



ГЕОГРАФИЧЕСКИЙ ФАКУЛЬТЕТ  
МГУ имени М.В. Ломоносова

# ХИМИЧЕСКИЙ СОСТАВ МИКРОЧАСТИЦ В ОКРУЖАЮЩЕЙ СРЕДЕ МОСКВЫ

2023



ГЕОГРАФИЧЕСКИЙ ФАКУЛЬТЕТ  
МГУ имени М.В. Ломоносова

# **Химический состав микрочастиц в окружающей среде Москвы**

2023



# **Chemical composition of microparticles in the environment of Moscow**

2023

УДК 550.42:504.054 (1-21)

ББК 26.82 (2-2М)

X 463

ISBN

## ХИМИЧЕСКИЙ СОСТАВ МИКРОЧАСТИЦ В ОКРУЖАЮЩЕЙ СРЕДЕ МОСКВЫ

Под редакцией

академика Н.С. Касимова, профессора Н.Е. Кошелевой

В сборнике представлены статьи, опубликованные коллективом авторов в ведущих российских и зарубежных журналах по проекту Российского научного фонда № 19-77-30004 (2019–2022): *Технология оценки экологического состояния мегаполиса на основе сопряженного анализа химического состава микрочастиц в системе «атмосфера–снег–дорожная пыль–почвы–поверхностные воды»*. Предложены новые теоретические, методические и прикладные подходы совершенствования междисциплинарной эколого-геохимической оценки городов, апробированные для Московского мегаполиса.

## CHEMICAL COMPOSITION OF MICROPARTICLES IN THE ENVIRONMENT OF MOSCOW

Editors

academician N.S. Kasimov, professor N.E. Kosheleva

The collection presents the articles published by a team of authors in leading Russian and foreign journals during the implementation of Russian Science Foundation project no.19-77-30004 (2019–2022): *Integrated technology for environment assessment of a megacity based on chemical analysis of microparticle composition in the «atmosphere–snow–road dust–soil–surface water» system*. New theoretical, methodological and applied approaches to improve multidisciplinary ecological and geochemical assessment of urban environment are proposed and tested for Moscow megacity.

© Московский государственный университет  
имени М.В. Ломоносова  
Географический факультет

© Коллектив авторов



# СОДЕРЖАНИЕ

## Введение

### 1. Общие вопросы экогеохимии городов

Кларки химических элементов как эталоны сравнения в экогеохимии.....	9
<i>Касимов Н.С., Власов Д.В.</i>	
Physicochemical properties of road dust in Moscow.....	16
<i>Kasimov N.S., Kosheleva N.E., Vlasov D.V., Nabelkina K.S., Ryzhov A.V.</i>	
Факторы накопления тяжелых металлов и металлоидов на геохимических барьерах в городских почвах.....	26
<i>Кошелева Н.Е., Касимов Н.С., Власов Д.В.</i>	
Supplement to Newly identified climatically and environmentally significant high latitude dust sources.....	39
<i>Meinander O. et al. (contribution from Aseyeva E.N., Kasimov N.S., Samonova O.A.)</i>	

### 2. Городские почвы

Contamination of urban soils with heavy metals in Moscow as affected by building development.....	43
<i>Kosheleva N. E. , Vlasov D. V. , Korlyakov I. D., Kasimov N. S.</i>	
Main features and contamination of sealed soils in the east of Moscow city.....	53
<i>Nikiforova E.M., Kasimov N.S., Kosheleva N.E., Timofeev I.V.</i>	
Уровни и факторы накопления металлов и металлоидов в придорожных почвах, дорожной пыли и их фракции PM <sub>10</sub> в Западном округе Москвы.....	61
<i>Власов Д. В., Кукушкина О. В., Кошелева Н. Е., Касимов Н. С.</i>	

### 3. Дорожная пыль

Enrichment of road dust particles and adjacent environments with metals and metalloids in Eastern Moscow.....	73
<i>Kasimov N. S., Vlasov D. V., Kosheleva N. E.</i>	
Spatial distribution and sources of potentially toxic elements in road dust and its PM <sub>10</sub> fraction of moscow megacity.....	84
<i>Vlasov D., Kosheleva N., Kasimov N.</i>	
Contamination levels and source apportionment of potentially toxic elements in size fractionated road dust of Moscow.....	97
<i>Vlasov D.V., Vasil'chuk J. Yu., Kosheleva N.E., Kasimov N.S.</i>	
Benzo[a]pyrene in Moscow road dust: pollution levels and health risks.....	113
<i>Kosheleva N.E., Vlasov D.V., Timofeev I.V. Samsonov T.E., Kasimov N.S.</i>	

### 4. Атмосферные осадки и снег

Partitioning and solubilities of metals and metalloids in spring rains in Moscow megacity.....	127
<i>Vlasov D. , Kasimov N. , Eremina I., Shinkareva G. , Chubarova N.</i>	
Daily variations in wet deposition and washout rates of potentially toxic elements in Moscow during spring season.....	140
<i>Vlasov D.V., Eremina I.D., Shinkareva G.L., Chubarova N.E., Kasimov N.S.</i>	

<b>Major ions and potentially toxic elements in atmospheric precipitation during the COVID-19 lockdown in Moscow megacity</b> .....	<b>152</b>
<i>Vlasov D., Kasimov N., Eremina I., Shinkareva G., Chubarova N.</i>	

<b>Dissolved and suspended forms of metals and metalloids in snow cover of megacity: partitioning and deposition rates in western Moscow</b> .....	<b>169</b>
<i>Vlasov D., Vasil'chuk J., Kosheleva N., Kasimov N.</i>	

## 5. Аэрозоли

<b>Impact of restrictive measures during the Covid-19 pandemic on aerosol pollution of the atmosphere of the Moscow megalopolis</b> .....	<b>186</b>
<i>Popovicheva O.B., Chichaeva M.A., Kasimov N.S.</i>	

<b>Seasonal, weekly, and diurnal black carbon in Moscow megacity background under impact of urban and regional sources</b> .....	<b>193</b>
<i>Popovicheva O., Chichaeva M., Kovach R., Zhdanova E., Kasimov N.</i>	

<b>Effects of braking conditions on nanoparticle emissions from passenger car friction brakes</b> .....	<b>206</b>
<i>Vojtíšek-Lom M., Vaculík M., Pechout M., Hopan F., Arul Raj A.F., Penumarti S., Horák J.S., Popovicheva O., Ondráček J., Doušová B.</i>	

<b>Black carbon in spring aerosols of Moscow urban background</b> .....	<b>216</b>
<i>Popovicheva O.B., Volpert E., Sitnikov N.M., Chichaeva M.A., Padoan S.</i>	

<b>Functional factors of biomass burning contribution to spring aerosol composition in a megacity: combined FTIR-PCA analyses</b> .....	<b>225</b>
<i>Popovicheva O., Ivanov A., Vojtisek M.</i>	

<b>Spring aerosol in urban atmosphere of megacity: analytical and statistical assessment for source impacts</b> .....	<b>237</b>
<i>Popovicheva O., Padoan S., Schnelle-Kreis J., Nguyen D.L., Adam T., Kistler M., Steinkogler T., Kasper-Giebl A., Zimmermann R., Chubarova N.</i>	

<b>Factors influencing aerosol and precipitation ion chemistry in urban background of Moscow megacity</b> .....	<b>248</b>
<i>Zappi A., Popovicheva O., Tositti L., Chichaeva M., Eremina I., Kasper-Giebl A., Tsai Y.I., Vlasov D., Kasimov N.</i>	

## 6. Речные воды

<b>Anthropogenic factors affecting the Moskva River water quality: levels and sources of nutrients and potentially toxic elements in Moscow metropolitan area</b> .....	<b>264</b>
<i>Shinkareva G., Erina O., Tereshina M., Sokolov D., Lychagin M., Kasimov N.</i>	

<b>Rainstorms impacts on water, sediment, and trace elements loads in an urbanized catchment within Moscow city: case study of summer 2020 and 2021</b> .....	<b>280</b>
<i>Chalov S., Platonov V., Erina O., Moreido V., Samokhin M., Sokolov D., Tereshina M., Yarinich Yu., Kasimov N.</i>	

\* \* \*

## Вместо заключения

<b>Загрязнение Московского мегаполиса: мониторинг химического состава микрочастиц в системе «атмосфера–снег–дорожная пыль–почвы–поверхностные воды»</b> .....	<b>294</b>
<i>Н.С. Касимов, Н.Е. Кошелева, О.Б. Поповичева, Д.В. Власов, Г.Л. Шинкарева, О.Н. Ерина, С.Р. Чалов, М.А. Чичаева, Р.Г. Ковач, Ю.А. Завгородняя, М.Ю. Лычагин</i>	

## ВВЕДЕНИЕ



Загрязнение компонентов окружающей среды (атмосферы, атмосферных осадков, снега, почв, дорожной пыли и поверхностных вод) признано одной из важных экологических проблем современности. Особенно остро она проявляется в крупнейших городах – мегаполисах, где проживают десятки миллионов человек, сосредоточены транспорт, промышленность, отходы хозяйственной деятельности, эмиссия которых приводит к формированию антропогенных аномалий различных поллютантов в городской среде, влияющих на здоровье населения. В последние десятилетия на территории многих городов, в том числе в России, выявлены высокие концентрации тяжелых металлов, полициклических ароматических углеводородов и других загрязнителей. В настоящее время значимой задачей является поиск и развитие методов интегральной оценки экологического состояния городов.

Среди них следует отметить четыре основные задачи исследований. Первая – развитие единого подхода к созданию технологий оценки территорий городов на основе сопряженного анализа уровней содержания, поведения и потоков поллютантов в системе «*атмосфера–снег–дорожная пыль–почвы–поверхностные воды*», который должен ассимилировать различные методики оценки загрязнения отдельных сред. Вторая – поиск объектов и показателей (индикаторов, маркеров), наиболее адекватно отражающих реальное загрязнение окружающей среды. Во многих, в том числе наших, работах показано, что основное загрязнение во всех компонентах среды сосредоточено в микрочастицах размером менее 10 микрон (PM<sub>10</sub>). Оно достаточно хорошо изучено в аэрозолях, которые сами являются микро- и наночастицами. Другие компоненты городской среды в этом отношении изучены существенно слабее, особенно в контексте влияния их химического состава на здоровье населения. Третья – идентификация конкретных источников загрязнения компонентов городской среды с количественной оценкой их вклада в общее загрязнение на основе статистических моделей технологии Source Apportionment, широко применяемой во всем мире, но меньше известной в России. И, наконец, четвертая задача – разработка подходов и методов оценки влияния различных загрязнителей, особенно в микрочастицах, на экологические риски заболеваемости населения.

Все эти задачи решались на примере Москвы – крупнейшего мегаполиса Европы, где проживает более 12 млн человек. В настоящем издании приводятся результаты междисциплинарных исследований коллектива сотрудников географического факультета (кафедры геохимии ландшафтов и географии почв, гидрологии суши, метеорологии и климатологии, картографии и геоинформатики, экономической и социальной географии России, лаборатории эрозии почв и русловых процессов), НИИ ядерной физики и факультета почвоведения

МГУ имени М.В.Ломоносова совместно с нашими партнерами из различных организаций. Исследования выполнены в 2019–2022 гг. по мероприятию «Проведение исследований научными лабораториями мирового уровня в рамках реализации приоритетов научно-технологического развития Российской Федерации» Президентской программы исследовательских проектов, реализуемых ведущими учеными. Работы велись по проекту Российского научного фонда № 19-77-30004 «Технология оценки экологического состояния Московского мегаполиса на основе анализа химического состава микрочастиц в системе «атмосфера–снег–дорожная пыль–почвы–поверхностные воды» (Мегаполис)», руководитель проф. Н.Е. Кошелева.

Основная часть работ по проекту выполнялась на кафедре геохимии ландшафтов и географии почв географического факультета МГУ, заведующий кафедрой академик Н.С. Касимов. Коллективом кафедры получен ряд значимых теоретических, методических и практических результатов в исследованиях антропогенных изменений ландшафтно-геохимических и почвенных систем в городах России, а также Польши (Иновроцлав), Кубы (Моа), Монголии (Улан-Батор, Дархан, Эрдэнэт), Эквадора (Кито).

Мы предлагаем читателю электронный дайджест, состоящий из 25 статей, опубликованных участниками проекта РФФИ в ведущих зарубежных и российских журналах. Материалы сгруппированы в шесть разделов. В первом рассмотрены общие методические и теоретические вопросы экогеохимии городов, включая оценку кларковых значений химических элементов, их фоновых уровней и механизмов формирования геохимических барьеров в городских почвах и других средах в зависимости от их физико-химических свойств и других природных и антропогенных факторов. Во втором разделе приводятся результаты исследования загрязнения почв и содержащихся в них микрочастиц PM<sub>10</sub> тяжелыми металлами и металлоидами в Восточном и Западном округах Москвы в связи с воздействием городской застройки, запечатыванием дорожными покрытиями и осаждением дорожной пыли. Третий раздел посвящен сравнительному анализу химического состава дорожной пыли в разных округах Москвы и количественной оценке вклада антропогенных источников в ее загрязнение потенциально токсичными элементами и ПАУ.

В четвертом разделе приводятся результаты исследований выпадения загрязняющих веществ из атмосферы в виде жидких и твердых (снега) осадков, их свойств и вымывающей способности по отношению к атмосфере. Пятый раздел содержит результаты измерительных компаний параметров городской атмосферы на Аэрозольном комплексе в Метеообсерватории МГУ, включая межгодовую, сезонную и суточную динамику содержания аэрозолей, черного углерода, основных ионов, микроэлементов и ПАУ с определением их источников. В шестом разделе представлены результаты эколого-геохимического мониторинга в бассейне реки Москвы, связанные с сезонной динамикой и распределением по длине реки биогенных и потенциально токсичных элементов в растворенной и взвешенной формах, поступающих из различных техногенных источников. Заключительный раздел посвящен разработке и апробации подходов к сопряженному анализу химического состава микрочастиц в транзитных (атмосферные аэрозоли и осадки, речные воды и взвесь) и депонирующих (дорожная пыль, снежный покров, почвы, донные отложения) средах.

Для сокращения объема дайджеста приводятся только тексты статей, без списков литературы и приложений, которые можно найти по ссылке на оригинальную публикацию каждой статьи.

*академик Н.С.Касимов  
профессор Н.Е.Кошелева*



# 1. ОБЩИЕ ВОПРОСЫ ЭКОГЕОХИМИИ ГОРОДОВ

## Кларки химических элементов как эталоны сравнения в экогеохимии \*

### ВВЕДЕНИЕ

А.Е. Ферсман в 1923 г. предложил среднее содержание химического элемента в земной коре или какой-либо ее части называть «кларком» в честь американского химика Ф. Кларка, посвятившего более 40 лет решению данной проблемы.

Кларки химических элементов в континентальной земной коре широко используются в качестве эталона сравнения различных геохимических систем, для оценки степени концентрации вовлекаемых в процесс техногенеза химических элементов, выявления региональной геохимической специализации фоновых ландшафтов и техногенной геохимической трансформации химического состава природных сред. Так, сравнение концентраций многих тяжелых металлов и металлоидов в почвах сельскохозяйственных угодий Европы с их кларками по [17, 20] показало, что относительно земной коры в агропочвах Европы накапливаются С, Se, S, Cd, околоскларковые значения характерны для Pb, As, P, Cs, Ti, Cr, Zn, Mn, La, Te, Bi, Ag, Mo, и существенно ниже кларков – V, Fe, Au, Ba, Co, Hg, Ni, Cu, Sn, Sr, Sb, U, Be, Tl, W, B, Ge [13].

Как известно, континентальная кора обычно подразделяется на три части: верхнюю (осадочный и гранитно-метаморфический слои), среднюю и нижнюю, по которым рассчитывается средний химический состав каждой из них, то есть выделяются кларки верхней, средней и нижней части коры, а также кларки континентальной коры в целом [24]. При этом только верхняя часть коры является резервуаром природных ресурсов, используемых человечеством, и главным источником большинства химических элементов, вовлеченных в техногенез [26].

Почвы и наземные ландшафты формируются на поверхности земной коры, что определяет целесообразность использования в качестве эталонов при эколого-геохимических исследованиях кларков ее верхней части, для расчета которых используются средневзвешенные величины химического состава магматических горных пород [5, 11, 14, 15, 22], или средний состав мелкозернистых обломочных осадочных пород, ледниковых отложений или ледниковых лессов в соответствии с концепцией геохимического баланса осадкообразования, согласно которой средний состав вторичных осадочных пород тождественен среднему составу первичных магматических пород [3, 16, 23, 27].

А.Е. Ферсман считал, что кларки представляют собой «новую константу мира». Однако исследования прошедшего полувека показали, что оценки кларков

различных авторов для многих элементов достаточно сильно отличаются. Так, по [3] кларки Mn, Cr, Ni и Cu в 2–5 раз больше, а S, I, Cl, N, Bi и C – в 2–16 раз меньше, чем по [27]. В свою очередь, кларки [5] по S в 23, Вг и Cd в 7, Cl в 4, Au в 3, В, Са, Ag, Sn, Sb, Bi в 1,5–2 раза больше, а I в 3 раза меньше, чем данные [20]. Основной причиной различий между оценками является применение авторами различных моделей соотношения главных типов (в основном, магматических – ультраосновные, основные, средние, кислые) горных пород в континентальной земной коре. Например, А.П. Виноградов [3] принял соотношение гранитов и базальтов 2:1, а S.R. Taylor, S.M. McLennan – 1:1 [11]. Различия современных оценок также определяются соотношением главных групп горных пород и их химическим составом: в осадочном слое – песков, песчаников, глин, эвапоритов и др.; в гранитно-гнейсовом слое – гранитов, гранодиоритов, базитов, сиенитов и др. [5]. Таким образом, развитие представлений о распространенности различных типов и групп горных пород, совершенствование аналитических методов ведут к уточнению кларков химических элементов, то есть «кларк» – это скорее набор условных констант, применяемых на определенном этапе развития науки, что необходимо учитывать при их использовании в качестве фоновых эталонов, в том числе в экогеохимии и геохимии ландшафтов.

### МАТЕРИАЛЫ И МЕТОДЫ

В качестве информационной базы использовались опубликованные данные о кларках химических элементов в верхней части земной коры, [2, 3, 5, 15, 17, 20, 22, 23, 27] (табл. 1). Из-за ограниченного перечня химических элементов не учитывались кларки земной коры и ее верхней части по [6, 9, 11, 19, 21, 25]. Анализировались в основном элементы 1, 2 и 3 классов опасности для окружающей среды.

### РЕЗУЛЬТАТЫ И ИХ ОБСУЖДЕНИЕ

#### Эталонные сравнения в экогеохимии

В экогеохимии для оценки экологической опасности загрязнения компонентов ландшафтов используют три основных «эталона» сравнения: гигиенические нормативы (предельно допустимые концентрации – ПДК, ориентировочно допустимые концентрации – ОДК), фоновые геохимические уровни и кларки химических элементов. Каждый из этих эталонов имеет свои достоинства и недостатки.

\* Касимов Н.С., Власов Д.В. // Вестник Московского университета. Серия 5: География. 2015;(2): 7–17.  
SJR 0.29

Таблица 1. Кларки химических элементов в верхней части континентальной земной коры, мг/кг

№	Элемент	А.П. Виноградов [1962]	А.А.Беус и др. [1976]	D.M.Shaw et al. [1976]	S.R.Taylor, S.M.McLennan [1985]	K.H.Wedepohl [1995]	S.Gao et al. [1998]	R.L.Rudnick, S. Gao [2003]	Z.Hu, S.Gao [2008]	Н.А.Григорьев [2009]
1	H	—	1000	—	—	—	—	—	—	1670
4	Be	3,8	2,5	1,3	3	3,1	1,95	2,1	1,9	2,3
5	B	12	10	9,2	15	17	28	17	47	34
6	C	230	300	—	—	3240	—	—	—	8100
7	N	19	26	—	—	83	—	83	—	106
9	F	660	720	500	—	611	561	557	—	510
11	Na	25 000	22 000	25 700	28 900	25 670	21 220	24 260	—	20 700
12	Mg	18700	12 000	13 500	13 300	13 510	15 800	14 950	—	17 700
13	Al	80500	80 000	77 400	80 400	77 440	74 990	81 500	—	76 100
15	P	930	800	655	—	665	698	655	—	690
16	S	470	400	600	—	953	309	62	—	1400
17	Cl	170	170	100	—	640	142	370	—	1500
19	K	25 000	27 000	25 700	28 000	28 650	22 250	23 240	—	22 300
20	Ca	29 600	25 000	29 500	30 000	29 450	24 600	25 660	—	38 900
22	Ti	4500	3300	3120	3000	3117	4010	3840	—	3900
23	V	90	76	53	60	53	98	97	106	121
24	Cr	83	34	35	35	35	80	92	73	92
25	Mn	1000	700	527	600	527	774	774	—	770
26	Fe	46 500	36 000	30 900	35 000	30 890	41 430	39 180	—	40 600
27	Co	18	7,3	12	10	11,6	17	17,3	15	17
28	Ni	58	26	19	20	18,6	38	47	34	50
29	Cu	47	22	14	25	14,3	32	28	27	39
30	Zn	83	51	52	71	52	70	67	75	75
32	Ge	1,4	1,3	—	1,6	1,4	1,34	1,4	1,3	1,3
33	As	1,7	1,9	—	1,5	2	4,4	4,8	5,7	5,6
35	Br	2,1	2,2	—	—	1,6	—	1,6	—	11
38	Sr	340	230	316	350	316	266	320	—	270
42	Mo	1,1	1,3	—	1,5	1,4	0,78	1,1	0,6	1,56
46	Pd	—	0,0001	—	0,0005	—	0,00146	0,00052	—	—
47	Ag	0,07	0,048	—	0,05	0,055	0,055	0,053	—	0,11
48	Cd	0,13	0,16	0,075	0,098	0,102	0,079	0,09	0,06	0,64
50	Sn	2,5	2,7	—	5,5	2,5	1,73	2,1	2,2	3,5
51	Sb	0,5	0,2	—	0,2	0,31	0,3	0,4	0,75	0,81
52	Te	0,001	0,001	—	—	—	—	—	0,027	—
53	I	0,4	0,5	—	—	1,4	—	1,4	—	0,49
55	Cs	3,7	3,8	—	3,7	5,8	3,55	4,9	4,9	5,5
56	Ba	650	680	1070	550	668	678	628	—	510
57	La	29	46	32,3	30	32,3	34,8	31	—	32
74	W	1,3	1,9	—	2	1,4	0,91	1,9	1,4	2,03
79	Au	0,0043	0,0012	0,00181	0,0018	—	0,00124	0,0015	—	0,00436
80	Hg	0,083	0,033	0,096	—	0,056	0,0123	0,05	—	0,065
81	Tl	1	1,8	0,524	0,75	0,75	1,55	0,9	0,55	—
82	Pb	16	16	17	20	17	18	17	—	17
83	Bi	0,009	0,01	0,035	0,127	0,123	0,23	0,16	0,23	0,29

Примечание. N — порядковый номер элемента в периодической таблице химических элементов Д.И. Менделеева.

ПДК и ОДК разработаны для узкого набора элементов и лишь для некоторых компонентов ландшафтов (почвы, воды, атмосферный воздух). При сравнении гигиенических нормативов и кларков становится понятно, что ПДК и ОДК некоторых элементов имеют околосларковые значения или даже ниже кларка. Так, ОДК Cd в песчаных почвах составляет 0,5 мг/кг, а его

кларк в верхней части земной коры — 0,64 мг/кг по [5], то есть различия не существенны. Незначительно ниже кларка ОДК Zn и Cu в песчаных почвах, а ОДК As и Ni в песчаных и кислых суглинистых почвах в 1,5-2 раза меньше, чем их кларки [5, 15, 17, 20], что снижает приемлемость и без того узкого перечня разработанных и утвержденных экологических нормативов.



Шире распространены оценки загрязнения с использованием фоновых уровней поллютантов, учитывающих региональные геохимические особенности территорий. Однако в ряде случаев оценка геохимического фона затруднена или невозможна. Например, поверхностные отложения транспортных дорог, часто именуемые «дорожной пылью», представляют собой специфический техногенный объект, фонового аналога которого не существует. Это также актуально для других техногенных объектов (угольные отвалы, хвостохранилища, осадки сточных вод и т.д.), для которых использование фоновых величин элементов в природных почвах, водах или донных отложениях достаточно условно. При эколого-геохимических оценках территорий со сложным геологическим строением и контрастным химическим составом пород (например, крупных речных бассейнов) необходим расчет геохимического фона для каждого типа пород, что не всегда возможно и целесообразно. При эколого-геохимических оценках городских почв их загрязнение часто оценивается относительно фоновых аналогов, в то время как рыхлые субстраты в городах не всегда можно определить в качестве почв с традиционных почвенно-генетических позиций [4], поэтому сравнение их с фоновыми зональными почвами также весьма условно.

При невозможности применения гигиенических нормативов или геохимического фона в качестве эталона часто используются кларки химических элементов. Однако они также имеют ряд недостатков, среди которых основной – большие различия оценок разных исследователей (рис. 1). Использование разных величин кларков одних и тех же элементов создает проблему сравнения полученных выводов о геохимической специализации компонентов ландшафтов, а также контрастности и распространенности геохимических аномалий элементов. Все это вызывает необходимость детального исследования оценок

среднего химического состава верхней части континентальной земной коры.

В СССР и России для научных и практических целей часто применялись кларки верхней части земной коры А.П. Виноградова [3], за рубежом более популярны оценки К.Н. Wedepohl [27], S.R. Taylor, S.M. McLennan [23] и др. И хотя считается, что корректировка предложенных А.П. Виноградовым кларков химических элементов не способна существенно повлиять на основополагающие выводы геохимии (проблема минеральных природных ресурсов, в основном – редких элементов; установление геохимического фона биосферы и выявление ее геохимической неоднородности и др.) [11], вопросу использования заниженных или завышенных значений кларков в экогеохимии не уделялось должного внимания [7, 18].

Так, при расчете кларков концентрации или рассеяния химических элементов с использованием низких относительно данных других исследователей кларков могут быть выявлены «ложные» геохимические аномалии элементов или сильно завышены их площади. При высоких значениях кларков элементов в верхней части земной коры относительно данных других авторов контрастность и площади аномалий могут быть сильно занижены. С другой стороны, химический состав земной коры пространственно неоднороден в связи с ее геодинамической и возрастной гетерогенностью, что создает определенную проблему количественной оценки различий [11].

В качестве примера приведем расчеты кларков концентраций КК и рассеяния КР<sup>1</sup> химических элементов в городских придорожных почвах южной части Восточного округа г. Москвы (ВАО). В почвах газонов ведущим фактором почвообразования является антропогенный, поскольку они созданы и их свойства поддерживаются человеческой дея-

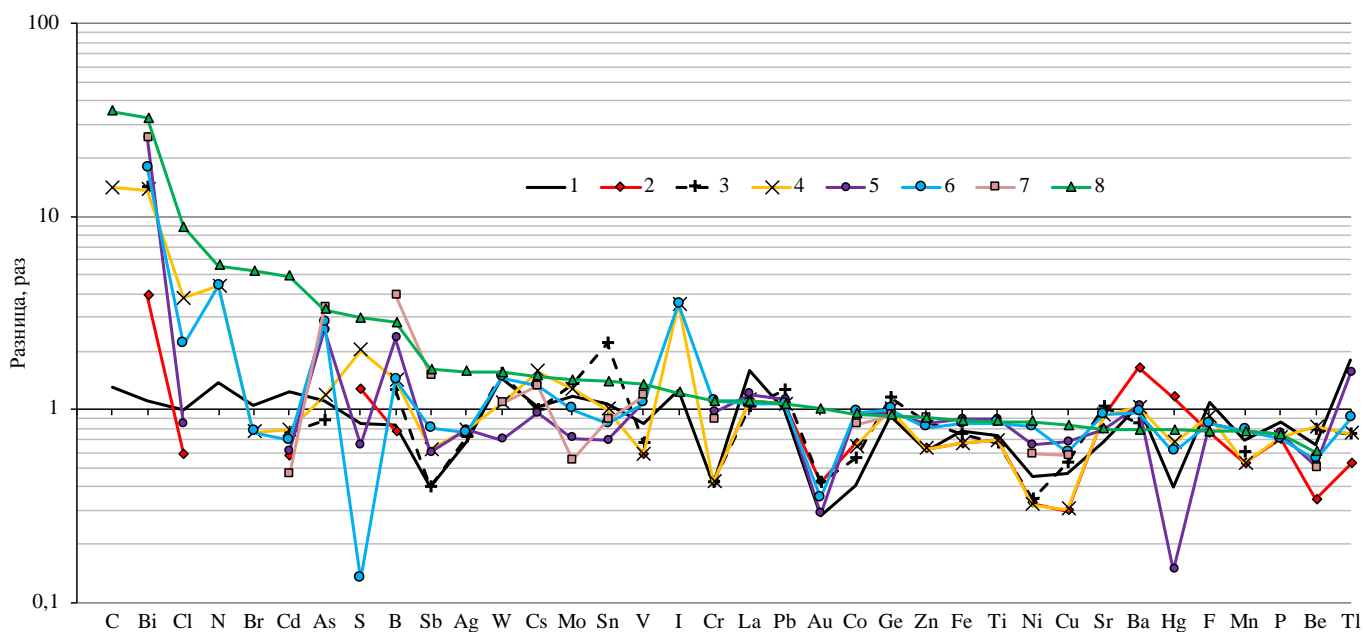


**Рис. 1.** Кларки химических элементов в верхней части континентальной земной коры. За 1 приняты кларки А.П. Виноградова [3]. Цифрами обозначены кларки: 1 – [2], 2 – [22], 3 – [23], 4 – [27], 5 – [15], 6 – [20], 7 – [17], 8 – [5]

<sup>1</sup> Кларки концентрации КК =  $C/K$  и рассеяния КР =  $K/C$ , где  $C$  – содержание элемента в почвах, мг/кг;  $K$  – кларк элемента в верхней части континентальной земной коры, мг/кг.

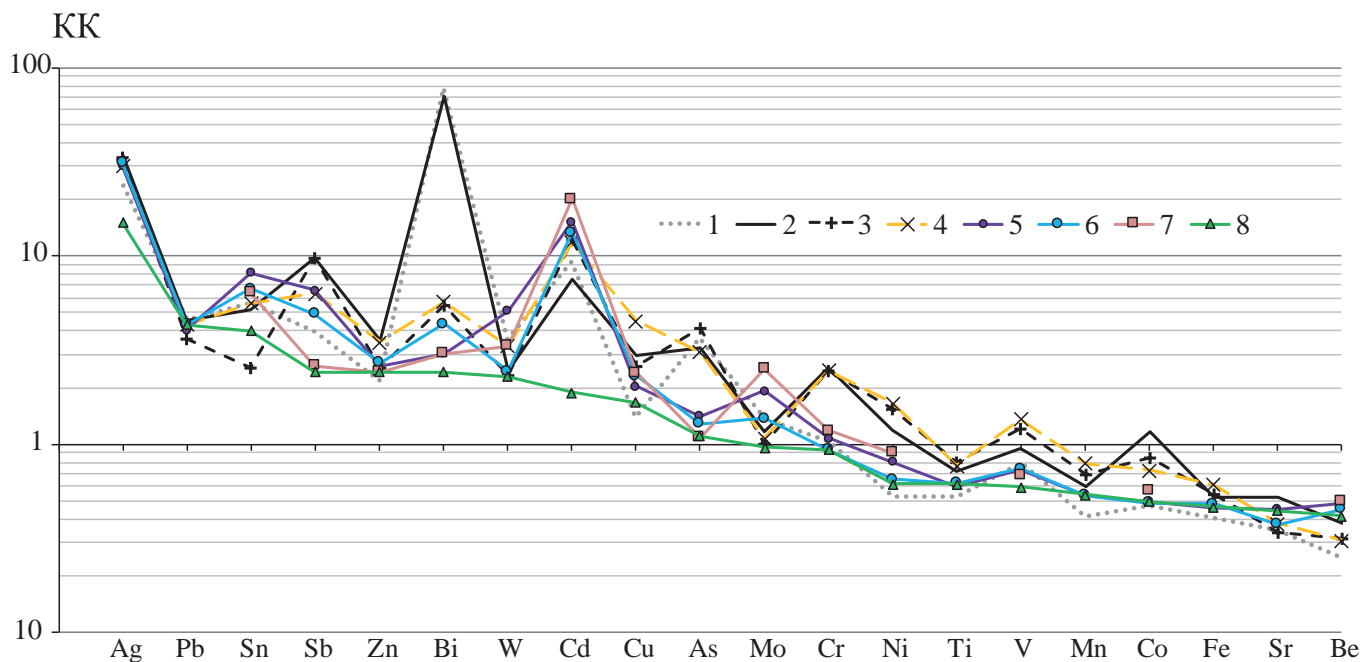


**Рис. 2.** Кларки концентрации КК и рассеяния КР элементов в придорожных почвах Восточного округа г. Москвы. Цифры – показатели, рассчитанные относительно оценок: 1 – [3], 2 – [2], 3 – [23], 4 – [27], 5 – [15], 6 – [20], 7 – [17], 8 – [5]

тельностью. Они также подвержены сильному техногенному воздействию транспорта. И хотя часто при разбивке придорожных газонов применяются торфо-компостные смеси, природные составляющие которых изымаются из фоновых ландшафтов, сравнение придорожных почв с зональными дерново-подзолистыми почвами не совсем корректно. Поэтому в качестве эталона нами использовались кларки верхней части континентальной земной коры (рис. 2).

В придорожных почвах ВАО при применении кларков по [2, 3] выявляются очень контрастные аномалии Bi, в то время как при расчете КК по другим оценкам Bi накапливается слабо. Cd по [5] имеет околочларковые концентрации, а по [2, 3, 15, 17, 20, 23, 27] характеризуется сильным накоплением (КК 7,5-20). По [5, 15, 17, 20] As образует не-контрастные аномалии, в то время как по другим оценкам он накапливается интенсивнее. По кларкам отдельных авторов Mo, Cr, Ni, Co и V слабо накапливаются, а по другим – рассеиваются. Большие разбросы значений КК и КР установлены у Sn, Sb, W.

Карты распределения КК Cd в поверхностном горизонте почв южной части ВАО показывают значительные различия в распространенности и контрастности геохимических аномалий металла (рис. 3). Наименьшие площади имеют аномалии Cd при использовании кларка по [5], а наиболее контрастные с максимальным распространением их центров – по [15]. При кларке Cd по [3] получаем промежуточную оценку степени загрязнения территории (рис. 3б). Этот пример иллюстрирует неоднозначность оценок экологического состояния среды при использовании кларков различных авторов. Такие сильные различия аномальности характерны и для многих других элементов.

### Оценка различий кларков элементов

Неоднородность геохимических систем оценивают с помощью показателя *абсолютного разброса*, как отношения максимального фонового содержания элемента в одной составной части геохимической системы к минимальному фоновому содержанию этого же элемента в другой составной части этой же системы; для земной коры такими частями являются разные типы горных пород [1]. При анализе различий между кларками в верхней части земной коры предлагается использовать *показатель геохимического диапазона кларков элементов* (ГД), равный отношению максимального и минимального значения содержания *i*-го элемента:  $ГД = C_{i\max} / C_{i\min}$ .

По величине ГД химические элементы разделены на четыре группы (табл. 2, рис. 4), которые по степени экологической опасности и экогеохимической изученности далее подразделялись на подгруппы: 1, 2, 3 и без классов опасности в почвах.

*Элементы с очень малым ГД* ( $\leq 1,5$ ) – кларки верхней части земной коры у разных исследователей практически не отличаются: F, Pb, Al, K, Na, P, Ti, Ge. Для этих элементов незначительная разница в кларках позволяет в качестве эталонов сравнения использовать любые оценки.

*Элементы с малым ГД* (1,5–2,5). В эту группу входят элементы, у которых кларки верхней части земной коры незначительно отличаются у разных исследователей, делящиеся на четыре подгруппы (здесь и далее индекс–величина ГД, подгруппы приведены через запятую): Zn<sub>1,6</sub>; Co<sub>2,5</sub>; V<sub>2,3</sub>W<sub>2,2</sub>Ba<sub>2,1</sub>Mn<sub>1,9</sub>Sr<sub>1,5</sub>; Ag<sub>2,3</sub>H<sub>1,7</sub>Cs,La,Ca,Mg<sub>1,6</sub>Fe<sub>1,5</sub>.

Из этой группы элементов наиболее экологически опасен Zn, хотя явно выделить экстремальные оценки его кларков трудно из-за небольшой разницы значений разных авторов. Однако в целом кларк

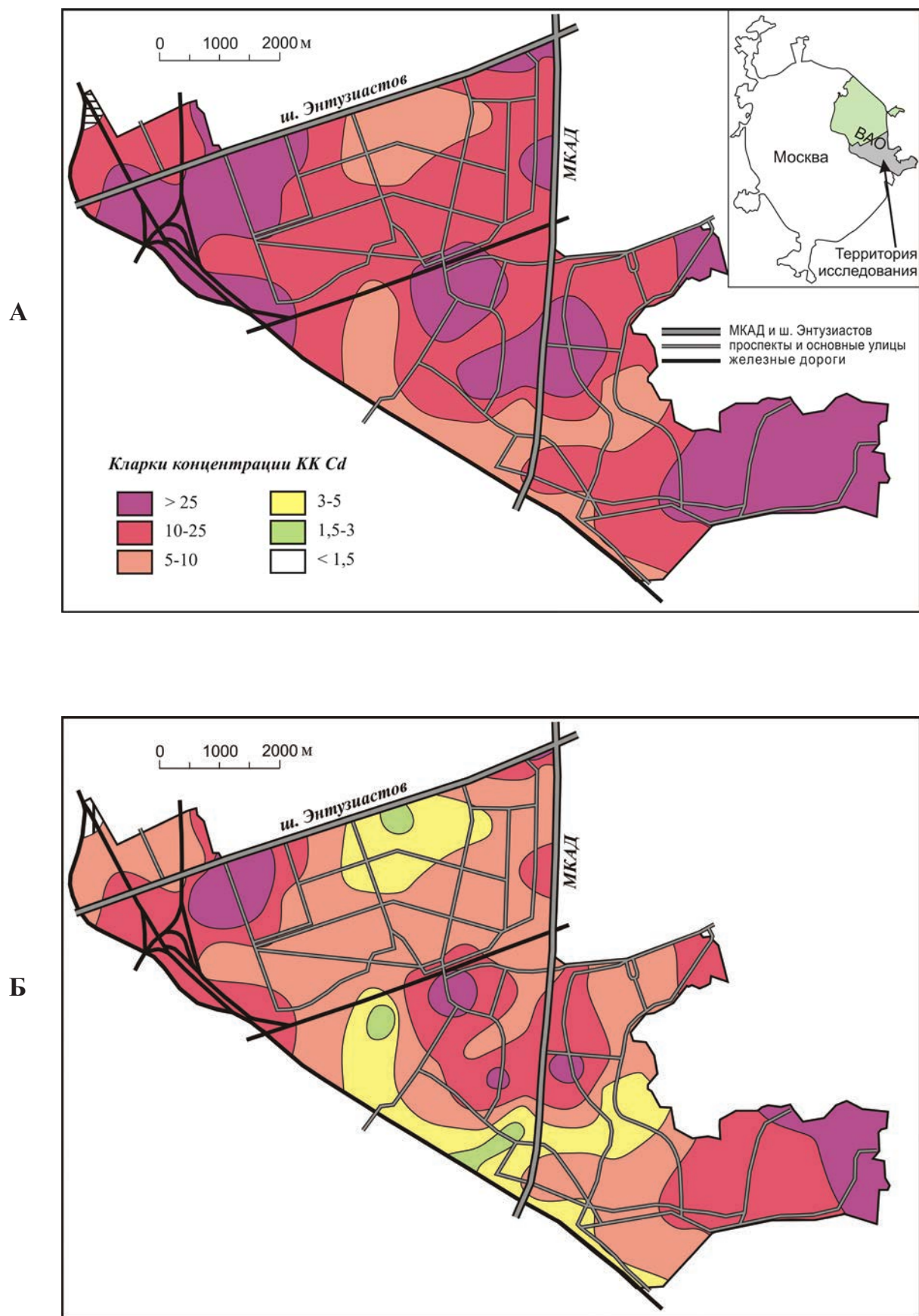


**Рис. 3.** Кларки концентрации Cd в поверхностном горизонте почв. От кларков зависит оценка степени загрязнения территории ВАО кадмием: а – сильное загрязнение по [17]; б – среднее загрязнение по [3]; в – слабое загрязнение по [5]





Таблица 2. Группирование элементов

Группы элементов (величина ГД)	Подгруппы элементов			
	Классы опасности в почвах			Прочие
	1	2	3	
> 5,0	Cd, Hg	B	–	Bi, Br, C, Cl, N, Pd, S, Te
2,5–5,0	As	Cr, Cu, Mo, Ni, Sb	–	Au, Be, I, Sn, Tl
1,5–2,5	Zn	Co	Ba, Mn, Sr, V, W	Ag, Ca, Cs, Fe, H, La, Mg
≤ 1,5	F, Pb	–	–	Al, Ge, K, Na, P, Ti

Примечание. Классы опасности элементов в почвах населенных мест по [10]

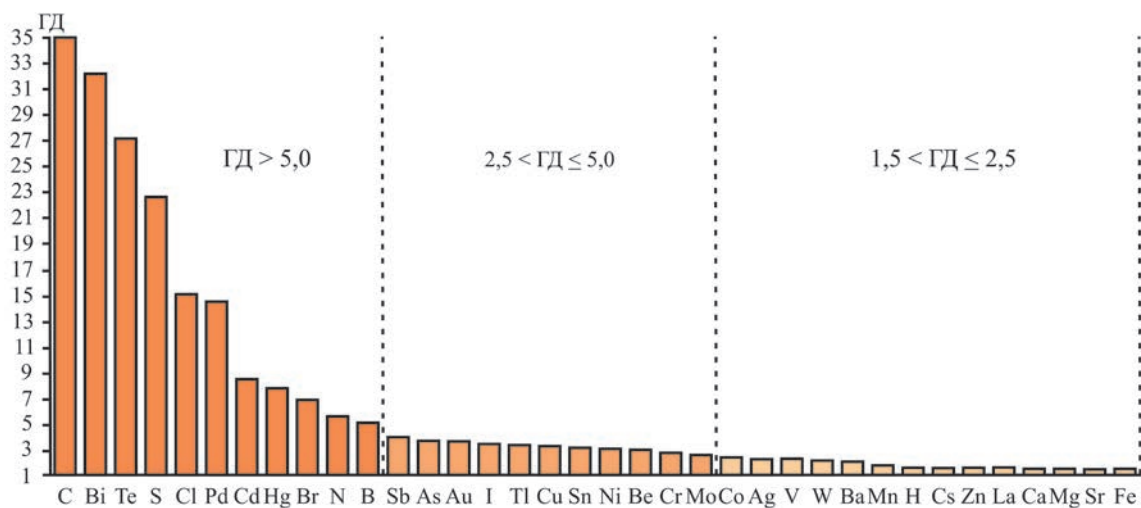


Рис. 4. Геохимический диапазон (ГД) кларков химических элементов в верхней части континентальной земной коры [2, 3, 5, 15, 17, 30, 20, 22, 23, 27]. Показаны элементы с ГД > 1,5

Zn по [3, 5, 15, 20] выше, чем по [2, 22, 27]. Для Co оценка по [2] меньше в 1,6-2,5 раза, чем другие оценки. Среди элементов третьей и четвертой подгрупп в первую очередь выделяется Mg, кларки которого по [2] отличаются от оценок других авторов в 1,1-1,6 раза в большую или меньшую стороны. Аналогичная ситуация характерна для Mn и Fe, для которых максимальные оценки у Виноградова [3], для W – минимальный кларк рассчитан Gao et al. [15], для Ba с максимальной оценкой у Shaw et al. [22], Ag и Ca – у Григорьева [5].

*Элементы со средним ГД (2,5–5,0)* с заметной разницей величин кларков верхней части земной коры у разных исследователей, которые также делятся на три подгруппы: As<sub>3,8</sub>; Sb<sub>4,0</sub>Cu<sub>3,4</sub>Ni<sub>3,1</sub>Cr<sub>2,7</sub>; Au<sub>3,6</sub>I<sub>3,5</sub>Tl<sub>3,4</sub>Sn<sub>3,2</sub>Be<sub>2,9</sub>.

Наиболее опасным для окружающей среды с высоким диапазоном кларков (3,8) является As. С течением времени каждая последующая оценка кларка As была выше предыдущей за исключением минимальной по [23], что необходимо учитывать при анализе региональных геохимических особенностей фоновых территорий, так как использование ранних (относительно низких) кларков приводит к переоценке вклада As в геохимическую специализацию района и искусственно увеличивает контрастность и опасность выявляемых аномалий элемента.

Так, в фоновых почвах монгольской части бассейна р. Селенги среднее содержание As составляет 8,6, в донных отложениях – 8,5, в речной взвеси – 40, в пылевой составляющей снежного покрова – 24 мг/кг [8, 12]. При использовании кларков Виноградова (1,7 мг/кг), Беуса (1,9), Taylor, McLennan (1,5) и Wedepohl (2) выявлено очень сильное концентрирование As во всех компонентах ландшафтов, а при расчете относительно Gao et al. (4,4 мг/кг) Rudnick, Gao (4,8), Hu, Gao (5,7) и Григорьева (5,6) сильное накопление характерно только для речной взвеси и пылевой составляющей снега.

Среди элементов второго класса опасности кларк Sb, по Григорьеву, в 1,6-4,0 раза выше, чем у других исследователей. Кларк Cu по Shaw et al. и Wedepohl в 1,6-3,4 раза меньше, чем по другим оценкам. У Mo очень низкий кларк по [15, 17], и ГД металла составляет 2,6. Отдельно выделяются Cr и Ni, объединяемые общей особенностью – их кларки по Виноградову и в наиболее поздних работах [5, 15, 17, 20] в несколько раз превышают оценки по [2, 22, 23, 27]. В третьей подгруппе кларк Au по Григорьеву в 2,4-3,6 раза выше, чем у других исследователей. Явно занижены кларки Sn по Gao et al. [15] и Be по Shaw et al. [22], которых в 1,2-3,2 и 1,5-2,9 раза меньше, чем по другим оценкам.

*Элементы с большим ГД (> 5,0).* В эту группу входят элементы с самой значительной разницей кларков верхней части земной коры разных исследователей. В ней выделяются три подгруппы: Cd<sub>8,5</sub>Hg<sub>7,8</sub>; V<sub>5,1</sub>; C<sub>35</sub>Bi<sub>32</sub>Te<sub>27</sub>S<sub>23</sub>Cl, Pd<sub>15</sub>Br<sub>6,9</sub>N<sub>5,6</sub>.

Cd и Hg являются наиболее опасными загрязнителями окружающей среды. При анализе их кларков видно, что оценка Hg по Gao et al. [15] и Cd по Григорьеву [5] сильно отличается от остальных. При игнорировании этих экстремальных значений ГД снижается до 1,5-2. Бор – элемент второго класса опасности, его кларк по [17] значительно отличается от оценок других авторов.

Для элементов третьей подгруппы оценка одного или нескольких исследователей сильно отличается от всех остальных оценок, в результате чего у этих элементов сильно возрастает величина ГД. Так, по [2] кларк Pd в 5-15 раз ниже, чем оценки других авторов. Кларки S и Cl [5] заметно выше кларков других исследователей (в 1,5-23 раза для S и в 2,3-11 раз для Cl). Для S наибольшая разница в оценках характерна для двух наиболее поздних работ [5, 20]. У Bi, C и N кларки Виноградова и Беуса значительно меньше других исследователей в 3,5-32, 11-35 и 3,2-5,6 раза соответственно. Эти сравнения можно продолжить.

Таким образом, кларки химических элементов в верхней части континентальной земной коры Виноградова [3], Беуса и соавт. [2], Shaw et al. [22] и Taylor, McLennan [23] значительно отличаются от современных оценок. Особо стоит отметить очень широкое применение кларков Виноградова в эколого-геохимических исследованиях российских ученых. При использовании кларков верхней части континентальной коры необходимо учитывать различные оценки для одних и тех же химических элементов, что особенно актуально для элементов с большой разницей в оценках кларков и наиболее опасных поллютантов: Cd, Hg, B, As, Cr, Cu, Mo, Ni, Sb, Bi, Br, C, Cl, Pd, S, Te, Zn, Co, Ba, Mn, Sr, V, W.

При эколого-геохимических исследованиях ландшафтов в качестве эталонов сравнения целесообразно использовать любую из существующих оценок кларков элементов с очень малыми геохимическими диапазонами – F, Pb, Al, K, Na, P, Ti, Ge [2, 3, 5, 15, 17, 20, 22, 23, 27]; для Zn, Co, V, W, Mn, Sr, H, Cs, La и Fe – любую из современных оценок [5, 17, 20], а Ba, Ag, Ca и Mg из-за сильного отличия оценок Григорьева от остальных – кларки по [20]. Для элементов со средними и высокими геохимическими диапазонами стоит уделять повышенное внимание к выбору эталонов сравнения (табл. 2). Так, в качестве кларков Cl, Br, C, N, S, Tl и Sn целесообразно применять оценки [27], Cd, Pd, Mo и Au – [20], Te, Bi и Cu – [17], B, Hg, Ni, Cr, As, Sb, I и Be – [5]. Близость к среднему между различными оценками кларков и современность этих оценок – ключевые условия выбора рекомендуемых эталонов сравнения в экогеохимии.

## ВЫВОДЫ

1. В экологической геохимии и геохимии ландшафтов в качестве эталонов сравнения широко используются кларки химических элементов, сильно различающиеся между оценками разных авторов, то есть кларки представляет собой набор условных констант, применяемых на определенном этапе развития науки.

2. Количественной мерой различий оценок предлагается считать геохимический диапазон химических элементов (ГД) – отношение между максимальным и минимальным значением кларка одного и того же элемента. По величине ГД химические элементы делятся на четыре группы: с большим (> 5,0), средним (2,5–5,0), малым (1,5–2,5) и очень малым диапазоном (< 1,5). Каждая группа в зависимости от экологической опасности и геохимической изученности элементов разделена на несколько подгрупп.

3. В качестве кларков отдельных элементов целесообразно применять оценки К.Н. Wedepohl, R.L. Rudnick, S. Gao, Z. Hu или Н.А. Григорьева.

## Physicochemical properties of road dust in Moscow \*

### INTRODUCTION

Road dust is a multicomponent substance formed as a result of washing out and deflation of roadside soils, wear of different components of transport infrastructure and vehicles, crushing of solid waste and residues of deicing agents (DIAs), and atmospheric precipitation of particulate matter (Ladonin and Plyaskina 2009; Nazzal et al. 2013; Prokofieva et al. 2015). Road dust originates from various sources and indicates pollution level of urban landscapes, since its particles are the carriers for many pollutants, including heavy metals and metalloids (HMMs). In turn, road dust itself may be a source of secondary pollution of the atmosphere and roadside soils. Road dust is lifted into the air by traffic and it is one of the six most important sources of suspended particulate matter (PM) in urban atmosphere (Belis et al. 2013; National Emissions Inventory 2017).

In the major cities of the world, road dust is increasingly being considered as an object of environmental and geochemical monitoring (Vlasov et al. 2015; Demetriades and Birke 2015; Jayarathne et al. 2017; Yang et al. 2017). Extensive literature is devoted to elemental composition of road dust; however, the physicochemical properties inherited from its different components have been studied to a much lesser extent, although they are the ones that determine the potential of the dust to fix pollutants. Usually, such parameters as pH, organic carbon content ( $C_{org}$ ), electrical conductivity (EC), and particle size distribution are evaluated (Wang and Qin, 2007; Al-Khashman 2007; Hu et al. 2011; Acosta et al. 2011). The studies of atmospheric dust focus on particles with an aerodynamic diameter of 10  $\mu\text{m}$  or smaller ( $\text{PM}_{10}$ ). This PM fraction is the most important indicator of air quality in many cities around the world, since it can penetrate the human respiratory tract, cause asthma in children and increase the risk of mortality from diseases of the cardiovascular system (Tager 2005; Fonova 2017; Report... 2017). The same particle size fraction is also important when studying road dust, since the particles  $\text{PM}_{10}$  contain up to 40–60% of the total amount of HMMs and the concentrations of Cd, Ag, Sb, Sn, Se, Cu, Bi, Pb, Zn, Mo, and W in this fraction are 4–22 times higher than their abundances in the upper continental crust (Vlasov et al. 2015; Vlasov 2017).

When road dust settles on the surface of urban soils it changes their physicochemical properties. Road dust has a weak alkaline reaction and can form or increase the capacity of the existing alkaline geochemical barrier, which control the accumulation of many HMMs (Kosheleva et al. 2015). The presence of organic matter in dust causes the formation of organo-mineral geochemical barrier and the occurrence of various-size dust particles leads to the appearance of sorption-sedimentation geochemical barriers.

In this study for the first time a comprehensive analysis of the road dust properties and their spatial distribution has been made for the entire urban area of Moscow, the largest megacity of Russia and Europe. Moscow has numerous industrial enterprises, heating power plants (HPPs), an extensive road and transport network, and over 4.6 million cars. Similar but limited in scope studies were previously conducted only for individual districts of Moscow (Ladonin and Plyaskina 2009; Vlasov et al. 2015; Prokofieva et al. 2015; Bitjukova et al. 2016; Ladonin 2016). The purpose of this study was to evaluate the main physicochemical properties and the accumulation potential of the Moscow's road dust with respect to pollutants as its chemical composition is one of the important indicators of urban environment quality.

The specific objectives of the study were:

- to obtain a representative data set for the territory of Moscow that characterizes the dust on its roads in regard to various traffic intensity in different administrative districts of the city;
- to determine main physicochemical parameters of the road dust: pH, EC,  $C_{org}$ , and particle size distribution;
- to identify their spatial trends within the city;
- to assess the extent of technogenic geochemical transformation of the dust properties on the roads and to evaluate its accumulation potential with respect to inorganic pollutants (e.g., HMMs).

### SOURCES OF ROAD DUST

Motor transport. It is the main source of air pollution in Moscow that presents up to 95% of total emissions, or 880–930 thousand tons per year (Report... 2017; Bitjukova and Saulskaya 2017). The length of Moscow roads is 3,600 km, they occupy about 8% of its area (Fig. 1). The density of the road network is 4.2  $\text{km}/\text{km}^2$ , including the main network 1.54  $\text{km}/\text{km}^2$  (Khusnullin 2013). At the beginning of 2017, the automobile fleet of Moscow was about 4.6 million units of which 90.4% were passenger cars, 8.5% were trucks, and 1.1% buses. The number of vehicles is constantly increasing; the car ownership level is 340 per 1000 people.

Deposition of atmospheric aerosols resulting from anthropogenic emissions is one of the factors controlling the accumulation of road dust. Motor transport emissions consist of carbon monoxide (63%), nitrogen oxides (22%), and volatile hydrocarbons (13%) (Report... 2017). Particulate matter accounts for about 1% of the traffic emissions and non-exhaust emissions coming from abrasion of the road surface and road marking, break and tire wear, which ranges, according to various estimates, from 2.5 to > 5 thousand tons per year depending on traffic conditions – type, speed, and numbers of maneuvers (Nazzal et al. 2013). The particulate fraction  $\text{PM}_{10}$  is

\* Kasimov N.S., Kosheleva N.E., Vlasov D.V., Nabelkina K.S., Ryzhov A.V. // Geography, Environment, Sustainability. 2019;12(4):96-113.



largely associated with emissions of diesel cargo transport (61%) and buses (29%), despite the fact that their number is much smaller than that of passenger transport; however, they have higher emission intensity and mileage and a smaller share of engines of high environmental classes. An apportionment of the sources of PM<sub>10</sub> in Hatfield Tunnel (United Kingdom) showed that 60% of the particulate fraction is composed of particles originated from wear of road surfaces, tires, and brake pads, and re-suspension of the dust (i.e. non-exhaust emissions); while engine exhausts produce only 40% of PM<sub>10</sub> (Lawrence et al. 2016).

The maximum concentrations of pollutants in the air are observed in close proximity to roads. Within a distance of 1 m from a roadway the average dust load is 1.77 g/m<sup>2</sup> per day and at a distance of 5 meters it is 0.47 g/m<sup>2</sup> per day, which is 262 and 67 times higher, respectively, than the background level (Achkasov et al. 2006). Even in the eastern industrial part of Moscow, the dust load near roads is 1.2–2 times more intensive than near industrial areas (Kasimov et al. 2012).

The generation of particles during braking of vehicles due to friction between parts of the brake system is one of the significant sources of road dust (Garg et al. 2000). Therefore, the contribution of the road dust loading to suspended PM in urban environment can be quantitatively assessed using markers of particles originated from brake and tire wear, which include Cu and Sb (Weckwerth 2001), as well as tracers of road wear – Ca, Al, Si, Ti, and Fe (Diapouli et al. 2017).

Deicing reagents. The DIAs used in Moscow are chloride-based. They comprise at least 93% of technical salt (sodium chloride). The salt is usually mixed with marble chips that after snowmelt mark the places where the DIAs were applied (Nikiforova et al. 2016). A single road treatment requires 80–200 g/m<sup>2</sup> of the DIA (Sister and Koretsky 2004). The total permitted salt load in Moscow reaches 420–500 thousand tons (as dry matter) during the winter season, or 37 kg of the DIAs per person (Khomyakov 2015). The DIAs include combined (solid and liquid) agents. The municipal services of Moscow use liquid DIAs at temperatures higher 16°C; at lower temperatures combined agents which include 50–60% of marble chips, crystals of calcium chloride, and formic acid salts are applied. The solubility of marble is low; with decreasing chip-size, it increases in the presence of dissolved calcium chloride and particles of road surface (Greinert et al. 2013). In the courtyards and adjacent areas, sidewalks, and pedestrian streets, only combined DIAs are allowed to be applied. Additionally, grains of crushed granite with a diameter of 2–5 mm can be used, mainly in yard areas and on dangerous road sections.

Industrial enterprises and construction. In Moscow, there are over 30,000 stationary sources of pollutant emissions concentrated in the industrial zones (Fig. 1 a). In different years, the total emission load ranged from 60 to 70 thousand tons per year with a contribution of solids of about 3%. Thirteen HPPs in Moscow account for almost 50–65% of atmospheric emissions from stationary sources, while 20–30% comes from oil refineries, 2–3% and about 2% are derived from engineering enterprises, and from food processing and building materials production, respectively (Bityukova and Saulskaya 2017).

The sources of aerosol emissions to the atmosphere also include about 700 objects of urban construction

– residential buildings, urban infrastructure, road and transport facilities (Bityukova and Saulskaya 2017). Many stages of construction are accompanied by intense dust generation. In the near future, the number of construction projects in Moscow is expected to increase owing to the adoption of the law aimed at renovation the old housing stock. Accordingly, about 5,000 buildings needs to be demolished and rebuilt. Besides, in Moscow, some industrial zones are being redeveloped into residential areas.

Soil deflation. Dust contamination of roads increases due to wind erosion of poorly vegetated soils. Within the Moscow Ring Road (MRR), artificially created or highly transformed soils – urbanozems (Prokofieva and Stroganova 2004) – dominate; they have more alkaline pH, higher levels of C<sub>org</sub> and readily soluble salts, increased accumulation potential and higher proportion of clay, which control binding of HMMs in soils (Kosheleva et al. 2015). Extraneous material of anthropogenic origin, e.g., construction and household waste, are common in urban soils.

The composition of solid atmospheric fallout on the roadside areas of Moscow reflects its mixed origin. The coarse fractions consist mainly of quartz grains, feldspars, carbonates, and asphalt fragments; the fine fractions, in addition, carry carbon-containing matter, paint, glass, plastic, brick and other fragments (Prokofieva et al. 2015). The PM<sub>2.5</sub> fraction (particles with an aerodynamic diameter of 2.5 μm or smaller) is formed by soluble inorganic salts, mainly sulfates and nitrates (4–32% of the aerosol mass), insoluble mineral particles, carbon-containing material (1.2–48%) usually represented by elemental carbon (Privalenko and Bezuglova 2003; Da Costa and Oliveira 2009).

## MATERIALS AND METHODS

The road dust was tested in Moscow within the MRR on roads with different traffic intensity in June–July 2017 in 9 administrative districts (Fig. 1), as well as inside courtyards with local driveways and parking lots. The courtyards protected from the winds often act as traps for inorganic pollutants which are accumulated in urban soils of residential areas (Kosheleva et al. 2018b). The sampling grid density was defined as one sample per approximately 4 km<sup>2</sup> (Demetriades and Birke 2015; Kasimov et al. 2016). The dust samples that represent geochemical background in urban environment were collected on pedestrian paths in natural forest parks (the Losiny Ostrov, the Izmaylovsky and Bitsevski parks), at the most remote locations from the highways. In total, 173 dust samples were collected on the roads, 36 – in the courtyards, and 5 – in the forest parks.

In terms of traffic intensity, all roads were divided into several types by the width of the roadway and the number of lanes: (1) MRR, (2) the Third Ring Road (TRR), (3) major radial highways with more than four lanes in one direction, (4) large roads with three to four lanes, (5) medium roads with two lanes, and (6) small roads with one lane, and (7) local driveways and parking lots of courtyards. Table 1 shows the number of samples taken on different types of roads.

The fieldwork period was characterized by wet and rainy weather conditions; in June–July 2017 the precipitation norm for Moscow was exceeded nearly twice (Weather and Climate, 2017). The accumulation of the

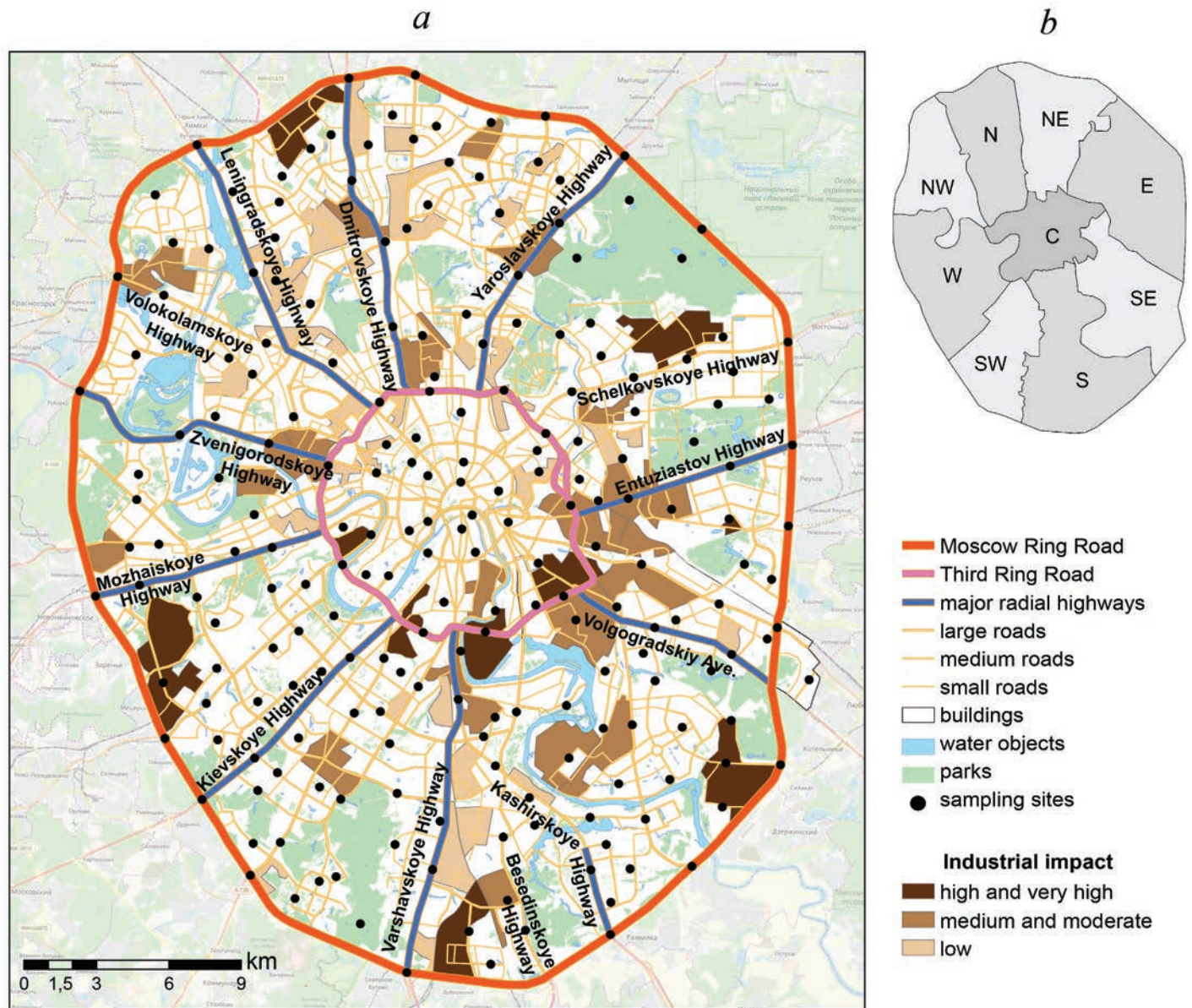


**Fig. 1.** Mobile and stationary sources of technogenic impact and road dust sampling locations in Moscow (a) and the administrative districts of Moscow within the Moscow Ring Road (b)

Impact levels of industrial zones are given according to Bityukova and Saulskaya (2017). Capital letters indicate the names of administrative districts (okrugs): N – Northern, NE – Northeastern, E – Eastern, SE – Southeastern, S – Southern, SW – Southwestern, W – Western, NW – Northwestern, C – Central

road dust was hampered by intensive surface drainage and daily road cleaning by public utilities. The sampling was carried out in days as dry as possible and no earlier than 24 hours after the rain and full road drying. Composite 300–500 g samples were collected along the curb on both sides of the road with a plastic scoop and brush, in 3–5 replications at a distance of 3–10 m from each other. On large and major radial roads, the samples were taken on the dividing strip; in the courtyards they were collected from the parking lots.

The main physicochemical properties of the dust samples were analyzed at the Ecological and Geochemical Center of the Faculty of Geography, Lomonosov Moscow State University. The pH values were measured in aqueous solutions (dust:water 1:2.5) by the potentiometric technique, the electrical conductivity (EC) – in aqueous solutions (dust:water 1:5) using EC meter,

the content of organic carbon was determined by the Tyurin (wet oxidation) method followed by titration, and the analysis of particle size distribution was performed by laser granulometry. The definition of particles is given according to the classification of N.A. Kachinsky adopted in Russia.

The obtained data were analyzed by statistical methods. For each district and road type, the following measures were calculated: sample averages ( $\bar{m}$ ), their errors, standard deviations  $\sigma$ , variation coefficients ( $Cv = \sigma/\bar{m} \cdot 100\%$ ), minimum and maximum values. The variation of the parameters depending on a set of factors (type of road, spatial location of the sampling point in the city, particle size class, base-acid reaction, and  $C_{org}$  content) were estimated by the regression trees method in S-Plus package (MathSoft®). The visualization of the geochemical data was done in ArcGIS 10 package.



## RESULTS AND DISCUSSION

The physicochemical properties analyzed (Tables 1, 2), in general, fall into the range of values comparable to what has been found in other cities of the world where pH,  $C_{org}$  content and EC varied between 7–9, 1–17%, and 100–2800  $\mu\text{S}/\text{cm}$ , respectively (Wang and Qin 2007; Al-Khashman 2007; Ladonin and Plyaskina 2009; Acosta et al. 2011; Yisa et al. 2011; Hu et al. 2011; Sutherland et al. 2012).

The results of multivariate regression analysis (Fig. 2) revealed the leading factors determining the physicochemical properties of road dust.

### Urbanized background

The road dust in the urban forest parks (Table 1) had the lowest values of pH (7.1) and EC (70  $\mu\text{S}/\text{cm}$ ). The DIAs are not applied in these territories; there is no pollution by particles formed during mechanical deterioration of vehicle parts, and atmospheric deposition is hampered by vegetation. The main components of the

dust in these background areas are plant residues and soil particles. In the forest parks, natural sod-podzolic soils (Retisols) with slightly acidic reaction and the prevalence of fulvic acids in the surface horizon owing to plant litter (Prokofeva et al. 2013, Rozanova et al. 2016) are still present. Foliage residues serve as a natural source of  $C_{org}$ , which determined its increased concentrations – 4.1%, on average. Unlike the forest parks, fallen leaves are removed from the public gardens and parks, as well as in many residential yards and green lawns, thereby reducing the new addition of organic matter into the soil. Also, the background dust had specific granulometric composition: in all 5 samples collected, a coarse particle size fraction 250–1000  $\mu\text{m}$  prevailed (> 50%).

### Base-acid reaction

The average pH of the dust sampled on the roads and in the courtyards is 7.4. The differences between the administrative districts were insignificant; the values that exceed the maximum and the average pH were typical of the western, southern and eastern parts of Moscow, while

**Table 1.** Physicochemical properties of the dust collected from different road types

Roads (number of samples)	pH		EC, $\mu\text{S}/\text{cm}$		$C_{org}$ , %		Share of $\text{PM}_{10}$ , %	
	Average (min–max)	$C_v$ , %	Average (min–max)	$C_v$ , %	Average (min– max)	$C_v$ , %	Average (min–max)	$C_v$ , %
forest parks (5)	7.1 (6.7–7.4)	3.2	70 (66–88)	17	4.1 (2.5–7.4)	42	13 (6.3–18)	37
MRR (20)	7.3 (6.8–7.9)	3.1	256 (98–521)	41	2.7 (1.5–4.9)	33	18 (5.4–31)	36
TRR (10)	7.4 (7.0–7.6)	2.4	277 (136–712)	57	2.8 (0.85–3.6)	29	18 (6.2–22)	25
major radial (19)	7.5 (7.1–8.0)	3.5	256 (118–537)	45	2.0 (1.0–4.0)	36	15 (4.1–29)	63
large (47)	7.4 (6.9–8.0)	3.9	257 (88–523)	49	2.1 (0.17–4.8)	41	16 (5.7–33)	44
medium (44)	7.4 (6.8–8.1)	3.7	174 (33–450)	55	2.3 (0.87–4.6)	38	13 (3.2–27)	52
small (34)	7.4 (6.4–8.1)	4.2	193 (47–525)	58	2.4 (0.91–4.8)	36	14 (4.0–39)	52
courtyards (36)	7.2 (6.6–8.1)	3.7	162 (63–483)	50	4.1 (1.1–6.7)	32	14 (5.2–28)	45

Note. Hereinafter, share of  $\text{PM}_{10}$  represents the share (%) of particles with a diameter of 10  $\mu\text{m}$  and smaller in a bulk sample of the road dust (considering particles of all diameters).

**Table 2.** Physicochemical properties of the road dust collected in different administrative districts of Moscow

District (number of samples)	pH		EC, $\mu\text{S}/\text{cm}$		$C_{org}$ , %		Share of $\text{PM}_{10}$ , %	
	Average (min–max)	$C_v$ , %	Average (min–max)	$C_v$ , %	Average (min–max)	$C_v$ , %	Average (min–max)	$C_v$ , %
Eastern (21)	7.4 (7.0–8.0)	3.8	174 (33–519)	67	2.2 (0.17–4.9)	51	14 (6.7–30)	46
Western (29)	7.4 (6.9–8.1)	4.0	183 (98–376)	40	2.5 (1.1–5.67)	45	16 (4.1–28)	41
Northern (12)	7.3 (7.1–7.9)	2.9	211 (97–537)	58	2.6 (1.4–3.8)	22	19 (6.9–28)	34
Northeastern (23)	7.3 (6.4–7.7)	3.7	199 (65–352)	40	3.1 (1.6–5.1)	34	17 (6.7–29)	34
Northwestern (16)	7.2 (6.7–8.0)	4.6	248 (90–459)	45	2.7 (0.85–5.1)	38	18 (7.2–29)	35
Central (32)	7.3 (6.8–8.1)	3.9	243 (80–712)	56	2.4 (0.85–4.8)	46	14 (4.2–24)	47
Southern (27)	7.4 (6.8–8.1)	4.2	214 (73–483)	42	2.8 (1.3–6.6)	49	12 (5–26)	55
Southeastern (30)	7.4 (6.6–8.0)	4.3	242 (47–525)	64	2.7 (0.91–6.7)	46	15 (3.2–39)	62
Southwestern (20)	7.4 (7.1–7.8)	2.4	176 (53–521)	61	2.4 (1.4–4.7)	38	14 (4.1–34)	55
Moscow (210)	7.4 (6.4–8.1)	3.9	211 (33–712)	56	2.6 (0.17–6.7)	44	15 (3.2–39)	48



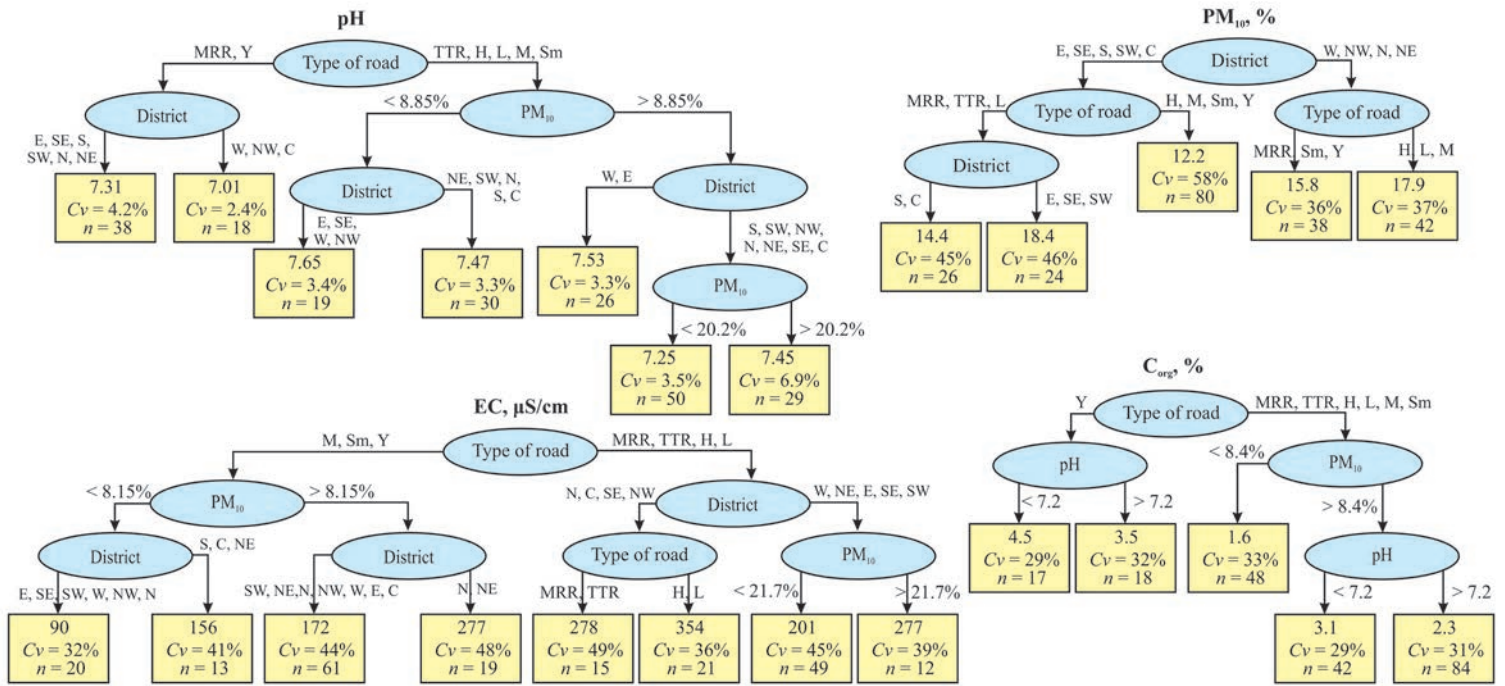


**Fig. 2.** Differentiation of the physicochemical properties of the Moscow’s road dust in relation to the type of the road, the administrative district, and the particle size distribution

For each terminal node, the average value of the parameter, the coefficient of its variation Cv, and the number of sampling points n are given. Types of roads: H – major radial highway, L – large, M – medium, Sm – small, Y – courtyards. For the names of the districts please see the footnote of Fig. 1

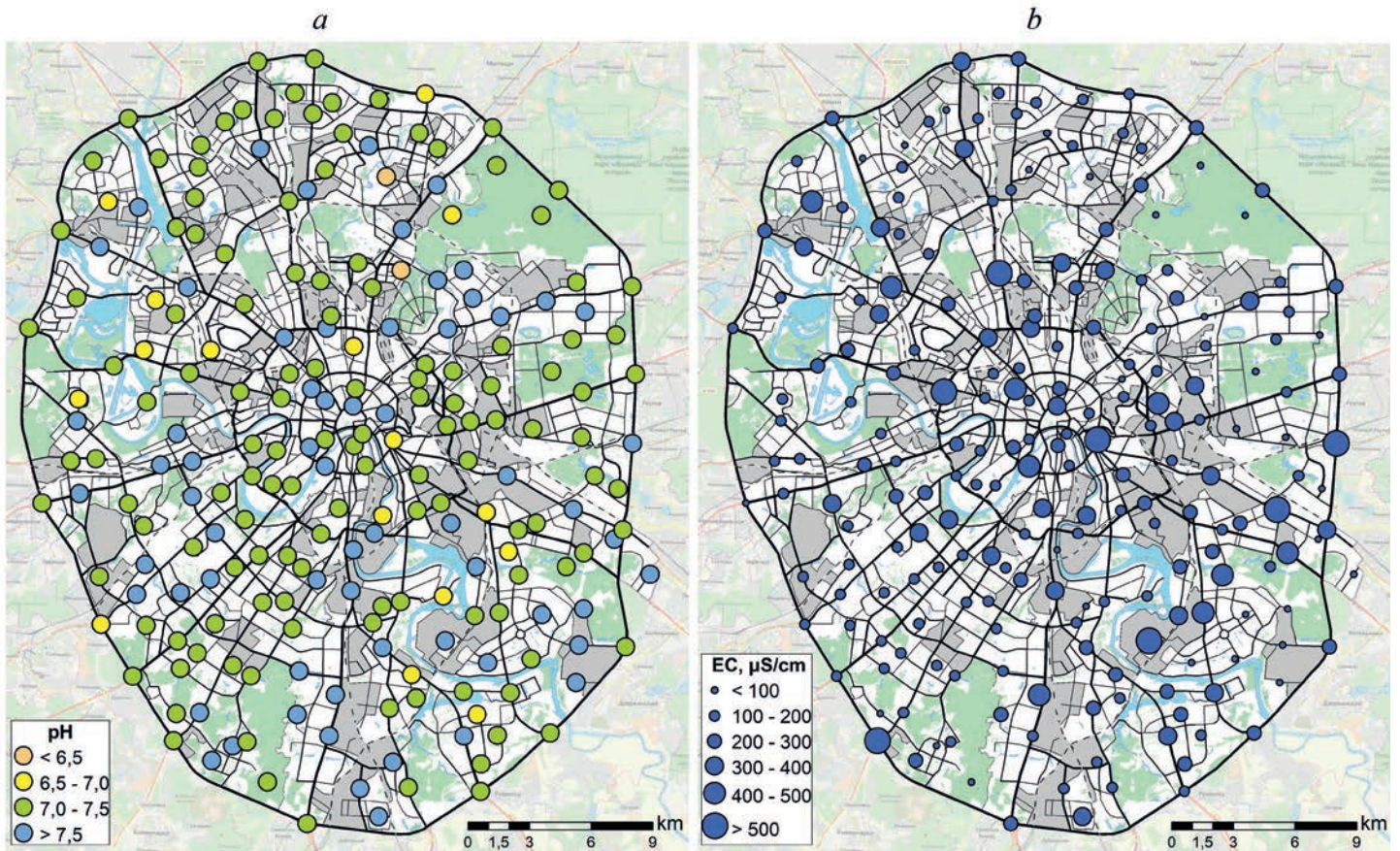


**Fig. 3.** Base-acid reaction (a) and the results of electrical conductivity measurements of the road dust in Moscow (b)



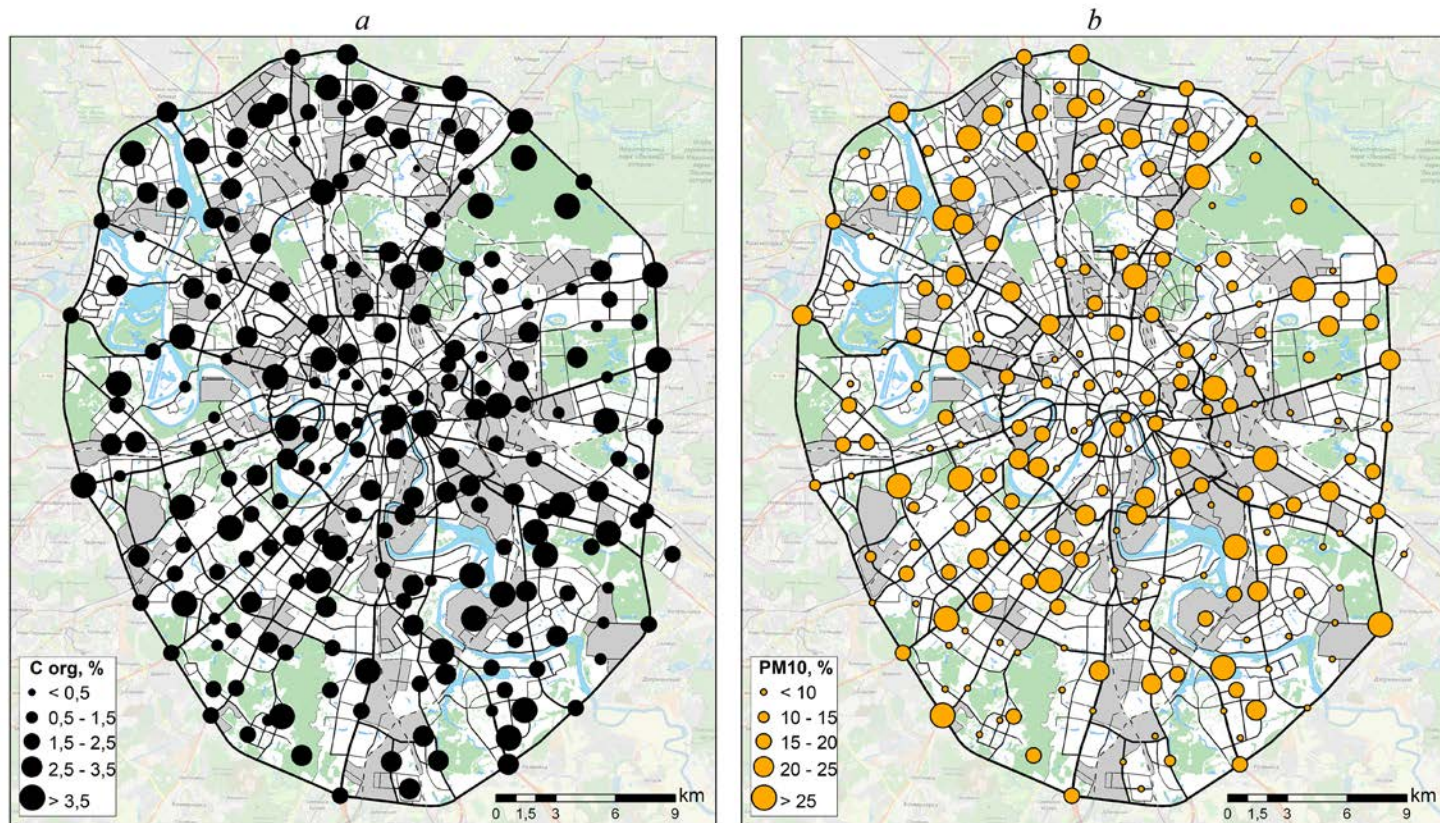


Fig. 4. The  $C_{org}$  content (a) and the proportions of  $PM_{10}$  fraction in the road dust samples in Moscow (b)

minimum values were observed in its northern part (Table 2, Fig. 3a). The lowest average pH of 7.2 was recorded in the Northwestern district due to the prevailing northerly winds which contribute to the translocation of alkaline technogenic dust to the south of Moscow (Lokoshchenko 2015) – the road dust pH in the Southern, Southeastern and Southwestern districts, as well as in the Eastern and Western districts, exceeded the value of 7.4. The coarse sand fraction (particles with diameter  $>500 \mu\text{m}$ ) is suspended at wind speeds exceeding 10 m/s; the coarse silt (with diameter 10–50  $\mu\text{m}$ ) and smaller particles may suspend in fairly weaker winds. Particles with diameter of 1–2  $\mu\text{m}$  at wind speeds of 2–3 m/s are removed from the soil surface, enter the surface aerosol, and remain suspended for quite a long time (Gendugov and Glazunov 2007). The particles' pH rises when their size decreases. Thus, in Western district, the pH in the aqueous extract of  $PM_{50}$  (with diameter  $\leq 50 \mu\text{m}$ ) was 0.6 units higher than that of  $PM_{>50}$  (with diameter  $>50 \mu\text{m}$ ); on large roads, this difference increased to almost 1 unit (Bityukova et al. 2016).

High pH values ( $\geq 8$ ) in most cases are caused by the influx of alkalinizing substances during the repair of the roadway and laying paving slabs (Greinert et al. 2013). The maximum pH of 8.1 turned out to be lower than the average (8.2) and maximum (8.9) pH of road dust collected in the summer of 2013 for the eastern part of the city (Vlasov et al. 2015) when the weather was rather dry and hot. Low pH values in the summer of 2017 may be associated with intensive removal of carbonate dust by precipitation and surface runoff.

The pH values of the dust correlate well with the types of roads. The pH tends to increase in the following order: courtyards and small roads  $\rightarrow$  large and major radial roads. The exception is the road dust collected on the MRR which shows the intermediate pH values. The

lowest average pH is restricted to the inner yard territories (7.2), while the highest – is registered for the major radial highways (7.5); which supports the idea that pH increases with the increasing road width and intensity of traffic. Roadway abrasion is higher on large roads (even small ruts are formed here), the material of which has a slightly alkaline reaction with a pH of 7.4. The highest pH variability with both the minimum (6.4) and maximum (8.1) values was observed on small roads.

The pH rise with increasing road-size might be explained by a more active use of strong alkaline detergents on large roads. During summer period, roads are cleaned daily by sweeping dust and periodic washing of the road surface. Detergent products with high pH (9–11) are used (“Chistodor,” “Tornado”). After deposition on road surfaces and drying they become one of the significant dust alkalinizing agents. The pH of the dust is minimal on parking lots in courtyards and on the MRR as they are not regularly washed (Fig. 2) while the road dust pH is much higher on the TRR, major radial, large, medium, and small roads, especially in Eastern, Southeastern, Western and Southwestern districts.

The predominance of the coarse particle size fractions in the road dust (Fig. 2) determines a more alkaline environment, which is associated with the input of slightly soluble particles of marble chips in winter season. The bulk of the DIAs used consists of particles with a diameter of 1–10 mm; the number of particles  $<1 \text{ mm}$  does not exceed 15–20%.

#### Electrical conductivity

The Moscow's road dust has high EC, which is due to the presence of large quantities of soluble substances of technogenic and natural origin, detected in aqueous



extracts. The average EC value of Moscow road dust was 211  $\mu\text{S}/\text{cm}$ , which is about 3 times higher than the background value in the forest parks (70  $\mu\text{S}/\text{cm}$ ). The EC varies between the districts from 173 (Eastern district) to 248  $\mu\text{S}/\text{cm}$  (Northwestern district) and within the districts, where the EC variation coefficients are also significant ( $C_v$  40–67%).

In winter time, the main source of readily soluble salts are the DIAs. With their excessive application, some of the reagents are not removed by the melt water, but remain in the solid form on the roadway, increasing the road dust EC. With decreasing particles' size, their EC rises: in Western district, the EC of  $\text{PM}_{50}$  is 2 times higher than that of  $\text{PM}_{>50}$  (Bityukova et al. 2016).

The clear relationship between road-size and the EC was detected: the EC values on medium and small roads and in courtyards were 1.5 times lower than those on the MRR, TRR, major radial highways and large roads, especially in Northern, Central, Southeastern and Northwestern districts (Fig. 2) due to a high content of  $\text{PM}_{10}$  (Table 2). A similar effect was observed in Amman, Jordan (Al-Khashman 2007). The smallest average EC (161  $\mu\text{S}/\text{cm}$ ) was typical of courtyards with parking lots, while the highest (277  $\mu\text{S}/\text{cm}$ ) of the TRR. The minimum value was found on the medium-size roads in Eastern district (33  $\mu\text{S}/\text{cm}$ ), and the maximum (712), at the crossroad of the Zvenigorodskoye Highway and the TRR.

The map (Fig. 3b) shows that increased EC are confined to the area stretching from the north-west to south-east. Most likely, the high EC values in this area are associated with greater density of the road transport network and industrial facilities. Outside this area in the north-east of Moscow, there is a large forest park Losiny Ostrov, and in the south-west, the Bitsevski forest park.

### Organic carbon

The pool of carbon in road dust is formed by soil particles containing humus and organic compounds of technogenic origin. In the traffic zone, the composition of organic matter is dominated by insoluble organic compounds, generally not susceptible to destruction by soil microorganisms, which increases their accumulation. Sources of these compounds are asphalt pavement and emissions from industries and motor vehicles (Faure et al., 2000). In the recreational and residential areas (forest parks and courtyards), the organic matter usually consists of natural fractions of humus (Lodygin et al. 2008); it is possible that in wet conditions (as it was in summer 2017), the fungi mycelium was an additional source of organic carbon (Prokofieva et al. 2015). The increase in the  $C_{\text{org}}$  content in the forest parks is caused by the decomposition of plant litter as a natural source of  $C_{\text{org}}$ ; in the courtyards, it is associated with the application of organic fertilizers (Vodyanitskii 2015).

The average content of  $C_{\text{org}}$  in road dust of Moscow was 2.6% ranging from 2.2% in Eastern district to 3.1% in Northeastern district with the variation coefficient up to 50% (Table 1, Fig. 4a). In dust of different types of roads, the minimum content of  $C_{\text{org}}$  of 2.0% was associated with the major radial highways and large roads; the maximum of 4.0%, close to the background level of 4.1%, was observed in the courtyards (Fig. 2), where organic matter comes from soil particles that are blown out from lawns and carried on wheels of cars parked on bare ground. The lawn soils have a high content of  $C_{\text{org}}$  and

nutrients, primarily nitrates (Kosheleva et al. 2018a). The addition of organic matter also occurs during idling of car engines responsible for increased emissions of soot and other organic compounds.

The  $C_{\text{org}}$  content in the road dust is positively correlated with  $\text{PM}_{10}$  fraction, which is partially derived from automobile exhaust containing various organic compounds, including soot particles and lubricating oils (Grigoriev and Kissel 2002). The fine particle size fraction in the road dust also includes fine topsoil particles (1–2  $\mu\text{m}$ ), which are blown out by moving vehicles (Gendugov and Glazunov 2007). The smaller are the particles, the greater is the likelihood of them being blown out of the soil surface and getting into the dust. This explains the direct relationship between  $C_{\text{org}}$  and  $\text{PM}_{10}$ . The effect of pH on the  $C_{\text{org}}$  content (Fig. 2) relates to the contribution of soil particles, which, compared with technogenic material, have a more acidic reaction.

### Particle size distribution

The granulometric composition of the Moscow's road dust was fairly uniform; it mainly contains sand (50–1000  $\mu\text{m}$ ) and coarse silt (10–50  $\mu\text{m}$ ) fractions, consisting predominantly of quartz and feldspar, respectively (Prokofieva et al. 2015). There were no significant differences in the particle size distributions between the road dust samples collected in different administrative districts and on different road types; the differences did not exceed 2–6% (Table 1, 2, Fig. 4b). Within the district groups, the share of  $\text{PM}_{10}$  in the road dust varied depending on the type of roads (Fig. 5). The road dust in Southern, Southeastern and Southwestern districts and on the large roads and the MRR was slightly dominated by  $\text{PM}_{5-10}$  and  $\text{PM}_{10-50}$  fractions (Fig. 5).

The dust with a high content of the  $\text{PM}_{10}$  was typical for the Leningradskoye and Yaroslavskoye Highways, some of the busiest highways in Moscow, and for large roads at some distance from TRR and the city center. The  $\text{PM}_{10}$  content increases as a result of daily congestion of vehicles with long idling, which leads to an increase in emissions of fine particles and soot. This is especially pronounced in local depressions of the relief, where the most favorable conditions for the deposition of particles are formed.

The maximum content of coarse fractions was observed on the medium and small roads, as well as in Central, Eastern, Southeastern and Southwestern districts. The most likely reason for the predominance of coarse fractions in the road dust of the Southeastern district is the coarse parent material of Meshchera lowland; there, a flat sandy plain is composed of fluvio-glacial sands and sandy loam (Kasimov et al. 2016).

### Technogenic transformation of the dust properties and the dust ability to accumulate pollutants.

Physicochemical properties of the road dust in the city are affected by technogenic sources. The comparison of the road dust with the dust sampled in the forest parks allowed us to estimate the intensity of the technogenic transformation of its properties (pH, EC,  $C_{\text{org}}$ , and the  $\text{PM}_{10}$  content) within Moscow. However, a comprehensive assessment of such transformation is difficult due to differences in the units of measurement and the variability of the parameters studied. To bring the heterogeneous



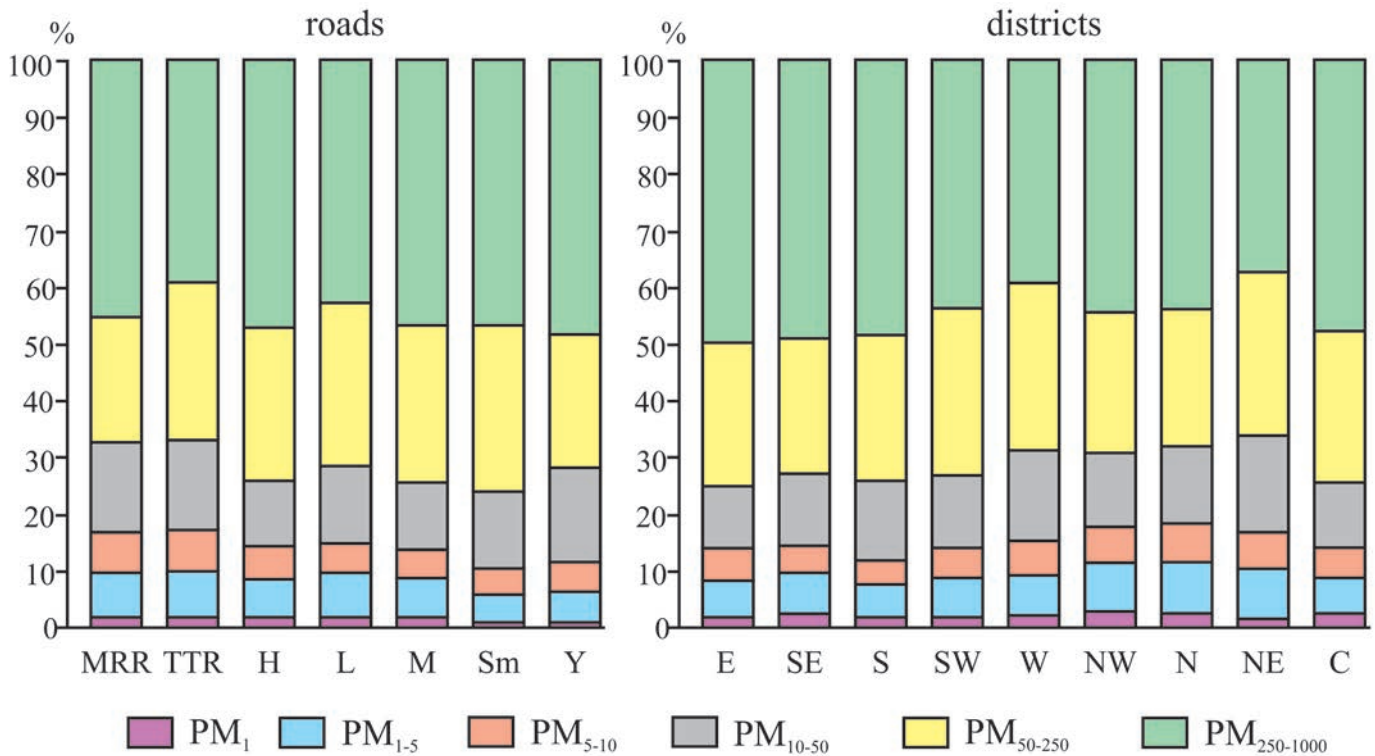


**Fig. 5.** The granulometric composition of the road dust on various types of roads and in different administrative districts of Moscow. Types of roads are deciphered in Fig. 2.

data to a single scale, physicochemical properties of the road dust were normalized (Tikunov 1997):

$$X'_i = |X_i - X_b| / |X_{ex} - X_b|,$$

where  $X_i$ ,  $X'_i$  are the initial and normalized values of a property at the  $i$ -th sampling point, respectively;  $X_b$  is the background value of the property in the dust of forest parks;  $X_{ex}$  is the extreme value of the property ( $X_{max}$  or  $X_{min}$ ) most deviating from the background value  $X_b$ . As a rule,  $X_{ex} = X_{max}$ . If  $|X_{min} - X_b| > |X_{max} - X_b|$ , then  $X_{ex} = X_{min}$ .

Then the degree of technogenic transformation ( $R$ ) at the  $i$ -th sampling point can be defined as the total value of the normalized deviations of all parameters from the background values of  $\sum X'_{ij}$ , where  $j$  is the considered physicochemical property (in our case  $j = 1, 2, 3, 4$ ). We set the approximate gradations of  $R$  depending on its range in the study area  $\Delta R = R_{max} - R_{min}$  (Table 3).

Analysis of the spatial distribution of  $R$  (Fig. 6a) showed that the greatest transformation of the physicochemical properties of road dust was associated with the sections of major radial highways located near the industrial zones and bus depots: in Southern district – it was the Varshavskoye Highway (electrical substations,

meat processing plant, bus and trolleybus depots, factory for the production of optoelectronic devices); in Eastern district – Schelkovskoye Highway (HPP-23); in Northern district – Dmitrovskoye Highway (bus depot, mechanical plants); in Northwestern district – Volokolamskoye Highway (bus depot, reinforced-concrete plant) and Zvenigorodskoye Highway (bus depot and HPP-16); in Western district – Mozhaiskoye Highway (HPP-25, wood processing plant, champagne wines plant, beer and non-alcoholic beverages plant); and in Central district – the Garden Ring road.

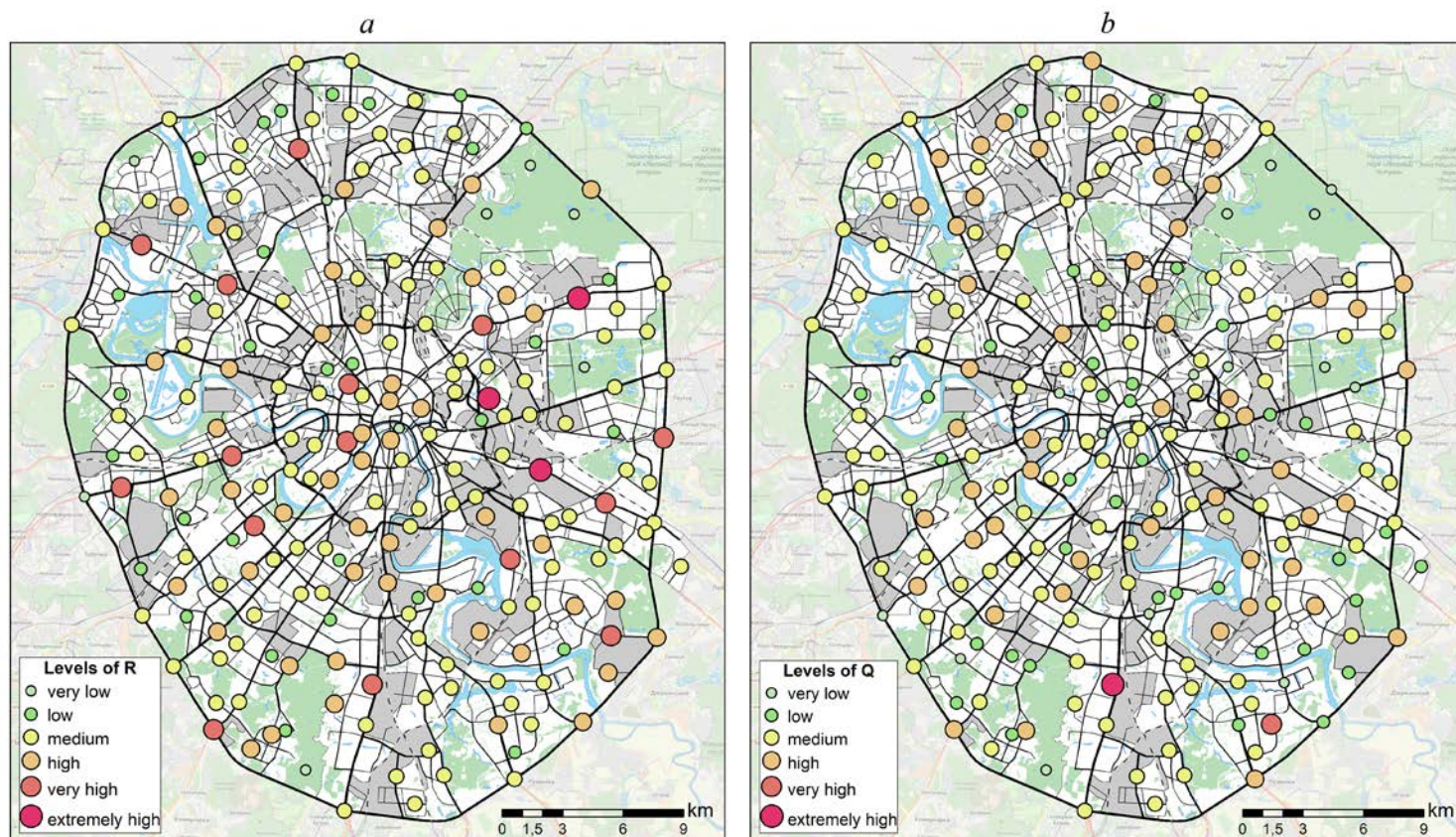
An increase in the  $pH$ ,  $C_{org}$  and the  $PM_{10}$  contents in soils leads to the formation of technogenic alkaline, organo-mineral, and sorption-sedimentation geochemical barriers (Vodyanitskii 2008; Vodyanitskii 2015), whose capacity increases with the growth of these parameters (Kosheleva et al. 2015). Considering that roadside soils play an important role in the formation of the mineral part of road dust and supply a significant amount of toxic chemical elements and compounds, an increase in  $pH$ ,  $C_{org}$  and the  $PM_{10}$  content in the road dust, as in other mineral components of urban landscapes will contribute to the growth of its accumulation potential in relation to

**Table 3.** Levels of technogenic transformation ( $R$ ) of the road dust physicochemical properties

Level of technogenic transformation	Limit values of $R$	Ranking categories of $R$ for Moscow
very low	$R \leq R_{min} + 0.1 \cdot \Delta R$	$R \leq 0.417$
low	$R_{min} + 0.1 \cdot \Delta R < R \leq R_{min} + 0.25 \cdot \Delta R$	$0.417 < R \leq 0.776$
medium	$R_{min} + 0.25 \cdot \Delta R < R \leq R_{min} + 0.5 \cdot \Delta R$	$0.776 < R \leq 1.374$
high	$R_{min} + 0.5 \cdot \Delta R < R \leq R_{min} + 0.75 \cdot \Delta R$	$1.374 < R \leq 1.972$
very high	$R_{min} + 0.75 \cdot \Delta R < R \leq R_{min} + 0.9 \cdot \Delta R$	$1.972 < R \leq 2.330$
extremely high	$R > R_{min} + 0.9 \cdot \Delta R$	$R > 2.330$

**Table 4.** Ranking categories of the accumulation potential (Q) of the road dust

Accumulation potential	Limit values of Q	Ranking categories of Q for Moscow
very low	$Q \leq Q_{\min} + 0.1 \cdot \Delta Q$	$Q \leq 0.796$
low	$Q_{\min} + 0.1 \cdot \Delta Q < Q \leq Q_{\min} + 0.25 \cdot \Delta Q$	$0.796 < Q \leq 1.052$
medium	$Q_{\min} + 0.25 \cdot \Delta Q < Q \leq Q_{\min} + 0.5 \cdot \Delta Q$	$1.052 < Q \leq 1.478$
high	$Q_{\min} + 0.5 \cdot \Delta Q < Q \leq Q_{\min} + 0.75 \cdot \Delta Q$	$1.478 < Q \leq 1.905$
very high	$Q_{\min} + 0.75 \cdot \Delta Q < Q \leq Q_{\min} + 0.9 \cdot \Delta Q$	$1.905 < Q \leq 2.160$
extremely high	$Q > Q_{\min} + 0.9 \cdot \Delta Q$	$Q > 2.160$

**Fig. 6.** The degree of technogenic transformation (R) of physicochemical properties (a) and the accumulation potential (Q) of the road dust (b)

many HMMs.

To assess the spatial variability of the accumulation potential of the Moscow's road dust with respect to HMMs, the normalized index  $Q = \sum X'_{ij}$  was calculated, with  $j = 1, 2, 3$ ;  $(X'_{ij}) = (X_i - X_{\min}) / (X_{\max} - X_{\min})$ . The following ranking categories were adopted for the accumulation potential (Q) of road dust in Moscow taking into account its range in the study area  $\Delta Q = Q_{\max} - Q_{\min}$  (Table 4).

The spatial distributions of the two indices – Q and R – differed for several reasons. First, the calculation of Q did not take into account the data on the EC of the aqueous extract of the road dust, since the EC's effect on the accumulation potential of mineral components has not been sufficiently studied. Secondly, the accumulation potential considers only the increase in pH values and the content of  $C_{\text{org}}$  and  $PM_{10}$ , whereas the index of technogenic transformation R summarizes both positive and negative deviations from the background conditions.

The analysis of the Q index distribution suggests the

predominance of road dust with high and average accumulation potential in the traffic zone in all districts of the city. Medium levels of technogenic transformation and accumulation potential were typical of the MRR and the TRR, which might be explained by rapid "regeneration" of dust material as a result of frequent road sweeping by municipal services. The largest accumulation potential of the road dust was detected in south of Moscow (along the Varshavskoye Highway), in the south-east (in courtyards and on medium-size streets between the Kashirskoye and Besedinskoye Highways), and in the north of Moscow (along the MRR and medium-size streets near the HPP-21, pipe plant, and fish and meat processing plants).

## CONCLUSIONS

The dust in the urban forest parks of Moscow is mainly derived from the natural sources with minimal impact of anthropogenic fallout. Formed mainly by soil particles, it has the background properties most similar to those ob-



served in the upper horizon of zonal sod-podzolic soils. It has neutral pH (average 7.1), low EC (70  $\mu\text{S}/\text{cm}$ ), high content of  $C_{\text{org}}$  (4.1%) and a significant amount of the coarse particle size fraction ( $> 250 \mu\text{m}$ ). The high content of  $C_{\text{org}}$  in the forest parks is caused by decomposition of plant litter.

The dust on the roads has a more alkaline reaction (pH 7.4), high EC (211  $\mu\text{S}/\text{cm}$ ), and lower content of  $C_{\text{org}}$  (2.6%), which is explained by motor vehicles emissions and the proximity to the industrial areas, as well as with a large volume of DIAs applied. The road dust is alkalized by detergents and particles formed by abrasion of roadways and blown out from construction sites. A three-fold excess of the EC over the background values is mainly due to the use of the DIAs and roadway maintenance. The concentration of  $C_{\text{org}}$  in the Moscow's road dust is on average 2 times lower compared to the background values. In the courtyards, the increased content of  $C_{\text{org}}$  is associated with the application of organic fertilizers. In general, the road dust is composed mainly of sand-size particles (50–1000  $\mu\text{m}$ ) and coarse silt (10–50  $\mu\text{m}$ ) fraction. The variations in the share of particle size fractions by districts and different types of roads, as a rule, do not exceed 2–6%.

The most significant factor determining the physicochemical properties of the road dust is the type of road. The dust on large roads including TRR has higher pH, EC, and  $\text{PM}_{10}$  values, which is caused by the intense traffic and, as a result, the greater amount of particles formed through roadway and vehicle wear. The content of  $C_{\text{org}}$  in the road dust is reduced due to the lower contribution

of soil particles. The spatial trends in the dust properties across the city territory are poorly expressed; to a large extent they are masked by other factors such as proximity to industrial zones and to large forest parks, the DIAs composition, frequency of the roadway cleaning and washing, and the contribution of soil particles of various genesis in different districts of Moscow.

The settling of airborne technogenic substances in the traffic zone increases the accumulation potential of the road dust with respect to pollutants binding compared to the dust of the forest parks. The most pronounced transformation of the road dust properties was found along some segments of the major radial highways that are located near the industrial areas and bus depots, especially in Southern, Eastern, Northern, Northwestern, Western and Central districts. In Southern, Southeastern and Central districts dust has the greatest accumulation potential. Cleaning roadways by municipal services reduces technogenic transformation of the road dust properties and thereby diminish its ability to bind pollutants, what is most pronounced on MRR and TRR. Therefore, regular cleaning of all types of roads, including those in courtyards of residential areas, is an effective measure to improve the quality of urban environment by reducing the level of its contamination with dust and dust associated pollutants. Thus, these results and the approved methodology for studying the physicochemical properties of road dust can be useful in assessment of urban environmental pollution, as well as in planning and rationalizing activities for cleaning streets from road dust.

## Факторы накопления тяжелых металлов и металлоидов на геохимических барьерах в городских почвах \*

### ВВЕДЕНИЕ

Промышленные объекты и транспорт в городах поставляют большое количество вредных выбросов, оказывая негативное воздействие на состояние окружающей среды. Загрязняющие вещества осаждаются из атмосферы на поверхность почв и накапливаются в них, изменяя морфологические и физикохимические свойства верхних горизонтов. Выпадение карбонатной пыли приводит к росту рН поверхностных горизонтов, тонкие фракции пыли и ила, а также гумусовые вещества увеличивают емкость поглощения [7, 17, 18, 29, 40, 42]. Утечки воды из распределительных сетей обуславливают подтопление, а запечатывание, то есть размещение на поверхности почв зданий, покрытие их асфальтом и т. д., приводит к уплотнению и уменьшению пористости почв с нарушением их газового режима [10]. В результате в поверхностных горизонтах городских почв образуются щелочной, сорбционный, глеевый, окислительный и комплексные геохимические барьеры (ГХБ), на которых накапливаются токсичные тяжелые металлы и металлоиды (ТМ) [5, 6, 10, 11, 17, 18, 34, 42, 46, 51, 61, 65]. Их емкость, как правило, гораздо больше, чем у природных аналогов [18], что является важным фактором ускоренного накопления ТМ.

Свойства этих барьеров, отсутствующих или слабо выраженных в природных почвах, в значительной степени определяют дальнейшую судьбу ТМ. Закономерности аккумуляции ТМ на барьерах в условиях города изучены недостаточно даже для хорошо известных в геохимическом и экологическом отношении металлов, таких как Cu, Zn, Pb, Cd, Cr, Ni, Co, для Bi, Sb и As такая информация практически отсутствует. Анализ поведения ТМ в городских почвах предполагает определение зависимостей между формами нахождения химических элементов и совокупностью антропогенных факторов и ландшафтных условий, влияющих на миграционную способность ТМ и определяющих скорость их накопления на ГХБ [14, 23]. Темпы накопления ТМ зависят от прочности связей с почвенными компонентами (оксидами и гидроксидами Fe и Mn, глинистыми минералами, органическим веществом), которая обусловлена химическими свойствами элемента, формами поступающих из техногенных источников соединений и геохимической обстановкой, то есть окислительно-восстановительными и кислотно-щелочными условиями [5, 16, 31, 42, 59].

Главным источником ТМ в городских почвах является техногенная пыль. Химический состав выпадающих из атмосферы частиц сильно различается в зависимости от их размера и происхождения. Они состоят из крупных частиц  $PM_{10}$  диаметром  $< 10$  мкм, мелких –  $PM_{2.5}$  ( $< 2.5$  мкм) и  $PM_1$  ( $< 1$  мкм) и очень

мелких частиц  $PM_{0.1}$  ( $< 0.1$  мкм). В городах в  $PM_{10}$  концентрируются Zn, Pb, в меньшей степени – As, Cr, Sb, Cu, Ni, Sn, Sr, Cd, Mo, Ag.  $PM_{2.5}$  обогащены V, Cr, Mn, Zn, Se, Pb, Ni, Cd, Pt, Pd, Rd [62]. Доля биологически доступных форм Ag, Co, Mn, Mo и Sb в  $PM_{2.5}$  и  $PM_{10}$  составляет 40-60%, Cu, Ni и Zn – 60-80%, а Cd, Pb и Tl – более 80% [49].

Миграционная способность ТМ оценивается путем сопоставления данных о валовом содержании и концентрациях подвижных форм химических элементов [2, 20, 23, 25, 26, 35, 56]. Наиболее подвижными являются обменные формы ТМ, представленные легкогидролизуемыми соединениями, которые чаще всего извлекаются из почв ацетатно-аммонийным буферным раствором (ААБ) с рН 4.8 или ААБ с этилендиаминтетрауксусной кислотой (ЭДТА) [16, 25, 28, 30, 31]. ТМ переходят из почвы в раствор путем ионного обмена, а также гидролиза под действием ионов водорода и образования растворимых ацетатных или аммонийных комплексных соединений [25].

Исследование форм ТМ в почвенном покрове города совместно с природными и антропогенными факторами их накопления дает возможность определить механизмы и условия формирования ГХБ по комбинации факторов, при которых наблюдается максимальная аккумуляция ТМ в почвах. В число факторов, помимо основных почвенных свойств, необходимо включать ландшафтные характеристики: рельеф, почвообразующие породы, положение в катене, характер растительности, а также антропогенные факторы – функциональное назначение территории, структуру и плотность застройки, характер транспортной сети, количество выпадающей пыли, мощность техногенных отложений и др. Количественный анализ такой ландшафтно-геохимической информации позволяет понять роль этих факторов в накоплении ТМ в городских почвах и определить доминирующие классы техногенных ГХБ.

Цель работы – оценить условия формирования и параметры основных видов техногенных ГХБ путем анализа распределения валовых и подвижных форм ТМ в городских почвах при различных сочетаниях ландшафтных и антропогенных факторов. Объектом изучения явился почвенный покров Восточного административного округа (ВАО) Москвы. Ландшафтно-геохимические исследования ВАО как модельной урбанизированной территории ведутся на географическом факультете МГУ с 1990-х гг. За 20-летний период накоплен значительный статистический материал, установлены особенности миграции и динамика накопления ТМ в разных компонентах ландшафтов и функциональных зонах округа, а также формы накопления Pb в почвах [19, 22, 33-36, 42].

В настоящей работе решались следующие задачи:

\* Кошелева Н. Е., Касимов Н. С., Власов Д. В. // Почвоведение. 2015;(5):536–553.

[DOI: 10.7868/S0032180X15050032](https://doi.org/10.7868/S0032180X15050032)

Kosheleva N. E., Kasimov N. S., Vlasov D. V. // Eurasian Soil Science. 2015;48(5):476–492.

[DOI: 10.1134/S1064229315050038](https://doi.org/10.1134/S1064229315050038)

IF 1.4

- установить валовое содержание, концентрации подвижных форм и подвижность<sup>1</sup> Bi, Sb, As, Cd, Cu, Pb и Zn в поверхностном слое городских почв;
- определить ландшафтные условия, включая физико-химические свойства почв, и комплекс антропогенных факторов, влияющих на интенсивность аккумуляции ТМ в почвах, и по сочетанию факторов диагностировать основные классы техногенных ГХБ;
- выявить особенности пространственного распространения ГХБ на территории ВАО;
- оценить изменение емкости ГХБ в результате техногенной трансформации физико-химических свойств почв.

## МЕТОДЫ ИССЛЕДОВАНИЯ

Изучалась южная, наиболее загрязненная часть ВАО, где расположен ряд крупных промышленных зон, автомагистралей, ТЭЦ-11, районная тепловая станция «Перово». Все эти объекты являются основными источниками загрязнения почвенного покрова, который достаточно сильно изменен под воздействием процессов урбанизации и техногенеза [33]. Территория относится к южно-таежным ландшафтам Подмоскворной Мещеры и представляет собой плоскую зандровую равнину с абсолютными высотами 150-160 м. На большей части ВАО сформировались специфические антропогенно-преобразованные почвы: урбодерново-подзолистые, урбаноземы, индустриоземы, экраноземы, а также техноземы, развитые на

водно-ледниковых песках и супесях и техногенных отложениях мощностью 1–4 и более метров [10, 43].

Исследования проводились летом 2010 и 2011 гг. на основе функционального зонирования территории [24]. Из-за аккумуляции металлов в поверхностных горизонтах техногенно-измененных почв опробовался верхний (0-15 см) дерново-гумусовый горизонт. Всего было отобрано 73 смешанных пробы почв в трех повторностях и 10 – на фоновой территории (рис. 1). При оценке контрастности техногенных педогеохимических аномалий в качестве эталонов были использованы фоновые дерново-подзолистые почвы Национального природного парка «Мещера» в 200 км к востоку от Москвы, которые характеризуют региональные ландшафтно-геохимические условия неурбанизированных территорий Подмоскворной Мещеры.

Физико-химические свойства почв и подвижные формы ТМ определялись в Эколого-геохимическом центре географического факультета МГУ: рН водной вытяжки – потенциометрическим методом, гранулометрический состав – на лазерном гранулометре (Fritsch, Германия), содержание органического углерода – методом Тюрина. Валовое содержание Cd, Pb, Sb, As, Bi, Zn, Cu, MnO и Fe<sub>2</sub>O<sub>3</sub> анализировалось масс-спектральным и атомно-эмиссионным методами с индуктивно связанной плазмой на приборах Elan-6100 и Optima-4300 (Perkin Elmer, США) во ВНИИ минерального сырья (Москва), подвижные формы ТМ – в вытяжке ААБ с ЭДТА на атомно-абсорбционном спектрометре novAA-400 (Analytik-Jena AG, Германия).



**Рис. 1.** Основные источники техногенного воздействия и точки отбора проб поверхностных горизонтов почв на территории ВАО. Функциональные зоны: Р – рекреационная, В – жилая застройка повышенной этажности, С – жилая застройка средней этажности, Н – жилая застройка низкой этажности, ПА – постагрогенная

<sup>1</sup> Подвижность (%) – отношение содержания подвижных форм химического элемента к его валовому содержанию.



Материалы исследований организованы в виде геоинформационной системы, содержащей координаты 73 точек опробования, характеристику ландшафтных условий и антропогенных факторов, физико-химические свойства почв и концентрации в них ТМ.

Геохимические особенности фоновых почв выявлялись путем сравнения содержания ТМ  $C_{\phi}$  с их кларком  $K$  в верхней части континентальной коры по [15]. С этой целью рассчитывались кларки рассеяния  $KP = K / C_{\phi}$  при  $C_{\phi} \leq K$ . Среднее содержание элементов в фоновых дерново-подзолистых почвах определено на основе собственных данных авторов и сведений из [1, 36]. Техногенная геохимическая трансформация городских почв характеризовалась коэффициентами накопления относительно регионального фона:  $K_c = C / C_{\phi}$ , где  $C$  – содержание элемента в городских почвах. Химический состав почв определялся формулой, в нижних индексах которой указаны  $K_c$  рассматриваемых элементов.

Факторы аккумуляции ТМ, представленные как количественными, так и качественными переменными, определены путем построения в пакете SPLUS (MathSoft, 1999) регрессионных деревьев, связывающих уровни содержания ТМ с наиболее сильно влияющими факторами. Метод регрессионных деревьев заключается в последовательном делении таблицы данных по одному из факторов на две части таким образом, чтобы каждая из них была максимально однородной [57]. Однородность полученных групп характеризуется вариабельностью прогнозируемого признака

$$D = \sum_i (y_i - \bar{y})^2,$$

где  $i$  – количество наблюдений в группе,  $\bar{y}$  – среднее значение по всем наблюдениям  $y_i$ . Затем каждая из групп делится еще на две части и т.д. Каждое деление можно рассматривать как ветвление по одной из переменных-предикторов; структура и количество ветвей результирующего дерева зависят от числа уровней деления.

При наличии базы данных (БД) с  $n$  столбцами, содержащими переменные-предикторы  $x_1, x_2, x_3, \dots, x_n$ , и столбцом  $\bar{y}$ , представляющим результирующую функцию-отклик, регрессионное дерево (дендрограмма) строится по следующему алгоритму. Предварительно задаются два параметра:  $M_{split}$  и  $M_{group}$  – минимальное количество наблюдений (строк таблицы) в группе до начала деления и после деления соответственно. Затем для каждой переменной-предиктора формируются все возможные деления БД на две группы.

Метод формирования групп зависит от типа переменной. Если переменная количественная, тогда вся таблица БД сортируется по столбцу с этой переменной, а затем делится на две части, каждая из которых имеет длину не меньше  $M_{group}$ . Если переменная порядковая, то предварительно выделяются подмножества БД, имеющие одинаковые значения этой переменной, а затем из этих подмножеств формируются все возможные комбинации. Общее возможное число делений по порядковой переменной равно  $2^{k-1}-1$ , где  $k$  – число градаций переменной.

Все деления по всем переменным сравниваются по величине  $\Delta D$ , которая характеризует уменьшение общей вариабельности функции-отклика  $y$  в результате деления. Для этого оценивается вариабельность в исходной группе  $D = \sum_i (y_i - \bar{y})^2$  и вариабельности

$$\text{в левой } D_L = \sum_L (y_i - \bar{y}_L)^2,$$

$$\text{и в правой } D_R = \sum_R (y_i - \bar{y}_R)^2,$$

ветвях, где индексы  $L$  и  $R$  обозначают наборы номеров образцов в ветвях деления. Выбирается тот вариант ветвления, который максимизирует величину

$$\Delta D = D - D_L - D_R.$$

В пределе рекурсивное деление большой БД может дать дерево с очень большим количеством конечных узлов. Есть вероятность, что прогностическая возможность такого большого дерева будет ограничена, так как нижние ветви будут показывать специфичность малых групп образцов. Для того, чтобы избежать такой переопределенности, дерево «обрезают». Существует несколько способов обрезки. Оптимальное количество ветвей можно определить путем проверки значимости различий средних между ветвями с помощью  $t$ -теста ( $\alpha = 0,05$ ).

Процесс разбиения заканчивается, если  $n$  становится меньше заранее установленного (6-8) или если проверка гипотезы о значимости различий между средними значениями с помощью  $t$ -теста дает отрицательный результат. Для каждого конечного узла дендрограммы по  $n$  точкам опробования рассчитываются средняя концентрация (или подвижность) металла и коэффициент вариации  $C_v$ . Метод позволяет прогнозировать уровни содержания поллютантов в почвах при различных сочетаниях факторов, а также оценить значимость последних [21, 33, 34].

Статистические модели распределения и подвижности ТМ в почвах ВАО Москвы строились в зависимости от следующих факторов и условий:

- антропогенные: вид использования городской территории; пылевая нагрузка; выбросы автотранспорта; структура и плотность застройки; мощность техногенных отложений; запечатанность почв;

- ландшафтные: геохимическая позиция (вид элементарного ландшафта); тип рыхлых отложений; подтопление почв; озелененность территории; физико-химические свойства почв – кислотность (рН), содержание ведущих фазносителей ТМ (органического вещества, оксидов Fe и Mn, фракций ила (< 1 мкм), мелкой (1–5), средней (5–10) и крупной (10–50) пыли), а также тонкого (50–250), среднего и крупного (250–1000 мкм) песка.

Функциональная принадлежность территории определялась по карте зонирования ВАО масштаба 1:25000, составленной на основе космических снимков 2009 г. сверхвысокого разрешения со спутника QuickBird (2.4 м, Digital Globe, США) [24]. Удельный выброс автотранспорта на каждой магистрали рассчитан В.Р. Битюковой по статистическим данным, пылевая нагрузка в каждой точке по [19]. Остальные антропогенные и ландшафтные факторы оценены по картам из [22, 43].

При диагностике ГХБ в почвах использовалась типология Глазовской [13], в которой барьеры группируются в зависимости от механизмов закрепления элементов и соединений. Ею описаны механический, биогеохимический органоминеральный (органическое вещество гумусовых горизонтов), щелочной (проявляется при повышении рН), хемосорбционный (связан с аморфными гидроксидами и органоминеральными соединениями Fe, Mn и Al) и сорбционно-седиментационный (обусловлен аккумуляцией элементов фракциями частиц различного диаметра).

## АНТРОПОГЕННЫЕ ФАКТОРЫ И ЛАНДШАФТНЫЕ УСЛОВИЯ

Количество, мощность, специализацию и состав выбросов источников загрязнения отражает функциональная структура урбанизированной территории. В пределах ВАО выделены промышленная, транспортная, рекреационная, постагрогенная и селитебная – жилой застройки низкой (1–5 этажей), средней (5–9 этажей) и повышенной этажности (10 и более этажей). Предприятия энергетики, машиностроения и металлообработки, химии и нефтехимии, производства стройматериалов, мусоросжигательный завод в Руднево сосредоточены в основном в крупных промзонах («Соколиная гора», «Прожектор», «Перово» и др). В округе густая сеть автодорог, среди наиболее крупных – МКАД, шоссе Энтузиастов, Вешняковская ул., Зеленый проспект, Перовская ул. Жилая зона повышенной этажности расположена в основном за МКАД в микрорайонах Новокосино и Кожухово, застройка средней этажности – в границах МКАД. Низкая застройка соответствует старым жилым кварталам в Косино-Ухтомском р-не. Относительно большие участки рекреационной зоны представлены лесопарками Кусково (Вешняки), Терлецким (Ивановское), Перовским (Новогиреево), а также Косинским Триозерьем (Косино-Ухтомский). Постагрогенная зона в настоящее время представлена Косинским лесопарком (Косино-Ухтомский район).

Пылевая нагрузка распределена по территории ВАО крайне неравномерно. Наиболее сильно загрязнена территория промышленной (40 кг/км<sup>2</sup> в сут.) и транспорт-

ной (55 кг/км<sup>2</sup> в сут.) зон (рис. 2). Максимальная наблюдавшаяся зимой 2009/10 гг. суточная нагрузка пыли в кленово-березовой лесопосадке в 30 м от МКАД составила 213 кг/км<sup>2</sup>, что в 21 раз выше фонового значения [19]. Техногенная геохимическая специализация твердой фракции снега отражает состав пыли в холодное время года и заключается в накоплении Mo ( $K_c=19$ ), Ag, Sb, As, W, Sn (4–6), V, Fe, Cr, Sr, Ni (2–3.9), Cd, Co, Bi (1.5–1.7). В выпадениях доминируют Mo ( $K_d^*=176$ ), W, Sb, As, Ag (14–18), Sn, Fe, Sr, V, Cr, Ni (6–10), Co, Zn, Mn, Cu, Bi, Cd, Ti (3–5). Наиболее интенсивные выпадения элементов характерны для автомагистралей и промышленных зон. По В.Р. Битюковой, наибольшая величина удельных выбросов автотранспорта приурочена к МКАД (до 57 мг выбросов на 1 км пробега) и ш. Энтузиастов (4–7 мг выбросов на 1 км пробега); наименьшая – к внутриквартальным улицам – менее 1 мг выбросов на 1 км пробега.

Степень антропогенной нарушенности почвенного покрова территории характеризуют также структура застройки и запечатанность почв. Высокая плотность застройки (> 10000 м<sup>2</sup>/га) характерна для среднеэтажных и частично низкоэтажных кварталов в районах Перово и Новогиреево, а также для высокоэтажных районов Новокосино и Косино-Ухтомский. Плотность застройки низкой этажности и промзон в основном средняя (5000–10000 м<sup>2</sup>/га), а за МКАД – низкая (<5000 м<sup>2</sup>/га). Чаще всего встречаются четыре типа застройки: периметральная, групповая, строчная и усадебная.

Запечатанность создает механические барьеры на пути нисходящих потоков атмосферных осадков,

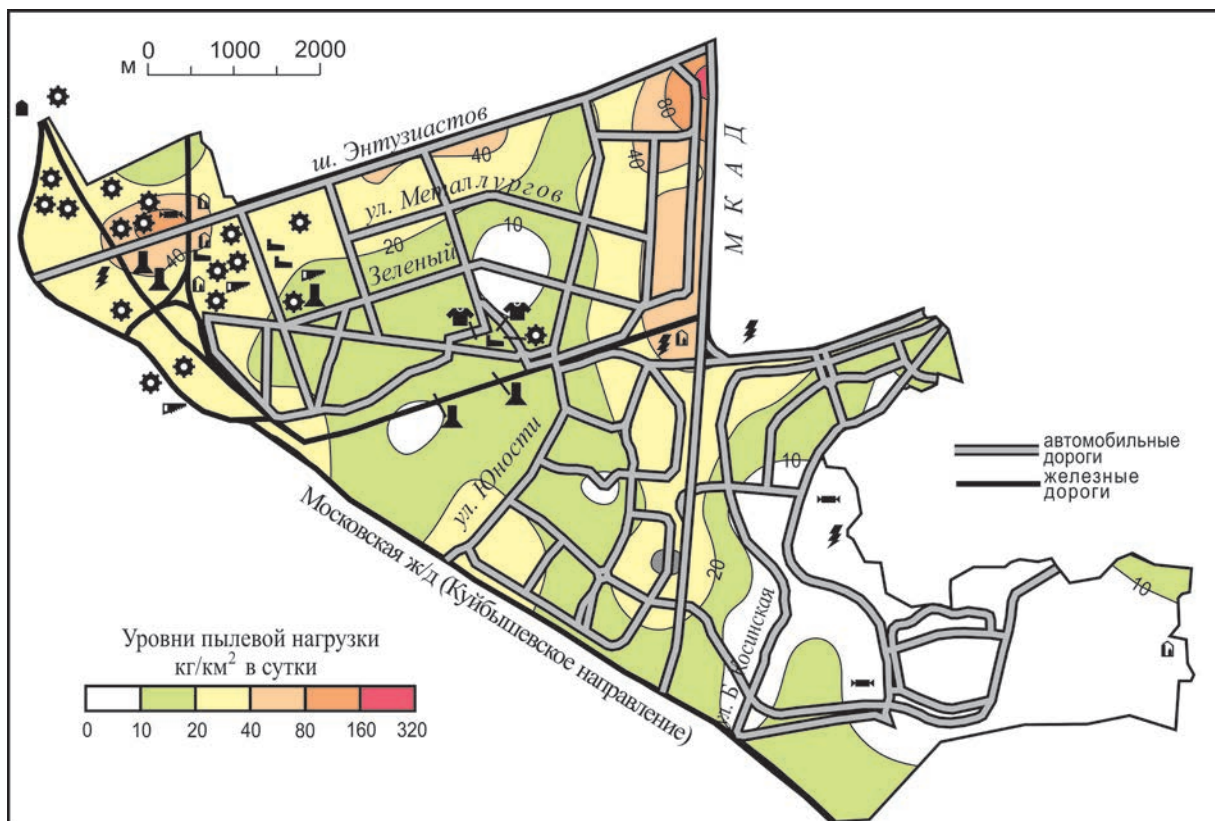


Рис. 2. Выпадения пыли на территории ВАО (2010 г.). Составлено по данным [19]. Условные обозначения на рис. 1.

\* $K_d = D/D_{\phi}$  – коэффициент превышения выпадений ТМ над фоном,  $D$  и  $D_{\phi}$  – выпадение элемента в округе и на фоновой территории соответственно, мг/км<sup>2</sup> в сутки.

в результате резко снижается радиальная миграция элементов [12]. Наибольшая запечатанность почв (50–70%) свойственна территориям ВАО с административными, торговыми и коммунально-складскими объектами и промзонами. Меньше (20–50%) запечатаны почвы районов жилой застройки различной этажности. Наименее запечатанными являются почвы лесопарковых территорий.

К ландшафтными факторам отнесены характеристики рыхлых отложений, на которых формируются городские почвы. Их гранулометрический и минералогический состав в значительной степени определяют уровни содержания ТМ в почвах. Среди рыхлых отложений преобладают водно-ледниковые каменистые пески, местами перекрытые маломощными покровными суглинками, и древнеаллювиальные водно-ледниковые пески и супеси с прослоями суглинков, характерные для обширных флювиогляциальных равнин в центральной части и террас реки Москвы на севере и юго-востоке рассматриваемой территории ВАО. Моренная равнина, сложенная валунными суглинками, встречается небольшими участками в северной части исследуемого района. Древние озерные котловины, расположенные в южной части ВАО вокруг озер Белое и Святое, заполнены озерноледниковыми суглинками с прослоями песков. Лощинно-балочные песчано-суглинистые отложения приурочены к днищам ручьев и балок, а аллювиальные, преимущественно песчаные – к поймам рек Рудневки, Пономарки, Нищенки, Серебрянки [3, 22].

Положение в рельефе определяет геохимическую обстановку, интенсивность латеральной миграции и зоны аккумуляции ТМ в почвах. В округе преобладают элювиальные и трансаккумулятивные элементарные ландшафты. Первые занимают повышенные элементы мезорельефа при относительно глубоком (> 1 м) уровне грунтовых вод и приурочены к водно-ледниковым равнинам, вторым соответствуют более низкие гипсометрические позиции долинных зандров. Трансэлювиальные ландшафты распространены на небольших участках покатых склонов речных долин, а супераккумулятивные – в древнеозерных котловинах и днищах лощин и балок [22].

Вследствие утечек из водоподводящих и коллекторных сетей на большей части территории округа наблюдается повышение уровня грунтовых вод [43]. Подтопляемые участки с глубиной залегания грунтовых вод менее 1 м приурочены к озерным понижениям и засыпанным поймам малых рек Пономарки, Нищенки, Серебрянки; неподтопляемые территории с

глубоким, более 3 м залеганием грунтовых вод, находятся на юго-востоке округа в бассейне р. Рудневки; остальные территории подтопляются периодически. Для подтопляемых и периодически подтопляемых участков характерна более высокая увлажненность почв и переменные окислительно-восстановительные условия.

Наименьшая степень озелененности (< 50%) отмечена в высотных жилых кварталах Новокосино и Косино-Ухтомского р-на, а также в среднеэтажной застройке районов Перово и Соколиная гора; наибольшая (> 70%) – в южной части Косино-Ухтомского р-на, прибрежной части оз. Белое и северной части р-на Вешняки; средняя (50–70%) – в среднеэтажной и малоэтажной застройке районов Ивановское, Новогиреево и Вешняки [22].

## РЕЗУЛЬТАТЫ И ОБСУЖДЕНИЕ

### Свойства фоновых почв и содержание в них ТМ

Для поверхностных горизонтов фоновых дерново-подзолистых почв в Национальном парке «Мещера» характерна кислая реакция среды со средней величиной рН 4,8 при варьировании от 4.0 до 5.5. Содержание органического углерода составляет в среднем 2.3% при колебаниях от 0.9 до 5.0%; среднее количество оксидов Fe – 0.80%, Mn – 0.046%. Преобладают супеси с содержанием физической глины около 12%.

Содержание Pb в верхнем горизонте почв близко к его кларку в верхней части континентальной коры (табл. 1), для остальных элементов характерно рассеяние (КР 2–3). Низкие концентрации элементов в почвах объясняются их незначительным содержанием в почвообразующих водноледниковых песках [1].

### Физико-химические свойства городских почв

Техногенная трансформация исходных природных почв на территории ВАО проявляется, прежде всего, в изменении основных физико-химических свойств и их микроэлементного состава. По сравнению с фоновыми условиями резко повышается рН поверхностных горизонтов – в среднем с 4.8 (кислая реакция) на фоне до 7.1 (нейтральная, с повышением местами до 8.5 – щелочной). Наиболее высокие значения рН характерны для почв промышленной зоны (7.6) и автомагистралей (7.4), слабокислая реакция (6.3) выявлена в почвах парков. Подщелачивание почв, связанное с выбросами пыли и золы, установлено во многих других городах и на пригородных территориях, при

**Таблица 1.** Валовое содержание (Сф вал.), концентрации подвижных форм (Сф подв.) и подвижность Bi, Sb, As, Cd, Cu, Pb и Zn в поверхностном горизонте фоновых почв Национального парка «Мещера» (n=10) в сравнении с кларками (К) верхней части континентальной коры [15]

Геохимические показатели	Элемент						
	Bi	Sb	As	Cd	Cu	Pb	Zn
К, мг/кг	0.29	0.81	5.6	0.64	39	17	75
Сф вал., мг/кг	0.13	0.36	2.0	0.21	20	14	37
Сф подв., мг/кг	0.004	0.01	0.04	0.08	4.2	8.5	1.0
Подвижность, %	3	4	2	39	21	61	3
Кларк рассеяния (КР)	2.2	2.2	2.8	3.0	2.0	1.2	2.0



этом воздействие нередко столь интенсивно, что приводит к смене класса водной миграции элементов с H-Fe на Ca [7, 19, 29, 42, 46].

В городских почвах относительно фона увеличивается количество органического вещества и физической глины. Содержание общего углерода в верхнем горизонте почв ВАО колеблется от 0.1 до 10.4% при среднем значении 3.5%, что в 1.5 раза выше аналогичного показателя в фоновых почвах. Содержание общего углерода по функциональным зонам варьирует слабо, максимум наблюдается в жилой застройке средней и низкой этажности, что обусловлено внесением торфо-компостных смесей.

По содержанию физической глины (16%) почвы ВАО в основном супесчаные, хотя локально в лесопосадках близ МКАД – тяжелосуглинистые (содержание физической глины > 40%). Утяжеление гранулометрического состава городских почв связано с повышенным поступлением техногенной пыли, а также с подсыпкой почвы при рекультивационных работах городских служб. Наиболее легкий состав (11% физической глины) имеют поверхностные горизонты почв промышленных зон из-за сильной опесчаненности исходных пород – флювиогляциальных песков; наиболее тяжелый – почвы постагрогенной зоны (25%) из-за унаследования свойств, сформированных при сельскохозяйственном использовании территории (рыхление почвы, внесение минеральных и органических удобрений, мелиорантов и т. д.). Количество оксидов Fe в почвах ВАО по сравнению с фоном увеличивается в среднем в 3.6 раза и составляет 2.84%, а Mn – в 1.4 раза (0.063%).

По сравнению с данными 2005 г. [34] pH поверхностного горизонта почв ВАО незначительно снизился (в среднем с 7.5 до 7.1), однако возросло содержание органического вещества – с 2.7 до 3.5%, что можно объяснить заменой загрязненного верхнего слоя чистым материалом и широким применением торфо-компостных смесей.

Изменения физико-химических свойств почв в сочетании со значительными атмосферными поставками ТМ приводят к формированию в поверхностных горизонтах техногенных аномалий, в которых концентрируется широкая ассоциация ТМ. В почвах ВАО с разной интенсивностью аккумулируются все изученные элементы, которые по значениям  $K_c$  образуют ряд:  $Cd_{7.6} > Bi_{4.9} > Sb, Zn_{4.8} > Pb_{4.5} > As_{3.9} > Cu_{2.9}$  (табл. 2). Содержание ТМ пространственно

очень изменчиво: у Cu, Zn, Sb коэффициенты вариации  $C_v$  составляют 60–70%, у Cd и Bi увеличиваются до 130–140%. К основным источникам поллютантов относится автотранспорт, а также промышленные предприятия. Выбросы топливно-энергетического комплекса, как правило, обогащены Pb, Zn, Cu, машиностроения и металлообработки – Zn, Sb, Cu, Pb, As, химии и нефтехимии – Cd, Sb, Zn, Cu, Bi, Pb, As, заводов по производству стройматериалов – Pb, Sb, Zn, Bi, Cu, мусоросжигательных заводов – Bi, Pb, Cd, Sb, As, Zn, Cu; дорожная пыль содержит значительное количество Pb, Cu, Zn, Cd, Sb [9, 55].

Техногенная пыль, как правило, сильно обогащена подвижными формами элементов [49, 51], поэтому содержание обменных и органоминеральных форм ТМ, извлекаемых ААБ с ЭДТА, заметно больше фоновых:  $Zn_{35.5} > Bi_{21.9} > As_{10.5} > Sb_{6.6} > Cu_{4.8} > Cd_{3.1} > Pb_{1.3}$ . Наибольшая подвижность у Cu (34%), средняя (15–20%) – у Zn, Pb, Cd и Bi. Относительно малоподвижны Sb и As с долей подвижных форм около 5%. По сравнению с фоном в городских почвах наиболее сильно увеличивается подвижность Zn (в 6.7 раза) и Bi (в 4.3 раза), подвижность Pb и Cd, напротив, уменьшается, что указывает на преобладание в составе техногенных выпадений слабоподвижных форм этих металлов. Вариабельность концентраций ( $C_v$ ) подвижных форм ТМ в городских почвах существенно выше, чем валового содержания – от 105% у Cu и As до 348% у Bi.

#### Статистическое моделирование накопления тяжелых металлов и металлоидов в городских почвах и классы ГХБ.

Результаты моделирования по методу регрессионных деревьев позволили оценить пространственное варьирование валового содержания и подвижности ТМ при изменении ландшафтных условий и антропогенных факторов и диагностировать ГХБ, обуславливающие формирование контрастных техногенных аномалий. Диагностика ГХБ проводилась по дендрограммам, характеризующим связь между новообразованными физико-химическими свойствами почв и закреплением элементов на ГХБ (рис. 3, 4), что позволило выделить основные механизмы закрепления ТМ и определить классы ГХБ, доминирующие в поверхностных горизонтах городских почв (табл. 3).

**Таблица 2.** Статистические и геохимические показатели для валового содержания ( $C_{вал.}$ ) и подвижных форм ( $C_{подв.}$ ) Bi, Sb, As, Cd, Cu, Pb и Zn в поверхностном горизонте почв ВАО Москвы ( $n=73$ )

Показатель	Элемент						
	Bi	Sb	As	Cd	Cu	Pb	Zn
$C_{вал.}$ , мг/кг	0.61 (0.12–6.1)*	1.71 (0.45–6.3)	7.8 (3.0–55)	1.6 (0.3–14)	59 (13–220)	63 (13–330)	179 (46–690)
$K_c$ вал.	4.9	4.8	3.9	7.6	2.9	4.5	4.8
$C_{подв.}$ , мг/кг	0.08 (0.001–2.4)	0.09 (0.001–1.0)	0.39 (0.02–2.2)	0.25 (0.1–0.39)	20 (2.0–84)	11 (0.56–131)	36 (2.1–235)
$K_c$ подв.	21.9	6.6	10.5	3.1	4.8	1.3	35.5
Подвижность, %	13 (0.1–39)	5 (0.01–30)	5 (0.4–39)	16 (2–93)	34 (10–86)	18 (2–101)	20 (3–98)

Примечание. Верхняя строка – среднее значение, в скобках – минимальное и максимальное содержание.

Предполагалось, что увеличение подвижности элемента при росте содержания тех или иных гранулометрических фракций связано с его выпадением в составе этих фракций.

*Свинец.* Свинец типичный халькофильный элемент, в соединениях находится в двух- и четырехвалентной формах. В восстановительной обстановке халькофильные элементы и элементы группы железа восстанавливаются до двухвалентных и образуют нерастворимые сульфиды [38], что объясняет их накопление в речных илах. Основные компоненты почвы, связывающие Pb – карбонаты, глинистые минералы, оксиды Fe и Mn, а также гумус [6, 8]. Органическое вещество оказывает большее влияние на иммобилизацию Pb, чем карбонаты или гидроксиды, которые осаждаются в почве только при высоких pH [59]. При больших концентрациях Fe подвижность Pb уменьшается с ростом pH, что объясняется увеличением устойчивости гидроксидов Fe в щелочной обстановке [23, 37]. При увеличении техногенной нагрузки в дерново-подзолистых почвах возрастает доля обменной и специфически сорбированной фракций Pb [26].

Валовое содержание Pb в почвах ВАО изменяется в зависимости от геохимической позиции с максимальным накоплением в подчиненных геохимических ландшафтах. В супераквальных ландшафтах более интенсивной аккумуляции Pb способствует изменение окислительно-восстановительного режима почв при подтоплении и увеличение количества почвенного гумуса. В элювиальных, трансэлювиальных

и трансаккумулятивных ландшафтах Pb накапливается в оксидах Fe и Mn. При низком содержании оксидов Fe (< 2.9%) Pb концентрируется в основном в частицах среднего и крупного песка; увеличение доли частиц илистой фракции влечет за собой снижение накопления Pb в почвах.

Поступление подвижных форм Pb связано с фракцией средней пыли. При ее концентрации < 11.7% в почвах, развитых на озерноледниковых суглинках и ложинно-балочных песчано-суглинистых отложениях, подвижность Pb больше, чем в почвах на других типах отложений. Увеличение пылевой нагрузки и запечатанности почв сопровождается ростом подвижности Pb. В то же время при суточной пылевой нагрузке более 14.2 кг/км<sup>2</sup> подвижность Pb в почвах высотной, среднеэтажной застройки и промышленной зоны выше, чем в рекреационной и транспортной зонах.

Наиболее контрастные аномалии Pb в городских почвах приурочены к комплексному сорбционному и биогеохимическому органоминеральному барьеру, обязанному своим образованием значительным концентрациям оксидов Fe и Mn и органического вещества (> 2.9, 0.06 и 4.0% соответственно). Накоплению Pb также способствует поступление частиц крупного песка (> 10%), вероятно, техногенного происхождения, обогащенного этим металлом. При этом их контрастность и емкость заметно больше в подчиненных геохимических ландшафтах за счет более сильного увлажнения, способствующего иммобилизации Pb, и высокого содержания гумуса.

**Таблица 3.** Влияние антропогенных факторов и ландшафтных условий на накопление и подвижность ТМ в поверхностном (0–15 см) слое почв ВАО Москвы

Фактор		Валовое содержание						Подвижность							
		Pb	Cu	Zn	Cd	Bi	Sb	As	Pb	Cu	Zn	Cd	Bi	Sb	As
Ландшафтные	Почвенно-геохимические свойства	pH		2+	2+	3+						2–			
		Сорг	2+					2, 4+	2+				3–		2+
		ил	3–								4+				
		мелкая пыль				2+									
		средняя пыль				4+	1+			1+	3–				6–
		крупная пыль			3–			5–				2+	1+		
		мелкий песок								4+				2–	5+
	средний и крупный песок	4+				2–								1+	
	Fe <sub>2</sub> O <sub>3</sub>	2+	1+	1+		1+	3, 5+	1, 3+	5–		3–		2–		
	MnO	3+			5+	3+	4+					3–			
Ландшафтные	Тип рыхлых отложений							3	2		1		1	3	
	Ландшафтно-геохимическая позиция	1									1				
	Подтопление почв				4										
Антропогенные	Функциональная зона		3	3	3	3, 4	1		4, 5	2	5		4	1	4
	Озелененность						5+			3–				3–	
	Запечатанность почв				3–				4+			3–			
	Пылевая нагрузка		4+						3+						
	Выбросы транспорта									1+					
Структура застройки										6				3	

Примечание. Ранги от 1 до 6 показывают уменьшение значимости фактора; «+» – рост показателя способствует увеличению концентрации (подвижности) элемента, «–» – его уменьшению; для качественных показателей характер связи не определяется.

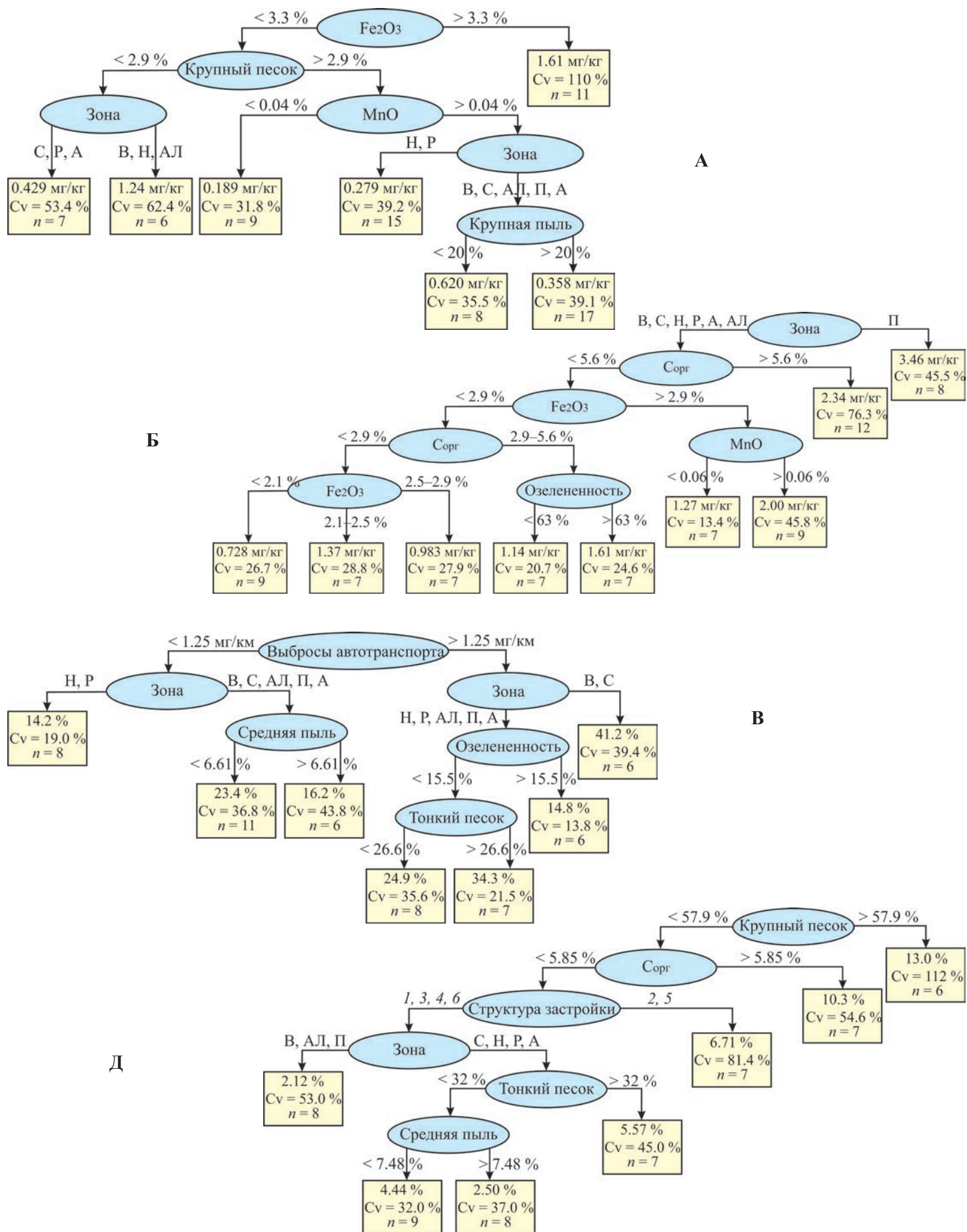


**Рис. 3.** Распределение валового  $V_i$  (а),  $S_b$  (б) и подвижности  $Cu$  (в),  $As$  (г) в почвах ВАО при различных сочетаниях антропогенных и ландшафтных факторов. Для каждого конечного узла приводится среднее значение концентрации ТМ, коэффициент вариации  $C_v$  и число точек опробования  $n$ . Структура застройки: 1 – без застройки, 2 – групповая, 3 – смешанная, 4 – строчная, 5 – периметральная, 6 – усадебная.



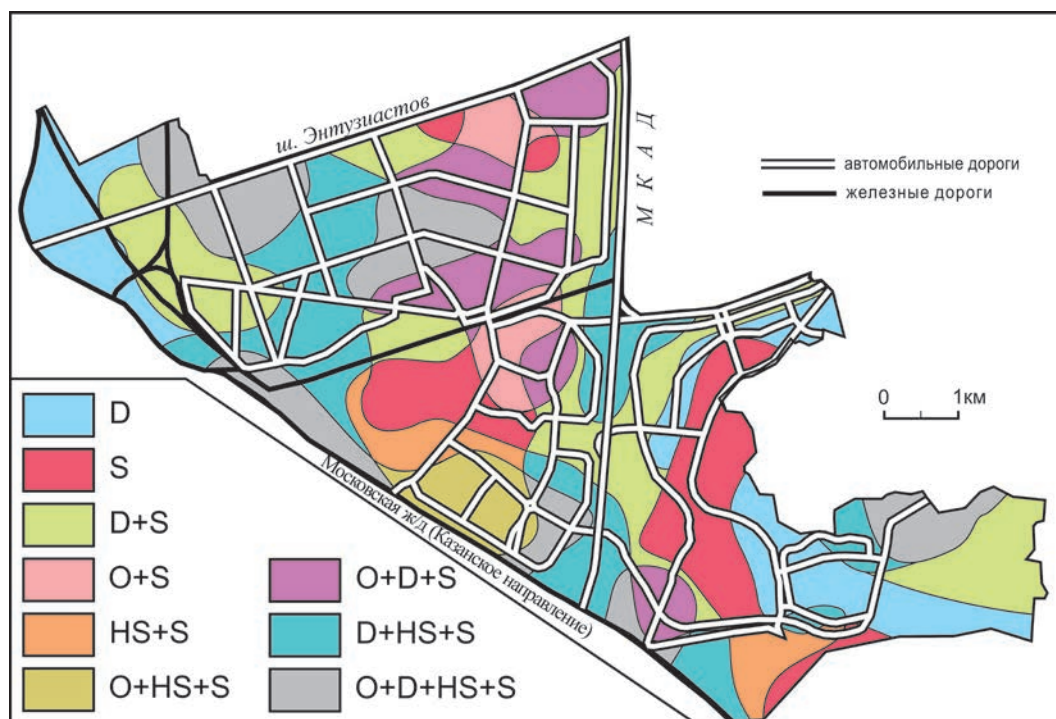


**Рис. 4.** Геохимические барьеры в поверхностных горизонтах почв ВАО г. Москвы: D – щелочной (Cd, Cu, Zn), S – сорбционно-седиментационный (Cd, Cu), HS – хемосорбционный (Pb, Bi, Sb, As, Cu, Zn), O – органоинеральный (Pb, Sb, As) и их сочетания.

Медь связывается органическим веществом почв, карбонатами, гидроксидами Fe и Mn, глинистыми частицами [54]. В дерново-подзолистых почвах при увеличении техногенной нагрузки способность органического вещества к сорбции Cu резко снижается, что сначала приводит к увеличению доли специфически сорбированной, а затем и обменной фракции металла [26]. В восстановительной среде подвижность Cu уменьшается [4]. Количество растворимой Cu в почвах имеет положительную корреляционную связь с валовым содержанием Cu и отрицательную – с pH [59]. В почвах Смоленско-Московской возвышенности связь подвижных форм Cu с ее валовым содержанием положительная и выражена более четко в гумусовых и органогенных горизонтах. Значимое влияние на распределение подвижной Cu оказывают концентрация подвижных форм Mn и Fe, а также окислительно-восстановительные условия. Связанные в оксидах Fe формы Cu более подвижны, чем в оксидах Mn [23].

Валовое содержание Cu в почвах ВАО увеличивается с ростом концентрации оксидов Fe. При низком содержании оксидов Fe (< 3.1%) накопление Cu контролируется щелочно-кислотными условиями. В кислой и нейтральной среде (pH < 7.0) почвы селитренной и постагрогенной зон аккумулируют Cu интенсивнее, чем почвы рекреационной и транспортной. В щелочных условиях (pH > 7.0) с увеличением доли частиц крупной пыли валовое содержание Cu уменьшается. При доле крупной пыли в почвах менее 35% концентрация Cu возрастает одновременно с увеличением пылевой нагрузки.

Подвижность Cu положительно коррелирует с выбросами автотранспорта (рис. 3, В). При значениях удельного выброса автотранспорта менее 1.25 мг/км пробега наименьшая подвижность Cu характерна

для почв низкоэтажной застройки и рекреационной зоны. В остальных зонах при увеличении доли средней пыли подвижность Cu снижается. Если удельный выброс автотранспорта превышает 1.25 мг/км пробега, наибольшая подвижность элемента наблюдается в почвах селитренной зоны, в других зонах она уменьшается с ростом озелененности территории, так как растения поглощают подвижные, доступные для них формы ТМ.

Наиболее интенсивно Cu накапливается в почвах на хемосорбционном барьере, который формируется при значительных концентрациях оксидов Fe (> 3.1%), а также на щелочном барьере, образованном выпадениями карбонатной пыли.

Цинк аккумулируется в поверхностных горизонтах почв, сорбируясь органическим веществом и глинистыми частицами, причем при pH < 7 происходит катионный обмен, а при pH > 7 – хемосорбция [54]. В щелочных условиях Zn адсорбируется наиболее сильно, в этих условиях возможно включение Zn в решетку глинистых минералов [51]. Концентрация Zn увеличивается по мере уменьшения размера частиц и в илстой фракции достигает 60% от валового содержания [41]. Ведущую роль в накоплении подвижных форм Zn играет содержание подвижных форм Mn и Fe [23]. Среди влияющих факторов отсутствуют валовое содержание Zn и органическое вещество [23, 59].

Моделирование распределения валового содержания Zn в почвах ВАО выявило его увеличение с ростом концентраций оксидов Fe в почвах. При малом содержании оксидов Fe (< 3.2%) велика роль щелочно-кислотных условий. В кислых и нейтральных почвах (pH < 7) Zn аккумулируется интенсивнее всего в почвенном покрове селитренной и постагрогенной зон, а в более щелочных условиях – при снижении

запечатанности почв. В почвах с запечатанностью более 38% рост числа частиц средней пыли приводит к более интенсивной аккумуляции Zn, причем при доле этих частиц более 4.1% росту валового содержания Zn способствует увеличение концентраций оксидов Mn.

Подвижность Zn в почвах зависит от типа рыхлых отложений: она наибольшая в почвах на лощинно-балочных песчано-суглинистых и аллювиальных преимущественно песчаных отложениях. В почвы, сформированные на других типах отложений, подвижные формы металла поступают в основном с частицами ила и крупной пыли, при этом подвижность Zn снижается за счет его фиксации оксидами Fe. При относительно высоком содержании оксидов Fe ( $> 2.54\%$ ) и небольшой доле частиц ила ( $< 2.5\%$ ) наибольшая подвижность Zn характерна для почв высокоэтажной жилой застройки, промышленной и транспортной зон.

Таким образом, Zn накапливается преимущественно на хемосорбционном и сорбционно-седиментационном барьерах, где он фиксируется оксидами Fe, Mn и частицами средней пыли. В аккумуляции Zn участвует также щелочной барьер, очевидно, меньшей емкости.

*Кадмий* обладает большим сродством к сере, нежели цинк, поэтому он более подвижен в кислых условиях [51]. В окислительной кислой и нейтральной средах (при  $\text{pH} < 7$ )  $\text{Cd}^{2+}$  подвижен, в сильно-щелочной среде образуются менее растворимые нейтральные и анионные формы –  $\text{CdCO}_3$ ,  $\text{Cd}(\text{OH})_2$ ,  $\text{Cd}(\text{OH})_3^-$  [27]. В кислых условиях водорастворимые, обменные, органоминеральные и непрочносорбированные формы Cd составляют до 88% от валового содержания [48]. Следовательно, миграция Cd в основном контролируется щелочно-кислотными условиями [39]. Доказана сорбция Cd органическим веществом почв [45]. В накоплении Cd также велика роль валовых концентраций Fe, Mn, насыщенности основаниями, глинистых частиц, органического углерода [54].

В почвах ВАО валовое содержание Cd возрастает при увеличении доли частиц средней и мелкой пыли. При доле фракции мелкой пыли 3.6–6.0% Cd аккумулируется более интенсивно в почвах жилой застройки средней этажности, постагрогенной и транспортной зон по сравнению с жилой застройки низкой этажности и рекреационной зоной. В почвах с большим количеством мелкой пыли ( $> 6.0\%$ ) отчетливо проявляется влияние на поведение Cd щелочно-кислотных условий: в кислых и нейтральных почвах ( $\text{pH} < 6.8$ ) он накапливается слабее, чем в более щелочных. При  $\text{pH} > 6.8$  содержание Cd зависит от окислительно-восстановительного режима почв: элемент интенсивнее аккумулируется в периодически подтопляемых, нежели в подтопленных почвах.

Поступление подвижных форм Cd в городские почвы связано в основном с частицами крупной пыли. Подвижность металла в почвах сильно снижается с ростом pH и при переходе от элювиальных и трансэлювиальных ландшафтов к трансаккумулятивным и супераккумулятивным. Дальнейшее снижение подвижности Cd в подчиненных ландшафтах при  $\text{pH} > 6.85$  связана с увеличением запечатанности.

Максимальная аккумуляция Cd в городских почвах определяется его закреплением на щелочном и сорбционно-седиментационном барьерах. Емкость

последнего обусловлена преимущественно фракцией частиц средней и мелкой пыли. Контрастность и емкость этих классов барьеров заметно увеличиваются за счет иммобилизации элемента в подчиненных геохимических ландшафтах.

*Висмут.* Поведение Bi в окружающей среде изучено слабо. Известно, что в окислительных условиях он слабоподвижен. Bi способен образовывать карбонатные соединения ( $\text{Bi}_2\text{O}_2\text{CO}_3$ ), что снижает его миграционную способность [54]. Bi активно сорбируется органическим веществом и оксидами металлов. Установлено, что с аморфными оксидами металлов связано около 25% валового Bi, и примерно столько же – с органическим веществом почв [52].

В почвах ВАО Bi накапливается преимущественно в оксидах Fe, с ростом количества которых увеличивается и его валовое содержание (рис. 3, А). При концентрациях оксидов Fe  $< 3.3\%$  накопление Bi в почвах снижается с ростом содержания бедной этим элементом фракции среднего и крупного песка. Если содержание этой фракции не превышает 2.9%, наиболее высокие концентрации Bi приурочены к почвам жилой застройки и бывшим агроландшафтам за пределами МКАД. При большем количестве среднего и крупного песка ( $> 2.9\%$ ) интенсивная аккумуляция валового Bi в почвах большинства функциональных зон определяется повышенным ( $> 0.04\%$ ) содержанием оксидов Mn. С увеличением числа частиц крупной пыли в почвах этих зон валовое содержание Bi уменьшается.

Подвижность Bi в почвах, также как и Zn зависит от типа рыхлых отложений: наибольшая подвижность характерна для почв на лощинно-балочных песчано-суглинистых и аллювиальных песчаных отложениях. Для почв, подстилаемых остальными типами отложений, характерна иммобилизация Bi за счет фиксации металла оксидами Fe. При относительно высоком содержании оксидов Fe ( $> 2.5\%$ ) Bi сорбируется также органическим веществом почв и оксидами Mn, в результате чего его подвижность снижается. При малых ( $< 0.0645\%$ ) концентрациях оксидов Mn подвижность Bi в почвах селитебной и рекреационной зон выше, чем в промышленной и транспортной зонах.

Максимальное накопление Bi обусловлено формированием в почвах хемосорбционного барьера, емкость которого определяется содержанием оксидов Fe ( $> 3.0\%$ ) и Mn ( $> 0.04\%$ ), которое максимально в верхней части ландшафтно-геохимических катен, где господствует окислительная обстановка. Ведущая роль оксидов Fe и Mn в аккумуляции Bi подтверждается и тем, что наименьшие концентрации Bi выявлены почвах с их незначительным содержанием и высокой долей крупного песка.

*Мышьяк.* As хорошо адсорбируется гидроксидами Fe, илом, накапливается в тяжелых минералах [30]. В глинистой фракции может сорбироваться 27–90% от валового содержания As [31]. Многими исследователями особо подчеркивается роль накопления As минералами, содержащими Fe и Mn [47]. В интервале pH 3–10 количество адсорбированного  $\text{As}^{5+}$  на оксидах Fe уменьшается с ростом pH, тогда как адсорбция  $\text{As}^{3+}$  увеличивается, достигая максимума при pH 9 [53]. В отсутствие гидроксидов Fe и Mn роль главных фаз-носителей As выполняют Al-содержащие минералы и карбонаты [63]. При pH 7–9 миграционная способность As резко уменьшается [54].



Регрессионный анализ данных по ВАО выявил увеличение содержания в почвах валового As с ростом концентрации оксидов Fe. При низком (< 3.6%) содержании Fe<sub>2</sub>O<sub>3</sub> накопление As определяет органическое вещество – наибольшие концентрации As приурочены к многогумусным (С орг. > 5.2%) почвам, сформированным на лощинно-балочных песчано-суглинистых отложениях днищ ручьев и балок, а также аллювиальных песчаных отложениях пойм рек Рудневки, Пономарки, Нищенки, Серебрянки.

Выявлены положительные связи между подвижностью As и содержанием органического вещества, среднего и крупного песка (рис. 3, Г). При содержании песка менее 58% и органического углерода менее 5.8% на его подвижность оказывают влияние структура застройки и принадлежность к функциональной зоне. В почвах селитебной, рекреационной и транспортной зон подвижность As положительно связана с содержанием тонкого песка, и отрицательно – с концентрацией средней пыли.

Отсюда следует, что As аккумулируется в основном на комплексном хемосорбционном и биогеохимическом органоминеральном барьере, хорошо выраженный при концентрациях оксидов Fe > 3.6% и органического вещества > 5.2%.

**Сурьма.** Поведение Sb в ландшафтах также изучено слабо, однако выяснению условий миграции этого элемента уделяется все больше внимания из-за его токсичности и накопления в осадках сточных вод [54]. В геохимическом отношении Sb во многом сходна с As: Sb легко сорбируется гидроксидами Fe и Mn, а также органическим веществом [44, 50, 54]. На сорбцию Sb влияет состояние поверхности сорбента и величина pH: сорбция на гидроксидах Fe достигает максимума в кислом диапазоне и сохраняется до pH 7 [60].

Валовое содержание Sb в почвах ВАО контролируется видом использования территории и свойствами почв: содержанием гумуса, оксидов Fe и Mn (рис. 3, Б). Максимум Sb в почвах промзон обусловлен техногенными выпадениями, в остальных зонах содержание Sb увеличивается с ростом запасов гумуса. Если они меньше 5.6%, основную роль в аккумуляции Sb играют оксиды Fe и Mn, а также озелененность территории.

Подвижность Sb в первую очередь определяется принадлежностью к функциональной зоне: в почвах постагрогенной и промышленной зон она больше, чем в остальных зонах. В первых двух зонах подвижность металлоида наибольшая при доле тонкого песка 26.4–32.0%; при уменьшении или увеличении содержания тонкого песка подвижность Sb уменьшается. При доле тонкого песка менее 26.4% установлена отрицательная связь между подвижностью Sb и степенью озелененности территории. Присутствие песка в количестве более 32% обуславливает наибольшую подвижность металлоида в почвах на лощинно-балочных песчано-суглинистых отложениях и озерно-ледниковых суглинках с прослоями песков.

Накопление Sb в почвах приурочено к участкам локализации комплексного хемосорбционного и биогеохимического органоминерального барьера (рис. 4), обусловленного значительным количеством оксидов Fe, Mn и органического вещества (> 2.9, 0.06 и 5.6% соответственно). Определенный вклад в накопление Sb вносит механический барьер, выраженный на территориях с высокой долей озелененности (бо-

лее 63%). Древесная растительность замедляет скорость ветра в приземном слое воздуха, что приводит к оседанию пылевых частиц, содержащих поллютанты. Кроме того, городские растения активно вовлекают Sb в биогеохимический цикл [64].

**Обобщение результатов моделирования накопления ТМ в почвах ВАО** в зависимости от комплекса факторов и условий показало, что их валовое содержание находится в прямой зависимости от концентрации оксидов Fe и Mn (формирующих хемосорбционный барьер для Bi, Sb, As, Cu, Pb, Zn), органического вещества (органоминеральный барьер для Sb, As, Pb), гранулометрического состава (сорбционно-седиментационный барьер для Cd, Cu) и pH (щелочной барьер для Cd, Cu, Zn). Усиление роли сорбционных барьеров объясняется преобладанием в округе почв с повышенным по сравнению с фоном содержанием Fe<sub>2</sub>O<sub>3</sub>, MnO и пылевых частиц, что согласуется с данными других исследователей [6, 26].

На аккумуляцию Sb и Pb в городских почвах сильное влияние оказывают и иные факторы: накопление Pb происходит преимущественно в подчиненных геохимических позициях, а содержание Sb наиболее ощутимо изменяется в зависимости от вида функционального использования территории, который определяет техногенное поступление элемента. Влияние последнего фактора прослеживается также у Bi, Cd, Cu и Zn. Остальные ландшафтные и антропогенные факторы имеют меньшее значение и выявляются лишь у отдельных элементов: аккумуляция Zn зависит от запечатанности почв, Cu – пылевой нагрузки, Sb – степени озелененности.

В поверхностные горизонты почв большая часть ТМ поступает из атмосферы, поэтому формы и подвижность элементов в выпадениях в значительной степени передаются городским почвам. Анализ подвижности ТМ в зависимости от крупности частиц позволил определить формы элементов в составе тех или иных гранулометрических фракций (табл. 2). Преимущественное поступление Pb со средней пылью, Cd и Zn – с крупной, а As – с песчаной фракцией увеличивает миграционную способность этих металлов в почвах за счет высокой доли подвижных форм элементов в выпадениях, в то время как Cu, As в составе средней пыли, а Sb в мелком песке присутствуют в прочносвязанных формах, которые не извлекаются ААБ с ЭДТА. С ростом содержания оксидов Fe происходит иммобилизация Pb, Zn, Bi. Роль оксидов Mn и почвенного органического вещества проявляется в прочной фиксации Bi и усилении подвижности As. Рост pH и запечатанности почв, изменяющей их окислительно-восстановительный потенциал, напротив, снижает подвижность Cd.

**Пространственное распространение ГХБ в городских почвах.** Карта ГХБ составлена на основе анализа карт физико-химических свойств почв (pH, содержания органического вещества, оксидов Fe, ила, мелкой, средней и крупной пыли, тонкого и крупного песка) с выделами, соответствующими максимальным концентрациям ТМ, а также карт элементарных геохимических ландшафтов и функциональных зон.

При построении карт почвенных свойств использовались их градации, установленные в ходе регрессионного анализа по дендрограммам для отдельных



металлов. Для нижних уровней дендрограмм учитывались значения ландшафтных и антропогенных факторов вышележащих уровней. Так, в дендрограмме, характеризующей дифференциацию Sb в почвенном покрове ВАО (рис. 3, Б), хемосорбционный барьер выделяется по содержанию  $Fe_2O_3 > 2.9\%$  (третий уровень дендрограммы), при этом учитывается, что содержание органического углерода в этом выделе, который включает все функциональные зоны, кроме промышленной (первый уровень), меньше 5.6%.

Локализация сорбционно-седиментационного барьера для Cd и Cu в почвах элювиальных, трансэлювиальных и трансаккумулятивных ландшафтов определялась по содержанию ила  $> 1.5\%$  и концентрации  $Fe_2O_3 < 2.9\%$  при доле крупного песка  $> 10\%$ , а также по содержанию средней пыли  $> 11.1\%$  при доле мелкой пыли  $> 6.0\%$ . Границы хемосорбционного барьера для Bi, Sb, As, Cu, Pb, Zn соответствуют концентрациям  $Fe_2O_3 > 3.1\%$ ; к ним добавляются участки с содержанием  $Fe_2O_3 > 2.9\%$  в элювиальных, трансэлювиальных и трансаккумулятивных ландшафтах; а также локальные границы с  $Fe_2O_3 > 2.9\%$  с одновременным содержанием органического углерода  $> 5.6\%$  во всех зонах, кроме промышленной.

Органоминеральный барьер для Sb, As, Pb формируется в почвах с количеством органического углерода  $> 5.2\%$  и концентрациями  $Fe_2O_3 < 3.6\%$ ; в почвах супераккумулятивных ландшафтов – при содержании органического углерода  $> 4.0\%$ ; а также в почвах всех функциональных зон, кроме промышленной с содержанием углерода  $> 5.6\%$ .

Пространственное распространение щелочного барьера (дендрограммы для Cd, Cu, Zn) определялось по величине  $pH > 6.8$  с одновременным содержанием в почвах мелкой пыли  $> 6\%$  и средней пыли  $< 11.1\%$ . При  $pH > 7.0$  он выделялся для концентраций  $Fe_2O_3 < 3.2\%$ .

Карты отдельных классов почвенных ГХБ строились методом кригинга в пакете Surfer 10. Результирующая карта получена путем оверлея этих карт (рис. 4). Ее анализ показал, что на территории округа широко распространены комплексные ГХБ. При этом наибольшие площади занимает щелочной барьер, который формируется в почвах повсеместно, за исключением участков Кусковского и Терлецкого парков, а

также рекреационной зоны Косинского Триозерья. Остальные классы ГХБ занимают в ВАО меньшие площади. Сорбционно-седиментационный барьер в основном приурочен к транспортной зоне, его образование обусловлено высокими уровнями выпадения пыли. Еще меньшие площади занимает хемосорбционный барьер, локализованный в промзоне «Прожектор», вдоль МКАД и на прилегающих территориях, занятых в основном жилой застройкой низкой этажности. Наименьшие площади характерны для органоминерального ГХБ, который встречается небольшими участками в пределах МКАД (газоны во дворах селитебной зоны и вдоль автомагистралей); а также эпизодически за пределами МКАД – в рекреационной зоне вблизи Косинского Триозерья и в постагрогенной зоне рядом с мусоросжигательным заводом в Руднево.

Изменение емкости почвенно-геохимических барьеров в условиях города. Регрессионные деревья позволяют оценить изменение емкости ГХБ в городских почвах по сравнению с фоновыми. На основе значений в конечных узлах дендрограмм определены валовые содержания ТМ в тех же точках опробования и с теми же факторами техногенной нагрузки, но при физико-химических параметрах фоновых почв. Так, при фоновом количестве в почвах оксидов Fe ( $< 3.2\%$ ), частиц крупного песка ( $> 2.9\%$ ), оксидов Mn ( $> 0.04\%$ ) содержание валового Bi составляет 0.279 мг/кг в низкоэтажной застройке и рекреационной зоне и 0.358 мг/кг в остальных зонах, так как фоновая доля крупной пыли  $> 20\%$  (рис. 3, А). Среднее по округу модельное содержание валового Bi с учетом количества точек опробования, попадающих в указанные конечные узлы, равно  $0.279 \cdot 15 / (15+8+17) + 0.358 \cdot 25 / (15+8+17) = 0.33$  мг/кг (табл. 4). Разница между фактическими и полученными концентрациями характеризует количество ТМ, которое закрепилось в городских почвах на ГХБ за счет увеличения их поглощающей способности.

Изменение характеристик городских почв по сравнению с фоновыми приводит к приращению среднего валового содержания всех элементов на 33–99% (табл. 4, рис. 5). При этом доля закрепленных Bi, Pb и Cd составляет 45–50, Sb и As – 40, Cu – 30, а Zn – 26%. В городских почвах снижается подвиж-

**Таблица 4.** Среднее содержание и подвижность ТМ в поверхностных горизонтах почв ВАО г. Москвы и их изменение за счет увеличения емкости геохимических барьеров

Элемент	Валовое содержание ТМ, мг/кг				Подвижность, %		
	модельное (М)	фактическое (R)	прирост d, %	доля прироста p в R	модельная (M m)	фактическая (Rm)	Rm–Mm
Cd	0.80	1.59	+ 99	50	30.3	37.7	+ 7.4
Pb	33	63	+ 89	48	14.3	9.7	– 4.6
Bi	0.33	0.61	+ 83	46	9.0	11.7	+ 2.7
Sb	1.03	1.71	+ 67	40	1.8	2.1	+ 0.3
As	4.68	7.76	+ 66	40	6.0	4.3	– 1.7
Cu	41	59	+ 44	30	23.9	23.2	– 0.7
Zn	133	179	+ 33	26	11.4	12.3	+ 0.9

Примечание. R, Rm – содержание и подвижность ТМ в городских почвах; M, Mm – рассчитанные по модели содержание и подвижность ТМ при фоновых свойствах почв (мг/кг); прирост  $d = (R-M)/M \cdot 100$  (%);  $p = (R-M)/R \cdot 100$  – доля (%) закрепленного элемента за счет техногенной трансформации физико-химических свойств городских почв.

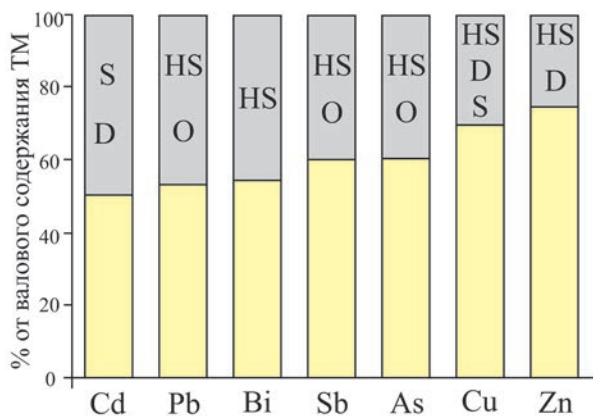


**Рис. 5.** Накопление ТМ в поверхностных горизонтах почв ВАО г. Москвы за счет увеличения емкости (серый цвет) геохимических барьеров: S – сорбционно-седиментационного, HS – хемосорбционного, D – щелочного, O – органоминерального.

ность Pb и As и увеличивается подвижность Cd и Bi, для остальных элементов она остается неизменной (табл. 4). Благодаря физико-химическим свойствам городских почв поступающие из атмосферы подвижные Pb и As частично нейтрализуются и становятся менее доступными для растений. Скорость аккумуляции подвижных Cd и Bi опережает темпы роста их валового содержания, что ведет к увеличению экологической опасности загрязнения городских почв этими элементами. Эти результаты свидетельствуют о том, что в условиях города аккумуляция ТМ на техногенных барьерах необязательно сопровождается уменьшением их подвижности, в некоторых случаях она может даже возрастать. Это объясняется высокой интенсивностью выпадения подвижных форм ТМ из атмосферы, которая превосходит скорость их выщелачивания из поверхностного горизонта почв.

## ВЫВОДЫ

1. В результате техногенного воздействия промышленных предприятий и автотранспорта в почвах ВАО по сравнению с фоновыми возрастают концентрации ТМ с коэффициентами накопления  $K_c$  2.9–7.6. Особенно сильно городские почвы обогащены подвижными формами элементов:  $Zn_{36} > Bi_{22} > As_{10} > Sb_7 > Cu_5 > Cd_{3.1} > Pb_{1.3}$ . Заметно увеличивается по сравнению с фоном подвижность Zn (в 6.7 раза), Bi (4.3), As (2.5), Cu (1.6). У Pb и Cd в выпадениях преобладают труднорастворимые соединения, поэтому их подвижность, напротив, уменьшается.

2. Накопление химических элементов в почвах ВАО контролируется целым рядом факторов, обуславливающих формирование различных классов ГХБ: хемосорбционного (оксиды Fe и Mn – Bi, Sb, As, Cu, Pb, Zn), биогеохимического органоминерального (органическое вещество почв – Sb, As, Pb), сорбционно-седиментационного (гранулометрический состав почв – Cd, Cu) и щелочного (кислотно-основные свойства – Cd, Cu, Zn). Заметное влияние на харак-

теристики ГХБ оказывает функциональная принадлежность территории (Sb, Bi, Cd, Cu и Zn). Формирование комплексных ГХБ обусловлено выпадением карбонатной пыли с повышенным содержанием тонких фракций, внесением в почву торфо-компостных смесей с высоким содержанием гумусовых веществ, подтоплением и запечатыванием почв, нарушающими их газовый и окислительно-восстановительный режимы. При этом аккумуляция ТМ на техногенных барьерах не всегда сопровождается снижением их подвижности, при высокой интенсивности выпадений подвижных форм ТМ из атмосферы, превосходящей скорость их выноса из поверхностного горизонта почв, она может возрастать.

3. Наибольшие площади в ВАО занимает щелочной барьер, встречающийся повсюду, за исключением участков рекреационной зоны. Сорбционно-седиментационный ГХБ приурочен к транспортной зоне, хемо-сорбционный барьер формируется в почвах промзоны Прожектор, вдоль МКАД и на прилегающих территориях. Органоминеральный ГХБ занимает наименьшую площадь – в пределах МКАД это газоны во дворах жилой зоны и вдоль автомагистралей, за ее пределами – небольшие участки рекреации вблизи Косинского Триозерья и бывших агроландшафтов в Руднево. Характерной особенностью городских почв является широкое распространение комплексных ГХБ.

4. Техногенная трансформация физико-химических свойств городских почв (рост pH, увеличение количества органического вещества, оксидов Fe и Mn, утяжеление гранулометрического состава) по сравнению с фоновыми приводит к приращению среднего валового содержания всех элементов на 33–99%. Сравнительная оценка емкости комплексных ГХБ в поверхностных горизонтах городских и фоновых почв показала, что доля закрепленных в городских почвах ТМ составляет 40–50% от валового содержания для Bi, Pb, Cd, Sb и As, 26–30% – для Zn и Cu.

## Supplement to

# Newly identified climatically and environmentally significant high latitude dust sources \*

The central part of the East European Plain, with the wide occurrence of silty soils derived from loess-like sediments and reduced natural vegetation, is a potential aeolian dust source (Bullard et al., 2011; Sweeney and Manson, 2013). However, this region currently lacks observations on dust lifting and transport. The gap for observations in the central part of the East European Plain for potential HLD source updates is filled here with new data in Figs. S2–S4 on the partitioning of elements among the five particle-size fractions separated from the natural soils of a rural area 100 km southwest of Moscow (Fig. S1). The study area (55.12°–55.13°N, 36.21°–36.22° E) belongs to the southeastern part of the Smolensk–Moscow Upland (314 m a.s.l.), representing a marginal area of the Middle Pleistocene (MIS 6) glaciation with moraine topography modified by post-glacial erosional and fluvial processes. The major soil reference group is Retisol (IUSS Working Group WRB, 2015), developed on the loess-like loam. About 50% of the soils in the interfluvial area were subjected to arable farming. A new and unpublished independent dataset on 33 elements in topsoil horizons was obtained with a higher-accuracy ICP-MS/AES analysis (compared to the DC-ARC-AES dataset of Samonova and Aseyeva, 2020).

### **SUPPLEMENT: Central part of the East European Plain: partitioning of chemical elements among five particle-size fractions**

Topsoil (0–10 cm) samples were collected along several transects (Samonova and Aseyeva, 2020), crossing two small erosional landforms—a gully and a balka (Fig S1). The collected bulk samples (n=22) were physically fractionated into five particle-size fractions (250–1000, 50–250, 10–50, 1–10, and <1 μm, n=100). The boundaries among particle size classes were defined according to the Russian conventional fraction groups: coarse and medium sand (250–1000 μm), fine sand (50–250 μm), coarse silt (10–50 μm), medium and fine silt (1–10 μm), and clay (<1 μm). The concentrations of Al, Fe, Mn, Ti, Li, Be, Sc, V, Cr, Co, Ni, Cu, Zn, Ga, As, Rb, Mo, Cd, Sn, Sb, Cs, Pb, Ta, Tl, Bi, Th, Y, Nb, Ba, U, Zr, Sr, and Hf were determined on Elan-6100 and Optima-4300 DV spectrometers (Perkin Elmer Inc., USA) by ICP-AES/MS after the samples were digested in a mixture of acids (NSAM-499-AES/MS method). In physical fractionation, the sand fractions were separated from the bulk soil samples by wet sieving, while the silt and clay fractions were obtained by sedimentation and siphoning during times determined by Stokes' law.

The measured concentrations and element distribution among soil particle-size fractions are shown in Figs. S2, S3, and S4. Because of the different ways in which the elements can occur in the soils (Samonova and Aseyeva, 2020), their distribution among particle-size fractions varies. However, some common patterns in partitioning the elements exist, which allowed us to combine them into several distinct groups (groups A, B, and C). According to our results, most of the elements (Al, Cd, Zn, Sc, V, Tl, Pb, Rb, Ti, Nb, Th, Y, U, Li, Cs, Be, and Ga) showed the progressive accumulation from the coarser to the finer fractions and a maximum of the element concentration in the clay fraction (Fig. S2). The predominant accumulation of metals in the fine fractions was reported earlier for the natural and polluted soils (Hardy and Cornu, 2006; Ljung et al., 2006), suggesting these elements are mainly found in the secondary minerals such as phyllosilicate clays, where they occur as structural components or adsorbed ions. A more detailed study of the element partitioning showed that group A was not homogeneous because of some differences in the distribution of the elements between the two sand fractions, which allowed us to identify several subgroups of the elements. The first subgroup (Al, Cd, Zn, Sc, V, Tl, Pb, and Rb) included the elements partitioned equally between the two sand fractions. The second contained Ti, Nb, Th, Y, and U, with higher affinity to the finer sand fraction, presumably due to the preferential accumulation of stable minerals like rutile and titanite in the fine sand and silt fractions. The third included the lithophile elements (Li, Cs, Be, Ga) associated more closely with the coarser sand fraction than the fine sand fraction.

Unlike group A, the elements from group B had minimal concentrations, not in the sand but the silt fractions, specifically the coarse silt fraction (Cr, Ni, Sn, Bi, Sb, As, Mn, and Co) or both silt fractions (Fe and Mo). However, the particle-size fraction that hosts the major amounts of the elements remained the same (the clay fraction). Most of the elements comprising this group participate in redox reactions and belong to the arsenic group or represent typical elements of the ferro-family. The latter group can occur in soils as structural components of primary ferrous minerals or/and as co-precipitates in secondary Fe-Mn (hydr)oxides. Most of the elements from group B did not concentrate in the sand fractions, except for Mn, Co, and Mo, which, in some cases, displayed two concentration maxima (one in clay and one in sand). Such bimodal distribution was reported earlier and can be explained by the presence of several hosting minerals and phases having high

\* Meinander O. et al. (contribution from Aseyeva E.N., Kasimov N.S., Samonova O.A.) // Atmospheric Chemistry and Physics. 2022; 22:11889–11930.



retention for these metals. In the clay, Mn and Co are associated with secondary clay minerals. However, in the sand, they seem to be bound to newly formed Mn (hydr)oxides. The last group (group C) incorporated stable elements Zr and Hf. Their maximum concentrations were observed in the silt fractions, with a maximum in the coarse silt and a minimum in the coarse and medium sand fractions. Such distribution among different particle-size fractions can be explained by the occurrence of these elements in detrital grains of primary accessory minerals, such as zircon, usually concentrated in the fine sand to coarse silt fractions.

In conclusion, our geochemical study conducted in the central part of European Russia showed that most

of the elements in the upper horizons of typical silty soils displayed progressive accumulation in the finer fractions. However, our data also proves that the preferential association of the elements with particle-size fractions is not limited to the clay fraction. Metals such as Mn and Co tend to have bimodal distribution with concentration maxima in the clay and sand fractions. The partitioning of Zr, Hf, Nb, Ti, U, and Y accumulating in the silt fractions is governed by their presence in the mineral structure of accessory minerals that are stable during transport, physicochemical weathering, and soil formation. In many cases, the coarse silt fraction, with particle sizes of 10–50  $\mu\text{m}$ , is depleted in elements, which can stem from its loessial origin.

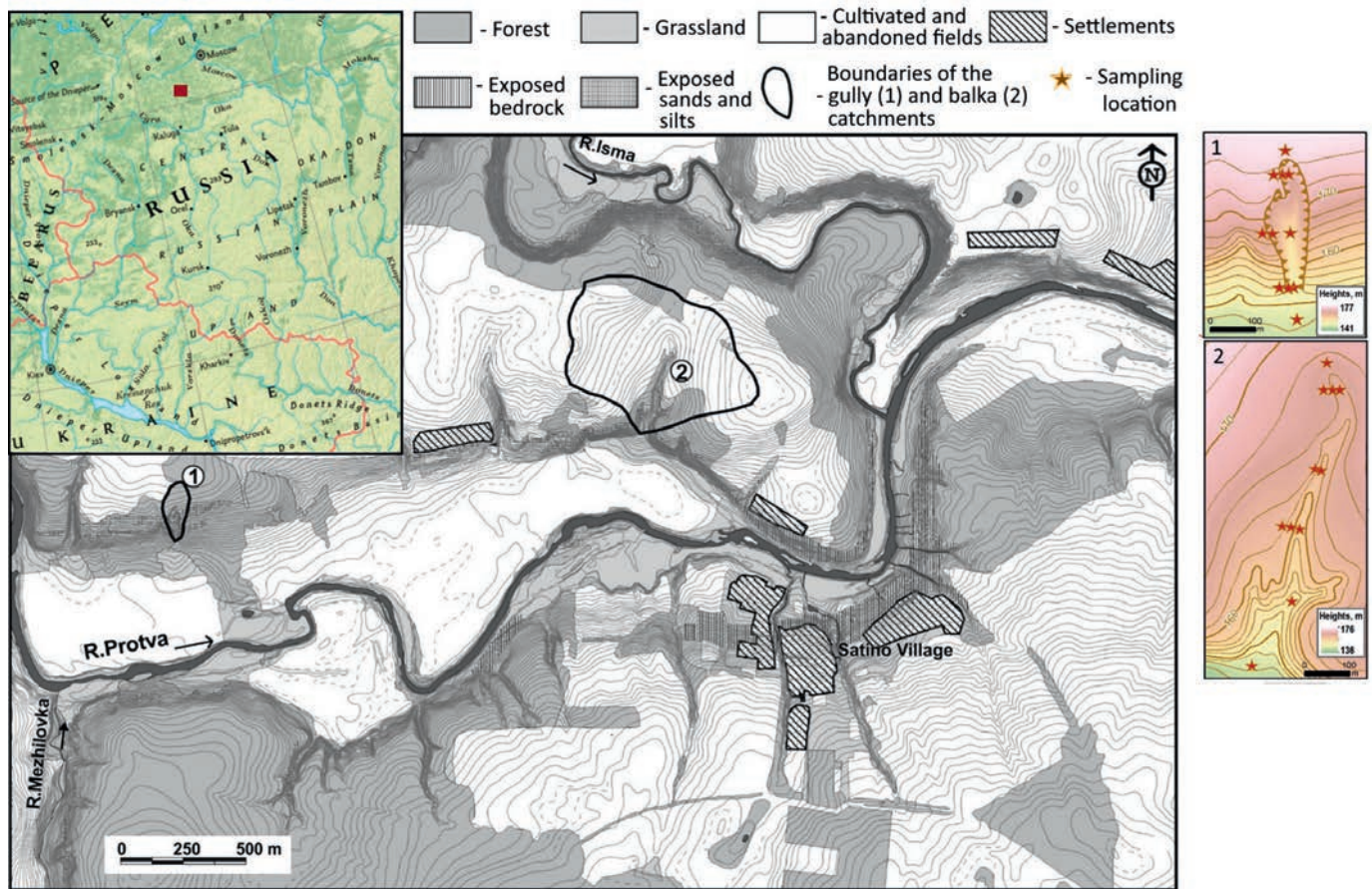


**Figure S1.** Map of the study area in Central European Russia (modified after Panin et al., 2009) with the study objects and sampling locations

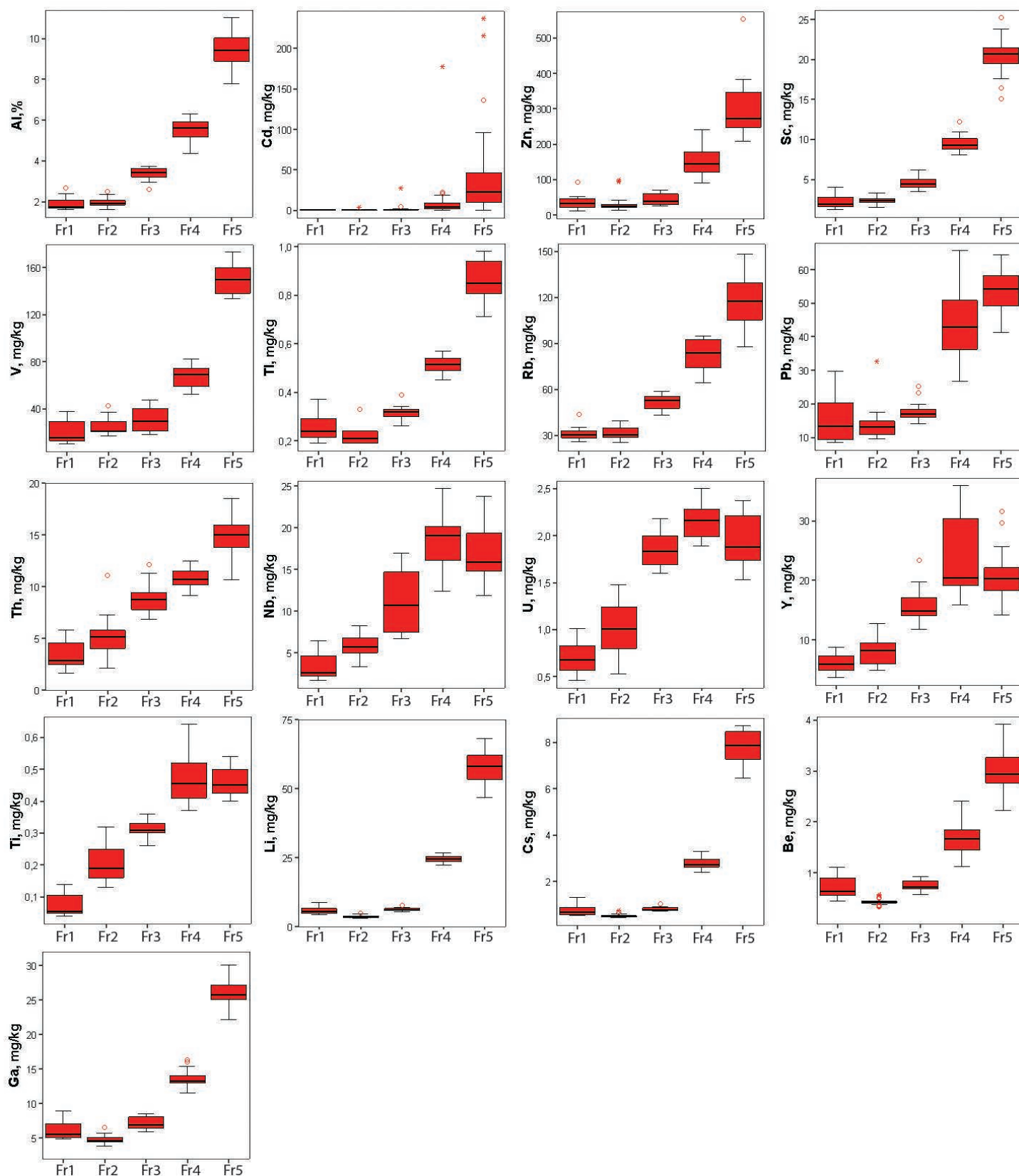


**Figure S2.** The abundances of elements (group A) in the soil particle-size fractions. Median is indicated as a line across the box. X-axis: particle size fractions Fr1 – coarse and medium sand (250–1000 μm); Fr2 – fine sand (50–250 μm); Fr3 – coarse silt (10–50 μm); Fr4 – medium and fine silt (1–10 μm); Fr5 – clay (<1 μm).

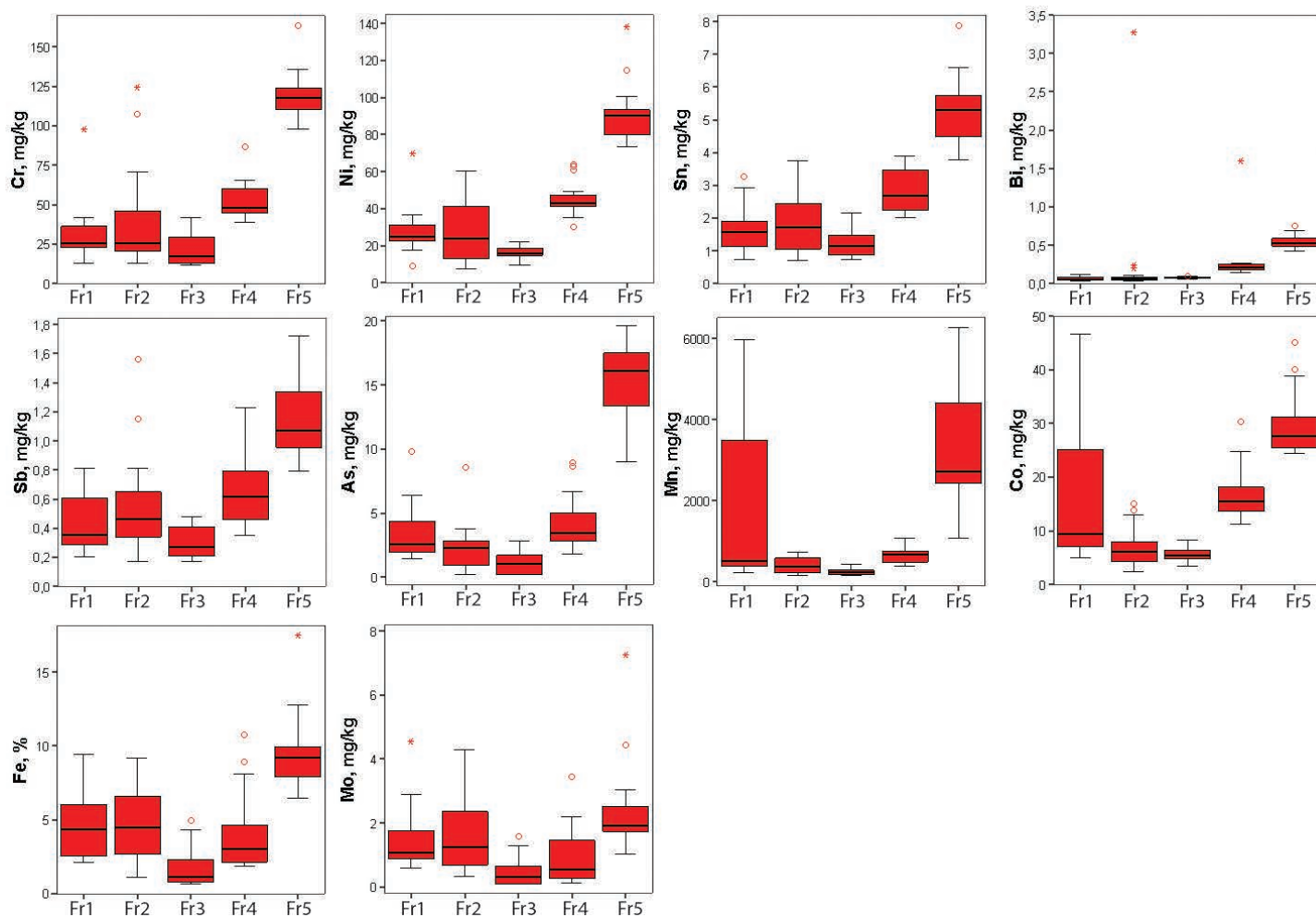


**Figure S3.** The abundances of elements (group B) in the soil particle-size fractions. Median is indicated as a line across the box. X-axis: particle size fractions Fr1 – coarse and medium sand (250–1000 μm); Fr2 – fine sand (50–250 μm); Fr3 – coarse silt (10–50 μm); Fr4 – medium and fine silt (1–10 μm); Fr5 – clay (<1 μm).

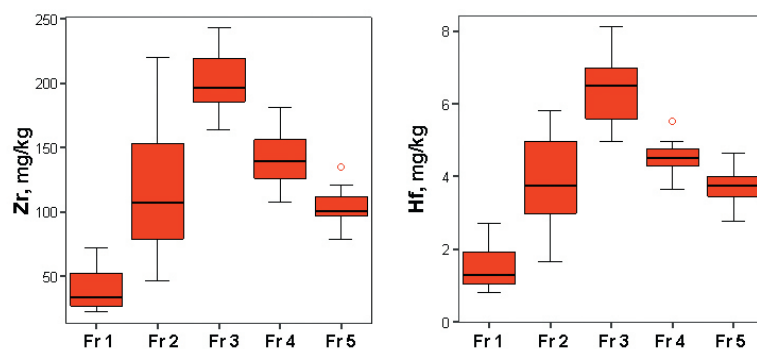


**Figure S4.** The abundances of elements (group C) in the soil particle-size fractions. Median is indicated as a line across the box. X-axis: particle size fractions Fr1 – coarse and medium sand (250–1000 μm); Fr2 – fine sand (50–250 μm); Fr3 – coarse silt (10–50 μm); Fr4 – medium and fine silt (1–10 μm); Fr5 – clay (<1 μm).



## 2. ГОРОДСКИЕ ПОЧВЫ

### Contamination of urban soils with heavy metals in Moscow as affected by building development \*

#### 1. INTRODUCTION

Cities have become the centers of intensive impact contamination of the environment because of high concentration of population and industry within relatively small areas. The ecological situation in many cities of Russia and other countries is close to the critical one (Kasimov et al., 2014). The strongest technogenic impact on the environment and humans is typical for multimillion megalopolises. According to the intensity and area of contamination, they represent specific technogenic geochemical and biogeochemical provinces (Saet et al., 1990; Johnson et al., 2011; Kasimov et al., 2014). Emissions from industrial enterprises and transport into the atmosphere are responsible for the development of geochemical anomalies in other components of urban terrain: snow cover, vegetation, soils, and hydrosphere.

A great number and uneven distribution of the technogenic emission sources in combination with diverse weather conditions create a complex and highly changeable pattern of geochemical fields and geochemical anomalies in the atmosphere of megalopolises. The content of contaminated aerosols in the air is highly variable, because particles of different sizes are transported by air flows to different distances (Hitchins et al., 2000; Baldauf et al., 2008; Hagler et al., 2009). Therefore, in order to assess the average level of contamination of the urban environments and the degree of ecological comfort in separate districts and quarters of the city, it is reasonable to test urban soils that accumulate pollutants for many years.

Distribution of atmospheric pollutants is controlled by the meteorological factors specifying the dispersing and accumulative capacities of the atmosphere (Baklanov et al., 2008; Glazunov, 2014; Demin et al., 2016). A significant influence on them is exerted by the topographical conditions and building patterns. High-rise residential blocks represent a complex system of air-blown multi-surfaces at different heights and with different slopes. Buildings considerably transform the wind regime of the atmospheric boundary layer creating “wind shades” in closed yards and “canyon effects” along large streets (Lifanov, 2006; Moussiopoulos et al., 2010; Samsonov et al., 2015). A decrease in wind speed in closed courtyards leads to the deposition of dust particles enriched in pollutants and their accumulation in the soils; in the wellventilated areas, pollutants are carried away. Thus, depending on their orientation, buildings can either protect the area from pollution, or enhance it.

A multivariate statistical analysis of soil-geochemical data and parameters of building patterns in the cities makes it possible to describe the spatial geo-

chemical heterogeneity of the urban environment and to delineate the zones of predominate accumulation of the pollutants in the soils and other depositing media (Dimopoulos et al., 2004; Tsiros et al., 2009). However, such studies are few in number, and the geometry of urban development in them is insufficiently considered.

The aim of our study was to evaluate barrier and protective functions of city buildings via a joint analysis of the contents of heavy metals and metalloids (HMMs) in the upper horizon of urban soils, physicochemical properties of the soils specifying their capacity to fix HMMs, and parameters of surrounding buildings. Residential area of the Eastern Administrative District (EAD) of Moscow was selected as the key object. This district is characterized by the high technogenic loads on the urban environment and various residential development with high-rise and low-rise buildings arranged in patterns of different densities.

The specific objectives of the study were as follows:

- to assess the physicochemical properties of urban soils and the intensity and spatial patterns of their pollution with HMMs;
- to determine parameters of building patterns – distance to the buildings, their height, and their area on different directions from soil sampling points – with the use of high-resolution satellite imagery and geoinformation analysis; and
- to determine threshold parameters of the artificial relief of the city favoring an increase or a decrease in concentrations of HMMs in urban soils.

#### 2. STUDY AREA

Soils in the southern part of the EAD within Sokolinaya gora, Perovo, Ivanovskoe, Novogireevo, Veshnyaki, Novokosino, and Kosino-Ukhtomskii municipalities (Fig. 1) were studied.

Low-rise (up to five storeys) houses are typical of the old quarters in Perovo, Ivanovskoe, Novogireevo, and Veshnyaki municipalities and of the zone of individual house construction in Kosino-Ukhtomskii municipality. Middle-rise (six-nine storeys) houses are typical of residential areas within the Moscow Ring Road (MRR), and high-rise houses (>ten storeys) are found beyond the MRR in Novokosino and Kosino-Ukhtomskii municipalities (Kasimov et al., 2016). Depending on the mutual arrangement of buildings, the following four development patterns can be distinguished: arranged (along perimeter, in groups, in lines), and isolated (manor-type) patterns.



**Fig. 1.** Sources of technogenic emissions and soil sampling points in the residential zone of the EAD. UTM system. Sampling points in the area of Veshnyakovskaya Street are shown on the inset map. Municipal areas: Sokolinaya gora (I), Perovo (II), Ivanovskoe (III), Novogireevo (IV), Veshnyaki (V), Novokosino (VI), and Kosino-Ukhtomskii (VII). Here and in Figs. 4 and 5 the following industrial zones are shown: A – Sokolinaya gora, B – Prozhektor, C – Perovo, D – Kosino-1, E – Kosino-2, F – Rudnevo.

Motor transport is the major source of pollution of the urban atmosphere and urban landscapes; it contributes to nearly 80% of total emissions (Kasimov et al., 2014). The largest highways are the MRR; Entuziastov and Nosovikhinskoe highways; Slobodnyi and Zelenyi avenues; and Perovskaya, Plekhanova, Yunosti, Veshnyakovskaya, and some other streets. Exhaust gases contain Cu, Pb, and Sr; engine oil is the source of Fe, Mo, Zn, Cu, Pb, and Sb; tire abrasion pollutes the environment with Cd, Mn, Fe, Zn, Pb, Co, Ni, Cr, Cu, and Sb; and wear of brake pads, with Fe, Cu, Sb, Mn, Zn, Ti, and Pb (Limbeck and Puls, 2011; Adachi and Tainosho, 2004; Iijima et al., 2007; Gietl et al., 2010; Quiroz et al., 2013). In the production of bearings, antifriction alloys based on Sn and Pb are used; these alloys also contain Sb, Cu, Cd, Ni, As (Vlasov et al., 2015).

Stationary sources of the anthropogenic pollution are the enterprises of heat power engineering, metal pro-

cessing, machine building, chemistry and petrochemistry, production of building materials, pulp and paper, food, and some other industries, whose emissions contain HMMs. Emissions of thermal power plants contain V, Ni, Pb, Mo, Ge, Cr, Zn, W, Cu, Ag, and Sn; of incineration plants, Bi, Ag, Sn, Pb, Cd, Sb, Cu, Zn, Cr, Hg, and As; of chemical and petrochemical enterprises, W, Hg, Cd, Sb, Sn, Ag, Zn, Cu, Bi, Pb, Mo, and Co; and of mechanical engineering and metalworking plants, W, Mo, Zn, Sn, Sb, Ni, Cr, Cu, Mn, Pb, Co, V, and As (Saet et al., 1990; Demetriades and Birke, 2015). The enterprises are mainly found in the industrial zones, such as Sokolinaya gora, Prozhektor, Perovo, Rudnevo, Kosino-1, and Kosino-2.

The study area belongs to the marginal part of the Meshchera swampy and slightly dissected glaciolacustrine plain slightly inclined toward the southeast and covered by

Quaternary glaciofluvial, alluvial, and anthropogenic sediments of considerable thickness (Shmidt, 2012). The soil cover of residential areas consists of the anthropogenic urbanozems (Urbic Technosols), sealed soils (Ekranic Technosols), replantozems (Urbic Technosols Umbric), and recreazems (Urbic Technosols Humic). In the recreation zone, both native and anthropogenically transformed soils are found: soddy-podzolic and soddy urbopodzolic soils (Retisols) and their gleyed variants and soddy and mucky-peat alluvial soils (Fluvisols). In the postagrogenic zone (former cropland included in the urban territory), postagrogenic agrozems and agrosoddy-podzolic regraded soils are distinguished (Shmidt, 2012; Kasimov et al., 2016).

Southern, western, and eastern winds predominate in this area; thus, the EAD receives pollutants from industrial objects located to the west and southeast of its area. The frequency of calm days varies from 3 to 22%, which means that the EAD territory is sufficiently well blown through with the removal of the pollutants beyond its boundaries. Northeastern air flows predominate in the north and northeast of the studied area, northwestern air flows, in the center; and southwestern air flows, in the south. This should be taken into account in the analysis of the input of the pollutants from the adjacent industrial zones and the atmospheric transport of the pollutants toward neighboring suburban areas (Lifanov, 2006).

### 3. MATERIALS AND METHODS

In order to characterize distribution of the pollutants in the soil cover of the EAD, the geochemical survey of the residential area around the Veshnyakovskaya Street was performed in July 2015. The samples were taken in the nodes of the regular grid; sampling points were spaced apart at about 200 m distance from each other. Mixed soil samples from the surface soil layer (0-10 cm) were taken using an envelope sampling pattern. Overall, 24 mixed soil samples (Fig. 1) were collected. In

addition, data on 28 mixed soil samples obtained in the residential zone of the EAD in summer 2011 were used (Kasimov et al., 2016).

The major physicochemical properties and the contents of HMMs were determined in the samples using traditional methods (Krechetov and Dianova, 2009). The bulk contents of HMMs were analyzed by the mass spectrometry and atomic emission spectrometry with inductively coupled plasma (ICP-MS and ICP-AES methods, respectively) on Elan-6100 and Optima-4300 DV (Perkin-Elmer, USA) spectrometers in the Fedorovsky All-Russia Research Institute of Mineral Resources. For a detailed analysis, data on 14 elements belonging to the first (Zn, As, Pb, Cd), second (Co, Ni, Mo, Cr, Cu, Sb), and third (V, W) hazard classes accepted in Russia (GOST 17.4.1.02-83) and on Sn and Bi were selected. The major physicochemical soil properties – pH and the contents of organic carbon ( $C_{org}$ ), physical clay (particles with diameter  $b$  0.01 mm,  $PM_{10}$ ), and Fe and Mn oxides – were determined in the Eco-Geochemical Center of the Faculty of Geography, Moscow State University.

The contours of buildings were obtained from the OpenStreetMap database. The heights of buildings (H) were determined by visual interpretation of GeoEye-1 satellite image (2015) using the database 2GIS. The area occupied by the individual buildings (S) was determined by a special tool for calculating the geometry (Calculate Geometry, Area) in the software package ArcGis 10.0. The distance (L) from the sampling points to the buildings was measured using a distance tool (Generate Near Table), which allowed also to identify the directions of the lines connecting the sampling points and the buildings.

Building parameters were determined in the zone with radius of 50 m around a sampling point (Fig. 2). The building parameters were averaged ( $\bar{S}$ ,  $\bar{L}$ ,  $\bar{H}$ ) and summed ( $\Sigma S$ ) for each sampling point using one-way ANOVA analysis of variance (Statistica 8.0 software). In addition, paramet-

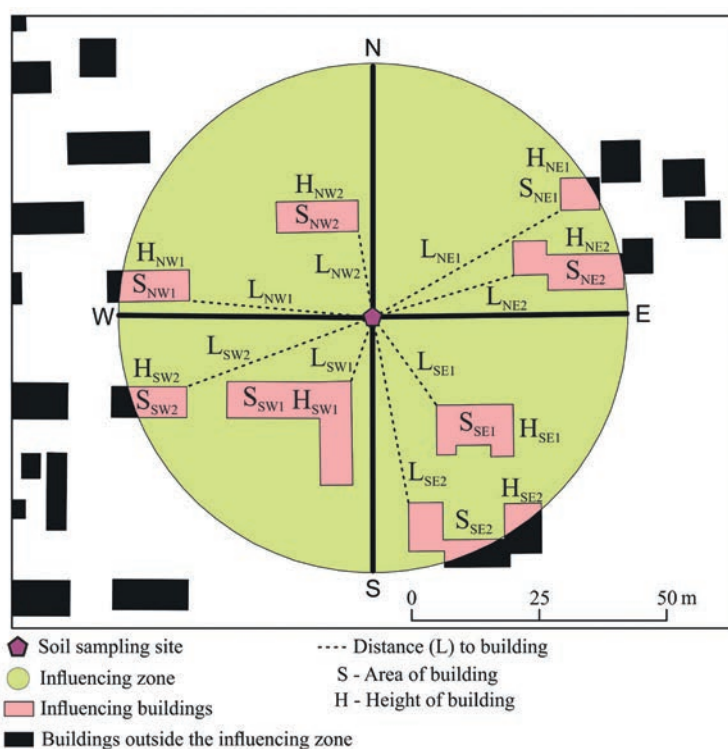


Fig. 2. Example of determination of the building development parameters within the 50-m zone around a sampling point.



ric statistics was calculated for four major azimuthal sectors (northeastern, northwestern, southeastern, and southwestern) of the influencing zone to judge the degree of "closeness" of sampling points with respect to the winds.

The spatial geochemical heterogeneity of the soil cover in relation to building parameters and a complex of soil factors was assessed using S-PLUS software by the method of regression trees. In essence, this method consists of the consecutive division of the data table according to one of the factors into two parts with maximum inner homogeneity (Rawls and Pachepsky, 2002). The homogeneity of the obtained group is characterized by the variability of the forecasted index  $D = \sum_i (y_i - \bar{y})^2$ , where  $i$  is the number of observation in the group, and  $\bar{y}$  is the average value of  $y_i$  according to all the observations. Each of the groups is then divided into two parts, etc. Thus, each of the divisions can be considered as branching along one of the variables—predictors; the structure and number of branches in the final tree depend on the number of division levels.

The division is terminated, if  $n$  is less than the preset value (usually, 6–8), or if testing of the hypothesis about significance of the difference between the averages with the help of t-test gives a negative result. For each final node of the dendrogram, the average concentration of the metal and the coefficient of its variation  $C_v$  are calculated for  $n$  sampling points. This method makes it possible to predict the concentrations of the pollutants in soils upon different combinations of the factors and to evaluate the significance of these factors (Nikiforova and Kosheleva, 2007; Kasimov et al., 2016; Kosheleva et al., 2015).

The anthropogenic geochemical transformation of urban soils was assessed by the enrichment factor  $EF = C_u/C_b$  and dispersion factor  $DF = C_b/C_u$ , where  $C_b$  and  $C_u$  are concentrations of analyzed elements in the background and urban soils, respectively (Saet et al., 1990). Data on the background soils were obtained in the Meshchera National Park located approximately 150 km to the east of Moscow (Kasimov et al., 2016). The total contamination of the soils with HMMs was estimated with the help of the integral contamination index  $Z_c$  widely applied in Russia:  $Z_c = \sum EF - (n - 1)$ , where  $n$  is the number of elements with  $EF > 1$  (Saet et al., 1990). The hygienic hazard of the soil contamination was estimated using the values of maximum permissible concentrations (MPC) accepted in Russia for Sb (4.5 mg/kg) and V (150 mg/kg), or the values of tentatively permissible concentrations (TPC) established for Ni (80 mg/kg), Cu (132 mg/kg), Zn (220 mg/kg), As (10.0 mg/kg), Cd (2.0 mg/kg), and Pb (130 mg/kg) (GN 2.1.7.2041-06; GN 2.1.7.2511-09). The coefficient of ecological hazard  $K_d$  shows by how many times the actual concentration of an element exceeds the MPC or TPC values.

The associations of HMMs characterized by similar behavior patterns in soils and having the same sources were determined with the help of cluster and correlation analyses.

## 4. RESULTS AND DISCUSSION

### 4.1. Physicochemical properties of soils and concentrations of HMMs

Surface horizons of urban soils in the residential zone of the EAD are characterized by a significant increase in pH values up to the neutral (pH 7.5) or even alkaline

(pH 8.6) reaction in comparison with the background soils of the Meshchera National Park. This is related to dust and ash emissions or to the dissolution of various technogenic inclusions in the soils. The pH of concrete, shingle, and clinker brick debris is about 8.0, and the pH of plaster and slate debris is up to 11–12 (Greinert et al., 2013). The technogenic alkalization of the soils and the corresponding change in the conditions of water migration of the elements have been found for urban soils of many Russian and European cities (Birke et al., 2011; Charzyński et al., 2013; Kasimov et al., 2014).

The soils of the EAD are also characterized by the increased contents of  $C_{org}$  and physical clay ( $PM_{10}$ ) particles. Thus, the  $C_{org}$  content in the surface horizon of studied urban soils varies from 0.2 to 9% and averages 3.9%, which is 1.6 times higher than the background level. The soils of the residential zone have a loamy sandy texture with the average physical clay content of 11%; in some sampling points, sandy loamy and silty loamy soils with the physical clay content up to 29.7% have been found. A heavier texture of urban soils on some plots is due to the increased dust load on the surface and to the application of loamy soil material during soil reclamation works by municipal workers (Kosheleva et al., 2018).

The background soils of the Meshchera National Park are depleted of most HMMs (Table 1), which is due to their low concentrations in the sandy parent materials.

A comparison of data on the concentrations of HMMs in urban soils of the EAD and in the background soils at tests to a significant accumulation of many HMMs in the urban soils; the accumulated elements can be arranged into the following sequence according to their  $EF$  values (subscripts):  $Cd_{8.6}W_{6.3}Bi_{5.5}Zn_{5.1}As_{4.2}Cr_{3.8}Sb_{3.6}Pb_{3.5}Cu_{3.0}$ . These geochemical features of urban soils reflect the influence of several pollution sources. The major source is automobile transport, which is confirmed by the data on the elemental composition of road dust and its separate particle-size fractions with the high concentrations of Cd, Sb, W, Bi, and Pb (Vlasov et al., 2015). Some contribution to the soil pollution is caused by emissions from engineering, metalworking, petrochemical, electric power, construction materials, and incineration plants (Saet et al., 1990; Limbeck and Puls, 2011; Vlasov et al., 2015). It is known (Saet et al., 1990) that the ash of waste-incin-

**Table 1**  
Concentrations of HMMs in the surface horizons of soils background soddy-podzolic soils of the Meshchera National Park and in the residential zone of the EAD.

HMMs	Background soils, mg/kg (n* = 10)	Urban soils, mg/kg (n = 52)				EF
		mean	median	min	max	
Cd	0.2	1.8	0.91	0.30	19	8.6
W	0.69	4.3	3.1	0.72	16	6.3
Bi	0.12	0.69	0.35	0.12	4.4	5.5
Zn	37	190	150	46	750	5.1
As	2	8.3	6.3	3	55	4.2
Cr	26	98	70	24	530	3.8
Sb	0.36	1.3	1.1	0.45	3.7	3.6
Pb	14	50	47	13	200	3.5
Cu	20	61	40	13	290	3
Ni	11	27	24	11	67	2.5
Sn	4.4	10	8	1.5	38	2.3
Co	4.3	7.2	7.2	3	11	1.7
V	36	55	56	18	93	1.5
Mo	0.86	1.2	1.1	0.54	2.7	1.4

\*n is the number of analyzed samples.

eration plants is enriched in many HMMs:  $\text{Bi}_{10000}\text{Cd}_{380-770}\text{Zn}_{120-360}\text{Cr}_{10-200}\text{Cu}_{15-64}$  (excess of element concentrations in the ash relative the natural abundances in the upper part of the continental crust is given in subscripts). Therefore, the soils near incineration plants actively accumulate these elements:  $\text{Cd}_{27}\text{Cu}_{11}\text{Zn}_9\text{Sn}_6$  ( $EF$  values are indicated in subscripts) (Birke et al., 2011). Various organic and mineral fertilizers are applied to the soils of the residential zone, including phosphorus fertilizers containing elevated concentrations of Cd, As, Sn, and Pb (Motuzova and Karpova, 2013).

The considered HMMs compose relatively stable associations with similar spatial distribution patterns: Cr-Cd-Cu-Zn-Bi-W-Ni (the coefficient of correlation between the contents of these elements  $r = 0.83-0.95$ , significant at  $P = 95\%$ ), Sb-Pb ( $r = 0.87$ ), V-Co ( $r = 0.76$ ), and Mo-Sn ( $r = 0.43$ ). The former two associations mainly consist of the technogenic elements released into the environment in the course of various anthropogenic (technogenic) activities, whereas the latter two associations represent anionogenic elements (except for Co) that are not accumulated (or only slightly accumulated) in the urban soils.

The integral index of the soil contamination with HMMs ( $Z_c$ ) averages 68, which corresponds to the high contamination level ( $64 < Z_c < 128$ ) (Saet et al., 1990; Kasimov et al., 2016). The high  $Z_c$  values have been identified on 25% of the surveyed territory. Moderate contamination level ( $32 < Z_c < 64$ ) has been found on a larger part (62%) of the territory, and very high contamination level ( $Z_c > 128$ ) has been found on 10% of the territory. Only 3% of the surveyed residential zone is characterized by the low total contamination level ( $16 < Z_c < 32$ ).

The most significant excess of hygienic norms in the soils of residential area of the EAD is typical of Cd (Kd up to 9.5) and As (up to 5.5). Less dangerous contamination levels are typical of Zn (Kd  $< 3.4$ ), Cu ( $< 2.2$ ), and Pb ( $< 1.5$ ). The concentration of Zn exceeds the corresponding TPC on about 23% of the territory; the concentration of As, on 19%; Cd, on 14%, Cu, on 10%, and Pb, on 2% of the territory. The concentrations of V, Ni, and Sb are lower than the corresponding norms.

#### 4.2. The influence of building patterns on the distribution of HMMs in urban soils

Statistical models characterizing distribution patterns of HMMs in soils of the residential area of the EAD have been developed based on the following factors and conditions:

- parameters of the building development within the 50-m radius zone around soil sampling points and also in the four azimuthal sectors (total area under buildings, average area and height of the buildings, and average distance to the buildings);
- characteristics of soil components that serve as the major carriers of HMMs (Vodyanitskii, 2008): the contents of organic carbon ( $C_{org}$ ), physical clay ( $\text{PM}_{10}$ ), and Fe and Mn oxides; and
- acid-base conditions (pH) affecting the migration capacity of HMMs.

The results of the multiple regression analysis (Table 2, Fig. 3) indicate that the building development is one of the major factors affecting the distribution of

HMMs in the urban soils of the EAD. It may both enhance and diminish the degree of soil contamination in dependence of the parameters of the buildings and their arrangement with respect to the prevailing winds.

First, buildings may serve as protective screens on the migration pathways of the pollutants from motor vehicles and industrial objects toward residential yards. In the yards protected from winds, the input of dust enriched in HMMs from the atmosphere considerably decreases with a corresponding decrease in the concentration of the pollutants in the soils. This effect was clearly pronounced for As, Co, Pb, Sb, Sn, and W. For these elements, a positive relationship between their concentrations in the soils and the average distance to the surrounding buildings was observed. With a decrease in the distance to the buildings, the concentration of Sn decreased by three times (Fig. 3), and the concentrations of other HMMs decreased by 1.2–2.8 times, if the buildings were found no further than 23–35.7 m from the sampling points (Table 2). For most of the elements, the protective effect of the buildings was most clearly pronounced in the north-western sector, which is in agreement with the direction of predominant winds.

The protective function of the buildings is also proved by the negative relationship between the concentrations of Cr, Mo, Ni, and Sn and the average height of the buildings. For Cr, the protective effect of the buildings is only seen in the yards between relatively high buildings (with the average height above 20.7 m). In such yards, the concentration of Cr in the upper soil horizon decreases by 1.3 times. The concentrations of Sn and Ni in the soils of the yards decrease by 1.9 times in the case of the average height of the buildings above 15 and 11 m, respectively (Fig. 3). The concentration of Mo decreases by 1.4 times in the case of the average height of the buildings above 7.5–8.5 m. Dense building patterns protect the soils from contamination with As: if the total area under buildings in the given sector within the radius of 50 m exceeds 657 m<sup>2</sup>, the concentration of As in the soils decreases by 1.3 times.

The enhancement of the soil pollution is observed in the case of densely arranged high-rise buildings, when the inner yards serve as “traps” for atmospheric flows. They sharply decrease wind velocity, so that contaminated dust particles precipitate from the atmosphere and are accumulated in the soils. This barrier effect of dense building patterns is especially pronounced for Cd, Bi, and Cu: their concentrations in the soils are positively correlated with the average height of the buildings (the concentrations of these elements increase by 1.5–1.7 times upon an increase in the average height of the buildings from 8.5 to 20 m and more). For Cd and Cu, this effect is only seen in the north-western sector.

The concentrations of Cd, Cu, Zn, W, and Mo display positive relationship with the total area under the buildings within the 50-m radius. Threshold values, upon which the concentrations of these HMMs in the soils increase by 1.2–1.7 times are equal to 323, 760, 760, 1000, and 1300 m<sup>2</sup>, respectively. For Co, Sb, and Pb, a positive relationship of their concentrations in the urban soils with the average area under the buildings in the northeastern and southwestern sectors is observed (Fig. 3). The threshold values are equal to 118, 311, and 323 m<sup>2</sup>, respectively. If the area under the buildings is larger, the concentrations of these pollutants in the soils increase by 1.3–1.7 times.

A negative relationship between the concentrations of Cr and Sn in the urban soils and the average distance to the surrounding buildings also points to the existence of the zone of active fallout of these elements from the atmosphere: when the distance to the buildings is < 25–30 m, the concentrations of these elements in the soils increase by 1.3–1.9 times.

Differences between threshold values of building parameters resulting in the enhancement of the soil contamination with HMMs in the residential zone of the district can be explained by the uneven distribution of HMMs in dust particles of different diameters carried by wind flows to different distances (Hitchins et al., 2000; Baldauf et al., 2008; Hagler et al., 2009). This is confirmed by data on the chemical composition of particle-size fractions of road dust sampled in the EAD (Vlasov et al., 2015). In comparison with the upper part of the continental crust, these fractions are enriched in the following elements:

fraction  $PM_1$   $Cd_{25}Sb_{23}Zn_{15}Sn_{12}Cu_{11}Pb_{10}W_9Bi_8Mo_6$ ,  
fraction  $PM_{1-10}$   $Cd_{23}Sb_{22}Sn_{12}Cu_9Bi_9Pb_8Zn_7Mo_7$ ,

fraction  $PM_{10-50}$   $Cd_{12}Sb_{11}Zn_7Sn_7W_7Cu_6Mo_6Pb_5Bi_5$ ,  
fraction  $PM_{>50}$   $Cd_8Sb_6Zn_5Cu_5Mo_5Sn_5$ .

The absence of As, Co, Cr, Ni, and V in these sequences attests to the insignificant role of the atmospheric input of these elements to the soils of the residential zone.

The level of soil pollution with HMMs in the residential zone of the EAD also varies in dependence on the soil texture. A positive relationship between the contents of physical clay and the pollutants attests to the input of HMMs into the soils together with fraction  $PM_{10}$ , and a negative relationship between them indicates that the atmospheric input of HMMs into the soils takes place with dust particles of larger sizes. With an increase in the portion of fraction  $PM_{10}$ , concentrations of Co, Ni, and V in the soils increase, whereas concentrations of As, Bi, Cd, Sb, Pb, and Sn become lower (Table 2). For Cr, Cu, W, and Zn, this relationship is uncertain, which may be explained by the input of these elements from several sources with different sizes of the emitted dust particles.

**Table 2.** Ranking the parameters of building development and physicochemical soil properties affecting the accumulation of HMMs in the surface horizons of urban soils of eastern Moscow.

HMM	Factors								
	building development (parameters of buildings)				soil properties				
	average distance	average height	average area	total area	pH	C <sub>org</sub>	physical clay	Fe <sub>2</sub> O <sub>3</sub>	MnO
As	4+ NW (> 23 m)	n/a	n/a	4- (<657 m <sup>2</sup> )	n/a	n/a	2-	1,3+	5+
Bi	n/a	3+ (>18.5 m)	n/a	n/a	n/a	n/a	1-	n/a	2+, 3-
Cd	n/a	3+ NW (>20 m)	n/a	2+ NE (>323 m <sup>2</sup> )	n/a	n/a	1-	5-	n/a
Co	3+ (>26.4 m)	n/a	3+ SW (>118 m <sup>2</sup> )	n/a	2-	n/a	1+	2,3+	n/a
Cr	3- (<25.2 m)	4- (<20.7 m)	n/a	n/a	n/a	n/a	1,3-, 2+	n/a	n/a
Cu	n/a	3+ NW (>8.5 m)	n/a	4+ (>761 m <sup>2</sup> )	n/a	n/a	1,3-, 2+	n/a	n/a
Mo	n/a	4- (<8.5 m)	n/a	3+ (>1299 m <sup>2</sup> )	2-	2,5+	n/a	n/a	1+
Ni	n/a	2- (<11.1 m)	n/a	n/a	3-	n/a	4+	1+	2-
Pb	1+ NW (>35.7 m)	n/a	3+ NE (>323 m <sup>2</sup> )	n/a	2-	n/a	4-	n/a	3+
Sb	2+ (>32.7 m)	n/a	3+ (>311 m <sup>2</sup> )	n/a	1-	n/a	2-	4+	n/a
Sn	2+ NW, 3- (>28.1 m)	1- (<15.2 m)	n/a	n/a	n/a	n/a	2-	3+	n/a
V	n/a	n/a	n/a	n/a	2-	n/a	1,2+	3+	n/a
W	3+ NW (>28.1 m; >34.8 m)	n/a	n/a	4+ (>997 m <sup>2</sup> )	n/a	n/a	1,4-, 2+	n/a	n/a
Zn	n/a	n/a	n/a	3+ (>758 m <sup>2</sup> )	n/a	n/a	1-, 2+	n/a	3+
Zc	n/a	3+ NW (>20 m)	n/a	n/a	n/a	4+	1-	n/a	2+, 3-

**Note:** Ranks from 1 to 5 correspond to a decrease in the significance of a given factor; (+) and (-) signs mean positive and negative relations, respectively. In brackets – threshold values of building parameters, upon which the concentrations of HMMs in the urban soils of residential areas of the EAD tend to increase, n/a – not available. Here and in Fig. 3, letters indicate the particular parameters with respect to the azimuthal directions (NW – northwestern, SW – southwestern, and NE – northeastern).



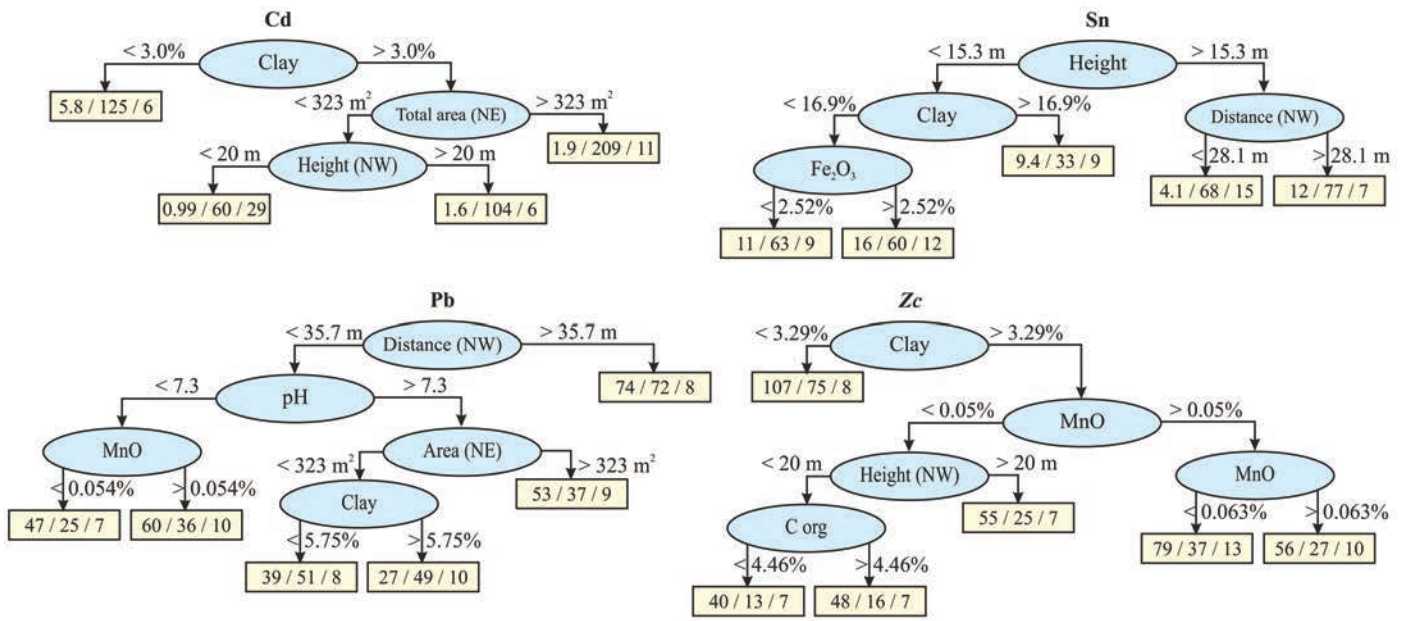


**Fig. 3.** Distribution patterns of Cd, Sn, Pb, and integral contamination index Zc in the soils of eastern Moscow for different combinations of the factors. For each final node (in the boxes), average concentrations of the elements (mg/kg) or Zc values are given; the coefficients of variation Cv and the number of sampling points n are also indicated in the following sequence: mean /Cv / n.



**Fig. 4.** Distribution of the integral contamination index (Zc) in the soils of the residential zone of the EAD.



**Fig. 5.** Manifestation of the (a) protective and (b) barrier effects of the buildings on the accumulation of HMMs in soils of the EAD.



**Table 3**

Occurrence frequencies of the protective and barrier effects of the buildings affecting the accumulation of HMMs in urban soils of the EAD.

HMM	Occurrence frequency <i>f</i> , %	
	protective effect	barrier effect
As	48.1	0
Bi	0	21.2
Cd	0	32.7
Co	15.4	13.5
Cr	13.5	21.2
Cu	0	28.8
Mo	23.1	11.5
Ni	13.5	0
Pb	84.6	17.3
Sb	19.2	36.5
Sn	86.5	13.5
W	59.6	13.5
Zn	0	23.1
Zc	0	13.5

The accumulation of As, Bi, Cd, Co, Mo, Ni, Pb, Sb, Sn, V, and Zn in urban soils also depends on the sorption capacity of the soils related to the presence of Fe and Mn oxides, whereas the accumulation of Mo is controlled by the organic matter ( $C_{org}$ ) content. The content of Co, Mo, Ni, Pb, Sb, and V depends on pH conditions and generally increases in the weekly alkaline medium compared with a neutral one due to immobilization of most HMMs.

The multielemental contamination of the soils ( $Z_c$ ) depends on the contents of fine fractions, organic matter, and Mn oxides (Fig. 3).

Among building parameters, the most significant influence on the soil contamination is exerted by the height of the buildings; the  $Z_c$  value increases by about 10 units in the northwestern direction from the sampling points (Fig. 3). Anomalous concentrations of HMMs are usually found in the yards in close proximity to the highways (Fig. 4). The highest  $Z_c$  values in the soils of the residential zone were found near the Veshnyakovskaya Street in the center of the studied area, near the Perovskaya Street in the northwest, Nosovikhinskoe highway in the east, and Kosinskoe highway in the southeast. All these anomalies are due to precipitation of HMMs from car exhausts and from the emissions of the incineration plant.

To reveal spatial localization of the barrier and trapping effects of residential buildings, we have developed schematic maps (Fig. 5). The intensity of these effects is illustrated by the number of HMMs, whose content in the soils depends on the earlier described parameters of the buildings. These values were determined from the sets of points included in the one or other final nodes of the dendrograms.

The protective effect is manifested for virtually all the studied points, whereas the barrier effect exists in a much lower number of plots. The latter is completely absent in the area of low-rise buildings in the Kosino-Ukhtomskii municipality in the southeast of the territory and most pronounced in the yards between high-rise buildings near the Veshnyakovskaya Street. A more frequent occurrence of the protective effect can be explained by the predominance of line and cluster building patterns in comparison with the perimetral

building pattern creating efficient multielemental barriers (wellshaped yards encircled by the buildings). At the same time, the protective effect of the buildings in the EAD is manifested for a smaller number of HMMs (up to 7 elements) in comparison with the barrier effect (up to 10 elements).

For many of the studied points, barrier and protective effects of the buildings are superposed. For instance, for some elements, the buildings serve as screens hampering element migration, whereas for other elements they serve as traps favoring the accumulation of elements in the yards surrounded by the buildings. This can be explained by different particle-size composition of the emissions from various sources of HMMs.

The spreading of particular HMMs depends on the location and character of their sources. The frequency of occurrence  $f$  of the protective screens and barriers as compared with the total number of sampling points (Table 3) shows that the protective effect is most frequently pronounced for Sn and Pb ( $f = 85\text{--}86\%$ ) and for W and As ( $f = 48\text{--}60\%$ ). These particular elements are rarely captured by the traps. Such a behavior is typical of the coarse fractions of aerosols emitted into the atmosphere from relatively low sources. For these fractions, even low-rise buildings serve as efficient screens. This situation is typical of the entire territory, which attests to the major role of motor vehicles as the sources of Sn, Pb, W, and As. A larger part of emissions from the vehicles does not reach considerable heights, at which the barrier effect becomes more pronounced.

Barrier effect has been found for most of the studied HMMs, though its occurrence frequency for most of the elements is lower than that of the protective effect. Only for Cu, Cd, and Sb, the occurrence frequency is within 29–37%. For the remaining eight elements, it varies within 11–23%. This effect is most pronounced for the fine fractions of the aerosols. As for the integral contamination index  $Z_c$ , both effects are virtually absent, because dust particles responsible for them in this case have different sizes.

## 5. CONCLUSIONS

The soil-geochemical survey performed in the residential area of the Eastern Administrative District of Moscow included evaluation of the barrier and protective functions of urban development by means of a joint analysis of the contents of HMMs in the upper horizon of urban soils, their physicochemical properties, and the parameters of the buildings. The main findings of this study are the following:

- (1) The soils of residential zone in the eastern Moscow intensely accumulate  $Cd_{8.6}W_{6.3}Bi_{5.5}Zn_{5.1}As_{4.2}Cr_{3.8}Sb_{3.6}Pb_{3.5}Cu_{3.0}$  (subscript indicates the  $EF$  value). Most of the urban soils are strongly contaminated with HMMs, which creates dangerous ecological situation. The hygienic norms are exceeded for As, Cd, Zn, Cu, Pb.
- (2) The level of soil contamination in the residential zone is spatially differentiated and depends on parameters of the buildings. At distances of < 23–36 m from the buildings, their total area  $\geq 660$  m<sup>2</sup>, and their average height  $\geq 7.5\text{--}21$  m, these buildings create protective screens for the yards, where the



concentrations of As, Cd, Co, Cr, Mo, Ni, Pb, Sb, Sn, and W in the soils decrease by 1.2–3 times. An opposite effect of the buildings is manifested in the inner yards – traps of HMMs. Such barriers appear at distances of < 25–30 m from the buildings having the average height  $\geq 8.5$ –20 m, average area  $\geq 118$ –323 m<sup>2</sup>, and total area  $\geq 323$ –1300 m<sup>2</sup>. In such traps, the concentrations of Bi, Cd, Co, Cr, Cu, Mo, Pb, Sb, Sn, W, and Zn in the soils increase by 1.2–1.9 times.

- (3) The effects of these two different building patterns are only manifested upon certain directions of air flows. In eastern Moscow, southern, western, and eastern winds predominate. Buildings located in the northwestern sector relative to the sampling point protect it from the aerial pollution. An increase in the height of these buildings and a decrease in the distance to the sampling point favor the reduction of concentrations of As, Cr, Mo, Ni, Pb, Sn, and W in the soils. An opposite effect – the development of the zones of active fallout from the atmosphere – is observed for Cd, Pb, and Co upon an increase in the average or total area of the buildings in the northwestern or southeastern sectors relative to the sampling point. The protective effect of the buildings is more widespread, which may be explained by the predominance of building arrangement in lines or in groups (clusters) in comparison with perimetral arrangement creating wellshaped yards that serve as multielemental traps. For many sampling points, both protective and barrier effects of the buildings can be observed: for some elements, buildings are screens protecting the soils from contamination, whereas for other elements, buildings are barriers enhancing the soil contamination.
- (4) The obtained quantitative data on the influence of building patterns on the accumulation of HMMs make it possible to perform the ecological assessment of construction plans for new urban areas. When planning new residential quarters, the relative positioning and parameters of the buildings should be taken into account; these buildings should not create barriers to the specific priority pollutants coming from local sources. The role of soil properties in the accumulation of HMMs is also great, and this should be considered in the remediation of urban soils. Enhanced accumulation capacity of soil reclamation substrates with the high content of organic matter leads to a strong fixation and accelerated accumulation of HMMs coming from technogenic sources. In this relation, it is necessary to optimize the parameters of reclamation substrates that ensure the sustainable functioning of urban soils and the biological diversity of soil microbiota.
- (5) The results obtained provide the basis for improving local and city-scale air quality models, which take into account deposition of dust particles enriched in HMMs. Geochemical data can be used to verify large eddy simulation models via adjusting deposition parameters to ensure fitting of the calculated and actual areas with an increased or a decreased accumulation of pollutants.

## Main features and contamination of sealed soils in the east of Moscow city\*

### INTRODUCTION

Sealed soils (Ekranic Technosols; Russian: Ekranozems, from ekran—screen, membrane) are urban soils covered by road pavements (asphalt, concrete), buildings, and various constructions. These soils represent a specific form of technopedogenesis (Glazovskaya et al., 1986) and include both human transformed natural soils and artificially created soils developed from cultural layers or redeposited sediments, as well as from translocated, geochemically extraneous, material, and fill substrates (Gerasimova et al., 2003; Prokofieva, 1998). According to the FAO definition (FAO, 2006), Ekranic Technosols are the soils with a low permeability of the surface layer because of its screening or strong compaction under the impact of natural and/or anthropogenic processes. In the classification WRB (2015) Ekranic Technosols are defined as soils composed of technic hard material with properties substantially different from those of natural materials.

In Russia, urban soils have mainly been studied in open (not sealed) areas, and the obtained data have been extrapolated on the entire urban territory with an assumption that the soil properties are similar. The first time of sealed soil study is 1995 (Stroganova & Prokofieva, 1995). In the recent decade, an attempt to distinguish a separate group of sealed soils (Ekranozems) and to include it into the general classification system of Russian soils and parent materials has been made (Prokofyeva et al., 2011). Now the study of sealed soils becomes an immanent part of the ecogeochemical assessment of the state of the soil cover on urban territories. The morphology, physicochemical properties, evolution, and classification of sealed soils are being studied together with those of open soils on urban territories (Levin et al., 2017).

The most evident consequence of soil sealing is the creation of protective screen between the atmosphere and the soil surface, this screen hampers the further development of sealed soils. An increased compaction of sealed soils in comparison with open soils is related to the high technogenic vibration loads. A low permeability of road pavements decreases with time, which eases the inflow of pollutants into the soil. The lifetime of road pavements in cities of the humid zone is about 10 years (Gesentsvey et al., 1985). Every year, the thickness of the paved layer decreases by about 4–5 mm forming up to 160–200 t/ha of the products of its destruction (Manuylov & Moskovkin, 2016).

Soil sealing decreases the evapotranspiration and increases rainstorm runoff, it strongly transforms the heat balance of the soil: The higher the density of constructions, the higher the temperature of the soil surface under asphalt. In hot summer days, the difference in temperatures between sealed and open soils may reach 2–3°K,

the saturation deficit of air diagnosed by a darker color of sealed soils (Burghardt, 2017).

Data on the physicochemical and microbiological properties and the level of heavy metal contamination of sealed soils obtained in some administrative districts of Moscow (Stroganova & Prokofieva, 1995) indicate that the soil under artificial pavements continues its functioning and does not become an abiotic body. The moisture and heat supplies in these soils are sufficient for vegetation growing (Prokofieva, 1998). However, the biological activity of sealed soils is low. These soils are characterized by the specific communities of microorganisms with a dominance of nitrogen-fixing *Azotobacter chroococum*. This causes the low intensity of the nitrogen cycle and, particularly, the low rate of nitrification and denitrification processes. Psychrotrophic microorganisms developing under low temperatures ( $t < 6.5$  °C) prevail, whereas spore-forming bacteria are suppressed (Zabelina & Zlyvko, 2015).

Despite the predominance of sealed soils in the soil cover of large cities (“EEA” 2017), specific features of their functioning and their contamination levels are studied insufficiently. Data on the migration of pollutants in sealed soils of Moscow and on the accumulation and distribution of priority pollutants in their profiles are few in number, the location of anomalous concentrations of organic and inorganic pollutants in the sealed soils of Moscow is unknown. The aim of this paper is to characterize the main properties and the level of pollution of sealed soils in different land use zones of the Eastern administrative district (EAD) of Moscow and to compare them with background natural soils and with open urban soils. The concentrations of both organic (petroleum products (PPs) and benzo[a]pyrene (BaP)) and inorganic (heavy metals and metalloids (HMMs)) are considered.

The particular goals of the study are as follows:

- (i) To compile the map of soil sealing on a scale of 1: 50 000 for different land use zones in the EAD
- (ii) To determine the morphological features and major physicochemical properties (actual increases by 10–20% (Wessolek, 2008). The weakening of gas exchange processes leads to the deficit of acidity pH water, the organic carbon content oxygen and excess of carbon dioxide under the asphalt, where extremely low values of the oxidation–reduction potential can be found. They can be Corg, particle-size distribution, degree of salinity) of sealed soils in land use zones of the district
- (iii) To evaluate the levels of contamination of sealed soils in the EAD with priority pollutants (PPs, BP, and HMMs) and to assess the ecological hazard of their anomalous concentrations

\* Nikiforova E.M., Kasimov N.S., Kosheleva N.E., Timofeev I.V. // Environmental Geochemistry and Health. 2022;44:1697–1711.

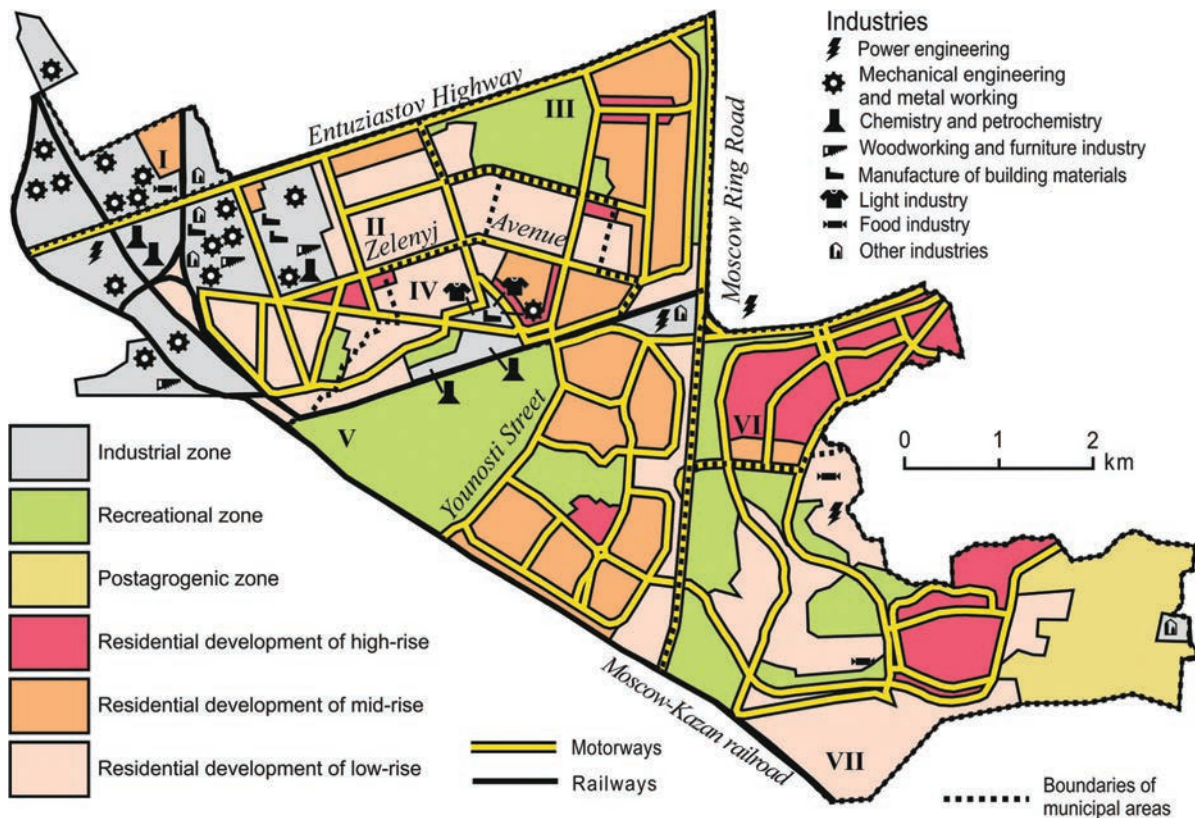


**Fig. 1** Map of the land use zoning of the territory with the main industrial enterprises in the southern part of the EAD of Moscow, scale 1: 50,000. UTM coordinate system. Municipal areas: Sokolinaya gora (I), Perovo (II), Ivanovskoe (III), Novogireevo (IV), Veshnyaki (V), Novokosino (VI), Kosino-Ukhtomsky (VII)

## POLLUTION SOURCES

There are some ways how the pollutants enter into the sealed soils. A certain amount of HMMs and polyarenes is inherited from parent rocks and can be determined from data on their content in undisturbed background soils. Another portion of pollutants were falled out from the atmosphere and accumulated in the soils before they were sealed. After sealing, the stock of pollutants in soils is constantly replenished due to leaching from asphalt and seepage through cracks of polluted storm and melt water.

Motor traffic is the main source of environmental pollution in the EAD of Moscow, its contribution to the total aerial emissions reaches 85–90%. There are also more than 50 factories, which are concentrated in several industrial zones, waste incineration plant in Rudnevo, and two large thermal power stations (TPS) in the EAD (Fig. 1). Despite the decline in the industrial production at the end of the twentieth century (Bityukova & Saulskaya, 2017), the impact of these industrial facilities on the modern eco-geochemical state of soils in the EAD has been significant (Kosheleva & Nikiforova, 2016). Aerial emissions, effluents, and solid wastes enriched in various pollutants enter the upper horizons of sealed soils with rainwater and runoff flows upon fracturing concrete asphalt. With an average lifetime of road covering in cities of the humid zone of about 10 years (Gesentsvey et al., 1985), the first cracks are formed already in the first years after road repairs.

Asphalt coating is another source of pollutants in sealed soils (Legret et al., 2005). It represents an artificial material obtained via compacting asphalt mixture,

sand, mineral powder, and bitumen (Gezentsvei, 1985). Bitumen supplies the bulk of PAHs to sealed soils. It consists of solid and semiliquid residues of oil distillation, which contain many PAHs inherited from the tar and asphaltene of the initial oil or newly formed as a result of industrial production of bituminous materials. The naphthalene type of contamination with a share of naphthalene homologues of 65.2% of the total PAHs is typical for asphalt concrete of road pavements (Nikiforova et al., 2019). Among trace elements in asphalt concrete Mn, Ba, Sr, Zn, V, Ni, Cr, and Co have the highest bulk concentrations (Adachi & Tainosho, 2004; Kupiainen et al., 2005). For Mn, Sr, and Zn a high proportion of mobile forms is typical (von Gunten et al., 2020).

The range of substances and separate chemical elements entering migration flows from technogenic sources is very large. The priority soil contaminants in the EAD are PPs and their derivatives, BaP—the most dangerous carcinogenic substance from the group of polycyclic aromatic hydrocarbons (PAHs), and HMMs (Kasimov et al., 2016). Emitted pollutants are partly dispersed around their sources forming local technogenic geochemical anomalies in different components of urban landscapes (Birke et al., 2011; Đuriš, 2011; Kasimov et al., 2016, 2017; Lianga et al., 2019; Tume et al., 2019; Vodyanitskii, 2009). Their other part is involved in regional geochemical fluxes resulting in the increasing concentrations of these pollutants in the natural media (Chen et al., 2020; Fernández et al., 2000; Foti et al., 2017; Jiao et al., 2021; Nam et al., 2009; Wild & Jones, 1995).

Petroleum products are technogenic carbonaceous substances such as unsaturated hydrocarbons, PAHs, and their derivatives entering the environment in the course



of the work of oil refineries. The greatest danger to human health arises from the inhalation of hydrocarbon solvents (hexane, benzene, toluene, xylene, etc.). They suppress oxidation–reduction processes, disturb tissue respiration, inhibit cardiac activity, and hamper the functions of the liver, digestion, thyroid, and some other organs (Pikovskiy et al., 2015).

When soils are polluted with organic compounds, benzo[a]pyrene (BaP) – a high molecular weight PAH, which causes carcinogenic, mutagenic, and neurotoxic effects on animals and humans, – presents the high risk (Gennadiev & Pikovskiy, 1996; Jacob, 2008; Tarafdar & Sinha, 2017). Benzo[a]pyrene is often considered an indicator of the overall carcinogenic activity of the entire PAH group in the environment (Nikiforova & Kosheleva, 2011). The sources of BaP are emissions from industrial plants, heating and transportation systems, and products of incineration of wastes and various fuels (Alegbeleye et al., 2017; Khalili et al., 1995; Larsen & Baker, 2003). An additional source of PAHs in sealed soils is asphalt concrete pavements, produced on the base of bitumen – an organic binder, which is a solid and semiliquid residues from the distillation of oil. PAHs in their composition were inherited from oil tar and asphaltenes (Pikovskiy et al., 2015).

Vehicle emissions are enriched with a wide range of HMMs, they also are widely applied in various industries. The flow of HMMs from motor vehicles is caused by exhaust gases (Pb, Cu, and Sr), tire particles (Cd, Fe, Mn, Zn, Ba, Pb, Co, Ni, Cr, Cu, and Sb), brake pads (Fe, Cu, Ba, Sb, Mn, Zn, Ti, and Pb), abrasion of the road surface (Ag, Be, As, Zn, W, Cr, V, Fe, Ti, and Co), and windblowing of road dust and soil particles (Fe, Mn, Ti, Pb, Cr, and Sr) accumulating near the curbs (Adachi & Tainosho, 2004; Charlesworth et al., 2011; Limbeck & Puls, 2010; Turer et al., 2001). The chemical composition of industrial emissions depends on the kind of industry and the composition of raw materials, whereas the quantity of exhausts is controlled by technologies of production and purification of emissions. Enterprises producing and distributing electricity emit V, Ni, Pb, Mo, Ge, Cr, Zn, W, Be, Cu, Ag, and Sn; engineering and metalworking industries, W, Mo, Zn, Sn, Sb, Ni, Cr, Cu, Mn, Pb, Co, V, and As; chemistry and petrochemistry, W, Hg, Cd, Sb, Sn, Ag, Zn, Cu, Bi, Pb, Mo, and Co; construction materials–Ag, Pb, W, Sb, Zn, Bi, Mo, Sn, Cu, Ba, Ni, V, Cr, and Sr (Demetriades & Birke, 2015). Incineration of solid domestic wastes is accompanied by the emissions of Bi, Ag, Sn, Pb, Cd, Sb, Cu, Zn, Cr, Hg, and As (Bezuglaya & Smirnova, 2008; Kasimov et al., 2014; Saet et al., 1990).

## MATERIALS AND METHODS

The study is based on the results of soil-geochemical surveys of sealed soils in September 2016 and August 2017 and on the published analytical data on open (not sealed) soils of the EAD (Kasimov et al., 2016). Seven municipalities – Sokolinaya Gora, Perovo, Ivanovskoe, Novogireevo, Veshnyaki, Novokosino, and Kosino-Ukhtomskii – in the southern part of the EAD were investigated. This territory belongs to southern taiga landscapes of the Meshchera lowland and represents a vast outwash plain on the Moskva–Klyaz'ma interfluvium with absolute heights of 150–160 m a.s.l. It is composed of glaciofluvial and ancient alluvial sediments (Ecological atlas of Moscow, 2000).

Eco-geochemical study of sealed soils was preceded by land use zoning of the EAD (Kasimov et al., 2012) with the use of high-resolution satellite images (2.4 m, Quick Bird). Five land use zones were distinguished according to predominant type of land use: industrial, traffic, residential (low-, middle-, and high-rise), recreational, and post-agrogenic (Fig. 1). The latter is a former agricultural land currently built up with residential areas.

Sealed soils were studied in pits and trenches made by various municipal services. The upper part of the soil profile with a thickness of 15–50 cm located under the asphalt and the underlying sand–gravel beds was sampled. Overall, 47 mixed samples composed of 3–4 individual ones were taken from 35 soil pits. The morphological structure of the profile of Ekranozems was studied in four overburden pits with a depth of 1.5–2.0 m. When describing soils, the amount of anthropogenic inclusions (artifacts) was assessed visually (in % of the total mass of fine fractions). The sampling procedure was the same for all types of soils, then the samples were dried, ground, and sieved, according to conventional preparation methods. For comparison, we used data on 49 surface samples of open (not covered with asphalt) soils and on ten soil samples taken in the undisturbed Meshchera lowland region to the east of Moscow (Kasimov et al., 2014). The physicochemical and chemical properties of sealed and open urban soils and background natural soils were determined in the Eco-Geochemical Center of the Geographical Faculty of Moscow State University: actual acidity (pH water) in an aqueous suspension by the potentiometric method (pH340i/set), soil organic carbon ( $C_{org}$ ) by the method of I.V. Tyurin with a titrimetric ending, and particle-size distribution by the laser diffraction method (“Analysette 22. Laser klasse 1” granulometer, Fritsch), and soluble electrolytes, according to the electrical conductivity of water extract on SevenEasy S30 (Mettler Toledo) conductivity meter. The contents of PPs and BaP in the soils were analyzed by the of luminescent bituminological and low-temperature spectrofluorimetry methods in the Laboratory of Carbonaceous Substances of the Biosphere at the Geographical Faculty of Moscow State University. The bulk contents of HMMs were determined by the inductively coupled plasma mass spectrometry (ICP-MS) and atomic emission spectrometry (ICP-AES) methods in the N.M. Fedorovskiy All-Russia Institute of Mineral Raw Materials on Elan-6100 and Optima-4300 (PerkinElmer, USA) spectrometers. For a detailed analysis, 11 elements belonging to the first (Zn, As, Pb, and Cd), second (Cr, Cu, Ni, and Sb), and third (Ba, V, and W) hazard classes according to Russian State Standard (Vodyanitskii, 2016), and Sn and Bi were selected.

Processing of soil-geochemical data included calculations of the contamination factor coefficients of pollutant accumulation in sealed soils relative to their open analogs  $S = Cs/Cu$ , where  $Cs$  and  $Cu$  are concentrations of pollutants in the sealed and open soils, respectively, and the integral soil contamination index  $Zc = \sum CF - (n-1)$ , where  $CF = Cs/Cb$  is the contamination factor for particular HMM in the sealed soils relative to their background content  $Cb$ , and  $n$  is the number of elements with  $CF > 1.0$  (Saet et al., 1990). This index has five grades denoting contamination level and ecological hazard: low, nonhazardous ( $Zc < 16$ ), moderate, moderately hazardous ( $16 < Zc < 32$ ), high, hazardous ( $32 < Zc < 64$ ), very high, very hazardous ( $64 <$

$Z_c < 128$ ), and maximum, extremely hazardous ( $Z_c > 128$ ) (Kasimov et al., 2016; Saet et al., 1990). Mapping sealed soils contaminated with PPs, BaP, and HMMs were performed using ArcGIS 10 software. The ecological and geochemical assessment of soils was performed using the maximum permissible concentration (MPC) of a given element according to international hygienic norms (Crommentuijn et al., 2000).

Mapping sealed soils included an unsupervised classification of multispectral QuickBird images with determination of the proportion between open surfaces and surfaces covered with asphalt and buildings (Khaybrahmanov et al., 2017). Within each of the land use zones, the areas with the low, moderate, and high degree of soil sealing were determined, the particular criteria were specific of each land use zone. In the ArcGIS software, satellite images with predetermined major classes (water objects, vegetation), and anthropogenic objects (asphalt pavements, buildings) were compared with polygons of the land use zones (land use classes). For each of the latter, the number of pixels of particular classes was calculated. Their sum gave us the areas occupied by each of the land use classes. The percent of sealed soils in the total area of the land use zone was calculated.

## RESULTS AND DISCUSSION

### Soil sealing in the EAD

The map of soil sealing in the southern part of the EAD (Fig. 2) demonstrates the distribution of sealed soils in different land use zones of the district. Colors on the map indicate land use zones; the darker the color, the more soils are sealed.

The highest degree of sealing (> 70%) is typical of the industrial and traffic zones, and the lowest (< 10%) is observed in the recreation zone. High percent of sealed soils is also typical for the old parts of the EAD: industrial and residential zones of Perovo with the high building density. Moderate degree of sealing is typical of the new-rise multi-story residential areas in Novokosino and Kosino-Ukhtomskii municipalities. The low degree of sealing corresponds to older residential areas with a high and medium degree of greenery adjacent to the Kusk-

ovsky Park. The map of soil sealing for the EAD has a lot common features with the map of soil sealing in the Southeastern administrative district (SEAD) of Moscow (Strogonova and Prokofieva 1995). The high percent of sealed soils (up to 90%) in the SEAD is observed in the industrial zone. In the natural (recreation) zone and agricultural zone of the SEAD, the percent of sealed reaches 20%, in residential areas, it varies from 20 to 75%.

### MORPHOLOGY AND PHYSICOCHEMICAL PROPERTIES OF SEALED SOILS

Soils sealed under road pavements may include virtually all types of soils found in the city. The morphologies of their profiles are diverse. In the most strongly transformed types of sealed soils in the industrial or traffic zone, natural genetic horizons may be completely absent. Such soils are composed of human-made (technogenic) layers. As a rule, the profile of sealed soils includes a combination of the artificial layers differing in their color and thickness. Their boundaries are usually smooth and sharp. The laying of asphalt is often accompanied by the removal of the topsoil, or its replacement with an artificial substrate. Other genetic horizons of the profile also become transformed, which complicates their morphological study and identification.

The analysis of the profile of sealed soils includes identification of the diagnostic horizons (Fig. 3) differing not only in their morphological features but also in their chemical and physicochemical properties (Prokof'eva et al., 2014). Soil names are directly related to the presence, thickness, and specific combination of the horizons in the studied profile.

Asphalt concrete (ASC) as the most common road pavement is the artificial construction material consisting of gravels and sand with admixtures of fine mineral powder and organic bitumen (Gesentsvey et al., 1985). The ASC layer is usually underlain by sandy gravelly pads (SGPs) of different thickness.

The major diagnostic horizon of sealed soils is the urbic horizon UR. This is a synlithogenic horizon forming in the course of regular input of various substances onto the surface of urban soils, including deposition of aerosols from the polluted aboveground atmosphere. Urbic

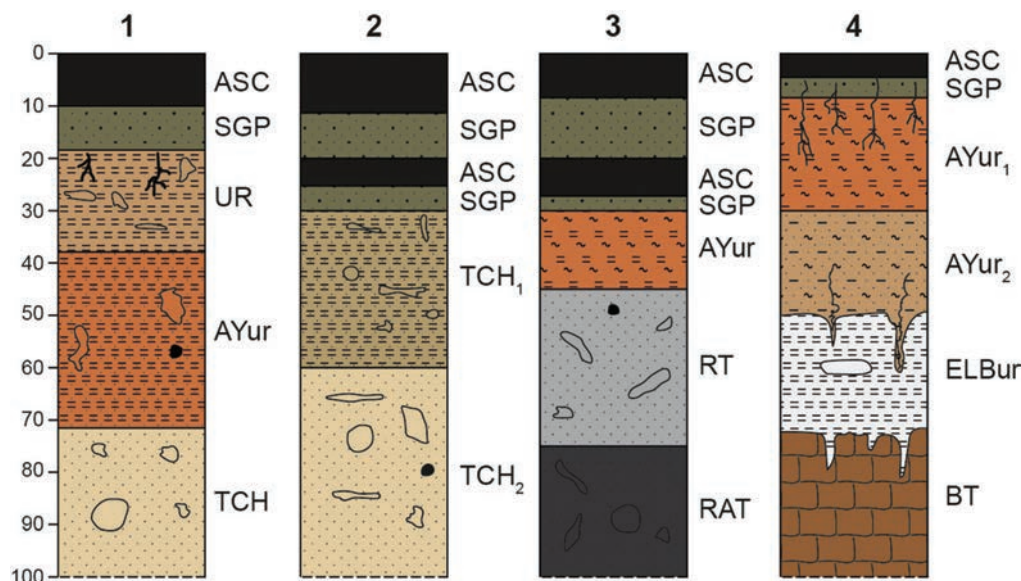
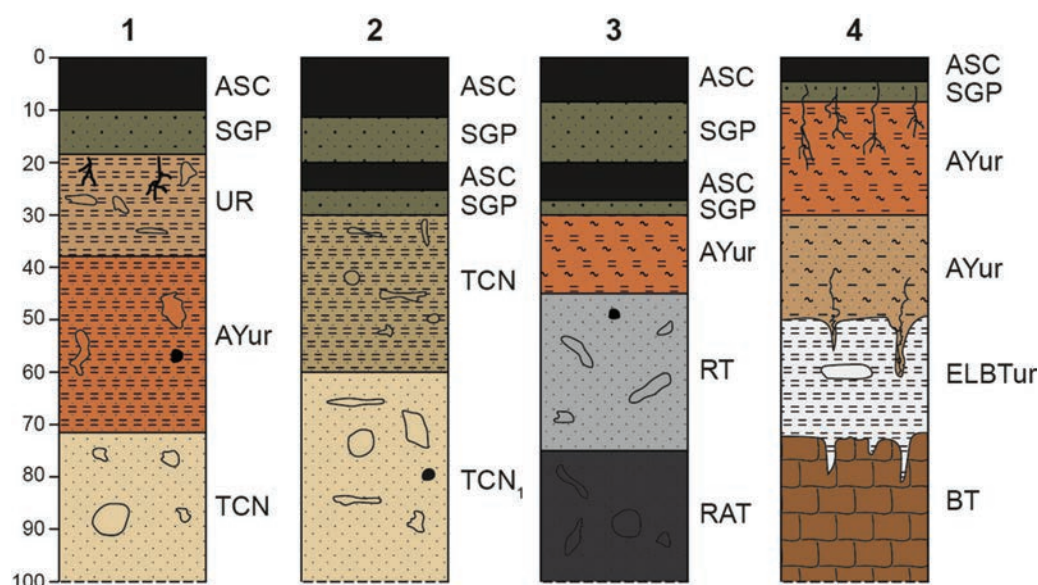


Fig. 2 Sealing degree of soil cover in various land use zones of the southern part of the EAD in Moscow, scale 1: 50,000





**Fig. 3** Morphological profiles of sealed soils in various land use areas of the EAD of Moscow: 1–Urban Ekranic Technosol in Kosino-Ukhtomsky District, Ukhtomsky settlement, low-rise residential area; 2–Ekranic Technosol (Toxic) in Perovo District, industrial zone; 3–Technic hard material over Eutric Albic Retisol (Areninovic, Technic) in Veshnyaki District, traffic zone; 4–Technic hard material over Mollic Someric Umbrisol (Areninovic, Technic) in Novokosino District, Triozerye, recreation area. Diagnostic horizons and anthropogenic layers (WRB indices are indicated in brackets): ASC–technic hard material (asphalt); SGP–Sand and gravel pad; UR (Au)–urbic; AYur (Au)–mollic horizon with artifacts ( $\leq 10\%$ ); TCH (Cu) – mixed human disturbed parent material with artifacts ( $\leq 20\%$ ); RT (O)–technogenic layer with organic material ( $\leq 30\%$  (peat-containing mixture); RAT (A)–technogenic layer with organic material ( $\leq 30\%$ ); ELBur (EBt)–eluvialilluvial horizon with urbic properties; BT (Bt), Illuvial horizon

horizons have a continuous character, gray or brown-gray color, predominantly coarse texture with a considerable silt content, an increased water content in its upper part immediately under asphalt pavement, and more than 10% artifacts (construction and household wastes). Effervescence with HCl is usually observed.

The humus horizon with urbic properties (AYur) is formed in the upper part of soil profile. It has an even gray-brown or dark brown-gray color, crumb or granular–crumb structure (often, with features of subhorizontal plating), loamy texture, abundant coaly particles. It is slightly dry or wet (immediately under the asphalt) and contains relatively loose ochreous Fe and dark gray Mn segregations and anthropogenic inclusions ( $< 10\%$ ), usually, it is slightly effervescent.

The upper UR and AYur horizons of sealed soils in the EAD are characterized by the slightly alkaline reaction, sandy loamy, or silty loamy texture, and an increased content of  $C_{org}$ , whereas the background natural soils are acid, loamy sandy, and have a low  $C_{org}$  content (Table 1). The highest  $C_{org}$  content is typical of the sealed soils in the recreation zone, and the highest pH values are typical of the sealed soils in the residential and industrial zones. Judging the mean values of electrical conductivity (EC) of the soil solution, these soils are nonsaline despite regular application of deicing mixtures and fertilizers to the surrounding open soils. The average EC in sealed soils is  $0.22 \text{ mS cm}^{-1}$ , which is 13.6 times lower than the allowable level of  $3.0 \text{ mS cm}^{-1}$  (Ganjara 2005).

In comparison with neighboring open urban soils, sealed soils are impoverished in  $C_{org}$  (by 1.8 times), have approximately the same reaction (pH 7.5), and do not accumulate salts in the upper horizons (Table 1).

Similar values of parameters were obtained by other researchers studying morphology and properties of sealed soils in Moscow (Prokofieva, 1998; Stroganova

and Prokofieva 1995). They found that in some urban districts, the acidity of sealed soils is considerably lower than that in the background zonal soddy–podzolic soils (Albic Retisols), the pH of sealed soils is in the range of 6.5–9.3. The  $C_{org}$  content in sealed soils varies from 0.5 to 6.0%, which is higher than the range for the zonal natural soils. The soil texture is loamy sandy or sandy loamy. Anthropogenic inclusions (artifacts) may comprise up to 50% of the soil mass.

#### Contamination of sealed soils with petroleum products, benzo[a]pyrene, and heavy metals and metalloids

According to the level of pollution with BaP and PPs, sealed soils strongly differ from the background natural soils (Table 1). The distribution of the pollutants in them is uneven, and the average contents of the pollutants are considerably higher. The average BaP content in sealed soils is 9.6 times higher than the maximum permissible concentration (MPC,  $0.02 \text{ mg kg}^{-1}$ ), the background content of BaP in the natural soils is exceeded by 56 times. The qualitative composition of PPs in the sealed soils is described as a mixture of oxidized substances with the high content of resinous components (Pikovskiy et al., 2015). The allowable PPs content ( $300 \text{ mg kg}^{-1}$ , Ganjara, 2005) in the sealed soils is exceeded by 9.5 times. The highest degree of BaP pollution is typical of the sealed soils in the industrial zone, and the highest degree of PPs pollution is typical of the sealed soils in the traffic and recreation zones. In general, the degree of contamination of sealed soils with BaP and PPs is 3.4–3.5 times lower than that of open urban soils. The slight accumulation of BaP in sealed soils is explained with the predominance of low molecular weight PAHs in them (Nikiforova et al., 2019).



**Table 1.** Physicochemical and chemical properties of the upper horizons of background soils, sealed soils, and unsealed soils in the EAD of Moscow

Index	Depth, cm	C <sub>org</sub> , %	pH <sub>water</sub>	EC, dS m <sup>-1</sup>	< 0.01 mm, %	BaP, mg kg <sup>-1</sup>	PP, mg kg <sup>-1</sup>
Background soddy-podzolic soils of Meshchera (n* = 10)							
Mean	0–25	0.73	4.9	0.03	12.0	0.0034	0.00
Industrial zone of EAD (n = 9)							
Mean		1.62	7.45	0.172	29.9	0.366	1923
min–max	3–55	0.24–3.32	6.34–8.1	0.080–0.334	9.4–41.1	0.004–1.68	42–10,000
Traffic zone (n = 11)							
Mean		2.03	7.37	2.49	32.6	0.110	3983
min–max	4–128	0.0–7.01	6.16–8.65	0.083–1.14	4.1–53.7	< 0.001–0.934	10–30,800
Residential zone (n = 21)							
Mean		1.57	7.72	0.265	29.6	0.119	716
min–max	5–120	0.03–5.88	6.41–9.37	0.086–1.03	11.5–57.2	< 0.001–1.13	< 5–5000
Recreational zone (n = 6)							
Mean		2.99	7.16	0.086	30.8	0.194	4188
min–max	5–60	0.75–6.34	6.49–7.70	0.059–0.116	10.5–62.1	< 0.001–0.54	< 5–14,500
All ekranozems of EAD (n = 47)							
Mean		1.87	7.51	0.221	30.5	0.169	2155
min–max	3–128	0.3–7.01	6.16–9.37	0.059–1.138	4.1–62.1	< 0.001–1.68	< 5–30,800
Unsealed soils of EAD (n = 49)							
Mean	0–20	3.35	7.8	0.48	33.0	0.644	10,000**

\*n–Number of samples

\*\*According to (Pikovskiy et al. 2012)

Our data are in agreement with the results obtained for sealed soils of the city of Vladimir, in which the average content of PPs in the upper horizons of sealed soils in different land use zones varies from 560 to 910 mg/kg, corresponding to the moderate degree of pollution (Zabelina & Zlyvko, 2015).

The concentrations of most HMMs in the sealed soils of EAD are two to four times higher than their concentrations in the background natural soils. V, Sn, Cr, and Ba are an exception, as their concentrations in the sealed soils are close to the background concentrations. In comparison with open soils, the accumulation of HMMs in sealed soils is less pronounced, whereas the distinctions between sealed soils of different land use zones are better manifested (Table 2). Thus, As, Ba, Cr, Cu, Ni, Pb, Sb, and Sn are more intensely accumulated in the sealed soils of the industrial zone. As is also accumulated in the sealed soils of the traffic zone, V, in the sealed soils of the residential zone, and Cd, Zn, and W, in the sealed soils of the recreation zone. In the industrial zone, the concentrations of Cu, Sb, and Pb are even higher than those in open soils, the concentrations of Ni, As, Sn, Ba, and W are close in the sealed and open soils. These proportions between the elements are observed under high anthropogenic load and considerable degree of soil sealing, which prevents infiltration of snowmelt and rainwater into the sealed soils and the leaching of HMMs from them.

In the industrial zone with the high degree of sealing, HMMs tend to accumulate more actively than in the sealed soils of other zones, because large amounts of HMMs emitted by plants and factories are transferred by runoff flows into the soils through cracks. Low S coefficients are typical of a number of HMMs in the sealed soils of other zones that are well drained owing to small sealed areas, which is consistent with the results of a research in the Polish city of Torun (Charzynski et al., 2017).

A comparison of the HMM concentrations in the sealed soils of the EAD with MPC levels (Crommentuijn et al., 2000) indicates that the norms for Ba and Cu are exceeded in sealed soils of all the land use zones. Besides, in the industrial zone MPC levels are exceeded for Sb and Pb.

#### SPATIAL DISTRIBUTION PATTERNS OF THE POLLUTANTS

The spatial pattern of pollution of the upper horizons of sealed soils with organic pollutants is displayed on two maps of the EAD (Fig. 4). In relation to the very high variability in the PPs and BaP concentrations in these horizons, the interpolation of data obtained seems to be unreasonable. These data are directly indicated as circles of different diameters (graduated symbols) in the sampling points. The polygons shown on the map reflect the degree of soil sealing in different land use zones of the EAD of Moscow (Fig. 2).

Several contrasting technogenic (human-induced) anomalies of PPs with the concentrations up to 14,500 mg kg<sup>-1</sup> in the upper part of sealed soils have been revealed. These concentrations exceed the allowable level by 17–48 times. Such anomalies are mainly allocated to sealed soils of the traffic zone. The maximum concentration of PPs (30 800 mg kg<sup>-1</sup>) has been identified in the sealed soil under the Nosovikhino highway. In the sealed soils of the industrial and residential zones, the high levels of PPs pollution have been found for the areas with the high and moderate degree of sealing, not far from the major highways. The level of contamination of sealed soils in the recreation zone with PPs is two times higher than that in the industrial zone, which is explained by the proximity of many parks to the major highways. The minimum average content of PPs (716 mg kg<sup>-1</sup>) was found in the sealed soils of the residential zone.

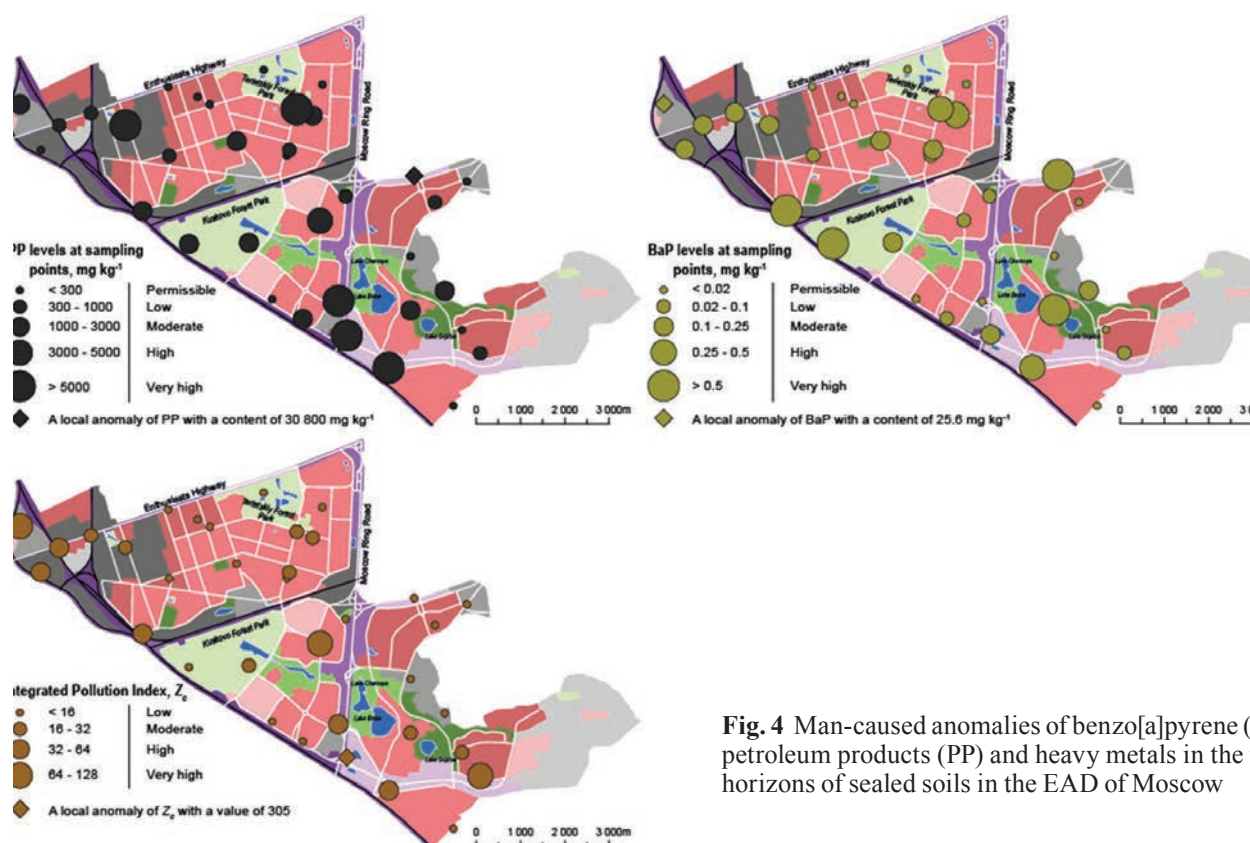


Fig. 4 Man-caused anomalies of benzo[a]pyrene (BaP), petroleum products (PP) and heavy metals in the upper horizons of sealed soils in the EAD of Moscow

Spatial distribution of BaP in the surface horizons of sealed soils (Fig. 4) is close to the distribution of PPs, because both organic pollutants are hydrocarbons of the same origin. However, some differences between them should be noted. Thus, maximum concentrations of BaP are found in the sealed soils of the industrial zone (15–20 MPC, on the average). An extremely high concentration of BaP ( $25.6 \text{ mg kg}^{-1}$ ) exceeding the MPC level by 1280 times has been determined in the sealed soils of the Sokolinaya gora industrial zone. High concentrations of BaP are also present in the sealed soils of the recreation zone. They are only two times lower than those in the industrial zone. Against the high spatial variability in the BaP concentrations and the presence of several local anomalies (with BaP concentration of 45 MPC and higher) in the southeast and east of the EAD the average concentrations of BaP in the sealed soils of the traffic and residential zones are three times lower than those in the industrial zone. The allowable and low level of contamination with BaP (1–5 MPC) is typical of the sealed soils in the residential zone and, partly, in the traffic zone (under local small streets).

A comparison of data on the mean content of BaP in the sealed soils (Table 1) and in the open soils of the EAD (Kasimov et al., 2017; Kosheleva & Nikiforova, 2011) indicates that the soils of open plots are generally characterized by the higher content of BaP (data on 2010), the difference reaches 3.4 times. Taking into account the low permeability of asphalt concrete, the concentration of BaP in the sealed soils is high, which may be explained by the low values of the oxidation–reduction potential in these soils. This favors long-term preservation and accumulation of BaP in the sealed soils. As shown earlier, BaP may be preserved in such soils for decades (Chernyanskii et al., 2001).

In general, the geochemical state of the sealed soils of EAD with respect to the contents of BaP and PPs is ecologically hazardous. Human-caused accumulations of

these hydrocarbons with the high degree of contrast are formed in the sealed soils of all land use zones. However, they are more common in the soils of the industrial and traffic zones with the high degree of soil sealing.

With respect to the integral index of contamination with HMMs, the studied sealed soils belong to the nonhazardous ( $Z_c < 16$ ) or moderately hazardous ( $16 < Z_c < 32$ ) levels. Only three local (point-size) anomalies with the extremely dangerous concentrations of HMMs ( $64 < Z_c < 128$ ) have been identified. One of them is in the industrial zone of the Sokolinaya gora municipality, and two other anomalies are allocated to crossroads with heavy traffic. An extremely high contamination with HMMs has been found in the sealed soil of the industrial zone near the Moscow Ring Road. This soil is affected by both industrial and traffic exhausts.

## CONCLUSIONS

Mapping of sealed soils showed their dominant position in the soil cover of the EAD. The highest degree of sealing (50–70%) is characteristic of soils in industrial and residential zones in the central part of the district with high building density. A high degree of sealing is typical for areas of new high-rise development outside the Moscow Ring Road. The low degree of sealing corresponds to older residential areas with a high and medium degree of greenery adjacent to the Kuskovsky Park.

The artificial asphalt screen on the soil surface affects the character of the soil functioning, changing its water and air regimes, morphological profile, physicochemical properties, and contamination levels. Sealed soils of the EAD have a medium content of  $C_{\text{org}}$  (2.24% on the average), alkaline reaction (pH 8.0), coarse texture (fraction  $< 0.01 \text{ mm}$  is 23.2%). The maximum  $C_{\text{org}}$  was found in the soil of the recreation zone, and the alkaline reaction (with  $\text{pH} > 8.0$ )

**Table 2** Contents of heavy metals and metalloids in the upper part of the sealed soils in comparison with unsealed soils for the Eastern Administrative district of Moscow, lg g<sup>-1</sup>

Parameter	V	Cr	Ni	Cu	Zn	As	Cd	Sn	Sb	Ba	W	Pb	Bi
MPC*	43	100	38	40	160	34	1.6	53	3.5	165	–	140	–
<i>Background sod-podzolic soils of Meshchera (n** = 10)</i>													
mean	36	26	11	20	37	2.0	0.21	4.4	0.36	238	0.69	14	0.125
<i>Industrial zone (I) of EAD (n = 9)</i>													
mean	40.6	49.7	30.7	329	150	6.34	0.93	14.2	4.45	483	3.81	143	0.26
min	21.1	19.2	9.11	10.1	36.3	0.89	0.11	0.77	0.03	273	0.55	12.3	0.074
max	57.0	144	108	1315	257	13.3	3.52	67.2	25.4	986	12.7	644	0.47
S	0.52	0.54	0.88	3.74	0.52	0.78	0.66	0.95	1.23	1.06	0.61	1.25	0.37
<i>Traffic (T) zone (n = 11)</i>													
mean	39.1	28.6	19.5	35.1	111	5.20	0.40	2.22	0.60	357	1.38	34.1	0.30
min	24.9	11.5	10.9	4.35	25.9	1.56	0.068	0.67	0.063	221	0.21	9.59	0.077
max	59.5	49.2	27.3	111.7	247	14.0	1.40	4.78	1.80	592	4.12	78.9	1.32
S	0.52	0.32	0.61	0.52	0.60	0.87	0.33	0.13	0.38	0.90	0.33	0.57	0.38
<i>Residential (H) zone (n = 21)</i>													
mean	43.8	39.6	19.9	29.3	110	3.95	0.54	3.49	0.96	341	2.51	41.4	0.24
min	18.6	8.49	6.71	6.92	24.8	0.94	0.08	0.57	0.21	92.5	0.55	9.08	0.06
max	86.2	152	36.1	108	306	9.27	3.69	20.8	2.79	481	16.5	131	1.36
S	0.56	0.38	0.67	0.49	0.58	0.54	0.39	0.29	0.67	0.78	0.53	0.69	0.38
<i>Recreational (R) zone (n = 6)</i>													
mean	40.5	33.9	16.7	28.0	108	3.68	1.51	2.95	0.89	341	3.50	27.3	0.19
min	28.1	17.8	12.3	16.5	84.2	1.85	0.20	1.00	0.53	238	0.65	15.7	0.09
max	55.3	58.1	21.8	53.1	133	6.18	5.15	5.03	1.40	444	9.47	42.3	0.41
S	0.54	0.34	0.58	0.56	0.74	0.58	0.72	0.23	0.77	0.90	1.09	0.56	0.34
<i>All ekranozems of EAD (n = 47)</i>													
mean	41.7	38.4	21.4	87.9	116.9	4.67	0.70	5.17	1.56	372	2.62	57.3	0.25
min	18.6	8.49	6.71	4.35	24.8	0.89	0.07	0.57	0.03	92.5	0.21	9.08	0.06
max	86.2	152	108	1315	306	14.0	5.15	67.2	25.4	986	16.5	644	1.36
S	0.54	0.39	0.73	1.41	0.61	0.71	0.52	0.39	1.00	0.89	0.55	0.96	0.40
<i>Unsealed soils of EAD (n = 49)</i>													
I (n = 5)	78	92	35	88	286	8.1	1.4	15	3.62	456	6.2	114	0.71
T (13)	75	90	32	67	183	6	1.2	17	1.56	398	4.2	60	0.78
H (22)	77.5	103	29.6	59.2	190	7.37	1.38	12.1	1.43	436	4.70	60.1	0.628
R (9)	75	101	29	50	147	6.4	2.1	13	1.16	377	3.2	49	0.56
mean	77.4	99.4	29.2	62.4	191	6.55	1.35	13.4	1.56	418	4.73	59.6	0.628

\*According to (Crommentuijn et al., 2000)

\*\*n—Number of sample

was found in the sealed soils of the residential and industrial zones. Despite the application of deicing mixtures and mineral fertilizers, the studied sealed soils are not saline: The electrical conductivity of the soil solution in the upper horizon is almost 15 times lower than the allowable level.

In comparison with open urban soils, sealed soils of the EAD have a lower organic matter content, approximately the same pH, and somewhat coarser texture, they are non-saline. The norms for BaP and PPs contents in the sealed soils are exceeded by almost ten times, which is 3.5 times lower than for the open urban soils. The highly contrasting technogenic accumulations of hydrocarbons are mainly typical of the sealed soils in the industrial and traffic zones.

The concentrations of most HMMs in the sealed soils exceed background levels by 1.2–4.4 times. In comparison with open soils of the EAD, the accumulation of HMMs in the sealed soils is lower, whereas the difference between sealed soils of different land use zones is more pronounced. The most active accumulation of Cu, Sb, Pb, W, Zn, Cd, As, Bi, and Ni has been found in the sealed soils of the industrial zone with the high degree of sealing. According to the integral contamination index  $Z_c$  (38.9), these are the most polluted soils (their  $Z_c$  is two times higher than that in the other zones). Hygienic norm for Ba and Cu is exceeded in the sealed soils of all

land use zones. In addition, the concentrations of Sb and Pb are higher than the MPC level in the sealed soils of the industrial zone. Though the zonal percolation type of the water regime in the sealed soils is not fully realized, some part of precipitation carrying pollutants penetrates under the asphalt and creates contrasting geochemical anomalies of hydrocarbons and HMMs.

Unfavorable changes in the properties of urban soils upon their sealing under asphalt create additional dangers to the urban environment and human health. In many countries, soil sealing is under control. In Europe, it is believed that the low degree of sealing is favorable for the citizens, because it decreases the degree of technogenic transformation of the urban environment. Urban areas need a sound approach to city planning. It is desirable to decrease the degree of sealing wherever possible, implement additional greening measures, and apply semipermeable coverings, such as tiled and stone-paved sidewalks (Burghardt & von Bertrab, 2016; Charzyński et al., 2017). As shown by the European and Russian experience (Levin et al., 2017; Piotrowska-Długosz & Charzyński, 2015; Romzaykina et al., 2020), the planned transformation of a part of sealed soils in Moscow into open soils should contribute to the improvement of ecological situation in the capital.



## Уровни и факторы накопления металлов и металлоидов в придорожных почвах, дорожной пыли и их фракции $PM_{10}$ в Западном округе Москвы.\*

### ВВЕДЕНИЕ

Одной из глобальных экологических проблем в последние десятилетия стала урбанизация, которая сопровождается ростом числа мегаполисов, где концентрируются опасные загрязняющие вещества, поступающие с выбросами промышленности, транспорта и бытовыми отходами. Москва является крупнейшим городом Европы, поэтому изучение химического состава почвенного покрова и дорожной пыли представляет особый интерес: оно позволяет оценить накопление и распределение тяжелых металлов и металлоидов (ТММ) в городских ландшафтах, выявить приоритетные загрязнители и определить факторы, влияющие на локализацию их техногенных аномалий [11, 43, 44].

Выбросы отработанных автомобильных газов и жидкостей, остатки смазочных масел и других нефтепродуктов, частицы шин и тормозных колодок, обогащенные ТММ, поступают в дорожную пыль и придорожные почвы [21, 38]. Выдувание частиц дорожной пыли и почв способствует росту загрязнения атмосферного воздуха в городах [50], увеличивая в том числе риск оксидативного стресса клеток организма человека [32, 60].

Основной депонирующей средой для ТММ являются почвы, так как в отличие от атмосферы, грунтовых и подземных вод возможность их самоочищения весьма ограничена. Почвы являются одним из главных источников материала дорожной пыли [62], однако для микрочастиц дорожной пыли характерен более высокий уровень загрязнения ТММ, чем придорожных почв [31]. Особый интерес вызывают микрочастицы с диаметром  $<10$  мкм (англ. “particulate matter” –  $PM_{10}$ ) и более тонкие фракции [9, 34, 42, 49, 53, 54, 59]. По Качинскому [13]  $PM_{10}$  – это фракция физической глины, состоящая из ила, мелкой и средней пыли. С уменьшением размера частиц концентрации ТММ в них увеличиваются, что связано с ростом удельной площади поверхности, сорбционной емкости и емкости катионного обмена, увеличением количества органического вещества и содержания глинистых минералов и одновременным снижением доли кварца в минералогическом составе [33].

Дорожная пыль формируется в результате осаждения промышленных и транспортных выбросов, а также при дефляции придорожных почв летом и противогололедных реагентов (ПГР) зимой [36]. Поэтому частицы пыли являются фазой-носителем многих поллютантов, в первую очередь, ТММ. С дорожного полотна пыль легко выдувается в воздух,

особенно частицы  $PM_{10}$ , а затем поступает в городские почвы, способствуя их загрязнению. Химический состав дорожной пыли и ее отдельных фракций изучается во всем мире, но в России он по-прежнему анализируется редко и для ограниченного числа ТММ [7, 8, 41, 45, 52]. Подобные исследования проведены в ряде округов Москвы, однако загрязнение мелкодисперсных частиц пыли оценивалось далеко не всегда [16, 27, 37, 48, 57].

Цель работы – дать эколого-геохимическую оценку состоянию придорожных почв и дорожной пыли, а также их фракции  $PM_{10}$  по содержанию ТММ на примере Западного административного округа (ЗАО) Москвы, где расположены крупнейшие дорожные магистрали города.

Решались следующие задачи:

- проанализировать основные физико-химические свойства почв и дорожной пыли на разных типах дорог, способствующие фиксации загрязняющих веществ, и сравнить их с фоновыми уровнями;
- определить уровни накопления элементов – приоритетных поллютантов в верхних горизонтах почв и дорожной пыли, а также их фракции  $PM_{10}$  на дорогах разной крупности;
- выявить физико-химические свойства депонирующих сред, ландшафтные и антропогенные факторы, влияющие на аккумуляцию ТММ в почвах и дорожной пыли;
- оценить степень загрязнения и связанную с ней экологическую опасность поллютантов по суммарному показателю загрязнения.

### ОБЪЕКТ И МЕТОДЫ ИССЛЕДОВАНИЯ

Большая часть территории ЗАО расположена на Теплостанской возвышенности, которая отличается максимальными для Москвы высотой и перепадом высот, а также сильной расчлененностью речной и овражно-балочной сети. В рельефе преобладают плоские поверхности, пологие и крутые склоны моренной холмистой, пологоувалистой аккумулятивной равнины с выраженной латеральной твердофазной миграцией поллютантов в результате плоскостного смыва и овражной эрозии. Центральная часть округа расчленена пологими и крутыми склонами долины р. Сетунь и ее притоков, способствующими латеральной миграции веществ; на юге долины местами засыпана и значительно преобразована хозяйственной деятельностью. Пространства между холмистой равниной и речными долинами представлены выположенными участками флювиогляциаль-

\* Власов Д. В., Кукушкина О. В., Кошелева Н. Е., Касимов Н. С. // Почвоведение. 2022;(5):538–555.

[DOI: 10.31857/S0032180X22050112](https://doi.org/10.31857/S0032180X22050112)

Vlasov, D.V., Kukushkina, O.V., Kosheleva, N.E., Kasimov N. S. // Eurasian Soil Science. 2022;55(5):556–572.

[DOI: 10.1134/S1064229322050118](https://doi.org/10.1134/S1064229322050118) IF 1.4

ной аккумулятивной равнины с менее интенсивной боковой миграцией поллютантов. Северо-восток ЗАО занимает долинный комплекс р. Москвы и ее притоков, включающий пойму, первую надпойменную террасу и ее склоны [2].

В почвообразовании в ЗАО преобладают техногенные факторы, поэтому здесь распространены антропогенные почвы, в основном урбаноземы и квазиземы [18], состоящие из пылевого-гумусового субстрата с примесью бытового и строительного мусора, иногда подстилаемые водонепроницаемыми материалами, например, бетоном и др. Квазиземы отличаются от урбаноземов более легким гранулометрическим составом и большим количеством гумуса, они включают несколько привнесенных гумусированных слоев и слоев подстилающего техногенного грунта. Для всех антропогенно-измененных почв характерно нарушение почвенного профиля и несогласованное залегание горизонтов.

Летом 2017 г. в ЗАО отобрано 29 смешанных проб придорожных почв из верхнего (0–10 см) горизонта в 2–3 м от дорожного полотна и 29 смешанных проб дорожной пыли на разных типах дорог вдоль бордюров (рис. 1). Смешанные пробы составлялись из 3–5 индивидуальных, взятых на расстоянии 3–10 м друг от друга. Автомобильные дороги разделялись на типы в зависимости от количества полос движения в одну сторону и плотности выбросов транспорта [17]: Московская кольцевая автомобильная дорога (МКАД) (5 полос с выбросами 1000–1500 т/км<sup>2</sup> в год) – по 4 пробы почв и дорожной пыли; главные радиальные дороги (4 полосы, 1500–2000 т/км<sup>2</sup> в год) – по 4 пробы; крупные (3 полосы, 1500–2000 т/км<sup>2</sup> в год) – по 10 проб; средние (2 полосы, 2000–4000 т/км<sup>2</sup> в год) – по 3 пробы; малые дороги (1 полоса, 500–1000 т/км<sup>2</sup> в год) – по 3 пробы. Дворы (плотность выбросов транспорта до 1000 т/км<sup>2</sup> в год), где отобрано 5 проб в пределах автопарковок и 5 проб почв рядом с парковками, представлены своеобразными “колодцами-ловушками” из двух–четырех 9–16-этажных домов с узкими проездами [15], которые формируют зону застоя приземного воздуха и способствуют осаждению поллютантов [39]. В качестве фоновых эталонов для почв и пыли использовались дерново-подзолистые почвы (14 проб) на покровных суглинках в Коралловском лесничестве Одинцовского района Московской области, в 50 км к западу от Москвы, развитые под разнотравным елово-березовым лесом.

Фракция РМ<sub>10</sub> почв и пыли выделялась методом отмучивания после диспергирования образцов с помощью влажного растирания [3]. Полученный раствор фильтровали через мембранный фильтр с диаметром пор 0.45 мкм. Физико-химические свойства пыли и почв определялись в Эколого-геохимическом центре географического факультета МГУ: рН и удельная электропроводность (ЕС<sub>1:5</sub>) водной вытяжки – потенциометрическим и кондуктометрическим методами, содержание органического углерода (С<sub>орг</sub>) – методом Тюрина с титриметрическим окончанием, гранулометрический состав – лазерной гранулометрией.

Содержание ТММ в общих пробах почв, пыли и частицах РМ<sub>10</sub> определялось масс-спектральным (ICP-MS) и атомно-эмиссионным спектральным (ICP-AES) методами с индуктивно-связанной плазмой во ВНИИ минерального сырья им. Н.М. Федо-

ровского. Анализировались ТММ разных классов опасности: I класса (Zn, As, Cd, Pb); II (Cr, Co, Ni, Cu, Sb, Mo); III (V, W, Sr, Mn), а также Bi, Sn, Fe, Ta. Большинство выбранных для анализа элементов характеризуются интенсивным накоплением в аэрозолях [5], атмосферных осадках [55, 56], снежном покрове [1, 58], речной взвеси [14, 26], дорожной пыли и ее отдельных гранулометрических фракциях [10, 16, 27], а также в верхних горизонтах почв [39, 46, 51] Москвы.

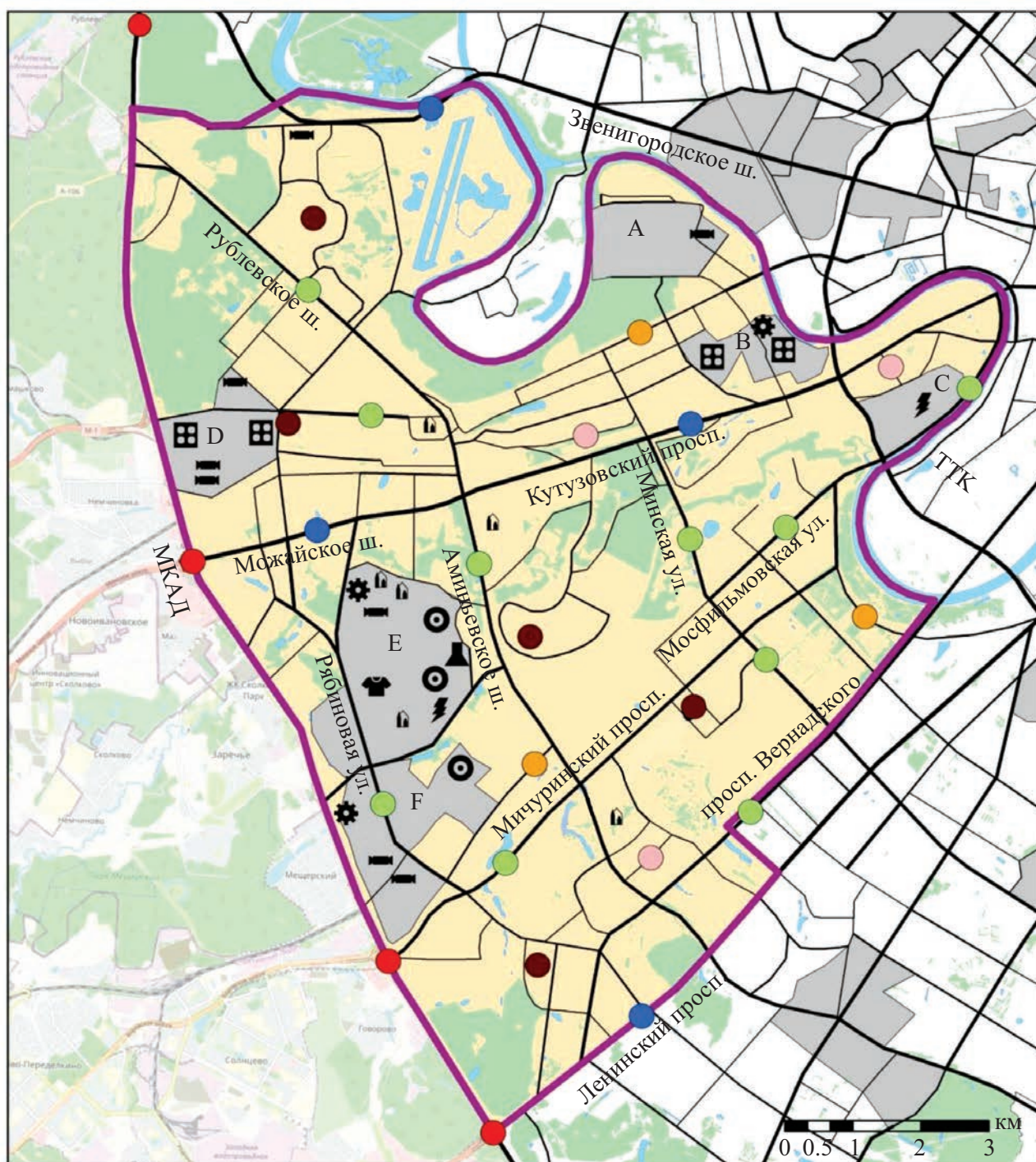
Данные анализировались в пакете Statistica 10. Для каждого из 18 изучаемых элементов в придорожных почвах, дорожной пыли и фракции РМ<sub>10</sub> рассчитывались коэффициенты накопления  $K_c = C_i/C\phi$ , где  $C\phi$ ,  $C_i$  – концентрация изучаемого элемента в фоновых почвах и в городских почвах или пыли, соответственно, или коэффициенты рассеяния  $K_p = C\phi/C_i$  при  $C\phi/C_i > 1$ . Расчет суммарного показателя загрязнения  $Z_c = \sum K_c - (n - 1)$ , где  $n$  – число химических элементов с  $K_c > 1$ , позволил определить категорию загрязнения: <16 – низкое, неопасное, 16–32 – среднее, умеренно опасное, 32–64 – высокое, опасное, 64–128 – очень высокое, очень опасное, >128 – максимальное, чрезвычайно опасное [11]. Вклад фракции РМ<sub>10</sub> дорожной пыли или придорожных почв в содержание ТММ в общей пробе пыли или почв оценивалось по доле  $D_i$  (%):  $D_i = C_{i0} \times P_{i0}/C_i$ , где  $C_{i0}$  – концентрация элемента в РМ<sub>10</sub>, мг/кг фракции,  $P_{i0}$  – доля фракции РМ<sub>10</sub> в пробе пыли или почв, %.

Коэффициенты экологической опасности  $K_o = C_i/ПДК(ОДК)$  вычислялись для As, Cd, Pb, Zn, Ni, Cu, Sb, V, Mn, у которых существуют утвержденные в РФ предельно допустимые (ПДК) или ориентировочно допустимые концентрации (ОДК) в почвах [20].









Влияние природных и техногенных факторов на аккумуляцию ТММ в придорожных почвах, дорожной пыли и в их фракции РМ<sub>10</sub> оценивалось в программном пакете S-PLUS с помощью метода регрессионных деревьев [39]. Дендрограммы строились в зависимости от следующих факторов и условий: геохимическая позиция (положение в рельефе), свойства почв или пыли, определяющие их сорбционную способность по отношению к ТММ (рН, удельная электропроводность ЕС<sub>1:5</sub>, содержание РМ<sub>10</sub>, то есть частиц физической глины, и С<sub>орг</sub>), тип дороги, объем выбросов автотранспорта (неопубликованные данные о выбросах предоставлены проф. В.Р. Битюковой).

Для учета ландшафтно-геохимической неоднородности территории использованы данные об абсолютных высотах в каждой точке, определенных по цифровой модели рельефа (данные SRTM, Shuttle Radar Topography Mission). Повышенные и выровненные плоские поверхности (абс. высоты 182–204 м), пологие и крутые склоны (184–199 м) моренной равнины, сложенной валунными суглинками, соответствуют автономным элювиальным и трансэлювиальным ландшафтам, соответственно (рис. S1). Засыпанные участки долины р. Сетунь и ее притоков на техногенных отложениях (166–170 м) и выложенные участки флювиогляциальной аккумулятивной равнины (161–170 м), сложенной песками, песчано-гравелистыми отложениями и суглинками, представлены трансэлювиально-аккумулятивными ландшафтами. Пониженные участки пологих и крутых склонов долины р. Сетунь и ее притоков (146–





### Промышленные предприятия

-  Электроэнергетики
-  Химии и нефтехимии
-  Легкой промышленности
-  Машиностроения и металлообработки
-  Производства резины и пластика
-  Производства электрооборудования
-  Пищевой промышленности
-  Прочих отраслей

### Точки отбора проб пыли и почв

- МКАД
- Радиальные шоссе
- Крупные дороги
- Средние дороги
- Малые дороги
- Дворы

**Рис. 1.** Точки отбора проб почв и дорожной пыли в западной части Москвы (лето 2017 г.). Промышленные зоны (показаны серой заливкой): А – Фили, В – Западный порт, С – Бережковская набережная, D – Кунцево, E – Северное Очаково, F – Южное Очаково.



154 м) с преимущественно песчаными отложениями относятся к трансэлювиальным ландшафтам, а пойма, первая надпойменная терраса р. Москвы и ее притоков и ее пологие склоны (123–142 м) с песками, супесями и суглинками с прослоями торфа, в значительной степени перекрытыми техногенными отложениями, относятся к супераквальным ландшафтам.

## РЕЗУЛЬТАТЫ И ОБСУЖДЕНИЕ

**Основные физико-химические свойства придорожных почв и дорожной пыли.** Более половины проб почв имеет легкосуглинистый состав, содержание частиц  $PM_{10}$  в придорожных почвах более чем в полтора раза меньше, чем на фоновых участках. Наблюдаются колебания содержания крупных фракций (крупнее  $PM_{10}$ ), которое максимально на МКАД, минимально на радиальных многополосных шоссе и малых дорогах. Реакция среды в придорожных почвах всюду близка к нейтральной со средним рН 7.26. Наибольшие величины рН отмечаются на МКАД и во дворах. Почвы вблизи крупных и малых дорог обладают нейтральной реакцией среды (табл. 1), тогда как для фоновых дерново-подзолистых почв характерна слабокислая реакция. Основной причиной подщелачивания почв в городе является строительная пыль, применение ПГР и сильнощелочных моющих средств с рН 9–11.

Средняя удельная электропроводность  $EC_{1:5}$  водной вытяжки из почв ЗАО составляет 190 мкСм/см, что почти в три раза выше фонового уровня.  $EC_{1:5}$  варьирует от минимальных значений в почвах вблизи малых дорог до максимальных рядом с крупными магистралями и МКАД. Увеличение  $EC_{1:5}$  связано с применением ПГР зимой, которые весной лишь частично смываются талыми водами и осадками. Среднее содержание  $C_{орг}$  = 4.67%, что в полтора раза выше фона за счет органических частиц техногенного происхождения – асфальта, выбросов автотранспорта и промышленности [28]. Минимальные величины  $C_{орг}$  приурочены ко дворам, малым дорогам и радиальным шоссе. Больше всего органического вещества содержится в почвах рядом с МКАД и крупными дорогами.

Почвенные свойства варьируют в зависимости от крупности дорог и интенсивности движения автотранспорта. Наибольшие колебания характерны

для  $EC_{1:5}$  (в 1.9 раза) и содержания  $C_{орг}$  (в 1.5 раза). Варьирование содержания частиц  $PM_{10}$  (физической глины) можно отнести к среднему (в 1.3 раза), наименьшие колебания значений характерны для рН. По сравнению с фоновыми почвами рН придорожных почв почти на единицу больше, их отличает в 3 раза более высокая электропроводность, повышенное в 1.4 раза содержание  $C_{орг}$  и более легкий гранулометрический состав.

Дорожная пыль имеет супесчаный состав, содержание фракции  $PM_{10}$  в пыли практически в два раза меньше, чем в фоновых почвах. Максимум тонких фракций наблюдается на крупных дорогах, минимум – на малых дорогах и во дворах, что, вероятно, связано с активной поставкой  $PM_{10}$  при истирании шин и металлических деталей тормозных механизмов автомобилей [50].

Реакция среды пыли близка к слабощелочной со средним значением 7.44 при незначительных колебаниях на разных типах дорог. Максимальные значения характерны для шоссе и средних дорог, минимальные – для МКАД и дворов. Применение моющих средств на радиальных шоссе и крупных дорогах приводит к подщелачиванию пыли. Из-за применения ПГР средняя  $EC_{1:5}$  составляет 180 мкСм/см, что превышает фоновый уровень дерново-подзолистых почв в 2.8 раза. Наибольшие значения  $EC_{1:5}$  зафиксированы на крупных и средних дорогах, наименьшие – во дворах с автопарковками. Содержание  $C_{орг}$  составляет в среднем 2.5% при колебаниях от 1.35% на крупных дорогах до 4.42% во дворах, куда  $C_{орг}$  поступает с близлежащих газонов, с выхлопами автотранспорта и при истирании шин.

По сравнению с придорожными почвами дорожная пыль имеет более легкий гранулометрический состав, содержит в 1.5 раза меньше мелкодисперсных частиц и в 3 раза меньше  $C_{орг}$ . Реакция среды и электропроводность в водной вытяжке из почв и пыли имеют близкие значения – 7.3–7.45 и 180–190 мкСм/см.

**ТММ в придорожных почвах и их фракции  $PM_{10}$ .** Приоритетные поллютанты придорожных почв ЗАО – W, Sb, Mo, Cu, Cd, Sn, Zn, Bi (*Kc* 2.4–6.0) (табл. 2). По сравнению с фоновыми почвами наиболее активно аккумулируется W (средний *Kc* 6.0) с сильным варьированием концентраций на дорогах с разной интенсивностью движения. Основными источни-

**Таблица 1.** Основные физико-химические свойства придорожных почв и дорожной пыли (приведены средние значения)

Территория	Придорожные почвы				Дорожная пыль			
	$PM_{10}$ , %	рН	$C_{орг}$ , %	$EC_{1:5}$ , мкСм/см	$PM_{10}$ , %	рН	$C_{орг}$ , %	$EC_{1:5}$ , мкСм/см
МКАД	22.5	7.46	5.4	247	15.3	7.16	2.8	156
Радиальные шоссе	17.3	7.22	4.3	173	10.7	7.68	1.3	175
Крупные дороги	19.4	7.15	5.6	221	19.4	7.53	2.1	211
Средние дороги	20.4	7.25	3.8	185	16.5	7.62	1.8	210
Малые дороги	17.5	7.10	4.7	132	13.6	7.53	2.6	193
Дворы с автопарковками	21.1	7.36	4.2	181	13.2	7.13	4.4	136
Среднее по ЗАО	19.7	7.30	4.7	190	14.8	7.44	2.5	180
Фоновые почвы	31.9	6.40	3.3	65.5	–	–	–	–

ками W являются износ шин и дорожного покрытия, а также промышленные выбросы [57, 63]. Максимальное накопление W зафиксировано в почвах рядом со средними и крупными магистралями, рядом с МКАД и радиальными шоссе его концентрация снижается в три и два раза соответственно. Похожая картина аккумуляции наблюдается у Sb, которая после W вносит наибольший вклад в загрязнение почв ТММ (рис. S2). К увеличению концентрации Sb приводит износ тормозных колодок транспорта [61]. Наибольшая концентрация Sb выявлена вблизи средних внутрирайонных дорог; на МКАД и во дворах с автопарковками она накапливается в три раза слабее.

Концентрация Mo и Cu достигает максимальных значений ( $K_c$  3.2 и 2.7 соответственно) на средних дорогах, на магистралях с более интенсивным движением постепенно уменьшается, минимальные значения приурочены ко дворам с автопарковками. Обогащению почв Cu и Mo способствуют также выбросы заводов машиностроения и металлообработки [19], а также невыхлопные выбросы автотранспорта [47]. На увеличение концентраций Cu влияют предприятия по производству электролитической медной фольги и оптоэлектронных устройств. Zn, Cd и Sn аккумулируются в почвах вблизи всех ти-

пов дорог довольно равномерно ( $K_c$  2.4–2.45). Основным поставщиком Zn являются железнодорожный транспорт, выбросы промышленных предприятий и автотранспорт – Zn присутствует в шинах в неорганических формах (ZnS и ZnO) и в виде органического стеарата [23]. Высокие концентрации Cd и Sn характерны для шин, дорожной разметки, тормозных колодок и других деталей автомобилей [47]. Для Pb, As, Ni свойственно слабое накопление ( $K_c$  1.3–1.5), Ta, Cr, Co, V, Sr, Mn рассеиваются ( $K_p$  1.7–1.1).

Тонкие частицы  $PM_{10}$  обладают большей способностью поглощать загрязнители, поэтому все ТММ отличаются высокой интенсивностью аккумуляции в этой фракции придорожных почв (рис. 2). Наибольший  $K_c = 15.6$  у W с максимальными концентрациями на крупных и средних дорогах, наименьшие значения свойственны МКАД и дворам. Близкое распределение концентраций на разных типах дорог характерно для Mo и Sn ( $K_c$  8.8 и 5.4 соответственно). Как и в валовых пробах, вторым по значимости поллютантом для фракции  $PM_{10}$  является Sb с одинаковым уровнем аккумуляции (10.8) на разных типах дорог, который вдвое больше, чем в почвах в целом. Значительно больше в частицах  $PM_{10}$  по сравнению с валовыми пробами содержание Zn и Cu

**Таблица 2.** Среднее содержание элементов (мг/кг) в придорожных почвах, дорожной пыли и их фракции  $PM_{10}$  на разных типах дорог и во дворах с автопарковками в ЗАО Москвы

Объект и дороги		V	Cr	Mn	Fe	Co	Ni	Cu	Zn	As	Sr	Mo	Cd	Sn	Sb	Ta	W	Pb	Bi
Почвы	МКАД	67	55	515	27890	9.7	25	41	166	5.8	132	1.9	0.47	3.8	1.8	0.62	5.6	28	0.32
	радиальные шоссе	54	42	412	25127	6.8	33	45	131	3.4	116	1.6	0.42	4.2	2.0	0.45	7.2	21	0.58
	крупные дороги	52	38	390	25054	7.7	32	56	147	5.4	126	1.7	0.39	4.1	1.9	0.40	7.0	27	0.27
	средние дороги	66	45	462	27161	9.6	35	61	162	6.9	139	1.7	0.35	5.6	2.2	0.49	7.9	33	0.41
	малые дороги	47	38	379	18628	6.1	26	44	165	4.0	114	1.1	0.62	3.6	1.5	0.37	4.6	32	0.25
	дворы с автопарковками	58	52	446	21109	7.5	34	38	258	4.9	114	1.0	0.76	3.2	1.4	0.43	3.3	36	0.49
$PM_{10}$ почв	МКАД	92	69	777	42670	14	37	61	301	9.1	110	3.6	0.76	7.5	3.1	0.80	10	48	0.58
	радиальные шоссе	87	67	649	38069	13	35	80	320	5.9	123	4.5	0.76	8.9	4.7	0.86	17	39	0.78
	крупные дороги	82	80	636	41197	15	44	120	386	9.8	136	5.4	0.63	10	5.2	0.87	21	54	0.78
	средние дороги	86	63	684	41876	15	39	107	334	11	134	4.4	0.53	11	4.7	0.81	19	55	0.78
	малые дороги	90	78	804	42886	14	42	95	437	8.6	116	3.4	1.2	9.6	4.0	0.83	11	79	0.92
	дворы с автопарковками	84	74	673	38253	13	42	69	580	6.3	119	2.6	1.0	5.8	2.6	0.85	8.6	51	0.78
Дорожная пыль	МКАД	65	56	424	29918	8.9	21	52	335	0.8	156	1.3	0.20	4.6	3.0	1.3	6.3	15	0.26
	радиальные шоссе	57	43	393	25505	6.5	21	67	220	1.8	134	1.5	0.20	3.7	1.3	0.57	2.2	26	0.19
	крупные дороги	66	53	409	30131	6.1	24	51	156	1.4	168	2.6	0.22	4.8	2.7	0.53	4.2	24	0.27
	средние дороги	61	55	403	26718	5.1	24	47	128	1.7	182	3.3	0.24	4.3	1.8	0.56	2.5	22	0.51
	малые дороги	48	34	341	21939	4.5	16	50	143	1.7	130	2.1	0.19	4.9	1.3	0.58	2.4	63	0.18
	дворы с автопарковками	39	38	319	21123	5.7	17	29	262	2.2	138	1.7	0.26	3.1	1.3	0.27	3.9	25	0.20
$PM_{10}$ дорожной пыли	МКАД	90	57	620	42106	17	35	144	1045	2.7	182	4.1	0.48	14	14	0.52	27	37	1.0
	радиальные шоссе	99	78	718	49626	19	46	200	1364	3.0	200	6.2	0.57	25	14	0.63	22	60	1.8
	крупные дороги	85	72	661	46618	16	45	222	879	2.5	191	6.2	0.62	25	13	0.63	28	154	1.9
	средние дороги	74	62	597	41624	14	41	188	618	2.3	197	6.2	0.77	25	12	0.36	21	66	2.0
	малые дороги	71	62	584	37057	13	45	142	692	1.5	161	4.1	0.60	22	7.1	0.44	22	111	1.4
	дворы с автопарковками	87	56	736	41743	16	53	147	1282	2.3	207	2.6	1.0	19	7.3	1.9	31	75	1.5
Фоновые почвы		86	55	1006	25398	9.4	24	18	71	3.6	137	0.50	0.20	1.7	0.40	0.80	1.0	19	0.20

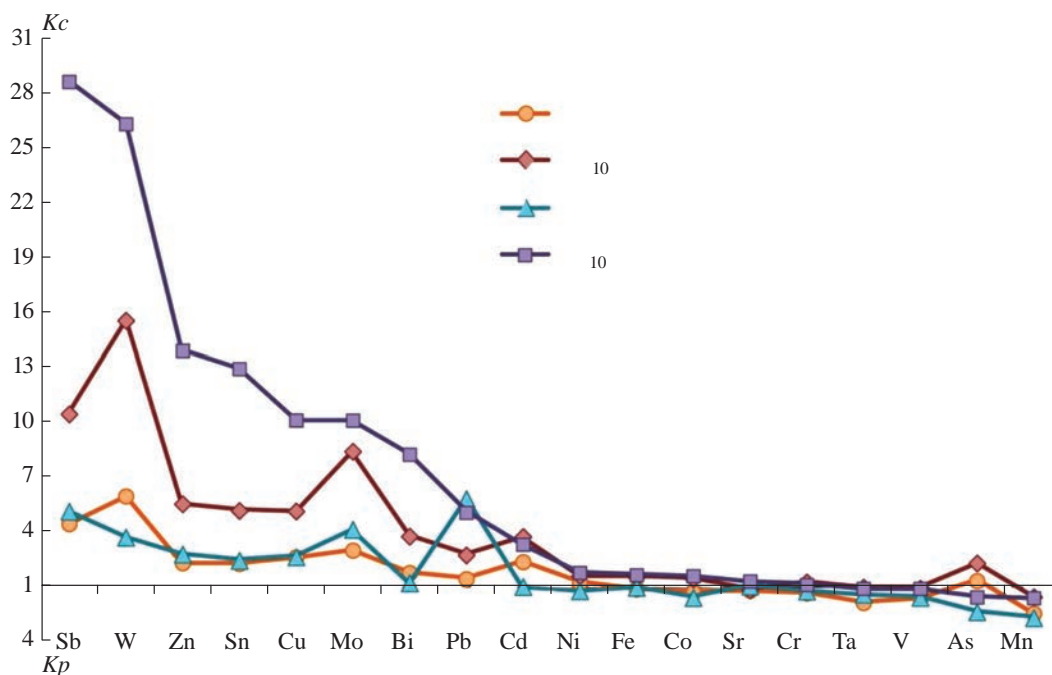


Рис. 2. Геохимические спектры ТММ в придорожных почвах, дорожной пыли и их частицах  $PM_{10}$  в ЗАО г. Москвы.

( $K_c \geq 5.3$ ), которое не дифференцировано по типам дорог. В мелкодисперсных частицах накапливаются также Bi, Cd, Pb, As ( $K_c$  2.4–4.5) и менее активно Ni, Co, Fe и Cr ( $K_c$  1.3–1.7). V, Sr и Mn рассеиваются ( $K_p$  1.1–1.5).

ТММ в дорожной пыли и ее фракции  $PM_{10}$ . Основными загрязнителями дорожной пыли ЗАО являются Sb, Mo и W ( $K_c$  3.8–5.3) (табл. 2). Концентрация главного поллютанта – Sb примерно одинакова на всех магистралях, кроме МКАД, на которой значения превышают средние в 3 раза (рис. S2). Варьирование содержания Mo и W невелико, с максимальными значениями на средних дорогах и минимальными на малых дорогах, во дворах (для Mo) и на МКАД и крупных дорогах (для W). Слабее в дорожной пыли аккумулируются Zn, Cu и Sn, которые распределены на всех автомагистралях и дворах с парковками довольно равномерно, за исключением высокой концентрации Zn на МКАД и низкой – Cu во дворах. Содержания Cd, Bi, Sr и Fe близко к величинам в фоновых почвах, а As, Cr, Co, Ni, V, Mn и Ta рассеиваются.

Набор приоритетных загрязнителей в дорожной пыли такой же, как и в почвах, однако содержание Sb и Mo в пыли в 1.2 и 1.4 раза больше, а W в 1.6 раза меньше. Это объясняется тем, что дорожная пыль отражает актуальную геохимическую нагрузку на городские ландшафты в теплый сезон, тогда как придорожные почвы аккумулируют некоторые поллютанты многие десятилетия, другая их часть может вымываться из верхнего горизонта (рис. S3).

В тонкодисперсных частицах  $PM_{10}$  все ТММ накапливаются намного интенсивнее по сравнению с общими пробами. Во фракции  $PM_{10}$  пыли содержание приоритетных загрязнителей W и Sb в 1.7 и 2.7 раза выше, чем в  $PM_{10}$  придорожных почв. Относительно почвенного фона наиболее интенсивно (средний  $K_c$  29.4) накапливается Sb с максимумом на МКАД и радиальных шоссе ( $K_c$  35.1) и минимумом ( $K_c$  18.5) на малых дорогах и во дворах. Второй по значимости загрязнитель – W со средним  $K_c$  26.3

(табл. 2) и размахом колебаний на разных дорогах в 1.5 раза. Максимальные концентрации W наблюдаются во дворах, минимальные – на средних дорогах. Высока аккумуляция Zn и Sn ( $K_c$  13.9 и 13.4 соответственно), в почвах содержание этих элементов в 2.5 раза меньше. Активно накапливаются Cu, Mo и Bi, которые распределены на всех автомагистралях и дворах с парковками довольно равномерно. Концентрация Pb в тонких фракциях незначительно снижается относительно содержания в валовых пробах ( $K_c$  5.8 и 5.0 соответственно). Содержание Cd во фракции  $PM_{10}$  в 3 раза выше, чем в валовых пробах ( $K_c$  3.4 и 1.1 соответственно), оно слабо варьирует на всех типах дорог. Концентрации Cr, Co, Ni, V, Sr, Fe, Ta, As и Mn близки к фоновым.

Связь накопления ТММ в частицах придорожных почв и дорожной пыли. Известно, что одним из источников материала дорожной пыли служат придорожные почвы, но одновременно выражен и обратный процесс – поставка частиц дорожной пыли в придорожные почвы [31, 62], то есть существует “круговорот” частиц в пыли и почвах, в который включается дополнительная поставка поллютантов из других техногенных источников. Это движение частиц и содержащихся в них ТММ обуславливает геохимические связи между почвами и дорожной пылью, что подтверждает отмеченное ранее совместное накопление Ag, Sb, Sn, W, Bi, Cd, Cu, Pb, Zn в обоих компонентах в восточной части Москвы [37]. В почвах, дорожной пыли и их микрофракциях  $PM_{10}$  Западного округа аккумулируются W, Sb, Sn, Mo, Zn, Cu (средние  $K_c > 2$ ), к которым в почвах,  $PM_{10}$  почв и  $PM_{10}$  пыли добавляется Cd, в дорожной пыли и  $PM_{10}$  почв и пыли – Pb, а в  $PM_{10}$  почв и  $PM_{10}$  дорожной пыли – Bi (рис. 2), то есть в целом перечень входящих в парагенезисы ТММ на западе и востоке Москвы практически не отличается.

Формирование геохимических связей между дорожной пылью, почвами и их фракцией  $PM_{10}$  на западе Москвы подтверждает корреляционный анализ



содержания ТММ в четырех изученных компонентах (всего проанализировано шесть возможных пар компонентов, указанных в табл. 3).

В подсистемах почвы –  $PM_{10}$  почв и дорожная пыль –  $PM_{10}$  дорожной пыли выявлены наиболее высокие  $r$ , которые указывают на существенный вклад связанных с микрочастицами  $PM_{10}$  ТММ в их валовое содержание (рис. 3). В придорожных почвах ЗАО фракция  $PM_{10}$  содержит 40–60% Mo, W, Bi, Sb, Zn и Sn от запасов этих ТММ, а также 40–60% Cu, Cd, Pb, Mo и Co и более 60% Zn, Sn, Sb, Bi и W от их запасов в дорожной пыли.

В подсистеме  $PM_{10}$  почв –  $PM_{10}$  дорожной пыли значимые  $r$  установлены для Cu (0.65), Mo (0.56) и Sb (0.47), что указывает на общие источники этих ТММ в почвах и дорожной пыли и на ведущую роль микрочастиц  $PM_{10}$  в переносе Cu, Mo и Sb между изучаемыми компонентами городской среды (рис. 4). Эти корреляционные связи сохраняются в подсистеме почвы –  $PM_{10}$  дорожной пыли, где к Cu ( $r = 0.63$ ), Mo (0.56) и Sb (0.44) добавляется Sn (0.38), что свидетельствует о поступлении этих ТММ с микрочастицами из дорожной пыли в почвы. Следовательно, фракция  $PM_{10}$  является одной из наиболее важных носителей ТММ, особенно в дорожной пыли, что определяет ее повышенную экологическую опасность для населения ЗАО.

Для других ТММ значения  $r$  не значимы при  $p < 0.05$ , вероятно, из-за большего участия более крупных частиц в миграции ТММ, неоднородности источников загрязнения (дорожная пыль накапливает поллютанты в теплый сезон, почвы – за многолетний период), наличия емких геохимических барьеров в почвах и их слабой выраженности в дорожной пыли и т.д. Определить основные факторы накопления ТММ в почвах и дорожной пыли позволяет нелинейный регрессионный анализ.

Факторы накопления ТММ. Для оценки роли различных факторов накопления ТММ в придорожных почвах, дорожной пыли и их микрочастицах  $PM_{10}$  использован метод регрессионных деревьев. Для Cr, Mn, Sr, Ta и V регрессионный анализ не проводился, поскольку во всех изучаемых компонентах они практически не накапливаются.

В придорожных почвах аккумуляция большинства ТММ зависит от геохимической позиции участка опробования и содержания тонких частиц  $PM_{10}$  (табл. 4), что согласуется с концепцией о ве-

дущей роли рельефа в перераспределении поллютантов в техногенных ландшафтах и результатами оценки подвижности Sb, Pb, As и Hg в почвах горнопромышленных ландшафтов муниципалитета Лена (Испания) в зависимости от геоморфологических и климатических факторов [24]. Геохимическая позиция, отражающая положение в рельефе и тип почвообразующей породы, определяет накопление в придорожных почвах Bi, Cd, Fe, Mo и Ni, которое достигает максимума на отметках 199–204 м в автономных ландшафтах, соответствующих выровненным плоским поверхностям моренной равнины.

Гранулометрический состав оказывает наибольшее влияние на распределение Cu, Sb, Sn, W и Zn в почвах вблизи различных типов автодорог: чем меньше частиц  $PM_{10}$  и состав почв ближе к супесчаному, тем интенсивнее они накапливают ТММ. Кислотно-основные условия и крупность дорог влияют на накопление шести и десяти ТММ соответственно, однако для большинства ТММ эти факторы не являются главными. pH является ведущим только для Co и вторым по значимости для As, Cd, Sn и W. С ростом pH концентрации этих ТММ увеличиваются, за исключением анионогенного As, который активнее мигрирует в щелочной среде [12]. Крупность автотрасс является вторым по значимости фактором для Bi, Cd, Cu, Mo и Zn, третьим – для Co, Ni, Sb, Sn и W.

Ключевую роль в аккумуляции наиболее опасных загрязнителей – W и Sb – в придорожных почвах играет гранулометрический состав (табл. 4). В суглинистых почвах (при содержании  $PM_{10} > 20\%$ ) W накапливается в 2.2 раза интенсивнее на высотных отметках  $>165$  м (трансэлювиально-аккумулятивные ландшафты засыпанных участков долины р. Сетунь и ее притоков и выположенных участков флювиогляциальной аккумулятивной равнины), чем на более низких отметках, приуроченных в основном к трансэлювиальным ландшафтам пологих и крутых склонов долины р. Сетунь и ее притоков, а также к супераккумулятивным ландшафтам поймы, первой надпойменной террасы р. Москвы и ее пологим склонам (рис. S1). В супесчаных почвах накопление W зависит от реакции среды: в слабощелочных, близких к нейтральному, условиях ( $pH > 7.1$ ) содержание металла в среднем в 2.7 раза больше, чем в более нейтральных условиях ( $pH < 7.1$ ). Это можно объяснить тем, что источником W также являются подщелачивающие агенты: ПГР, выпадения карбонатной строительной пыли, износ

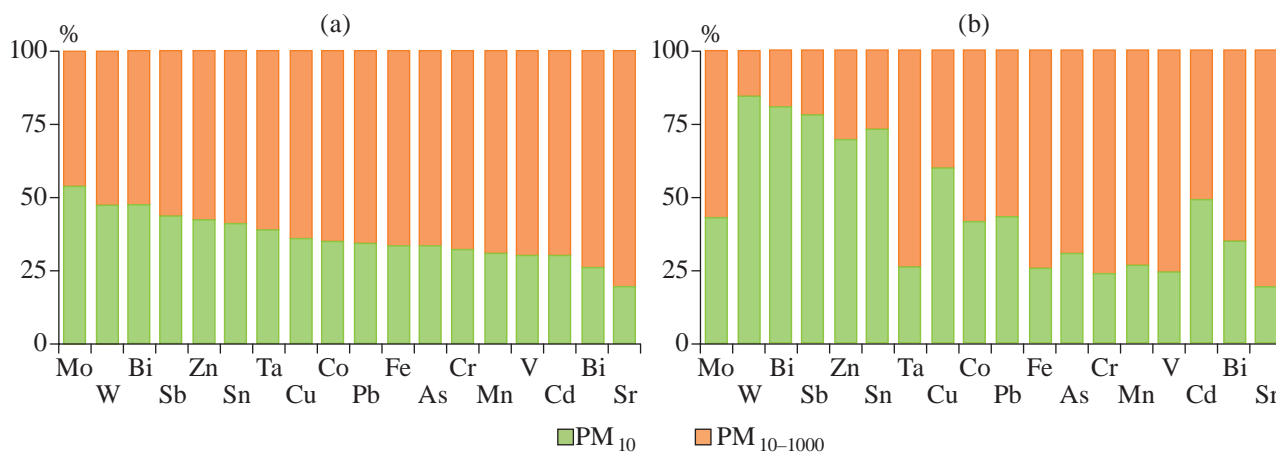


Рис. 3. Фракционный состав ТММ в придорожных почвах (а) и дорожной пыли (б) ЗАО Москвы.

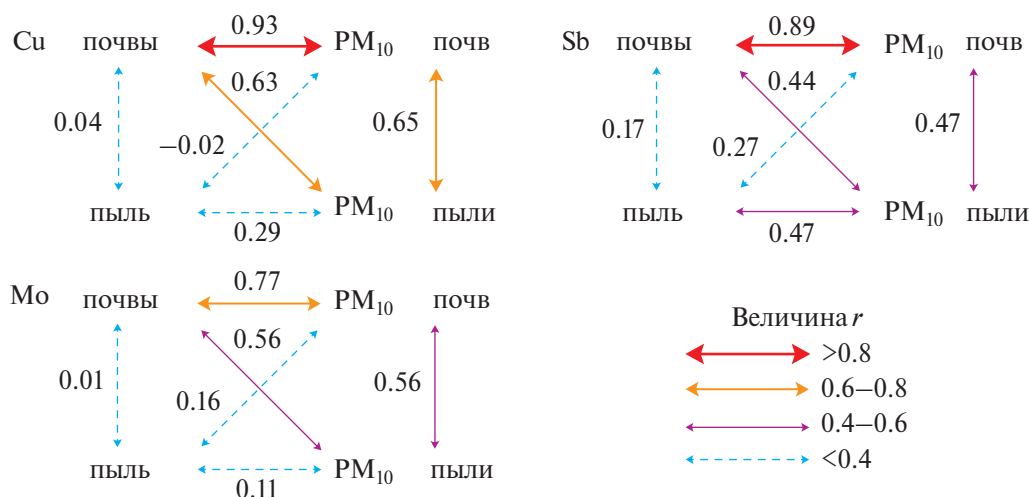


Рис. 4. Корреляционные связи Cu, Mo и Sb в системе почвы–дорожная пыль–PM<sub>10</sub> почв–PM<sub>10</sub> дорожной пыли.

Таблица 3. Коэффициенты корреляции Пирсона  $r$  между содержанием ТММ в подсистемах почвы–дорожная пыль, PM<sub>10</sub> почв–PM<sub>10</sub> дорожной пыли, почвы–PM<sub>10</sub> почв, дорожная пыль–PM<sub>10</sub> дорожной пыли, почвы–PM<sub>10</sub> дорожной пыли и дорожная пыль–PM<sub>10</sub> почв

ТММ	Величина $r$ в подсистемах					
	почвы – пыль	PM <sub>10</sub> почв – PM <sub>10</sub> пыли	почвы – PM <sub>10</sub> почв	пыль – PM <sub>10</sub> пыли	почвы – PM <sub>10</sub> пыли	пыль – PM <sub>10</sub> почв
V	0.03	-0.07	0.28	<b>0.42</b>	0.09	-0.17
Cr	-0.07	0.02	0.16	<b>0.41</b>	-0.15	-0.07
Mn	0.20	0.06	<b>0.57</b>	0.18	0.24	0.02
Fe	0.04	-0.14	<b>0.41</b>	<b>0.40</b>	0.11	-0.16
Co	0.05	-0.29	<b>0.43</b>	<b>0.57</b>	-0.01	-0.31
Ni	0.03	-0.07	0.36	0.04	0.21	-0.35
Cu	0.04	<b>0.65</b>	<b>0.93</b>	0.29	<b>0.63</b>	-0.02
Zn	0.20	0.33	<b>0.92</b>	<b>0.84</b>	0.19	0.28
As	0.11	0.07	<b>0.58</b>	-0.04	-0.10	0.17
Sr	0.02	0.10	<b>0.73</b>	0.24	0.05	-0.06
Mo	0.01	<b>0.56</b>	<b>0.77</b>	0.11	<b>0.56</b>	0.16
Cd	0.07	0.04	<b>0.84</b>	<b>0.62</b>	0.18	-0.08
Sn	0.18	0.33	<b>0.90</b>	0.17	<b>0.38</b>	0.29
Sb	0.17	<b>0.47</b>	<b>0.89</b>	<b>0.47</b>	<b>0.44</b>	0.27
Ta	0.29	-0.05	0.22	-0.22	-0.02	-0.18
W	-0.14	-0.32	<b>0.93</b>	<b>0.56</b>	-0.30	-0.13
Pb	0.15	0.27	<b>0.86</b>	<b>0.99</b>	0.18	0.21
Bi	-0.04	0.21	<b>0.55</b>	-0.07	-0.06	0.19

карбонатных материалов, в том числе применяемых в дорожном строительстве. На последнее указывает то, что концентрации W в почвах увеличиваются с ростом транспортной нагрузки, достигая наибольших уровней (в среднем 12.8 мг/кг) на МКАД, радиальных шоссе и средних дорогах.

Sb аккумулируется в супесчаных почвах элювиальных ландшафтов плоских поверхностей и трансэлювиальных ландшафтов пологих и крутых склонов моренной равнины (абсолютные высоты >188 м) в полтора раза интенсивнее, чем на более низких отметках, где содержание ТММ определяется крупностью дорожной сети – на МКАД, радиальных

шоссе и средних дорогах оно в 1.6 раза меньше, чем на крупных дорогах и во дворах (рис. 5а). В суглинистых почвах накопление Sb зависит от типа автодороги: максимальные концентрации металлоида наблюдаются на крупных и средних дорогах. Здесь наибольшее количество светофоров, а аккумуляция Sb во время частых маневров, таких как начало движения, торможение, поворот, происходит наиболее активно [29].

Ведущими факторами аккумуляции Mo и Cd являются геохимическая позиция и тип дороги, на втором месте физико-химические свойства почв: pH и EC<sub>1:5</sub> для Cd и содержание C<sub>орг</sub> для Mo. Так,

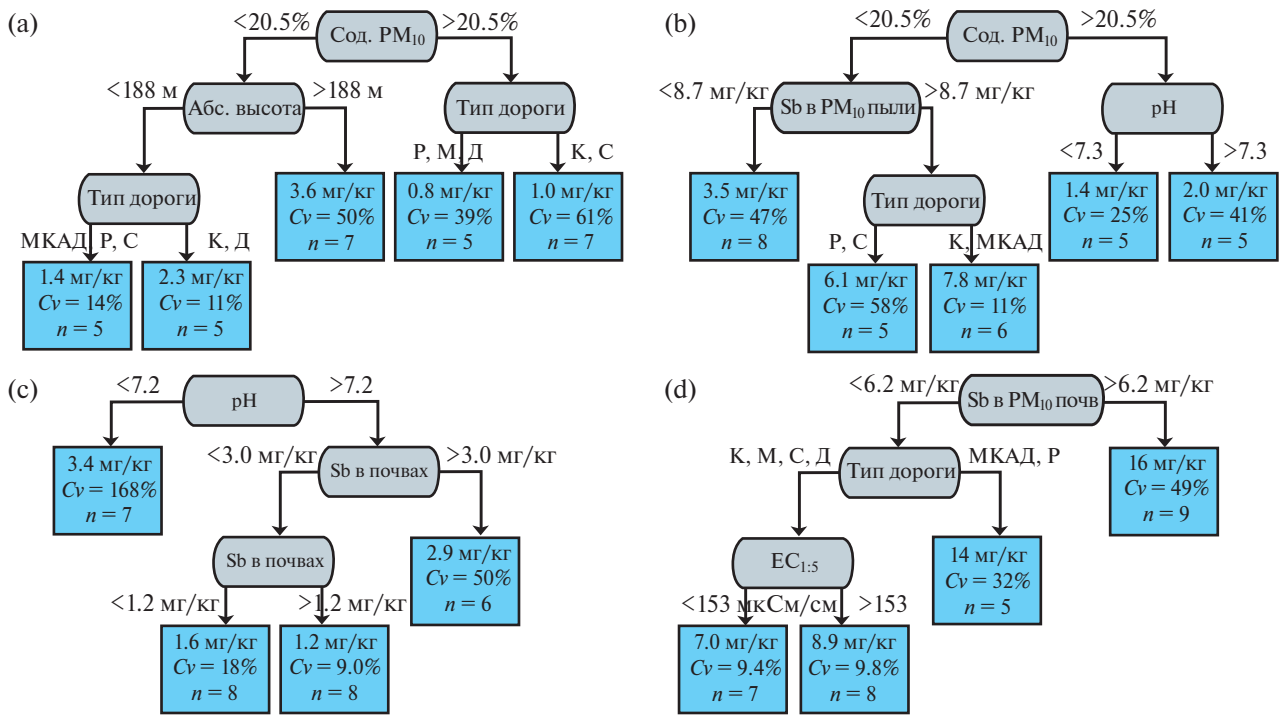


**Рис. 5.** Факторы накопления Sb в придорожных почвах (а), фракции  $PM_{10}$  почв (б), дорожной пыли (с) и фракции  $PM_{10}$  дорожной пыли (д) в ЗАО Москвы. Типы дорог: Р – радиальные шоссе, К – крупные, С – средние, М – малые дороги, Д – дворы с автопарковками;  $EC_{1.5}$  – удельная электропроводность водной вытяжки.

чем больше абсолютная высота и крупнее дорога, тем интенсивнее накапливаются Mo и Cd. В более насыщенных органическим веществом почвах накопление Mo интенсивнее из-за наличия органоминерального геохимического барьера [4]. Cd активнее аккумулируется в слабощелочных почвах, причем чем больше электропроводность водной вытяжки, тем меньше его концентрация. Это связано с тем, что при увеличении количества водорастворимых солей в почвах, в первую очередь, хлоридов (и соответственно при росте  $EC_{1.5}$ ), подвижность Cd также увеличивается, что может приводить кускоренному вымыванию комплексов  $CdCl_n^{2-n}$  из верхних горизонтов почв атмосферными осадками [30] и уменьшению валового содержания металла.

В суглинистых почвах (при содержании  $PM_{10} \gg 20\%$ ) Cu, Sn и Zn накапливаются интенсивнее, чем в супесчаных, причем концентрация Sn и Zn возрастает в щелочном диапазоне, а Cu – с уменьшением электропроводности. Последнее объясняется тем, что с ростом  $EC_{1.5}$  увеличивается подвижность Cu, что в условиях избыточного увлажнения приводит к ускоренному вымыванию  $Cu^{2+}$  из почв [41]. Кроме физико-химических свойств, вторым по значимости фактором аккумуляции Cu, Sn и Zn является тип дороги: концентрации металлов возрастают на крупных дорогах, что связано с интенсивной транспортной нагрузкой и более высокими объемами выбросов.

В частицах  $PM_{10}$  почв, в отличие от валового содержания ТММ, их аккумуляция в большей степени зависит от pH и гранулометрического состава почв, эти факторы определяют накопление девяти и одиннадцати ТММ соответственно, причем pH (щелочной геохимический барьер) является ведущим фактором для Co, Fe и Ni, а гранулометрический состав

(сорбционно-седиментационный геохимический барьер, по [4]) – для Bi, Cd, Cu, Sb, Sn, W и Zn (табл. 4). Менее значимыми факторами являются тип дороги и геохимическая позиция. Распределение W и Sb контролируется гранулометрическим составом и кислотно-основными свойствами, наименьшее влияние оказывает крупность дороги (рис. 5b, рис. S3). От содержания частиц  $PM_{10}$  в почвах зависит и аккумуляция Cd, Cu, Sn, Co, Fe, Ni и Zn в этих частицах. Реакция среды является вторым по значимости фактором в накоплении Bi, Cu, Sb, Sn, W и Zn. Концентрация Mo – одного из главных загрязнителей почв – контролируется содержанием элемента в частицах  $PM_{10}$  дорожной пыли, вероятно, выдувающихся с дорожного полотна и выпадающих на поверхность почв, а также объемом выбросов автотранспорта, гранулометрическим составом почв и типом дороги. Объем выбросов автотранспорта также значительно влияет на накопление Pb во фракции  $PM_{10}$  придорожных почв, на аккумуляцию As, Cu, Pb и Sb в  $PM_{10}$  влияет их содержание во фракции  $PM_{10}$  дорожной пыли.

В дорожной пыли для большинства ТММ ведущим фактором накопления является тип дороги, он определяет аккумуляцию восьми ТММ и является главным для W, Mo и As. Для Mo, Cu, Zn, Co, Fe и Ni аккумуляция происходит сильнее на крупных дорогах, однако Mo и Pb обнаруживают обратную тенденцию и накапливаются на дорогах с меньшей интенсивностью движения. Повышенное поступление Mo и Pb в дорожную пыль на малых дорогах, вероятно, связано с частыми маневрами транспорта и дорожными заторами. Mo и Pb входят в состав деталей тормозных механизмов автомобилей [47], а частое торможение приводит к росту выбросов автотранспорта и концентраций ТММ в дорожной пыли [25].



**Таблица 4.** Факторы накопления ТММ и их значимость в придорожных почвах и их фракции PM<sub>10</sub>, а также в дорожной пыли и ее фракции PM<sub>10</sub> в ЗАО Москвы

Факторы накопления ТММ	As	Bi	Cd	Co	Cu	Fe	Mo	Ni	Pb	Sb	Sn	W	Zn
Придорожные почвы													
Кислотно-основные условия (рН)	2-*	-	3+	1+	-	-	-	-	-	-	2+	2+	3+
Электропроводность EC <sub>1,5</sub>	1+	2-	4-	-	3-	2+	-	-	-	-	-	-	-
Содержание C <sub>орг</sub>	-	3+	-	-	-	-	3+	-	2-	-	-	-	-
Содержание PM <sub>10</sub>	-	-	-	-	1-	-	-	2+	-	1-	1-	1-	1-
Геохимическая позиция	-	1+	1+	2+	2+	1+	1+	1+	-	2+	-	4+	-
Тип дороги	-	2	2	3	2	-	2	3	-	3	3	3	2
Объем выбросов автотранспорта	-	-	-	-	-	3+	-	-	3-	-	-	-	-
Содержание элемента в пыли	-	-	-	4+	-	-	-	-	1+	-	-	-	-
PM <sub>10</sub> придорожных почв													
Кислотно-основные условия (рН)	-	2+	-	1+	2+	1+	-	1+	-	2+	2+	2+	2+
Электропроводность EC <sub>1,5</sub>	-	-	-	-	-	3-	-	-	-	-	2+	-	-
Содержание C <sub>орг</sub>	-	-	-	-	-	4-	-	-	-	-	-	-	-
Содержание PM <sub>10</sub>	-	1-	1-	2-	1-	2-	2-	2-	-	1-	1-	1-	1-
Геохимическая позиция	1-	-	-	-	-	-	-	-	-	-	-	-	-
Тип дороги	3	2	2	1	-	-	3	3	-	3	3	3	-
Объем выбросов автотранспорта	-	-	-	-	-	-	2+	-	2-	-	-	-	-
Содержание элемента в PM <sub>10</sub> пыли	2-	-	-	-	2+	-	1+	-	1+	2+	-	-	-
Дорожная пыль													
Кислотно-основные условия (рН)	-	-	-	2-	3-	-	-	4-	-	1-	2+	-	1-
Электропроводность EC <sub>1,5</sub>	-	3+	2+	-	-	1+	-	-	-	-	1+	4+	-
Содержание C <sub>орг</sub>	3+	2+	1+	-	-	-	-	-	3+	-	-	3-	3+
Содержание PM <sub>10</sub>	4-	-	-	-	-	-	4-	-	-	-	-	-	4-
Геохимическая позиция	-	1-	-	-	-	-	-	3-	-	-	-	-	-
Тип дороги	1	-	3	-	2	3	1	2	2	-	-	1	-
Объем выбросов автотранспорта	2-	-	-	1+	1+	2+	2+	1+	-	-	-	-	2+
Содержание элемента в почвах	-	-	4+	3+	-	4+	2-	-	1+	2+	3+	2+	-
PM <sub>10</sub> дорожной пыли													
Кислотно-основные условия (рН)	1+	-	-	-	-	-	-	2+	-	-	3-	-	1+
Электропроводность EC <sub>1,5</sub>	-	-	2+	3+	3+	3-	-	-	-	3+	2+	-	-
Содержание C <sub>орг</sub>	3-	1-	-	-	-	4-	-	1+	-	-	-	-	-
Содержание PM <sub>10</sub>	3-	-	3-	2-	-	-	-	-	-	-	-	2+	3-
Геохимическая позиция	-	-	-	-	4-	-	3-	-	-	-	-	-	-
Тип дороги	2	-	1	-	-	2	-	-	-	2	1	3	-
Объем выбросов автотранспорта	-	2-	-	1+	2+	-	2-	-	-	-	-	-	2+
Содержание элемента в PM <sub>10</sub> почв	-	3+	-	-	1+	1-	1+	-	1+	1+	-	1-	-

\* Ранги от 1 до 4 показывают уменьшение значимости фактора: "+" – рост показателя способствует увеличению концентрации элемента, "-" – уменьшению. Для качественных показателей характер связи не определяется.

Физико-химические свойства пыли занимают второе по значимости место (табл. 4). Реакция среды является ведущим фактором накопления Sb и Zn и влияет на концентрации Co, Cu, Ni и Sn на разных типах дорог. В отличие от почв, в дорожной пыли к аккумуляции ТММ приводит снижение рН, что может быть связано с усиленной поставкой ТММ при высокой транспортной нагрузке и интенсивных выбросах диоксидов азота, а также с активным применением на крупных дорогах хлоридных ПГР, которые могут являться подкис-

ляющими агентами [6]. Содержание органического вещества влияет на концентрации As, Bi, Cd, Pb, W и Zn, а электропроводность – на Bi, Cd, Fe, Sn и W в дорожной пыли, что обусловлено поставками ТММ из техногенных источников в составе органических и водорастворимых соединений. Увеличение содержания C<sub>орг</sub> в дорожной пыли можно объяснить интенсивным истиранием шин и выбросами выхлопных газов [22], а рост электропроводности – с увеличением поставок автотранспортом растворимых соединений [35].

Для Pb, Sb, Mo, Sn и W большое значение имеет уровень их содержания в придорожных почвах, что может указывать как на поступление этих ТММ в дорожную пыль при выдувании загрязненных частиц почв, так и на поставку ТММ в почвы при выдувании частиц дорожной пыли. Наименьшее влияние на аккумуляцию элементов оказывает гранулометрический состав пыли и геохимическая позиция точек отбора.

Ведущим фактором аккумуляции Sb в дорожной пыли являются кислотно-основные свойства последней: чем выше кислотность пыли, тем интенсивнее накапливается анионогенная Sb (рис. 5с). Активная поставка Sb из пыли в почвы и обратно подтверждается тем, что в щелочном диапазоне при высоком содержании Sb в придорожных почвах ( $>3$  мг/кг) аккумуляция загрязнителя в дорожной пыли усиливается в два раза по сравнению с обратной ситуацией, когда концентрации Sb в придорожных почвах не превышают 3 мг/кг.

Содержание Mo в дорожной пыли контролируется типом дороги, то есть интенсивностью движения, объемами выбросов автотранспорта и гранулометрическим составом пыли. На крупных, средних и малых дорогах концентрации Mo достигают максимальных значений, причем, если объем выбросов автотранспорта  $>23$  т/км в год, то содержание ТММ в пыли увеличивается в 1.5 раза. В супесчаных почвах (содержание  $PM_{10} < 17\%$ ) Mo накапливается активнее, чем в суглинистых. На МКАД, радиальных шоссе и во дворах аккумуляция Mo идет не столь интенсивно.

В частицах  $PM_{10}$  дорожной пыли ключевую роль в накоплении ТММ играет содержание загрязнителей в  $PM_{10}$  почв, для Cu, Fe, Mo, Pb, Sb и W этот фактор является ведущим (табл. 4, рис. 5d, рис. S3). Вторыми по значимости факторами являются объем выбросов автотранспорта (Co, Bi, Cu, Mo, Zn) и тип дороги (As, Cd, Fe, Sb, Sn, W). Значимыми факторами дифференциации  $PM_{10}$  дорожной пыли по содержанию ТММ являются также свойства дорожной пыли – pH (As, Zn, Ni, Sn) и Сорг (Bi, Ni, As, Fe). Содержание частиц  $PM_{10}$  и электропроводность водной вытяжки из дорожной пыли не относятся к ведущим факторам, однако содержание  $PM_{10}$  оказывает некоторое влияние на накопление Co, W, As, Cd и Zn, а величина  $EC_{1:5}$  – на Cd, Sn, Co, Cu, Fe, Sb.

Таким образом, валовое содержание ТММ в придорожных почвах и дорожной пыли контролируется различными факторами: в почвах определяющую роль играет геохимическая позиция участка опробования (его абсолютная отметка) и гранулометрический состав, химический состав дорожной пыли в основном контролируется антропогенными факторами – объемом выбросов автотранспорта и типом дороги. Кислотно-основные условия являются второстепенным фактором как для почв, так и для пыли.

Экологическая опасность загрязнения ТММ. Сравнение содержания девяти ТММ в почвах, дорожной пыли и их фракциях  $PM_{10}$  Западного округа Москвы с их ПДК и ОДК в почвах [20] показало, что наиболее опасно загрязнена фракция  $PM_{10}$  пыли, в которой концентрации Cu, Ni, Pb, Sb, Zn превысили нормативы практически повсеместно, а Cd и As – в 63 и 50% проб соответственно. При этом максимальные превышения ПДК/ОДК зафиксированы у Zn, Ni

и Pb (Ко 63, 47 и 28 соответственно). Несколько слабее загрязнена фракция  $PM_{10}$  почв с максимальными частотой и кратностью превышения нормативов у Ni (100%, Ко 31.6), Zn (100%, Ко 26.6), Cu (93%, Ко 7.7) и As (87%, Ко 10.1). Загрязнение валовых проб почв и пыли не столь интенсивно. Санитарно-гигиенические нормативы превышены почти в 100% проб у Zn, Ni и As с максимальными Ко 8.8, 31.6 и 5.0 соответственно, а у Cu, Cd и Pb – в 67, 27, 27% и максимальными значениями Ко 3.5, 2.8, 1.7. Таким образом, наибольшую экологическую опасность представляют три металла: Zn, Ni и Cu с близкой к 100% частотой превышения нормативов и очень высокими коэффициентами Ко для всех изучаемых компонентов. Дополнительную экологическую опасность создают высокие концентрации Pb, As, Cd и Sb в тонкодисперсных фракциях почв и пыли.

По среднему суммарному показателю загрязнения  $Z_c = 20$ , загрязнение ТММ придорожных почв ЗАО вблизи дорог разных типов относится к умеренно опасному с максимальными значениями на средних дорогах (25) и минимальными во дворах (18) и малых дорогах (16) (рис. 6). В частицах  $PM_{10}$  аккумуляция ТММ в 2.7 раза больше и средний показатель  $Z_c = 56$ . Загрязнение ТММ фракции  $PM_{10}$  почв высокое, опасное на многих дорогах, на крупных дорогах  $Z_c$  достигает максимума 71; на средних дорогах и радиальных шоссе показатель  $Z_c$  тоже высокий – 63 и 58 соответственно. Различия в суммарном загрязнении почв вблизи дорог разных типов существенны, наименее загрязненные – МКАД и дворы с автопарковками.

Полиэлементное загрязнение дорожной пыли относится к среднему, умеренно опасному уровню со средним  $Z_c = 18$ , наибольшим на МКАД и крупных дорогах (24 и 21 соответственно) и минимальным на радиальных шоссе (13) и во дворах с автопарковками (14). В мелкодисперсной фракции  $PM_{10}$  накопление ТММ превышает показатель в валовых пробах в 6.3 раза. Среднее значение суммарного показателя для частиц  $PM_{10}$   $Z_c = 113$ , что указывает на их очень опасное и высокое загрязнение ТММ на всех типах дорог. Максимальные значения наблюдаются на крупных дорогах и радиальных шоссе – 132 и 128 соответственно, наименьшие показатели характерны для малых дорог – 91.

## ЗАКЛЮЧЕНИЕ

Придорожные почвы в ЗАО по сравнению с фоновыми почвами более легкие, имеют повышенный до нейтральных значений pH, большее количество Сорг (4.7%) и в 3 раза более высокую электропроводность. Дорожная пыль имеет супесчаный состав, слабощелочную реакцию среды, такую же электропроводность  $EC_{1:5}$  и пониженное содержание Сорг. Крупность дорог на физико-химические свойства дорожной пыли и почв практически не влияет.

Приоритетными поллютантами придорожных почв и их фракции  $PM_{10}$  являются W, Sb, Mo, Cu, Cd, Sn, Zn, Bi, при этом в мелкодисперсной фракции  $PM_{10}$  концентрации большинства этих элементов заметно выше из-за большей удельной поверхности. Валовое содержание ТММ в почвах ЗАО варьирует в зависимости от геохимической позиции и гранулометрического состава почв, второстепенными фак-

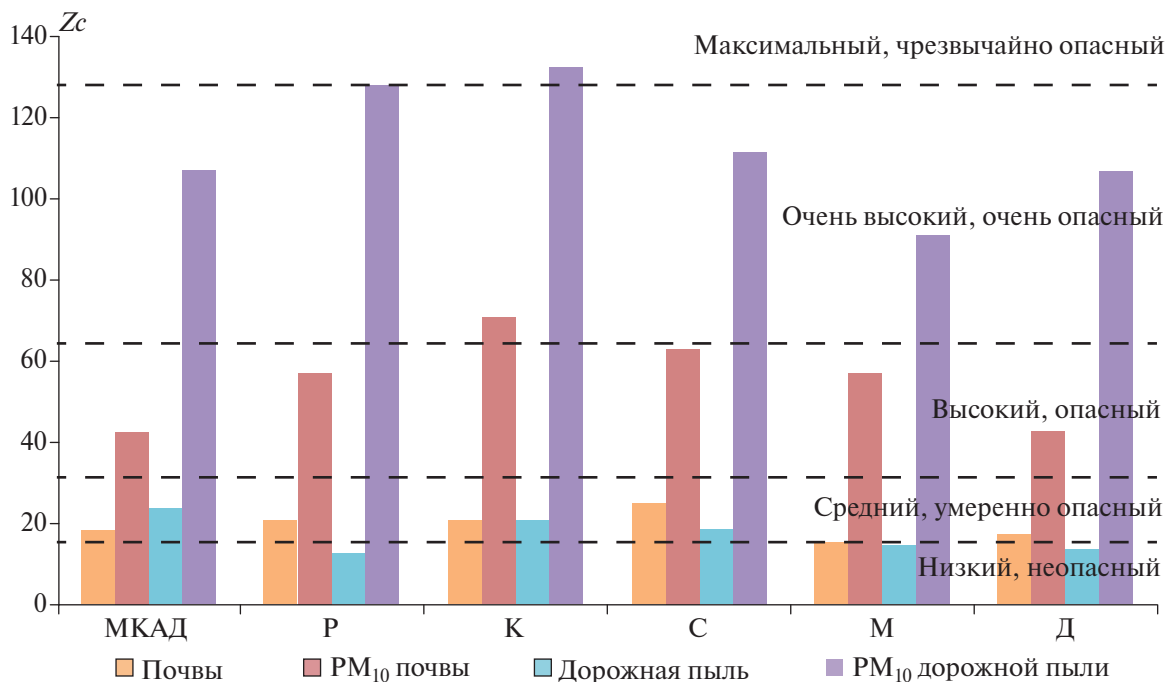


**Рис. 6.** Уровни суммарного показателя загрязнения  $Z_c$  и экологической опасности загрязнения придорожных почв и дорожной пыли ЗАО и их фракции  $PM_{10}$  ТММ на разных типах дорог и во дворах с автопарковками. Типы дорог: Р – радиальные шоссе, К – крупные, С – средние, М – малые дороги, Д – дворы.

торами являются реакция среды и тип дорог. Основным фактором накопления ТММ во фракции  $PM_{10}$  является гранулометрический состав почв, менее значимы положение в рельефе и приуроченность к тому или иному типу дороги или двору.

При одинаковых уровнях накопления количество приоритетных поллютантов в дорожной пыли несколько меньше, чем в почвах. В мелкодисперсных частицах  $PM_{10}$  дорожной пыли и почв набор приоритетных поллютантов совпадает, а уровни содержания во фракции  $PM_{10}$  пыли выше примерно в 2 раза. Ведущими факторами накопления большинства ТММ в дорожной пыли и частицах  $PM_{10}$  являются объем выбросов автотранспорта и тип дороги, физико-химические свойства пыли и поступление почвенных частиц.

В системе почвы–дорожная пыль– $PM_{10}$  почв– $PM_{10}$  дорожной пыли формируется парагенезис (совместное накопление ТММ с  $K_c > 2$ ) W–Sb–Sn–Mo–Zn–Cu. В подсистеме  $PM_{10}$  почв– $PM_{10}$  дорож-

ной пыли установлены значимые корреляции для Cu, Mo и Sb, что указывает на общие источники ТММ и преобладающую роль микрочастиц в обмене веществом и ТММ между изученными компонентами.

Загрязнение ТММ придорожных почв и дорожной пыли ЗАО относится к умеренно опасному с незначительными колебаниями на разных типах дорог. Существенно сильнее загрязнены мелкие частицы  $PM_{10}$  в почвах, их загрязнение является опасным на всех типах дорог, очень опасный уровень зафиксирован на крупных дорогах (средний  $Z_c = 71$ ). Мелкодисперсная фракция пыли загрязнена сильнее, чем в почвах, ее загрязнение является очень опасным и высоким (средний  $Z_c = 113$ ).

Полученные результаты могут быть использованы при планировании мероприятий, направленных на уменьшение негативного влияния загрязнения придорожных почв и дорожной пыли на городскую среду и здоровье населения.



### 3. ДОРОЖНАЯ ПЫЛЬ

## Enrichment of road dust particles and adjacent environments with metals and metalloids in eastern Moscow\*

### 1. INTRODUCTION

To assess the pollution level of urban environments with heavy metals and metalloids (HMMs), the chemical composition of various components of urban landscapes – atmospheric precipitation, urban soil, bottom sediments in water bodies and streams, vegetation, etc. – is studied.

Recently, increasing attention has been paid to road dust, since the negative impact of vehicles on environment in megacities (with a population of more than 10 million people) is very significant (Gurjar et al., 2008; D'Angiola et al., 2010; Goel and Guttikunda, 2015; Cheng et al., 2016; Kasimov et al., 2019c). The accumulation of HMMs in road dust was studied in various cities around the world (Škrbić et al., 2012; Wijaya et al., 2012; Saradhi et al., 2014) and in several cities of Russia – in the Selenga river basin (Republic of Buryatia), in the Perm region, Voronezh, Yekaterinburg, and some districts of Moscow (Kaigorodov et al., 2009; Ladonin and Plyaskina, 2009; Fedotov et al., 2014; Vlasov et al., 2015; Bityukova et al., 2016; Sereda, 2017; Prokof'eva et al., 2017; Seleznev, 2018; Kasimov et al., 2019b; Ladonin and Mikhailova, 2020). The distribution of Cd, Pb, Zn, Cu, Ni, Cr, Mn, and Fe has been well studied; less data are available for Sb, Bi, Mo, Ag, and As (Amato et al., 2009b; Quiroz et al., 2013; Dehghani et al., 2017). The amount and chemical composition of road dust are determined by the inflow of solid materials with fallout from the atmosphere, with blown off soil particles and particles formed due to pavement abrasion. The atmospheric supply of pollutants depends on the volume and composition of emissions from mobile sources, which include the emission of engine oil particles and fuel combustion products (Sb, Zn, Cu, Pb, and Mo), tire abrasion (Sb, Cd, Zn, Pb, Cu, Co, Ni, and Cr), wear of brake pads and alloy surfaces (Sb, Cu, Pb, Ag, Zn, Ni, W, and Cr) (Gietl et al., 2010; Charlesworth et al., 2011; Quiroz et al., 2013; Pant and Harrison, 2013; Grigoratos and Martini, 2015). In the manufacture of bearings, antifriction alloys based on Sn and Pb are used, which also include Sb, Cu, Cd, Ni, and As (State Standard GOST 1320-74, 2001).

Particulate matter emissions from diesel-powered cars running on Euro-5 and Euro-6 fuels are 28–36 times lower than those from engines working on Euro-1 and 5 times lower than those from engines working on Euro-4 (Emission standards, 2017). No less important is the mode of traffic, including the type, speed, and number of maneuvers associated with a stop (Irvine et al., 2009; Nazzari et al., 2013). As traffic intensities increase, the concentrations of Cd, Cu, Pb, Zn, Ni, Ti, Mo, Fe, Zr, K,

and Ca in road dust also increase (Apeageyi et al., 2011; Duong and Lee, 2011). Enhanced abrasion of road surface and road marking leads to the enrichment of road dust with Ag, Zn, As, W, Cr, V, and Co. The concentrations of Zn, Cu, and Cd are maximal in the dust accumulating near the curbstone, while Pb, Fe, and Ni concentrate at a distance of 1 m from the curbstone (Pal et al., 2011).

In turn, road dust itself can be a source of secondary pollution of atmospheric air and roadside soils with solid particles enriched with HMMs. There are coarse particles with a diameter of more than 2.5  $\mu\text{m}$  ( $\text{PM}_{2.5-10}$ ), fine particles ( $< 2.5 \mu\text{m}$ ,  $\text{PM}_{2.5}$ ), and very fine particles ( $< 1 \mu\text{m}$ ,  $\text{PM}_1$  and  $< 0.1 \mu\text{m}$ ,  $\text{PM}_{0.1}$ ). In the United States, road dust is the source of more than half the mass of  $\text{PM}_{10}$  particles and about a quarter of  $\text{PM}_{2.5}$  particles in the atmosphere, second only to fires in the latter case (United States, 2017). About 40% of  $\text{PM}_{10}$ , 15% of  $\text{PM}_{2.5}$ , and 3% of  $\text{PM}_1$  emissions are associated with road dust re-suspension from paved roads (Amato et al., 2009a; Chen et al., 2012; Lawrence et al., 2016). Road dust accounts for 60–100% Al, Si, Ca, and Ti; 40–60% Mg and Sr, 20–40% K, Fe, and Pb; and up to 20% S, Cl, Mn, Co, Ni, Cu, Zn, Sn, and Te in atmospheric particles  $\text{PM}_{2.5-10}$  (Grigoratos et al., 2014).

Dust particles enriched in HMMs and suspended in the surface air layer enter the human body with food and water (Revich, 2018; Khan and Strand, 2018).  $\text{PM}_{0.1}$  and  $\text{PM}_1$  are the most dangerous particles, as they penetrate into the pulmonary alveoli and bronchioles;  $\text{PM}_{1-2.5}$  are less dangerous as they enter the lungs and bronchi, and  $\text{PM}_{2.5-10}$  are retained by the upper respiratory tract (Tager, 2005). A decrease in the size of aerosol particles increases the risk of mutagenesis, the maximum of which is fixed for  $\text{PM}_{2.5}$  and smaller dust particles (Pagano et al., 1996). High ecological risk of fine particles of road dust compared with coarse ones is confirmed by data on an increase in the share of bio-available forms of Cu, Pb, Sb, Zn, Mn, Cr and Fe in fine fraction (Padoan et al., 2017).

Thus, in the traffic zone, there are two opposite processes – the entry of pollutants from the atmosphere and soils into road dust and the reverse migration of pollutants with road dust blown off from the roadway surface. To assess the distribution of pollutants between the components of urban landscapes, it is advisable to use geochemical paragenetic associations (parageneses) of the elements, i.e., those sets of the elements that have common sources and close migration pathways, so that they simultaneously accumulate in the particular environmental components (Perel'man and Kasimov, 1999). Data on the concentrations of

\* Kasimov N. S., Vlasov D. V., Kosheleva N. E. // Urban Climate. 2020;32(4):100638.

DOI: [10.1016/j.uclim.2020.100638](https://doi.org/10.1016/j.uclim.2020.100638). CiteScore 8.3, IF 6.7

pollutants in the snow cover, which is an indicator of air pollution, allow us to estimate the atmospheric addition, and data on the contents of HMMs in roadside soils are indicative for the pedolithogenic component in the road dust.

The contents of HMMs in the particle-size fractions of road dust in cities of the world – the fractional distribution of HMMs – remain insufficiently studied. Studies of the geochemical composition of road dust could be conditionally divided into two groups. The first one includes investigation of elements content in the different fractions of road dust. Recently studies have focused on the thoracic fraction (PM<sub>10</sub>), which poses a potential danger to public health (Ramírez et al., 2019; Kasimov et al., 2019a; Zhang et al., 2019; Tian et al., 2019), as well as fine PM<sub>2.5</sub> and PM<sub>5</sub> particles, which could be blown out from the road surface and could stay in the atmosphere for a long time (Kong et al., 2012; Padoan et al., 2017; Lanzerstorfer, 2018). At the same time little information is available about HMMs concentrations in the road dust particles with diameter less than 20 µm due to the difficulties in separation of this fraction by sieving (Lanzerstorfer, 2018).

Second group includes studies of fractional distribution of HMMs in road dust, specifically determination of a pollutants distribution between particle-size fractions in single road dust sample and definition of particles that are the main HMMs carriers. The main focus is on relatively coarse particles with sizes: < 125 and 125–200 µm (Abdel-Latif and Saleh, 2012), < 75, 75–180, 180–850, 850–2000 µm (Duong et al., 2006), < 63, 63–80 or 63–125 or 63–250 µm and some others, even more coarse fractions (Deletic and Orr, 2005; Han et al., 2008; Zafra et al., 2011; Han et al., 2014). But sometimes finer particles become the subject of research: < 38, 38–74, 74–125 µm in diameter (Shen et al., 2016), < 37, 37–50, 50–75, 75–100 µm (Fujiwara et al., 2011), < 20, 20–56, 56–90, 90–250 µm (Adamiec et al., 2016). Recent studies of the fractional HMMs distribution in road dust take into account fine particles < 5, 5–15, 15–35 µm and more coarse (Lanzerstorfer and Logiewa, 2019), and < 2.5, 2.5–10, 10–200, 200–2000 µm (Padoan et al., 2017). However, they do not consider the composition of the most ecologically dangerous PM<sub>1</sub> fraction. In our work, we tried to combine the methods and approaches used in both groups of studies.

Therefore, in our work special attention was paid to the fractional composition of road dust and the accumulation of HMMs in particles of different sizes. Thus, the purpose of our study was to identify the patterns of HMM accumulation in different particle-size fractions of dust on roads in eastern Moscow with different traffic intensities and their relationship with the composition of roadside soils and atmospheric precipitation in winter. Geochemical relationships between road dust and other environmental components were examined via isolating paragenetic groups of elements in the snow–road dust–soil system and in its individual subsystems (road dust–soil, road dust–snow dust, and snow dust–soil). One of the most polluted Eastern Administrative Okrug in Moscow, where detailed environmental and geochemical studies of the behavior of HMMs and organic pollutants in landscapes have been conducted since the 1980s, was chosen as the object of our study (Kasimov et al., 2016; Kasimov et al., 2017; Vlasov and Kasimov, 2016; Koshcheva et al., 2018; Vlasov et al., 2019).

*The following particular goals were set:*

- to determine the contents of HMMs in particle-size fractions of dust on roads with various traffic intensities;
- to identify the enrichment of road dust with HMMs relative to their background contents and to assess the environmental hazard of HMMs in road dust;
- to estimate the levels of HMM accumulation in atmospheric fallout and soils; and
- to evaluate the sources of pollutants in road dust and to identify paragenetic groups of HMMs in the particular components of urban landscapes in eastern Moscow.

## 2. MATERIALS AND METHODS

### 2.1. Study area

The main source of environmental pollution in eastern Moscow is motor transport, it contributes to about 80% of the total emissions (including gaseous compounds and particulate matter). This is slightly less than the average amount of motor transport emissions in Moscow (93%, or 980 thousand tons) (Bityukova and Mozgunov, 2019). Solid particles emissions in Moscow are less than 1% of all pollutant emissions from motor vehicles (Kul'bachevskii, 2018). However, these data greatly underestimate particulate emissions, because non-exhaust motor vehicle emissions that can account for more than half of the total exhaust and non-exhaust emissions of PM<sub>10</sub> by motor vehicles (Van der Gon et al., 2018), are not included. Sometimes their proportion in total emissions could reach 70–90% (Nagpure et al., 2016). However in 2005–2014 the annual mean emissions of CH<sub>4</sub> in Moscow rapidly decreased simultaneously with the reconstruction of the natural gas transportation, distribution, and consumption system; and the annual mean emissions of CO, NO<sub>x</sub>, and SO<sub>2</sub> slightly decreased too (Elansky et al., 2018). Deposition of carbonate dust, use of deicing reagents and decline of acidifying compounds emissions in Moscow led to the increase of snow pH values by 0.6 since 1999 to 2019 (Eremina and Vasil'chuk, 2019).

Stationary sources of pollution in eastern Moscow are represented by an incinerator, heat power plants, metal working and mechanical engineering, chemistry and petrochemistry, production of building materials, pulp and paper factories, food industry, and other industries concentrated in several industrial zones: Sokolinaya Gora, Prozhektor, Perovo, Rudnevo, Kosino-1, and Kosino-2 (Fig. 1). In the course of the zoning of eastern Moscow, the following land-use zones were identified: traffic; industrial and nonresidential buildings; residential low-rise (up to 5 floors), medium-rise (6–9), and high-rise (10 and more floors) zones; recreational; and post-agrogenic zones.

The study area is located in the marginal part of the Meshchera slightly dissected swampy glaciolacustrine plain inclined to the southeast and covered by a relatively large thickness of Quaternary glaciofluvial, alluvial, and technogenic deposits (Great Atlas of Moscow, 2012). The soil cover is represented by neutral, sometimes alkaline (pH up to 7.2–8.5) sandy and loamy sandy urban soils (Urbic Technosols), sealed soils (Ekranic Technosols), and replantozems (Urbic Technosols (Transportic)). Human-transformed and natural soils are developed in the recreational zone: soddy-podzolic and urban soddy-podzolic



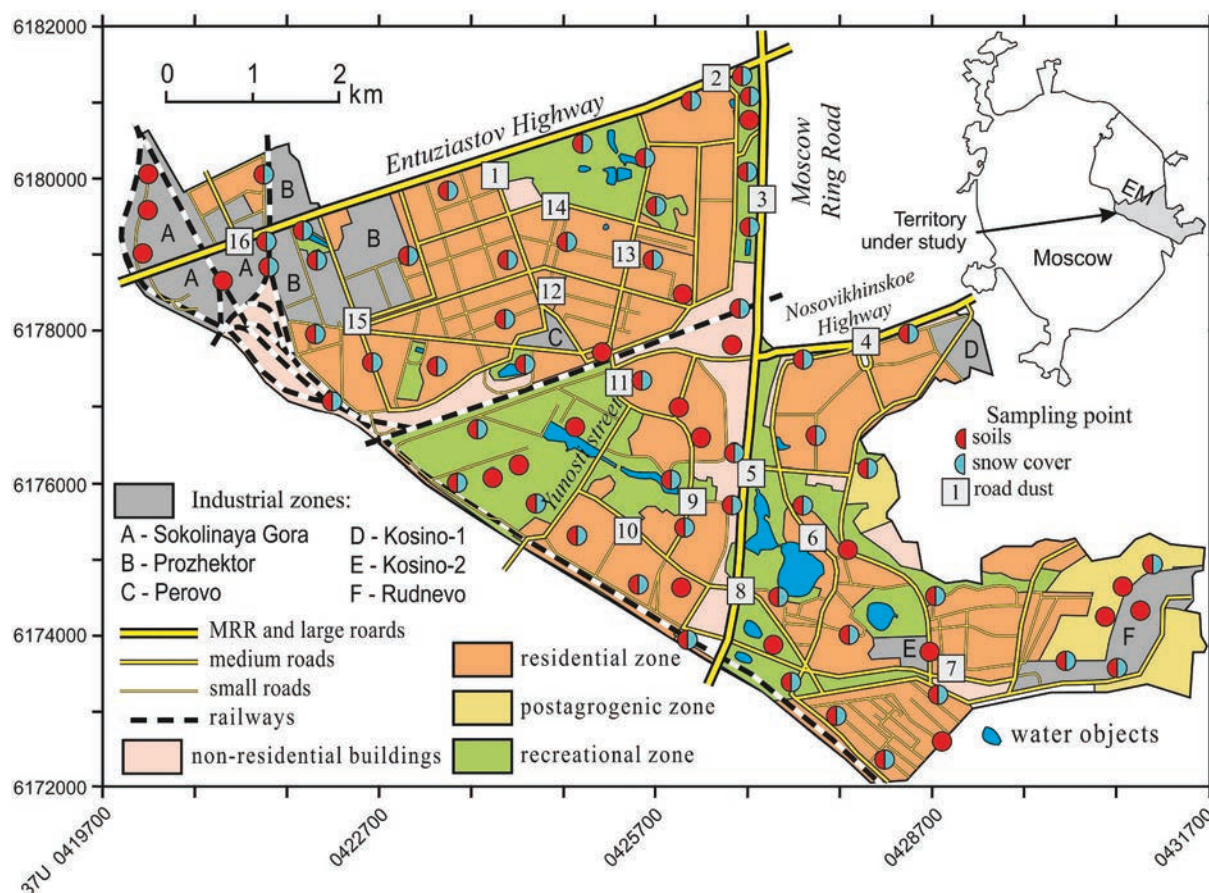


Fig. 1. Land-use zoning and snow, soil, and road dust sampling points in eastern Moscow (EM). UTM coordinate system.

soils (Eutric Albic Retisols (Prototechnic)) and their gleyic, gleyed, and swampy varieties (Great Atlas of Moscow, 2012; Kasimov et al., 2016). The surface horizons of urban soils in eastern Moscow are characterized by increased pH values (by almost three pH units), higher (by 2.7%) content of organic matter, considerably higher (by almost four times) adsorption capacity, 20% higher content of physical clay ( $< 0.01$  mm, or  $PM_{10}$ ), and three to seven times higher content of nutrients in comparison with the natural background soils owing to deposition of industrial and construction dust and application of peat composts and deicing mixtures (Kasimov et al., 2016).

## 2.2. Field work

Road dust was collected in July 2013 from the road surfaces with a plastic brush and dustpan in three replicates at distances of 5–10 m after a five-day dry period on roads with various traffic intensities (Fig. 1): Moscow Ring Road (MRR) with the traffic intensity of about 250 thousand cars per day (sampling points 3, 5, 8); large roads (80–100 thousand cars per day) – Entuziastov Highway (points 2, 16) and Nosovikhinskoe Highway (4); medium roads (40–55 thousand cars per day) – Bol'shaya Kosinskaya Street (6), Veshnyakovskaya Street (9, 11), Svobodnyi Prospect (13), and intersection of Zelenyi Prospect with Perovskaya and Plekhanov streets (15); small roads (20–25 thousand cars per day) – Novogireevskaya Street (1), Dmitrievskii Street (7), intersection of Moldagulova and Sniperskaya streets (10), Soyuznyi Prospect (12), and intersection of Metallurgov and Martenovskaya streets (14).

To determine the sources of the road dust, samples

from the surface (0–15 cm) horizon of urban soils ( $n = 73$ ) were taken; in winter, the snow cover ( $n = 51$ ) was sampled at a quasi-uniform grid with a step of 500–600 m, which made it possible to characterize the spatial distribution of HMMs in the study area.

Road dust is a specific technogenic object that does not have a background analogue; therefore, natural abundances of the elements in the upper part of the continental crust were used as reference standards. The following sources of data were used: (Rudnick and Gao, 2014) for Ag, Cd, and Mo; (Hu and Gao, 2008) for Bi, Co, Cu, and V; (Wedepohl, 1995) for Sn; and (Grigoriev, 2009) for As, Be, Cr, Fe, La, Mn, Ni, Mo, Pb, Sb, Sr, Ti, W, and Zn. For snow, the background reference data were obtained from five samples taken 45–50 km west of Moscow not far from the cities of Golitsyno and Zvenigorod, where the aerotechnogenic influence of Moscow is minimal. For soils, background reference data were obtained from ten samples of soddy-podzolic soils (Retisols) taken in the Meshchera Natural Park in Vladimir region, about 150 km east of Moscow, where the soils are developed from the same sediments of sandy, loamy sandy, and sandy loamy textures as in eastern Moscow.

## 2.3. Laboratory studies

Road dust samples were dispersed using wet rubbing, and particle-size fractions were isolated by elutriation (Vadyunina and Korchagina, 1986). Then, the obtained solutions were filtered through membrane filters with pore diameter of  $0.45 \mu\text{m}$ . Four particlesize fractions were separated: clay ( $< 1 \mu\text{m}$ ,  $PM_1$ ), fine and medium



silt (1–10  $\mu\text{m}$ ,  $\text{PM}_{1-10}$ ), coarse silt (10–50  $\mu\text{m}$ ,  $\text{PM}_{10-50}$ ), and sand (50–1000  $\mu\text{m}$ ,  $\text{PM}_{>50}$ ). To separate the solid particles from snow, snow samples after melting at room temperature were filtered through membrane filters with pore diameter of 0.45  $\mu\text{m}$ .

The concentrations of Ag, As, Be, Bi, Cd, Co, Cr, Cu, Fe, La, Mn, Mo, Ni, Pb, Sb, Sn, Sr, Ti, V, W, and Zn was determined in road dust and its particle-size fractions, soils, and dust component of snow by the mass-spectral and atomic emission methods with inductively coupled plasma on Elan-6100 and Optima-4300 quadrupole mass spectrometers (Perkin Elmer, USA) at the N.M. Fedorovsky All-Russia Research Institute of Mineral Raw Materials (Moscow).

## 2.4. Data treatment

The obtained analytical data were used to calculate several geochemical indicators for separate components of the urban environment.

### Road dust:

- Relative abundance coefficients (concentration clarkes,  $CC$ ):  $CC = C/K$ , where  $C$  is the content of a metal or metalloid in the road dust, mg/kg; and  $K$  is the natural abundance of the element in the upper part of the continental crust, mg/kg;
- Enrichment factor  $EF = (C/C_{ref})_{\text{sample}} / (C/C_{ref})_{\text{earth crust}}$ , where  $C$  and  $C_{ref}$  are the contents of the studied element and the reference element in the sample and in the upper continental crust, respectively. In our case, La was chosen as the reference element due to slight use in industrial production and low levels of emissions from transport (Avino et al., 2008);
- Total enrichment index ( $Ze$ ) of the road dust with pollutants:  $Ze = \sum EF - (n - 1)$  at  $EF > 1.5$ , where  $n$  is the number of elements with  $EF > 1.5$  (Vlasov et al., 2015). This index characterizes the levels of accumulation of chemical elements in the road dust solely under the impact of technogenic sources and excludes the effects related to blown off soils or surface materials. The grades of  $Ze$  are indicative for the degree of environmental hazard; with respect to dust load in the snow, the following grades of  $Ze$  are accepted in Russia: < 32, non-hazardous; 32–64, moderately hazardous; 64–128, hazardous; 128–256, very hazardous; and > 256, extremely hazardous (Saet et al., 1990; Kasimov et al., 2016).

### Snow cover:

- Daily dust load ( $P_n$ , kg/km<sup>2</sup> per day):  $P_n = 107 \cdot m / (n \cdot l \cdot S)$ , where  $m$  is the mass of solids in the snow, g;  $n$  is the number of snow samples taken with a cylinder of definite diameter;  $l$  is the number of days with the snow cover; and  $S$  is the cylinder crosssectional area, cm<sup>2</sup>, 107 is the conversion factor from g/cm<sup>2</sup> to kg/km<sup>2</sup>;
- Deposition of the elements ( $D$ , mg/km<sup>2</sup> per day):  $D = P_n \cdot C$ , where  $C$  is the concentration of a given elements in the suspended matter, mg/kg;
- Excess of an element deposition on the studied urban area over its deposition on the background area  $Kd = D/Db$ ;
- Total excess of deposition of the elements on the urban area over their deposition on the background area

$Zd$ :  $Zd = \sum Kd - (n - 1)$ , where  $n$  is the number of elements with  $Kd > 1.5$  (Kasimov et al., 2016). Snow cover and soils:

- Coefficient of concentration of the pollutants relative to the background level (relative enrichment factor)  $Kc = C / C_{\text{backgr}}$ , where  $C$  and  $C_{\text{backgr}}$  are element concentrations in the samples taken from the studied urban territory and from the background area;
- Total contamination of the studied samples with the chemical elements  $Zc$ :  $Zc = \sum Kc - (n - 1)$ , where  $n$  is the number of elements with  $Kc > 1.5$  (Saet et al., 1990). The following grades of environmental hazard according to  $Zc$  values are accepted in Russia: < 16, non-hazardous; 16–32, moderately hazardous; 32–64, hazardous; 64–128, very hazardous; and > 128, extremely hazardous (Saet et al., 1990; Kasimov et al., 2016).

## 3. RESULTS AND DISCUSSION

### 3.1. Heavy metals and metalloids in road dust

#### 3.1.1. The contents of HMMs in particle-size fractions of road dust

Particle-size distribution of road dust in eastern Moscow is characterized by the low content of  $\text{PM}_{10}$  fraction (1.8% on the average). The percent of particle-size fractions increases with an increase in their size; thus, the content of  $\text{PM}_{1-10}$  fraction is up to 13%;  $\text{PM}_{10-50}$ , up to 16%; and  $\text{PM}_{>50}$ , up to 69%. An increase in the traffic intensity leads to the rise in the content of sand fraction in road dust owing to blowing out of smaller particles. This is confirmed by an increased content of fractions  $\text{PM}_{1-10}$  and  $\text{PM}_{10-50}$  (16.5% and 34.6%, respectively) and a decreased content of fraction  $\text{PM}_{>50}$  (45.2%) in roadside soils as compared with road dust (13%, 16%, and 69%, respectively). Particle-size distribution of road dust of eastern Moscow is practically the same as of the rest of the city (Kasimov et al., 2019c). A small proportion of fine fractions in the total mass of road dust is also typical for other cities (Zhao et al., 2010; Zafra et al., 2011; Duong and Lee, 2011; Bourliva et al., 2017; Lanzerstorfer and Logiewa, 2019).

The concentrations of Cd and Sb in road dust samples from eastern Moscow are about six times higher than the natural abundances of these elements in the upper continental crust; the concentrations of Sn, Zn, Cu, Mo, Pb, Ag, Bi, and W are 2.5 to 4 times higher than the natural abundances of these elements (Table 1). Close data on element concentrations in road dust were obtained for many other world cities, e.g., for Tokyo (Japan), Mumbai (India), Tehran (Iran) (Wijaya et al., 2012; Saradhi et al., 2014; Dehghani et al., 2017).

The concentrations of virtually all elements in particle-size fractions of road dust from eastern Moscow tend to decrease with an increase in the size of the particles (Table 1). The exceptions are Ti and Sr: their maximum concentrations are typical of sand and coarse silt fractions entering road dust from the roadside soils. The presence of soil particles in road dust may also be the reason for the higher concentrations of W, Cr, V, Fe, and Mn in the coarse silt in comparison with the fine and medium silt.

The fractional geochemical pattern of road dust can be reflected by the percent of the elements in the particular particle-size fractions (mass loading)  $MG_i = C_i \cdot P_i /$

**Table 1.** Contents of HMMs in particle-size fractions of road dust (16 samples), the solid fraction of snow (51 samples), and soils (73 samples) of eastern Moscow and natural abundances of these elements (K) in the upper continental crust, mg/kg (for Fe and Ti, g/kg).

HMMs	Road dust					Solid fraction of snow	Soils	K
	fractions				total dust			
	PM1	PM1-10	PM10-50	PM > 50				
Ag	2.9 (0.45–8.2)	0.75 (0.38–1.6)	0.19 (0.003–1.3)	0.004 (0.002–0.01)	0.15 (0.08–0.34)	3.6 (0.01–110)	1.1 (0.25–17)	0.053 <sup>a</sup>
As	10 (6.5–19)	7.9 (4.9–12)	3.2 (1.7–6.5)	1.6 (0.41–3.2)	2.8 (1.4–4.2)	18 (0.82–167)	7.8 (3.0–55)	5.6 <sup>b</sup>
Be	1.2 (1.0–1.6)	0.87 (0.60–1.1)	0.71 (0.35–1.4)	0.70 (0.38–1.4)	0.75 (0.43–1.4)	1.9 (0.88–5.1)	0.96 (0.46–1.6)	2.3 <sup>b</sup>
Bi	2.0 (1.6–2.8)	1.8 (1.4–2.8)	0.88 (0.51–1.8)	0.31 (0.07–0.90)	0.61 (0.21–1.0)	2.7 (0.44–27)	0.61 (0.12–6.1)	0.23 <sup>c</sup>
Cd	2.3 (1.8–3.9)	1.8 (1.3–2.3)	0.76 (0.41–1.4)	0.35 (0.11–0.83)	0.61 (0.27–1.5)	3.5 (0.66–54)	1.6 (0.30–14)	0.09 <sup>a</sup>
Cu	308 (194–567)	218 (141–372)	113 (53–269)	65 (26–125)	93 (40–181)	762 (195–2466)	59 (13–220)	27 <sup>c</sup>
Co	24 (20–30)	16 (14–20)	9.5 (4.8–15)	5.8 (2.3–9.2)	8.0 (3.8–12)	17 (6.6–43)	8.5 (5.5–13)	15 <sup>c</sup>
Cr	158 (126–206)	65 (13–128)	70 (40–143)	40 (22–63)	50 (32–74)	118 (25–371)	94 (24–450)	92 <sup>b</sup>
Fe	54 (42–65)	24 (4.5–46)	30 (16–54)	19 (6.8–32)	22 (11–31)	43 (17–188)	20 (10–77)	40.6 <sup>b</sup>
La	34 (30–40)	28 (22–35)	22 (14–31)	16 (6.8–24)	18 (9.0–24)	26 (13–53)	23 (13–77)	32 <sup>b</sup>
Mn	838 (577–1261)	373 (90–753)	433 (265–650)	295 (116–493)	339 (176–473)	674 (369–1440)	491 (209–1937)	770 <sup>b</sup>
Mo	7.2 (5.2–9.9)	6.7 (4.0–14)	4.4 (2.5–14)	2.9 (1.2–7.5)	3.5 (1.7–6.4)	4.7 (0.07–25)	1.6 (0.57–6.1)	1.1 <sup>a</sup>
Ni	73 (61–117)	54 (42–79)	34 (17–57)	19 (7.3–35)	26 (13–46)	135 (53–419)	31 (14–120)	50 <sup>b</sup>
Pb	176 (112–576)	123 (65–412)	64 (32–146)	35 (10–83)	53 (20–130)	333 (73–777)	63 (13–330)	17 <sup>b</sup>
Sb	20 (14–26)	15 (6.8–25)	6.1 (2.9–14)	2.3 (1.3–5.5)	4.6 (2.7–6.8)	19 (4.9–62)	1.7 (0.45–6.3)	0.81 <sup>b</sup>
Sn	32 (25–45)	24 (16–34)	11 (6.4–21)	6.3 (3.7–17)	9.5 (5.4–15)	24 (9.7–53)	12 (2.3–73)	2.5 <sup>d</sup>
Sr	73 (56–131)	35 (6.4–81)	118 (43–209)	153 (90–301)	133 (87–251)	111 (50–256)	117 (61–230)	270 <sup>b</sup>
Ti	1.4 (1.0–1.8)	0.71 (0.15–1.4)	2.1 (0.87–4.3)	1.8 (0.43–3.2)	1.7 (0.56–2.8)	2.6 (1.3–5.1)	2.4 (1.2–3.3)	3.9 <sup>b</sup>
V	131 (117–141)	57 (12–106)	75 (42–117)	48 (13–84)	55 (23–79)	190 (87–470)	71 (39–94)	106 <sup>c</sup>
W	21 (2.8–54)	5.7 (0.5–17)	9.4 (0.2–27)	3.4 (0.6–7.3)	5.3 (1.1–10)	22 (8.1–46)	4.5 (0.72–14)	2.03 <sup>b</sup>
Zn	1180 (769–4167)	455 (81–1350)	350 (177–1036)	190 (119–619)	262 (160–705)	673 (335–3115)	179 (46–690)	75 <sup>b</sup>

Note: Minimal and maximal values are given in parentheses. Abundances of the elements in the upper continental crust are given according to <sup>a</sup> Rudnick and Gao, 2014; <sup>b</sup> Grigoriev, 2009; <sup>c</sup> Hu and Gao, 2008; <sup>d</sup> Wedepohl, 1995

$C_{dust}$ , where  $C_i$  and  $P_i$  are the concentration (mg/kg) of an element in the  $i$ -th fraction of the road dust and share (%) of the  $i$ -th fraction of particles in the total road dust, and  $C_{dust}$  is the concentration (mg/kg) of this element in the whole dust sample. The fractional distribution of HMMs in the road dust on the roads with different traffic intensities is displayed in Fig. 2.

With an increase in the traffic intensity, the percent of the elements increases in the sand fraction; decreases in the fine, medium, and coarse silt fractions; and remains stable in the clay fraction. Sand fractions of road dust sampled on small and medium roads concentrate Fe, Mn, Be, Ti, Sr, Sn, Cr, Mo, and V; sand fractions of road dust from large highways with heavy traffic concentrate virtually all HMMs. On small roads, the most environmentally hazardous particles PM<sub>1</sub> and PM<sub>1-10</sub> contain about 93% of Ag; 51–60% of Cd, Bi, As, Sb, and Sn; 31–50% of Cr, Mo, Pb, Ni, Zn, Co, and Cu; and up to 15–30% of W, V, Fe, Mn, Be, Ti, and Sr out of the total contents of these elements in bulk samples of the road dust. On larger roads, the share of elements concentrated in PM<sub>1</sub> and PM<sub>1-10</sub> particles decreases. In the road dust from the MRR, these particles contain 78% of Ag; 31–35% of Cd and Sb; 16–30% of Bi, As, Sn, Mo, Pb, Ni, Zn, Co, and Cu; 6–15% of W, Cr, V, Fe, Mn, and Be; and 2–5% of Ti and Sr out of the total contents of these elements in the road dust as a whole. The high sorption capacity of fine particles explains the fact that even in the topsoils of small erosional landforms located in the uncontaminated area of the

center of European Russia PM<sub>1</sub> and PM<sub>1-10</sub> accounts for 40–60% of Mn, Cu, Zn, Pb, Co, Ni, Cr (Samonova and Aseyeva, 2020).

### 3.1.2. Enrichment of road dust and its particle-size fractions with HMMs

The main sources of HMMs in road dust were identified using the enrichment factor  $EF$  calculated relative to La, which is weakly involved in the processes of technogenesis. The enrichment of dust as a whole and its individual fractions with Ag, Cd, Sb, Zn, Sn, Cu, Pb, W, Bi, and Mo ( $EF > 2$ ) indicates the input of these HMMs from technogenic sources (Fig. 3), among which motor transport emissions prevail. For As, Cr, Co, Ni, Fe, Sr, V, Mn, Ti, and Be ( $EF < 2$ ), natural (or crustal either terrigenous) and mixed sources – parent materials, soils, building materials for creating the roadways, etc. – predominate.

The enrichment of road dust with HMMs depends on the traffic intensity, which is related to the width of the roads. On average, road dust in eastern Moscow is enriched in Cd<sub>12</sub>Sb<sub>10</sub>Sn<sub>7</sub>Zn<sub>6</sub>Cu<sub>6</sub>Mo<sub>6</sub>Pb<sub>5</sub>Ag<sub>5</sub>W<sub>5</sub>Bi<sub>5</sub> (subscripts indicate  $EF$  values). Depending on the nature of the relationship with the intensity of the traffic, four groups of elements are distinguished: (a) Cd and Zn, in which a regular change in the  $EF$  value occurs with an increase in the traffic intensity ( $EF$  decreases for Cd and increases for Zn); (b) Be, Sn, Cu, Cr, Ni, and Mo with  $EF$  values increase in the following sequence: MRR < small roads < medium roads < large roads; (c) Co, V, Ti, Fe, and Mn, whose  $EF$  values slightly differ for different

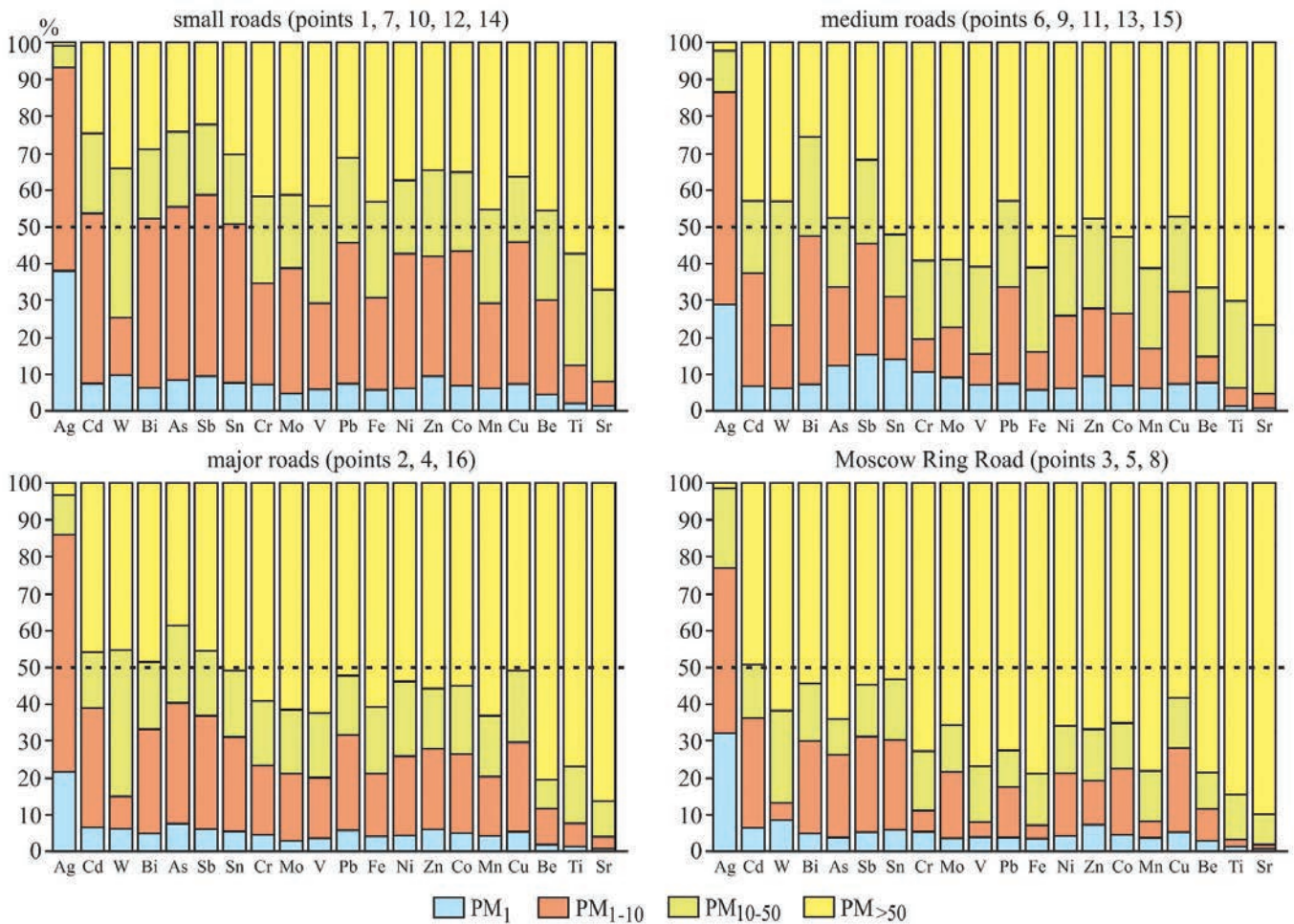


Fig. 2. Fractional distribution of HMMs in road dust of eastern Moscow.

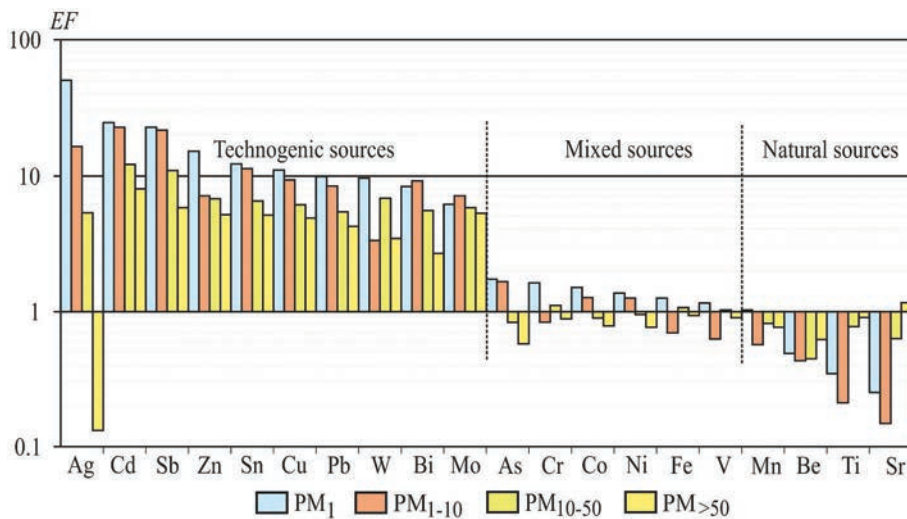


Fig. 3. Enrichment of particle-size fractions of road dust from eastern Moscow with HMMs ( $n = 16$ ).

roads; and (d) Ag, Bi, W, Pb, Sb, As, and Sr with  $EF$  values variations regardless of the size of the roads.

Fraction  $PM_1$  of road dust in eastern Moscow accumulates  $Ag_{51}Cd_{25}Sb_{23}Zn_{15}Sn_{12}Cu_{11}Pb_{10}W_9Bi_8Mo_6Co_2As_2Cr_2$ . On all roads,  $PM_1$  particles are very strongly ( $EF > 20$ ) enriched in Ag, Cd, and Sb; on MRR, Zn is added to them (Table 2). For Sn, Bi, Mo, Cr, and As, the difference in  $EF$  values between the roads with various traffic intensities is small; for V, Fe, Mn, Be, Co, Ni, Ti,

and Sr,  $EF$  is less than 1.5. There is no data on enrichment of the  $PM_1$  fraction of road dust in other cities, however, it was found that in the metropolitan area of Turin, Italy as in Moscow Zn, Sb, Cu, and Pb accumulate in  $PM_{2.5}$  fraction of road dust (Padoan et al., 2017).

Fraction  $PM_{1-10}$  is characterized by a weaker accumulation of Ag in comparison with fraction  $PM_1$ :  $Cd_{23}Sb_{22}Ag_{17}Sn_{12}Cu_9Bi_9Pb_8Zn_7Mo_7W_3Co_2As_2$ . Particles  $PM_{1-10}$  are strongly enriched in Cd on all roads,



**Table 2.** Fractional distribution of HMMs and total enrichment of road dust in eastern Moscow.

Fraction	Roads	EF levels				Ze
		> 20	20–10	10–5	5–2	
PM <sub>1</sub>	S	Ag <sub>63</sub> Cd <sub>22</sub> Sb <sub>21</sub>	Zn <sub>11</sub> Sn <sub>11</sub>	Cu <sub>9</sub> W <sub>9</sub> Pb <sub>8</sub> Bi <sub>8</sub> Mo <sub>6</sub>	As <sub>2</sub>	160
	M	Ag <sub>40</sub> Cd <sub>30</sub> Sb <sub>25</sub>	Pb <sub>14</sub> Sn <sub>14</sub> Cu <sub>12</sub> Zn <sub>12</sub> W <sub>11</sub> Bi <sub>10</sub>	Mo <sub>7</sub>	Cr <sub>2</sub> As <sub>2</sub>	166
	L	Ag <sub>37</sub> Sb <sub>24</sub> Cd <sub>23</sub>	Cu <sub>14</sub> Sn <sub>13</sub> Zn <sub>12</sub>	Pb <sub>8</sub> Bi <sub>8</sub> Mo <sub>7</sub> W <sub>5</sub>	As <sub>2</sub> Cr <sub>2</sub>	144
	MRR	Ag <sub>62</sub> Zn <sub>30</sub> Cd <sub>21</sub> Sb <sub>21</sub>	W <sub>13</sub> Sn <sub>10</sub>	Pb <sub>9</sub> Cu <sub>8</sub> Bi <sub>8</sub> Mo <sub>6</sub>	Cr <sub>2</sub> As <sub>2</sub>	181
	EM	Ag <sub>51</sub> Cd <sub>25</sub> Sb <sub>23</sub>	Zn <sub>15</sub> Sn <sub>12</sub> Cu <sub>11</sub> Pb <sub>10</sub>	W <sub>9</sub> Bi <sub>8</sub> Mo <sub>6</sub>	As <sub>2</sub> Cr <sub>2</sub>	163
PM <sub>1–10</sub>	S	Cd <sub>22</sub>	Sb <sub>18</sub> Ag <sub>14</sub> Sn <sub>10</sub>	Bi <sub>8</sub> Cu <sub>7</sub> Pb <sub>7</sub> Mo <sub>6</sub>	Zn <sub>4</sub> W <sub>2</sub> As <sub>2</sub>	90
	M	Cd <sub>25</sub> Sb <sub>22</sub>	Ag <sub>15</sub> Pb <sub>12</sub> Sn <sub>12</sub> Bi <sub>11</sub> Cu <sub>10</sub>	Mo <sub>7</sub> Zn <sub>6</sub> W <sub>6</sub>	–	118
	L	Sb <sub>27</sub> Cd <sub>22</sub> Ag <sub>21</sub>	Sn <sub>14</sub> Cu <sub>13</sub> Zn <sub>10</sub> Mo <sub>10</sub> Bi <sub>10</sub>	Pb <sub>7</sub>	As <sub>2</sub> W <sub>2</sub>	129
	MRR	Sb <sub>22</sub> Cd <sub>21</sub>	Ag <sub>18</sub> Zn <sub>10</sub>	Sn <sub>9</sub> Cu <sub>8</sub> Bi <sub>8</sub> Pb <sub>7</sub> Mo <sub>6</sub>	W <sub>2</sub> As <sub>2</sub>	104
	EM	Cd <sub>23</sub> Sb <sub>22</sub>	Ag <sub>17</sub> Sn <sub>12</sub>	Cu <sub>9</sub> Bi <sub>9</sub> Pb <sub>8</sub> Zn <sub>7</sub> Mo <sub>7</sub>	W <sub>3</sub> As <sub>2</sub>	109
PM <sub>10–50</sub>	S	–	Cd <sub>13</sub>	Sb <sub>8</sub> W <sub>8</sub> Sn <sub>5</sub> Zn <sub>5</sub> Pb <sub>5</sub>	Cu <sub>4</sub> Mo <sub>4</sub> Bi <sub>4</sub> Ag <sub>2</sub>	50
	M	–	Cd <sub>12</sub> Sb <sub>10</sub>	W <sub>7</sub> Pb <sub>7</sub> Cu <sub>6</sub> Sn <sub>6</sub> Zn <sub>5</sub> Mo <sub>5</sub> Bi <sub>5</sub>	Ag <sub>4</sub>	57
	L	–	Sb <sub>14</sub> Cd <sub>13</sub> Cu <sub>11</sub> Mo <sub>11</sub>	Sn <sub>9</sub> Bi <sub>8</sub> Zn <sub>7</sub> W <sub>6</sub> Pb <sub>5</sub>	Ag <sub>4</sub>	78
	MRR	–	Sb <sub>13</sub> Ag <sub>12</sub> Cd <sub>12</sub> Zn <sub>11</sub>	Sn <sub>7</sub> Cu <sub>6</sub> W <sub>6</sub> Bi <sub>6</sub> Mo <sub>5</sub> Pb <sub>5</sub>	–	73
	EM	–	Cd <sub>12</sub> Sb <sub>11</sub>	Zn <sub>7</sub> Sn <sub>7</sub> W <sub>7</sub> Cu <sub>6</sub> Mo <sub>6</sub> Ag <sub>5</sub> Pb <sub>5</sub> Bi <sub>5</sub>	–	62
PM <sub>&gt; 50</sub>	S	–	–	Cd <sub>9</sub> Mo <sub>6</sub> Cu <sub>5</sub> Sn <sub>5</sub> Sb <sub>5</sub>	Zn <sub>4</sub> W <sub>4</sub> Pb <sub>4</sub> Bi <sub>3</sub>	37
	M	–	–	Cd <sub>8</sub> Sn <sub>6</sub> Cu <sub>5</sub> Mo <sub>5</sub>	Sb <sub>4</sub> Zn <sub>4</sub> W <sub>4</sub> Pb <sub>4</sub> Bi <sub>2</sub>	33
	L	–	–	Sb <sub>8</sub> Cd <sub>7</sub> Cu <sub>7</sub> Mo <sub>7</sub> Sn <sub>6</sub> Zn <sub>5</sub>	Pb <sub>4</sub> Bi <sub>4</sub> W <sub>2</sub>	41
	MRR	–	–	Zn <sub>9</sub> Sb <sub>8</sub> Cd <sub>5</sub> Pb <sub>5</sub>	Mo <sub>4</sub> W <sub>4</sub> Cu <sub>3</sub> Sn <sub>3</sub> Bi <sub>3</sub>	37
	EM	–	–	Cd <sub>8</sub> Sb <sub>6</sub> Zn <sub>5</sub> Cu <sub>5</sub> Mo <sub>5</sub> Sn <sub>5</sub>	Pb <sub>4</sub> W <sub>3</sub> Bi <sub>3</sub>	36
Total road dust	S	–	Cd <sub>14</sub> Sb <sub>10</sub>	Ag <sub>7</sub> Sn <sub>7</sub> Cu <sub>6</sub> Bi <sub>6</sub> Zn <sub>5</sub> Mo <sub>5</sub> W <sub>5</sub> Pb <sub>5</sub>	–	60
	M	–	Cd <sub>12</sub>	Sb <sub>9</sub> Sn <sub>7</sub> Cu <sub>6</sub> Mo <sub>6</sub> Pb <sub>6</sub> W <sub>5</sub>	Zn <sub>4</sub> Ag <sub>4</sub> Bi <sub>4</sub>	53
	L	–	Sb <sub>12</sub> Cd <sub>10</sub>	Cu <sub>9</sub> Mo <sub>8</sub> Sn <sub>7</sub> Zn <sub>7</sub> Bi <sub>5</sub>	Pb <sub>4</sub> Ag <sub>4</sub> W <sub>3</sub>	61
	MRR	–	Zn <sub>11</sub> Sb <sub>10</sub>	Cd <sub>8</sub> Pb <sub>6</sub> Sn <sub>3</sub> Bi <sub>5</sub>	Cu <sub>4</sub> Mo <sub>4</sub> Ag <sub>4</sub> W <sub>4</sub>	51
	EM	–	Cd <sub>12</sub> Sb <sub>10</sub>	Sn <sub>7</sub> Cu <sub>6</sub> Zn <sub>6</sub> Mo <sub>6</sub> Pb <sub>5</sub> Ag <sub>5</sub> W <sub>5</sub> Bi <sub>5</sub>	–	56

Note: Roads: S – small; M – medium; L – large; MRR – Moscow Ring Road; EM – all roads of eastern Moscow on the average. Ze – total enrichment index. Dashes mean the absence of indicator fitting the accepted grade (the elements with  $EF \geq 2$  are shown).

in Sb on all roads except small ones, and in Ag only on large roads. The values of  $EF$  for Ag on small and medium roads and on MRR, and for Sn on all roads are almost the same. PM<sub>1–10</sub> particles do not concentrate Be, Ti, V, Cr, Mn, Fe, Co, Ni, and Sr on all roads in eastern Moscow. Close results showing the accumulation of Zn, Cu, Pb, Sb, Cd, Co, and As in PM<sub>5</sub> fraction were obtained for road dust of Wels, Austria (Lanzerstorfer, 2018).

Fraction PM<sub>10–50</sub> is even less enriched in most HMMs: Cd<sub>12</sub>Sb<sub>11</sub>W<sub>7</sub>Sn<sub>7</sub>Zn<sub>7</sub>Cu<sub>6</sub>Mo<sub>6</sub>Bi<sub>5</sub>Ag<sub>5</sub>Pb<sub>5</sub>. On large roads and MRR, PM<sub>10–50</sub> particles accumulate HMMs more actively than on medium and small roads. Moreover, the  $EF$  for Ag, Mo, and Zn on the MRR and for Cu and Mo on large roads is 1.5–2 times higher than that in the dust of other roads.

Fraction PM<sub>> 50</sub> weakly concentrates a significantly smaller number of elements: Cd<sub>8</sub>Sb<sub>6</sub>Zn<sub>5</sub>Cu<sub>5</sub>Mo<sub>5</sub>Sn<sub>5</sub>Pb<sub>4</sub>W<sub>3</sub>Bi<sub>3</sub>. The accumulation of Sb in this fraction is particularly pronounced on large roads and MRR; for Zn and Pb, maximum  $EF$  values are confined to road dust on the MRR; whereas the accumulation of Cd, Sn, Cu, and Mo is stronger on small, medium, and large roads. The ratios of Be, Ti, V, Cr, Mn, Fe, Co, Ni, As, Sr, and Ag to La in the PM<sub>> 50</sub> fraction virtually does not differ from the ratios of these elements in the upper continental crust ( $EF \sim 1$ ).

In general, the distribution of studied HMMs in particle-size fractions is characterized by a regular increase in element concentrations with a decrease in particle size. Thus in eastern Moscow, in PM<sub>1</sub> fraction, the concentra-

tions of Zn, Sb, W, Cd, As, Sn, Pb, Cu, Bi, Cr, Co, and Ni are 2.8–4.5 times (for Ag – up to 19 times), in PM<sub>1–10</sub> 1.1–3.3 times (for Ag – up to 5 times), in PM<sub>10–50</sub> up to 1.8 times more than in the total road dust (or in PM<sub>1000</sub> particles). A decrease in the HMM concentrations with the increase in particle size is common for road dust of different cities. For example, in Katowice, Poland, in PM<sub>20</sub> particles of road dust the concentrations of Cr, Zn, Pb, Ni, and Cu are 2–4.4 times, and Cd is up to 13 times higher than in PM<sub>> 250</sub> (Adamiec et al., 2016). In Dongying city, Shandong Province of China the content of HMMs in the PM<sub>10</sub> fraction of road dust is up to 3.3 times higher than in PM<sub>100</sub> (Kong et al., 2012). Element concentrations in PM<sub>5</sub>, PM<sub>15</sub>, and PM<sub>35</sub> fractions of road dust of Wels, Austria are up to 4.5 times higher than in PM<sub>250</sub> (Lanzerstorfer, 2018), and in PM<sub>63</sub> of road dust of Aberdeen, Scotland are 7–20 times higher than in PM<sub>> 500</sub> (Deletic and Orr, 2005). In addition in PM<sub>37</sub> of Buenos Aires HMM content is 1.5–3 times higher than in PM<sub>75–100</sub> (Fujiwara et al., 2011). These facts along with an increased resuspension ability of fine particles, increase their possible hazardous influence to the population. The same pattern was also revealed for atmospheric particles in many cities, for example, in Zabrze, Poland (Zwozdziak et al., 2017). Thus the tendency of HMM concentrations to decrease with increasing particle size is most pronounced for Cd, Sb, Cu, Co, Zn, Pb, and As, as was revealed in many studies. In eastern Moscow, the usually unexplored W, Sn, and Bi are added to these elements.



Fig. 4. Total enrichment of particle-size fractions of road dust in eastern Moscow with HMMs.

### 3.1.3. Total contamination of road dust

The concentration of HMMs in road dust was evaluated on the basis of the total enrichment index  $Z_e$ . Its calculations for the particle-size fractions of dust on the roads with various traffic intensities are shown in Figs. 4 and 5. The clay fraction  $PM_1$  is most contaminated with HMMs –  $Z_e = 115\text{--}266$ ; with an increase in particle size,  $Z_e$  values decrease from 74 to 146 in fine and medium silt  $PM_{1-10}$  to 47–104 in coarse silt  $PM_{10-50}$  and to 21–63 in sand fractions  $PM_{>50}$  (Fig. 4). On average, the total enrichment of  $PM_1$  particles with pollutants corresponds to a very dangerous level; of  $PM_{1-10}$  particles, to a dangerous level; and of  $PM_{10-50}$  and  $PM_{>50}$  particles, to a moderately dangerous level.

With increasing traffic intensity from small and medium roads to large roads, the contamination of  $PM_{1-10}$ ,  $PM_{10-50}$ , and  $PM_{>50}$  particles also increases. However, in the road dust from the MRR, the  $Z_e$  values in these fractions decrease by 5–25 units (Fig. 5). The  $PM_1$  fraction is characterized by a more complicated behavior: the maximum  $Z_e$  is typical of the particles from the MRR; the minimum, from large roads; and an intermediate position is occupied by the particles from small and medium roads. The total enrichment of  $PM_1$  with HMMs on small roads reaches a very dangerous level.

Different enrichment of silt fractions on roads with various traffic intensities can be explained by two reasons. The first is the traffic mode. On small and medium streets, vehicle emissions contain a greater amount

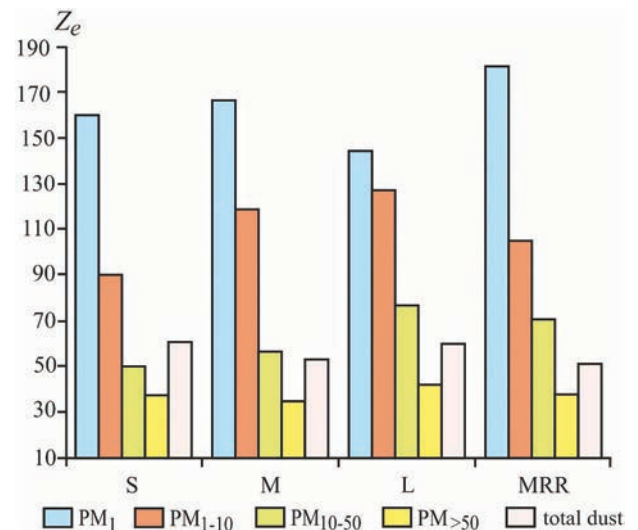


Fig. 5. Total enrichment of particle-size fractions of road dust in eastern Moscow with HMMs on roads of different sizes: S – small, M – medium, L – large, and MRR – Moscow Ring Road.

of fine particles generated by the abrasion of brake pads, tires, and pavement as a result of frequent stops at traffic lights, public transport stops, in traffic jams, etc. Traffic jams reducing the speed of the traffic flow to 20 km/h

lead to an increase in emissions by 30% (Bityukova and Sokolova, 2008); very strong traffic jam with a speed of 8 km/h or less enhances the emissions by 3–4 times (Choudhary and Gokhale, 2016). Car stops and their frequency also affect fuel consumption and the emission of pollutants (Ericsson, 2001). With a decrease in traffic speed, the size of ejected particulate matter sharply increases (Kittelson et al., 2004). In the center of Moscow, where traffic jams are very frequent, the concentration of CO and NO<sub>2</sub> in the air near the highways is almost two times higher than that away from the center – between the Third Transport Ring and the MRR (Kul'bachevskii, 2017). On large roads that are subjected to greater blowing, increasing traffic speeds lead to the removal of small particles of road dust by air flows, and the proportion of large particles gradually increases.

The second reason is the types and volume of the fleet. From 2011 to 2016, despite the strong expansion of the territory of Moscow in 2012 and an increase in the number of vehicles, particulate emissions from them decreased by 1.3 times – from 1643 to 1248 tons, which is associated with the use of more environmentally friendly brands of gasoline and an increasing efficiency of internal combustion engines: in 2002 in Moscow, Euro-0 class cars accounted for about 74%; Euro-1 class cars, 11% of all city cars. In 2012, most of the cars were of Euro-3 (35%), Euro-4 (33%), and Euro-5 (10%) classes (Donchenko et al., 2014). Up to 56% of all particulate matter entering the Moscow atmosphere with motor vehicle emissions is supplied by trucks weighing more than 3.5 tons; 29%, by buses; 10%, by cars; and 5%, by trucks weighing less than 3.5 tons (Kul'bachevskii, 2017). At the same time, the share of passenger transport (buses, trolleybuses, minibuses, etc.) is large on small and medium-sized intra-quarter roads, their number on large roads and MRR decreases simultaneously with an increase in the number of trucks and cars.

Thus, contrasting technogenic geochemical anomalies of Cd, Sb, Zn, Ag, and Sn are formed in road dust, especially in the smallest and most environmentally hazardous particles PM<sub>1</sub> and PM<sub>1–10</sub> even on small intra-quarter streets.

## 3.2. Heavy metals and metalloids in atmospheric fallout and soils

### 3.2.1. Atmospheric fallout

A comprehensive characteristic of atmospheric pollution during the cold period can be obtained by analyzing pollutant anomalies in the snow cover. Data on the content of solid particles in the snow cover and the concentration of HMMs in them make it possible to determine the amount of pollutants entering the soil and surface water during snow melting. Up to 2% of the mass of suspended particles in snow have a diameter of less than 25 μm, but they accumulate up to 80% of the total mass of HMMs contained in the snowmelt (Glenn and Sansalone, 2002). Mo ( $K_c = 19.1$ ), as well as Ag, Sb, As, W, and Sn (6.3–3.6) are intensively accumulated in the solid fraction of snow of eastern Moscow. The coefficient of concentration of V, Fe, Cr, Sr, Ni, Cd, Co, Bi are smaller ( $K_c = 2.1–1.5$ ). The concentrations of other metals (Zn, Mn, Pb, Cu, Be, Ti) in the snow of the urban territory are close to their background concentrations.

The amount of dust falling on the snow cover depends on the power and location of the emission sources,

the dispersing capacity of the atmosphere, the prevailing wind direction, etc. In eastern Moscow, it averages 27 mg/m<sup>2</sup> per day with fluctuations from 8 mg/m<sup>2</sup> per day in the southeastern part of the territory on open unaffected plots of former agricultural land to 40 and 55 mg/m<sup>2</sup> per day near industrial facilities and large roads. As a result, the coefficient of excess of HMM deposition in the city over the background deposition ( $\bar{K}_d$ ) differs by several orders of magnitude in individual sections of the study area. The fallout of many HMMs from the atmosphere in eastern Moscow significantly exceeds the background: for Mo, by 176 times; for W, Sb, As, and Ag, by 18–14 times (Kasimov et al., 2016). These elements are present in the emissions of motor vehicles, engineering and metalworking enterprises, chemical industry, heat power engineering, production of building materials, glass, etc. (Saet et al., 1990; Demetriades and Birke, 2015). Significantly lower  $\bar{K}_d$  values (from 3 to 12) are typical of Sn, Fe, Sr, V, Cr, Ni, Co, Zn, Mn, Cu, Cd, Bi, and Ti.

The intensity of atmospheric addition of HMMs in snow cover was estimated by calculating the total excess of deposition of the elements in the urban area over the background area  $Z_d$ . It depends not only on the content of HMMs in the solid fraction of snow (Table 1) but also on the total dust load. For eastern Moscow, the average  $Z_d$  coefficient is 296, which corresponds to a low pollution with a non-hazardous environmental situation (Kasimov et al., 2016). The input of metals in eastern Moscow mainly depends on the amount of deposited dust ( $r = 0.86$ ) and, to a lesser extent, on the dust composition ( $r = 0.30$ ). The average pollution level with a moderately hazardous environmental situation ( $1800 > Z_d > 1000$ ) is characteristic of the northwestern part of the territory and is mainly due to the emissions of Mo and W from motor vehicles and various industries.

### 3.2.2. Urban soils

A comparison of HMM concentrations in the topsoils of eastern Moscow (Table 1) with background values showed that 10 elements accumulate most intensively in the urban soils: Cd<sub>7.6</sub>W<sub>6.5</sub>Bi<sub>4.9</sub>Zn<sub>4.8</sub>Sb<sub>4.8</sub>Pb<sub>4.5</sub>Ag<sub>4.5</sub>As<sub>4.0</sub>Cr<sub>3.6</sub>Fe<sub>3.6</sub> ( $K_c > 3.0$ ). Cu, Ni, Sn, Be, Co, V, and Mo are characterized by weaker accumulation with  $K_c$  of 1.7–2.9; Ti and Mn have near-background concentrations.

Compared to the dust component of snow, the relative enrichment of urban soils with Mo is much less, which is probably due to the increased migration capacity of this element in alkaline and slightly alkaline urban soils (Perel'man and Kasimov, 1999). The lists of accumulating elements in the soils and road dust are identical, but the concentration (relative enrichment) coefficients in the soils are somewhat lower, which can be explained by a coarser texture of the urban soils in comparison with their background analogues.

The average  $Z_c$  of HMMs in the soils of the territory is 51, which corresponds to a moderately hazardous environmental situation (Kasimov et al., 2016). About 51% of the tested points have high and dangerous levels ( $32 < Z_c < 64$ ) of soil contamination; 11%, very high and very dangerous ( $64 < Z_c < 128$ ); and 6%, maximal extremely dangerous ( $Z_c > 128$ ) levels. Only 32% of the study area is occupied by slightly and moderately contaminated soils.



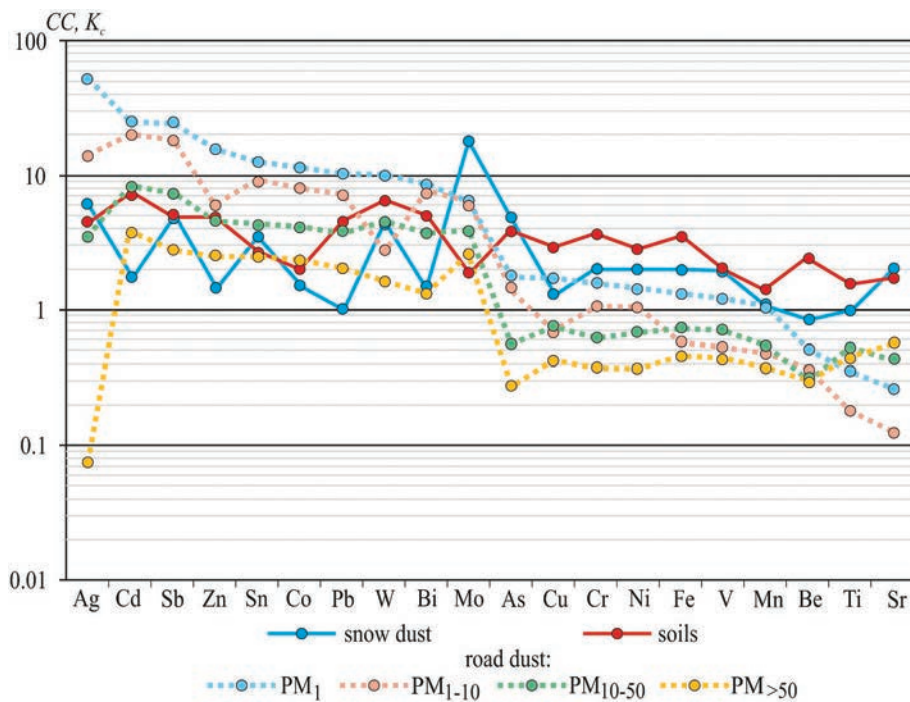


**Fig. 6.** Geochemical features of the solid fraction of snow (snow dust), urban soils, and particle-size fractions of road dust ( $PM_1$ ,  $PM_{1-10}$ ,  $PM_{10-50}$ ,  $PM > 50$ ) in eastern Moscow according to relative enrichment factors  $K_c$  (for snow dust and soils) and relative abundance coefficients  $CC$  (for road dust and particle-size fractions of road dust).

### 3.3. Comparison of the chemical compositions of road dust, atmospheric fallout, and urban soils

#### 3.3.1. Contrast of the anomalies of HMMs

The intense technogenic impact of transport and industrial facilities leads to the changes in the physico-chemical properties of depot media in eastern Moscow (Kasimov et al., 2016) and the formation of technogenic geochemical anomalies in them, which are usually characterized by the relative enrichment factors  $K_c$  (for snow dust and soils) and relative abundance coefficients  $CC$  (for road dust and particle-size fractions of road dust) of individual elements and by the total contamination indices  $Z_c$ ,  $Z_d$ .

Technogenic anomalies in the particular components of the landscapes of eastern Moscow have different geochemical specializations (Fig. 6) because of the migration of pollutants, the presence or absence of geochemical barriers (Kosheleva et al., 2015), the nature and characteristics of technogenic pollution sources, and the duration of exposure to pollution.

The components of urban landscapes concentrate the following HMMs (elements with  $K_c > 2.5$  are indicated in order of decreasing anomaly, pollutants with  $K_c$  or  $CC \geq 5$  are marked in bold):

*Road dust:* Cd, Sb, Sn, Zn, Cu, Mo, Pb, Ag, Bi, W;  
 its  $PM_1$  fraction – **Ag, Cd, Sb, Zn, Sn, Cu, Pb, W, Bi, Mo**;  
 $PM_{1-10}$  – **Cd, Sb, Ag, Sn, Cu, Bi, Pb, Mo, Zn, W**;  
 $PM_{10-50}$  – **Cd, Sb, Zn, W, Sn, Cu, Mo, Bi, Pb, Ag**;  
 $PM > 50$  – **Cd, Sb, Mo, Sn, Zn, Cu, Pb, W, Bi**;

*Atmospheric fallout (the solid fraction of snow):*

**Mo, Ag, Sb, As, W, Sn**;

*Surface soil horizons:*

**Cd, W, Bi, Zn, Sb, Pb, Ag, As, Cr, Fe, Cu, Ni, Sn.**

Fractions  $PM_1$  and  $PM_{1-10}$  of road dust and dust component of the snow are characterized by the maximum relative enrichment in HMMs and are most indicative of the ecological state of the urban environment. The anomalies of HMMs in the urban soils are less pronounced.

#### 3.3.2. Associations of HMMs in road dust and adjacent media

A comparative analysis of the geochemical composition of the dust component of snow, road dust, and surface soil horizons in eastern Moscow made it possible to identify pollutants that simultaneously accumulate in different components, i.e., form paragenetic associations (parageneses) of HMMs characterizing their sources (Vlasov and Kasimov, 2016). The geochemical composition of each component of the landscape was determined relative to its background analogue (for road dust, element abundances in the upper continental crust were taken), which made it possible to evaluate the changes in the chemical composition of each component of the environment under the impact of anthropogenic factors using parageneses of HMMs.

The landscapes of eastern Moscow are characterized by the formation of the Sb–Ag–Sn–W paragenetic association common to road dust, soil, and the dust component of snow. This element association, being an indicator of the impact of vehicles, enters the environment with the emission of motor oil and due to the wear of brake pads, metal parts, and tires (Kukutschová et al., 2009; Nazzal et al., 2013; Quiroz et al., 2013; Pant and Harrison, 2013; Grigoratos and Martini, 2015; Alves et al., 2018). In addition to motor vehicles, the sources of Ag are related to enterprises in the construction industry and those, burning fossil fuels, as well as sewage sludge used as a fertilizer for roadside soils (De Miguel et al., 1998; Eckelman and Graedel, 2007; Zuzolo et al., 2018).

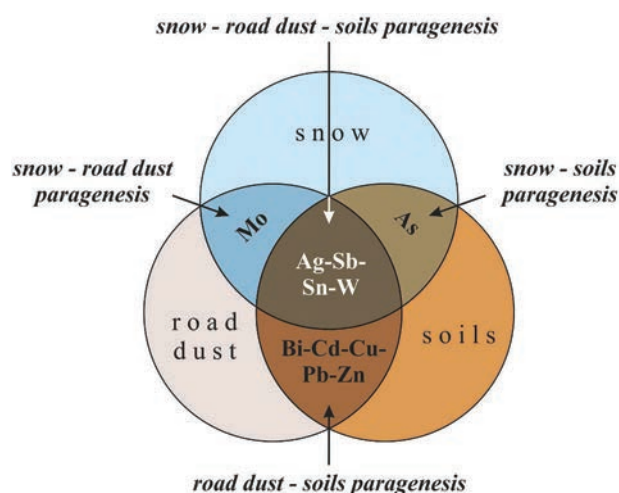


**Fig. 7.** Paragenetic associations of HMMs in mineral components of landscapes of eastern Moscow.

The accumulation of elements depends on their chemical properties. For anionic (migrating under alkaline conditions) As and Mo, atmospheric fallout is the major source of these elements in road dust and topsoil, which is confirmed by their paragenesis in the snow–road dust and snow–soil subsystems (Fig. 7). Molybdenum, whose mobility under alkaline conditions is higher than under acidic conditions, is not fixed in the topsoils with alkaline reaction upon its deposition on the soil surface. Its anomalies are found only in the snow–road dust subsystem. Therefore, Mo is not a part of the snow–soil paragenesis. The enrichment of road dust with As is very weak, which indicates input of this metalloid mainly from industrial emissions. Therefore, its anomalies are characteristic of only atmospheric precipitation (snow) and soils, in which this element is fixed on the biogeochemical barrier (Koshelva et al., 2015). Arsenic enters road dust in small quantities and, therefore, it is not included in the snow–road dust paragenesis.

The source of cationogenic Bi, Cd, Cu, Pb, and Zn, which are weakly mobile in slightly alkaline urban soils and alkaline road dust, is mainly associated with motor vehicle emissions; These elements are members of a paragenetic association in the soil–road dust subsystem. The migration of Bi, Cd, Cu, Pb, and Zn between road dust and roadside soils is caused by the resuspension of solid particles. Owing to the regional transfer of pollutants, the background snow accumulates Bi, Cd, Cu, Pb, and Zn (Kasimov et al., 2016); therefore, their Kc in dust load of snow is low, and anomalies of this paragenesis in the city snow are virtually absent. For this reason, the above-listed HMMs are not included in the snow–road dust and snow–soil parageneses.

Thus, the formation of various parageneses in the eastern part of Moscow is mainly due to the properties of HMMs (their mobility under alkaline conditions or accumulation at geochemical barriers) coming from vehicles and industrial facilities. Set of elements in parageneses

also depends on seasonal variations in the composition and amount of emissions from anthropogenic sources: snow cover accumulates pollutants emitted in winter, road dust characterizes summer emissions, and soils are indicative for the long-term pollution.

#### 4. CONCLUSIONS

Road dust in eastern Moscow as a whole and its particle-size fractions are enriched in Ag, Cd, Sb, Zn, Sn, Cu, Pb, W, Bi, and Mo emitted by vehicles; for other elements, natural and mixed sources, both natural and technogenic predominate. Among them, Cd, Sb, Zn, Ag, and Sn form the most contrasting anomalies in the fine fractions of road dust. The total enrichment of road dust with HMMs decreases with increasing particle size; it is maximum in PM<sub>1</sub> fraction and minimum in PM > 50 fraction. With increasing traffic intensity, the proportion of the majority of HMMs increases in particles PM > 50 and decreases in particles PM<sub>10–50</sub> and PM<sub>1–10</sub> being almost unchanged in PM<sub>1</sub> particles. The total enrichment with pollutants of the PM<sub>1</sub> fraction corresponds to a very dangerous level; of the PM<sub>1–10</sub> fraction, to a dangerous level; and of the PM<sub>10–50</sub> and PM > 50 fractions, to a moderately dangerous level.

A specific geochemical feature of the urban landscapes under consideration is the accumulation the Sb–Ag–Sn–W paragenetic association of elements in the road dust, snow, and soils. This association is indicative of the impact of emissions from vehicles and industrial facilities. The snow–road dust and snow–soil subsystems are characterized by the paragenesis of anionic As and Mo coming mainly from industrial sources, whereas the soil–road dust subsystem is characterized by the paragenesis of cationogenic Bi–Cd–Cu–Pb–Zn emitted mostly by motor vehicles. Thus, the set of elements forming paragenetic associations is specified by the particular sources of the pollutants, the chemical properties of the elements, and the indicative capacity of the components of urban environment in individual seasons (snow in the cold season, road dust in the warm season, and soil over the long-term period).

Differences in HMM pollution of total road dust on the roads of eastern Moscow with various traffic intensities are insignificant. However, the relationship with the size of the road and traffic intensity is manifested for individual road dust fractions: the total enrichment of PM<sub>1</sub> particles with HMMs is maximum on the MRR; it is also large on small roads, while the maximum enrichment of coarser particles (PM<sub>1–10</sub>, PM<sub>10–50</sub>, and PM > 50) is characteristic of large roads and the MRR. Thus, the negative impact of vehicles on the environment is evident not only on large roads, but also on intra-quarter streets, where small particles of PM<sub>1</sub> are highly enriched in HMMs. In the areas with a dense network of small roads, road dust particles being a source of toxic HMMs create an unfavorable environment for urban residents.

# Spatial distribution and sources of potentially toxic elements in road dust and its PM<sub>10</sub> fraction of Moscow megacity\*

## 1. INTRODUCTION

Solid microparticles, especially particulate matter PM<sub>10</sub> and PM<sub>2.5</sub> (with a diameter of up to 10 µm and 2.5 µm, respectively) represent one of the main contaminant of urban air. These particles can remain in the atmosphere for a long time in the suspended state and be transported over long distances. In Moscow, Europe's largest megacity, air pollution is significant: average annual concentrations of PM<sub>10</sub> in 2005–2014 amounted to 22–37 µg/m<sup>3</sup> (Elansky et al., 2018), while near the roads, their concentrations are two to three times higher than inside residential areas (Kul'bachevskii, 2019). An increase in the concentration of microparticles in the air and in the content of potentially toxic elements (PTEs) in them negatively affect the respiratory function of citizens, especially patients with asthma (Veremchuk et al., 2018), and causes oxidative stress resulting in oxidative modification of proteins and DNA and impairing leukocyte energy potential (Golokhvast et al., 2015).

Microparticles enter the atmosphere of cities with emissions from industrial enterprises and vehicles (Amato et al., 2016; Grigoratos et al., 2014; Pachon et al., 2020). In large cities, where the contribution of vehicles to total emissions predominates, particles with a diameter of 2.5 to 10 µm (PM<sub>2.5–10</sub>) mainly come from non-exhaust emissions of vehicles (abrasion of tires, brake pads and road pavement) and from resuspension of roadside soils and road dust, and fine fractions with a diameter of less than 2.5 µm (PM<sub>2.5</sub>) are mainly related to exhaust emissions (Pant and Harrison, 2013; Zhang et al., 2020). For instance, the PM<sub>10</sub> emission factor from wear between pavements and tires is of the order of 2 mg/km per vehicle (Alves et al., 2020a). At the same time, resuspended road dust can be one of the most important sources of microparticles in the atmosphere; for example, in Bogota, it supplies about 23% of the mass of PM<sub>10</sub> particles (Ramírez et al., 2018) and in the USA, more than a half of PM<sub>10</sub> and about a quarter of PM<sub>2.5</sub> particles (United States Environmental Protection Agency, 2020). This is especially true for cities with a high density of road network and large areas sealed under road pavements (Amato et al., 2011).

Road dust is formed due to resuspension of roadside soils in summer and deicing reagents in winter, as well as due to deposition of suspended atmospheric particles and precipitation (Kasimov et al., 2019c). The study of the chemical composition of road dust and its individual fractions is important from the environmental point of view, since they are enriched in many pollutants, including PTEs, and, therefore, pose a high risk to the respiratory system (Khan and Strand, 2018; Ramírez et al., 2019; Rissler et al., 2012).

The chemical composition of road dust and its individual particlesize fractions is studied all over the world,

but in Russia it is still rarely analyzed for a limited number of PTEs (Kamanina et al., 2019; Kasimov et al., 2019b; Kaygorodov et al., 2009; Konstantinova et al., 2020; Krupnova et al., 2020; Prokof'eva et al., 2017; Seleznev et al., 2020). In Moscow, such studies have been performed in some administrative districts (Ermolin et al., 2018; Fedotov et al., 2014; Kasimov et al., 2020; Ladonin, 2018; Ladonin and Mikhaylova, 2020; Ladonin and Plyaskina, 2009; Vlasov et al., 2015), whereas the general pattern of the road dust contamination with PTEs is still missing. When studying the composition of road dust and its pollution with PTEs, less attention is paid to PM<sub>10</sub> particles (Kong et al., 2012; Lanzerstorfer, 2018; Ramírez et al., 2020, 2019; Tian et al., 2019; Zhang et al., 2019), though their concentration is determined during air monitoring in cities.

The composition of road dust and its fractions depends on the intensity of anthropogenic loads: in industrial areas, due to the impact of industrial and construction facilities, road surface abrasion, and vehicle emissions, dust contains an increased amount of PM<sub>10</sub> particles in comparison with that in the areas of residential and commercial buildings road surfaces, the potential risk to public health decreases by about four times (Tian et al., 2019).

The purpose of our study was to analyze trace element composition of road dust and its PM<sub>10</sub> fraction in Moscow within the Moscow Ring Road (MRR) and assess its spatial variability. Specific objectives of this study were the following:

- to determine the bulk content of PTEs in the road dust of the megacity and the contribution of the PM<sub>10</sub> fraction;
- to characterize the spatial distribution of PTEs in road dust and its PM<sub>10</sub> fraction and to evaluate differences in the dust enrichment in PTEs on different types of roads;
- to identify the main sources of PTEs in road dust.

## 2. SOURCES OF ROAD DUST IN MOSCOW

The main sources of road dust in Moscow are motor vehicles, industrial emissions, dry deposition and precipitation from the atmosphere, application of deicing salts in winter, and wind erosion of soils in summer (Kasimov et al., 2019c; Vlasov et al., 2020b).

At the beginning of 2019, the car fleet of Moscow numbered about 4,380,000 vehicles, including 90.4% of cars, 8.6% of freight and light utility vehicles, and 1.1% of buses; the level of motorization of the population reached 347 cars/1000 people (Kul'bachevskii, 2019). The length of Moscow roads is about 3600 km, and they occupy about 8% of Moscow area. The density of the road network is 4.2 km/km<sup>2</sup>, including the highway network of 1.54 km/km<sup>2</sup> (Khusnullin, 2013). Motor vehi-

\* Vlasov D., Kosheleva N., Kasimov N. // Science of the Total Environment. 2021;761:143267.



cles contribute up to 98% of the total emissions, which amounted to 782,000 t in 2018 (Kul'batchevskii, 2019).

Overall, about 28,000 stationary emission sources concentrated in industrial zones of the city are registered in Moscow. Over the years, their emissions range from 60 to 70 thousand tons with the solids fraction of about 3%. In 2018, emissions from stationary sources amounted to 60,400 t (Kul'batchevskii, 2019), of which almost 50–65% were produced by 13 thermal power stations of Moscow; 20–30%, by oil refinery; 15–20%, by processing industries; 2–3%, by machine-building enterprises; 2–3%, by incinerators; and about 2%, by food and building materials industries (Bityukova and Saulskaya, 2017).

In Moscow, deicing salts of the chloride group are commonly applied; they consist of at least 93% of technical table salt mixed with marble or granite chips. In a single road treatment, the rates of application of deicing-mixtures vary within 80–200 g/m<sup>2</sup>. The total permitted salt load reaches 420–500 thousand tons of dry weight during the winter season (Khomyakov, 2015). The deicing agents are usually applied in Moscow till the end of March, or even till the first decade of April, depending on weather conditions. In spring due to excessive application of deicing salts, some of the reagents are not washed out by the melt water, but remain in the solid form on the roadway, increasing the road dust electrical conductivity (EC) up to 250 μS/cm in the central part of the city (which is 3 times higher than in the parks), and up to 720 μS/cm in dust on the roads with the highest traffic (Kasimov et al., 2019c). Precipitation during the warm season does not lead to the complete leaching of salts out of urban ecosystems and from road surfaces. Leaching of salts during summer only weakens, but does not completely eliminate the process of progressive salinization of Moscow soils (Nikiforova et al., 2014). An additional source of water-soluble compounds (e.g., Na<sup>+</sup>, NO<sub>3</sub><sup>-</sup>, PO<sub>4</sub><sup>3-</sup>, Cl<sup>-</sup>, Ca<sup>2+</sup>) in road dust is vehicle emissions (Alves et al., 2015). We have previously found the significant amounts of water-soluble K, Mn, Cd, Cu, Co, and NO<sub>3</sub><sup>-</sup> in the snow cover near roads in the western part of Moscow as a result of deicing agents application and vehicles emissions (Vlasov et al., 2020b).

Dustiness of roads increases due to wind erosion of urban soils poorly protected by surface vegetation and sod layer. Artificially constructed or highly transformed soils – urbanozems (Urbic Technosols) – predominate within the MRR and are characterized by increased pH values, higher contents of organic matter and soluble salts, higher exchange capacity, and higher percent of the physical clay fraction in their composition in comparison with the background natural soils, which contributes to the fixation of PTEs in them (Kosheleva et al., 2015).

The composition of solid atmospheric deposition in the roadside areas of Moscow reflects the main sources of dust. Coarse fractions mainly consist of quartz grains, feldspars, carbonate minerals, and asphalt fragments; fine fractions are supplemented with carbon-containing particles and small fragments of paint, glass, plastic, brick, and other materials (Prokof'eva et al., 2017). The PM<sub>2.5</sub> fraction is composed of the soluble inorganic salts (mainly, sulfates and nitrates: 4–32% of the aerosol mass), insoluble mineral particles, and carbonaceous materials (1.2–48%) usually represented by elemental carbon (Duarte and Duarte, 2009; Popovichva et al., 2020).

### 3. MATERIALS AND METHODS

The studies were conducted on the territory within the MRR. Before the official expansion of the city area in 2012 by 2.4 times, the area within the MRR comprised 83% of Moscow territory; after 2012, it reaches 35% of the total Moscow area. Road dust was collected in nine administrative districts of Moscow on roads with different traffic intensities (number of samples  $n = 173$ ), as well as inside courtyards with parking lots ( $n = 36$ ) from June 09 to July 30, 2017 (Fig. 1). The density of the sampling network was approximately 1 point per 4 km<sup>2</sup>. In terms of traffic intensity, all roads were divided into several types in accordance with the width of the roadway and the number of lanes: the MRR ( $n = 20$ ), the Third Ring Road (TRR,  $n = 10$ ), the main radial highways with more than four lanes in one direction ( $n = 18$ ), large roads with three–four lanes ( $n = 48$ ), medium roads with two lanes ( $n = 43$ ), and small roads with one lane in one direction ( $n = 35$ ). In the forest parks Losiny Ostrov, Izmailovsky, and Bitsevsky, on footpaths farthest from the roads, five samples of background dust were taken.

The period of field work was rainy; the rainfall in June–July 2017 in Moscow exceeded the average value by almost two times. Low intensity rains (<5 mm) fell on June 01–03, 16 and 22, and July 09, 16, 21, and high-intensity rains (>5 mm) fell on June 05, 13–15, 19, 21, 26, and July 01–04, 08, 12–14 and 31. So, the accumulation of road dust was impeded by intensive surface runoff and daily cleaning of roads by municipal services, which could also reduce road dust pollution by PTEs (Amato et al., 2010; Karanasiou et al., 2011; Zhang et al., 2017; Kim et al., 2019). However, there is evidence that the washing activities result merely in a road dust moistening without its effective removal (Karanasiou et al., 2014); sweeping and washing of roads did not significantly reduce non-exhaust emissions (Keuken et al., 2010). Therefore, sampling was performed under dry weather conditions, no less than 24 h after the low-intensity rains and no less than 72 h after the high intensity rains, when the road surface was completely dried out. Samples were taken along the curb on both sides of the roads using a plastic dust pan and a brush in three–five replicates at a distance of 3–10 m from one another; one mixed sample was composed of them. On the major radial highways and large roads, samples were taken from the dividing strip; in the yards, from parking areas. The bulk samples were then stored in self-sealed polyethylene bags for transportation to the laboratory.

All dust samples were dried for 48 h at room temperature. The dried samples were sieved through a 1-mm sieves to remove debris particles and gravel. Each sample was divided into a three subsamples. In the first ~10 g subsample particle-size distribution was analyzed on the Analysette 22 MicroTec plus laser particle sizer (Fritsch, Germany) with sodium pyrophosphate pretreatment for dispersing aggregates in the Environmental and Geochemical Center of the Lomonosov Moscow State University. In the second ~10 g subsample the separation of the particles fraction with a diameter of 10 μm or less (PM<sub>10</sub>) by wet grinding with further elutriation (Vadynina and Korchagina, 1986) was done. The obtained solutions were filtered through a membrane filter with pore diameter of 0.45 μm. The third ~10 g subsample was ground in an agate mortar and sieved through a 63-μm sieve to total PTE concentrations analysis.

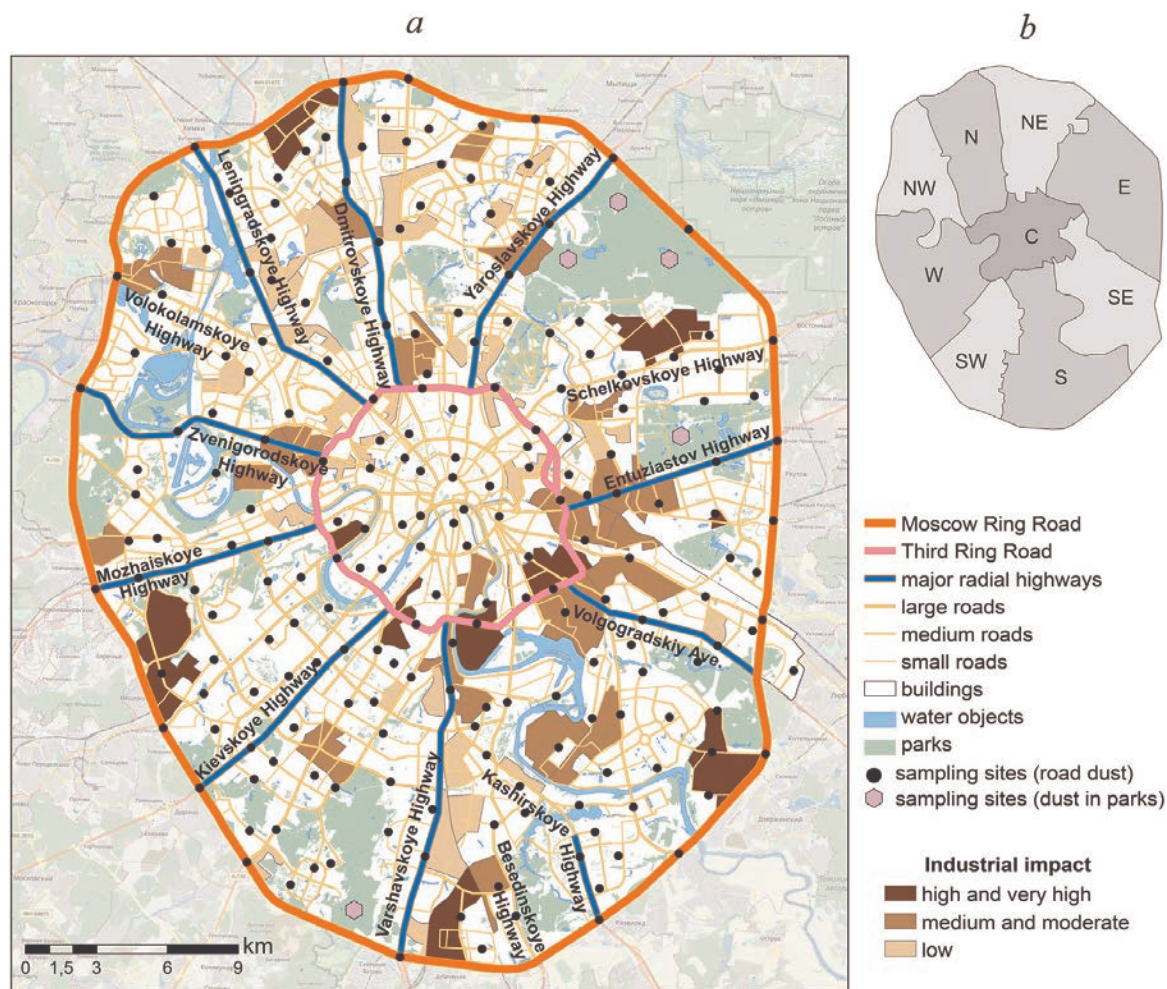


**Fig. 1.** (a) Mobile and stationary sources of anthropogenic emissions, sampling sites of road dust and background dust in parks in Moscow, and (b) administrative districts of Moscow within the MRR. Impact levels of industrial zones are given according to Bityukova and Saulskaya (2017). Capital letters indicate the names of administrative districts: N – Northern, NE – Northeastern, E – Eastern, SE – Southeastern, S – Southern, SW – Southwestern, W – Western, NW – Northwestern, and C – Central.

The contents of As, Bi, Cd, Co, Cr, Cu, Fe, La, Mn, Mo, Ni, Pb, Sb, Sn, Ti, V, W, and Zn were determined in road dust and PM<sub>10</sub> particles by mass (ICP-MS) and atomic emission (ICP-AES) spectrometry with inductively coupled plasma using an iCAP Qc mass spectrometer (Thermo Fisher Scientific, USA) and an Optima-4300 DV atomic emission spectrometer (Perkin Elmer, USA), respectively. The analysis was performed in the laboratory of the N.M. Fedorovsky All-Russian Research Institute of Mineral Raw Materials by certified methods (NSAM № 499 AES/MS, 2015) using blank samples and standard reference materials “SGHM-2. Aluminosilicate loose sediment (GSO 3784-86)”, “SGD-2a. Essexite gabbro (GSO 8671-2005)”, “CS-2a. Trap rock (GSO 8671-2005)” (Vinogradov Institute of Geochemistry SB RAS, Russian Federation), and “andesite AGV-2” and “basalt BHVO-2” (U.S. Geological Survey, USA). This laboratory is accredited in the international accreditation system Analytics (AAS.A.00255) and the national accreditation system (RA.RU.21GP11) and meets the requirements of the International Organization for Standardization (ISO Guide 34:2009 and ISO/IEC 17025:2017). The detection limits (DLs) were as follows (mg/kg): As, 0.11; Bi, 0.0028; Cd, 0.008; Co, 0.01; Cr, 0.78; Cu, 0.82; Fe, 8.6; La, 0.054; Mn, 0.18; Mo, 0.008; Ni, 0.43; Pb, 0.6; Sb, 0.005; Sn, 0.14; Ti, 17; V, 0.09; W, 0.043; Zn, 1.5. For all samples, for low concentrations

of PTEs (<5 DL) the relative standard deviation did not exceed 20%; for higher concentrations of PTEs (>5 DL), the relative standard deviation did not exceed 10%. Most of elements selected for analysis are highly accumulated in Moscow’s environment (Ermolin et al., 2018; Kasimov et al., 2020; Kosheleva et al., 2018, 2015; Nikolaeva et al., 2019; Romzaykina et al., 2020; Vergel et al., 2019; Vlasov et al., 2020a, 2020b, 2019). They are also good indicators of both anthropogenic and natural sources in road dust and can pose risks to public health (Adamiec and JaroszKrzemińska, 2019; Al-Shidi et al., 2020; Alves et al., 2020a; Kolakkandi et al., 2020; Lanzerstorfer and Logiewa, 2019; Men et al., 2020; Miazgowiec et al., 2020; Ramírez et al., 2019; Wang et al., 2020).

The obtained data were processed by the methods of mathematical statistics in the Statistica 10 software package. Sample mean ( $M$ ), standard deviation  $\sigma$ , coefficients of variation ( $Cv = \sigma/M \times 100\%$ ), and minimum and maximum concentrations of PTEs were calculated. The significance of the correlation coefficients  $r$  was checked using the t-test at  $p < 0.001$ .

The fractional distribution of PTEs in road dust was estimated from the share of an element in the PM<sub>10</sub> fraction relative its content in the bulk road dust sample:  $Di = Ci \times Pi/C_{dust}$ , where  $Ci$  is the element concentration in PM<sub>10</sub>, mg/kg fraction;  $Pi$  is the content of PM<sub>10</sub> fraction in the dust sample, %; and  $C_{dust}$  is the



concentration of the element in the bulk dust sample, mg/kg.

The contribution of anthropogenic sources of PTEs to individual road dust fractions was estimated using the enrichment factor  $EF = (C_i/C_{ref}) / (K_i/K_{ref})$ , where  $C_i$  and  $C_{ref}$  are the concentrations of the  $i$ -th and reference elements in the sample,  $K_i$  and  $K_{ref}$  are natural abundances (clarkes) of the  $i$ -th and reference elements in the upper continental crust (Rudnick and Gao, 2014), respectively. Composition of the upper continental crust was used as a reference for normalization because of the lack of background analogue for road dust, which is a specific anthropogenic object. The input of the reference element from anthropogenic sources should be minimal. Most often, Al is used for this purpose; less often, Li, Zr, Ti, Sc, Co, Fe, and Mn (Basha et al., 2010; Kara et al., 2014). In our study, we chose La as a reference element relatively weakly utilized by humans in comparison with many PTEs (Avino et al., 2008).

The EF was developed to elucidate the origin of elements in seawater, atmospheric air, and sediments; then, it was applied to study the chemical composition of soils, lake sediments, peat, tailings, and other environmental objects (Reimann and de Caritat, 2005). When using EF, it is assumed that the ratio of the studied and normalizing elements in natural processes is equal to this ratio in the Earth's crust and that it changes under anthropogenic impact. There are no generally accepted grades for the EF. In many studies of the chemical composition of atmospheric aerosols, it is accepted that the values of  $EF < 1$  indicate the predominant supply of elements from the Earth's crust, i.e., their terrigenous (crustal) origin. If EF is in the range from 1 to 10, sources of mixed anthropogenic–terrigenous origin probably operate; for  $EF \geq 10$ , PTEs are clearly of anthropogenic origin (Cheng et al., 2018). When assessing the composition of rainwater,  $EF \geq 100$  is sometimes used as a threshold level (Chon et al., 2015). We used EF gradations according to (Sutherland, 2000), which are often applied in the studies of road dust pollution:  $<2$  – depletion to minimal enrichment, suggestive of no or minimal pollution,  $2-5$  – moderate enrichment, suggestive of moderate pollution;  $5-20$  – significant enrichment and pollution;  $20-40$  – very high enrichment and very strong pollution, and  $>40$  – extremely enrichment and pollution.

The intensity of the total accumulation of PTEs was estimated by the total enrichment factor  $TEF = \sum EF - (n - 1)$ , where EFs of  $n$  elements with  $EF > 1$  were summed (Vlasov et al., 2015). The TEF values indicate the levels of accumulation in road dust and environmental hazards of a group of PTEs coming from anthropogenic sources:  $<32$ , nonhazardous;  $32-64$ , moderately dangerous;  $64-128$ , dangerous;  $128-256$ , very dangerous; and  $>256$ , extremely dangerous. These gradations were developed in Russia to estimate the total PTEs pollution of the dust component of the snow cover (Kasimov et al., 2012; Saet et al., 1990).

Visualization of geochemical data was performed in the ArcGIS 10 software. The data of the OpenStreetMap project were used as a cartographic base for geochemical maps. The boundaries of industrial zones occupying more than 17% of Moscow were delineated according to (Bityukova and Saulskaya, 2017). The current productive activity in many industrial zones is minimal, but separate stationary sources of emissions from the mainly nonproductive sphere, such as gas stations, car washes,

car repair shops, medical facilities, and others continue to function within their territory. Such industrial zones are barriers to the transport network and reduce the connectivity of the territory, which increases vehicle mileage and, therefore, creates higher levels of vehicle emissions. The maximum concentration of large industrial zones is typical of the eastern and southeastern parts of the city, next to which there are densely populated suburban areas. The anthropogenic impact of industrial zones (Fig. 1) was estimated using indicators of the volume, structure, toxicity, and area of atmospheric emissions from each source in the industrial zone, as well as the size of the industrial zone and its percent in the overall land use (Bityukova and Saulskaya, 2017). Very high and high levels of anthropogenic impact are characteristic of 11 industrial zones, which occupy more than 20% of the total industrial area of Moscow and supply more than 70% of the gross pollution of all industrial zones of the city. These industrial zones are located mainly in the eastern, southern, and southeastern sectors of Moscow, often adjacent to the TRR or MRR. In these sectors, considerable areas are also occupied by industrial zones with medium and moderate levels of anthropogenic impact on the environment.

## 4. RESULTS AND DISCUSSION

### 4.1. Particle-size distribution of road dust

The physicochemical properties of Moscow road dust generally fit into the range of values reported for other cities in the world: the pH, 7–12; the organic carbon (OC) content, 1–19%; and the electrical conductivity (EC), 100–2800  $\mu\text{S}/\text{cm}$  (Acosta et al., 2011; Al-Khashman, 2007; Alsbou and Al-Khashman, 2018; Ladonin and Plyaskina, 2009; Li et al., 2016; Pant et al., 2015; Sutherland et al., 2012; Wu and Lu, 2018; Yu et al., 2020). The most significant man-induced change in the properties of road dust in Moscow is characteristic of the segments of large roads near industrial zones and of bus depots (Kasimov et al., 2019c).

The texture of Moscow road dust is relatively homogeneous; it is composed of sand (50–1000  $\mu\text{m}$ ) and silt (10–50  $\mu\text{m}$ ) fractions with a predominance of quartz and feldspars, respectively (Prokof'eva et al., 2017). The fluctuations in the particle-size distribution for roads of different categories are small; the differences do not exceed 2–6%. Coarse particles ( $>50 \mu\text{m}$ ) account for 60–70% of the total mass (Kasimov et al., 2019c). The average content of  $\text{PM}_{10}$  particles in road dust is  $14.9 \pm 7.2\%$ ; a slight decrease in the content of these particles is observed with a decrease in the size of the roads: from  $17.7 \pm 6.5\%$  on the MRR and  $17.7 \pm 4.7$  on the TRR to  $16.1 \pm 7.4\%$  on the largest highways,  $14.4\% \pm 9.7\%$  on major radial highways,  $13.4 \pm 6.9\%$  on medium roads, and  $13.6 \pm 7.2\%$  on small roads increasing to  $14.3 \pm 6.5\%$  in the yards. In Moscow forest parks, road dust contains  $>50\%$  of coarse particles (250–1000  $\mu\text{m}$ ); the content of  $\text{PM}_{10}$  particles is slightly lower than that on the highways and amounts to  $12.9 \pm 5.3\%$ .

The spatial distribution of the  $\text{PM}_{10}$  fraction in road dust is shown in Fig. S.1 (Supplementary material). A slight increase in the content of  $\text{PM}_{10}$  on MRR and TRR is typical for places of big daily traffic jams, which leads to an increase in emissions of fine particles and soot. High shares of  $\text{PM}_{10}$  were also noted along the Leningradskoye and Yaroslavskoye highways, ones of the busiest highways



in Moscow. In road dust in the northern part of the city (Northern, Northeastern, and Northwestern administrative districts), on major highways and the MRR, the content of fine particles  $PM_{5-10}$  slightly increases. The maximum content of coarse ( $>50 \mu m$ ) fraction and, accordingly, the minimum content of fine ( $PM_{5-10}$ ) particles are observed in the center, east, and southeast of Moscow (Kasimov et al., 2019c). The most probable reason for the predominance of coarse fractions in the road dust of the eastern and southeastern parts of Moscow is that they belong to the Meshchera lowland, a flat outwash plain composed of glaciofluvial sands and loamy sands (Kasimov et al., 2016).

In other cities, the particle-size distribution of road dust varies significantly depending on a large number of factors – traffic intensity, number of congestions, wind erosion of roadside soils, abrasion of car parts and roadbed, sampling season, duration of the rainless period, frequency and quality of road cleaning from dust, wind speed, etc. (Bian and Zhu, 2009; Duong and Lee, 2011; Gietl et al., 2010; Li et al., 2015). However, despite the influence of various factors in most cities of the world, including Moscow, the share of  $PM_{10}$  particles in road dust is quite stable and rarely increases up to 10–25%. For instance, in Austrian Wels,  $PM_{10}$  particles account for 10–15% of the mass of the  $PM_{200}$  fraction (Lanzerstorfer, 2018); in Bogota – about 10% of the mass of bulk road dust (Ramírez et al., 2019), in Shanghai – about 20% (Shi et al., 2011), in Chelyabinsk – up to 17% (Krupnova et al., 2020), in Krakow, Katowice and Olkusz – up to 7–10% (Logiewa et al., 2020), in Philadelphia – less than 10% of the mass of road dust (O’Shea et al., 2020); in Alushta town – 22% of road dust and 31% of soils in the surface horizons (Kasimov et al., 2019a). Local sources of  $PM_{10}$  particles (e.g., industrial emissions, coal combustion) or natural factors (e.g., dust storms, dry periods) sometimes lead to a sharp increase in the proportion of  $PM_{10}$  in road dust. For instance, in Beijing and Shanghai – cities with heavy industrial impact, the  $PM_{10}$  content averages 59% and 65% of the  $PM_{100}$  fraction of road dust, respectively, whereas in coastal Hong Kong it is only 3% due to frequent rains (Tanner et al., 2008).

## 4.2. PTEs in road dust and in its $PM_{10}$ fraction

### 4.2.1. Contents of PTEs in bulk samples of road dust

Owing to the anthropogenic impact, the chemical composition of Moscow road dust is characterized by the concentration of Pb, Cd, Zn, Sb, and Cu by 2.4–3 times and Mo, W, Sn, and Bi by 1.2–3 times relative to their average contents in the upper part of the continental crust. Other elements (Ti, V, Cr, Mn, Fe, Co, Ni, As, and La) do not accumulate in the road dust of Moscow (Table 1).

On the paths of urban forest parks, only the concentrations of Cd, Bi, and Zn in the dust are higher than their natural abundances in the upper continental crust. Most likely, these elements enter the dust with windblown particles from the upper soil horizons, where they accumulate due to atmospheric deposition. In comparison with road dust, dust particles from the paths of forest parks are depleted of PTEs, which is due to a larger proportion of coarse particles with a diameter  $>50 \mu m$ , which have a relatively low sorption capacity: on average, their content in park dust and road dust is about 75 and 55–65%, respectively (Kasimov et al., 2019c). A decrease in the fraction of fine particles was also noted for the soils of parks in Bogotá, which were used as a background standard in the study of

city road dust. The content of  $PM_{10}$  particles in the road dust of this city was about 10%, whereas in the soils of parks, it was two times lower (Ramírez et al., 2019).

In Moscow road dust, the accumulation of Sb, W, Cu, Pb, and Sn is 3–4 times more intense than their accumulation in the dust sampled on paths in forest parks, and the accumulation of Mo, Cr, Zn, Fe, V, and Ni is 1.5–3 times higher (Table 1). Concentrations of Co, Ti, Mn, As, Cd, Bi, and La in the dust of parks and highways do not differ much. Many PTEs are characterized by strong variability of concentrations that increases several times in road dust in comparison with the dust of forest parks, which indicates a significant contribution from anthropogenic sources and spatial heterogeneity of anthropogenic impacts on the roads. The average coefficient of variation  $C_v$  for PTEs in park dust is 39%, and it increases to 87% in road dust. The highest variability is characteristic of anthropogenic elements, such as Pb ( $C_v$  in road dust is 12 times higher than  $C_v$  in park dust), W and Mo (6 times), and As (5 times), which may be due to a higher variability of industrial emissions in comparison with the emissions from vehicles. The variability of concentrations of Mn, Cd, and Bi in road dust slightly differs from that in park dust, which may be caused by a relatively large input of Mn with plant litter and of Cd and Bi with mineral fertilizers (Motuzova and Karpova, 2013).

In terms of the levels of PTEs in road dust, Moscow is in an intermediate position among other major cities of the world. For example, Moscow road dust is enriched with As relative to road dust in Tokyo, Osaka, and Kyoto (Wijaya et al., 2012) and Beijing (Men et al., 2018), but is depleted in this element in comparison with road dust of Lagos (Ogunsola et al., 1994). Another dangerous metalloid – Sb – is less actively accumulated in road dust of Moscow than in road dust of Dhaka, Kolkata, Lagos, and Tehran (Ahmed et al., 2007; Dehghani et al., 2017; Nath et al., 2007; Ogunsola et al., 1994). The pollution of road dust in Moscow with toxic Cd, Pb, and Zn is also generally lower than in many other large cities – London (Wang et al., 1998), Paris (Pagotto et al., 2001), Warsaw (Adamiec, 2017), Tokyo (Wijaya et al., 2012), Seoul (Lee et al., 2005), Shanghai (Tanner et al., 2008), Tehran (Dehghani et al., 2017), Karachi (Iqbal and Jilani, 2015), Mumbai (Saradhi et al., 2014), Guangzhou (Cai et al., 2013), and others.

Tehran road dust has the closest chemical composition to Moscow road dust (Dehghani et al., 2017). However, such an analysis of the geochemical specialization of road dust in megacities is rather arbitrary because of the comparison of the composition of particles with different diameters (50, 63, 75, 125, 150, 1000, 2000  $\mu m$ ) and the absence of generally recognized particle fractions that should be distinguished when assessing the intensity of dust pollution with PTEs. The crustal factor also plays an important role: the enrichment of some parent rocks and soil particles by certain PTEs can lead to a noticeable increase in their concentrations in road dust.

### 4.2.2. Concentrations of PTEs in $PM_{10}$ particles of road dust

$PM_{10}$  particles have an increased sorption capacity compared to road dust in general. This determines a 1.2–6.4 times higher concentration of many PTEs in  $PM_{10}$  than in the bulk samples of road dust (Table 1). At the same time, relative to Moscow parks, the  $PM_{10}$  fraction of Moscow road dust accumulates Sb, W, Sn, Bi, and Cu

**Table 1.** Element clarkes (K) in the upper part of continental crust (Rudnick and Gao, 2014) and concentrations of PTEs in road dust, park dust, and in their PM<sub>10</sub> fractions in Moscow, summer 2017.

Element	K, mg/kg	Road dust, n = 209			Park dust, n = 5			CF	PM <sub>10</sub> of road dust, n=209			PM <sub>10</sub> of park dust, n = 5			CF
		concentration, mg/kg	Cv, %	PI <sub>r</sub>	concentration, mg/kg	Cv, %	PI <sub>p</sub>		concentration, mg/kg	Cv, %	PI <sub>r</sub>	concentration, mg/kg	Cv, %	PI <sub>p</sub>	
As	4.8	2.0 (0.14–43)	203	0.4	2.0 (1.0–2.9)	41	0.4	1.0	2.0 (0.14–43)	71	0.4	6.9 (3.2–11)	48	1.4	0.3
Bi	0.16	0.273 (0.053–5.1)	151	1.7	0.371 (0.058–1.5)	170	2.3	0.7	1.5 (0.12–12)	65	9.2	0.41 (0.32–0.51)	19	2.6	3.6
Cd	0.09	0.244 (0.12–1.04)	43	2.7	0.32 (0.19–0.46)	39	3.6	0.8	0.82 (0.08–8.7)	102	9.1	1.1 (0.82–1.3)	19	12	0.8
Co	17.3	6.1 (2.5–16)	39	0.4	4.3 (3.4–5.2)	18	0.2	1.4	15 (1.0–85)	46	0.9	9.9 (8.6–11)	10	0.6	1.5
Cr	92	48 (12–312)	60	0.5	20 (14–26)	23	0.2	2.3	68 (2.2–493)	58	0.7	48 (39–56)	15	0.5	1.4
Cu	28	66 (8.3–556)	98	2.4	20 (9.8–30)	46	0.7	3.4	184 (12–906)	54	6.6	59 (44–72)	18	2.1	3.1
Fe	39,200	23,831 (7764–48,261)	31	0.6	11,904 (8253–14,059)	19	0.3	2.0	40,947 (2823–220,472)	42	1.0	29,588 (25266–37,904)	17	0.8	1.4
La	31	13 (5.6–50)	41	0.4	16 (7.1–38)	79	0.5	0.8	21 (1.6–170)	54	0.7	24 (21–26)	8.0	0.8	0.9
Mn	774	359 (132–852)	28	0.5	299 (209–403)	29	0.4	1.2	641 (58–4573)	50	0.8	1061 (894–1177)	11	1.4	0.6
Mo	1.1	2.2 (0.49–22)	83	2.0	0.79 (0.67–0.95)	14	0.7	2.8	4.9 (0.06–21)	54	4.5	2.5 (1.7–3.0)	23	2.2	2.0
Ni	47	23 (6.9–139)	60	0.5	14 (12–21)	26	0.3	1.6	46 (5.1–310)	56	1.0	36 (26–50)	24	0.8	1.3
Pb	17	51 (9.5–2488)	351	3.0	15 (8.3–20)	30	0.9	3.3	91 (6.5–923)	114	5.3	48 (40–54)	11	2.8	1.9
Sb	0.4	2.1 (0.40–11)	66	5.2	0.50 (0.30–0.64)	34	1.3	4.1	12 (0.45–48)	55	30	1.9 (1.3–2.4)	22	4.7	6.4
Sn	2.1	4.6 (0.84–22)	64	2.2	1.38 (0.78–1.96)	37	0.7	3.3	21 (1.0–137)	57	9.8	5.1 (3.9–6.4)	18	2.4	4.0
Ti	3840	2096 (659–5574)	38	0.5	1570 (1139–1918)	19	0.4	1.3	3053 (136–17,281)	45	0.8	2802 (2563–3077)	9.0	0.7	1.1
V	97	53 (16–136)	40	0.5	31 (24–41)	22	0.3	1.7	81 (5.4–501)	46	0.8	68 (54–88)	20	0.7	1.2
W	1.9	3.9 (0.56–40)	95	2.0	1.07 (0.76–1.18)	16	0.6	3.6	25 (1.2–167)	63	13	4.4 (3.1–6.3)	34	2.3	5.6
Zn	67	197 (54–1723)	81	2.9	88 (40–122)	42	1.3	2.2	1026 (48–7772)	91	15	386 (297–451)	17	5.8	2.7

Note: Minimum and maximum concentrations are given in parentheses. Global pollution index  $PI_r = Cr/K$ , where Cr is the concentration of PTE in road dust or its PM<sub>10</sub> particles, K is the concentration of PTE in the upper continental crust; for parks,  $PI_p = Cp/K$ , where Cp is the concentration of PTE in dust of parks or its PM<sub>10</sub> particles. Contamination factor  $CF = Cr/Cp$ .

3–6.5 times more actively, whereas the accumulation of Zn, Mo, Pb, and Co is 1.5–3 times less active. Relative to the natural element abundances in the upper part of the continental crust, PM<sub>10</sub> particles of road dust are enriched in Sb by 15 times, Zn by 14 times, W by 12 times; and Cd, Sn, Cu, Bi, Pb, and Mo by 5–9 times. The variability of the concentrations of all PTEs in PM<sub>10</sub> particles of road dust under the anthropogenic impact increases several times in comparison with these particles in park dust. Thus, the average Cv of PTEs in PM<sub>10</sub> particles of park dust is 19%, and it increases to 62% in PM<sub>10</sub> particles of road dust.

In Moscow, the PM<sub>10</sub> fraction concentrates more than 65% of the total contents of W, Bi, Sb, Zn, and Sn in road dust and slightly more than 50% of the total Cu content (Fig. 2). These elements are mainly associated with PM<sub>10</sub> particles actively migrating in the atmosphere over long distances and polluting the air and soil in different land use zones along the roads, including residential quarters. A fairly large (30–50%) amount of Cd, Pb, Mo, Co, and Ni in road dust is also associated with PM<sub>10</sub> particles. The remaining elements – Mn, Fe, As, V, Cr, and Ti – are mainly (75–80%) contained in coarser fraction with a diameter of more than 10 μm. In general, PM<sub>10</sub>

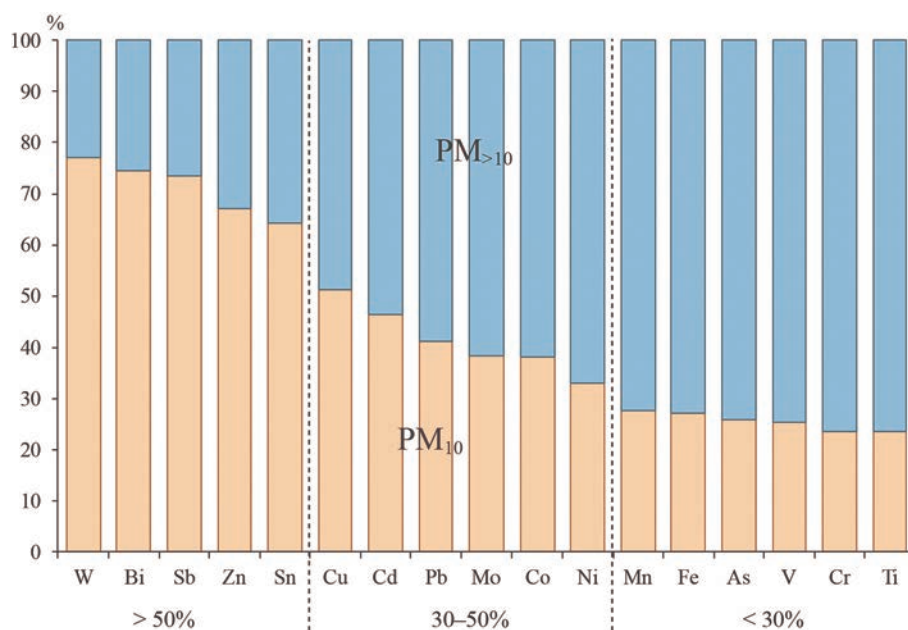


**Fig. 2.** Fractional composition of PTEs in road dust of Moscow (summer 2017).

particles are among the most important carriers of PTEs in Moscow road dust, which determines their increased environmental hazard to the population.

The pollution of the PM<sub>10</sub> fraction of road dust depends on the intensity of anthropogenic impact, which is indirectly characterized by the size of the city. For example, in Moscow, the concentrations of most PTEs (except for As) in PM<sub>10</sub> dust particles are 1.5–2 times higher than those in small towns, such as Alushta (Kasimov et al., 2019a) and Austrian Wels (Lanzerstorfer, 2018). A comparison with larger cities of the world allows us to determine the geochemical features of PM<sub>10</sub> particles in road dust of Moscow: a 2 to 12 times higher content of W in comparison with that in Barcelona, Zürich, and Girona (Amato et al., 2011), a 1.5–3 times higher content of Zn in comparison with that in Beijing, Tianjin, and Dongying (Chen et al., 2012; Kong et al., 2012; Zhang et al., 2019), and low contents of As, Sb, Bi, Mo, Sn, Cu, Cd, Pb, Cr, and Ni relative to those in most of these large cities, as well as in Hong Kong (Ho et al., 2003). High concentrations of W and Zn are likely to be associated with a large number of traffic jams, traffic lights, intersections and turns in Moscow compared to other cities, which contributes to faster tire abrasion and wear of brake pads containing significant amounts of these metals (Apeageyi et al., 2011). This is confirmed by the TomTom traffic load index, which takes into account data on traffic congestion in 416 cities from 57 countries, and according to which Moscow and the nearest suburbs in 2017–2019 ranked fifth– sixth place in the world (losing in different years to Bangalore, Manila, Bogotá, Mumbai, Pune, and New Delhi) with the traffic congestion level of 57–59%, which corresponds to 218–225 h of traffic loss for each driver (TomTom Traffic Index, 2020).

In terms of the levels of Co, Fe, Mn, Ti, and V in PM<sub>10</sub> particles of road dust, Moscow occupies an intermediate position among other large cities, which can be explained by the arrival of these PTEs with resuspended particles of roadside soils and road pavement, the intensity of which varies slightly from city to city. Thus, the level of pollution of road dust and its PM<sub>10</sub> fraction in Moscow with most PTEs is slightly lower than in many other large cities.

### 4.3. Spatial differentiation of contamination of road dust and PM<sub>10</sub> fraction with PTEs

In Moscow, PTEs in road dust and its PM<sub>10</sub> fraction can be subdivided into two groups with respect to their EF values (Fig. 3). Sb<sub>13</sub>Pb<sub>8</sub>Zn<sub>8</sub>Cd<sub>7</sub>Cu<sub>6</sub>Sn<sub>5</sub>Mo<sub>5</sub>W<sub>5</sub>Bi<sub>4</sub> (subscripts indicate EF values of corresponding elements in bulk samples of road dust) belong to the first group with high EF because of the anthropogenic impact. In this case, the road dust contamination with Sb, Pb, Zn, Cd, and Cu corresponds to significant ( $5 < EF < 20$ ) enrichment factor values, and contamination with Sn, Mo, W, and Bi corresponds to the moderate ( $2 < EF < 5$ ) values. The second group with lower EF levels includes Fe, Ni, Co, V, Mn, Ti, Cr, and As that enter road dust mainly due to blowing out of roadside soils, parent materials, and natural materials applied for roadbed construction. The PM<sub>10</sub> fraction of road dust in Moscow accumulates the same elements (Sb<sub>44</sub>Zn<sub>23</sub>W<sub>19</sub>Sn<sub>14</sub>Bi<sub>13</sub>Cd<sub>13</sub>Cu<sub>10</sub>Pb<sub>8</sub>Mo<sub>7</sub>), but is enriched with them by 2–4 times more intensively than the bulk samples. Therefore, the PM<sub>10</sub> particles contamination with Sb corresponds to the extremely high enrichment level ( $EF > 40$ ); with Zn, to very high level ( $20 < EF < 40$ ); and with W, Sn, Bi, Cd, Cu, Pb, and Mo, to significant level ( $5 < EF < 20$ ).

The spatial distribution of PTEs in road dust and its PM<sub>10</sub> fraction in Moscow is extremely heterogeneous; many PTEs are characterized by local anthropogenic geochemical anomalies of various contrasts (Fig. 4; Figs. S2–S9 in Supplementary material). Centers of geochemical anomalies are found in the Central (Zn, Sn, Cd, Cu, Pb), Eastern (Mo, Zn, W, Sn, Bi, Cd, Cu, Pb), Western (Pb, Zn, W, Sn, Bi), Southern (Cu, W, Sn, Cd, Pb), and Northern (Bi) districts of the city. Anomalies of Sb in road dust and PM<sub>10</sub> particles are detected in all parts of the city and are confined mainly to radial highways and the MRR. This is consistent with previous data on Sb as one of the main pollutants in urban environments of Moscow: in the dissolved and suspended phases of snow cover and precipitation (Kasimov et al., 2012; Vinokurov et al., 2017; Vlasov et al., 2020a, 2020b), atmospheric depositions and mosses (Vergel et al., 2019), soils (Kosheleva et al., 2018, 2015), bottom sediments

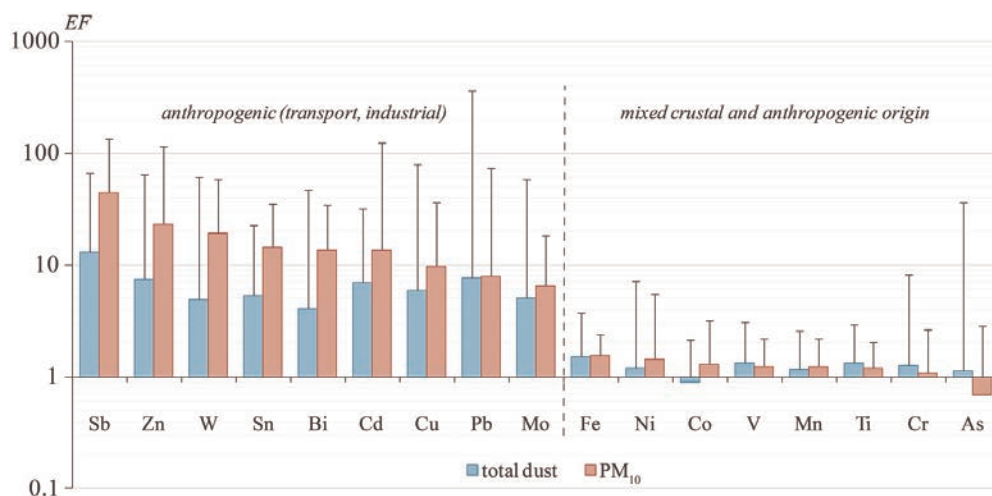


**Fig. 3.** Enrichment of road dust and its PM<sub>10</sub> fraction with PTEs in Moscow (summer 2017) upon their input from different sources. Vertical lines indicate maximum EF for each PTE.



of ponds and lakes (Vlasov et al., 2019), woody and herbaceous plants (Kasimov et al., 2016). The high accumulation of Sb in all parts of Moscow is due to the fact that the main source of emissions in the city is motor vehicles, which can supply large amounts of Sb because of the wear of brake pads (Pant and Harrison, 2013; Grigoratos and Martini, 2015; Zhu et al., 2020). An increase in road dust loadings is observed simultaneously with a decrease in vehicle speed and distance to closest braking zone (Pachon et al., 2020). Emission of Sb and other PTEs is high during frequent stop–start maneuvers and changes in vehicle trajectory movement (Nazzal et al., 2013; Ferreira et al., 2016). Frequent traffic jams in Moscow, which significantly reduce the traffic speed, cause intensive accumulation of Sb in road dust.  $PM_{10}$  is characterized by a decrease in the Sb accumulation rate with a decrease in the size of the road: the EF decreases from 63 on MRR to 46–50 on TRR, highways, large and

medium roads, to 35 on small roads and to 26 on roads and parking lots in the yards. The hypothesis that the main source of Sb in  $PM_{10}$  is motor transport is also confirmed by a sharp decrease in EF to 6 in parks, which are situated far enough from roads (Table 2).

Previous studies of the chemical composition of soils, the dust component of the snow cover, and various particle-size fractions of road dust in the east of Moscow demonstrated that all these components of the urban environment accumulate Sb, W, and Sn, and the fine fractions  $PM_1$  and  $PM_{1-10}$  additionally accumulate Cd, Zn, Cu, Pb, Mo, and Bi at a significant level ( $EF > 5$ ), especially in the roadside areas of MRR and major highways (Kasimov et al., 2020; Vlasov et al., 2020b).

Often geochemical anomalies of PTEs are small in length and are associated not only with the size of the road (i.e., with the intensity of the vehicles impact) but also with the influence of particular industrial zones.

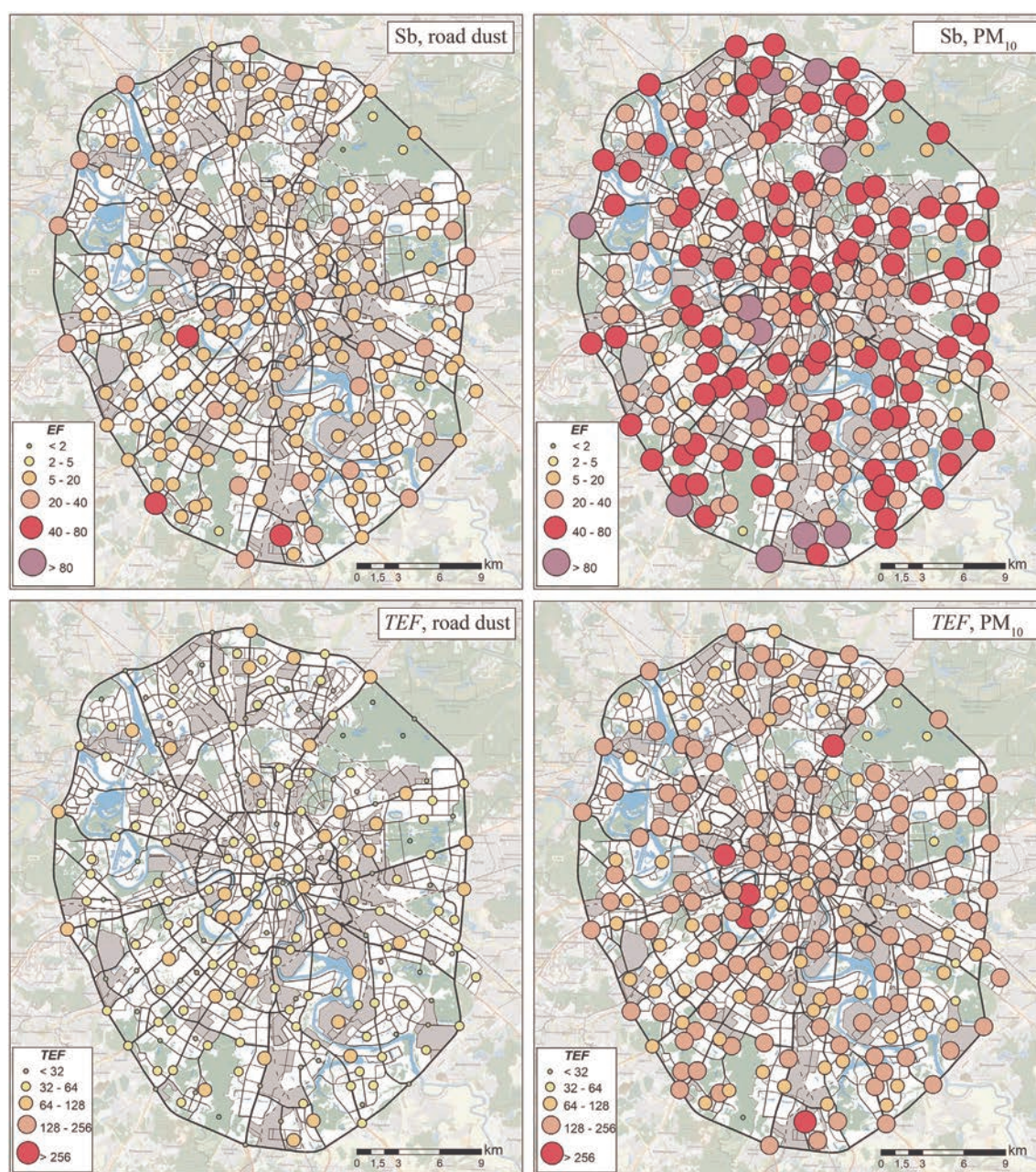


**Fig. 4.** Enrichment factor of Sb and the total enrichment factor (TEF) in road dust and  $PM_{10}$  fraction of road dust in Moscow (summer 2017).



**Table 2.** Enrichment of road dust and its PM<sub>10</sub> fraction with PTEs on roads of different sizes in Moscow (summer 2017).

Fraction	Area	Contamination levels and EF values					TEF
		Extremely high	Very high	Significant	Moderate		
		EF ≥ 40	EF 40–20	EF 20–10	EF 10–5	EF 5–2	
PM <sub>10</sub>	MRR	Sb <sub>63</sub>	Zn <sub>31</sub> W <sub>21</sub>	Sn <sub>12</sub> Bi <sub>11</sub> Cd <sub>10</sub>	Cu <sub>9</sub> Mo <sub>6</sub>	Pb <sub>5</sub>	163
	TRR	Sb <sub>46</sub>	Zn <sub>38</sub> W <sub>22</sub>	Sn <sub>17</sub> Bi <sub>16</sub> Cu <sub>12</sub>	Cd <sub>9</sub> Mo <sub>8</sub> Pb <sub>7</sub>	–	169
	H	Sb <sub>52</sub>	Zn <sub>21</sub>	Sn <sub>14</sub> W <sub>14</sub> Bi <sub>12</sub> Cu <sub>11</sub> Cd <sub>10</sub>	Mo <sub>8</sub> Pb <sub>6</sub>	–	143
	L	Sb <sub>50</sub>	–	Zn <sub>18</sub> W <sub>16</sub> Sn <sub>15</sub> Bi <sub>14</sub> Cd <sub>13</sub> Cu <sub>12</sub> Pb <sub>10</sub>	Mo <sub>8</sub>	–	151
	M	Sb <sub>48</sub>	Zn <sub>21</sub>	W <sub>19</sub> Cd <sub>16</sub> Sn <sub>16</sub> Bi <sub>14</sub> Cu <sub>10</sub>	Pb <sub>8</sub> Mo <sub>8</sub>	–	154
	Sm	–	Sb <sub>35</sub>	W <sub>19</sub> Zn <sub>17</sub> Sn <sub>14</sub> Cd <sub>14</sub> Bi <sub>13</sub>	Pb <sub>8</sub> Cu <sub>8</sub> Mo <sub>6</sub>	–	127
	Y	–	Zn <sub>27</sub> Sb <sub>26</sub> W <sub>22</sub>	Cd <sub>16</sub> Bi <sub>14</sub> Sn <sub>13</sub>	Cu <sub>8</sub> Pb <sub>7</sub>	Mo <sub>4</sub>	131
	Moscow	Sb <sub>44</sub>	Zn <sub>23</sub>	W <sub>19</sub> Sn <sub>14</sub> Bi <sub>13</sub> Cd <sub>13</sub> Cu <sub>10</sub>	Pb <sub>8</sub> Mo <sub>7</sub>	–	145
	P	–	–	Cd <sub>15</sub>	Zn <sub>8</sub> Sb <sub>6</sub>	Pb <sub>4</sub> Bi <sub>3</sub> Sn <sub>3</sub> W <sub>3</sub> Mo <sub>3</sub> Cu <sub>3</sub>	42
Total road dust	MRR	–	Sb <sub>21</sub>	Zn <sub>12</sub>	W <sub>7</sub> Cu <sub>6</sub> Cd <sub>6</sub>	Mo <sub>5</sub> Bi <sub>5</sub> Sn <sub>5</sub> Pb <sub>4</sub> Fe <sub>2</sub>	67
	TRR	–	–	Zn <sub>17</sub> Sb <sub>13</sub>	W <sub>8</sub> Sn <sub>7</sub> Cd <sub>6</sub> Cu <sub>6</sub>	Mo <sub>5</sub> Bi <sub>4</sub> Pb <sub>4</sub> Fe <sub>2</sub>	65
	H	–	–	Sb <sub>11</sub>	Cd <sub>6</sub> Zn <sub>6</sub>	Sn <sub>5</sub> Bi <sub>5</sub> Cu <sub>5</sub> Pb <sub>4</sub> W <sub>4</sub> Mo <sub>4</sub>	42
	L	–	–	Sb <sub>16</sub> Pb <sub>15</sub>	Cu <sub>9</sub> Sn <sub>7</sub> Cd <sub>6</sub> Zn <sub>6</sub>	Mo <sub>5</sub> W <sub>4</sub> Bi <sub>4</sub>	68
	M	–	–	Sb <sub>12</sub>	Cd <sub>7</sub> Zn <sub>6</sub> Cu <sub>6</sub>	Pb <sub>5</sub> Sn <sub>5</sub> Mo <sub>5</sub> W <sub>4</sub> Bi <sub>4</sub>	47
	Sm	–	–	Sb <sub>10</sub>	Cd <sub>7</sub> Pb <sub>7</sub> Sn <sub>6</sub> Zn <sub>6</sub> Cu <sub>6</sub>	Mo <sub>5</sub> W <sub>4</sub> Bi <sub>4</sub>	49
	Y	–	–	–	Zn <sub>9</sub> Sb <sub>8</sub> Cd <sub>8</sub> Pb <sub>6</sub> W <sub>6</sub> Mo <sub>6</sub>	Sn <sub>4</sub> Bi <sub>4</sub> Cu <sub>3</sub>	46
	Moscow	–	–	Sb <sub>13</sub>	Pb <sub>8</sub> Zn <sub>8</sub> Cd <sub>7</sub> Cu <sub>6</sub>	Sn <sub>3</sub> Mo <sub>5</sub> W <sub>5</sub> Bi <sub>4</sub>	54
	P	–	–	–	Cd <sub>8</sub>	Zn <sub>3</sub> Sb <sub>3</sub> Bi <sub>3</sub> Pb <sub>2</sub>	19

Note: MRR – Moscow Ring Road, TRR – Third Ring Road, H – major highways, L – large roads, M – medium roads, Sm – small roads, and Y – roads and parking lots in the yards; Moscow – average for all roads in Moscow; P – dust sampled in parks. Dashes mean the absence of the corresponding contamination level. Elements with EF < 2 are not shown.

Thus, Pb anomalies in the west of Moscow are most likely due to the impact of the M.V. Khrunichev Space Research and Production Center, Western River Port, Moscow Kiyevsky railway station, and bus depot No. 5 in the “Berezhkovskaya Embankment”, “Western Port”, and “Fili” industrial zones (Bityukova and Saulskaya, 2017). Increased Zn concentrations in the center of Moscow are associated with emissions of railway transport and of industrial enterprises at the border of the Central and Southeastern administrative districts: car repair and tire plants, refrigeration equipment factory in the “Serp i Molot” and “Volgogradskiy Prospekt” industrial zones. An increased concentration of Cu in road dust in the south of Moscow is caused by the impact of railway transport, nonferrous metal casting enterprises, production of electrolytic copper foil and optoelectronic devices (the “Copper Foil” factory in the “Verkhniye Kotly” industrial zone and the “Sapphire” factory in the “Chertanovo” industrial zone), electrical substations, brick factory, and bus and trolleybus parks in the “Chertanovo”, “Nagatino” industrial zones (Bityukova and Saulskaya, 2017). Zn is widely used in manufacturing of tires and metallic parts of vehicles (Alves et al., 2020a; Pant and Harrison, 2013), and production of galvanized steel for refrigerators (Sabnavis et al., 2018). Cu may be emitted by metallurgical plants, machinery companies (Vergel et al., 2019), and production of optoelectronic devices (Saet et al., 1990). Zn and Cu can be emitted by trolleybuses (Aprile et al., 2010) and brick factories (Cao et al., 2019). Railway transport is a significant source of Zn, Pb and Cu in the environment (Stojic et al., 2017; Vaiškūnaitė and Jasiūnienė, 2020).

As a rule, relatively contrasting geochemical anomalies of Sb, Zn, W, Cd, Sn, Cu, Bi, Pb, Mo and other PTEs are formed in the dust of the major highways of Moscow (Varshavskoye and Dmitrovskoye highways,

Prospekt Mira, Kutuzovskiy, Volgogradskiy, and Sevastopolskiy avenues, etc.), TRR, and MRR; less often, they are allocated to medium and small roads, or even to the yards of residential areas (Table 2). In addition to vehicle emissions, emissions from railroad transport participate in their formation (Cd anomalies in road dust are found in the area of the three railway stations – Kazansky, Yaroslavsky, and Leningradsky), as well as near various industrial enterprises. High levels of Cd, Cu, Zn, Pb, and As are also typical of soils in the area of the three railway stations and near the Belorusskiy railway station, especially at short (up to 10 m) distances from the railways, though the influence of railways can spread up to 1000 m (Makarov, 2014).

The total enrichment factor (TEF) was calculated for a comprehensive study of the enrichment of road dust and its PM<sub>10</sub> fraction with PTEs and preliminary assessment of spatial patterns of the environmental hazard. In general, TEF values of Moscow road dust correspond to a low level of environmental risk (average TEF = 54), whereas TEF values for PM<sub>10</sub> particles attest to a high level of environmental risk (TEF = 145) (Figs. 4, 5; Table 2).

The highest TEF values of bulk samples of road dust are typical for the MRR, TRR, and major highways; TEF values of PM<sub>10</sub> particles are the highest in road dust on the MRR and TRR in different parts of the city (Fig. 5; Table 2), where, in addition to cars, there are many large freight vehicles and public transport on the roads. In Moscow, up to 56% of all particulate matter entering the atmosphere with motor vehicle emissions is delivered by trucks weighing more than 3.5 tons, 29% by buses, 10% by cars, and 5% by trucks weighing less than 3.5 tons (Kul’bachevskii, 2019). The particularly high enrichment of PM<sub>10</sub> fraction with PTEs is observed within the central (enclosed inside the TRR) part of the city with a high density of the road network

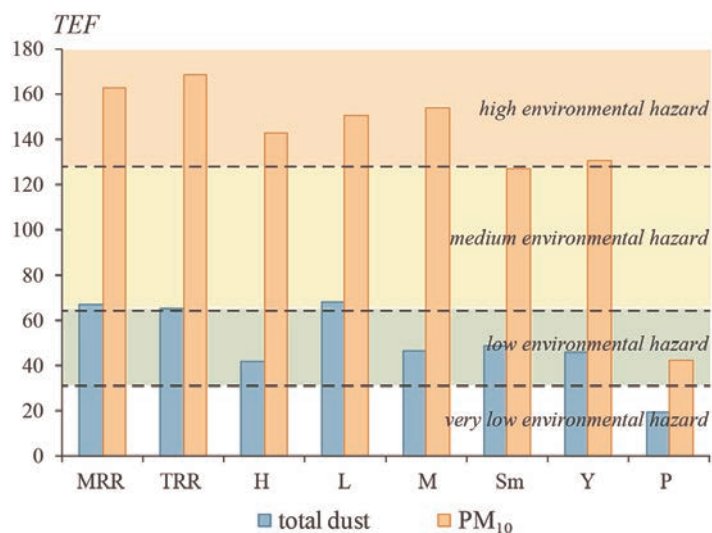


**Fig. 5.** Total enrichment factor TEF values and the levels of environmental hazard of road dust and its PM<sub>10</sub> fraction on different highways of Moscow (summer 2017). Roads: H – major radial highways, L – large roads, M – medium roads, Sm – small roads, Y – roads and parking lots in the yards; P – dust sampled in parks.

and intense traffic. On major radial highways, the TEF values of road dust are lower than on MRR, TRR, and large and medium roads because of frequent roadbed cleaning by municipal services on highways, which results in a regular renewal of road dust and, hence, lower accumulation of many PTEs in it.

Differences in the enrichment of road dust and its PM<sub>10</sub> fraction with PTEs on roads with different traffic flows can be explained by the following reasons. On small and medium roads, despite a decrease in traffic flow, emissions contain a greater amount of fine particles due to abrasion of brake pads, tires, and pavement as a result of frequent stops because of a large number of traffic lights, traffic jams, stops of public transport, etc. Congestion reducing the traffic flow rate to 20 km/h, leads to an increase in emissions by 30% (Bitjukova and Sokolova, 2008); very strong congestion with the flow rate of 8 km/h and less increases emissions by three–four times (Choudhary and Gokhale, 2016). With a decrease in vehicle speed, the size of ejected particulate matter sharply increases (Kittelson et al., 2004). The duration and frequency of vehicle stops has a strong impact on fuel consumption and pollutant emissions (Ericsson, 2001). In the center of Moscow, where traffic jams occur very often, the concentrations of CO and NO<sub>2</sub> in the air near the highways are almost two times higher than those away from the center, between the TRR and the MRR (Kul'bachevskii, 2019). With an increase in transport speeds on large roads and greater wind blowing intensity, small particles of road dust are resuspended to the atmosphere, and the proportion of large particles gradually increases. Therefore, an increase in the size of the road and the intensity of the traffic flow from medium to large and major highways leads to a decrease in the TEF of the PM<sub>10</sub> fraction.

In the yards of residential buildings, the TEF levels of road dust and PM<sub>10</sub> particles are only 1.1–1.5 times lower than those on major highways, MRR, and TRR. In the courtyards, traffic is low, but generally low wind speeds, tall buildings, and other constructions favor the

development of specific trap zones (well-shaped traps) that reduce the airborne migration of PM<sub>10</sub> particles and contributing to their deposition on the surface of soils and roads (Kosheleva et al., 2018). Thus, such areas require frequent cleaning to reduce the amount of dust and PM<sub>10</sub> particles.

#### 4.4. Source apportionment of PTEs

To identify the main sources of PTEs and their contribution to the composition of road dust and its PM<sub>10</sub> fraction in Moscow, the principal component analysis (PCA) was applied. This method allows one to reduce the number of factors required for interpretation by generalizing arrays of multidimensional data in several linear combinations of influencing variables (principal components) without significant loss of information. The results of PCA simplify the identification of various sources involved in the formation of the fractional composition of road dust. The initial data for the analysis were the concentrations of PTEs in road dust and in the PM<sub>10</sub> fraction (Table 1). The varimax normalized rotation method was used. Factors were distinguished by the magnitude of factor loadings: a strong relationship corresponded to the factor loading of more than 0.7, and a moderate relationship corresponded to the factor loading of 0.5–0.7. Classes on the distribution schemes of factor score values for each chosen factor (Figs. S.10 and S.11 in Supplementary material) were distinguished by the Jenks natural breaks classification method.

##### 4.4.1. Total road dust

For bulk samples of road dust, six principal factors explaining in total 68% of the total variance were identified (Fig. 6).

*The first factor (PC1)* is the most important and accounts for about 33.6% of the total variance. This factor reflects the contribution of roadside soil particles to road dust, which leads to the enrichment of road dust with siderophile and lithophile elements of the Earth's crust – Ti, V, Mn, Fe, and Co (Adachi and Tainosho, 2005; Gunawardana et al., 2012; Harrison et al., 2012; Morera-Gómez et al., 2020). The impact of this factor is observed ubiquitously (Fig. S.10 in Supplementary material). The input of these PTEs from a single source is confirmed by the high positive correlation coefficients  $r = 0.71–0.95$  between the concentrations of elements of this group (Table S.1 in Supplementary material).

*The second (PC2) and third (PC3) factors*, most probably, characterize the contribution of industrial enterprises. The second factor is responsible for 11.1% of the variance and is associated with the accumulation of Cu and As ( $r = 0.47$ ). It reflects the impact of enterprises for the casting of nonferrous metals, production of electrolytic copper foil, and optoelectronic devices (Saet et al., 1990), which manifests itself in the formation of Cu and As anomalies, especially in the southern part of the city (Fig. S.10 in Supplementary material).

The third factor characterizes the influence of machine building and metal processing, car repair and painting enterprises (Demetriades and Birke, 2015; Zheng et al., 2018), especially in the eastern part of the city. This factor accounts for about 9% of the total variance and is associated with increased concentrations of Ni, Cr, and Mo in road dust. There is a strong positive correlation



between Ni and Cr ( $r = 0.72$ ), while Mo with Ni and Cr are not strongly correlated ( $r = 0.30$  and  $0.35$ , respectively). The main reason of the strong positive correlation between Ni and Cr may be their joint emission as a result of mechanical abrasion of stainless steel surfaces or gilt metal objects, which is a source of coarse particles, enriched in Ni and Cr (Okuda et al., 2007).

The contributions of the fourth (PC4), fifth (PC5) and sixth (PC6) factors to the total variance comprise 7.2%, 7.0%, and 6.3%, respectively. These factors might be associated with non-exhaust emissions of vehicles. They are most clearly manifested on large roads (Fig. S.10 in Supplementary material), where traffic jams often occur and a large number of traffic lights are installed, which leads to frequent stops and an increased number of car maneuvers. Thus, PC4, which is responsible for the formation of Sb and Pb anomalies in road dust of Moscow ( $r = 0.49$ ), most likely characterizes the abrasion of brake pads and linings, where these metals are contained in high concentrations (antimony sulfide Sb<sub>2</sub>S<sub>3</sub> is a common component of brake lubricant) and often used as indicators of this process (Gietl et al., 2010; Grigoratos and Martini, 2015; Hulskotte et al., 2014; Quiroz et al., 2013; Ramírez et al., 2019).

The fifth factor (PC5) is responsible for the accumulation of Zn, W, Co, and Cd in the road dust as a result of tire and road surface abrasion. These PTEs are used as indicators of non-exhaust emissions (Apegyei et al., 2011; Pant and Harrison, 2013; Penkala et al., 2018; Song and Gao, 2011). Zinc and Cd are used in the manufacture of automobile tires (Harrison et al., 2012). Zn is present in tires either in inorganic forms (ZnS and ZnO) or as organic Zn stearate (Alves et al., 2020a; Pant and Harrison, 2013; Wik and Dave, 2009). Moreover Zn borates are used as an additive in the manufacture of polymers necessary for the production of automobile parts, glass, and fiberglass (European Borates Association, 2011). The operation of sources common to Zn, W, Co, and Cd in combination with the supply of certain elements from individual sources is the cause of weak correlation between these PTEs:  $r$  are significant and decrease from 0.42 for the W–Co pair and 0.36 for the Zn–Co pair to 0.26 for the Zn–W pair; correlations between Cd and other PTEs are characterized by low correlation coefficients ( $r < 0.15$ ) and are statistically insignificant (Table S.1 in Supplementary material).

The sixth factor (PC6) explains the formation of Cd, Sn, and Bi anomalies in the road dust. The sources of these elements are wearing metal parts of cars, tires, roadbed, and road markings. Thus, Cd and Bi can be present in high concentrations in tires and road markings; Sn, in brake pads and other details (Adachi and Tainosho, 2004; Budai and Clement, 2018; Grigoratos and Martini, 2015; Harrison et al., 2012; Thorpe and Harrison, 2008). Because of the difficulty of discrimination between various non-exhaust sources, this integral factor is sometimes called “vehicle abrasion” (Fabretti et al., 2009). A large number of these PTEs sources operating with different intensities are indicated by low  $r$  values that are significant only for the Cd–Sn (0.30) pair and insignificant for the Cd–Bi and Sn–Bi pairs (Table S.1 in Supplementary material).

An additional source of elements is related to various industrial emissions. Thus, Cr, Ni, Zn, Mo, Pb, and other PTEs can be emitted by the mechanical engineering and metalworking plants; Sb, Mo, Pb, Cd, Bi, and As are derived from incinerators; and Zn, Pb, Sb, Cd, Bi, and As can accumulate in roadside soils owing to the application

of fertilizers and reclamation mixtures (Adachi and Tainosho, 2004; Christian et al., 2010; Grigoratos and Martini, 2015; Hulskotte et al., 2014).

#### 4.4.2. PM<sub>10</sub> particles

The composition of PM<sub>10</sub> particles in Moscow road dust is more homogeneous compared to road dust in general, which is confirmed by a smaller number of principal components for PTEs concentrations in the PM<sub>10</sub> fraction and a more extensive list of elements, whose accumulation is controlled by them (Fig. 6; Table 2). Four principal factors were determined for PM<sub>10</sub> particles of road dust and accounted for 84.2% of the total variance.

The first principal component (PC1) indicates the entry of elements into the dust with particles of roadside soils polluted by emissions from vehicles and industrial facilities and contributing to the enrichment of PM<sub>10</sub> particles of Moscow road dust with most PTEs of the mixed anthropogenic-terrestrial (Ti, Fe, Mn, Ni, Co, V, Cr) and of the predominantly anthropogenic (Zn, Sn, W, Bi) origins. This factor is clearly pronounced on all types of roads (Fig. S.11 in Supplementary material) and accounts for 64.1% of the variance. The strongest correlative relationships are characteristic of the anthropogenic-terrestrial Ti, Fe, Mn, Co, V, Cr, and Ni ( $r = 0.84$ – $0.97$ ); for PTEs of predominantly anthropogenic origin (Zn, Sn, W, and Bi), correlative relationships between the elements are weaker ( $r = 0.42$ – $0.77$ ) for all element pairs, except for the Sn–Bi pair with  $r = 0.91$ .

The second (PC2) and third (PC3) principal components explain 7.8% and 6.3% of total variance, respectively. They are most probably associated with PTEs derived from vehicles, including their wearing parts, engine oil particles, and motor exhausts, as well as from road surface abrasion resulting in the increased concentrations of Mo, Sb, Cu, Sn, Cr, Ti, and Fe in PM<sub>10</sub> particles (PC2) with strong correlative relationships between the elements ( $r = 0.60$ – $0.94$ ) and of Cu, Pb, Cd, and Zn (PC3) with less strong relationships ( $r = 0.32$ – $0.65$ ). For example, Ti is present in metal parts of automobile brake systems, and Cr in a paint for road marking (Adachi and Tainosho, 2004). Both factors also reflect the impact of industrial enterprises, so they are most clearly revealed not only in the central part of the city, where the main impact is associated with emissions of vehicles but also in its southern, southwestern, southeastern, and eastern industrial parts (Fig. S.11 in Supplementary material).

The fourth principal component (PC4) is only applicable for As; this metalloid weakly accumulates in PM<sub>10</sub> particles (EF = 1.1); it is probable that there are no significant sources of this element in the urban environments of Moscow. This factor accounts for 6.1% of the total variance. The sources of As may be related to incinerators of urban wastes, organic residues, and biomass (Kumar et al., 2015; Niyobuhungiro and Blottnitz, 2013), as well as to industrial enterprises (Bencharif-Madani et al., 2019). Arsenic does not significantly correlate with any of the PTEs in the PM<sub>10</sub> particles of Moscow road dust (Table S.1 in Supplementary material).

Our results is close to the data obtained for other megacities in the world, for example, for China, where reconstructed PM<sub>10</sub> emissions embody 51–64% soil and cement dust, 26–40% tailpipe exhaust, 7–9% tire wear, and 1–3% brake wear (Zhang et al., 2020).

Copper and antimony are often used as indicators of brake pad abrasion. The Cu/Sb ratio in solid atmospheric

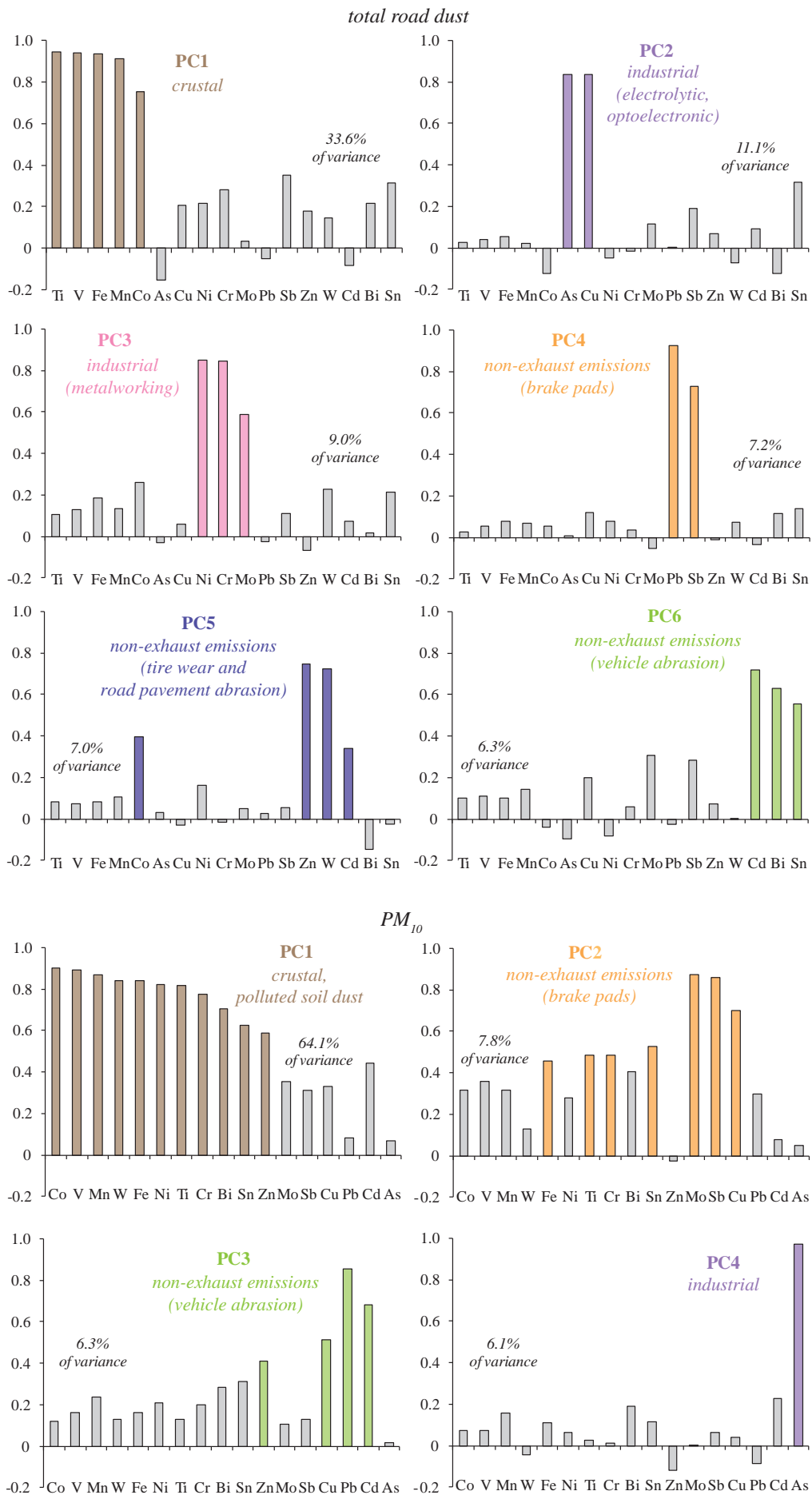


**Fig. 6.** Principal components responsible for the main sources of PTEs in the road dust and the PM<sub>10</sub> fraction of road dust in Moscow (summer 2017); calculated factor loadings are shown on the vertical axes.

particles in tunnels and road dust of different cities varies within 1.3–19 (Adachi and Tainosho, 2004; Alves et al., 2018, 2015; Amato et al., 2011; Bukowiecki et al., 2010; Fabretti et al., 2009; Gietl et al., 2010; Pant and Harrison, 2013; Ramírez et al., 2019; Stechmann and Dannecker, 1990), and within 5–18 in inhalable (PM<sub>10</sub>) fraction of road dust (Alves et al., 2020b, and references in it); this ratio in the upper part of the continental crust is much higher (70) (Rudnick and Gao, 2014). According to the PCA, the main source of Cu in the road dust of Moscow is related to industrial emissions, whereas the main source of Sb is related to motor vehicles. The enrichment of road dust with Cu and Sb from different sources is confirmed by the low correlation between them ( $r = 0.36$ ). In PM<sub>10</sub> particles, both elements mainly come from vehicle emissions, and the correlation between their concentrations is much stronger ( $r = 0.75$ ). The median value of the Cu/Sb ratio in Moscow road dust is 26; thus in the PM<sub>10</sub> fraction it equals 16. In the dust sampled in parks, it increases to 36 (road dust) and 28 (PM<sub>10</sub>). A sharp increase in this ratio in the road dust may indicate the input of Cu from industrial sources and with contaminated soil particles. With a decrease in the road size, the Cu/Sb ratio increases (Fig. S.12 in Supplementary material), which indicates a reduction in the Sb contamination and an increase in the Cu contamination.

Another example of a pair of elements, for which different sources have been identified for road dust and for PM<sub>10</sub> particles, is the Sb–Mo pair. The results of PCA suggest joint supply of these elements to PM<sub>10</sub> fraction with the products of abrasion of brake pads and other metal parts of automobiles. The presence of Mo in Moscow road dust is largely determined by industrial emissions. In Moscow road dust and PM<sub>10</sub> particles on different types of roads the Mo/Sb ratio is  $\leq 1$ ; in dust samples from parks, it increases to 1–2; in the upper part of the continental crust, it is close to 2.0 (Fig. S.12 in Supplementary material). The high indicative value of the Mo/Sb ratio is confirmed by the data for Palermo and Catania (Italy), where the sharpest increase in the Sb content compared to Mo is typical for the fine fractions (PM<sub>2.5</sub>) of atmospheric dust particles (Dongarrà et al., 2009).

In general, the PCA results indicate the presence of several sources of the same element in road dust and its PM<sub>10</sub> fraction in Moscow, which results in several principal components responsible for the same element supply. In turn, each of the PCs can characterize the source of many PTEs in the urban environment. For PM<sub>10</sub> particles, a more uniform composition in comparison with bulk samples of road dust is typical. Owing to their high migration capacity, PM<sub>10</sub> particles can migrate to considerable distances, so that the zones of influence of different sources often overlap one another.

## 5. CONCLUSIONS

For the first time, the contents of PTEs in road dust and its PM<sub>10</sub> fraction were studied in detail in Moscow, the largest megacity in Europe. The average content of PM<sub>10</sub> particles in Moscow road dust is  $14.9 \pm 7.2\%$ ; a tendency for a slight decrease in the share of these parti-

cles with a decrease in the size of the roads is observed: from  $17.7 \pm 6.5\%$  on the Moscow Ring Road to  $13.6 \pm 7.2\%$  on small roads; it increases again up to  $14.3 \pm 6.5\%$  in the yards. In Moscow forest parks, the proportion of PM<sub>10</sub> particles is lower than that in the road dust and averages  $12.9 \pm 5.3\%$ .

The main pollutants of bulk road dust and its PM<sub>10</sub> fraction in Moscow are Sb, Zn, W, Sn, Bi, Cd, Cu, Pb, and Mo. The pollution of Moscow road dust by dangerous Cd, Sb, Pb, and Zn is generally lower than in many other large cities of the world, but the PM<sub>10</sub> particles of Moscow road dust are characterized by a high W content, an increased Zn content, and relatively low contents of As, Sb, Cd, and Pb in comparison with other cities. This is related to a significant proportion of resuspended particles of roadside soils in the road dust: about 34% for bulk samples of road dust and 64% for its PM<sub>10</sub> fraction. Other factors that have the greatest impact on the chemical composition of road dust and PM<sub>10</sub> particles are non-exhaust vehicle emissions (~20% for road dust and ~14% for PM<sub>10</sub> particles) and industrial emissions (~20% and ~6%, respectively).

PM<sub>10</sub> particles are one of the most important carrier of W, Bi, Sb, Zn, and Sn (more than 65% of the total content); Cu (>50%); and Cd, Pb, Mo, Co, and Ni (30–50%) in the road dust of Moscow. The PM<sub>10</sub> fraction is, on average, 1.2–6.4 times more contaminated with PTEs than the total road dust. Owing to the susceptibility of PM<sub>10</sub> particles to resuspension from the roadway, their capacity to remain in the suspended state in the air for a long time and be transported over considerable distances, these particles pose an increased environmental hazard to citizens.

The chemical composition of road dust in general and its PM<sub>10</sub> particles is spatially heterogeneous. They are most heavily contaminated in the central part of the city due to the large number of cars and traffic congestion. Local anomalies of individual elements are observed near industrial zones mainly in the west, south, and southeast of Moscow. With decreasing road size and traffic intensity, the enrichment of road dust and its PM<sub>10</sub> fraction with PTEs decreases. In the yards of residential buildings, which are usually ignored in the ecogeochemical monitoring of urban areas, the level of total enrichment of road dust and its PM<sub>10</sub> fraction is only 1.1–1.5 times lower than on major highways, the Moscow Ring Road, and the Third Ring Road, which is serious danger to people spending a significant part of their lives in residential areas.

The results obtained in this study proved the need of further investigation of the PTEs distribution in different particle-size fractions of road dust. In addition they can be used to simulate the pollutant fluxes in the atmosphere of Moscow metropolitan area, since road dust is an important source of microparticles in the air. The spatial patterns of the PTEs distribution in the road dust and its PM<sub>10</sub> fraction should be taken into account while planning measures to remove dust and clean the road surface, especially for the most polluted parts of the road network of city, as it could assist in significant reduction of public health risks.



## Contamination levels and source apportionment of potentially toxic elements in size fractionated road dust of Moscow \*

### INTRODUCTION

Over the period from 1950 to 2015 the contribution of megacities to the urban population increased from 3 to 13%. The number of people living in such cities rose from 24 to 463 million (United Nations 2018), which created a high load on the urban environment (Baklanov et al. 2016). When assessing the hazard of environmental pollution in megacities and other urban areas by potentially toxic elements (PTEs), much attention is paid to road dust, whose chemical composition is determined by exhaust and non-exhaust traffic emissions and PTE deposition from the atmosphere (Haynes et al. 2020).

The chemical composition of road dust has received much attention in scientific publications (Semerjian et al. 2021; Vlasov et al. 2022a). It is important to assess not only the accumulation of pollutants in bulk samples of road dust but also in its individual particle size fractions, which have different abilities to be blown out from the road surface, the distance of transfer in the atmosphere, and the hazard to public health (Lanzerstorfer 2021). Fine particles enriched with PTEs can be easily resuspended from the road and penetrate deep into the human body, causing adverse health effects (Alves et al. 2020; Guo et al. 2021; Men et al. 2022), for instance, oxidative stress (Veremchuk et al. 2018), cellular mitochondrial activity, and the development of inflammatory responses (Yoon et al. 2018). Therefore, recently, many studies have focused on the distribution of PTEs in the “thoracic” road dust particles (or PM<sub>10</sub> fraction, i.e., particles with a diameter < 10 μm) (Amato et al. 2009; Ramírez et al. 2019; Zhang et al. 2019; Tian et al. 2019; Kasimov et al. 2019a; Levesque et al. 2021; Vanegas et al. 2021; Vlasov et al. 2022b; Jeong and Ra 2022b), as well as in the finer PM<sub>2</sub>, PM<sub>2.5</sub>, PM<sub>4</sub>, and PM<sub>5</sub> fractions (Acosta et al. 2011; Kong et al. 2012; Chen et al. 2012; Padoan et al. 2017; Lanzerstorfer and Logiewa 2019; Miazgowicz et al. 2020; Faisal et al. 2021).

When assessing the urban environment quality, it is essential to study not only fine particles of road dust but also relatively coarse fractions since those particles form the bulk of road dust mass (Adamiec et al. 2016; Bourliva et al. 2017; Seleznev et al. 2021) can be easily and effectively removed from the roadway together with particles > 100 μm during the cleaning (Majumdar et al. 2021). For instance, the PM<sub>50</sub> fraction and the finer particles account for about 5–15% of the road dust in Asian and European cities, while a proportion of coarse particles reaches more than 85% (Bian and Zhu 2009; Zhao et al. 2010; Duong and Lee 2011; Zafra et al. 2011). Considering coarse fractions of road dust can be characterized by a sufficiently high pollution level (Švédová et al. 2020; Jeong and Ra 2022a), especially in summer (Zhu et al. 2021), the collection of these particles by municipal services requires control over their further utilization. The chemical composition of fine fractions is significant-

ly affected by both remote and local sources, while the composition of coarse fractions is strongly influenced by local ones (Logiewa et al. 2020). Moreover, fine particles enter road dust mainly with vehicle emissions (Lingard et al. 2006), while coarse road dust fractions are derived from wind resuspension of roadside soil particles and mechanical abrasion of the road surface, as well as abrasion wear of car parts (Tanner et al. 2008). It is well known that PTE concentrations increase with decreasing particle size (Fujiwara et al. 2011; Jayarathne et al. 2017; Lanzerstorfer 2021). However, source apportionment of PTEs in size-fractionated road dust is performed rarely (Kolakkandi et al. 2020), although considering the chemical composition of different particle size fractions could provide a more detailed assessment of potential sources of pollutants in the entire mass of road dust.

Moscow is the largest megacity in Europe: the number of people living in the urban agglomeration exceeds 17 million (Mosstat 2020). As in many other megacities, the primary source of anthropogenic impact on the environment is motor transport, which supplies about 92% of total emissions (Kul’bachevskii 2020). Among stationary sources, the main contribution is made by enterprises for the production and distribution of electricity, gas, and water (65%) and manufacturing (29%). Industrial zones in Moscow occupy about 17% of its total area, which reduces the connectivity of the road network and leads to longer distances traveled by vehicles and a higher volume of pollutant emissions from motor transport. Off-gasses of industrial enterprises are dust sources too (Bityukova and Saulskaya 2017). A decrease in particle contamination with an increase in their size and a strong accumulation of Zn, Cu, Cd, Cr, Ni, Sn, Pb, S, and P in nanoparticles of road dust was identified (Fedotov et al. 2014; Ermolin et al. 2018). In the road dust of the southeastern part of the city, the concentrations of Pb, Ag, As, Cd, and Hg decreased by a factor of 1.5–3 from 2004 to 2017 due to the closure of many industrial enterprises, but the concentrations of Zn, Cu, Sb, Cr, and Ni increased 1.2–2.5-fold due to an increase in vehicle emissions (Ladonin and Mikhaylova 2020). High correlations were found between the content of PTEs in road dust and dust on exterior glass window surfaces of a high-rise building in Moscow, which confirms the significant role of road dust in urban air pollution (Nikolaeva et al. 2022). A contaminant profile for PM<sub>10</sub> particles was previously obtained in Moscow, and it comprises Sb, Zn, W, Sn, Bi, Cd, Cu, Pb, and Mo (Vlasov et al. 2021). However, comparing contaminant profiles of four particle size fractions of road dust in different parts of Moscow has not been conducted before.

Historically, the eastern Moscow part has been more industrialized than the western one: the intensity of the environmental impact of the eastern industrial zones determines 66% of the total industrial emissions versus 34% for the western part (Bityukova and Saulskaya

2017). The unevenness of industrial and traffic impact in the two parts of the city led to the difference in element concentrations: in the soils of the eastern part, the levels of Cd, Sb, Zn, W, Pb, Ni, Cr, and As were 1.5–2.5 times higher than their concentrations in the western part (Bityukova et al. 2016). Moreover, the number of people living in the Western and Eastern Administrative Okrugs of Moscow is 1.397 and 1.527 million, respectively, and the population densities in these two Okrugs are 7.2 and 9.9 thousand people per square km, respectively (Mossat 2020).

Therefore, the present study is aimed at comparing PTE partitioning in the road dust in the western part of Moscow with a developed motor transport network and the industrial eastern part. To achieve this aim, we (i) analyzed the mass fractions of different particles in the road dust of the western and eastern parts of the city, (ii) assessed PTEs enrichment levels in the dust particle size fractions and bulk samples, and (iii) performed source apportionment of PTEs in the particle size fractions of the road dust using the principal component analysis with multiple linear regression for the first time in Moscow. In the eastern, industrial part of the city, the distribution of PTEs across the  $PM_1$ ,  $PM_{1-10}$ ,  $PM_{10-50}$ , and  $PM_{50-1000}$  fractions of the road dust was analyzed earlier (Kasimov et al. 2020), but the comparison of the PTE content in four fractions in two parts of Moscow was studied for the first time.

## MATERIALS AND METHODS

### Study area and sampling

In the western part of Moscow, there is a more significant amount of major highways with high traffic intensity compared to the eastern part of the city. However, based on the data on transport emission density, the considered city's parts slightly differ: surface areas of roads with < 100 tons of traffic emissions per 1 km<sup>2</sup> account for 20% and 22%, while roads with 100–500 t/km<sup>2</sup> occupy 55% and 56% and roads with > 500 t/km<sup>2</sup> occupy 25% and 22% of the total area of the Western and Eastern Administrative Okrugs of the city, respectively (Bityukova and Mozgunov 2019). The higher average speed on the Moscow Ring Road (MRR) in the east (64 km/h) than in the west (60 km/h) indicates more significant congestion in the western part of the city.

In the western part, combined heat and power plants (CHPs) and boiler houses prevail among stationary emission sources due to de-industrialization and renovation of industrial zones. Two large CHPs (No. 12 and 25), Khru-nichev Space Center, a construction plant, an industrial complex “Ochakovo” (brewery and soft-drink plant), a rubber fabricating plant, the West Port, and a railway depot are located in this part of the city (Bityukova 2021). The industrial zones are also home to car repair businesses (Saulskaya 2018), reinforcing the similarity between industrial and traffic-related pollution. In the eastern part of Moscow, the stationary sources are represented by an incineration plant, thermal power plants, metalworking and mechanical engineering enterprises, chemical and petrochemical enterprises, food industry plants, plants that produce construction materials, pulp and paper, and other materials. After the CHPs, the incineration plant is ranking the largest among the industrial sources in terms of the volume of emissions supplying Fe, Zn, Pb, Hg, Cr, Sb, Ni, Al, Cd, Cu, Mn, Sn, Co, As, V, and Tl (Public Federal Register 2022).

Road dust samples ( $n=21$ ) were collected in the western part of the city in the Krylatskoye, Mozhaysky, and Novo-Peredelkino municipal districts in June 2014 (Fig. 1, Table S1). In the city's eastern part, samples ( $n=16$ ) were collected in the Sokolinaya Gora, Perovo, Ivanovskoye, Novogireyevo, Veshnyaki, Novokosino, and Kosino-Ukhtomsky districts in July 2013. Information on the fieldwork and results of studying the chemical composition of road dust and its particle size fractions in the eastern part of Moscow were described in detail in our previous paper (Kasimov et al. 2020), while in the current study, we focused on differences between two city parts.

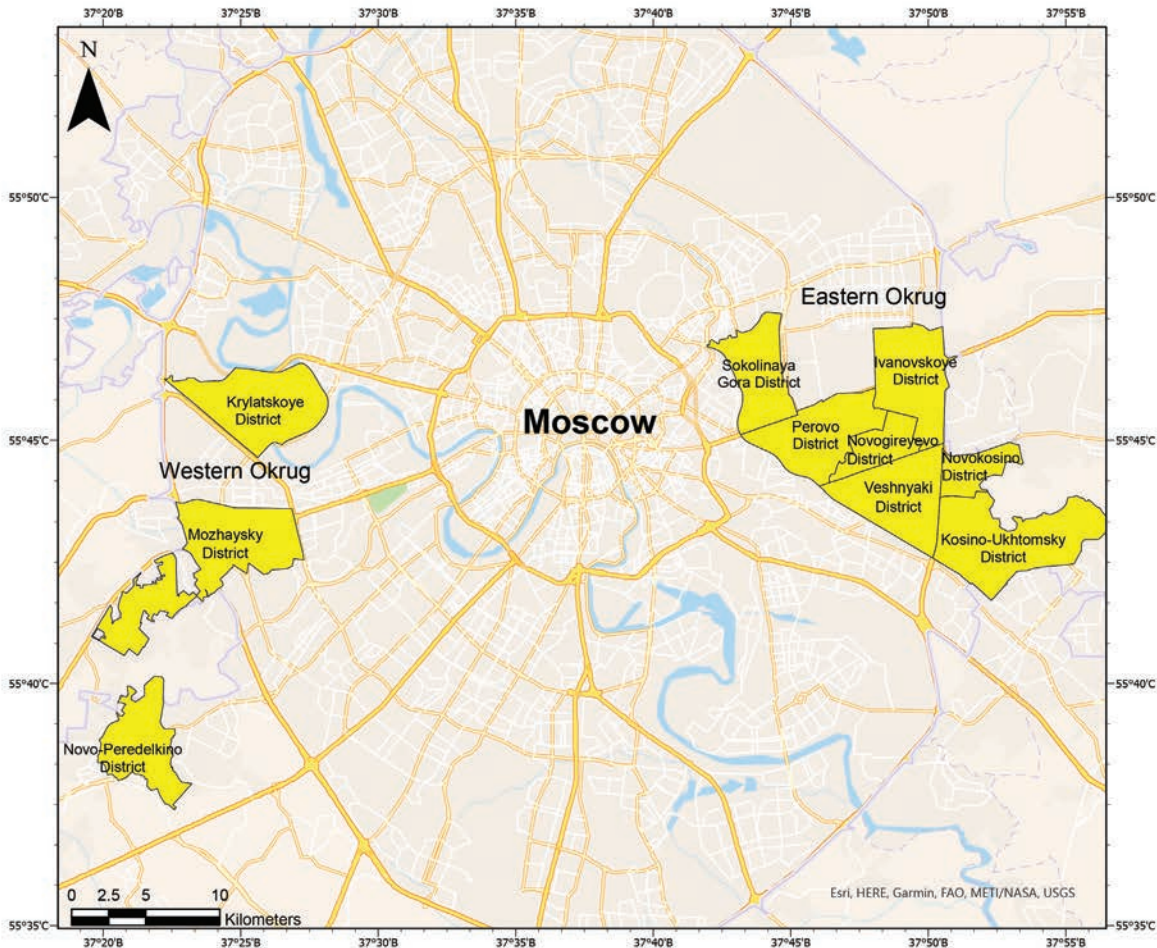
Sampling was carried out during the summer since there is a high probability of road dust resuspension from the roadway surface after a dry antecedent period, and it releases into the atmosphere, which poses a potential risk to public health. Roads were divided into four groups according to the number of lanes in one direction: MRR (5 lanes, 6 samples), large roads (3 lanes, 8 samples), medium roads (2 lanes, 10 samples), and small streets and courtyards (1 lane, 13 samples). In our study, the word “courtyard” refers to an innerblock space in residential areas used for vehicle parking and, therefore, undergoes traffic influence. The sampling was carried out from the road surface with a plastic brush and a scoop after a dry period of at least seven days. Triplicate samples were collected at a distance of 5–10 m and then stored in self-sealed polyethylene bags for transportation to the laboratory.

### Laboratory analyses

All dust samples were dried for 48 h at room temperature. The dried samples were sieved through 1-mm sieves to remove debris particles and gravel, according to N.A. Katschinski particle size classification (Katschinski 1956; Bezuglova et al. 2021). Each sample was divided into two subsamples. In the first – 10 g subsample, particle size distribution was analyzed using laser particle sizer “Analysette 22 MicroTec plus” (Fritsch, Germany) to assess the content of  $PM_1$  (particles with a diameter < 1  $\mu$ m),  $PM_{1-10}$  (1–10  $\mu$ m),  $PM_{10-50}$  (10–50  $\mu$ m), and  $PM_{50-1000}$  (50–1000  $\mu$ m) fractions. The analysis included sodium pyrophosphate pretreatment for dispersing aggregates and was performed at the Environmental and Geochemical Center of M.V. Lomonosov Moscow State University.

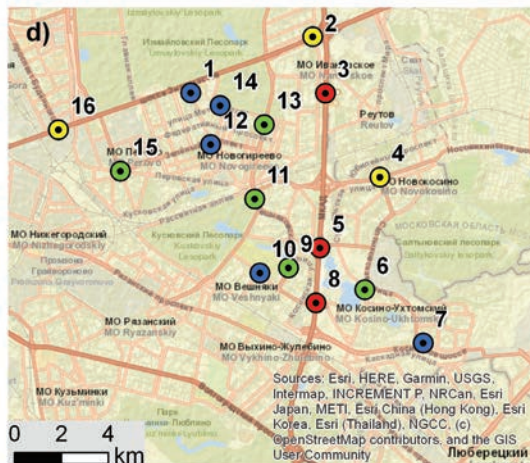
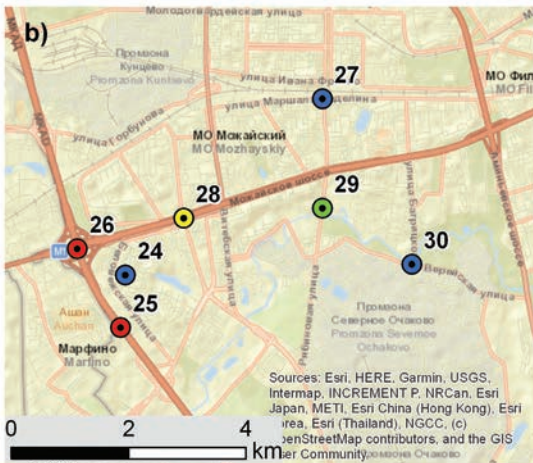
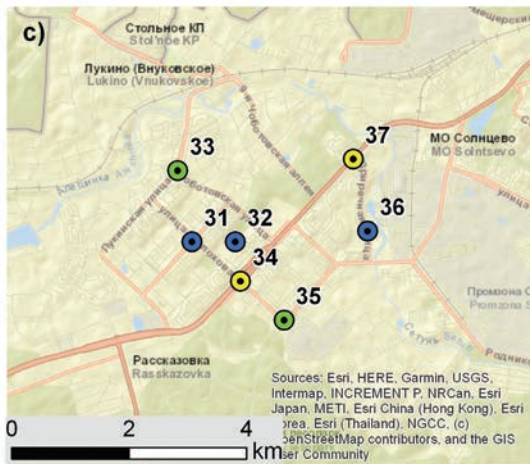
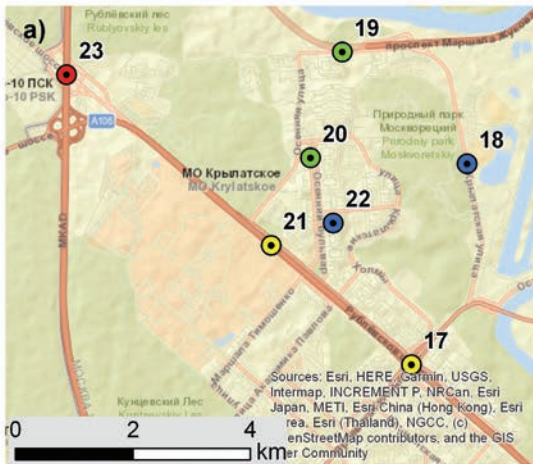
The second – 10 g subsample was fractionated into four size ranges, listed above, using dry sieving and sedimentation. On the first stage, bulk samples were sieved using the 50  $\mu$ m stainless steel sieve to separate  $PM_{50-1000}$  particles that could not pass through the sieve. The particles which passed through the 50  $\mu$ m sieve were fractionated with the sedimentation method based on Stokes' Law, which is described in detail elsewhere (Li et al. 2017). The pretreatment of the subsamples included preliminary liquid dispersing with ~ 1000 mL of deionized water without exposure of the dust samples to ultrasound in order to preserve particle structures, that is, to create conditions similar to the natural ones for wind resuspension. The dust solution was then transferred to a 1000-mL measuring cylinder. After an appropriate settling time, previously calculated with Stokes' Law, the supernatant was siphoned off at a fixed depth below the surface and collected. To ensure that each particle frac-





A

**Fig. 1.** Moscow districts where road dust samples were collected (A) and locations of the road dust sampling in the western and eastern parts of Moscow (B): (a) Krylatskoye District; (b) Mozhaysky District; (c) Novo-Peredelkino District; (d) southern part of the Eastern Administrative Okrug. A description of sampling sites is given in Table S1 (Supplementary Materials)



B

● MRR (Moscow Ring Road) ● Large roads ● Medium roads ● Small Roads



tion was completely separated, the remaining solution was subjected to repeated sedimentation and siphon until the supernatant was clear. The solutions obtained after physical fractionation were filtered through membrane filters with a pore diameter of 0.45  $\mu\text{m}$  (EMD Millipore, USA). After separation, all filters with particle size fractions of road dust were dried at 40  $^{\circ}\text{C}$ , weighed, and stored for further analyses. The particle size fractions of the road dust were analyzed for Al, As, Ba, Be, Bi, Cd, Co, Cr, Cu, Fe, Mn, Mo, Ni, Pb, Rb, Sb, Sn, Sr, Ti, V, W, and Zn concentrations by mass and atomic emission inductively coupled plasma spectrometry (ICP-MS/AES) using an "iCAP Qc" mass spectrometer (Thermo Fisher Scientific, USA) and an "Optima-4300 DV" atomic emission spectrometer (Perkin Elmer, USA). The analysis was performed in the analytical center of N.M. Fedorovsky All-Russian Research Institute of Mineral Raw Materials by certified methods (NSAM No. 499 AES/MS 2015) using blank samples and standard reference materials "GSO 3784–86," "GSO 8671–2005," "GSO 8671–2005" (Vinogradov Institute of Geochemistry SB RAS, Russia), "AGV-2," and "BHVO-2" (U.S. Geological Survey, USA). The laboratory is accredited by the international accreditation system Analytica (AAS.A.00255) and the national accreditation system (RA.RU.21GP11) and meets the requirements of the International Organization for Standardization (ISO Guide 34:2009 and ISO/IEC 17,025:2017). The detection limits (DLs,  $\mu\text{g/g}$ ) were as follows: Al, 12; As, 0.05; Ba, 0.54; Be, 0.001; Bi, 0.016; Cd, 0.003; Co, 0.01; Cr, 8.6; Cu, 0.51; Fe, 36; Mn, 0.19; Mo, 0.076; Ni, 0.84; Pb, 1.2; Rb, 0.08; Sb, 0.022; Sn, 0.07; Sr, 0.08; Ti, 5.8; V, 0.025; W, 0.024; and Zn, 0.93. For all samples, at low concentrations ( $< 5$  DL) of PTE, the relative standard deviation did not exceed 20%; at higher concentrations ( $> 5$  DL) of PTE, the relative standard deviation did not exceed 10%.

### Data processing and PCA/APCS-MLR analysis

Differences between the chemical composition of individual size fraction of the road dust and the content of PTEs in the bulk road dust sample were estimated using the coefficient  $D_x$ :

$$D_x = C_f / C_{tot} \quad (1)$$

where  $C_f$  is the concentration of the element in the  $f$ -th particle size fraction ( $\mu\text{g/g}$  fraction) and  $C_{tot}$  is the concentration of the element in the bulk dust ( $\mu\text{g/g}$  dust).

To determine the contribution of the particle size fractions to the overall contamination of the road dust by a specific pollutant, the grain size fraction loading (GSFL) was calculated for each size fraction  $f$  (Sutherland et al. 2012):

$$GSFL_f = C_f \times P_f / C_{tot} \quad (2)$$

where  $GSFL_f$  is the percentage of the PTE in the  $f$ -th particle size fraction of the road dust (%) and  $P_f$  is the share of the  $f$ -th fraction in the road dust (%).

The contribution of anthropogenic sources to the PTE content in the particle size fractions of the road dust samples was determined by the enrichment factor EF:

$$EF = (C_i / C_{Al}) / (K_i / K_{Al}) \quad (3)$$

where  $C_i$  and  $C_{Al}$  are the concentrations of the considered  $i$ -th element and a reference element in the sample and  $K_i$  and  $K_{Al}$  are the abundances of these elements in the

upper continental crust (Rudnick and Gao 2014). Al was chosen since it is commonly used as a reference element (Vodyanitskii and Vlasov 2021).  $EF < 1$  indicates the natural origin of the element in a sample (predominant supply from the earth's crust, i.e., primarily terrigenous origin),  $EF$  from 1 to 10 indicates the possible contribution from anthropogenic sources, and at  $EF \geq 10$ , PTEs have a clear anthropogenic origin (Cheng et al. 2018). For an integral assessment of the intensity of PTEs accumulation, the total enrichment factor TEF was calculated:

$$TEF = \sum EF - (n - 1) \quad (4)$$

where  $n$  is the number of the summable individual elements with  $EF > 1$ .  $TEF$  shows the levels of accumulation of chemical elements due to anthropogenic impact:  $< 32$ , low; 32–64, moderate; 64–128, high; 128–256, very high;  $> 256$ , extremely high (Vlasov et al. 2021). The  $TEF$  levels were chosen based on the integral index of pollution of the dust accumulated in snow cover, which is used in Russia to assess air pollution (Saet et al. 1990).

Statistical data processing was carried out in the Statistica 10 package. Application of the principal component analysis (PCA) made it possible to reduce the original dimension of data required for interpretation by transforming a set of multivariate data into several linear combinations and allowing the identification of the sources that control the chemical composition of the studied particle size fractions (Aminiyan et al. 2018). Four datasets were used in the PCA (each dataset for a separate particle size fraction of the road dust). They included data on concentrations of 22 PTEs in 37 samples (16 samples from the eastern and 21 samples from the western parts of Moscow). Prior to the analysis, Z-normalization was applied:

$$Z_{ik} = (C_{ik} - \bar{C}_i) / \sigma_i \quad (5)$$

where  $C_{ik}$  is the concentration of the  $i$ -th chemical element in the sample  $k$ ,  $\bar{C}_i$  is the average concentration of the  $i$ -th element for all samples, and  $\sigma_i$  is the standard deviation of the  $i$ -th element.

Kaiser–Meyer–Olkin (KMO) and Bartlett's sphericity tests were performed to examine the suitability of the data for PCA. KMO is a measure of sampling adequacy indicating the common variance proportion (Varol 2011). In this study, KMO is  $> 0.60$  for each dataset (0.65, 0.73, 0.66, and 0.63 for  $PM_{10}$ ,  $PM_{1-10}$ ,  $PM_{10-50}$ , and  $PM_{50-1000}$  of road dust, respectively), indicating that PCA may be useful. Bartlett's test of sphericity indicates whether a correlation matrix is an identity matrix and variables are unrelated (Varol 2011). The significance level of  $< 0.001$  for each dataset in this study indicates significant relationships among the variables and the suitability of using PCA.

The Varimax rotation method was used to simplify the interpretation of the factors and reduce the number of PTEs with high factor loadings (Guo et al. 2004). Only the principal components (PCs) that explained more than 5% of the total variance of the data set and with eigenvalues  $> 1$  (Kaiser's criteria) were used as factors. To assess the contribution of sources to the PTE concentrations, the PCA method was used with the calculation of Absolute Principal Component Scores (APCS) and the further application of Multiple Linear Regressions (MLR). PCA/APCS-MLR is a valuable technique to identify independent factors using the eigenvector decomposition of a matrix of pairwise correlations among compound concentrations (Thurston et al. 2011; Prakash et al. 2018).

APCS allow apportioning the total mass of each PTE among the components obtained by the PCA, that is, among the various sources. A detailed methodology for calculating APCS and using PCA/APCS-MLR can be found elsewhere (Thurston and Spengler 1985; Shi and Lu 2018; Liang et al. 2019; Chen et al. 2021). The main steps in this approach are summarized below.

As the factor scores obtained from PCA are normalized, with mean zero and standard deviation equal to unity, the true zero for each factor score was calculated by introducing an artificial sample with concentrations equal to zero for all variables. For this additional sample, normalized values for PTE concentrations will be as follows:

$$(Z_0)_i = (0 - \bar{C}_i) / \sigma_i = -\bar{C}_i / \sigma_i \quad (6)$$

The APCS for each component are then estimated by subtracting the factor scores for this artificial sample from the factor scores of each one of the true samples.

Regressing the PTE concentration data on APCS gives estimates of the coefficients, which convert the APCS into pollutant source mass contributions from each source for each sample (Thurston and Spengler 1985). The source contributions to  $C_i$  can be calculated by using MLR:

$$C_i = \xi_{0i} + \sum (APCS_p \times \xi_{pi}), p = 1, 2, \dots, n \quad (7)$$

where  $\xi_{0i}$  is the intercept of multiple regression for the  $i$ -th element,  $\xi_{pi}$  is the coefficient of multiple regression of the source  $p$  for pollutant  $i$ , and  $APCS_p$  is the scaled value of the rotated factor  $p$  for the considered sample.  $APCS_p \times \xi_{pi}$  represents the contribution of source  $p$  to  $C_i$ . The mean of the product  $APCS_p \times \xi_{pi}$  on all samples represents the average contribution of the sources (Ma et al. 2021). APCS uncertainty (UNC, %) was calculated as follows:

$$UNC = (C_{meas} - C_{model}) / C_{meas} \times 100\% \quad (8)$$

where  $C_{meas}$  is the measured concentration of PTE and  $C_{model}$  is the predicted concentration of PTE based on PCA/APCS-MLR results (Song et al. 2006).

## RESULTS AND DISCUSSION

### Mass fractions of particles in the road dust

In the western and eastern parts of Moscow, the average mass fractions of various particle sizes in the road dust differ significantly (Fig. 2). On the roads of the western part of Moscow, the dust had a sandy texture (Katschinski 1956) with the  $PM_{10}$  share of about 7.5%. In the eastern part, the road dust consisted mainly of sandy loam and showed a higher amount (about 14%) of the  $PM_{10}$  fraction. This can be explained by the fact that  $PM_{10}$  emissions are higher at a constantly low vehicle speed (Tang et al. 2019). In the eastern part, where the average traffic speed is lower, the proportions of  $PM_{10}$  and  $PM_{1-10}$  were higher than in the western part.

In the western part of Moscow, the share of  $PM_{10}$  was higher on roads with more traffic: it increased from small and medium roads to large roads and the MRR. This was probably due to the increased abrasion of roadways from road traffic and more intense wear of tires since it is known that up to 36% of the particles' masses originated due to the abrasion usually have a size of 20–50  $\mu m$  (Klöckner et al. 2021). In addition, major roads usually have high curbs and dust collectors to prevent the fine particles from their spread outside the road. In the eastern part of Moscow, an increase in traffic intensity was accompanied by a rise in  $PM_{50-1000}$  share, while the amount of other fractions decreased due to the blowing of particles from the roadway. The latter was confirmed by a higher share of  $PM_{1-10}$  and  $PM_{10-50}$  in the roadside soils compared to the dust: in the soils, the  $PM_{1-10}$  on average accounted for about 16%, the amount of this fraction in the road dust was 13%;  $PM_{10-50}$  in the soils and road dust accounted for 35% and 16%, respectively. The share of  $PM_{50-1000}$  was lower in the soils compared to the dust—45% versus 69% (Kasimov et al. 2016). In the road dust of small roads and in-yard areas, a larger proportion of  $PM_{50}$  can be explained by the widespread occurrence of closed courtyards, which act as a kind of “sink” for polluted atmospheric air coming from highways and numerous industrial sources located in the east of Moscow (Kosheleva et al. 2018). In courtyards, the

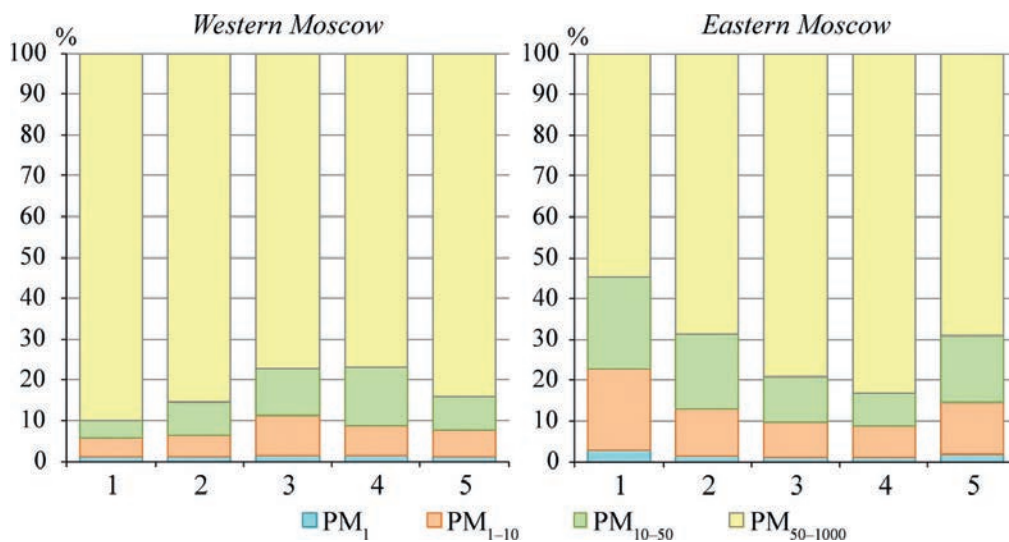


**Fig. 2.** Mass fractions of different particle sizes in the road dust on roads of various types in Moscow's western traffic and eastern industrial parts. Roads: 1—small roads and courtyards, 2—medium, 3—large, 4—MRR, and 5—average for all roads

atmospheric delivery of fine particles and mechanical cleaning, which removes mainly coarse particles, led to a gradual accumulation of fine fractions.

### PTEs content in the particle size fractions of the road dust

The total content of PTEs in the bulk samples of the road dust and their concentrations in particle size fractions in Moscow's western and eastern parts are given in Table 1. In the road dust of the western part of Moscow, the average total concentrations of Cu, W, and Pb were 10–30% higher compared to those in the eastern part, and Zn, Mo, Cd, Sn, Sb, and Bi were higher in the eastern part. High concentrations of Cu, Pb (Pant, Harrison 2013), and W (Vlasov et al. 2022b) in the western part of Moscow are caused by transport emissions, while Zn, Mo, Cd, Sn, Sb, and Bi in the eastern part of the city can be found in industrial emissions of incineration plant, thermal power plants, metalworking and mechanical engineering enterprises, chemistry and petrochemical enterprises, food industry plants, plants that produce construction materials, pulp and paper, and other materials (Kasimov et al. 2020). The differences in the concentration of PTEs in the individual fractions and the bulk road dust samples, in general, were reflected in the values of the  $D_x$  index (Eq. 1; Fig. 3).  $D_x$  for  $PM_1$  was significantly higher than for coarser fractions in both parts of Moscow. At the same time, the maximum concentrations of the PTEs coming from vehicles were confined to  $PM_1$  (Cr, Cu, Zn, Cd, and Sn) and  $PM_{1-10}$  (Be, Co, Ni, As, Rb, Sr, Sb, Ba, W, and Bi) in both parts of the city. However, as the particle size increases, the concentrations of these PTEs decrease. The coarser  $PM_{10-50}$  fraction, which mainly originates from soil minerals and pavement fragments, had high Ti contents, which decreased with decreasing particle size. Fe, Mn, and V had a similar distribution within particle size fractions: their maximum concentration was found in  $PM_{1-10}$ , and a minimum was registered in the coarsest  $PM_{50-1000}$  fraction. A bimodal distribution was typical of Mo and Pb: their high concentrations were found in  $PM_1$  and  $PM_{10-50}$ . In general, in the eastern part of Moscow, the concentrations of most PTEs in  $PM_1$  particles on average 3–5 times exceed those in  $PM_{50-1000}$ , and in the western part, the exceedance equals to 2–4 times.

PTE concentrations increased with a decrease in the size of the road dust particles due to an increase in their specific surface area, growth of sorption capacity and cation exchange capacity, changes in mineralogical composition accompanied by an increase in the percentage amount of clay minerals, and related decrease in quartz abundance (Bian and Zhu 2009; Duong and Lee 2011; Gunawardana et al. 2014). In addition, a higher amount of organic matter content (Kasimov et al. 2019b) can contribute to the accumulation of PTEs as fine particles contain more microbial humic-like substances, and larger ones are enriched in fulvic acids (Aryal et al. 2015). Chemical analyses of soils in the Central part of the East European Plain also demonstrate that the majority of elements (Al, Cd, Zn, V, Tl, Pb, Rb, Ti, Th, U, Li, and Cs) accumulate more intensively in finer fractions and show a maximum of the element concentration in  $PM_1$ . Furthermore, Mn, Co, Mo, and Fe showed accumulation both in coarser fractions  $PM_{250-1000}$  and  $PM_{50-250}$  and in the finest fraction  $PM_1$  (Meinander et al. 2022).

In coarse particles  $PM_{50-1000}$ , the differences in the content of most PTEs in the western and eastern parts of Moscow do not exceed 100% (Fig. 4). In finer particles, these differences are more distinct, which probably result from unequal traffic loading, different structure of the vehicle fleet, and an increased level of anthropogenic impact related to industrial facilities in the eastern part of the city. In summary, in the eastern part of the city, the concentrations of Sb, Mo, As, and Ni in  $PM_1$  and Sb, Mo in  $PM_{1-10}$  were more than twice the values in the western part of Moscow. These elements may indicate emissions from mechanical engineering and metalworking enterprises, chemical and petrochemical industries, the energy sector, incineration plants, and construction materials manufactures (Duan and Tan 2013; Li et al. 2020; Wong et al. 2021). The differences in the element concentrations in the bulk road dust and its particle size fractions registered in the eastern and western parts of the city can also arise from different cleaning techniques: frequent wet cleaning of the roadway in the west of Moscow and mechanical cleaning in the east. Furthermore, long-term exposure to dust on the roadway causes a stronger impact of different pollution sources, leading to an increase of PTEs concentrations in all particle sizes and, therefore, the reduction of disparities between particle size fractions (Zafra et al. 2011).

In summary,  $PM_1$  and  $PM_{1-10}$  of the road dust in the east of the city were characterized by increased levels of Sb, Mo, As, Ni, Bi, Cd, and Sn, while in the west, these fractions had higher concentrations of W, Cr, Cu, Ti, Sr, and Pb. The different industrial impact and traffic load in the city parts can explain the dissimilarity. Among the listed PTEs, the concentrations of Sb, Mo, Ni, and Cd in all fractions in the east exceeded those in the west, probably due to the higher impact associated with the industrial sector and especially the incineration plant (Public Federal Register 2022) and metalworking industry (Wei et al. 2021) that may emit those PTEs. The difference between the contents of other PTEs in the particle size fractions was much less pronounced.

### Partitioning of PTEs in the road dust

Figure 5 shows the distribution of PTEs within the particle size fractions of the road dust in the western and eastern parts of Moscow evaluated by the GSFL index (Eq. 2). Fractional composition (partitioning) of PTEs in the road dust for the roads of different sizes in the western and eastern parts of Moscow. The black line separates the proportion of fine particles ( $PM_1$  and  $PM_{1-10}$ ) from coarse ones ( $PM_{10-50}$  and  $PM_{50-1000}$ ).

The fractional composition of PTEs in the road dust was different for roads of various sizes. In the western part of the city, for most PTEs, the highest contribution of  $PM_1$  and  $PM_{1-10}$  was found on the large roads. With a reduction in traffic load, the contribution of these particle size fractions decreased due to a higher input from  $PM_{50-1000}$ . The lower contribution from fine particles was also observed on the MRR due to the higher share of PTEs associated with the  $PM_{10-50}$  fraction. In the eastern part of Moscow, the contribution of  $PM_1$  and  $PM_{1-10}$  declined with increasing traffic load, reaching the maximum for most PTEs on small roads and in courtyards. The main difference between the western and eastern parts of Moscow is that the eastern industrial part of the city was characterized by a recession in the contribution



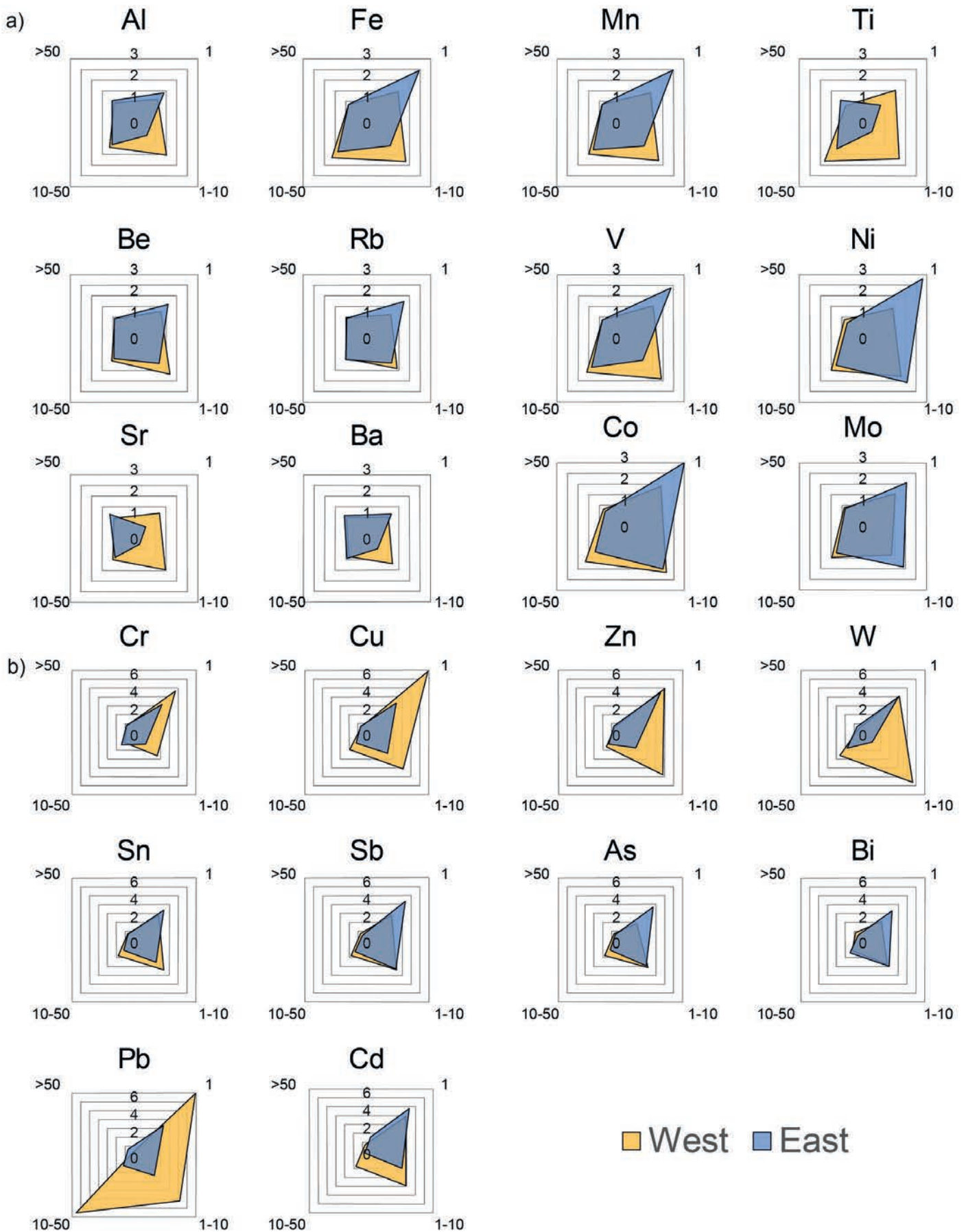


**Fig. 3.** The ratio of PTE concentrations in the fractions  $PM_1$ ,  $PM_{1-10}$ ,  $PM_{10-50}$ , and  $PM_{50-1000}$  (marked as > 50) to the total PTE content ( $D_x$  index) in the bulk road dust in the western and eastern parts of Moscow: (a) the PTEs with  $D_x < 3$ ; (b) the PTEs with  $D_x$  up to 7. The numbers in the corners of the squares indicate the size of PM in  $\mu m$

**Table 1.** PTE concentrations in the particle size fractions of the road dust in the western (traffic) and eastern (industrial) parts of Moscow and the PTE abundances in the upper continental crust (K),  $\mu\text{g/g}$ , for Al, Fe, and Ti— $\text{mg/g}$ . Minimum and maximum values are given in brackets. The abundances of PTEs in the upper continental crust are given according to (Rudnick and Gao 2014)

PTE	Western (traffic) part of Moscow, $\mu\text{g/g}$				Eastern (industrial) part of Moscow, $\mu\text{g/g}^a$				Bulk dust	K, $\mu\text{g/g}$	
	PM <sub>1</sub>	PM <sub>1-10</sub>	PM <sub>10-50</sub>	PM <sub>50-1000</sub>	Bulk dust	PM <sub>1</sub>	PM <sub>1-10</sub>	PM <sub>10-50</sub>			PM <sub>50-1000</sub>
Be	1.2 (0.17–2.0)	1.6 (0.52–2.5)	1.0 (0.59–1.3)	0.88 (0.53–1.8)	0.95 (0.68–1.7)	1.2 (0.98–1.6)	0.87 (0.60–1.1)	0.71 (0.35–1.4)	0.70 (0.38–1.4)	0.75 (0.42–1.3)	2.1
Al	35 (6.0–54)	49 (16–72)	37 (20–49)	30 (17–59)	32 (22–57)	38 (30–48)	16 (3.1–28)	28 (10–53)	28 (15–46)	27 (16–41)	81
Ti	4.1 (0.27–8.7)	4.6 (2.0–7.1)	4.9 (3.1–9.6)	2.2 (1.1–5.1)	2.7 (1.3–5.6)	1.4 (1.0–1.8)	0.71 (0.15–1.4)	2.1 (0.87–4.3)	1.8 (0.43–3.2)	1.7 (0.56–2.8)	3.8
V	88 (13–132)	109 (36–150)	91 (61–196)	49 (25–122)	57 (29–126)	131 (117–141)	57 (12–106)	75 (42–117)	48 (13–84)	55 (23–79)	97
Cr	243 (121–423)	136 (44–251)	58 (35–85)	41 (23–82)	52 (27–83)	158 (126–206)	65 (13–128)	70 (40–143)	40 (22–63)	50 (32–74)	92
Mn	559 (86–755)	708 (244–839)	592 (410–915)	347 (170–612)	397 (238–656)	838 (577–1261)	373 (90–753)	433 (265–650)	295 (116–493)	339 (176–473)	774
Fe	42 (6.9–63)	53 (21–74)	48 (26–114)	25 (12–47)	29 (17–51)	54 (42–65)	24 (4.5–46)	30 (16–54)	19 (6.8–32)	22 (11–31)	39
Co	15 (2.7–26)	17 (4.6–25)	13 (7.5–25)	6.4 (2.9–14)	7.9 (4.4–16)	24 (20–30)	16 (14–20)	9.5 (4.8–15)	5.8 (2.3–9.2)	8.0 (3.8–12)	17
Ni	32 (19–53)	40 (5.0–59)	28 (18–51)	17 (9.2–34)	20 (12–35)	73 (61–117)	54 (42–79)	33 (17–57)	19 (7.3–35)	26 (13–46)	47
Cu	674 (144–2139)	403 (44–1322)	192 (54–898)	60 (19–178)	98 (30–257)	308 (194–567)	218 (141–372)	113 (53–269)	65 (26–125)	93 (40–181)	28
Zn	1076 (115–2505)	1045 (282–2351)	357 (174–654)	127 (52–226)	218 (99–385)	1180 (769–4167)	455 (81–1350)	350 (177–1036)	190 (119–619)	262 (160–705)	67
As	4.2 (0.85–21)	7.2 (0.89–32)	4.1 (1.9–15)	1.6 (0.39–5.0)	2.3 (0.66–9.0)	10 (6.5–19)	7.9 (4.9–12)	3.2 (1.7–6.5)	1.6 (0.41–3.2)	2.7 (1.4–4.2)	4.8
Rb	46 (9.1–62)	58 (19–83)	39 (22–57)	40 (25–81)	41 (30–78)	68 (57–79)	45 (33–55)	39 (14–64)	37 (24–56)	39 (26–54)	84
Sr	206 (31–501)	252 (88–561)	170 (111–238)	164 (107–348)	172 (121–339)	73 (56–131)	35 (6.4–81)	118 (43–209)	153 (90–301)	133 (87–251)	320
Mo	2.6 (1.2–4.2)	2.3 (0.51–6.1)	2.5 (1.2–4.2)	1.5 (0.66–2.9)	1.7 (0.87–2.9)	7.2 (5.2–9.9)	6.7 (4.0–14)	4.4 (2.5–14)	2.9 (1.2–7.5)	3.5 (1.7–6.4)	1.1
Cd	1.6 (0.83–4.0)	1.6 (0.38–3.6)	0.72 (0.46–1.5)	0.28 (0.12–0.56)	0.41 (0.25–0.74)	2.3 (1.8–3.9)	1.8 (1.3–2.3)	0.76 (0.41–1.4)	0.35 (0.11–0.83)	0.61 (0.27–1.5)	0.09
Sn	27 (8.8–103)	23 (4.6–49)	12 (7.4–19)	4.5 (2.1–13)	6.7 (3.1–14)	32 (25–45)	24 (16–34)	11 (6.3–21)	6.3 (3.7–17)	9.5 (5.4–15)	2.1
Sb	6.7 (1.1–23)	8.1 (1.6–17)	4.3 (1.6–12)	1.7 (0.83–4.2)	2.4 (1.0–5.6)	20 (14–26)	15 (6.8–25)	6.1 (2.9–14)	2.3 (1.3–5.5)	4.6 (2.7–6.8)	0.4

Table 1 (continued)

PTE	Western (traffic) part of Moscow, $\mu\text{g/g}$					Eastern (industrial) part of Moscow, $\mu\text{g/g}$ <sup>a</sup>					K, $\mu\text{g/g}$	
	PM <sub>1</sub>	PM <sub>1-10</sub>	PM <sub>10-50</sub>	PM <sub>50-1000</sub>	Bulk dust	PM <sub>1</sub>	PM <sub>1-10</sub>	PM <sub>10-50</sub>	PM <sub>50-1000</sub>	Bulk dust		
Ba	353 (85–489)	417 (153–530)	295 (147–385)	343 (248–590)	348 (265–572)	350 (261–476)	152 (28–310)	152 (28–310)	286 (118–507)	328 (189–501)	305 (198–446)	628
W	30 (2.0–80)	41 (7.9–65)	19 (6.1–77)	3.2 (0.80–17)	7.3 (2.6–26)	21 (2.8–54)	5.7 (0.49–17)	5.7 (0.49–17)	9.4 (0.19–27)	3.4 (0.64–7.3)	5.3 (1.0–10)	1.9
Pb	861 (99–4129)	642 (24–2637)	814 (14–7186)	25 (16–36)	124 (29–734)	176 (112–576)	123 (65–412)	123 (65–412)	64 (32–146)	35 (10–83)	53 (20–130)	17
Bi	1.2 (0.22–4.9)	1.6 (0.39–5.4)	0.70 (0.31–2.1)	0.47 (0.053–6.0)	0.58 (0.13–5.4)	2.0 (1.6–2.8)	1.8 (1.4–2.8)	1.8 (1.4–2.8)	0.88 (0.51–1.8)	0.31 (0.069–0.90)	0.61 (0.21–1.0)	0.16

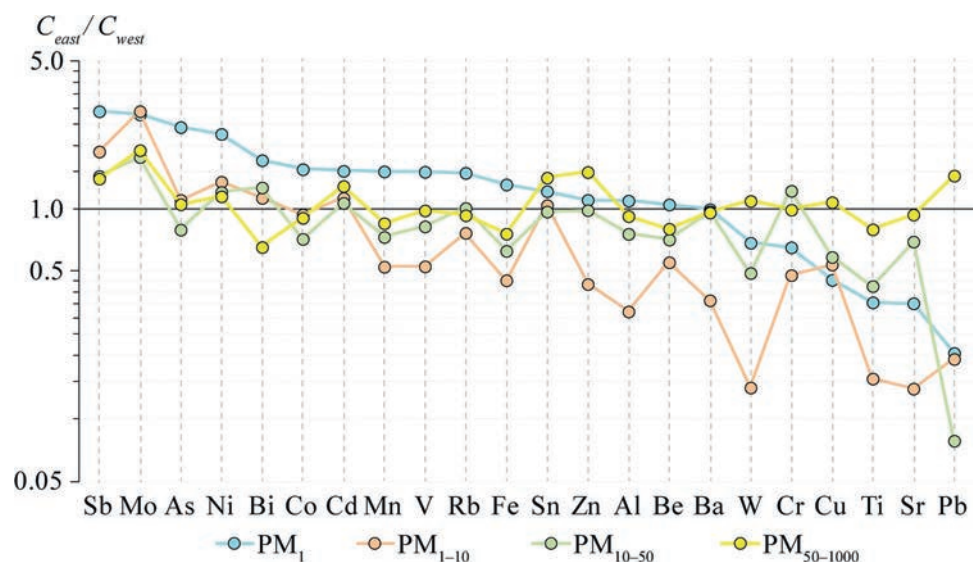


Fig. 4. The ratio of PTE concentrations in the road dust particles of the eastern ( $C_{east}$ ) part to the PTE concentrations in the western ( $C_{west}$ ) part of Moscow

of PM<sub>1</sub> and PM<sub>1-10</sub> with a rise in traffic. An opposite relationship was revealed for the west, probably due to differences in the traffic and industrial impacts and kind of road cleaning. In the eastern part of Moscow, a change in the contribution of PM<sub>1</sub> and PM<sub>1-10</sub> was mainly due to an increase in the loading of the PM<sub>50-1000</sub> fraction, and in the western part, it was caused by a higher contribution of PM<sub>10-50</sub>. At the same time, the PM<sub>1</sub> fraction in both parts of the city on all types of roads usually accounted for no more than 10% of the total PTE content, and the most significant contribution of PM<sub>1</sub> was found for Cu, Zn, Cd, Sb, Sn, W, Pb, Bi, and Cr.

W, Pb, Cd, Sn, Sb, Cu, Zn, Cr, and As compared to other PTEs are characterized by a high contribution of PM<sub>1</sub> and PM<sub>1-10</sub> fractions to the total concentrations of each PTE on all types of roads in both parts of the city. Bi was added to this list on the MRR, large and small roads. In the eastern part, all types of roads showed high peaks of Cu, Zn, As, W, Pb, and Sb. The list of the elements beside W, Pb, Cd, Sn, Sb, Cu, Zn, As, Cr, and Bi also included Mo, Ni, Co (on all types of roads), and Mn, Fe, V, Be (on small, medium and large roads) probably due to the presence of sources not typical for the western part of Moscow and associated with emissions from industrial enterprises.

#### Enrichment factors of chemical elements in size-fractionated road dust

Both parts of Moscow showed the enrichment of PM<sub>1</sub>, PM<sub>1-10</sub>, and PM<sub>10-50</sub> with Sb, Cd, Zn, Sn, Bi, W, Cu, and Pb associated with the delivery of the elements from anthropogenic sources ( $EF > 10$ ); Mo was added to this list in the eastern part of Moscow (Fig. 6). This is confirmed by data on the geochemical specialization of atmospheric aerosols in Moscow (Gubanova et al. 2021). Relatively high EFs, which can be explained by the impact of anthropogenic and natural (mostly terrigenous) sources, were revealed in the same particle size fractions for As, Cr, Ni, Co, Fe, Rb, Be, and Ba in both parts of Moscow, as well as for Mo, Ti, and Sr in the western part. Due to the low sorption capacity of the coarse particles,



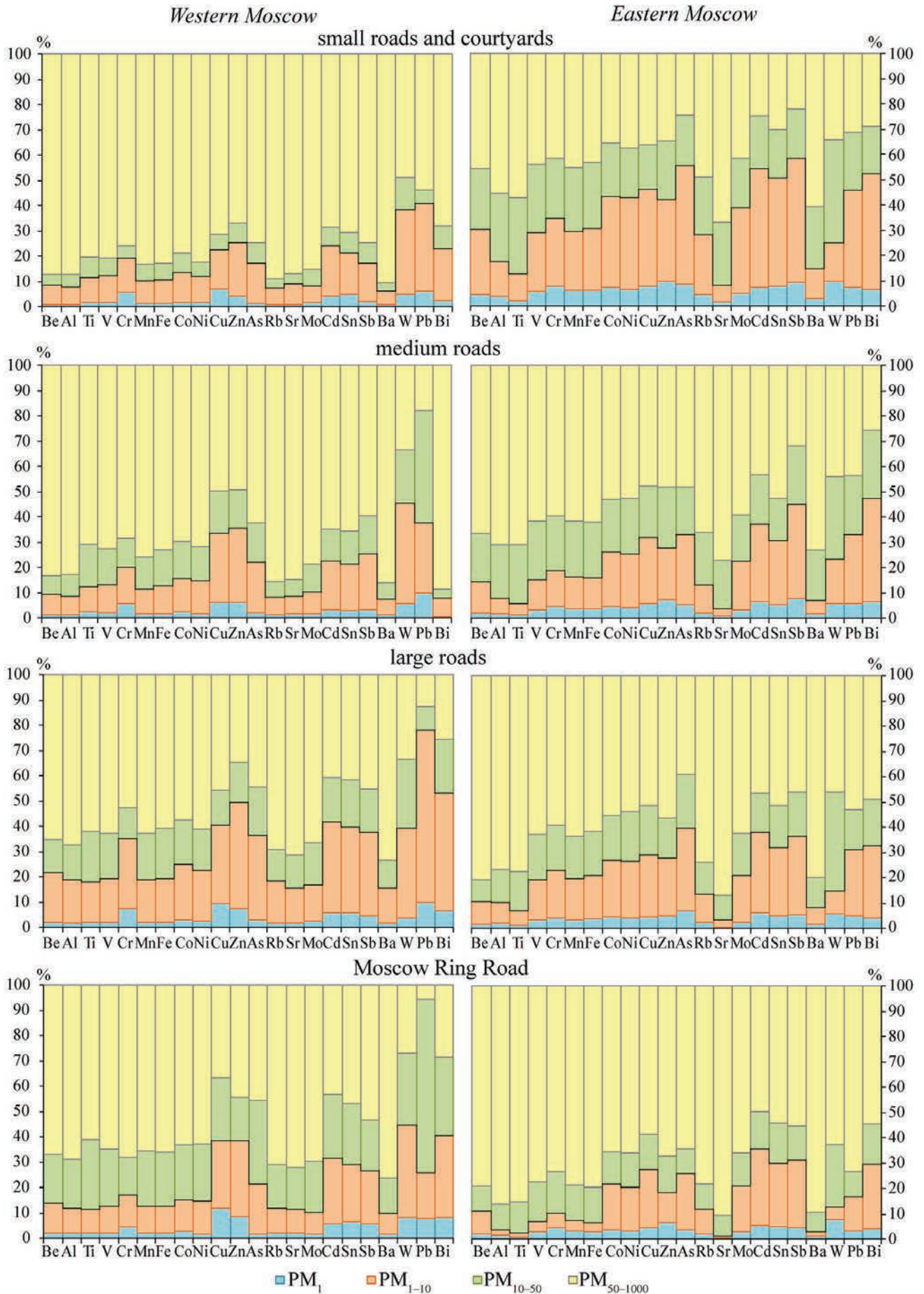


**Figure 5.** Fractional composition (partitioning) of PTEs in the road dust for the roads of different sizes in the western and eastern parts of Moscow. The black line separates the proportion of fine particles ( $PM_1$  and  $PM_{1-10}$ ) from coarse ones ( $PM_{10-50}$  and  $PM_{50-1000}$ )

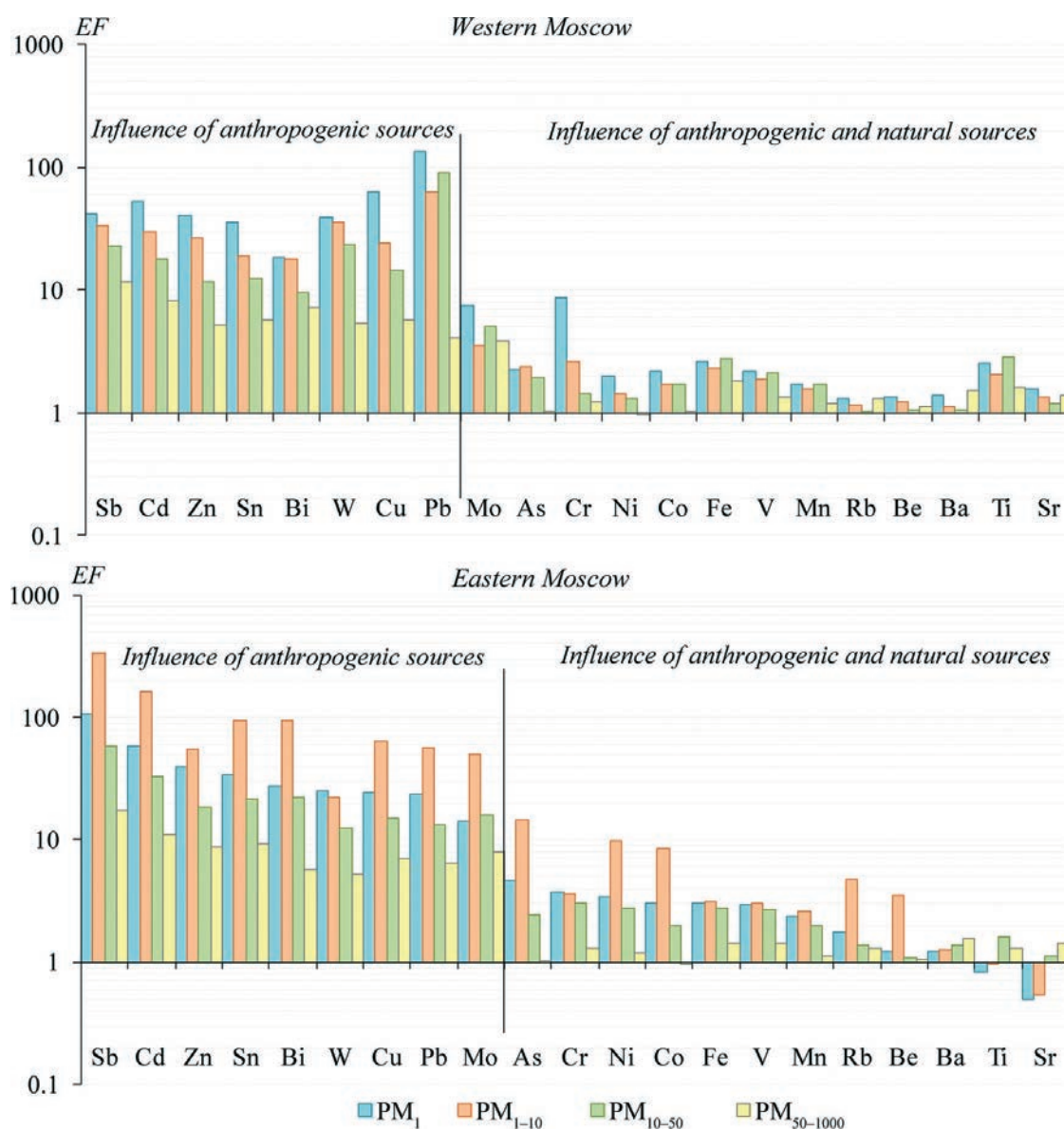


**Figure 6.** Enrichment of particle size fractions of the road dust with PTEs in the western (traffic) and eastern (industrial) parts of Moscow

the  $PM_{50-1000}$  fraction revealed lesser enrichment with most PTEs than the finer fractions. Eastern Moscow was characterized by elevated levels of the EF for Sb, Cd, Zn, Sn, Bi, Mo, As, Ni, Co, Rb, and Be, which indicates a significant contribution of industrial sources to road dust pollution. In the western part of the city, the EF levels for Pb, Cu, W, and Ti were higher than in the eastern part due to the stronger impact of traffic.

The main difference between the two parts of Moscow is that in the western part, the EF maxima of anthropogenic and natural-anthropogenic PTEs occur in the  $PM_1$  fraction, whereas in the eastern part, the EF maxima are associated with  $PM_{1-10}$ . This is because in the western part, the coefficient  $D_x$  of the reference element Al in  $PM_{1-10}$  particles is maximal, and in the east, on the contrary, it is minimal (Fig. 3). These values can be explained by the differences in the mineralogical composition of  $PM_1$ ,  $PM_{1-10}$ , and coarser fractions, as well as the unequal input of  $PM_1$  and  $PM_{1-10}$  during abrasion of the road surface and wear of vehicle tires. A large proportion of  $PM_{10}$  formed during abrasion of the road surface consists mainly of aluminosilicates, including about 40% of

plagioclase  $(Na,Ca)Al(Si,Al)Si_2O_8$  and 35–40% of hornblende  $Ca_2(Mg,Fe)_4Al(Si_7Al)O_{22}(OH,F)_2$  (Tervahattu et al. 2006). The ultrafine road dust particles contain a high proportion of Fe-rich carbonaceous particles with high contents of Al, Ca, S, and Si, supplied by brake wear, with fuel additives and engine oil (Kwak et al. 2014), as well as magnetite particles produced during abrasion of brake pads (Kukutschová et al. 2011; Ramírez et al. 2020).

The influence of the traffic intensity on the chemical composition of the road dust particle size fractions and the effect of the traffic flow structure were confirmed by the data on the EFs calculated for different road types (Table S2, Table S3). In the western part of the city, the EF values for most PTEs reached their maximum on the MRR and large roads. We observed a decrease in EF values on the medium and small roads and courtyards. Compared to  $PM_{10-50}$  and  $PM_{50-1000}$ , the EF values of PTEs in the fine fractions ( $PM_1$  and  $PM_{1-10}$ ) suggested more pronounced differences between various roads. The EF values of Be, Rb, Ba, Sr, Ni, As, V, Co, and Mn in the road dust were practically the same, regardless of road type, which in-

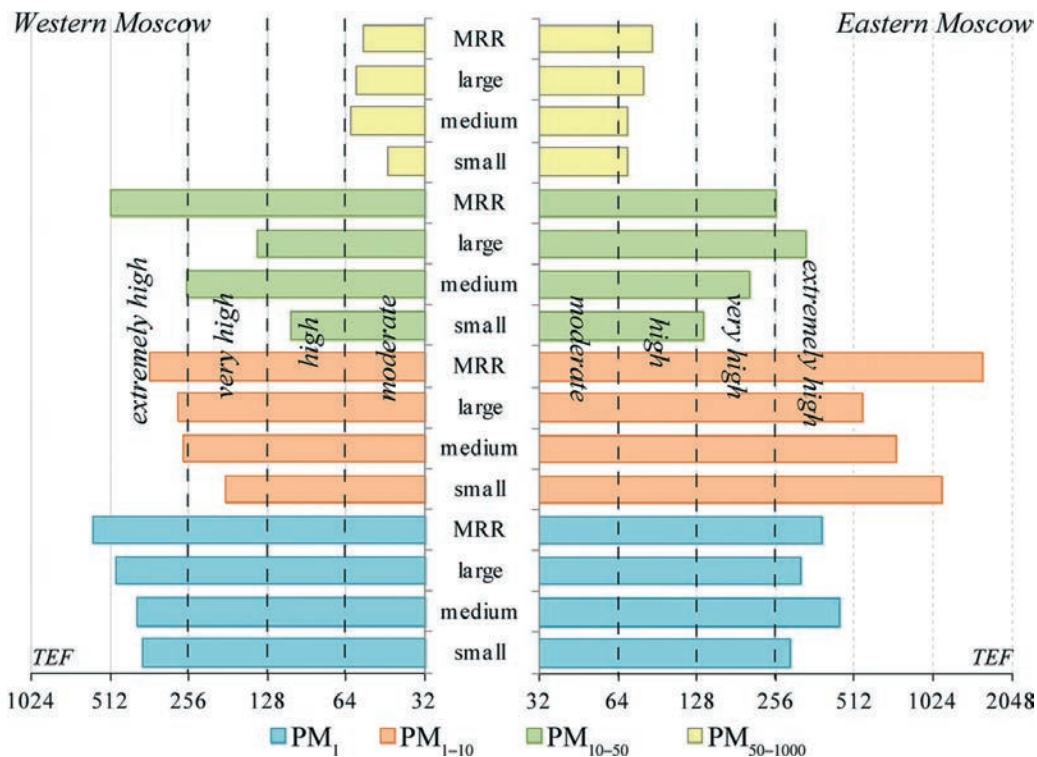


**Fig. 7.** Total enrichment of the road dust particles with PTEs on roads of different sizes in Moscow's western (traffic) and eastern (industrial) parts. TEF values are shown on the horizontal axis. MRR is Moscow Ring Road

indicates that the road size (and, accordingly, the intensity of traffic) had little effect on the accumulation of the elements from this group. EF value of Bi suggests its high enrichment in the  $PM_{50-1000}$  fraction on medium roads. In summary, in the western part of Moscow, many PTEs preferably accumulate in the road dust of large roads and the MRR, corresponding with increased emission of pollutants from motor vehicles at high speeds. The same pattern was observed in Ulsan (Republic of Korea), where the concentrations of PTEs reached maximal levels in the road dust of the main highways; in the central part of the city, on large bypass roads with a high proportion of busses and trucks, the concentrations of Cd, Cu, Zn, Ni dropped (Dung and Lee 2011).

The TEF index was used to assess the total enrichment of the dust particle size fractions with PTEs on various road types in the western and eastern parts of Moscow (Table S2, Table S3, Fig. 7).

According to TEF index values, the most polluted fraction differs in the city's two parts:  $PM_1$  in Western Moscow and  $PM_{1-10}$  in Eastern Moscow. In the western part of Moscow, the finest particles  $PM_1$  and  $PM_{1-10}$  demonstrate the trend of TEF values rising with the increase of road size, while in the eastern part of the city only coarse particles  $PM_{50-1000}$  show the same trend. The data on TEF show that in the western part of Moscow PTEs most intensively accumulated in the  $PM_1$  fraction (average TEF value = 444). On all roads, the TEF values in this particle size fraction ranged as extremely high (Fig. 7, Table S2). With increasing particle size, the TEF values decreased from 254 in  $PM_{1-10}$  to 208 in  $PM_{10-50}$  to 53 in  $PM_{50-1000}$ . The observed close TEF levels in  $PM_{1-10}$  and  $PM_{10-50}$  might be associated with high enrichment of Pb in large particles on medium roads, especially on the MRR. The accumulation of other PTEs in  $PM_{10-50}$  particles was less intensive than in

$PM_{1-10}$ . In the  $PM_1$  and  $PM_{1-10}$  fractions, the TEF values increased with traffic flow. In the  $PM_{50-1000}$  fraction, the TEF values grew from small to medium and large roads but slightly decreased on the MRR.

In the eastern part of Moscow, the average level of the TEF in the  $PM_1$  fraction was lower compared to that of the west of Moscow on all road types except for medium ones, while in the  $PM_{1-10}$  it was higher on all roads. In the western part, the TEF values in the fraction  $PM_{10-50}$  were higher on medium roads and the MRR by 56 and 255 units, respectively, than in the eastern part; but on small and large roads, they were lower by 31 and 195 units, respectively. In the eastern part of Moscow, PTEs accumulated in fine fractions on both small and large roads due to industrial impact. An increase in the TEF values associated with an increase in traffic load in the east of Moscow was noticeable only in the coarse fractions  $PM_{10-50}$  and  $PM_{50-1000}$ .

In summary, an extremely high enrichment in PTEs was observed in the fine fractions  $PM_1$  and  $PM_{1-10}$  not only on major highways but also on small roads and in courtyards. Relatively large particles of  $PM_{10-50}$  were also enriched with PTEs to extremely high levels on medium roads and the MRR in the western part of Moscow and on large roads in its eastern part.

### Source identification and apportionment

The data on PTE concentrations in four particle size fractions of the road dust was analyzed using principal component analysis (PCA). For  $PM_1$  and  $PM_{1-10}$ , four principal components (PCs) were extracted, explaining 80.7% and 81.5% of the total variance in the data, respectively, and for  $PM_{10-50}$  and  $PM_{50-1000}$ , five PCs were extracted, responsible for 84.2% and 73.5% of the total variance, respectively (Tables S4–S7).



The PCA/APCS-MLR receptor model was applied to the four extracted components for PM<sub>1</sub> and PM<sub>1–10</sub> particles and the five extracted components for PM<sub>10–50</sub> and PM<sub>50–1000</sub> to quantify the contributions of the sources to each measured PTE content. Statistical analysis results, including identified source profiles obtained by PCA/APCS-MLR, APCS uncertainty, and the coefficient of determination ( $R^2$ ) between predicted and observed concentrations of PTEs, are presented in Tables S8–S11 (Supplementary material). In APCS, source contribution estimates are not constrained to be nonnegative (Miller et al. 2002), which is physically impossible, i.e., PCA/APCS-MLR's ability to generate negative source contributions and inability to model extreme data are known concerns (Larsen and Baker 2003). For all studied PTEs, the uncertainty (UNC) did not exceed  $\pm 45\%$ , which indicates an acceptable level of modeling accuracy and is appropriate for source apportionment of PTEs in various particle size fractions of road dust in Moscow. For the majority of PTEs,  $R^2$  was more than 0.6. Relatively low  $R^2$  values ( $< 0.6$ ) were obtained in PM<sub>1</sub> for As (0.55), Cr (0.45), in PM<sub>1–10</sub> for Pb (0.55), in PM<sub>10–50</sub> for Zn (0.39), and in PM<sub>50–1000</sub> for Ni (0.48), Bi (0.24), and Pb (0.17). To assess the differences in the contribution of sources to the PTE content in dust and its particle size fractions in different parts of the city, the average values of  $APCS_p \times \xi_{pi}$  were calculated separately for the western and eastern parts of the city (Table S12). The results are presented in Fig. 8, where stacked bars display contributions by different sources to an element concentration. Only sources with a reliably established positive contribution to PTE concentrations were considered.

Source contribution (in percent) to size-fractionated road dust in Moscow obtained by PCA/APCS-MLR. The black line separates the contributions of terrigenous (below the line) and anthropogenic (above the line) sources

The terrigenous factor was identified in the PM<sub>1</sub> and PM<sub>1–10</sub> fractions, explaining 38.1% and 47.7% of the total variance of the data, respectively. It had high loadings of Al, Be, Ba, Fe, Rb, V, and Mn in the PM<sub>1</sub> fraction and high loadings of Al, Ba, Ti, Fe, V, Mn, Be, Sr, Cr, Rb, W, Zn, and Pb in the PM<sub>1–10</sub> fraction. The accumulation of Al usually indicates the addition of rock particles, while the enrichment with Fe, Mn, Rb, and Ba implies wind-induced emission of particles from polluted urban soils (Yu et al. 2018; Morera-Gómez et al. 2020; Konstantinova et al. 2022).

Additionally, this factor may be derived from the abrasion of the road surface since asphalt concrete contains relatively high amounts of Mn, Ba, Sr, V, and Ni (von Gunten et al. 2020) and can also be due to construction objects emitting high amounts of Sr (Amato et al. 2009), while concrete dust often is rich in Be (Frye et al. 2021). In general, in the western part of Moscow, the contribution of the terrigenous source to the concentrations of Pb, Sr, Cu, and W and notably of Cr in the PM<sub>1–10</sub> fraction was higher than in PM<sub>1</sub>, but its impact on Ni, Bi, Mo, Sb, and especially on As concentrations was significantly lower.

Two terrigenous factors were identified in the coarse fractions of the road dust: rock particles (including building materials) and wind-induced emissions of particles from polluted soils. The occurrence of two terrigenous factors in the coarse size fractions might be attributed to the significant additional impact of local soil (Logiewa et al. 2020). The fine fractions, however, are typically char-

acterized by intense air transport from remote sources, resulting in better mixing of particles coming from rocks and soils, and higher commonality in their chemical composition, in contrast to large ones. The influence of rock particles with high loadings of Rb, Ba, Al, Be, and Sr explained 38.0% of the total variance in PM<sub>10–50</sub>. In PM<sub>50–1000</sub>, this factor (with high loadings for Rb, Al, Ba, Sr, and Be) explained 12.6% of the total variance. Resuspension of polluted soil particles explained 9.0% and 36.6% of the total variance in the PM<sub>10–50</sub> and PM<sub>50–1000</sub> fractions, respectively, and had high loading for Ti, Mn, Co, V, Fe and Ti, Co, V, Fe, Mn, Cr, Cu, respectively.

In all particle size fractions of the road dust, the terrigenous factor had high relative contributions ( $> 50\%$ ) to the concentrations of Al, Ba, Rb, Sr, Be, Mn, V, Ti, and also Fe in the PM<sub>1</sub>, PM<sub>1–10</sub>, and PM<sub>50–1000</sub> fractions (Table S12). The most significant relative contributions of the terrigenous sources to the PTE concentrations were observed in the coarsest PM<sub>50–1000</sub> particles in both parts of the city (Fig. 8). Due to a more intense industrial impact, the contribution of the terrigenous factor to the PTE concentrations in the east in all particle size fractions was lower than that in the west. The PM<sub>10–50</sub> fraction in the eastern part of Moscow was little affected by wind-blown soil particles (the relative contribution from this source was less than 1–2% for all PTEs), but in the western part, soil factor contributed 30–40% to the total levels of Ti, Mn, and Fe and 10–20% to other PTEs. However, in total, both terrigenous sources—rocks and soils—made approximately the same relative contribution to the concentrations of most PTEs in PM<sub>10–50</sub> in both parts of Moscow.

The factor that was interpreted as the influence of motor transport (“traffic” factor) explained 21.2%, 19.2%, 9.2%, and 9.7% of the total variance in PM<sub>1</sub>, PM<sub>1–10</sub>, PM<sub>10–50</sub>, and PM<sub>50–1000</sub>, respectively, and had high loadings for W, Pb, Cu, Zn, and Bi in PM<sub>1</sub>, Sn, Bi, Cu, Zn, Sb, and Co in PM<sub>1–10</sub>, Cu, Pb, Bi, Cd, Sb, Co, V, and Zn in PM<sub>10–50</sub>, Sb and Zn in PM<sub>50–1000</sub>. It is known that W, Cu, Sb, and Pb are good brake pad wear indicators (Duan and Tan 2013; Moskovchenko et al. 2022; Ozaki et al. 2021), while Zn and Cd are tire abrasion indicators (Grigoratos and Martini 2015). The largest number of PTEs whose concentrations were significantly influenced by vehicles was found in the PM<sub>1–10</sub> and PM<sub>10–50</sub> fractions. However, in the west of Moscow, motor transport made a significant contribution (20–50%) to the concentrations of Zn, W, Pb, Bi, Cu, and Sr in PM<sub>1</sub>; in the east, the contribution of the transport sector to the element concentrations in the same fraction was lower by 15–30%. In the PM<sub>1–10</sub> fraction, the most significant relative contribution of vehicle transport ( $> 90\%$ ) was calculated for Bi in the west of Moscow. The contribution of this factor to Sn concentrations was described as “high” (about 70%), and for Cu, Sb, Cd, Zn, Mo, and Pb as “enhanced” (20–50%). In the east, the contribution of transport to the concentrations of most PTEs was nearly the same as in the west but differed only for Cu, W, Zn, and Pb. For these elements, the relative contribution of traffic factor was higher by 14–20%, probably due to frequent traffic jams caused by more significant congestion of major roads in the eastern part of Moscow and additionally by industrial impact (Bi et al. 2018; Jeong et al. 2020; Kasimov et al. 2021; Kelepertzis et al. 2020).

In general, in PM<sub>1–10</sub>, in comparison with PM<sub>1</sub>, the contribution of vehicle emissions to the concentrations

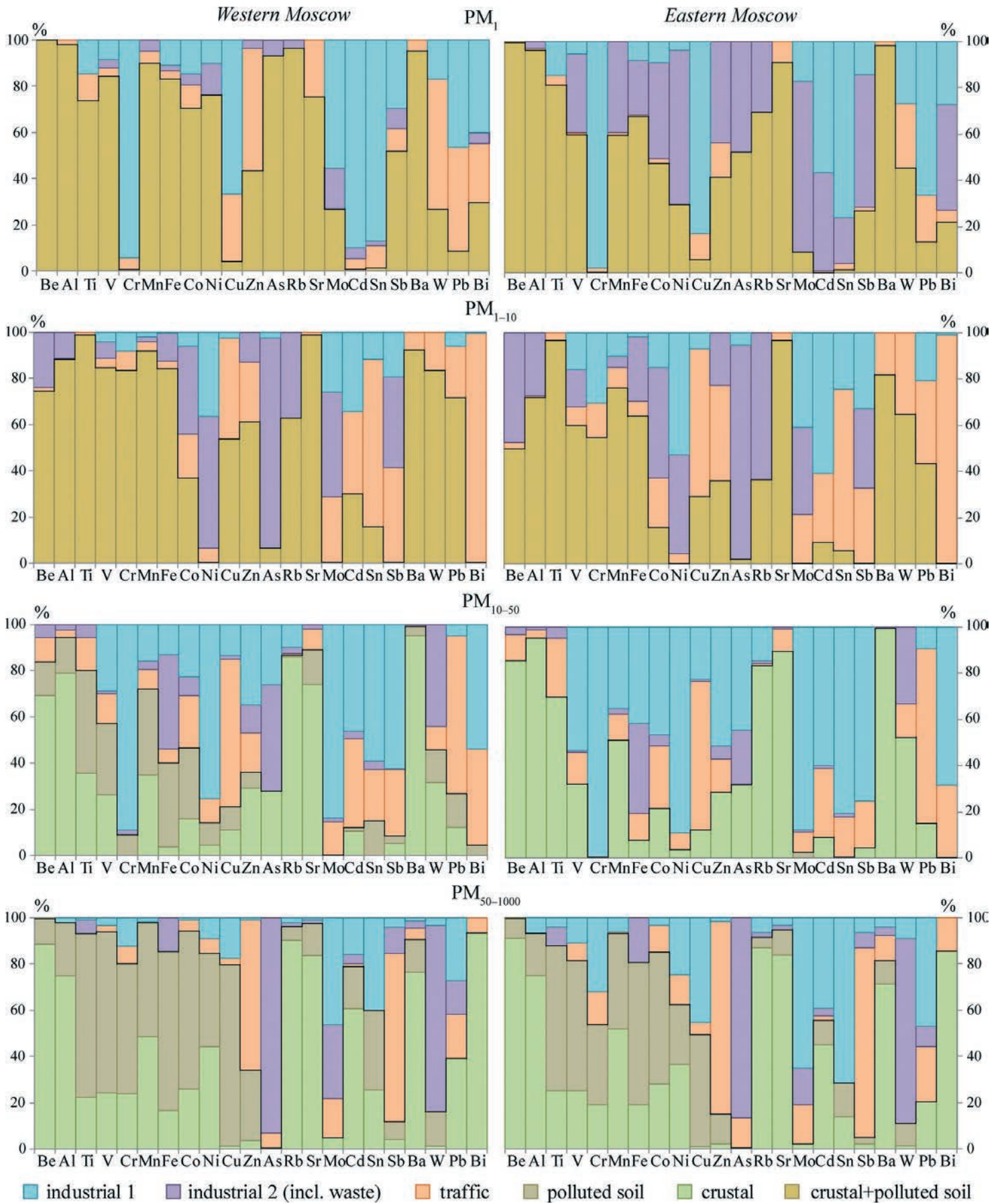


**Fig. 8.** Source contribution (in percent) to size-fractionated road dust in Moscow obtained by PCA/APCS-MLR. The black line separates the contributions of terrigenous (below the line) and anthropogenic (above the line) sources

of Sn, Cd, Sn, Mo, and Bi was higher. In the coarser particles, the contribution of motor transport to the accumulation of PTEs was roughly the same in different parts of the city. In the PM<sub>10–50</sub> particles, traffic-derived particles determined about 60% of the Pb and Cu concentrations and 20–40% of Bi, Cd, Sb, Sn, and Co. In the PM<sub>50–1000</sub> particles, a significant contribution of the transport factor (65–70%) was found only for Sb and Zn.

The factor associated with the influence of industrial facilities (“industrial 1” factor) explained 5.2%, 5.0%, 23.5%, and 8.1% of the total variance in PM<sub>1</sub>, PM<sub>1–10</sub>, PM<sub>10–50</sub>, and PM<sub>50–1000</sub>, respectively, and had high loadings for Sn, Cd, and Cu in PM<sub>1</sub>, Ni, Cd, and Mo in PM<sub>1–10</sub>, Mo, Cr, and Ni in PM<sub>10–50</sub>, Mo, Sn, and Cd in PM<sub>50–1000</sub>. A significant source of Mo, Cr, Cu, and Ni are emissions from metalworking, refinery, and petrochemical industries (Kim et al. 2014; Bozkurt et al. 2018; Wong et al. 2021). Cd is added to the environment with emissions from instrumentation, chemical, and rubber industries and also during plastics and paints production (Ciarrocca et al. 2015; Hossain et al. 2019). The largest number of PTEs whose concentrations were significantly influenced by industrial factor was established in the PM<sub>10–50</sub> fraction, but in the western part of Moscow, the largest relative contribution of industrial sources to the PTE concentrations was found in the PM<sub>1</sub> (55–95% for Mo, Cu, Sn, Cd, Cr and 30–50% for Sb, Pb, and Bi). In PM<sub>10–50</sub>, the relative contribution from industries varied within 50–80% for Mo, Sn, Bi, Sb, Cr, and Cd. In PM<sub>50–1000</sub> and PM<sub>1–10</sub>, the contribution of an industrial factor in the element concentrations was lower in comparison with PM<sub>10–50</sub> fraction: 10–45% for Mo, Sn, Pb, Cd, Cu, Cr, Ni in PM<sub>50–1000</sub> and 12–36% for Ni, Mo, Cd, Sn, Sb in PM<sub>1–10</sub>. In the eastern part of Moscow, where many industrial areas are located, the relative contribution of industries to the PTE concentrations was higher than the western part—by 10–30% in PM<sub>1–10</sub>, PM<sub>10–50</sub>, and PM<sub>50–1000</sub>. The PM<sub>1</sub> fraction had lower loadings of industrial sources in the eastern part of the city than in the western part, mainly due to an increase in the relative contribution of the “industrial 2” factor (see below), which was especially pronounced for Cd, Sn, Mo, and Pb.

The factor associated with the influence of mixed sources such as emissions from industrial facilities, waste processing, and incineration plants (“industrial 2” factor) explained 16.3%, 9.6%, 5.5%, and 6.6% of the total variance in PM<sub>1</sub>, PM<sub>1–10</sub>, PM<sub>10–50</sub>, and PM<sub>50–1000</sub>, respectively, and had high loadings for Mo, Sb, Ni, Co, V, Mn, Bi, Cd, Rb, and As in PM<sub>1</sub>, As, Rb, Co, and Ni in PM<sub>1–10</sub>, As, W, and Fe in PM<sub>10–50</sub>, W and As in PM<sub>50–1000</sub>. Typically, waste sorting, recycling, and incineration plants are sources of As, Cd, Sb, Rb, V, and Bi (Christian et al. 2010; Enamorado-Báez et al. 2015; Li et al. 2020), while Rb, Ni, and Co can serve as indicators of combustion processes (Song and Gao 2011; Kara et al. 2014; Yu et al. 2018). High contributions for both As and Fe can be associated with scrap metal recycling (Duan and Tan 2013) and the sorption of As by Fe oxides and hydroxides (Ouyang et al. 2020). A significant contribution of the “industrial 2” factor to the concentrations of a wide range of PTEs was revealed in the PM<sub>1</sub> and PM<sub>1–10</sub> particles. In the west of Moscow, the relative contribution of this factor to the concentrations of the PTEs in PM<sub>1</sub> reached 15% for Mo, Sb, Ni, Cd, Bi, As, Zn, Co, and Mn. In PM<sub>1–10</sub> it was > 40% for As, Ni, and Mo and 20–40%

for Sb, Rb, Co, and Be. In the eastern (industrial) part for most PTEs, the loadings of the mixed sources were higher than in the western part (Fig. 8). In the PM<sub>1–10</sub> fraction, the contribution of waste incineration and industrial emissions to the concentrations of As, Ni, Rb, Mo, Sb, Co, V, Be, and Al were higher in comparison with PM<sub>1</sub>. In the coarse particles in the west, “industrial 2” sources determined 12–46% of As, Fe, W, and Zn concentrations in PM<sub>10–50</sub> and 33–90% of As, W, and Mo concentrations in PM<sub>50–1000</sub>. In contrast to the fine particles, this factor in the coarser fractions contributes less in the east than in the west due to the higher loading of the separately identified “industrial 1” factor.

In general, our results on the relative contributions of different sources to the chemical composition of the road dust agree well with the loading levels obtained in other cities. So, significant relative contributions of terrigenous factors to the concentrations of Al, Co, Fe, and Sr (39–65%), and industrial sources and traffic to the concentrations of Cd, Cu, Ni, Pb, Sb, Zn, As, and Cr (41–72%) were established for the road dust in Chelyabinsk, Russia (Krupnova et al. 2020). In Xi’an (China), the contribution of natural sources prevailed in the PM<sub>63</sub> fraction of the road dust, where geogenic factor controlled the concentrations of Co, Ga, Mn, Ni, Rb, V, and Y (57–87%), while the main contribution to the concentrations of Ba, Cr, Cu, Pb, and Zn (59–70%) came from vehicle emissions (Shi and Lu 2018). In Guangzhou (China), road dust pollution was formed mainly under the influence of a mixed industrial and traffic factor which controlled 71% of Pb, 58% of Cr, and 48% of Zn concentrations. High relative contribution to the element concentrations came from traffic emissions, which comprised nearly 100% of Cu, 75% of Ni, 42% of Cr and Zn, 28% of Pb, and 24% of Co. An input with soil particles was a significant source for Co (up to 38%) and Ni (up to 18%) (Liang et al. 2019).

In summary, according to the relative contribution of various sources to the PTEs concentrations, the fine particles PM<sub>1</sub> and PM<sub>1–10</sub> are rather similar. According to the list of individual sources, the PM<sub>10–50</sub> particles occupy an intermediate position between the fine (PM<sub>1</sub> and PM<sub>1–10</sub>) and the coarse (PM<sub>50–1000</sub>) particles. The two parts of Moscow differ according to the contribution of various anthropogenic sources to the pollution of particle size fractions of the road dust: in the east of Moscow, industrial sources and waste incineration have high contributions to the PTE concentrations in all particle size fractions, while in the west, the contribution of traffic emissions increases significantly, especially in PM<sub>1</sub>, PM<sub>1–10</sub>, and PM<sub>10–50</sub>.

## CONCLUSIONS

For the first time, the partitioning of PTEs in the road dust was studied in detail, and the quantitative source apportionment of PTEs in four particle size fractions of road dust was carried out for western and eastern parts of Moscow that are associated with traffic and industrial impact, respectively. The difference in nature and intensity of impacts caused by traffic and industries was the reason for the greater proportion of relatively fine particle size fractions PM<sub>1–10</sub> and PM<sub>10–50</sub> in the road dust of the eastern part and the predominance of the coarse fraction PM<sub>50–1000</sub> in the western part of the city. PM<sub>1</sub> and PM<sub>1–10</sub> of the road dust in the east of the city were



characterized by increased levels of Sb, Mo, As, Ni, Bi, Cd, and Sn, while in the west, these fractions had higher concentrations of W, Cr, Cu, Ti, Sr, and Pb. The dissimilarity can be explained by the different industrial impact and traffic load in the city parts. Among the listed PTEs, the concentrations of Sb, Mo, Ni, and Cd in all fractions in the east exceeded those in the west, probably due to the higher impact associated with the industrial sector. In the west, the intensity of accumulation of most PTEs in the road dust and its particle size fractions increased with an increase in the traffic load. In the east, the differences between the roads of different sizes for most PTEs were less pronounced due to the “smoothing” effect of industries, and the fine particles on small roads were enriched with PTEs to the same extent as on the large ones. In both parts of the city, extremely high W, Pb, Cd, Sn, Sb, Cu, Zn, Cr, and As enrichment was found in PM<sub>1</sub> and PM<sub>1–10</sub> not only on major highways but also on small roads and in courtyards, which indicates the need to control their ecological and geochemical state.

A similar list of PTEs came from terrigenous sources in both parts of Moscow. They significantly contributed to the concentrations of Al, Be, Ti, Sr, Mn, Fe, Rb, and Ba in particles of all size ranges. Significant differences in the geochemistry of particle size fractions of the road dust were related to anthropogenic factors. In the western part of Moscow, dominated by the transport sector, the main pollutants with EF > 10 were Pb, Sb, Cd, and W, and in the eastern part, the polluting elements—Sb, Cd, Sn, Zn, Bi, Cu, and Mo—were derived from industrial sources. The maxima of the EFs for anthropogenic and mixed natural and anthropogenic PTEs were typical of the PM<sub>1</sub>

fraction in the western part and the PM<sub>1–10</sub> fraction in the eastern part of Moscow. In the eastern part, the relative contribution of industrial sources to the accumulation of PTEs in all particle size fractions was 10–30% more than in the western part of Moscow. In the west, the finest particles PM<sub>1</sub> and PM<sub>1–10</sub> demonstrate the rising of TEF values with the increase of road size, while in the eastern part of the city only coarse particles PM<sub>50–1000</sub> show the same trend. The most polluted fraction, according to TEF index values, differs in the two parts of the city: PM<sub>1</sub> in Western Moscow and PM<sub>1–10</sub> in Eastern Moscow.

Generally, our study confirms the trend distinguished in many other cities: an increase in the accumulation of PTEs with a decrease in particle size. In terms of the chemical composition and the intensity of PTE enrichment, the PM<sub>1–10</sub> particles were more similar to PM<sub>1</sub>, and the PM<sub>10–50</sub> particles were more similar to PM<sub>50–1000</sub>. These similarities were confirmed by the analysis aimed at quantifying the contributions of various sources to the PTE concentrations in the particle size fractions. In the fractions PM<sub>1</sub> and PM<sub>1–10</sub>, a significant contribution was made by anthropogenic sources; however, its role decreased in the coarse fractions—PM<sub>10–50</sub> and especially in PM<sub>50–1000</sub>—due to the influence of roadside soils and rocks.

The results can be used to minimize the adverse impact on public health associated with wind-induced re-suspension of road dust particles and improve the road dust cleaning system. The research results showed the need to include road dust and its particle size fractions in the ecological and geochemical monitoring system of the urban environment.

## Benzo[a]pyrene in Moscow road dust: pollution levels and health risks\*

### INTRODUCTION

Road dust is a multicomponent medium formed during the settling of aerosol particles derived from the engine and industrial emissions, wear and tear of vehicles and transport infrastructure, washing out and blowing out of roadside soils, the comminution of garbage, and from residues of deicing mixtures (Aguilera et al., 2021; Pachon et al., 2021; Seleznev et al., 2020; Zhang et al., 2019a). Its particles are the carrier phase of many pollutants, primarily polycyclic aromatic hydrocarbons (PAHs, or polyarenes) and heavy metals and metalloids (HMMs) (Alves et al., 2020b; Jayarathne et al., 2019; Vanegas et al., 2021; Wiseman et al., 2021; Vlasov et al., 2022). Therefore, in large cities, road dust increasingly often becomes an object of ecological and geochemical monitoring (Demetriades & Birke, 2015; Ramirez et al., 2019; Sager, 2020; Vlasov et al., 2021; Yang et al., 2017). Road dust particles, particularly those with a diameter of less than 10  $\mu\text{m}$  ( $\text{PM}_{10}$ ), are easily blown out from the roadways into the air, and the related pollutants enter human bodies through inhalation, ingestion, or dermal contact (Levesque et al., 2021; Lloyd et al., 2019; Rienda & Alves, 2021). Road dust is an essential source of particulate matter in the urban atmosphere, especially within street canyons (Kauhaniemi et al., 2011; Stojiljkovic et al., 2019). Moreover, road dust is a significant source of suspended particles in the atmosphere of the USA, supplying more than half of the mass of  $\text{PM}_{10}$  and about a quarter of  $\text{PM}_{2.5}$  (NEI, 2020). In the form of dry precipitates, road dust enters urban soils, as well as the surface of plants, contributing to their pollution, particularly, during mechanical cleaning of the roadway by city services (Polukarova et al., 2020). Migrating with storm runoff, it exerts a negative impact on urban water bodies, increasing the content of suspended matter and the concentrations of most HMMs, PAHs, salts, and nutrients (Lloyd et al., 2019; Nawrot et al., 2020). In the absence of snow cover, the chemical composition of road dust appears an informative indicator of the ecological state of the urban environment and the primary sources of pollution (Kasimov et al., 2019a; Ladonin & Mikhaylova, 2020; Švédová et al., 2020).

PAHs are distinguished as carcinogens and mutagens (IARC, 2010). Pyrogenic PAHs are mainly formed during the combustion of organic substances in motor vehicles and industrial plants; petrogenic PAHs are found in petroleum products. PAHs included in the polymeric materials, tires, and road surfaces can be classified as both pyrogenic and petrogenic (Stogiannidis & Laane, 2015). Among PAHs, the most dangerous is benzo[a]pyrene (BaP), which belongs to hazard class I substances, the ingestion of which into the human body can cause cancer (Dat & Chang, 2017; Jacob, 2008; US EPA, 2017). In cities, BaP is most often formed during incomplete combustion of fuels at industrial enterprises, transport

facilities, and in heating systems, as well as during biomass burning (Konstantinova et al., 2020a; Liao & Yu, 2020). PAHs in road dust have been the subject of many studies, especially in Asian cities with high amounts of road dust and with numerous sources of PAHs (Anh et al., 2019; Gbeddy et al., 2021; Khpalwak et al., 2019; Konstantinova et al., 2020b; Ma et al., 2017; Majumdar et al., 2017; Soltani et al., 2015; Wei et al., 2015). In the road dust of Moscow—the largest megacity of Russia and Europe—the dustiness of the roads is also quite high (Bityukova & Mozgunov, 2019). However, most of the studies of PAHs in Moscow are devoted to soils (Agapkina et al., 2007, 2018; Belinskaya et al., 2015; Kasimov et al., 2017; Kogut et al., 2006; Nikiforova & Kosheleva, 2011; Nikiforova et al., 2019; Nikolaeva et al., 2017; Smagin et al., 2021; Zavgorodnyaya et al., 2019), river water (Ermina et al., 2016), bottom sediments of water reservoirs (Kramer & Tikhonova, 2015), snow cover (Galitskaya & Romyantseva, 2012; Kasimov et al., 2017; Khaustov & Redina, 2019; Lebedev et al., 2012; Zavgorodnyaya et al., 2019), atmospheric precipitation (Polyakova et al., 2018), and aerosols (Popovicheva et al., 2020).

So, the behavior and distribution of BaP in Moscow road dust have not been studied in detail, there are only a few single measurements of the content of BaP in road dust on some city roads (Bykova et al., 2021; Karpuhin et al., 2017), although road dust is an important link reflecting the relationships between the urban environments—soils, water bodies, and atmospheric aerosols (Kasimov et al., 2020). In the road dust of Moscow, only HMMs were previously analyzed in detail (Ermolin et al., 2018; Fedotov et al., 2014; Kasimov et al., 2021; Ladonin & Mikhaylova, 2020; Vlasov et al., 2021). An important role in the distribution and accumulation of HMMs and BaP is played by the physicochemical properties of road dust, determining dust capacity to fix pollutants (Acosta et al., 2011; Hu et al., 2011; Kasimov et al., 2019b), and by the artificial relief: under urban conditions, buildings can both protect against pollution and contribute to the enhanced accumulation of pollutants (Kasimov et al., 2017; Kosheleva et al., 2018). Air pollution, and probably as a result, road dust, is especially high in deep street canyons with heavy traffic (Lv et al., 2020; Yuan et al., 2014). The isolation of street canyons from adjacent urban blocks leads to the fact that about 70% of the equivalent black carbon released into the atmosphere from intracanyon sources (vehicles) (Barreira et al., 2021). Owing to the turbulent air mixing in street canyons, a uniform distribution of PAH concentrations over height can be observed (De Nicola et al., 2013). BaP is one of the priority pollutants in Moscow soils; its contribution to the total equivalent toxicity of 16 PAHs is 37.5% (Agapkina et al., 2018). Road dust in Moscow is an important source of particles in the atmosphere (Gubanov et al., 2021), and increased concentrations of BaP in the surface air are one of the causes of population mortality in the city from

cancer (Andreeva et al., 2016). Thus, the study of road dust pollution with BaP in Moscow is extremely relevant. However, despite the serious danger of BaP for the city's population, the associated public health risks have not yet been estimated.

Our work aimed to characterize the content and leading factors contributing to the increased accumulation of BaP in the road dust in dependence on the type of road and geometry of street canyons in Moscow, to compare BaP contents in road dust and other urban environments, and to evaluate non-carcinogenic and carcinogenic risks to public health.

### Sources of road dust pollution

The main source of road dust pollution in Moscow is motor transport; in 2019, its emissions amounted to 345,000 tons, or 85% of the total volume of emissions into the atmosphere (Kul'batchevskii, 2020). Roads occupy about 8% of the city's area; their total length at the end of 2019 was 6625 km (Rosstat, 2020). With the area of Moscow reaching 2561 km<sup>2</sup>, the density of the road network in the city is 2.6 km/km<sup>2</sup>. In 2019, Moscow's car fleet totaled about 4419 thousand units, including 90% of cars, 9% of trucks and light-duty vehicles, and 1% of buses. The level of motorization was 349 units/1000 people. The average growth rate of the vehicle fleet in Moscow in 2014–2019 reached 18.2 thousand units/year, or 0.5%/year (Kul'batchevskii, 2020).

In Moscow's motor transport emissions (excluding abrasion of the road surface, markings, tires, and brake pads of cars), carbon monoxide accounts for 63%, nitrogen oxides 22%, volatile hydrocarbons 13%, and particulate matter about 1%. The largest amount of PM<sub>10</sub> is emitted by freight transport (61%) and buses (29%), although the number of these vehicles is an order of magnitude smaller than that of light cars. This is because of considerably higher specific emissions and mileage of heavy trucks and buses and a lower share of engines of high ecological classes corresponding to Euro-4, Euro-5, and higher European emission standards (Kul'batchevskii, 2020). The average dust load on the surface of roadside soils (within a 1 m zone) in the early 2000s was 1.77 g/m<sup>2</sup> per day, decreasing to 0.47 g/m<sup>2</sup> per day at a distance of 5 m from the road, which was 262 and 67 times higher, respectively, than the background dust deposition (0.007 g/m<sup>2</sup> per day) level (Achkasov et al., 2006). At present, dust deposition from the atmosphere within a few meters from the MRR averages 0.13 g/m<sup>2</sup> per day; it decreases to 0.10 g/m<sup>2</sup> per day near major highways and 0.03–0.04 g/m<sup>2</sup> per day near medium and small roads; in courtyards of residential buildings with parking lots, it is about 0.02 g/m<sup>2</sup> per day (Vlasov et al., 2020).

Exhaust emissions of BaP per 1 km of the mileage reach up to 0.1 mg for mopeds and motorcycles, 3.87 mg for cars, 2.03 mg for light trucks, 0.97 mg for heavy trucks, and 0.90 mg for buses (Ricchio et al., 2016). In addition to vehicle exhausts, the source of BaP in the traffic area is non-exhaust emissions, among which the most significant contribution is due to tire and roadway wear. The content of BaP in automobile tires can reach 1.39–2.5 mg/kg, in addition, the intensity of the supply of polyarenes during tire wear increases with increasing tire mileage or the degree of wear (Alves et al., 2020a). A significant source of PAHs and BaP in the traffic area is represented by railway transport facilities associated with

diesel engine exhaust gases; abrasion of brakes, wheels, and rails; dust blowing during the transportation of bulk minerals and slags; and wear and tear of sleepers and objects treated with various chemical compounds (Kim et al., 2016; Levengood et al., 2015; Lovett et al., 2018).

Emissions from industrial plants also contribute to road dust pollution. There are more than 30,000 stationary emission sources in the industrial zones of Moscow (Fig. 1).

In 2019, the volume of their emissions amounted to about 60,000 tons, with a share of solids of about 3% (Kul'batchevskii, 2020). Stationary sources are responsible for only 15% of the total emissions of pollutants in Moscow, of which 50–65% are due to 13 combined heat and power plants (CHPs); 20–30%, to oil refinery plants; 15–20%, to processing industries; and up to 7%, to machinebuilding enterprises, incinerators, and production of food and construction materials (Bityukova & Saul'skaya, 2017). Very high and high levels of anthropogenic impact are characteristic of 11 industrial zones, which occupy more than 20% of the total area of industrial territories and supply more than 70% of the gross pollution from all city's industrial zones (Bityukova & Saul'skaya, 2017). These industrial zones are located mainly in Moscow's eastern, southern, and southeastern sectors, often adjacent to the TRR or MRR. Industrial zones with medium and moderate levels of anthropogenic impact also occupy large areas near the TRR in these sectors. Dust sources are also represented by about 700 urban construction sites. These are residential buildings, urban infrastructure, and road and transport facilities. In addition, Moscow is currently redeveloping industrial zones into residential ones (Saul'skaya, 2018).

The dustiness of roads increases due to the windblowing of urban soil particles and the use of deicing mixtures (DIMs). Artificially created or intensely transformed soils—Technosols—prevail on territories bounded by the MRR (Prokof'eva et al., 2017). These soils are specified by higher pH values, contents of soluble salts, organic matter, PM<sub>10</sub> particles, and sorption capacity in comparison with the natural background soils (Umbric Albeluvisols), which contributes to the fixation of BaP in the urban soils (Kasimov et al., 2019b). In Moscow, DIMs of the chloride group (NaCl, CaCl<sub>2</sub>) mixed with marble chips are applied. In 2019, 324 thousand tons of DIMs were purchased by the City Hall, so for every 1 m<sup>2</sup> of road surfaces and courtyards (in total they occupy about 162 million m<sup>2</sup>) accounted for 2 kg of DIMs (Voronov et al., 2019).

### Materials and methods

#### *Sampling and chemical analyses of road dust*

Road dust was sampled in June–July 2017 within the territory limited by the MRR (Fig. 1). Sampling was carried out during the summer, since in autumn, winter, and spring the roadway is wet for a long period (due to snow melting or low temperatures that prevent the rapid evaporation of moisture), and in the summer, there is a high probability of road dust resuspension from the roadway surface after a dry antecedent period and release it into the atmosphere, which poses a potential risk to public health. Samples were taken in all districts of the city on roads with different traffic intensities: MRR (number of samples  $n = 19$ ), Third Ring Road (TRR) (7), major radial highways with more than four lanes in one direc-



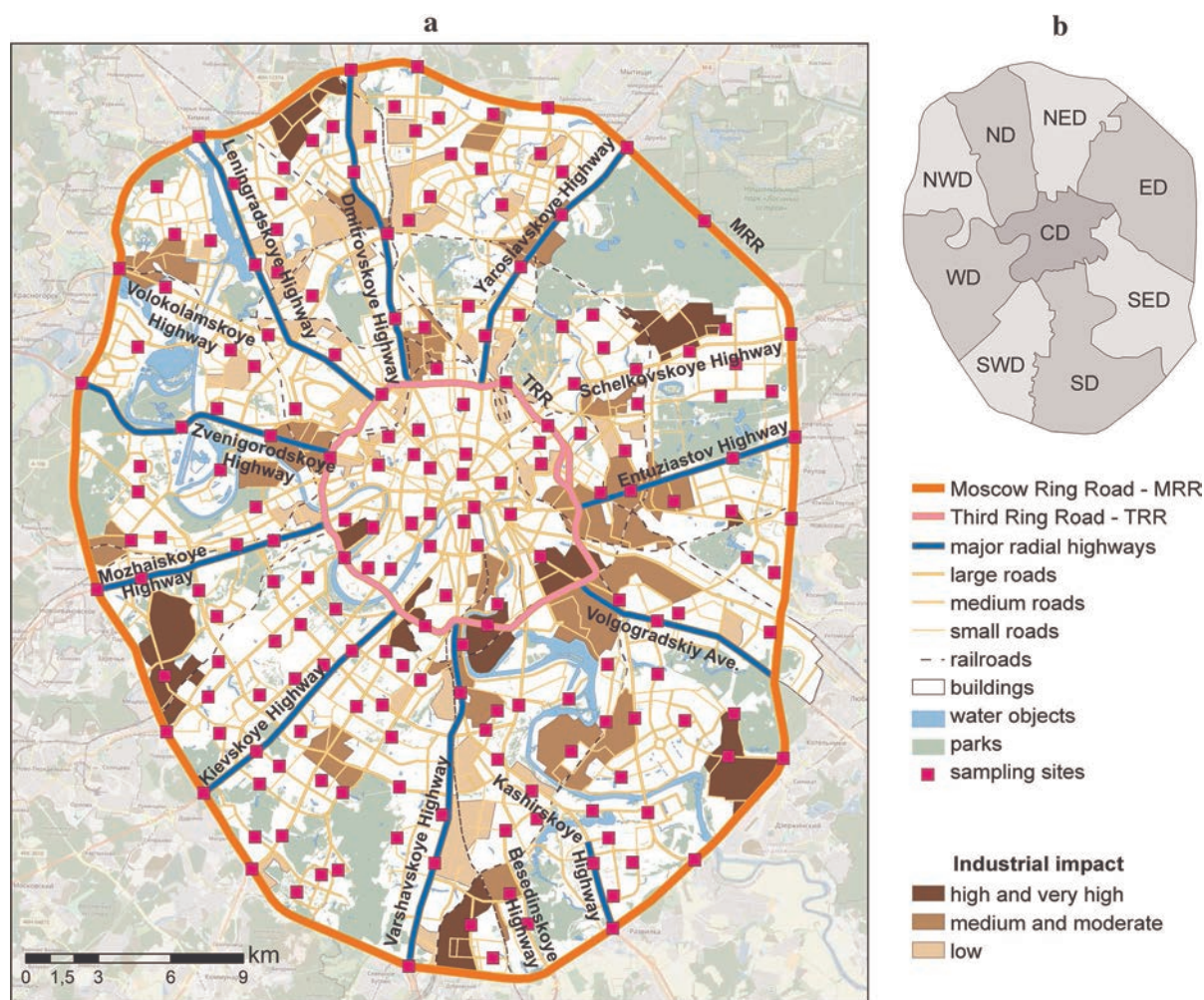


**Fig. 1.** Sources of industrial impact and road dust sampling sites (summer 2017) in Moscow (a) and the administrative districts of Moscow within the Moscow Ring Road (b): ND is Northern district, NED is Northeastern, ED is Eastern, SED is Southeastern, SD is Southern, SWD is Southwestern, WD is Western, NWD is Northwestern, CD is Central district. Industrial impact levels are given according to Bitjukova and Saul'skaya (2017)

tion (17), large roads with three–four lanes (46), medium roads with two lanes (42), and small roads with one lane in one direction (29). Overall, 160 dust samples were collected on highways and 33 dust samples in courtyards with parking lots (Table S1 in the Supplementary materials). The period of field work was rainy; the rainfall exceeded the average value by almost two times. Light rains with a volume of < 5 mm fell on June 1–3, 16, 22, and on July 9, 16, 21; rainfall events with a volume > 5 mm occurred on June 5, 13–15, 19, 21, 26, and on July 1–4, 8, 12–14, and 31. The accumulation of road dust was impeded by surface runoff and cleaning of roads by municipal services. So, sampling was performed under dry weather conditions, no less than 24 h after the rains with volume < 5 mm and no less than 72 h after the rains with volume > 5 mm, when the road surface was completely dried out. Samples were taken along the curb on both sides of the roads using a plastic dustpan and a brush in three–five replicates at a distance of 3–10 m from one to another; one mixed sample was composed of them. On the major radial highways and large roads, samples were taken from the dividing strip; in the courtyards, samples were taken from parking areas. The bulk samples were then stored in self-sealed polyethylene bags for transportation to the laboratory.

All dust samples were dried for 48 h at room temperature and then were sieved through 0.25-mm sieves to remove debris particles and gravel. The BaP content was determined in samples at the Laboratory of Carbonaceous Substances of the Biosphere (Faculty of Geography, Lomonosov Moscow State University) by high-resolution spectrofluorimetry at the temperature of liquid nitrogen (Shpol'skii spectroscopy) using a Fluorat-02-Panorama (Lumex Instruments, Saint-Petersburg, Russia) device supplemented with an LM-3 monochromator and a CRYO-1 cryogenic attachment. This method is widely used in the study of PAH concentrations in soils and mineral objects. The methodology is described in detail elsewhere (Tsibart et al., 2014). Briefly, 3 g of road dust samples were extracted with n-hexane (5 mL) at room temperature. The degree of extraction was controlled by the absence of extract luminescence under UV light. In cases of the presence of extract luminescence, the extraction was continued with 5 mL of n-hexane. The extract was frozen in liquid nitrogen (77 K). Then, the mixture in the frozen extract was irradiated by light, and the BaP luminescence spectra were recorded. The wavelengths of the excitation and emissions of luminescence used for the BaP identifications are 367 nm and 402 nm, respectively. High selectivity of the method is obtained by using a

spectra selection of BaP in the solution by scanning the narrow excitation wave band (Alekseeva & Teplitskaya, 1981). Identification and quantitative estimations of BaP were made by comparison of fluorescence and excitation spectra with the international certified reference standard solution 2260a of the National Institute of Standards and Technology (USA). The limits of detection (LOD) and quantification (LOQ) for BaP were 0.0001 mg/kg and 0.0005 mg/kg, respectively. The average error in determining BaP was 10–15% with a maximum error (near LOD) of 25%.

### Data processing

Statistical data treatment was performed in the Statistica 8 software package. The mapping of geochemical data was performed in the ArcGIS 10 package. Maps from the OpenStreetMap project ([www.openstreetmap.org](http://www.openstreetmap.org)) served as a cartographic basis for maps. The classification of numeric fields when using graded symbols was carried out using the Jenks natural breaks algorithm.

The method of regression trees in the S-PLUS software package was used to assess the effect of the physicochemical properties of dust, the uneven anthropogenic load in certain areas of the city, and the geometry of street canyons on the BaP content in road dust (Rawls & Pachepsky, 2002). The result of multiple partitioning of the matrix with predictor variables and the BaP content in Moscow road dust is a dendrogram reflecting the levels of the pollutant content for various combinations of quantitative and qualitative factors. For each terminal node of the dendrogram, the average content of BaP and the coefficient of variation  $C_v$  ( $C_v = \sigma/\text{mean} \times 100\%$ , where  $\sigma$  is standard deviation) were calculated for  $n$  sampling points. The following properties of road dust were taken into account: particle-size distribution, pH and the electrical conductivity (EC) of the water solution, and the organic carbon ( $C_{\text{org}}$ ) content. A detailed analysis of these properties of Moscow dust was made previously (Kasimov et al., 2019b), and the brief results are given in the Supplementary Materials (Text S1, Table S2). The anthropogenic impact of transport was characterized by the type of road, from which dust samples were taken, and by its belonging to one of the nine districts. The parameters of street canyons—height  $H$ , width  $W$ , canyon proportions  $H/W$ , length  $L$ , and orientation (direction)  $\theta$ —were determined for each sampling point using the OpenStreetMap data following the methodology described below.

The environmental hazard of road dust pollution with BaP was determined using the environmental hazard coefficient  $K_h = C/\text{MPC}$ , where  $C$  is the content of BaP in road dust, and MPC is its maximum permissible concentration. As the MPC of BaP for road dust has not been developed, the MPC for soils equal to 0.02 mg BaP/kg soil (SanPiN1.2.3685-21, 2021) was used as a hygienic standard. The reasons why we used MPC of BaP in soils are as follows: (1) the contribution of soil particles to the road dust mass in Moscow is significant (Vlasov et al., 2021), (2) soils are often used as a background in the study of road dust (Men et al., 2020), (3) resuspension of road dust particles from the roadway into the atmosphere and their further deposition on the soil surface can be an important source of urban soils pollution (Zhang et al., 2019b), (4) the same approach is used to assess the potential risk to public health from the exposure of road dust and soil particles (Gabarrón et al., 2017b).

### Determination of parameters of street canyons

The size of the road (the number of lanes) is an insufficient characteristic for analyzing the spatial distribution of pollutants within the urban area and quantitatively assessing its impact on the accumulation of BaP since this characteristic does not take into account the urban development surrounding the road. Previously, we have shown that building characteristics have a significant impact on the pollution level of the urban environment in Moscow (Kosheleva et al., 2018). Buildings can both prevent the transfer of pollutants from the streets to the surrounding areas (which can increase the level of dust pollution on the roads), and in some cases, on the contrary, certain building characteristics can contribute to the blowing of pollutants off the streets, which can potentially reduce dust pollution by various contaminants. Therefore, we expanded the set of parameters characterizing the geometry of streets with traffic flows and used formal methods of its description within the framework of the concept of urban canyons. An urban canyon is a three-dimensional volume bounded by the surface of the Earth from below and by the walls of buildings from both sides of the street and open at the top (Fig. S1a, Supplementary materials). This concept is widely used in urban climatology to model the processes occurring in the interaction zone of the boundary layer of the atmosphere, the Earth surface, and urban built-up (De Nicola et al., 2013; Fellini et al., 2020; Nunez & Oke, 1977; Oke, 1987). The micro-canyon is defined by a pair of neighboring buildings, but dispersion of pollutants in urban environment appears in a larger scale, specifically along the streets, which are formed by multiple canyons arranged in a row. To formalize such arrangement, Samsonov et al. (2015) introduced the concept of the macro-canyon (Fig. S1b, Supplementary materials). With the correct planning of the street network in relation to the wind rose, the macro-level canyons are ventilation corridors, along which the urban atmosphere is blown through, and the concentration of pollutants in it decreases (Ren et al., 2018). In this work, macro-level canyons are called *street canyons*.

The main parameters of the micro-canyon are the height  $h$  and the width  $w$ , which determine the proportions of the canyon, the  $h/w$  ratio (Text S2, Supplementary Materials). The similar parameters  $H$ ,  $W$ , and  $H/W$  of the street canyon are determined by averaging the  $h$ ,  $w$ , and  $h/w$  values for its constituent micro-canyons (Samsonov et al., 2019). Additional geometric characteristics of the street canyon are its length  $L$  and orientation (direction)  $\theta$ , which is defined in the range from  $0^\circ$  to  $180^\circ$  (because mutually opposite orientations are equivalent). Street canyon characteristics for each sampling point in Moscow were determined based on the data from OpenStreetMap. The variability of the characteristics is shown by their distributions (Fig. 2), and their characteristic values are shown in the bottom line of Table 1. The average values of the canyon's height  $H$  and width  $W$  are 17.5 m and 120.3 m, respectively, which determines the prevalence of small values of the canyon proportions ( $H/W < 0.5$ ). The distribution of canyon lengths also suggests that shorter canyons ( $< 3000$  m in length) are more common. The main mode of orientations corresponds to the direction  $102.2^\circ$ , while the directions perpendicular to it are also widespread (for clarity, the directions  $0^\circ$ – $180^\circ$  are duplicated in the graph by equivalent directions  $180^\circ$ – $360^\circ$ ).



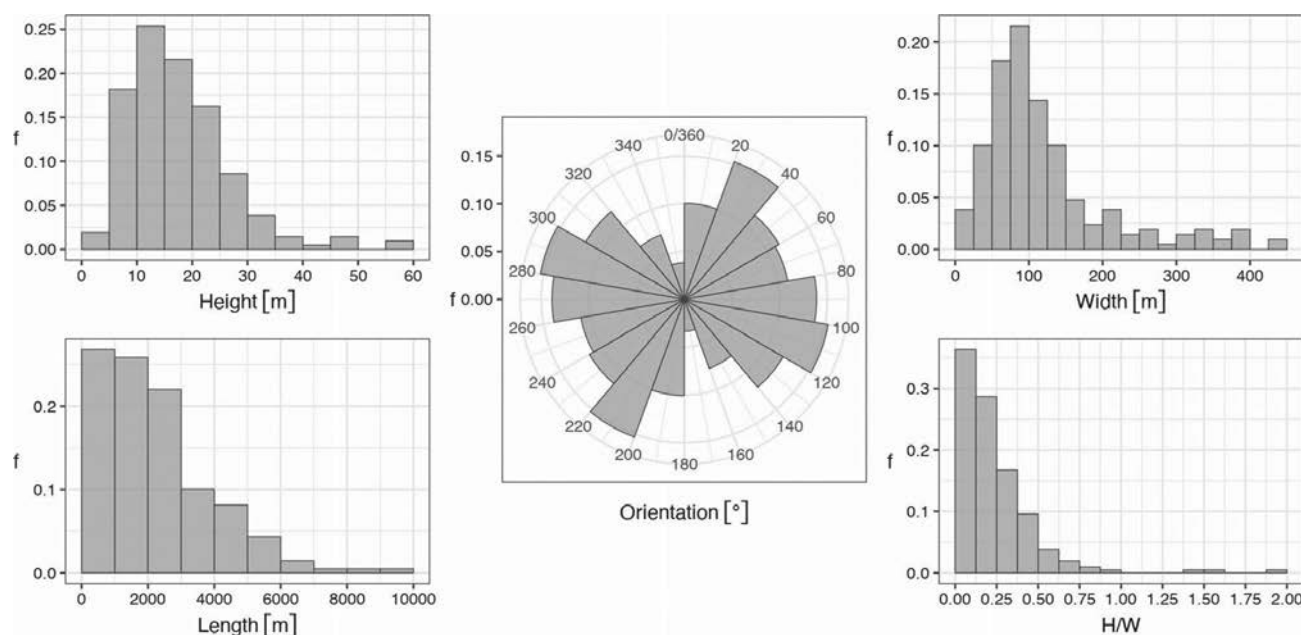


**Fig. 2** Distribution of the parameters of street canyons at sampling sites (frequencies of occurrence) in Moscow

**Table 1** Typical values of street canyon parameters in Moscow

Road	Height ( $H$ ), m	Width ( $W$ ), m	Length ( $L$ ), m	$H/W$	Orientation ( $\theta$ ), °
MRR	12.1	304.1	4,650	0.053	110.6
TRR	13.4	157.1	2,232	0.110	120.7
Major radial highways	16.7	143.2	4,424	0.136	61.6
Large	17.8	129.2	2,744	0.166	34.9
Medium	15.9	92.7	1,675	0.213	41.6
Small	18.2	76.9	1,170	0.284	74.1
Courtyards	23.0	58.5	588	0.522	92.6
All roads	17.5	120.3	2,199	0.240	102.2

Mean values are given for  $H$ ,  $W$ ,  $L$ , and  $H/W$ ; modal values are indicated for  $\theta$

The average characteristics of the street canyons are expected to differ depending on the type of road along which the canyon is located. The corresponding distribution densities are shown in Fig. 3; mean values of  $H$ ,  $W$ ,  $L$ , and  $H/W$  and modal values of  $\theta$  are given in Table 1. It can be seen that the change in the type of road from the courtyard roads to the MRR is accompanied by a regular decrease in the mean height of the canyons from 23 to 12.1 m, an increase in the mean width from 58.5 to 304.1 m, an increase in the mean length from 588 to 4650 m, and a decrease in the canyon proportions from 0.522 to 0.053. This general pattern is interrupted by relatively short TRR canyons with the mean length of 2232 m, which is obviously due to the higher curvature of the TRR, at which the rectilinear sections are relatively short. Another exception is represented by canyons along medium roads, which are less high (15.9 m) than canyons along small (18.2 m) and large (17.8 m) roads, which can be explained by the peculiarities of street development. However, there is no complete differentiation of the parameters of the canyons depending on the types of roads; their distributions partially overlap one another. This determines the need to consider all the parameters of the canyons when analyzing the factors of BaP accumulation in the road dust of Moscow.

### Assessment of public health risks

The health risks of adults and children were assessed using a model developed by the US EPA (US EPA, 1989, 2002), which takes into account three pathways of the entry of contaminated road dust particles into the body: oral via ingestion (ingest), dermal via skin contact (dermal), and respiratory via inhalation (inhal). For BaP, the risk is determined by the average daily dose (ADD) of chronic consumption of contaminated dust coming in three ways:

$$ADD_{\text{ingest}} = \frac{C_u \times \text{IngR} \times \text{EF} \times \text{ED}}{\text{BW} \times \text{AT}} \times \text{CF}, \quad (1)$$

$$ADD_{\text{inhal}} = \frac{C_u \times \text{InhR} \times \text{EF} \times \text{ED}}{\text{BW} \times \text{AT} \times \text{PEF}}, \quad (2)$$

$$ADD_{\text{dermal}} = \frac{C_u \times \text{SA} \times \text{AF} \times \text{ABS} \times \text{EF} \times \text{ED}}{\text{BW} \times \text{AT}} \times \text{CF}, \quad (3)$$

where  $C_u$  is the content of BaP in road dust (mg/kg), IngR and InhR are the amounts of ingested (mg/day) and inhaled ( $\text{m}^3/\text{day}$ ) particles, EF is the exposure frequency (days/year), ED is the exposure duration (year), BW is the average human body weight (kg),  $\text{AT} = \text{ED} \times 365$



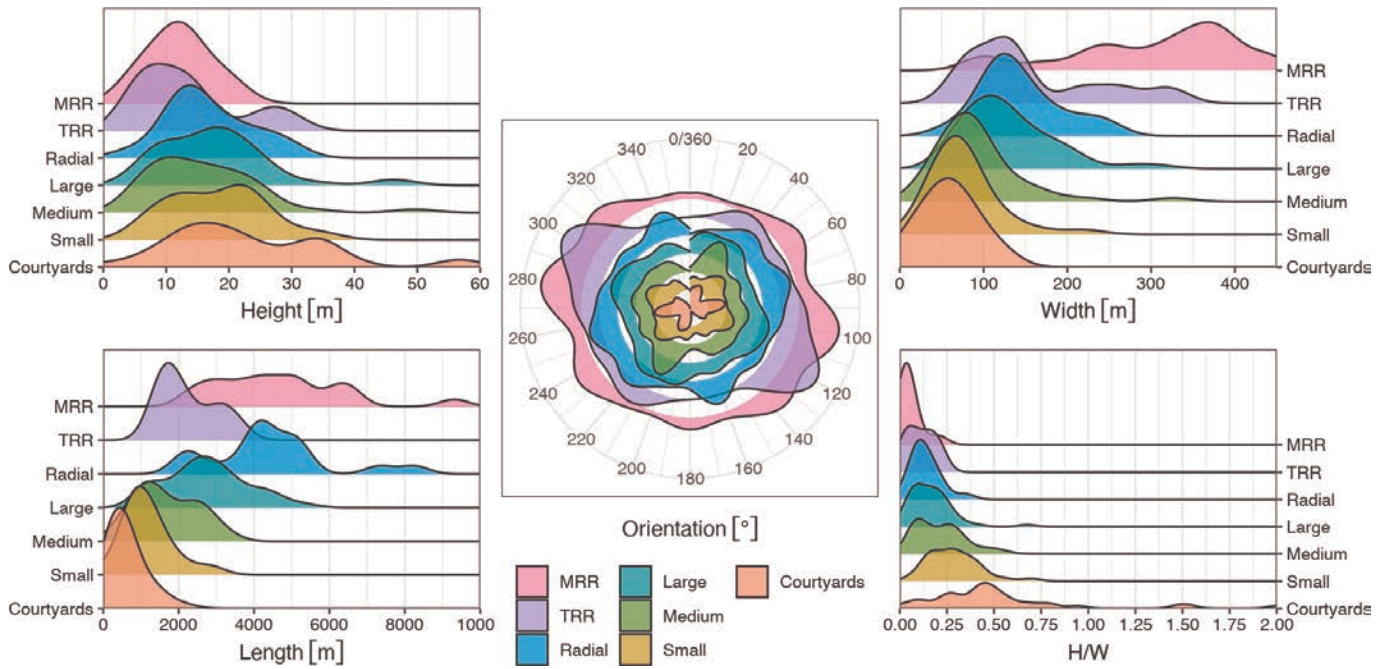


**Fig. 3** Distribution densities of the parameters of street canyons by types of roads in Moscow

is the average time of BaP influence (days), CF is the conversion factor ( $1 \times 10^{-6}$  kg/mg), PEF is the particle emission factor ( $1.36 \times 10^9$  m<sup>3</sup>/kg), SA is the surface area of the skin in contact with road dust particles (cm<sup>2</sup>), AF is the coefficient of dust adhesion to the skin (mg/cm<sup>2</sup>), and ABS is the absorption coefficient of BaP. The values of the variables differ for adults and children (Table 2).

**Table 2** Values of variables for adults and children used in the assessment of public health risks

Variable	Value		References
	Adults	Children	
IngR (mg/day)	30	60	(US EPA, 2002)
InhR (m <sup>3</sup> /day)	21.4	16.74	(US EPA, 2011)
EF (days/year)	350	350	(US EPA, 2002)
ED (year)	72	6	(US EPA, 2002)
BW (kg)	80	15	(US EPA, 1989, 2002)
AT (days)	26,280	2190	(US EPA, 2002)
SA (cm <sup>2</sup> )	5700	2800	(US EPA, 2002)
AF (mg/cm <sup>2</sup> )	0.07	0.2	(US EPA, 2002)
ABS	0.13	0.13	(RSL, 2017)

The danger of BaP is determined by the ratio of ADD<sub>i</sub> to the reference dose RfD:

$$HQ_{\text{ingest}} = \frac{ADD_{\text{ingest}}}{RfD_o} \quad (4)$$

$$HQ_{\text{inhal}} = \frac{ADD_{\text{inhal}}}{RfD_i} \quad (5)$$

$$HQ_{\text{dermal}} = \frac{ADD_{\text{dermal}}}{RfD_{\text{ABS}}} \quad (6)$$

Reference dose RfD is a daily dose, which, being consumed for a long period, does not lead to the development of pathological changes or diseases detected by modern research methods at any time in the life of the present or subsequent generations. To date, the following reference doses have been established for BaP: for oral intake,  $RfD_o = 3 \times 10^{-4}$  mg/kg per day, and for inhalation,  $RfD_i = 2 \times 10^{-6}$  mg/kg per day (RSL, 2017; US EPA, 1989). According to the recommendations by the US EPA (2002),  $RfD_{\text{ABS}}$  is calculated by multiplying the reference dose for oral intake by the gastrointestinal absorption coefficient, which equals 1.0 for BaP (RSL, 2017). Thus,  $RfD_{\text{ABS}} = RfD_o$ .

Hazard index  $HI = \sum(HQ_{\text{ingest}} + HQ_{\text{inhal}} + HQ_{\text{dermal}})$  considers the admission of contaminated dust particles in all possible ways. Indicators HQ<sub>i</sub> and HI are graded into four levels of hazard for human health: none (< 0.1), low (0.1–1), moderate (1–10), and high (> 10) (Lei et al., 2016; Lemly, 1996; Man et al., 2010; US EPA, 2002).

The carcinogenic risk for adults was assessed by calculating the incremental lifetime cancer risk (ILCR) under the impact of BaP (AT = 72 yr = 26 280 days) (US EPA, 1989, 2002):

$$ILCR_i = ADD_i \times CSF_i \times \sqrt[3]{BW/70}, \quad (7)$$

where CSF<sub>i</sub> is the cancer slope factor (mg/kg per day) for different pathways of dust particles into human body (*i* = ingest, dermal, inhal):  $CSF_{\text{ingest}} = 7.3$ ,  $CSF_{\text{inhal}} = 3.85$ ,  $CSF_{\text{dermal}} = 25$  (Knafla et al., 2006; Peng et al., 2011; Yang et al., 2014). The total carcinogenic risk (TR) under the influence of BaP arriving in various ways was determined as the sum of individual risks:

$$TR = \sum ILCR_i \quad (8)$$

Indicators ILCR<sub>i</sub> and TR are graded into five levels (Fryer et al., 2006; US EPA, 1989): very low (< 10<sup>-6</sup>), low (10<sup>-6</sup>–10<sup>-5</sup>), medium (10<sup>-5</sup>–10<sup>-4</sup>), high (10<sup>-4</sup>–10<sup>-3</sup>), and very high (> 10<sup>-3</sup>).

**Table 3** Mean, minimum and maximum concentrations (mg/kg), and environmental hazard of BaP in the dust on different types of Moscow roads and parking lots in courtyards (summer 2017)

Roads (number of samples)	Mean $\pm$ $\sigma$	Min	Max	$C_v$ , % <sup>a</sup>	$K_h$
MRR (19)	0.26 $\pm$ 0.20	0.030	0.91	77	13.1
TRR (7)	0.14 $\pm$ 0.11	0.045	0.33	81	7.1
Major radial highways (17)	0.17 $\pm$ 0.98	0.022	0.36	58	8.5
Large roads (45)	0.29 $\pm$ 0.19	0.026	0.77	68	14.4
Medium roads (42)	0.25 $\pm$ 0.13	0.042	0.56	54	12.3
Small roads (29)	0.22 $\pm$ 0.13	0.036	0.56	59	10.8
Courtyards (33)	0.37 $\pm$ 0.21	0.101	1.02	57	18.6
All roads (193)	0.26 $\pm$ 0.18	0.022	1.02	67	13.2

<sup>a</sup> $C_v$  is the coefficient of variation

<sup>b</sup> $K_h$  is the environmental hazard coefficient

## Results and discussion

### *The contents and spatial distribution of BaP in road dust*

The mean BaP content in the road dust of Moscow is 0.26 mg/kg (Table 3, Table S3 in Supplementary materials), which is almost 53 times higher than the background level (0.005 mg/kg) in the natural topsoils (Umbric Albeluvisols) of the Meshchera lowland, 50 km east of the city (Kasimov et al., 2017), the level in postagrogenic soils (0.005 mg/kg) in the east of Moscow (Kasimov et al., 2017), and the level in natural soils of the Losinyi Ostrov National Park (0.008 mg/kg) in the northeast of Moscow (Zavgorodnyaya et al., 2019). In the soils of forest parks, which fall under the influence of industrial facilities and transport, the BaP content is only 1.5–1.6 times lower than that in the road dust of Moscow and averages 0.16 mg/kg for the eastern industrial part of the city with variation from 0 to 0.80 mg/kg (Kasimov et al., 2017). In Moscow's northeastern and northern parts, the BaP content in the dust of forest parks averages 0.17 mg/kg with variation from 0.04 to 0.49 mg/kg. The BaP content in soil fractions < 1  $\mu$ m and 1–2  $\mu$ m is higher (0.27 mg/kg and 0.45 mg/kg, respectively) than that in road dust because of the high sorption capacity of clay particles (Kogut et al., 2006). Comparison of BaP concentrations in road dust with the level in the background and urban soils is carried out quite often (Men et al., 2020) since there is no background analog for road dust (all roads are of anthropogenic origin), and soils are an important source of road dust material and its PM<sub>10</sub> particles in Moscow (Vlasov et al., 2021) and other cities (Ramírez et al., 2019).

The highest content of BaP was determined in road dust from courtyards in residential blocks (mean, 0.37 mg/kg; maximum, 1.02 mg/kg) (Table 3). This is due to the impact of organized and unorganized car parking, low vehicle speeds, and frequent vehicle maneuvers in courtyards. In addition, the accumulation of BaP can increase in specific “trap wells” in courtyards, where the velocity of airflows decreases and more active fallout of aerosols takes place (Kosheleva et al., 2018). Among different types of roads, road dust is most contaminated with BaP on large roads and the MRR with the high traffic intensity and a large number of trucks. On the contrary, in the road dust of medium and small roads, the BaP content is lower because of lower traffic intensity induced by public transport and numerous traffic lights and turns, which increase the number of maneuvers and contribute to traffic

congestion. The least contaminated is the road dust from radial highways and TRR because of the absence of traffic lights and regular renewal of the dust during sweeping and washing of the roadbed by city services.

Thus, the environmental hazard of BaP pollution is maximal in courtyards with parking lots (mean  $K_h$  = 18.8, maximum 51), the second place belongs to major radial highways (mean  $K_h$  = 15, maximum 33.5), and road dust from the MRR ranks third (mean  $K_h$  = 13, maximum 40.5) (Table 3). The share of dust sampling points, in which  $K_h$  exceeds 10, on different types of roads decreases in the following order: courtyards with parking lots (79%) > MRR (63%) > medium roads (60%) > large roads (57%) > small roads (48%) > radial highways (35%) > TRR (29%). The points with the highest contamination ( $K_h$  > 30) are found in courtyards with parking lots (12% of the total number of sampling points in courtyards), on major radial highways (7%), and the MRR (5%) (Fig. 4).

The distribution of BaP in road dust of Moscow is uneven; the highest mean contents are typical for the Northern, Southeastern, Eastern, Central, and Southern administrative districts (Fig. 5), where traffic jams are frequent and large industrial facilities are located. Waste incineration plants are located in the Eastern, Southern, and on the border of the Northern and Northeastern districts. Many heat power plants are located in the Southern district and on the border of Southern and Southwestern districts. The maximum content of BaP (1.02 mg/kg) in the road dust exceeding the background level in Umbric Albeluvisols by more than 200 times was found in the Central district, where the density of the road network is higher than in other districts of Moscow, and the minimum content (0.022 mg/kg), in the Southern district. The lowest mean BaP content (0.10 mg/kg) was in the road dust from the Southeastern district. We obtained a value close to the previously reported (0.13 mg/kg) for this area (Karpuhin et al., 2017).

On most of Moscow's highways, a hazardous environmental situation has developed with an excess of the MPC for BaP by 13–15 times. The maximum excesses with the coefficient of environmental hazard  $K_h$  = 30–50 are observed near large industrial zones within the TRR and the area between the TRR and the Moscow Central Circle railroad (Table 3). Only the Southeastern district is characterized by a low excess of the BaP content in the road dust relative to the MPC (on average, by 2.2 times), which can be explained by the predominance of volatile low-molecular-weight PAHs (naphthalene homologs) in the emissions of the oil refinery. According to the per-



**Fig. 4** Percent of road dust samples with different levels of  $K_h$  in the districts and on different types of roads. The decoding of the designations of the administrative districts is given in the caption to Fig. 1.

Roads: MRR is Moscow Ring Road, TRR is Third Ring Road, RH is radial highways, LR is large roads, MR is medium roads, SR is small roads, YA is yards with parking lots

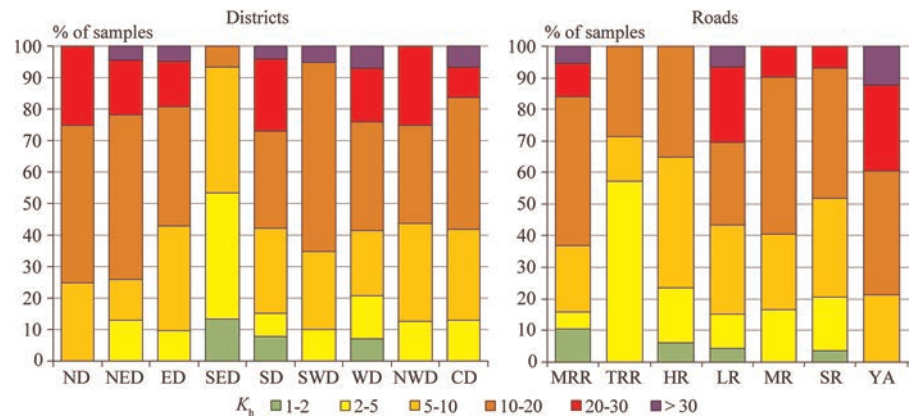
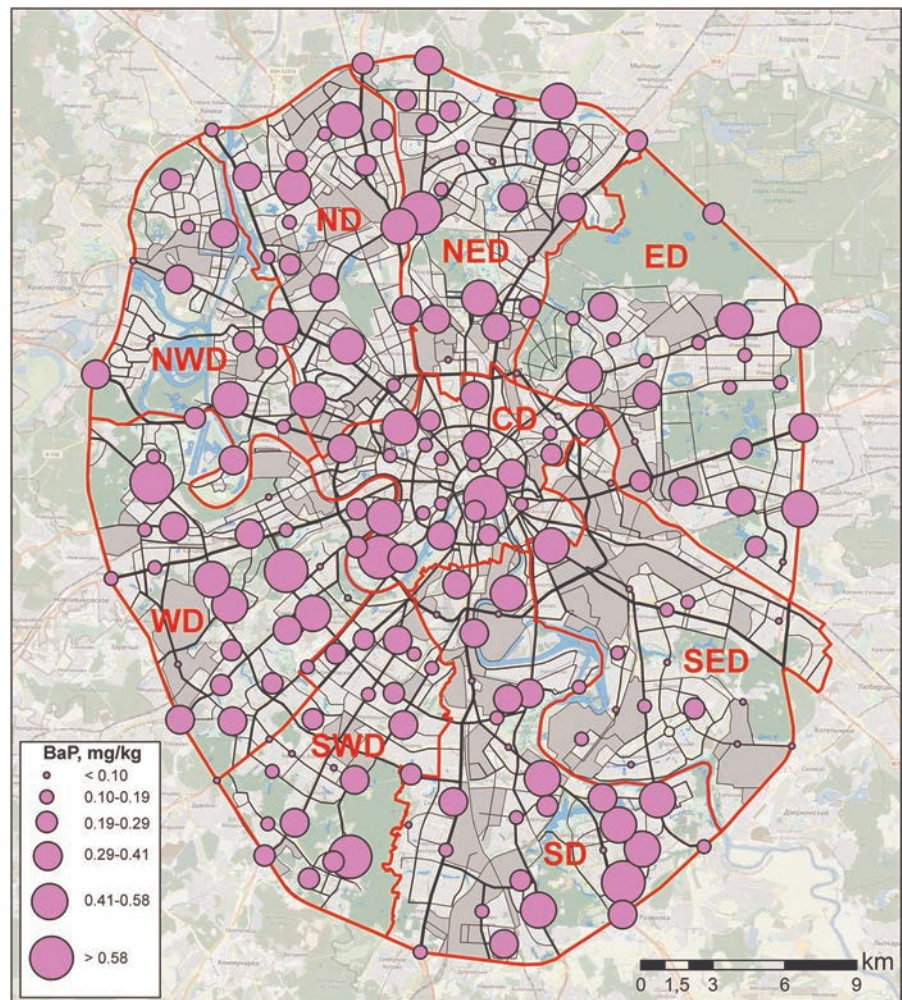


**Fig. 5** Distribution of BaP in road dust of Moscow (summer 2017)



centage of dust sampling points, in which  $K_h$  exceeds 10, relative to the total number of sampling points (Fig. 4), the districts of Moscow can be arranged into the following sequence: ND (75%) > SED (74%) > SWD (65%) > WD (59%) > CD and SD (58%) > ED (57%) > NWD (56%) > SED (7%). The most polluted points with  $K_h > 30$  were found in WD (7% of samples), CD (6%), ED and SWD (5%), and SED and NWD (4%).

#### Comparison of BaP contents in road dust and other components of Moscow environment

Since there were no previous assessments of road dust pollution in Moscow with BaP, it was impossible to understand what “place” in terms of pollution level road

dust occupies among other environments of the city. This is important because it is not clear whether further detailed studies on the distribution of BaP and other PAHs in road dust are needed, or research needs to be focused on other environments to assess public health risks. So, the chemical composition of road dust as an indicator of urban pollution can be assessed by comparing it with the composition of atmospheric precipitation in the form of snow and rain, soils, and bottom sediments in water-courses and reservoirs.

#### Precipitation

The fallout of PAHs with snowfalls onto the earth surface near roads in Moscow is 3–6 times higher than that in the recreational area and residential blocks (Zavgorod-



nyaya et al., 2019) (Fig. 6, Table S3 in Supplementary materials). The BaP concentration in the filtrate of melted snow near major roads often exceeds the MPC for water (0.005 mg/L) (Mazur et al., 2021), reaching 0.003 mg/kg to 0.140 mg/kg near major highways (Khaustov & Redina, 2019), and 0.005–0.493 mg/L near the MRR (Lebedev et al., 2012). The insoluble phase in the city's snow (dust component of the snow) accounts for about 90% of the total BaP content (Galitskaya & Rumyantseva, 2012). In the dust component of snow of the high-rise residential, agricultural, and recreational areas, the BaP content is slightly lower than that in road dust. In the low-rise and middle-rise residential areas and near roads it rises up to 0.60 mg/kg, 1.22 mg/kg, and 5.73 mg/kg, respectively, which is several times higher than in road dust (Kasimov et al., 2017).

In spring, the BaP concentration in the rainwater of Moscow varies within 0.0006–0.03 mg/L and, in most cases, exceeds the MPC for water (Polyakova et al., 2018). High correlation coefficients between the contents of BaP and pyrene, fluoranthene, chrysene, benzo[*a*]anthracene, indeno[*1,2,3-c,d*]pyrene, and benzo[*g,h,i*]perylene in atmospheric aerosols of Moscow indicate the supply of PAHs with emissions from com-

bustion of natural gas and the operation of domestic heating plants together with emissions from combustion of gasoline and diesel fuels by vehicles (Popovichcheva et al., 2020).

### Urban soils

According to the long-term monitoring data, the BaP content in the soils of different land-use zones of Moscow averages 0.02–0.04 mg/kg and varies from 0.003 to 2.30 mg/kg (Kosheleva & Tsykhman, 2018; Kul'bachevskii, 2020), which is generally less than that in the road dust. However, most publications provide averaged data on the BaP content in the soils of several land-use zones, including slightly polluted recreational zones, which underestimates the BaP pollution of urban soils. According to these estimates, the average BaP content in soils is 0.023 mg/kg in the south of the city (Maksimova et al., 2014), 0.043 mg/kg in the northeast (Namestnikova, 2017), and 0.080 mg/kg in the southeast (Karpuhin et al., 2017), though averages of 0.115–0.125 mg/kg in different parts of the city have also been reported (Agapkina et al., 2007; Belinskaya et al., 2015).

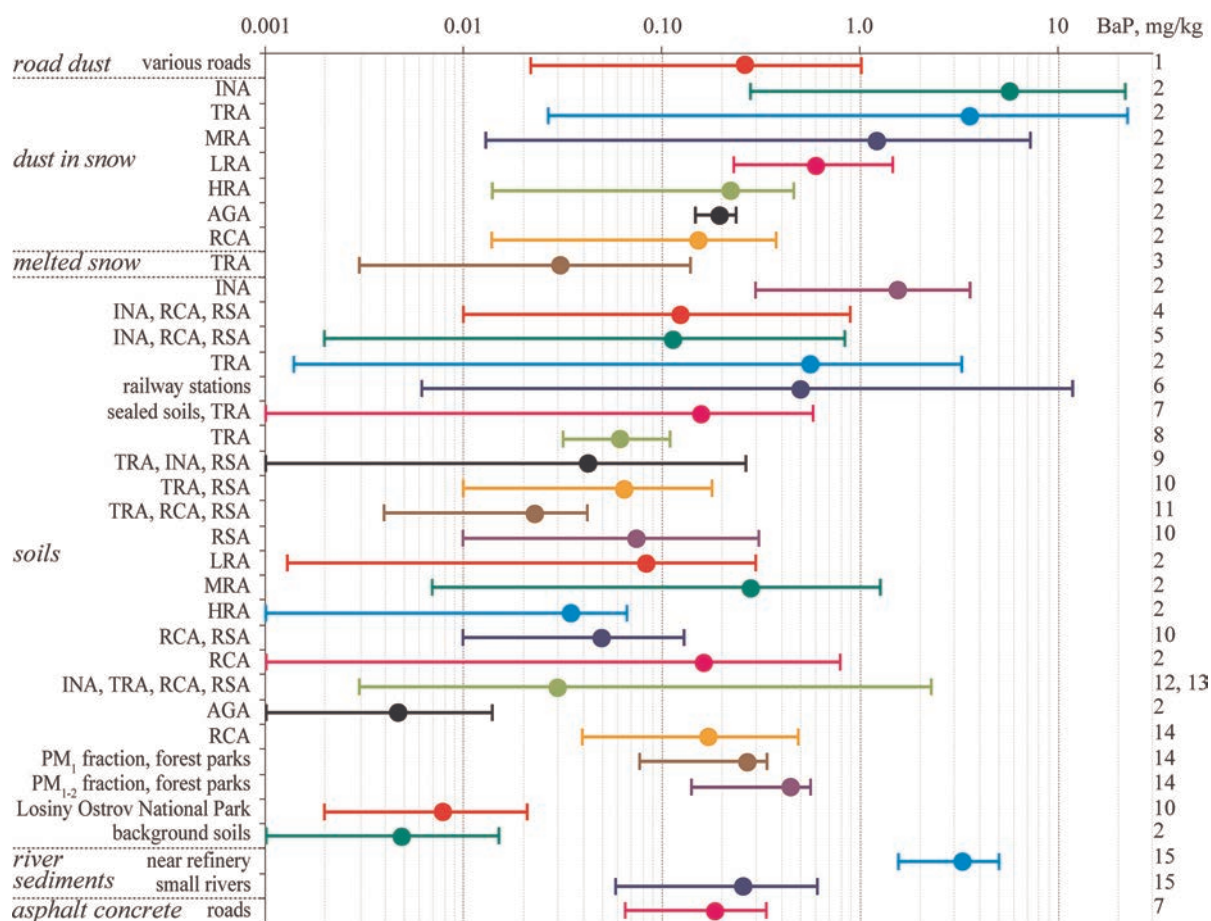


**Fig. 6** Contents of BaP in the urban environments of Moscow. Lines indicate the ranges, and bubbles indicate the mean concentrations. Information on the components of the urban environment and land-use areas (INA is industrial, TRA is traffic, RSA is residential, LRA is lowrise residential, MRA is medium-rise residential, HRA is high-rise residential, AGA is agricultural, RCA is recreational) are indicated in the left columns. The numbers in the right column indicate reference sources: 1—this study; 2—Kasimov et al. (2017); 3—Khaustov and Redina (2019); 4—Belinskaya et al. (2015); 5—Agapkina et al. (2007); 6—Makarov (2014); 7—Nikiforova et al. (2019); 8—Nikolaeva et al. (2017); 9—Namestnikova (2017); 10—Zavgorodnyaya et al. (2019); 11—Maksimova et al. (2014); 12—Kul'bachevskii (2020); 13—Kosheleva and Tsykhman (2018); 14—Kogut et al. (2006); 15—Kramer and Tikhonova (2015)

In soils of the residential zone, the BaP content is varying from 0.035 mg/kg in new high-rise residential areas to 0.075 mg/kg and 0.084 mg/kg in the densely built-up and low-rise residential areas (Kasimov et al., 2017; Zavgorodnyaya et al., 2019). These values are almost three times lower than the BaP content in road dust. However, in old medium-rise residential blocks, where a large number of people who own vehicles live for a long time, the BaP content in soils increases to an average of 0.28 mg/kg (Kasimov et al., 2017), which is comparable to its content in road dust.

In the soils of the traffic zone, the highest concentrations of PAHs are observed within 30–50 m from roads, which indicates a significant supply of PAHs from roads, especially in densely built-up areas (Nikolaeva et al., 2017; Zavgorodnyaya et al., 2019). This is confirmed by a threefold increase in the ratio of BaP to benzo[*g,h,i*]perylene in urban soils as compared to undisturbed soils of forest parks (Zavgorodnyaya et al., 2019). In the soils of the traffic zone in a 50-m strip along the roads, the BaP content averages 0.062–0.065 mg/kg (Nikolaeva et al., 2017; Zavgorodnyaya et al., 2019), increasing to 0.57 mg/kg within few meters from major highways and ranging from 0.001 to 3.28 mg/kg (Kasimov et al., 2017), which is twice as more as in the road dust. In the traffic zone near large railway stations, the BaP content in soils varies from 0.006 to 11.9 mg/kg with an average of 0.50 mg/kg (Makarov, 2014), which is almost two times higher than in the road dust.

In industrial zones, a significant source of BaP is emissions from enterprises of various industries; therefore, the average concentration of BaP in soils is 1.56 mg/kg varying from 0.30 to 3.61 mg/kg, which is higher than in the traffic zone (Kasimov et al., 2017) and is almost six times higher than in road dust.

A more intense accumulation of BaP in roadside soils compared to road dust was previously found in some other cities (Bezberdaya et al., 2022) and could be associated with increased organic matter content in soils treated with peat-compost mixtures, contributing to the active fixation of polyarenes on the geochemical sorption barrier (Kosheleva & Nikiforova, 2011). In addition, soils accumulate BaP for decades, whereas the accumulation time in road dust is limited to a few days or weeks in the warm season because the dust material is regularly renewed due to its partial blowing and road cleaning by communal services. The road surface provides an additional supply of BaP to soils and road dust. The average BaP content in the asphalt concrete pavement of Moscow is 0.19 mg/kg with a variation from 0.066 to 0.34 mg/kg, and its content in sealed soils under the asphalt pavement averages 0.16 mg/kg, increasing to 0.51 mg/kg in some places (Nikiforova et al., 2019), which is about 1.5 times lower than in the road dust.

With an increase in the number of benzene rings, the rate of PAH biodegradation decreases (Patel et al., 2020); therefore, the concentration of highmolecular-weight BaP during its long-term accumulation in soils is 2.5 times higher than in melted snow, which accumulates BaP during several cold months (Zavgorodnyaya et al., 2019). However, at the first stages of the operation of new sources of BaP, and owing to the active replacement of contaminated soil material with a cleaner one, soils become relatively depleted (four–seven times) in BaP compared to the dust component of snow (Kasimov et al., 2017).

### **Bottom sediments**

When particles contaminated with BaP enter the watercourses, they accumulate actively in the bottom sediments of small rivers. Thus, in bottom sediments of the Los' River in the Losiny Ostrov National Park in the northeast of Moscow, the BaP content is 0.059 mg/kg; in bottom sediments of the Nishchenka River in its southeastern part, it increases from 1.58 to 5.05 mg/kg along the river course, which is due to the strong industrial impact, including that of the old refinery located near the river (Kramer & Tikhonova, 2015). Due to low solubility in water, BaP molecules migrate mainly together with fine particles as part of sorption organic and organomineral complexes (Kogut et al., 2006). Therefore, despite the fairly high levels in soils and road dust, BaP in the Moskva River virtually does not migrate in dissolved form (Eremina et al., 2016). In bottom sediments of small rivers of Moscow—the Los', Kotlovka, Businka, and Tarakanovka—the mean BaP content is 0.26 mg/kg with a variation from 0.059 to 0.61 mg/kg, which is close to its content in road dust (Kramer & Tikhonova, 2015) and attests to a significant role of emissions from vehicles and washing off road dust in the pollution of water bodies in the city.

So, the BaP content in Moscow road dust is, on average, several times lower than that in winter atmospheric precipitation and is close to that in the soils of most land-use zones and bottom sediments of watercourses of the city. This is due to the supply of dust contaminated with BaP both from the atmosphere and from the blown out soil particles. Lower levels of BaP in road dust and soils compared to snow are due to a higher degradation rate of BaP in the warm season, the removal of contaminated dust material from roads by communal services, and the addition of clean material to the urban soils.

### **Factors of BaP accumulation in road dust**

The role of various factors of BaP accumulation in road dust was determined using the method of regression trees, which makes it possible to estimate the BaP content under different combinations of influencing factors according to the dendrogram. To construct it, the following groups of factors were used: (1) physicochemical properties of dust (Table S2, Supplementary materials); (2) the level of anthropogenic load, determined by the type of road and its allocation within a particular part of the city (administrative districts) as well as the geometry of street canyons (its length *L*, height *H*, width *W*, *H/W* ratio, and orientation of the canyon  $\theta$  relative to the cardinal points). The inclusion of physicochemical properties among the factors in regression analysis is reasonable, since organic matter, its composition and structure, as well as the presence of clay minerals and fine particle fractions (especially PM<sub>10</sub> and PM<sub>2</sub> due to the large surface area, negative charge, and high content of organic matter), play a significant role in the accumulation of PAHs and BaP; the degradation of PAHs depends on the pH and EC values, which determine the activity of microbial communities (Gennadiev et al., 2015; Gabarrón et al., 2017b; Dehghani et al., 2018; Emoyan et al., 2018). In general, physicochemical properties of road dust in Moscow (Text S1, Supplementary materials) fit into the range of values typical for other cities of the world: pH 7–9, C<sub>org</sub> 1–17%, EC 100–2800  $\mu\text{S}/\text{cm}$  (Abbasi et al.,



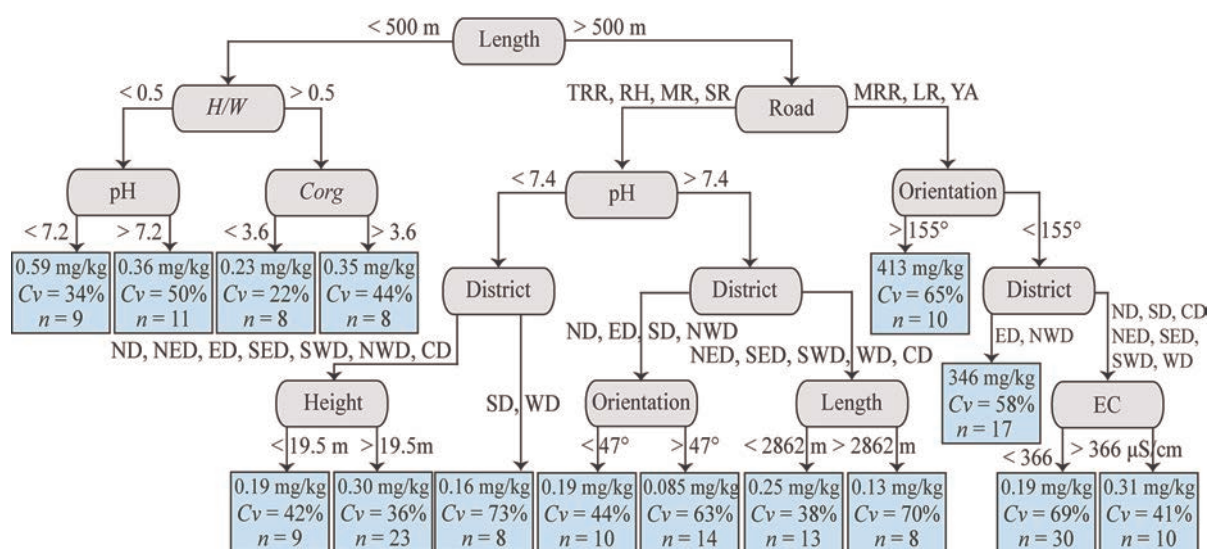


**Fig. 7** Factors of BaP accumulation in road dust of administrative districts in Moscow. The decoding of the designations of the administrative districts is given in the caption to Fig. 1, the types of the roads—in Fig. 4

2017; Acosta et al., 2011; Bartkowiak et al., 2017; Dong et al., 2020; Gabarrón et al., 2017a, 2017b; Gelhardt et al., 2021; Padoan et al., 2017; Sutherland et al., 2012; Wu & Lu, 2018). Other factors used in regression trees are analyzed above.

The results of regression analysis made it possible to determine the threshold values of the influencing factors and showed a significant role of the geometry of street canyons in the accumulation of BaP in road dust (Fig. 7). With a canyon length  $L < 500$  m, which is typical for courtyards with parking lots, the BaP content in road dust is maximum, on average, 0.39 mg/kg. In relatively wide street canyons ( $H/W < 0.5$ ), BaP accumulation in road dust is 1.6 times more intense than in narrow canyons. This can be explained by a larger number of cars in wide canyons and the protective role of buildings in narrow canyons that act as barriers preventing air flows contaminated with BaP from entering the courtyards. Previously, an inverse relationship was revealed; air pollution in canyons with high  $H/W$  values was higher than in canyons with low  $H/W$  values (Merbitz et al., 2012). However, such a relationship was observed in a large street canyon with heavy traffic.

A secondary factor of BaP accumulation in short ( $L < 500$  m) and wide ( $H/W < 0.5$ ) canyons is the acid–base properties of dust; in a neutral medium, the BaP content is 1.6 times higher than in an alkaline medium, which can be explained by dust acidification by nitrogen oxides with an increase in traffic load. In short ( $L < 500$  m) and narrow ( $H/W > 0.5$ ) canyons, a positive relationship between the BaP and organic matter contents is observed, which is caused by a significant proportion of soil particles in the road dust of courtyards. The organic matter of the traffic zone mainly consists of difficultly soluble compounds, the sources of which are the asphalt pavement and emissions from the industrial sector and vehicles (Faure et al., 2000), and the influence of organic matter on the sorption of PAHs is generally known (Minkina et al., 2019).

Most of the samples (about 80%) were taken in relatively long ( $L > 500$  m) canyons, where the average concentration of BaP is 0.24 mg/kg with some differentiation by road type. On the MRR and major highways, the average BaP content reaches 0.28 mg/kg with an increase

in accumulation when the canyon is directed from north to south ( $\theta > 155^\circ$ ). With a different orientation of the canyons, various intensities of polyarene accumulation are seen in different parts of the city, as well as in dust with various EC caused by the use of DIMs (Fig. 7). An increase in EC by 1.7 times enhances the accumulation of BaP, which is confirmed by soil studies in the Eastern district of Moscow (Kosheleva & Nikiforova, 2011), as well as in Tyumen city (Konstantinova et al., 2020a).

In long ( $L > 500$  m) canyons on the TRR, radial highways, medium and small roads, as well as in short wide ( $L < 500$  m,  $H/W < 0.5$ ) canyons, pH has a noticeable effect on the BaP content in road dust; in a neutral medium ( $pH < 7.4$ ), it is 1.5 times higher than in an alkaline medium. High pH values ( $pH \geq 8$ ) are due to the input of alkalinizing materials during repair works on the roads and the laying of paving slabs (Greinert et al., 2013). A similar negative relationship between the pH value of the water extract of road dust and the BaP content was established in Tyumen (Konstantinova et al., 2020a). Moreover, the excess of the average height of the canyon  $H > 20$  m on these types of roads in all districts of Moscow, except for the Southeastern district, leads to a noticeable (1.6 times) increase in the accumulation of BaP because of the slowing down air flows in the canyons (Kauhanieni et al., 2011).

Hence, the maximum accumulation of BaP in the road dust of Moscow occurs in relatively wide ( $H/W < 0.5$ ) and short ( $L < 500$  m) canyons, and is favored by the neutral reaction of the dust typical of courtyards with parking lots, and meridional orientation of segments of major roads (MRR, radial highways) perpendicular to the direction of the prevailing winds, which impairs blowability of these segments.

#### Assessment of environmental hazard of BaP and human health risk

The health risk of the urban population is determined by the chronic average daily dose (ADD) of BaP-contaminated dust. The consumption of BaP with dust particles which enter the body of an adult and a child by different pathways varies greatly from  $2.8 \times 10^{-9}$  mg/kg



**Table 4** Average daily doses of BaP (10–5 mg/kg per day) entering the bodies of adults/children with contaminated road dust particles on the roads with different traffic intensities

District	MRR	TRR	Radial highways	Street roads			Courtyards
				Large	Medium	Small	
Oral pathway: ADD <sub>ingest</sub>							
ND	8.1/86.7	n/a	9.1/96.7	n/a	10.9/116.3	14/149.2	9.8/104.3
NED	10.8/114.8	n/a	7.9/84	17.3/184.8	6.3/66.8	6.6/69.9	12.2/129.6
ED	20.1/214	n/a	10.1/107.6	6.4/68.4	9.3/99.5	7.4/78.7	12.4/132.7
SED	5.6/59.6	5.4/58.1	7.5/79.8	4.7/49.8	3.7/39.3	3.1/33.3	4.7/49.6
SD	6.7/71.3	n/a	3/32.3	8.8/93.8	13.3/142	5.8/61.6	15.3/162.8
SWD	7.6/81.3	n/a	8.3/88.6	9.4/100.1	7.1/75.8	8.5/90.7	14.5/154.7
WD	7.7/82.1	n/a	4.6/48.8	13.2/140.9	4.4/46.5	10.3/109.6	11.8/125.4
NWD	3.5/37.8	n/a	5/53.1	9.4/100.1	11.8/126.2	6.3/66.7	12.2/129.9
CD	n/a	5.1/54.2	n/a	9.8/104.5	10.2/109.1	9.5/101.1	23/245.4
Dermal pathway: ADD <sub>dermal</sub>							
ND	14.1/105.2	n/a	15.7/117.3	n/a	18.9/141.1	24.2/181	16.9/126.6
NED	18.6/139.3	n/a	13.6/101.9	30/224.2	10.8/81.1	11.3/84.8	21/157.3
ED	34.7/259.7	n/a	17.4/130.5	11.1/83	16.1/120.7	12.8/95.5	21.5/161
SED	9.7/72.4	9.4/70.5	12.9/96.8	8.1/60.4	6.4/47.7	5.4/40.4	8/60.2
SD	11.6/86.6	n/a	5.2/39.2	15.2/113.8	23/172.3	10/74.7	26.4/197.5
SWD	13.2/98.7	n/a	14.4/107.5	16.2/121.5	12.3/91.9	14.7/110.1	25.1/187.7
WD	13.3/99.6	n/a	7.9/59.2	22.8/170.9	7.5/56.5	17.8/132.9	20.3/152.2
NWD	6.1/45.8	n/a	8.6/64.5	16.2/121.5	20.5/153.1	10.8/81	21.1/157.7
CD	n/a	8.8/65.8	n/a	16.9/126.8	17.7/132.3	16.4/122.6	39.8/297.7
Inhalation pathway: ADD <sub>inhal</sub>							
ND	0.0043/0.0178	n/a	0.0048/0.0198	n/a	0.0057/0.0239	0.0073/0.0306	0.0051/0.0214
NED	0.0056/0.0236	n/a	0.0041/0.0172	0.0091/0.0379	0.0033/0.0137	0.0034/0.0143	0.0064/0.0266
ED	0.0105/0.0439	n/a	0.0053/0.0221	0.0034/0.014	0.0049/0.0204	0.0039/0.0162	0.0065/0.0272
SED	0.0029/0.0122	0.0029/0.0119	0.0039/0.0164	0.0024/0.0102	0.0019/0.0081	0.0016/0.0068	0.0024/0.0102
SD	0.0035/0.0146	n/a	0.0016/0.0066	0.0046/0.0192	0.007/0.0291	0.003/0.0126	0.008/0.0334
SWD	0.004/0.0167	n/a	0.0044/0.0182	0.0049/0.0205	0.0037/0.0155	0.0045/0.0186	0.0076/0.0318
WD	0.004/0.0168	n/a	0.0024/0.01	0.0069/0.0289	0.0023/0.0096	0.0054/0.0225	0.0062/0.0257
NWD	0.0019/0.0078	n/a	0.0026/0.0109	0.0049/0.0205	0.0062/0.0259	0.0033/0.0137	0.0064/0.0267
CD	n/a	0.0027/0.0111	n/a	0.0051/0.0214	0.0054/0.0224	0.005/0.0207	0.0121/0.0504

Here and in Table 5, n/a denotes the absence of data. Colors (from green to red) indicate increasing ADD values for each type of road, each administrative district, and each pathway of BaP intake into human bodies

**Table 5** Total carcinogenic risk (TR) associated with traffic intensities on different roads

District	MRR	TRR	Highways	Street roads			Courtyards	Average in district
				Large	Medium	Small		
ND	$1.56 \times 10^{-3}$	n/a	$1.74 \times 10^{-3}$	n/a	$2.10 \times 10^{-3}$	$2.69 \times 10^{-3}$	$1.88 \times 10^{-3}$	$2.11 \times 10^{-3}$
NED	$2.07 \times 10^{-3}$	n/a	$1.52 \times 10^{-3}$	$3.33 \times 10^{-3}$	$1.21 \times 10^{-3}$	$1.26 \times 10^{-3}$	$2.34 \times 10^{-3}$	$2.01 \times 10^{-3}$
ED	$3.86 \times 10^{-3}$	n/a	$1.94 \times 10^{-3}$	$1.23 \times 10^{-3}$	$1.79 \times 10^{-3}$	$1.42 \times 10^{-3}$	$2.39 \times 10^{-3}$	$1.97 \times 10^{-3}$
SED	$1.08 \times 10^{-3}$	$1.05 \times 10^{-3}$	$1.44 \times 10^{-3}$	$8.98 \times 10^{-4}$	$7.09 \times 10^{-4}$	$6.01 \times 10^{-4}$	$8.96 \times 10^{-4}$	$8.25 \times 10^{-4}$
SD	$1.29 \times 10^{-3}$	n/a	$5.84 \times 10^{-4}$	$1.69 \times 10^{-3}$	$2.56 \times 10^{-3}$	$1.11 \times 10^{-3}$	$2.94 \times 10^{-3}$	$1.93 \times 10^{-3}$
SWD	$1.47 \times 10^{-3}$	n/a	$1.60 \times 10^{-3}$	$1.81 \times 10^{-3}$	$1.37 \times 10^{-3}$	$1.64 \times 10^{-3}$	$2.79 \times 10^{-3}$	$1.78 \times 10^{-3}$
WD	$1.48 \times 10^{-3}$	n/a	$8.81 \times 10^{-4}$	$2.54 \times 10^{-3}$	$8.40 \times 10^{-4}$	$1.98 \times 10^{-3}$	$2.26 \times 10^{-3}$	$1.88 \times 10^{-3}$
NWD	$6.82 \times 10^{-4}$	n/a	$9.59 \times 10^{-4}$	$1.81 \times 10^{-3}$	$2.28 \times 10^{-3}$	$1.20 \times 10^{-3}$	$2.34 \times 10^{-3}$	$1.77 \times 10^{-3}$
CD	n/a	$9.79 \times 10^{-4}$	n/a	$1.89 \times 10^{-3}$	$1.97 \times 10^{-3}$	$1.82 \times 10^{-3}$	$4.43 \times 10^{-3}$	$1.94 \times 10^{-3}$

Colors from green to red indicate a rise in the average TR value for different types of roads in each administrative district

to  $4.75 \times 10^{-3}$  mg/kg per day. The ADD values averaged for the administrative districts of Moscow decrease in the following order: ND > NED > ED > CD > SD > WD > SWD > NWD > SED.

There is also a strong differentiation of this indicator depending on the type of road (Table 4).

Ingestion of dust particles with food and while playing, walking, etc., is the main pathway of BaP intake into the bodies of both adults and children. ADD values indicate that adults and children receive 90.6% and 93.3% of BaP orally, respectively. BaP entering human bodies through skin contact is 9.3% and 6.7% of the total ADD for these two groups, respectively. Less than 0.2% of BaP is received through inhalation. The total hazard index HI is highly differentiated by administrative districts of the city with the highest average values both for adults and children in the Northern district and the lowest values in the Southeastern district (Fig. S2, Supplementary materials).

For adults, average HI values do not exceed 3.34 in all districts of Moscow, which corresponds to the mod-

erate level of health hazard. However, children are more susceptible to exposure to pollutants per unit weight because of their physiological and behavioral characteristics, such as ingestion of significant amounts of soil and dust during playing and walking outdoors, increased gastrointestinal absorption of certain substances and air consumption per unit weight, etc. (Gabarrón et al., 2017b; Qu et al., 2012). Thus, for a child, average HI values in administrative districts of Moscow vary from 3.37 to 8.62, corresponding to the moderate health hazard level. The maximum HI (28.9) was determined for courtyards in the Central district, where children are more likely to contact contaminated dust particles during walks. The lowest HI values were found in the Southeastern district, which can be explained by the predominance of volatile low-molecular weight PAHs in the refinery emissions.

Almost all values of the carcinogenic risk associated with the oral and dermal exposure ways are in the range from  $10^{-5}$  to  $10^{-3}$ , which corresponds to moderate and high risk levels; the risk associated with inhaled BaP is very low:  $10^{-9}$  to  $10^{-7}$ . Therefore, the total risk (TR) is

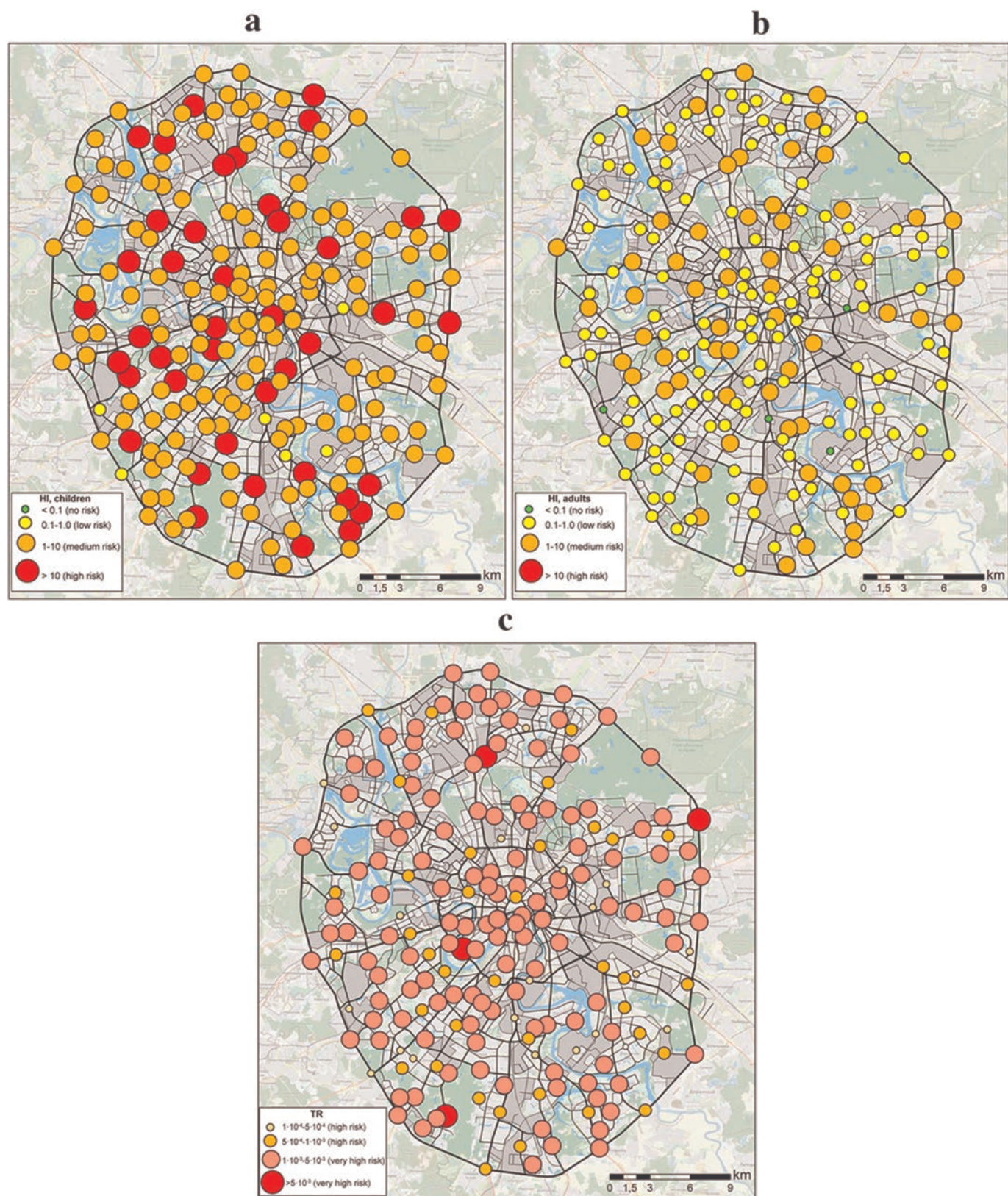


**Fig. 8** Distribution of the total hazard index HI for a children and b adults; c total carcinogenic risk TR at sampling points of Moscow road dust (summer 2017)

high and very high with  $TR > 10^{-4}$ . The highest average value of the  $TR = 4.43 \times 10^{-3}$  is in the Central district. Increased contents of PAHs in road dust and other environments lead to an increased risk of developing cancer cells, including lung, skin, and bladder cancer (Abdel-Shafy & Mansour, 2016; Armstrong et al., 1994; Boström et al., 2002; Kim et al., 2015; Zhang et al., 2020). In addition to

carcinogenic effects a direct relationship has been established between the long-term exposure to microparticles contaminated with polyarenes and the decrease in birth weight (Wilhelm et al., 2012), poor cognitive development (Edwards et al., 2010), obesity, and the risk of diarrhea (Wu et al., 2021). The contribution of different ways of entry to the total risk follows the sequence: ingestion



> skin contact > inhalation, which is consistent with the results obtained by other researchers (Alghamdi et al., 2021; Gope et al., 2018; Jiang et al., 2014; Mihankhah et al., 2020; Zhang et al., 2020).

The variation in the TR values depending on the type of roads in different districts of Moscow is given in Table 5. The highest average values are observed in the Southern, Southwestern, Northwestern, and Central administrative districts (Fig. 8) for courtyards with parking lots, which is most likely associated with the idling of cars while waiting for passengers. In the Central, Northeastern, and Western districts, maximum TR values are typical of the roads with several lanes. In the Eastern and Southeastern districts, maximum TR values are allocated to the MRR and major radial highways, respectively, due to frequent traffic congestions since many residents from the southeastern suburbs commute to work on these roads every day.

### Limitations of the study

Our results are a first assessment of risk for public health from road dust polluted with BaP in Moscow megacity based on snapshot observations during one of the seasons of the specific year. Therefore, the risk assessment results in our study have the following limitations. Firstly, the sampling represents only one season, which did not allow taking into account the inter-annual variability in the accumulation of dust on the roads. To assess seasonal differences in the level of pollution of the urban environment with BaP, a comparative analysis of pollutant concentrations in various environments, such as snow cover which characterizes pollution during the cold period, urban soils, and bottom sediments of water bodies which are indicators of long-term pollution, was carried out. For a more accurate risk assessment, further studies of the distribution of BaP in road dust in different seasons and under various meteorological conditions are required. Secondly, the study of only BaP did not make it possible to do a source apportionment study using receptor models and statistical methods such as principal component analysis or positive matrix factorization. Further expansion of the list of analyzed pollutants could remove this limitation. Thirdly, the distribution of BaP in various particle size fractions of road dust of Moscow has not yet been studied, which may affect the assessment of the risk to public health, since the ability of particles to be blown off the roadway, as well as their ability to penetrate the human body, largely depends on particle size. For a more detailed assessment of the health risk, it is necessary to determine the content of BaP in different particle size fractions of road dust. Finally, the obtained results show the risk levels averaged over various types of roads and different administrative units of the city. In the absence of knowledge about the degree of road dust pollution with BaP in Moscow, the task was to obtain the average level of contamination in order to understand whether further more detailed studies of BaP in road dust in Moscow are needed. It will be helpful to take into account the spatial variability of BaP concentrations in road dust when assessing health risks in future, for example, applying Monte Carlo simulation or using not only mean concentrations, but also the median, 90th and 95th percentiles of BaP concentrations.

### CONCLUSIONS

For the first time, the pollution levels and the spatial distribution of BaP in road dust in Moscow were determined considering the geometry of street buildings (canyon effect) and the physicochemical properties of the dust. In addition, the health risks of the adult and child population arising from BaP contamination were assessed, including the average daily dose of contaminated dust, the hazard index, and the carcinogenic risk under the influence of BaP entering the human body through dermal, ingestion, and inhalation pathways.

The average BaP content in Moscow road dust is 53 times higher than the background level in Umbric Albeluvisols and 1.6 times lower than the BaP content in dust fallout from the atmosphere. The highest contents and environmental hazard of BaP pollution with a maximum in the Central district of Moscow are confined to the courtyards with parking lots. The pollution with BaP in these places is intensified due to the formation of “trap wells” creating zones of air stagnation and deposition of aerosols. Road dust pollution with BaP depends on the type of road: large street roads and the MRR with high traffic intensity are the most polluted, while radial highways and the TRR with a low number of traffic lights are the least polluted roads.

Important factors of BaP accumulation in road dust of Moscow are geometry patterns of street canyons. The BaP content in road dust is maximum when the canyon length is less than 500 m, and relatively wide canyons accumulate BaP 1.6 times more actively than narrower street canyons. In longer canyons, road dust pollution with BaP is less pronounced, but the pollution level is not the same on different types of roads and depends on their orientation relative to the cardinal points. On the TRR, radial highways, and medium and small street roads with high (> 20 m) street canyons, there is a noticeable increase in the accumulation of BaP. The influence of the physicochemical properties of road dust and allocation in different districts of the city is manifested locally.

On most of Moscow's highways, an extremely dangerous environmental situation has developed with an excess of the MPC for BaP by 13–15 times. The maximum excess of the MPC ( $K_h$  30–50) is observed near large industrial zones within the TRR and in the territories between the TRR and the Moscow Central Circle railroad. The high content of BaP in road dust negatively affects the health of citizens. The main way of BaP intake by adults and children is oral ingestion, which accounts for more than 90% of the total BaP intake. For adults in all districts, the HI index corresponds to a low–moderate level of danger, for children, to a moderate level with a maximum in the central part of the city. The carcinogenic risk is the highest in the courtyards of the Southern, Southwestern, Northwestern, and Central districts.

The results showed the need for further study of BaP in the road dust of Moscow, seasonal dynamics of pollution and the effect of precipitation on the washing of dust from roads. The results can be useful for identifying urban areas with the most dangerous level of BaP pollution and for increasing the efficiency of road cleaning measures.



## 4. АТМОСФЕРНЫЕ ОСАДКИ И СНЕГ

### Partitioning and solubilities of metals and metalloids in spring rains in Moscow megacity\*

#### 1. INTRODUCTION

Rain plays an important role in purifying the atmospheric air by removing solid particles, metals and metalloids (MMs), and other pollutants during the warm season. At low precipitation intensity (<0.1 mm/h), more than 99% of the aerosol mass is washed out from the atmosphere during in-cloud processes (elements sorption on raindrops inside the cloud), and up to 50%–80% during below-cloud processes (washout of the aerosol solid particles in the atmospheric surface layer) (Zhang et al., 2004). The most significant factors determining the rate of atmospheric pollutant washout by rains are the sizes of the solid atmospheric particles and raindrops as well as the amount, intensity, and duration of the rainfall event (Bayramğlu Kars, 1 et al., 2018; Cizmecioglu and Muezzinoglu, 2008; Guo et al., 2015; Khan et al., 2018; Ma and Kang, 2018; Ouyang et al., 2015; Park et al., 2015; Tripathee et al., 2020; Uchiyama et al., 2017). Although research on the composition of atmospheric precipitation over long periods of time (annual and perennial) has been extensively carried out, short-term changes have been scarcely investigated (Pan et al., 2017). Urban air pollution depends on many factors such as the city functional zone (e.g., recreational, transport, industrial), parameters of street canyons, distance to the pollutant source, and others. It was reported that building development in cities changes turbulent wind-velocity fluctuations (Glazunov, 2014) and creates geochemical heterogeneity via redistributing atmospheric pollutant fluxes and forming sedimentation zones in urban soils and other deposition media (Kosheleva et al., 2018). Local maxima of air pollution and atmospheric precipitation are characteristic of regions near industrial zones and major highways. For instance, in Moscow, Europe's largest city, the average annual concentrations of atmospheric PM<sub>10</sub> near highways were 1.4 times higher than those in residential areas (Kul'bachevskii, 2019). PM<sub>10</sub> concentrations in the city were found to decrease by an average of 3.7% annually from 2005 to 2014, mostly on the weekends (Elansky et al., 2020, 2018). The heterogeneity of urban air pollution was also confirmed by data on the variations in the ionic composition of precipitation in Moscow (Yeremina et al., 2014). However, the occurrence of medium-range transport of atmospheric pollution might suggest that in megacities, rainwater contamination with MMs is only slightly larger in the city center than in the suburbs (Garnaud et al., 1999).

In rainwater, usually the soluble fraction of chemical elements is investigated because this fraction is the most reactive and highly migratory, with the capability of getting incorporated in the biological cycles, including bio, hydro, and pedogeochemical processes. However, the insoluble fraction of MMs accumulates in the surface layers of urban soils and road dust, acting as a source of secondary air pollution when particles are blown away from the surface (Cerqueira et al., 2014; Grigoratos et al., 2014; Kasimov et al., 2019b; Ma et al., 2019; Seleznev et al., 2019, 2020; Talovskaya et al., 2018, 2019). A comprehensive study of the composition of the solid and liquid phases of MMs as well as MM partitioning in rainwater provides a detailed description of pollution and may be used to control atmospheric inputs and environmental health (Guo et al., 2017). In rainwater, ecologically hazardous Cd, V, Cu, Zn, Sr, Na, and Ca are highly soluble, while the solubilities of Cr, Ni, Co, and Pb are generally considerably lower (Báez et al., 2007; Chudaeva et al., 2008; Cizmecioglu and Muezzinoglu, 2008; Garnaud et al., 1999; Kamei-Ishikawa et al., 2016; Kaya and Tuncel, 1997; Morselli et al., 2003). Al and Fe, which are the components of the coarse aerosol fraction, together with Cs, Ga, Y, Sc, and Mo, prevail in the insoluble form (Al-Momani, 2008; Báez et al., 2007; Bayramoğlu Kars and Alagha, 2004; Chudaeva et al., 2008; Kamei-Ishikawa et al., 2016; Özsoy and Örnektekin, 2009). The concentrations of MM forms in rainwater are strongly influenced by rainfall parameters (e.g., rainfall amount and duration), and by the physicochemical properties of rainwater, which determine the transition of soluble MMs to insoluble ones and vice versa. These properties include pH, concentration and the size of solid particles in rainwater, electrical conductivity (EC), cation and anion balance, and redox potential (Conko et al., 2004; Di Marco et al., 2020; Garcia et al., 2006; Kamani et al., 2014; Morselli et al., 2004; Singh et al., 2016; Tripathee et al., 2020).

Detailed studies have been conducted on the elemental composition of precipitation in many cities around the world. In Russia, considerable research attention has focused on analyzing the composition of snow cover, while much less research has been devoted to rainwater (Chudaeva et al., 2008; Elpat'evskii, 1993; Golubeva et al., 2010; Kokorin and Politov, 1991; Semenets et al., 2017; Udachin et al., 2010; Yanchenko and Yaskina, 2014). Studies of snow cover pollution in Moscow with solid particles enriched with environmentally hazardous MMs and benzo(a)pyrene were carried out in different

\* Vlasov D., Kasimov N., Eremina I., Shinkareva G., Chubarova N. // Atmospheric pollution research. 2021;12(1):255–271.

functional zones in various parts of the city; Cd, Sb, Zn, Pb, Cu, Mo, Sn, and Bi were among the main pollutants identified (Achkasov et al., 2006; Bogatyrev et al., 2018; Kasimov et al., 2017, 2012; Lebedev et al., 2012; Sokolov and Astrakhan, 1993; Vinokurov et al., 2017, 2014). There are also studies relating to polycyclic aromatic hydrocarbons, polychlorinated biphenyls, organophosphates, dialkylphthalates, phenols, alkylpyridines and other organic compounds present in the rainwater (Polyakova et al., 2018). Research on MM partitioning in rainwater in Moscow has not yet been conducted, although this is necessary to define the fate of pollutants after their deposition and understand the interrelationships between the components of the urban environment (e.g., between precipitation, soils, road dust, and surface waters).

Thus, this study was aimed to compile and analyze the first dataset of the soluble and insoluble MM fractions in the rainwater in Moscow. The experiments were conducted during the spring season at the Meteorological Observatory of Lomonosov Moscow State University (MO MSU); the spring season was selected because the most diverse meteorological conditions and levels of air pollution are usually observed in this season. The research objectives include the following: (1) study of MM partitioning in Moscow rainwater; (2) determine MM solubility in the precipitation and the factors influencing it; and (3) identify the probable sources of MMs in the precipitation.

## 2. MATERIALS AND METHODS

### 2.1. Rainwater sampling

A study on the chemical composition of atmospheric precipitation was carried out in April and May 2018, at the MO MSU (55.707°N, 37.522°E; Fig. 1), located in the MSU Botanical Garden. MO MSU is situated far from industrial pollution sources and major highways and is considered a background meteorological observatory.

Rainwater samples (15 events) were collected using a rigid-vinyl plastic funnel 80 × 80 cm, placed at a height of 2 m from the ground, atop a plastic bucket. We analyzed each rainfall event from the beginning to its end on the current or adjacent days: April 6–7th, 10–11th, 17–18th, 18–19th, 21st, 21–22nd, 25th, and 26th, as well as May 1st, 2nd, 4th, 5–6th, 17–18th, 18–19th, and 19–20th.

### 2.2. Laboratory analysis, quality assurance and quality control

pH of the rainwater samples was measured using a pH meter (Seven Compact S220; Mettler Toledo, Switzerland; accuracy:  $\pm 0.002$ ); EC was measured using an EC meter (Seven Compact Cond meter S230; Mettler Toledo, Switzerland; accuracy:  $\pm 0.5\%$ ). To determine the forms of MMs, all samples were filtered through membrane filters with a pore diameter of 0.45  $\mu\text{m}$  (EMD Milipore, USA) to separate the solid phase (filter retained



Fig. 1. Spring rains sampling site in Moscow.



the solid particles) from the liquid (filtrate) phase. Filters and filtrates were analyzed separately. The content of solid particles in rainwater ( $X$ , mg/L) was estimated based on the mass of the suspension on the filter  $m$  (mg); this was weighed using an analytical balance (Discovery DV114C; Ohaus, Switzerland; repeatability: 0.1 mg) and determined using Equation (1):

$$X = m/V \quad (1)$$

where  $V$  is the amount of the filtered rainwater (L). Concentrations of Al, As, Ba, Be, Bi, Ca, Cd, Co, Cr, Cs, Cu, Fe, K, Li, Mg, Mn, Mo, Na, Ni, Pb, Rb, Sb, Sc, Se, Sn, Sr, Th, Ti, Tl, U, V, W, Y, Zn, and Zr were determined in the laboratory of the All-Russian Research Institute of Mineral Resources named after N.M. Fedorovskii using ICPMS (mass spectrometer iCAP Qc; Thermo Fisher Scientific, USA) and ICP-AES (atomic emission spectrometer Optima-4300DV; PerkinElmer, USA) methods according to certified methods (NSAM № 499 AES/MS, 2015; NSAM № 520 AES/MS, 2017). This laboratory is accredited in the international analytical system Accreditation (AAC.A.0025), the national accreditation system (RA.RU.21III11), and complies with the requirements of the International Standards ISO Guide 34:2009 and ISO/IEC 17025:2017. It also conducts metrological examinations of measurement techniques in Russian Federation (accreditation certificate No. 01.00115–2013). The analysis was conducted using instrument blanks, method blanks, and standard reference materials. For determining soluble MMs “Trace metals in Drinking Water (TMDW)” (High-Purity Standards, USA) reference material was used. The detection limits (DLs) were as follows ( $\mu\text{g/L}$ ): Li, 0.04; Be, 0.004; Na, 60; Mg, 7.0; Al, 1.0; K, 10; Ca, 18; Sc, 1.0; Ti 0.05; V, 0.05; Cr, 0.1; Mn, 0.5; Fe, 9.0; Co, 0.006; Ni, 0.1; Cu, 0.1; Zn, 0.3; As, 0.09; Se, 0.3; Rb, 0.006; Sr, 0.2; Y, 0.006; Mo, 0.2; Zr, 0.006; Cd, 0.007; Sn, 0.009; Sb, 0.06; Cs, 0.005; Ba, 0.04; W, 0.01; Tl, 0.004; Pb, 0.03; Bi, 0.006; Th, 0.006; U, 0.007. For insoluble MMs “SGHM-2. Aluminosilicate loose sediment (GSO 3784–86)” (Vinogradov Institute of Geochemistry SB RAS, Russian Federation) reference material was used. The DLs were as follows ( $\mu\text{g/L}$ ): Li, 0.034; Be, 0.001; Na, 3.0; Mg, 0.9; Al, 9.0; K, 3.7; Ca, 10; Sc, 0.022; Ti 2.8; V, 0.05; Cr, 0.1; Mn, 0.07; Fe, 3.4; Co, 0.004; Ni, 0.17; Cu, 0.1; Zn, 0.2; As, 0.06; Se, 0.06; Rb, 0.004; Sr, 0.05; Y, 0.007; Mo, 0.003; Zr, 0.142; Cd, 0.003; Sn, 0.03; Sb, 0.002; Cs, 0.001; Ba, 0.13; W, 0.018; Tl, 0.001; Pb, 0.24; Bi, 0.001; Th, 0.002; U, 0.001. For rainwater samples, for low concentrations of MMs ( $<5$  DL) the relative standard deviation did not exceed 20%; for higher concentrations of MMs ( $>5$  DL), the relative standard deviation did not exceed 10%.

### 2.3. Data processing

To identify the probable source regions of air masses arriving at Moscow, backward trajectories were analyzed for each rain sample collection date using the HYSPLIT transport and dispersion model (Rolph et al., 2017; Stein et al., 2015). Modeling was carried out at heights of 500, 1000, and 1500 m above the Earth’s surface with an interval of 120 h from the middle of the rainfall event; this was determined by the difference between the time of its end and beginning.

Volume-weighted concentrations ( $C_w$ ) were calculated using Equation (2):

$$C_w = \sum_n^{i=1} (C_i \cdot X_i / X_s) \quad (2)$$

where  $C_i$  is the content of the soluble or insoluble fraction of the element ( $\mu\text{g/L}$ );  $X_i$  is the precipitation amount ( $\text{L/m}^2$ ) in the  $i$ -th rain event; and  $X_s$  is the precipitation amount for the entire study period ( $\text{L/m}^2$ ).

To define the predominant fraction of elements in precipitation, the share of their soluble fraction or solubility ( $K_z, \%$ ) was calculated as:

$$K_z = 100\% \cdot C_S / C_T \quad (3)$$

$$C_T = C_I + C_S \quad (4)$$

where  $C_S$  is the concentration of the soluble MM fraction,  $\mu\text{g/L}$ ;  $C_I$  is the concentration of the insoluble MM fraction,  $\mu\text{g/L}$ ; and  $C_T$  is the total content of the soluble and insoluble fractions,  $\mu\text{g/L}$ . All studied elements were divided into four groups using the following  $K_z$  scale: (1)  $>75\%$ , a sharp predominance of the soluble MM fraction; (2)  $50\%–75\%$ , presence of MMs mainly in the soluble fraction; (3)  $25\%–50\%$ , MMs present mainly in the insoluble fraction; and (4)  $<25\%$ , a sharp predominance of the insoluble MM fraction.

The contribution of anthropogenic sources to MM content in rainwater was estimated using the enrichment factor ( $EF$ ):

$$EF = (C_i / C_{AI}) / (K_i / K_{AI}) \quad (5)$$

where  $C_i$  and  $C_{AI}$  are the contents of the  $i$ -th and reference elements in the rainwater sample respectively; and  $K_i$  and  $K_{AI}$  are the concentrations of the  $i$ -th and reference elements in the upper continental crust, respectively (Rudnick and Gao, 2014). The reference element in atmospheric aerosols should ideally have no anthropogenic source. Al is most often used as a reference element; Li, Ca, Mg, Zr, Ti, Sc, Co, Fe, and Mn are much less commonly used (Basha et al., 2010; Kara et al., 2014). It is assumed that in natural processes, the ratio of the studied and reference elements remains almost permanent and is equal to the ratio in the continental crust, changing only under anthropogenic impact. Comparison with the distribution of elements in the continental crust is justified, as particulate matter in atmospheric air consists of soil and rock particles transported by wind from the Earth’s surface (Reimann and de Caritat, 2005). In our study, Al was selected as the reference element. An  $EF < 10$  indicates the natural origin of elements in the rainwater samples (mainly from the Earth’s crust).  $EF$  values from 10 to 100 denote the probability of anthropogenic element sources, whilst  $EF > 100$  signifies that elements definitely have an anthropogenic origin (Chon et al., 2015).

Statistical processing of the results was conducted using Statistica® 8 software (Statsoft/Dell, USA). To evaluate the correlation between the properties of precipitation and rainwater, and solubility of MMs, the non-parametric Spearman rank correlation coefficients  $r_s$  were calculated, with a significance level of  $p < 0.05$ . Cluster analysis was carried out to define the MM groups with similar distribution patterns in Moscow rainfall. MM grouping was carried out using the Ward’s amalgamation rule, with a measure of similarity  $d = 1 - \text{Pearson } r$ .



### 3. RESULTS AND DISCUSSION

#### 3.1. Meteorological conditions and rainfall parameters

In the beginning and middle of April, during the rainfall period, the cyclonic type of atmospheric circulation prevailed with the advection of air from the western and northern regions. On April 25–26th, a low gradient baric field was observed with a predominant air advection from the northern regions. On May 1–6th, air outflow from the south and southwest dominated, and from May 17th to 20th, air advection from the west was observed with a cyclonic type of circulation.

The average monthly meteorological parameters for April and May 2018 were analyzed relative to the measurement data of the MO MSU for 1954–2013. In 2018, the average monthly air temperature was 2–3 °C higher than the corresponding temperatures for 60 years from 1954 to 2013 (Chubarova et al., 2014). In April 2018, the average air temperature was 8.4 °C (it was 6.2 °C for 1954–2013), and in May it was 16.7 °C (it was 13.3 °C for 1954–2013); this is consistent with the general climate warming trend. Lower values of relative humidity were also noted. The precipitation amount was within the normal range; in April it was 38 L/m<sup>2</sup> compared to 41 L/m<sup>2</sup>, and in May it was 50 L/m<sup>2</sup> compared to 55 L/m<sup>2</sup> based on the long-term measurements.

Most of the rainfall events in April–May 2018 were characterized by light rains with a volume of less than 5 L/m<sup>2</sup> (Table 1). Rainfall events with a volume greater than 5 L/m<sup>2</sup> were observed on April 18–19th and 26th, 2018, as well as May 5–6th, 17–18th, 18–19th, and 19–20th, 2018. The duration of these rainfall events varied from short (less than 4 h) on April 6–7th and 21st, and May 2nd, 4th, and 5–6th to 17 h events on May 18–19th, and a 25 h event on April 17–18th. As such, rainfall intensity also changed significantly during the study duration; from 0.2 to 2.9 L/m<sup>2</sup> per hour (Table 1).

Acidity analysis highlighted a significant excess in the proportion of acid rain (with pH < 5.0) in April 2018 (66%) compared to the measurement data of the MO MSU for 1982–2017 (17%). There was lower proportion of acid rain in May 2018 (28% and 35%, respectively). All rainfall events were characterized by a pH ranging from weakly acidic to almost neutral; in the first rainfall event of the season on April 6–7th the pH recorded was 4.05, and for the rainfall event on April 21st, the pH was 6.35. The average pH of the rainwater in April and May 2018 was 5.0 and 5.2, respectively (with mean perennial values of 5.0 and 4.8). The highest EC (572 μS/cm) was detected for the first rainfall event on April 6–7th, following the winter period. In other samples, the EC varied from 21 to 217 μS/cm.

The average mineralization value for the duration of the experiment was 21.7 mg/L; this is consistent with the data of 22.8 mg/L for 1982–2017. Mineralization was dependent on the precipitation amount; it was found to be an average of 18.5 mg/L for a precipitation amount greater than 3 L/m<sup>2</sup>, and 56.1 mg/L for a precipitation amount less than 3 L/m<sup>2</sup>. However, the acidity had only differed slightly, along with the predominant cation and anion concentrations. During the experiment, Ca<sup>2+</sup> was the predominant cation in the rainwater samples (Eremina, 2019). The main source of Ca<sup>2+</sup> in the atmosphere is chemical weathering and dissolution of minerals (Gon-

zález and Aristizábal, 2012). In cities, an additional source of Ca is the construction and demolition dust (Crilley et al., 2017; Ramírez et al., 2020). The predominant anion was Cl<sup>-</sup> consistent with the observations of the last 13 years (Eremina, 2019). Weathering products of rocks, marine aerosols, and de-icing reagents were the sources of Cl<sup>-</sup> (Eremina et al., 2015).

#### 3.2. Concentrations of soluble and insoluble MMs

The contents of soluble and insoluble element fractions and the total MM concentrations in rainwater are given in Table 2. The contents of almost all MMs in April were 1.3–4.1 times higher than those in May. This was likely to be caused by a more intense input of MMs into the atmosphere from industrial sources in April due to the active heating season, which was no longer active in May. In April, grass cover had not yet developed, and as such, dust particles on roads were blown into the atmosphere; their further partial dissolution contributed to the MM content (Kylloñen et al., 2009). In spring, there was a sharp increase in the coarse particle fraction in the atmosphere (Chubarova et al., 2011). Moreover, in April, after snow melting and before streets were washed with city services, road dust particles (especially PM<sub>10</sub>, PM<sub>1</sub>, PM<sub>0.25</sub>) were found to be highly enriched with Pb, W, Sb, Cd, Cu, and other MMs (Ermolin et al., 2018; Fedotov et al., 2014; Kasimov et al., 2020; Vlasov, 2017), which were actively transported by wind from the road surface into the atmosphere. In May, the intensity of particle resuspension decreased due to road washing and precipitation. Previous research on atmospheric PM<sub>10</sub> seasonal variations in Moscow have also demonstrated that the highest PM<sub>10</sub> concentrations were observed in March–April due to snow melting and the accompanying wind transport of fine soil and de-icing reagent particles that accumulated during the winter (Elansky et al., 2018).

The highest concentrations of MMs are characteristic of the first rainfall event that occurs following a dry period (Kamani et al., 2014; Naimabadi et al., 2018; Ouyang et al., 2019). Thus, the maximum concentrations of soluble and insoluble MMs were observed in the first rainfall event after the winter period on April 6–7th, when the air masses moved mainly from southwestern (Spain, Portugal), southern, and southeastern Europe (Fig. A1).

An increase in the precipitation amount led to a decrease in the average concentrations of MMs. Typically, the dependence of MM concentrations on the precipitation amount may be described as:

$$C = C_o X^{-\beta} \quad (6)$$

where  $C$  is the concentration of a soluble or an insoluble MM or the total MM concentration in the precipitation;  $X$  is the precipitation amount; and  $C_o$  and  $\beta$  are constants (Takeda et al., 2000). The higher the  $\beta$  coefficient, also called the scavenging index (Shimamura et al., 2006), the more rapid and intensive is the chemical element washout. In Moscow, the highest  $\beta$  coefficients (>0.9) were common for elements of predominantly terrigenous (crustal) and partially anthropogenic origin (soluble Li, K, Na, Mn, U, Ca, V, Co, Cs, Zr, Sn, W, and Bi, and insoluble Na, U, Zr, Y, W, Zn, and Be). This was likely to be caused by the accumulation of these MMs by large particles, transported from the surface of soils or roads during the dry period and then quick-

**Table 1** Main parameters of rainfall in the territory of the MO MSU in April–May 2018.

Date	Precipitation	Duration of rainfall	Rainfall intensity,	Antecedent	Solid particles	pH	EC,
amount, L/m <sup>2</sup>	event, h	L/m <sup>2</sup> per hour	dry period, h	content, mg/L			μS/cm
April:							
6–7th	0.7	3.6	0.2	65	150	4.05	572
10–11th	2.4	8.1	0.3	89	45	5.05	108
17–18th	12.4	25.2	0.5	138	76	4.75	85
18–19th	5.2	9.8	0.5	0	9.2	4.65	32
21st	4.1	1.5	2.7	58	87	6.35	78
21–22nd	2.7	10.3	0.3	2	24	5.40	21
25th	2.4	6.2	0.4	56	80	4.90	119
26th	7.8	6.6	1.2	14	18	4.75	24
May:							
1st	4.3	6.9	0.7	98	75	5.35	64
2nd	1.2	0.75	1.6	31	183	5.85	217
4th	1.3	0.92	1.4	43	102	6.15	115
5–6th	5.1	2.3	2.3	12	45	5.15	61
17–18th	14.9	5.2	2.9	292	40	5.30	27
18–19th	15.4	17.4	0.9	5	6.8	4.40	29
19–20th	7.4	13.2	0.6	9	6.1	4.45	27

**Table 2** Concentrations of MMs in rainwater samples in April–May of 2018, μg/L.

MM	Soluble fraction (CS)			Insoluble fraction (CI)			Total (CT)		
	Mean <sup>a</sup>	Min.–Max. <sup>a</sup>	Cw <sup>b</sup>	Mean	Min.–Max.	Cw	Mean	Min.–Max.	Cw
Li	0.17	0.02 <sup>c</sup> -0.74	0.079	0.88	0.017 <sup>c</sup> -3.0	0.64	1.1	0.037-3.7	0.72
Be	0.023	0.002 <sup>c</sup> -0.065	0.020	0.054	0.001-0.17	0.038	0.077	0.002-0.24	0.059
Na	818	63-6550	339	367	3.2-1442	247	1185	66-7992	587
Mg	326	52-1268	178	512	12-1639	354	837	64-2907	532
Al	141	15-924	70	1946	46-6965	1370	2087	69-7889	1439
K	455	11-2392	218	681	26-2146	476	1135	68-3572	694
Ca	7840	982-37,621	3761	1188	38-3525	779	9027	1049-41,029	4539
Sc	0.5 <sup>c</sup>	0.5 <sup>c</sup> -0.5 <sup>c</sup>	0.5 <sup>c</sup>	0.40	0.011 <sup>c</sup> -1.5	0.28	0.90	0.51-2.0	0.78
Ti	0.60	0.08-2.4	0.30	139	3.4-503	96	139	3.6-506	96
V	0.82	0.06-5.5	0.38	3.8	0.091-15	2.6	4.6	0.15-20	3.0
Cr	0.60	0.16-3.5	0.30	2.3	0.16-8.7	1.6	2.9	0.32-12	1.9
Mn	26	2.0-103	13	22	0.83-66	15	48	2.9-150	29
Fe	184	38-1217	102	1970	76-6558	1407	2154	156-7775	1509
Co	0.42	0.042-2.0	0.21	0.50	0.016-1.8	0.35	0.92	0.058-3.7	0.56
Ni	0.95	0.19-4.9	0.48	1.4	0.086-5.0	0.95	2.4	0.28-9.9	1.4
Cu	13	3.1-63	8.8	5.1	0.16-13	3.9	18	4.3-76	13
Zn	66	13-284	37	12	0.30-37	7.2	78	15-304	44
As	0.18	0.11-0.62	0.12	0.060	0.03 <sup>c</sup> -0.22	0.047	0.24	0.14-0.84	0.17
Se	0.18	0.15 <sup>c</sup> -0.52	0.15	0.39	0.067-1.0	0.32	0.57	0.22-1.2	0.48
Rb	0.83	0.081-4.6	0.40	2.4	0.087-8.4	1.7	3.2	0.20-9.9	2.1
Sr	17	2.8-62	10	7.8	0.23-29	5.3	25	3.9-90	16
Y	0.13	0.013-0.83	0.067	0.55	0.004 <sup>c</sup> -1.7	0.39	0.68	0.023-2.6	0.45
Zr	0.073	0.003 <sup>c</sup> -0.36	0.041	6.6	0.071 <sup>c</sup> -23	4.5	6.7	0.074-23	4.6
Mo	0.1 <sup>c</sup>	0.1 <sup>c</sup> -0.1 <sup>c</sup>	0.1 <sup>c</sup>	0.13	0.002 <sup>c</sup> -0.60	0.078	0.23	0.10-0.70	0.18
Cd	0.15	0.037-0.53	0.095	0.021	0.002 <sup>c</sup> -0.073	0.012	0.17	0.039-0.57	0.11
Sn	0.066	0.010-0.17	0.035	0.77	0.033-2.9	0.56	0.84	0.043-3.1	0.60
Sb	5.5	1.1-16	3.2	0.25	0.019-0.94	0.17	5.8	1.1-17	3.4
Cs	0.018	0.003 <sup>c</sup> -0.071	0.010	0.081	0.002-0.24	0.060	0.099	0.005-0.31	0.070
Ba	22	6.1-51	16	22	0.46-86	15	44	9.3-132	31
W	0.074	0.014-0.45	0.036	0.93	0.009 <sup>c</sup> -4.4	0.60	1.0	0.023-4.8	0.64
Tl	0.016	0.002 <sup>c</sup> -0.051	0.010	0.016	0.001-0.050	0.011	0.031	0.003-0.10	0.021
Pb	148	23-973	112	32	1.1-76	24	180	31-1026	136
Bi	0.042	0.003 <sup>c</sup> -0.20	0.024	0.14	0.014-0.63	0.10	0.18	0.018-0.83	0.12
Th	0.017	0.003 <sup>c</sup> -0.066	0.010	0.21	0.001 <sup>c</sup> -0.60	0.15	0.22	0.004-0.67	0.17
U	0.027	0.004 <sup>c</sup> -0.14	0.013	0.076	0.001-0.22	0.054	0.10	0.004-0.35	0.067

<sup>a</sup> Mean, Min.–Max. – mean, minimum and maximum concentrations.

<sup>b</sup> Cw – volume-weighted concentrations.

<sup>c</sup> Concentration was below DL, thus for further calculations the half of it was used.

ly washed out from the atmosphere by light and short rainfall events. In Higashi (Takeda et al., 2000), Lhasa (Guo et al., 2015), Singapore (Hu and Balasubramanian, 2003), and Tokyo (Shimamura et al., 2006), high  $\beta$  values were also found mainly for elements of terrigenous origin, whereas MMs of anthropogenic origin were characterized by lower  $\beta$  coefficients. A similar dilution effect (a decrease in MM concentrations with an increase in the precipitation amount) was previously reported for many urban, rural, and remote territories (Ma and Kang, 2018; Park et al., 2015; Song and Gao, 2009; Tripathy et al., 2020).

The MM content in rainwater varies greatly depending on the intensity of the anthropogenic impact, the territory class (urban, suburban, rural, and remote areas), proximity to the sea coast, precipitation amount, season, and other factors (Table 3).

In the present study, the concentration of the soluble fractions of Cr, Ni, As, Se, and Cd were lower in Moscow as compared with those in many other cities, and were close to the concentrations of these elements in rainwaters in the suburban and rural territories, and in some cases, the background territories. Particularly high concentrations of these MMs in the rainwater were observed in industrial zones; for example, in Daya Bay located on the edge of the Pearl River Delta area, where large coal-fired thermal power plants and the petrochemical zone are situated (Wu et al., 2018). The contents of the soluble fractions of Al, V, Fe, and Co in Moscow rainwater were close to those in most other cities. Among the main pollutants, Zn, Pb, and Sb dominated. Concentrations of soluble fractions of Ba, Mn, Cu, Zn, Pb, and Sb in rainfall were greater than in many cities of the world due to the high emissions from the transport sector, including those from non-exhaustive sources, e.g., resuspension of road dust, tires and brake pads wear, abrasion of road surfaces (Grigoratos and Martini, 2015; Grivas et al., 2018; Jeong et al., 2019), and traffic jams. This is confirmed by our data on the composition of Moscow road dust (Kasimov et al., 2020; Vlasov et al., 2015).

Regarding the insoluble MM fraction, in comparison with the Mexico City (Báez et al., 2007), Ankara (Kaya and Tuncel, 1997), Mersin (Özsoy and Örnektekin, 2009), and the Mediterranean coast of Turkey near Antalya (Al-Momani et al., 1998), the contents of Al, V, Mn, Fe, Cu, Pb, Sr, and Ba in the rainwater in Moscow were higher, whilst the concentrations of Cr, Co, Ni, Zn, and Cd were lower.

Thus, spring rainfall in Moscow was an important factor in the purification of atmospheric air contaminated with the insoluble and soluble fractions of many MMs. A comparison with the element concentrations in the rainwaters of other cities showed that the levels of elements in the MO MSU data may be used as background urban levels in the city's rainwater during future studies of environmental pollution of this megacity.

### 3.3. Sources of MMs in spring rains of Moscow

#### 3.3.1. Cluster analysis

Based on the results of cluster and correlation analysis (Fig. B1), five associations of soluble MM fractions with a similar distribution pattern in spring rainfall were identified: (1) Li–Mg–Sr–Ca–Co–Zn–Ni–Cd–Cs ( $r = 0.93–0.99$ ); (2) Na–Al–V–Fe–Y–Cr–W–Cu–Pb–Se ( $r =$

$0.87–0.99$ ); (3) Zr–U–Bi–Tl–Th ( $r = 0.89–0.99$ ); (4) K–Rb ( $r = 0.97$ ); and (5) Ti–Mn–Sb–Ba ( $r = 0.91–0.97$ ). The insoluble fraction of the MMs was characterized by slightly different associations: (1) Li–Cs–Tl–Be–Y–K–Th–U–Cu ( $r = 0.91–0.99$ ); (2) Mg–Mn–Zr–Ca ( $r = 0.94–0.99$ ); (3) Na–Sr–Ti–Fe–Co–Al–Sc–V–Rb–Ba–Cr–Sn–Ni–Mo ( $r = 0.97–0.99$ ); (4) Zn–Cd–Pb ( $r = 0.72–0.98$ ); and (5) As–Sb–W–Bi ( $r = 0.90–0.96$ ). Only soluble As, Sn, and Be and suspended Se were weakly associated with other MMs.

The associations of soluble Li–Mg–Sr–Ca–Co–Zn–Ni–Cd–Cs and Na–Al–V–Fe–Y–Cr–W–Cu–Pb–Se, and insoluble Mg–Mn–Zr–Ca and Na–Sr–Ti–Fe–Co–Al–Sc–V–Rb–Ba–Cr–Sn–Ni–Mo were mainly formed through the wind transportation of de-icing reagents particles (Na, Ca, Mg), carbonate dust emissions from constructional facilities (Ca, Mg, Sr, Ti and Li), and the resuspension of urban soil and road dust particles (Al, Ti, V, Fe, Y, Co) contaminated with transport emissions (e.g., during the abrasion of metal parts of cars and road surfaces; Ba, Zn, Cd, Cr, Sn, Mo, Cu) (Adachi and Tainosho, 2004; Crilley et al., 2017; Grigoratos and Martini, 2015; Kasimov et al., 2019a, 2020; Saet et al., 1990; Vlasov et al., 2015). In spring, rainwater usually contains a large amount of solid dust particles of natural origin. This can be attributed to the large open areas of soils unoccupied by vegetation, and increased intensity of winds, which together, lead to the enrichment of rainwater with crustal elements (Pan and Wang, 2015). Another reason is the long-distance transport of soil particles from continental areas, as indicated by the presence of Al, Y, Fe, and Se in the association. For example, Se usually accumulates in fine particles (diameter of  $0.25–0.35 \mu\text{m}$ ) that can migrate for hundreds of kilometers (Gallorini, 2000). Emissions from coal-burning power plants (Ketris and Yudovich, 2005; Landing et al., 2010), marine and continental aerosols (Suess et al., 2019), as well as forest fires and other sources associated with biomass burning (De Santiago et al., 2014; Lynam et al., 2015) significantly contribute to Se content in atmospheric precipitation.

Long-distance transport, fuel burning in heating plants, and biomass burning also formed associations of soluble Zr–U–Bi–Tl–Th and K–Rb and insoluble Li–Cs–Tl–Be–Y–K–Th–U–Cu. It has been reported that Th, Tl, U, and Bi often indicate coal burning (Landing et al., 2010), as high concentrations of K, Th, Tl, Be, U, and Cu are found in coal-originated soot particles (Ketris and Yudovich, 2005). Elements of these associations may also originate from the wind transport of soil particles, where MMs are present in soil minerals (Grivas et al., 2018; Reid et al., 2005; Yu et al., 2018).

Associations of soluble Ti–Mn–Sb–Ba and insoluble Zn–Cd–Pb were mainly due to the influence of motor vehicles connected to the abrasion of tire wear (Zn, Cd, Mn, Sb), brake pads (Sb, Ba, Pb, Zn), and road surfaces (Ti, Mn) (Adachi and Tainosho, 2004; Grigoratos and Martini, 2015; Nazzari et al., 2013). The source of biogenic Mn may be plant pollen, which intensively migrates in the spring during the plant flowering season (Dikareva and Rumiantsev, 2015).

The association of insoluble As–Sb–W–Bi originated from industrial enterprises, especially incinerators (Demetriades and Birke, 2015; Saet et al., 1990), located in the southern, northern, and eastern parts of Moscow, and to a lesser extent from motor vehicle emissions.



**Table 3** Concentrations of the soluble MMs in rainfall in various regions of the world, µg/L.

Area	Class <sup>a</sup>	Al	V	Cr	Mn	Fe	Co	Ni	Cu	Zn	As	Se	Mo	Cd	Sb	Ba	Pb	Conc. <sup>b</sup>	Ref. <sup>c</sup>	
Moscow, Russia	UB	141	0.81	0.60	26	184	0.42	0.95	13	66	0.18	0.18	0.10	0.15	5.5	22	148	1	1	
Moscow, Russia	UB	70	0.38	0.30	13	102	0.21	0.48	8.8	37	0.12	0.15	0.10	0.09	3.2	16	112	2	1	
Lhasa, China	UB	130	0.31	0.43	7.7	221	1.6	0.58	1.7	14	0.64	-	-	0.03	-	-	1.6	2	2	
Higashi, Japan	UB	6.1	0.23	-	1.6	-	-	0.26	0.62	4.8	-	-	-	0.06	-	0.37	0.063	2	3	
Izmir, Turkey	UB	124	5.5	0.7	10	108	0.45	4.2	8.9	25	-	-	-	0.65	-	8.3	5.9	2	4	
Tehran, Iran	UB	456	-	1.7	-	235	-	7.1	21	81	-	-	-	0.67	-	-	70	2	5	
Shiraz, Iran	UB	430	-	1.6	24	306	-	4.1	13	63	-	-	-	-	-	12	10	1	6	
Kathmandu, Nepal	UB	145	-	1.1	5.8	171	0.69	0.49	1.3	17	-	-	-	0.07	-	-	0.98	1	7	
Dhunchu, Nepal	UB	52	-	0.2	2.2	52	0.38	1.0	0.87	9.8	-	-	-	0.06	-	-	0.91	1	7	
Lucknow, India	UB	56	7.1	9.5	6.9	69	0.11	0.74	0.37	18	-	0.06	0.17	-	-	-	1.2	1	8	
Gwangju, Republic of Korea	UB	13	-	0.06	4.6	11	-	0.28	1.7	19	-	-	-	0.09	-	-	3.1	2	9	
Montreal, Canada	UB	17	0.75	1.5	9.5	90	0.13	2.8	4.0	28	-	-	0.72	0.2	0.35	-	5.1	1	10	
Mexico City, Mexico	UB	15	4.8	0.26	8.3	-	-	3.0	-	-	-	-	-	0.37	-	-	1.6	2	11	
Tainan, Taiwan	UB	14	1.2	0.4	9.9	-	0.2	7.2	993	64	1.0	-	-	-	-	7.9	1710	1	12	
Ankara, Turkey	UB	47	0.92	0.4	-	31	-	2.2	3.7	0.02	-	-	-	8.6	-	-	3.3	2	13	
Chuncheon, Republic of Korea	UB	14	0.14	-	3.2	-	-	0.52	1.7	9.9	0.38	-	-	0.07	-	-	1.7	1.5	2	14
Mersin, Turkey	UB	6.5	-	1.0	3.2	3.2	1.3	2.6	1.6	37	-	-	-	0.5	-	1.6	5.1	2	15	
Zagreb, Croatia	UB	92	0.75	6.5	4.2	82	0.062	0.64	3.7	7.6	0.16	0.07	0.06	0.06	0.17	4.6	1.2	1	16	
Daya Bay, China	UB, CL	2800	13	16	230	1130	0.87	10	25	510	20	3.2	8.1	7.6	-	1320	40	2	17	
Istanbul, Turkey	UB, CL	7660	6.6	0.58	-	2750	0.32	0.77	1450	-	-	-	-	-	-	-	1.5	1	18	
Singapore	UB, CL	18	3.5	1.6	2.8	24	0.57	3.9	5.6	7.2	-	-	-	0.33	-	-	3.4	2	19	
Jiaozhou Bay, China	UB, CL	34	-	0.77	28	16	0.1	-	-	28	-	0.84	-	0.15	-	-	2.6	2	20	
Pensacola, Florida, USA	UB, CL	53	0.27	0.10	1.1	26	0.03	0.37	0.31	2.2	0.19	0.26	-	0.01	0.05	1.0	0.31	1	21	
Reston, Virginia, USA	SB	57	0.47	0.17	2.2	25	-	0.27	0.76	4.4	0.1	-	-	0.06	-	-	0.47	2	22	
Bangi, Malaysia	SB	18	-	-	2.4	20	-	1.6	2.4	28	-	-	-	-	-	-	2.2	1	23	
suburbs of Vladivostok, Russia	SB, CL	24	0.56	0.52	7.2	26	0.12	2.5	4.8	37	0.69	-	1.2	0.24	0.45	17	0.69	1	24	
Ajloun neighborhood, Jordan	RR	90	1.3	0.77	1.1	60	-	1.2	1.8	6.0	-	-	0.28	0.29	0.14	-	1.5	2	25	
Southeast Nigeria	RR	8.7	0.79	1.5	66	19	6.0	10	5.7	118	0.56	-	-	0.67	-	22	13	1	26	
Sakhalin Island, Russia	RR, CL	13	0.26	0.24	5.3	18	0.11	0.69	1.3	22	0.38	-	0.8	0.08	0.42	6.1	0.56	1	24	
20 km west of Antalya, Turkey	RR, CL	73	-	3.7	-	-	-	11	3.1	124	0.02	0.27	-	4.3	0.19	-	6.4	1	27	
Mount Everest, northern slope (4276 m)	B	2.9	0.02	0.05	0.6	4.6	0.03	0.15	0.06	0.47	0.04	-	0.01	0.005	-	-	0.036	1	28	

<sup>a</sup> Class: UB – urban areas, SB – suburban areas, CL – coastal territories, RR – rural areas, BG – remote (background) areas.

<sup>b</sup> Conc.: 1 – mean values, 2 – volume-weighted concentrations. Dash means no data available.

<sup>c</sup> Ref.: 1 – our data; 2 – (Guo et al., 2015); 3 – (Takeda et al., 2000); 4 – (Yatkin et al., 2016); 5 – (Kamami et al., 2014); 6 – (Mirzaei et al., 2018); 7 – (Tripathee et al., 2014); 8 – (Singh et al., 2007); 9 – (Chon et al., 2015); 10 – (Poissant et al., 1994); 11 – (Báez et al., 2007); 12 – (Cheng and You, 2010); 13 – (Kaya and Tuncel, 1997); 14 – (Kim et al., 2012); 15 – (Özsoy and Örnektekin, 2009); 16 – (Orlović-Leko et al., 2020); 17 – (Wu et al., 2018); 18 – (Uygur et al., 2010); 19 – (Hu and Balasubramanian, 2003); 20 – (Xing et al., 2017); 21 – (Landing et al., 2010); 22 – (Conko et al., 2004); 23 – (Nadzir et al., 2017); 24 – (Chudaveva et al., 2008); 25 – (Al-Momani, 2008); 26 – (Nganje et al., 2015); 27 – (Al-Momani et al., 1998); 28 – (Cong et al., 2015).

### 3.3.2. Enrichment of rains with MMs

Among the main sources of pollutants in atmospheric precipitation, anthropogenic emissions, migration of marine aerosols, and continental dust, are usually considered (Song and Gao, 2009). The contribution of anthropogenic sources to the composition of rainwater in Moscow was estimated using the enrichment coefficient,  $EF$ . The average composition of seawater is sometimes used as a reference standard when calculating  $EF$ ; in this case, Na was used as an indicator element (Cheng et al., 2011). Less often, Mg or Ca are used instead of Na. The seawater reference makes it possible to estimate the contribution of anthropogenic and crustal sources to elemental content in rainwater.

In this study, the  $EF$  was calculated using the data on the average composition of seawater (Gordeev and Lisitzin, 2014) and Na as a reference element.  $EF$  values varied greatly between the chemical elements (Fig. 2). Very high  $EF$  values (106–109) were characteristic of Pb and crustal elements such as Fe, Al, Sc, Mn, Ti, and Y. This indicated a strong influence of solid particles blown from the surface to the precipitation compound. Smaller, though still significant  $EF$  values (103–107), were obtained for MMs that were primarily of anthropogenic origin: Zn, Be, Co, Cu, W, Se, Cr, Ni, Tl, V, Cd, Ba, and As.

The  $EF$  value, that was calculated relative to the average composition of the upper continental crust and Al as a reference element for Moscow rainwater, also showed considerable differences between the elements (Fig. 2). Thus, for the soluble MM fraction, this  $EF$  varied from 0.1 for Ti to 10,603 for Sb, and for the insoluble fraction, from 0.5 for Na to 657 for Se. The highest  $EF$  of the insoluble fraction was characteristic of Se, which has also been reported for other regions of the world (Shimamura et al., 2006; Xing et al., 2017). The anthropogenic origin ( $EF \geq 10$ ) was confirmed for the soluble and insoluble fractions of Sb, Pb, Cd, Zn, Cu, Bi, W, and Sn as well as the predominantly soluble fractions of Ca, Mo, Sr, As, Sc, Ba, Mn, Na, Mg, Tl, Co, Be, K, and Ni (Fig. 2). High  $EF$  values ( $>10$ ) with Al as a reference element were also found for most MMs in Tainan, Taiwan (Cheng and You, 2010), Gwangju and Taean, Republic of Korea (Chon et al., 2015; Jung et al., 2011), Lhasa, China (Guo et al., 2015), Tehran, Iran (Kamani et al., 2014), Aliaga, Turkey (Kara et al., 2014), and the southeastern part of the Atlantic Ocean (Chance et al., 2015).

Greater enrichment with the soluble fraction of MM compared to the insoluble fraction was observed in the rainwater of northern Jordan (Al-Momani et al., 2002). The main sources of these elements were motor vehicle emissions resulting from fuel combustion, tire, brake pads, and other metal vehicle parts wear, road surface abrasion, wind transport of roadside soil particles, industrial emissions, and macro-regional pollutant migration (Adachi and Tainosho, 2004; Demetriades and Birke, 2015). The latter is likely contribute significantly to the general atmospheric precipitation pollution, as the enrichment coefficients were the highest for the soluble MM fraction. This means that the elements accumulate in higher quantities in the smallest particles, which could pass through filter pores during the filtration processes. These particles may migrate over significant distances of hundreds or even thousands of kilometers, and contribute to the formation of precipitation as condensation nuclei (Ponette-Gonzalez et al., 2018; Sakata et al., 2006; Tri-

pathee et al., 2014). For example, in rainfall of Northern China, Cu, Zn, Pb, Cd, As, Se, and Tl are associated mainly with fine particles, while Na, K, Ca, Ba, Mg, Co, V, Mo, Ni, Cr, and Mn all have a bimodal distribution with concentration peaks in particles of 0.43–0.65  $\mu\text{m}$  and 4.7–5.8  $\mu\text{m}$ . In Moscow, the road dust resuspension also makes a significant contribution to the enrichment of MMs in spring rains. This is confirmed by the intensive accumulation of Zn, Cu, Pb, Cd, W, and Sn in rainwater. These elements are the indicators of motor vehicle emissions and were found in high concentrations in the Moscow road dust (Kasimov et al., 2020).

### 3.3.3. Contribution of anthropogenic, crustal, and marine sources to the concentrations of MMs in rainwater

There are several sources of each chemical element present in the atmosphere and rainfall. To quantify the contribution of anthropogenic ( $A$ ), crustal or terrigenous ( $T$ , e.g., particles of soils, rocks, that have been blown from the surface) and marine ( $M$ , e.g., ocean aerosol migration) sources to MM concentrations in atmospheric precipitation, the share of each source was calculated (Zhang et al., 2007) using the following Equations (7)–(11):

$$M = 100/EF_{Na} \quad (7)$$

$$T = 100/EF_{Al} \quad (8)$$

$$A = 100 - M - T \quad (9)$$

$$EF_{Na} = (C_i/C_{Na})/(CM_i/CM_{Na}) \quad (10)$$

$$EF_{Al} = (C_i/C_{Al})/(K_i/K_{Al}) \quad (11)$$

where  $C_i$ ,  $C_{Al}$ ,  $C_{Na}$  represent the contents of the  $i$ -th and reference elements (Al and Na) in the rainwater sample, respectively;  $K_i$  and  $K_{Al}$  are the concentrations of the  $i$ -th and reference elements (Al) in the upper continental crust (Rudnick and Gao, 2014); and  $CM_i$  and  $CM_{Na}$  are concentrations of the  $i$ -th and reference element (Na) in seawater (Gordeev and Lisitzin, 2014). The contribution of each source was calculated separately for the soluble and insoluble fractions of MMs (Fig. 3).

The soluble fraction of most MMs was characterized by a very large contribution from anthropogenic sources; this was  $>90\%$  for Sb, Pb, Se, Cd, Zn, Cu, Bi, Ca, Mo, Sc, Ba, As, W, Sr, Mn, Sn, Co, Tl, Ni, and Be. Crustal sources prevailed for lithophilic Zr, Ti ( $>99\%$ ), and Th ( $>90\%$ ). Their contribution was also significant for Cs, Fe, Y, Cr, Li, V, Rb, and U (17%–43%). Marine aerosol accounted for 1%, 2%, 6%, 7%, and 23% of Rb, Sr, K, Li, and Mg concentrations, respectively; and had a negligible effect ( $<1\%$ ) on the concentrations of other soluble elements.

For the insoluble fraction of MMs, the role of anthropogenic factors decreased because of the increase in crustal material contribution, likely due to the influence of the particles transported by wind from the soil surface and road dust resuspension (Bencharif-Madani et al., 2019; Kamani et al., 2014). Anthropogenic sources accounted for more than 90% of Se, Pb, Bi, Sb, W, Sn, more than 80% of Cu, Cd, and Zn, more than 70% of Mo, and approximately 50% of Fe. For the remaining insoluble elements, crustal sources were predominant. The

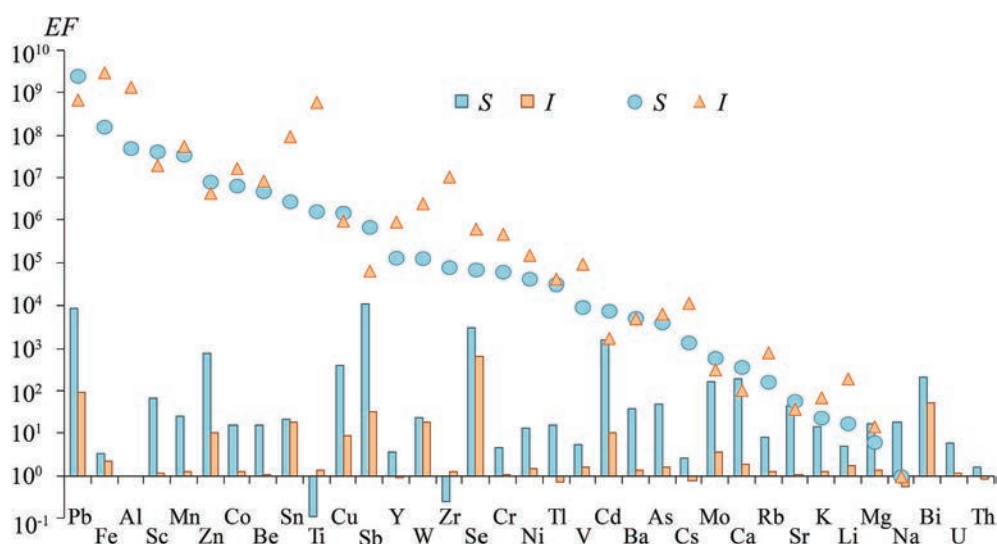


**Fig. 2.** Enrichment factors of soluble (S) and insoluble (I) MM fractions in rainwater of the MO MSU during April–May 2018. For bars, Al was used as reference element, and the average composition of the upper continental crust was used as a reference standard. For triangles and circles, Na was applied as reference element and the average composition of seawater was used as a reference standard. MMs are arranged in decreasing order of EF for soluble fractions.

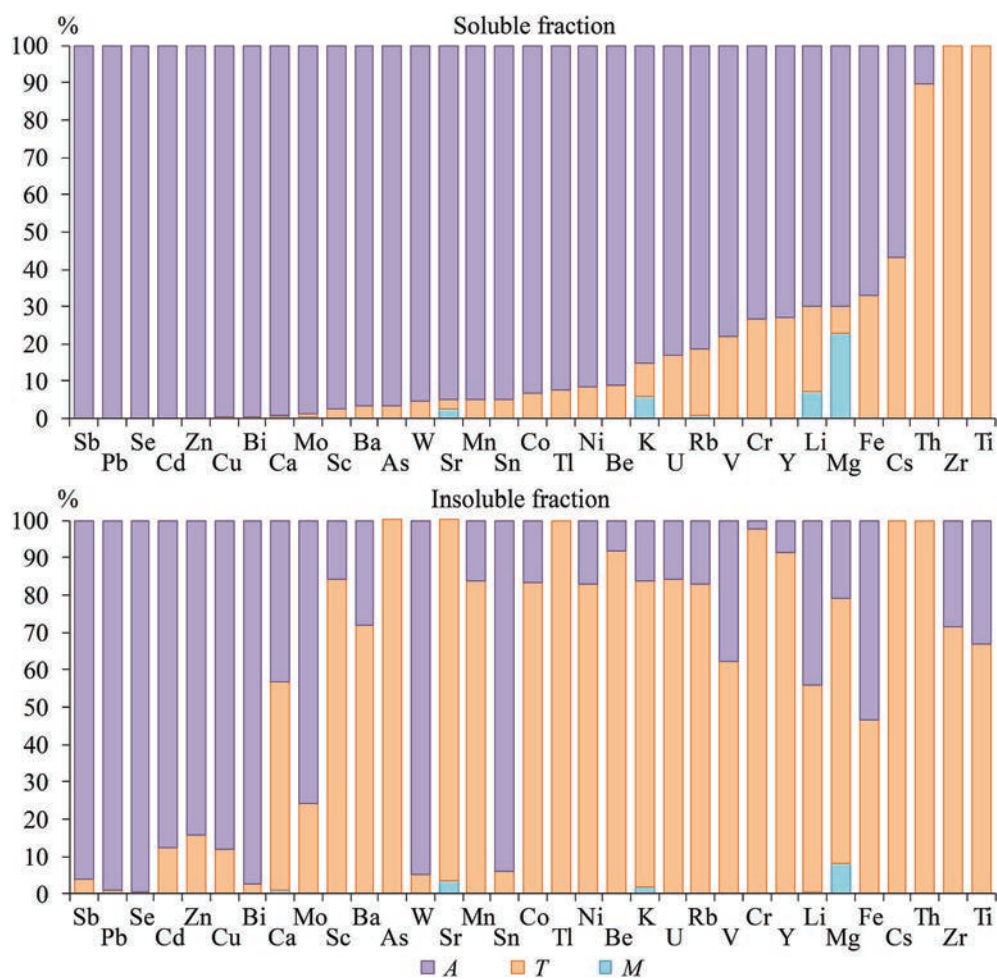


**Fig. 3.** Contribution of anthropogenic (A), crustal (T) and marine (M) sources to the contents of soluble and insoluble MM fractions. Elements are arranged in decreasing order of the anthropogenic sources contributing to the soluble MM fraction content.



contribution of ocean aerosols to the content of insoluble fractions of elements in precipitation was also insignificant (<1%) for most MMs; only for Ca, Li, K, Sr, and Mg it accounted for 1%–8%.

### 3.4. Partitioning of MMs in rainwater

#### 3.4.1. Solubilities of MMs

All MMs investigated in this study were divided into four groups based on the ratio of soluble to insoluble fractions. The first MM group, with a sharp predominance of the soluble fraction (solubility  $K_z > 75\%$ ) included Sb, Zn, Ca, and Cd (Fig. 4a). A similar pattern for Cd and Zn was observed for precipitation in Paris, France, and Bologna, Italy, the causative factors being vehicular emissions and thermal power plants (Garnaud et al., 1999; Morselli et al., 2003). Previous research on MM partitioning in snow cover of Western Moscow shows that at the MO MSU, the soluble fractions of Na, Ca, and K prevailed, whilst for Cd, Ni, Sr, Zn, and Mg the soluble fraction ranged between 55% and 70% (Vlasov et al., 2020). A higher amount of insoluble MM fractions in snow cover in comparison with rainwater was associated with long-term solid particle accumulation by snow, including dry atmospheric deposition.

In Moscow, a sharp predominance of the insoluble fraction ( $K_z < 25\%$ ) was characteristic of the second group consisting of Ti, Zr, Al, Sn,

Fe, W, Th, Li, V, Cs, Bi, and Y. This was also common for other cities, such as Mersin and Istanbul in Turkey (Başak and Alagha, 2004; Özsoy and Örnektekin, 2009) and some cities in Northern China (Pan and Wang, 2015).

An intermediate position was occupied by Cr, Rb, U, Be, Se, K, Ni, Mg, and Co, mainly found in the insoluble fraction ( $K_z 25\%$ –50%, third group); and Mn, Tl, Ba, Mo, Na, Sc, Sr, Cu, Pb, and As, with rather high proportion of the soluble fraction ( $K_z 50\%$ –75%, fourth group). The predominance of insoluble Cs and a high proportion of soluble Sr were found in wastewater during rainfall in Morioka, Japan (Kamei-Ishikawa et al., 2016). In rainfall in the Far East (Russia), the share of the soluble fraction of most elements was higher than that in the rainwater in Moscow (Chudaeva et al., 2008), most likely because of the more intensive dissolution caused by a higher precipitation volume and a lower amount of fine solid particles washed out from the atmosphere. A significant proportion of the soluble fraction of anthropogenic elements in atmospheric precipitation has also been noted in other regions of the world (Al-Momani, 2008; Báez et al., 2007; Cizmecioglu and Muezzinoglu, 2008; Connan et al., 2013; Heal et al., 2005).

#### 3.4.2. Influence of rainfall parameters on the partitioning of MMs in rainwater

A large proportion of the insoluble fraction may be attributable to two main causes. The first is associated with the MM input into the atmospheric air together with solid soil or dust particles (Bencharif-Madani et al., 2019; Padoan et al., 2016). This is typical for crustal elements and other metals, which exist mainly in weakly mobile and practically insoluble forms, such as Ti, Zr, Al, Fe, Th, Li, Cs, Bi, and Rb. Experimental data on MM leaching from the  $PM_{2.5}$  fraction to an aqueous solution as a result of the contact between solid aerosol particles with mimicking fog water showed that the solubility of Al, Cr, and

Sr was much lower than that of Cd and Rb (Di Marco et al., 2020).

The second cause is the properties of rainwater and those of the chemical elements themselves. It is known that the soluble fraction of MMs in rainwater strongly depends on acid-base conditions, redox potential, and solid particle size (Morselli et al., 2004). In general, Ba, Na, Sr, Cu, Pb, Ca, Zn, and Cd are mobile under acidic conditions and migrate in the form of cations (Kasimov et al., 2019). In the acidic environment of urban rainwater with pH 4.0–6.4 these elements may easily be transferred into the aqueous solution and therefore generally become predominant in the soluble fraction. In acidic precipitation (pH < 5), the solubility of many MMs is often much higher than in rainfall with a higher pH (Báez et al., 2007; Conko et al., 2004; Kamani et al., 2014). In Moscow rainfall, this fact was most pronounced at pH < 4.5 (Fig. 5). At the same time, pH had the greatest influence on MMs with medium solubility, as elements with high solubility were already present in the soluble fraction (Garcia et al., 2006; Kaya and Tuncel, 1997). Thus, in Moscow spring rainfall events, the largest difference in MM solubility (20%–50%) in acid rains with pH < 4.5, compared to non-acid rains with pH > 5.0, was observed for Y, Pb, U, Be, Na, Ni, Th, Cu, W, Fe, Mg, Cr, Tl, and Ba. A lower variability in solubility (5%–20%) was common for Co, Cs, Sr, Mo, Li, Zn, Sc, Al, V, Ca, Se, Cd, Mn, and the smallest (<5%) variability was observed for As, Zr, Sb, Sn, Ti, K, and Bi (Fig. 5). Low pH may be a cause of increased MM solubility and an indicator of the MM input due to anthropogenic impacts. There were two main sources of elements; (1) industrial enterprises and thermal power plants supplying sulfates, and (2) transport, which is a source of nitrates. Sulfates together with nitrates cause the acidify rainwater with its pH decreasing to 5 or lower. The acidification of rainwater in Moscow is also affected by chlorides from de-icing reagents (Eremina et al., 2015). A high temporal heterogeneity in the ratio of the MM fractions in individual rainfall events was observed in Moscow (Fig. 4b and c, Fig. 6).

If there were dry days prior to the rainfall event, the majority of elements were found in the insoluble form, associated with solid particles. A stable linear correlation between the share of soluble MM fraction and the length of the antecedent dry period was determined for Cr ( $r_s = -0.68$ ), Sc (-0.65), Mo (-0.63), Cd (-0.63), Ba (-0.60), Rb (-0.60), Na (-0.56), Th (-0.54), and V (-0.53). However, all elements except Se  $r_s$  had negative values, which means that with an increase in the duration of the antecedent dry period, the share of the soluble fraction of MMs had decreased, while that of the insoluble fraction had increased. Moreover, the influence of solid particles on the MM solubilities was shown by the stable negative linear correlation between the share of the soluble MM fraction and the solid particle content in rainwater for Sc ( $r_s = -0.91$ ), Mo (-0.89), Cd (-0.76), Ba (-0.63), Pb (-0.60), Cr (-0.58), and the negative correlation for all other MMs (Table C1). A large proportion of elements in the insoluble fraction was typical for the rainfall on April 21st where there was a predominance of air masses from southwestern Europe at 1500 m altitude, from the Atlantic Ocean at 1000 m, and from the Baltic Sea at 500 m. Other rainfall events with a high share of insoluble elements were recorded on April 17–18th, May 1st and 17–18th, 2018, when air masses arrived mainly from southeastern, central, and southern Europe and the

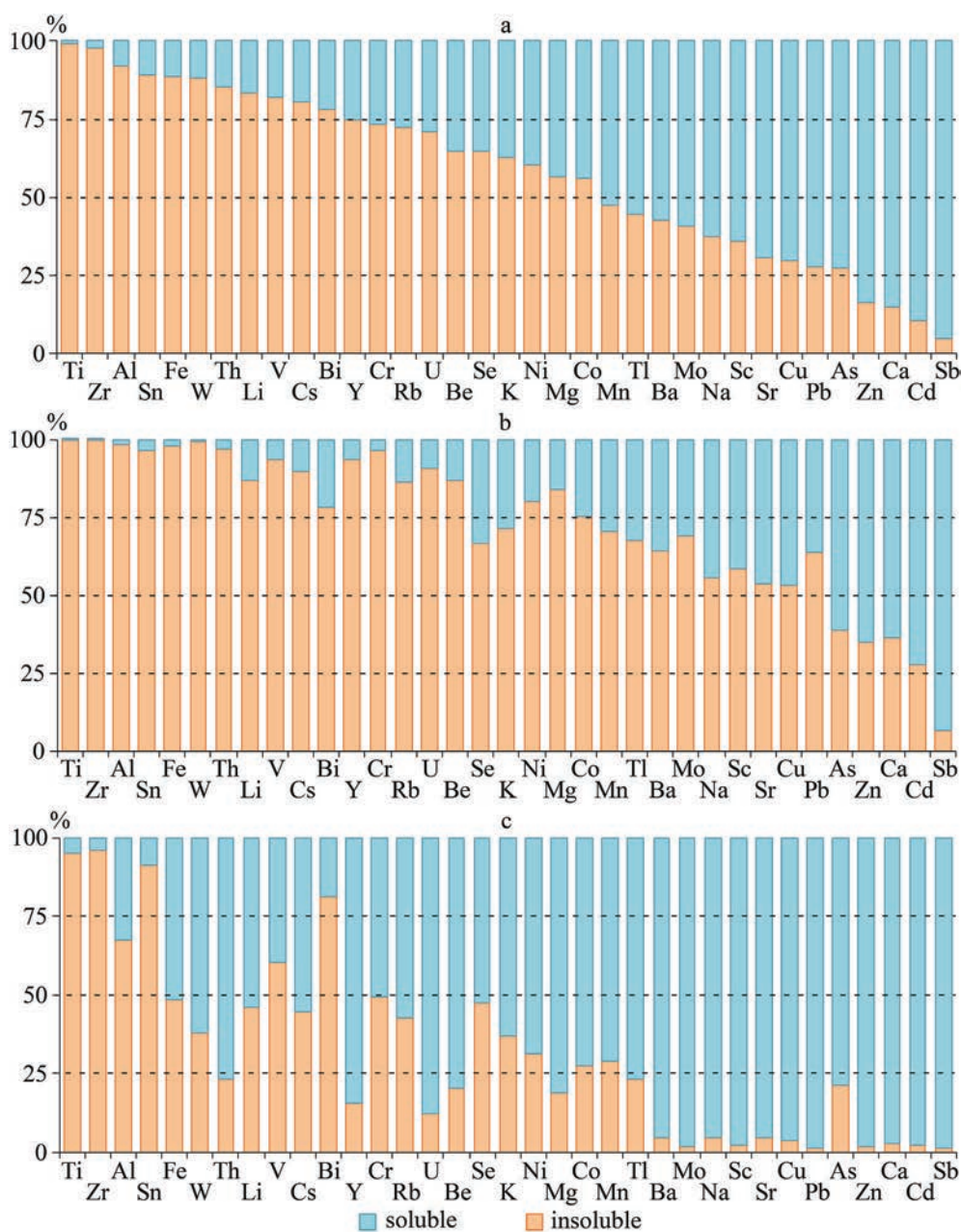


**Fig. 4.** Proportion of soluble and insoluble MM fractions in the precipitation of the MO MSU territory: (a) on average in April–May 2018; (b) April 21st, the episode with the highest proportion of insoluble MM fraction; (c) May 19–20th, the episode with the largest proportion of soluble MM fraction. MMs are arranged in order of increasing average proportion of soluble fraction for the entire observation period.

Balkans, which may have facilitated the atmospheric migration of solid particles (Fig. A1).

With prolonged rainfall (over several days in a row) on the second and subsequent days, the share of the soluble fraction of MMs sharply increased due to a decrease in the content of solid particles in the rainfall from its prolonged scavenging from the atmosphere. This was typical for rains in the territory of MO MSU on April 18–19th, 21–22nd and 26th, 2nd, 18–19th, and especially May 19–20th. Thus, the solid particle concentration in a rain sample from April 18–19th was more than eight times lower than in the samples from the previous rainfall event on April 17–18th (9 and 76 mg/L, respectively). This was especially pronounced for Pb ( $r_s$  between the rainfall event duration and the share of the soluble element fraction was 0.78), Cd (0.68), Cu

(0.62), Be (0.61), Zn (0.56), Sc (0.55), and Mo (0.55). For other MMs, although the  $r_s$  showed positive values, it was not significant. It is known that in the first episode of precipitation after a long antecedent dry period, rainfall events are enriched with MMs due to in-cloud scavenging (rainout mechanism) and the below-cloud scavenging (washout mechanism). Moreover, in subsequent events of prolonged rainfall, the below-cloud scavenging processes are weakened due to the gradual removal of particles from the atmosphere (Bayramoğlu Kars, *et al.*, 2018). This means that during the initial rainy days, an increased amount of aerosol particles precipitate from the atmosphere, and on subsequent days, the rainfall washes out smaller amounts of pollutants due to lower concentrations of aerosols remaining in the air. With an increase in the solid particle content in pre-



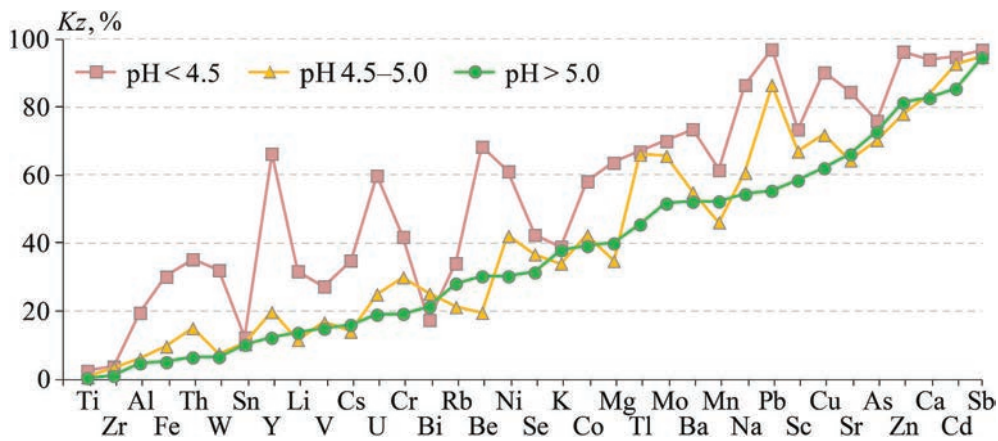


**Fig. 5.** Proportion of soluble elements fraction (or solubility, Kz) in acidic rains with pH <4.5 and pH 4.5–5.0 and non-acidic rains with pH 5.0–6.4 in the MO MSU territory in April–May 2018.

MM <sup>a</sup>	April <sup>b</sup>								May <sup>b</sup>							A <sup>c</sup>	M <sup>c</sup>	WP <sup>c</sup>
	6–7th	10–11th	17–18th	18–19th	21st	21–22nd	25th	26th	1st	2nd	4th	5–6th	17–18th	18–19th	19–20th			
Ti	0	1	0	2	0	0	0	0	0	1	0	0	0	2	5	1	1	1
Zr	2	3	1	12	0	1	1	1	1	1	1	1	1	6	4	2	2	2
Al	12	11	5	8	2	3	6	5	4	7	6	5	2	15	32	6	10	8
Sn	5	42	5	20	3	7	12	4	1	13	11	2	1	23	9	12	9	11
Fe	16	13	6	12	2	5	11	10	4	5	4	5	3	24	51	9	14	11
W	9	15	4	15	1	4	6	6	5	10	10	4	4	25	62	7	17	12
Th	10	12	4	25	3	4	7	25	4	7	12	7	3	19	77	11	18	15
Li	20	25	10	10	13	8	16	11	6	27	19	10	3	22	54	14	20	17
V	27	31	11	28	6	16	14	15	9	19	15	16	8	15	40	18	17	18
Cs	23	27	14	14	10	9	17	12	14	21	20	24	3	27	56	16	24	19
Bi	24	39	23	30	22	23	25	23	11	22	24	23	8	10	19	26	17	22
Y	32	24	18	32	7	13	20	10	11	14	14	11	6	83	84	19	32	25
Cr	29	37	14	42	4	42	18	47	6	33	15	10	8	47	50	29	24	27
Rb	15	37	12	36	14	26	13	25	18	59	33	26	12	31	57	22	34	28
U	38	41	24	28	9	12	29	19	9	24	33	18	5	54	88	25	33	29
Be	27	47	24	16	13	67	27	12	39	8	26	12	29	98	80	29	42	35
Se	48	26	69	18	34	37	25	35	22	13	37	56	28	27	53	36	34	35
K	38	48	25	58	28	38	22	32	24	67	39	36	24	17	63	36	39	37
Ni	49	48	35	28	20	22	41	66	31	57	34	17	15	66	69	38	41	40
Mg	44	50	21	52	16	37	27	39	27	55	47	46	42	67	81	36	52	43
Co	53	64	37	55	25	30	47	31	31	60	41	40	23	49	73	43	45	44
Mn	56	66	39	59	30	49	48	40	44	76	59	59	36	58	71	48	58	53
Tl	51	64	46	92	32	29	37	91	50	50	59	52	28	74	77	55	56	55
Ba	35	68	42	78	36	48	43	57	41	61	55	58	52	91	95	51	65	57
Mo	14	71	38	97	31	76	29	98	38	40	30	73	55	98	98	57	62	59
Na	82	87	56	89	44	61	49	49	27	67	54	59	37	83	95	65	60	63
Sc	25	69	44	91	42	81	47	86	52	50	47	65	63	97	98	61	67	64
Sr	68	81	54	77	46	55	64	62	50	78	75	75	70	90	95	64	76	69
Cu	83	82	74	81	47	68	73	60	66	69	51	61	54	91	96	71	70	70
Pb	95	81	86	97	36	74	81	82	74	29	33	57	59	98	99	79	64	72
As	74	89	61	72	61	72	72	76	72	87	61	68	72	76	79	72	74	73
Zn	93	94	88	49	65	88	88	87	83	81	80	85	77	98	98	82	86	84
Ca	92	92	80	91	64	80	85	79	78	91	88	90	79	94	97	83	88	85
Cd	92	95	90	98	72	95	87	96	85	80	84	91	82	95	97	91	88	89
Sb	95	98	94	98	93	92	95	92	95	97	97	97	87	98	95	96	95	95

<sup>a</sup> MM are arranged in order of increasing of the average solubility for the entire observation period.

<sup>b</sup> The metals and metalloids solubilities in precipitation: < 25%, 25–50%, 50–75%, > 75%.

<sup>c</sup> Column A contains April mean values, column M – May mean values, column WP – mean values for the whole period.

**Fig. 6.** Proportion of the soluble fraction (solubility) of MMs in the rainfall of the MO MSU in April–May 2018, reported as a percentage.

precipitation, their gradual dissolution intensifies, leading to an increase in the concentration of soluble MMs. At the same time, the rate of decrease in the concentrations of V, Ni, Zn, Pb, and Cd of anthropogenic origin during rainfall is lower, likely due to the in-cloud scavenging processes (Guo et al., 2015; Hu and Balasubramanian, 2003; Özsoy and Örnektekin, 2009; Poissant et al., 1994). Therefore, an increase in the soluble MM fraction during prolonged precipitation episodes indicates an increase in the contribution of in-cloud scavenging compared to below-cloud scavenging processes from rainfall pollution.

A similar situation depicting decreasing concentration of solid particles during prolonged rainfall was typical

for other extended periods of rainfall (Table 1). This pattern was not consistent on May 1st and 2nd, 2018. On the first day, the rainfall contained 75 mg/L of solid particles, whilst on the second day it contained 183 mg/L solid particles. This was probably due to the active departure of citizens to suburban summer cottages, causing a sharp increase in transport emissions. The second reason could be burning a large amount of charcoal and plant biomass during the holidays celebrated in Russia in early May. As a result, there was an increased amount of particulate matter in the air due to the low intensity of washout from the atmosphere together with the small precipitation amount (only 4.3 L/m<sup>2</sup> on May 1st and 1.2 L/m<sup>2</sup> on May 2nd).



During the May holidays, air advection from the south and southwest prevailed. At the same time, in the MO MSU territory, high ratios of black carbon (BC) content to the concentration of PM<sub>10</sub> in the atmospheric air were observed; this was due to long-distance transport of particles originated from biomass burning in southern Russia and western Europe on May 1st and 5–7th. The BC/PM<sub>10</sub> ratio was 0.15–0.19, while BC concentrations equaled 3–7 µg/m<sup>3</sup>. On the unpolluted days of April and May 2018, the BC/PM<sub>10</sub> ratio was 0.01–0.06, with a BC concentration <2 µg/m<sup>3</sup> (Popovicheva et al., 2020). From April 30th to May 5th increased PM<sub>10</sub> concentration in the air was measured to be approximately 34 µg/m<sup>3</sup>; however, it sharply decreased to 23 µg/m<sup>3</sup> from May 6th to 12th. This is likely due to the short and intense rains on May 2nd, 4th and 5–6th, 2018 (Chubarova et al., 2019).

On May 17–18th, the share of insoluble MM in rainfall was high due to a prolonged antecedent dry period (11 days), when, on May 13–17th, a large amount of aerosol had accumulated in the air and PM<sub>10</sub> concentrations increased to an average of 40 µg/m<sup>3</sup> (Chubarova et al., 2019).

The proportion of the soluble fraction was also affected by rainfall intensity. This was especially pronounced for Cu ( $r_s = -0.66$ ), Y ( $-0.61$ ), Zn ( $-0.58$ ), Bi ( $-0.58$ ), Fe ( $-0.57$ ), Pb ( $-0.55$ ), and Cd ( $-0.54$ ). For other MMs, the  $r_s$  was not significant, although it was negative with the exception of Mg, Sr, Mo, and Ba. This negative correlation was likely due to the fact that during heavy rainfall, an intensive washout of solid particles from the atmosphere occurred; this in turn led to an increase in the proportion of the soluble MM fraction.

#### 4. CONCLUSIONS

Spring rainfall in Moscow was characterized by a significant temporal heterogeneity of MM content and a large variability in the concentrations of soluble elements. In general, the contents of most MMs in the rainwater in April were higher than in the rainwater in May. This was attributable to the considerable contribution to the MMs from industrial sources during the winter heating season, high atmospheric aerosols pollution in April, and the dilution effect due to the increase in the precipitation amount in May.

In this study, Ti, Zr, Al, Sn, Fe, W, Th, Li, V, Cs, Bi, and Y dominated in the insoluble form, and Sb, Zn, Ca, and Cd in the soluble form in the rainwater. This indicates the high pollution risk of Zn, Cd, and Sb in the Moscow environment, as soluble pollutant fractions can easily be incorporated into the biogeochemical cycles, which should be taken into account in further ecological and geochemical urban assessments. A large share of the insoluble fraction of elements was associated with the supply of solid soil or road dust particles to the atmosphere. MM solubilities in rainfall increased with decreasing pH and increasing duration of rainfall, and declined with an increase in rainfall intensity, the length of the antecedent dry period, and the content of solid particles in rainwater. With prolonged rainfall on the second and subsequent days, the proportion of soluble fraction of almost all MMs sharply increased. This highlights the necessity of detailed analysis of air pollution by MMs during prolonged precipitation as a part of environmental monitoring. During the celebration of public holidays in Russia at the beginning of May, the proportion of insoluble MM forms increased. This was due to the sharp increase in transport emissions due to the mass departure of citizens from the city to suburban summer cottages combined with the burning of large amounts of charcoal and plant biomass during the holidays.

The enrichment of spring rainfall with a soluble MM fraction was more pronounced than with insoluble fractions because of the very large contribution (>90%) of anthropogenic sources to the content of the former for most MMs. In contrast, for the insoluble MM fraction, the influence of crustal material transported by wind from the soil surface had increased.

The concentrations of the soluble fractions of Cr, Ni, As, Se, and Cd in Moscow rainfall were lower than in many other cities of the world, and were close to the levels of these elements in the rainfall of suburban, rural, and background territories. This leads us to recommend the use of data obtained in this study as urban background values for environmental and geochemical monitoring of the entire Moscow city. For a better understanding of the seasonal variability, nature, and intensity of rainfall scavenging of the MM fractions, it is necessary to conduct longer and more detailed studies on the chemical composition of rainfall and snow.

## Daily variations in wet deposition and washout rates of potentially toxic elements in Moscow during spring season\*

### INTRODUCTION

The study of the chemical composition of atmospheric precipitation makes it possible to assess the washout rates of potentially toxic elements (PTEs), particulate matter, organic pollutants and ions (such as sulfates, nitrates, ammonium, etc.) from the atmosphere and to evaluate wet deposition fluxes on the Earth's surface (Al-Momani 2008; Cizmecioğlu and Muezzinoglu 2008; Bayramoğlu Karşı et al. 2018; Talovskaya et al. 2018, 2019; Ma et al. 2019; Tian et al. 2020; Cherednichenko et al. 2020; Park et al. 2020; Loya-González et al. 2020; McHale et al. 2021). PTEs usually include a large number of elements, e.g. carcinogenic As, Cd, Pb, Cr, Be, Ni, and Co, as well as causing general toxic damage to the body or individual organs and systems Sb, Zn, Cu, Mo, W, Sn, Se, Ba, Mn, and others (R 2.1.10.1920-04 2004; U.S. EPA 2020). Atmospheric precipitation is the most important factor in the self-purification of atmospheric air during the warm season (Ouyang et al. 2019; Long et al. 2020; Orlović-Leko et al. 2020). Wet deposition compared to dry one is more efficient in removing PTEs from the atmosphere and causes higher pollutants input into terrestrial or aquatic systems (Ouyang et al. 2015). Although estimates of wet deposition of PTEs over long periods of time (one-year or long-term) are carried out quite often, short-term changes in the chemical composition of rainwater are still poorly investigated (Pan et al. 2017).

The elemental composition of atmospheric precipitation has been studied in detail in many cities around the world. In Russia, the main attention is paid to the analysis of the individual chemical elements distribution in the rains, but those are usually snap-shot observations (Elpat'evskii 1993; Golubeva et al. 2005; Chudaeva et al. 2008; Udachin et al. 2010; Yanchenko and Yaskina 2014; Semenets et al. 2017; Svistov et al. 2017; Kuderina et al. 2018; Bufetova 2019). In Moscow – the largest megacity in Europe – complex meteorological observations are being carried out since the mid-1950s (Chubarova et al. 2014) at the Meteorological Observatory of the Lomonosov Moscow State University (MO MSU). Since 1982, these observations have been supplemented with monitoring of the physicochemical properties and macrocomponent composition of atmospheric precipitation (Eremina 2019). The atmospheric air pollution in Moscow with particulate matter (PM) and gaseous pollutants, especially sulfur dioxide due to the use of natural gas by electric and thermal power plants, is lower than in other megacities (Elansky et al. 2018). In Moscow, research on the individual rain samples pollution with organic compounds was carried out (Polyakova et al. 2018). Our previous study of the solubility and partitioning of PTEs during spring rains in Moscow showed that anthropogenic sources contributed significantly to the concentration of soluble PTEs; for the insoluble PTEs, crustal materials were the important contributors (Vlasov et al. 2021a). The spring period was chosen because of the largest va-

riety of meteorological conditions, typical for both cold and warm seasons, and emissions of pollutants into the atmosphere from various sources that were previously observed during spring months (Chubarova et al. 2019; Elansky et al. 2020; Popovicheva et al. 2020a). However, studies of the intensity of soluble PTEs washout from the atmosphere by rains within the city have not been previously conducted. Therefore, the aims of this study are to estimate wet deposition of soluble PTEs forms and to identify the rain parameters that affect PTEs washout from the atmosphere during the spring period.

### MATERIALS AND METHODS

The study of the rainwater chemical composition was carried out in April-May 2018 at the MO MSU during the AeroRadCity experiment (Chubarova et al., 2019). The MO MSU is located in the southwestern part of the city at the territory of the MSU Botanical Garden, far from industrial sources of pollution and major highways; and therefore is considered as a background city station (Fig. 1). Rain samples ( $n = 15$ ) were taken at a height of 2 m from the ground surface using a vinyl plastic funnel 80x80 cm in size and a white plastic bucket. Each rainfall event was analyzed from its beginning to the end on the current or adjacent days, that is, individual rainfall events: on April 6–7, 10–11, 17–18, 18–19, 21, 21–22, 25, 26, and May 1, 2, 4, 5–6, 17–18, 18–19, 19–20.

The pH and electrical conductivity (EC,  $\mu\text{S}/\text{cm}$ ) were measured in rainwater samples by potentiometric and conductometric methods, respectively. To isolate soluble forms of PTEs, samples were filtered through Millipore® filters with a pore diameter of 0.45  $\mu\text{m}$ . According to the mass of suspension on the filter, the content of solid particles in rainwater ( $S$ ,  $\text{mg}/\text{L}$ ) was estimated as  $S = m / V$ , where  $m$  is the mass of particles on the filter,  $\text{mg}$ ;  $V$  is the volume of filtered rainwater,  $\text{L}$ . Concentrations of Al, As, B, Ba, Be, Bi, Ca, Cd, Co, Cr, Cu, Fe, K, Mn, Mo, Na, Ni, P, Pb, Rb, S, Sb, Se, Sn, W, and Zn in the filtrate were determined using mass spectral (ICP-MS) and atomic emission methods (ICP-AES) with inductively coupled plasma on the mass spectrometer «iCAP Qc» (Thermo Scientific, USA) and atomic emission spectrometer «Optima-4300 DV» (Perkin Elmer, USA) in the laboratory of the All-Russian Scientific-research Institute of Mineral Resources named after N.M. Fedorovsky according to certified methods (NSAM № 520 2017).

In this study, the term wet deposition ( $D$ ) means the mass of a chemical element fallout from the atmosphere with rainfall per unit area of the Earth's surface for the entire precipitation event ( $\mu\text{g}/\text{m}^2$  per event):  $D = C \cdot X$ , where  $C$  is the PTEs content in rainwater,  $\mu\text{g}/\text{L}$ ;  $X$  is the precipitation amount,  $\text{mm}$  (which corresponds to  $\text{L}/\text{m}^2$ ). The term washoutrate ( $Dh$ ) means the mass of a chemical element fallout from the atmosphere with rainfall per unit area of the Earth's surface per unit time ( $\mu\text{g}/\text{m}^2$  per hour). The washout rate shows how effectively

\* Vlasov D.V., Eremina I.D., Shinkareva G.L., Chubarova N.E., Kasimov N.S. // Geography, Environment, Sustainability. 2021;14(1):219-233.



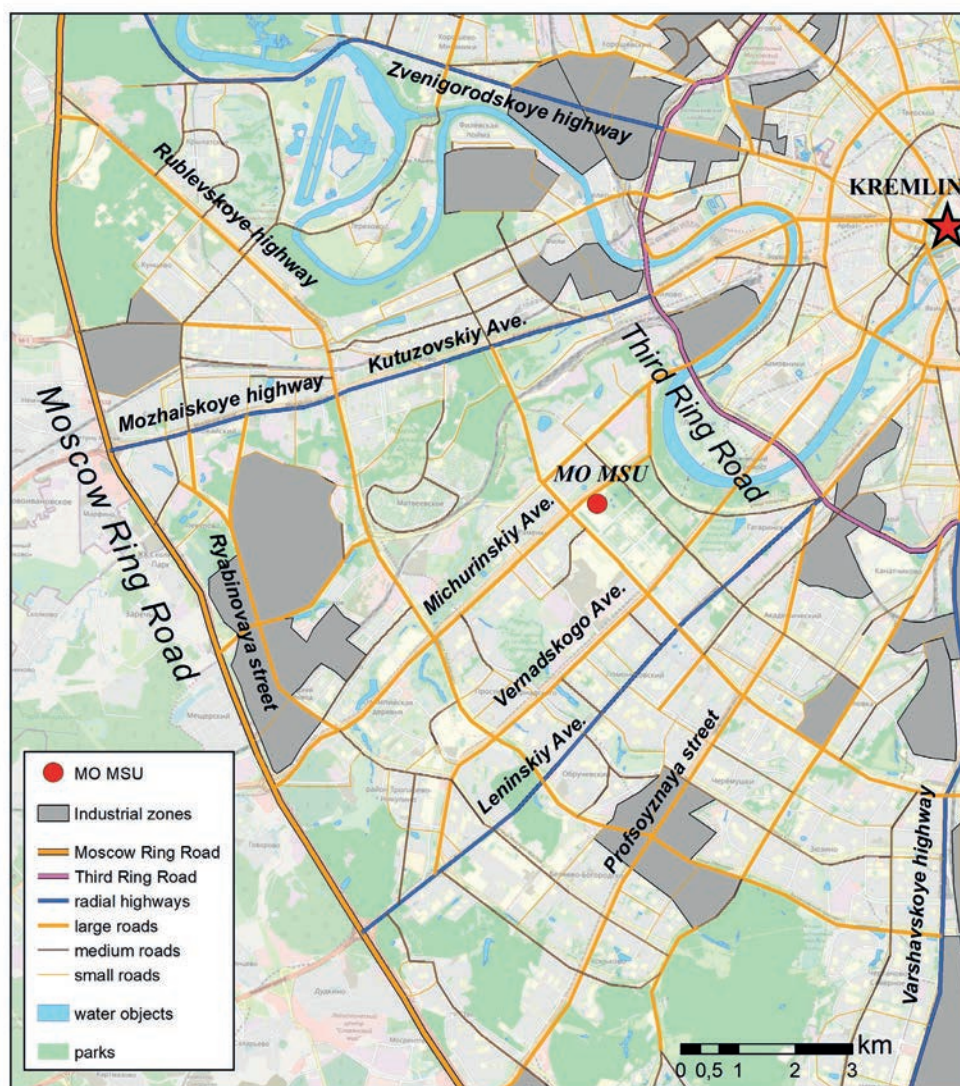


Fig. 1. Rains sampling site (MO MSU) in the southwestern part of Moscow

(quickly) the pollutant is washed out from the atmosphere:  $Dh = C \cdot X / t$ , where  $t$  is the duration of precipitation, hours. The  $Dh$  index allows to compare precipitation events of various duration to determine the effect of rainfall parameters on the intensity of PTEs washout from the atmosphere. The duration of precipitation was calculated as a difference between the end and the beginning times of a particular precipitation event. These data were obtained from the standard meteorological TM-1 tables and have an error in determining the beginning and the end of the precipitation event on the order of 1–2 minutes, which is more accurate than the 10-minute time resolution of measurements obtained with the pluviograph. At the same time, good correspondence was observed between the data on the duration of precipitation and the pluviograph data. The precipitation intensity ( $U$ , L/m<sup>2</sup> per hour) was also estimated as  $U = X / t$ . From the time difference between the end of the precipitation event and the beginning of the next one, the length (in hours) of the dry period  $R$  between rain events was calculated.

Due to big variation in wet deposition between particular PTEs, for a comprehensive assessment of each separate precipitation event, all data were normalized:

$D'_i = (D_i - D_{\min}) / (D_{\max} - D_{\min})$ , where  $D_i$  and  $D'_i$  are the initial and normalized values of PTEs wet deposition in the  $i$ -th precipitation event, respectively;  $D_{\max}$  and  $D_{\min}$  are the maximum and minimum values of PTEs wet deposition for the entire observation period. Then the total normalized wet deposition ( $ND$ ) in the  $i$ -th precipitation event can be defined as  $\sum D'_{ij}$ , where  $j$  are all considered PTEs (in our case,  $j = 1, 2, 3, \dots, 24, 25, 26$ ). The normalization was done for the wet deposition of PTEs to the Earth's surface ( $ND$ ), as well as for data on the washout rate of PTEs from the atmosphere ( $NDh$ ).

Statistical processing of the results was performed in the Statistica® 8 software. To assess the correlation between precipitation parameters ( $X$ ,  $t$ ,  $U$ ,  $R$ ) and the physicochemical properties of rainwater (pH, EC, S) on one hand, and values of PTEs wet deposition ( $D$ ) and the washout rates of PTEs from the atmosphere ( $Dh$ ) on the other hand, the nonparametric Spearman's rank correlation coefficients  $r_s$  were calculated, the significance of which was tested at a level of  $p < 0.05$ . To determine the PTEs groups with a similar distribution of wet deposition, cluster analysis was performed using the PTEs grouping by the Ward's method with the similarity measure  $d = 1 - \text{Pearson's } r$ .



## RESULTS AND DISCUSSION

### Rain parameters and physicochemical properties of rainwater

To characterize weather conditions and identify periods with typical synoptic situations in April–May 2018, meteorological data from the MO MSU and a synoptic maps archive were used (Weather maps... 2020). An analysis of the atmospheric circulation features showed that in early and mid-April, during the period of rainfall, the cyclonic type of circulation prevailed with air advection from the western and northern regions. On April 25–26, a low-gradient baric field was observed with a predominance of air advection from the northern regions. In the first decade of May, air masses from the south and southwest prevailed, and from May 17 to May 20, air advection from the west with a cyclonic type of circulation was observed.

In 2018, the average monthly air temperature values were 2–3°C higher than the corresponding values for 1954 to 2013 and amounted to 8.4°C in April and 16.7°C in May, which matches with the general trend of climate warming (Chubarova et al. 2014). The amount of precipitation fell within the normal range: in April it was 38 mm compared to 41 mm, in May – 50 mm compared to 55 mm according to the long-term measurements. The duration of precipitation varied from short-term rains (less than 4 hours) on April 6–7 and 21, May 2, 4 and 5–6 to 17 hours on May 18–19, and even 25 hours on April 17–18, thus, the rain intensity varied from 0.2 L/m<sup>2</sup> per hour to 2.9 L/m<sup>2</sup> per hour depending on the event (Fig. 2). With an increase in the rain events duration, the precipitation amount also increases ( $r_s = 0.60$ ; Fig. 3a), whilst the content of solid particles in rainwater decreases ( $r_s = 0.60$ ; Fig. 3b) due to their in-

tensive washout from the atmosphere at the beginning of precipitation event. As the duration of precipitation increases, the precipitation intensity usually decreases (Fig. 3c).

An excess of the acid precipitation (with pH < 5.0) frequency in April in comparison with the mean values for 35 years at the MO MSU (66% and 17%, respectively) was revealed. At the same time, a lower acid precipitation frequency was found for May (28% and 35%, respectively). All rains were characterized by a slightly acidic to almost neutral reaction with pH variability from 4.05 on April 6–7 to 6.35 on April 21 (Fig. 2). The average pH of rainwater in April and May 2018 was 4.7 (versus the average long-term values for these months of about 5.0 and 4.8, respectively). The highest EC value (572 μS/cm) was also found on April 6–7. In rainwater samples from other days the EC varied from 21 μS/cm to 217 μS/cm (Fig. 2). During the spring experiment, as in the last 13 years, Ca<sup>2+</sup> was the predominant cation, and Cl<sup>-</sup> was the predominant anion in precipitation (Eremina 2019; Eremina and Vasil'chuk 2019). The increase in EC values in rainfall is probably due to the partial dissolution of particulate matter washed out from the atmosphere, as indicated by the strong rank correlation ( $r_s = 0.85$ ) between EC and the content of solid particles in rainwater (Fig. 3e). The ranking is based on the increase in the values of rainwater properties and precipitation parameters – high ranks correspond to high values of indicators.

The average solid particles content in rainwater during the spring experiment was 63 mg/L, varying from 6.1 mg/L in the last episode of prolonged precipitation in late May to 183 mg/L on May 2 during the public holidays (1–9 May) celebrated in Russia (Fig. 2) which were also characterized by elevated aerosol loading due to predominant air advection from the south and south-western regions (Chubarova et al. 2020). The amount of solid par-

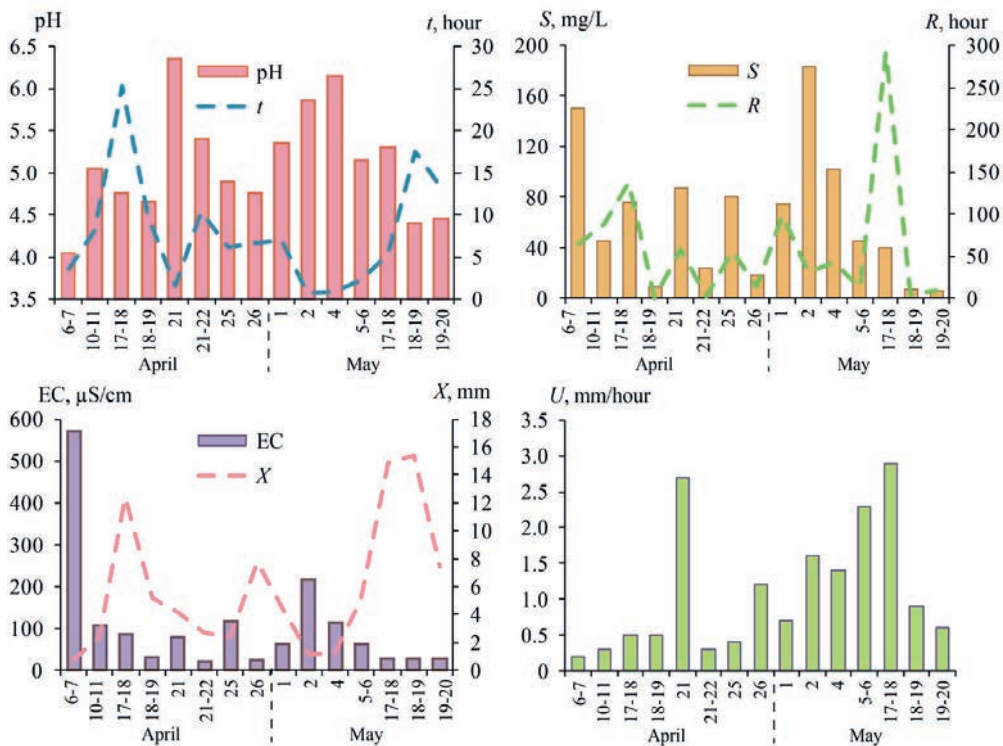


**Fig. 2.** Physicochemical properties of rainwater and rainfall parameters during the spring experiment. X – precipitation amount, t – duration of precipitation, R – length of the antecedent dry period, S – solid particles content in rainwater, U – precipitation intensity, EC – electrical conductivity

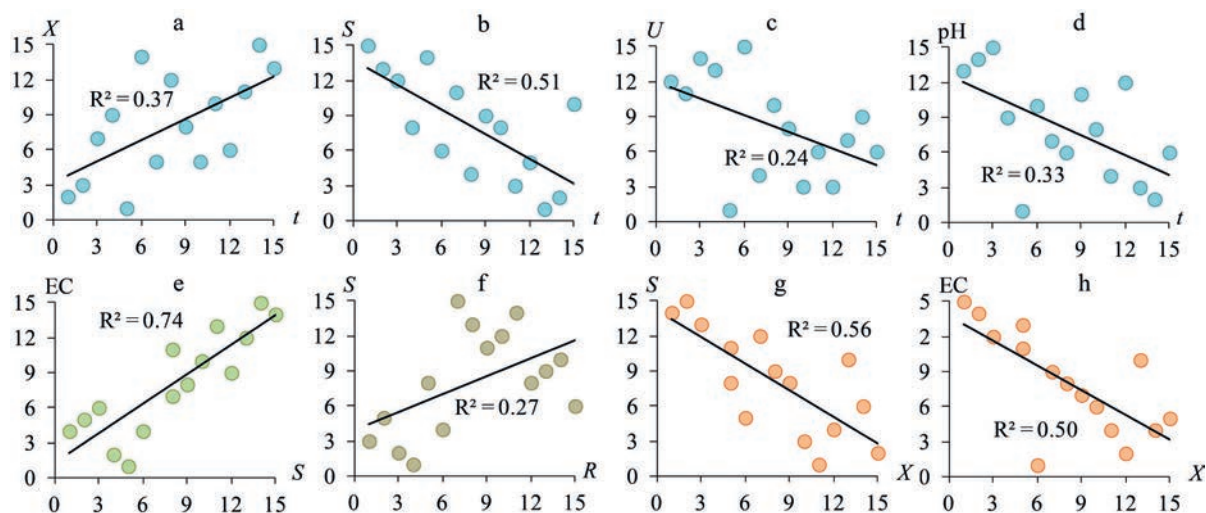


**Fig. 3.** Rank correlation between the ranks of the physicochemical properties of rainwater and rain parameters: X – precipitation amount, t – duration of precipitation, R – length of the antecedent dry period, S – solid particles content in rainwater, U – precipitation intensity, EC – electrical conductivity. High ranks correspond to high values of indicators. The color indicates the dependences on the same parameters of rain or the properties of rainwater (horizontal axis): (a)-(d) duration of precipitation, (e) solid particles content in rainwater, (f) length of the antecedent dry period, (g)-(h) precipitation amount

ticles washed out with rains depends on the length of the antecedent dry period prior to precipitation event ( $r_s = 0.53$ ; Fig. 3f), which is associated with the accumulation of coarse aerosol particles in the air during a long dry period and their subsequent washout with precipitation. A significant correlation between the solid particles content in rainwater and precipitation amount ( $r_s = -0.75$ ; Fig. 3g) was revealed. This is likely due to the dilution effect, namely the mineralization and the content of solid particles in rainwater decrease with increasing precipitation amount (Park et al. 2015). A decrease in EC with an increase in the precipitation amount ( $r_s = -0.72$ ) is associated with the same phenomenon (Fig. 3h). The decrease in solid particles content in rainwater is influenced by an increase in the duration of precipitation ( $r_s = -0.70$ ), probably due to the more intensive washout rate of solid particles in the first minutes and hours after the beginning of a rainfall event (Fig. 3b). A decrease in the solid particles content in rainwater with increasing duration of precipitation leads to a decrease in rainwater pH (Fig. 3d) since high pH is associated with the partial dissolution of particulate matter (Singh et al., 2016).

Thus, the most important rain parameters for wet deposition are precipitation amount, duration and intensity as well as the length of the dry period. All of them affect the pH and EC values along with the content of solid particles in rainwater.

### Wet deposition and washout rates of PTEs from the atmosphere

The wet deposition of PTEs in spring varies greatly – on average from 21884  $\mu\text{g}/\text{m}^2$  per episode for Ca to 0.12  $\mu\text{g}/\text{m}^2$  per episode for Be (Table 1).

The highest levels of wet deposition ( $> 100 \mu\text{g}/\text{m}^2$  per event) are typical for  $\text{Ca} > \text{S} > \text{Na} > \text{K} > \text{Pb} > \text{Fe} > \text{Al} > \text{Zn} > \text{P}$ , while highest washout rates from the atmosphere ( $> 50 \mu\text{g}/\text{m}^2$  per hour) are common for  $\text{Ca} > \text{S} > \text{K} > \text{Na} > \text{Fe} > \text{Al} > \text{Pb} > \text{Zn}$ . For other PTEs, the wet deposition as well as washout rates are much lower and decrease

(Table 1). Ca, S, Na, and K are macroelements of atmospheric precipitation and natural waters; the presence of macroelements of the continental crust (Al and Fe) in high concentrations relative to other PTEs in rainwater is associated with crustal and terrigenous sources input; high washout rates of Zn, Pb, Mn, Ba, and Cu are caused by the industrial and vehicular impact, which is typical for most large cities (Galloway et al. 1982; Song and Gao 2009; Kamani et al. 2014; Vlastos et al. 2019).

A comprehensive assessment of the temporal heterogeneity of wet deposition and washout rates of PTEs from the atmosphere was carried out by calculating the total normalized values of wet deposition (ND) and total normalized values of washout rates of PTEs (NDh) for the entire experiment period. Changes in the ND and NDh values are shown in Fig. 4.

The highest ND values for the majority of PTEs were found for rains on April 17–18, when one of the three rainfall events with the highest precipitation amount (12.4 mm) was observed. These maxima are also associated with the highest aerosol concentration before the beginning of rainfall: from April 11 to April 16, the maximum  $\text{PM}_{10}$  concentration was observed over the entire period of the experiment and was equal to 43  $\mu\text{g}/\text{m}^3$  (Chubarova et al. 2019). Afterwards, from April 17 to April 22, due to the precipitation and washing out of aerosols, a sharp decrease in the PM content (to 24  $\mu\text{g}/\text{m}^3$ ) was determined, which in turn caused the high values of total normalized wet deposition on April 17–18 and total normalized washout rates on April 21. Increased levels of total normalized wet deposition of PTEs, relative to other days, were observed on May 17–19, which is also due to a high level of aerosol pollution of the atmospheric surface layer in the previous dry period (Chubarova et al. 2019), large precipitation amount (14.9–15.4 mm) and high rain intensity on May 17–18 (2.9 mm/hour, the most intense rain of the entire experiment period).

The washout rates of PTEs from the atmosphere have a slightly different pattern in temporal changes compared to ND (Fig. 4). Very high total normalized washout rates

**Table 1.** PTEs' wet deposition to the Earth's surface and washout rates from the atmosphere at the MO MSU territory

PTEs	Wet deposition, $\mu\text{g}/\text{m}^2$ per event		Washout rates, $\mu\text{g}/\text{m}^2$ per hour	
	mean	minimum–maximum	mean	minimum–maximum
Ca	21884	85152–3546	6881	31420–344
S	3519	12279–660	991	3496–64
Na	1979	9113–466	497	1608–35
K	1269	3691–173	546	3828–10
Pb	650	3186–38	79	190–6.0
Fe	592	2615–104	111	238–10
Al	406	1860–39	96	300–3.8
Zn	214	922–42	58	247–4.0
P	123	481–16	42	278–0.92
Ba	95	272–17	24	82–1.6
Mn	76	264–15	28	165–1.1
Cu	51	213–10	10	35–0.98
B	32	161–3.1	7.6	34–0.31
Sb	19	83–3.1	5.4	23–0.30
Ni	2.8	13–0.51	0.78	4.1–0.050
Rb	2.3	5.8–0.63	1.0	7.4–0.061
Cr	1.7	6.9–0.43	0.43	2.1–0.042
Co	1.2	5.9–0.20	0.35	1.6–0.020
Se	0.89	2.3–0.18	0.17	0.43–0.039
As	0.73	1.7–0.14	0.17	0.74–0.029
Mo	0.58	1.5–0.070	0.11	0.29–0.020
Cd	0.55	1.9–0.13	0.14	0.45–0.012
W	0.21	1.0–0.038	0.048	0.18–0.004
Sn	0.2	0.96–0.027	0.057	0.23–0.003
Bi	0.14	0.73–0.024	0.034	0.11–0.002
Be	0.12	0.53–0.009	0.018	0.058–0.001

Note. PTEs are arranged in descending order of their average wet deposition

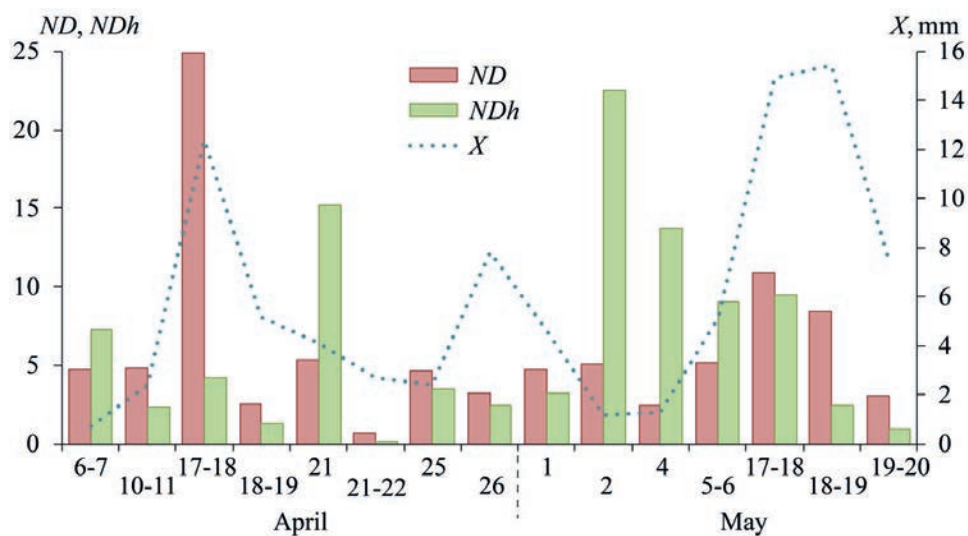


**Fig. 4.** Total normalized values of wet deposition of PTEs (ND, left axis) and washout rates of PTEs from the atmosphere (NDh, left axis), as well as precipitation amount (X, mm, right axis) on the MO MSU in April–May 2018



of PTEs (NDh) were revealed for May 1–6, when air advection from the south and southwest prevailed. The beginning of this period of public holidays (May 1) is characterized by rather low washout rates of PTEs. However, already on May 2 it increased sharply due to the anthropogenic emission of PTEs to the atmosphere from the biomass burning in suburban areas and the territory of the MSU Botanical Garden, together with the coal burning during picnics near MSU and vehicle emissions due to the large number of traffic jams that occur when residents leave the city. This is confirmed by the increase in the levels of wet deposition of K, Rb, Mn, Sn, Sb, and As these days, which are often used as indicators of controlled biomass and coal combustion or forest fires (Landing et al. 2010; Samsonov et al. 2012; Grivas et al. 2018). Thus, the spring period is characterized by a strong influence of forest fires in the Moscow region and the biomass burning in residential areas on the composition of atmospheric particles in Moscow (Popovicheva et al. 2020a), which is indicated by the high values of the black carbon (BC) to the PM<sub>10</sub> content ratio in the atmosphere (Popovicheva et al. 2020b), since BC is a marker of biomass burning or fuel combustion.

From April 30 to May 5, a high concentration of PM<sub>10</sub> of 34 µg/m<sup>3</sup> was observed, which sharply decreased to 23 µg/m<sup>3</sup> in the period from May 6 to May 12 (Chubarova et al. 2019), probably due to short and intense rains on May 2, May 4 and May 5–6, which caused high values of the total normalized washout rates of PTEs. On May 17–18, the PTEs washout rates were also high due to the previous long dry period (11 days), with a large amount of aerosol accumulated in the air on May 13–17, which resulted in high PM<sub>10</sub> values (Chubarova et al. 2019). During prolonged rains, which lasted several days with only short breaks, wet deposition and PTEs washout rates significantly decreased, which is typical for May 18–19, May 19–20 and April 26, but especially noticeable for April 18–19 and April 21–22 (Fig. 4). These data confirm the hypothesis about the deposition of the main pollutants' masses in the first hours after the onset of rain due to the active washout of aerosols from the atmosphere (Lim et al. 1991).

Thus, the highest ND levels for most PTEs were found on April 17–18 and May 17–18 due to a long dry period before these precipitation events (138 hours and 292 hours, respectively) and high aerosol concentrations in the surface atmospheric layer. The maximum NDh was observed on April 21, May 2, May 4, May 5–6, and May 17–18 with relatively short and intense (1.4–2.9 mm/hour) precipitation.

### Sources of PTEs in rainwater

In order to estimate the contribution of anthropogenic sources to the content of PTEs in precipitation the enrichment factor (EF) could be used:  $EF = (D_i / D_{Al}) / (K_i / K_{Al})$ , where  $D_i$  and  $D_{Al}$  are wet deposition of the *i*-th and the reference elements,  $K_i$  and  $K_{Al}$  are the abundances of the *i*-th and the reference elements in Sn<sub>19</sub>, Na<sub>16</sub>, Co<sub>14</sub>, Ni<sub>12</sub>, Be<sub>11</sub>, K<sub>11</sub>) and the content of PTEs in the upper continental crust is used as a reference standard with Al as a reference element (Basha et al. 2010).  $EF < 10$  indicates a crustal (or terrigenous) origin of elements,  $EF$  from 10 to 100 shows probability of anthropogenic PTEs sources, and at  $EF \geq 100$  PTEs definitely have an anthropogenic source (Tian et al. 2020).

High EFs in the Moscow rains in April–May 2018 certainly indicating the anthropogenic origin of the PTEs, were determined for (the EF values are shown in the subscript) Sb<sub>9392</sub>, Pb<sub>7680</sub>, Se<sub>1987</sub>, Cd<sub>1232</sub>, and S<sub>1138</sub>. A significant contribution of anthropogenic sources was also observed for Zn<sub>641</sub>, B<sub>373</sub>, Cu<sub>368</sub>, Bi<sub>175</sub>, Ca<sub>171</sub>, and Mo<sub>106</sub>. In many other cities, a substantial enrichment of atmospheric precipitation with these PTEs was also found (Koulousaris et al. 2009; Song and Gao 2009; Özsoy and Örnektekin 2009; Landing et al. 2010; Kamani et al. 2014; Chon et al. 2015), and for Zn, Cd, and Cu it was reported even for the southeastern part of the Atlantic Ocean (Chance et al. 2015). This indicates the significant role of wet deposition processes for the PTEs input into terrestrial landscapes. The main sources of most of these PTEs are vehicle emissions, fuel combustion, tires and brake pads wear, road surface abrasion, roadside soil particles blowing, industrial enterprises emissions, as well as macroregional long-distance transport of pollutants (Demetriades and Birke 2015; Grigoratos and Martini 2015; Grivas et al. 2018; Konstantinova et al. 2020; Liyandeniya et al. 2020; Logiewa et al. 2020; Orlović-Leko et al. 2020; Ramírez et al. 2020; Seleznev et al. 2020; Tian et al. 2020), which is confirmed by the previously identified sources of snow cover pollution in the western part of Moscow (Vlasov et al. 2020). The remaining PTEs on the territory of the MO MSU were apparently of mixed anthropogenic-terrigenous sources (P<sub>38</sub>, Ba<sub>31</sub>, As<sub>30</sub>, W<sub>22</sub>, Mn<sub>20</sub>, Sn<sub>19</sub>, Na<sub>16</sub>, Co<sub>14</sub>, Ni<sub>12</sub>, Be<sub>11</sub>, K<sub>11</sub>) and terrigenous origin (Rb<sub>6</sub>, Cr<sub>4</sub>, Fe<sub>3</sub>), which indicates the influence of solid particles blown out from the Earth's surface and included in the atmospheric precipitation.

For a more detailed determination of PTEs sources, a cluster analysis was carried out. Based on its results, four associations of soluble forms of PTEs with similar deposition patterns were identified: (1) Zn–Sb–Ni–Ca–Co–Bi–Sn–Al–W–Cr–Fe–Na–P; (2) Cu–Ba–Pb–Cd–S–B; (3) Se–Mo–As–Be; and (4) K–Rb–Mn (Fig. 5).

The first geochemical association (Zn–Sb–Ni–Ca–Co–Bi–Sn–Al–W–Cr–Fe–Na–P) includes PTEs coming from anthropogenic (Zn, Sb, Bi, Ca), anthropogenic-terrigenous (W, Sn, Co, Ni, Na, P) and terrigenous (Al, Fe, Cr) sources. Sb, Zn, Sn, Bi, W, and Ni indicate the resuspension of road dust and its various grain size particles, since in Moscow and some other cities road dust is highly enriched with these PTEs (Ladonin and Plyaskina 2009; Fedotov et al. 2014; Ermolin et al. 2018; Kasimov et al. 2019a; Ladonin and Mikhaylova 2020; Vlasov et al. 2021b). For example, in the eastern part of Moscow, the fine fraction PM<sub>1</sub> and the coarser PM<sub>1–10</sub> of road dust are significantly ( $EF > 5$ ) enriched in Sb, W, Sn, Cd, Zn, Cu, Pb, Mo, and Bi, especially on Moscow Ring Road and highways (Vlasov et al. 2015; Kasimov et al. 2020). Al, Fe, and Na are emitted by blowing out particles of contaminated urban soils (Morera-Gómez et al. 2020). This source is somewhat less significant for W, which is presented in the surface horizons of Moscow soils (Kosheleva et al. 2018). Blown-out soil particles are also a source of P in atmospheric aerosols and precipitation (Bencharif-Madani et al. 2019). Deicing agents can supply Na and Ca, since CaCl<sub>2</sub> and marble chips (Ca, Mg)CO<sub>3</sub> are among the main deicing agents after NaCl in Moscow (Vlasov et al. 2020). Mentioned deicing agents are found in high concentrations in road dust and surface soil horizons in the spring season. Cr, Ni, and Co can come due to abrasion of the asphalt pavement (Song and Gao 2011). Thus, the Zn–Sb–Ni–Ca–Co–Bi–

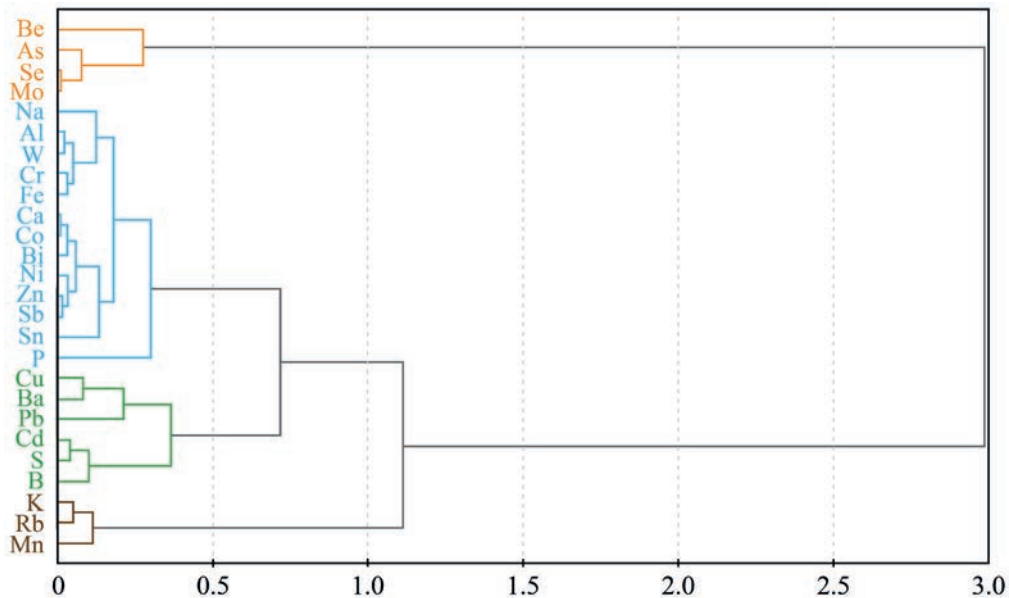


**Fig. 5.** Dendrogram of wet deposition of PTEs in the MO MSU on April–May 2018 (clustering was done using Ward's method; the similarity measure is  $d = 1 - \text{Pearson's } r$ )

Sn–Al–W–Cr–Fe–Na–P association is mainly formed by the blown out particles of urban soils, road dust and deicing agents, which could be partially dissolved in rainwater. For instance, at the very beginning of the contact of an acidic (pH 4.7) mimicking fog water with atmospheric PM<sub>2.5</sub>, a significant part of K, Cd, Mn, Mo, V, Ba, Al, Fe, Sb, Cu, and Cr are transferred to the soluble form (Di Marco et al. 2020).

*The second association* Cu–Ba–Pb–Cd–S–B includes elements with high EFs, that are coming from anthropogenic sources (Cu, Pb, Cd, S, B), as well as anthropogenic-terrestrial Ba. Copper, as well as Pb and Cd, are used in large quantities in vehicle brake pads and linings (Fabretti et al. 2009; Grigoratos and Martini 2015). Barium sulfates used in the brake pads manufacturing as a friction modifier can supply S and Ba to atmospheric particles and precipitation (Pant and Harrison 2013). Boron also comes from vehicles, since it is used as an additive in the manufacture of polymers, glass and fiberglass, as well as in the production of lubricants, antifreeze and fuel additives (U.S. Borax 2020). Waste incineration can be an additional source of Sb, Cd, and other PTEs (Christian et al. 2010). High S concentrations also often indicate a large contribution of long-distance transport of secondary inorganic aerosols (Cheng et al. 2015).

*The third association* (Se–Mo–As–Be) is formed by elements with very high (Se, Mo) and high (As, Be) EFs, which indicates their predominantly anthropogenic origin in atmospheric precipitation. Likely sources of Mo include metalworking, car repair and painting companies (Demetriades and Birke 2015; Zheng et al. 2018), widespread in Moscow. Arsenic, Se, Be and sometimes Mo can come from waste incineration and diesel fuel combustion (Kumar et al. 2015; Bencharif-Madani et al. 2019), while Se is also used as a coal combustion indicator (Wu et al. 2018). Despite the fact that coal is not used at Moscow thermal power plants, Se accumulated in fine particles (0.25–0.35  $\mu\text{m}$ ) could migrate hundreds of kilometers (Gallorini 2000) from those territories where coal is burned (suburbs, summer cottages, even transboundary transfer).

*The fourth association* (K–Rb–Mn) is probably determined by the biomass burning, since these PTEs, as noted above, are widely used as indicators of this type of impact (Samsonov et al. 2012; Grivas et al. 2018). High EFs values are found for Mn and K, while for Rb low EF is defined, probably due to its poor solubility in rainwater (Yu et al. 2018) and relatively high abundance in the upper continental crust.

Thus, the Zn–Sb–Ni–Ca–Co–Bi–Sn–Al–W–Cr–Fe–Na–P geochemical association is formed by the PTEs input mainly with blowing out of soil particles and road dust as well as deicing agents' resuspension. The main source of Cu–Ba–Pb–Cd–S–B association is vehicle emissions, while Se–Mo–As–Be association is particularly emitted from industrial sources as well as during waste incineration and long-distance air mass transport. In addition, biomass combustion (including forest fires) and atmospheric migration of plant pollen are responsible for the formation of K–Rb–Mn geochemical association.

#### **Influence of rain parameters on the washout rates of PTEs from the atmosphere**

A nonparametric correlation analysis was carried out to determine the main factors affecting the wet deposition of PTEs to the Earth's surface and the PTEs washout rates from atmospheric air.

The precipitation amount determines the wet deposition values of anthropogenic PTEs with high EFs (Table 2, Fig. 6): Se, Mo ( $r_s = 0.96$ ), As, Pb, Ba, and Cd ( $r_s$  0.83, 0.65, 0.59, and 0.57, respectively). Other researchers also noted a similar positive correlation, for instance, in cities and suburbs of Northern China for Cu, Zn, Cd, As, and Se (Pan and Wang 2015), and Izmir, Turkey for Cr, Cd, Pb, and Ni (Cizmecioglu and Muezzinoglu 2008). Less strong inverse correlation was found between the precipitation amount and the washout rates of soluble PTEs from the atmosphere:  $r_s$  values are significant only for anthropogenic-terrestrial Na and P (–0.53); for other elements, except for Se, Mo, and Pb, they are also negative (Table 3, Fig. 7). A decrease in the PTEs washout rates is associated, as noted earlier, with the dilution effect, which reduces the

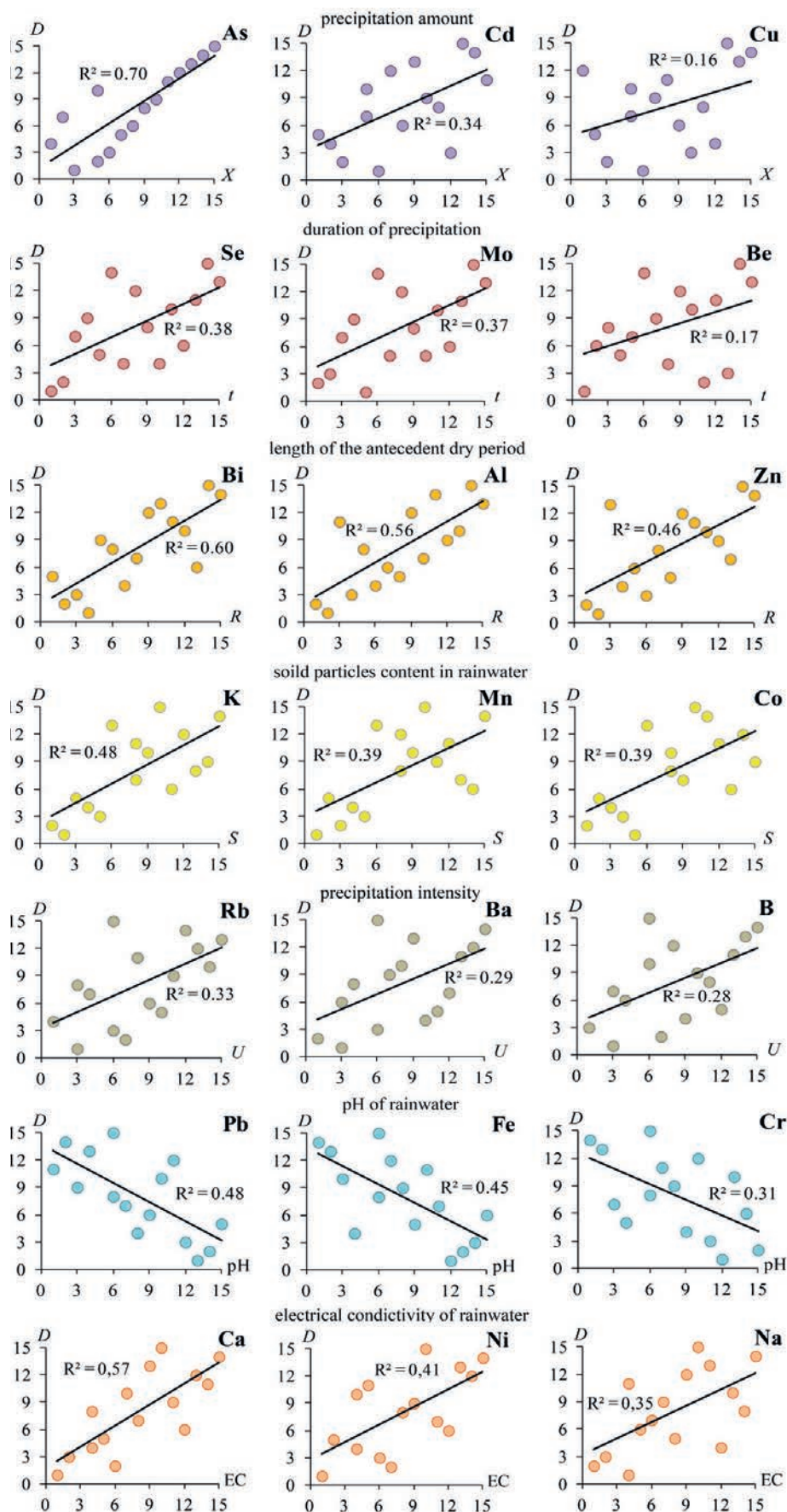


Fig. 6. Examples of rank correlation of wet deposition of PTEs (vertical axis) with the physicochemical properties of rainwater or rain parameters (horizontal axis; designations are shown in caption of Fig. 2). High ranks correspond to high values of indicators. The color shows the correlation with the same rain parameters or properties of rainwater



**Table 2.** The Spearman's correlation coefficient ( $r_s$ ) values between wet deposition of PTEs on the Earth's surface, physicochemical properties of rainwater, and rain parameters on the MO MSU territory

PTEs	Physicochemical properties of rainwater			Rain parameters			
	pH	EC	Solid particles content	Precipitation amount	Duration of precipitation	Precipitation intensity	Length of the antecedent dry period
Be	-0.01	-0.17	-0.10	0.38	0.42	-0.11	0.47
B	0.29	-0.02	0.14	0.39	-0.13	<b>0.51</b>	<b>0.56</b>
Na	-0.07	<b>0.57</b>	<b>0.52</b>	-0.15	-0.16	-0.09	<b>0.66</b>
Al	-0.25	0.45	0.38	0.09	0.02	-0.06	<b>0.75</b>
K	0.46	0.46	<b>0.68</b>	-0.17	-0.49	0.39	<b>0.70</b>
P	0.10	0.31	0.36	-0.12	-0.21	0.08	0.25
S	0.06	0.27	0.28	0.21	-0.05	0.25	<b>0.72</b>
Ca	0.07	<b>0.74</b>	<b>0.74</b>	-0.31	-0.35	0.03	<b>0.68</b>
Cr	<b>-0.57</b>	0.36	0.15	0.15	0.17	-0.19	0.39
Mn	0.46	0.42	<b>0.61</b>	-0.05	-0.40	0.43	<b>0.69</b>
Fe	<b>-0.68</b>	0.15	-0.07	0.36	0.41	-0.27	0.47
Co	0.06	<b>0.62</b>	<b>0.63</b>	-0.15	-0.26	0.04	<b>0.79</b>
Ni	-0.18	<b>0.63</b>	<b>0.56</b>	-0.10	-0.08	-0.09	<b>0.63</b>
Cu	-0.39	0.18	0.06	0.39	0.28	-0.00	<b>0.60</b>
Zn	-0.10	0.38	0.33	0.19	0.01	0.14	<b>0.68</b>
As	-0.47	-0.47	<b>-0.60</b>	<b>0.83</b>	<b>0.53</b>	0.24	0.05
Se	-0.48	<b>-0.69</b>	<b>-0.72</b>	<b>0.96</b>	<b>0.60</b>	0.22	-0.05
Rb	0.45	0.36	<b>0.51</b>	0.06	-0.37	<b>0.55</b>	<b>0.65</b>
Mo	-0.35	<b>-0.72</b>	<b>-0.75</b>	<b>0.96</b>	<b>0.60</b>	0.31	-0.08
Cd	-0.18	-0.06	-0.18	<b>0.57</b>	0.24	0.30	0.35
Sn	0.06	<b>0.59</b>	0.48	-0.14	-0.11	0.00	0.48
Sb	0.00	0.27	0.18	0.29	0.01	0.30	0.49
Ba	0.06	-0.06	-0.06	0.59	0.14	0.53	0.44
W	-0.42	<b>0.52</b>	0.30	-0.03	0.19	-0.37	<b>0.64</b>
Pb	<b>-0.70</b>	-0.20	-0.40	<b>0.65</b>	<b>0.63</b>	-0.19	0.13
Bi	0.09	0.35	0.46	0.01	-0.24	0.12	<b>0.77</b>

Note. The  $r_s$  values significant at  $p < 0.05$  are shown in **bold**

PTEs concentrations and, as a consequence, the mass of pollutants' washout per unit time.

The duration of precipitation has a significant positive correlation with the wet deposition of PTEs of anthropogenic origin including Pb, Mo, Se, and As ( $r_s$  0.63–0.53), and a negative correlation with the washout rate from the atmosphere for all PTEs (Tables 2 and 3, Figs. 6 and 7). Such relations are significant for all PTEs, except for Be and Pb, with  $r_s$  values ranging from -0.52 for Mo to -0.90 for Mn. The reason for this is a sharp decrease in PTEs concentrations in atmospheric air by the end of the precipitation event in comparison with its beginning, when the highest PTEs levels are usually found, due to the removal of pollutants from the atmosphere during prolonged precipitation (Ouyang et al. 2015).

The length of the antecedent dry period is one of the most important factors contributing to an increase in wet deposition and the washout rates of PTEs from the atmosphere especially in conditions with elevated aerosol content (Tables 2 and 3, Figs. 6 and 7). This is most pronounced for the wet deposition of PTEs of anthropogenic (Bi, S, Zn, Cu, B, Ca), anthropogenic-terrigenous (Co, K, Mn, Na, Ni, W) and terrigenous (Al, Rb) origin. For the washout rates of most PTEs, such relations are less pronounced, while the correlation coefficients are positive for all PTEs and are significant for W, Ni, B, Be, Rb, and Cu (0.65–0.51). That is, with an increase in the dry period, the washout rate of PTEs increases.

The first rain after a long dry period is enriched with PTEs due to in-cloud and below-cloud scavenging processes. During a short dry period, due to frequent precipitation, the below-cloud scavenging processes weaken with the gradual removal of solid particles from the atmosphere (Bayramoğlu Karşı et al. 2018). During prolonged precipitation, an increased amount of aerosols is removed from the atmosphere within the first days. On the subsequent days, due to low concentrations of atmospheric aerosols, the rains wash out smaller amounts of pollutants. An increase in the pollutant concentrations in precipitation after a long dry period and a large load of contaminants in the early stages of river runoff are often referred to as the «first flush effect» that was investigated in detail on urban territories (Schiff et al. 2016; Shen et al. 2016; Liu et al. 2019; Mamoon et al. 2019).

Solid particles content in rainwater contributes to an increase in the wet deposition and washout rates of PTEs from the atmosphere due to the intensification of the gradual dissolution of particles, which in turn leads to an increase in the concentration of soluble forms of PTEs (Table 3, Fig. 7).

The rain intensity proved to have a positive correlation with the wet deposition of most PTEs. High significant  $r_s$  were found for terrigenous Rb (0.55), anthropogenic-terrigenous Ba (0.53), and anthropogenic B (0.51) (Table 2, Fig. 6). The washout rate is characterized by stronger correlation

**Table 3.** The Spearman's correlation coefficients ( $r_s$ ) values between washout rates of PTEs from the atmosphere, physicochemical properties of rainwater, and rain parameters on the MO MSU territory

PTEs	Physicochemical properties of rainwater			Rain parameters			
	pH	EC	Solid particles content	Precipitation amount	Duration of precipitation	Precipitation intensity	Length of the antecedent dry period
Be	0.43	0.28	0.48	-0.06	-0.50	0.54	0.52
B	<b>0.66</b>	0.28	<b>0.54</b>	-0.05	<b>-0.68</b>	<b>0.77</b>	<b>0.54</b>
Na	0.45	<b>0.69</b>	<b>0.82</b>	<b>-0.53</b>	<b>-0.81</b>	0.38	0.45
Al	0.43	<b>0.72</b>	<b>0.87</b>	-0.49	<b>-0.82</b>	0.42	0.50
P	0.45	<b>0.64</b>	<b>0.78</b>	<b>-0.53</b>	<b>-0.78</b>	0.34	0.31
S	<b>0.58</b>	<b>0.61</b>	<b>0.77</b>	-0.43	<b>-0.83</b>	<b>0.56</b>	0.48
K	<b>0.65</b>	<b>0.56</b>	<b>0.82</b>	-0.47	<b>-0.87</b>	<b>0.54</b>	0.50
Ca	0.50	<b>0.67</b>	<b>0.82</b>	-0.47	<b>-0.85</b>	<b>0.51</b>	0.47
Cr	0.34	<b>0.63</b>	<b>0.78</b>	-0.42	<b>-0.82</b>	0.45	0.46
Mn	<b>0.65</b>	<b>0.59</b>	<b>0.83</b>	-0.50	<b>-0.90</b>	<b>0.53</b>	0.47
Fe	0.30	<b>0.68</b>	<b>0.82</b>	-0.49	-0.82	0.38	0.48
Co	<b>0.51</b>	<b>0.68</b>	<b>0.84</b>	-0.49	<b>-0.87</b>	0.49	0.46
Ni	0.45	<b>0.69</b>	<b>0.86</b>	-0.46	<b>-0.80</b>	0.44	0.55
Cu	0.43	<b>0.52</b>	<b>0.70</b>	-0.23	<b>-0.71</b>	<b>0.61</b>	<b>0.51</b>
Zn	<b>0.51</b>	<b>0.66</b>	<b>0.83</b>	-0.43	<b>-0.83</b>	<b>0.53</b>	0.49
As	0.41	0.19	0.37	-0.13	<b>-0.77</b>	<b>0.78</b>	0.26
Se	0.34	0.01	0.21	0.13	<b>-0.67</b>	<b>0.90</b>	0.16
Rb	<b>0.63</b>	<b>0.57</b>	<b>0.76</b>	-0.43	<b>-0.85</b>	<b>0.59</b>	<b>0.51</b>
Mo	0.49	-0.19	0.03	0.31	<b>-0.52</b>	<b>0.96</b>	0.09
Cd	<b>0.54</b>	<b>0.63</b>	<b>0.80</b>	-0.43	<b>-0.84</b>	<b>0.54</b>	0.49
Sn	0.44	<b>0.76</b>	<b>0.81</b>	-0.50	<b>-0.66</b>	0.28	0.50
Sb	<b>0.53</b>	<b>0.62</b>	<b>0.78</b>	-0.35	<b>-0.76</b>	<b>0.56</b>	0.50
Ba	<b>0.53</b>	0.39	<b>0.57</b>	-0.07	<b>-0.65</b>	<b>0.76</b>	0.38
W	0.34	<b>0.74</b>	<b>0.85</b>	-0.46	<b>-0.68</b>	0.29	<b>0.65</b>
Pb	-0.38	0.11	0.09	0.35	-0.09	0.09	0.43
Bi	<b>0.56</b>	<b>0.61</b>	<b>0.83</b>	-0.48	-0.85	0.47	0.45

Note. The  $r_s$  values significant at  $p < 0.05$  are shown in **bold**

(Table 3, Fig. 7) with rain intensity for a large number of PTEs: high  $r_s$  values were found for Ca, Mn, Zn,

Be, K, Cd, S, Sb, and Rb (0.51–0.59), Cu (0.61), Ba, B, As (0.76–0.78), and Se (0.90). For other PTEs, except for Pb,  $r_s$  is also positive and amounts to 0.37 and even higher. A positive correlation between the amount of PTEs washed out from the atmosphere and rain intensity is typical for precipitation in Kyoto and regions of Japan (Sakata et al. 2006), as well as for southwestern Taiwan, when during the typhoon, the amount of washed-out pollutants sharply increased compared to the usual precipitation levels (Cheng and You 2010).

Long dry periods before the onset of precipitation event lead to an increase in the solid particles' content in rainwater, which in turn contributes to an increase in the rainwater pH as a result of the partial dissolution of the suspended matter (Yeremina et al. 2014; Singh et al. 2016). Such partial dissolution of road dust particles can contribute to an increase in precipitation pH since its values for the water extract of road dust in Moscow is 6.4–8.1 (Kasimov et al. 2019b). Therefore, with an increase in the length of the dry period, as well as the amount of solid particles in rainwater and pH value, the intensity of PTEs washout by rain from the atmosphere also increases (Table 3, Fig. 7). The largest  $r_s$  values are typical for B, K, Mn, and Rb ( $r_s$  0.66–0.63), as well as Co, Ba, Bi, Cd, Sb, S, and Zn (0.58–0.51). Due to the acidifying effect of industrial and thermal power plants emissions (e.g., on account of sulfate-ion formation as a

result of a chemical reaction of emitted sulfur dioxide and water in the atmosphere), vehicle emissions (e.g., nitrate ion formation as a result of chemical reactions of emitted nitrogen oxides and water), and also deicing chloride reagents (Eremina et al. 2015), a decrease in the rainwater pH is accompanied by an increase in the wet deposition of Pb ( $r_s = -0.70$ ), Fe (-0.68), and Cr (-0.57), as well as Be, Na, Al, Ni, Cu, Zn, As, Se, Mo, Cd, and W (Table 2, Fig. 6). At the same time, a decrease in the rainwater pH in this case is not the reason for the growth of wet deposition of PTEs, but an indicator of the anthropogenic sources' impact on supplying these PTEs to the urban environment.

*Electrical conductivity* indirectly shows the amount of ions in the solution (rainwater). Therefore, EC has positive a correlation with the level of wet deposition of many PTEs, and especially Ca, Ni, Co, Sn, Na, and W ( $r_s$  0.74–0.52). For some PTEs, this correlation is negative. This is possible because, due to the predominantly low levels of deposition of these PTEs (first of all, Be, Se, As, Mo, Cd, and Ba), their contribution to EC is insignificant. Therefore, the pattern of EC change is determined precisely by the behavior of elements with high concentrations in rainwater and, accordingly, high levels of wet deposition, e.g. Ca, Na, Fe, Mn, Al, S, etc. (Tables 2 and 3, Figs. 6 and 7). This is confirmed by the fact that positive significant  $r_s$  values were found between the washout rates of the majority of PTEs and the EC value.

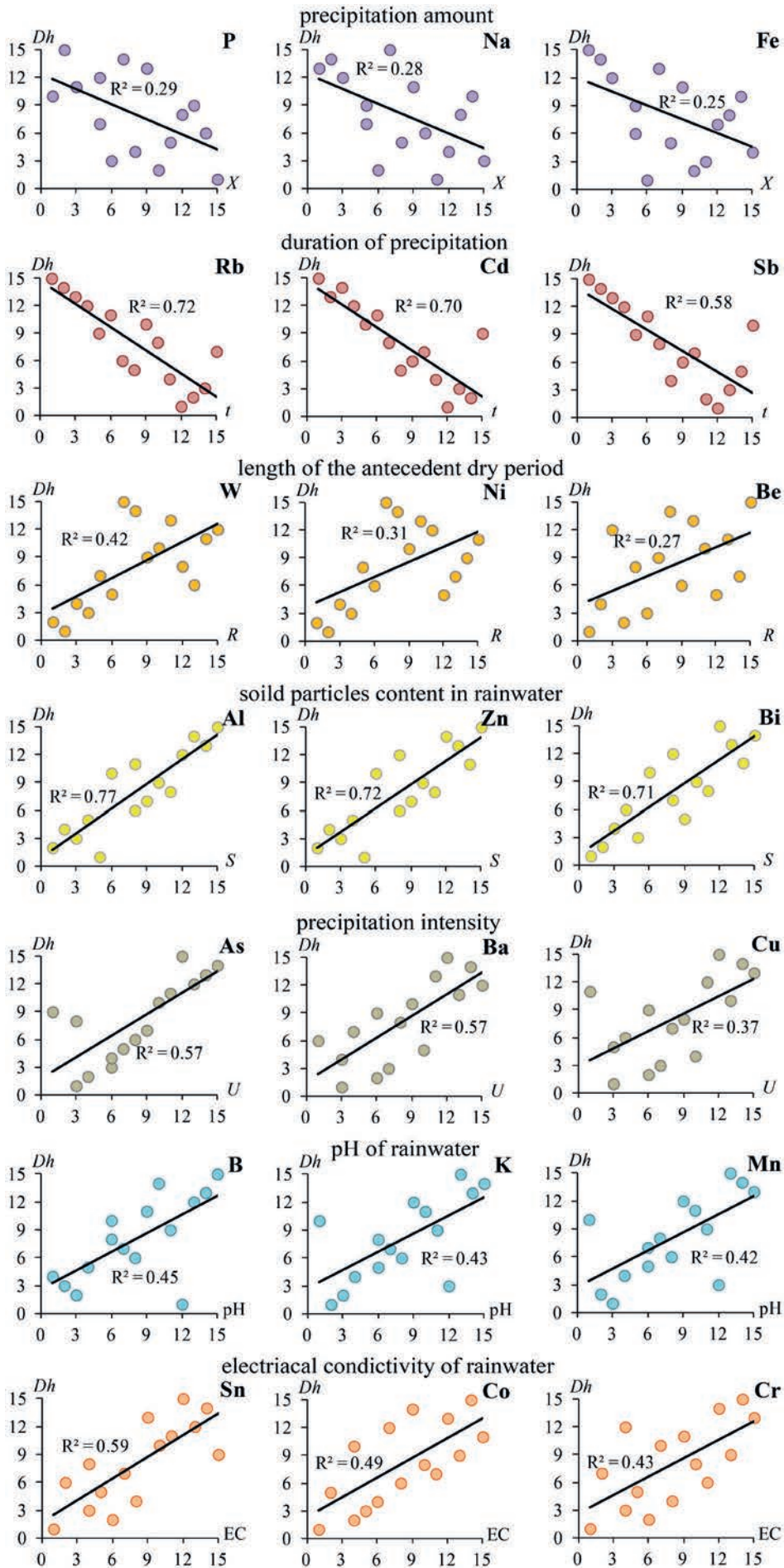


**Fig. 7.** Examples of rank correlation of washout rates of PTEs (vertical axis) with the physicochemical properties of rainwater or rain parameters (horizontal axis; designations are shown in caption of Fig. 2). High ranks correspond to high values of indicators. The color shows the dependences on the same rain parameters or properties of rainwater



## CONCLUSIONS

In urban conditions, rain is an important factor in the atmosphere purification from PTEs. The contaminated particles of road dust and urban soils input into the atmosphere during wind-blowing, the impact of transport and industrial facilities, waste incineration and biomass burning lead to a strong enrichment of rainwater with soluble forms of Sb, Pb, Se, Cd, and S, as well as P, Ba, As, W, Mn, Sn, Na, Co, Ni, and Be. High levels of PTEs wet deposition were revealed for the public holidays (May 1–6), which is due to the anthropogenic supply of PTEs to the atmosphere during the combustion of organic residues and coal in suburbs, the strong impact of transport and the elevated aerosol content due to predominant air advection from southern and south-western regions. During prolonged rains, the wet deposition of PTEs sharply decreases on the second and subsequent days due to the active below-cloud scavenging of aerosols during the initial moments of precipitation.

In Moscow, one of the most significant rainfall parameters affecting the level of PTEs wet deposition from

the atmosphere is the length of the dry period before the beginning of atmospheric precipitation when aerosol particles accumulate in the air, which leads to an increase in rainwater pH. This factor has a particularly strong effect on the deposition and washout of PTEs of mainly anthropogenic origin (W, Zn, Bi, Cd, Sb, Ni, B, S, K, and Cu). Another important factor in atmosphere purification from PTEs is the rain intensity, which depends on the amount and duration of precipitation. An increase in these parameters leads to an increase in wet deposition and washout rates of most PTEs, especially of anthropogenic Se, As, B, Cu, Sb, S, and Cd, anthropogenic-terrigenous Ba and K, and terrigenous Rb.

The first data obtained for Moscow on the rain parameters affecting the levels of wet deposition and washout rates of PTEs from the atmosphere in April–May are preliminary. However, these results can be useful for urban environmental quality assessment in Moscow and can provide a better understanding of atmospheric deposition processes in urban areas.

# Major ions and potentially toxic elements in atmospheric precipitation during the COVID-19 lockdown in Moscow megacity\*

## 1. INTRODUCTION

The rapid spread of a new coronavirus infection caused the introduction of mobility restrictions for inhabitants to reduce the population's morbidity, which significantly affected the state of the environment, economy, and society (Hartwell et al., 2021). Such lockdowns were introduced in many major cities around the world in the spring and summer of 2020 (Shakil et al., 2020), which reduced the number of vehicles both within cities and between (Marinello et al., 2021b; Zeng and Bao, 2021), the passenger traffic intensity on public transport (Sahraei et al., 2021), amount of air traffic (Suzumura et al., 2020), vehicle (Cao et al., 2021) and industrial emissions (Zheng et al., 2021).

Lockdowns represent a real-time experiment in monitoring the state of the urban atmosphere under the rapidly and significantly changing anthropogenic load (Jia et al., 2021). Restrictions led to the reduction of air pollution levels in cities with many contaminants (Adam et al., 2021; Marinello et al., 2021a), primarily  $\text{NO}_x$  (Barré et al., 2021; Volta et al., 2022),  $\text{PM}_{10}$  (Fan et al., 2021),  $\text{PM}_{2.5}$  (Balamurugan et al., 2022),  $\text{PM}_1$  (Clemente et al., 2022), nanoparticles and ultrafine particles (Eleftheriadis et al., 2021; Straaten et al., 2022), volatile organic compounds and non-methane hydrocarbons (Gu et al., 2022; Pakkattil et al., 2021), black carbon (Petit et al., 2021), polycyclic aromatic hydrocarbons (Ambade et al., 2021). Although electricity production and demand have declined on a macro-regional scale (Ali et al., 2021), shelter-in-place restrictions have led to an intensification of energy consumption in cities, especially by the private sector, and, accordingly, an increase in particulate matter from the residential burning of coal (Tyagi et al., 2021). Moreover, the results of observations over 540 traffic, background, and rural stations, from 63 cities covering 25 countries showed no clear signal between population mobility and the reduction of pollutants other than  $\text{NO}_2$  and  $\text{NO}_x$ , which indicates the influence of factors other than the reduced vehicular impact on improving air quality (Sokhi et al., 2021). Such a factor can be meteorological conditions (Das et al., 2021; Lv et al., 2022), which cause up to 36–49% of the decrease in black carbon,  $\text{PM}_{2.5}$ , and  $\text{NO}_2$  concentrations in Nanjing, China (Lin et al., 2021) and up to 1/3 of the decrease in  $\text{PM}_{2.5}$  concentrations over China and South Korea (Kang et al., 2020). Thus, the impact of restrictive measures on the state of the environment is ambivalent and can contribute to both a decrease and an increase in pollution.

However, there are few assessments of the impact of lockdown on the content of potentially toxic elements (PTEs) and water-soluble ions in aerosols (Chanchpara et al., 2021; Li et al., 2021; Liu et al., 2021b; Manchanda et al., 2021; Wang et al., 2021a) compared to the number of studies on the assessment of atmospheric gas pollution. Most often, there is a decrease in the level of

PTEs in atmospheric aerosols and dust due to the lesser vehicles impact, construction, dust blowing out, and in some cases to the lesser industrial emissions (Clemente et al., 2022; Millán-Martínez et al., 2022; Nguyen et al., 2021; Rabin et al., 2022) while waste burning and unfavorable meteorological conditions for the dispersion of pollutants contribute to an increase in aerosol pollution by PTEs and Cl during lockdowns (Nguyen et al., 2021; Wang et al., 2022b). The decreasing levels of atmospheric pollution during the lockdown are also manifested in a decrease in the amount of dry deposition of settleable particulate matter by 73–97% and the content of Al, Ca, Fe, Mg, Mn, and Na in it by up to 75% (Lara et al., 2022). However, for most megacities, estimates of the impact of lockdowns on aerosol pollution with PTEs are not available.

Under normal (without lockdowns) conditions, precipitation is a significant factor in the purification of the atmosphere from pollutants (Vithanage et al., 2022): for instance, 26–43% of  $\text{PM}_{2.5}$  is removed by the wet deposition in different seasons (Wang et al., 2021b). During the lockdown, a decrease in the level of wet and dry depositions of S and N from the atmosphere in Monterrey, Mexico, has been reported (Solís Canul et al., 2021). Heavy rainfall, which had already significantly reduced air pollution by  $\text{PM}_{10}$  and  $\text{PM}_{2.5}$  in the State of São Paulo, Brazil, prior to the lockdown, was the reason for the weak air pollution decline during the lockdown itself (Rudke et al., 2021). In Hangzhou, China, the concentrations of total and water-soluble Fe in  $\text{PM}_{2.5}$  decreased by 62–78%, but the solubility of Fe increased as a result of the atmospheric oxidizing capacity increase, which promoted the formation of more acidic species and further enhanced the dissolution of aerosol Fe (Liu et al., 2021a). During the lockdowns, PTEs content in mosses (Vergel et al., 2022; Yushin et al., 2020; Zupančič and Bozau, 2021) and snow pits (Wang et al., 2022a), reflecting atmospheric deposition, were studied. Nevertheless, the impact of the lockdown on the chemical composition and pollution level of atmospheric precipitation with PTEs has not been previously assessed in detail.

In Moscow, restrictive measures were introduced from the very end of March until the beginning of summer. From early April to mid-May, air pollution decreased due to a fourfold reduction in traffic load: for  $\text{CO}_2$  by 28–38%, for  $\text{NO}_2$  by 33–55%, for NO by 63–66%, and for  $\text{PM}_{10}$  by 17–28% (Ginzburg et al., 2020). Under the urban background conditions in the west of Moscow during the lockdown, the concentrations of  $\text{PM}_{10}$ , CO, NO,  $\text{NO}_2$ ,  $\text{CH}_x$ , and  $\text{SO}_2$  in the air decreased, and the concentrations of  $\text{O}_3$  increased due to reduced vehicle emissions and atypical meteorological conditions, which were manifested in the smoke air advection on the verge of the lockdown, as well as advection of clean air from the northern regions (Chubarova et al., 2021) with the reduction in cloud condensation nuclei concentrations

\* Vlasov D., Kasimov N., Eremina I., Shinkareva G., Chubarova N. // Urban Climate. 2023; 48: 101422.

during the lockdown (Shuvalova et al., 2022). In this period, the contribution of fuel combustion to the air pollution by black carbon in the city decreased, but the contribution of biomass burning in the residential areas in the suburbs (waste, wood and plant residues burning) and agricultural fires around the city increased (Popovicheva et al., 2021). After the restrictions were lifted, concentrations of black carbon and PM<sub>2.5</sub> increased significantly (Popovicheva et al., 2021), and concentrations of Ba, Sn, K, Cu, Bi, B, Mo, As, Sb, and Pb associated with PM<sub>10</sub> emitted from vehicles and industrial sources as well as Sr, Mg, Ca originated from construction and demolition processes, and Zr, P, Mn, Fe emitted with road dust and soil particles resuspension also increased (Kasimov et al., 2021). At the same time, PM<sub>10</sub> concentrations remained almost the same due to the washing out of particles by precipitation (Popovicheva et al., 2021). After the restrictions were lifted in early May, compared to April, the concentrations of P, Pb, Al, S, Ni, Sn, Sb, Bi, Se, and Th in size-segregated aerosols in the center of Moscow began to increase (Gubanova et al., 2021). However, the lack of data on pre- and post-lockdown PTEs levels did not allow assessing the lockdown impact on air pollution and the role of precipitation in the purification of the atmosphere from pollutants during the lockdown remains unclear.

Observations of the chemical composition of precipitation, including the content of PTEs forms, have been carried out in Moscow since the beginning of 2020, which made it possible to study the changes in the chemical composition of precipitation before, during, and after the lockdown in order to achieve the following goals: (1) to determine the change in physicochemical properties and major ion composition of precipitation before, during and after the lockdown; (2) to study the ratio of soluble and insoluble forms of PTEs in precipitation during these periods; (3) to identify sources and evaluate the impact of the lockdown on the change in their contribution to precipitation pollution.

## 2. MATERIALS AND METHODS

### 2.1. Study period

The investigation of the chemical composition of precipitation was carried out in January–July 2020 on the territory of the Meteorological Observatory of Lomonosov Moscow State University (MO MSU; 55.707°N, 37.522°E), located in the south-west of Moscow on the territory of the Botanical Garden away from industrial sources and major highways (Fig. S1).

Meteorological conditions in the studied period were previously described in detail (Chubarova et al., 2021). Briefly, winter 2019/2020 turned out to be dry (Hydrometcenter of Russia, 2021); the air temperature was significantly higher compared to 1954–2013 in all winter months and at the beginning of spring and summer: by 7.8°C in January, by 7.2°C in February, by 6.2°C in March, and by 1.5°C in June (Chubarova et al., 2014). The air temperature in April and May was lower than the long-term average values by 1.4°C and 1.7°C, respectively, which is associated with the predominance of air advection from the northern regions (Chubarova et al., 2021). The year 2020 was unique in terms of precipitation patterns. In January and February (56 mm and 35 mm respectively), precipitation amount was close to the long-term average annual for these months (47 mm and

40 mm), while in March (49 mm), it was 1.3-fold higher than average (37 mm) due to active cyclonic atmospheric processes, and in April – 2.4-fold lower (17 mm in April as opposed to 41 mm average). However, in May and June, unprecedented precipitation occurred (168 mm and 193 mm), almost three times higher than the long-term monthly mean (55 mm and 76 mm for May and June, respectively). Thus these months became the rainiest in 200 years of meteorological observations in Moscow (Lokoshchenko, 2020). In July, 113 mm of precipitation fell against the average value of 81 mm. As a result, a large amount of precipitation in late spring and early summer contributed to the purification of the atmosphere from pollutants.

On the other hand, there was a decrease in the anthropogenic load during the study period as starting from March restrictions were introduced to prevent the spread of the COVID-19 outbreak (Table S1). The self-isolation (lockdown) period for the majority of residents was introduced on March 30, and the access control regime began on April 13. Since June 1, car dealerships, non-food stores, weekend fairs, and some consumer services enterprises have resumed their work, and since June 9, the access control regime and self-isolation have been canceled (Measures against coronavirus in Moscow, 2020). During the lockdown, the number of vehicles on the roads has been drastically reduced (Fig. 1).

An average decrease in the number of vehicles on the weekdays of April was 40% (Kirilina, 2020), which resulted in the lowest level of road congestion for 2020 in Moscow in April (TomTom Traffic Index, 2020). During the pandemic, “Yandex” developed the self-isolation index (YSII), which demonstrated the lockdown level (the level of city activity compared to the typical day before the pandemic) in various cities, including Moscow: when YSII < 2.4, it means that there are many people on the streets; when YSII changes from 2.5 to 2.9 – there are many people on the streets; from 3.0 to 3.5 – some people on the street; from 3.6 to 3.9 – most people stayed at home; from 4.0 to 5.0 – streets are almost empty (Yandex, 2021). The changing of the YSII values in Moscow (Fig. 1) had a negative correlation with vehicles number (Kirilina, 2020), levels of road congestion (TomTom Traffic Index, 2020), as well as concentrations of PM<sub>10</sub>, CO, NO, NO<sub>2</sub>, CH<sub>x</sub>, SO<sub>2</sub> in the air of Moscow background area and positive correlation with O<sub>3</sub> (Chubarova et al., 2021).

The following periods have been identified to assess the impact of the lockdown on PTEs pollution of atmospheric precipitation.

Pre-lockdown period (PL) was from January 1 through March 31, since the precipitation on March 30–31 (the first days of the lockdown) washed out the pollutants that had accumulated in the atmosphere during the long rainless period started from March 15, which was before the restrictions. In January and February of 2020 (subperiod PL1), snow and mixed precipitation prevailed; in March of 2020 (subperiod PL2), it rained.

The lockdown period (LP) was from April 1 to May 31. Since in Moscow, air pollution is significantly affected by emissions of the power industry (Elansky et al., 2018), LP was divided into two subperiods: LP1 (April 1 – May 11) during the active heating season; and LP2 (May 12–31) during the lockdown, but after the end of the heating season. Starting from May 12, the number of vehicles on the roads of Moscow started to increase in



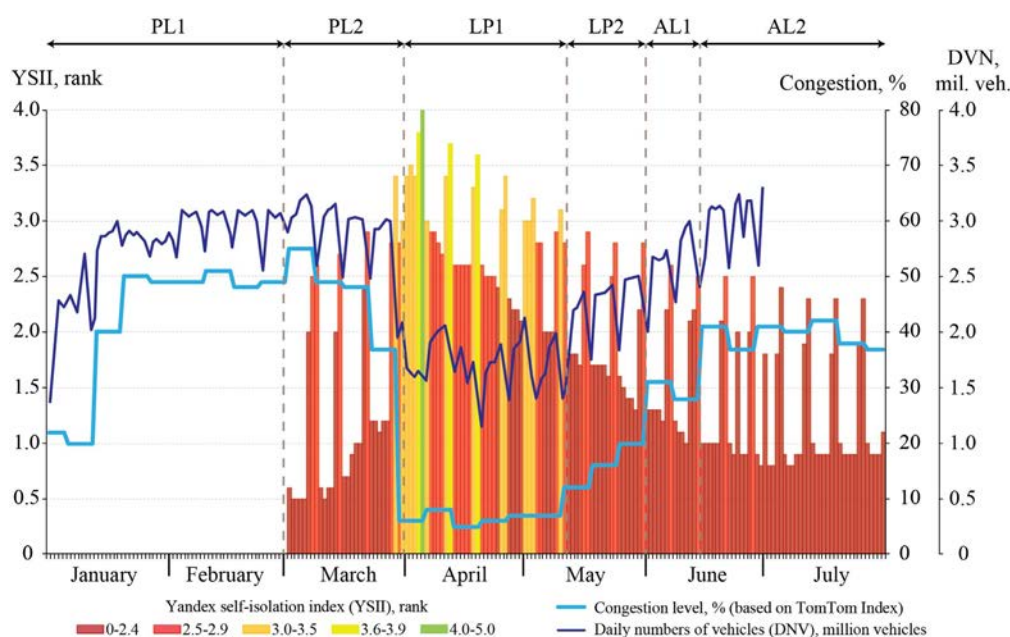


**Fig. 1.** The change of Yandex self-isolation index (YSII, ranks), levels of road congestion (mean % for every week, based on TomTom Index data), and daily vehicles number on the roads (DVN, millions of vehicles, based on data (Kirilina, 2020)) in Moscow in January–July 2020 during pre-lockdown periods (PL1, PL2, see comments in text), lockdown periods (LP1, LP2) and after lockdown periods (AL1, AL2).

comparison with April–early May 2020 (Kirilina, 2020); that is, on May 12, the influence of the lockdown on the intensity of the traffic load began to weaken. In addition, the non-working days’ regime in Russia, introduced on March 30, was canceled that day, leading to the restoration of transport and industrial activity.

After lockdown period (AL) lasted from June 1 until the end of the precipitation composition analysis campaign on July 27. Even though the access control regime and self-isolation have been canceled since June 9, it took longer to restore economic and transport activity fully. According to (TomTom Traffic Index, 2020), differences in road congestion in Moscow in the summer of 2020 compared to 2019 were < 20% starting from week 25, i.e., from June 15 (Fig. S2, Supplementary materials). Therefore AL was divided into two subperiods: AL1 (June 1–14) – the beginning of the lockdown canceling; and AL2 (June 15 – July 27) – the recovery of road traffic and industry activity. In June, in general, the number of vehicles on the roads of Moscow gradually returned to the level of 2019 (Kirilina, 2020).

## 2.2. Sampling and laboratory techniques

Precipitation samples ( $N = 87$ ) were taken on the MO MSU territory using a polyvinyl chloride funnel (80 × 80 cm), located at the height of 2 m from the ground surface, and a white plastic bucket. Each case of precipitation was analyzed from its beginning to the end on the current or adjacent day.

The pH and specific conductivity (EC,  $\mu\text{Sm}/\text{cm}$ ) was measured using an “Expert-001” ionometer and “Expert-002” conductivity meter (Econix, Russian Federation; accuracy:  $\pm 0.01$  and  $\pm 0.5\%$ , respectively). The soluble cations ( $\text{Ca}^{2+}$ ,  $\text{Mg}^{2+}$ ,  $\text{Na}^+$ ,  $\text{K}^+$ ,  $\text{NH}_4^+$ ) and anions ( $\text{SO}_4^{2-}$ ,  $\text{Cl}^-$ ,  $\text{NO}_3^-$ ) concentrations were determined by ion chromatography on a “JETchrom” instrument (Portlab, Russian Federation). The detection limits for cations and anions were calculated at a 95% confidence level

for three parallel measurements of the sample and blank measurements. For  $\text{SO}_4^{2-}$  and  $\text{Na}^+$  they are 0.04 mg/L, for  $\text{Ca}^{2+}$  and  $\text{K}^+$  – 0.03 mg/L, for  $\text{Cl}^-$ ,  $\text{NO}_3^-$ ,  $\text{NH}_4^+$ , and  $\text{Mg}^{2+}$  – 0.02 mg/L. Concentrations of  $\text{HCO}_3^-$  were obtained by titration with a solution of sulfuric acid with control of solution pH. The results showed a good convergence between the sum of equivalents of cations and anions with  $R^2 = 0.995$  (Fig. S3).

To determine the soluble and insoluble forms of PTEs, samples were filtered through membrane filters with a pore diameter of 0.45  $\mu\text{m}$  (EMD Millipore, USA) for separation of the solid phase (filter with suspended particles) from the liquid phase (filtrate), which were analyzed separately. Suspended particles concentration (SPC, mg/L) was estimated based on data on the mass of suspended particles deposited on the filter ( $m$ , mg) and the volume of filtered water ( $V$ , L):

$$\text{SPC} = m / V \quad (1)$$

Filter weight was determined on an analytical balance Discovery DV114C (Ohaus, Switzerland; repeatability: 0.1 mg).

Concentrations of Al, Ag, As, Ba, Bi, Cd, Co, Cr, Cs, Cu, Fe, Mn, Mo, Ni, P, Pb, Rb, S, Sb, Sc, Sr, Ti, Tl, W, and Zn in the filtrate and on the filter was obtained at the All-Russian Scientific Research Institute of Mineral Raw Materials named after N.M. Fedorovsky using ICP-MS and ICP-AES methods on mass spectrometer “iCAP Qc” (Thermo Fisher Scientific, USA) and atomic emission spectrometer “Optima-4300 DV” (Perkin Elmer, USA). This laboratory complies with ISO Guide 34:2009 and ISO/IEC 17025:2017. The analysis was conducted using instrument blanks, method blanks, and standard reference materials. For determining soluble PTEs, “Trace metals in Drinking Water” (High-Purity Standards, USA) reference material was used. The detection limits (DLs) were as follows ( $\mu\text{g}/\text{L}$ ): Al, 0.084; Ag, 0.005; As, 0.009; Ba, 0.016; Bi, 0.005; Cd, 0.003; Co, 0.005; Cr, 0.04;

Cs, 0.0025; Cu, 0.04; Fe, 2.5; Mn, 0.022; Mo, 0.036; Ni, 0.13; P, 4.0; Pb, 0.06; Rb, 0.004; S, 61; Sb, 0.005; Sc, 0.022; Sr, 0.22; Ti, 0.025; Tl, 0.0029; W, 0.007; Zn, 0.12. For insoluble PTEs, "GSO 3784–86" (Vinogradov Institute of Geochemistry SB RAS, Russian Federation) reference material was used. The DLs were as follows ( $\mu\text{g/g}$ ): Al, 53; Ag, 0.054; As, 0.12; Ba, 0.11; Bi, 0.02; Cd, 0.074; Co, 0.09; Cr, 1.1; Cs, 0.02; Cu, 0.85; Fe, 67; Mn, 4.1; Mo, 0.046; Ni, 1.1; P, 39; Pb, 0.1; Rb, 0.12; S, 47; Sb, 0.092; Sc, 0.085; Sr, 0.22; Ti, 0.025; Tl, 0.008; W, 0.03; Zn, 1.3. For low concentrations of PTEs ( $<5$  DLs), the relative standard deviation (RSD) did not exceed 20%; for higher concentrations of PTEs ( $>5$  DLs), RSD did not exceed 10%.

Due to the strong variability, for a correct comparison of the periods, volume-weighted concentrations of the soluble PTEs forms, major ions, and mineralization were calculated:

$$C = \sum_{i=1}^n (C_i \times X_i) / X_j \quad (2)$$

where  $C_i$  are concentrations of the soluble PTEs ( $\mu\text{g/L}$ ), major ions ( $\mu\text{eq/L}$ ), or mineralization ( $\text{mg/L}$ ),  $X_i$  is the amount of fluid (mm) that fell during  $i$ -th precipitation episode,  $n$  is the number of precipitation episodes in period  $j$ ,  $X_j$  is the amount of fluid that fell during of period  $j$  (mm). Concentrations of the insoluble PTE forms are measured in  $\mu\text{g/g}$ ; therefore, the average concentrations over the periods were calculated by simply averaging without considering the amount of precipitation.

Changes in PTEs concentrations ( $\delta$ , %) in the studied periods relative to each other were calculated as follows:

$$\delta = 100 \times (C_2 / C_1 - 1) \quad (3)$$

where  $C_2$  and  $C_1$  are the mean volume-weighted PTE concentrations in two compared periods.

To define the predominant fraction of elements in precipitation, the share of their soluble fraction or solubility ( $K_z$ , %) was calculated as:

$$K_z = 100\% \times C_{sol} / C_{tot}, \quad (4)$$

$$C_{tot} = C_{ins} + C_{sol}, \quad (5)$$

$$C_{ins} = C_g \times \text{SPC} / 1000, \quad (6)$$

where  $C_{sol}$  is the concentration of the soluble PTE,  $\mu\text{g/L}$ ;  $C_{ins}$  is the concentration of the insoluble PTE,  $\mu\text{g/L}$ ;  $C_{tot}$  is the total content of the soluble and insoluble fractions,  $\mu\text{g/L}$ ; SPC is the suspended particles concentration,  $\text{mg/L}$ ,  $C_g$  is the PTE content in suspended particles, washed out by precipitation,  $\mu\text{g/g}$ .

### 2.3. Assessment of the PTEs sources contribution to the pollution of precipitation

PTE sources in rains were estimated using the enrichment factor (EF):

$$\text{EF} = (C_i / C_{Al}) / (K_i / K_{Al}), \quad (7)$$

where  $C_i$  and  $C_{Al}$  are the contents of the  $i$ -th and reference (Al) elements in the precipitation sample, respectively;  $K_i$  and  $K_{Al}$  are the concentrations of the  $i$ -th and reference elements in the upper continental crust, respec-

tively (Rudnick and Gao, 2014).  $EF$ s were calculated using the volume-weighted PTE concentrations.  $EF < 10$  for the soluble phase and  $EF < 1$  for the insoluble phase show the predominant supply of PTE from terrigenous (crustal) sources;  $10 \leq EF < 100$  for soluble and  $1 \leq EF < 10$  for insoluble phases indicate the presence of both anthropogenic and terrigenous PTE sources;  $EF \geq 100$  for soluble phase (Chon et al., 2015) and  $EF \geq 10$  for insoluble one (Cheng et al., 2018) prove anthropogenic PTE origin in precipitation. Most often, for the soluble PTEs and total concentration of PTEs in rains, the gradation of  $EF \geq 100$  for anthropogenic sources is used (Koulousaris et al., 2009; Özsoy and Örnektekin, 2009; Samayamanthula et al., 2021; Tripathee et al., 2020), for the insoluble PTEs in precipitation and snow cover, lower  $EF$  gradations may be applied (Xu et al., 2022b). It has been proved that the threshold for evaluating the anthropogenic origin of metals in precipitation samples should be higher than that of aerosol samples Xu et al., 2022b). Since large particles blown from the surface of soils and roads make a significant contribution to the chemical composition of aerosols washed out from the atmosphere by rains, the gradations of  $EF$  adopted for soils and road dust ( $EF < 1$  for terrigenous sources, and  $EF \geq 10$  for anthropogenic sources) can be applied for insoluble phases (Adimalla et al., 2020; Bourliva et al., 2017; Liang et al., 2019; Morera-Gómez et al., 2020). Therefore, in our work, we used different gradations of  $EF$  for precipitation's soluble and insoluble phases.

For main PTEs sources identification, principal component analysis with multiple linear regression (PCA-MLR) was used in Statistica 8 software and R programming environment. As input data for PCA and another source apportionment method, positive matrix factorization, the PTE concentrations in each precipitation episode are often used without prior normalization to the precipitation volume (Al-Momani, 2003; Bisht et al., 2022; Jain et al., 2019; Keresztesi et al., 2020; Mirzaei et al., 2018; Samayamanthula et al., 2021; Tian et al., 2020) since the volume-weighted concentrations are usually used to average the PTE concentrations over a period of time, such as a month, season, or year (Ma et al., 2019; Tripathee et al., 2020). If the concentration of each PTE in each precipitation episode is replaced by the volume-weighted concentration, then the PTE content obtained after the application of MLR can only be averaged over the entire study period. This approach will not make it possible to estimate the change in the contributions of identified sources to the PTE concentration in each of the six studied subperiods. For PCA, data on the PTE deposition rates are sometimes used (Cereceda-Balic et al., 2020). There is a direct relationship between the deposition rate of PTEs and the amount of precipitation, which has been repeatedly confirmed (Cherednichenko et al., 2021; Cizmecioglu and Muezzinoglu, 2008; Pan and Wang, 2015; Takeda et al., 2000; Tripathee et al., 2020), including by our previous studies of Moscow rains (Vlasov et al., 2021a). The aim of the current research did not include the assessment of the PTEs deposition rate from the atmosphere. Therefore, when performing PCA-MLR, we used the concentrations of PTEs in soluble and insoluble phases of each precipitation episode.

The ultimate goal of performing PCA-MLR is to determine the percent contribution of different PTEs sources for a given precipitation sample. The detail process of the PCA-MLR model was described in previous

studies (Larsen and Baker, 2003; Thurston and Spengler, 1985). Only the principal components with eigenvalues  $>1$  (Kaiser's criteria) were used as factors. Prior to the analysis, Z-normalization was applied (Larsen and Baker, 2003):

$$Z_{ik} = (C_{ik} - \bar{C}_i) / \sigma_i, \quad (8)$$

where  $C_{ik}$  is the concentration of the  $i$ -th chemical element in the sample  $k$ ,  $\bar{C}_i$  is the average concentration of the  $i$ -th element, and  $\sigma_i$  is the standard deviation of the  $i$ -th element. Kaiser-Meyer-Olkin (KMO) and Bartlett's sphericity tests were performed to examine the suitability of the data for PCA (Varol, 2011). KMO is a measure of sampling adequacy that indicates the proportion of variance that is common, i.e., the variance that may be caused by underlying factors. In this study, KMO is 0.84 (meritorious level) for datasets of soluble and insoluble forms of PTEs, indicating that each dataset is adequate and PCA may be helpful. Bartlett's test of sphericity indicates whether a correlation matrix is an identity matrix and whether variables are unrelated. The significance level of  $<0.001$  for each dataset in this study indicates significant relationships among the variables.

Source contribution was estimated with PCA-MLR, for which the total PTEs concentrations were calculated separately in soluble ( $\sum C_{sol}$ ) and insoluble ( $\sum C_{ins}$ ) phases of precipitation. The MLR equation can be expressed as:

$$\hat{Z}_{\sum C_{sol}} = \sum (B_k \times FS_k), \quad (9)$$

where  $\hat{Z}_{\sum C_{sol}}$  is the standard normalized deviate of the sum of the soluble PTEs concentrations,  $B_k$  represents the regression coefficients, and  $FS_k$  is factor (principal component) scores calculated by the PCA analysis. Thus, the mean percentage contribution of source  $k$  (MPCS, %) was calculated as:

$$MPCS = 100 \times B_k / \sum B_k, \quad (10)$$

and the mass contribution of each source  $k$  (MCS,  $\mu\text{g/L}$ ) was estimated as:

$$MCS = \text{mean}_{\sum C_{sol}} \times (B_k / \sum B_k) + B_k \times \sigma_{\sum C_{sol}} \times FS_k \quad (11)$$

where  $\sigma_{\sum C_{sol}}$  is the standard deviation of  $\sum C_{sol}$  (947  $\mu\text{g/L}$ ), and  $\text{mean}_{\sum C_{sol}}$  is the mean of  $\sum C_{sol}$  (968  $\mu\text{g/L}$ ). The same calculations were performed for the insoluble PTE phase of precipitation at  $\sigma_{\sum C_{ins}}$  equal to 26,696  $\mu\text{g/g}$  and  $\text{mean}_{\sum C_{ins}}$  equal to 90,077  $\mu\text{g/g}$ . Based on the results of PCA-MLR, volume-weighted mean concentrations of PTEs were calculated for the studied subperiods.

To identify the probable source regions of air masses arriving at Moscow, backward trajectories were analyzed for each rain sample collection date using the HYSPLIT transport and dispersion model (Rolph et al., 2017). Modeling was carried out at heights of 500, 1000, and 1500 m above the Earth's surface with an interval of 72 h from 12 UTC of the day with the precipitation. In addition, an analysis of the possible advection of a smoke cloud from agricultural fires was carried out; this methodology was described in detail by Chubarova et al., 2020, Chubarova et al., 2021. Briefly, to do so, the data from the FIRMS fire monitoring service using MODIS/Terra satellite images was used together with the actual data on the oc-

currence of detected fires within a 50 km radius from the particle transfer line, determined by the HYSPLIT backward trajectory method at the height of 500 m with a time step of one day. If the number of fires in the region (Moscow, Moscow region, and adjacent regions) was small and/or the fires were located on the border of a 50 km region, then the AERONET data on the Absorption Angstrom Exponent (AAE) were additionally used. The impact of fires was proved for March 17–18 and 25–29, April 4, 7, 9, 13, 23, and June 18.

### 3. RESULTS AND DISCUSSION

#### 3.1. Changes in the physicochemical properties of precipitation and major ions content during the lockdown

Data on the physicochemical properties of precipitation and major ions content during PL, LP, and AL periods in Moscow in the winter and summer of 2020 are shown in Table 1. In 2020, the decrease in precipitation pH from winter to summer (Fig. 2) was entirely consistent with its long-term annual variation (Chubarova et al., 2014). During each of the LP2, AL1, and AL2 periods, a considerable amount of precipitation occurred, comparable to the sum of precipitation of the PL1 + PL2 periods, which lasted three months. The daily average for LP2, AL1, AL2, and PL1 + PL2 was 6.7 mm, 9.3 mm, 5.4 mm, and 1.6 mm, respectively. At the same time, the intensity of precipitation increased from the beginning of the year to the summer season. This contributed to the intensification of pollutant washout from the atmosphere from PL1 (3.7 mm/episode) and PL2 (4.9 mm/episode) to LP1 (5.0 mm/episode) and especially LP2 (11 mm/episode) and AL1 (16 mm/episode), decreasing at PL2 (8.8 mm/episode). The level of precipitation pollution was affected by the uneven distribution of the amount and intensity of the precipitation. The average content of solid particles and EC was the highest in LP1 despite the introduced lockdown restrictions and the lowest in AL1 due to dilution. High concentrations of particulate matter and EC during LP1 were also associated with frequent episodes of smoke advection (April 4, 7, 9, 13, and 23) and aerosol accumulation in the atmosphere during a long two-week period without rainfall before the first April precipitation (April 18).

The highest volume-weighted concentrations of all ions were observed during LP1, which coincide mainly with April, when the highest long-term annual content of ions is usually recorded (Chubarova et al., 2014). The main reason for this is the inverse relation of these concentrations with precipitation and lack of snow cover. At the same time, the herbaceous cover is not yet developed in April, so partially dissolving soil particles, with an increase in convection, end up in the surface air layer. Therefore, in 2020, the maximum mineralization value was obtained for LP1 with the minimum amount of precipitation, which is associated with increased concentrations of  $[\text{HCO}_3^-]$ ,  $[\text{Cl}^-]$ , and  $[\text{Na}^+]$ , by factors of 2.6, 1.6, and 3.6, and decreased concentrations of  $[\text{SO}_4^{2-}]$  and  $[\text{NO}_3^-]$  by factors of 2.0 and 1.4 respectively in LP1 relative to the long-term annual data for April in 2000–2019. The concentration of  $[\text{SO}_4^{2-}]$  has been gradually decreasing in all seasons of recent years, and the decrease of  $[\text{NO}_3^-]$  content in LP1 relative to long-term data can be associated with a significant decrease in traffic load



**Table 1.** The amount of precipitation, physicochemical properties of precipitation, and volume-weighted content of major ions in the periods before (PL1, PL2) during (LP1, LP2) and after lockdown (AL1, AL2) in Moscow in 2020.

Parameters	Periods					
	PL1	PL2	LP1	LP2	AL1	AL2
	Jan 01–Feb 29	Mar 01–Mar 31	Apr 01–May 11	May 12–May 31	June 01–June 14	June 15–July 27
X, mm	91	50	50	135	130	167
X per episode, mm	3.2	4.9	5.0	11	16	8.8
pH	6.6	6.4	5.9	5.6	5.2	5.1
EC, $\mu\text{S}/\text{cm}$	34	40	69	25	14	28
SPC, mg/L	18	34	51	17	12	15
$\text{HCO}_3^-$ , $\mu\text{eq}/\text{L}$	55	69	80	23	4.1	7.1
$\text{SO}_4^{2-}$ , $\mu\text{eq}/\text{L}$	24	34	45	22	12	30
$\text{Cl}^-$ , $\mu\text{eq}/\text{L}$	117	127	319	93	49	106
$\text{NO}_3^-$ , $\mu\text{eq}/\text{L}$	23	29	29	17	12	27
$\text{Ca}^{2+}$ , $\mu\text{eq}/\text{L}$	112	153	240	75	41	88
$\text{Mg}^{2+}$ , $\mu\text{eq}/\text{L}$	7.8	8.9	26	8.7	4.7	13
$\text{Na}^+$ , $\mu\text{eq}/\text{L}$	39	45	59	19	5.7	17
$\text{K}^+$ , $\mu\text{eq}/\text{L}$	7.3	11	11	7.9	3.9	10
$\text{NH}_4^+$ , $\mu\text{eq}/\text{L}$	41	38	121	39	14	36
Mineralization, mg/L	14	17	29	9.9	4.7	11
$\sum\text{anions}/\sum\text{cations}$	1.06	1.02	1.03	1.04	1.12	1.04

X is the precipitation amount, EC is electrical conductivity, and SPC is the solid particle content.

and, accordingly, nitrogen oxide emissions during the period of strict restrictions. An increase in  $[\text{NO}_3^-]$  concentrations due to the traffic load recovery was also observed in AL2 (from 12  $\mu\text{eq}/\text{L}$  in AL1 to 27  $\mu\text{eq}/\text{L}$  in AL2) and in LP2 (to 17  $\mu\text{eq}/\text{L}$ ), despite the substantial dilution of samples due to high precipitation amount.

The ion balance in precipitation during the studied periods changed (Fig. 3). The contribution of  $[\text{HCO}_3^-]$  to the sum of the ions decreased from January to July: from 13% in PL to 8.1% in LP and 2.3% in AL (Fig. 3, Fig. S4), which coincides with the trend of decreasing pH from winter to summer. In LP1, contributions of  $[\text{NO}_3^-]$  and  $[\text{SO}_4^{2-}]$  decreased due to reduced transport and industry emissions (Fig. S4, Fig. S5), but the contribution of  $[\text{Cl}^-]$  and  $[\text{NH}_4^+]$  increased slightly, and starting from LP2, the contribution of  $[\text{NO}_3^-]$  and  $[\text{SO}_4^{2-}]$  began to increase, due to the secondary formation of aerosols during transboundary transport as one of the reasons (Hassan et al., 2022; Zheng et al., 2020): ammonium sulfate (Pearson correlation coefficient  $r$  between  $[\text{NH}_4^+]$  and  $[\text{SO}_4^{2-}]$  was 0.69), ammonium nitrate ( $r$  between  $[\text{NH}_4^+]$  and  $[\text{NO}_3^-]$  was 0.43) and ammonium chloride ( $r$  between  $[\text{NH}_4^+]$  and  $[\text{Cl}^-]$  was 0.81) (Fig. S6). An increase of a secondary inorganic aerosol contribution to the major ions and trace elements content in  $\text{PM}_{2.5}$  in Wuhan was noted for local air masses with a simultaneous decrease in the contribution of industrial processes, coal combustion, biomass burning, vehicle emissions, and road dust (Zheng et al., 2020). In Delhi, during the lockdown, the contribution of vehicular emissions, domestic coal combustion, and semi-volatile oxygenated organic aerosol in  $\text{PM}_{2.5}$  concentrations in the air decreased by 86–96%, while the contribution of secondary chloride, power plants, dust-related, hydrocarbon-like organic aerosols, and biomass burning related emissions changed only slightly and depended mainly on meteorological conditions (Manchanda et al., 2021). However,

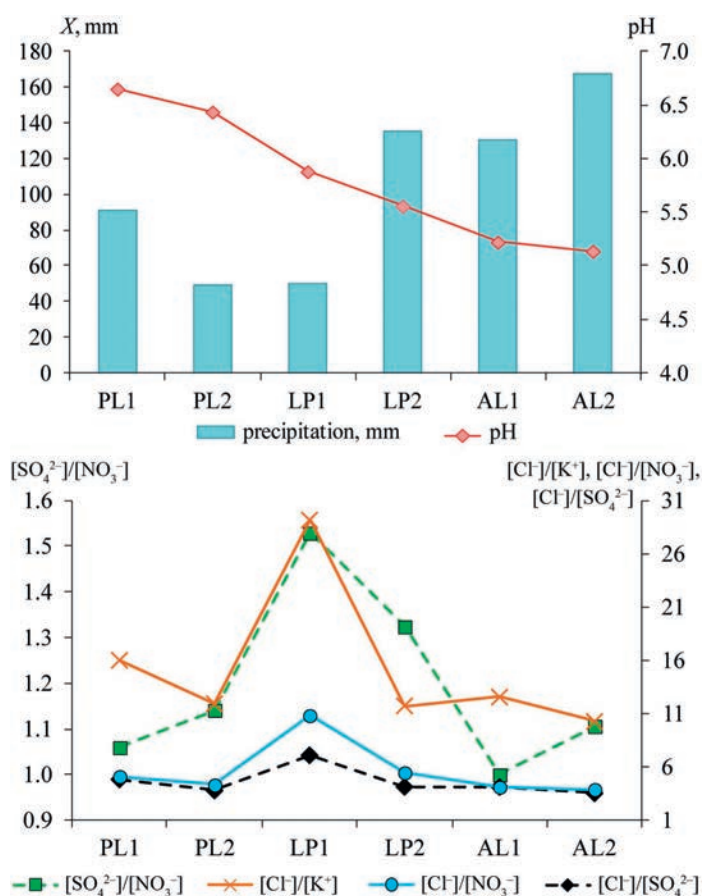


**Fig. 2.** Precipitation amount (X, mm), pH value, and  $[\text{SO}_4^{2-}]/[\text{NO}_3^-]$ ,  $[\text{Cl}^-]/[\text{K}^+]$ ,  $[\text{Cl}^-]/[\text{NO}_3^-]$ ,  $[\text{Cl}^-]/[\text{SO}_4^{2-}]$  ratios in rains that fell during the studied subperiods in Moscow in 2020.

the assessment of the role of  $[\text{Cl}^-]$  in the formation of secondary inorganic aerosols in Moscow requires further detailed investigation in different seasons.

The increase in the contribution of  $[\text{Cl}^-]$  in LP could be explained as follows. In Moscow, de-icing mixtures are used, up to 60–80% of the mass of which accounts for NaCl, and the rest are  $\text{CaCl}_2$ , crushed marble ( $\text{CaCO}_3$ ), KCl,  $\text{HCOONa}$ ,  $\text{MgCl}_2$ ; liquid solutions of  $\text{CaCl}_2$  and NaCl are also used (Order N 05-14-650/1, 2011). It is known that in the warm season, chloride de-icing mixtures can be a significant factor in the acidification of atmospheric precipitation in Moscow due to the formation of HCl (Eremina et al., 2015), which can lead to the increase in soluble PTE forms in precipitation (Vlasov et al., 2021b). Substantial  $[\text{Cl}^-]$  input may be due to the influence of the de-icing mixtures in Moscow (Zappi et al., 2023), as a very high  $r$  value (up to 0.95) was defined between  $[\text{Cl}^-]$  and  $[\text{Ca}^{2+}]$  in precipitation in January–July of 2020 (Fig. S6). However, the high correlation between  $[\text{Na}^+]$  and  $[\text{Cl}^-]$  ( $r = 0.84$ ,  $R^2 = 0.705$ ) was lower than typical for precipitation influenced by marine aerosol ( $R^2 > 0.9$ ) (Terzi et al., 2010) and dissolution of de-icing mixture particles, blown out from the road and soil surfaces after snowmelt, which indicates an additional source of  $[\text{Na}^+]$  and  $[\text{Cl}^-]$ . It was reported that such a source of  $[\text{Cl}^-]$  in aerosols and precipitation could be waste incineration (Liu et al., 2018), open biomass burning, and its burning in residential areas (Fourtziou et al., 2017; Yang et al., 2018). The increase in  $[\text{Cl}^-]$  contribution to the sum of the ions in Moscow precipitation was observed in LP1 (from 24.8% in PL2 to 34.3% in LP1) when part of the city residents moved to suburban areas where they burned waste and heated by burning coal and wood due to low air temperatures. This probably caused a sharp increase in  $[\text{Cl}^-]/[\text{SO}_4^{2-}]$  and  $[\text{Cl}^-]/[\text{NO}_3^-]$  ratios in LP1 up to 7.1 and 11, respectively, at the ranges of 3.8–4.8 and 4.3–5.1 in PL1 and PL2, as well as 3.5–4.1 and 3.9–5.5 in LP2, AL1, and AL2. Wherein the  $r$  value was higher between  $[\text{Cl}^-]$  and  $[\text{SO}_4^{2-}]$  (0.70) in comparison with  $r$

between  $[\text{Cl}^-]$  and  $[\text{NO}_3^-]$  (0.61; Fig. S6). An increase in biomass and coal burning contribution to aerosol pollution by polycyclic aromatic hydrocarbons during lockdown with a simultaneous decrease of traffic contribution was revealed in Jamshedpur, India (Ambade et al., 2021). In Suzhou, during the Chinese New Year and the lockdown, the contribution of coal combustion and industrial emissions to the  $\text{PM}_{2.5}$  content increased by 2.9 and 1.7 times, and traffic contribution decreased by 22% only (Wang et al., 2021a). An increase in  $[\text{Cl}^-]/[\text{SO}_4^{2-}]$  ratio up to 6–10 and higher indicates that biomass burning and waste combustion could be an essential  $[\text{Cl}^-]$  source in aerosols (Luo et al., 2019) and, accordingly, precipitation, which also supports our hypothesis.

Potassium ion  $[\text{K}^+]$  is often used as another biomass burning indicator (Achad et al., 2018). However, it could also migrate with sea salt (Fourtziou et al., 2017) and terrigenous dust particles (Yu et al., 2018) and be associated with de-icing mixtures (Order N 05-14-650/1, 2011). Correlation between  $[\text{K}^+]$  and  $[\text{Cl}^-]$  during the studied periods in Moscow was high ( $r = 0.67$ ), and episodes with a sharp increase in  $[\text{K}^+]$  and  $[\text{Cl}^-]$  in general were observed at the end of March and the first half of April, as well as on April 24. On these dates, frequent smoke advectations of polluted air from the suburbs (Fig. 4) with very high  $\text{PM}_{10}$  and  $\text{PM}_{2.5}$  concentrations were recorded (Gubanova et al., 2021) that were also observed in the atmospheric column (Chubarova et al., 2021). During LP1, an average  $[\text{Cl}^-]/[\text{K}^+]$  value sharply increased up to 29, from 12 to 16 during pre-lockdown, and decreased afterward in LP2, AL1, and AL2 to 10–13 (Fig. 2), which indicates a significant  $[\text{Cl}^-]$  input as a result of waste burning. Such features have been identified in other cities during the lockdown, for instance, in Pudong (China), concentrations of Cl in atmospheric  $\text{PM}_{2.5}$  increased due to waste incineration (Wang et al., 2022b), and in Hangzhou (China) particles containing biomass burning tracers increased up to 155% (Xu et al., 2022a).

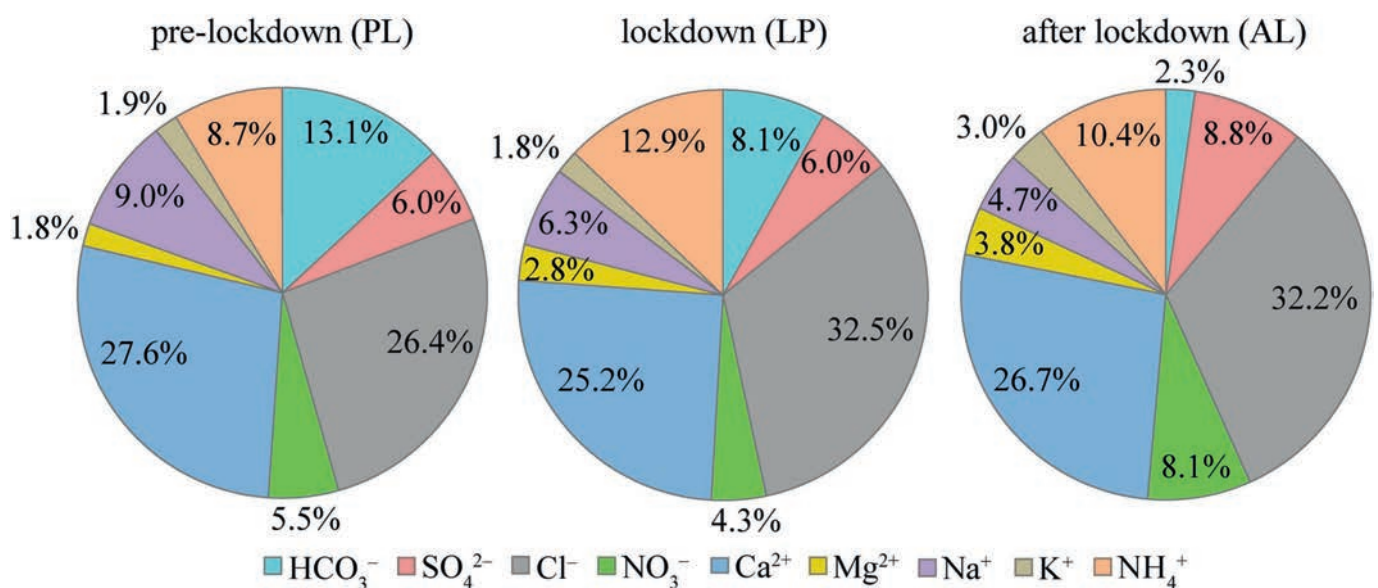


Fig. 3. The ion balance in Moscow precipitation before, during, and after the lockdown in January–June of 2020.



The smoke advection from the suburbs and the concomitant decline in city vehicle emissions during the lockdown led to a dramatic change in the  $[\text{SO}_4^{2-}]/[\text{NO}_3^-]$  ratio, which increase shows an amplification of the influence of stationary sources, and a decrease identifies the transport sources (Naimabadi et al., 2018; Zeng et al., 2021). In PL, the  $[\text{SO}_4^{2-}]/[\text{NO}_3^-]$  ratio was 1.06–1.14, which sharply increased later in LP1 up to 1.53 due to an increase in  $[\text{SO}_4^{2-}]$  concentrations and relatively unchanged  $[\text{NO}_3^-]$  concentrations. The increase in  $[\text{SO}_4^{2-}]$  concentrations in LP1 may be related to the waste, biomass, and coal burning in the suburbs (the sources of  $\text{SO}_2$  emissions), which was considered above when analyzing the  $[\text{Cl}^-]/[\text{SO}_4^{2-}]$  ratio. In LP2, it decreased to 1.32 due to a faster decline in  $[\text{SO}_4^{2-}]$  concentrations compared with  $[\text{NO}_3^-]$ . In Moscow, natural gas is mostly used for heating, but in towns from the Moscow suburbs fuel oil may be additionally used, so higher air temperatures (late spring), the end of the heating season, and less waste and fuel combustion in the suburbs in LP2 could be the reason for the decrease in  $\text{SO}_2$  emissions and, as a consequence, a decrease in  $[\text{SO}_4^{2-}]$  concentrations in the precipitation. The significant role of satellite towns in air pollution in Moscow during the lockdown is confirmed by data on the contamination of the moss *Pleurozium schreberi* with trace

elements on the territory of the entire Moscow region (Vergel et al., 2022). After the lockdown, this ratio decreased even further, amounting to 1.00–1.11 (Fig. 2). This is due to the increase in  $[\text{NO}_3^-]$  concentration in AL2 on account of the restoration of transport activity, the growth of vehicle emissions, including  $\text{NO}_x$ . Nevertheless,  $r$  between  $[\text{SO}_4^{2-}]$  and  $[\text{NO}_3^-]$  was 0.70 for the entire study period (Fig. S6), reaching 0.76–0.94 in PL1, PL2, LP1 and AL1, but reducing to 0.58–0.61 in LP2 and AL2. This indicates ion input from fuel combustion in most precipitation episodes before and during the first part of the lockdown, as well as immediately after the restrictions were lifted.

During AL, the contribution of  $[\text{Ca}^{2+}]$  began to increase slightly due to the intensification of the ion supply during the blowing out of soil and dust particles in the summer after the end of long and intense rains. Simultaneously the contribution of  $[\text{NH}_4^+]$  and  $[\text{Na}^+]$  decreased due to the blowing out of a lesser amount of de-icing mixture residuals to the summer. After the restrictions were lifted, the  $[\text{NO}_3^-]$  contribution doubled. This growth began in the second phase of restrictions (the second half of May) when the traffic load began to increase gradually, and the share of  $[\text{NO}_3^-]$  increased from 3.2% in LP1 to 5.6% in LP2, continuing to grow in AL1 and AL2 to 8.1–8.2% (Fig. S4).

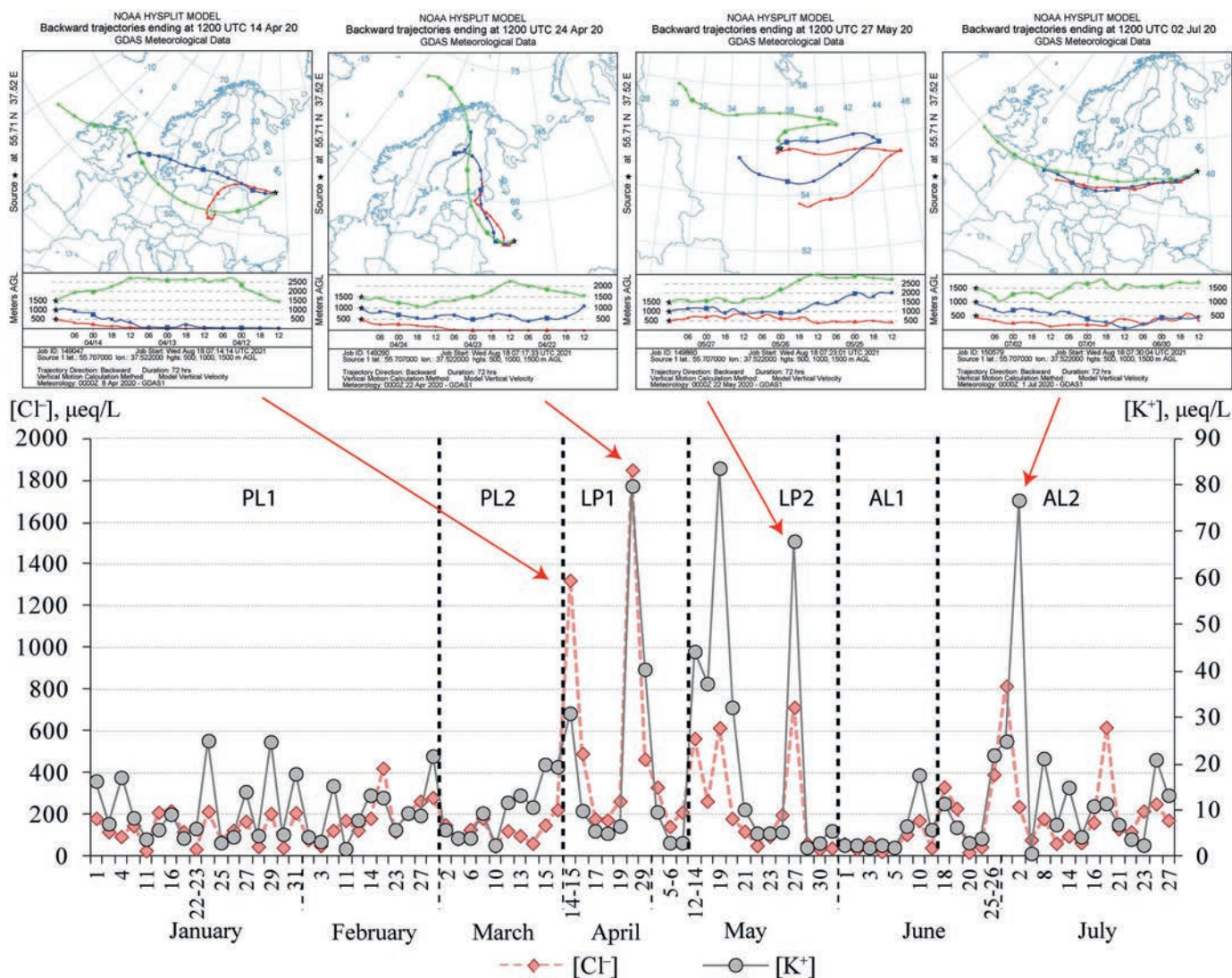


Fig. 4. Concentrations of  $[\text{Cl}^-]$  and  $[\text{K}^+]$  in atmospheric precipitation in Moscow in January–July 2020 by individual episodes.



### 3.2. Content and solubilities of PTEs during periods

The content of soluble and insoluble forms of PTEs in atmospheric precipitation during the studied periods in Moscow is given in Table S2. Concentrations of soluble forms are highly dependent on precipitation amount due to dilution processes (Tripathee et al., 2020), therefore, volume-weighted concentrations were used for the correct comparison of the periods.

Before the lockdown, mixed precipitation (rains and snow) fell in January–February, rains prevailed in March, and the amount of precipitation in PL2 was almost two times less than in PL1, which contributed to a relative

increase in PTE concentrations. In the last quarter of March, a powerful positive pressure anomaly and unfavorable meteorological conditions for the dispersion of impurities were observed, which led to a sharp short-term increase in the concentrations of CO and PM<sub>10</sub> (Ginzburg et al., 2020). Smoke advection also contributed to the additional contamination effect since it happened on March 21–27, which, together with the absence of precipitation, led to the intensification of pollution (Chubarova et al., 2021). As a result of the combined effect of anthropogenic impact in the first half of PL2 and meteorological parameters in the second half of PL2, the concentrations of the soluble form of most PTEs increased compared to PL1 (Fig. 5, Fig. 6, Figs. S7–S9, Table S3), while the in-

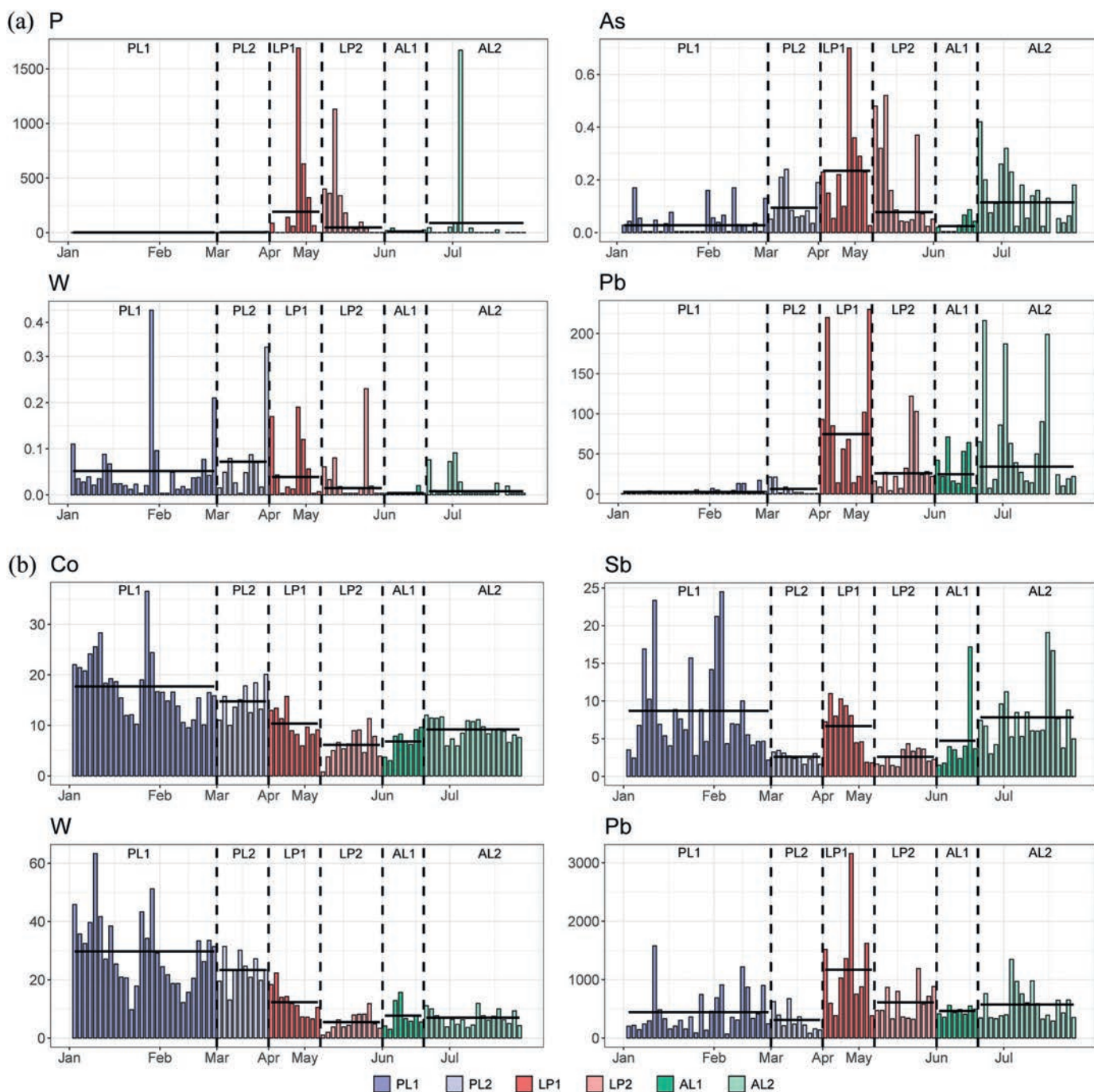


**Fig. 5.** The content of (a) soluble,  $\mu\text{g/L}$ , and (b) insoluble,  $\mu\text{g/g}$ , forms of some PTEs in Moscow precipitation in January–July of 2020. Horizontal lines show volume-weighted soluble PTEs concentrations over the subperiod and averaged insoluble PTEs concentrations over the subperiod. Subperiod designations are indicated in the text. Plots for other PTEs are shown in Figs. S7 and S8 in the Supplementary Materials.

soluble form of all PTEs, on the contrary, decreased due to the beginning of anthropogenic load reduction from local (intraurban) sources. The concentrations of soluble PTEs, emitted during the waste incineration – As, P, Ag, and emissions from industries – Sb, Mo, Al, Pb, Ag increased dramatically ( $> 60\%$ ) (Kara et al., 2014; Kasimov et al., 2020; Zheng et al., 2018).

During the lockdown, compared to the PL period, concentrations of soluble P ( $>3000\%$ ), Ag ( $>2000\%$ ), Pb ( $>800\%$ ), and Sb ( $>500\%$ ) increased dramatically, which is associated with the waste and plant residues burning in suburban areas, as well as the biomass burning before the lockdown. During the lockdown, the biomass burning contribution to the content of black carbon in Moscow was 20%, and after the restrictions were lifted, it decreased to 13%, while the contribution of fossil fuel combustion increased from 79% to 87%; the largest contribution of biomass burning was characteristic of air advection from the northeast and northwest (Popovicheva et al., 2021). Smoke advection was often observed during the lockdown period in April (Chubarova et al., 2021), which was also confirmed by high correlation coefficients  $r$  between  $[K^+]$  and P (0.81), as well as  $[Cl^-]$  and Sb (0.88) (Fig. S6). An intensive increase in the concentrations of soluble PTEs forms was observed mainly in the first lockdown subperiod (LP1) in April and the first half of May. An increase

in PTE concentrations in precipitation and snow during the lockdown was also found in the urban area in Thessaloniki, Greece, due to the higher central heating emissions during this period (Tsamos et al., 2022). In the second half of May (LP2), the end of the heating season in Moscow, a decrease in traffic load and a significant amount of precipitation, as well as the advection of the cleanest Arctic air with low values of the pollutants (Chubarova et al., 2021) and contributed to a sharp decrease in the concentrations of soluble forms of PTEs.

Fine particles migrate most in the atmosphere. After being washed out by precipitation and during filtration, these particles pass through the filter pores, i.e., form the soluble phase of precipitation. This is especially true for S, Pb, Zn, K, Sb, Bi, Mn, Mo, Sn, P, Cu, and Co, up to 25% of which in  $PM_{10}$  in Moscow is accounted for by  $PM_{0.5}$  (Gubanova et al., 2021). Therefore, during episodes of smoke advection, the concentrations of soluble PTEs mainly increased, while the content of insoluble forms of most PTEs contained in particles larger than  $0.45 \mu m$  (filter pore diameter) increased in LP1 and decreased in LP2 (Fig. 6, Fig. S9). The impact of smoke advections on air quality in Moscow during the lockdown is confirmed by the increase in concentrations of P, Pb, Bi, Se, Ni, Sn, and Sb in aerosols in the city center in late March and early May compared to April (Gubanova et

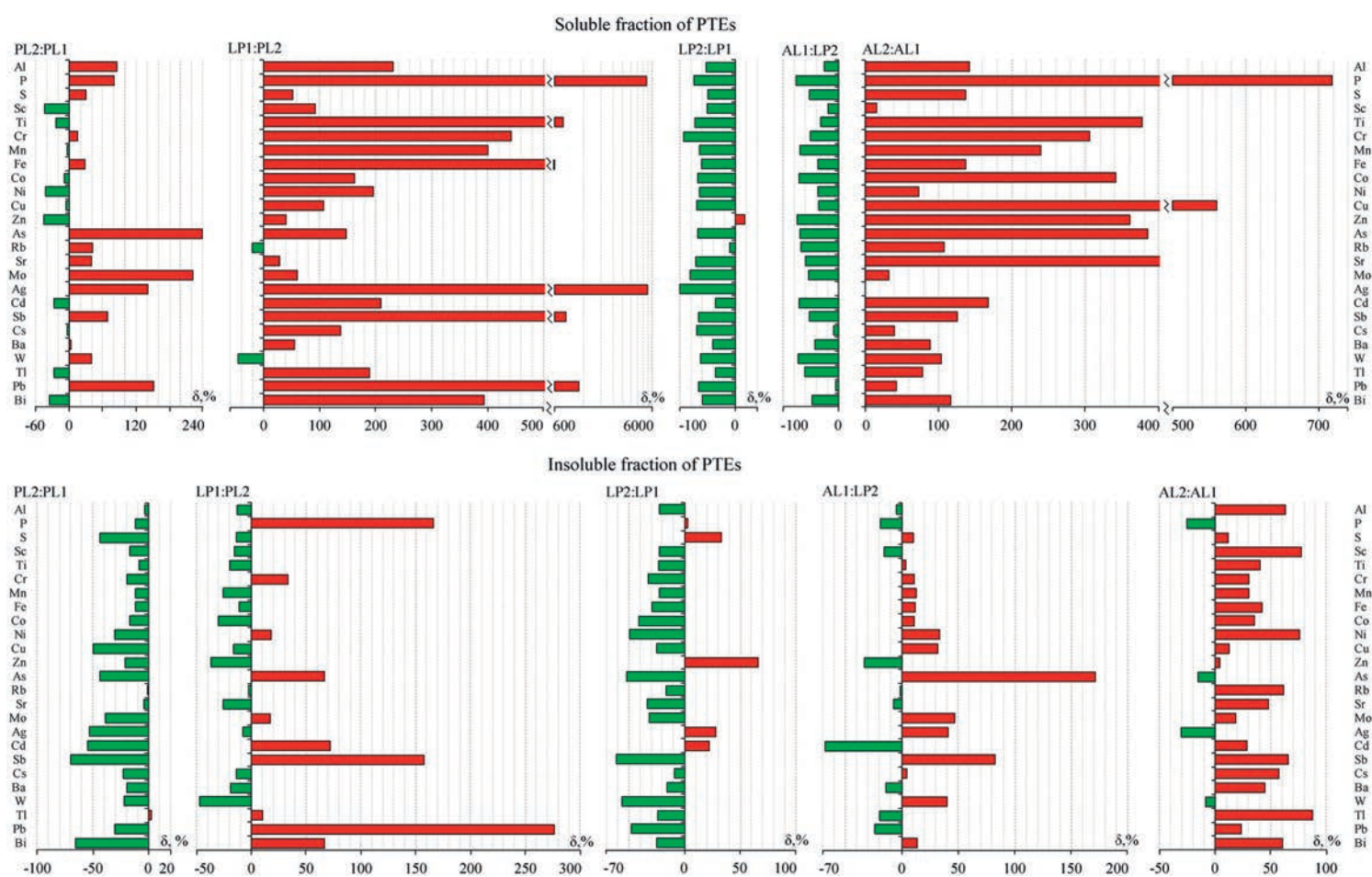


**Fig. 6.** Lockdown effect: change in concentrations ( $\delta$ , %) of soluble and insoluble PTEs in atmospheric precipitation in Moscow in the studied periods in January–July 2020. Positive  $\delta$  are shown in red, and negative  $\delta$  are shown in green. (For interpretation of the references to colour in this figure legend, the reader is referred to the web version of this article.)



al., 2021). In LP2, compared with LP1, concentrations of almost all PTEs, besides Zn, decreased by 10–99%. Over the entire LP, compared to PL, the concentrations of insoluble P and Pb in precipitation increased by 146% and 112%, respectively. Simultaneously the concentrations of W, Cu, and Co decreased by 50–70%; Sr, Ag, Bi, Mn, S, Sc, Sb, Ba, and Ni by 35–50%; and of the remaining PTEs by <35%. This indicates a less intensive PTEs supply from intraurban sources: vehicle emissions and blowing out of road dust particles due to sharply reduced traffic, which is confirmed by TomTom data (TomTom Traffic Index, 2020). In other cities, a decline in particulate matter concentrations in the atmosphere during the lockdown was also determined by a decrease in transport activity. In Lublin, Poland, its reduction by a factor of five also reduced the doses of traffic-related PM<sub>1</sub> and PM<sub>0.1</sub> particles inhaled by road users (Polednik, 2021). In cities and regions of Spain, the decrease in PM<sub>10</sub> concentrations was more significant than that of PM<sub>2.5</sub> due to a reduction in non-exhaust transport emissions and construction/demolition dust (Querol et al., 2021). In the Moscow precipitation, positive  $r$  values between  $[K^+]$  and insoluble PTEs (the effect of smoke advection) were found only for P, Pb, and Cd and amounted to 0.56, 0.45, and 0.25, respectively (Fig. S6).

An increase in the content of soluble PTEs and a decrease in insoluble ones led to a sharp increase in the PTEs' solubility during the lockdown (Fig. 7, Fig. S10), especially for Ag (67%), P (45%), Mn, Pb, Sb, and As (>15%). The irregular change in concentrations of PTEs' forms in precipitation led to the fact that the PTEs' solubility increased significantly in the first subperiod of lockdown LP1, while this trend slowed down in the second lockdown subperiod LP2.

After the lockdown, a record amount of precipitation in 200 years of meteorological observations was reported, which, despite the restoration of traffic load in Moscow, led to the purification of the atmosphere from PTEs due to the strong dilution. Thus, after the restrictions were lifted,

the concentrations of soluble PTEs decreased by 17–97% for all PTEs except for Cu (an increase of 65%) and Ti (an increase of 23%). This may be associated with the supply of Cu and Ti from vehicles since both metals are used in the brake pads (Adachi and Tainosho, 2004; Borawski, 2020). The effect of dilution is indicated by the negative  $r$  between the amount of precipitation and the concentrations of all soluble PTEs except for Ag (Fig. S6); the  $r$  value is significant at  $p < 0.01$  for S, Rb (–0.31), Sc, Ni, Ba (–0.30), Cs (–0.28). The most significant increase in the concentrations of soluble forms of PTEs in rains was observed in AL2 at the end of June and July, even despite a large amount of precipitation during that time. That is, the washout by precipitation did not compensate for the increase in PTEs supply from anthropogenic sources. After the restrictions were lifted, the pollution recovery of precipitation by PTEs occurred gradually, probably also due to the time lag between the recovery of emissions on the one hand and the level of atmospheric pollution by aerosols on the other. In European countries, even a few months after the end of the lockdown, NO<sub>2</sub> concentrations in the air were 20% lower than the modeled ones, that is, the recovery of air pollution levels after the lifting of restrictions occurred gradually (Solberg et al., 2021).

For insoluble forms of PTEs, the increase in concentrations started already in AL1, despite the intensive washing out of solid particles from the atmosphere by prolonged rains in the first half of June. In AL2, at the end of June and July, the concentrations of insoluble PTEs in precipitation continued to increase. In general, over the period AL relative to LP, the concentrations of insoluble As, Sb, Ni, Bi, Cs, and Mo, which are indicators of the impact of industrial facilities and transport, increased the most (>35%). At the same time, the concentrations of Cd (by 58%), Pb (37%), P (32%), W (16%), and Zn (16%) decreased, likely due to reduced emissions from suburban waste burning and less frequent smoke advection.

All this led to the fact that the solubility of Ag and Mo in AL decreased by 64% and 22%, respectively, while of

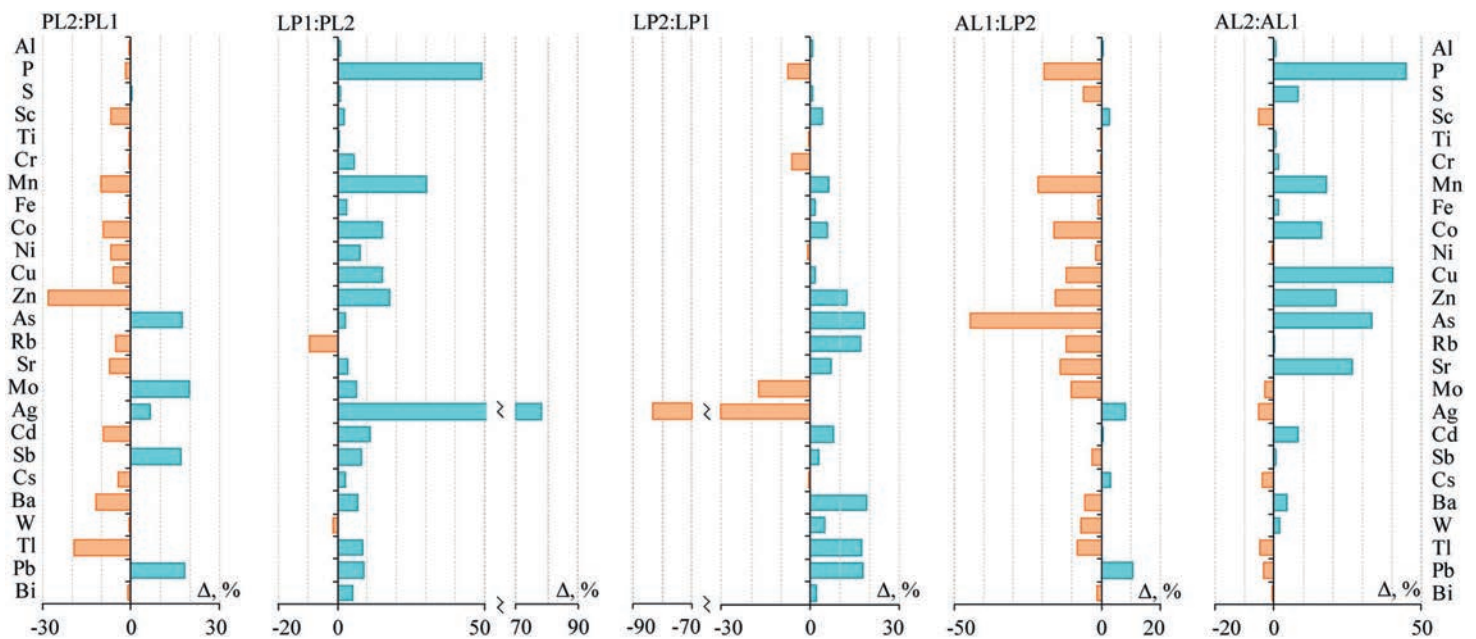


**Fig. 7.** Change in the solubility of PTEs ( $\Delta$ , %) in atmospheric precipitation in Moscow during the studied periods in January–July 2020. Positive  $\Delta$  are shown in blue, and negative  $\Delta$  are shown in brown. (For interpretation of the references to colour in this figure legend, the reader is referred to the web version of this article.)



Cu, Pb, Sr, and P increased by 12–21%; for the remaining PTEs, the changes did not exceed 10%. The solubility of most PTEs rapidly decreased almost immediately after the restrictions were lifted due to an increase in the concentrations of insoluble forms in AL1 and significantly increased again due to prolonged precipitation in AL2 (Fig. 7).

The high PTEs solubility in June–July and its general increase from winter to summer is associated with a general trend of a decrease in the precipitation pH from 6.6 in winter to 5.1–5.2 in the first half of summer (Table 1) since lower pH promotes an accelerated PTEs transition in precipitation from the insoluble form to the soluble one (Kamani et al., 2014; Vlasov et al., 2021b). A particularly strong influence of a pH decrease on the increase in PTEs solubility in precipitation was revealed by significant  $r$  values at  $p < 0.01$  (Fig. S6) for Pb (−0.90), Fe, Cd, Cu, Sb, Zn, Ba, Al (−0.50 to −0.66), as well as significant  $r$  between the  $[\text{HCO}_3^-]$  in precipitation and the solubility of Pb, Cd, Zn (−0.56 to −0.60).

### 3.3. Source identification and apportionment

#### 3.3.1. Enrichment factors

The  $EF$  has been widely used as the first step to identify the relative contribution of crustal or anthropogenic sources to certain chemical elements and compounds

in atmospheric precipitation (Cable and Deng, 2018; Keresztesi et al., 2019; Rivera-Rivera et al., 2020; Samayamanthula et al., 2021; Tian et al., 2020). Fig. 8 shows the  $EF$  of soluble and insoluble PTEs forms in precipitation in PL, LP, and AL in Moscow in January–July 2020.

Significantly higher  $EF$  values were obtained for soluble forms than for insoluble ones. This may be due to the fact that the PTEs are accumulated in higher quantities in the finest particles, which may participate in regional transport over hundreds of kilometers, contributing to the formation of precipitation as condensation nuclei, and could also pass through filter pores during filtration processes (Ponette-González et al., 2018; Tripathee et al., 2014). In addition,  $EF$  values of most elements in precipitation samples are higher than those of totally dissolved in aerosol samples (Xu et al., 2022b), which may be related to the higher solubility of PTEs than reference elements (e.g., Al) in dilute acid. For instance, similar greater enrichment with the soluble PTEs compared to the insoluble ones was also observed in the rainwater of Northern Jordan (Al-Momani et al., 2002). In Moscow, this was especially pronounced for Sb, S, Zn, Cd, Sr (average  $EF$  for periods for the soluble form was 125–457 times higher), and Pb, As, Ba, Cu, Ag, Tl (on average 38–84 times higher). Only for Tl, Cr, and Fe, the differences in  $EF$  values between the two forms were

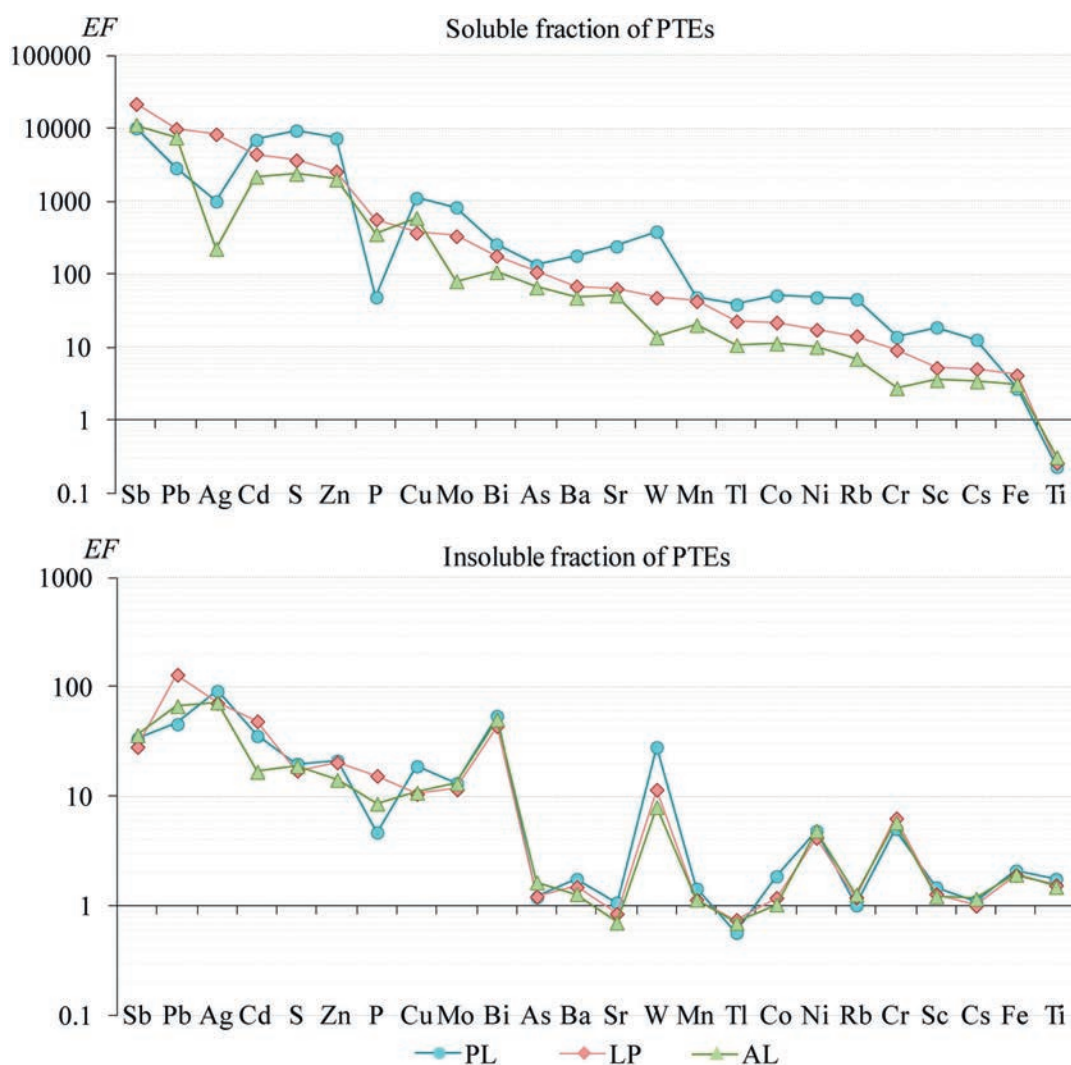


Fig. 8.  $EF$  value for soluble and insoluble PTEs forms in atmospheric precipitation in the studied periods in January–July 2020.

insignificant (up to 1.7 times on average, Fig. 8). Sb, S, Zn, Cd, Pb, Cu, Ag, Mo, W, Bi with  $EF > 100$  for soluble forms and  $EF > 10$  for insoluble ones had a certain anthropogenic origin on average over periods. In addition, in soluble form, this group included P, Sr, and As. Soluble Sc, Cr, Cs, Fe, Ti, and insoluble Sr and Tl came from terrigenous sources. The remaining PTEs can be attributed to the group of mixed natural-anthropogenic origin.

During all three periods, soluble and insoluble forms of Sb, Pb, Ag, Cd, S, Zn, Cu, Mo, and Bi with  $EF > 100$  and  $EF > 10$ , respectively, were supplied from anthropogenic sources. Before the lockdown, soluble As, Ba, Sr, W, and insoluble W were supplied from anthropogenic sources. After the restrictions were introduced due to the anthropogenic load reduction, the  $EF$  values for most soluble and insoluble PTEs began to decrease. This continued even after the restrictions were lifted, probably due to the washing out of pollutants from the atmosphere by heavy rains that fell during this period and due to dilution. Only for soluble Sb, Pb, Ag, and P and insoluble Pb, Cd, and P  $EF$  values increased during lockdown due to the impact of suburban waste burning, which was discussed earlier.

The most significant differences in the  $EF$  values between all three studied periods were characteristic of the soluble PTEs forms. Thus, the largest  $EF$  for the majority of soluble elements was calculated for the period before the lockdown, and the smallest – after the restrictions were lifted (Fig. 8). This indicates a more significant change in the supply of ultrafine aerosols from anthro-

pogenic sources as a result of lockdown measures and greater dependence of soluble PTEs concentrations on changes in rain parameters (frequency, intensity, length of the dry period between rains, etc.) from episode to episode (Vlasov et al., 2021a). Thus, the chemical composition of solid particles washed out from the atmosphere by precipitation is more stable and changes less significantly with a decrease in anthropogenic activity.

### 3.3.2. Principal component analysis

For potential sources of PTEs identification Principal Component Analysis (PCA) was used. For soluble forms of PTEs, four Principal Components (PC) that explained 74.0% of the total variance were defined (Table 2).

PC1 is responsible for 50.4% of the variance and has high factor loadings ( $> 0.5$ ) for P, Ti, Cd, As, Co, S, Mn, and Rb with correlation coefficients of 0.45–0.86 (Fig. S6). P, As, Cd, Rb, and S could derive from waste, fuel, and biomass combustion (Bozkurt et al., 2018; Hu et al., 2015; Lun et al., 2018). Ti, Cd, Co, and S may also come from non-exhaust vehicle emissions, e.g., during tire wear and road surface abrasion (Alves et al., 2020; Zannoni et al., 2016). High S concentrations may also indicate long-range transport of secondary inorganic aerosol (Cao et al., 2017), which is confirmed by the high  $r$  between the content of S and  $[\text{NH}_4^+]$  in precipitation, equal to 0.78 (Fig. S6). Thus, PC1 was indicated as the influence of waste and fuel combustion, and vehicle emissions.

**Table 2.** Varimax-rotated component matrix following principal component analysis of the soluble fraction of PTEs in precipitation in Moscow (loadings  $> 0.5$  are highlighted in bold).

PTEs	Rotated component number			
	PC1	PC2	PC3	PC4
Al	0.114	<b>0.927</b>	0.130	0.155
P	<b>0.967</b>	0.031	0.111	-0.013
S	<b>0.647</b>	0.131	<b>0.523</b>	0.380
Sc	0.099	0.250	<b>0.588</b>	0.555
Ti	<b>0.805</b>	0.421	0.027	0.124
Cr	0.265	0.433	<b>0.613</b>	0.074
Mn	<b>0.522</b>	0.487	<b>0.528</b>	0.236
Fe	0.180	<b>0.889</b>	0.136	0.093
Co	<b>0.682</b>	0.277	<b>0.537</b>	0.082
Ni	0.384	0.482	<b>0.624</b>	0.219
Cu	0.200	<b>0.646</b>	0.122	0.133
Zn	0.083	<b>0.510</b>	-0.017	0.330
As	<b>0.676</b>	0.327	0.376	0.219
Rb	<b>0.502</b>	0.101	0.259	<b>0.536</b>
Sr	0.113	<b>0.648</b>	0.333	0.215
Mo	0.124	0.026	<b>0.720</b>	0.235
Cd	<b>0.778</b>	0.120	0.073	0.376
Sb	0.432	<b>0.694</b>	0.426	0.111
Cs	0.166	0.235	0.297	<b>0.826</b>
Ba	0.139	<b>0.767</b>	0.343	0.250
W	0.090	0.037	<b>0.728</b>	0.156
Tl	0.246	0.211	0.264	<b>0.842</b>
Pb	0.050	<b>0.746</b>	-0.063	-0.081
Bi	0.451	<b>0.630</b>	0.226	0.360
Eigenvalue	12.1	2.7	1.8	1.2
Variance explained, %	50.4	11.1	7.6	4.8
Estimated source	Waste and fuel combustion, vehicle emissions	Road dust and non-exhaust emissions, soils	Industrial	Mineral
Source contribution, %	41.8	19.7	22.3	16.2

Silver was not considered due to a large number of samples with concentrations below the detection limit. Source contribution was determined using PCA-MLR.

PC2 explains 11.1% of the total variance and has high factor loadings Al, Fe, Ba, Pb, Sb, Cu, Sr, Bi, and Zn with correlation coefficients of 0.23–0.92. The least pronounced relations were found between Zn and Pb with other PTEs. Such a range of elements indicates the brake pads abrasion (Grigoratos and Martini, 2015; Pant and Harrison, 2013) with the accumulation of Sb, Cu, Ba, Pb, Zn, and Bi in road dust and its individual particle size fractions in Moscow (Bykova et al., 2021; Ermolin et al., 2018; Kasimov et al., 2020; Vlasov et al., 2021c, Vlasov et al., 2022). Fe and Sr can originate from terrigenous sources – soils and rocks (Morera-Gómez et al., 2020; Ramírez et al., 2019; Shinkareva et al., 2022), as well as Al, which is often used in *EF* calculations as a reference element (Mirzaei et al., 2018; Orlović-Leko et al., 2020; Vodyanitskii and Vlasov, 2021). Thus, PC2 was identified as a factor indicating the input of road dust, soils and non-exhaust vehicle emissions.

PC3 explains 7.6% of the total variance and has high factor loadings W, Mo, Ni, Cr, Sc, Co, Mn, and S with correlation coefficients of 0.33–0.85. The least pronounced relations were found between W and Mo with the rest elements. Most PTEs can come from industrial enterprises, especially metalworking production and mechanical engineering (Bozkurt et al., 2018; Zheng et al., 2018), which are important sources of environmental pollution in Moscow (Bityukova and Saulskaya, 2017). This is confirmed by the accumulation of W, Mo, and S in the snow cover in the city west (Vlasov et al., 2020). Alloy steel processing

enterprises, mechanical wear of chrome steel, and galvanic industries can also supply Cr, Ni, and Co (Bozkurt et al., 2018; Okuda et al., 2007). In Moscow, we previously found high correlations between Cr and Ni in road dust and its PM<sub>10</sub> fraction (0.72 and 0.86, respectively), in the insoluble and soluble forms of snow in the city west (0.96 and 0.82, respectively), and in the insoluble and soluble forms of spring rains at the MO MSU (0.99 and 0.98, respectively), amounting to 0.66 in 2020 (Fig. S6). This fact indicates the common input of these elements into the atmosphere in different seasons (Vlasov et al., 2020, Vlasov et al., 2021b, Vlasov et al., 2021c). PC3 was indicated as the influence of industrial sources.

PC4 is responsible for 4.8% of the total variance and has high factor loadings for Tl, Cs, Sc, and Rb with correlation coefficients of 0.42–0.88. *EF* for Tl, Cs, Sc, and Rb does not exceed 20 in LP, and AL and 40 in PL, indicating the terrigenous sources input. Thus, Tl is included in sulfide minerals (pyrite, sphalerite, marcassite, etc.), feldspars, and micas in which it can be found in high concentrations due to similar ionic radius with K and Rb (Liu et al., 2019). Cs, Rb, and Sc are also present in feldspars and other soil minerals (Kabata-Pendias, 2011). Thus PC4 was identified as a mineral source.

For insoluble forms of PTEs in the precipitation of Moscow, five PCs were identified, which account in total for 79.3% of the total variance (Table 3).

PC1 explains 43.8% of the total variance and has high factor loadings for Ba, W, Sr, Co, Mn, Cu, Ti, Fe, and

**Table 3.** Varimax-rotated component matrix following principal component analysis of the insoluble fraction of PTEs in precipitation in Moscow (loadings >0.5 are highlighted in bold).

PTEs	Rotated component number				
	PC1	PC2	PC3	PC4	PC5
Al	<b>0.519</b>	0.096	<b>0.828</b>	-0.078	0.025
P	-0.390	0.088	-0.063	<b>0.783</b>	0.120
S	0.206	<b>0.818</b>	0.204	0.318	0.049
Sc	0.351	0.155	0.447	-0.100	-0.318
Ti	<b>0.758</b>	0.275	0.495	-0.062	0.078
Cr	-0.018	<b>0.922</b>	0.112	0.054	-0.054
Mn	<b>0.836</b>	0.204	0.385	-0.063	-0.032
Fe	<b>0.716</b>	0.186	<b>0.576</b>	-0.128	0.170
Co	<b>0.860</b>	0.201	0.243	-0.049	0.011
Ni	0.052	<b>0.860</b>	-0.004	-0.081	-0.011
Cu	<b>0.781</b>	0.435	0.061	0.236	0.099
Zn	0.403	0.396	-0.068	0.449	-0.281
Rb	0.186	0.224	<b>0.910</b>	-0.024	0.009
Sr	<b>0.874</b>	0.045	0.305	-0.075	0.005
Mo	0.404	<b>0.773</b>	0.096	-0.084	0.166
Ag	0.231	<b>0.772</b>	-0.033	0.120	0.188
Cd	0.393	0.162	-0.075	<b>0.699</b>	-0.161
Sb	0.240	0.311	0.120	-0.011	<b>0.735</b>
Cs	0.237	<b>0.694</b>	<b>0.555</b>	0.187	0.058
Ba	<b>0.878</b>	0.001	0.172	0.029	-0.009
W	<b>0.878</b>	0.190	0.028	-0.041	-0.005
Tl	0.162	-0.106	<b>0.882</b>	0.064	0.190
Pb	-0.295	-0.046	0.153	<b>0.629</b>	<b>0.500</b>
Bi	0.470	0.367	0.229	0.166	0.239
Eigenvalue	10.5	3.6	2.2	1.7	1.0
Variance explained, %	43.8	15.0	9.2	7.0	4.3
Estimated source	Vehicle emissions, road dust, construction dust	Industrial	Soils, mineral	Waste combustion	Brake pads
Source contribution, %	34.2	18.6	38.8	2.3	6.1

Arsenic was not considered due to a large number of samples with concentrations below the detection limit. Source contribution was determined using PCA-MLR.



Al, with correlation coefficients of 0.47–0.92 (Fig. S6). The most likely sources of Cu, Ti, W, Ba, Fe, and Al are non-exhaust vehicle emissions and blowing out of road dust particles (Ramírez et al., 2019; Srimuruganandam and Shiva Nagendra, 2012) and the accumulation of these particles in urban canyons (Kosheleva et al., 2022). Sr and Ba input is associated with the emission of construction and demolition carbonate (Amato et al., 2014). Thus, PC1 was indicated as the influence of vehicle emissions, road dust, and construction dust.

PC2, explaining 15.0% of the total variance, is indicated as industrial emissions input, as PC2 has high factor loadings for Cr, Ni, S, Mo, Ag, and Cs with correlation coefficients of 0.51–0.87 (Fig. S6).

PC3 is responsible for 9.2% of the total variance and is associated with the input of PTEs with mineral and soil particles since it has high factor loadings for Rb, Tl, Al, Fe, and Cs with correlation coefficients of 0.45–0.88 (Fig. S6).

PC4 accounts for 7.0% of the total variance and has high factor loadings for P, Cd, and Pb, likely originated from waste combustion. A fairly high  $r$  among these PTEs was found between the P and Pb (0.64); P and Cd (0.31); as well as Cd and Pb (0.12). It was reported that during waste combustion, Pb can also be supplied to the atmosphere in addition to P and Cd (Li et al., 2019).

PC5, accounting for 4.3% of the total variance, has a strong positive correlation with Sb and Pb, which can be indicators of car brake pad wear (Ozaki et al., 2021). After the ban on ethylated gasoline in many countries, brakes and road surface markings became the most important source of Pb in vehicle emissions (Aguilera et al., 2021; Bourliva et al., 2018).

### 3.3.3. PCA-MLR receptor model

Multiple linear regression analysis of the sum concentration of all measured soluble and insoluble PTEs was performed by selecting the PCA factor scores as the independent variables to determine the mass apportionment of the four principal components in the soluble phase and five principal components of the insoluble phase in precipitation samples.

For soluble PTEs, the resulting equation was as follows:

$$\hat{\sum C_{sol}} = 0.752 \times FS_1 + 0.354 \times FS_2 + 0.401 \times FS_3 + 0.292 \times FS_4 \quad (R^2 = 0.936).$$

By expanding  $\hat{\sum C_{sol}}$  and rearranging terms, the multiple linear regression equation becomes:  $\sum C_{sol} = 0.752 \times \sigma_{\sum C_{sol}} \times FS_1 + 0.354 \times \sum C_{sol} \times FS_2 + 0.401 \times \sigma_{\sum C_{sol}} \times FS_3 + 0.292 \times \sigma_{\sum C_{sol}} \times FS_4 + \text{mean}_{\sum C_{sol}}$ , where  $\sigma_{\sum C_{sol}}$  was 947  $\mu\text{g/L}$ , and  $\text{mean}_{\sum C_{sol}}$  was 968  $\mu\text{g/L}$ .

For insoluble PTEs, the resulting equation was as follows:

$$\hat{\sum C_{ins}} = 0.610 \times FS_1 + 0.331 \times FS_2 + 0.693 \times FS_3 + 0.041 \times FS_4 + 0.110 \times FS_5 \quad (R^2 = 0.976).$$

By expanding  $\hat{\sum C_{ins}}$  and rearranging terms, the multiple linear regression equation becomes:

$$\sum C_{ins} = 0.610 \times \sigma_{\sum C_{ins}} \times FS_1 + 0.331 \times \sigma_{\sum C_{ins}} \times FS_2 + 0.693 \times \sigma_{\sum C_{ins}} \times FS_3 + 0.041 \times \sigma_{\sum C_{ins}} \times FS_4 + 0.110 \times \sigma_{\sum C_{ins}} \times FS_5 + \text{mean}_{\sum C_{ins}}$$

where  $\sigma_{\sum C_{ins}}$  was 26,696  $\mu\text{g/g}$ , and  $\text{mean}_{\sum C_{ins}}$  was 90,077  $\mu\text{g/g}$ .

The PCA-MLR results showed that the average percentage contribution of the soluble PTEs content in Moscow precipitation over the entire study period was 41.8% for waste and fuel combustion and vehicle emissions; 22.3% for industrial emissions; 19.7% for road dust and non-exhaust emissions, and soil particles resuspension; and 16.2% for the mineral source (Table 2). For insoluble PTEs, the results slightly differ: 38.8% for soil particles resuspension and mineral source; 34.2% for vehicle emissions, road dust resuspension, and construction dust; 18.6% for industrial emissions; 6.1% for brake pads abrasion; and 2.3% for waste combustion (Table 3).

In Figs. 9, S11, and S12, the time series of the total concentrations of soluble ( $\sum C_{sol}$ ) and insoluble ( $\sum C_{ins}$ ) PTEs forms coming from distinguished sources are shown, as well as the contribution of each source to  $\sum C_{sol}$  and  $\sum C_{ins}$  in each precipitation sample.

The results showed that PCA-MLR gives a more accurate estimate of the sources' contributions to the content of insoluble PTEs forms compared to soluble ones: for the latter, modeling showed a negative contribution (which is physically impossible) of PC1 to the content of PTEs in 7% of individual samples of atmospheric precipitation, of PC2 – in 13%, of PC3 – in 20%, of PC4 – in 25%. For insoluble forms, a negative contribution was obtained only for PC3 (3.5%), PC4 (3.5%), and PC5 (2.3%). PCA's ability to generate negative source contributions and inability to effectively model extreme data are known concerns (Larsen and Baker, 2003). Therefore, in Figs. 9, S11, and S12 for separate precipitation episodes, the sum of percentage contributions in  $\sum C_{sol}$  and  $\sum C_{ins}$  is <100% due to excluding negative source contributions in the calculations. A significant change in the sources' contributions to precipitation pollution in Moscow during and after the lockdown was found (Fig. 9).

For soluble PTEs, the contribution of industrial emissions sharply decreased in LP2, that is, after the end of the heating season. In PL, the contribution of this source was 38% in PL1 and 66% in PL2, reaching 40% in LP1 and decreasing to 6% in LP2. Immediately after the restrictions were lifted, the contribution of industrial emissions amounted to 7%, decreasing to almost zero in AL2. In LP2, when the population activity began to increase, the contribution of road dust and non-exhaust emissions, as well as soil particles resuspension began to restore, amounting to 8–15% in PL1, PL2, and LP1, rising to 17% in LP2 and sharply increasing to 28–30% after restrictions were lifted. This is due not only to an increase in the traffic load but also to the intensification of blowing out of dust particles from the road surface, especially in the second half of July. At this time, after intensive precipitation of up to 41 mm in early summer, moderate rains of 0.7–8.5 mm occurred. The recovery of transport activity after the lockdown was reflected in the growth of the contribution of waste and fuel combustion and vehicle emissions. Specifically, in PL1, PL2, and LP1, a such contribution was 24–37%, increasing in LP2 to 58%, and after the lifting of restrictions, it amounted to 56–65%. It is crucial that in LP1, despite a slight change in the relative contribution of waste and fuel combustion and vehicle emissions, there was a sharp increase in PTEs concentrations coming from these sources. This was also confirmed by the overlap of the  $[\text{Cl}^-]$  and  $[\text{K}^+]$  concentration peaks with the concentration of PTEs coming

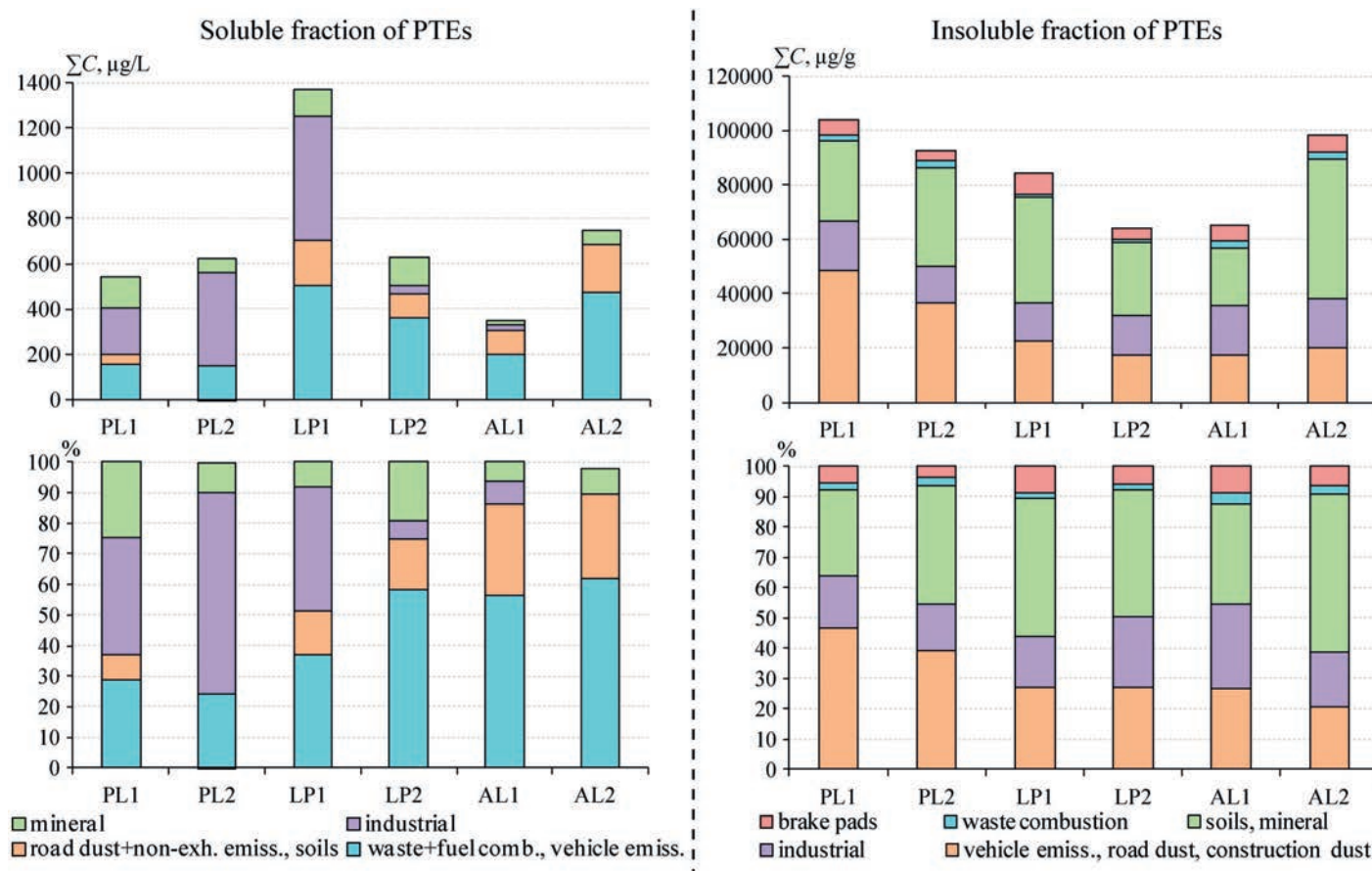


**Fig. 9.** The contribution of the factors distinguished using PCA to the total concentrations of soluble PTEs forms and the total concentrations of insoluble PTEs forms in the precipitation of Moscow during the studied subperiods in January–July 2020 estimated using MLR. The upper graphs show the absolute contribution to the concentrations; the lower ones show the percentage (normalized by the sum of the contributions of the sources) contribution to the concentrations. The PTE concentrations in the studied subperiods are presented as volume-weighted means.

from the waste and fuel combustion and vehicle emissions factor on April 24 and 29, May 12–14 and 19, and also on July 2 (Fig. S13). In June–July, the  $[Cl^-]$  and  $[K^+]$  peaks were most likely associated with the influence of road dust and non-exhaust emissions, as well as soil particles resuspension, while in the first half of April, with the industrial factor (Fig. S13). The PTEs concentrations associated with the mineral source sharply decreased by a factor of 2–6.5 in AL1 compared to the other periods due to a large amount of precipitation, which contributed significantly to dilution.

For insoluble PTEs, the most significant differences in the sources' contribution between the studied periods were defined for vehicle emissions, road dust resuspension, and construction dust. Concentrations of PTEs, coming from this mixed source, gradually decreased from 39–46% in PL to 27% in LP and AL1 and continued to decrease to 21% in AL2. This change is associated with a decrease in traffic activity and the suspension of work at many construction sites due to the lockdown. After the restrictions were lifted, the contribution of vehicle emissions, road dust resuspension, and construction dust did not recover due to the rapid washing out of particulate matter from the atmosphere during heavy precipitation. Moistened soils also prevented the blowing out of particles from their surface. This was reflected in a decrease in the contribution of soil particles resuspension and mineral source: in PL in winter and in March, the contribution of this source was 28–39%, increasing in

LP1 to 46%, and decreasing in LP2 to 42% and in AL1 to 33%. In AL2, after heavy rains subsided, the contribution of soil particle resuspension and mineral source increased to 52%. At the same time, the percentage contribution of brake pads abrasion and waste combustion to the precipitation contamination with insoluble PTEs was insignificant and changed slightly in the studied periods, amounting to 4–9% and 2–4%, respectively.

During the studied subperiods, the concentrations of insoluble PTEs coming from industrial emissions changed insignificantly and averaged 13,900–18,200  $\mu\text{g/g}$ . However, in relative terms, this source contribution increased from 15–18% in PL and LP1 to 23% in LP2 and 28% in AL1, which is associated with a decrease in the concentrations of PTEs coming from other sources. That is, the contribution of industrial emissions to precipitation pollution with soluble PTEs decreased as restrictions were introduced and dropped to almost zero after the end of the heating season, while the lockdown and the end of the heating season had almost no effect on the concentrations of insoluble PTEs.

#### 4. CONCLUSIONS

The first data on the impact of the COVID-19 lockdown on changes in the physicochemical properties, ionic composition, content, and ratio of PTEs forms in precipitation in Moscow have been obtained. The dual nature of the lockdown impact on the composition of pre-

precipitation has been revealed. On the one hand, the content of the most soluble and insoluble PTEs decreased by 10–99% and 9–61%, respectively, which is consistent with the decreasing air pollution levels observed in other cities during the lockdown. On the other hand, the burning of wood, coal, waste and agricultural residues in the suburbs typical for Moscow contributed to an increase in precipitation pollution with PTEs during the lockdown, especially with soluble P, Ag, Pb, Sb, As, Cd,  $[\text{Cl}^-]$ ,  $[\text{K}^+]$ , and insoluble P, Pb, Cd. Smoke air advections to the city also exacerbated the precipitation pollution, which is confirmed by the growth of the ratios  $[\text{SO}_4^{2-}]/[\text{NO}_3^-]$ ,  $[\text{Cl}^-]/[\text{NO}_3^-]$ ,  $[\text{Cl}^-]/[\text{SO}_4^{2-}]$ , and  $[\text{Cl}^-]/[\text{K}^+]$ . Due to the time lag between the increase in atmospheric pollution and the washing out of aerosols by precipitation, the recovery of the PTEs level in precipitation occurred gradually after the restrictions were lifted.

Our research during the lockdown made it possible to show that the chemical composition and the sources' contribution to the PTEs content in solid particles in precipitation are more stable and change less significantly with a decrease in anthropogenic activity in contrast to the soluble precipitation phase. The greatest changes in

the contribution of sources were established in the second stage of the lockdown and after the lockdown, when the contribution of industrial sources to the content of soluble PTEs sharply decreased (from 38–66% to 6%) due to the increased contribution of road dust and non-exhaust emissions, and soil particles resuspension (from 8–15% to 17–30%), waste and fuel combustion and vehicle emissions (from 24–37% to 56–65%). For insoluble PTEs, the most significant differences in the sources' contribution were defined for vehicle emissions, road dust resuspension, and construction dust, which input decreased from winter to summer due to the lockdown and a large amount of precipitation in late May–June.

These results can be helpful in studying the effect of anthropogenic load variability on precipitation pollution by PTEs in megacities to define the factors influencing the ratio of PTEs forms and their potential hazard to the urban population. Unlike other cities, in Moscow in the first half of 2020, the lockdown overlapped with an unprecedented amount of precipitation, which requires further investigation of the chemical composition of precipitation and aerosols in similar time periods in subsequent years.



# Dissolved and suspended forms of metals and metalloids in snow cover of megacity: partitioning and deposition rates in western Moscow\*

## 1. INTRODUCTION

Urban air pollution with particulate matter is a recognized environmental problem, especially relevant for megacities. Contaminated air is responsible for about 80% of premature deaths; it causes ischaemic heart disease, stroke, chronic obstructive pulmonary disease, and lung cancer [1], and increases the risk of adenocarcinomas [2]. Increased concentrations of particulate matter with high proportions of metals and metalloids (MMs) affect the external respiratory function of citizens, especially of asthma patients [3].

Due to its long occurrence and ability to accumulate pollutants over the entire cold period of the year, snow cover is a natural, informative, and convenient component indicating air pollution with particulate matter and MMs in northern cities [4–7]. Snow pollution with MMs correlates well with the overall Air Quality Index (AQI) and the level of atmospheric pollution with PM<sub>10</sub> and PM<sub>2.5</sub> [8]. In comparison to rains, snow more effectively absorbs pollutants and washes them out of the atmosphere due to the higher surface area and porosity of snowflakes compared to raindrops [9]. The intensity of snow cover pollution is determined from the mass of MMs entering soils and surface waters during snow melting. MMs in liquid (dissolved or soluble) form could be included into the biogeochemical cycle, while solid (suspended or insoluble) forms of MMs accumulate in surface horizons of urban soils and road dust [10–12]. The ratio of these forms of MMs and its variations are also frequently used informative indicators of different types of pollution sources [13–16]. In recent studies on snow cover pollution, special attention has been paid to the chemical composition of accumulated particulate matter and the determination of its mass [4,17–22].

Major sources of pollutants in the snow cover of cities are emissions of vehicles, industries and the fuel and energy complex, as well as de-icing salts (DISs). High level of snow cover pollution along roads is caused by reduced efficiency of automobile engines when air temperatures are below zero [23,24]. The most often used chemical DISs are chlorides and carbonates of Na, Ca, Mg, and K, as well as organic compounds, glycols and other alcohols, etc. [25,26]. However, the most commonly applied NaCl causes salinization and solonchikicity of soils, suppresses urban vegetation, and increases salinity of water bodies [27–31]. During snow melting, chloride meltwater increases the mobility of many metals contained in soil particles and their environmental hazard, probably due to the formation of MMs chlorides [32–34].

Moscow is the largest megacity in Europe, with more than 12.6 million citizens, and more than 17 million people inhabiting the agglomeration. As in many other large cities the main source of anthropogenic impact on the environment is motor transport, generating about 93% of

the total emissions to the atmosphere. Heat and power stations and the oil refinery are responsible for the majority of stationary source emissions [35]. In spite of active deindustrialization since the 1990s, industrial zones still occupy about 17% of the city area, thus reducing the connectivity of road network and leading to excessive motor traffic and higher release of pollutants [36,37].

The studies of snow cover pollution in certain administrative okrugs and districts of Moscow and the Moscow Oblast are quite numerous [29,30,38–50]. However, most of the studies did not consider the ratio of MMs forms (i.e., MMs partitioning) and its change under anthropogenic impact; nor did they include comprehensive assessment of snow cover pollution with MMs near roads of different types. It is therefore necessary to collect and constantly update data about geochemical pressure on urban landscapes, especially in the traffic zone.

The western part of Moscow is considered to be less polluted with industrial emissions due to predominant westerlies and the concentration of large industrial zones in the eastern and southeastern sectors of the city, where they produce about 2/3 of the total industrial emissions [36]. Therefore, the Western Administrative Okrug (WAO), with a population of 1.4 million and with about 2800 cars per 1 km<sup>2</sup>, was chosen to assess the vehicles' impact on MMs accumulation in snow [35]. Our main objective is to assess anthropogenically-induced changes in the chemical composition of snow cover in the traffic zone of the WAO. The aims of this study were the following: (1) identification of changes in macro-component composition and physical-chemical properties of the snow meltwater in the WAO relative to the background territory; (2) determination of snow cover contamination by dissolved and suspended forms of MMs near roads and at car parking lots in the yards of residential buildings; (3) analysis of the ratio of MMs forms in the snow cover of the traffic zone; (4) assessment of the atmospheric deposition rates of pollutants along the roads and potential anthropogenic load on the urban landscapes of WAO during snow melting.

## 2. MATERIALS AND METHODS

### 2.1. Study area and snow sampling

Southerly and westerly winds prevail in Moscow during the year, resulting in the regional transfer of pollutants in the north and east directions; the repeatability of easterly winds is also high [51]. Moreover, Moscow is a “heat island”, created by burning the great amount of fuel from the end of September to the second half of April [52]. The resulting upward air currents in the city center promote the inflow of relatively clean air from suburban territories to the city. This contributes to self-purification of the atmospheric air and, consequently, diminishes snow cover pollution [53].

\* Vlasov D., Vasil'chuk J., Kosheleva N., Kasimov N. // Atmosphere. 2020;11(9):907.

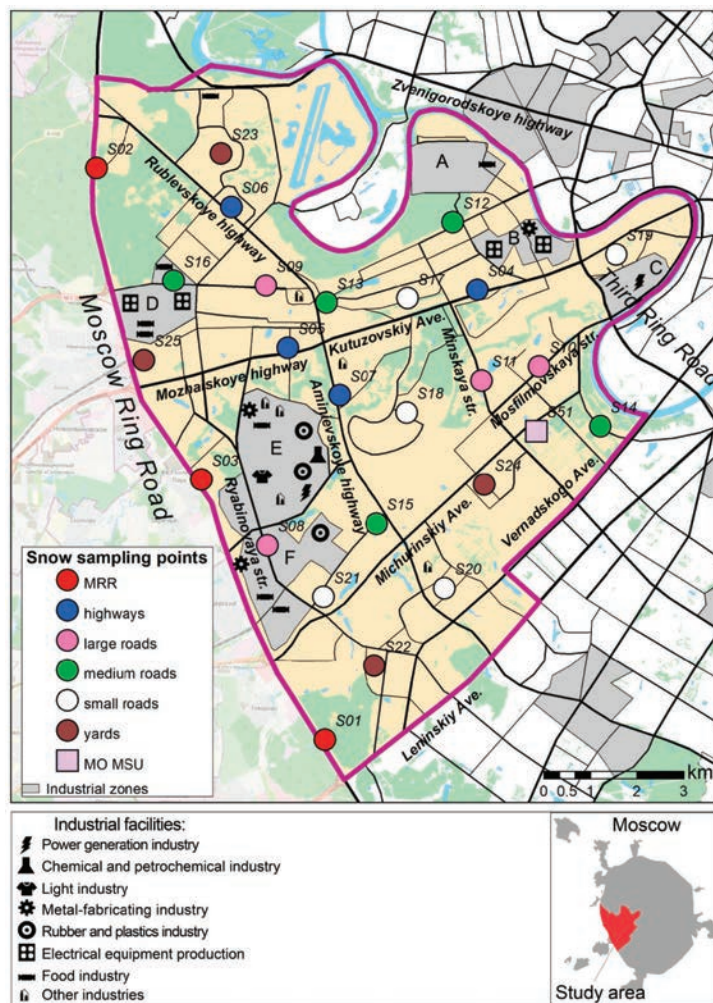


**Figure 1.** Snow cover sampling sites in the western part of Moscow (March 2018). Industrial zones: A–Fili, B–Western Port, C–Berezhkovskaya Embankment, D–Kuntsevo, E–Severnoye Ochakovo, F–Yuzhnoye Ochakovo.

Large highways and interchanges (Moscow Ring Road–MRR, Rublevskoye and Mozhaiskoye highways, Kutuzovskiy and Michurinskiy avenues, etc.) are the main sources of anthropogenic impact in WAO. There are also six industrial zones within its territory: Fili (Figure 1, letter (A)), Western Port (B), Berezhkovskaya Embankment (C), Kuntsevo (D), Severnoye Ochakovo (E), and Yuzhnoye Ochakovo (F), which include heat and power stations No. 25 (Severnoye Ochakovo industrial zone) and No. 12 (Berezhkovskaya Embankment industrial zone), metal-fabricating enterprises, electrical equipment production, enterprises of rubber, chemical, light and food industries (Figure 1).

Geochemical survey of snow cover was carried out in mid-March 2018 in maximum snow cover thickness. Due to frequent thawing weather in winter of 2017–2018, permanent snow cover was formed only at the end of the first decade of January 2018. The thickness of snow cover in WAO differed only slightly from the long-term mean values (35–45 cm) [51,54] and averaged 42–50 cm near roads, increasing to 55–65 cm (averaged 61 cm) within the background areas. It is known that MMs concentrations in the surface layer of snow cover are usually lower than in the underlying layers [12]. To avoid underestimation of snow cover pollution, snow samples were taken along the full depth of undisturbed snow cover. In total, 26 mixed samples were taken within the territory of WAO (Fig-

ure 1), each consisting of 10–15 individual samples taken at a distance of 3–5 m by plastic pipe with the cross-section area of 20 cm<sup>2</sup> (one plastic pipe corresponded to one snow core, i.e., snow column) along the following roads: the MRR (3 sites), highways with four lanes in one direction (4 sites), large roads with three lanes in one direction (4 sites), medium roads with two lanes in one direction (5 sites), and small roads with one lane in one direction (5 sites). The yards of residential buildings with car parking lots (four sites) and the Meteorological Observatory of the Lomonosov Moscow State University (MO MSU) were also sampled. The background area was chosen to be sufficiently distant from the city to avoid its polluting influence. Thus, three sampling sites were selected more than 120 km west of Moscow in the Mozhaisk and Volokolamsk districts of the Moscow Oblast.

## 2.2. Laboratory analysis and data processing

Snow cover samples were melted in the laboratory at 20–22 °C. The main physicochemical characteristics of meltwater were determined at the Ecological and Geochemical Center of the Lomonosov Moscow State University, Faculty of Geography. The pH of the resulting solution was measured using the potentiometric method with the pHMeter “SevenCompact S220” (Mettler Toledo, Greifensee, Switzerland; accuracy: ±0.002). Filtra-



tion through membrane filters with pore diameter of 0.45  $\mu\text{m}$  (EMD Millipore, Burlington, MA, USA) was applied to isolate filtrate with dissolved (or soluble) forms of MMs and particles on the filter with suspended (or insoluble) forms. Filters with pore diameter of 0.45  $\mu\text{m}$  are widely used to separate the dissolved and suspended forms of MMs when studying the composition of snow cover, rainfall runoff, or river waters [8,16,55,56].

The anionic composition of filtrate ( $\text{SO}_4^{2-}$ ,  $\text{Cl}^-$ ,  $\text{NO}_3^-$ ) was determined using the "Stayer" liquid ion chromatograph (Akviron, Moscow, Russia); and the cationic composition ( $\text{Ca}^{2+}$ ,  $\text{Mg}^{2+}$ ,  $\text{K}^+$ ,  $\text{Na}^+$ ) using the atomic absorption spectrometer with flame atomization "novAA-400" (Analytik-Jena AG, Jena, Germany). The detection limits for cations and anions were calculated at 95% confidence level for three parallel measurements of the sample and blank measurements. For  $\text{SO}_4^{2-}$  and  $\text{Na}^+$ , they are 0.04 mg/L, for  $\text{Ca}^{2+}$  and  $\text{K}^+$  – 0.03 mg/L, for  $\text{Cl}^-$ ,  $\text{NO}_3^-$ , and  $\text{Mg}^{2+}$  – 0.02 mg/L. The concentration of  $\text{HCO}_3^-$  ions was calculated as the difference between the sums of cations and anions equivalents. In aerosol chemistry, the ammonium plays a significant role in chemical processes, including the formation of secondary ammonium sulfate and ammonium nitrate fine inorganic aerosols [57]. However, previous studies on the chemical composition of snow in Moscow showed that the ammonium in urban snow is about 5%-eq. from the amount of cations [58]. That is, the ammonium does not play a significant role in the balance of cations in Moscow snow meltwater. Therefore, the concentrations of ammonium in snow cover of WAO were not measured.

The content of solid particles in snow meltwater ( $X$ , mg/L) was estimated (Equation (1)) based on the mass of suspension on the filter  $m$  (mg), weighed on an analytical balance "Discovery DV114C" (Ohaus, Greifensee, Switzerland; repeatability: 0.1 mg):

$$X = m/V, \quad (1)$$

where  $V$  is the amount of meltwater (L).

Concentrations of dissolved and suspended forms of Al, As, Ba, Bi, Ca, Cd, Co, Cr, Cu, Fe, K, Mg, Mn, Mo, Na, Ni, Pb, Rb, Sb, Sn, Sr, Ti, V, W, and Zn were measured at the laboratory of the N.M. Fedorovsky All-Russian Research Institute of Mineral Raw Materials (VIMS) by ICP-MS and ICP-AES methods using the "iCAP Qc" mass spectrometer (Thermo Fisher Scientific, Waltham, MA, USA) and the "Optima-4300DV" atomic emission spectrometer (Perkin Elmer, Waltham, MA, USA) according to the certified methods [59,60]. The VIMS laboratory is accredited to the Analytics international accreditation system (AAS.A.00255) and the national accreditation system (RA.RU.21ГП11); it meets the requirements of the International Standards ISO Guide 34:2009, ISO/IEC 17025:2017, and ISO/IEC 17043:2010. The VIMS laboratory is also accredited to certificate measurement techniques and provide metrological examination in Russian Federation (accreditation certificate No. 01.00115-2013). The analysis was conducted using replicates, method blanks, field blanks, and standard reference materials in order to maintain the standard quality. For dissolved MMs, the detection limit (DL), which is defined as three times the standard deviation of replicate blank measurements, were as ( $\mu\text{g/L}$ ): Na, 18; Mg, 100; Al, 0.57; K, 100; Ca, 19; Ti 0.55; V, 0.4; Cr, 1.0; Mn, 0.33; Fe, 0.53; Co, 0.034; Ni, 3.4; Cu, 0.32; Zn, 0.23; As, 0.10; Rb, 0.005; Sr, 0.02; Mo, 0.05;

Cd, 0.004; Sn, 0.01; Sb, 0.007; Ba, 0.01; W, 0.03; Pb, 0.05; Bi, 0.002. For suspended MMs the DL were as ( $\mu\text{g/L}$ ): Na, 16; Mg, 2.2; Al, 22; K, 9.1; Ca, 25; Ti, 1.6; V, 0.12; Cr, 0.38; Mn, 0.18; Fe, 8.6; Co, 0.01; Ni, 0.29; Cu, 0.52; Zn, 1.0; As, 0.02; Rb, 0.01; Sr, 0.12; Mo, 0.009; Cd, 0.001; Sn, 0.08; Sb, 0.005; Ba, 0.31; W, 0.05; Pb, 0.6; Bi, 0.003.

Snow cover contamination with dissolved and suspended forms of MMs was evaluated (Equation (2)) using the contamination factor ( $CF$ ):

$$CF = C_{urb}/C_b \quad (2)$$

where  $C_{urb}$  and  $C_b$  are MMs concentrations in snow cover in the city and in the background area, respectively ( $\mu\text{g/L}$ ).

The mass of each MMs coming to the Earth's surface from the atmosphere ( $\mu\text{g}/\text{m}^2$  per day), that is, the deposition rates of suspended and dissolved MMs were calculated (Equations (3) and (4)):

$$D_{urb} = C_{urb} \cdot P/t \quad (3)$$

$$D_b = C_b \cdot P/t \quad (4)$$

where  $D_{urb}$  and  $D_b$  are deposition rates in the city and in the background area, respectively ( $\mu\text{g}/\text{m}^2$  per day);  $P$  is the water supply in snow cover ( $\text{L}/\text{m}^2$ );  $t$  is the number of days of snow cover occurrence (61–63 days depending on the date of snow sampling).

Water supply in snow cover was calculated according to Equation (5) below:

$$P = V/(a \cdot t \cdot S) \quad (5)$$

where  $a$  is the number of plastic pipes with snow (i.e., snow columns or snow cores) collected at the site;  $S$  is the area of the plastic pipe cross-section,  $\text{m}^2$ .

The dust deposition rate was estimated as (Equation (6)):

$$P_n = m/(a \cdot t \cdot S). \quad (6)$$

The intensity of anthropogenic pressure was determined (Equation (7)) as the excess of an element deposition rate on the studied urban area over its deposition rate on the background area:

$$DF = D_{urb}/D_b. \quad (7)$$

Comprehensive assessment of snow cover pollution with dissolved and suspended MMs was obtained by calculating the total contamination factor of snow ( $TCF$ , Equation (8)) and the total excess of MMs deposition rates in the city above the background ( $TDF$ , Equation (9)):

$$TCF = \sum CF - (n - 1), \quad (8)$$

$$TDF = \sum DF - (n - 1), \quad (9)$$

where  $n$  is the number of chemical elements with  $CF$  or  $DF > 1$ ; when calculating  $TCF$  and  $TDF$ , only  $CF$  and  $DF > 1$  are summed [61,62]. The environmental hazard of MMs snow pollution was determined in line with the  $TCF$  gradations adopted in Russia: <32–low, non-dangerous, 32–64–medium, moderately dangerous, 64–128–high, dangerous, 128–256–very high, very dangerous, >256–maximum, extremely dangerous [61,62].

The spatial distribution patterns of the  $TCF$  and  $TDF$  totals were evaluated in the ArcGIS software package (Esri, Redlands, CA, USA). Cluster analysis to separate stable paragenetic associations of MMs was performed



by the Complete Linkage method in the STATISTICA 8 software (Statsoft/Dell, Tulsa, OK, USA) with a measure of similarity  $d = 1 - \text{Person } r$  and amalgamation rule Complete Linkage. The significance of Pearson correlation coefficients  $r$  and Spearman correlation coefficients  $r_s$  was checked against the t-criterion at  $p < 0.05$ .

### 3. RESULTS AND DISCUSSION

#### 3.1. Physicochemical properties and macrocomposition of snow meltwater

Background snow waters in the western part of Moscow are slightly acidic (pH 5.6), with low mineralization (6.4 mg/L); the ionic composition of water is calcium bicarbonate (Table 1). The obtained data correlates with the findings of physicochemical properties of snow in Moscow suburbs [40,58,63]. The concentration of solid particles in snow water in background conditions is low (about 9 mg/L), while the intensity of daily dust load (9 mg/m<sup>2</sup> per day) corresponds to the average level for background non-urbanized areas in the East European Plain (about 10 mg/m<sup>2</sup> per day) [61].

pH value is an integral indicator of acidifying and alkalizing compounds' ratio and reflects the influence of these compounds on the carbonatic equilibrium. According to 2018 data, the pH value of contaminated snow meltwater in WAO ranged from 7.3 to 8.8 with an average of 8.1; that is, the alkalization of snow cover in the city is intensive and exceeds the background by 2.5 pH units. The highest pH values 7.6–8.8 are common for roads; with an average pH of 8.2, the alkalization of meltwater decreases in the following sequence of roads: large (8.6) > highways (8.4) > medium (8.2) > small and the MRR (8.0). The rising pH value of snow meltwater with an increase in traffic intensity was also recorded in Lahti, Finland [55]. The intensity of alkalization in WAO is lower in the yards of residential buildings with car parking lots—the average pH of snow meltwater is 7.4 with slight variations from 7.3 to 7.5. The pH of snow water in the territory of the MO MSU is 7.3, which is close to the mean value for residential zones. In Moscow,

like most other cities, there is alkalization of surface soil horizons [29,30,64–66], road dust particles [65,67,68], and bottom sediments of lakes and ponds [69]. Previous studies on Moscow soil water extract and the composition of salts in soils showed a significant increase in the amount of carbonates [29], as opposed to the background sod-podzolic soils that do not contain carbonates at all. This, together with results of research in other cities [70], indicates significant influence of carbonates on the soils' pH value. The sources of carbonaceous compounds in the urban environments, aside from natural-originated carbonate particles, are dust from construction and demolition activities, as well as road dust particles mainly related to tire wear, motor exhaust, and brake wear [71–73]. Thus, rather high pH values of snow meltwater are associated with partial dissolution of incoming urban soils and road dust particles on snow cover surface. It is known that partial dissolution of solid particles of various geneses increase the rainwater pH values [74]. Greater pH values of roadside snow meltwater sampled near large roads confirm the hypothesis of road dust particles being the most important alkalizing agent for the snow of WAO. The pH of road dust water extract for Moscow large roads varies from 6.9 to 8.1 and decreases in the yards [68]. An additional source of alkalizing agents in snow cover is marble chips, which is a commonly used DIS in Moscow [75]. On the contrary, chloride DISs can slightly reduce the pH of precipitation and snow due to the formation of gaseous HCl, ClNO<sub>2</sub>, and Cl<sub>2</sub> as a result of the reaction of NaCl with gaseous HNO<sub>3</sub>, H<sub>2</sub>SO<sub>4</sub>, N<sub>2</sub>O<sub>5</sub>, and ClONO<sub>2</sub> [76].

The intensive geochemical impact of transport and industrial facilities and the application of DISs led to a significant increase in the concentration of solid particles in snow cover (2–5-fold), the intensity of dust load (2–7-fold), and mineralization (5–18-fold), as well as to the change in the ionic composition of snow meltwater in WAO relative to the background. The mineralization of meltwater next to roads in the western part of Moscow averages 100 mg/L, varying from 18 to 331 mg/L; in the yards of residential buildings, it varies from 18 to 63 mg/L and amounts 32 mg/L in the territory of the MO

**Table 1.** Physicochemical properties, snow cover thickness, and ion content in snow meltwater in the western part of Moscow and the background territory.

Parameter	Roads *					R (n = 21)	Y (n = 4)	MO MSU (n = 1)	B (n = 3)
	MRR (n = 3)	H (n = 4)	L (n = 4)	M (n = 5)	Sm (n = 5)				
pH	8.0	8.4	8.6	8.2	8.0	8.2	7.5	7.3	5.6
Mineralization, mg/L	144	233	87	73	58	113	35	32	6.4
Solid particles, mg/L	93	83	28	31	24	48	15	17	9.0
Dust load, mg/m <sup>2</sup> per day	133	102	35	41	30	62	20	21	9.0
Snow cover thickness, cm	50	42	46	45	42	45	45	45	61
Water supply, L/m <sup>2</sup>	91	73	83	80	77	80	79	77	67
Na <sup>+</sup> , µeq/L	1126	2357	505	594	436	951	262	236	8
K <sup>+</sup> , µeq/L	9	25	14	9	11	14	16	28	1
Mg <sup>2+</sup> , µeq/L	17	20	38	12	12	19	9	19	4
Ca <sup>2+</sup> , µeq/L	1039	1459	707	498	394	773	226	178	69
Cl <sup>-</sup> , µeq/L	1400	3353	607	719	434	1229	278	240	7
NO <sub>3</sub> <sup>-</sup> , µeq/L	22	28	29	25	26	26	24	29	24
SO <sub>4</sub> <sup>2-</sup> , µeq/L	92	104	79	63	82	83	70	59	15
HCO <sub>3</sub> <sup>-</sup> , µeq/L	678	374	550	305	310	420	141	134	38

\* Roads: H—highways, L—large, M—medium, Sm—small; R—average for roads; Y—yards with parking lots; B—background; n—number of mixed samples.

MSU. In terms of the mineralization of snow meltwater, the roads of WAO form a following series: highways (233 mg/L) > MRR (144) > large (87) > medium (73) > small (58 mg/L). In Moscow, the average annual concentrations of atmospheric PM<sub>10</sub> in 2018 totaled 0.7 of the maximum permissible concentrations (that is, about 40 µg/m<sup>3</sup>); near highways, the concentration of PM<sub>10</sub> was 1.4 times higher than inside residential areas [35]. At the same time, PM<sub>10</sub> concentrations in the city decreased by an average of 3.7% annually in 2005–2014 [77]. Our data on snow cover pollution show an increase in the content of solid particles by almost four times in snow meltwater near roads compared to the yards of residential buildings with car parking lots, which indicates a significant contribution of particles larger than PM<sub>10</sub> to atmospheric deposition, as well as the presence of an additional source of solid particles in snow, e.g., DISs. A sharp increase in the content of particulate matter in snow cover when using DISs was also found in other cities, for example, in Yekaterinburg (Russia); where the content of particulate matter in the snow cover of roads and footpaths is 4–5 times higher than in the snow cover of lawns and car parking lots in the yards [21].

The ionic composition of snow meltwater near the Moscow Ring Road, the highways, and large and medium roads differs slightly. It is almost everywhere of calcium-sodium chloride type, which compares favorably with the results of long-term (1999–2019) studies of acidity and chemical composition of snow and rainfall in Moscow and Moscow Region [58,63,78]. Only at sampling points on the streets of Molodogvardeiskaya (point S16 in Figure 1) and Ryabinovaya (point S08) near the construction sites and industrial zones Severnoye Ochakovo and Yuzhnoye Ochakovo is the water of calcium-sodium bicarbonate-chloride type. Snow meltwater near small roads, at car parking lots in the yards of residential buildings, and on the territory of the MO MSU has the same composition with slightly higher proportion of bicarbonates, nitrates, sulfates, and calcium and lower proportion of chlorides and sodium, probably due to smaller amounts of DISs, which is also confirmed by low mineralization of meltwater on these territories as compared to other roads.

Water supply in the snow cover next to the roads is average 80 L/m<sup>2</sup>, slightly decreasing in the yards (79 L/m<sup>2</sup>) and the MO MSU (77 L/m<sup>2</sup>). Water supplies in the background snow cover are lower and amounts to 67 L/m<sup>2</sup> as a result of partial snow blowing by the wind. Snow cover in the city is less susceptible to blowing due to higher density resulting from slightly higher air temperatures (heat island) and, accordingly, more frequent temperature transitions around 0°C in March (during snow cover sampling period) and the earlier start of snow melting.

## 3.2. MMs concentrations in snow cover

### 3.2.1. Dissolved forms of MMs

Average, minimum, and maximum concentrations of MMs forms in snow cover near roads, in the yards of residential buildings, near the MO MSU, and in the background area are given in Table 2. The value of contamination factor *CF* (Table 4) shows the excess of MMs forms' concentrations above the background level and, therefore, the level of snow cover contamination.

The maximum content of dissolved forms of most MMs is observed in roadside snow cover, because of ve-

hicular impact; it gradually decreases in the yards and at the MO MSU down to minimum levels in snow cover of the background territory in the suburbs. The *CF* factor varies quite a lot along the roads with different traffic intensities in WAO. The snow cover is most heavily contaminated with dissolved Na, the *CF* of which regularly declines as the road size decreases: from 280 near the highways, 134 near the MRR and 50–70 near large, medium and small roads, and down to 28–31 in the yards of residential buildings and at the MO MSU. The main source of dissolved Na is DISs; thus, dissolved Ca and Sr actively accumulate in snow cover too. Their *CF*s also decline as the road size decreases: from 14–23 at the MRR and highways to 6–10 on large, medium, and small roads, and down to 3–6 in the yards and at the MO MSU. High values of correlation coefficient *r* for pairs Na–Cl<sup>-</sup> (0.99), Ca–Cl<sup>-</sup> (0.87), and Sr–Cl<sup>-</sup> (0.94) indicate the entry of these metals with chloride-type DISs, applied frequently in Moscow. This is confirmed by the studies of snow cover composition in the southwestern part of Moscow, where the use of DISs contributed to a sharp increase in Na, Ca, and K concentrations [39].

Motor vehicle emissions could be an additional source of Na. Petrol Euro 3, 4, 5 and diesel Euro 3, 4 vehicles emit up to 1310 µg Na per 1 km [80]. Strontium is probably an impurity in DISs, since this metal is often a part of calcium compounds. Concentrations of dissolved forms of MMs in snow cover depend on the intensity of transport impact; they are also associated with different amounts of DISs applied on different roads. For example, the concentrations of Na in snow of Novi Sad (Serbia), those of Cu, Fe, Zn, and Pb in snow of Beijing (China), and those of Al, Co, Cr, Cu, Mn, and Ni in snow of Lahti (Finland) increase with larger road size, while the concentrations of Zn in Novi Sad and Cl<sup>-</sup> in Beijing decrease [4,12,55].

In the western part of Moscow, several MMs showed local maxima of concentrations in the yards and at the MO MSU, where large areas are occupied by parking lots. Thus, high levels of dissolved K are probably due to the active fuel combustion during car engine idling; this is confirmed by the value of *r* = 0.57 between the content of dissolved K and NO<sub>3</sub><sup>-</sup>. It is known that NO<sub>3</sub><sup>-</sup> is produced by fuel burning, in particular by motor transport [81], amounting up to 2280 µg NO<sub>3</sub><sup>-</sup> per 1 km [80]. Even larger amounts of water-soluble NO<sub>3</sub><sup>-</sup> are released when burning diesel fuel [82]. Therefore, K is used as an indicator of vehicle emissions when studying the composition of aerosols [83,84]. It occurs in unleaded gasoline [85] and comes abundantly with road dust, especially in tunnels, and with direct tailpipe emissions of cars [80,86,87]. Fuel burning also causes the release of V into the environment [88,89], and therefore its concentrations are high in the snow cover near parking lots. In general, MMs emissions over cruise conditions are substantially different from the emissions over a transient cycle or while idling [90].

Besides the above-mentioned Na, Ca, Sr, K, and V due to the transport impact, the snow cover near all types of roads is highly polluted (*CF* > 3) with dissolved Mo and Mg, with W, Co, and Ba near the MRR, with W, Sn, Bi, Co, Ni, Ba, Sb, Fe, and Ti near highways, with Sb and Co near large roads, with Cd, Mn, and Co near medium roads, and with Sb, Ba, and Ni along small roads. The possible source of these MMs could be non-exhaust vehicle emissions [91–94], which is supported by the data

**Table 2.** Concentrations of dissolved and suspended forms of MMs in snow cover near roads, at car parking lots in the yards of residential buildings, at the MO MSU and in the background area in March 2018, µg/L.

MMs	Dissolved Forms												Suspended Forms																			
	Roads (n = 21)				Yards (n = 4)				MO MSU (n = 1)				Background (n = 3)				Roads (n = 21)				Yards (n = 4)				MO MSU (n = 1)				Background (n = 3)			
	Mean	Min.	Max.	Mean	Mean	Min.	Max.	Mean	Mean	Min.	Max.	Mean	Mean	Min.	Max.	Mean	Mean	Min.	Max.	Mean	Mean	Min.	Max.	Mean	Mean	Min.	Max.	Mean	Mean	Min.	Max.	Mean
Na	21870	2830	85900	6022	1960	15620	5430	193	170	210	193	50*	50*	50*	50*	932	69	10907	103	54	172	109	24	17	38							
Mg	233	100	840	107	100	120	230	50*	50*	50*	50*	50*	50*	50*	50*	1110	102	12610	145	83	228	148	28	22	39							
Al	75	31	227	65	39	111	53	58	47	69	58	47	69	58	4216	351	48798	526	299	822	638	165	103	270								
K	531	100	1210	617	260	950	1110	50*	50*	50*	50*	50*	50*	50*	836	106	8660	157	85	242	164	61	36	108								
Ca	15498	2820	46160	4535	2800	5800	3570	1387	1230	1690	1387	1230	1690	1387	4010	251	44960	462	227	778	478	50	30	81								
Ti	2.0	0.3*	13	0.85	0.55	1.1	1.0	1.1	1.0	1.2	1.1	1.0	1.2	1.1	345	30	3900	48	29	76	45	8.3	1.9	18								
V	0.92	0.2*	2.9	0.76	0.2*	1.7	1.1	0.2*	0.2*	0.2*	0.2*	0.2*	0.2*	0.2*	12	1.1	135	2.1	1.4	2.7	2.8	0.27	0.16	0.45								
Cr	0.66	0.5*	3.9	0.5*	0.5*	0.5*	0.5*	0.5*	0.5*	0.5*	0.5*	0.5*	0.5*	0.5*	11	0.44	140	1.1	0.59	1.6	8.8	0.71	0.53	1.0								
Mn	11	3.8	84	12	3.2	34	3.9	4.5	3.2	6.2	4.5	3.2	6.2	4.5	55	5.5	603	8.4	4.5	14	8.1	3.0	1.2	5.8								
Fe	93	25	440	68	37	93	46	49	43	56	49	43	56	3848	452	39098	680	383	1036	678	139	94	218									
Co	0.28	0.12	1.0	0.18	0.1	0.3	0.11	0.071	0.054	0.091	0.071	0.054	0.091	1.6	0.13	19	0.19	0.11	0.31	0.22	0.037	0.02	0.058									
Ni	4.6	1.7*	28	1.7*	1.7*	1.7*	3.6	1.7*	1.7*	1.7*	1.7*	1.7*	1.7*	6.1	0.51	76	1.1	0.67	1.4	1.7	0.45	0.3	0.67									
Cu	5.2	2.5	13	4.1	2.8	4.9	4.9	2.8	2.5	3.1	2.8	2.5	3.1	17	2.1	121	3.8	2.5	4.7	6.1	0.65	0.58	0.7									
Zn	16	8.7	29	18	12	23	24	22	15	31	22	15	31	33	3.9	311	6.9	3.7	9.2	18	1.1	0.63	1.7									
As	0.05*	0.05*	0.05*	0.05*	0.05*	0.05*	0.05*	0.05*	0.05*	0.05*	0.05*	0.05*	0.05*	0.27	0.013	2.6	0.077	0.014	0.11	0.12	0.013	0.01	0.016									
Rb	0.43	0.22	0.88	0.35	0.25	0.52	0.34	0.19	0.17	0.23	0.19	0.17	0.23	3.1	0.42	32	0.56	0.33	0.81	0.60	0.2	0.12	0.38									
Sr	14	4.9	40	7.2	5.2	11	7.0	1.2	1.0	1.3	1.2	1.0	1.3	17	1.6	191	2.7	1.8	4.1	4.4	0.41	0.23	0.74									
Mo	0.26	0.025	3.4	0.071	0.025	0.16	0.025*	0.025	0.025	0.025	0.025	0.025	0.025	0.71	0.083	7.0	0.17	0.1	0.21	0.25	0.02	0.015	0.025									
Cd	0.068	0.019	0.61	0.064	0.028	0.12	0.061	0.033	0.017	0.047	0.033	0.017	0.047	0.053	0.008	0.42	0.018	0.009	0.025	0.025	0.006	0.001	0.012									
Sn	0.015	0.005	0.21	0.012	0.005	0.033	0.005*	0.005	0.005	0.005	0.005	0.005	0.005	1.3	0.35	9.6	0.59	0.38	0.75	0.56	0.063	0.04*	0.098									
Sb	0.38	0.1	4.0	0.12	0.095	0.16	0.12	0.068	0.063	0.074	0.068	0.063	0.074	0.79	0.11	8.0	0.21	0.16	0.25	0.26	0.029	0.022	0.044									
Ba	9.2	4.2	31	6.7	4.1	8.6	7.7	2.7	2.1	3.3	2.7	2.1	3.3	34	4.9	341	7.5	5.8	9.9	9.3	1.7	0.95	3.2									
W	0.11	0.02*	0.88	0.02*	0.02*	0.02*	0.02*	0.02*	0.02*	0.02*	0.02*	0.02*	0.02*	2.6	0.25	28	0.33	0.19	0.47	0.27	0.045	0.025	0.068									
Pb	0.35	0.13	1.8	0.28	0.18	0.44	0.54	0.70	0.50	0.83	0.70	0.50	0.83	5.0	0.46	38	1.8	1.5	2.0	8.6	0.84	0.67	1.0									
Bi	0.003	0.001	0.029	0.002	0.001	0.006	0.001*	0.001	0.001	0.001	0.001	0.001	0.001	0.094	0.023	0.66	0.035	0.031	0.036	0.047	0.011	0.007	0.02									

Notes. \* Concentrations below detection limits were assigned a value equal to a half of it [79]. MMs are listed in the order of increasing numbers in Mendeleev's Periodic Table.



Object (Number of Mixed Samples)	Values of Contamination Factor <i>CF</i>					<i>TCF</i>
	>50	25–50	10–25	5–10	3–5	
MRR ( <i>n</i> = 3)	<i>DS</i> Na <sub>134</sub> Ca <sub>385</sub> W <sub>258</sub> Co <sub>219</sub> Ti <sub>203</sub> Mg <sub>199</sub> Sr <sub>198</sub> Na <sub>194</sub> <i>SP</i> Mo <sub>141</sub> Al <sub>128</sub> Fe <sub>122</sub> Zn <sub>120</sub> Sb <sub>113</sub> Mn <sub>88</sub> As <sub>86</sub> Ba <sub>85</sub> Cu <sub>78</sub> Cr <sub>78</sub> Ni <sub>66</sub> Rb <sub>66</sub> Sn <sub>63</sub> K <sub>60</sub>	—	Ca <sub>15</sub> Sr <sub>14</sub> Pb <sub>19</sub>	W <sub>7</sub> K <sub>7</sub> Co <sub>5</sub>	Mo <sub>4</sub> Mg <sub>4</sub> Ba <sub>4</sub> V <sub>3</sub>	194 3212
Highways ( <i>n</i> = 4)	<i>DS</i> Na <sub>280</sub>	—	Sr <sub>23</sub> Ca <sub>21</sub> K <sub>20</sub> W <sub>19</sub> Sn <sub>11</sub> <i>SP</i> W <sub>47</sub> Co <sub>31</sub> Ti <sub>31</sub> Sr <sub>29</sub> V <sub>29</sub> Mg <sub>28</sub> Na <sub>27</sub> Mo <sub>36</sub>	Bi <sub>8</sub> Co <sub>6</sub> Mo <sub>6</sub> Mg <sub>5</sub> Ni <sub>5</sub> V <sub>5</sub> Cd <sub>7</sub> Bi <sub>6</sub> Ni <sub>6</sub> Cr <sub>6</sub> Sr <sub>9</sub> Mg <sub>9</sub> Fe <sub>9</sub> Ba <sub>8</sub> Al <sub>7</sub> Rb <sub>6</sub> Mn <sub>6</sub> Bi <sub>6</sub> Cd <sub>5</sub> K <sub>5</sub> Ni <sub>5</sub> Pb <sub>5</sub> Sr <sub>9</sub> Ca <sub>7</sub> K <sub>7</sub> Cd <sub>6</sub> Mn <sub>5</sub> Co <sub>5</sub>	Ba <sub>4</sub> Sb <sub>3</sub> Fe <sub>3</sub> Ti <sub>3</sub> Pb <sub>4</sub> V <sub>4</sub> Co <sub>3</sub> Cr <sub>4</sub> V <sub>4</sub> Mg <sub>3</sub> Mo <sub>3</sub>	414 481 156 235 116
Large roads ( <i>n</i> = 4)	<i>DS</i> Na <sub>64</sub>	—	Zn <sub>24</sub> Mo <sub>22</sub> Fe <sub>20</sub> Sn <sub>17</sub> Al <sub>17</sub> Sb <sub>16</sub> Cu <sub>15</sub> Ba <sub>14</sub> As <sub>13</sub> Mn <sub>13</sub> Rb <sub>11</sub> K <sub>10</sub> Sb <sub>17</sub> K <sub>11</sub> Ca <sub>10</sub> Ca <sub>24</sub> W <sub>21</sub> Cu <sub>17</sub> Mo <sub>16</sub> Zn <sub>14</sub> Sr <sub>13</sub> Co <sub>12</sub> Sn <sub>12</sub> Sb <sub>11</sub> Mg <sub>11</sub> V <sub>11</sub> Ti <sub>10</sub> As <sub>10</sub> Na <sub>10</sub>	—	—	240
Medium roads ( <i>n</i> = 5)	<i>DS</i> Na <sub>71</sub>	—	Cu <sub>22</sub> Ca <sub>21</sub> W <sub>19</sub> Mo <sub>18</sub> Sn <sub>14</sub> Sb <sub>13</sub> V <sub>13</sub> Sr <sub>13</sub> Zn <sub>12</sub> Ti <sub>11</sub> Mg <sub>11</sub> Co <sub>11</sub> As <sub>11</sub> Na <sub>10</sub> Fe <sub>10</sub>	—	Cd <sub>4</sub> Ni <sub>4</sub> Cr <sub>4</sub> Pb <sub>4</sub>	240
Small roads ( <i>n</i> = 5)	<i>DS</i> Na <sub>52</sub>	—	—	K <sub>9</sub> Sr <sub>7</sub> Ca <sub>6</sub> V <sub>6</sub> Mo <sub>5</sub> Sr <sub>9</sub> Co <sub>9</sub> Ti <sub>8</sub> Mg <sub>7</sub> Na <sub>6</sub> Ba <sub>6</sub> Al <sub>5</sub> Mn <sub>5</sub> Bi <sub>5</sub> Sb <sub>6</sub> W <sub>6</sub> Mg <sub>5</sub> V <sub>5</sub>	Sb <sub>4</sub> Ba <sub>4</sub> Ni <sub>4</sub> Mg <sub>3</sub> Cd <sub>4</sub> Ni <sub>4</sub> Rb <sub>4</sub> K <sub>4</sub> Pb <sub>3</sub> Cr <sub>3</sub> Co <sub>4</sub> Sn <sub>3</sub> Ba <sub>3</sub>	98 179 187
Average for roads ( <i>n</i> = 21)	<i>DS</i> Na <sub>113</sub>	—	Mo <sub>17</sub> V <sub>15</sub> Ca <sub>13</sub> Sn <sub>12</sub> W <sub>12</sub> Cu <sub>12</sub> Sb <sub>11</sub> As <sub>10</sub> Zn <sub>10</sub> Fe <sub>10</sub> Sr <sub>12</sub> Ca <sub>11</sub> K <sub>11</sub> Mo <sub>10</sub> As <sub>22</sub> Sn <sub>21</sub> Ba <sub>20</sub> Mn <sub>19</sub> Al <sub>25</sub> Rb <sub>15</sub> Cr <sub>15</sub> K <sub>14</sub> Ni <sub>14</sub>	—	—	695
Yards with car parking lots ( <i>n</i> = 4)	<i>DS</i> Ca <sub>80</sub> W <sub>57</sub>	—	Co <sub>44</sub> V <sub>44</sub> Sr <sub>42</sub> Ti <sub>41</sub> Mg <sub>40</sub> Na <sub>39</sub> Mo <sub>36</sub> Zn <sub>30</sub> Fe <sub>28</sub> Sb <sub>27</sub> Cu <sub>25</sub>	—	—	66
MO MSU ( <i>n</i> = 1)	<i>DS</i> Na <sub>31</sub>	—	K <sub>12</sub>	Sr <sub>6</sub> Bi <sub>8</sub> Pb <sub>6</sub>	V <sub>4</sub> Ca <sub>3</sub>	103
	<i>SP</i> Na <sub>28</sub>	—	—	—	—	71
	<i>DS</i> Na <sub>28</sub>	—	K <sub>22</sub> Zn <sub>16</sub> Mo <sub>15</sub> Cr <sub>12</sub> Sr <sub>11</sub> V <sub>10</sub> Pb <sub>10</sub> Ca <sub>10</sub>	Sr <sub>9</sub> Ca <sub>9</sub> Mo <sub>8</sub> V <sub>8</sub> Sb <sub>7</sub> W <sub>7</sub> Sr <sub>6</sub> Zn <sub>6</sub> As <sub>6</sub> Ti <sub>6</sub> Cu <sub>6</sub> Co <sub>5</sub> Mg <sub>5</sub> Fe <sub>5</sub> V <sub>6</sub> Sr <sub>6</sub> Mg <sub>5</sub> Cu <sub>9</sub> As <sub>9</sub> Sn <sub>9</sub> Sb <sub>9</sub> W <sub>6</sub> Co <sub>6</sub> Ba <sub>5</sub> Ti <sub>5</sub> Mg <sub>5</sub> Fe <sub>5</sub> Na <sub>5</sub>	—	156

**Table 3.** Accumulation of dissc

*Notes.* The *CF* value of each element is written in the subscript. *DS*—dissolved (blue background), *SP*—suspended (orange background) forms.

on the intensive enrichment of Moscow road dust and especially its fractions PM<sub>1</sub> and PM<sub>1–10</sub> with Sb, W, Sn, Bi, and Cd [67,95,96], and nanoscale particles of road dust enriched with Pb, Cu, Zn, Ni, Cd, Cr, Co, and Sn [97]. Therefore, the highest *CF* values for many of these MMs, in particular W and Sn, are characteristic of snow cover along the MRR and highways. High levels of dissolved Na, K, Mg, Fe, Al, Zn, Sr, Cu, and other MMs comparable to our data were also found in snow cover near the MRR in 2011 [48].

The most intensive accumulation of dissolved Mo and Sb in the western part of Moscow was observed in snow cover along large roads. Mo and Sb probably come with emissions from heat and power station No. 25 and other thermal power plants in WAO, as indicated by increased *r* coefficients in pairs Mo–Sb (0.99), Mo–SO<sub>4</sub><sup>2-</sup> (0.48), and Sb–SO<sub>4</sub><sup>2-</sup> (0.45). During long and severe frosts, fuel oil is used as an additional fuel for power plants along with natural gas, thus contributing to higher SO<sub>2</sub> emissions [77] and increasing SO<sub>4</sub><sup>2-</sup> concentrations in snow cover. The accumulation of Mo and Sb in snow cover is also characteristic of the eastern part of Moscow, where these elements are actively emitted by heat and power stations, as well as by metalworking, mechanical engineering, and petrochemical enterprises [46].

The MO MSU and the background territory are characterized by higher concentrations of dissolved Zn and Pb compared to snow cover along the roads and in the yards. The increased content of dissolved Zn in snow cover near the MO MSU compared to roadside snow cover was indicated earlier [40]. This is probably due to the regional transfer of pollutants from urbanized areas of the Moscow Oblast and the nearest regions, to the macro-regional transfer from Europe and global migration of pollutants. It is confirmed by the data on the accumulation of metals in the dust component of background snow cover near Zvenigorod in the western part of Moscow Oblast [46], in snow cover of the background regions of the Ryazan Meshchera [98], and the Polar Plateau in Antarctica [99]. High levels of Cd at the urban reference sites not polluted by traffic compared to snow near the roads were detected in Innsbruck, due to the input of metal from non-transport sources [23]. In Moscow, the snow cover composition at the MO MSU showed 2–3 times higher content of Fe, V, Co, and Ba; minor difference in content of Al, Mn, Ni, Cu, As, and Cd; and 2–3 times lower content of Cr, Zn, Sr, and Mo compared to the territory of the Botanical Garden next to the MO MSU [40].

Different rates of *CF* value increment with increasing anthropogenic impact make it necessary to consider the behavior of all studied pollutants simultaneously and make an integral assessment of contamination. For this purpose, total contamination factor *TCF* of snow cover with dissolved and suspended MMs was calculated. The spatial distribution of *TCF* is shown in Figure 2.

The maximum levels of MMs contamination in the dissolved phase of snow causing extreme-

ly dangerous environmental situations ( $TCF > 256$ ) are characteristic of the sections along Kutuzovskiy Avenue, Mozhaiskoye Highway (near the industrial zones Severnoye Ochakovo and Yuzhnoye Ochakovo), Rublevskoye Highway and Minskaya Street, mainly because of the application of DISs. Very high level of snow cover pollution and very dangerous environmental situations is characteristic of the MRR, Aminievskoye Highway, several medium (Molodogvardeiskaya St. near the Kuntsevo industrial zone and Bolshaya Filevskaya St. near the Fili and Western Port industrial zones) and small (Koshtoyantsa St., sampling point S20 in Figure 1) roads. Territories along almost all studied small roads and at the MO MSU have the high level of pollution (with  $TCF$  64–128) and a dangerous environmental situation. The amount of applied DISs is lower in most yards, and the impact of transport decreases as well, but it does not completely disappear because of the presence of car parking lots. The decrease is also due to protective functions of buildings that act as barriers to air pollutant flows from the highways to the yards of residential buildings [100]. Buildings prevent the spread of emissions from vehicles, thus decreasing snow cover pollution to medium level (with  $TCF$  32–64) and a moderately dangerous environmental situation.

### 3.2.2. Suspended forms of MMs

The content of suspended forms of all MMs in roadside snow cover is higher than in snow cover of the yards, the MO MSU, and the background territory. Application of DISs on roads and further blowing of their particles by the wind leads to their inclusion into roadside snow. This accounts for the fact that the highest  $CF$  values of Ca (385, 64, and 24, respectively) were found in snow cover of the MRR, highways, and large roads, decreasing on medium roads, small roads, in yards, and at the MO MSU (21, 13, 9, and 10, respectively). Suspended forms of all MMs, except K, Mo, and Sb, are accumulated much more intensively than dissolved ones, due to enrichment of the dust component of snow cover with MMs and the high content of solid particles in snow cover. Solid particles' input to the snow cover is due to precipitation from the atmosphere, DISs application on roads, blowing of road dust and soils particles from snow-free areas, and spraying of mud sediment from the surface of roadways during snow melting. Resuspended road dust is reported to be one of the most important sources of microparticles in the atmosphere; for example, in Bogota, it supplies about 23% of the mass of  $PM_{10}$  particles [101] and in the USA, more than a half of  $PM_{10}$  and about a quarter of  $PM_{2.5}$  particles [102]. In Paris, the contributions of road dust emissions were estimated to be 13% of atmospheric  $PM_{10}$ , while the sum of vehicle exhaust and wear accounted for 47% of  $PM_{10}$  [103]. Moreover, for the north cities, the spraying of mud sediment from the surface of roadways is an essential source of suspended particles and MMs in roadside snow cover [21].

On large roads, dissolved Mo and Sb accumulate more intensively compared to its suspended forms, which is probably due to the increased pH of snow meltwater (an average of 8.6 on large roads, 8.0–8.4 on other roads). These elements are typical anionogenic elements and migrate well in alkaline conditions, so the higher pH values could contribute to the acceleration of their dissolution [104]. A positive correlation of dissolved Mo content

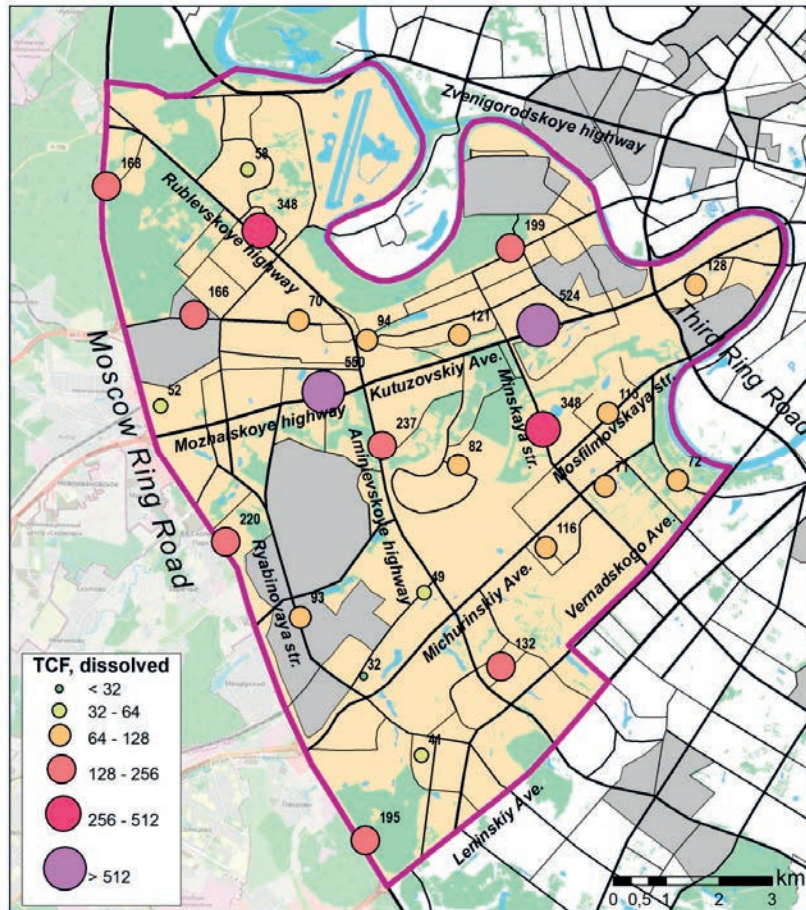
with pH values of river water and snow was also found in the basins of rivers flowing into the Gulf of Bothnia [105].

Smaller roads have lower traffic intensity, resulting in a decrease of accumulation of suspended MMs forms. Ca, W, Co, Ti, Mg, Sr, Na, Mo, Al, Fe, Zn, Sb, Mn, As, Ba, Cu, Cr, Ni, Rb, Sn, and K are accumulated intensively ( $CF > 50$ ) in snow cover near the MRR. The  $CF$  decreases sharply for all MMs along the highways, reaching 64 for Ca, 27–47 for W, Co, Ti, Sr, V, Mg, and Na and less than 25 for other MMs. Along large and medium roads, the  $CF$  of Ca, W, Cu, Mo, Zn, Sr, Co, Sn, Sb, Mg, V, Ti, As, Na, Cu, and Fe decrease to 10–25, and to 5–17 near small roads. Higher content of solid particles in snow cover at the MO MSU leads to the increase in  $CF$  values for Zn, Mo, Cr, Sr, V, Pb, and Ca up to 10–16, as compared with the yards where  $CF$  values of these MMs are 5–9. High levels of Zn at the MO MSU are probably due to the influence of transport, since car parking lots are located nearby, where intense accumulation of the metal is typical [106]. Our studies on the chemical composition of dust component in snow cover of the eastern industrial part of Moscow showed that the following MMs are the ones that accumulate most intensively (the  $CF$  value is written in subscript):  $Mo_{19}Sb_{4.9}As_{4.6}W_{4.3}Sn_{3.6}V_{2.1}Fe_{2.1}Cr_{2.0}$  [46]. However, foregoing data include areas with low levels of snow cover pollution, namely recreational and agricultural zones; therefore,  $CF$  levels for MMs are lower than those obtained for the traffic zone in the western part of the city.

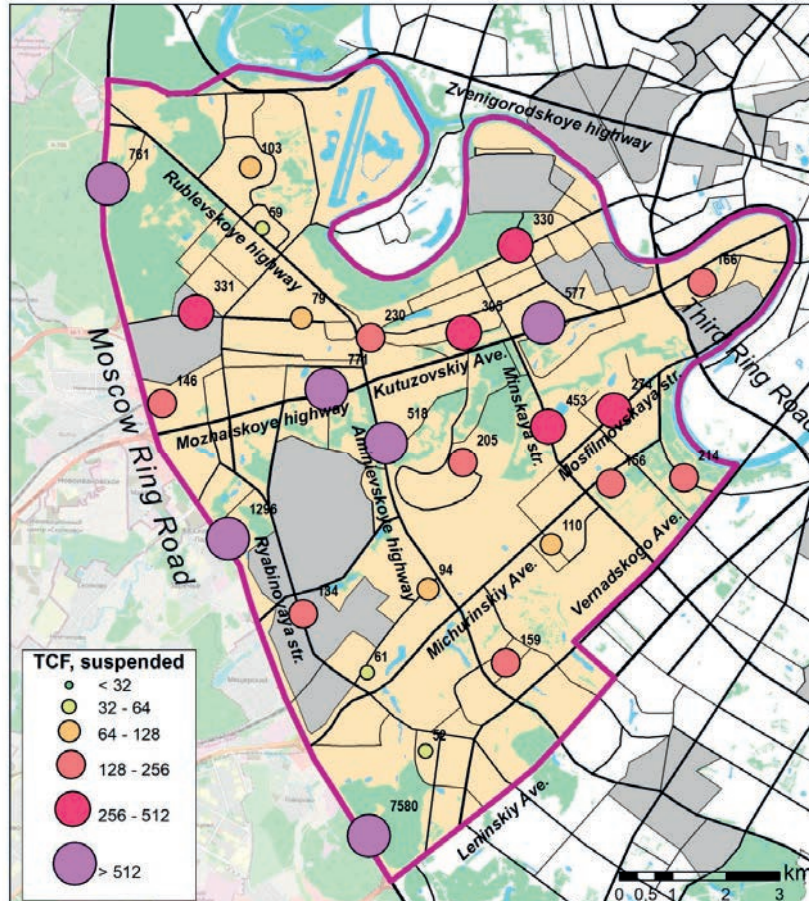
The  $TCF$  values of suspended MMs increase considerably and the levels of environmental hazard increase by one gradation at many points, as compared to the total pollution of snow cover with dissolved forms. The highest increase of  $TCF$  for suspended forms is at the MRR, where the extremely dangerous environmental situation and the maximum  $TCF$  values were found, ranging from 761 in the northern part of the study area (4.5 times higher than the  $TCF$  for dissolved MMs forms) to 1296 on the average (6 times higher) and 7580 in the southern part (39 times higher). In other territories, the growth of  $TCF$  for suspended forms relative to the dissolved ones is less pronounced, reaching 1.2 to 3 times. The exception is Rublevskoye Highway, where the  $TCF$  is almost 6 times lower due to the low dust content in snow cover (12 mg/L compared to 102 mg/L near the MRR). The low dust content in snow cover could be attributed to the large distance of sampling point from the highway itself—there is both an alternate route and a car parking lot on the roadside, which separate the sampling point from the highway.

Extremely high snow cover pollution on the territory near the intersection of the MRR and Leninskiy Avenue, one of the busiest highways in Moscow, is probably the result of very intense MMs inflow with vehicle emissions (enormous numbers of cars and traffic congestions), as well as the blowing of contaminated road dust microparticles. An extremely dangerous situation ( $TCF > 256$ ) also occurs on Kutuzovskiy Avenue, Mozhaiskoye and Aminievskoye highways, and a number of large (Minskaya and Mosfilmovskaya streets) and medium (Molodogvardeiskaya and Bolshaya Filevskaya streets—sites S16 and S12 in Figure 1, respectively) roads. In the yards of residential buildings, snow cover pollution with suspended forms of MMs as compared to dissolved ones increases to the high level ( $TCF$  64–128), and to very high





(a) Dissolved MMs



(b) Suspended MMs

**Figure 2.** Distribution of TCF values for dissolved and suspended MMs in the western part of Moscow.



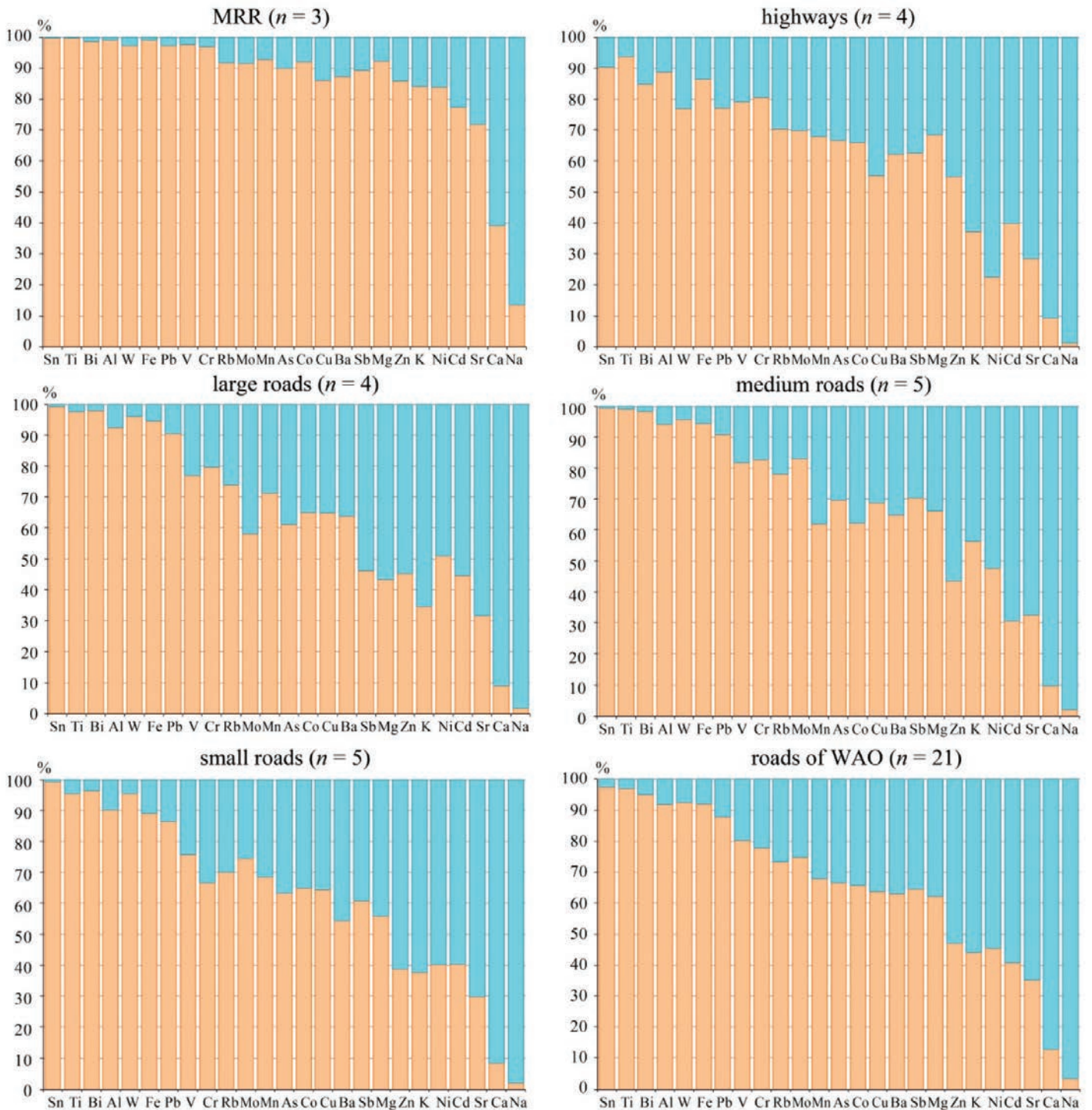


**Figure 3. (with continuation)** Proportions of dissolved and suspended MM forms in snow cover along different types of roads, at car parking lots in the yards of residential buildings and at the MO MSU in the western part of Moscow, and in the background area.

level ( $TCF$  128–256), and very dangerous environmental situation for small and some medium roads.

Thus, snow cover pollution on the roadside territories in the western part of Moscow is mainly due to particulate matter. It is enriched with Ca, W, Co, V, Sr, Ti, Mg, Na, Mo, Zn, Fe, Sb, and Cu. The MMs content in suspension along the roads is on average 25 times or more above the background. Na, Sr, Ca, K, Mo, Sb, and W are the main dissolved pollutants; their content in the snow of certain areas of the WAO is six or more times above the background level. The spatial pattern of the total contamination factor  $TCF$  is characterized by the formation of common centers of abnormally high values for

both dissolved and suspended MMs forms on the MRR, Kutuzovskiy Avenue, Rublevskoye, Mozhayskoye, and Aminievskoye highways and some other streets. The anomalies appear due to the application of DISs, vehicle emissions, as well as the impact of enterprises in the adjacent industrial zones, such as Severnoye Ochakovo, Yuzhnoye Ochakovo, Kuntsevo, Fili, and Western Port.

### 3.3. Partitioning of MMs

Studying the ratio of MMs forms is important for predicting the pollutants' behavior during and after snowmelt, since the dissolved phase has a higher migratory ability. Therefore, the risk of contamination

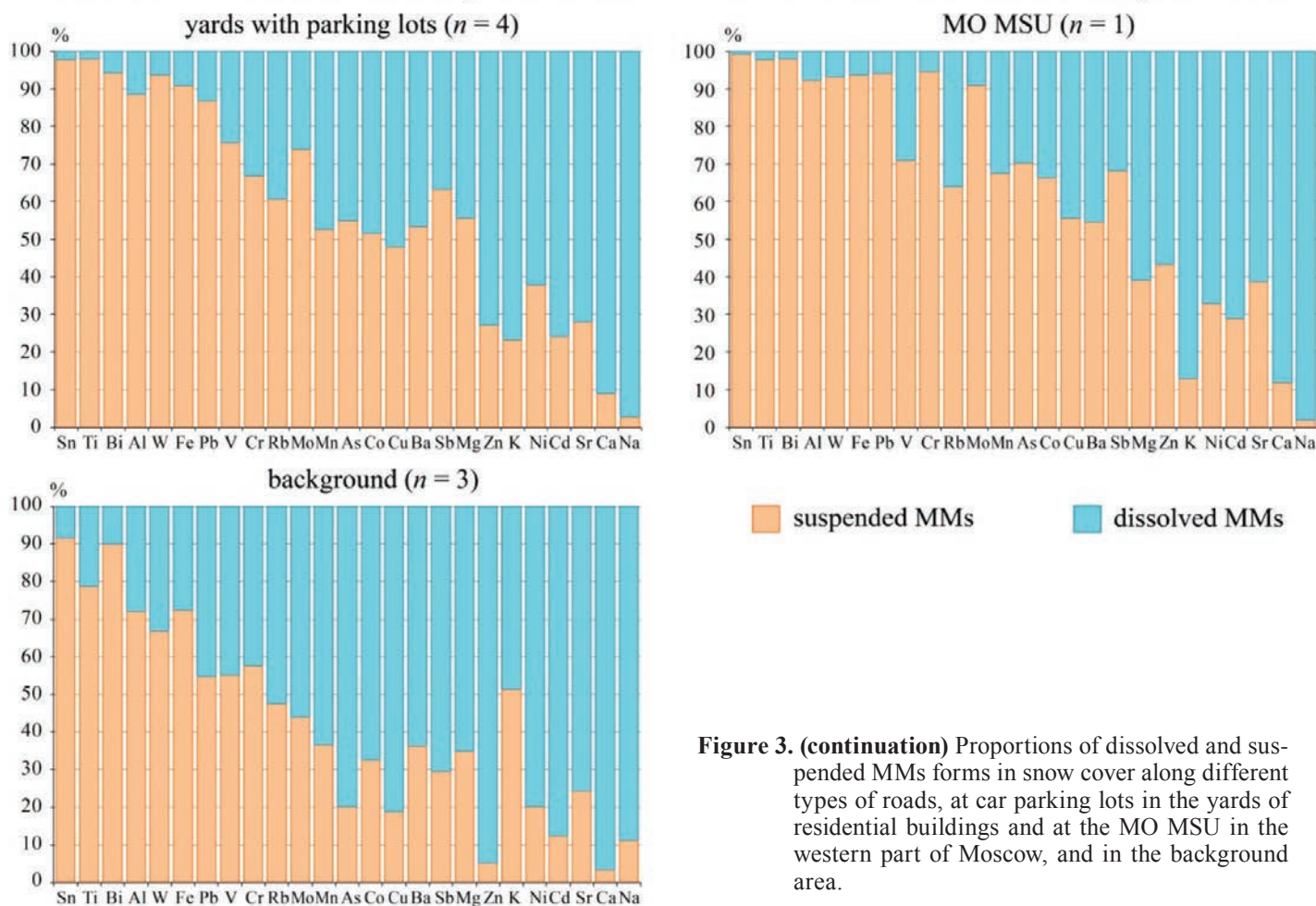


**Figure 3. (continuation)** Proportions of dissolved and suspended MMs forms in snow cover along different types of roads, at car parking lots in the yards of residential buildings and at the MO MSU in the western part of Moscow, and in the background area.

greatly depends on the MMs' ability to transform from a non-dissolved phase to a dissolved one. To define the predominant phase of elements in snow, the share of their dissolved phase, or solubility ( $K_z$ , %) was calculated:  $K_z = 100\% \cdot C_{dis} / (C_{dis} + C_{sus})$ , where  $C_{dis}$  is the concentration of dissolved phase of MMs,  $\mu\text{g/L}$ ;  $C_{sus}$  is the concentration of suspended phase,  $\mu\text{g/L}$ .

Most MMs in snow cover of the background territory prevail in dissolved form: the proportion of dissolved forms of Ca, Zn, Na, Cd, Ni, As, Cu, and Sr is more than 85%; 60–70% for Sb, Co, Mg, Mn, and Ba, and 52–56% for Rb and Mo (Figure 3). These MMs are most likely washed out from the atmosphere and could enter the snow cover during in-cloud processes, i.e., elements' sorption on snowflakes inside the cloud [107]. Another source is washing out from the atmosphere with an ultrafine ( $<0.45 \mu\text{m}$ ) fraction of aerosols, which passes through filters in the process of snow meltwater filtration in the laboratory. The predominance of dissolved forms of MMs could also be attributed to a slightly acidic reaction (pH 5.6) of snow meltwater in background areas, as the cationogenic Ca, Zn, Na, Cd, Ni, Cu, Sr, Co, Mg, and Ba could be easily transferred from insoluble to soluble form in acidic waters [104,108,109].

Other MMs are found predominately in suspended forms, which accounts for 80–90% of Sn and Bi, 60–80% of Ti, Al, Fe, and W, and 50–60% of Pb, V, Cr, and K. An increase in the proportion of suspended forms of MMs is related to the washout of the solid aerosol particles in the atmospheric surface layer by below-cloud scavenging processes [107]. In the background area, most

of these MMs enter the atmosphere with relatively large soil particles blown from snow-free surfaces, thus contributing to higher proportion of suspended MMs forms. Thin snow cover, strong wind, and the absence of woody vegetation could significantly increase the soil particles supply to the roadside snow. Regional transport of contaminated atmospheric aerosol particles of different sizes also contributes to the higher proportion of suspended MMs forms. For example, in Northern China, Al and Fe in precipitation are mainly associated with large particles and Pb with thin ones, while K, V, and Cr have a bimodal distribution with peak concentrations within particle size intervals of  $0.43\text{--}0.65$  and  $4.7\text{--}5.8 \mu\text{m}$  [110].

In urban areas, mass deposition of solid particles from the atmosphere and the application of DISs on roads with their subsequent blowing out and re-depositing on the surface of roadside snow cover significantly increase the role of suspended MMs forms. This is most pronounced in snow cover along roads (Figure 3), where the proportion of suspended forms is above 90% for Sn, Ti, Bi, Al, W, and Fe, 80–90% for Pb, V, and Cr, 50–80% for Rb, Mo, Mn, As, Co, Cu, Ba, Sb, Mg, and Zn. The dissolved phase prevails for K, Ni, Cd, and Sr (it accounts for 50–65%), as well as for Ca (87%) and Na (97%).

The effect of dust deposition on the increasing proportion of suspended forms of MMs is confirmed by the high significant negative coefficients of rank correlation  $r_s$  between the dust load and the proportion of dissolved forms for almost all MMs:  $r_s$  are less than  $-0.67$  for all MMs, except K ( $-0.57$ ), Sb ( $-0.56$ ), Ni ( $-0.41$ ), and insignificant for Mo, W, and Na. Insignificant cor-



relation between Mo and W solubility and dust load is due to numerous points with concentrations below the detection limit, for these elements. Weak Na solubility correlation with amount of dust particles is due to Na input mainly with DISs and their subsequent rapid dissolution, providing for just little effect on the dust load. High positive  $r_s$  between the concentrations of  $\text{Cl}^-$  in meltwater and the proportion of suspended forms of all MMs ( $r_s = 0.49\text{--}0.75$ ), except Sr (0.44), Ca (0.40), K, Ni, Mo, W (0.15–0.34), and Na (–0.28) indicate the presence of MMs as slightly soluble impurities in chloride DISs. High proportion of suspended MMs in snow cover of the WAO could be also explained by the change of subacidic conditions in background snow meltwater (pH 5.6) to neutral, weak alkaline, and even alkaline in the city (pH 7.5–8.6). Under such alkaline conditions, the cationogens Bi, Fe, Pb, Rb, Mn, Co, Cu, Ba, Mg, and Zn are poorly dissolved from the suspended particles. This is confirmed by the negative significant  $r_s$  between the pH value of meltwater and the proportion of dissolved forms of Cu, Cd, Ba, Bi, Fe, Sn, Al, and W.

A comparative analysis of the chemical composition of atmospheric dust, snowmelt-runoff, and rainfall-runoff in Beijing showed the leading role of dust in the formation of precipitation composition. Its presence in the snow cover results in the predominance of suspended forms of pollutants [12]. High proportions of many MMs in the suspension along with the dissolved forms of Na, K, Ca, Sr, and Sb were also identified in snow cover on the windward slope of the Salt Lake Valley (central Wasatch Mountains), Utah, USA [111]. The predominance of suspended forms of most MMs seems to be typical of urban areas, as supported by the data on Cr, Pb, Cu, Ni, Al, and Fe in snow in Östersund [15] and on Pb, Cu, Zn, and Cd in snow in Luleå and Umeå, Sweden [16].

Concentrations of Al, Fe, Mn, and V in snow cover of the traffic zone increase with increasing particle size reaching the maximum in particles  $>1000\ \mu\text{m}$ , while the concentrations of Zn and Pb are the highest in particles  $<100\ \mu\text{m}$  [21]. This trend is observed even in small cities with no industrial enterprises, where the increasing contributions of 0.45–1.2  $\mu\text{m}$ , 1.2–8  $\mu\text{m}$ , and  $>8\ \mu\text{m}$  fractions to the total concentrations of these MMs in snow cause lower proportion of dissolved forms of Al, Si, Mn, Fe, and Zn compared to the background territories, as shown by the Valday case study [112]. A summary of the results of studies on the chemical composition and the ratio of pollutants in water runoff from roads at 294 monitoring points on six continents showed that Pb and Cr predominate in road runoff in suspended form, while Zn, Cu, Ni, and Cd in dissolved form [14]. At the same time, the proportion of suspended forms of MMs in snow meltwater is usually greater than in rainwater [113]. The MRR stands out among all types of roads of the WAO in terms of the ratio of MMs forms in snow cover—the highest proportion of suspended forms of all MMs was recorded next to this highway. Mass input of dust particles leads to the dominance of suspended form for most MMs in snow cover (more than 85%); only Cd and Sr account for 72–77%. Ca and Na entering snow cover with easily soluble DISs prevail in dissolved forms (61% and 86%, respectively). Medium roads, similar to the MRR, are characterized by a significant proportion ( $>80\%$ ) of suspended forms for Sn, Ti, Bi, Al, W, Fe, Pb, V, Cr, and Mo and relatively low ones for Zn and Cd (43% and 31%, respectively). A high proportion of dissolved Zn

reaching 70% is typical of traffic area runoff [14], and of dissolved Cd and Zn for snowmelt water, in which the solubility of these metals could reach 100% and 81%, respectively [15].

The ratio of MMs forms on large, small roads, and highways is scarcely different from the average level for all WAO roads.

Anthropogenic load in the yards and at the MO MSU is less pronounced compared to roads; it is evident from the content of solid particles in snow meltwater (15 and 17 mg/L compared to 48 mg/L on the roads). Therefore, the contribution of suspended MMs to the total content of elements in snow cover decreases. The MO MSU is located between two small roads – Academician Khokhlov Street and Michurinskiy Alley, used for the passage and parking of vehicles of the MSU employees. Thus, the ratio of suspended and dissolved MMs forms is close to that in the yards. At the same time, the share of dissolved Cd, K, Zn, Mg, Ba, Cu, and Rb increases by 10% and more in snow cover at the MO MSU and in the yards of residential buildings compared with roads. The source of these MMs could be fine particles (less than 0.45  $\mu\text{m}$ ) emitted during the heating of car engines at car parking lots in the yards and near the MO MSU.

This is confirmed by laboratory studies on the influence of air temperatures and the operation modes of car engines on snow pollution with particulate matter and MMs. The studies have shown that motor vehicles emissions enrich snow with particles of 50–400 nm, which are high in MMs content [19]. Therefore, when a solid phase is separated from meltwater using filters with 0.45  $\mu\text{m}$  pore diameter, a large number of fine MMs-contaminated particles enters the dissolved phase. Nanoparticles account for 71% of the total number of particles with 3 nm to 10  $\mu\text{m}$  diameter in snow of Montreal, and up to 19% of particles are less than 100 nm [114]. Particle number density of ultrafine particles (0.01–0.1  $\mu\text{m}$  in diameter) in snow is dozens and hundreds of times larger than that of 0.1–0.2  $\mu\text{m}$  and 0.2–0.5  $\mu\text{m}$  particles. However, a significant proportion of Al, Cr, Mn, Co, Ni, Cu, As, Cd, and Pb is in suspended form, that is, it is associated with particles larger than 0.2  $\mu\text{m}$ , although the ultrafine fraction also plays an important role in the formation of total MMs content in snow [22].

Study of the composition of atmospheric particles in Hong Kong revealed that the proportion of water-soluble MMs in  $\text{PM}_{2.5}$  fraction is 10–25% higher than in the  $\text{PM}_{10}$  fraction. Moreover, Ca, Mg, Cd, Zn, V, Cu, Mn, and Ni prevail in dissolved form in  $\text{PM}_{2.5}$  fraction, compared to just Ca, Mg, Cd, and Zn in  $\text{PM}_{10}$  [84]. Residential buildings often form enclosed spaces, or “well traps”, in which the migration of particles in the atmosphere diminishes sharply and soil pollution with MMs in the yards increases [100] due to deposition of fine particles, thus contributing to a higher proportion of dissolved forms of MMs in snow cover. Probably for the same reason, the proportion of dissolved forms of most MMs (except Ni, K, and Mg) in snow cover of the yards is higher than at the MO MSU. The traffic intensity at car parking lots is low—even near stores, the vehicles’ turnover usually does not exceed 50 units per day per 1 parking place [115]; nevertheless, the runoff from these areas is usually highly enriched with many MMs as compared to highways with light traffic intensity [14].

Thus, Sn, Ti, Bi, Al, W, Fe, Pb, V, Cr, Rb, Mo, Mn, As, Co, Cu, Ba, Sb, and Mg dominate in suspended form





in snow cover in the western part of Moscow. Ca and Na prevail in the dissolved form, and the contribution of suspended and dissolved forms of Zn, K, Ni, Cd, and Sr to their total content ranges from 40 to 60%, that is, they lack a clearly pronounced predominant form of occurrence.

### 3.4. Deposition rates of dissolved and suspended MMs

To assess geochemical impact on the components of urban landscapes during the snow occurrence period, it is necessary to determine the accumulated supplies of MMs released during snow melting. The content of particulate matter and MMs in snow meltwater of urban areas is greater than in rainfall-runoff, indicating the crucial role of snow melting for the formation of chemical composition of river runoff [12,15]. Snow-covered areas near different types of roads, in the yards, and in the background territory are quite different, because the city territory is severely fragmented by the road network and buildings. Therefore, the correct comparison of the supplies of pollutants in snow cover of different territories is only possible using specific parameters (per unit area). Normalizing of supplies by the number of days of snow occurrence shows the accumulation of pollutants per unit area and per time unit, i.e., the daily intensity of deposition (flux) of pollutants from the atmosphere. Since the concentrations of dissolved and suspended forms of MMs are expressed in  $\mu\text{g/L}$ , data on water content in snow cover in  $\text{L/m}^2$  are used to estimate the intensity of pollutants deposition.

The mean, minimum, and maximum values of the dissolved and suspended forms of MMs deposition from the atmosphere near the roads, in the yards of WAO, at the MO MSU, and in the background area are given in Table 4.

High levels of daily deposition in dissolved form are typical for major elements in precipitation, namely Na, Ca, K, and Mg; elements of the upper continental crust, i.e., Al and Fe, as well as Ti, are added to them if we consider the deposition in suspended form. Deposition of dissolved Na, Ca, Sr, Mo, K, W, Sb, V ( $DF > 5$ ) and suspended Ca, W, Co, V, Ti, Sr, Mg, Na, Mo, Zn, Fe, Sb, Al, Cu, As, Sn, Ba ( $DF > 25$ ) in roadside snow cover showed the largest excess above the

background values. The list of priority pollutants is shorter at car parking lots in the yards of residential buildings of the Moscow WAO and the MO MSU. In the yards compared to the background areas, the highest excess of deposition rates are found for dissolved Na, K, and Sr ( $DF > 5$ ) and suspended Ca, Sn, and Mo ( $DF > 10$ ), while dissolved Na, K, Sr, and V and suspended Zn, Mo, Cr, Sr, V, Pb, Cu, Ca, As, Sn, and Sb are characterized by the highest excess of deposition rates at the MO MSU, compared to the background areas. Thus, the snow cover composition and MMs deposition intensity for the MO MSU territory showed intermediate values between yards and roads. This is mainly due to the amount and composition of deposited dust within MO MSU, since the distribution pattern of the dissolved forms is practically similar to the yards.

The total excess of MMs deposition rates over the background level is represented by the integral *TDF* index. For the dissolved MMs phase, the *TDF* value depends on the size of the road: it is maximum for the highways (446), on the MRR it is 264; it decreases to 186 on large roads, to 143 on medium roads and to 116 on small ones (Figure 4).

High *TDF* values are marked for Kutuzovskiy Avenue and Mozhaiskoye highway—648 and 529, respectively (Figure 5). Increased values of the integral index ( $TDF > 250$ ) were also calculated for the MRR, Rublevskoye, and Aminievskoye highways and Minskaya Street (a large road). *TDF* values are approximately the same in the yards and at the MO MSU (82 and 83, respectively). In addition, the changes in *TDF* values are determined by the accumulation of Na: the share of this metal to *TDF* is 67–68% for the MRR and the highways, decreasing to 59% for medium roads due to the less intensive use of DISs, to 51% for small roads, 45% in the yards, and 38% at the MO MSU. However, the contribution of Na is only 38% for large roads, because of the intensive input of dissolved forms of Mo and Sb ( $DF$  40 and 19, respectively). A significant contribution of Ca, Sr, and K is common to all types of roads.

The maximum value of the integral *TDF* index for suspended phase, reaching 4039, is found for the MRR, due to intense deposition of a wide range of MM, among which ( $DF > 100$ , and written in subscript) are  $\text{Ca}_{491}\text{W}_{328}\text{Co}_{281}\text{Ti}_{261}\text{V}_{261}\text{Sr}_{255}\text{Mg}_{246}\text{Na}_{243}\text{Mo}_{173}\text{Al}_{161}\text{Fe}_{153}\text{Zn}_{147}\text{Sb}_{140}\text{Mn}_{113}\text{Ba}_{109}\text{As}_{105}$ .

Similar to suspended MMs, *TDF* values for dissolved MMs decrease with diminishing road size: it is 553 for

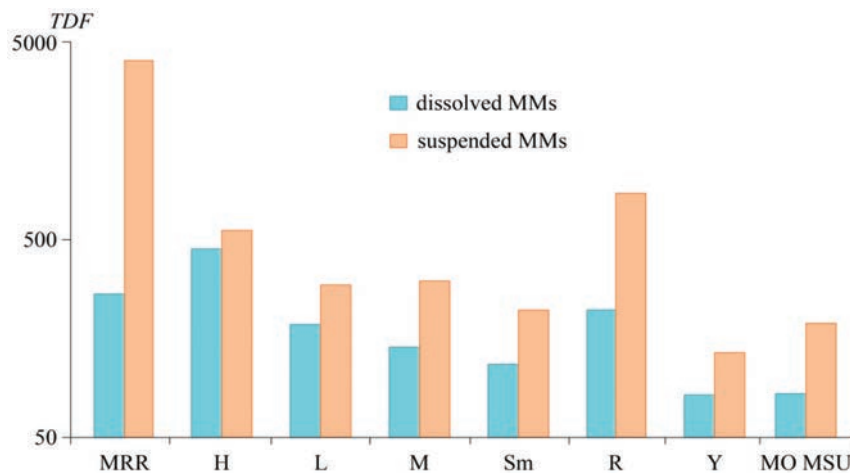
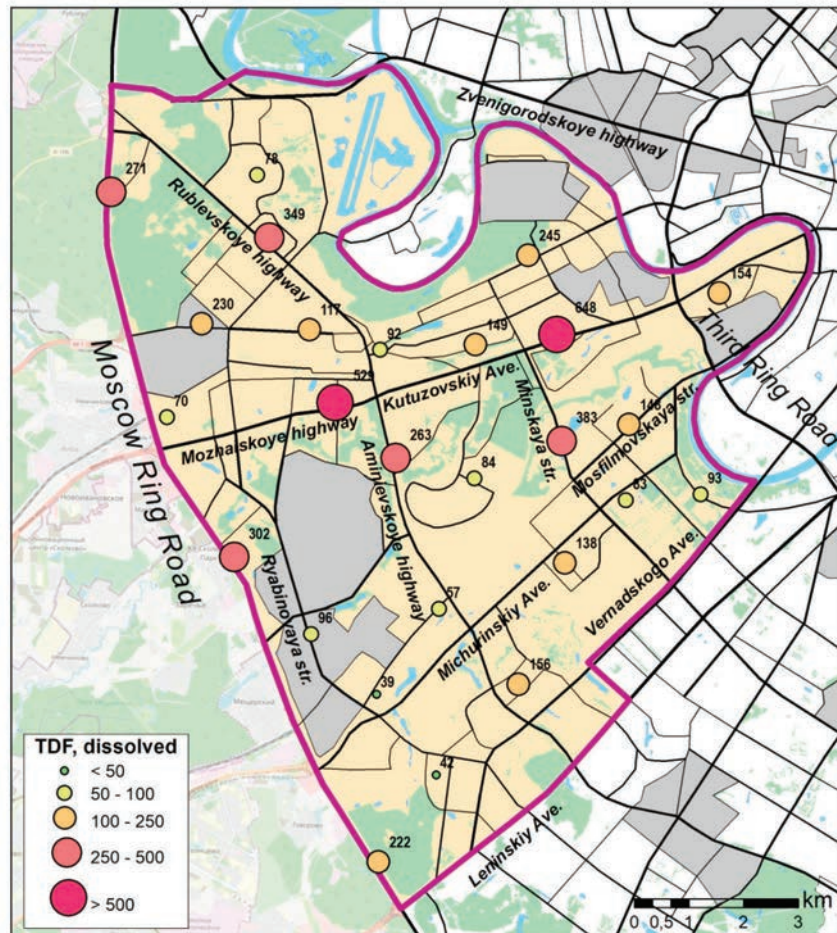


**Figure 4.** Total excess of daily deposition of dissolved and suspended forms of MMs over the background level for different territories: H—highways, L—large roads, M—medium roads, Sm—small roads, R—all roads of the Moscow WAO, Y—car parking lots in the yards of residential buildings.



(a) Dissolved MMs



(b) Suspended MMs

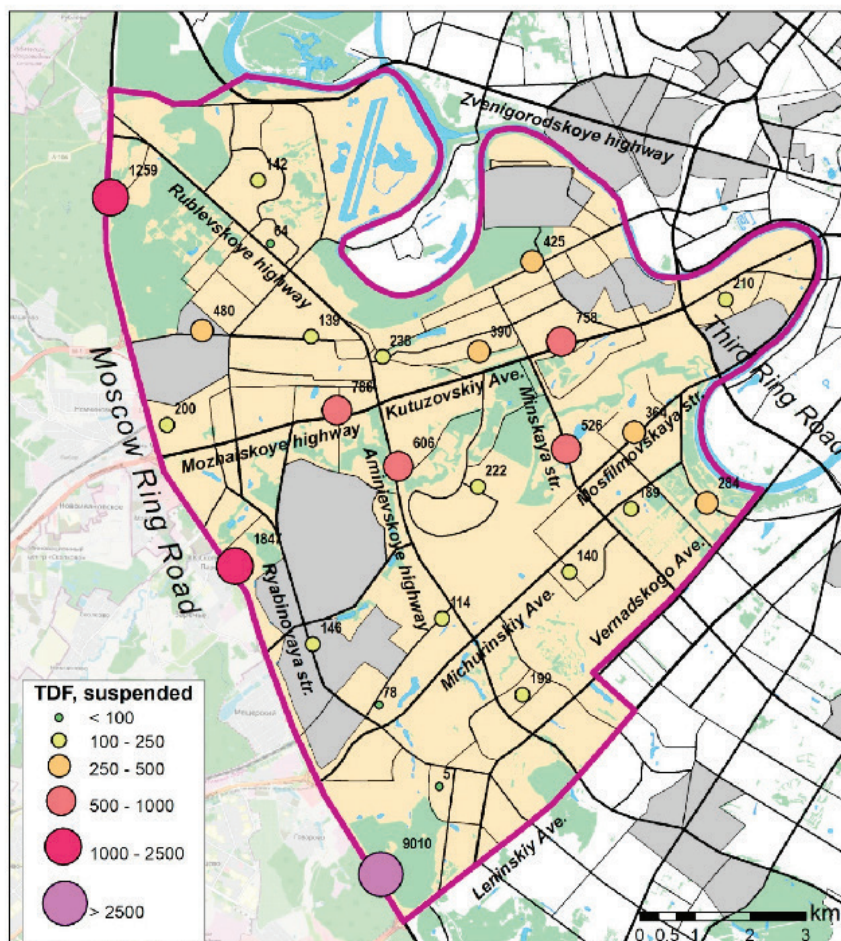


**Figure 5.** Distribution of integral *TDF* index values for dissolved and suspended MMs forms in the western part of Moscow.



the highways, 294 and 308 for large and medium roads, respectively, 220 for small ones and 135 for the yards (Figure 4). The highest *TDF* values at all points studied on the MRR and the increased values ( $TDF > 500$ ) on Kutuzovskiy Avenue, Mozhaiskoye and Aminievskoye highways, and Minskaya Street (Figure 5) evidence that the anomalies of dissolved and suspended MMs depositions generally coincide. Lower *TDF* values of suspended MMs on Rublevskoye highway could be caused by the low content of solid particles in meltwater (12 mg/L compared to 78–102 mg/L in snow cover next to the MRR, 170 mg/L along Kutuzovskiy Avenue and 95 mg/L along Mozhaiskoye highway).

The *TDF* value for suspended MMs within the MO MSU area lies between values for small roads and yards and equals to 189. There is no particular element leading in its contribution to *TDF* in suspended phase compared with dissolved one: the input of Zn averages 10%, those of Ca, V, Cr, Cu, As, Sr, Mo, Sn, Sb, and Pb–6–8%, and 5% or less of other MMs. On the roads, the contribution of

Ca is 7–13%, W–7–10%, Mo and Cu–below 9%, Co and V–below 8%, Sn and Ti–below 7%, Sb, Zn, Sr, Mg, and Na–below 6%, and the rest MMs–5% or less. In the yards, the contribution of Ca is 9%, Mo, Sn, Sb, W, V, Zn, As, Ti, and Sr–6–8%, and the rest MMs–5% or less.

The average *TDF* value for suspended forms is 864; the elements form the following series in terms of DF values:  $Ca_{100}W_{71}Co_{56}V_{54}Ti_{52}Sr_{52}Mg_{49}Na_{48}Mo_{43}Zn_{36}Fe_{34}Sb_{33}Al_{32}Cu_{30}As_{26}Sn_{25}Ba_{25}Mn_{23}Rb_{19}Cr_{17}K_{17}Ni_{16}Cd_{11}Bi_{10}Pb_7$ . This pattern of deposition differs from what we received earlier for the roads of the Eastern Administrative Okrug of Moscow, where the *TDF* value for suspended MMs was 609 with the following excesses of deposition over the background:  $Mo_{380}W_{45}Sb_{31}As_{27}Sn_{18}Fe_{15}Sr_{14}V_{13}Co_{11}Cr_{11}Mn_{10}Ni_9Ti_8Zn_8Cu_7Bi_6Ag_6Cd_5Be_4Pb_3$  [46]. However, the calculation of *TDF* in the Eastern Okrug did not consider major elements that play an important role in snow cover pollution, such as Ca, Mg, Na, K, and Al, as well as Ba and Rb. If these elements are ignored, the *TDF* for the Western Okrug will be 574, which is very close to its value in the eastern industrial part of Moscow.

### 3.5. Indication of sources (Cluster Analysis)

Sources of dissolved and suspended MMs in the snow cover of the western part of Moscow were identified by cluster analysis (Figure 6). Seven MMs associations were distinguished for dissolved forms, i.e., Cl–Na–Sr–Ca ( $r = 0.86–0.99$ ), Mg– $HCO_3^-$  ( $r = 0.50$ ), Mo–Sb– $SO_4^{2-}$  ( $r = 0.45–0.99$ ), K– $NO_3^-$  ( $r = 0.57$ ), Mn–Cd–Cu–Co–Rb ( $r = 0.50–0.95$ ), Ti–Fe–Pb–Al–Sn–Bi–W ( $r = 0.78–0.97$ ), Cr–Ba–Ni ( $r = 0.82–0.87$ ); no associations for V and Zn were found. It is well known that coarse particles in the snow are carried over shorter distances compared to fine particles ( $< 0.45 \mu m$ ), so their composition is more uniform and depends mainly on the adjacent sources. Therefore, fewer associations of suspended forms of MMs are formed compared to dissolved ones (4 vs 7), but they contain greater number of MMs, i.e., Ni–Al–Mg–Ti–Ca–Sr–Mn–Co–W–K–Rb–Ba–Ni–Fe–V ( $r = 0.94–0.99$ ), Cr–Zn ( $r = 0.97$ ), Mo–Sb–Cd–As ( $r = 0.91–0.97$ ), Sn–Bi ( $r = 0.91$ ); no associations for Cu and Pb were identified.

DISs are a most important source of MMs in the snow cover of WAO, which is clearly manifested in the associations of dissolved Cl–Na–Sr–Ca and Mg– $HCO_3^-$ , since Na, Ca, and Mg chlorides, as well as Ca and Mg carbonates are mainly used as DISs in Moscow [75]. Their consumption for single road treatment is 80–200 g/m<sup>2</sup> [116]. Moscow community services apply liquid DISs at temperatures higher than  $-16 \text{ }^\circ\text{C}$ ; at lower temperatures, combined ones are applied, which include marble chips (up to 50–60%), and crystals of calcium chloride and formic acid salts. The solubility of marble is low, but it increases with diminishing size of its chips in the presence of dissolved calcium chloride and pavement particles [70]. Only combined DISs are approved for application in the yards, grounds surrounding residential buildings, sidewalks, and pedestrian streets of Moscow. DISs and the construction dust of carbonate composition could also be a source of Sr, since this metal is often contained in Ca and Mg carbonates [117].

Large amounts of MMs accumulate in snow cover as a result of soil and road dust particles transfer. They are resuspended from the road surface during long snowless periods and from the snow-free areas [4], as well as when

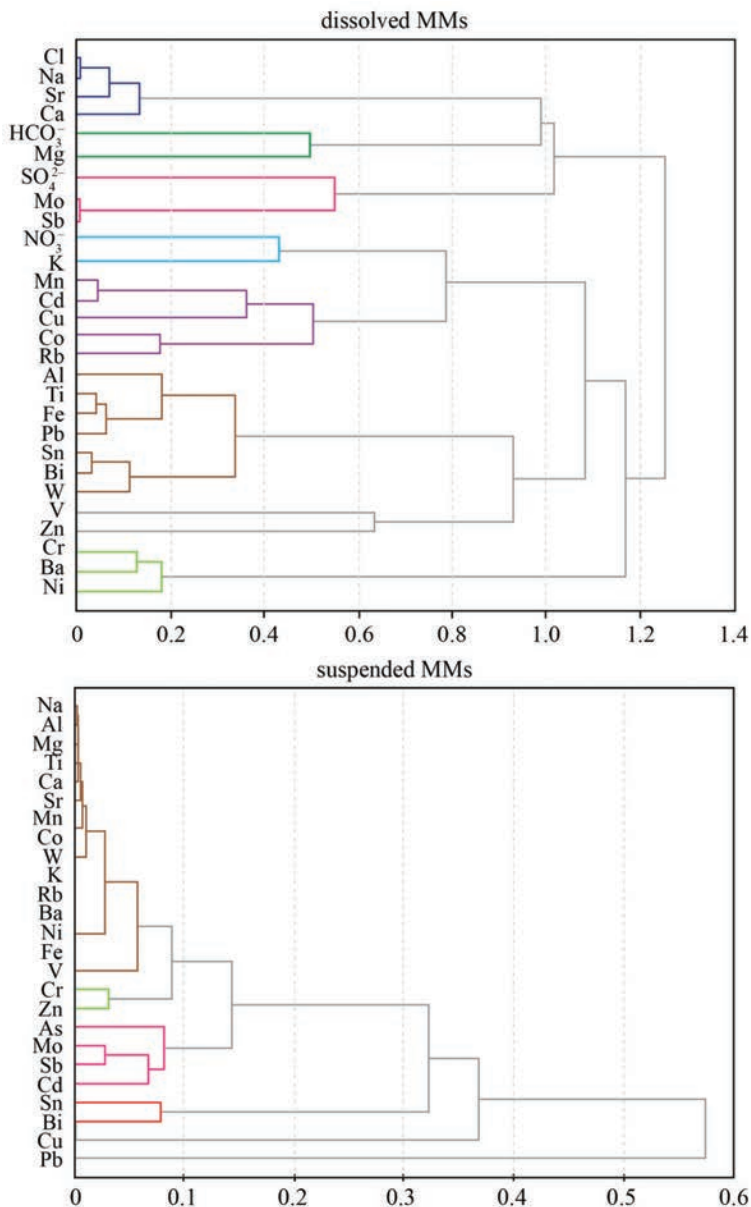


**Figure 6.** Dendrograms of dissolved and suspended MMs in snow cover of the western part of Moscow. Results of cluster analysis (amalgamation rule: Complete Linkage, distance measure:  $d = 1 - \text{Pearson } r$ ).

cars spray particles of contaminated material accumulated on the road surface and consisting of snow, DISs, dirt from the car wheels, and a large mass of soil particles [21]. Input of a large group of MMs as a result of blowing and splashing mud material from the surface of roads is indicated by the formation of associations of suspended Ni–Al–Mg–Ti–Ca–Sr–Mn–Co–W–K–Rb–Ba–Ni–Fe–V and dissolved Ti–Fe–Pb–Al–Sn–Bi–W. Thus, Al, Ti, Fe, Mn, Rb, and K come predominantly with soil particles upon blowing [118–120]; Na, Ca, Mg, and Sr – with construction dust and large DISs particles; W, Sn, Bi, Co, Ni, Ba, Pb, and Ti – with various size fractions of road dust [67,95,119,121–125].

The input of elements into snow cover from roadside areas is difficult to separate from their entry with car emissions, since both road dust and roadside soils are partly polluted with MMs by vehicles emissions. Therefore, wear of brake pads and other metal parts of vehicles leads to the formation of associations of dissolved Cr–Ba–Ni and suspended Cr–Zn, and probably dissolved Mo–Sb–SO<sub>4</sub><sup>2-</sup> together with suspended Sn–Bi and Mo–Sb–Cd–As in roadside snow. The assumption is supported by the results of studies in which Ba, Zn, Sb, Sn, Mo, Bi, Cr, and Ni were proved to be indicator elements for such effects of motor vehicles [91,93,118,120,126–130]. Ba and Sb sulphates used as a friction modifier in the production of brake linings [131], as well as antimony sulfide (III)–Sb<sub>2</sub>S<sub>3</sub>, which is a component of brake lubricant [92] could be sources of sulfate ion in snow cover.

Abrasion of tires and the roadway surface causes the formation of the association of dissolved Mn–Cd–Cu–Co–Rb in roadside snow cover of the Moscow WAO. These MMs are often used as indicators of this type of transport impact [89,93,118,126,127]. In addition, Zn, Cr, Mo, and Sb are indicators of tire abrasion [122,127], while Cu, Cd, and Mn indicate brake pads and linings wearing [89,119,121,122,126]. However, the consideration of brake pads abrasion and tire wear as separate factors is rather questionable because they form a wide range of MMs associations. Therefore, the abrasion of brake pads and tires is sometimes classified as a single “vehicle abrasion” factor [118]. Vehicle exhausts contribute to the formation of dissolved K–NO<sub>3</sub><sup>-</sup> association in roadside snow cover. Most commonly, the input of K is attributed to the combustion of organic residues, biomass, or coal [132–134]. However, there are no significant sources of biomass combustion within the WAO territory, and power plants burn mainly natural gas in winter, so the input of K and NO<sub>3</sub><sup>-</sup> from vehicles seems more likely. Moreover, significant correlations of NO<sub>3</sub><sup>-</sup> with dissolved Cu ( $r = 0.62$ ) and Rb ( $r = 0.42$ ), and of dissolved K with dissolved forms of Rb ( $r = 0.75$ ), Cu ( $r = 0.64$ ), Sr ( $r = 0.52$ ), Co ( $r = 0.52$ ), W ( $r = 0.47$ ), Cl ( $r = 0.41$ ), and Na ( $r = 0.39$ ) are typical of snow cover in WAO. This may indicate additional input of K and NO<sub>3</sub><sup>-</sup> with DISs (in the form of KCl, or as impurities to the DISs of chloride composition), as well as when blowing and splashing road dust and soil particles, sometimes with admixed potassium and nitrogen fertilizers.

The anthropogenic impact of industrial enterprises in the western part of Moscow is less intense than that of vehicles, but this source could contribute to the formation of dissolved Mo–Sb–SO<sub>4</sub><sup>2-</sup> association in snow cover. Despite the fact that Moscow thermal power plants burn mainly natural gas during the heating season, fuel oil is also used there during severe and prolonged frosts as an additional fuel. This contributes to higher SO<sub>2</sub> emissions into the atmospheric air [77] and, probably, increases SO<sub>4</sub><sup>2-</sup> concentrations in snow cover.

Both the dissolved forms of V and Zn, and suspended forms of Cu and Pb could come in different amounts from all the above-discussed sources. Thus, no close associations with other MMs were found for these elements.

#### 4. CONCLUSIONS

The undertaken studies proved the significant impact of motor transport, industrial facilities, and DISs on urban snow cover pollution. The obtained data made it possible to define in detail the snow cover pollution pattern of snow over in the western part of Moscow, which could be used to predict the after-snowmelt fate of MMs in other urban environments.

In the western part of Moscow, anthropogenic impact caused a significant increase of dust load (2–7 times), concentration of solid particles in snow cover (2–5 times), mineralization of snow meltwater (5–18 times), and the change of its ionic composition from calcium bicarbonate to calcium-sodium chloride (as compared with background snow cover).

Suspended forms of Ca, W, Co, V, Sr, Ti, Mg, Na, Mo, Zn, Fe, Sb, and Cu are primary pollutants in the traffic zone of the western part of Moscow; their concentrations in roadside snow cover are more than 25 times in excess over the background. Na, Sr, Ca, K, Mo, Sb, and W dominate among the dissolved forms, with six and more times excess over the background. The location of the anomalies of dissolved and suspended MMs concentrations matches those of the deposition of mentioned MMs forms in snow cover within the WAO. These anomalies are localized near the MRR and many large and medium roads. Na is the most important pollutant; its contribution to total deposition of pollutants increases with growing amount of DISs application – from 38–45% at the MO MSU and in the yards to 51–68% on the roads.

In WAO, the following anthropogenic sources supply different groups of chemical elements that form specific paragenetic associations of MMs in snow cover: DISs (dissolved Cl–Na–Sr–Ca and Mg–HCO<sub>3</sub><sup>-</sup>); resuspension of road dust and blowing of soil particles (suspended Ni–Al–Mg–Ti–Ca–Sr–Mn–Co–W–K–Rb–Ba–Ni–Fe–V and dissolved Ti–Fe–Pb–Al–Sn–Bi–W); wear of metal parts of the cars (suspended Cr–Zn, Mo–Sb–Cd–As and dissolved Cr–Ba–Ni, Mo–Sb–SO<sub>4</sub><sup>2-</sup>); abrasion of tires and roadway surfaces (dissolved Mn–Cd–Cu–Co–Rb); vehicle exhausts (dissolved K–NO<sub>3</sub><sup>-</sup>); and emissions of heat power plants (dissolved Mo–Sb–SO<sub>4</sub><sup>2-</sup>).

## 5. АЭРОЗОЛИ

### Impact of Restrictive Measures during the Covid-19 Pandemic on Aerosol Pollution of the Atmosphere of the Moscow Megalopolis\*

In the second half of the 20th century, a response to economic growth around the world was an increase in the concentration of pollutants in the atmosphere [1] and, as a result, an increase in environmental damage [2]. The contribution of human economic activity to this process, including emissions from vehicles, heat power engineering, and industrial facilities, has already exceeded the contribution of natural sources—fires and dust storms.

*Pollution of the urban atmosphere.* At present, air quality is determined by mass concentrations of the most dangerous gaseous pollutants CO, NO<sub>2</sub>, O<sub>3</sub>, SO<sub>2</sub>, and fine particles less than 10 μm in size (PM<sub>10</sub>)<sup>1</sup>. The chemical composition of PM<sub>10</sub> is determined by anthropogenic and natural sources. Particular attention is paid to the smallest respirable fraction of aerosols less than 2.5 μm in size (PM<sub>2.5</sub>), which are formed in emissions of primary sources (transport, industry, construction, road dust, fires) and those formed in the atmosphere as a result of photochemical reactions of gaseous emissions of SO<sub>2</sub> and NO<sub>2</sub> from thermal power plants and internal combustion engines. High PM<sub>2.5</sub> concentrations cause toxic effects on the human body, exacerbation of asthma, lung cancer, and cardiopulmonary diseases [3, 4]. In this context, the World Health Organization (WHO) and environmental protection agencies in different countries have introduced maximum permissible concentrations for the average annual and daily content of PM<sub>10</sub> and PM<sub>2.5</sub> in the air (Table 1). The most polluted are megalopolises with a PM<sub>2.5</sub> level exceeding 89 μg/m<sup>3</sup>, and the cleanest, with an annual average PM<sub>2.5</sub> value of less than 10 μg/m<sup>3</sup> [5].

Black carbon (BC) is a product of incomplete combustion of fossil fuels in transport engines, thermal power plants, and biomass in the residential sector, as well as the fumes of agricultural and forest fires. It is formed as agglomerates 100–200 nm in size, consisting of nanoparticles with a diameter of 20–50 nm (Fig. 1a). Global anthropogenic black carbon emissions are estimated at about 7.2 Tg (teragrams) per year and amount to ~15% of the mass concentration of PM<sub>2.5</sub>; for the transport sector, this value reaches 50% [6]. The anthropogenic influence of the city is identified by the characteristic daily trend of black carbon, which reflects the variability of the intensity of emissions of combustion products in accordance with the operating mode of enterprises and transport

[7]. In the process of fuel combustion, a unique structure of graphite microcrystallites is formed (Fig. 1b), due to which black carbon remains the only component of aerosols that absorbs solar radiation well and determines the radiation balance of the atmosphere and climate.

Black carbon is the most dangerous and toxic component of PM<sub>2.5</sub> from the point of view of the impact of emissions of combustion products on public health in comparison with other sources. In large cities, the risk of chronic and respiratory diseases increases owing to the high degree of air pollution with black carbon from the exhaust of automobile engines [8]. Emissions of burnt fossil fuel are the most significant environmental threat to children's health worldwide [9]. Due to a number of characteristic properties, black carbon is today considered one of the most important indicators of the impact on human health and the environment [8]. Its mass concentration is accepted by the world environmental protection agencies as a characteristic of continuous monitoring of the degree of aerosol pollution of the atmosphere [10].

Moscow is one of the largest megacities in the world with a high population density and a developed transport, heat and power, and industrial infrastructure that uses natural fuels (gas, diesel, gasoline), which is accompanied by large volumes of aerosol emissions into the atmosphere. The capital has about 630 industrial enterprises registered in various branches of machine building and metalworking, energy, chemistry and petrochemistry, light and food industries, and construction. About 50% of pollutants are emitted by enterprises that produce and redistribute energy, gas, and water. Industrial pro-

**Table 1.** Air quality standards and MPCs (μg/m<sup>3</sup>) adopted by the WHO, the US Environmental Protection Agency (EPA), the European Union (EU), and the Russian Federation

	Period	WHO	EPA	EU	RF*
PM <sub>2.5</sub>	Annual average	10	12	25	25
	Daily	25	35		25
PM <sub>10</sub>	Annual average	20	–	40	40
	Daily	50	150	50	60

\* Hygienic standards GN 2.1.6.3492-17 “Maximum Permissible Concentrations (MPC) of Pollutants in the Air of Urban and Rural Settlements.”

<sup>1</sup> PM stands for particulate matter.



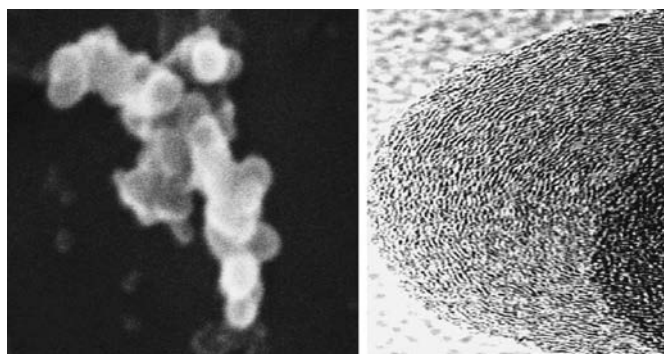


**Fig. 1.** Structure of black carbon microparticles: agglomerates in the emission of (a) a diesel engine of automobile transport [33] and (b) the internal structure of graphite microcrystallites [35].

duction zones occupy about 17% of the city's area; the 14 largest enterprises provide up to 85% of gross pollution from stationary sources [11]. The total volume of industrial emissions is dominated by processing plants and electricity distribution enterprises; gas accounts for 96.7% of fuel consumption. A central heating system operates in Moscow, and biomass is not used for heating, in contrast to large cities in China and Europe [12, 13]. The combustion of biomass is believed to contribute a small share to the pollution of a city's atmosphere.

In 2019, the average annual concentrations of  $PM_{10}$  and transport emissions in the capital amounted to 0.8 MPC (see Table 1) and up to 93% of gross pollution [14]. Analysis of the dynamics of the main pollutants that determined air quality in 2005–2014 showed that Moscow is comparable in this indicator with European cities [15]. However, the Russian Federation has not yet adopted a method for monitoring combustion products in the atmosphere; there are no MPC standards for black carbon. Its mass concentrations are only measured for scientific purposes [16, 17]. In August 2010, during extreme pollution by smoke emissions from fires around the Moscow metropolis, abnormally high concentrations of  $PM_{10}$  and black carbon were recorded, 34 times higher than the MPC according to EU standards (see Table 1) and seven times the MPC level in a normal period [18].

*The state of the environment during the pandemic.* The COVID-19 pandemic, announced by WHO on March 11, 2019, has had a significant impact on public health and economic activity around the world. Many

countries introduced a self-isolation regime and a number of measures limiting economic activity and traffic. It has become clear that the impact of the pandemic is an unprecedented experiment in quantifying the impact of collective responses on the environment, including urban air quality. Analysis of data on global air quality showed a significant decrease in the concentrations of oxides  $NO_2$  and CO, which dominate the emissions of internal combustion engines of road transport, compared to the level of 2019 [19]. European cities recorded a decrease in  $CO_2$  emissions from 8 to 75% (<https://www.icos-cp.eu/event/933>) and  $NO_2$  down to 62% [20]. A decrease in atmospheric concentrations of primary pollutants ( $NO_x$ , CO,  $SO_2$ , volatile organic components) led to a change in the ozone concentrations of secondary organic aerosols, depending on the meteorological conditions of the region [21]. It was assumed that the decline in economic activity would lead to a significant reduction in  $PM_{2.5}$  in the aerosol load of the atmosphere. However, measurements carried out in the largest cities of the world showed different levels of the decrease in the mass concentrations of  $PM_{2.5}$ , from the maximum, by 35% [20], to the absence of any changes [22], owing to the ambiguous dependence of transformation processes occurring in the emissions of primary sources into the atmosphere.

Black carbon, as a direct product of fuel combustion, has become one of the most significant indicators of the impact of changes in transport intensity and industrial production on the environment during the pandemic. According to the observations of 17 European stations, the emission of black carbon in Europe dropped by 11% compared to the same period in previous years [23]. Significant temporal changes in the concentration of black carbon occurred in the countries that introduced the most stringent restrictive measures. In large cities, its average concentration during quarantine dropped by 35–47% compared to the period before the epidemic [24, 25]. The decrease in the concentration of indicators of primary vehicle emissions—the number of fine particles and black carbon, registered on roads of different traffic intensity classes—reached 60–68% and 22–46%, respectively [26]. The highest emission of black carbon was observed in the spring of 2020 in the residential sector of cities due to the intensive combustion of biomass at low air temperatures [23].

In Moscow, the number of reported cases of COVID-19 increased from April to June 2020, but by the end

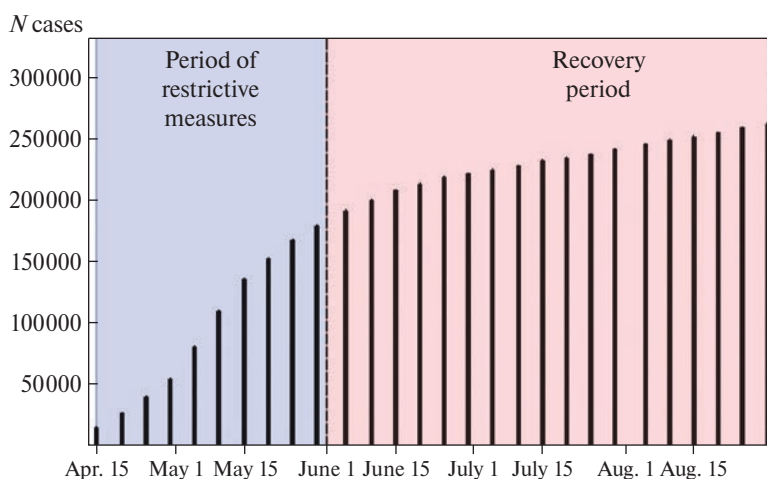


**Fig. 2.** COVID-19 cases recorded in Moscow from April to August 2020.

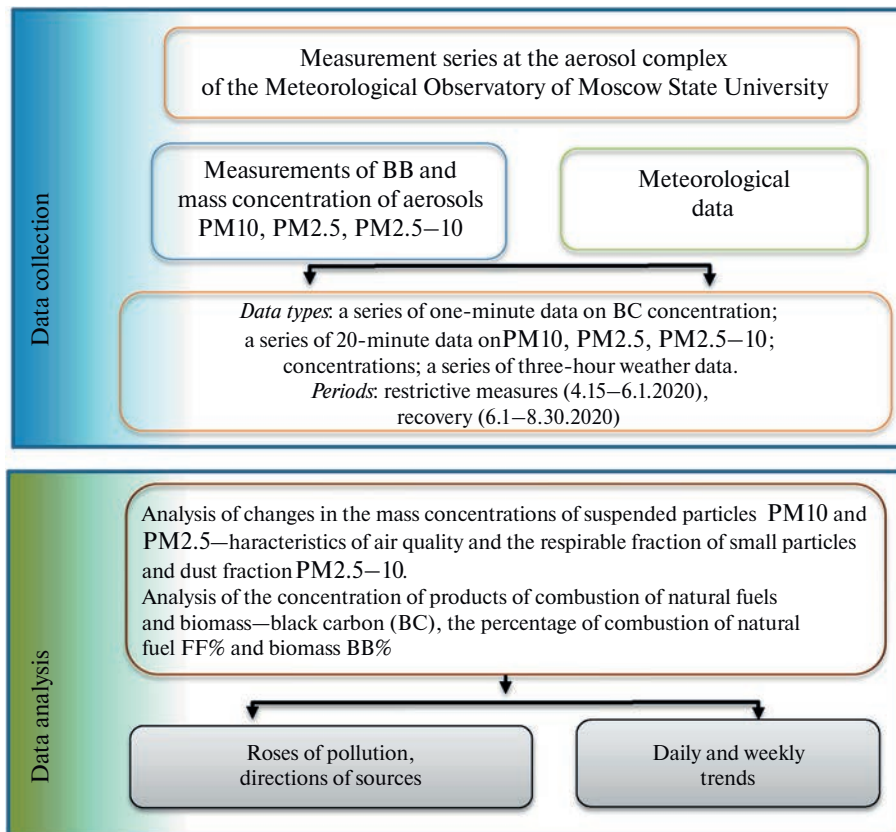


Fig. 3. Collection and analysis of data on aerosol load of the atmosphere during the COVID-19 pandemic.

of summer the situation had stabilized ([https://www.rospotrebnadzor.ru/region/korono\\_virus/epid.php](https://www.rospotrebnadzor.ru/region/korono_virus/epid.php)) (Fig. 2). Restrictive measures during the pandemic influenced the intensity of the economic activity of the metropolis. The quarantine lasted from March 26 to May 12, after which some enterprises received permits to work. On June 1, Moscow began to ease strict restrictions on movement and work of the population. On June 1, the period of restrictive measures ended, and the recovery period began. By June 18, business activity returned to its former course, and by the end of the summer life in the city returned to normal. Estimates of changes in the concentration of the gaseous pollutants CO, NO<sub>2</sub>, NO, and PM<sub>10</sub>, according to Mosecomonitoring data, are recorded in [27], which presents the results of the analysis of aerosol pollution of the atmosphere of the Moscow megalopolis during the COVID-19 pandemic based on measurements of the most important indicators of hazardous impact on the environment and human health—black carbon and the mass concentration of PM<sub>2.5</sub>. The influence of the decline in economic activity and the intensity of the traffic flow during the period of restrictive measures in spring 2020 and the subsequent increase in activity during the recovery period in the summer of 2020 on the change in the mass concentration of black carbon, its daily and weekly trend, and the direction of sources of high concentrations is shown.

*Technique for measurement of aerosol contamination.* The aerosol load in the atmosphere and meteorological parameters were measured in the southwestern part of Moscow, at the Meteorological Observatory of Moscow State University, located far from large enterprises and highways, which means that it can characterize the conditionally background state of the urban environ-

ment. The main stages of data collection and analysis are shown in Fig. 3. The mass concentration of PM<sub>10</sub> was determined using a TSI OPC optical particle counter after calibration with a TEOM 1405 (Thermo Fisher Scientific, United States). The respirable fraction of particles less than 2.5 μm in size (PM<sub>2.5</sub>) and the dust fraction of the largest particles ranging in size from 2.5 to 10 μm (PM<sub>2.5–10</sub>) were estimated. The optical properties of aerosols were measured using an AE33 aethalometer (Magee Scientific, United States) at seven wavelengths in the range from ultraviolet to infrared. The mass concentration of black carbon was determined from the change in the attenuation of radiation at a wavelength of 880 nm. By the difference in spectral absorption of emissions from high-temperature combustion of fossil fuel (FF) in engines and low-temperature biomass burning (BB), depending on the wavelength, the contribution determined by the percentage of FF% and BB% was estimated based on the model [28]. The black carbon concentration data and wind directions as a pollution rose made it possible to identify the location of local sources of maximum BC concentrations. The regional distribution of biomass burning sources (fires) around the Moscow megalopolis was determined by the ratio of the calculated trajectories of air mass transfer for the entire period to the black carbon concentration at the time of their arrival at the observation point [29]. An array of reverse trajectories of air mass transfer with a step of 48 hours back at an altitude of 500 m, obtained on the basis of the HYSPLYT model and archived meteorological data from GDAS, was used for the calculations (<http://www.arl.noaa.gov/ready>).

*Changes in the mass concentration of black carbon during the pandemic.* During the period of restrictive measures, low values of black carbon were observed: on

**Table 2.** Mean and root-mean-square errors of the mass concentration of black carbon (BC), PM<sub>10</sub>, PM<sub>2.5</sub>, and PM<sub>2.5–10</sub>, the share of fossil fuel combustion FF%, biomass BB%, and meteorological parameters during the period of restrictive measures and during the recovery period. Meteorological parameters: temperature (T), wind speed (WS), and precipitation

Characteristic	Period of restrictive measures	Recovery period
BC and PRM		
BC, $\mu\text{g}/\text{m}^3$	$0.9 \pm 0.7$	$1.6 \pm 1.4$
PM <sub>2.5</sub> , $\mu\text{g}/\text{m}^3$	$3.5 \pm 2.7$	$5.1 \pm 3.0$
PM <sub>2.5–10</sub> , $\mu\text{g}/\text{m}^3$	$12.4 \pm 8.1$	$11.2 \pm 7.0$
PM <sub>10</sub> , $\mu\text{g}/\text{m}^3$	$16 \pm 10$	$16.3 \pm 9.3$
Fraction of fuel and biomass burned		
FF%	$79.5 \pm 9.9$	$86.8 \pm 3.8$
BB%	$20.5 \pm 9.9$	$13.2 \pm 3.8$
Meteorological parameters		
T, deg	$8.3 \pm 4.6$	$18.5 \pm 3.5$
WS, m/s	$2.0 \pm 0.8$	$1.7 \pm 0.6$
Precipitation, mm	$4.3 \pm 7.0$	$3.9 \pm 8$

average  $0.95 \pm 0.7 \mu\text{g}/\text{m}^3$  (Table 2), the minimum was  $\sim 48 \text{ ng}/\text{m}^3$ . During the recovery period, its concentration increased significantly and amounted to  $1.6 \pm 1.4 \mu\text{g}/\text{m}^3$ , the maximum values reaching  $\sim 13.6 \mu\text{g}/\text{m}^3$ . Changes in the mean concentrations during these intervals are shown in Fig. 4. During the transition from one period to the other, there was a significant increase in the mean concentration of black carbon, which was 75% due to the resumption of transport and economic activity in Moscow. During the restrictive measures after May 12, when a number of enterprises received work permits, the average concentration of black carbon increased by 22%.

These numbers matched well with TomTom's traffic statistics ([https://www.tomtom.com/en\\_gb/traffic-index/moscow-traffic](https://www.tomtom.com/en_gb/traffic-index/moscow-traffic)). In Moscow, during the period of restrictions (April 15–June 1, 2020), the average daily level of road congestion ranged from 2 to 20%, and during the period of economic recovery (June 1–August 31, 2020), it increased on weekdays to 36–72% and on weekends to 40–45%.

During the transition from the period of restrictive measures to the recovery period, the percentage of fossil fuel combustion (FF%) increased from 79 to 87% (see Fig. 4), which indicated an increase in its consumption with the restoration of traffic intensity and the work of the energy and industrial sectors. The black carbon component from biomass combustion is not directly related to economic activity. It shows the opposite trend: a high percentage of biomass burning ( $\sim 20\%$ ) was observed precisely during the period of restrictive measures (see Fig. 4). Since biomass is not used in the Moscow heating system, the sources of its combustion should be sought in emissions from incineration plants and among emissions from waste and wood burning in the residential sector of Moscow oblast. During the most stringent self-isolation, a significant part of Muscovites were forced to move out of town and live in dachas in Moscow oblast, where biomass is widely burned for heating houses and garbage disposal. The period of restrictions included the holidays of May 1 and 9, during which a particularly high proportion of the population lived outside the city.

Since the COVID-19 epidemic coincided with the spring season of agricultural activity around Moscow, plumes of smoke from fires may have contributed to the aerosol composition of the urban environment, as was established in the spring of 2017 [30]. During the period of restoration of economic activity of the population from June 1, there was a decrease in the fraction of biomass burning on average to 13%; later this value did not change. Apparently, this level corresponds to the pollution of Moscow's urban environment by emissions from biomass burning in the summer season.

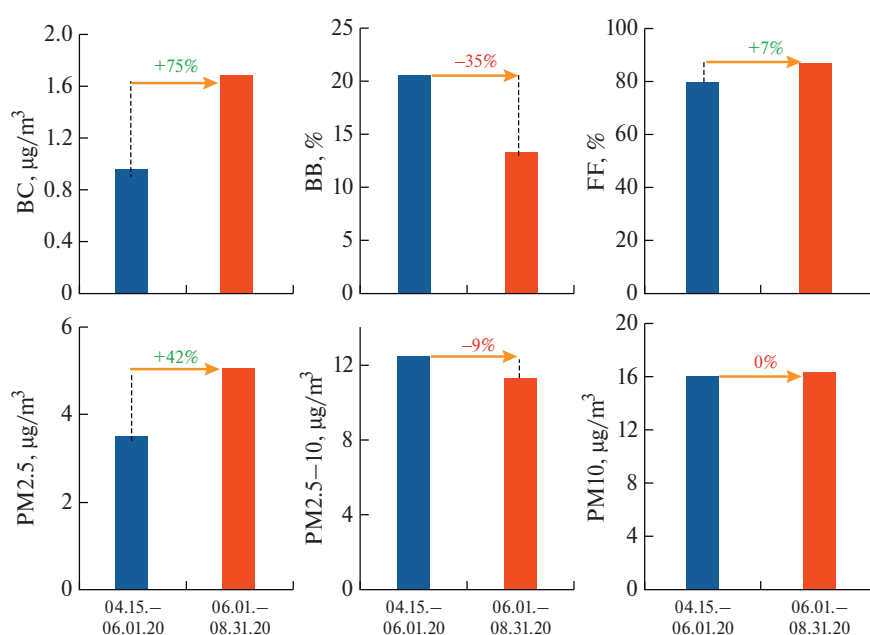


**Fig. 4.** Average mass concentrations of black carbon (BC), the share of combustion of biomass BB% and natural fuel FF%; average mass concentrations of PM<sub>2.5</sub>, PM<sub>2.5–10</sub>, and PM<sub>10</sub> during the period of restrictive measures and during the recovery period. Percentage changes over the recovery period are shown in relation to the period of restrictive measures.



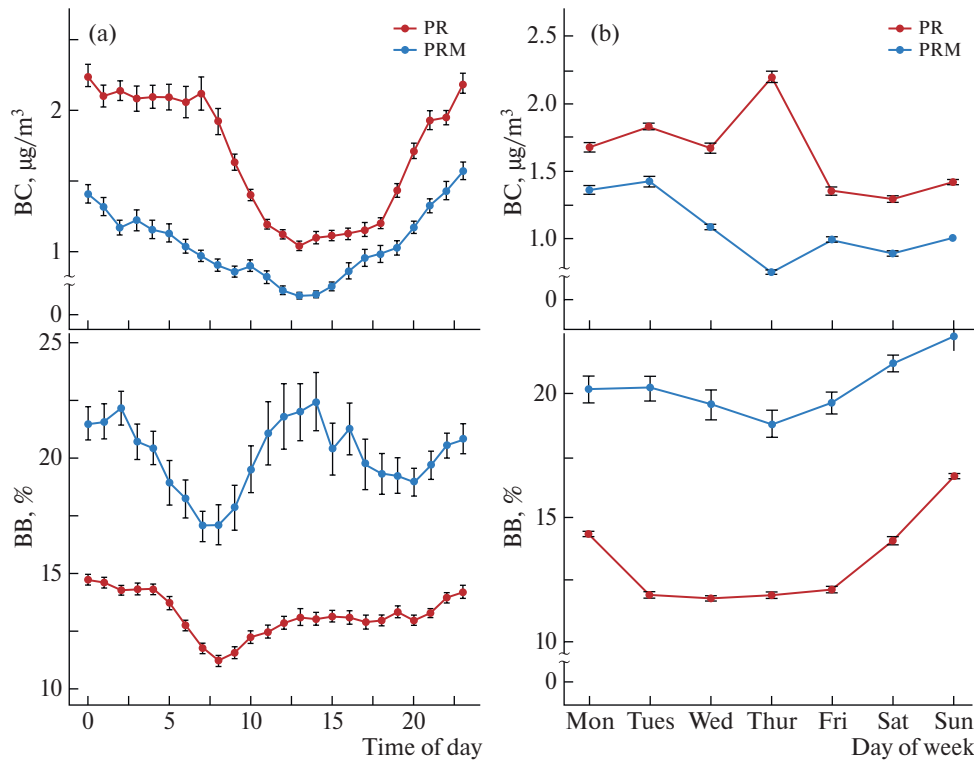


**Fig. 5.** (a) Daily and (b) weekly variations in the mass concentration of black carbon (BC) and the fraction of combustion of biomass BB% during the period of restrictive measures (PRM) and during the period of recovery (PR).

*Impact of restrictive measures on the change in the daily and weekly trend of black carbon concentrations.* The daily variation in aerosol concentrations depends on the height of the atmospheric boundary layer, which is determined by the processes of heating, mixing, and photochemical activity, as well as the variability of emissions from sources. During the restrictive measures in Moscow, the daily BC variation differed significantly from the recovery period by lower hourly averaged values and flat dynamics with the absence of a morning maximum (Fig. 5). Such a diurnal variation was formed due to the low traffic intensity and moderate economic activity of the city, in contrast to the typical course for large cities in the spring–summer time, when the maximum concentration of black carbon is observed in the morning hours due to the increase in the traffic intensity and the maximum energy load [7, 31]. At night, its level rose to  $1.4 \mu\text{g}/\text{m}^3$ , similar to that measured by employees of the Meteorological Observatory of Moscow State University in the spring of 2017–2018 [30]. Since diesel engine exhaust contains much more black carbon than gasoline-fueled engines, its high level at night is the result of the peculiarities of the regulation of cargo transportation in Moscow, where the entry of heavy vehicles into the city center is limited during the day. A similar diurnal variation with high nighttime concentrations is observed in cities with a regulated flow of cargo transport, which is allowed to travel only at night [32]. During the recovery of economic activity, a significant increase in the black carbon concentrations was observed at any time of the day, as was a change in the shape of the diurnal cycle. The recovery of economic activity has led to a consistently high level of pollution by emissions from fuel combustion products at night and in the morning, which is typical of an urbanized environment.

During the period of restrictive measures, the nature

of the diurnal variation for the fraction of biomass burning was distinguished by a long daily maximum (see Fig. 5), which in spring with an average air temperature of about  $8^\circ$  (see Table 2) corresponded to the economic activity of the population in intensive waste burning and heating country houses. In summer, during the recovery period, the average daily temperature increased to  $18^\circ$ , the percentage of biomass burning fell, and the diurnal variation leveled off.

The weekly variation of the black carbon concentration during the restrictions shows the lowest level in the middle of the week and its increase by the weekend (see Fig. 5), as could be expected in the situation of long non-working days during the period of significant restrictions on the working activity of the urban population. The recovery in economic activity changed the weekly trend of black carbon: its high concentrations shifted to working days, which is typical of the normal life of the city. The flat weekly BC trend during the recovery period is typical of the summer vacations of a significant part of the population, when there is practically no difference in emissions from transport and enterprises between working days and weekends.

Changes in the direction of sources of high concentrations of black carbon during the pandemic. The roses of black carbon pollution show that during the restrictive measures its concentration rarely exceeded  $3 \mu\text{g}/\text{m}^3$ ; until May 7, sources of high concentrations—more than  $4 \mu\text{g}/\text{m}^3$ —were located 4 km to the southwest of the Moscow State University Meteorological Observatory—the Ochakovo industrial zone and the largest HPP-25 (Fig. 6). After the central heating was turned off, the direction of the highest recorded concentrations changed to the northwest—from the side of the Fili industrial zone. During the recovery period, the concentration of black carbon increased to  $5\text{--}6 \mu\text{g}/\text{m}^3$  towards the source in the

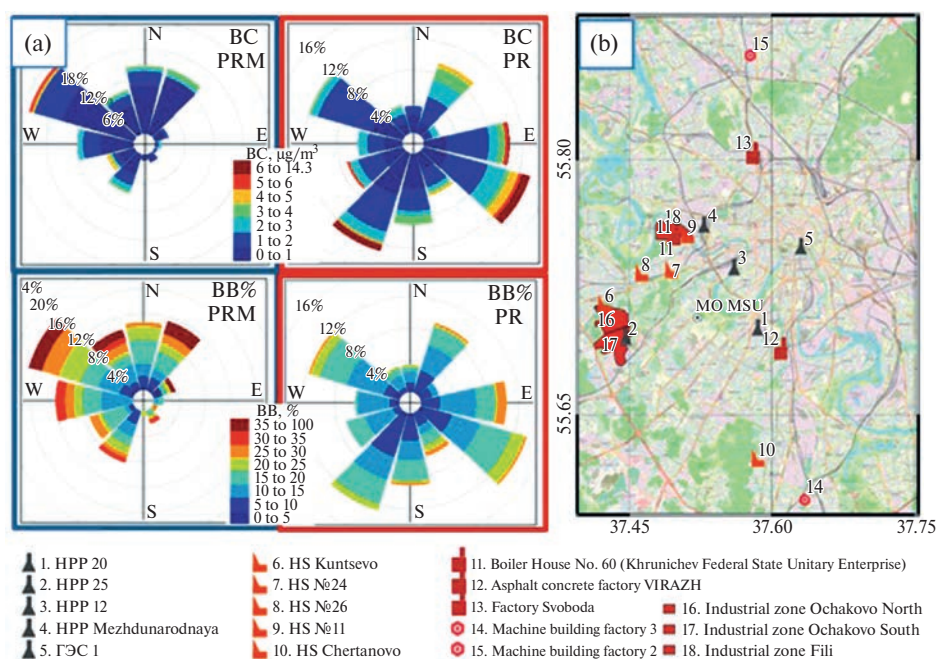


**Fig. 6.** (a) Pollution roses with black carbon (BC) and the share of combustion of biomass BB% during the period of restrictive measures (PRM) and during the period of recovery (PR); (b) the locations of the industrial zones and facilities of the fuel and energy sector (HPPs, heating stations (HSSs), and boiler houses), oil refineries, and waste incineration plants closest to the Moscow Observatory (MO) of Moscow State University (MSU).

southwest from the Ochakovo industrial zone, as well as in the southeast, where the facilities of HPP-20 and ABZ PK Virazh, Moscow's asphalt and concrete company, are located closest to the observatory.

During the period of restrictive measures, the maximum value of the fraction of biomass burning ( $\sim 20\%$ ) was recorded in the directions of the northeasterly and northwesterly winds (see Fig. 6). A potential source could be Moscow's largest waste incineration Special Plant No. 2, located in the industrial zone of the Northwestern Administrative Okrug, which processes up to 160 000 t of waste per year. Other sources associated with the transfer of air masses from Moscow oblast with dense residential development of settlements and summer cottages, where wood is widely used for heating houses and is burned during garbage disposal, could have made a large contribution.

In April–May around Moscow, smoke emissions from agricultural fires make a significant contribution to the aerosol load on the atmosphere [34]. In 2020, during this period, satellite data of anomalous thermal glow showed high fire activity in the Moscow region. Figure 7 shows the regional distribution of biomass burning sources (fires) around Moscow, which determine the BB% during the restrictive measures and in the recovery period. The highest concentrations of smoke emission sources were found in the north of Moscow. During the recovery period, which lasted all summer, the maximum BB% did not exceed 14%; no significant sources of biomass combustion were observed (see Fig. 7). At that time, according to satellite data, forest fires were recorded only south of Moscow.

Changes in the mass PM concentration during the pandemic. Analysis of the daily variation of the mass concentration of  $\text{PM}_{2.5}$ , carried out by the staff of the Meteorological Observatory of Moscow State University from 2011 to 2013, indicates common anthropogenic sources of the most dangerous gaseous atmos-

pheric pollutants and primary aerosols [34]. The values of the mass concentrations of  $\text{PM}_{10}$  were 1.5–2 times higher than those of  $\text{PM}_{2.5}$ , which was determined by a significant contribution to the total mass of the coarse dust fraction and soil particles in the range from 2.5 to 10  $\mu\text{m}$  ( $\text{PM}_{2.5-10}$ ). During the period of strict restrictions until June 1, 2020, the Meteorological Observatory recorded a low value of the mass concentration of  $\text{PM}_{2.5}$ , on average  $3.5 \pm 1.7 \mu\text{g}/\text{m}^3$  (see Table 2), which increased by 43% in the recovery period (see Fig. 4). The growth of air pollution by fine particles with the recovery of economic activity indicated a deterioration in air quality in the megalopolis. The same trend was observed during the recovery of industrial production and the activity of road transport in Moscow after the crisis of 2008–2009 [34]. The fraction of black carbon in  $\text{PM}_{2.5}$  during the restrictions was  $33 \pm 2\%$ ; there was no noticeable change in the ratio of BC to  $\text{PM}_{2.5}$  during the recovery period.

The dynamics of changes in the mass concentration of the larger dust fraction  $\text{PM}_{2.5-10}$  during the pandemic turned out to be opposite to  $\text{PM}_{2.5}$  (see Table 2). Its increase during the restrictions demonstrated the most significant aerosol pollution of the atmosphere for the spring period from the underlying surface after the melting of the snow cover and the beginning of the process of soil dusting. From June 1 to 18, during the maximum precipitation that reached 7.5 mm (see Table 1), the lowest concentration of  $\text{PM}_{2.5-10}$  was observed – on average  $7.8 \pm 4.2 \mu\text{g}/\text{m}^3$  – as a result of the washing out of large particles from the atmosphere with rain.

During the period of strict restrictions until June 1, 2020, the average mass concentration of  $\text{PM}_{10}$  was at the level of  $16 \pm 10 \mu\text{g}/\text{m}^3$ ; no changes were recorded during the recovery period. It can be concluded that the mass concentration of  $\text{PM}_{10}$  is the least identifiable of changes in the economic activity of the city population.

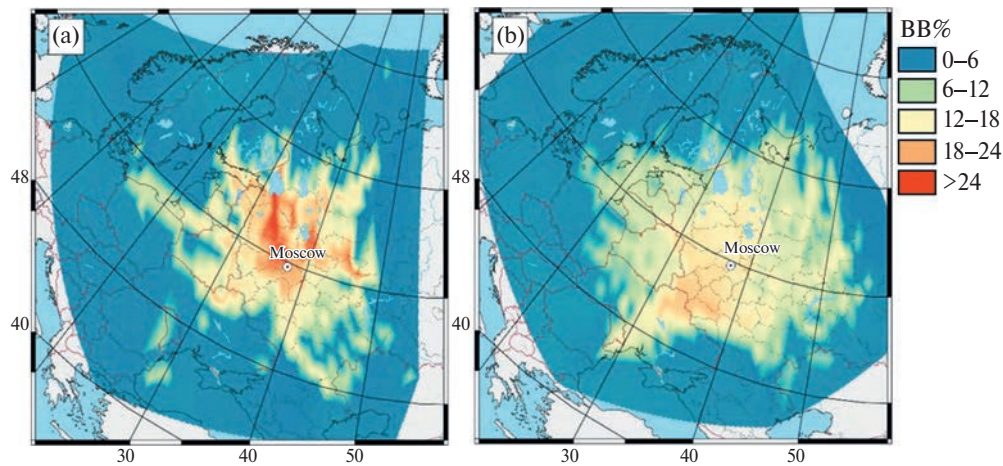


**Fig. 7.** Regional distribution of the share of BB% of biomass combustion (fires) around Moscow during (a) the period of restrictive measures and (b) the recovery period.

\* \* \*

During the COVID-19 pandemic in the spring of 2020, the introduction of strict measures of restrictions and self-isolation led to an improvement in the ecological state of the atmosphere in Moscow compared to the subsequent summer period. Black carbon in the emissions from the combustion of fuels used by transport and city enterprises turned out to be an effective indicator of reducing the aerosol load of the atmosphere and the emission of hazardous toxic substances into the atmosphere. The decrease in the flow of vehicles led to low values of the concentration of black carbon and a flat dynamics of its daily variation due to the reduced energy load in the morning hours. The change in the operating mode of enterprises affected the redistribution of emission intensities from working days to weekends. The

fraction of biomass burning exceeded the summer level of normal life in the region due to increased emissions of waste and wood burning in the residential sector of Moscow oblast and seasonal agricultural fires. During the period of recovery of economic activity in the summer of 2020, the intensity increased and the direction of sources of high concentrations of black carbon from large industrial zones and HPP enterprises changed. The mass concentration of  $PM_{2.5}$  in the respirable aerosol fraction increased significantly, about 30% of which was the most dangerous and toxic component—black carbon. Experimental study of short-term changes in the state of the atmosphere during a rapid extreme fall and subsequent recovery of economic activity makes it possible to understand better the processes taking place in the economy–society–environment system of large cities.



## Seasonal, weekly, and diurnal black carbon in moscow megacity background under impact of urban and regional sources \*

### INTRODUCTION

High population and multi-profile activities in megacities objectively leads to large-scale ecological impact, emphasizing a need to assess the sources of atmosphere pollution. In the complex situation of the plurality of anthropogenic emissions, an important research task remains to identify contributions of major urban sources as well as an impact of the region around. Among anthropogenic aerosol sources, black carbon (BC) is mainly formed by the incomplete combustion of fossil fuels (diesel, gasoline, gas, coal) in emissions of transport, energy production, residential heating, and biomass burning (domestic and wildfires). BC is the light-absorbing component of aerosols, it contributes to atmosphere warming by direct and indirect radiative forcing [1], thus it is accepted as a critical climate forcer. High-weight organic carbon (OC) emitted together with BC is attributed to brown carbon (BrC) due to high light absorption at short wavelengths [2].

BC is mainly present in aerosols of urban environment [3,4,5], thus it concerns air quality and population health [6]. Freshly emitted BC particles are aggregated by hundreds of monomers with fractal structure [7,8] and later tend to be mixed with other atmospheric components such as organics, dust, and sulfates [9]. The toxicity of diesel-emitted particles affects the respiratory system and exacerbates cardiovascular and allergic diseases [10]. Epidemiological evidence links the exposure to BC with cardiopulmonary hospital admissions and mortality [11]. Diesel exhaust, which comprises high amounts of BC, is classified as a carcinogen for humans by the International Agency for Research on Cancer (IARC).

BC is found particularly high in most urbanized Asian cities where the rapid industrial and economic development has been accompanied by serious fine particle pollution of the atmosphere [4,12,13]. Seasonal variations are found less pronounced in urban locations in Europe [4]. The diurnal pattern of an atmospheric constituent such as BC aerosol (which is not produced by photochemical oxidation) is tied closely to the source strengths of its emissions and evolution of the atmospheric boundary layer. BC mass concentrations in large cities peak during morning and evening hours when the atmospheric boundary layer is shallow and anthropogenic emissions are high [5,13,14,15]. BC concentrations had a weekly cycle with higher concentrations on weekdays and lower on weekends, this is apparently related to the lower traffic rates on weekends [16]. Between the meteorological variables, such as wind speed, temperature, relative humidity, pressure, and rainfall, wind speed had the highest influence on BC concentrations with an inverse relationship [16,17].

Long-range transport from the surrounding regions has been identified as one of the main factors affecting BC concentrations in the urban environment, also exhibiting strong seasonal dependence [14,17]. The concentration weight trajectory (CWT) analysis is being success-

fully used to determine which province is the most likely source region for aerosols present over a particular urban location [18]. Aged plumes from large-scale wildfires and biomass burning activity affect the aerosol pollution of megacity [19,20,21]. In early spring, high-pollution events are observed due to agriculture grass fires [22].

Herein, a BC source apportionment approach is intensively developed in order to estimate the most significant combustion sources [12,23,24]. In large EC and US cities, fossil fuel combustion emissions from transportations and industry are found to be the major contributing source while the impact of wood burning related to the domestic heating is increasing preferably during the winter period. In Asia cities, solid fuel sources such as coal combustion, domestic biofuels, and biomass burning are found to be predominant during the pollution haze episodes [13,23].

Biomass burning can produce light-absorbing aerosols containing BrC that exhibit much stronger spectral dependence than high-temperature combustion of fossil fuels, such as diesel/gasoline in transport systems [25]. The contribution of fossil fuel and wood burning in the urban environment are quantified through the application of the multi-wavelength absorption analyses [3,5,26].

The European part is the most populated region in Russia, with the developed industrial infrastructure where fossil fuel (gas, diesel, gasoline, coal) is widely used by transport, industry, power plants, and the domestic sector [27]. According to BC emissions from fires in northern Eurasia, on average ~58% of BC was emitted in spring (March, April, May), 31% in summer (June, July, August), and 10% in fall (September, October, November) [28].

The Moscow megacity is one of the densely populated sources of anthropogenic pollutants in the eastern part of Europe. Annual average mass concentrations of particles with a diameter less than 2.5  $\mu\text{m}$  (PM<sub>2.5</sub>) are found at the level of 20–30  $\mu\text{g m}^{-3}$ , which is comparable to large European cities but lower than in Asian megacities [29]. Accordingly, the air quality in Moscow is similar to megacities in Europe and North America [30]. Air mass transportation can seriously impact the particulate loading and composition during the intensive wildfires and peat burning in the regions around the megacity [31,32].

The first step to aerosol source apportionment in Moscow was carried out in spring, based on organic and elemental carbon, ions, and organic marker species [33]. The main factors of traffic, biomass burning, biogenic activity, and secondary aerosol formation were revealed. Advanced source apportionment by means of combined ambient data and statistical analysis differentiated daily aerosol chemistry by low and high absorption Angstrom Exponent (AAE) related to fossil fuel and biomass burning affected spectral features [34].

BC measurements in the Moscow center addressed the level of air pollution substantially lower than in Beijing [35]. BC concentrations measured in spring of 2018

\* Popovicheva O., Chichaeva M., Kovach R., Zhdanova E., Kasimov N. // Atmosphere. 2022; 13(4):563.

DOI: [10.3390/atmos13040563](https://doi.org/10.3390/atmos13040563) CiteScore=3.7, IF=3.1

and 2019 in Moscow urban background was found comparable to the less polluted city in Europe, Helsinki city [36]. A possible relationship of BC and fire events was observed in [37,38]. However, black carbon emissions inventories and their spatial-temporal effects of urbanization are widely developed [27,39,40].

The absence of an official BC emission inventory in a megacity and Russian Federation as a whole prevents the development of scientific assessments for air pollution and its mitigation. A lack of BC observations performed over different time scales, including annual, weekly, and diurnal, still limits the understanding of the temporal variations of BC aerosol concentrations.

Despite an increasing number of BC source apportionment studies in Europe, Asia, and the United States [41], combustion sources assessments in Moscow metropolitan area remain a big issue. Centralized heating systems operate in Moscow from the end of September until the beginning of May, but their impact has not been considered yet. Especially, the impact of biomass burning is under question because any biomass and coal is not used for heating and energy supply in Moscow, other than many European and Asian cities where the domestic sector widely uses these types of fuel in the cold season [42,43,44,45]. Biomass burning is not taken into consideration by environmental agencies as a potential source of Moscow pollution. However, there is a huge residential area in the region around the Moscow megacity, called the Moskovskaya Oblast, where the usage of wood for oven heating and cooking, especially during weekends and holidays, is very common and must be considered. The impact of air mass transportation during the seasonal wildfires in the regions around the megacity should be quantified separately.

This paper is devoted to seasonal data of aerosol light absorption characteristics in the Moscow megacity back-

ground. It aims at filling a gap covering the seasonal, weekly, and daily temporal scales for BC concentration variations, together with the influence of meteorology and air mass transportation. Both daily and weekly cycles, as well as weekend effects, are analyzed. Transport, centralized heating, and power supply in industry are emphasized as the major fossil fuel combustion sources in the urban environment. Source-specific measure of spectral absorption, Angstrom Absorption Exponent (AAE), identifies the biomass burning residential sources in autumn and winter as well as agricultures fires and wildfires impacts in warm seasons. We use the CWT modeling to show the origin of regional sources for observed high BC concentrations.

## 2. MATERIALS AND METHODS

### 2.1. Description of Sampling Site and Campaigns

Moscow megacity is located in the middle of the East European Plain (see map in Figure 1). The Moscow Metropolitan area ( $55^{\circ}45' N$ ;  $37^{\circ}37' E$  at the city center) is the largest as well as the northernmost and coldest megacity in Europe. It covers an area of  $2561 \text{ km}^2$  and has a registered population exceeding 13.8 million. Moderate average air temperatures, low solar UV radiation levels, and good ventilation make the accumulation of primary emitted pollutants and the photochemical formation of secondary pollutants less intensive [46]. The analysis of measured daily mean  $\text{PM}_{10}$  concentrations and calculated ones by chemical transport model showed the influence of atmospheric processes and local sources in Moscow urban background [47,48].

Today, Moscow accounts for 10% of the Russian vehicle fleet, over 4.6 million cars were registered by the end of 2017 [49]. While automobilization is growing in Moscow, intensive implementation of higher ecological

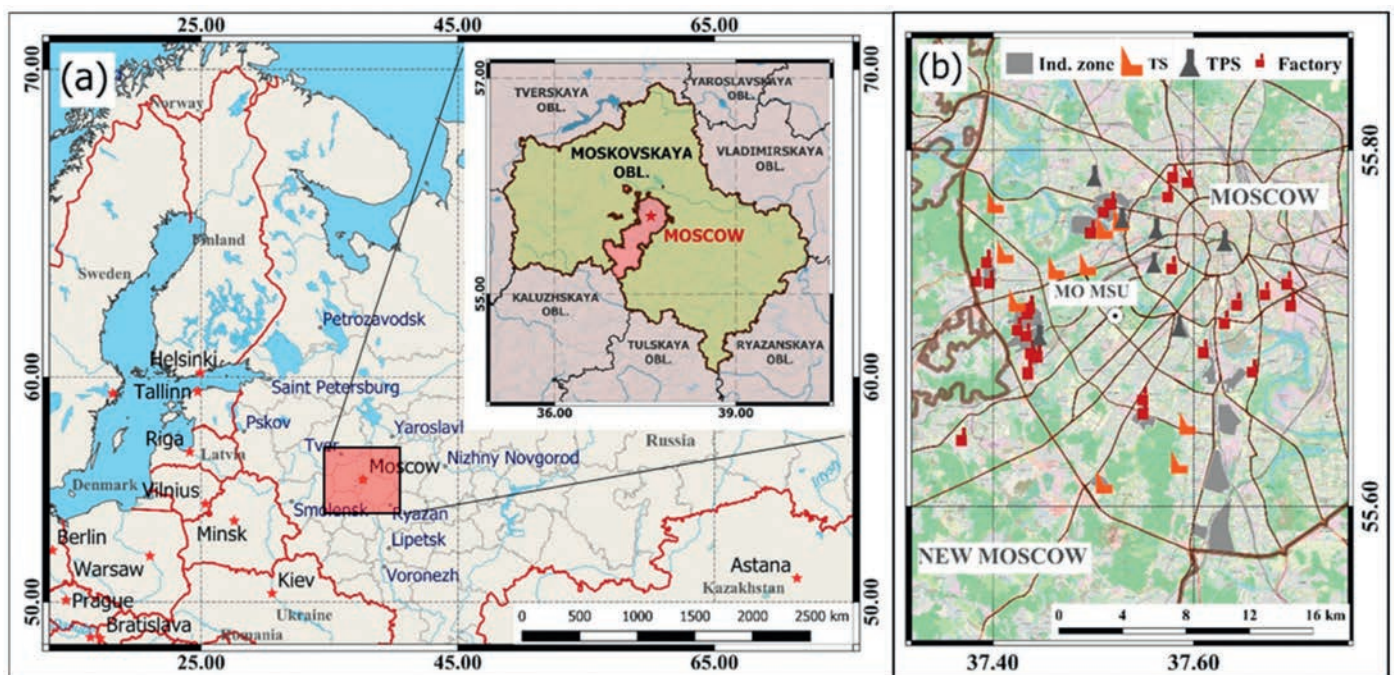


**Figure 1.** (a) Location of Moscow in the European part of Russia. Insert at the right top is a map of Moscow City and Moskovskaya oblast. (b) Southwest sector of Moscow area including New Moscow. Location of sampling site at Meteorological Observatory of Moscow State University (MO MSU) ( $55^{\circ}42' N$ ;  $37^{\circ}31' E$ ) is indicated. Industrial zones (Ind.zone), thermal power stations (TPS), thermal stations (TS) and factories (Factory) are shown.



classes of engines, a declining share of trucks, and better quality of fuel promote the improvement of vehicle ecological parameters. Standards below the Euro-5 have been banned since January 2016. By 2014, up to 50% of motor fuels in Moscow corresponded to class 5. Over the past 7 years, large-scale road construction, development of public transport, and improvement of the structure of vehicle fleet led to a density of emissions does not exceed 500 tons/sq.km/year for 70% of the territory of a city [49]. Nevertheless, presently, the Moscow megacity often faces serious traffic congestion problems because of the vehicle number increasing. Economic losses due to traffic jams are significant, as a car stuck in a traffic congestion emits an average of 30% more pollutants [49].

Gaseous exhaust from automobile transport composes 93% of total megacity emissions [49]. Of industrial gaseous emissions, 50–65% relate to combined heat and power plants, producing and redistributing energy, gas, and water, 20–30% are emitted by refineries, and 15–20% by manufacturing industries. A remaining 2–3% of industrial gaseous emissions originate from the machinery and equipment industry, incinerators, food production, and construction. Heat and power plants, and the residential sector in a city are almost totally supplied with natural gas (gas composes 96.7% of fuel consumption), distinguishing Moscow from many European and Asian cities. In Moscovskaya Oblast the fraction of heat plant emissions is high, as much as 40% from the total stationary sources while the using of coal is significantly decreasing, different from Asian part of Russia [50].

The characteristic feature of Moscow is the high air pollution level in its northwest and northeast sectors where the main industrial and transportation sources are concentrated [30]. The Moscow center is cleaner despite heavy traffic because the absence of industrial enterprises. The lowest pollutant concentrations are observed in the southwestern sector which address the urban background.

In spring and summer, fires are usually observed in the European part of Russia and in the Moscow Oblast; they impact the aerosol properties as well [51]. The agriculture practice of the last year grass removing on fields is widespread in the spring season.

BB including waste burning is pronounced in residential areas around a city, especially during May holidays from 1 to 10 May, as recorded in 2017 and 2018–2019, in [33,36], respectively.

Measurement campaigns of this study are conducted at the Aerosol Complex located at the territory of the Meteorological Observatory of Moscow State University (MO MSU), southwest of Moscow city (Figure 1). MO MSU takes place at about 800 m south of a residential area and a highway. Industrial areas are situated at a distance of 3 km and greater from MO MSU. This enables the revealing the trends of aerosol composition as parameters of background urban pollution [47].

Real-time BC measurements were carried out at the MO MSU site with time resolution 1 min. Aerosol equivalent BC (eBC) concentrations were measured using custom made portable aethalometer. This instrument was purposely designed for mobile measurement campaigns and was successfully used at different platforms and in various regions [36,52,53].

The light attenuation caused by the particles depositing on a quartz fiber was analyzed at three wavelengths (450, 550, and 650 nm). eBC concentrations were determined by converting the time-resolved light attenuation to eBC

mass at 650 nm and characterized by a specific mean mass attenuation coefficient, as described elsewhere [52].

Calibration parameter for quantification eBC mass was derived during parallel long-term measurements against an AE33 aethalometer (Magee Scientific) that operates at the same three wavelengths, for more details see elsewhere [36]. The light attenuation coefficient  $batn$  of the collected aerosol was calculated as

$$batn=A(m^2) \cdot \delta ATN/V(m^3) \quad (1)$$

where  $A$  is the filter exposed area and  $V$  is the volume of air sampled and  $\delta ATN$  is the light attenuation defined as follows:

$$\delta ATN=ln(I_0/I) \quad (2)$$

where  $I_0$  and  $I$  is the light intensity transmitted through unexposed and exposed parts of the filter, respectively. A wavelength of 660 nm was used further to represent eBC concentration. A good linear correlation between the aethalometer's attenuation coefficient  $batn$  and the EBC concentrations calculated with the AE33 aethalometer (at 660 nm) was achieved ( $R^2=0.92$ ). This allowed estimation of EBC mass concentrations using the regression slope and intercept between  $batn$  at 650 nm and EBC of the AE33 aethalometer at 660 nm:

$$EBC(ng/m^3)=3.3 \times 10^5 \cdot A(m^2) \cdot \frac{\delta ATN}{V(m^3)} \quad (3)$$

where  $3.3 \times 10^5$  is the correction factor that includes the specific mass absorption coefficient for the MSU aethalometer calibrated against the AE33 aethalometer assuming the Mass Absorption Cross section (MAC) adopted by AE33 equal to  $9.89 \text{ m}^2 \text{ g}^{-1}$ . The uncertainty of EBC measurements from both aethalometers depends on the accuracy of the MAC value used for the conversion of the light absorption coefficient to mass concentration. The constant MAC value adopted here is an approximation, assuming a uniform state of mixing for BC in atmospheric aerosol. Absolute uncertainties of the reported MAC values remain as high as 30–70% due to the lack of appropriate reference methods.

Aethalometer filters were changed manually at the latest when ATN values approached 70 but at most times filters were changed at lower values. During rough and wet weather conditions, water droplets affected the measurements adding higher noise to the recorded ATN signal and big uncertainties. These short data periods were either excluded from the dataset or, where possible, treated manually by establishing an adjusted baseline for the reference ATN values. BC is commonly used as a term for black carbon, further we will use it instead eBC.

Particles with diameter less than  $10 \mu\text{m}$  ( $\text{PM}_{10}$ ) were collected on 47 mm quartz fiber filters in 24 h intervals from 5 p.m. of a given day to 5 p.m. next day. Air was sampled at the flow of  $16 \text{ l/min}$ ; the pumped volume was reported at standard atmosphere conditions. Measurements of meteorological parameters (temperature, relative humidity, pressure, precipitation, wind speed and wind direction) were performed each 3 h by MO MSU meteorological service.

Sampling campaigns were performed from the end of April 2019 until January 2020. The measurement time is divided on five periods with following designations: spring time from 30 April 2019 to 7 May 2019 (SPRING 1), spring time from 7 May 2019 to 31 May 2019



(SPRING 2), summer time from 1 June 2019 to 1 August 2019 (SUMMER), autumn time from 23 September 2019 to 30 November 2019 (AUTUMN), and winter time from 1 December 2019 to 19 January 2020 (WINTER). Central heating season ended on 7 May 2019 (when during 5 days temperature was higher 8 °C) and started again on 23 September 2019 (when during 5 days temperature was less 8 °C). Therefore, the separation of springtime into two periods relates to the ending of the heating system operation at the end of SPRING 1 period.

In order to compare the BC variabilities in spring 2019 using the pollution rose analyses with ones in spring of 2017 and 2018 [36], we combine SPRING1 and SPRING2 into one SPRING period. Because samples had not been collected for AAE measurements during spring of 2019 (due to technical reasons) we present here AAE data obtained for spring of 2018 (SPRING 2018) in order to complete the seasonal analyses for light absorption properties as well.

## 2.2. Meteorological Observations

Meteorological parameters (air temperature, water vapor pressure, precipitation, and wind speed) for separated seasonal periods of 2019 as well as for SPRING 2018 are presented in Table S1. Winter and autumn periods with averaged air temperature 0.4 °C and 5.4 °C, respectively, relate to cold seasons in Moscow. In order to describe meteorological parameters in comparison with previous years we calculated the deviations of their means from climatic ones in the period from 1981 to 2010, based on MO MSU observation data. Such deviations are called as “anomaly”.

The positive anomaly for air temperature during SPRING1 and SPRING2 periods was 1.5 °C and 3.6 °C, respectively. May of 2018 and 2019 were warmer by 3.0 °C and 2.9 °C than climatic mean, respectively. In May 2018, atmospheric pressure was increased due to the activity of the northeastern ridges of the Azores high while in May 2019 atmospheric pressure was low. The maximum air temperature in SPRING2 and SPRING 2018 periods was 29.2 °C on 29 May 2019 and 27.8 °C on 2 May 2018, respectively.

By contrast, during SUMMER the temperature was below than climatic mean by 0.3 °C. July was the coldest summer month. Its negative anomaly of 2.9 °C was associated with the displacement of Atlantic cyclones to the Arctic seas coast and the north of the European part of Russia. At that time the Moscow region was often affected by the northern and northwest air flows in the rear cold parts of cyclones. The maximum air temperature of 31.4 °C was observed in 8 June 2019.

Autumn had its warmest in the last 60 years due to stable anticyclonic weather in October and November, with anomaly air temperature 2.3 °C. Precipitation was below climatic mean in Autumn. In winter, anomaly air temperature approached 6.1 °C. The largest positive anomaly of monthly averaged air temperature was observed as high as 5.9 °C in December, due to the increased cyclonic activity over the North Atlantic area of the Icelandic low pressure. The snow covers in winter 2019–2020 was unstable, it was observed only during 22 days for the period. The average snow depth was 3 cm, the maximum snow depth was only 15 cm on 31 January 2020. Difference from the climatic means in the circulation conditions was in winter when the west wind was prevailed. Negative anomaly in the range 0.4–0.6 m/s was observed for the wind speed.

## 2.3. Methods and Analyses

Off-line examination of light attenuation on quartz filter samples was performed using a multiple-wavelength light transmission instrument (transmissometer), based on the method described in [54]. The intensity of light transmitted through quartz filters was measured at seven wavelengths from the near-ultraviolet to near-infrared spectral region. Five different spots were exposed to evaluate the homogeneity of the filter sample, and we repeated the measurements at least three times. This procedure provided uncertainties of ~10%. Then, the averaged attenuation (ATN) was used for the parametrization of the attenuation (ATN) dependence on the wavelength  $\lambda$  using a power law relationship:

$$\text{ATN} = k\lambda^{-\text{AAE}} \quad (4)$$

where the Absorption Angstrom Exponent (AAE) is a measure of a strength of the spectral variation of aerosol light absorption. AAE is assigned to source-specific optical marker because aerosols produced by motor vehicles and biomass burning can be distinguished by different wavelength ( $\lambda$ ) dependences in the light absorption [32,53,54].

Pollution rose techniques are well known as an informative way for identifications what is the direction that the highest pollutant concentrations associated are. Bivariate polar plot is a useful method for graphic visualization of the joint wind speed direction dependence of aerosol concentrations [55]. This approach allows to trace the source location, preferably at scale ~1–10 km where the wind direction is remaining quasi-constant while back-trajectories provides a limited support thanks to the low spatial resolution of the model employed [54]. For bivariate polar plots construction, the wind data are partitioned into wind speed direction bins, and the mean concentration calculated for each bin. Wind direction intervals at 10 degrees and 30 wind speed intervals in the range 0 to 20 m s<sup>-1</sup> capture the sufficient details of the concentration distribution. Smoothing techniques is chosen for the estimate of the square root-transformed concentrations as a function of the bivariate wind components. Plotting the concentration data in polar coordinates is useful for the purposes of source identification [56].

Traffic data were taken from TomTom maps and traffic data system [https://www.tomtom.com/en\\_gb/traffic-index/moscow-traffic/](https://www.tomtom.com/en_gb/traffic-index/moscow-traffic/), accessed on 20 November 2021. Traffic congestion is provided in % of time what a driver takes for a trip compared with free-flow travel times. TomTom provides hour-by-hour congestion averaged for each day of week.

Backward trajectories (BWT) were generated using NOAA Hybrid Single-Particle Lagrangian Integrated Trajectory (HYSPPLIT) model of the Air Resources Laboratory (ARL) [57] with the coordinate resolution equal to 1° × 1° of latitude and longitude. The potential source areas were investigated using 2 day BWT for air masses arriving each one hour at 250 m height above ground level (A.G.L.). Such height corresponds to the level of the boundary layer in Moscow as taking place at 250–300 m, as evaluated in [30]. Concentration weighted trajectory (CWT) analysis is an effective tool that is combined with BWT data and pollutant concentrations to trace the source origin [18]. For each grid cell, the mean concentration of a pollutant species is calculated as follows:

$$\ln(\overline{C_{ij}}) = \frac{1}{\sum_{k=1}^N \tau_{ijk}} \sum_{k=1}^N \ln(C_k) \quad (5)$$

where  $C_{ij}$  is the average weighted concentration in the grid cell  $(i,j)$ ,  $i$  and  $j$  are grid indices,  $k$  is the index of trajectory,  $N$  is the total number of trajectories used,  $C_k$  is the pollutant concentration measured upon arrival of  $k$  trajectory, and  $\tau_{ijk}$  is the residence time of  $k$  trajectory in a grid cell  $(i,j)$ . A high value of  $C_{ij}$  means that air parcels passing over cell  $(i,j)$  would cause high concentrations at the receptor site.

Fire information was obtained from Resource Management System (FIRMS) operated by the NASA/GSFC Earth Science Data Information System (ESDIS) (<https://firms.modaps.eosdis.nasa.gov/map>, accessed on 1 November 2021). It is based on satellite observations which register the thermal spots (open fires) with temperature above 2000 K. For the best identification of fire location data, this work uses data arrays on the spatial location of fire centers from the Visible Infrared Imaging Radiometer Suite (VIIRS). Daily maps were related to the computed trajectories, providing a clear picture of the geographical location of fires nearby the trajectory pass not more than 500 km, with the several kilometer resolutions.

### 3. RESULTS

#### 3.1. Seasonal, Diurnal, and Weekly BC Concentrations

The time series of eBC concentrations during the seasons of 2019 and winter of 2020 are shown in Figure 2. The variations from 0.2 to 8.8  $\mu\text{g}/\text{m}^3$  are observed for the whole duration of the study. The descriptive statistics for all seasons are presented in Table 1. The seasonal mean

BC concentration for the whole period of study is  $1.7 \pm 1.4 \mu\text{g}/\text{m}^3$ . Maximum mean BC equal to  $2.2 \pm 1.8 \mu\text{g}/\text{m}^3$  is observed in SPRING1, it is higher than in SPRING2,  $1.8 \pm 1.3 \mu\text{g}/\text{m}^3$ , respectively, that can relate to the end of the heating period in Moscow.

BC concentrations in SPRING 2018 [36] are summarized in Table 1 together with data for 2019. Mean of BC concentrations during approximately same periods of spring 2017 is found to be similar,  $1.7 \pm 1.4 \mu\text{g}/\text{m}^3$ , to spring 2019. In spring 2018 the BC mean is smaller,  $1.1 \pm 0.9 \mu\text{g}/\text{m}^3$ , than in spring 2019. For comparison, observations in the Moscow center in spring 2014 and 2016 showed the mean BC concentrations of 4.4 and 1.7  $\mu\text{g}/\text{m}^3$  while at the suburban background station they were consistently less, 3.0 and 1.05  $\mu\text{g}/\text{m}^3$ , respectively [37]. In AUTUMN and WINTER periods, mean BC are lower,  $1.7 \pm 1.1$  and  $1.1 \pm 0.7 \mu\text{g}/\text{m}^3$ , than in SUMMER when mean BC is found  $2.0 \pm 1.8 \mu\text{g}/\text{m}^3$ .

Seasonal BC in different cities of the globe brings out the importance of typical urban sources such as traffic, industry, heating, and residential emissions as well

**Table 1.** Mean, maximum (max), and minimum (min) concentrations of black carbon ( $\mu\text{g}/\text{m}^3$ ) for separated seasonal periods of 2019 and 2020, and SPRING 2018; standard deviations (S.T.D.).

Period	Mean	Max	Min	S.T.D.
SPRING 1 2019	2.2	11.1	0.17	1.8
SPRING 2 2019	1.8	10.7	0.15	1.3
SUMMER 2019	2.0	12.1	0.03	1.8
AUTUMN 2019	1.7	8.1	0.01	1.1
WINTER 2019–2020	1.1	4.2	0.03	0.7
SPRING 2018	1.1	10.0	0.1	0.9

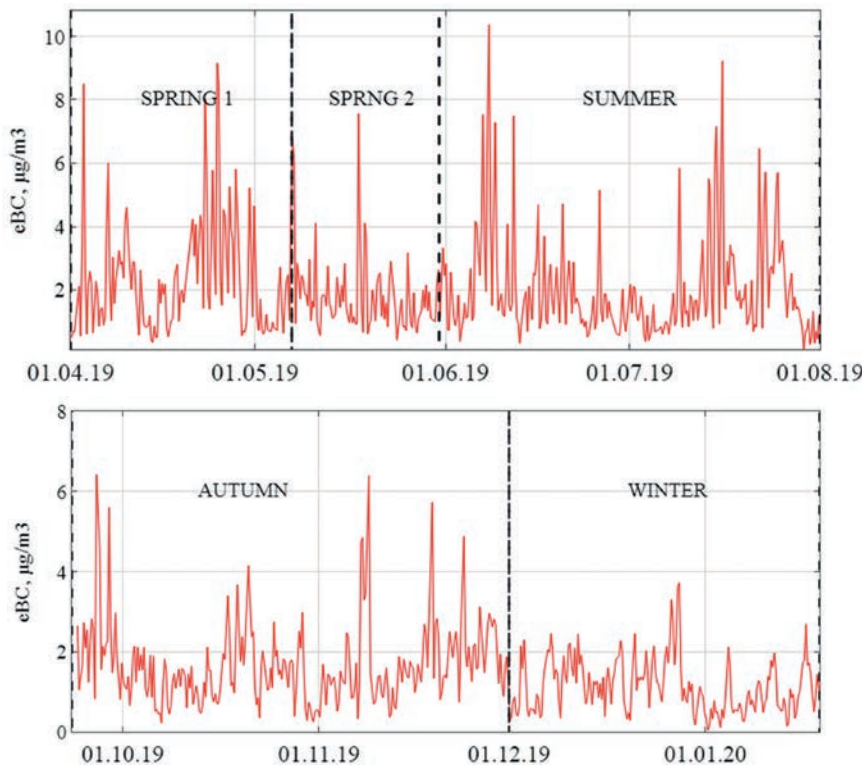


**Figure 2.** Time series of 12 h mean eBC concentrations during SPRING 1, SPRING 2, SUMMER, AUTUMN and WINTER periods of 2019 and 2020 years. Dash lines separates the durations of periods.

as of meteorology and the long-range transport over a particular location. Seasonal variations are found less pronounced in urban locations in Europe than in India and China [4]. In European less polluted cities such as Zurich, Basel, Gent, and Helsinki the seasonal variations in mean BC concentrations are observed from 1 to 2  $\mu\text{g}/\text{m}^3$  [4,16] with maximums in fall and late winter due to the weakened mixing and enhanced emissions related to heating needs. In the Athens megacity, one of the most polluted cities in Europe, BC concentrations are equal to  $2.4 \pm 1.0 \mu\text{g}/\text{m}^3$  and  $1.6 \pm 0.6 \mu\text{g}/\text{m}^3$  during the cold and the warm period, respectively; the contribution from wood burning in residential sector is significantly higher during the cold period [5]. Observation of maxima in seasonal BC concentrations in spring in our study may indicate the particular impact of agriculture fires and long-range transport from surrounding regions (as will be shown later). Wintertime in 2019 and early 2020 was anomaly warm, therefore heating and energetic supplies operated at reduced potential.

The diurnal evolution of aerosols is influenced mainly by the space-time variation in atmospheric boundary layer (ABL) and source strengths of emissions. The ABL exhibits a definitive diurnal structure, its evolution over land is closely coupled with the heating of the surface by the Sun radiation. In urban environment, the atmospheric abundance of BC is affected by both the stability of the ABL and anthropogenic activities [4]. In large cities, the BC morning peak is well observed in diurnal mass concentrations; it is attributed to the combined influence of

the ABL height and vehicle traffic enhancement in the morning [4,13,15]. The minimum BC concentrations is found during midday when there are fewer anthropogenic BC emissions, while the deeper boundary layer leads to a faster dispersion resulting in the pollution dilution. The surface inversion after sunset results in the accumulation of BC, causing even higher concentrations in the late evening.

In our study, the daily trend of BC concentrations differs in SPRING and SUMMER from AUTUMN and WINTER (Figure 3). In SPRING and SUMMER, a noticeable peak in concentrations exists in the morning between 6:00 and 9:00, relating to rush hours of traffic and maximum of the morning loading for heating and energy city supply. There is the daytime decrease to minimal values at approximately 15:00. A gradual growth in the evening to the night is observed after 20:00. We note that similar diurnal trend with a morning peak was observed in spring of 2017 [36]. There is a significant difference between maximum (around 3  $\mu\text{g}/\text{m}^3$ ) in morning times and minimum (around 1  $\mu\text{g}/\text{m}^3$ ) in daytime for diurnal trends in SPRING and SUMMER.

It is worth to consider the daily variations in CO concentrations, the most relevant to automobile emissions in Moscow. Due to the centralized heat supply of both residential and industrial sectors from large heat and power plants (HPP) using natural gas, the main source of CO in Moscow is automobile transport (approximately 85–90% of all emissions) [58]. CO daily variations measured during nine years at 49 stations in the Moscow megacity

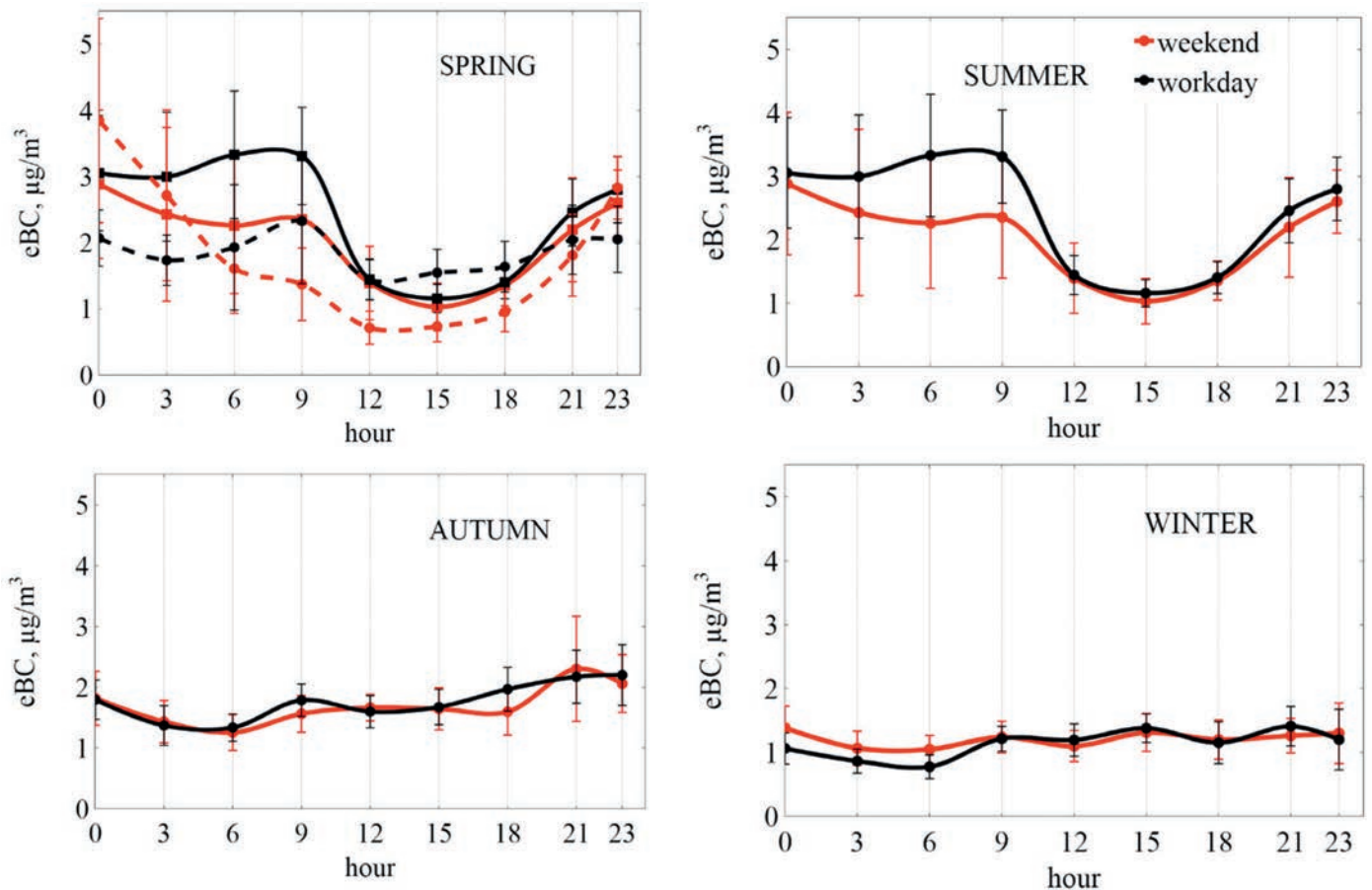


**Figure 3.** Weekday and weekend diurnal variations of hourly black carbon concentrations during SPRING, SUMMER, AUTUMN, and WINTER periods. SPRING is separated on SPRING 1 (line) and SPRING 2 (stroke). Workdays and weekend are marked in black and red. Plotted points are average values for aggregated data from the subsequent three hours during each day of the study, standard deviation is show with error bars.



showed that on weekdays the CO concentrations reach daily maxima from 5:00 to 9:00 [58]. Such an increase is caused not only by heavy traffic but also their accumulations below the surface temperature inversion which is usually begins breaking up at 6:00–7:00 in summer. The similar diurnal trend we found for BC in SUMMER (Figure 3).

In AUTUMN and WINTER, the daily trend of BC concentrations is characterized by a smooth course and insignificant morning peak (Figure 3). The difference between maxima in morning times and minimum in daytime hardly approaches hundreds nanograms per m<sup>3</sup>. We note that in autumn and winter, the time of surface temperature inversion destroying is later, at 08:00–09:00. Such seasonal variation in temperature stratification may be responsible for absence of clear observed significant variation in diurnal trend in cold seasons.

In SPRING on weekends, the diurnal pattern is different considerably from that on weekdays (Figure 3). In SPRING 1 maximum values were measured in the morning. The biggest impact of weekend is observed in SPRING 2 (in the beginning of this period related to May holidays) by the prominent BC peak during morning rush hours in weekdays and almost its absent in weekend. We should note that Friday, Saturday, and Sunday are the most typical days for Moscow inhabitants to go out of the city for a weekend to their country houses and then back to a city. The raised nocturnal concentrations for weekend in SPRING 2 are caused by the numerous private cars travelling almost in evening and night hours. In SUMMER (a period of vacations), the differences between weekdays and weekend are not so prominent. We note that regular travels of inhabitants from Moscow city on weekends are typical for spring–summer seasons and less in autumn–winter. It is more specific and quite different from other European cities, for example, Helsinki, where high road traffic activity towards the suburbs of a city is observed during the whole year leading to the prominent weekend effect [16].

Weekly cycles of air quality are the characteristics of large cities related to the highest amount of pollutants emitted on working days. In SPRING, average BC of

Tuesday, Wednesday and Thursday is much higher while in Friday its significant decrease is observed (Figure 4). Such a trend can be associated with the migration of the population from a city to the Moscovskaya Oblast for weekend. Moreover, SPRING 1, the period of central heating system operation, differs from SPRING2 by the more prominent morning peak that is related to higher emissions due to intensive energetic loading in the morning. The working activity in the middle of the week, in Thursday and Friday, is the most prominent in AUTUMN (Figure 4). In SUMMER and WINTER there is no strong difference between working days, always the minimum of BC relates to the weekend and Monday.

During weekdays, a strong increase of traffic congestion, according Tom Tom system, well relates to a morning peak of BC while its decrease after 10:00 correlates with the BC drop (Figure 5). Correlation between BC and strong increase of traffic congestion is clearly observed after 15:00. High BC nocturnal level occurs mostly due to the shallow ABL resulting in the trapping of pollutants. Difference in population activity in a megacity is well demonstrated by the opposite correlation between traffic congestion and BC during weekend (Figure 5). Maximum transport activity happens at the middle of a day, contrary to a minimum of BC.

### 3.2. Relationships between BC and Meteorological Parameters

Wind roses for separated seasons of 2019 are shown in Figure S1. SPRING 1 is different from SPRING 2 by the eastern direction of prevailing winds. In SUMMER, the high frequency of northwestern (NW) winds are observed. AUTUMN and WINTER are similar by prevailing southwestern (SW) and western (W) winds.

The pollution roses show the variations of prevailed wind directions and BC concentrations from season to season (Figure 6). SPRING period is characterized by the most frequent NE and E wind directions with a repeatability frequency up to 18% and the highest BC concentrations from 6 to 12  $\mu\text{g}/\text{m}^3$ . During SUMMER, the maximum BC was observed from all wind directions

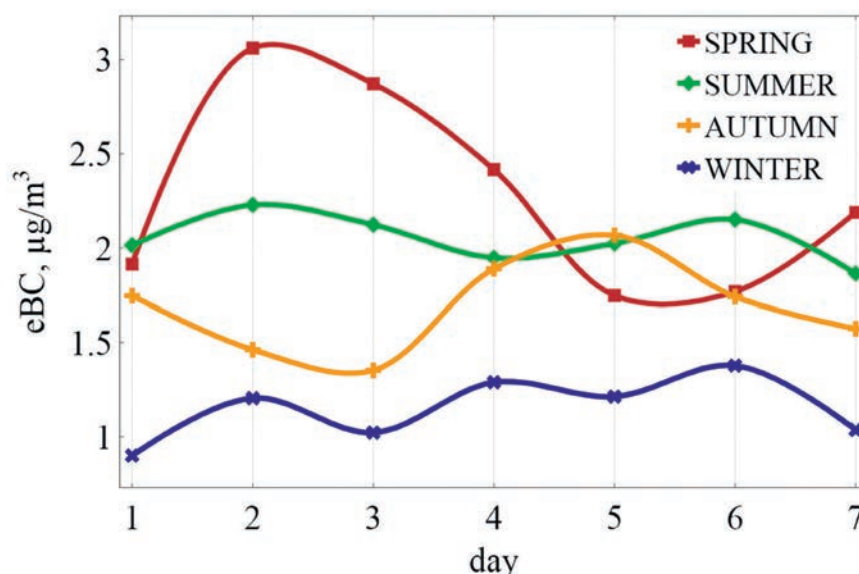


**Figure 4.** Weekly trends of black carbon concentration during SPRING, SUMMER, AUTUMN, and WINTER periods.

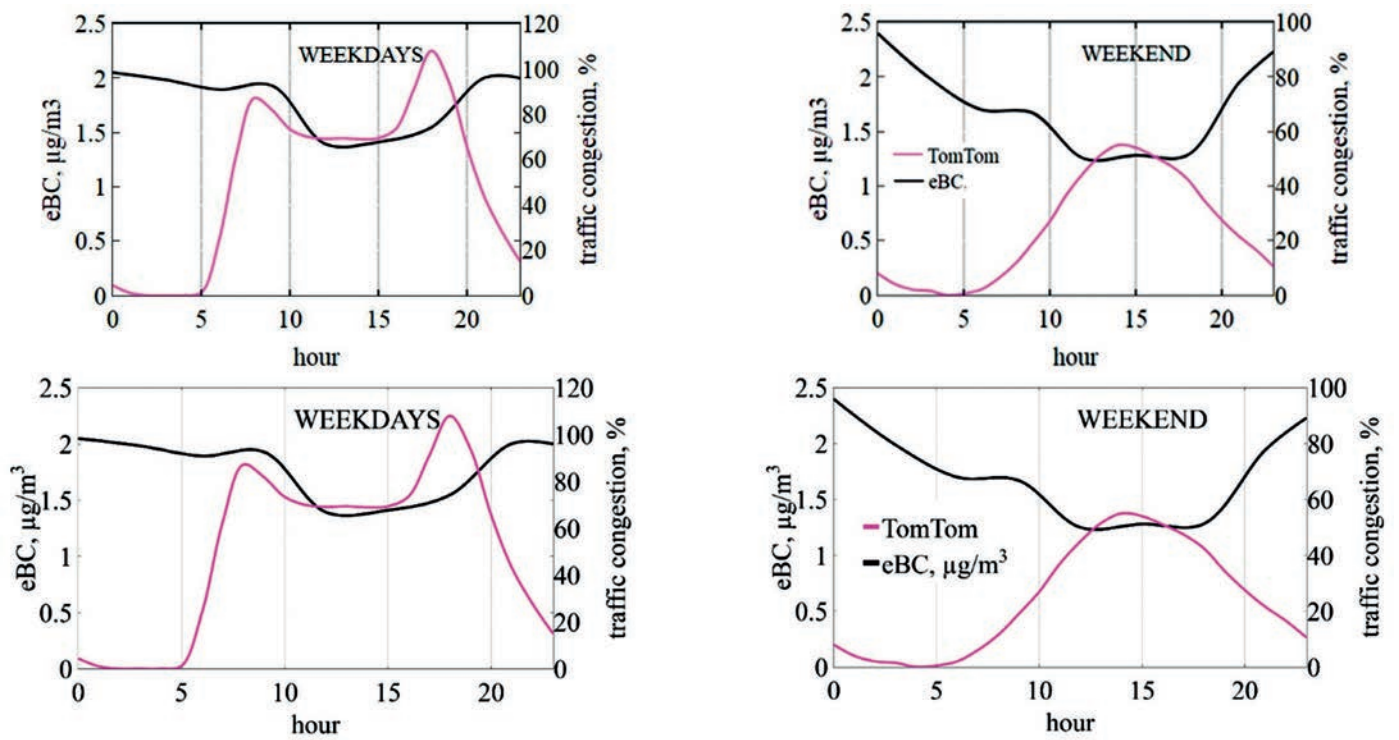


Figure 5. Diurnal variations of hourly black carbon concentrations and Tom Tom traffic congestion during the whole period of study for weekdays (left) and weekend (right).

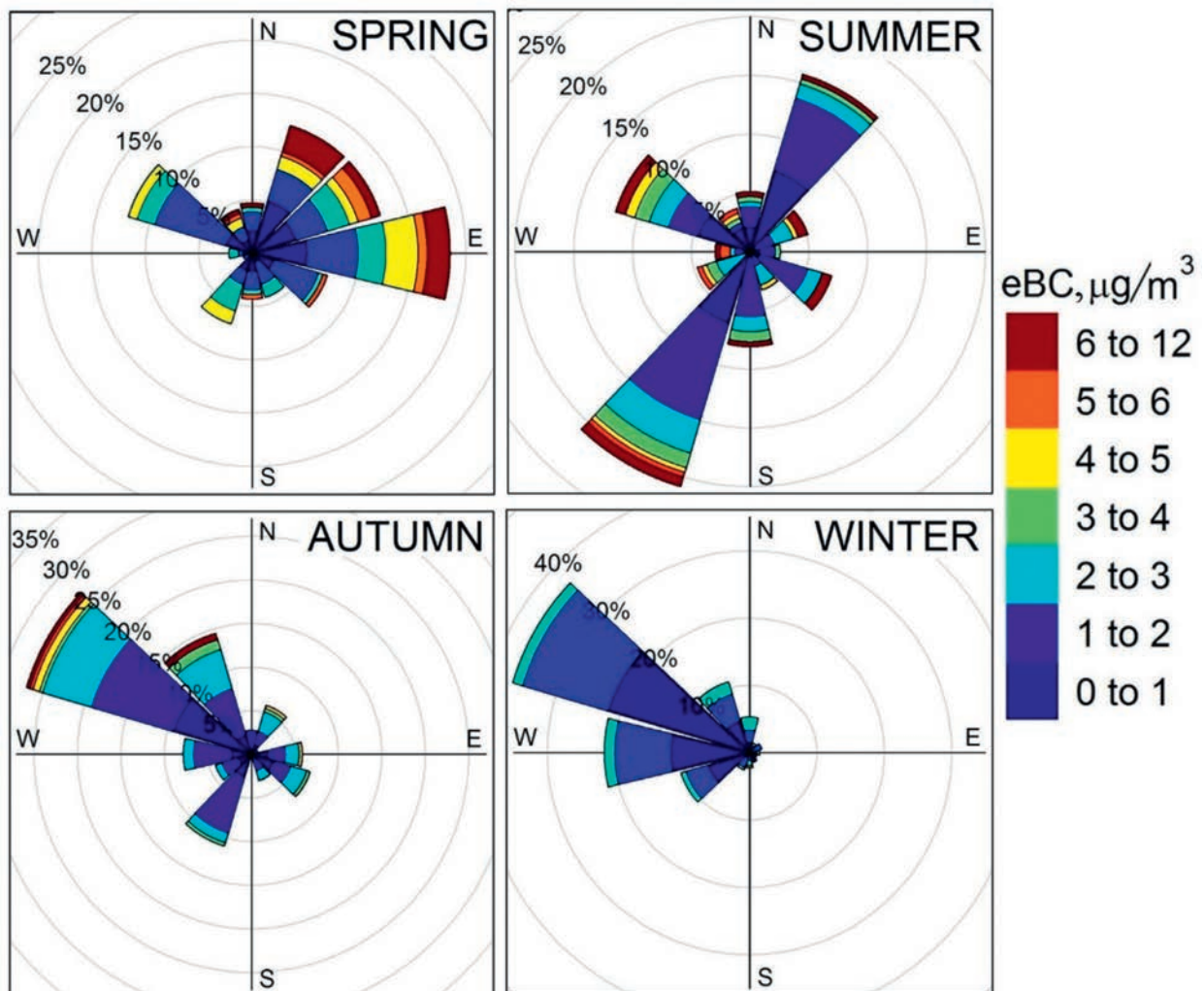


Figure 6. Black carbon pollution roses during SPRING, SUMMER, AUTUMN, and WINTER periods.



with the highest frequency from the southwest. This finding confirms the observations of the SW prevailing wind direction in the air layer from 40 to 500 m at the MO MSU [59]. Pollution roses in AUTUMN and WINTER are similar with respect to the direction of the highest pollution concentrations. In WINTER, the NW direction with a repeatability frequency up to 35% occurs, the SW direction is observed more rarely while the maximum of BC approaches only  $3 \mu\text{g}/\text{m}^3$ .

Relationships among the source contribution, wind direction and speed are commonly derived from polar plots [60]. Figure 7 represents bivariate plots of BC concentrations in polar coordinates of wind speed and direction at the MO MSU, they indicate the origin of the main BC emission sources. Map in Figure 1 highlights the southwestern sector of Moscow city where the sampling site takes place. Industrial zones, thermal power stations (TPS), thermal stations (TS), and factories (of mechanical engineering, metallurgical, food production, reinforced concrete, chemical, and pharmaceutical) are shown, those ones which are located in the area around 10 km from the MO MSU. In WSW and N directions from the MO MSU the biggest industrial zones "Ochakovo" and "Fili" are located, respectively.

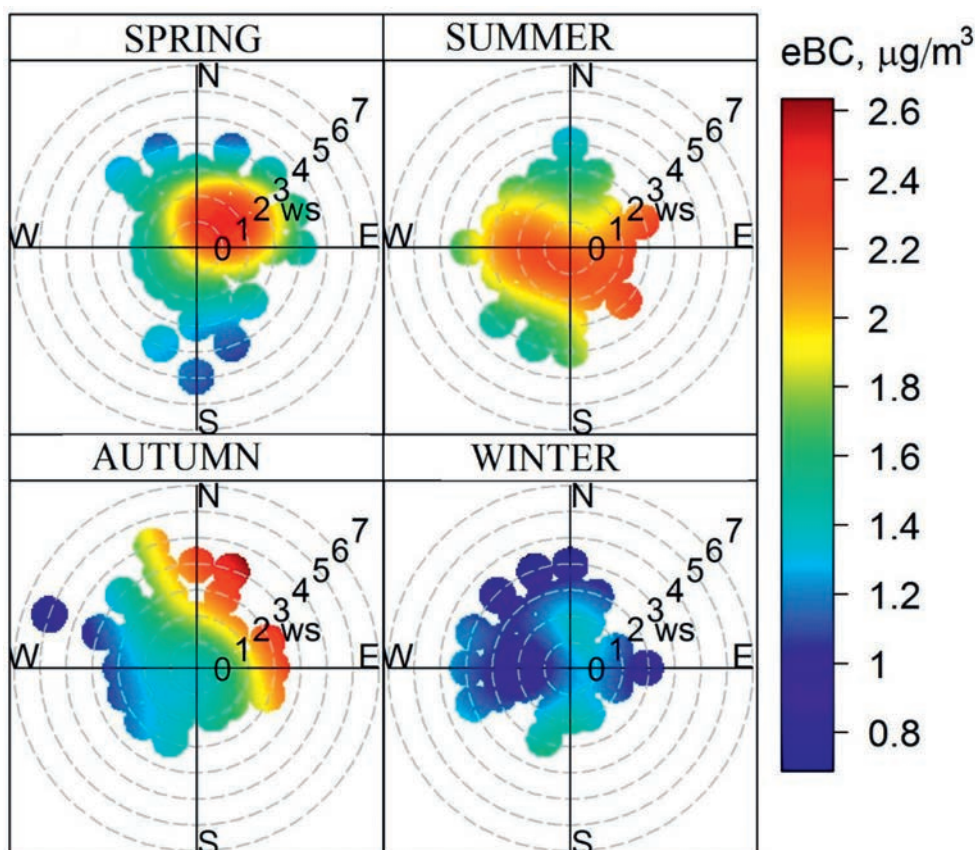
In SPRING, the BC polar plot indicates the dominant influence of sources in the NE direction. Highest concentrations (above  $2.2 \mu\text{g}/\text{m}^3$ ) occur at lowest wind speed during the days of windless weather, indicating the local emissions distributed around the MO MSU site. Such a picture is a typical feature of non-buoyant ground level sources as traffic. At wind speed  $\sim 2 \text{ m/s}$  remote sources such as the industrial zone "Fili", a number of TPSs and

TS, and factories could impact BC at the MO MSU when the site occurred downwind the emission stacks.

The SUMMER polar plot shows a similar picture such as the BC homogeneously distributed sources around the sampling site at all wind directions and wind speeds up to  $2 \text{ m/s}$ . It also identifies emissions from the NW and W direction of the industrial zone "Kunzevo" and "Ochakovo", respectively. The biggest thermal power station in Moscow, TPS-25, is located in "Ochakovo", its pollution dispersion area covers the territory of the MSU campus [61].

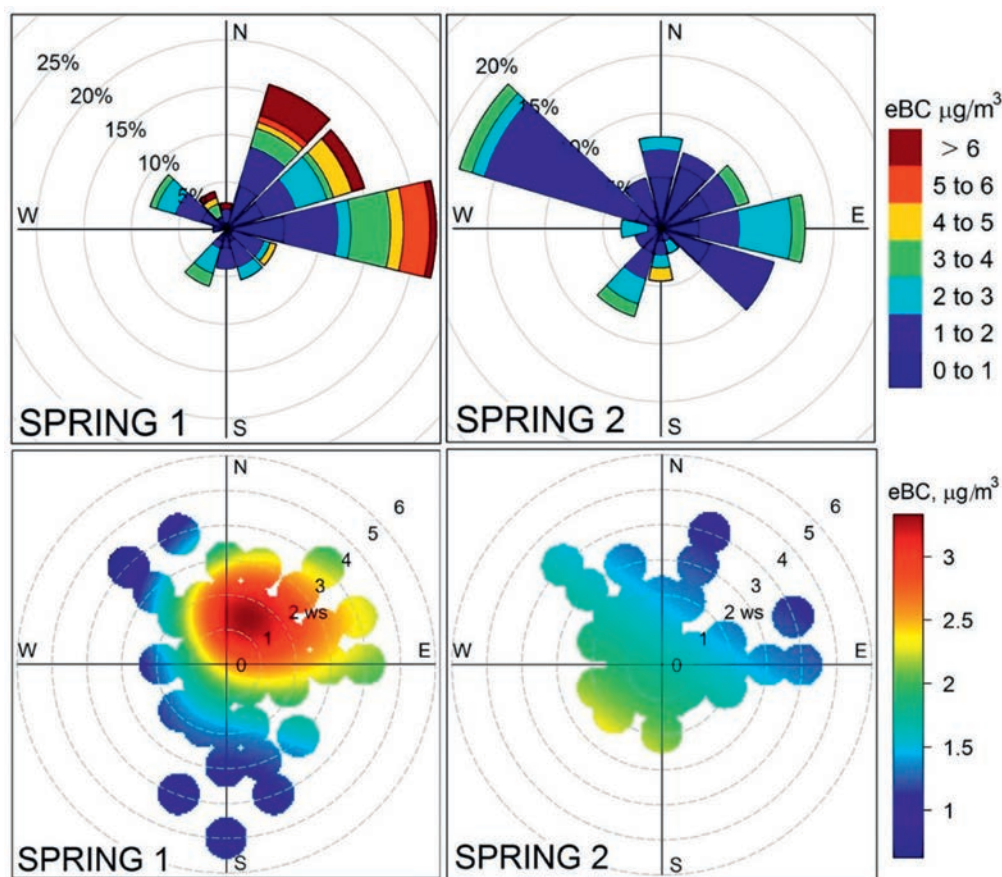
In AUTUMN, the situation is noticeably changed, its polar plot reveals the biggest impact from relatively remote sources in the NE at wind speeds higher than  $2 \text{ m/s}$ . A number of TPS takes place in this direction. The WINTER polar plot is characterized by the low BC concentrations (below  $1.4 \mu\text{g}/\text{m}^3$ ) with homogeneous source distribution. Week (in comparison with other seasons) sources may be noted in the N and S directions.

Figure 8 shows BC pollution roses and polar plots separately for two spring periods, SPRING 1 and SPRING 2. The change of highest BC concentrations from the NE to NW, with a decrease of BC concentrations from the highest values (above  $6 \mu\text{g}/\text{m}^3$ ) during the heating period to lower ones (below  $4 \mu\text{g}/\text{m}^3$ ) after, is observed. On polar plots the highest BC concentrations during the heating period are observed at wind speed around  $2 \text{ m/s}$ , that indicates a source in the direction of the industrial zone "Fili" and a number of HPPs. The situation is noticeably changing after the end of the central heating system operation. BC concentrations decreased, and the origin of emission sources were changed to the NW, hardly identified at wind speeds above  $2 \text{ m/s}$ .



**Figure 7.** Polar plots of BC concentrations for SPRING, SUMMER, AUTUMN, and WINTER periods (right). Wind speed (ws) is indicated in m/s.





**Figure 8.** Black carbon pollution roses (upper) and polar plots (bottom) for SPRING 1 and SPRING 2 periods.

### 3.3. Biomass Burning-Related Sources

Light absorption by particulates emitted from fossil fuel combustion sources exhibits a weak wavelength dependence with the Absorption Angstrom Exponent (AAE) close to 1.0 [2]. Wood smoke aerosols are distinguished by a strong wavelength dependency, showing AAE about 2.5. Large AAE near 4.0 indicates wood and debris burning in smoldering phase [62]. For ambient aerosols the study [43] recommended AAE values of 0.9 and 1.68 related to traffic and wood smoke, respectively, for specific wavelength pairs by comparing the BC source apportionment results using the Aethalometer model [25] with 14C measurements.

Observations in urban environment had related the AAE variation to biomass burning impact [54]. The increased AAE above 1.0 was suggested for identification of periods most affected by biomass burning [5], termed as “BB-affected”. Elevated light absorption with AAE up to 4.1 was observed in Moscow urban environment for days affected by peat burning plumes [32]. Parametrization of AAE relating to fossil fuel and biomass burning-affected values below 1.3 and high, above 1.3, values, respectively, has supported the contribution of traffic/industry and agriculture fires/residential biomass burning in Moscow urban background [34].

The spectral dependence of the aerosol light attenuation during a study period is well approximated by a power law equation (1), providing the estimate for AAE. Variation of AAE during SPRING 2018, and SUMMER 2019, AUTUMN 2019, and WINTER 2019–2020 exhibits the range from 0.6 to 1.9 (Figure 9). The seasonal maximum mean AAE is reached in WINTER 2019–2020 equal to  $1.3 \pm 0.2$  (Table 2). Winter time is especially dis-

tinguished by the exceeding SPRING 2018, AUTUMN 2019, and SUMMER 2019 mean, max, and min values. New Year holidays (days of 01.01 and 02.01.2020), when fireworks use is very intensive, are clearly seen by AAE approaching 1.9. Frequency of observations with AAE > 1 is 98%, the highest one between other seasons.

AUTUMN 2019 also demonstrates the high frequency of observations for AAE > 1, 78%. Together with WINTER 2019–2020, it reveals the biggest biomass burning impact in the cold seasons. At first sight, this finding looks surprising, considering that the local domestic heating using biomass burning is absent in Moscow megacity, in contrary from many other European cities, because the gas-fueled centralized heating supply continuously operates during the cold season. However, we should assume the strong influence of a huge residential area in the Moscovskaya Oblast located around the Moscow megacity.

In SPRING 2018 and SUMMER 2019, approximately the same mean AAE is obtained,  $1.0 \pm 0.2$ , with similar frequency of AAE > 1 observations, 58% and 50%, respectively. From 07 of May and during SUMMER periods the central heating system did not operate in Moscow. However, the warm period is traditionally related with the intensive weekend migration of population to the suburban area and also to vacation time when the elevated temperature stimulates the intensive residential activity around Moscow city such as garden cleaning, grass burning, and barbecue. Moreover, the spring season is traditional time for agriculture fires induced by grass burning on fields.

In a few days of study periods low AAE values were observed, even as low as 0.6 in SPRING 2018. Chemical

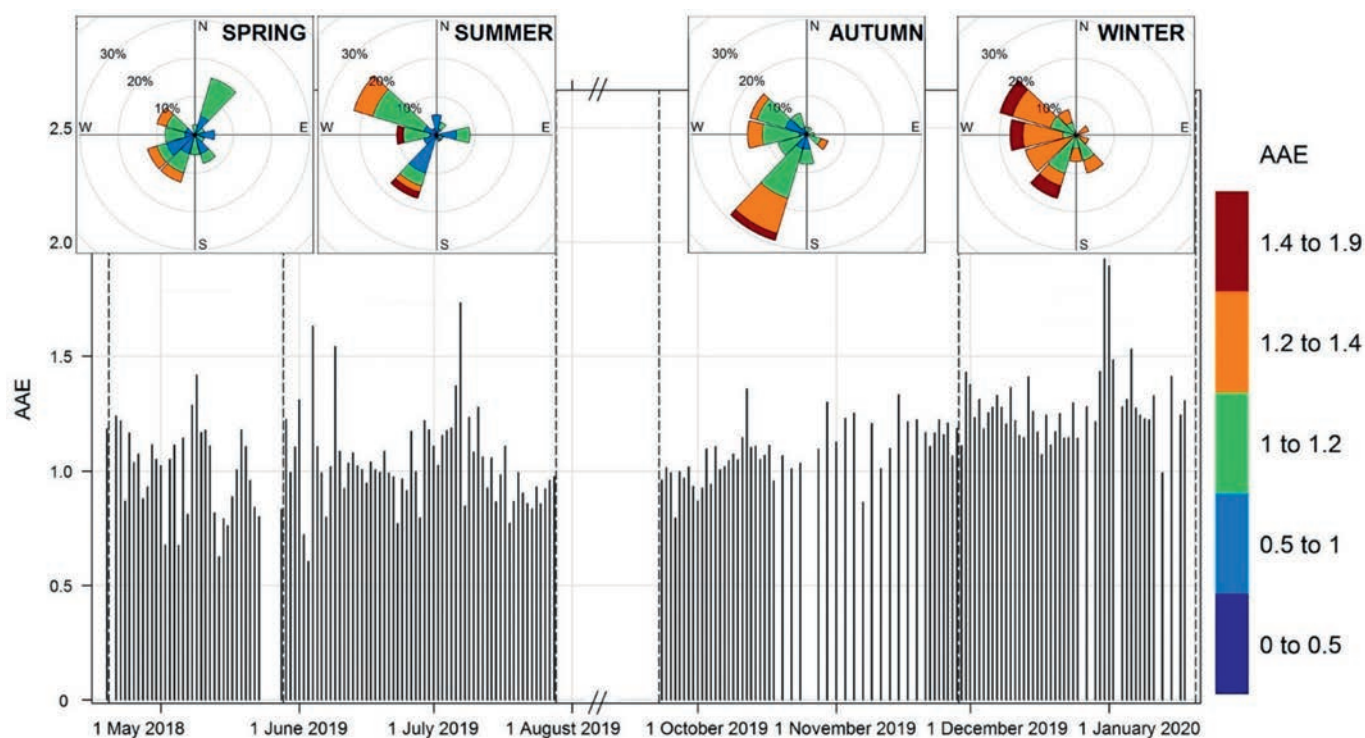


**Figure 9.** Absorption Angstrom Exponent (AAE) during SPRING 2018, and SUMMER 2019, AUTUMN 2019 and WINTER 2019–2020. AAE roses for each period are presented.

**Table 2.** Mean, maximum (max), and minimum (min) of Absorption Angstrom Exponent (AAE) during separated seasonal periods of 2019–2020 years and of SPRING 2018, standard deviations (S.T.D.), and frequency of observations for AAE > 1.

Period	Mean	max	min	S.T.D.	AAE > 1(%)
SPRING 2018	1.0	1.4	0.6	0.2	58
SUMMER 2019	1.03	1.7	0.6	0.2	50
AUTUMN 2019	1.09	1.4	0.8	0.1	78
WINTER 2019–2020	1.3	1.9	0.9	0.2	98

evolution of aerosol mixing state, particle morphology, and size distribution after emissions and atmospheric aging can influence aerosol absorption, which can be noticed especially for the long-range transported air masses [63,64,65]. The AAE for the aged aerosols measured during a few periods as low as 0.6 could be addressed mostly to the aerosol size distribution (large particles) and internally mixed BC particles [63]. As shown by modeling studies [66] pure BC particles coated by non-absorbing coating can have AAE in the range from <1 to 1.7, depending also on the morphology of the fractal aggregates [65].

Directions of the high AAE (above 1) indicated by AAE roses are SW, W, and NW in WINTER 2019 while only SW is dominant in AUTUMN 2018 (Figure 9). We should note that AAE roses do not show the similar direction as for BC concentrations for the same periods, see Figure 6 for comparison. This finding indicates that the biomass burning source does not impact much the BC concentrations in Moscow urban environment, having its own location distribution different from fossil fuel combustion. Moreover, the same directions but with lower AAE is observed in SPRING 2018 and SUMMER 2019.

### 3.4. Regional Sources of Black Carbon

Air masses arriving to a city may impact urban air quality, especially if the direction of their long-range transportation well correlates with fire-affected area. We use the CWT modeling to identify the origin of regional sources for observed high BC concentrations at the MO MSU site. Figure 10 shows CWT analyses for BC concentrations during four seasons of 2019–2020. In SPRING the source region of high concentrations (above  $3 \mu\text{g}/\text{m}^3$ ) is extended far north and south, encompassing the large area of European part of Russia as a region of the BC origin. In SUMMER, the total area of high BC is reduced and localized into a dense area around Moscow megacity and stretched with a loop toward south. In AUTUMN and WINTER, sources for comparable high BC concentrations are no more observed, regions of lower (below  $3 \mu\text{g}/\text{m}^3$ ) BC concentrations are rather homogeneous and large extended.

Fire activity is traditionally high in spring when temperature rises; agriculture practice with a purpose to remove the last year grass on the fields is widespread



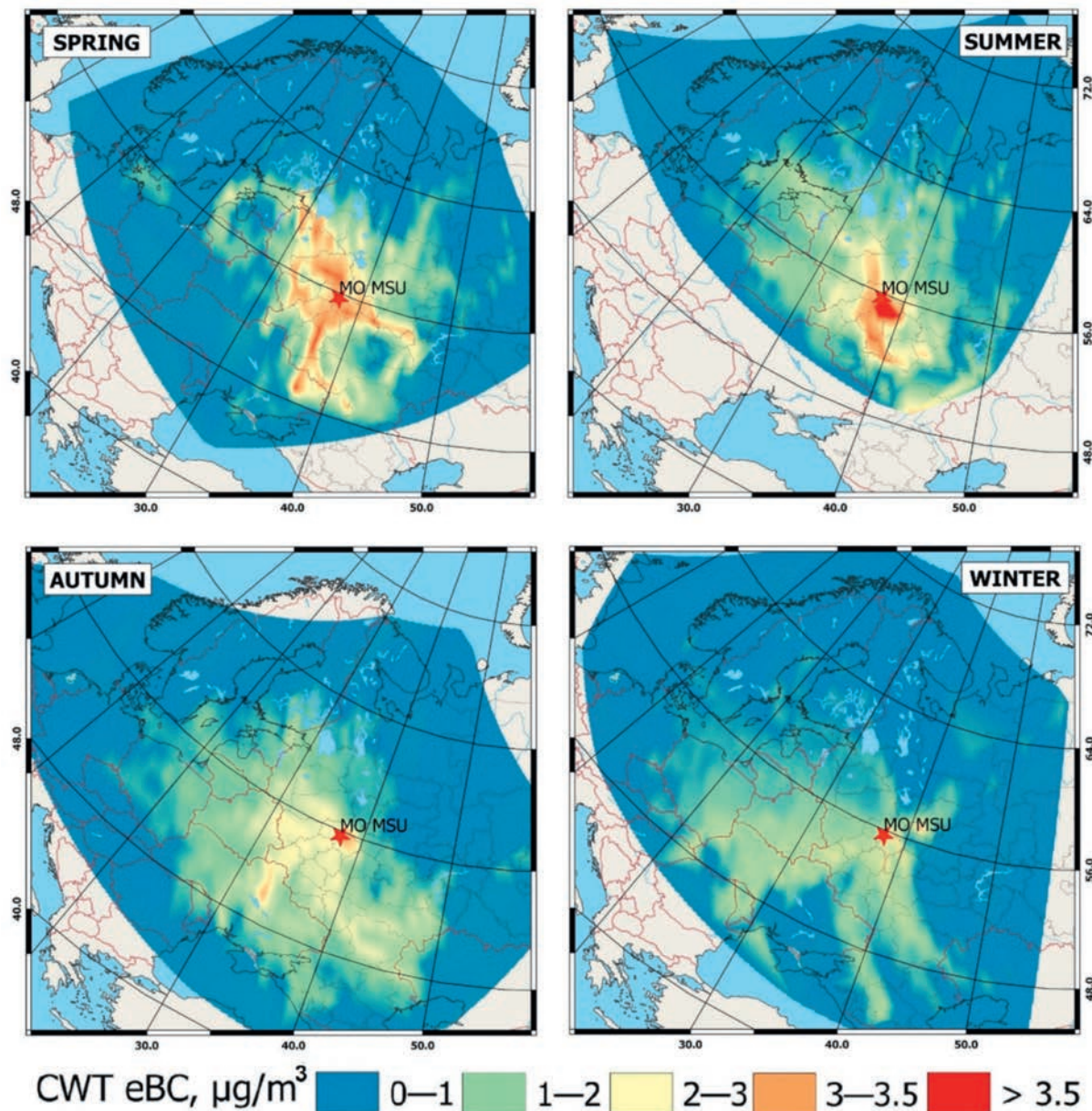


**Figure 10.** Concentration weighted trajectory (CWT) analysis for black carbon during SPRING, SUMMER, AUTUMN, and WINTER periods of 2019–2020 years. Color bars represent concentrations in  $\mu\text{g}/\text{m}^3$ .

in this season. The majority of wildfire emissions occurs in the European part of Russia from March to late May [27]. In spring of 2018, the biggest number of open flaming fires occurred in the south-east direction from the Moscow area at the end of April [36]. Figure 11 shows backward trajectories of air mass transportation during days of increased AAE. Values above 1.3 were recorded at 8 May and 9 May in SPRING 2018 and at 1 June, 4 June, 6 June in SUMMER 2019, indicating the biggest biomass burning impact. The air mass transportation from areas with high fire activity is demonstrated: from northwest for 8 May and 1 June, from northeast for 9 May and 4 June, and from southwest for 6 July. Thus, AAE analyses in our study confirm that high atmospheric pollutions in Moscow could be mainly caused by the transport of biomass burning pollutions from the rural agricultural regions over a distance of hundred kilometers as well as from residential sector of Moscovskaya Oblast.

#### 4. CONCLUSIONS

Moscow megacity is remaining to be low estimated densely populated source of potentially dangerous pollutants in the eastern part of Europe. A need to assess air quality in Moscow megacity led to the long real time BC measurements at the urban background site, on Aerosol Complex of MO MSU. Seasonal, weekly, and daily BC variations show the impact of urban sources, population activity, meteorology, and long-range transport over the site location. Level of BC in the range of seasonal variability similar to European cities indicates the comparable impacts of major urban sources such as traffic with intensive implementation of modern environmental requirements; heating power plants, producing and redistributing energy, gas, and water; and manufacturing industries. The specific source for Moscow megacity is the centralized heat supply for both residential and industrial sectors using natural gas.



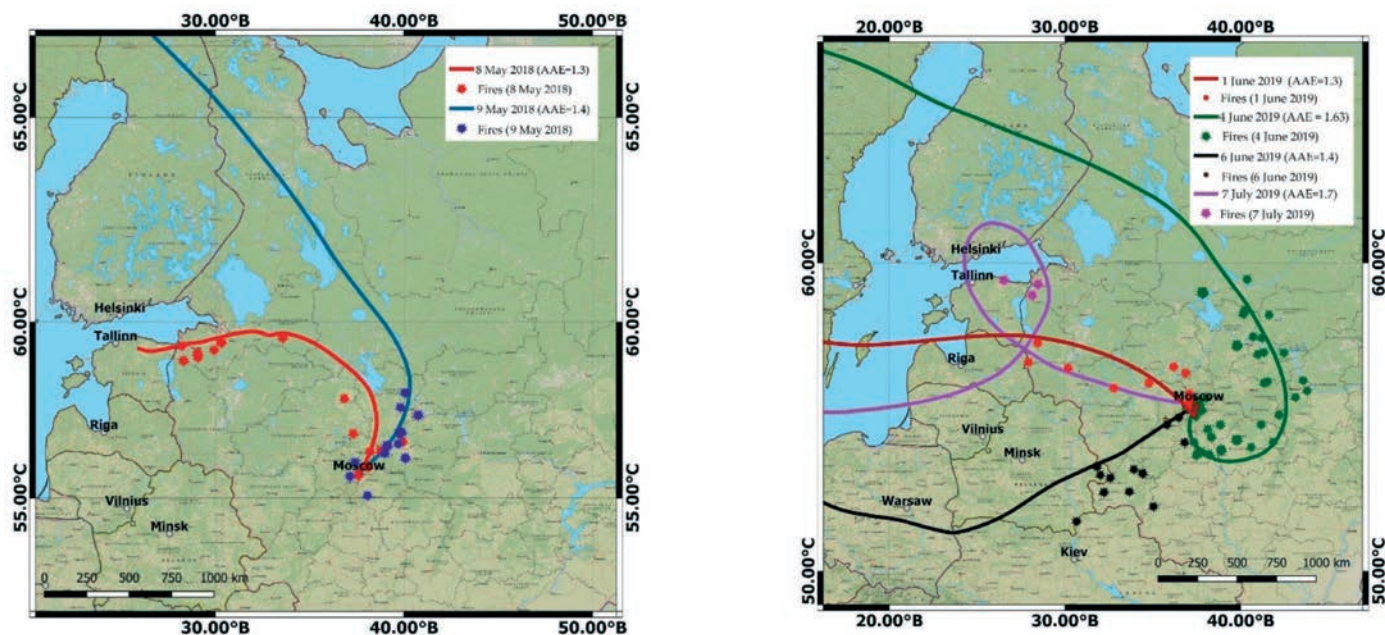


**Figure 11.** Trajectories of air mass transportation during days of increased AAE above 1.3 in SPRING 2018 (left) and SUMMER 2019 (right), shown at 12:00 UTC. Fires near trajectory pathway at those days are indicated by the same color.

Diurnal patterns in the spring and summer seasons shows the typical for large cities two peak structure during morning and evening hours when the atmospheric boundary layer (ABL) is shallow while traffic, heat, and energy supply are high. Seasonal variations in the ABL height and time of the surface temperature inversion smooth the diurnal trend in autumn and winter. BC has a weekly cycle with higher concentrations on weekdays relating to the largest combustion emissions on working days and a strong traffic congestion. Lower BC on Friday, Saturday, and Sunday is apparently related to the lower traffic rates and migration of the population from a city to the Moscovskaya Oblast for weekend.

Directions of the highest BC pollution concentrations are seasonally changed, as discovered by pollution roses. Polar plots indicate the origin of main BC emission sources nearby the MO MSU such as traffic, heating power plants, factories, and industrial zones in correla-

tion with wind direction and wind speed. Parametrization of source-specific measure of spectral absorption, Angstrom Absorption Exponent (AAE), and its frequency of observations above 1 supports the seasonal source apportionment. The biggest impact of biomass burning occurs in the cold seasons (winter and autumn) that almost relates to the impact of a huge residential area around megacity while local domestic biomass burning is absent in Moscow. In the warm seasons of the elevated temperature, the weekend migration of population to the suburban area (particular activity of Moscow inhabitants) and vacation time stimulates the intensive residential BB activity around Moscow city. The transport of biomass burning aerosols from the rural agricultural fire-affected regions over a distance of hundred kilometers as well as from residential sector of peri-urban areas of Moscow can confirm high atmospheric BC pollutions in Moscow in spring and summer.

# Effects of braking conditions on nanoparticle emissions from passenger car friction brakes\*

## 1. INTRODUCTION

Traffic is a main source of air pollutants in urban areas and consequently daily peak exposures tend to occur during transportation. Traffic nonexhaust sources represent anthropogenic dust source such as inorganic material emitted from vehicle brake pads, tires and mechanical parts and resuspension of road dust (Saraga et al., 2021). Brake wear particles were reported to be a major component of vehicular emissions (Bukowiecki et al., 2010; Grigoratos and Martini, 2014; Thorpe and Harrison, 2008) and the main source of magnetite particles (Gonet et al., 2021). There are marked differences in PM chemical composition depending on transport mode. Enhanced concentrations of Zn and Cu in cars and buses were related with brake and tire wear particles (Martins et al., 2021). These results evidence the importance of considering the transport mode in exposure assessment studies.

Friction brakes are currently the most common way to decelerate and stop road vehicles. Two common designs are used – disc brakes, where brake pads are pressed against a rotor (disc) connected to the rotating wheel, drum brakes, where brake shoes are pressed against the inner surface of a rotating drum. Brake pads and shoes comprise of a steel structural element, to which a friction lining is attached. The lining material is a complex mixture of binders, fibers, fillers, lubricants and abrasives (Grigoratos and Martini, 2015). During braking, the kinetic energy of the vehicle is transformed into heat. For safety reasons, the brakes are designed with sufficient reserve capacity, so that the main factor limiting the deceleration rate is the adhesion of the tire to the road surface. Both friction surfaces wear with use and are replaced periodically, with frequency depending primarily on the operating patterns of the vehicle.

The wear particles comprise of larger particles generated by physical abrasion of the material, and smaller particles formed by condensation of vapors resulting from high temperatures at friction surfaces (material volatilized at high temperature and newly formed compounds). The larger particles originating from mechanical processes are of diameters of several micrometers and higher. The smaller particles are typically nanoparticles with a diameter on the order of 10 nm formed by nucleation, with larger particles formed by condensation, coagulation and other processes (see Hinds, 1999 for a review for aerosol physics).

To date, there has been only a small number of studies evaluating the brake particle emissions. Approximately 40% of the particle mass was reported to be particles with an aerodynamic diameter smaller than 10  $\mu\text{m}$  (Kukutschová et al., 2011; Grigoratos and Martini, 2015, and references therein). Particle number distributions reported by (Zum Hagen et al., 2019) show peaks around 10 nm and 2–3  $\mu\text{m}$ , suggesting that these are the most frequent sizes of particles from high temperature and mechanical processes, respectively.

On one set of brake pads and rotor studies by (Zum Hagen et al., 2019), the total number of particles emitted remained relatively very low below a certain threshold brake pad temperature, beyond which the particle number per stop increased exponentially with increasing temperature. No relationship between the particle number and either the total energy dissipated was observed. The total particle mass, on the other hand, did not correlate to the brake pad temperature, but increased (not linearly) with the total energy dissipated during the stop. The threshold temperature varied from 140 to 170  $^{\circ}\text{C}$  and gradually increased with consecutive tests. Kukutschová et al. (2011) report a similar observation, but with the higher temperature at which low metallic pads emit large quantities of nano-size particles, around 300  $^{\circ}\text{C}$ . Also, when milled sample of the pad material was heated to 300  $^{\circ}\text{C}$ , ignition of carbonaceous material was observed.

Mathissen et al. (2018) report observations from two braking cycles developed to mimic real-world operation, a short, 3-h version of the Los Angeles City Traffic cycle, and a newly developed WLTP brake cycle based on the collection of driving patterns used for the development of the World Harmonized Light Vehicle Test Procedure. Over the 3 h-LACT cycle (Mathissen and Evans, 2019), the particle number stays relatively low below brake pad temperature of about 170  $^{\circ}\text{C}$ , and increases exponentially with temperature for higher temperatures. For the entire WLTP brake cycle, the brake pad temperature is below 170  $^{\circ}\text{C}$  and no increase in particle number emissions is observed.

Yet, at the same time, the brake wear emissions are reported to be relatively low during “average” driving simulated in the WLTP brake cycle. They are also known to be very high during extreme braking events which are parts of various durability tests, such as internationally recognized standards ISO 26867 and SAE J2522.

The goal of this study was to elucidate the effects of braking conditions, such as brake temperature, initial and terminal speed, and the severity of braking, on the production of nanoparticles. (Note: There is no unified formal definition of nanoparticles. In this study, we consider both nanoparticles, as well as ultrafine particles, to be particles with a diameter smaller than 100 nm. Since this definition does not necessarily follow the particle size distributions, this study also includes particles in the hundreds of nm range, believed to generally originate from thermal processes.) The experiments were conducted partly as a part of a broader effort to map the sources and the fate of antimony in the environment, and partly as a part of the ongoing effort to quantify brake wear emissions. The specific vision behind this study was to provide a guidance to citizens and legislators in terms of how to reduce nanoparticles from brake wear from the existing vehicle fleet.

\* Vojtišek-Lom M., Vaculík M., Pechout M., Hopan F., Arul Raj A.F., Penumarti S., Horák J.S., Popovicheva O., Ondráček J., Doušová B.// *Science of the Total Environment*. 2021;788:147779.  
DOI: [10.1016/j.scitotenv.2021.147779](https://doi.org/10.1016/j.scitotenv.2021.147779). CiteScore 14.1, IF 10.8



## 2. EXPERIMENTAL

### 2.1. Brake dynamometer

The tests were carried out on a brake testing dynamometer at the Technical University of Ostrava. A front brake assembly consisting of an original caliper and a typical rotor of one of the most popular (per vehicle registrations) passenger cars in the Czech Republic was coupled to a full scale brake dynamometer (Link M2800). The rotor is coupled by a rotating shaft to an asynchronous electric motor and a flywheel. The assembly is accelerated by the asynchronous motor to the desired speed. Upon command or when prescribed conditions, typically brake rotor temperature, are reached, hydraulic pressure is supplied via actuator to the brake caliper. The hydraulic pressure is regulated to match either the target brake line pressure or the target deceleration rate. Rotor temperature near the surface is measured by a thermocouple inserted in a hole drilled radially into the rotor. Details of the experimental setup are given in (Kukutschová et al., 2011).

The rotor and the brake assembly are housed in an airtight enclosure (Fig. 1), through which air was circulated by fans a flow rate of 40 m<sup>3</sup>/min (2400 m<sup>3</sup>/h) to provide cooling for the brake assembly and to scavenge fumes and smaller brake wear debris from the enclosure. Part of the outlet duct was replaced by a 40 cm diameter, approximately 5 m long pipe, serving as a dilution tunnel for particulate matter sampling. The sampling port was installed approximately 3.5 m from the last bend and 5.5 m from the brake assembly, corresponding to a residence time (for the particles to travel to the sampling point) of approximately 0.75 s.

For this experiment, four different brake pads, representing the most popular types and makes for the vehicle model, were procured from local dealers: one set of pads sold as original part by the vehicle authorized dealer (“OEM”), without any information about the actual manufacturer of the pads, and three sets of aftermarket pads, selected as most popular based on a survey among local part dealers, labeled according to their trade labels “Ferrodo”, “Zimmermann” and “ABE”. The dynamometer was set to the rolling radius of 308 mm, equivalent test mass of 690 kg corresponding to 37.5% of the gross vehicle weight of 1840 kg (75% of the braking power at front and 25% at the rear axle), and inertia of 65.5 kg·m<sup>2</sup>.

### 2.2. Test procedure

Standardized brake wear testing procedures typically comprise a range of extreme events, including a simulation of brake fading during prolonged hill descent and during repeated hard stops from very high speeds. These tests are intended to assess the brake performance during most extreme conditions rarely encountered during ordinary operation. To represent, as much as possible, ordinary operation, sections without extreme events were selected from two standard brake test procedures: ISO 26867 (Sections 3; 5; 8) and SAE J2522 (Sections 4.1; 4.2; 4.3; 6; 7; 11). The initial and final speed, the nominal brake pressure in bar, the initial brake rotor temperature, and the final brake rotor temperature observed during the run with OEM brake pads are plotted in Fig. 2.

Prior to the test, all four sets of pads were degreased (ISO 26867 Section 1) and stabilized (ISO 26867 Section 2, commonly known as “burnish”: 80 km/h initial speed, 30 km/h release speed, 10 stops at 30 bar and rotor initial temperature of 150 °C, and 32 stops at 15–50 bar and rotor initial temperature of 200 °C).

Additionally, another set of Zimmermann brake pads (labeled “Zimmermann V”) was subjected to a milder degreasing (64 stops, initial rotor temperature of 150 °C, initial speed 80 km/h, release speed 30 km/h, variable brake pressure), representing a “compromise” between burnish procedures prescribed in ISO 26867 Section 2 (32 stops at 200 °C initial rotor temperature) and SAE J2522 Section 1 (128 stops at 100 °C initial rotor temperature). This set was subjected to the above described test, and in addition, to three repeats of the newly developed WLTP brake testing procedure (Mathissen et al., 2018). This procedure, developed for the purposes of brake wear emissions tests, was crafted to represent typical vehicle operating conditions, analogous to the WLTC (World Harmonized Light Duty Vehicle Test Cycle) chassis dynamometer cycle used as part of exhaust emissions type approval procedures. The WLTP brake test procedure consists of 10 trips, totaling 192 km and 4 h 39 min of net run time, not including cooling periods between the trips. All 10 trips were run consecutively, allowing for the rotor to cool to below 30 °C prior to each trip, and the entire WLTP brake test was repeated three times. The cooling flow rate was kept constant at 2400 m<sup>3</sup>/h to suppress nucleation of semi-volatile compounds



Fig. 1. Brake assembly (left) and brake dynamometer enclosure (right).



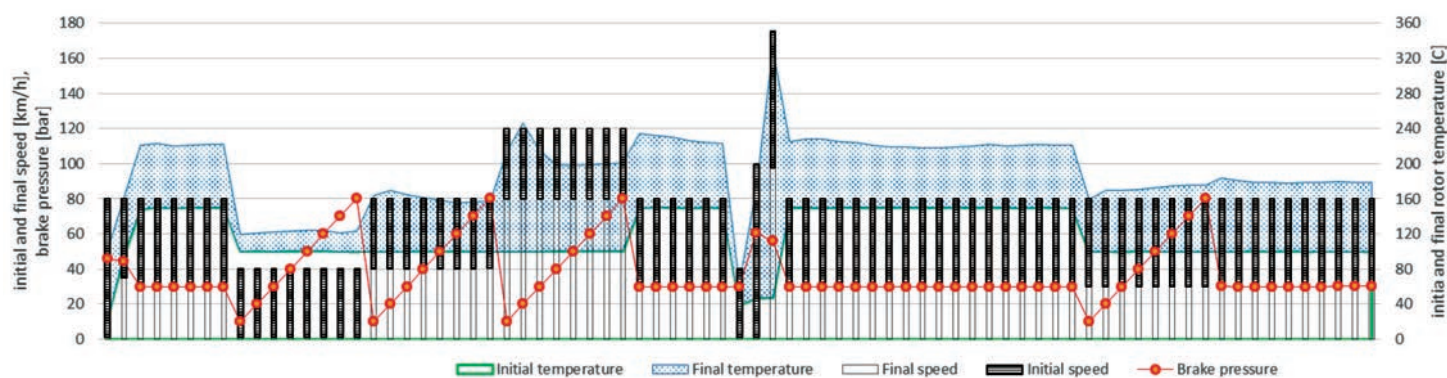


Fig. 2. Brake test sequence.

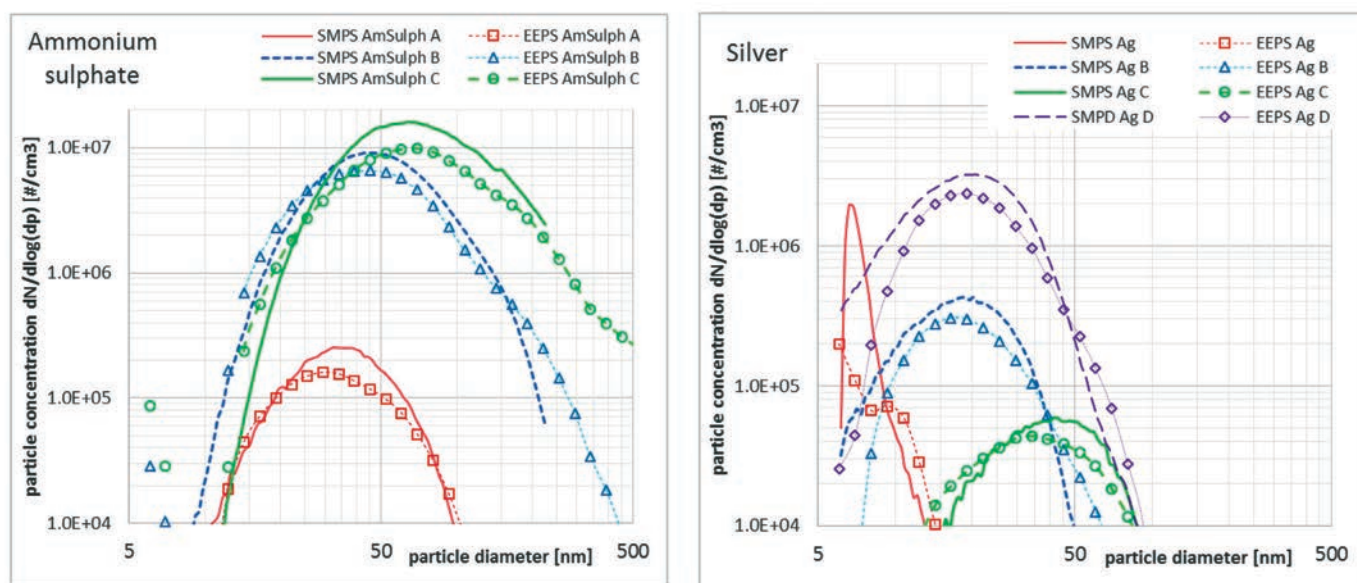


Fig. 3. Response of the electric mobility particle sizer to ammonium sulfate (left) and silver (right) nanoparticles (reference: SMPS+CPC).

and to allow for the particle classifiers to work without additional dilution.

### 2.3. Instrumentation

Particle concentrations were measured online by an electric mobility particle sizer (Engine Exhaust Particle Sizer, EEPS, TSI) and an aerodynamic particle sizer (ELPI, Dekati). Particles were also sampled using a 13-stage cascade impactor (DLPI, Dekati) and two high-volume samplers with PM<sub>2.5</sub> head. Of these, the EEPS data were deemed to be most relevant to the evaluation of the effects of operating conditions on nanoparticle production and are the only data reported on in this work.

### 2.4. Particle sizer response to non-exhaust particles

The EEPS charges the particles using two corona chargers in series, one with negative and one with positive voltage. The particles then travel between two concentric cylinders and are repelled by positive electric voltage applied to the inner cylinder to a stack of 22 electrometer rings forming the inner surface of the outer cylinder. Smaller particles tend to deposit on the upper electrometers and larger ones on the lower electrometers. The particle number distributions are calculated from the electrometer currents, after adjusting for time delay, mul-

tiples charges, and other factors, by a proprietary inversion matrix. The instrument has been designed and calibrated for engine exhaust particles, and with these, it has been known to provide slightly different responses for different characteristics of particulate matter, such as its fractal dimension. For this reason, in addition to the “default” conversion matrix used by the instrument to obtain particle number distribution from electrometer currents, specific matrices, such as “soot”, have been developed. To provide at least a rough check of the instrument response to metallic and inorganic particles expected to originate from brake wear, ammonium sulphate and silver nanoparticles were sampled by the EEPS and by a scanning mobility particle sizer (SMPS, TSI) coupled with a condensation particle counter as a reference. Selected results from this comparison are shown in Fig. 3. The EEPS reported concentrations are in general somewhat lower and the particle diameters reported by the EEPS are slightly lower compared to the reference. The disagreement on 10 nm silver nanoparticles is attributed to unstable distribution over the SMPS scan time of 3 min.

### 2.5. Calculations

The background particle concentration was calculated as the average particle diameter (particle size) distri-

bution measured over 15 s before the brake event, and subtracted from the size distributions measured during and after the brake event. The particle production during each brake event was calculated as the sum of particle distributions measured during and after the brake event, with the summing window determined manually for each event as the time period over which the total particle number concentration was visually assessed to be clearly above the background levels. The total number of particles per stop was obtained as the sum of particles in all size bins (unless otherwise noted, 32 bins from 5.6 to 560 nm), multiplied by the flow in the tunnel, and is denoted PN. In some places the sum of particles larger than 23 nm is provided (23–560 nm) – this sum is denoted PN23, and for differentiation, the sum of all channels (PN) is reported as PN5.6.

To account for the fact that braking from higher speeds logically leads to higher number of particles produced, particles are expressed in both per stop and per kWh dissipated. This is analogous to the expression of exhaust emissions on brake-specific basis, per kWh of engine output, and allows for comparison across a range of vehicle masses.

The average braking power has been calculated as the ratio of the total energy dissipated and the time during which the brakes were applied. The vehicle specific power (VSP), typically defined as the product of speed and positive acceleration, was calculated here as the product of average speed and average deceleration rate. Additionally, the product of energy dissipated and average power (in kWh·kW) is used as an arbitrary variable with no theoretical justification.

Unless otherwise noted, all data are reported for the one front wheel brake tested. Distance-specific (per km) emissions for the WLTP test were also estimated for the whole vehicle by dividing the emissions per wheel by

0.375, which was set as the ratio of the equivalent mass of one front wheel to the gross vehicle weight. This was done under a rough assumption that the one front wheel absorbing 37.5% of braking power has the same, 37.5%, share on total brake wear emissions from the vehicle. The emissions per kWh are the same whether expressed per brake or per vehicle.

### 3. RESULTS

#### 3.1. Detection limit and background

The EEPS measured background (the sum of instrument noise and the background particle concentrations) levels were 1123–5582 particles per  $\text{cm}^3$  ( $\#/\text{cm}^3$ ) during the ISO/SAE based tests, corresponding, at the tunnel flow of 2400  $\text{m}^3/\text{h}$ , to a mean background of  $0.7\text{--}3.7 \times 10^9 \#/\text{s}$ . The mean value of individual background before each brake event was  $3.9 \times 10^9 \#/\text{stop}$ . During the three runs of the WLTP brake cycle sequence, the background concentrations were 2060 to 45,147  $\#/\text{cm}^3$  (the 5th and 95th percentiles of the background concentrations were 2749 and 8130  $\#/\text{cm}^3$ ), with a mean of 4727  $\#/\text{cm}^3$ , corresponding to the mean background of  $3.15 \times 10^9 \#/\text{s}$ . All data given in this paper (except for background concentrations) are corrected for background.

#### 3.2. WLTP brake cycle tests

The WLTP brake test consists of 10 trips, totaling 192 km. The average particle number emissions per km, obtained by dividing the total particle number emissions for each segment by the length of the segment, are plotted in Fig. 4. The average emissions for the three tests were  $1.35 \times 10^{10} \#/\text{km}$  for the one front wheel brake and  $3.3 \times 10^{10} \#/\text{km}$  for the entire vehicle, about twenty times

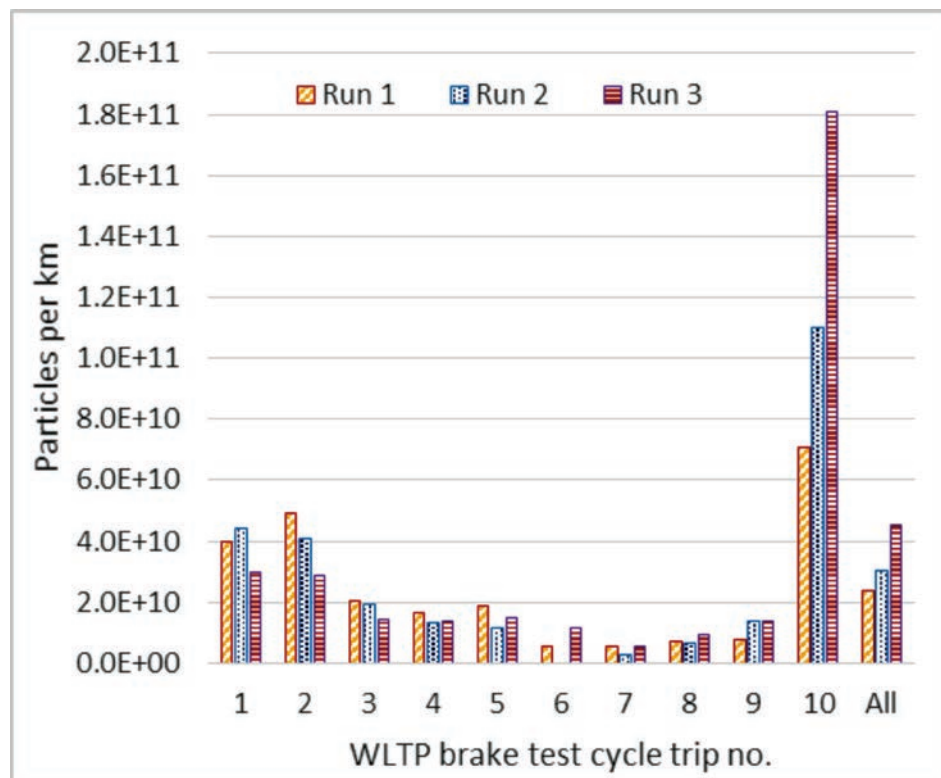


Fig. 4. Mean emissions of particles per km during 10 trips of the WLTP brake cycle.



lower than the  $6 \times 10^{11}$  #/km limit on non-volatile exhaust particles for light duty vehicles. The PN reported here represents all particles of 5.6–560 nm electric diameter, without removal of volatile particles, and is therefore higher than the total number of non-volatile particles “larger than 23 nm”, a typical metric for exhaust particles. (In reality, about 50% of 23 nm particles should be detected, with detection efficiency being higher for larger particles and lower for smaller particles, and there is no “hard” particle size limit.) Therefore, overall, the particle production over the WLTP brake cycle, at least as measured here, does not seem to be a problem. The variance among the three runs (the difference between maximum and minimum divided by the mean) ranged from 26% for Trip 4 to 91% for Trip 10, with 65% for the whole cycle, is dominated by the variance in trip 10, and within this trip, by the variance during two dominant braking events (no. 106 from 132 to 34 km/h, and no. 103 from 81 to 35 km/h). The distribution of the initial and final rotor temperatures, with further analysis, is reported later in this work.

### 3.3. SAE/ISO tests

The brake emissions per stop are plotted for the OEM brake pads in Fig. 5. The highest emissions per stop ( $3.5 \times 10^{13}$  per EEPS) were observed during braking from 175 to 100 km/h, followed by more intensive variants of the 120 to 80 km/h braking (up to  $1.6 \times 10^{12}$  #/stop per EEPS), and more intensive variants of the 80 to 30 km/h braking. This observation differs from that of Mathissen et al. (2018), where the number of particles per stop was around 109 #/stop until about 165 °C average rotor temperature and increased exponentially with the rotor temperature. First, there is no major difference between particle production during 80 to 30 km/h braking starting at 150 °C rotor temperature and similar (80 to 40 km/h and 80 to 30 km/h, both at comparable pressure) braking starting at 100 °C. Second, during 120 to 80 km/h and 80 to 30 km/h braking, the particle production tends to increase with the brake pressure, despite the average rotor

temperature being comparable. As a qualitative indicator of the particle size, the production of particles larger than 23 nm is plotted, together with the sum of all particles (5.6–560 nm), in Fig. 5. It is apparent that the stops with higher total particle production have a significant contribution of particles in 5.6–23 nm range. Examination of the size distributions, shown in Fig. 6 for EEPS (left), shows a consistent peak at 200–250 nm. Additionally, for stops with higher particle production, there is a strong peak at roughly 10 nm; this is typical for nucleation driven production of particles during high temperature processes. This observation is consistent with that of Namgung et al. (2017) on subway brakes, where, in addition to peaks in hundreds of nm, peaks in 10–100 nm range were observed at higher braking power.

The total PN emissions per stop for ELPI, shown in Fig. 5 (plotted as bold triangles), are generally consistent with EEPS, however, ELPI has shown a considerably higher background (plotted as thin line triangles) and also a considerably higher noise. The ELPI size distributions, shown in Fig. 6, show signs of peaks around 10 nm, weak signs of peaks around 200 nm, and signs of a coarse mode peak at 1–2  $\mu\text{m}$ .

To assess the effect of the degreasing procedure, and the overall test repeatability, the results of the two tests of the Zimmermann pads are compared in Fig. 7. One set of pads was tested at the beginning of the test campaign, and the degreasing consisted of 32 stops from 80 to 30 km/h at 200 °C initial rotor temperature, while the other set of pads was tested after the three others makes of pads, and its degreasing consisted of 64 stops from 80 to 30 km/h at 150 °C initial rotor temperature, a compromise between SAE and ISO procedures. The results show that both initially and overall, the pads degreened at 200 °C showed higher particle production than the 150 °C pads, with the difference ranging from tens of percent to an order of magnitude. The combined effects of differences in degreasing, the effects of the rotor being new during the first set of tests, and various factors affecting the repeatability of the test, were therefore, at the maximum, one order of magnitude.

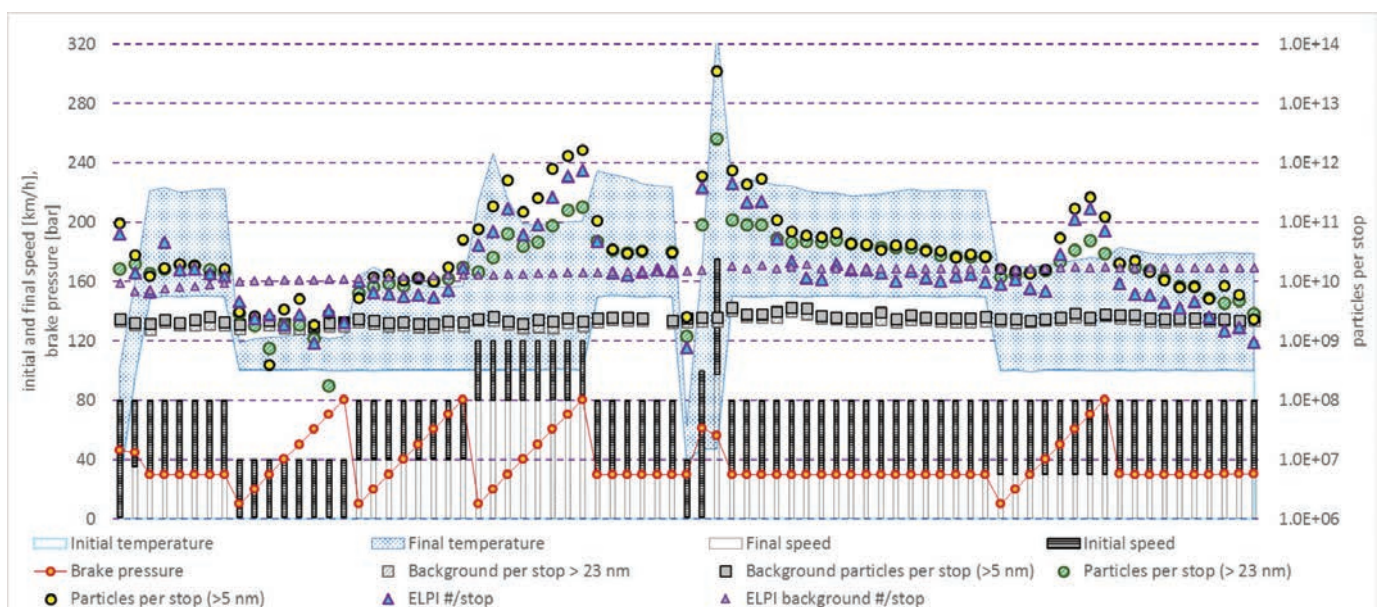


**Fig. 5.** Total number of particles (EEPS size ranges 5.6–560 nm and 23–560 nm, ELPI size ranges 9 nm–10  $\mu\text{m}$ ) per stop produced by OEM pads.



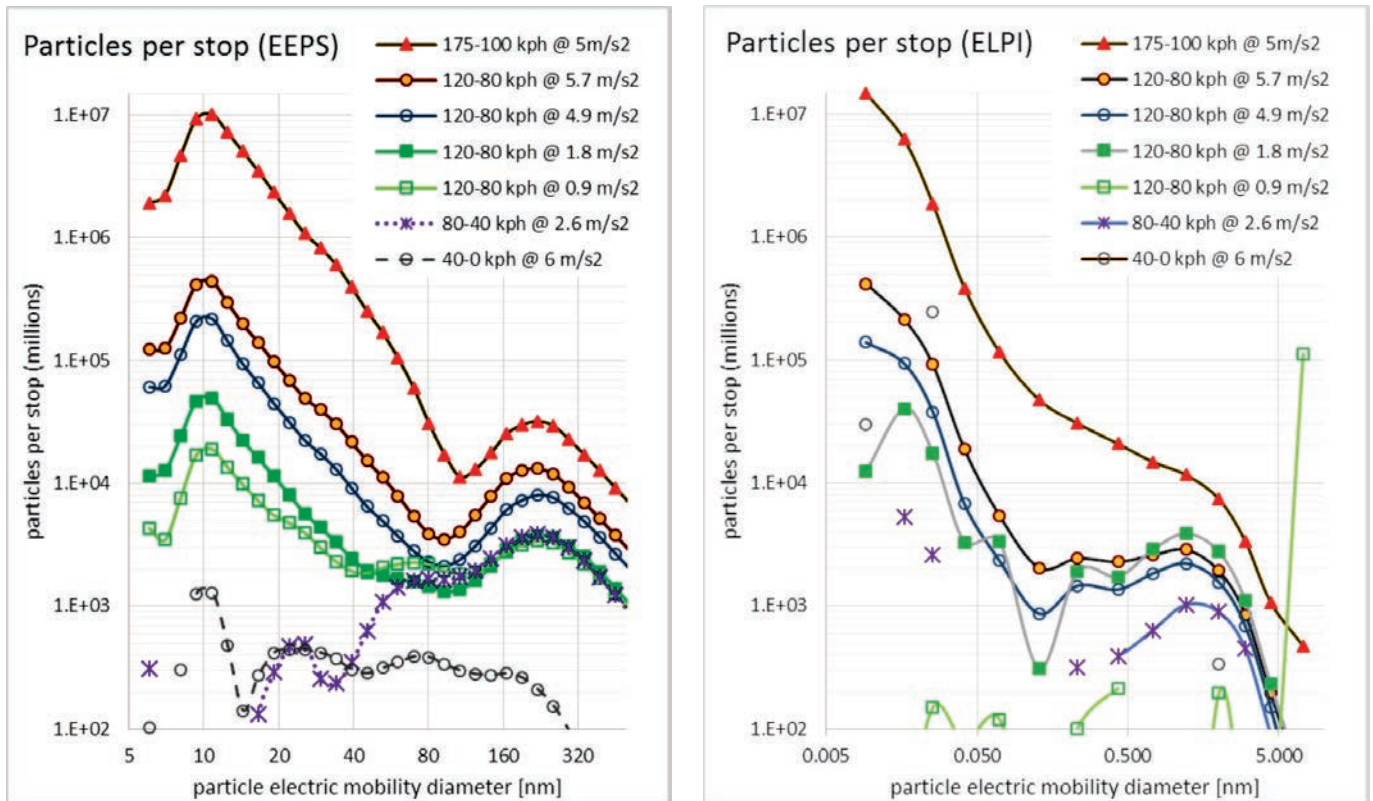


**Fig. 6.** Size distributions measured by EEPS (left) and ELPI (right) at selected initial speeds and decelerations for OEM pads.

The total particle production for all four sets of pads, normalized to particles per kWh dissipated, shown in Fig. 8 (from this point, only EEPS data are reported), shows up to two orders of magnitude difference among the pads in particle production during individual brake events, but with differences among the pads not being consistent among the brake events. For example, Zimmermann pads produced nearly two orders of magnitude more particles than ABE during 120 to 80 km/h braking, but nearly an order of magnitude less particles than ABE during 175 to 100 km/h braking.

In addition to the higher particle production (normalized to kWh of energy dissipated) at higher brake pres-

ures, a hysteresis effect was observed during 120 to 80 km/h stops on the OEM pads (Fig. 8) and on both sets of Zimmermann pads (Fig. 7 and Fig. 8). This effect was studied in detail by Niemann et al. (2020) and attributed to the decomposition of an organic binder in brake pads, an effect observed when a certain temperature is reached for the first time, with subsequent braking at similar temperatures producing less particles. Niemann et al. (2020) also reported, for a series of defined stops at a defined temperature, lower particle production in cases where brake pads were previously exposed to higher temperatures. In this study, stops from 80 to 30 km/h at 100 °C initial rotor temperature, at the end of the test sequence,

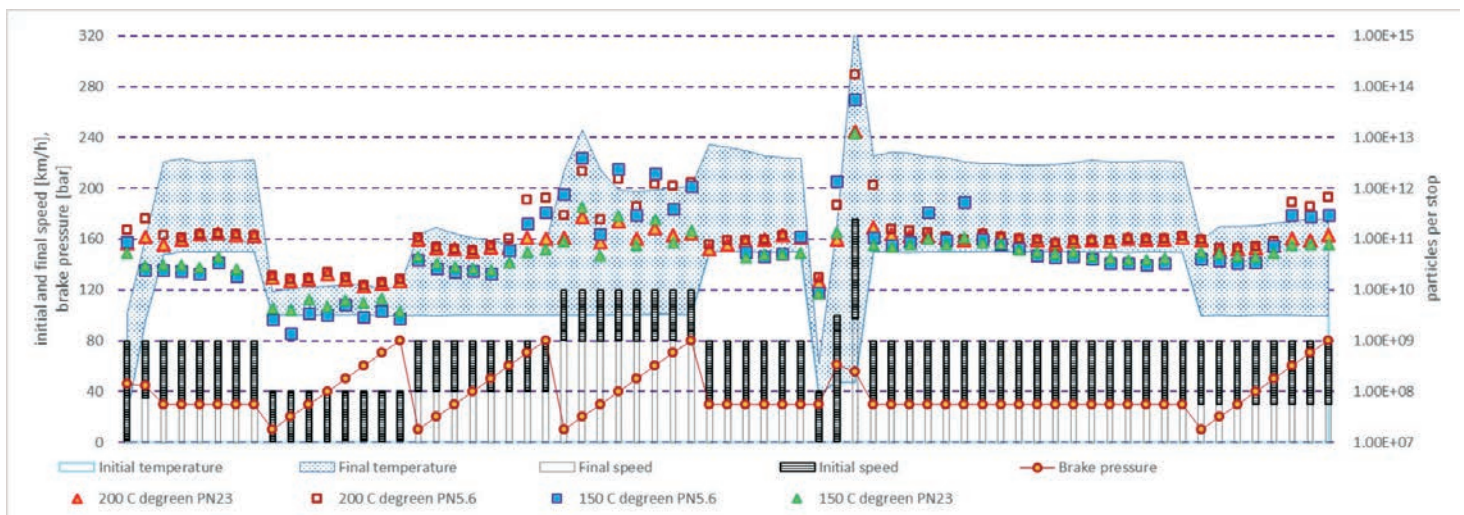


**Fig. 7.** Comparison of tests of Zimmermann pads with degreening by 80 to 30 km/h stops, 32 stops at 200 °C vs. 64 stops at 150 °C.

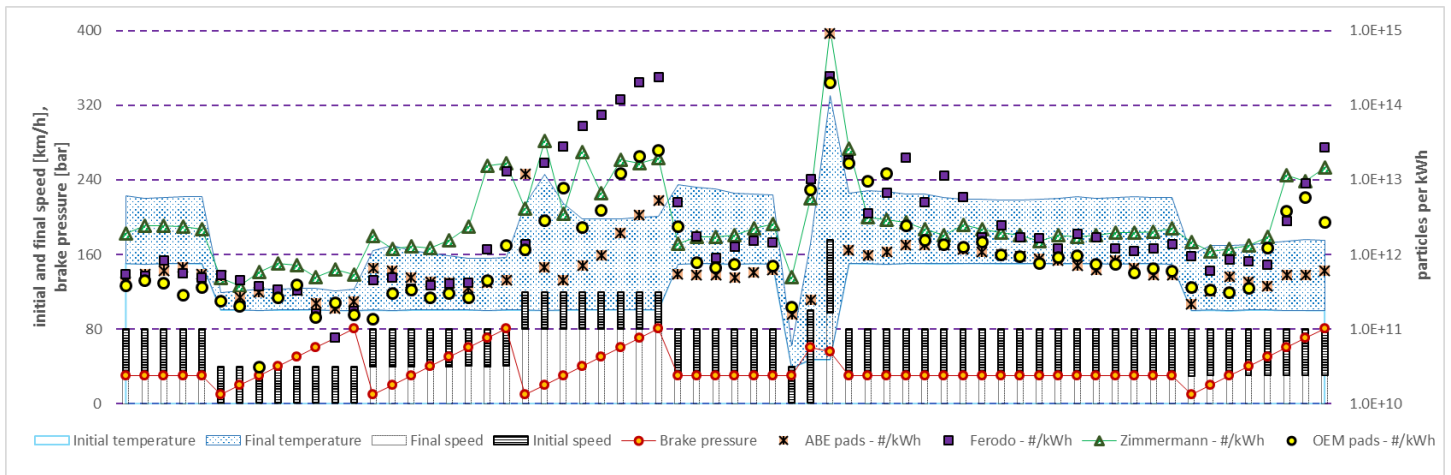


Fig. 8. Total number of particles per kWh dissipated – comparison among different pads.

preceded by a high-speed stop and a series of 80 to 30 km/h stops at 150 °C initial rotor temperature, show similar particle emissions as the 80 to 40 km/h stops run in the first third of the sequence.

### 3.4. Correlation of particle production with braking conditions

For the Zimmermann pads, which were also subjected to three runs of the complete WLTP sequence, the particle production per stop and per kWh is plotted, for each stop, in Fig. 9 as a function of the final temperature of the brake rotor (which in this work shows a considerably higher correlation to the particle emissions than initial or average temperature). Each bubble represents one stop. On the left graph showing particles per stop, the diameter of the bubble represents the average vehicle specific power (average speed multiplied by the average deceleration rate). It is apparent that not only the rotor temperature has an effect on the particle production, but also the VSP. The graph shows low VSP events with rotor temperature over 200 °C and emissions under 1010 #/stop as well as high VSP events just under 200 °C with emissions up to 1012 #/stop.

In the graph on the right, particles per kWh power are plotted, with the area of the bubble proportional to the average braking power. This expression, in #/kWh, compensates for the higher production of particles solely due to braking from higher speed, with more energy dissipated. The graph shows that even on per-kWh basis, both higher rotor temperature and higher braking power (more intensive braking) lead to higher particle production. Therefore, it appears that the particle production is not merely a function of the rotor temperature as measured by a thermocouple embedded in the rotor.

The final rotor temperature at the end of the braking is a function of the rotor temperature at the beginning of the braking, which is given by the history of braking events and cooling conditions, the brake design, and the energy dissipated. For practical purposes, energy dissipated can be inferred from speed data available through on-board diagnostics and/or position data from a GPS.

The relationship between the particle production and both the average braking power and the total energy dissipated is given in three graphs in Fig. 10. The left graph shows, on logarithmic scales, a dependency on the particles per stop on the total energy dissipated, with bubble area proportional to the average braking power. While particle

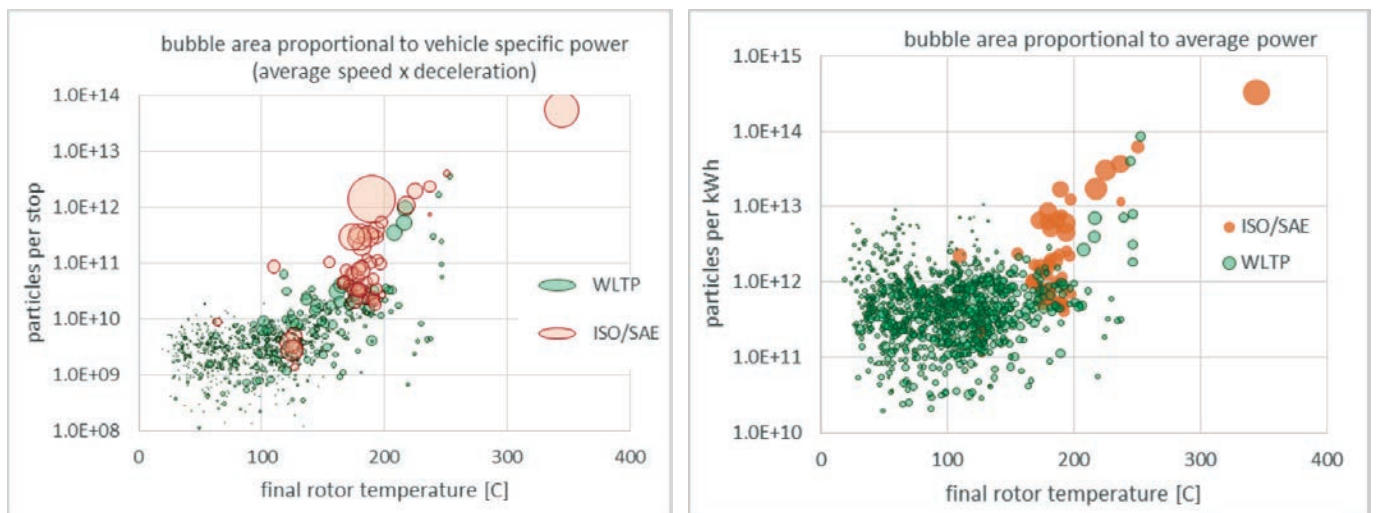
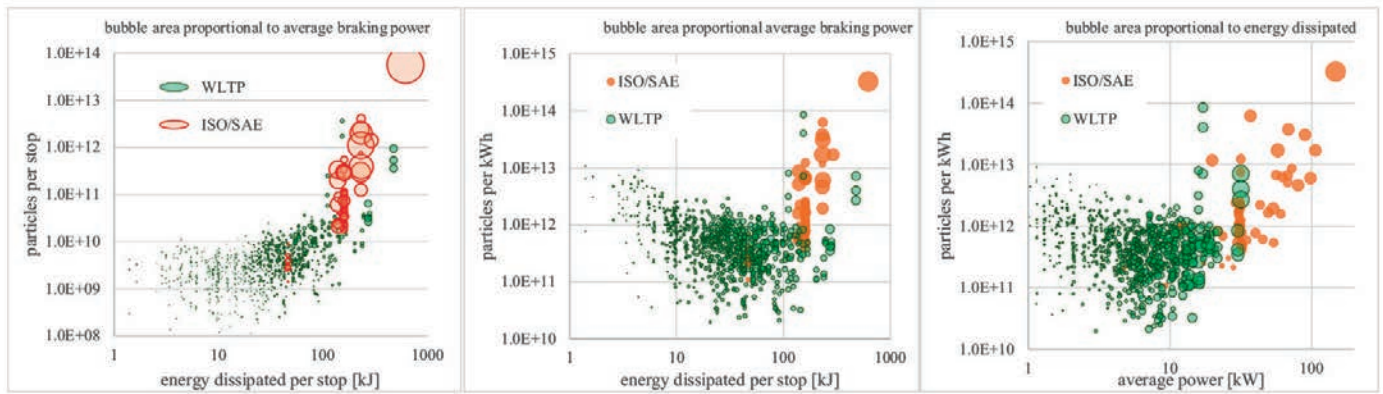
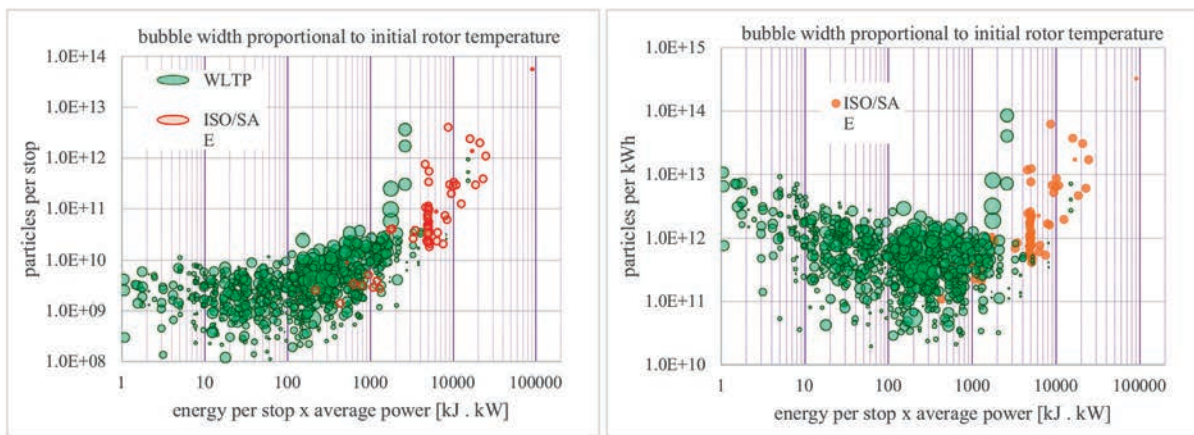


Fig. 9. Total number of particles emitted per stop (left) and per kWh dissipated (right) as a function of the rotor temperature at the end of the test. Left: The bubble diameter is proportional to the vehicle specific power (the product of average deceleration and initial speed). Right: The bubble area is proportional to the average power.





**Fig. 10.** Effects of braking intensity on particle production. Left and middle: Particles per stop (left) and per kWh (right) as a function of energy dissipated, with bubble area proportional to average braking power. Right: Particles per kWh as a function of average power, with bubble area proportional to the energy dissipated per stop.



**Fig. 11.** Particles per stop (left) and per kWh (right) as a function of the product of energy dissipated per stop and average braking power, with bubble area proportional to the rotor temperature at the beginning of the braking.

production is expected to increase with the energy dissipated, this relationship appears to be proportional until about 1010 # and 100 kJ per stop, after which the number of particles increases sharply with increasing energy dissipated, with higher braking power being somewhat associated with higher particle production. This dividing point is shown in the middle graph showing similar relationship, but with particles per kWh on the vertical axis. On the right graph, the average power is shown on the horizontal axis and the energy dissipated is expressed as the area of the bubble. Overall, it is clear that both the energy dissipated and the power play a role. (Note: The correlation of particle emissions with VSP was not as good as the correlations shown here.)

As a theoretical construct based on the above observations, the particle production is plotted as a function of the product of energy dissipated and power in Fig. 11, on the left in #/stop, on the right in #/kWh. The width of the bubble is proportional to the initial rotor temperature and suggests that outliers (higher particle emissions for stops around 200 kJ·kW) can be attributed to higher initial rotor temperature due to previous braking. It should be noted that the highest production per stop and per kWh was during 175 to 100 km/h braking with a rather low initial rotor temperature.

Fig. 12 shows a different representation of the particle emissions per stop, categorized based on the initial speed (horizontal axis), with different series of data elucidating the effects of deceleration rates the differences among the four models of brake pads.

#### 4. DISCUSSION

The relatively low particle number emissions over the WLTP brake cycle, developed to represent typical driving, are in a sharp contrast with the relatively high contribution of brake wear to the total particle emissions, discussed in the Introduction section. This can be partly explained by the source apportionment studies being performed on a mass basis, while particle number has been used as the metric here. Still, the findings seem to suggest that “off-cycle” emissions must represent a significant portion of the overall brake wear emissions, and can therefore potentially be of paramount importance. This has been confirmed in this study, where a single braking event from 175 km/h produced, under laboratory conditions, five orders of magnitude more particles than many milder, lower speed events, corresponding to several thousands of km of driving along the WLTP cycle.

It can be argued that the dilution conditions under on-road operation are different, and that the dilution ratio increases with speed, making the conditions less favorable for the formation of semi-volatile particles. In this study, a rather high tunnel flow rate (and cooling flow rate) of 2400 m<sup>3</sup>/h, on the higher end of a reasonable range, has been used. Nonetheless, the dilution at high speeds might be faster on the road than in the laboratory. This being said, high particle number concentrations at higher concentrations have been reported by other studies, including those considering only non-volatile particles. There-



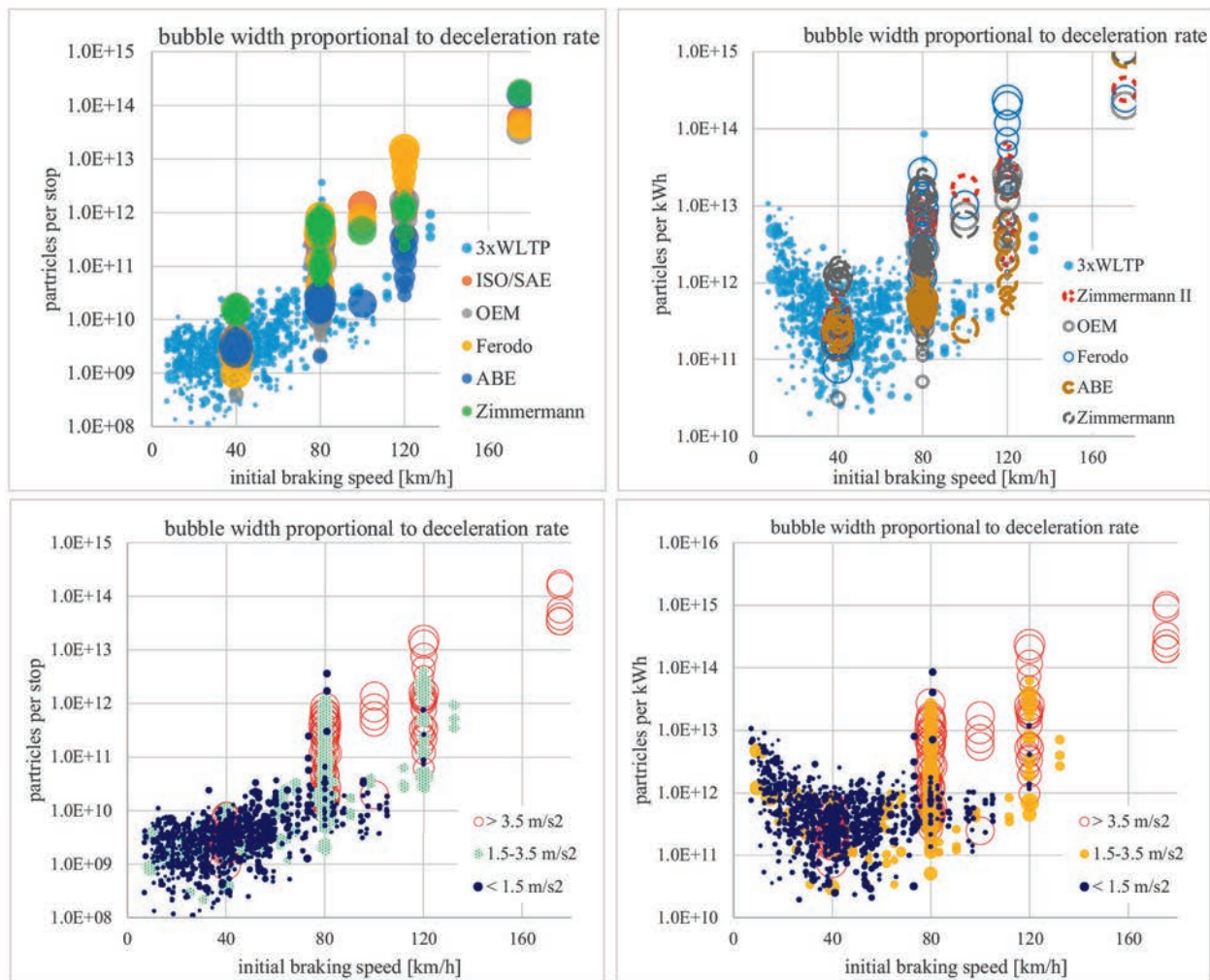


**Fig. 12.** Particles per stop as a function of the initial braking speed; bubble width is proportional to the deceleration rate, expressed per stop (left graphs) and per kWh (right graphs), with different brake pad models plotted in separate series in the upper graphs and different deceleration rates in the lower graphs.

fore, in our opinion, the real difference on the road might be lower than demonstrated here, but still considerable and most likely of several orders of magnitude.

In terms of practical guidance to the vehicle operators and traffic planners, as apparent from data plotted in Fig. 5, Fig. 6 and summary graphs in Fig. 12, all, even intensive, stops from 40 km/h resulted in rather low emissions per stop and per kWh, suggesting decent city driving respecting the 50 km/h limit and avoiding accumulation of heat in brakes by frequent accelerations and braking, should lead to emissions on the order of  $10^9$ – $10^{10}$  #/stop and  $10^{11}$ – $10^{12}$  #/kWh. Assuming the consumption of mechanical power in the 0.1–0.2 kWh/km range for passenger cars, the particle number emissions in such case should be around or below  $10^{11}$  #/km, including semi-volatile matter and including particles in the 5.6–23 nm range, both generally excluded in the Euro 6 solid particle limit of  $6 \times 10^{11}$  #/km for exhaust emissions.

With increasing speed, the overall particle production increases, notably at higher braking power (an order of magnitude effect during 120 to 80 km/h braking), and therefore, harsh braking at higher speeds is to be avoided. For example, braking from 175 to 100 km/h (at  $5.28 \text{ m}\cdot\text{s}^{-2}$  relatively harsh but still far from the  $7$ – $9 \text{ m}\cdot\text{s}^{-2}$  limit of modern vehicles) has caused 4–5 orders of mag-

nitude more particles per stop and roughly 3 orders of magnitude particles per kWh compared to the majority of WLTP braking events at 20–70 km/h.

The findings in this study are consistent with the thermal origin of the nanoparticles observed by Kukutschová et al. (2011) and discussed in detail in Niemann et al. (2020), with strong temperature effects observed by Mathissen et al. (2018) and Zum Hagen et al. (2019). From a thermodynamic perspective, higher deceleration rates most likely lead to higher local temperature at and very near the friction surfaces, where decomposition and volatilization of material is likely to take place. The changes in local temperatures are likely to be much faster than the changes measured by a thermocouple inserted in the rotor, albeit a very short distance from the rotor surface, therefore, local temperatures can temporarily reach values much higher than the average or final rotor temperature reported in the cited studies as well as in this study. The effects of volatilization of semi-volatile binders on subsequent operation are likely to depend on the thickness of the layer that was affected; the data shown in Fig. 7, Fig. 8 show short-term hysteresis but long-term effects (with tens of stops in between), assessed by comparing decelerations from 80 km/h within the first third and at the end of the test sequence, were not readily observed.

Data shown in Fig. 7, Fig. 8 also show that 80 to 30 km/h deceleration produced higher emissions after high-speed braking than during the same deceleration at the beginning of the test sequence (after deburring and degreasing), an opposite trend than what was reported by Niemann et al. (2020) and what would be expected based on the thermal treatment hysteresis. This is not likely a matter of higher background concentrations as these were assessed prior to each braking event. The deposition and reentrainment of semi-volatile materials, typical for exhaust systems of internal combustion engines, examined, for example, in (Vojtisek-Lom et al., 2015), should have much smaller effects on brakes, where there are, compared to engines, far less surfaces on which the deposits can accumulate. While not all answers may be immediately available, overall, there is a significant history effect which is difficult to quantify on a general level.

Despite hysteresis effects, up to two orders of magnitude differences among four makes of brake pads, and up to an order of magnitude combined degreasing effects and repeatability, there is a clear sign that harsher, more intensive braking, both in terms of the total energy dissipated and in terms of the average braking power, leads to disproportionately high emissions of ultrafine particles. The harshest deceleration, from 175 to 100 km/h at  $5.28 \text{ m}\cdot\text{s}^{-2}$ , has produced 8.4 to  $38 \times 10^{13}$  particles (per stop per vehicle), corresponding to, at mean emissions of  $3.3 \times 10^{10}$  particles/km during the WLTP brake cycle, to 2.5–11.5 thousands of km of WLTP-like driving.

From the operator perspective, the aggressivity of driving can be monitored using inexpensive accelerometers and OBD and GPS data, as it is also associated with higher fuel consumption, higher emissions, higher tire wear, and in many cases by increased probability of an accident due to reduced margin of safety.

From the traffic planning and regulatory perspective, the data clearly demonstrates the benefits of enforcing the speed limits, as well as the benefits of reducing motorway speed limits in regions with poor air quality. Both have been proposed and, in some regions, implemented to reduce the emissions of  $\text{CO}_2$ , particulate matter and nitrogen oxides.

Setting a legislative limit on the deceleration rate is not feasible, however, adherence to the general safety recommendations in road design and marking (adequate deceleration lanes, advanced warnings about necessary deceleration, appropriate speed limits), and enforcement of the safe following distance between vehicles, could prevent at least inadvertent harsh braking.

It is the opinion of the authors that given the variance among brake design and friction materials, including the variances among four brake pads observed in this study, there is not sufficient data at this point to provide any specific speed and deceleration thresholds, any quantitative empirical data for modeling purposes, recommendations as to the specific brands of brake pads, and other generalizations and recommendations.

## 5. CONCLUSIONS

In this study, four different sets of brake pads for a common passenger car were subjected, on a brake test-

ing dynamometer, to those parts of standardized brake performance tests believed to be reasonably realistic for common driving. One set of brake pads was also subjected to three runs of the WLTP cycle developed for brake wear particle measurements. Particle size distributions were measured online by Engine Exhaust Particle Sizer sampling from the outlet tunnel of the brake dynamometer enclosure.

While the total particle number (5.6–560 nm electric mobility particle diameter, without removal of volatile particles) was  $3.3 \times 10^{10}$  particles/km on the WLTP brake cycle (for the whole vehicle, average of the three runs of all 10 sections), non-linear increase of the total particle number was observed at higher braking powers and higher total energy dissipated. The harshest deceleration, from 175 to 100 km/h at  $5.28 \text{ m}\cdot\text{s}^{-2}$ , has produced 8.4 to  $38 \times 10^{13}$  particles (per stop per vehicle), corresponding to 2.5–11.5 thousands of km of WLTP-like driving.

Contrary to the findings reported by others, correlating an increase of PN production with the average brake rotor temperature during the braking event, a more complex relationship has been observed in this study. The particle number production appears to be affected by the combination of the initial rotor temperature, total energy dissipated and average dissipated power. At higher particle number emissions, a dominant 10 nm peak was observed, likely caused by nucleation of material volatilized at localized high temperatures at and near the friction surfaces. The product of total energy dissipated and the average dissipated power appears to correlate well with the total particle number production.

## 6. IMPLICATION

From a driver behavior and regulatory perspective, it appears that everything else being equal, nanoparticle emissions from brake wear increase both with the initial speed and with the deceleration rate. Therefore, limiting harsh braking and braking from high speeds has a potential to substantially decrease emissions of brake wear nanoparticles. While an order of magnitude differences were observed among the four sets of brake pads, and what is an acceptable level of brake wear emissions is subject to discussions, and therefore no specific thresholds or limits are recommended here, the findings suggest that there may be benefits of lowering the speed limits on motorways in areas that are congested or otherwise prone to harsh braking. The findings also support the benefits of contemplative, predictive, defensive, smooth driving, reducing the need for braking in general, and reducing the intensity of braking. Many recommendations aiming at road safety, such as highway design and safe driving, and at reducing fuel consumption and exhaust emissions, such as reducing speed and vehicle mass and smooth driving style, are also believed to lower brake wear nanoparticle emissions.

From the brake wear particle measurement perspective, it appears that “off-cycle” braking events, even if relatively infrequent, may be associated with exponentially higher emissions and non-negligible share of the total emissions, and therefore should not be taken out of the consideration.

## Black carbon in spring aerosols of Moscow urban background\*

### INTRODUCTION

At present, air pollution by the smallest suspended particles (aerosols) is recognized as one of the most important environmental problems. Particulate matter characterized by a small aerodynamic diameter of less than 10  $\mu\text{m}$  ( $\text{PM}_{10}$ ) contains environmentally hazardous components and it is recommended by the World Health Organization (WHO) as an air quality indicator. In accordance with the WHO air quality standards for  $\text{PM}_{10}$ , a daily mean maximum permissible mass concentration of 50  $\mu\text{g}/\text{m}^3$  is established (Who 2005). Black carbon (BC) is the light-absorbing component of aerosols, warming the atmosphere and thus affecting the Earth's radiation balance on a global scale (Bond et al. 2013). Estimates suggest that BC is the second most critical factor, following by carbon dioxide, contributing to global warming by direct forcing (Jacobson 2010). BC has drawn a considerable attention because of its environmental significance (Ramachandran and Rajesh 2007; Ahmed et al. 2014; Diapouli et al. 2017).

BC is mainly present in aerosols in urban environment (Mousavi et al. 2018), and thus it concerns local air quality and population health (Janssen et al. 2011). BC-containing particles are small enough to be readily inhaled into the human body and affects the respiratory system leading to exacerbate respiratory, cardiovascular, and allergic diseases, thus relating to adverse health effects (Pope III and Dockery 2006; Steiner et al. 2013). Epidemiological evidence links the exposure to BC with cardiopulmonary hospital admissions and mortality (WHO 2012).

Assessments of the ability for BC to affect the environment and health require a comprehensive study of the aerosol composition as well as a deep understanding of aerosol-related impacts. The comprehensive characterization of aerosols in the urban atmosphere makes it possible to identify sources of pollution and assess the consequences of effects of their emissions on air quality and human health. BC is increasingly recognized as the most important pollution contributor originating from anthropogenic activities, such as fossil fuel combustion (transport, energy production, residential heating) and biomass burning (domestic and wildfires). Diesel exhaust, which comprises high amounts of BC, is classified as a carcinogen for humans by the International Agency for Research on Cancer (IARC). Impact of traditional agriculture biomass burning (BB) activities on regional air quality is a major environmental concern, indicating that it may profoundly affect public health in urban areas (Popovicheva et al. 2017b).

BC emissions are found particularly large in most urbanized Asian cities where the rapid industrial and economic development has been accompanied by serious fine particle pollution of the atmosphere (Ohara et al. 2007; Chen et al. 2014). For US and European cities the source apportionment approach is intensively devel-

oped in order to estimate the most significant and dangerous combustion sources (Herich et al. 2011; Healy et al. 2017). An actual review on the status of ambient pollution in global megacities showed that the five most polluted megacities are Delhi, Cairo, Xi'an, Tianjin and Chengdu, all of which had an annual average concentration of  $\text{PM}_{2.5}$  greater than 89  $\mu\text{g}/\text{m}^3$  (Cheng et al. 2016). European megacities (London, Moscow and Paris) had much lower annual average concentrations between 18 and 21  $\mu\text{g}/\text{m}^3$ . However, these concentrations still are above the air quality guideline set by WHO to 10  $\mu\text{g}/\text{m}^3$  (WHO 2005).

Moscow megacity is the leader among all large cities of Russia on total number of inhabitants. However, for Moscow the situation is currently complicated by the existing lack of the aerosol composition and BC pollution assessments. High anthropogenic emissions of PM in Moscow can occur due to traffic, industry, heating, waste recycling, and construction. Additionally, secondary aerosol formation and long transportation can impact the particulate loading and composition, as it was occurred during an extreme smoke events related to intensive wildfires near the city (Popovicheva et al. 2014; Popovicheva et al. 2019).

However, Environmental Protection Agency "Moscomonitoring" conducts the measurements for only  $\text{PM}_{10}$  and  $\text{PM}_{2.5}$  mass concentrations at some monitoring stations. The analysis of measured daily mean  $\text{PM}_{10}$  concentrations and calculated ones by chemical transport model CHIMERE showed the high temporal variability reflecting the influence of local sources and atmospheric processes (Kuznetsova et al. 2011; Gubanova et al. 2018). Presently, BC is not a subject of the consistent monitoring, it is remaining as a topic of a few scientific research performed in the Moscow center (Golitsyn et al. 2015; Kopeikin et al. 2018).

The purpose of this study is the analysis of the aerosol pollution related to BC in total  $\text{PM}_{10}$  mass in the urban background of the Moscow megacity. Spring season is chosen because this time is characterized by an elevated number of BC sources including the seasonal agriculture fires in surrounding areas and residential BB around the city. We measure and examine the diurnal variability of BC concentrations under real conditions of the diversity of urban sources of emissions and meteorological factors. Wind speed and direction affect BC concentrations while air mass transportation from fire-affected regions support the increased level of BC pollution in spring in the urban background.

### MATERIALS AND METHODS

#### Measurement site

Moscow megacity covers an area of 2 561  $\text{km}^2$  and has a registered population exceeding 12.5 million in 2018. It is the largest city of Russia, and generally represents

\* Popovicheva O.B., Volpert E., Sitnikov N.M., Chichaeva M.A., Padoan S. // *Geography, Environment, Sustainability*. 2020;13(1):233-243.



a typical urban area. Presently, in Moscow megacity 26 gaseous and particulate pollutants ( $PM_{10}$  and  $PM_{2.5}$ ) are under continuous measurements (Kul'bachevskii 2017). Around 630 industrial enterprises of various branches of mechanical engineering and metal working, power engineering, chemistry and petrochemistry, light and food industry, production of construction materials (including 30 000 stationary emissions sources) are registered. Around 50% of all pollutant emissions from industrial sources are emitted by enterprises producing and redistributing energy, gas, and water. Gaseous Automobile transport exhaust composes 95% of total city emissions. According the reports from the Moscow Committee of environmental protection and natural resources and the Department of the Federal State Statistics Service, industrial production zones occupy around 17% of the city area, from stationary sources fourteen biggest enterprises provide up to 85% of gross pollution (Bityukova and Saulskaya 2017) while transport emissions compose up to 93 % of gross pollution from mobile sources (Kul'bachevskii 2017). In total industrial emissions the processing productions, the production of oil products, and the production and power distribution of gas and water are dominated while gas composes 96.7% of fuel consumption. The biggest fractions of industrial emissions are  $NO_x$  (50%), CO (15%),  $SO_2$  (16%) and 11% of volatile organic compounds. The Moscow city often faces serious traffic congestion problems because of the increased vehicle numbers; the total count of vehicles was registered as much as 4.6 million by the end of 2017 (Kul'bachevskii 2017). High speed of construction in Moscow additionally increases the aerosol loading in the atmosphere.

Black carbon mass concentration measurements were conducted at the rooftop of two-story building of the Meteorological Observatory of Moscow State Uni-

versity (MO MSU). MO is located at the territory of the MSU campus, southwest of the Moscow city ( $55^{\circ}07'N$ ,  $37^{\circ}52'E$ ) (Fig. 1).

It takes place in an area of hills Vorobievy Gory which is well ventilated. There is no any industrial plants or commercial areas nearby (Fig. 2). At about 800 m to the north from the MO MSU there is the residential area and to the north-west the Lomonosovsky prospect highway is located. The closed industrial enterprises are central and quarter heating stations, and industrial areas which take place at the distance of 3 km and longer from the MSU. Therefore, MO MSU is considered operated as an urban background site.

### Data collection

Aerosol equivalent BC concentrations (eBC) were measured using the portable aethalometer custom made by MSU/CAO. In this instrument the light attenuation caused by the particles depositing on a quartz fiber was analyzed at three wavelengths (450, 550, and 650 nm). eBC concentrations were determined by converting the time-resolved light attenuation to EBC mass at 650 nm and characterized by a specific mean mass attenuation coefficient as described elsewhere (Popovicheva et al. 2017a). Calibration parameter for quantification eBC mass was derived during parallel longterm measurements against an AE33 aethalometer (Magee Scientific) that operates at the same three wavelengths. Attenuation coefficient  $b_{atn}$  is defined as

$$b_{atn} = A \delta ATN V \quad (1)$$

where  $A$  is the filter exposed area,  $V$  is the volume of air sampled, and  $\delta ATN$  is the light attenuation defined as follows:



**Fig. 1.** Location of the portable aethalometer on the roof of Meteorological Observatory (MO) of MSU during spring campaigns of 2017 and 2018. MO MSU is on a Moscow city map



**Fig. 2.** The map of industrial areas and heating plans in Moscow around MSU. The black dot marked location of MO MSU. CHP - Central Heating Plan, DHS - District Heating Station

$$\delta ATN = \ln(I_0 / I) \quad (2)$$

where  $I_0$  and  $I$  is the light intensity transmitted through unexposed and exposed parts of the filter, respectively. Good linear correlation between the aethalometer's attenuation coefficient  $b_{atm}$ , and the eBC concentrations calculated with the AE33 aethalometer (at 660 nm) was achieved ( $R^2 = 0.92$ ). This allowed the estimation of eBC mass concentrations using the regression slope and intercept between  $b_{atm}$  at 650 nm and eBC of the AE33 aethalometer at 660 nm:

$$EBC = 3.3 * 10^5 * A * \delta ATN / V \quad (3)$$

where  $3.3 \times 10^5$  is the correction factor that includes the specific mass absorption coefficient for the MSU aethalometer calibrated against the AE33 aethalometer. Equation (3) assumes the mass absorption cross-section (MAC) adopted by AE33 equal to  $9.89 \text{ m}^2 \text{ g}^{-1}$ , values for  $A$  and  $V$  used to be in  $\text{m}^2$  and  $\text{m}^3$ . The constant MAC value adopted here is an approximation, assuming a uniform state of mixing for BC in atmospheric aerosol. This can be considered as a valid assumption in case of background aerosol measurements performed in this study. The level of uncertainty of eBC measurements was  $30 \text{ ng/m}^3$  for a 6 min integration time. Aethalometer filters were changed manually, when ATN approach the threshold value around 70 that corresponds the twice decreasing of light intensity transmitted.

Measurements were performed from 17 April to 25 May of 2017 and from 19 April to 23 May of 2018. Continuous measurements of meteorological parameters (temperature, relative humidity, pressure, precipitation, wind speed and wind direction) were performed each 3 hours routinely by MO MSU meteorological service.  $\text{PM}_{10}$  mass concentrations were collected by Moscomonitoring using the tampered element oscillating microbalance TEOM 1400a (Thermo Environmental Instruments Inc., USA). These data were used for the comprehensive database of whole sampling runtime.

In spring time fires are usually observed on the South of the Moscow city, the agriculture practice with a purpose to remove the last year grass on the fields is widespread in this season. Biomass burning in residential areas around city is pronounced, especially during May holidays from 1 to 10 May. Therefore, air mass arriving to urban area due to long-range transportation may impact the air quality of the city, especially if direction of their transportation well correlates with fire-affected regions. To evaluate the air mass transportation impact the backward trajectories (BWT) were generated using NOAA Hybrid Single-Particle Lagrangian Integrated Trajectory (HYSPPLIT) model of the Air Resources Laboratory (ARL) (Stein et al. 2015) with coordinate resolution equal to  $1^\circ \times 1^\circ$  of latitude and longitude. The potential source areas were investigated using 2-day backward trajectories for air masses arriving each 12 hours to the MO MSU at 500 m heights above sea level (A.S.L.). Fire information was obtained from Resource Management System (FIRMS), operated by the NASA/GSFC Earth Science Data Information System (ESDIS). It is based on satellite observations which register the open flaming with temperature above 2000 K. Daily maps were related to the computed trajectories, providing a clear picture of the geographical location of fires, with the several kilometer resolutions. A number of fires which could affect air masses transported to the MO MSU was calculated as a sum of fires occurred at distance  $0.5^\circ$  on both latitude and longitude from BTW. The number of fires passed by BWT was estimated as the sum of the amounts of all points of fire caught on the back trajectories points or in their neighborhood of no further than  $0.5^\circ$  along the latitude and longitude. Number of fires indicates the BB-influenced days.

## RESULTS AND DISCUSSION

### Diurnal BC patterns

The diurnal eBC mass concentrations measured in spring seasons of 2017 and 2018 are shown in Figure 3.



On a daily basis of 2017, there is an increase in concentrations starting from 04:00, and the relatively prominent morning peak occurs at 7:00-09:00. eBC concentrations are found to be the smallest during midday until the evening, around 19:00. After this time the gradual increase of eBC is observed, reaching the maximum at 21:00-22:00. During 2018, the mean diurnal BC mass concentration is found to be constant from midnight to 04:00, the poorly noticeable peak occurs at around 05:00, and after the gradual decrease is marked until 20:00. Morning peak similar observed in spring of 2017 is not observed anymore in spring of 2018. The diurnal variation in mean BC mass concentrations is appeared around  $1 \mu\text{g}/\text{m}^3$ , approaching maximum 2 and 1.8 and minimum 0.9 and  $0.5 \mu\text{g}/\text{m}^3$  during spring of 2017 and 2018, respectively.

The atmospheric abundance of BC is affected by both the stability of the boundary layer and anthropogenic activities in an urban environment (Ramachandran and Rajesh 2007). The nocturnal boundary layer depth is shallower than its daytime counterpart by a factor of 3-5. The development of a well-mixed layer height begins from 08:00, reaching maximum value around 14:00, decreases after 17:00, and later drops to the lowest level at night. The surface inversion after sunset results in the accumulation of BC, causing even higher concentrations in the late evening. It should be noted that in many urban areas the evening peak is happened between 21:00 and 22:00 (Ramachandran and Rajesh 2007; Kozlov et al. 2011; Chen et al. 2014).

In large cities the BC morning peak is well observed

for diurnal mass concentrations; it is attributed to the combined influence of the lower mixing layer height and vehicle traffic enhancement in the morning (Ramachandran and Rajesh 2007; Kozlov et al. 2011; Chen et al. 2014). The minimum BC concentrations are found during midday when there are fewer anthropogenic BC emissions, while the deeper boundary layer leads to a faster dispersion resulting in a dilution of BC concentrations at midday.

Diesel and petrol are the major fossil fuels used for road transportation, the main part of the diesel vehicles are heavy-duty vehicles. Diesel vehicles are known to produce much more BC than the vehicles which run on gasoline (Weingartner et al. 1997). Heavy duty (e.g., trucks, buses etc.) diesel vehicle can contribute an average 42% BC to particulate matter (Reddy and Venkataraman 2002). Vehicles which run on leaded petrol and unleaded petrol (which do not have catalytic converters) can give rise to 6 and 23% of BC in PM mass. They include two-wheelers such as scooters, motor bikes in addition to cars. In Moscow, a mixture of all vehicles runs on the roads and contributes to BC. In 2017 the Uniform interdepartmental information and statistical system ([www.fedstat.ru](http://www.fedstat.ru)) reported around 4640 000 vehicles, including 90.4 and 8.5 % of light and heavy duty cars and trucks, respectively, as well as 1.1 % of buses.

Stable high mean BC concentration from midnight to pre-dawn is observed especially prominent in 2018 (Fig. 3). Such diurnal profile is different from observed in large Russian city Tomsk (Kozlov et al. 2011) and Indian city Ahmedabad (Ramachandran and Rajesh 2007), and in

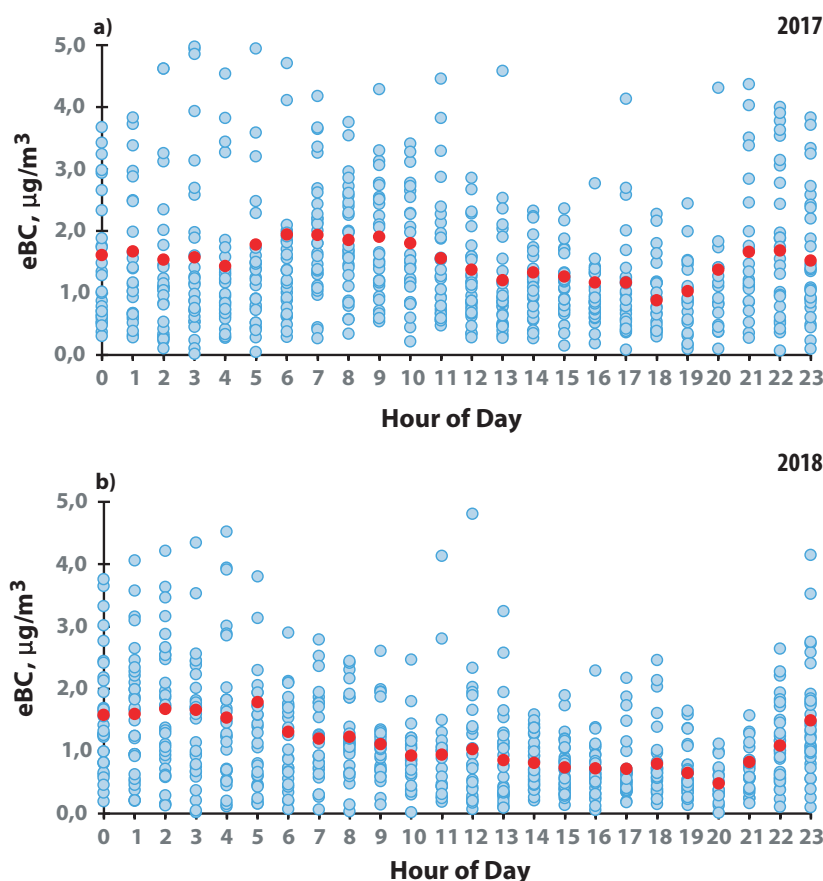


**Fig. 3.** Diurnal variations of hourly eBC concentrations during the sampling periods of a) 2017 and b) 2018 spring seasons. Plotted red points are the average values for aggregated data from the subsequent one hour on available days



megacity Athens (Diapouli et al. 2017). One reason may be related to increased emissions from diesel trucks (especially after 22:00) which could contribute to the higher BC concentration in the late evening (Garland et al. 2008). Here we should confirm that there is a restriction for heavy duty cargo vehicles to enter the Moscow city center during daytime, they are allowed to bring cargo only after midnight. Therefore, probably stable high BC observed later evening and during night time is due to the significant impact of diesel running vehicle emissions (almost from heavy duty cargo transport) in Moscow megacity.

### Relationships between BC and meteorological parameters

The physical and chemical processes of BC emission, transformation, transportation, and accumulation in the atmosphere relate to meteorological conditions, i.e. wind speed and direction, transport of air masses, and the intensity of precipitation. The wind roses at MO MSU in both 2017 and 2018 spring seasons show the relatively homogeneous distribution of the wind direction during the sampling period, with the prevailing south-west direction and with a repeatability frequency up to 10% in this direction (Fig. 4). This finding confirms the observations of the South-West prevailing wind direction in the air layer from 40 to 500 m for the period of 2004-2014 at the MO MSU (Lokoshchenko 2015). The western component of the wind strengthens in spring and summer, that means that the South- Southwest direction is registered more rarely, and the West-Southwest one, more frequently.

The highest frequency of eBC pollution, around 13%, is found during northern wind, according to the eBC pollution roses (Fig. 5), when eBC mass concentrations approached 7 and 5  $\mu\text{g}/\text{m}^3$  in 2017 and 2018, respectively. Other directions of SW (225°), NW (315°), and NE (45°) relating to the high frequency of 6, 5, and 8%, respectively, indicate the most relevant emission source locations. Analysis of the geographical locations on a map shows that in the direction of SW (270-225°) the industrial area "Ochakovo" is located, and two quarter thermal stations take place in the direction of NNW and NW (around 335°), central heating plants can pollute MO MSU from north and NE (45°) (Fig. 2).

Wind speed is an important factor affecting BC concentrations: higher wind speeds contribute to stronger BC dispersion. It is probable that due to higher wind speeds BC produced from local sources are transported to other locations. Such phenomenon is typically observed in polluted urban area (Chen et al. 2014). It was found from BC measurements made in urban sites in Toronto that low wind speeds lead to much less dispersion of BC and the traffic emissions remain concentrated around the emission site (Sharma et al. 2002). It was also noted that as the traffic density was relatively constant through the measurement period, higher wind speeds have a dilution effect on BC. Correlation between wind speeds and BC mass concentrations may give an indication of the proximity of BC sources at the measurement site, while the absence of significant correlation shows that the BC originates from distant sources.

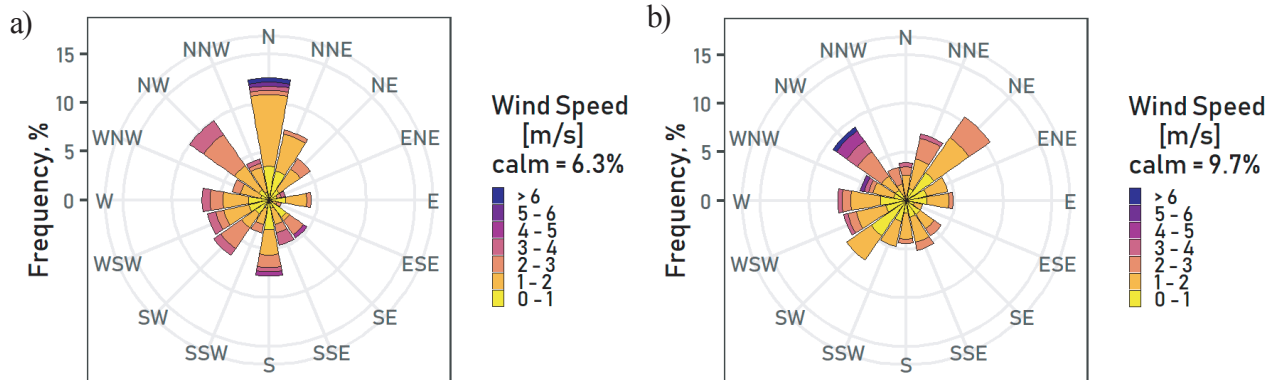


Fig. 4. Wind rose during spring season of a) 2017 and b) 2018

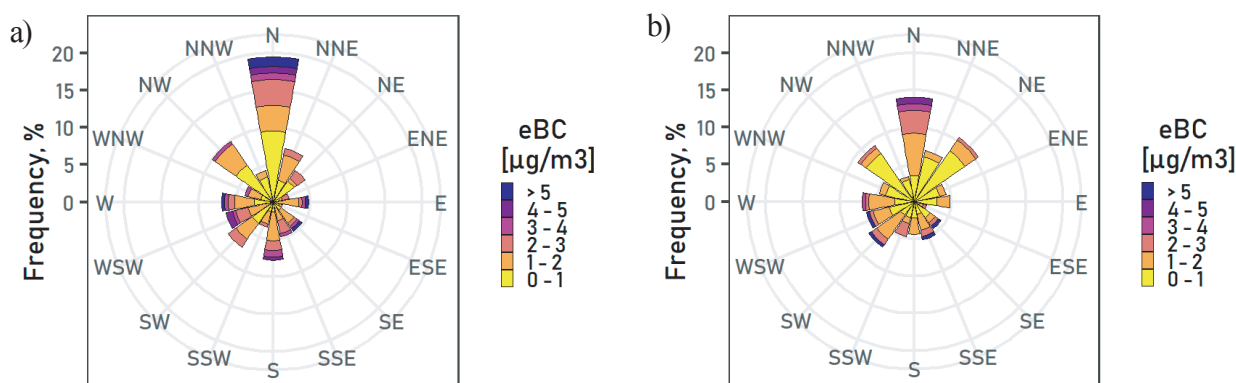
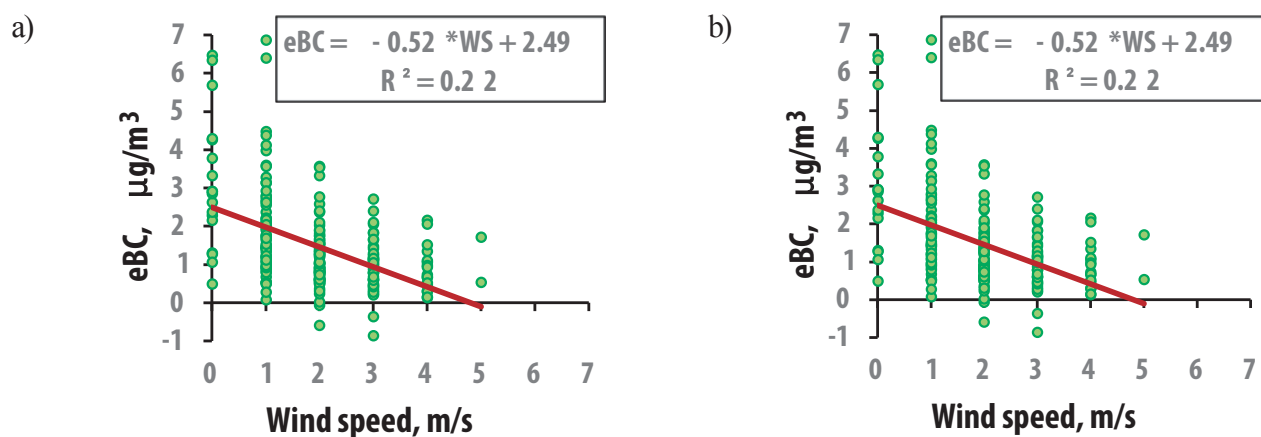


Fig. 5. eBC pollution rose during spring season of a) 2017 and b) 2018



**Fig. 6.** Correlation of eBC mass concentration and wind speed (WS) during the sampling period of a) 2017, and b) 2018 spring seasons. Negative slope is obtained for linear fit of measurement points

A regression of BC mass concentrations with wind speed at MO MSU during spring seasons yield a negative regression coefficient (slope)  $-0.51$  and  $-0.41$ , respectively (Fig. 6). This indicates that with increase in wind speeds the BC mass concentrations would decrease, as seen. Such correlation between wind speeds and BC mass concentrations gives an indication of the intensive BC sources in a megacity.

### Seasonal PM<sub>10</sub> variations

The time series of PM<sub>10</sub> mass concentrations over the whole period of observation is depicted in Fig. 7 and 8 for two-year spring seasons. In 2017, 1h mean PM<sub>10</sub> concentrations showed a strong variation from lowest of  $8 \mu\text{g}/\text{m}^3$  up to the highest value of  $82 \mu\text{g}/\text{m}^3$ , on average  $22 \pm 16 \mu\text{g}/\text{m}^3$ . In 2018, the PM<sub>10</sub> variations from 2

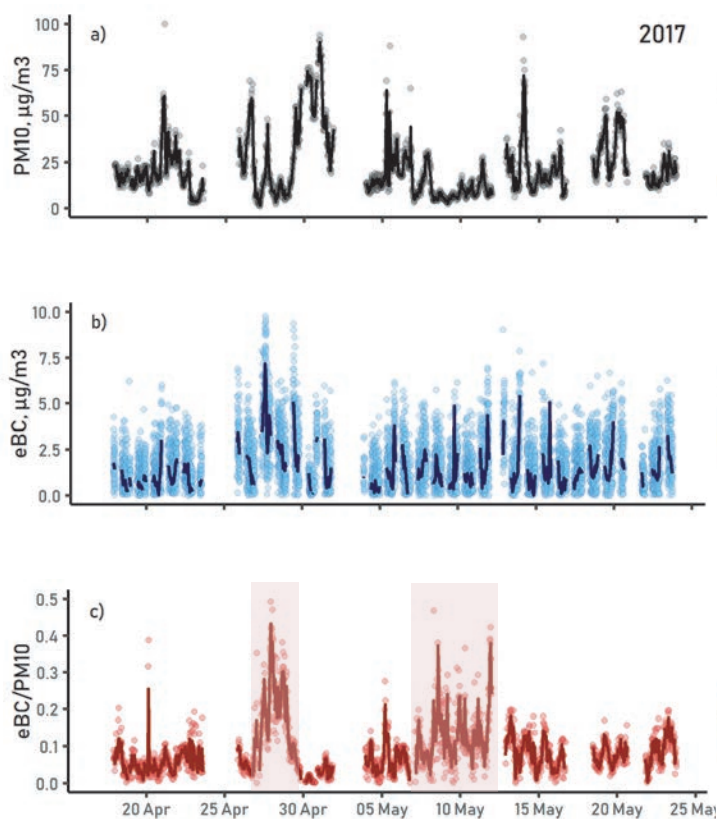


**Fig. 7.** 1-h mean (curve) and 1 min mean (dots) a) PM<sub>10</sub> mass concentrations, b) eBC mass concentrations, and c) eBC/PM<sub>10</sub> ratio in sampling period 2017 on the MO MSU. Pollution episodes are indicated.

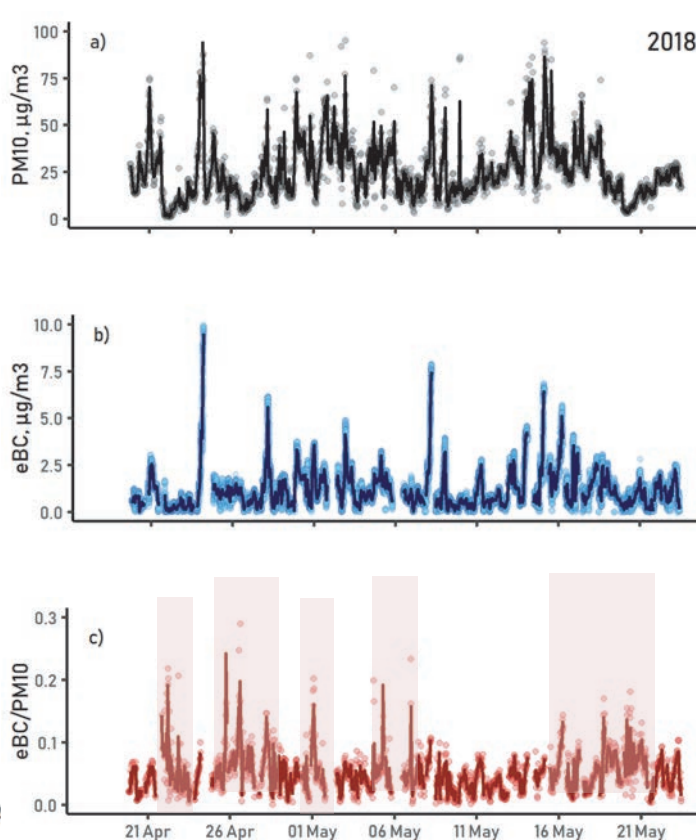


**Fig. 8.** 1-h mean (curve) and 1 min mean (dots) a) PM<sub>10</sub> mass concentrations, b) eBC mass concentrations, and c) eBC/PM<sub>10</sub> ratio in sampling period 2018 on the MO MSU. Pollution episodes are indicated.

to  $90 \mu\text{g}/\text{m}^3$  were even more frequent but on short-term, on average  $26 \pm 16 \mu\text{g}/\text{m}^3$ . These values are comparable to  $\text{PM}_{10}$  concentrations averaged over warm season (May-September) obtained from the data for 236 urban background monitors in Europe in the periods of 2003-2006, on averaged amounts to  $19.9 \text{ g}/\text{m}^3$  (Konovalov et al. 2009). For spring periods of 2014 and 2016  $\text{PM}_{10}$  concentrations was  $30.0$  and  $25.4 \mu\text{g}/\text{m}^3$ , and  $22.5$  and  $17.8 \mu\text{g}/\text{m}^3$  in the Moscow center and at the suburban station, respectively; the difference of 26% between their average values is caused by an addition from urban sources (Kopeikin et al. 2018).

During spring seasons of our study  $\text{PM}_{10}$  concentrations exceeded the daily mean maximum permissible mass concentrations from one to seven times in 2017 and 2018, respectively. The longest episode of the highest  $\text{PM}_{10}$  was observed at MO MSU from 30 April until 3 May of 2017, on average  $55 \pm 19 \mu\text{g}/\text{m}^3$ . Almost at the same days, from 29 April until 2 May the ambient temperature has approached an abnormally high level for this season,  $+ 21 \text{ }^\circ\text{C}$  (Fig. 9). In observation period of 2018, the permissive maximum  $\text{PM}_{10}$  values were exceeded seven times. the ambient temperature has approached  $+ 21^\circ\text{C}$  twice, on 1 and 18 May.

Such exceeding of the air quality standards can occur during meteorological conditions unfavorable for pollutant dispersion, passage of cold atmospheric fronts, and arrival of air masses polluted by fires around the city (Kuznetsova et al. 2011). Analysis of location impact showed that the maximum  $\text{PM}_{10}$  concentration was observed at the stations in the eastern sector of the Moscow city and less often in the west of Moscow, at the MO MSU station (Kuznetsova et al. 2011). This apparently reflects both local sources and a windward position in respect to the prevailing urban transfer. In the Moscow suburban station in Zelenograd city, both measured and calculated daily mean  $\text{PM}_{10}$  concentration was almost always lower than at all urban stations, which confirms that a megalopolis is a significant source of aerosol emissions. Observation of  $\text{PM}_{10}$  in summer showed a distinct correlation between short-term episodes of high  $\text{PM}_{10}$  with the local temperature maximums (Kuznetsova et al. 2011).

A substantial positive correlation between temperature variations and  $\text{PM}_{10}$  measurements at the European stations in the summer months was also established from the numerical analysis (Konovalov et al. 2009).

The existence of this correlation can be attributed to the fact that, as a rule, high-temperature periods are followed by an anticyclonic (blocking) situations promoting the build-up of the atmospheric pollutants (Kuznetsova et al. 2011). The  $\text{PM}_{10}$  concentration maximum is reached directly before or at the moment of the passage of cold front after the period of stagnation. A high  $\text{PM}_{10}$  concentration can also be a result of the wind uplift of aerosols due to wind strengthening before the front passage in a warm sector of a cycle with sufficient precipitation and the air mass change, whereas the situation was preceded by dry weather favorable for the soil erosion.

In our study we observe relatively good correlation between high  $\text{PM}_{10}$  and the local temperature maximums, with correlation coefficient  $R^2$  equal 0.68 and 0.57 for 2017 and 2018, respectively (Fig. 10). It is expected that intensive precipitation may lead to strengthened wet aerosol deposition. Analysis of 24-h  $\text{PM}_{10}$  variation with daily precipitation, shown on Fig. 10, indicates the decrease of  $\text{PM}_{10}$  in relation with days of rain. The most prominently this phenomenon is observed for 18-20 May when during the period of the most intensive rains (more than  $7.4 \text{ mm}$ ) we observed the lowest  $\text{PM}_{10}$  mass (around  $13 \mu\text{g}/\text{m}^3$ ).

### Seasonal BC and level of pollution variations

The time series of 1-h mean eBC concentrations over the spring periods of sampling show the high eBC variability, ranged from 0.1 up to 5 and  $10 \mu\text{g}/\text{m}^3$ , on average  $1.5 \pm 1.3$  and  $1.1 \pm 0.9 \mu\text{g}/\text{m}^3$ , in 2017 and 2018, respectively (Fig. 7 and 8). Observations performed in the Moscow center showed the averaged BC concentrations of 4.4 and  $1.7 \mu\text{g}/\text{m}^3$  while on suburban background station they were consistently less than 3.0 and  $1.05 \mu\text{g}/\text{m}^3$ , in spring 2014 and 2016 (Kopeikin et al. 2018).

Table 1 presents the mean BC concentrations obtained during the spring seasons at MO MSU, and rural and remote sites in different world locations. Comparisons show BC at MO MSU is lower than in European large cities like London ( $2.7 \mu\text{g}/\text{m}^3$ ) (Kendall et al. 2001) and Budapest ( $2.95 \mu\text{g}/\text{m}^3$ ) (Salma et al. 2004). However, the sites in these cities are classified as urban ones taking place in the city center. The closest to the measured BC value for MO MSU we find with the spring mean BC in the less polluted city in the Europe Helsinki,  $1.03 \mu\text{g}/\text{m}^3$  (Jarvi et al. 2008). The biggest BC was observed in the

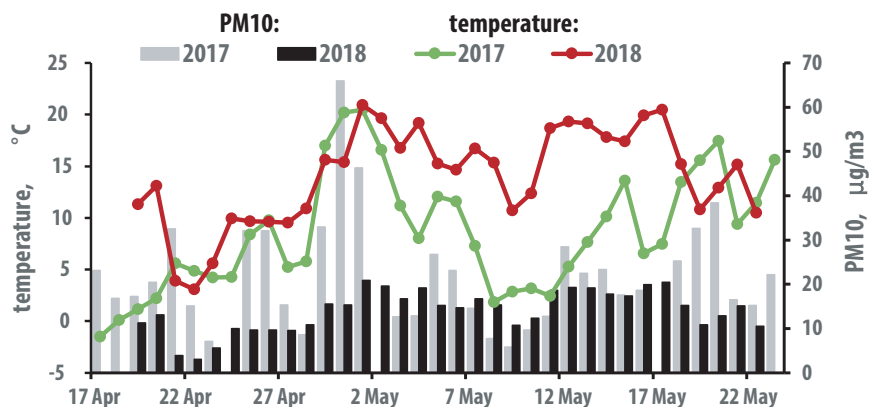


Fig. 9. 24-h mean temperature during the sampling period in 2017 (orange line) and 2018 (red line) and 24-h average  $\text{PM}_{10}$  mass concentrations in 2017 (grey) and 2018 (black)



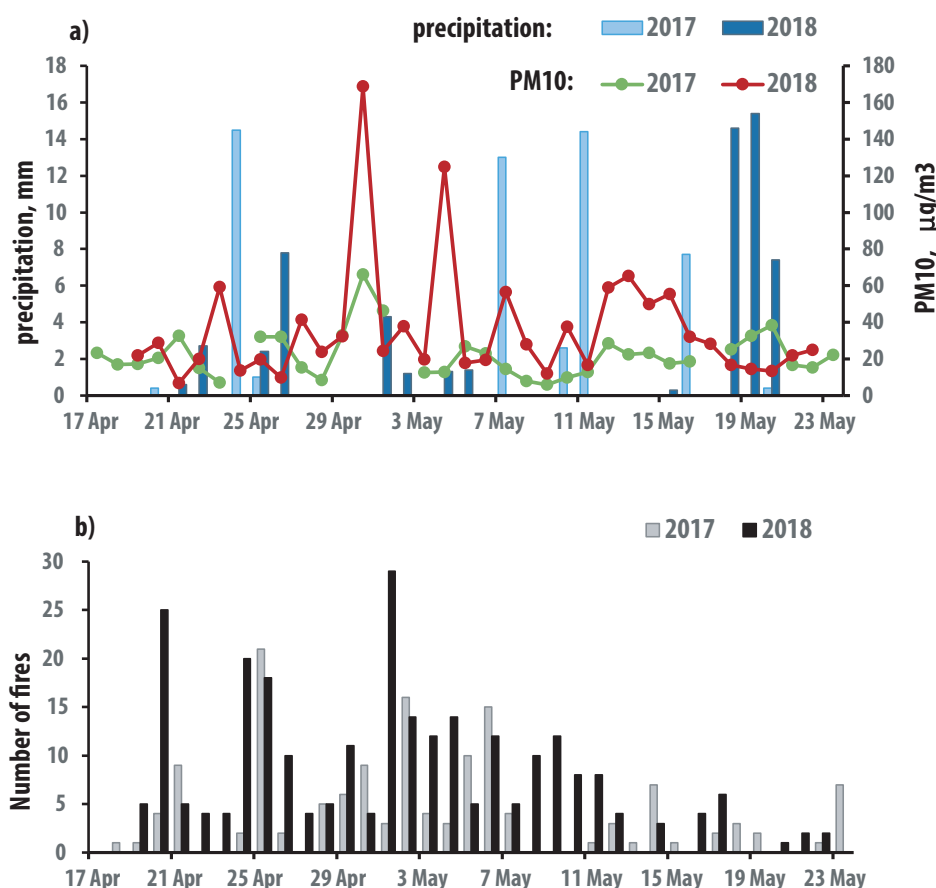


Fig. 10. a) Precipitation and 24-h average  $PM_{10}$  mass concentrations and b) number of fires during the spring seasons of 2017 and 2018

Table 1. Mean season BC concentrations ( $\mu\text{g}/\text{m}^3$ ) at rural and remote sites in different world locations

Site	Sampling period	BC	Reference
<b>URBAN</b>			
MO MSU, Moscow, Russia	April-May	1.1	this work
Helsinki, Finland	2017 – 2018	1.0	Jarvi et al. 2008
Budapest, Hungary	Spring 2004 – 2005	2.9	Salma et al. 2004
London 1, United Kingdom	April-May 2002	2.4	Kendall et al. 2001
Zurich, Switzerland	Spring 1996	1.2	Herich et al. 2011
La Reunion Island, France	Summer 2009 – 2010	0.5	Bhugwant and Brémaud 2001
Dhanbad, India	March-April 1998	5.5	Singh et al. 2015
Nanjing, China	March-April 2012	4.0	Wang et al. 2017
Mexico City, Mexico	April-May 2014	3.4	Salcedo et al. 2006
Guangzhou, China	April 2003	8.9	Wu et al. 2013
<b>RURAL</b>			
Yongxing Island, China	May-June 2008	0.5	Wu et al. 2013
Near Guangzhou, China	May-June 2008	2.6	Wu et al. 2013
Xilinhot, China	April 2005	2.0	Niu and Zhang 2010
Payerne, Switzerland	Summer 2008 – 2010	0.4	Herich et al. 2011

Indian and Chinese cities: around 5.5 and 8.8  $\mu\text{g}/\text{m}^3$  in Dhanbad, the coal capital of India, and Guangzhou, the biggest megacity of South China (Singh et al. 2015) and (Wu et al. 2013), respectively.

Episodes of BC pollution can be identified by the increased ratio of eBC to  $PM_{10}$  (eBC/ $PM_{10}$ ). In 2017, the highest ratio more than 40% was observed from 27 April to 2 May, and around 9 and 13 May (Fig. 7). High temperature in the period of observations approaching

a maximum at those days (Fig. 9) could relate to intensive biomass burning in the region around a city. Analyses of BWT arrived to the MO MSU during sampling period shows the highest number (48.9%) originating from North-West of the Moscow city. The remaining BWT arrived from North-East (28.1%), North – West (16.9%), and South – East (6.2%). Analyses of days of air mass transportation through fire areas demonstrates that the biggest number of open flaming fires occurred on

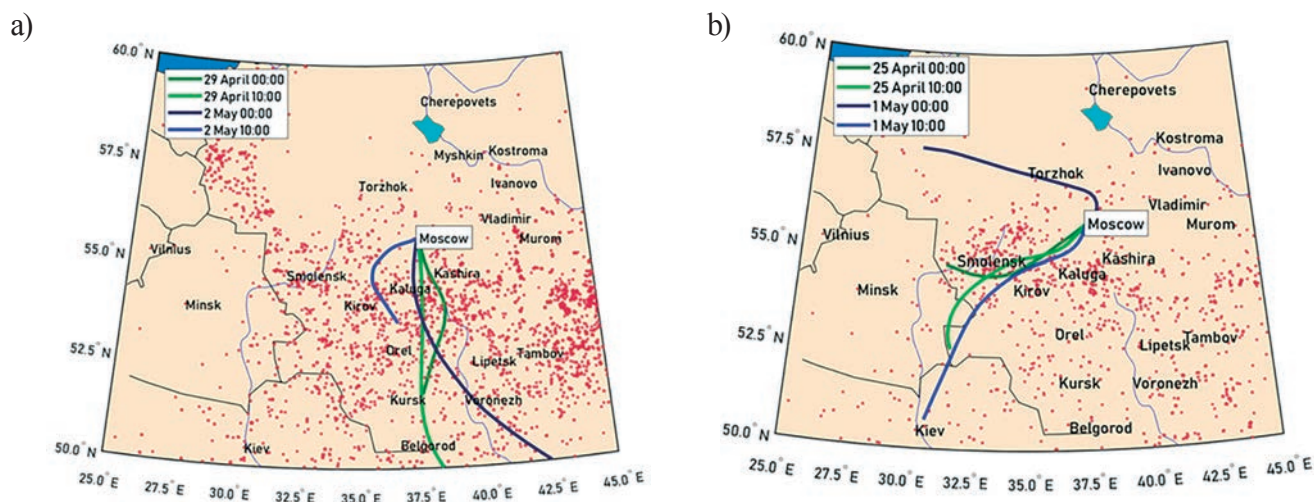


**Fig. 11.** 2-day backward air mass transportation from HYSPLIT model in the days of highest fires observed by FIRMS, 500 m a.s.l., a) 29 April and 2 May 2017, and b) 25 April and 1 May 2018. There are two trajectories for each day: one finished at 00:00 and second at 10:00 of the day.

26 April, 1-5 May (Fig. 10). Figure 11 shows the BWT arrived on 29 April and 2 May from areas with most intensive agriculture fires in south of Russia and Western Europe. Relation of abnormal temperature and the biggest number of open fires to the highest eBC/PM<sub>10</sub> at the days around 2 May confirms the reason of the BC pollution episode on urban background level. In the days of the biggest precipitations (07, 11, and 16 May) the low eBC/PM<sub>10</sub> ratios around 3-5 % were observed, relating to the washout effect.

In 2018, the level of pollution related to eBC/PM<sub>10</sub> showed the periodically repeated increased values of eBC/PM<sub>10</sub>, up to 10 % (Fig. 8). Analyses of BWT arrived to the MO MSU during sampling period shows the highest number (34%) originating from north-east of the Moscow city. The remaining BWT arrived from South - West and North - West (25%), and South - East (16%). The biggest number of open flaming fires occurred in the South-East direction from the Moscow area at the days 20, 24-25 April, and 1 May (Fig. 10). Figure 11 shows the BWT arrived on 25 April and 1 May from areas of most intensive agriculture fires in South of Russia and Western Europe. Such observations confirm that high atmospheric pollutions in Moscow are mainly caused by the transport of pollutions from the regions with intense emissions over a distance of hundred kilometers (Golitsyn et al. 2015).

## CONCLUSIONS

Measurements performed at the Meteorological Observatory MSU improve the luck of the analysis for the aerosol pollution related with BC as the most important pollution contributor in total PM<sub>10</sub> mass in the urban background of Moscow megacity. The highest level of BC pollution, up to 40%, was observed in the days of the May holiday in Russia, related with abnormal high temperature and intensive agriculture fires in the south of Russia and biomass burning around the city. Diurnal profile in the spring season is observed to be different from other large cities: we note stable high BC at night, the less pronounced morning peak in comparison with nocturne BC concentrations, and significant increase of mean diurnal BC late in the evening. As Moscow is an urban, industrialized and densely populated city, the diurnal variations in BC mass concentrations can mainly be attributed to the vehicular emissions and transport from the surrounding regions. Mean spring BC concentrations at urban background of Moscow megacity are observed similar to one in European cities and significantly lower than in industrialized Asian cities, in well relations with intensive transport and using of gas, diesel, and gasoline instead of coal in Asia.

# Functional factors of biomass burning contribution to spring aerosol composition in a megacity: combined FTIR-PCA analyses\*

## 1. INTRODUCTION

Air pollution due to particulate matter (PM) is one of the most important emerging environmental problems. Atmospheric processes and numerous aerosol emissions determine PM chemical properties impacting air quality [1] and human health [2]. The analysis of aerosol chemical composition provides insight into source contributions and strengthens links between particle constituents, health, and environmental impacts. However, the diversity of molecular constituents in the PM organic fraction poses challenges for characterization; detailed chemical analysis is far from being achieved at a molecular level [3].

Fourier transform infrared (FTIR) spectroscopy is a powerful tool for characterizing the aerosol properties, behavior, and origins of the complex organic fraction [4]. It is an analytical technique that captures the signature of a multitude of aerosol constituents and give rise to feature-rich spectral patterns over the mid-IR wavelengths [5]. Aerosol functionalization is highly source-dependent; it varies considerably between urban and rural regions and populated and remote areas, attributing to various classes of oxygen, hydrogen, and nitrogen-containing compounds [6,7].

Particulate emissions from fossil fuel (FF) combustion (motor vehicles, heating plants, energy production) is dominated in urban environment. Health-related properties of aerosols assigned to the biological accessibility and inflammatory potential indicates the importance of the functionalized structure of transport engine-produced particles [8]. For apportionment organic functional groups to sources, recurring FTIR spectral features were associated with available emission tracers [4]. The FF combustion factor had found as a mixture of alkane, hydroxyl, and carboxylic acid groups, with small contributions of amine and carbonyl groups. FF factors have characteristic peak locations common with fuel standards: gasoline, diesel, and oil [9]. Diesel emission analyses based on an evaluation of the relationship between engine, fuel, operating condition, and particle composition highlight the functional markers of the organic structure [10,11].

The main part of the diesel transport is heavy-duty vehicles (e.g., trucks, buses, tractors, etc.), which produce more black carbon than vehicles that run on gasoline [12]. However, the examination of carbonaceous PM emissions and secondary organic aerosol (SOA) formation from modern diesel particle filter (DPF) and catalyst-equipped diesel cars showed that they are markedly lower than from gasoline vehicles [13]. This emphasizes a need for additional quantification of functional markers of gasoline emissions as well.

Biomass burning (BB) affects the composition of particles by a large amount of incompletely oxidized products related to a significant proportion of basic sugars, fatty acids, and aldehydes [14]. Wood combustion releases

oxygenated polyromantic hydrocarbons (PAH) and acids with increased temperatures, whereas wood combustion releases oxygenated phenolic compounds and sugars derivatives at lower temperatures [15,16]. Alkane, carboxylic acid, amine, and alcohol functional groups are mainly associated with FF-related sources, while non-acid carbonyl groups are likely from BB events [6].

Multivariate calibration methods were developed to quantify the ambient aerosol organic functional groups and inorganic compounds [17,18]. They are associated to sources of emissions with the highest consistent contributions [4]. Apportionment of organic functional groups has identified FTIR spectral features of emission factors of the respective sources such as FF combustion, biogenic, BB, and ocean sources. Compositional analysis, functional group correlations, and back trajectories were used to identify three types of periods with source signatures: primary biogenic-influenced, urban-influenced, and regional background [7].

However, a complete set of internal standards for calibration of organic components in the atmosphere is not available, in part because the ambient particle composition is not fully known. Quantitative source apportionment developed for FTIR data can be applied only on a given instrument where the calibration was done. This leaves a need for further developing the chemometric techniques to apply to spectroscopy data analyses. In addition, the complexity of ambient mixtures of organic compounds in the atmosphere results in mixtures that cannot be fully resolved by FTIR spectroscopy [3], which requires the application of complementary aerosol characterization. From the other side, optical aerosol characteristics such as spectral absorption can act as complementary for identifying the source impact on the aerosol composition [19,20,21,22].

A promising approach for analyzing the FTIR spectral data is a chemometric tool such as principal component analysis (PCA). It had been used for determination of the physico-chemical properties of multi-component mixtures and discrimination between different chemical compositions [14,23,24]. The advantage of combined FTIR-PCA is that it can investigate chemical variations between well-defined species that can provide a clear parametrization for the analyses of spectral differences and identification of characteristic chemical components [25]. In urban areas, the apportionment of multifunctional aerosol compounds remains largely uncertain because of the plurality of emission sources. In the Mexico City Metropolitan Area (the second largest megacity in the world), FTIR-based studies found motor vehicle emission, oil burning, BB, and crustal components to be the main sources [6].

Moscow is the largest city in Europe. Moscow often faces serious traffic congestion problems because of the increased vehicle numbers; the total count of vehicles was registered as much as 4.6 million by the end of 2017 [26]. The uniform interdepartmental information

\* Popovicheva O., Ivanov A., Vojtisek M. // Atmosphere. 2020; 11(4):319–339.



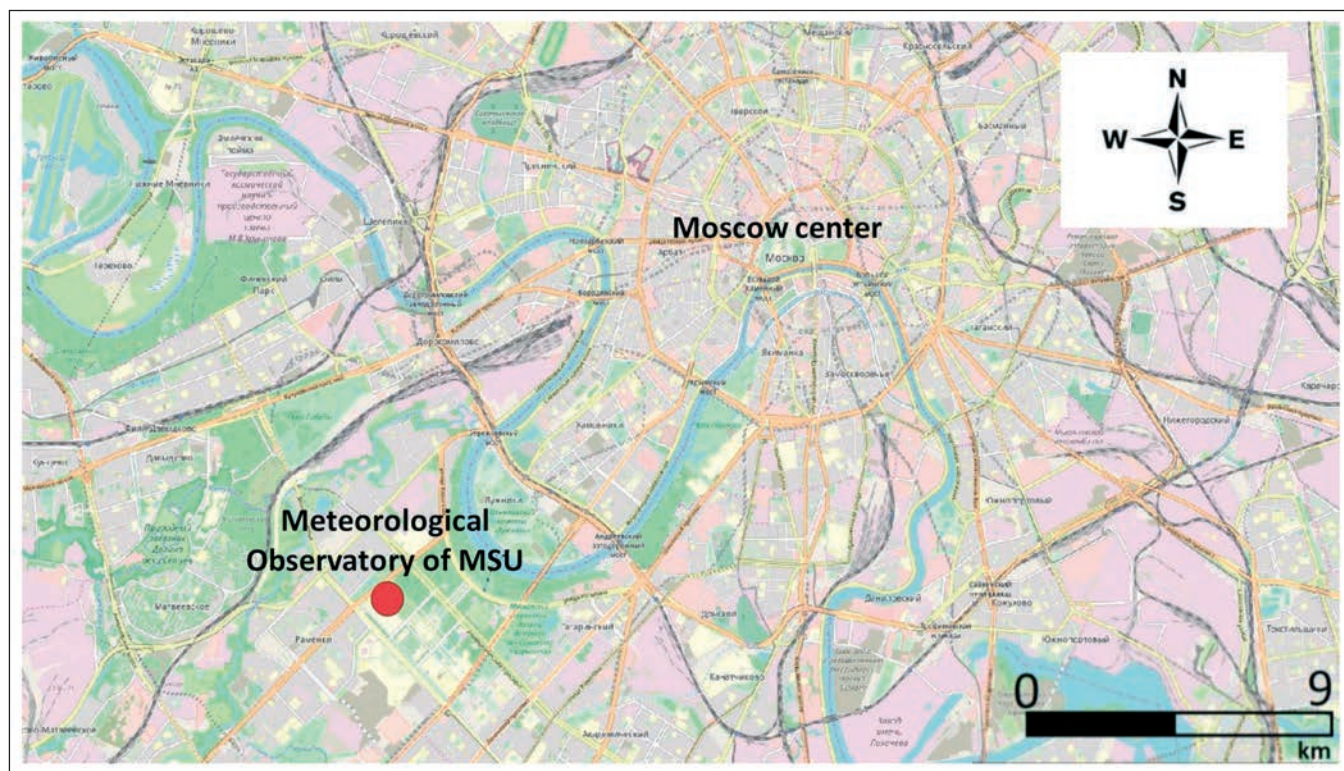


**Figure 1.** Map of Moscow city. Meteorological station of Moscow State University is indicated.

and statistical system ([www.fedstat.ru](http://www.fedstat.ru)) reported around 4,640,000 vehicles, including 90.4% and 8.5% of light- and heavy-duty cars and trucks, respectively, as well as 1.1% of buses. According to the Department of the Federal State Statistics Service, in the Moscow megacity, transport gaseous emissions compose up to 93% of the gross pollution from mobile sources [26].

Despite Moscow facing air quality problems [27], a lack of aerosol chemical characterization is significant. The pollution data presented for Moscow between global megacities are available only for particulate mass of size less than  $10\ \mu\text{m}$  ( $\text{PM}_{10}$ ) and  $2.5\ \mu\text{m}$  ( $\text{PM}_{2.5}$ ) masses [28]. The impact of BB is assumed negligible because the central heating system is operated. However, during an extreme smoke event in the Moscow megacity, a waste range of hydroxyl, aliphatic, aromatic, acid and non-acid carbonyl, and nitro compounds had indicated the intensive wildfires around a city as a major source of pollution [29]. The first steps to source the apportionment on the bases of organic and inorganic composition characterization was made in

This paper is devoted to aerosol characterization of the Moscow megacity urban background in spring season, when the megacity is most affected by a plurality of emission sources. FTIR spectroscopy complemented by the functional groups represent the classes of compounds in the entire aerosol composition. Analyzed spectral absorption provides the parametrization of Angstrom Absorption Exponent for identification of the periods dominated by FF and affected by agriculture and residential BB. Functional markers for diesel emissions related to modern engine technology and driving cycles as well as regional BB indicate to which extent the FF and BB emission sources impact the aerosol composition in urban environment. Because the identification of functional markers for gasoline car emissions had not been

done before, we have conducted the sampling campaign and characterize the functional structure of gasoline particulate emission, based on European standard protocols. Comparison of the day-to-day functional group composition shows the changes over the range of major functional factors influenced the aerosol composition. We attempted to interpret each PC loading in terms of chemical composition, relating them to functional factors.

## 2. EXPERIMENTS

### 2.1. Ambient Sampling Campaign

The intensive campaign was performed in the southwest of the Moscow city from 17 April to 25 May 2017. Aerosol sampling was conducted at the rooftop of two-story building of the Meteorological Observatory of Moscow State University (MO MSU) ( $55.07'\ \text{N}$ ,  $37.52'\ \text{E}$ ) (Figure 1). MO MSU is located at the territory of the MSU campus, in an area of Vorob'evy Gory hills, which is well-ventilated. There are no industrial plants or commercial areas nearby. At about 800 m to the north and north-west from the MO MSU, there are the residential area and the Lomonosovsky prospect highway, respectively. The closed industrial enterprises are central heating stations at a distance of 3 km from the MSU. Therefore, the MO MSU is considered an urban background station. The recent aerosol and its radiative effects observed at MO MSU during the AEROCITY 2018 experiment was presented in [30].

Sampling of particles with diameter less than  $10\ \mu\text{m}$  ( $\text{PM}_{10}$ ) was performed on 47 mm quartz fiber filters (preheated at  $600\ ^\circ\text{C}$  in advance) at 24 h intervals from 8 p.m., totaling 38 samples. Measurements of meteorological parameters (temperature, precipitation) was performed each 3 h by the MO MSU meteorological ser-

vice. PM<sub>10</sub> mass concentrations were collected by the Mosecomonitoring Agency using the tampered element oscillating microbalance TEOM 1400a (Thermo Environmental Instruments Inc. Franklin, MA, USA).

To evaluate the air mass transportation impact, the backward trajectories (BWT) were generated using the HYbrid Single-Particle Lagrangian Integrated Trajectory (HYSPLIT) model of the Air Resources Laboratory (ARL) [31] with a coordinate resolution equal to 1° × 1° of latitude and longitude. The potential origin areas were investigated using two-day back trajectories for air masses arriving each 12 h to the MO MSU at 500 m heights above sea level (A.S.L.). Fire information was obtained from Resource Management System (FIRMS), operated by the Earth Science Data Information System (ESDIS). Daily maps were related to the computed trajectories, providing a clear picture of the geographical location of fires, with a resolution of several kilometers. The number of fires that could affect air masses transported to the MO MSU was calculated as the sum of fires that occurred at a distance of 0.5° on both latitude and longitude from the BWT.

## 2.2. Near-Gasoline Source Sampling Campaign

A Ford Focus car with a downsized three-cylinder 1.0-L turbocharged gasoline direct injection (DISI) Eco-Boost engine (12-valve, 999 cm<sup>3</sup> displacement, Euro 6) and a Škoda Fabia car with a naturally aspirated multi-point injection (MPI) engine (1394 cm<sup>3</sup> displacement, Euro 5) were used for emission sampling. Ordinary gasoline without oxygenated compounds with a nominal research octane number of 95, meeting CSN EN228 specifications, was obtained from a local gas station (EurOil). The Ford Focus car was tested on a chassis dynamometer using the full length of the Common Artemis Driving Cycles (CADC), including urban, rural, and motorway (130 km/h maximum speed) parts. The exhaust was routed into a full-flow dilution tunnel, from which samples were taken on quartz fiber and Teflon membrane filters during three runs of the CADC. The results of vehicle emissions tests have been described previously elsewhere [32].

## 2.3. Methods and Techniques

FTIR spectra of filter samples were acquired using an IRPrestige-21 spectrometer (Shimadzu, Kyoto, Japan) in a diffuse reflection mode, described in details elsewhere [10,11]. Spectra were recorded in the 450 to 4000 cm<sup>-1</sup> range with 4 cm<sup>-1</sup> resolution and 100 accumulated scans. IR Solution software was applied to subtract the spectrum of blank substrates as well as to perform the Kubelka-Munk (K-M) conversion into a quasi-quantitative spectrum correlating with the sample concentration. Basis line correction was done by a subtraction of basis line function spectra.

To address the possible inhomogeneity of the sample loading, spectra were collected from three–five different spots on each sample. One spectrum was taken as representative of the entire sample, because it shared the biggest number of common absorption bands with others. Spectra in the range 3600–4500 and 1790–2500 cm<sup>-1</sup> were not considered because dominant absorption of water vapors and CO<sub>2</sub>, respectively. Because blank quartz filters exhibit strong absorption bands in the 770–860 and 972–1530 cm<sup>-1</sup> spectral ranges, causing the majority

of uncertainty, their examination was excluded from the following analyses.

The FTIR spectrum was divided into the vibration band regions, which are unique for each chemical compound [33]. Extensive knowledge is required for the identification of the functional groups. The common approach used in FTIR studies for the interpretation of the IR absorbance peaks is based on the referencing to spectroscopic guides and bands observed in previously published data [34,35]. Because of the possible overlapping of vibration bands and in order to avoid the discrepancy obtained in measurements performed by various spectral modes and apparatus, the interpretation of the IR spectra in this work was based on the database purposely built using the measurements performed on the same FTIR setup. We based our methods on the approach for identification of functional groups represented by wavenumbers of the absorption bands typical for ambient aerosols, according to previous comprehensive field observations and calibrations [5,18,34]. Additionally, the analyses of IR spectral features of near-source emissions performed in previous studies on the same apparatus [10,36] were summarized.

The database was completed through the use of a set of authentic chemical standards. Supplementary Materials Table S1 lists classes and compounds included into the database. We address 16 classes of organic compounds (alkanes, alkenes, polyaromatics, carboxylic acids, carbohydrates, amino acids, amines, aldehydes, ketones, esters, lactones, quinones, nitrocompounds, formats, alcohols, humic-like substances (HULIS), and sugars) and inorganic compounds (sulfates, nitrates, carbonates, and sulfuric acid). Absorbance peaks related to organic (hydroxyl O-H, carbonyl C=O, aliphatic C-C-H and C=C-H, polyaromatic C=C and C=C-H, C-O, N-H, C-N, -NO<sub>2</sub>, C-O-C) as well as ionic (NO<sub>3</sub><sup>-</sup>, CO<sub>3</sub><sup>2-</sup>, NH<sub>4</sub><sup>+</sup>, SO<sub>4</sub><sup>2-</sup>) functional groups are assigned in Table S2.

Off-line examination of light attenuation of particles deposited on quartz filter samples was performed using the multiple wavelength light transmission instrument (transmissometer) based on the methodology of [19]. The intensity of light attenuation through quartz filters was measured at seven wavelengths from the near-ultraviolet to near-infrared spectral region. Five different areas of the sample filter were analyzed in order to assess the possible heterogeneity of the sample. Then, the averaged attenuation (ATN) was used for the parametrization of the dependence of the attenuation (ATN) on the wavelength  $\lambda$  using a power law relationship:

$$ATN = k\lambda^{-AAE} \quad (1)$$

where the Absorption Angstrom Exponent (AAE) is a measure of a strength of the spectral variation of aerosol light absorption. It was shown that light attenuation is primarily due to particle light absorption [37]. In the optical transmission method employed here, the aerosol particles were collected using reflective quartz fiber filters, which brings uncertainty because light scattering by the filter fibers provides the embedded particles multiple opportunities to absorb light. Black carbon (BC) produced by high-temperature combustion sources fit within the Rayleigh scattering regime for near-visible wavelengths with a theoretical  $\lambda^{-1}$  relationship [38]. Weak spectral dependence of ATN with AAE around 1 was found for diesel soot and urban aerosols produced by fossil fuels combustion [19], and as much as 4.1 for peat burning



[39]. Spectral absorption of BB shows the combined impact of both BC absorbing from 670 nm down to 500 nm and brown carbon (BrC), which increases the absorption below 500 nm.

## 2.4. Functional Markers

Fuel combustion processes yield the basis particulate functionalized structure determined by a high and low combustion temperature [4,16,40]. Characterization of near-source emissions was conducted in order to emphasize the specific atmospheric pollutant functional patterns from the major local sources and then to compare them with those identified in the urban environment [22,29]. Observations of dominant alkane functionalities of particles emitted by an Opel Astra diesel engine [41] and BMW and John Deere engines operating at the stationary and transient conditions [42] are in a good agreement with the quantification of total aliphatic compounds in diesel emission constituting 68% carbon by weight [43]. Aromatic C=C functionalities accompanies aliphatic C-C-H, with less prominent carbonyl C=O and nitro-ONO<sub>2</sub> functionalities, in the particulate emission of the most widely used Iveco Tector heavy-duty diesel engine operated in a World Harmonized Transient Cycle (WHTC) using conventional EN 590 diesel fuel [11]. A similar functional pattern was observed in emissions of off-road diesel engines [10] operated in standard Non-Road Steady State cycle, which is identical to the ISO-8178 non-road engine emission certification procedure.

Therefore, we assumed that diesel transport emissions significantly impact the aerosol composition in Moscow environment. Then, we suggested that the diesel emission functionalized structures of the common transport system operated at the most widely distributed fuels and driving cycles described above as functional markers for transport impact onto Moscow aerosol composition. Since real-world engine operating conditions are best represented by a transient cycle (where both engine speed and fuel consumption vary) [44], we took into account the functional patterns of particulates emitted during transient diesel engine operation cycles as markers for the following source apportionment.

In order to address the gasoline transport emission, the functionalized patterns of particulate matter emitted from the DISI engine, using gasoline fuel with an octane number of 95 of CSN EN228 specifications, were analyzed. For this study, spectra obtained at an urban ARTEMIS driving cycle commonly applied in a city were used as a functional marker for diesel transport emission.

Since BB occurs in various phases and for different biomasses, we identified the functional pattern that can represent the regional BB features impacted the aerosol composition in a city. With a purpose to quantify the functional markers for Moscow regional wildfire and residential emission, the small-scale experimental open fires were conducted in the Moscow region at the location where intensive forest fires were observed [29]. Both combustion phases (low-temperature smoldering and open flame (flaming)) represent the BB process [45]. Therefore, for the purpose of this study, we used both spectral data for smoldering and flaming of regional BB as functional markers. To address agriculture fires relating to grass combustion, the inside and above grass burning spectra data were additionally considered, which were collected from the measurement campaign conduct-

ed during the peat burning event near Moscow [39].

Carbonates (CO<sub>3</sub><sup>2-</sup>) were identified in the range 880–860 cm<sup>-1</sup>; their presence in the PM size fraction was confirmed by thermo-optical measurements of carbonates in form of carbonate carbon [46]. Relative concentrations of carbonates increased from low to high amounts of smoke, thus showing the impact of re-suspended soil particles during intensive agricultural fires on the composition of coarse ambient aerosols. We should also note the prominent similarity of the position of the 880 cm<sup>-1</sup> vibration band of carbonates in ambient aerosols, similar to spectra of flaming emission. This indicates the wide distribution of dust in the urban atmosphere as well as dust of soil evolved by air convection during fires impacted the city atmosphere [22].

The soil-related particles are due to transportation, construction, agriculture, and wind erosion. Dust functionalities are specific features of coarse particles related to soil; Blanco and McIntyre (1972) reported quartz, silicates, and kaolinite to be the main constituents of coarse PM. We refer to the published data for the bands of dust-related functionalities in silicates, quartz, and kaolinite [47]. The band that appeared at 914 and 950 cm<sup>-1</sup> is attributed to Al-OH vibrations in the octahedral sheet structure of kaolinite [48] and Si-OH stretching [49], respectively.

## 2.5. Principal Component Analyses

PCA is a well-known chemometric procedure that allows the rotating the space spanned by the original variables to a new space, spanned by the Principal Components (PCs), in which most of the information contained in the original data is reported in the first (generally two or three) PCs [50]. The PCs are obtained using both the covariance data matrices (scaling by mean-centered data). Visualizing the two-dimensional (2D) plot of PC1 vs. PC2 (and/or PC3) allows studying the behavior of samples (in the scores plot) and variables (in the loadings plot).

For the preparation of the data matrix for PCA analyses, after conversion to K-M mode, the smoothing of the FTIR spectra was performed by a method of smoothing spline, using the minimizing of the mischief function and penalties for irregularities. Then, spectra were subjected to secondary derivatization by an approach described elsewhere [25]; the second derivative is beneficial in highlighting the difference between spectrum and minimization of the noise. A matrix for 25 daily FTIR spectral intensities and variables of 797 wavenumbers was built. Principal component analysis (PCA) decomposes the data matrix and concentrates the source of the variability into the first few PCs.

## 3. RESULTS AND DISCUSSIONS

### 3.1. FF and BB-Affected Periods

PM<sub>10</sub> mass concentrations over the sampling period show a strong variation from the lowest of 8 µg/m<sup>3</sup> to the highest value of 64 µg/m<sup>3</sup>, on average 22 ± 16 µg/m<sup>3</sup> (Figure 2). The longest episode of the highest PM<sub>10</sub> was observed at MO MSU on 29 and 30 April, on average 55 ± 19 µg/m<sup>3</sup>. On nearly the same days, from 29 April until 2 May, the ambient temperature approached an abnormally high level for this season: +21 °C. We observed



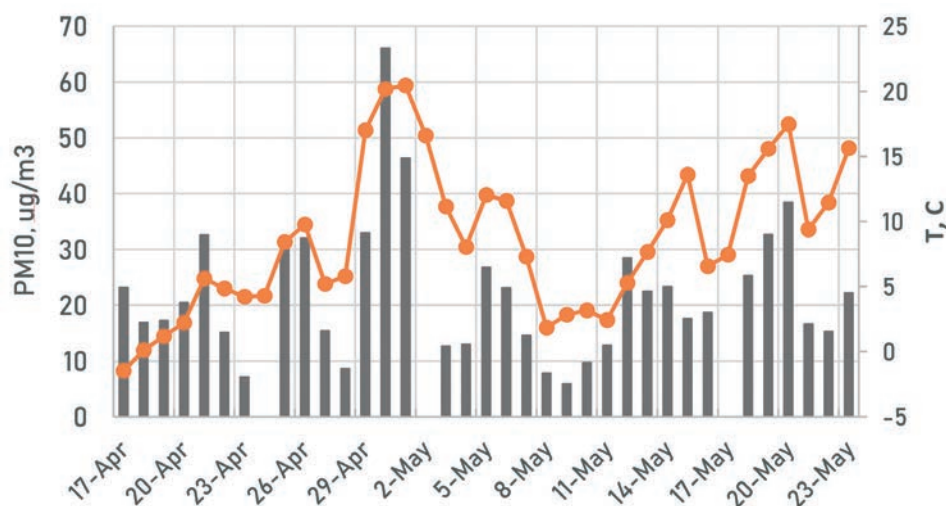


Figure 2. PM<sub>10</sub> mass concentrations and temperature over the sampling period at MO MSU.

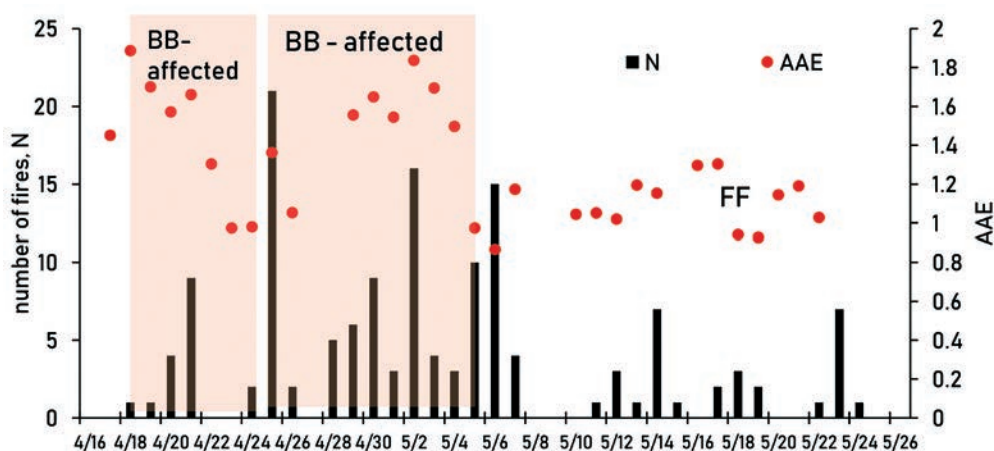


Figure 3. Absorption Angstrom Exponent (AAE) obtained from spectral dependence of aerosol light attenuation and number of fires (N) passed by air masses.

relatively good correlation between high PM<sub>10</sub> and the local temperature maximums (Figure 2), with correlation coefficient  $R^2$  equal 0.68.

The spectral dependence of the light attenuation (ATN) for daily samples was found to be well approximated by a power law equation (1). The Absorption Angstrom Exponent (AAE) was obtained as the slope of the linear regression with  $R^2$  around 0.9. Variation of the ATN spectral dependence during the whole sampling period exhibits the range of AAE from 1.03 to 1.95 (Figure 3). The values above 1.0 may indicate that brown carbon (BrC) associated with organic carbon in addition to BC contributes significantly to the measured light absorption of biomass smoke aerosols in ultraviolet and visible spectral regions [51]. The authors in [19] obtained a high value of 2.5 for smoke of savanna fires, while peat bog burning near Moscow region was characterized by AAE around 4.2 [39].

In spring time, fires are usually observed south of Moscow, an agriculture practice with the purpose to remove last year's grass on the fields that is widespread in this season. BB in residential areas around the city can also be pronounced, especially during the May holidays from 1 to 6 May, because of the high temperatures during that time. Therefore, we could assume that the analyses of the aerosol spectral dependence of light absorption during the studied time can indicate the impact of fire-af-

ected air mass on the aerosol chemistry in Moscow.

From 17 to 22 April, AAE values higher than 1.4 were observed (Figure 3). During this period, the air masses were transported from the north and passed the agriculture fires close to Moscow (Figure 4). On 23 April, the direction of air mass transportation changed to the west, while from 25 April to 2 May the direction was consistently from the south. On 23 and 24 April, the AAE dropped to 1.0. Since 25 April, the AAE became higher again, in correlation with a large number of fires observed in the south of Moscow (Figure 4). Moreover, the period from 30 April–5 May coincided with a vacation period in Russia when the warm temperatures (Figure 2) stimulated intensive residential activity around Moscow city, such as garden cleaning, grass burning, and barbecues. After 4 May, the direction of air mass transportation changed to the arctic region (Figure 4), leading to a drop of temperatures of a few degrees. On 11–13 May and 17–20 May, the air mass changed its direction from the west and east, respectively (Figure 4). On 5 May, the AAE dropped to 0.97 and no longer exceeded 1.3, even though the trajectories passed the regions of fires. This can be explained by small amounts of fires and frequent precipitation in this period.

The light spectral absorption can be applied as a source-specific optical marker for impact of BB on urban aerosols. The sampling period of our study can be divid-

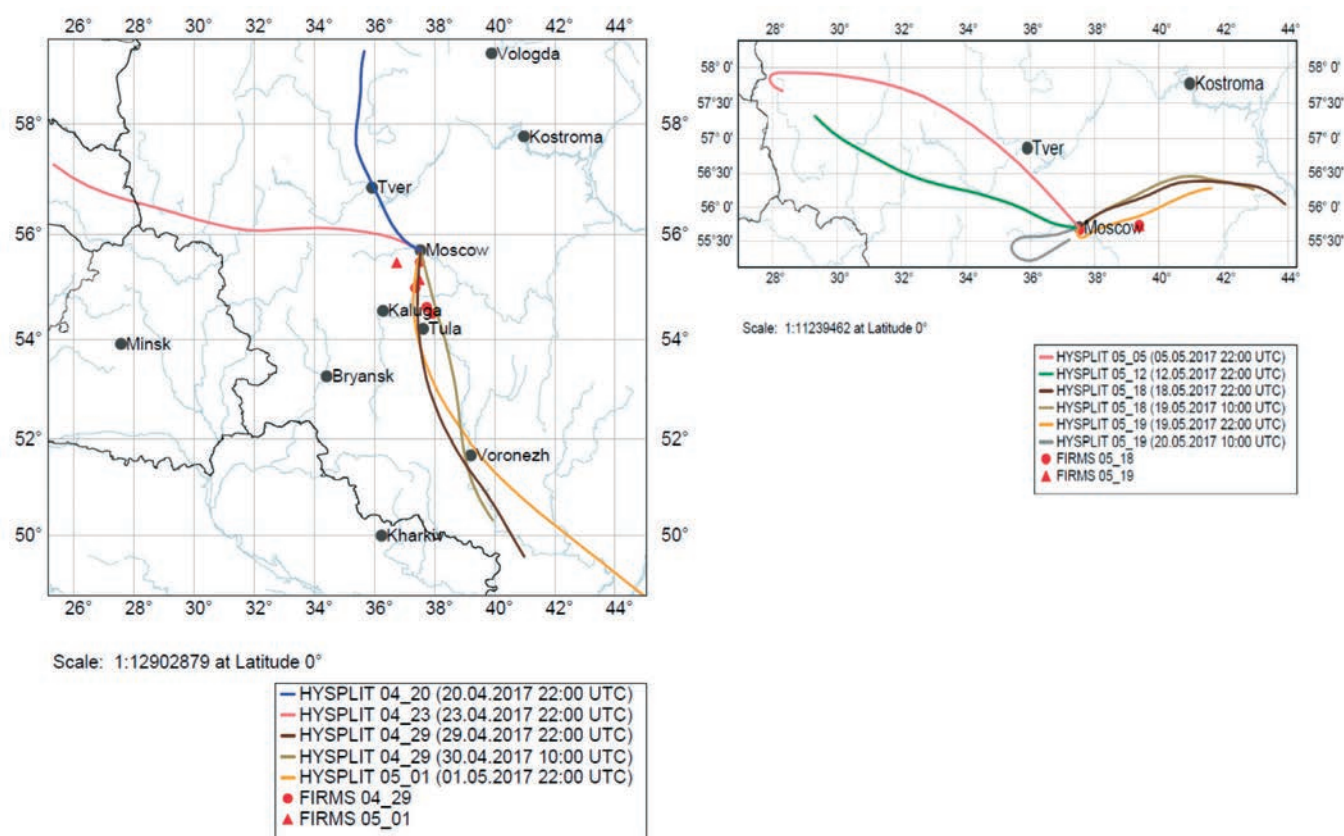


**Figure 4.** Two-day back air mass transportation from the HYSPLIT model in the days of the BB-affected period (left) and FF period (right), 500 m A.S.L. Fires observed by FIRMS in indicated days are marked by circles and triangles.

ed into periods of low and high AAE. The formal criteria for parametrization were chosen to be based on the observations performed in an urban environment, where the separation between BB-affected and FF periods was proposed at an AAE level of around 1.3 [21]. Thus, we addressed the days of the weak spectral dependence with  $AAE = 1.08 \pm 0.02$  to the dominant impact of fossil fuel combustion emissions with less impact of biomass burning during the “FF” period (Figure 3). Days of the dominant impact of biomass burning emissions during “BB-affected” period show a high spectral dependence with an averaged value  $AAE = 1.61 \pm 0.02$ . Similar results for traffic emissions were obtained in the Hanoi megacity with an AAE equal to 1.3 (Popovicheva et al., 2017b), indicating that traffic produces significantly less BrC and more BC than biomass burning. The number of fires passed by air masses relates to BB-influenced days (Figure 3).

### 3.2. FF-Related FTIR Spectral Features

In the Moscow megacity, anthropogenic PM emissions occurred due to traffic, industry, heating, waste recycling, and construction. Biomass was not used as a fuel for domestic burning because of the central heating system, which is different from many European cities. Various absorption bands relating to different classes of organic and ionic compounds were observed in FTIR spectra of spring aerosols; the most frequently indicated wavenumbers are shown in Figures S1 and S2. Saturated C-C-H, unsaturated C=C-H, and aromatic C=C and C=C-H vibrations suggest the presence of alkanes, alkenes, and polyaromatic hydrocarbons (PAH), respective-

ly. Carboxyl C=O groups represent functionalities in carboxylic acids, ketones, esters, anhydrides, and quinones. Hydroxyl -OH groups are associated with alcohols, while aromatic -NO<sub>2</sub> and -NH groups indicate the presence of nitrogen-oxy compounds and amines, respectively. Attributes of salts are SO<sub>4</sub><sup>2-</sup> and CO<sub>3</sub><sup>2-</sup> bands in sulfates and carbonates, respectively.

FTIR spectra of days assigned to the FF period are shown in Figure S1. The most frequent feature of all spectra are the aliphatic C-C-H symmetric/asymmetric stretches (2926–2855 cm<sup>-1</sup>) of methylene > CH<sub>2</sub> groups in alkanes. At higher wavenumbers, at around 3223 and 3405 cm<sup>-1</sup>, the vibrations of ammonium NH<sub>4</sub><sup>+</sup> and N-H amine groups, respectively, were prominent. In the same range, the O-H groups in alcohols and sugars can be identified. The most frequently observed bands in the range of 1738–1715 cm<sup>-1</sup> and 1587 cm<sup>-1</sup> are carbonyl C=O and C=C, respectively. C=C stretching is attributed to either aromatic compounds or microcrystalline structure of soot particles due to its polyaromatic character [52,53]. In both cases, the IR-inactive C=C mode is augmented by either sufficient asymmetry of the carbon material polyaromatic structure (e.g., by defects) or related to carbonyl groups conjugated with aromatic segments [54]. At 880 cm<sup>-1</sup> carbonate CO<sub>3</sub><sup>2-</sup> groups dominate.

The representative spectra for two days of the FF period (05.18 and 05.19) are shown in Figure 5, together with representative spectra of transport source emissions. In order to assign the absorption bands of ambient aerosols to the transport impact, the correlation with a pattern of a functional marker for diesel and gasoline particulate emissions was analyzed. Spectra of particulate emissions from heavy-duty diesel, off-road diesel, and gasoline

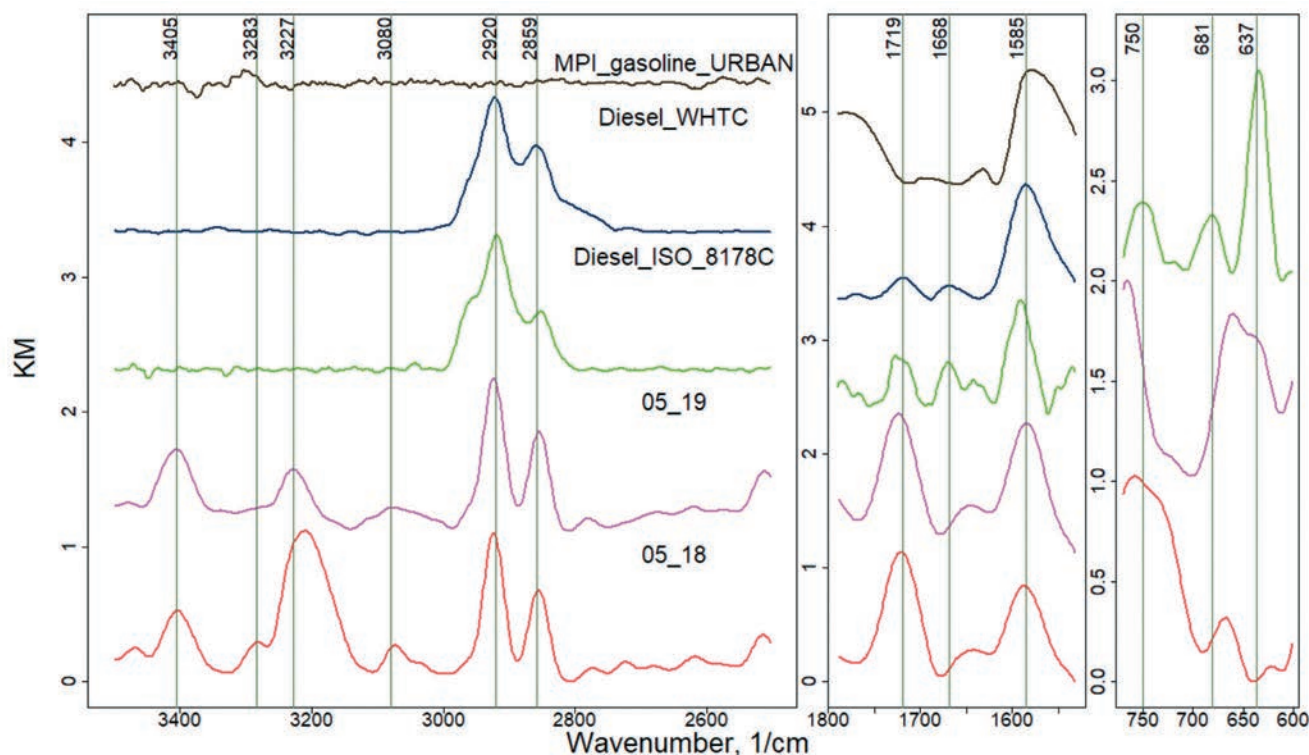


**Figure 5.** FTIR spectra for 05.18 and 05.19 from the FF period. Spectra of a heavy-duty diesel engine operated in the World Harmonized Transient Cycle and with conventional EN 590 diesel fuel engine (Diesel\_WHTC), an off-road diesel engine operated in a Non-Road Steady State cycle ISO-8178 (Diesel\_ISO\_8178), and an multi-point injection (MPI) gasoline engine operated in an Urban cycle (MPI\_gasoline\_URBAN) represent road and off-road diesel and gasoline emissions, respectively.

direct injection engine operated in World Harmonized Transient cycle (Diesel\_WHTC), Non-Road Steady State cycle ISO-8178 (Diesel\_ISO-8178), and Urban portion of the Artemis cycle (term as MPI gasoline URBAN), respectively, are shown in Figure 5. Both diesel engine emissions demonstrate the high similarity for bands at 1585, 1668, 1719, and 2920–2859  $\text{cm}^{-1}$  of aromatic C=C, aldehydes, acids/ketones C=O, and alkane C-C-H functional groups, respectively. Gasoline engine emission coincides by a wide band of C=C group. It is worth to note that a prominent band at 1589  $\text{cm}^{-1}$  associated with carbonyls was persistently observed in high-temperature combustion emissions, which was also found in gas flaring particulates [40]. Such findings prove that soot produced at high-temperature combustion can be identified by the similar chemical structure related to the aromatic ring stretching mode enhanced in intensity by O-containing functional groups.

There is a band in the representative spectra for two days of the FF period which always coincides for all spectra in Figure 5, it is one peaked at 1589  $\text{cm}^{-1}$  and other at

1719  $\text{cm}^{-1}$  for C=C and C=O, respectively. Bands of alkanes peaked at 2926–2855  $\text{cm}^{-1}$ ; moreover, alkenes observed at 1645  $\text{cm}^{-1}$  are identical between spectra of the FF period and diesel emissions functional markers, but different from the gasoline ones. Polyaromatic C=C=H at 750  $\text{cm}^{-1}$  are similar for spectra of the FF period and Diesel\_ISO-8178. Thus, we considered that C-C-H, C=C, and C=O groups in alkane, aromatic, and oxidized compounds act as a functional marker of transport vehicle emissions in the Moscow environment (Table 1).

Additionally, to organic functionalities, in the FF period sulfates,  $\text{SO}_4^{2-}$  in various salts and sulfuric acids are well observed in the wide range of 661 to 617  $\text{cm}^{-1}$ . Sulfates were consistently observed in transport vehicle emissions [10,41,42] due to fuel and lubrication oil contaminations. They show the prominent absorption band on the spectra of off-road diesel engine operated in Non-Road Steady State cycle ISO-8178 (Figure 5).

Secondary particles that are mainly ammonium sulfate and nitrate formed in the air from regional or local gaseous emissions of sulfur dioxide and oxides of nitro-

**Table 1.** Patterns of functional groups acting as functional markers of transport vehicle and regional BB smoldering and flaming emissions in Moscow megacity.

Wavenumbers, $\text{cm}^{-1}$	Diesel /Gasoline Transport	Wavenumbers, $\text{cm}^{-1}$	Smoldering /Flaming
637	$\text{SO}_4^{2-}$	617-621	$\text{SO}_4^{2-}$
750	C=C-H	762	C=C-H
1585	C=C	1530	-NO <sub>2</sub>
1668	C=O	1618	C=C
1719	C=O	1730-1680	C=O
2920-2859	C-C-H	2926-2851	C-C-H
		~3401	O-H,N-H



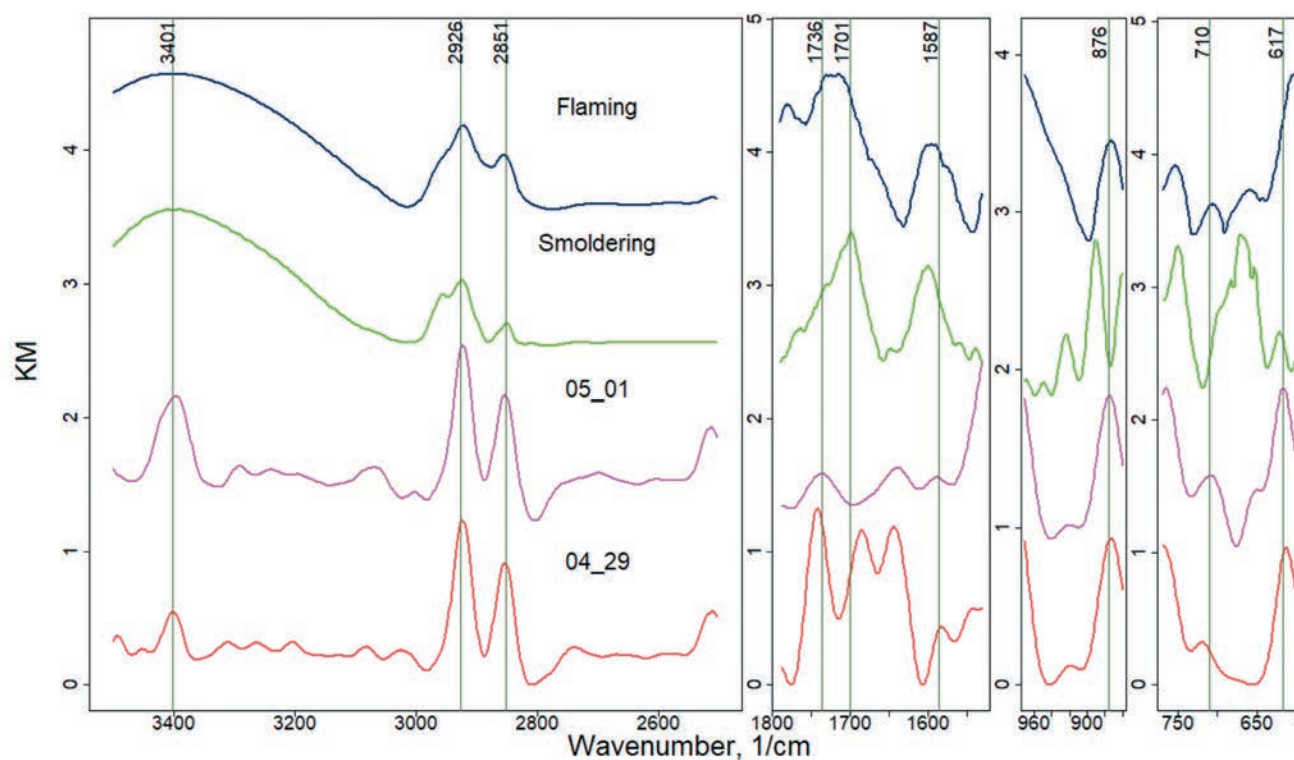


**Figure 6.** FTIR spectra for 05.01 and 04.29 from the BB-affected period. Spectra of the Moscow regional biomass represented by spruce flaming and mixture smoldering fires.

gen reacting with ammonia [55].  $\text{SO}_4^{2-}$  is well correlated with the  $\text{NH}_4^+$  absorption band at 3227 and 638  $\text{cm}^{-1}$ , due to the formation of internally mixed particles during long-term transport from urban sources [7] and BB season [46].

The bands observed in the FF period at 3405  $\text{cm}^{-1}$  can be associated to N-H in amines and amino acids, and to O-H in alcohols. Functionalities of amino acids are found to be well correlated with hydroxyls and carbohydrates; they are classified as biogenic functional groups because they originate from biogenic sources [7]. Additionally, the band at 3474  $\text{cm}^{-1}$ , assigned to O-H in sugars, alcohols, and carbohydrates, may prove the biogenic impact to aerosol composition. Such compounds are not emitted by diesel/gasoline transport; together with sulfates and ammonium, they demonstrate the mixing of secondary and biogenic aerosols in ambient urban environment. Related to sugars, alcohols, and carbohydrates, the band at 3474  $\text{cm}^{-1}$  is also prominent during the FF period, indicated by the biogenic emission already observed during spring time in other studies [56].

### 3.3. BB-Related FTIR Spectral Features

FTIR spectra of days assigned to the BB-affected period are shown in Figure S2. The most frequent feature of all spectra are the aliphatic C-C (symmetric/asymmetric) stretches (2926–2851  $\text{cm}^{-1}$ ) of methylene  $>\text{CH}_2$  groups in alkanes. Besides this group, other functionalities are much more variable and difficult to be described for comparison only by observation.

In Figure 6, the representative spectra for two days of the BB-affected period (05.01 and 04.29) are shown, together with spectra for smoldering and flaming of Moscow regional biomass. BB spectra of both biomasses exhibit a very wide unresolved band near 3401  $\text{cm}^{-1}$  from

various O-H and N-H in carbohydrates (including levoglucosan), alcohols, and amines. Aliphatic C-C-H and C=C stretching of aromatic rings are observed at 2926–2851 and 1614  $\text{cm}^{-1}$ , respectively. A wide band of oxidized functionalities in the range from 1730 to 1700  $\text{cm}^{-1}$  relates to carbonyl C=O groups. Polyaromatic C=C-H at 754 and 710  $\text{cm}^{-1}$ , as well as features of sulfates at 617  $\text{cm}^{-1}$ , are prominent for flaming, while strong absorption was observed at 667  $\text{cm}^{-1}$  due to sulfate emissions in  $\text{K}_2\text{SO}_4$ ,  $\text{MgSO}_4$ , and  $\text{Na}_2\text{SO}_4$  in the smoldering phase. The presence of  $\text{SO}_4^{2-}$  absorption bands at 617  $\text{cm}^{-1}$  and their slightly prominent feature in smoldering smoke indicate the formation of secondary sulfates in the Moscow environment, a phenomenon usually relating to the aging of biomass burning aerosols [57].

It should be noted that during an extreme smoke event, observed in the Moscow megacity in August 2010, smoldering and flaming of regional wildfires near a city were a source for very intensive persistent carbonyls found near 1736  $\text{cm}^{-1}$  [29]. The photochemical aging of BB smoke could result in the formation of secondary organic aerosols (SOA), which are represented through high dicarboxylic acid concentrations [58]. Additionally, in flaming spectra, a band of organic  $-\text{NO}_2$  groups are located at 1530  $\text{cm}^{-1}$ , similar to the very prominent vibrations there were observed in the peat bog smoke inside and above the grass during long-lasting peat burning near the Moscow region [39].

Analyses of the correlation between absorption bands of aerosols during the days of the BB-affected period and regional BB spectra indicate many similarities. In the range of the highest wavenumbers, ambient aerosols have a prominent peak at the same wavenumber of 3401  $\text{cm}^{-1}$ , defining the similar absorption compounds with regional BB; however, it is much narrower and likely dominated by N-H amines. A wide band of oxidized

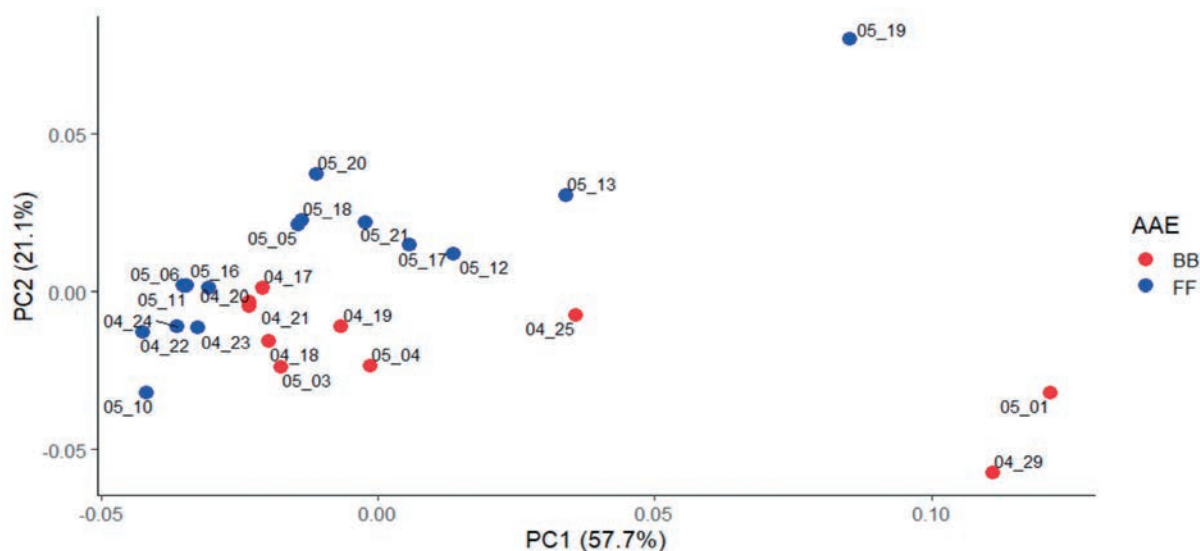


**Figure 7.** PCA score plots (PC1 × PC2) for FTIR spectra of sampling days marked by red and blue for AAE in the range of  $1.61 \pm 0.02$  and  $1.08 \pm 0.02$ , relating to the BB-affected and FF periods, respectively.

functionalities is localized near  $1736 \text{ cm}^{-1}$ , while  $-\text{NO}_2$  is always prominent at  $1530 \text{ cm}^{-1}$ . Polyaromatic  $\text{C}=\text{C}=\text{H}$  at  $765$  and  $710 \text{ cm}^{-1}$  are similar to the regional BB spectra; sulfates always dominate at  $617 \text{ cm}^{-1}$ , which are related to the vibrations in  $\text{Ca}_2\text{SO}_4$ . The representative spectra in Figure 6 show the days of the highest fire impact when BWT indicates the areas of fires (Figure 3). Therefore, we justify that a BB functional marker pattern of OH, N-H, C-C-H, C=O, C=C, C=C-H,  $-\text{NO}_2$ , and  $\text{SO}_4^{2-}$  groups in carbohydrates, alcohols, amines, alkanes, oxidized compounds, aromatic, nitrocompounds, and sulfates can act as a functional marker of regional BB emissions in the Moscow environment (Table 1). The presence of small absorption at  $3474 \text{ cm}^{-1}$  reflects the co-existence of BB and bioaerosols, which was already observed during spring time [56].

Dust functionalities related to soil appeared at  $923 \text{ cm}^{-1}$ , attributed to  $\text{Al}(\text{OH})$  vibrations in kaolinite, and related to Si-OH stretching around  $950 \text{ cm}^{-1}$ . Carbonates ( $\text{CO}_3^{2-}$ ) were identified in the range  $880\text{--}860 \text{ cm}^{-1}$ ; their presence in the PM size fraction was confirmed by thermo-optical measurements of carbonates in the form of carbonate carbon [46]. Relative concentrations of carbonates are increasing from low to high smoke, thus showing the impact of re-suspended soil particles during intensive agricultural fires on the composition of coarse ambient aerosols. The IR spectra of the coarse samples exhibited a peak around  $870 \text{ cm}^{-1}$ , which was due to asymmetric vibrations of calcium carbonate ( $\text{CaCO}_3$ ) [59]. During the BB-affected period, we should note the prominent similarity of the position of  $880 \text{ cm}^{-1}$  vibration band of carbonates  $\text{CO}_3^{2-}$  in ambient aerosols, similar to spectra of flaming emission. This indicates the wide distribution of dust in the urban atmosphere as well as that evolved by air convection during biomass burning, which impacted the city atmosphere [22].

### 3.4. Combined FTIR-PCA Analyses

In order to investigate the variations in functionalized structures and detect similarities between daily aerosol chemistry, a combined FTIR spectroscopy and PCA were

used. The score  $\text{PC1} \times \text{PC2}$  plots calculated using the FTIR spectra data matrix for the whole sampling period is shown in Figure 7. The highest principal component (PC) axes 1, 2, and 3 account for 57.7, 21.1, and 11.1% of the total variance in the data set, respectively. There are three days, namely 04.29, 05.01, and 05.19, for which FTIR spectra show very high PC1 variability with respect to the other ones, described by the highest PC1 values. Additionally, these days were when the highest temperature and  $\text{PM}_{10}$  mass concentrations were observed (Figure 2).

The scatter plot of PC1 against PC2 shows the similarities as well as the differentiation between aerosol composition of days separated on two episodes according to the AAE parametrization. A big group of days assigned to the high AAE is clustered at negative PC2, their chemical composition is characterized by a similar pattern of the functional groups. It indicates that there is a BB-related factor that strongly influences aerosol chemistry, separating those days into the negative direction of PC2. On the other hand, the  $\text{PC2} \times \text{PC3}$  plot does not demonstrate such separation well. The loadings plot in Figure 8 show the spectral variability explained by the first PCs. Marked extremums are the absorption bands identified on FTIR spectra of daily samples.

Table 2 summarizes the results of PCA analysis providing the most important variables as functional factors. It shows the principal components explaining PC1 (Factor 1, 58%), PC2 (Factor 2, 21%), and PC3 (Factor 3, 11%), totaling 89.9% of the data set variance. Factor 1 had the highest absolute value 0.21 for dust carbonates  $\text{CO}_3^{2-}$  ( $878 \text{ cm}^{-1}$ ), showing the impact of re-suspended soil particles, dust generated by the wind erosion, and transportation during spring season. Polyaromatics ( $762 \text{ cm}^{-1}$ ) from combustion emissions and sulfates ( $617 \text{ cm}^{-1}$ ) of BB features were also described by a high PC1, equal to 0.133. On the other hand, alkanes ( $2926\text{--}2855 \text{ cm}^{-1}$ ), alkenes ( $1645 \text{ cm}^{-1}$ ),  $\text{C}=\text{C}$  ( $1591 \text{ cm}^{-1}$ ) related to diesel/gasoline transport, and esters/carboxylic acids ( $1736 \text{ cm}^{-1}$ ) showed a PC1 value in the range of 0.046–0.023. In Factor 2, sulfates ( $621 \text{ cm}^{-1}$ ) from secondary aerosols demonstrated a high variability, with a PC2 value of 0.21.

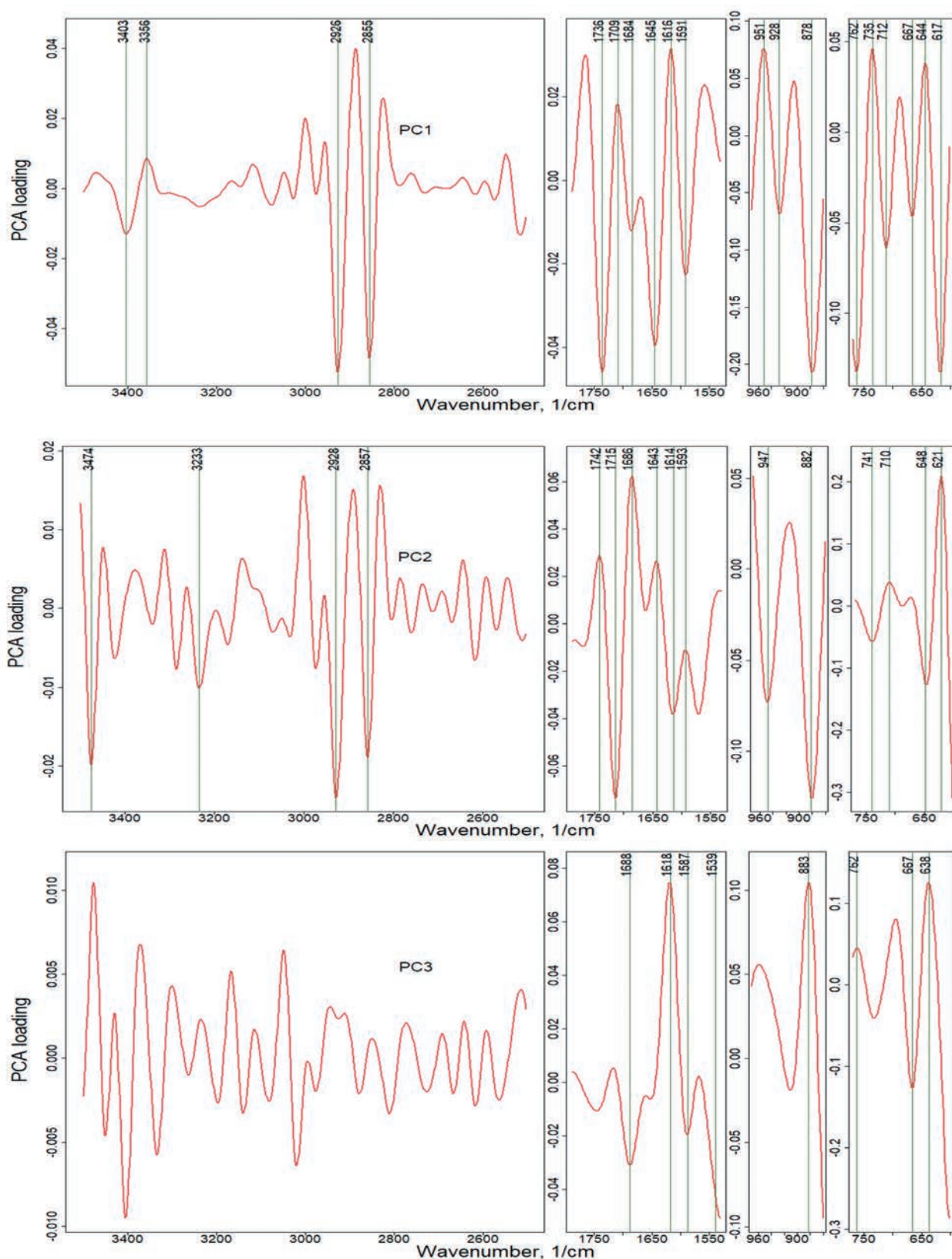


**Figure 8.** PC1, PC2, and PC3 loadings. Marked extremums are the absorption bands identified on FTIR spectra of daily samples.

Furthermore, dust-related features ( $947$  and  $882\text{ cm}^{-1}$ ) with carboxylic acids/ketones ( $1715\text{ cm}^{-1}$ ) from transport and aldehydes ( $1686\text{ cm}^{-1}$ ) in BB emissions were best explained by PC2 in the high absolute value range of  $0.13$ – $0.06$ . Strong features of sugars/alcohols/carbohydrates ( $3474\text{ cm}^{-1}$ ) were observed in biogenic aerosols,

characterized by an absolute value of PC2 equal to  $0.02$ . Factor 3 reveals the biggest impact of various sulfates ( $667$ ,  $638\text{ cm}^{-1}$ ) of long transportation, as well of dust carbonates ( $883\text{ cm}^{-1}$ ) at the highest PC3 near  $0.13$ , supported by C=C ( $1618\text{ cm}^{-1}$ ) agriculture/residential fires with a PC3 of  $0.075$ .



Table 2. Functional factors presented by principal components of PCA analysis of FTIR data.

Wavenumber, 1/cm	PC1 Loading (58%)	PC2 Loading (21%)	PC3 Loading (11%)	Functional Groups
617	-0.133			SO <sub>4</sub> <sup>2-</sup> sulphates
621		0.21		SO <sub>4</sub> <sup>2-</sup> sulphates
638			0.126	SO <sub>4</sub> <sup>2-</sup> sulfuric acid, sulphates
644	0.038			SO <sub>4</sub> <sup>2-</sup> sulfuric acid
648		-0.125		SO <sub>4</sub> <sup>2-</sup> sulfuric acid, sulphates
667	-0.046		-0.126	SO <sub>4</sub> <sup>2-</sup> sulphates, sulfuric acid
710		0.038		CO <sub>3</sub> <sup>2-</sup> carbonates; SO <sub>4</sub> <sup>2-</sup> sulphates; C=C-H polyaromatics
712	-0.064			CO <sub>3</sub> <sup>2-</sup> carbonates; C=C-H polyaromatics
735	0.046			C=C-H polyaromatics
741		-0.058		C=C-H polyaromatics
762	-0.132		0.046	C=C-H polyaromatics
878	-0.207			CO <sub>3</sub> <sup>2-</sup> carbonates; C=C-H polyaromatics
882		-0.126		CO <sub>3</sub> <sup>2-</sup> carbonates; C=C-H polyaromatics
883			0.105	CO <sub>3</sub> <sup>2-</sup> carbonates; C=C-H polyaromatics
928	-0.068			O-H organic acids
947		-0.073		O-H organic acids
951	0.076			O-H organic acids
1539			-0.043	-NO <sub>2</sub> nitrocompounds
1587			-0.019	N-H amino acid; -NO <sub>2</sub> nitrocompounds
1591	-0.023			N-H amino acid; C=C polyaromatics
1593		-0.011		N-H amino acid; C=C polyaromatics
1614		-0.038		C=C polyaromatics; N-H amino acid
1616	0.032			C=C polyaromatics; N-H amino acid
1618			0.075	C=C polyaromatics; N-H amino acid
1643		0.027		C=C alkenes
1645	-0.04			C=C alkenes
1684	-0.012			C=O aldehydes
1686		0.063		C=O aldehydes
1688			-0.031	C=O aldehydes, carboxylic acid
1709	0.018			C=O carboxylic acid, ketones, aldehydes
1715		-0.074		C=O carboxylic acid, ketones, aldehydes
1736	-0.046			C=O esters, carboxylic acid
1742		0.029		C=O esters, carboxylic acid
2855	-0.049			C-C-H aliphatic hydrocarbons; O-H organic acids
2857		-0.019		C-C-H aliphatic hydrocarbons; O-H organic acids
2926	-0.053			C-C-H aliphatic hydrocarbons; C=C alkenes
2928		-0.024		C=C alkenes
3233		-0.01		NH <sub>4</sub> <sup>+</sup> ammonium
3356	0.009			N-H amino acid; O-H carbohydrates and alcohols
3403	-0.013			N-H amines and amino acid; O-H alcohols
3474		-0.02		O-H sugar, alcohols and carbohydrates

#### 4. CONCLUSIONS

Spring aerosols in the Moscow urban background were analyzed for particle-associated organics, ions, and dust functionalities. Classes of organic/inorganic compounds in the aerosol composition were inferred from analyses of FTIR spectral absorbance. Sixteen organic compound classes and two ionic inorganic and dust-related species were identified in spring aerosols. The composition of daily ambient aerosols demonstrated aliphatic, aromatic, carbonyl, and sulfate compound absorbance as features of traffic emissions. The functionalities of diesel/gasoline emission were found in ambient aerosols by their functional markers, showing the dominant impact of transport emissions from the diesel/gasoline vehicles operated in the Moscow megacity at the most common engine cycle conditions. Specific bands of amines, sugars, alcohols, and carbohydrates indicated the biogenic activity, while prominent ammonium and sulfates absorbance was assigned to secondary inorganic formation typical for urban environment. Because the sampling site at the Meteorological Observatory took place in a residential area, far from highways and industrial and agricultural activities, the main source of ammonium sulfates in PM were likely from secondary aerosols. Dust-related functionalities were proved by carbonates and kaolinites.

Complex chemistry and devised organic composition requires a source-specific optical marker for the assessment of a potential impact of biomass burning on urban aerosols. Parametrization of the sampling duration on FF and BB-affected periods by low (below 1.3) and high (above 1.3) AAE supports the relative contribution of agriculture fires/residential BB to urban Moscow aerosol composition, which is dominated by FF combustion. The BB functional marker reveals the pattern of carbohydrates, alcohols, amines, alkanes, oxidized compounds,

aromatic, nitrocompounds, and sulfates observed in regional BB emissions. Air mass arriving in the Moscow area due to long-term transportation from the south of Russia impacts the air quality of the city, especially when the direction of transportation correlates well with fire-affected regions.

For the first time for the Moscow megacity environment, a factorial analysis such as principal component analysis (PCA) was used complementary to FTIR.

FTIR-PCA allowed the distinguishing between daily aerosol composition according to high AAE, which identified BB spectral features during BB-affected periods. Chemometric techniques discriminated day-to-day changes in a range of major factors influenced by the aerosol composition. PCA analysis for FTIR data provided the most significant variables in main PC loadings showing the functional factors of transport, biomass burning, biogenic, dust, and secondary aerosol spring source impacts. Factor 1, explaining 57.7% of the variability, demonstrated the highest impact of carbonates, polyaromatics from combustion emissions, and BB-related sulfates following by alkanes, alkenes, esters/carboxylic acids, and C=C functional marker related to diesel/gasoline transport. Factor 2 explained 21.1% of the variability; sulfates from secondary aerosols dominated, while dust, carboxylic acids/ketones from transport, aldehydes in BB emission, and sugars/alcohols/carbohydrates of biogenic sources explained the aerosol composition to a large extent. Factor 3 explained 11.1% of the variability, revealing the biggest impact of sulfates and dust carbonates, supported by the C=C marker of agriculture/residential fires. Based on the combined FTIR-PCA analyses, it was suggested that traffic and biogenic emissions affected by biomass burning were the dominating sources of particle-bound organic compounds in spring aerosols in the urban background of the megacity environment.

# Spring aerosol in urban atmosphere of megacity: analytical and statistical assessment for source impacts \*

## INTRODUCTION

The physical and chemical processes of particulate matter (PM) accumulation in the atmosphere depend on environment, anthropogenic and natural emissions, and transport of air masses. In order to take actions to reduce an exposure to air pollution, it is essential to know the sources and activities contributing to a level of pollution. Following a meta-analysis of recent studies, six major source categories for PM can be defined in the urban environment: traffic, resuspension of crustal/mineral dust, industrial sources, sea/road salt, biomass burning (BB), and atmospheric formation of secondary inorganic aerosols (Belis et al., 2013).

Chemical characterization of aerosol composition is a powerful tool for source apportionment (Gu et al., 2013; Chen et al., 2014; Li et al., 2018). However, due to the molecular complexity of PM, the chemical speciation of classes and individual organic compounds associated to the various sources is challenging. Identification of chemical compounds can act as molecular markers in the polluted atmosphere (Gu et al., 2013; Li et al., 2018). This approach is based on composition profiles for urban fossil fuel (FF) sources including gasoline- and diesel-powered vehicles (Kotianová et al., 2008), motor oil (Schauer et al., 2002), and heating plants (Bi et al., 2008). The relevance of BB emissions to residential heating in Europe cities (Pietrogrande et al., 2011; Nava et al., 2015) and long-range transport from wildfires to urban aerosol composition (Diapouli et al., 2014) is supported by organic and inorganic characterization. Humic-like substances (HULIS), originated in secondary reactions of volatile organic compounds (VOCs) emitted from both anthropogenic and biogenic sources (Kuang et al., 2015), attract an attention due to their effects on the radiation budget (Park and Yu, 2016).

Optical aerosol characteristics such as spectral absorption are useful for identifying the source impact on aerosol composition (Kirchstetter et al., 2004; Diapouli et al., 2017; Healy et al., 2017; Popovicheva et al., 2017). Biomass burning can produce light-absorbing aerosols that exhibit much stronger spectral dependence than high-temperature combustion of fossil fuels, such as diesel/gasoline of transport emissions.

Numerous and changeable aerosol sources as well as the diversity of molecular constituents in the organic and inorganic fraction of PM poses the need for the using of chemometric tools to provide the statistical analyses. Multivariate principal component analysis (PCA) was recently applied to analyze the FF and BB sources' contribution to urban particle-associated organic compounds (Pietrogrande et al., 2011; Li et al., 2018). However, due to a limited number of organic compounds characterized in those studies, a series of uncertainties remains and stimulates the further developing of the combined analytical and statistic approach. The extension of PCA anal-

yses by including the light absorption data for absorption Ångström exponent (AAE) as an optical marker for identification of the BB impact on aerosol composition can be a promising approach.

High population and a wide range of activities in a megacity lead to large-scale ecological impact which requires assessment by advanced aerosol characterization and statistic approaches. At present, the evaluation of PM composition in many megacities is performed (Cheng et al., 2016). Moscow is the largest megacity, and generally represents a typical urban area. In Moscow, mass concentrations of fine particulate matter with a diameter of less than 10  $\mu\text{m}$  ( $\text{PM}_{10}$ ) were found to be comparable or slightly higher than in other big European cities (around 20–30  $\mu\text{g m}^{-3}$  in yearly average) and lower than in Asian megacities (50–100  $\mu\text{g m}^{-3}$ ) (Cheng et al., 2016). Temporal variability of  $\text{PM}_{2.5}$ , the aerosol optical depth (AOD), temperature, humidity, and wind speed have been considered at the urban background site (Gubanova et al., 2018). However, no aerosol characterization approaches and source assessment analyses were applied for Moscow urban aerosols yet. Only case during extreme smoke event was recorded when a huge increase of PM and black carbon (BC) mass concentrations as well as the AOD, carbon-containing compounds, and BB markers have demonstrated the wildfire smoke pollution on urban environment (Chubarova et al., 2012; Popovicheva et al., 2014).

This work develops the advanced analytical and statistical approach for the comprehensive characterization of multicomponent aerosols in the Moscow urban background in the complex situation of the plurality of emissions in a megacity. Spring is considered as the multi-source season when the impact of both urban combustion sources and agriculture/residential fires in surrounding areas could be significant in accordance of biogenic activity. A large set of organic and ionic compounds characterizes the variability and source-dependent composition of aerosols. Both optical and chemical markers as well as meteorological data are applied for the identification of BB-affected periods. PCA analyses identifies a number of emission sources impacted the aerosol composition in the Moscow background.

## EXPERIMENTAL

### Measurement campaign and air mass transportation

The PM sampling setup was installed on the roof of the Meteorological Observatory of Moscow State University (MO MSU), located at the territory of the MSU campus, southwest of Moscow city center (Fig. 1). MO MSU is located on Vorobievy Gory ("Sparrow Hills"), in an area which is well ventilated with no industrial facilities or major roads located nearby. Therefore, MO

\* Popovicheva O., Padoan S., Schnelle- Kreis J., Nguyen D.L., Adam T., Kistler M., Steinkogler T., Kasper-Giebl A., Zimmermann R., Chubarova N. // *Aerosol and Air Quality Research*. 2020;20:702-719.  
DOI: [10.4209/aaqr.2019.08.0412](https://doi.org/10.4209/aaqr.2019.08.0412) CiteScore 6.5



MSU can be characterized as an urban background site. Sampling of PM<sub>10</sub> was performed on 47 mm quartz fiber filters (preheated at 600°C in advance) in 24 h intervals from 8 p.m. Measurements of meteorological parameters were performed by the MO MSU meteorological service. At the same time PM<sub>10</sub> mass concentrations were continuously monitored by the State Environmental Protection Institution, “Mosecomonitoring,” using a tapered element oscillating microbalance (TEOM 1400a; Thermo Environmental Instruments Inc., USA).

Measurements were performed between 17 April and 25 May of 2017. In this period backward air mass trajectories (BWTs) were generated, using the NOAA Hybrid Single-Particle Lagrangian Integrated Trajectory (HYSPLOT) model of the Air Resources Laboratory (ARL) (Stein et al., 2015) with the coordinate resolution equal to 1° × 1° of latitude and longitude. The potential source areas were investigated using 24 h BWTs for air masses at 500 m heights above sea level (a.s.l.). Fire information was obtained from Resource Management System (FIRMS), operated by the NASA/GSFC Earth Science Data Information System (ESDIS). The daily fire maps were related to the computed trajectories. A number of fires which could affect air masses was calculated as a sum of fires occurred at distance 0.5° on both latitude and longitude from BWTs. The number of fires passed by BWTs was estimated as the sum of amounts of all fires caught on the BWT points or in their neighborhood of no further than 0.5° along the latitude and longitude.

### Optical measurements

An off-line examination of light attenuation on quartz filter samples was performed using the multiple-wavelength light transmission instrument (transmissometer) described in Kirchstetter et al. (2004) and Popovicheva et al. (2017). The intensity of light transmitted through quartz filters was measured at seven wavelengths from the near-ultraviolet to near-infrared spectral region. At

least five different areas of the sample filter were analyzed in order to assess the possible heterogeneity of the sample. The light absorption was approximated by light attenuation (ATN) caused by the particle deposit defined as follows:

$$ATN = \ln(I_0/I)$$

where  $I_0$  and  $I$  is the light intensity transmitted through unexposed and exposed parts of the filter, respectively. The dependence of ATN on the wavelength  $\lambda$  was parameterized using a power law relationship:

$$ATN = k\lambda^{-AAE}$$

where the AAE (absorption Ångström exponent) is a measure of the spectral variation of aerosol light absorption.

### Analytical chemistry methods

A DRI 2001 Analyzer was used for the determination of the organic carbon (OC) and elemental carbon (EC), according to the IMPROVE\_A protocol (Chow et al., 2007). In the first heating stages, OC was thermally desorbed from the filter under a flow of helium with controlled temperature ramps. In the second stage, 2% O<sub>2</sub> is introduced with carrier gas, the original EC component plus any remaining pyrolyzed OC formed during the first heating stage were oxidized and desorbed. Correction of pyrolysis charring from OC is made by continuously monitoring the filter reflectance via an He-Ne 632.8 wavelength laser throughout an analysis cycle.

The in situ derivatization thermal desorption-gas chromatography and time-of-flight mass spectrometry (IDTD-GC-TOFMS) was used, as developed by Orasche et al. (2011). Hydroxyl and carboxyl groups of compounds such as anhydrous sugars were targets of the silylation derivatization procedure. Punches of quartz fiber filters were



Fig. 1. Location of Meteorological Observatory of MSU on a Moscow city map.

spiked with two isotope-labeled internal standard mixtures consisted of 1) fifteen deuterated PAHs, two deuterated oxy-PAHs and four deuterated alkanes and 2)  $^{13}\text{C}_6$ -levoglucosan (Omicron Biochemicals, USA),  $^{13}\text{C}_6$ -vanillin (Larodan, Sweden) and D31-palmitic acid (CIL, USA). The analytical precision of all studied analytes were below 17% within a calibration range, from 22 pg for abietic acid up to 342 ng for levoglucosan. Limits of quantification (LOQs) for PAHs were between 1 pg for fluoranthene and 8 pg as well as 17 pg for levoglucosan. Following organic species were quantified: thirteen PAHs, eight oxy-PAHs, eight hopanes, fifteen alkanes, three anhydrosugars, dehydroabietic acid methyl ester and dehydroabietic acid, 1,8-naphthalic anhydride and 1,8-naphthalaldehydic acid, and nicotine.

Humic-like-substance-bound OC (HULIS-C) was quantified by simultaneous analysis of two fractions with different (pH-dependent) solubility and thus with different molecular weight ranges (Limbeck et al., 2005; Feczko et al., 2007). Extracted samples were injected to the flow system of the total organic carbon measurement (FI-SPE-TOC). Eluent 1 (0.01 M  $\text{HNO}_3$ ) forwarded the sample to the anion exchanger (SAX) micro-column. HULIS were eluted from SAX by Eluent 2 (0.06 M  $\text{HN}_4\text{OH}$ ) and were introduced into a catalytic oven (900°C). Humic acid (HA; Fluka, ~20% of ash) was used for calibration. The water-soluble HULIS-C (HULIS-C-WS) and alkali-soluble HULIS-C (HULIS-C-AS) were measured separately for each sample. The limit of detection (LOD) was 17  $\text{ng m}^{-3}$  mainly due to a complex isolation procedure.

Water-soluble ions ( $\text{Li}^+$ ,  $\text{Na}^+$ ,  $\text{NH}_4^+$ ,  $\text{K}^+$ ,  $\text{Mg}^{2+}$ ,  $\text{Ca}^{2+}$ ,  $\text{F}^-$ ,  $\text{Cl}^-$ ,  $\text{SO}_4^{2-}$ ,  $\text{PO}_4^{3-}$ ,  $\text{BO}_3^{3-}$ , acetate, formate, lactate) were determined from the effluents collected after the isolation of HULIS. Anions were separated by an ion exchange column (IonPac AS17A) in isocratic conditions using 1.8 mM  $\text{Na}_2\text{CO}_3$  + 1.7 mM  $\text{NaHCO}_3$ . Cations were separated on IonPac CS12A using 38 mM methane sulfonic acid (MSA), the CSRS suppressor and a conductivity detector. Calibration for each ion was performed using external standards diluted from stock solutions (Merck). Filter blanks were measured and subtracted. Nitrite and nitrate ( $\text{NO}_2^-$  and  $\text{NO}_3^-$ ) were measured but due to usage of nitric acid during the sample preparation the quantification was not conducted. The limits of detection varied between 2 and 20  $\text{ng m}^{-3}$  and were lowest for lithium, sodium, and chloride and highest for organic ions, due to poor separation of those species.

Fourteen water-soluble saccharides (including polyols, anhydrosaccharides, primary and secondary saccharides) were analyzed from the effluents collected after the C18-extraction step of HULIS by high-performance anion exchange chromatography with pulsed amperometric detection (HPAE-PAD), as described by Inuma et al. (2009). The effluents were injected directly to a Dionex ICS-3000 system, equipped with a CarboPac MA1 column. Quantification was done using external standards (Fluka; Merck). The LOD was 1  $\text{ng m}^{-3}$  for most compounds. Galactosan, sucrose, and cellobiose showed poorer resolution resulting in higher LODs (3–6  $\text{ng m}^{-3}$ ). Because the GC-MS method was more sensitive than HPAE-PAD, data for three anhydrosugars were taken from GC-MS. On average, the results for anhydrosugars obtained with HPAE-PAD and GC-MS showed a 20% deviation for levoglucosan and 30% for mannosan.

## Correlation and principal component analyses

Multivariate principal component analysis is one of the most common multivariate explorative techniques which decomposes the data matrix and concentrate the source of variability into the first few principal components (PCs; Wold et al., 1987). By autoscaling, all data are mean-centered and then divided by the standard deviation of the variables. From PCA analysis, scores and loading plots are obtained, they allow an easy visualization of samples and variables. Hotelling analysis calculates the covariance ellipsoid corresponding to 95% confidence level. Data outside of the ellipsoid are considered as outliers and discarded from further analyses. PCA correlation loading plot contains two ellipses that indicate how much variance is taken into account, so the quantity of information each variable can explain. The outer ellipse is the unit circle and indicates 100% explained variance. The inner ellipse indicates 50% of explained variance.

PCA decomposes the data matrix of a set of observation variables (chemical compounds) into a set of values of linearly independent PCs, which represent the compounds of the biggest explained variability. PCs subsequently interprets as potential source factors. In our approach we would like to partially reduce the total amount of variables in the dataset of chemical compounds in order to minimize the redundant information and to try to maintain only the significant information for the optimal description of the samples. For that purpose, we restrict the number of variables choosing only representative compounds for the entire dataset of a given chemical class, the ones which are able to describe it in the most appropriate way. PCA is performed with all classes of organic and inorganic compounds found in spring aerosols while we take into account variables with the highest loadings. These are the most informative variables to explain the dataset. The considered variables have been evaluated together with the highest analytical validity of the corresponding chemical compounds.

A number of statistical techniques, such as LDA (linear discriminant analysis) and PMF (positive matrix factorization), requires an exact ratio between the number of samples (or observations) and variables. In the case of PCA there is no strict rule about the number of samples and variables to be taken into account. However, in order to show the differences in the calculation results, we verify a number of variables in PCA calculations further.

## RESULTS AND DISCUSSION

### Meteorology, light absorption, and air mass transportation

April and May in the Moscow area are typical spring months when temperature, biological and vegetation activity is increasing. From 29 April until 2 May the ambient temperature approached an abnormally high level for this season, +24°C (Fig. S1). During three days in April (25, 29, and 30) and twelve days in May (3, 5–7, 13–15, 18, 22, 24, 26, and 27) the solar shortwave radiation was very high and exceeded the 90% quantile of the maximum hourly doses in summer 2017 which is 24  $\text{MJ m}^{-2}$  (Fig. S1). During indicated days we expect the most favorable conditions for photochemical aerosol generation and agricultural activities in the south of Russia and Moscow's surrounding areas.

The spectral dependence of the aerosol light attenuation is well approximated by a power law equation (Eq.



(2)), providing the estimate for absorption Ångström exponent, as shown in Fig. 2. Variation of the AAE during the whole sampling period exhibits the range from 1.03 to 1.95 (Fig. 3). From 18 to 22 April air masses were transported from the north and passed the numerous agriculture fires close to Moscow (Fig. S2), the AAE higher than 1.4 was observed (Fig. 3). On 23 and 24 April the maximum of precipitation was occurred, up to 14 mm, the AAE was dropped. Since 25 April it became higher again, well in correlation with a large number of fires observed in the south of Moscow (Fig. S2). Fig. 4 shows the BWTs arrived on 26 April and 2 May from areas of intensive agriculture fires in the south of Russia and western Europe. High AAE value observed from the light absorption measurements also supports the effect of BB (Fig. 1). We should note that the period from 30

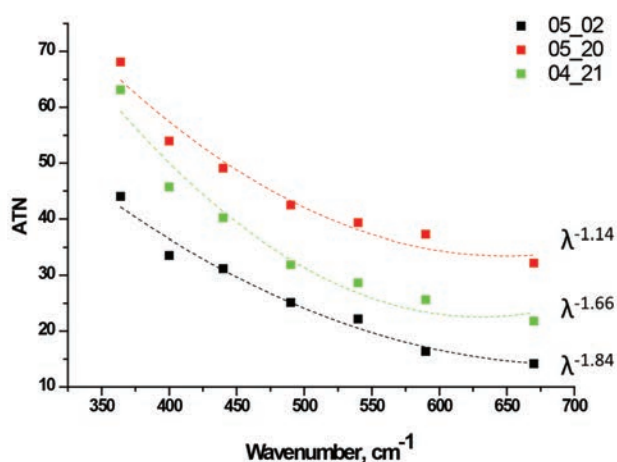


**Fig. 2.** Spectral dependence of the light attenuation (ATN) for days with highest (21 April and 2 May) and low (20 May) AAE values. The solid lines are generated using a power law Eq. (2), values of the  $\lambda$  exponent are chosen to fit the data.

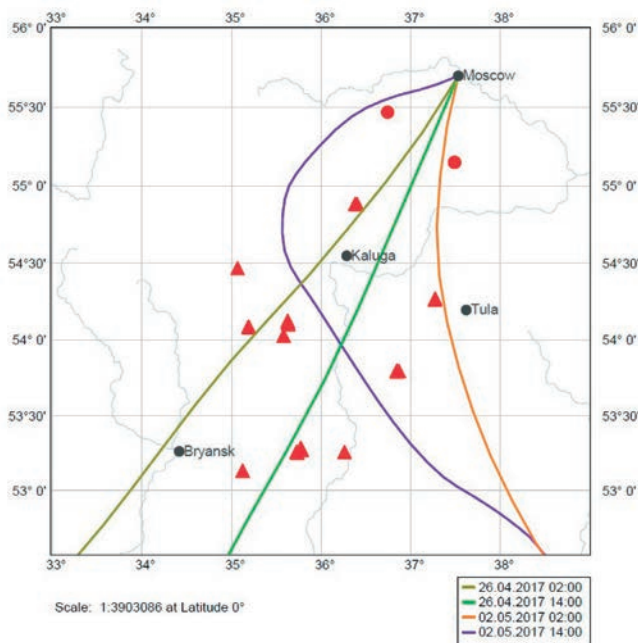


**Fig. 4.** 2-day back air mass transportation from HYSPLIT model in days of BB-affected period, 500 m a.s.l. Fires observed by FIRMS on 26 April and 2 May are marked by circles and triangles, respectively.

April–5 May coincides with a holiday period in Russia when warm weather stimulated the intensive residential activity around the Moscow city, such as garden cleaning, grass burning, and barbecue. After 4 May the direction of air mass transportation changed back to the Arctic region, relating to a temperature decrease (Fig. S1). On 5 May the AAE dropped to 0.97 and did not exceed 1.3 anymore.

Light absorption by particulates emitted from fossil fuel combustion sources exhibits relatively weak wavelength dependence with the AAE close to 1, indicating that black carbon is the dominant absorbing aerosol component (Kirchstetter et al., 2004; Popovicheva et al., 2017). While biomass burning aerosols are distinguished by stronger wavelength dependency, showing AAE of about 2.5 for wood smoke (Kirchstetter et al., 2004). This

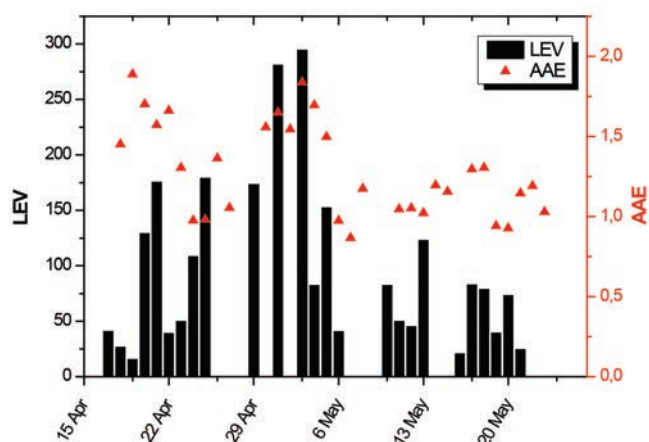


**Fig. 3.** Angstrom Absorption Exponent (AAE, red triangles) and levoglucosan concentrations (LEV) in the sampling period of spring of 2017 on the MO MSU. BB-affected periods identified by correlation of large AAE and Lev days is indicated in pink color.

indicates that brown carbon (BrC) associated with high-weight OC, in addition to BC contributes significantly to the measured light absorption in ultraviolet and visible spectral regions. Observations performed in urban environment show the variation of AAE indicating the impact of BB on urban aerosol, the AAE level above 1.3 was suggested to identify periods most affected by biomass burning (Diapouli et al., 2017) termed further as “BB-affected periods.”

### PM mass and aerosol composition

PM<sub>10</sub> mass daily concentrations show a strong variation from the lowest of 8  $\mu\text{g m}^{-3}$  to the highest value of 63  $\mu\text{g m}^{-3}$ , on average  $22 \pm 16 \mu\text{g m}^{-3}$  (Fig. 5). Maximum was recorded on 30 April due to air mass advection from south and south-east regions of Russia. Main constituents of spring aerosols are OC and EC followed by inorganic ions (Fig. 5). OC concentrations follow the PM<sub>10</sub> trend featuring an average OC concentration of 5.6  $\mu\text{g m}^{-3}$ . The highest values are observed in the period from 29 April till 1 May (up to 17.4  $\mu\text{g m}^{-3}$ ). Average EC is 1.9  $\mu\text{g m}^{-3}$ , ranging from 0.3 to 3.9  $\mu\text{g m}^{-3}$ . In urban environment the ratio of EC/TC characterizes the impact of combustion emission to carbonaceous aerosol composition.



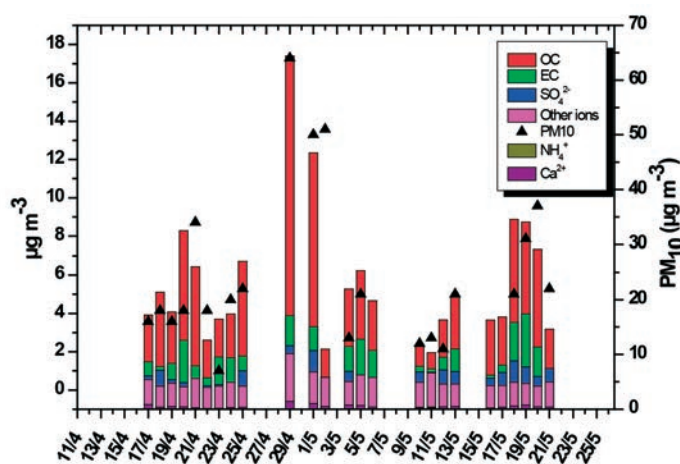


Fig. 5. 24 h averaged PM<sub>10</sub> and aerosol composition (ions, OC, EC) during sampling period.

During sampling period of our study, it approaches 20%. OC/EC ratio in the urban environment OC can be comparable to EC, dominated by vehicle emissions (Samara et al., 2014). Increased ratios of OC/EC between 4 and 15 are associated with wildfires in different regions over the world (Pio et al., 2011; Jung et al., 2016) due to the high OC content of BB emissions, especially from the smoldering combustion phase (Kalogridis et al., 2018). In our study average OC/EC is 2.1 at low AAE and increases to 30% during days of higher AAE. The maximal OC/EC reaches 3.8 (Fig. 5) in the days of air mass transportation from agriculture-fire-affected regions. Moreover, meteorological conditions, such as high temperature and solar radiation (Fig. S1) favor the formation of secondary organic aerosols due to condensation of heavy hydrocarbons, acid-catalyzed reactions, and oxidation in smoke plumes (Alves et al., 2010), that influences the OC/EC ratio as well.

Daily variability of individual organic compounds is shown in Fig. 6. The evolution of fifteen target PAH concentrations, namely four semivolatile PAHs with 4 rings, i.e., pyrene (P<sub>Y</sub>R), fluoranthene (FLU), benz[a]anthracene (BaA), chrysene (CRY), and eleven PAHs with 5 and 6 rings, i.e., sum benzo[b,k]fluoranthene (sumB), acephenanthrylene (ACE), perylene (PER), dibenz[a,h]anthracene (DiBaA), retene (RET), benzo[e]pyrene (BeP), benzo[a]pyrene (BaP), indeno[1,2,3-c,d]pyrene (IND), benzo[ghi]perylene (BgP), coronene (COR) and anthanthrene (ANT) shows maximum observed from 29 April–1 May. Ten oxy-PAHs, namely 9H-fluoren-9-one (9HFLUone), xanthone, 9,10-anthracenedione (ANQ-DO), cyclopenta[def]phenanthrenone (CPPH-O), 1,8-naphthalaldehydic acid (NAP-AC), 1,8-naphthalic anhydride (NAP-AN), 11H-benzo[a]fluorene-11-one (11HBaFone), 11H-benzo[b]fluorene-11-one (11HBbFone), 11H-benzo[c]fluorene-11-one (11HBcFone) and 7H-benz[de]anthracene-7-one (7HBdeAone) are dominant in April and at the end of sampling periods. Between hopanes we quantify 18 $\alpha$ (H)-22,29,30-trisnorhopane (Ts), 17 $\alpha$ (H)-22,29,30-trisnorhopane (Tm), 17 $\alpha$ (H),21 $\beta$ (H)-30-norhopane (29ab), 17 $\beta$ (H),21 $\alpha$ (H)-30-norhopane (29ba), 17 $\alpha$ (H),21 $\beta$ (H)-hopane (30ab), 17 $\beta$ (H),21 $\alpha$ (H)-hopane (morethane) 30ba, 22S-17 $\alpha$ (H),21 $\beta$ (H)-homohopane (31abS), 22R-17 $\alpha$ (H),21 $\beta$ (H)-homohopane (31abR), 22S-17 $\alpha$ (H),21 $\beta$ (H)-bishomohopane (32abS) and

22R-17 $\alpha$ (H),21 $\beta$ (H)-bishomohopane (32abR). They show the concentration minimum from 6 to 12 May. Maximum concentrations for n-alkanes with carbon number from 20 to 34 are found for the compounds C20 and C29. Nicotine is a marker of tobacco smoking; it shows relatively high variability.

Levoglucosan (Lev) is widely deployed as a BB marker for both near-source smoke (Engling et al., 2006) and fire long-range transportation (Fu et al., 2010), resulting from thermal decomposition of cellulose. During smoldering Lev can reach up to 30% of PM mass (Kalogridis et al., 2018). In our study Lev varies from 16 to 281 ng m<sup>-3</sup> having its maximum on 21, 25–29 April and 5 May, at the same days when a maximum of the fire numbers and AAE is observed (Fig. S2). Thus, AAE and Lev can act as optical and chemical marker, respectively,

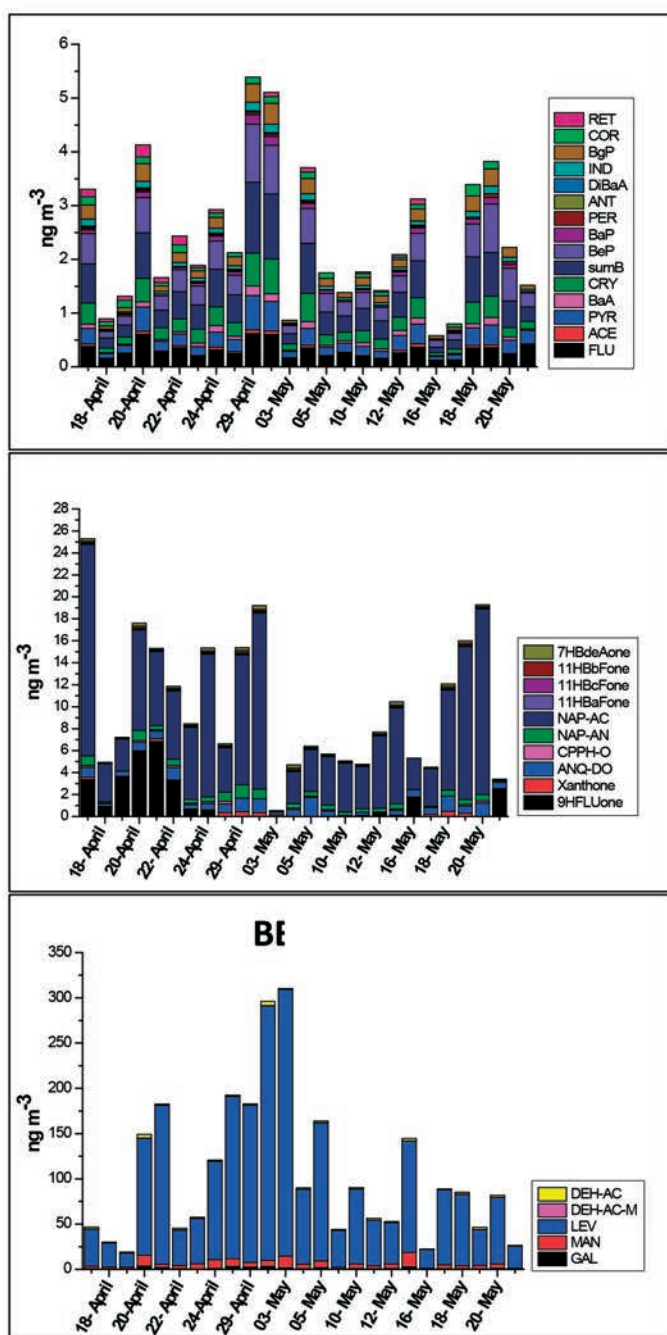


Fig. 6. Variation of organic and inorganic compound concentrations.

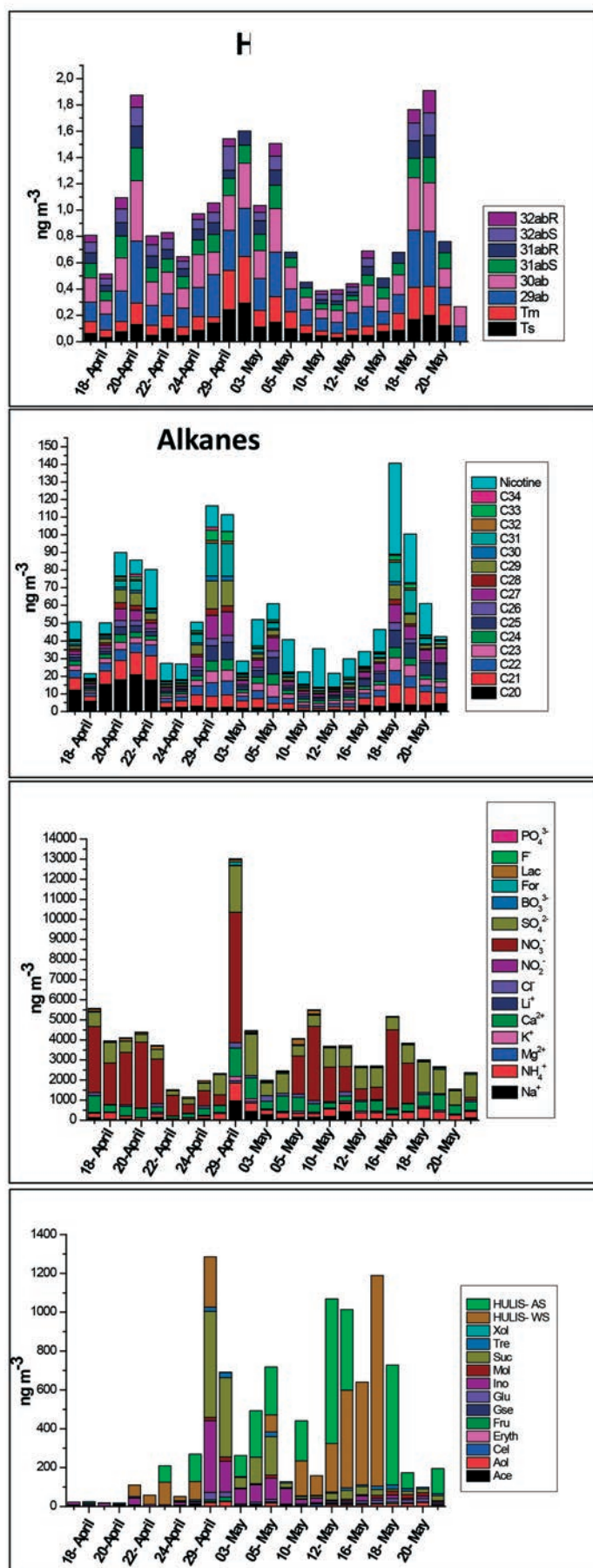


Fig. 6. (continued).

identifying BB-affected days as 20.04, 21.04, 25.04, 29.04, 1.05, 3.05, and 4.05, as shown in Fig. 3. Dehydroabietic acid (DEH-AC) is a tracer of coniferous wood burning (Simoneit et al., 1999), its concentration is not increased in the BB-affected period. The Lev/Man ratio during BB-affected days is significantly higher than during FF period (24 and 16, respectively). The aerosol composition during other days was influenced mostly by urban sources of fossil fuel combustion, further we term these days as “FF period.” The Lev concentration level was less than in BB-affected period, in the range from 20 to 75  $\text{ng m}^{-3}$ , once up to 120  $\text{ng m}^{-3}$  (Fig. 3). Here we note that Lev concentrations larger than 30  $\text{ng m}^{-3}$  are reported for European sites affected by wood burning in summer and winter (Puxbaum et al., 2007; Yttri et al., 2011).

Time trends of anhydrosaccharides and polyols are related to each other and show three characteristic periods (Fig. 7). Until 25 April the concentrations of anhydrosaccharides showed a strong variability with high peaks from day to day (up to factor of 5), whereas polyols remain constantly low indicating the clear BB influence. This situation changed in the period from 27 April till 5 May, when both anhydrosaccharides and polyols followed the same rising trend. This situation reflects the co-existence of BB and bioaerosols, which was already observed during spring-time in other studies (Bauer et al., 2008). This can be explained by a significant abnormal temperature increase in these days in relation with intensive biological activities (Fig. S1). Moreover, the co-existence of polyols, primary and secondary sugars with anhydrosaccharides may be explained by suspension of soil and plant debris in the heat wave of wildfires (Medeiros et al., 2006). From 6 May, Lev and Man decreased eventually, pointing to a reduction of the BB influence. Polyols remained at the same level indicating the spring impact of biological sources as fungal spores, bacteria and plant pollen, which seems reliable due to enhanced air temperature (Fig. S1).

Averaged over the whole sampling period the composition of saccharides was dominated by sucrose and inositol with average concentrations of 75.2 and 49.8  $\text{ng m}^{-3}$ , respectively. It reached a maximum during the period of the highest  $\text{PM}_{10}$  concentrations (Fig. 6). The average contribution of polyols (inositol (Ino), erythritol (Eryth), arabitol (Aol), mannitol (Mol)), primary saccharides (glucose (Glu), fructose (Fru)), trehalose (Tre), sucrose (saccharides) is higher than those of anhydrosaccharides (levoglucosan (Lev), mannosan (Man), galactosan (Gal)). Total HULIS-C ranged from  $< \text{LOD}$  ( $0.02 \mu\text{g m}^{-3}$ ) to  $1.83 \mu\text{g m}^{-3}$ , with an average of  $0.61 \mu\text{g m}^{-3}$  (Fig. S3). It is not possible to identify any trend for the contribution of water-soluble (HULIS-C-AC) and alkali-soluble (HULIS-C-AS).

The total ionic concentration is found on average 2.2  $\mu\text{g m}^{-3}$  and follows the trend of OC and EC concentrations (Fig. 5). The concentration of ions varied strongly from day to day (Fig. 6), the dominant ionic species are  $\text{SO}_4^{2-}$ , followed by  $\text{Ca}^{2+}$ ,  $\text{NH}_4^+$ , and  $\text{Na}^+$ .

Analyses of the aerosol concentrations averaged according to FF and BB-affected periods show that the main difference is visible for OC concentrations, which are 2  $\mu\text{g m}^{-3}$  higher during the days of BB impact (Fig. S4(a)). The absolute EC values are almost identical, but in relation to the sum of the main constituents, the contribution of EC is higher during the FF period. Most inorganic ions are slightly higher for BB-affected periods: The total sum



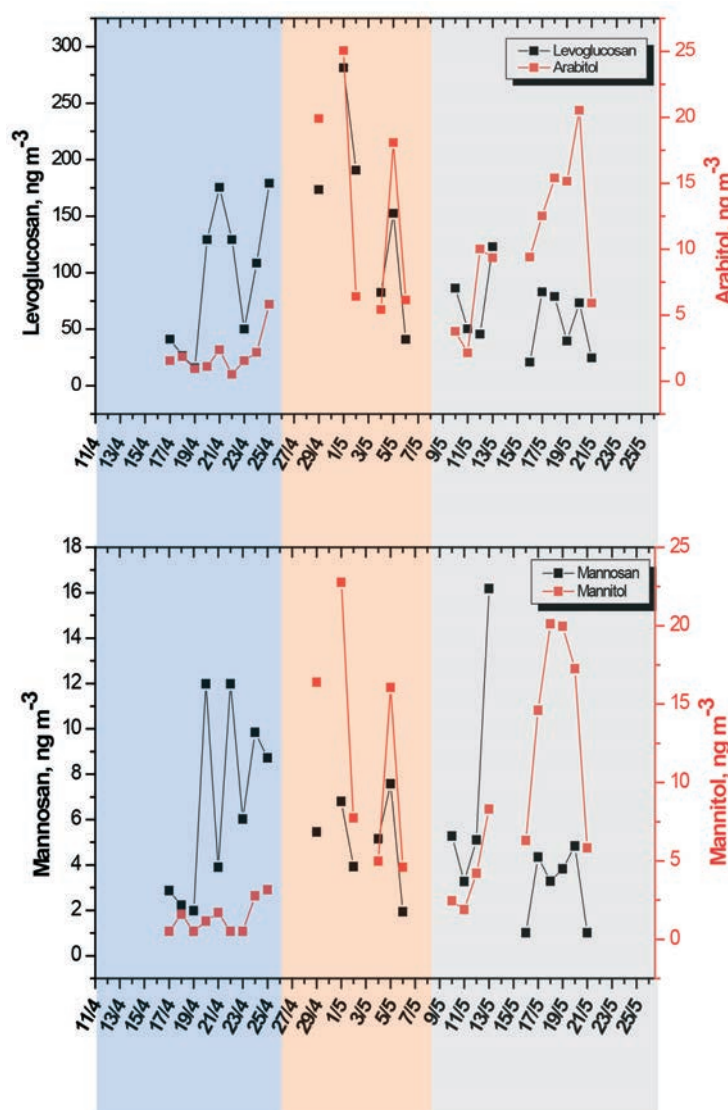


**Fig. 7.** The trend of anhydrosugars (levoglucosan and mannosan) and polyols (arabitol and mannitol). Three characteristic time-periods are indicated.

concentration is  $2.4 \mu\text{g m}^{-3}$  in comparison to  $2.0 \mu\text{g m}^{-3}$ . The  $\text{Na}^+$  concentration shows the highest relative increase during the BB-affected period (by 50% and by  $0.12 \mu\text{g m}^{-3}$  in terms of mass concentration). Additionally,  $\text{K}^+$  correlates with other saccharides (e.g., trehalose and polyols) and with other ions, which indicates a multisource character of  $\text{K}^+$  (e.g., soil, biogenic aerosol and BB). The spread between BB-affected and FF periods can be observed for median Lev and ranges from 71% to 45%. The contribution of inositol is higher during the BB period (14%) than during FF period (10%). Against the expectations that HULIS can act as BB marker, higher HULIS-C concentrations are observed during FF period. The share of HULIS-C in OC was much higher during the FF period (Fig. S4(b)) but recent studies (Kuang et al., 2015) denied that HULIS can be related to vehicle emissions.

### Source-related composition

At present, in Moscow megacity twenty-six gaseous and particulate pollutants ( $\text{PM}_{10}$  and  $\text{PM}_{2.5}$ ) are under continuous measurements (Mosecomonitoring, 2017).

Around 630 industrial enterprises of various branches of mechanical engineering and metal working, power engineering, chemistry and petrochemistry, light and food industry, production of construction materials (including 30,000 stationary emissions sources) are registered. Around 50% of all pollutant emissions from industrial sources are emitted by enterprises producing and redistributing energy, gas, and water. All gaseous automobile transport exhaust composes 95% of total city emissions (Mosecomonitoring, 2017). Aerosol emissions are produced by FF combustion (of gas in industry and energy production as well as of diesel and gasoline by transport systems). The absence of BB-based residential heating (due to city-wide central heating systems) distinguishes Moscow from other European megacities.

PAHs and their derivatives are produced by incomplete combustion of organic material mostly arising from anthropogenic emissions and wildfires. PAHs vary significantly in urban environment and are mainly influenced by transport-related gasoline, diesel and fuel oil combustion as well as domestic emissions (Ravindra et al., 2008; Ladino et al., 2018). Due to the different stability of PAHs against degradation the atmospheric aging can influence their ratios. BaP, sumB, IND, and BaA are prominent in emissions from non-traffic sources (natural gas combustion and domestic heating plants) while BgP is specific for gasoline and diesel exhausts (Pietrogrande et al., 2011). Several of these compounds have proven to be mutagenic and/or carcinogenic (Pedersen et al., 2009). The correlation matrix for PAHs highlights that PYR, FLU, BaA, CRY, sumB, ACE, BeP, BaP, IND, and BgP are well correlated with each other ( $R > 0.8$ ) confirming their common source. PER, DiBaA, ANT, COR, and RET are not well correlated with the rest of PAHs, which indicates different sources.

Oxy-PAHs are emitted from primary sources or formed by atmospheric reactions between PAHs and atmospheric oxidants such as  $\text{NO}_x$  and  $\text{O}_3$  (Bandowe et al., 2014; Lee et al., 2018). Naphthalic anhydride (NAP-AN) and xanthone indicate the increased reactivity of PAHs adsorbed on particles exposed to atmospheric oxidants ( $\text{O}_3$ , OH and  $\text{NO}_2/\text{O}_3$  mixture) (Ringuet et al., 2012), probably stimulated by photochemical activity leading to oxidation of PAHs. PCA analyses showed that the major sources of oxy-PAHs and PAHs are vehicle emissions and biomass burning (Lee et al., 2018) which can be taken to represent secondary organic aerosol (SOA) formed by photochemical reactions in the atmosphere.

Hopanes are used as markers of traffic emissions because engines that use lubricating oil emit hopanes (Lin et al., 2010). n-Alkanes are emitted by both biogenic and anthropogenic sources which can be differentiated according to n-alkane carbon numbers (He et al., 2006; Ladji et al., 2009). The most abundant n-alkanes in traffic emission are C20–C30 mainly from lubricating oil and fuel with a maximum for C25 for gasoline-powered vehicles and C20 for heavy-duty diesel trucks (Kotianová et al., 2008). While the heavier n-alkanes ( $> \text{C}27$ ) and sugars are mainly emitted from biogenic sources or due to incomplete biomass combustion (Rissanen et al., 2006; Fu et al., 2009).

A good correlation between anhydrosugars is observed in wood combustion as well as in ambient air affected by BB (Caseiro et al., 2009; Lee et al., 2010; Reche et al., 2012).



In this study a rather poor correlation can be observed between Lev and Man ( $R^2 = 0.23$ ). If the periods of FF and BB-affected are considered separately, a better correlation is observed for the days with lower anhydrosugar concentrations ( $R^2 = 0.56$ ) while during the other period a correlation is not visible at all. Such relation can be possible if more than one BB source is contributing to the anhydrosugar burden. This reason can be justified by the long holiday period from 1 to 10 May where a lot of residents in the Moscow region may have burnt garden waste, made bonfires and had barbeques. Lev and Gal correlates well along the whole sampling period ( $R^2 = 0.65$ ). Maximum ratio of 49 is observed during May holidays. Such high ratios are known for burning of hard wood, scrublands and grass pointing to a mixture of these sources in the Moscow region.

Atmospheric HULIS are defined as water-soluble macromolecular compounds with complex and often polymeric structures. They are reported as part of brown carbon related to BB (Lin et al., 2010) and combustion processes in urban environments (Kristensen et al., 2015). Assuming the main source of HULIS are secondary atmospheric reactions, Kim et al. (2016)'s analyses of HULIS-WS-C showed that their origin is mainly from transport of organic aerosols other than BB, while higher contributions of water-insoluble organic carbon (WISOC) can point to BB. Taking this into consideration we can expect that at least a certain part of HULIS-C-AS analyzed can be related to the WISOC fraction described by Kim et al. (2016) and, thus, associated with the transported BB aerosols.

The amount of ions is not only driven by primary gaseous emissions, but also by changes of air temperature, humidity and in air mass transport processes (Stelson and Seinfeld, 1982). Organic ions (formate and lactate) can be associated with natural sources like soils and natural forest emissions but also traffic (Khare et al., 1999, and literature cited therein). Sea salt (or de-icing salts) and soil mineral dust are represented within ions like  $\text{Na}^+$ ,  $\text{Cl}^-$ ,  $\text{Ca}^{2+}$ ,  $\text{Mg}^{2+}$ , and  $\text{K}^+$ . Latter one is also known to be present in BB emissions and was used as a marker in different studies (e.g., Pachon et al., 2013, and literature cited therein).

### Correlation loading analyses of PM compounds

For a deeper understanding of the role of PM compounds as source markers in Moscow urban background in spring, the combined analytical and statistical approach is applied. For the analytical chemistry part, it is suggested to take into account the compounds with the lower analytical uncertainty in the quantification. Correlation analyses estimates how strong they correlate with others and highlight the highest correlations. The correlation matrix uses the Pearson's correlation coefficient as a measure of the linear relation between two variables. It is suggested to take in account the variables with the highest explained variance.

Fig. S5 show the correlation loadings for all classes of quantified compounds. For PAHs it shows three different positions of variables: In the upper right part close to the outer ellipse, that represents 100% of the total explained variance. In the middle of the two ellipses, and out of the inner ellipse, that represents 50% of the total explained variance. From the first group of variables with the highest explained variance, the following analytes with low-

er analytical uncertainty have been chosen: BaP, BgP, SumB, IND and ACE. The same approach has been used to choose FLU from the second group and RET from the third group. As well COR has been chosen as marker for possible different sources.

The correlation matrix for oxy-PAHs highlights well a correlation ( $R > 0.8$ ) between 11HBaFone, 11HBbFone, 11HBcFone, and 7HBdeAone while a lower correlation factor is found for 9HFLUone, xanthone, ANQ-DO, CPPH-O, NAP-AC and NAP-AN. The correlation loading of o-PAHs shows a cluster of chemical compounds quite close to the outer ellipse that represents 100% of the total explained variance containing 11HBaFone, 11HBbFone, 11HBcFone, 7HBdeAone and NAP-AN. To perform the final PCA from the first group of variables with the highest explained variance, the analyte with the lower analytical uncertainty has been chosen: NAP-AN. By the same approach CPPH-O and xanthone have been chosen.

The correlation matrix highlights well a correlation ( $R > 0.8$ ) between 29ab, 30ab, 31abS, 31abR. The correlation loadings of PC1 vs. PC2 show three clusters containing 31abS, 31abR, 30ab, and 29 ab; 32 abR and 32 abS; and Tm and Ts, respectively. 29ab and 30ab are chosen as representative compounds for hopanes because the concentrations of others are negligible. To perform the final PCA, from the groups of variables with the highest explained variance, analytes with the lower analytical uncertainty have been chosen: 29ab and 30ab.

The correlation matrix shows well a correlation ( $R > 0.7$ ) between alkanes from C22 to C33, which is confirmed by the correlation loading. A significant correlation is also shown between C20 and C21, and between C21 and C22 while there is a low correlation ( $R < 0.4$ ) between C20 and C22. C34 does not show any correlation with any other alkane. To perform the final PCA, C20, C23, C24, C25, C27, C29, C32, and C33 have been chosen as the representative alkanes.

Correlations are observed between Aol, Mol, Fru, Glu, Tre, and Suc. Cellobiose (Cel), Eryth, xylitol (Xol), and galactose (Gse) are present in very low concentrations, and they are not significantly correlating with other sugars, beside a significant relation between xylitol and fructose. Strong and multiple correlations between polyols, primary and secondary saccharides point to the fact that these sugars are related to each other. These sugars were reported to originate from biological aerosols: Fungal spores, bacteria and plant debris, as compiled by Caseiro et al. (2007), are often observed in rising amounts during spring season (Yttri et al., 2007). This points to a rising activity of biological sources, like plant pollen, bacteria, and fungal spores. This can be due to the vicinity of the MO MSU location to the botanic garden of the MSU campus. To perform the final PCA, Xol, Aol, Mol, Glu, Suc and Ino have been chosen. Lev, Man, and Gal in the correlation loading are quite distant indicating a clear difference in source. For the final PCA we take into account all BB markers, namely Lev, Man, Gal, and DEH-AC.

Because for both HULIS-C fractions many values are found below LOD no significant correlation of HULIS-C and other compounds is recognized. In the correlation loading analysis HULIS-C fractions are situated outside the inner ellipse which means that this fraction does not contribute significantly to the explanation of the variance. Due to this fact, HULIS is not used in the final PCA.

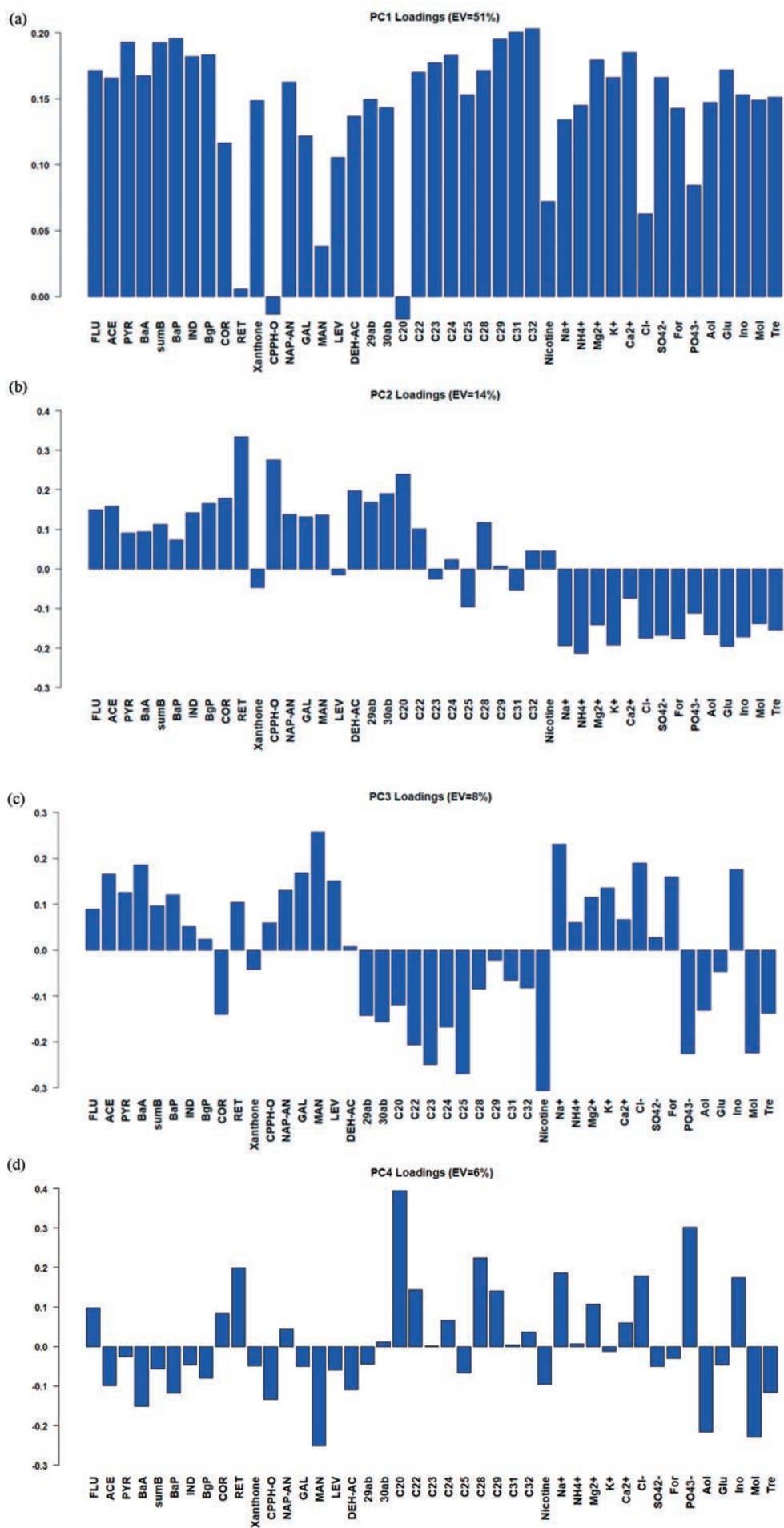


Fig. 8. Loadings of the four most significant PCs with their explained variances (EV).

The correlation loadings of ions show a first cluster composed of  $\text{SO}_4^{2-}$  and  $\text{NH}_4^+$ , a second cluster composed of  $\text{K}^+$ ,  $\text{Mg}^{2+}$ ,  $\text{Ca}^{2+}$ , For, and  $\text{Na}^+$  (Fig. S5(g)). These two clusters are close to the outer ellipse that represents 100% of the total explained variance. In between two ellipses, in different position in the plot, stand BO33– and Lac. Lying on the inner ellipse and completely out of it, that represents 50% of the total explained variance, and in different position in the plot, are  $\text{Cl}^-$ ,  $\text{Li}^+$ ,  $\text{PO}_4^{3-}$ , and  $\text{Cl}^-$ . To perform the final PCA, from the groups of variables with the highest explained variance, analytes with the lower analytical uncertainty have been chosen:  $\text{SO}_4^{2-}$ ,  $\text{Cl}^-$ ,  $\text{K}^+$ ,  $\text{Na}^+$ ,  $\text{Ca}^{2+}$ , FOR, and  $\text{BO}_3^{3-}$ .

For more detailed description of correlation loadings for quantified compounds see “Supplemental Materials.”

### PCA for aerosol composition and source identification

PCA is a common method used in order to describe the impact of source categories in urban environment (Pietrogrande et al., 2011; Lee et al., 2018). The approach developed in this study has formally considered not only number of compounds but also their relations to sources which is different for different compounds in the same class of compounds. Thirty-four representative compounds of various classes of organics (PAHs, oxy-PAHs, hopanes, alkanes, and sugars including Lev, Man and Gal) and seven inorganic ions have been chosen for final PCA, based on their relevance as molecular markers and with a purpose to identify the various sources. Nicotine is added as well.

Four significant PCs describe 78% of the explained variance (EV) contained in the dataset. The loading factors with associated variance are reported in Fig. 8(a). The PC1 (EV = 50%) presents the loading Factor 1, it contains variables of highest variability with absolute values for positive and negative variability ( $> 0.6$ ) for almost all PAHs except COR and RET, oxy-PAN except CPPH-o, hopanes, alkanes except C20, ions except  $\text{Na}^+$ ,  $\text{Cl}^-$ ,  $\text{PO}_4^{3-}$ , and sugars except Man and Lev. The PC1 loading contains almost all the variables describing different emission sources: combustion, natural and biological sources, all presenting strong positive loadings ( $\geq 0.5$ ).

PAHs in Factor 1 indicate emissions from various FF, natural gas combustion and heating plants. C21–C28 are associated with a combination of 4–5-ring PAHs, which are predominant in the emissions from gasoline- and diesel-powered vehicles. C25 confirms the high impact of gasoline-powered vehicles, also supported by 29ab and 30ab from traffic emissions. This observation corresponds well to the present situation in the megacity relating to an increasing fraction of modern vehicle fleets comprised of gasoline direct injection vehicles (Zimmerman et al., 2016). Oxy-PAHs such as 1,8-naphthalic anhydride were found in southern European cities as the compounds associated with secondary organic aerosol formation (Alves et al., 2017). NAP-AN and xanthone in Factor 1 can indicate presence of SOA in the Moscow atmosphere.

$\text{K}^+$  in Factor 1 exhibits the highest variability in contrast to other BB markers (Lev, Man, Gal) and similar to DEH-AC, which presence in the air is an indicator of forest fires and conifer wood domestic burning.  $\text{SO}_4^{2-}$  and  $\text{NH}_4^+$  represent well the secondary inorganic aero-

sols. The high input of  $\text{Ca}^{2+}$  and  $\text{Mg}^{2+}$ , as well as the presence of  $\text{K}^+$  is a hint that PC1 describes also crustal dust sources, like abrasion of soils or construction activities. All sugars are of the similar highest variability demonstrating the same biogenic emission source. This is also confirmed by high loadings of higher alkanes C29, C31, also known as plant waxes (Kotianova et al., 2008). Thus, Factor 1 is interpreted as a mixed factor identifying the sources of traffic, biomass burning, secondary inorganic aerosol, crustal dust and intensive photochemical and biogenic activity.

The PC2, explaining 14% of the total variance, shows strong positive loadings ( $\geq 0.4$ ) for the most of PAHs, o-PAHs, hopanes, and alkane chains (Fig. 8(b)), explaining emissions from FF combustion. Loading Factor 2 presents variables of highest variability for RET, CPPH-O, and C20. Retene is derived by degradation of specific diterpenoids from conifer trees. Therefore, it is a major product of pyrolysis of conifer wood (Vicente et al., 2011). Eicosane C20 (n-alkane with lower carbon number) characterizes heavy-duty diesel truck emissions. In Moscow the diesel truck entry is allowed only after the middle of the night that presently limits its impact to total emission. Thus, marker significance in Factor 2 is an indicator of wood combustion/forest fires and heavy-duty transport impacts. The PC2 with strong negative loadings ( $\leq 0.4$ ) for all ions and sugars explains the natural source.

The PC3 explains 8% of the total variance (Fig. 8(c)). Loading Factor 3 presents the main markers of BB emissions, Lev, Man, Gal, DEH-AC and  $\text{K}^+$ , all showing strong positive loadings ( $\geq 0.3$ ). Other variables with highest positive variabilities are benz[a]anthracene, nicotine and coronene. COR is produced in the petroleum-refining process of hydrocracking and shows the highest negative variability.  $\text{Na}^+$  and  $\text{Cl}^-$  from aged marine aerosols, also  $\text{Mg}^{2+}$  and  $\text{K}^+$  show enhanced loadings in Factor 3. The molar ratio of  $\text{Cl}^-$  to  $\text{Na}^+$  is on average 0.3 indicating a strong depletion of  $\text{Cl}^-$  (Li et al., 2016) which is in accordance with the fact that Moscow lies around 1000 km away from the sea coast. It is possible that some NaCl can originate from the resuspension of de-icing salt, which is used in Moscow megacity but the current factor does not point to other components, which can be expected along with resuspension of soil.  $\text{PO}_4^{3-}$  indicates a specific tracer for plastics burning (Simoneit et al., 2005). Thus, Factor 3 indicates the impact of smoking, local waste burning, and strongly aged marine aerosols, strongly influenced by transport over the land. Highest variability of the PC4 with loading Factor 4 with only 6% of explained variance is presented by C20 from sources which impact is the lowest (Fig. 8(d)).

Scores plot of PC1 (EV = 50%) vs. PC3 (EV = 8%) shows the variation of aerosol chemistry during the sampling period (Fig. 9). 29 April and 1 May present the highest concentrations of all chemical compounds confirming the strong impact of various sources during holidays. Days of 20.04, 21.04, 25.04, 29.04, 1.05, 3.05, and 4.05, indicated by both AAE and Lev marker, are prominent by positive PC3, clearly determining the similarity of aerosol composition during BB-affected period.

Since some statistical techniques assume the PCA performance with the less number of variables in comparison with observations we perform additional calculations with a reduced number of variables, see the results in “Supplemental Materials.”



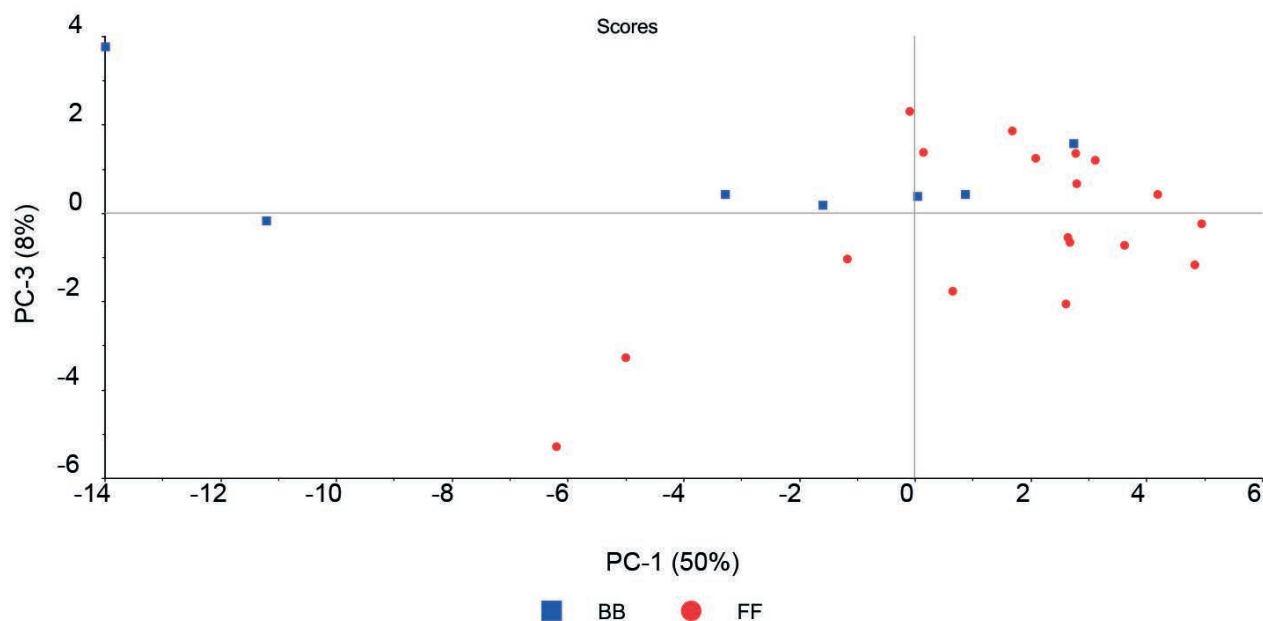


**Fig. 9.** Score PC1&PC3 plot for daily chemistry. Days of BB-affected periods identified by both AAE indicator and Lev marker are indicated by blue, others are indicated by red and related to FF period.

## CONCLUSIONS

A comprehensive approach has been developed for air quality assessment in the environment of a megacity. First, we characterize the aerosol composition in the megacity of Moscow using data on the carbon content, organic compounds, BB molecular tracers, and inorganic ions obtained from April till May, a season exhibiting significant changes in the air temperature, mass advection, and biological activity. The OC, EC, and ions accounted for a large percentage of the total  $PM_{10}$  concentrations. A wide range of optical and analytical tools is applied to quantify organic and inorganic compounds in the aerosol. The optical and chemical markers of the absorption Ångström exponent (AAE) and the levoglucosan concentration, which are strongly correlated, indicate the relative contributions of agricultural fires and residential BB near the city to the urban aerosol composition.

The aerosol compounds of the lowest analytical uncertainty and the highest explained variance are the preferred variables in our suggested analytical approach,

which enhances the data quality from an analytical point of view in addition to indicating the applicability of principal component analysis (PCA). Such an approach permits us to select variables that describe the impact of various sources in Moscow during spring. Statistical analysis of the correlation loadings reveals a number of compounds that represent the aerosol in terms of chemical composition and suggest different emission sources. PCA highlights possible emissions from gas combustion, gasoline-powered and heavy-duty transport, agricultural and residential fires, and biogenic activity. It also emphasizes the formation of secondary organic and inorganic aerosol and the occurrence of photochemical processes during periods of increased biogenic activity. The daily changes in the chemistry, which is mostly affected by air masses transported from agricultural fires in southern Russia, in addition to residential activity, are prominent. The computed PCA factors, distinguishable by their unique loadings, are interpreted as marker species that represent different sources, thus providing one step in the process of source apportionment for a megacity.

## Factors influencing aerosol and precipitation ion chemistry in urban background of Moscow megacity \*

### INTRODUCTION

Airborne particulate matter (PM) is one of the atmospheric pollutants of major concern associated not only to major air quality issues in connection with adverse effects on health (WHO, 2013) and the environment, but also with climate change (Fuzzi et al., 2015). PM is a multiphase system including a large number of components, of both primary and secondary origin, and in most cases prone to further physicochemical modifications (Pöschl and Shiraiwa, 2015; Pöschl, 2005; Raes et al., 2000). Owing to the recognized importance of this complex pollutant, great efforts have been applied worldwide in order to monitor and characterize it as well as to fix thresholds and regulations, allowing to prevent or limit adverse effects on human health and environment. The understanding of the processes leading to PM formation and origin requires to associate them to source profiling and quantification. For these reasons PM chemical speciation is of utmost importance since it allows to identify harmful substances as well as sources, providing tools for mitigation and prevention of potential hazards.

The major components of PM are elemental and organic carbon, sea salt, crustal materials from soil/road dust, and water soluble species (ammonium, sulfate, and nitrate) known as Secondary Inorganic Aerosol (SIA) (Seinfeld and Pandis, 2016). Among the PM components, ions play a major role both because of their abundance and massive contribution to aerosol mass load. Each ion determined is associated to specific sources of emission and formation pathways (Raes et al., 2000). Due to their water-soluble nature, ions also affect the acidity of precipitation. They are a key in precipitation formation processes, thus contributing to the hydrological cycle (Weber et al., 2016; Dadashazar et al., 2019).

In European urban areas, ammonium sulfate and nitrate concentrations are abundant (Putaud et al., 2010; Tositti et al., 2014). Dusts (Brattich et al., 2015; Tositti et al., 2021) may contribute to calcium and magnesium, usually in the form of relatively soluble carbonates capable, beside ammonia, to add neutralization potential to acidic species (Morozzi et al., 2021; Tositti et al., 2018a). Coastal areas are affected by sea salt compounds starting from the most abundant, i.e. NaCl, and extending to further saline compounds (Koçak et al., 2007; Lung et al., 2004). In inland cities during the cold period the sources of particulate sodium and chloride are de-icing agents (DIAs) (Kolesar et al., 2018; Kotowski et al., 2020; Stieger et al., 2018; Tositti et al., 2018a).

Ambient organic ions are associated with secondary organic aerosol (SOA), mainly produced by oxidation of volatile organic compounds (VOCs) (Kawamura and Bikkina, 2016; Pavuluri et al., 2010; Yang and Yu, 2008). Though at significantly lower concentration level

than SIA, they are present in significant “chemodiversity” (Tositti et al., 2018a). The speciation and profiling of SOA is a very hard and complex task (Gentner et al., 2017; Pio et al., 2005; Schauer et al., 2002; Wang et al., 2006), owing to a number of precursors and complexity of oxidation patterns. Oxidation, in fact, is carried out by a series of oxidizing species in the troposphere such as OH and NO<sub>3</sub> radicals, group of peroxy-radicals and ozone (Seinfeld and Pandis, 2016).

High polarity of both SIA and SOA is a key in the so-called cloud processing, wherein aerosol particles induce water vapor condensation upon cloud condensation nuclei until water droplets or snow crystals are formed. Precipitation chemistry largely reflects the composition of precursor aerosols (Pruppacher and Klett, 2010) whose degree of neutralization affects precipitation acidity (pH). Acidity of rains constituted an extremely serious environmental problem in Europe which, owing to effective policies of fuel management, led to a substantial solution of acid rain problems from the late 70’s to date (Tositti et al., 2018b; Vet et al., 2014; Vuorenmaa et al., 2018).

Factors influencing ion chemistry are more important in the urban environment where exposure and hazard to air pollution are sensibly higher, owing to the significant population density and related activities such as industry, transport, and heating etc. In this respect, megacities such as Moscow with over ten million inhabitants require a special focus, since emissions and consequent air quality standards might reveal even more unsafe for human health, material infrastructures as well as cultural heritage (Baklanov et al., 2016).

Emission sources in Moscow as a high latitude megacity have several specific features. Centralized heating supply is seasonally operated from the end of September until the beginning of May. Moscow power and heating plants are almost totally supplied with natural gas. Biomass and coal are not used either for industrial, domestic heating, or individual purposes, differently from many European and Asian cities (Diapouli et al., 2017; Nava et al., 2015). Biomass burning (BB) is not recognized by the local Environmental Agency as a significant source of aerosol pollution in Moscow (Kul’bachevskii, 2021). However, largely populated region in the city outskirts (Moscovskaya Oblast) applies biomass for many scopes, such as wood burning for domestic stoves, agricultural cleaning work, and summer recreational activities, that should be considered for air quality assessment. Seasonal light absorption measurements supported the assessment for the BB contribution in the region around Moscow in autumn and winter (Popovicheva et al., 2022). Moreover, combined organic and statistical analysis differentiated the impact of agriculture fires in spring (Popovicheva et al., 2020b).

\* Zappi A., Popovicheva O., Tositti L., Chichaeva M., Eremina I., Kasper-Giebl A., Tsai Y.I., Vlasov D., Kasimov N. // *Atmospheric Environment*. 2023; 294:119458.

Differently from the rest of Europe (Finardi et al., 2014; Font et al., 2019; Tang et al., 2014), the knowledge of Moscow megacity aerosol and its sources is limited. Black carbon (BC) pollution in the Moscow urban background (Popovicheva et al., 2020a) as well as in the Moscow center (Golitsyn et al., 2015) indicated a strong impact of transport. The first comprehensive aerosol characterization in the urban background of Moscow megacity included ions in spring only (Popovicheva et al., 2020c). BB markers (levoglucosan and  $K^+$  ions) proved the impact of wildfires during the extreme smoke event in August of 2010 (Popovicheva et al., 2014) and agricultural fires (Popovicheva et al., 2020c). Annual records of precipitation in 2012 in Moscow showed the significant increase of its acidity due to the presence of deicing salts (Eremina et al., 2015). The total ionic composition in rains did not change in the last years, while chloride and sodium concentrations were increased. Such finding was associated with DIAs, abundant due to the winter road management in Moscow (Eremina et al., 2015). Despite long-term statistical data for rain acidity and composition (Chubarova et al., 2014), a limited knowledge about factors influencing both particulate and precipitation ions chemistry is available to date for Moscow environment. This situation is further deteriorated by the fact that the Environmental Protection Agency “Mosecomonitoring” conducts the measurements for only  $PM_{10}$  and  $PM_{2.5}$  mass concentrations at some monitoring stations, without any PM speciation.

This paper therefore aims to cover an existing data gap for the aerosol and precipitation ion chemistry in Moscow urban background. We present the results for the seasonal variation of ionic composition obtained in a sampling campaign carried out in periods of spring 2018, summer and autumn 2019. Descriptive statistics are used to provide  $PM_{10}$  and ion seasonal characteristics as well as the comparison between Moscow and some large cities. Constraints of aerosol electroneutrality highlights the ion chemistry of neutralizing agents such as ammonia and carbonates. Varimax and correlation analyses trace the main sources of aerosol and rain ionic species. Black carbon and levoglucosan are considered together with ionic species for improved source apportionment in summer. The relevance of the aerosol chemical speciation to meteorological parameters and air mass transportation are investigated by using the both the conditional probability function (CPF) based on the bivariate polar plot and the Lagrangian integrated trajectory (HYSPLIT) model with the cluster analyses.

## 1. MATERIALS AND METHODS

### 1.1. Study area

Moscow metropolitan area ( $55^{\circ} 45' N$ ;  $37^{\circ} 37' E$  at the city center; mean altitude 150 m a.s.l.) is located in the center of the European part of Russia (map in Fig. 1). Moscow covers an area of 2561 km<sup>2</sup> and has a registered population exceeding 12.5 million, which makes it one of the most densely populated northernmost megacities in Europe. Moscow is characterized by a humid continental climate (Dfb according Köppen climate classification) with ~685 mm precipitation per year (Chubarova et al., 2014) which are represented by snow for about one third of year (mainly from late October to March), and by rain for the other part of the year with a maximum rainfall amount in summer (on average ~61 mm in June).

According to the record of the Meteorological Observatory (MO) MSU over the 60-year period (1954–2013) (Chubarova et al., 2014), significant warming of regional climate with a positive temperature trend of 0.07 °C/year is observed. Southwestern wind (5–10 m/s) prevails during all seasons (<https://weatherspark.com>). Highest wind speeds are typical of fall and winter. Clean Arctic air masses transported from the North are recorded especially in winter while aged plumes from agriculture and wildfires pollute the Moscow atmosphere in spring and summer. Moderate average air temperatures, low solar UV radiation levels, and good ventilation make the accumulation of primary emitted pollutants and the photochemical formation of secondary pollutants less intensive in Moscow (Elansky et al., 2018). Operation of centralized heating system begins and ends in Moscow when the temperature decreases below 8 °C and increases above 8 °C, respectively. Thus, the heating period divides the whole year formally on cold and warm with respect to its operation.

According to air quality characterization, Moscow is classified among the slightly polluted megacities in Europe and North America (Elansky et al., 2018). Traffic exhaust constitutes 93% of the overall gaseous megacity emissions (Bityukova and Mozgunov, 2019). While automobilization is growing in Moscow, intensive implementation of higher ecological classes of engines, a declining share of trucks and better quality of fuel promote the improvement of vehicle ecological parameters. Assuming that currently in Moscow the vehicles are powered with desulphurized fuels, traffic is no longer a significant source of SO<sub>2</sub>. However, high concentrations of NO<sub>x</sub> and CO are still an issue (Elansky et al., 2014), with the potential contributing significantly to SIA by means of active oxidation capacities of the atmosphere (Prinn, 2003; Seinfeld and Pandis, 2016). Around 50% of all pollutant emissions from industrial sources and thermal power stations are emitted by companies producing and redistributing energy, gas, and water. The currently fast urban expansion especially in New Moscow area (Fig. 1) additionally contributes to an aerosol buildup in Moscow.

### 1.2. Aerosol and precipitation sampling

The sampling campaign was conducted at the Aerosol Complex located at Meteorological Observatory of Moscow State University (MO MSU) in the MSU campus, southwest of Moscow city (Fig. 1). MO MSU is not directly affected by local pollution sources such as large transport roads or industrial facilities, the residential area and a highway takes place about 800 m south of the observatory, and industrial area is situated at about 3 km. MO MSU site can be therefore classified as an urban background (Chubarova et al., 2014).

Sampling of particulate matter and precipitation was performed during three seasons: spring 2018 (from April 3rd to May 22nd), summer 2019 (from May 29th to July 31st), and autumn 2019 (from September 5th to December 31st). In this work the term “seasons” is used according to the astronomical and not the meteorological convention. PM sampling was not available after December 31st due to the harsh weather conditions which compromised the sampler, preventing the collection of further winter samples. Samples collected in December (11) were merged to the autumn dataset according to the



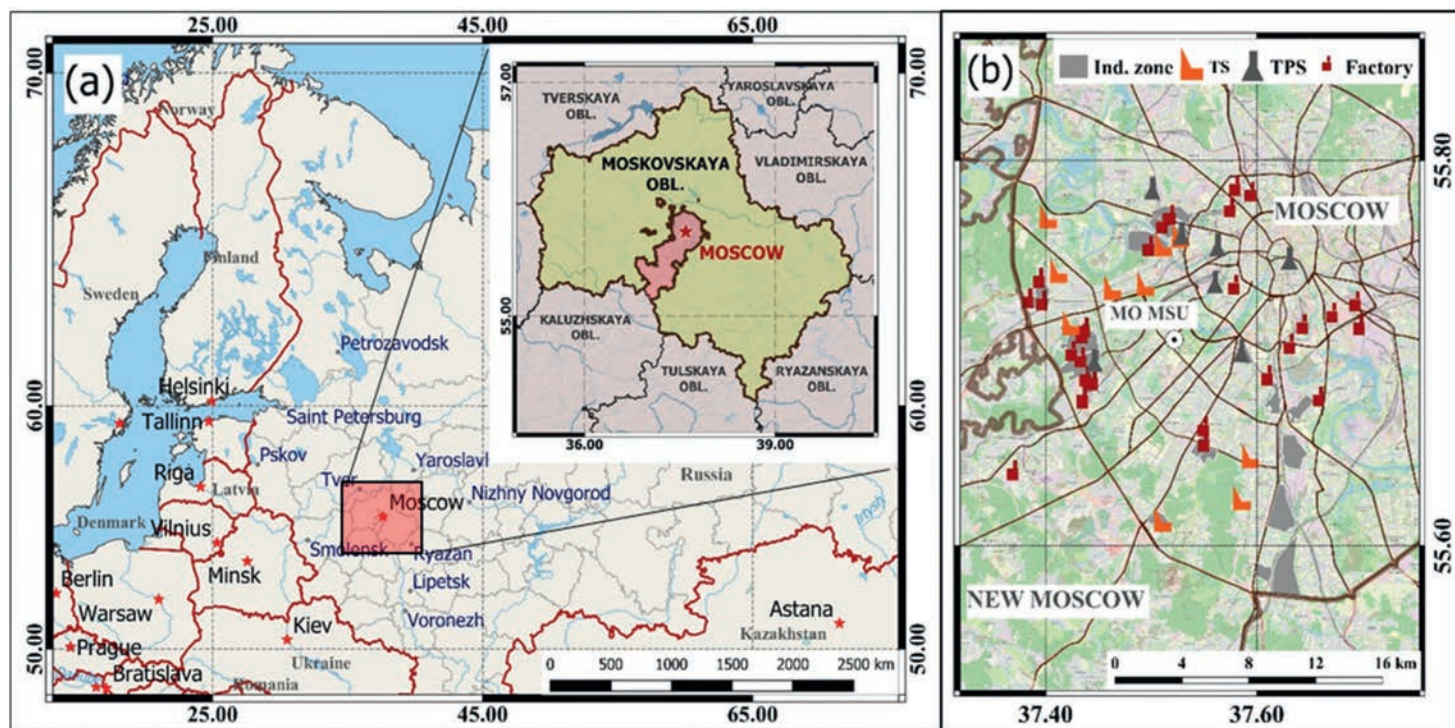


**Fig. 1.** a) Location of Moscow megacity in European part of Russia. Insert is Moscow and Moskovskaya Oblast nearby. b) Southwest sector of Moscow area including New Moscow. Location of sampling site at Meteorological Observatory of Moscow State University (MO MSU) ( $55^{\circ} 42' N$ ;  $37^{\circ} 31' E$ ) is indicated. Industrial zones (Ind.zone), thermal power stations (TPS), thermal stations (TS), and factories in the southwest sector of Moscow are indicated.

astronomical convention, therefore relating December to autumn as an overall cold season.

Particles with a diameter less than or equal to  $10 \mu\text{m}$  ( $\text{PM}_{10}$ ) were daily collected over 24-h periods from 5 p.m. of a given day to 5 p.m. of the next day. In spring and autumn sampling was performed on 47 mm quartz fiber filters (Pall Science, New York, USA), previously heated at  $600^{\circ}\text{C}$  for 5 h. Polyethylene terephthalate 47 mm filters (Merck, Germany) were used for summer sampling. An aspirator using a  $\text{PM}_{10}$  impactor was operated at an air flow of  $1 \text{ m}^3/\text{h}$  by, and the pumped volume was reported in standard atmospheric conditions. Totally, 35, 56 and 67 aerosol samples were collected in spring, summer, and autumn, respectively.

Both types of precipitation (rainfall and snow) were collected at a height of 2 m from the ground surface, using a PVC funnel with an exposed area of  $1600 \text{ cm}^2$  and a polyethylene vessel as a bulk collector. Totally, 16, 23 and 45 precipitation samples were collected in spring, summer, and autumn, respectively.

Meteorological parameters (temperature, relative humidity, pressure, precipitation, wind speed, and wind direction) were obtained at a 3 h time resolution by the MO MSU meteorological service.  $\text{PM}_{10}$  mass concentrations were collected using the tapered element oscillating microbalance TEOM 1400a (Thermo Environmental Instruments Inc., Waltham, MA, USA) by Mosecomonitoring (<https://mosecom.mos.ru/home-page/>). Additionally, continuous aerosol equivalent BC (eBC) concentrations were measured using the custom made portable aethalometer, for more details see elsewhere (Popovicheva et al., 2020a). BC is mainly formed by the incomplete combustion of fossil fuels (diesel, gasoline, gas, coal) in emissions of transport, energy production, residential heating

and biomass burning. Therefore, in this study BC is used as a marker of combustion for the source apportionment together with ions. Further in the text we will call eBC as BC according to commonly accepted terminology.

### 1.3. Analytical procedures

Aerosol samples were analyzed for water-soluble ionic species, namely cations, including sodium ( $\text{Na}^+$ ), ammonium ( $\text{NH}_4^+$ ), potassium ( $\text{K}^+$ ), magnesium ( $\text{Mg}^{2+}$ ) and calcium ( $\text{Ca}^{2+}$ ), and anions including chloride ( $\text{Cl}^-$ ), nitrate ( $\text{NO}_3^-$ ), and sulphate ( $\text{SO}_4^{2-}$ ), using ion chromatography as described elsewhere (Golobokova et al., 2020; Popovicheva et al., 2020c; Tsai and Kuo, 2013). For the extraction phase, the polyethylene terephthalate filter was placed in 5.0 mL of ultrapure water, then shaken for 90 min and filtered through an ester acetate syringe membrane of pore size  $0.2 \mu\text{m}$ . Quartz filter were extracted with 8 ml ultrapure water in an ultrasonic bath for 30 min, then the solution was filtered through acetate cellulose filters (porosity  $0.2 \mu\text{m}$ ). Anions of spring samples were separated by an ion-exchange column (Ion Pac AS17A, Thermo Fisher, USA) in isocratic conditions using  $1.8 \text{ mM Na}_2\text{CO}_3 + 1.7 \text{ mM NaHCO}_3$ , an AMMS suppressor and conductivity detection. Cations were separated on Ion Pac CS12A using  $38 \text{ mM}$  methane sulfonic acid (MSA), the CSRS suppressor and a conductivity detector. The detection limits varied between 2 and  $20 \text{ ng/m}^3$ , the lowest values were obtained for sodium and chloride.

In summer and autumn samples, inorganic cations were determined using a Dionex ICS-1000 equipped with a gradient pump (ICS-3000 Model SP-1), Dionex CSRS Ultra 4mm self-regenerating suppressor, conduc-

tivity detector, and an Ion Pac CS12A analytical column. Inorganic anions as well those from carboxylic acids (formate, acetate, oxalate, carboxylic di-lactate, succinate, and glutarate) were analyzed using a Dionex ICS-5000+ IC, which was equipped with a gradient pump (ICS-3000 Model SP-1) and AMMS 300 MicromembraneTH suppressor and conductivity detector. The guard column and analytical column were Dionex IonPac™ AG11-HC and Dionex IonPac™ AS11-HC, respectively. The MDLs for carboxylates varied between 0.88 and 4.05 ng/m<sup>3</sup>, were lowest for formate and highest for succinate at a nominal sampling volume of 24 m<sup>3</sup> for each typical 24 h PM sampling period.

Additionally, in summer samples sugars (glucose and mannose) and anhydrosugars (levoglucosan and mannosan) were determined using a Dionex ICS-5000+ IC equipped with a pulsed amperometric detector, a CarboPac MA1 guard column and an anion-exchange analytical column, and a Dionex ICS-5000 Electrochemical Detector. The MDLs for sugars and anhydrosugars varied between 1.59 and 3.35 ng/m<sup>3</sup>, were lowest for levoglucosan and highest for glucose at a nominal sampling volume of 24 m<sup>3</sup> for each typical 24 h PM sampling period.

In precipitation samples the concentrations of SO<sub>4</sub><sup>2-</sup>, Cl<sup>-</sup>, NO<sub>3</sub><sup>-</sup> and H<sup>+</sup>, Ca<sup>2+</sup>, Mg<sup>2+</sup>, Na<sup>+</sup>, K<sup>+</sup>, NH<sub>4</sub><sup>+</sup> ions as well as hydrogen carbonate (HCO<sub>3</sub><sup>-</sup>) and pH were measured. HCO<sub>3</sub><sup>-</sup> and pH were analyzed immediately after sampling. Precipitation samples were tested for pH using a pH-meter SP-701 (Suntex, Taipei, Taiwan) calibrated by standard pH solutions before measurements. H<sup>+</sup> concentration was calculated from pH values. Hydrogen carbonate was determined by acidimetric titration with 0.005N HCl by an ionmeter (Econics, RF). The concentrations of other cations and anions were analyzed by using ion chromatography on a JetChrom instrument (Portlab, Moscow, Russia). Detection limits varied between 0.02 mg/L for NO<sub>3</sub><sup>-</sup>, Mg<sup>2+</sup>, NH<sub>4</sub><sup>+</sup>, and K<sup>+</sup>, and 0.03 mg/L for SO<sub>4</sub><sup>2+</sup>, Na<sup>+</sup> and 0.05 mg/L for HCO<sub>3</sub><sup>-</sup>, Cl<sup>-</sup>, Ca<sup>2+</sup>.

#### 1.4. Statistical methods

In order to compare PM<sub>10</sub> and ion data from different seasons and check for similarities between seasons and variables, Mann-Whitney test (Mann and Whitney, 1947) and Spearman correlation indexes (Spearman, 2010) were used. We decided to use such tests, instead of the classical Student's t-test and Pearson correlation, because these are non-parametric. They allow the robust comparison even in the absence of normally-distributed data, as typically observed for atmospheric variables (Ott, 1990). For Mann-Whitney test, compositional data were divided into three groups, based on the three analyzed seasons, and for each variable the comparisons between each couple of seasons were computed. Results are expressed in terms of p-values, used in this case as a "similarity index": p-values higher than the chosen significance level (0.05) indicates that the two compared variables are not statistically different, while p-values lower than 0.05 indicate a statistically relevant difference.

Method based on the bivariate polar plot (Carslaw and Ropkins, 2012) shows how the concentration of species varies jointly with wind speed and wind direction in polar coordinates. This approach allows to trace the

source location, preferably at scale ~1-10 km where the wind direction is remaining quasi-constant while the calculations of air mass transportation provides a limited support thanks to the low spatial resolution of the model employed (Carslaw and Beevers, 2013). The highest values of concentrations identify the directions of emission source.

Backward trajectories (BWT) were generated using NOAA Hybrid Single-Particle Lagrangian Integrated Trajectory (HYSPLIT) model of the Air Resources Laboratory (Stein et al., 2015), with coordinate resolution equal to 1° × 1° of latitude and longitude. The potential source areas were investigated using 3 days back for air masses arriving each one hour at 500 m height above sea level (A.S.L.). BWTs were calculated in 1 hour for all periods of sampling.

Cluster analysis of trajectory data is an effective method of grouping the origin-like trajectories by combining the geographically close data, it takes into account the features of seasonal atmospheric circulation. The angular method is selected in which the matrix of angular distances shows how similar are two points of the BWT in dependence on their angle with respect to the initial location (Cui et al., 2021). Fire information was obtained from Resource Management System (FIRMS), database MODIS (<https://firms.modaps.eosdis.nasa.gov/map>), operated by the NASA/GSFC Earth Science Data Information System (ESDIS).

The scavenging ratio is a parameterization of the loss rate for gas or aerosol particles from the atmosphere by their incorporation into larger drops. This factor can be calculated by taking into account the volumes or masses of the chemical species being exchanged (Engelmann, 1971; Kasper-Giebl et al., 1999). The scavenging ratio in our study is the quotient of the concentration of ions in precipitation related to the concentration of those ions in aerosols. The scavenging ratios for each ion ( $\omega$ ) were calculated using the following formula:

$$\omega = (C_p / (\rho_p)) / (C_a / \rho_a), \quad (1)$$

where  $C_p$  is the ion concentration in precipitation,  $\mu\text{g/L}$ ,  $C_a$  is the concentration of the same ion in aerosols,  $\mu\text{g/m}^3$ ,  $\rho_p$  is the density of the precipitation, 1.0 kg/L,  $\rho_a$  is the density of the air. Air density was assumed to be constant during all sampling periods (1.2 kg/m<sup>3</sup>). With formula (1), it is possible to estimate the impact of rainfall for the different chemical species. In this work we have limited our calculation to season averages and to SIA ions, since their origin is more safely attributable to wet deposition as the aerosol scavenging processes; the other ion species may come from dry deposition which cannot be solved using a bulk precipitation collector.

Source apportionment was performed for both particulates and precipitation by factor analysis using the Vari-max algorithm (Van Espen and Adams, 1983), that is an extension of principal component analyses (PCA) with a rotation of the principal components space to convert the PCs into factors. In this way, each factor can be considered as the common source for the variables having higher loading values for that factor. This method was preferred to other more efficient models such as Positive Matrix Factorization owing to statistical constraints dictated by the limited number of observed parameters (Hopke, 2016).



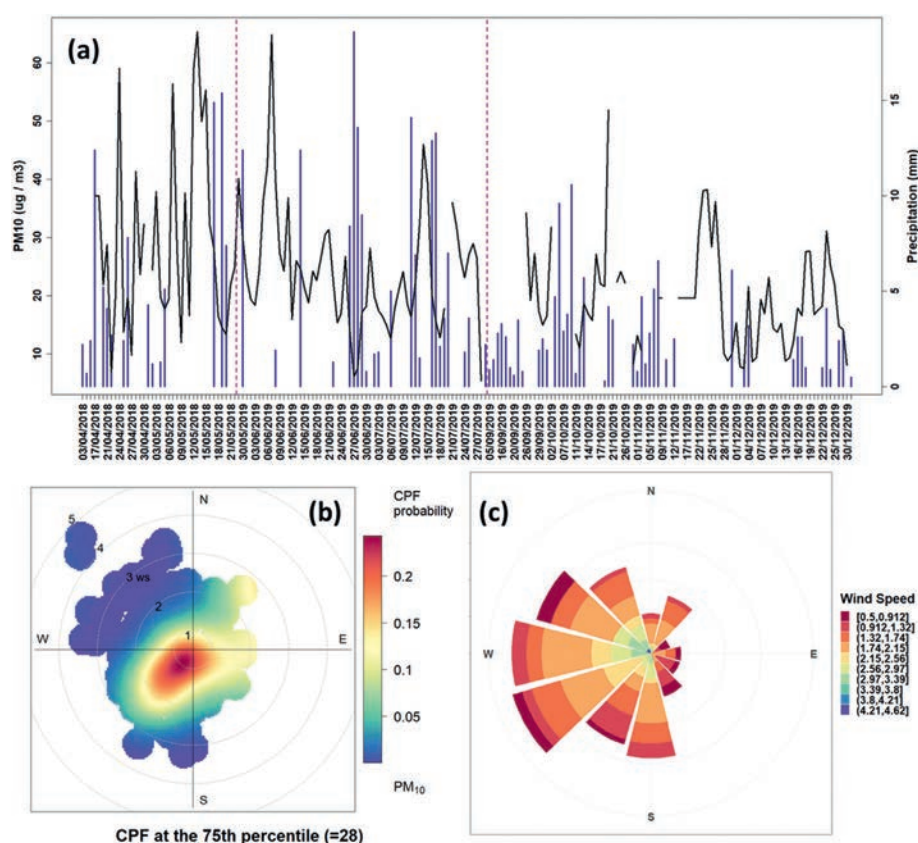


**Fig. 2.** a) Time series of  $PM_{10}$  (black lines) and precipitation (blue bars), dashed lines indicate the separation between three seasons; b) CPF bivariate polar plots showing the wind speed (ws) and wind direction dependence of  $PM_{10}$  concentration at 75th percentile, radial axis for wind speed in m/s; c) wind rose for the whole period of study. (For interpretation of the references to color in this figure legend, the reader is referred to the Web version of this article.)

## 2. RESULTS AND DISCUSSION

### 2.1. Aerosol data overview

#### 2.1.1. $PM_{10}$ and meteorological parameters overview

Table S1 presents the seasonal statistics of meteorological variables. Springtime of 2018 and summertime of 2019 with mean temperature  $14 \pm 4.7^\circ\text{C}$  and  $18.7 \pm 3.8^\circ\text{C}$ , respectively, corresponded to the warm period while autumn with low mean temperature  $3.2 \pm 5.4^\circ\text{C}$  belong to the cold period. The season with the highest precipitation ( $6.53 \pm 1.3$  mm) was summer. Time series of  $PM_{10}$  mass in three seasons, i.e., spring 2018, summer 2019, and autumn 2019 was shown in Figure 2.  $PM_{10}$  did not exceed the EU threshold of  $50 \mu\text{g}/\text{m}^3$  during any day if not in rare cases. The plot of  $PM_{10}$  vs. the main meteorological variables reveals that higher values were detected in association with periods of low or no precipitation (Figure 2a), and low wind predominant from the southwest (Figure 2b). The wind rose for the studied period is shown in Figure 2c, confirming westerly and south-westerly winds with speeds between 0.5 and 2.5 m/s, similar to the predominant wind direction for the MO MSU reported by (Chubarova et al., 2014). No particular correlation was observed between  $PM_{10}$  and temperature (Figure S1a). Lower  $PM_{10}$  was encountered in connection with lower pressure (Figure S1b), usually coinciding with higher precipitation (Figure 2a) and rel-

ative humidity (Figure S1c), responsible for aerosol wet scavenging, in agreement with the  $PM_{10}$  wet removal. The biggest differences between meteorological parameters were found for temperature and relative humidity by boxplots in Figure 3.

#### 2.1.2. Descriptive statistics

Basic statistics on seasonal concentrations of  $PM_{10}$ , inorganic ions ( $\text{SO}_4^{2-}$ ,  $\text{NO}_3^-$ ,  $\text{Cl}^-$ ,  $\text{Ca}^{2+}$ ,  $\text{K}^+$ ,  $\text{Na}^+$ , and  $\text{Mg}^{2+}$ ), carboxylic acids, and sugars is shown in Table S1 for the whole period of study. Oxalate and nitrite ( $\text{NO}_2^-$ ) could be measured above DL additionally to inorganic ions in spring, and in autumn and summer, respectively. Carboxylates (oxalate, acetate, formate, lactate, glutarate and succinate) as well as sugars (mannose, glucose) and anhydrosugars (levoglucosan and mannosan) were considered for summertime only. Also, total inorganic ions (TII), total organic ions (TOI) and total sugars (TS) are estimated in Table S1.

Maximum mean  $PM_{10}$  ( $33.5 \pm 28.2 \mu\text{g}/\text{m}^3$ ) was found in spring and minimum ( $19.5 \pm 8.6 \mu\text{g}/\text{m}^3$ ) in autumn. Statistically significant difference was estimated between autumn as compared to other two seasons. In both spring and autumn mean concentrations for inorganic anions and cations was found as following:  $\text{SO}_4^{2-} > \text{NO}_3^- > \text{Cl}^-$  and  $\text{Ca}^{2+} > \text{K}^+ > \text{Na}^+ > \text{Mg}^{2+}$ . In summer this tendency is the same, except for  $\text{Na}^+$ , higher than  $\text{K}^+$ .

Boxplots for inorganic ions are shown in Figure 3.  $\text{Na}^+$  showed the largest variability between seasons,



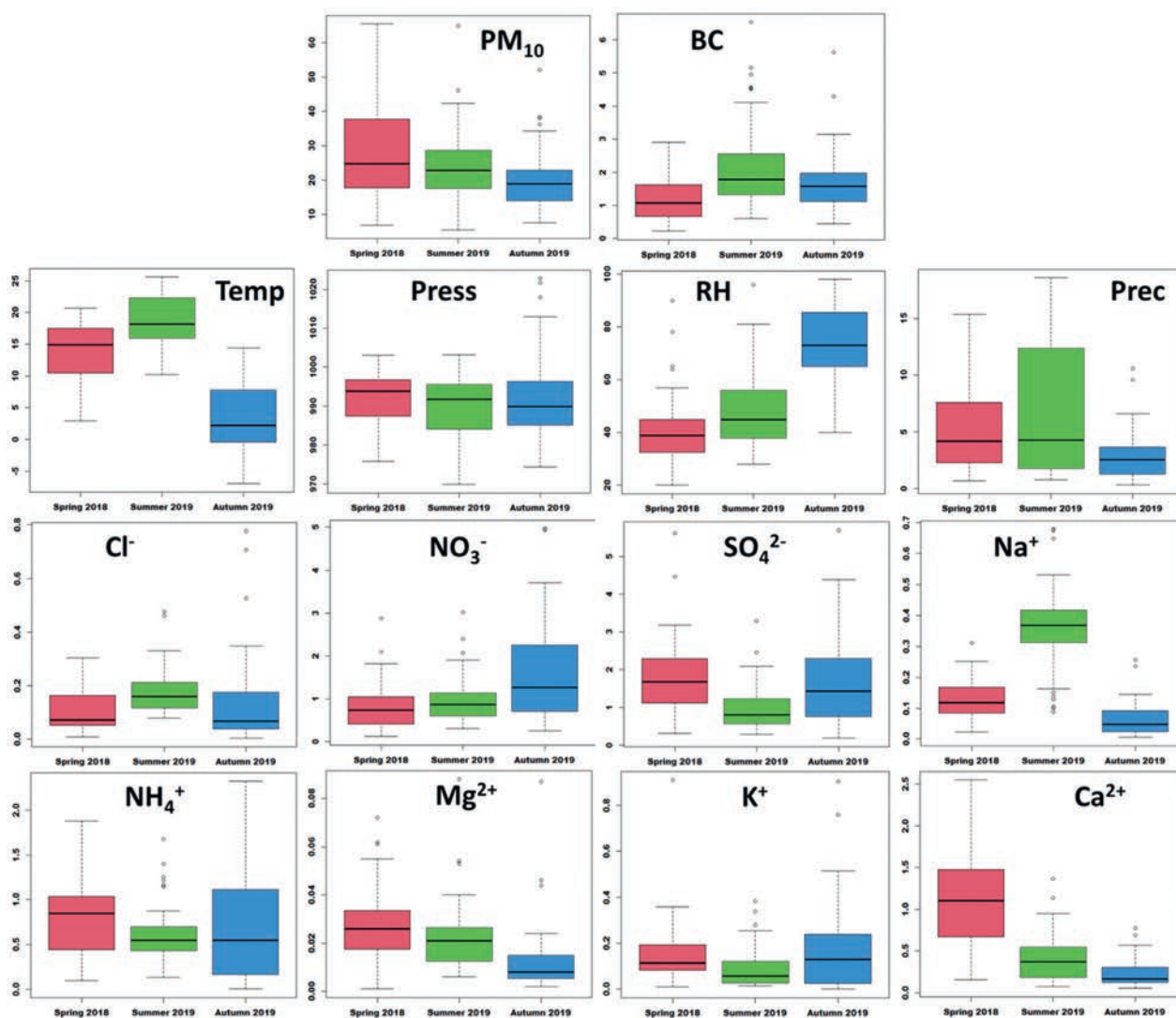


**Fig. 3.** Boxplots of aerosol  $\text{PM}_{10}$ , BC, temperature (Temp, °C), pressure (Press, hPa), relative humidity (RH, %), and Precipitation (Prec, mm), and inorganic ions concentrations ( $\mu\text{g}/\text{m}^3$ ) for spring 2018, summer 2019, and autumn 2019. Units of measure are the same of Table S1. Red, green, and blue boxes indicate spring, summer, and autumn, respectively. (For interpretation of the references to color in this figure legend, the reader is referred to the Web version of this article.)

with a median of  $0.37 \mu\text{g}/\text{m}^3$  and maximum of  $0.67 \mu\text{g}/\text{m}^3$  in summer and a median of  $0.05 \mu\text{g}/\text{m}^3$  and minimum of  $0.01 \mu\text{g}/\text{m}^3$  in autumn, respectively. Its variability is well-captured by Mann-Whitney tests comparing chemical values between seasons: p-values are all statistically significant ( $< 10^{-4}$ ), indicating significant differences between all couple of seasons. A similar behavior was found also for  $\text{Ca}^{2+}$ , although in this case a maximum ( $1.11 \mu\text{g}/\text{m}^3$ ) in spring and a minimum ( $0.16 \mu\text{g}/\text{m}^3$ ) in autumn were observed, all Mann-Whitney p-values are statistically significant.  $\text{K}^+$  is different by the highest median of  $0.11 \mu\text{g}/\text{m}^3$  and maximum in spring of  $0.99 \mu\text{g}/\text{m}^3$ , and in autumn ( $0.124$  and  $0.76 \mu\text{g}/\text{m}^3$ ) with significant differences (p-value  $< 0.5$ ) in summer. Median  $\text{Cl}^-$  ( $0.17 \mu\text{g}/\text{m}^3$ ) and  $\text{SO}_4^{2-}$  ( $1.0 \mu\text{g}/\text{m}^3$ ) also demonstrate the significant differences in summer while similarities are found for these ions in the other seasons. Median  $\text{NO}_3^-$  ( $1.6 \mu\text{g}/\text{m}^3$ ) and  $\text{Mg}^{2+}$  ( $0.12 \mu\text{g}/\text{m}^3$ ), instead, showed significant differences in autumn as compared to other seasons, while a median  $\text{NH}_4^+$  ( $0.8 \mu\text{g}/\text{m}^3$ ) exhibited a slightly significant difference (p-value = 0.04) only

when comparing spring and summer values.

Massive contribution of measured species to  $\text{PM}_{10}$  for each season is shown in Figure 4. Total inorganic ions (TII) constitute the largest fraction of aerosol mass in the cold period reaching a maximum of 27% in autumn, and a minimum of 16.5% in summer. Sulfates and nitrates dominate among the major anion components, with maximum contribution of 38 and 34% to TII in autumn, respectively. Cations are mainly represented by calcium and ammonium.  $\text{Ca}^{2+}$  had a maximum of 21% in spring and minimum of 5% in autumn. Seasonality of  $\text{NH}_4^+$  was not prominent, ~15-17% in any season. A lower though significant fraction of inorganic ions in TII was represented by sodium and chloride; in summer the percentage of both  $\text{Cl}^-$  and  $\text{Na}^+$  approached their maxima respectively of 5 and 11%, dropping to minima of 1.6 and 2% in autumn, respectively. Finally, maximum of  $\text{K}^+$  fraction of 3% was observed in spring and autumn.

In European urban areas, ammonium sulfate and nitrate concentrations may reach up to 21-28% of  $\text{PM}_{10}$ , owing to the extensive use of combustion at all the scales from industry down to domestic and individual uses

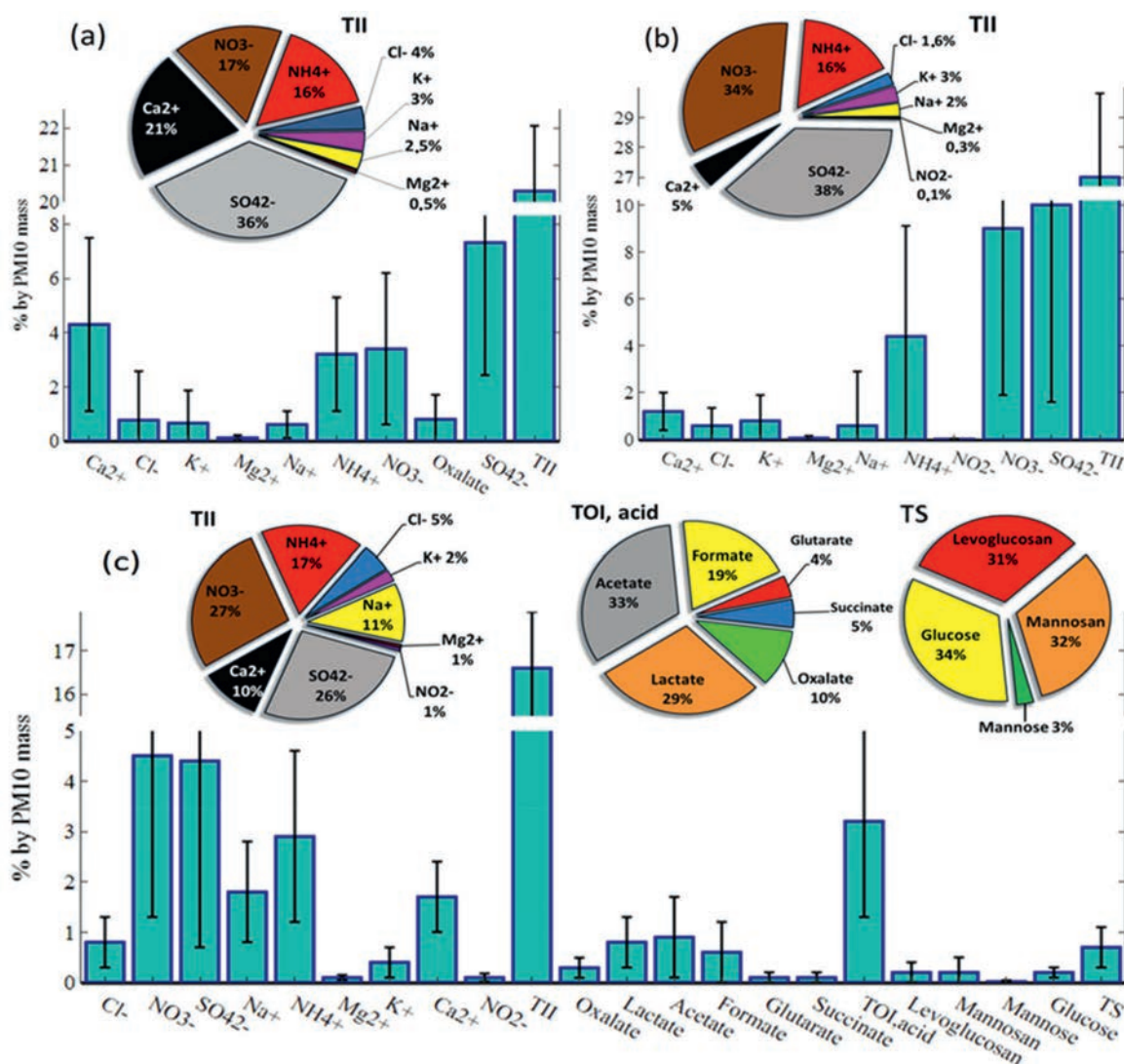


**Fig. 4.** Percentage contribution in PM<sub>10</sub> mass of inorganic ions and oxalate in spring 2018 (a), of inorganic ions and NO<sub>2</sub><sup>-</sup> in autumn 2019 (b), and of inorganic ions, organic ions, sugars and anhydrosugars in summer 2019 (c). Contribution of total inorganic ions (TII), total organic ions (TOI) and acids, and total sugars (TS) including anhydrosugars is shown. Pie diagrams show the relative abundance of individual measured species in total.

(Putaud et al., 2010; Tositti et al., 2014). In Moscow urban background we have obtained the maximum contribution of ammonium sulfate and nitrate to PM<sub>10</sub> around 15% in the cold period.

Summer species analyses showed that total inorganic fraction in PM<sub>10</sub> was higher (16.5%) than total carboxylates (3.5%), and total sugars and anhydrosugars (0.8%). Acetate and lactate dominated total organic ions (TOI), 33% and 29%, respectively. Acetate constitutes 1% to PM<sub>10</sub> mass in summer samples. Levoglucosan and mannan were the most prominent components of total sugars with respectively 31% and 32%.

### 2.1.3. Comparing Moscow PM data with other large cities

Aerosol sources are seasonally modulated by a number of meteorological factors, e.g., precipitation, atmospheric circulation as well as solar radiation, all influencing the planetary boundary layer height and, therefore, air pollutant concentrations. Urban emissions may be also influenced by seasonal variability, as in the case of domestic heating. In Table 1, data obtained for Moscow urban background are compared with a few large cities such as Am-

sterdam, London, Athens, and Paris. The comparison was carried out with urban background sites of big cities taking place also at the similar northern latitudes as Moscow. Mean PM<sub>10</sub> in Amsterdam (Hama et al., 2018) is slightly lower than Moscow but SIA concentrations are higher. SIA concentrations in London are also higher (Beccaceci et al., 2015). In Athens NO<sub>3</sub><sup>-</sup> concentrations are comparable with Moscow while other SIA are higher. The average PM<sub>10</sub> in Paris suburbs is almost twice higher while the concentrations of SIA are 3-12 times higher (Srivastava et al., 2018). Continental Toronto downtown, that is found at a similar latitude than Moscow but is influenced by the Great Lakes, shows SIA (Jeong et al., 2020) comparable to those observed in Moscow. Here we note that data for Toronto and Athens are presented for PM<sub>2.5</sub>. However, the comparison hold for SIA species may be reasonably considered because the SIA populating the submicron range is common to both PM<sub>10</sub> and PM<sub>2.5</sub>.

Despite Moscow has the largest population among European and Canadian cities of our comparison (with exception of London closer with its 9 million of inhabitants) though their size is not comparable, our data shows that Moscow urban background has the lowest SIA content with minima of SO<sub>4</sub><sup>2-</sup> and NH<sub>4</sub><sup>+</sup>, and comparable

$\text{NO}_3^-$ . Such finding is well related to a fact that nitrogen oxides constitute a large fraction of gaseous atmospheric pollution in Moscow, and their concentration is comparable to most of largest cities in industrialized countries while the average concentration of sulfur dioxide, ozone, and carbon monoxide is much lower than in the majority of world megacities (Elansky et al., 2007). The reason for that is the dominant using of gas as a fuel, leading mainly to the emissions  $\text{NO}_x$  and CO from heat and power plants (Elansky, 2014).

$\text{Na}^+$  and  $\text{Cl}^-$  concentrations in all the cities mentioned above with marine climate are higher than in Moscow a few times, indicating direct sea salt impact on their airsheds. Under ordinary circulation conditions, sea salt cannot exceed a few kilometers from the coast-line inward. In Toronto (Srivastava et al., 2018),  $\text{Na}^+$  and  $\text{Cl}^-$  are significantly less, revealing the absence either sea-salt or road management impact on the ion composition. The similar trend of strongly higher  $\text{Mg}^{2+}$  concentrations are found for coastal cities, probably the indication of the impact of sea salt aerosols on water-soluble species as well. Road salt aerosol driving wintertime atmospheric chlorine chemistry have been observed for inland cities (McNamara et al., 2020) and related to pseudo-marine factor relating to winter street management (Tositti et al., 2014). Thus,  $\text{Cl}^-$  and  $\text{Na}^+$  concentrations at the MO MSU site can be attributed to the impact of de-icing agents (DIAs) on aerosol composition in agreement with previous work by Eremina et al. (Eremina et al., 2015). Indeed, icy winters with long-lasting snow deposits require an intensive road management in Moscow to prevent traffic inconveniences. The composition of solid and liquid DIA used in Moscow megacity is dominated by NaCl salts, as reported in Supplementary

Material. DIAs resuspension by traffic-induced turbulence significantly alter the snow composition along the roadsides (Vlasov et al., 2020). Near the MO MSU, soil salinization persists throughout the year and practically does not depend on the moisture regime affecting aerosol composition by soil resuspension in a continuous way and a modulation controlled by local circulation.

Mean  $\text{PM}_{10}$  in Moscow is comparable with continental large cities such as Berlin (Wieprecht et al., 2004) and Prague (Schwarz et al., 2019), and slightly lower than in Sofia (Hristova et al., 2020) and Bucharest (Perrone et al., 2018). All mentioned cities are characterized by higher  $\text{SO}_4^{2-}$  and  $\text{NH}_4^+$  concentrations than in Moscow.  $\text{NO}_3^-$  is higher for Prague and Berlin, and comparable for Sofia and Bucharest. Transport of marine aerosols and impact of road salt along with aged sea salt increases  $\text{Na}^+$  and  $\text{Cl}^-$  concentrations in Sofia (Hristova et al., 2020). In Prague, road salt along with aged sea salt provide the similar concentrations as in Moscow (Schwarz et al., 2019). Moreover, in Prague, the concentrations of  $\text{Mg}^{2+}$  is comparable while  $\text{Ca}^{2+}$  is two times lower than in Moscow. In Budapest,  $\text{Na}^+$  concentrations are lower, and  $\text{Mg}^{2+}$  concentrations are comparable to Moscow.  $\text{K}^+$  is only one ion which concentration data for Moscow and other cities are very similar, an exception is Sofia where three times higher pollution by potassium related to residential heating is observed.

Although a longer sampling campaign would be required to draw conclusive considerations, our data indicate that the pollution in Moscow is comparable, if not lower, than that of also smaller cities. Paris and London, moreover, have significative higher pollution, but with certainly lower dimensions and populations.

**Table 1.** Mean  $\text{PM}_{10}$  and ions concentrations, in  $\mu\text{g}/\text{m}^3$ , in Moscow and large European and North America cities over periods indicated. Sites of comparison are described.

City, period	$\text{PM}_{10}$	$\text{Cl}^-$	$\text{NO}_3^-$	$\text{SO}_4^{2-}$	$\text{Na}^+$	$\text{NH}_4^+$	$\text{Mg}^{2+}$	$\text{K}^+$	$\text{Ca}^{2+}$	site
Moscow, Russia Apr–May 2018, Jun–Dec 2019	23.3	0.14	1.20	1.46	0.18	0.69	0.02	0.13	0.48	urban background
Amsterdam, Netherlands Apr 2013–May 2014	20.7	0.98	4.79	2.2	0.86	1.75	0.13	0.10	0.27	urban background
London, UK Jan 2013–Dec 2013	–	1.34	3.41	2.16	1.05	1.25	0.14	0.09	0.39	urban background
Paris, France 6–21 March 2015	49.0	0.58	14.4	4.3	0.41	5.66	0.06	0.14	0.86	suburban background
Athens, Greece June 2005–Sep 2006	24.2*	0.26*	1.42*	4.19*	0.73*	1.32*	0.12*	0.18*	1.2*	suburban background
Toronto, Canada Mar 2004–May 2014	13.0*	0.03*	1.70*	1.88*	0.04*	0.91*	0.01*	–	–	Downtown
Sofia, Bulgaria Jan 2019–Jan 2020	30.9	0.31	1.87	3.03	0.37	0.75	0.12	0.36	0.76	urban background
Budapest, Hungary Feb 2015–May 2015	29.9	–	1.9*	2.0*	0.13*	1.2*	0.02*	–	–	urban background
Prague-Libuš, Czech Rep. Apr 2008–Mar 2009	26.7	0.22	3.15	2.86	0.16	1.67	0.03	0.13	0.22	suburban background
Berlin, Germany Sep 2001–Sep 2002	22.3	–	2.4	3.9	–	1.8	–	–	–	urban background

Note. \*Data are given for  $\text{PM}_{2.5}$ .



## 2.2. Aerosol data analysis

### 2.2.1. Cations and anions balance

For sake of electroneutrality constraints, cations and anions have been analyzed for their charge balance. Ion data, converted into equivalents, show a deficit of anions in spring and summer, 33% and 35%, respectively (Fig. S2). This fact may be ascribed to carbonate ions, that were not analyzed directly. Their concentration was calculated from calcium and magnesium concentrations (Alastuey et al., 2004; Popovicheva et al., 2020d; Tositi et al., 2014) attributed to the mineral components associated to soil resuspension (Chow et al., 2015). Once added  $\text{CO}_3^{2-}$  to anions, linear regressions are computed for three seasons (Fig. 5). Table 2 shows  $R^2$ , slopes, and intercepts, and their relative standard deviations,  $\sigma$ , for the three seasons. Results indicate that spring aerosol is substantially electroneutral with the slope and intercept not significantly different from their ideal values of 1 and 0, respectively. Summer data, instead, show a slope slightly, but significantly different from 1 ( $p$ -value = 0.01). This indicates a slight excess of cations, but such a low difference, given that the intercept is not significantly different from 0, is most likely due to the experimental uncertainties, characterizing summer aerosol as almost neutralized. Autumn regression, instead, shows both slope and intercept significantly different from 1 and 0 ( $p$ -values 0.005 and 0.0001). This suggests an excess of anions, probably due to the presence of not neutralized  $\text{H}^+$  which can be a result of the gas to particle conversion of  $\text{SO}_2$  and  $\text{NO}_x$  to their respective acids and ammonium salts (not measured and therefore unaccounted in the charge balance), due to a temporary reduction of alkaline substances such as gaseous  $\text{NH}_3$ . It is to note that

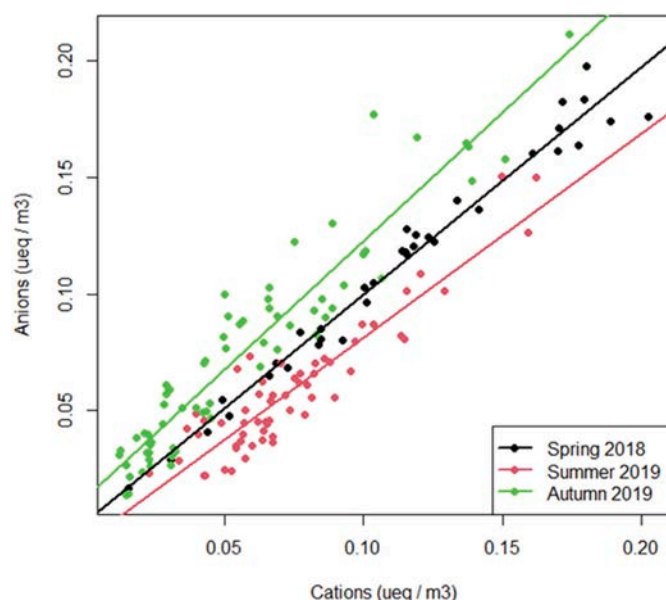


**Fig. 5.** Linear regressions of anions vs cations for spring 2018, summer 2019, and autumn 2019 with the contribution of  $\text{CO}_3^{2-}$  added to anions.

**Table 2**

Regression lines parameters for ion charge balance for three seasons.

Season	$R^2$	Slope	$\sigma_{\text{slope}}$	Intercept	$\sigma_{\text{intercept}}$
Spring 2018	0.97	0.97	0.03	0.002	0.0035
Summer 2019	0.84	0.87	0.05	-0.006	0.0039
Autumn 2019	0.89	1.10	0.04	0.012	0.0032

for Moscow atmosphere this component may include not only actual soil and road components, but also the additional carbonate fraction and, what's more,  $\text{CaCl}_2$  in DIA used for road management leading to a not predictable split of Ca and consequent bias in the charge balance (Eremina et al., 2015; Vlasov et al., 2021).

### 2.2.2. Chloride depletion

We check for the occurrence of chloride depletion in Moscow urban background, deriving from the likely interactions of  $\text{HNO}_3$  with  $\text{NaCl}$  (Hoffman et al., 2004; McNamara et al., 2020). The reaction involved is the following:



It was previously shown that the appearance of hydrogen chloride in the atmosphere of Moscow is the result of heterogeneous multiphase chemical reactions, including the above one, with the participation of DIAs (Eremina et al., 2015).

In order to evaluate the chloride depletion in three seasons, regressions were computed using  $\text{Na}^+$  as independent variable, owing to its remarkable chemical stability in the environment, and  $\text{Cl}^-$  as the dependent variable. The results are reported in Figure 6 and Table 3. Ion concentrations reveal a poor but positive ( $R^2 > 0.4$ ) correlation in spring and autumn with slopes of 0.87 and 2.02, respectively. Both slopes are far from 1.54, the value expected for  $\text{NaCl}$  composition. In spring,  $\text{Cl}^-$  concentration is less than expected in sodium chloride, demonstrating a feature of chlorine depletion following the snow melt and the remobilization of DIA in road dust.

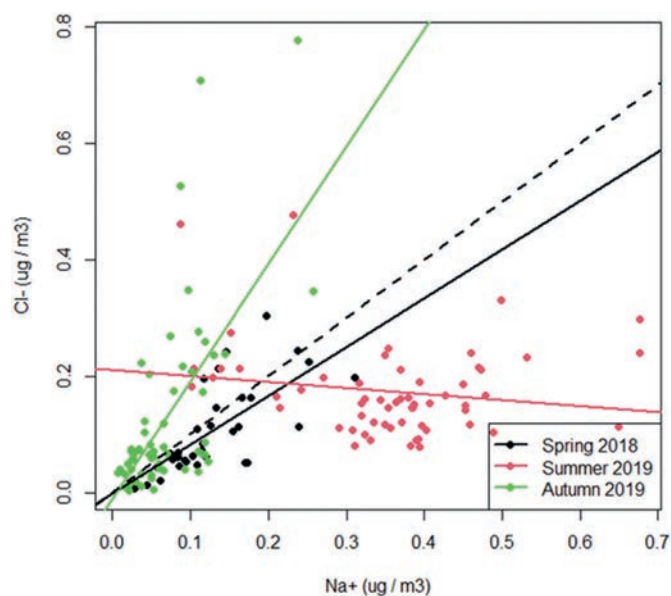


**Fig. 6.** Correlation of  $\text{Na}^+$  and  $\text{Cl}^-$  for the three seasons. Dashed line corresponds to concentration ratio of  $\text{Na}^+$  and  $\text{Cl}^- = 1:1$ .

**Table 3**

Regression lines parameters for chloride depletion in three seasons.

Season	$R^2$	Slope	$\sigma_{\text{slope}}$	Intercept	$\sigma_{\text{intercept}}$
Spring 2018	0.49	0.87	0.14	-0.003	0.02
Summer 2019	0.01	-0.10	0.08	0.21	0.03
Autumn 2019	0.41	2.02	0.31	-0.01	0.025

In summer, the correlation between  $\text{Cl}^-$  and  $\text{Na}^+$  is negative, suggesting a significant influence of reaction (2) in displacing chloride from sodium chloride. Probably, DIAs are not washed off efficiently by snow thawing and runoff as soon as the weather becomes milder, allowing for its aerosolization at the inception of warmer and drier conditions in summer.  $\text{NaCl}$  resuspension is promoted by both a significant low-level turbulence and dryness and the required photochemistry leading to  $\text{HNO}_3$  accumulation, less easily neutralized by ammonia which reacts preferably to  $\text{H}_2\text{SO}_4$  (Hewitt, 2001; Seinfeld and Pandis, 2016).

### 2.2.3. Secondary inorganic aerosol (SIA)

SIA derives from the oxidation of  $\text{SO}_2$  to  $\text{H}_2\text{SO}_4$  and of  $\text{NO}_x$  to  $\text{HNO}_3$ , respectively, under the influence of photochemically driven oxidation processes (Hewitt, 2001). These reactions are followed by variable degrees of neutralization by two alkaline substances, i.e. gaseous  $\text{NH}_3$ , the most abundant atmospheric alkaline substance, and to a lesser extent  $\text{CaCO}_3$  of mineral origin (Fountoukis and Nenes, 2007; Heal et al., 2012; Karydis et al., 2020; Tositti, 2018). It is to note that the neutralization of  $\text{H}_2\text{SO}_4$  by  $\text{NH}_3$  is thermodynamically favored as compared to the analogous reaction with  $\text{HNO}_3$ , while  $\text{NH}_4\text{NO}_3$  is less thermally stable, both conditions promoting the availability of  $\text{HNO}_3$  for reaction (2) and the subsequent chloride depletion.

Lai et al. (Lai et al., 2007) proposed two methods to evaluate the degree of neutralization of ammonia as sulfate or nitrate by using the correlation between the concentration of  $\text{NH}_4^+$  and that calculated from the concentrations of  $\text{SO}_4^{2-}$  and  $\text{NO}_3^-$ . Both methods are based on stoichiometric considerations and are based respectively on the neutralization of  $\text{H}_2\text{SO}_4$  and  $\text{HNO}_3$  by ammonia as  $\text{NH}_4\text{NO}_3$  and  $\text{NH}_4\text{HSO}_4$  (method 1), or as  $\text{NH}_4\text{NO}_3$  and  $(\text{NH}_4)_2\text{SO}_4$  (method 2). In our work, we used  $\text{nss-SO}_4^{2-}$  fraction instead of total  $\text{SO}_4^{2-}$ . The results obtained are depicted in Figure 7, Table 4 shows the regression results. According to Lai et al., the good correlations ( $R^2 > 0.7$ ) and intercepts not significantly different from

zero indicate that sulfates and nitrates are fully neutralized by ammonia in spring and summer. In autumn, the intercept is significantly higher than 0, sulfate and nitrate are not fully neutralized by ammonia, but other cations (as  $\text{Mg}^{2+}$  and  $\text{Ca}^{2+}$ ) contribute to the equilibrium. Ammonia, indeed, is supposedly less abundant in autumn owing to a decrease in biogenic activities and to soil capping due to snow cover as soon as the cold season proceeds. These seasonal features of ammonium participation in the formation of SIA and their further washing out by precipitation lead to the fact that the share of ammonium in the total amount of ions in the snow cover is on average about 6% (Eremina and Vasil'chuk, 2019), while in precipitation during the warm period it averages 11-12% (Eremina, 2019). The slope closer to 1, found by method 2, suggests that nitrate and sulfate exist mostly as  $\text{NH}_4\text{NO}_3$  and  $(\text{NH}_4)_2\text{SO}_4$  in all seasons.

## 2.3. Potential source analyses

### 2.3.1. Anemological analysis

Meteorological factors contribute significantly to variability of the ionic content in aerosols (Dadashazar et al., 2019). Relationships among the source factor and wind direction and speed, i.e. anemological analysis, are derived from polar plots (Saraga et al., 2021). Figure 8 shows the bivariate concentration polar plots during spring 2018, summer and autumn 2019, providing a graphical representation of the source origin for the

**Table 4**

Parameters of the regression lines for neutralization of sulfates, nitrates, and ammonia as  $\text{NH}_4\text{NO}_3$  and  $\text{NH}_4\text{HSO}_4$  (method 1), and as  $\text{NH}_4\text{NO}_3$  and  $(\text{NH}_4)_2\text{SO}_4$  (method 2).

Method 1	$R^2$	Slope	$\sigma_{\text{slope}}$	Intercept	$\sigma_{\text{intercept}}$
Spring 2018	0.87	0.65	0.043	0.072	0.040
Summer 2019	0.74	0.74	0.056	-0.002	0.038
Autumn 2019	0.79	0.67	0.042	0.305	0.039
<b>Method 2</b>					
Spring 2018	0.90	1.05	0.057	0.087	0.053
Summer 2019	0.76	1.06	0.076	-0.036	0.052
Autumn 2019	0.80	0.97	0.058	0.413	0.054

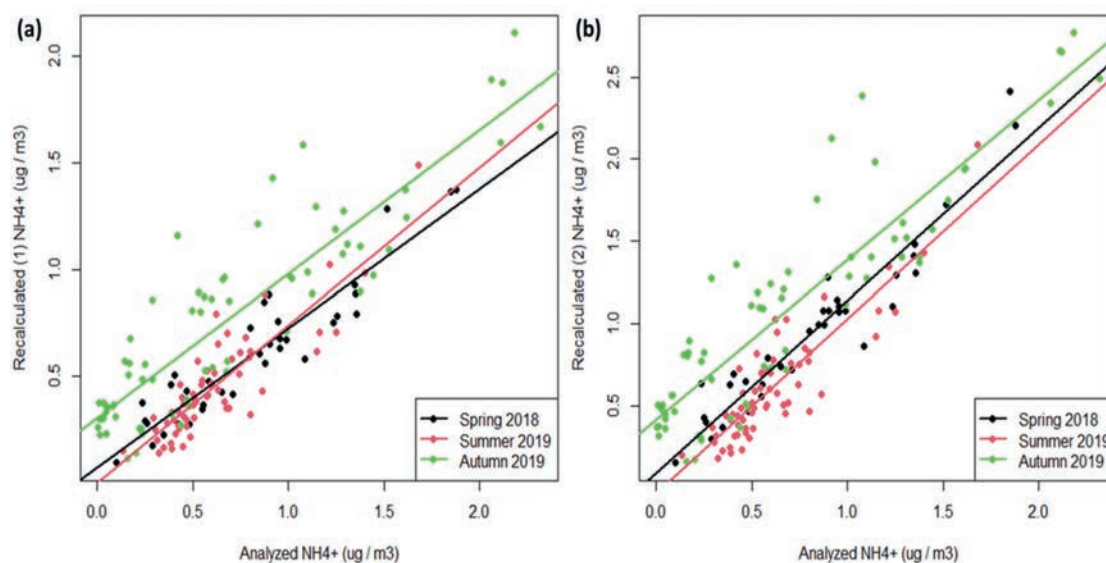


**Fig. 7.** Regression lines of recalculated vs analyzed  $\text{NH}_4^+$  concentrations according to a) method 1 and b) method 2 (Lai et al., 2007).



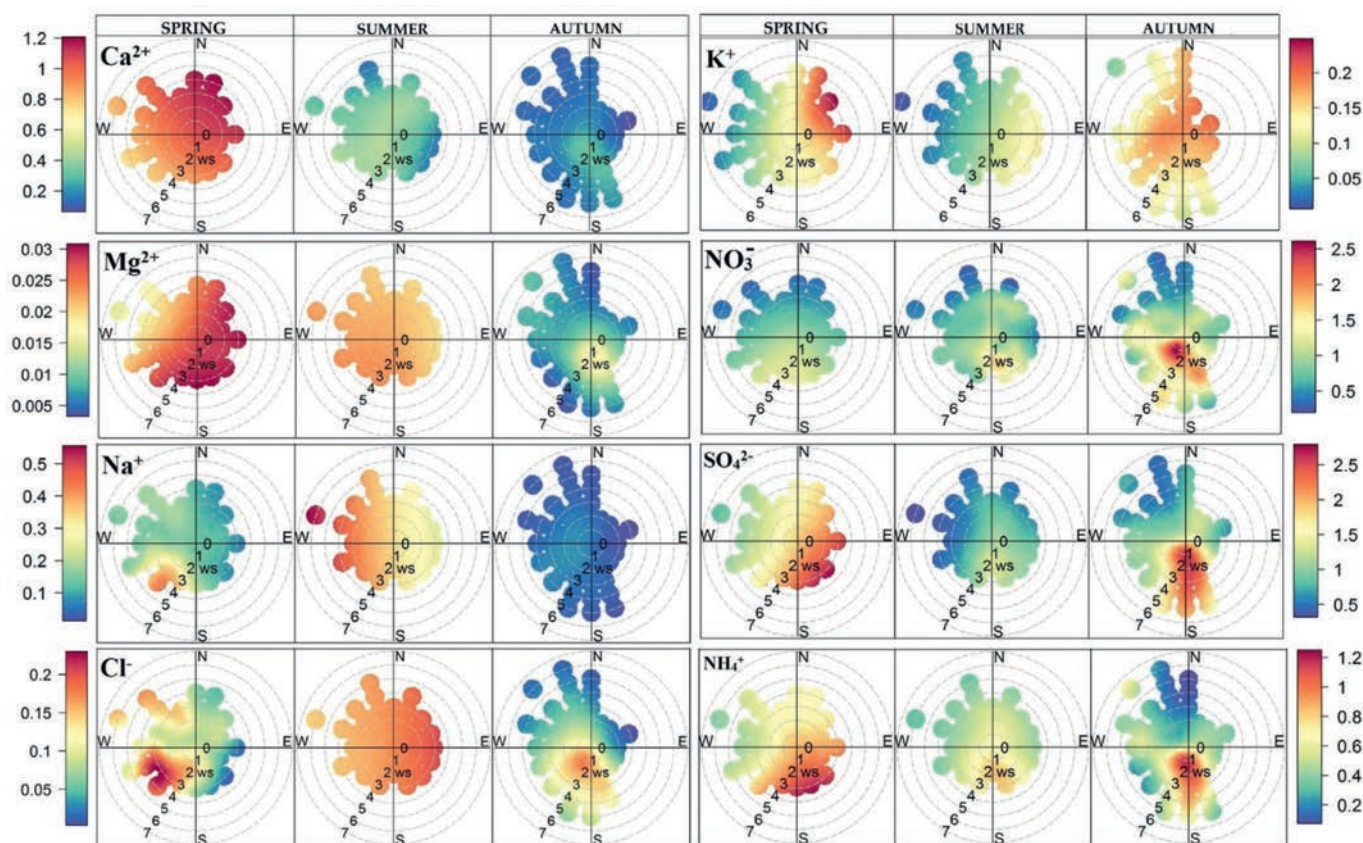


**Fig. 8.** Concentration bivariate polar plots showing the wind speed and wind direction dependence during spring 2018, summer and autumn 2019. The radial axis is wind speed in m/s and the color scale is the concentrations in  $\mu\text{g}/\text{m}^3$ . (For interpretation of the references to color in this figure legend, the reader is referred to the Web version of this article.)

MO MSU site. Map of Figure 1 depicts the MO MSU sampling site located in the southwest sector of Moscow, where industrial facilities are placed within a distance up to 10 km, including thermal power stations, thermal stations, mechanical engineering, metallurgical, food, reinforced concrete, chemical and pharmaceutical factories.

Polar plots of  $\text{SO}_4^{2-}$  and  $\text{NH}_4^+$  show a very similar pattern indicating the same origin for ammonium sulfates and reflects the high correlation between these ions as a result of the significant thermodynamic stability of ammonium sulfates originated from  $\text{SO}_2$  gas-to-particle conversion (Hewitt, 2001). In spring and autumn, they indicate the pollution sources in the southeast where the most industrially developed area takes place in Moscow (Bityukova and Saulskaya, 2017). Prevailing winds were from north and northwest in summer, therefore the MO MSU site is not downwind the heavily impacting sources as in spring and autumn.

High concentrations of  $\text{NO}_3^-$  (about  $1.5 \mu\text{g}/\text{m}^3$ ) in spring and summer are observed at weak wind conditions when non-buoyant ground-level sources such traffic are important. Increasing wind speed generally results in lower concentrations due to dispersion and mechanical turbulence. In autumn,  $\text{NO}_3^-$  increases probably due to the centralized heating system operation when the MO MSU site is downwind from southwest stacks of the large industrial zone (in particular, from the thermal power stations (Fig. 1)) as well as from the southeast industrial region.

$\text{Cl}^-$  and  $\text{Na}^+$  polar plots in spring indicate high concentrations, above  $0.2$  and  $0.32 \mu\text{g}/\text{m}^3$ , respectively, from southwest at wind speeds higher than  $2 \text{ m/s}$ . In fact, it coincides with heavily trafficked roads southwest MO NSU

where efficient road management aiming at reducing snow/ice deposits in the cold period is carried out systematically. In summer, the amount of salts in soil interstitial water drops by 2-7 times (Nikiforova et al., 2014). Also,  $\text{Cl}^-$ ,  $\text{Na}^+$  and  $\text{NO}_3^-$  decrease due to salt leaching, runoff, and absorption of nitrates by biota, but  $\text{Ca}^{2+}$ ,  $\text{Mg}^{2+}$  and  $\text{HCO}_3^-$  increase because dust and crushed marble chips accumulation in the upper horizon (Koshelova et al., 2018). Complete leaching of salts from the soil profile does not occur during summer, that leads together with soil solonchization to a progressive salinization of Moscow surface soils and to its substantial and everlasting availability to air-resuspension in the periods without snow cover (Nikiforova et al., 2017). Moreover, due to the greater amount of precipitation in summer compared to other seasons,  $\text{Cl}^-$  can migrate to the middle part of the soil profile while  $\text{Na}^+$  fixed in surface soil horizon can be resuspended into the atmosphere.  $\text{Na}^+$  polar plot in summer shows the resuspension of  $\text{Na}^+$ -enriched soil particles at any wind directions and speeds. Later, in autumn road salt is likely trapped in snow and ice with consequent scarce resuspension and no pronounced features of sources by polar plot.

For  $\text{Ca}^{2+}$  and  $\text{Mg}^{2+}$ , the high concentrations above  $0.025$  and  $0.63 \mu\text{g}/\text{m}^3$ , respectively, in spring occurs from all the wind directions, relating to local source of soil resuspension after snow thaw.  $\text{Ca}^{2+}$  polar plot in summer shows additional source areas southwest and southeast, associated with intensive building activities in the New Moscow area. In the other seasons these ion sources are not clearly emerging.

$\text{K}^+$  can be originated from soil (mineral potassium) and biomass burning. It is to note that mineral potassi-



um is less soluble than the corresponding fraction from biomass burning, owing to strong crystal lattice bonds in the rocks and minerals.  $K^+$  in our experimental data, obtained from ion chromatography, represents most likely soluble potassium source. Thus,  $K^+$  polar plot indicates biomass burning in spring from the east and in summer from the southeast at wind speeds higher than 2 m/s, with a likely dominating influence of remote sources in Moskovskaya Oblast as well as seasonal wildfires. Autumn plot, instead, indicates the presence of a major source of  $K^+$  from all the directions and low wind speeds, though more intense from west and southeast. Since in autumn no wildfires are observed in the northern European part of Russia, the likely origin for  $K^+$  is biomass burning in the region surrounding Moscow. The spectral dependence of the aerosol light attenuation observed in Popovicheva et al. (Popovicheva et al., 2022) supported the assessment for a contribution of biomass burning in the region around Moscow. We note that autumn is a cold season requiring domestic heating since September, it is recognized that the residential sector near Moscow employs wood for heating.

### 2.3.2. Backward trajectory analysis

Air pollutant transport relates to the atmospheric circulation and spatial distribution of regional sources. In spring and summer agriculture fires and wildfires may occur in the region around Moscow, thus providing the

strong impact on city air quality. Additionally, the residential sector in Moscovskaya Oblast can impact with using of biomass for house heating and cleaning the gardens. Major directions of air mass transportations by BWT cluster analysis are shown in Figure 9. In spring, the main cluster C1 includes 36% of analyzed BWTs and indicates the northwestern and western direction as dominant. Clusters C2 (29%) and C3 (18%) of northwestern and southern directions support the prevalent air mass transportation, respectively. 17% of BWTs compose the cluster C4 from the north. In summer, the largest number of BWTs came from the northwestern direction (48%), they compose the cluster C1. The northern and southern directions include the cluster C2 and C3, characterized by 22% and 17%, respectively, while the trajectories coming from the southwest directions make a less significant percentage contribution to the cluster C4 (13%).

Pie diagrams in Figure 9 show ions concentrations related to trajectories within the clusters C1 of the prevalent air mass transportation for each season.  $SO_4^{2-}$ ,  $NO_3^-$ , and  $NH_4^+$  of 38%, 17%, and 18% and 23%, 28%, and 17% of total ion concentrations, compose the highest SIA source in the northwestern direction in spring and summer, respectively. Highest frequencies of BWTs in this direction relate to the area of large fires occurred in the European part of Russia and around Moscow in both seasons. High  $K^+$  concentrations observed in this direction act as a marker of BB source impacted the air pollution of a megacity.

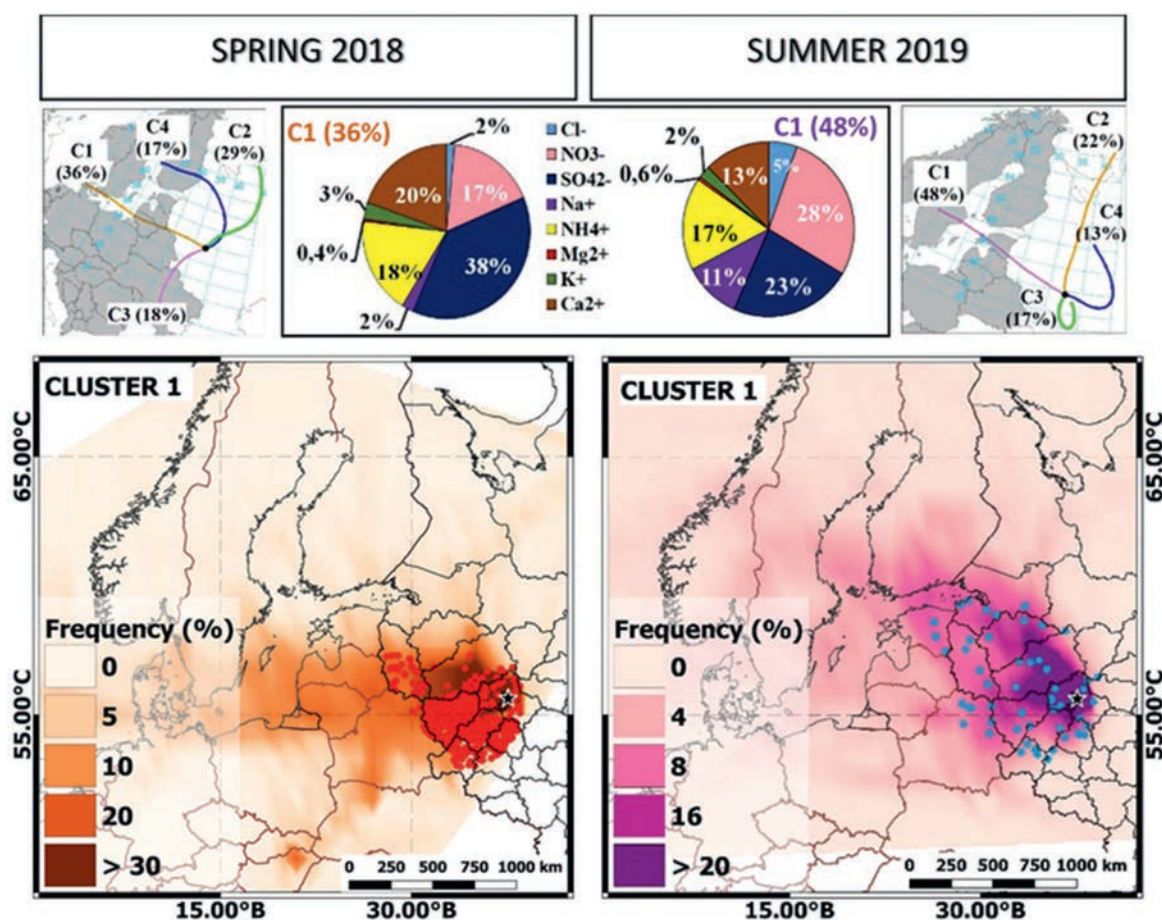


Fig. 9. BTW cluster analysis and pie diagrams for ion concentrations which correspond to the trajectories within clusters C1 for spring 2018 (left) and summer 2019 (right) (top panel). 72-hour BWT frequencies of C1 cluster for spring 2018 (left) and summer 2019 (right) (bottom panel). Fire locations related to the time of BWT pass are indicated by stars, MO MSU site is marked by black star.

### 2.3.3. Varimax analysis: ions and BC sources

In order to obtain the aerosol source profile, the receptor modelling and factor analysis was applied (Hopke, 2016). In our study, Varimax analysis was computed using ion and BC data for the whole dataset, with the aim of finding the potential common sources. Five factors were chosen as the best solution, being the one explaining more than 80% of the total variance. Table 5 shows the Varimax loadings obtained by the model.

**Table 5.** Varimax loadings for ion and BC concentrations during the whole study period. Bold values correspond to the most representative variables for each factor. EV stands for the explained variance, F for a factor.

	F1	F2	F3	F4	F5
EV(%)	27.6	20.8	13.3	13.1	12.1
Cl <sup>-</sup>	-0.050	0.040	0.089	<b>-0.898</b>	-0.123
NO <sub>3</sub> <sup>-</sup>	<b>-0.541</b>	0.187	-0.149	-0.236	0.048
SO <sub>4</sub> <sup>2-</sup>	<b>-0.550</b>	-0.102	0.044	0.160	-0.128
Na <sup>+</sup>	0.252	-0.340	-0.342	-0.287	0.359
NH <sub>4</sub> <sup>+</sup>	<b>-0.578</b>	-0.142	-0.015	0.014	0.210
Mg <sup>2+</sup>	-0.051	<b>-0.622</b>	-0.096	-0.070	-0.061
K <sup>+</sup>	0.043	-0.067	-0.048	-0.056	<b>-0.873</b>
Ca <sup>2+</sup>	-0.031	<b>-0.654</b>	0.138	0.079	-0.098
BC	-0.030	0.070	<b>-0.905</b>	0.094	-0.131

The five factors reported in Table 5 were considered as corresponding to as many emission sources. Factor 1 (F1) shows high loadings for NO<sub>3</sub><sup>-</sup>, SO<sub>4</sub><sup>2-</sup>, and NH<sub>4</sub><sup>+</sup>, indicating SIA as the dominant PM<sub>10</sub> component, corresponding to a non-resolvable cumulative contribution from all high temperature emission sources encompassing traffic, heat and power generation, and industry (Seinfeld and Pandis, 2016). The absence of BC in this factor indicates that there is no direct link to combustion sources like those using fossil fuel. SIA is originated in secondary processes which are not directly related to primary sources as BC but rather reflect the regional emissions affecting a megacity due to the relatively low chemical kinetics of formation and to non-local air mass transportation (Fig. 9). Moreover, comparable patterns of concentration polar plots for SO<sub>4</sub><sup>2-</sup> and NH<sub>4</sub><sup>+</sup> (Fig. 8) confirm their common source as well. Factor 2 (F2) associates Ca<sup>2+</sup> and Mg<sup>2+</sup>, indicating the mineral component of which calcium is a proxy. It represents the more abundant components in crustal materials so-called soil/road dust resuspension, derived from rock reworking, soil development, and the built environment (Lai et al., 2007). Factor 3 (F3) indicates the BC sources associated with fossil fuel combustion i.e. traffic, heating system, and industry in a megacity (Popovicheva et al., 2022). High loading only for BC in this factor suggests the absence of any strong ion relevance to combustion sources. The decoupling of BC from K<sup>+</sup> likely indicates that the main source of BC in the Moscow atmosphere is fossil fuel combustion while K<sup>+</sup> is a marker of biomass burning presenting the highest loading in Factor 5 (F5). Cl<sup>-</sup> derived from road salt, is found alone in Factor 4 (F4). It is to note that the decoupling from Na<sup>+</sup> does not mean that Cl<sup>-</sup> is not due to road salt, their association has been shown above. Relatively significant loadings of

Na<sup>+</sup> are found both in F2 and F4. This reasonably means that, differently from chloride, which is a highly reactive mobile substance and can be degassed by atmospheric processing, the same does not hold for Na<sup>+</sup>. Sodium is a highly conservative ion, which accumulates in the course of years in soil, where it is stabilized by ion exchange chemistry in the soil matrix to be recirculated in the lower troposphere following soil resuspension. Note that previously cited research work on the effects of DIA on soil water chemistry in Moscow revealed a decoupling of chloride ion from its cation partner Na<sup>+</sup>, circumstance which may support the occurrence of Cl<sup>-</sup> in factor 4 without other significant correlation.

### 2.3.4 Varimax analysis in summer case study: organic ions and sugars sources

For summer ion chemistry and BC are integrated by a series of chemical species including carboxylic and di-carboxylic acids, anhydrosugars (levoglucosan with its isomer mannosan), and sugars. These species were analyzed only in summer since this is the only season of high photochemistry as well as biogenic activities and biomass burning in Russia. Although it is not possible to evaluate the seasonal variation of such species, their presence in summer samples can be used to evaluate their source, also in correlation with inorganic ones. The whole dataset is subjected to an independent elaboration for receptor modelling using Varimax factor analysis (Table 6).

Factor 1 (F1) presents high loadings of SIA and oxalates, confirming the role of photochemistry in the formation of both inorganic and organic secondary aerosols (Tsai et al., 2013). In particular, oxalates and sulfates undergo a similar chemical processing mainly associated with cloud processing (Laongsri and Harrison, 2013). Factor 2 (F2) includes Cl<sup>-</sup>, BC, K<sup>+</sup>, and levoglucosan. Time series of BC, nss-K, and levoglucosan in Figure S3 show a remarkably good agreement throughout the summer period. It indicates the variable influence of biomass burning which relates to large wildfires observed in the European part of Russia and particular in the region around Moscow, as shown by BWT cluster analyses (Fig. 9). It is to note that the high loading of Cl<sup>-</sup> in F2, similar

**Table 6** Varimax loadings of the summer case-study. Bold values correspond to the most representative variables for each factor. EV stands for the explained variance, F for a factor.

	F1	F2	F3	F4	F5	F6
EV(%)	18.8	18.1	13.7	13.5	12.0	7.80
Cl <sup>-</sup>	-0.121	<b>0.533</b>	-0.116	-0.007	-0.019	-0.080
NO <sub>3</sub> <sup>-</sup>	<b>0.453</b>	-0.075	-0.143	-0.006	-0.023	0.100
SO <sub>4</sub> <sup>2-</sup>	<b>0.497</b>	-0.024	-0.021	0.017	0.188	-0.047
Na <sup>+</sup>	-0.085	-0.098	-0.260	<b>0.399</b>	0.256	0.228
NH <sub>4</sub> <sup>+</sup>	<b>0.424</b>	-0.095	-0.047	0.196	0.154	-0.055
Mg <sup>2+</sup>	0.048	-0.020	0.059	<b>0.570</b>	-0.021	-0.039
K <sup>+</sup>	0.030	<b>0.518</b>	-0.014	-0.053	-0.055	0.058
Ca <sup>2+</sup>	0.047	0.047	0.049	<b>0.464</b>	-0.249	-0.066
BC	0.140	<b>0.321</b>	-0.064	0.125	-0.082	0.013
Oxalate	<b>0.454</b>	0.116	-0.035	-0.067	0.040	-0.096
Lactate	-0.141	0.178	<b>-0.544</b>	0.205	0.209	-0.222
Acetate	0.050	-0.035	<b>-0.484</b>	-0.218	-0.290	0.001
Formate	0.005	-0.068	<b>-0.548</b>	-0.092	-0.026	0.181
Glutarate	0.140	0.027	0.011	0.020	<b>-0.567</b>	0.074
Succinate	0.105	0.019	0.009	0.116	<b>-0.530</b>	-0.035
Levoglucosan	0.064	<b>0.425</b>	0.073	-0.122	0.090	0.039
Mannosan	0.015	-0.095	-0.085	-0.112	-0.053	<b>0.707</b>
Mannose	0.238	0.121	0.119	-0.207	0.230	0.074
Glucose	-0.024	0.246	0.164	0.238	0.077	<b>0.559</b>



to BB markers, shows its seasonal distinct source together with a complex relationship to local origin. It means that  $\text{Cl}^-$  is contributed by two sources, i.e. road salts from which it is partially removed to the gaseous phase, and biomass burning, as was also observed by Brattich et al. (Brattich et al., 2021).

Factor 3 (F3) includes three carboxylic acids sharing similar sources. In particular, acetate is correlated with biomass burning (Tsai et al., 2013). Acetate comes mostly from primary emissions, while formate come from secondary transformations. The mass ratio of acetate and formate (A/F) is used to distinguish primary and secondary sources of these acids (Tsai et al., 2013). An A/F ratio higher than 1 indicates a prevalence of primary sources, while A/F lower than 1 indicates the contrary. In our case, the mean A/F mass ratio is 2.19, therefore the main source of these acids can be considered the urban primary sources, probably vehicular emissions (Tsai et al., 2013; Wang et al., 2007).

Factor 4 (F4), including  $\text{Ca}^{2+}$ ,  $\text{Mg}^{2+}$ , and  $\text{Na}^+$ , represents the influence of road dust and soil resuspension contribution thanks to the low-level turbulence and relatively drier conditions of summer, capable to recirculate these components. Succinate and glutarate in Factor 5 (F5) relates to oxalate and SIA as products of secondary formation from organic precursors by photochemical and heterogeneous reactions (Guo et al., 2021). Factor 6 (F6) with a little influence on the overall variance has a high loading of mannosan and glucose. Since mannosan is acting as biomass burning marker, and glucose is the product of biogenic activity, they both reflect the co-existence of biomass burning and bioaerosols which was observed in other studies (Bauer et al., 2008; Popovicheva et al., 2020). High temperature in summer (Fig. S1a) definitely relates with intensive biological activities. Moreover, the co-existence of sugars with anhydrosugars may be explained by suspension of soil and plant debris in the heat wave of wildfires (Medeiros et al., 2006).

## 2.4. Precipitation chemistry

Precipitation in the form of rain and snow reflects the aerosol composition through complex in-cloud and below clouds removal. The ion composition and pH are a function of the amount of condensed water and the relative degree of neutralization of SIA, while pH may affect solubility of removed aerosols and of those trapped in rain/snow bulk collectors (Pruppacher and Klett, 2010; Tositti et al., 2018b; Vlasov et al., 2021).

Long-term records of precipitation chemistry at MO MSU site show the significant increase of the acid precipitation number from almost absence until the level of 30% in last years (Eremina et al., 2015). The percentage of acid precipitation with  $\text{pH} < 5$  was 20.7% for a year on average, 31.0% for a warm season, and only 5.7% for winter. The total ionic mineral composition does not change in average, while chloride and sodium concentration were increasing.

Figure 2a shows precipitation events scattered throughout three seasons, they appear more abundant in summer and autumn (Table S1). In the end of autumn, in December, rainfall was subsequently substituted by snowfall. The pH recorded in precipitation reveals a certain tendency towards lower values in spring and summer (Fig. 10), such a fact is typically recognized as pertaining to acid rains (Bricker and Rice, 2003). Observed pH in spring and summer oscillate around 5-5.6.

Since during some time in autumn soil is frozen and covered with snow at the Moscow latitude, the agricultural contribution is likely negligible while traffic and industrial sources (with the support of ventilation) appear to be the most important ones. These leads to scarce availability of ammonia and therefore to a reduced neutralizing effect on sulfuric and nitric acids formed by  $\text{SO}_2$  and  $\text{NO}_x$  oxidation rather than to an excess of acidifying species. Increase of pH in colder seasons, above 5.6, suggests both the neutralizing influence of ammonia and

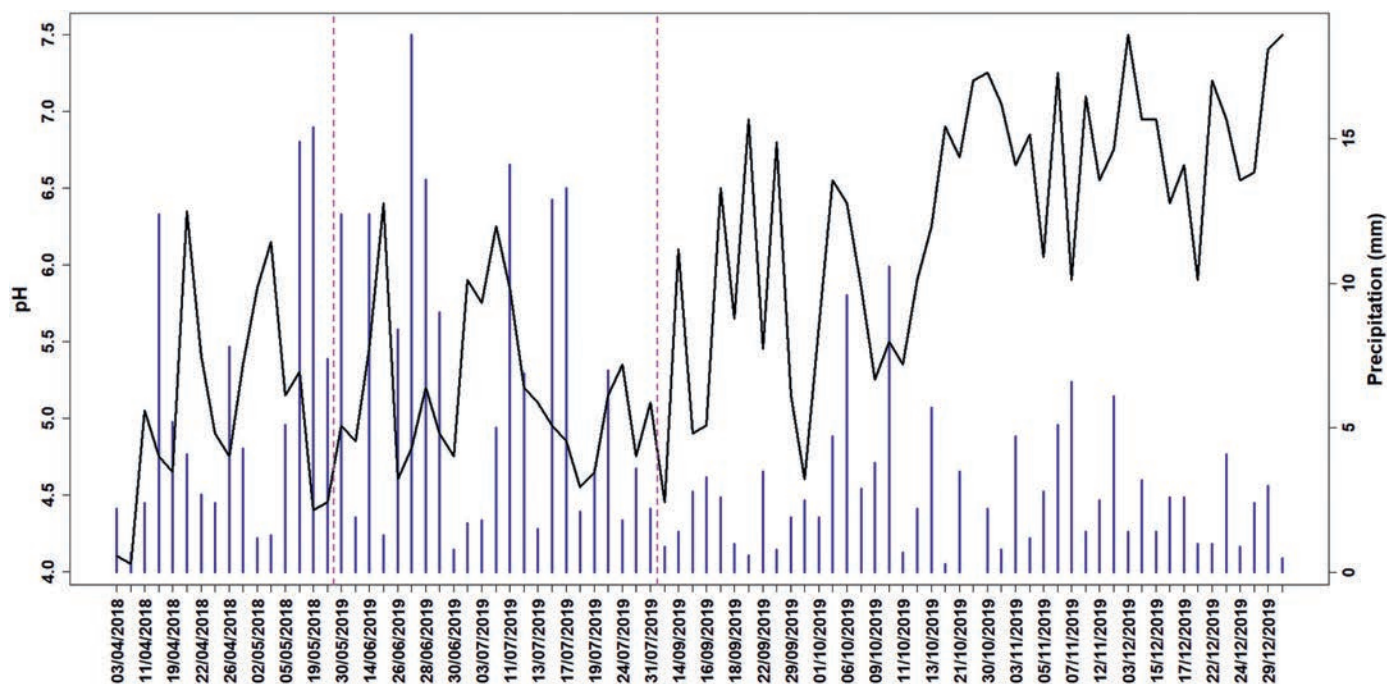


**Fig. 10.** pH (black line) and precipitation intensity (blue bars) for the whole period of study. (For interpretation of the references to color in this figure legend, the reader is referred to the Web version of this article.)



**Table 8**

Scavenging ratios calculated for SIA compounds during three seasons.

	$\omega\text{NO}_3^-$	$\omega\text{SO}_4^{2-}$	$\omega\text{NH}_4^+$
<b>Spring 2018</b>	$7.70 \cdot 10^3$	$2.12 \cdot 10^3$	$3.17 \cdot 10^3$
<b>Summer 2019</b>	$3.45 \cdot 10^3$	$2.40 \cdot 10^3$	$2.70 \cdot 10^3$
<b>Autumn 2019</b>	$5.29 \cdot 10^3$	$3.31 \cdot 10^3$	$2.74 \cdot 10^4$

the contribution from carbonates in resuspended alkaline urban soils (Nikiforova et al., 2017), road dust (Kasimov et al., 2019), and undissolved DIAs (Korolev and Gornyakov, 2018).

Precipitation ion chemistry and data variability is associated with the seasonal precipitation rate as well as with the type of precipitation event in terms of total volume of the deposited hydrometeor as well as of the progression of the single event. Table 7 reports basic statistics for precipitation during three seasons, together with pH and ion concentrations. The highest mean precipitation is observed in summer while in autumn it is the lowest. The highest mean and median concentrations for almost all ions were observed in spring, except  $\text{HCO}_3^-$ . Its maximum is in autumn, that is generally consistent with observations in previous years according to which the average concentrations of  $\text{HCO}_3^-$  in September-December are higher than in April-May (Eremina et al., 2017).

Spearman correlation analysis has been carried out. Based on Spearman indexes, it is found that ions pertaining to SIA appear highly correlated ( $> 0.70$ ) in connection with their origin and source. Other correlations are in general lower than those observed for SIA ( $< 0.7$ ), suggesting multiple sources for the other ions. An exception is represented by the ions already cited as coming from road management practices ( $\text{Ca}^{2+}$ ,  $\text{Mg}^{2+}$ , and  $\text{Na}^+$ , correlations between 0.65 and 0.75). This likely reflects the influence of soil resuspension in dry periods on the precipitation chemistry, since precipitation is collected as bulk deposition, i.e. the sum of wet and dry deposition, and not with a wet only approach (Tositti et al., 2018b). Finally,  $\text{H}^+$  and  $\text{HCO}_3^-$  appear uncorrelated in respect to all the other ions ( $< 0.3$ ) and they are reciprocally anticorrelated ( $-0.936$ ). This is reasonably due to the neutralizing effects of calcium and magnesium carbonates from soil resuspension acting as neutralizing agents toward  $\text{H}^+$  which is decreased through the formation of  $\text{HCO}_3^-$ . In Moscow, during years with a deficit of acid precipitation, the predominant anion in precipitation is  $\text{HCO}_3^-$ , the source of which is carbonates of alkali and alkaline earth metals. This is confirmed by the results of thermo-

dynamic calculations; in episodes with an excess of acids in precipitation it is associated with the absorption of ammonia from the atmosphere (Eremina et al., 2017).

Efficiency of wet removal can be appreciated analyzing simultaneously the trend of  $\text{PM}_{10}$  and precipitation, as reported in Figure 2a. Seasonal variability of scavenging ratios ( $\omega$ ) of SIA species (Table 9) have been calculated by taking into account the ion concentrations in aerosols, their concentrations in precipitation, and the air density, using eq. 1. Scavenging ratios are determined on a seasonal basis because they have less variability compared to ones calculated using precipitation event concentrations and consider the average ion concentrations in  $\text{PM}_{10}$  during both precipitation and dry periods (Cheng and Zhang, 2017).

The lowest  $\omega\text{NO}_3^-$ ,  $\omega\text{NH}_4^+$ , and  $\omega\text{SO}_4^{2-}$  are determined in summer and spring, respectively. The maximum  $\omega\text{NO}_3^-$  is found in spring, in autumn we observe the maximum  $\omega\text{SO}_4^{2-}$  and  $\omega\text{NH}_4^+$ . Gaseous species such as  $\text{HNO}_3$ ,  $\text{SO}_2$ , and  $\text{NH}_3$  can influence the SIA scavenging ratios since the composition of the precipitation is determined by the scavenging process of both gases and particles. That might be the reason of the overestimated levels of  $\omega$  especially in spring and summer, when the formation of SIA is favored by the photochemical reactions (Oduber et al., 2021). For instance, 88-96% of  $\text{NO}_3^-$  content in rainwater is formed due to gas-phase scavenging of  $\text{HNO}_3$ , whereas 89-96% of  $\text{SO}_4^{2-}$  concentration in rainwater may be due to particulate sulfate (Kasper-Giebl et al., 1999). However, our findings showing  $\omega$  decreasing in summer and increasing in autumn and spring are consistent with estimates obtained for atmospheric air and precipitation at Canadian rural locations (Cheng and Zhang, 2017).

Comparing the obtained values with those found in other works (Cheng and Zhang, 2017; Encinas et al., 2010) the secondary  $\omega\text{SO}_4^{2-}$ ,  $\omega\text{NO}_3^-$  and  $\omega\text{NH}_4^+$  resulted to be comparable with those calculated in our study.

Though the scavenging ratio is widely used, it must bear in mind that its meaning and use have some limitation. In fact, owing to the complexity of aerosol wet removal processes (Andronache, 2003), many uncertain-

**Table 7** Statistics of precipitation, pH, and ions concentrations (in  $\mu\text{g L}^{-1}$ ) in three seasons

	Spring 2018				Summer 2019				Autumn 2019			
	mean	median	min	max	mean	median	min	max	mean	median	min	max
Precipitation (mm)	5.59	4.20	0.70	15.4	6.53	4.30	0.80	18.6	2.91	2.55	0.30	10.6
pH	5.04	4.98	4.05	6.35	5.16	5.03	4.45	6.40	6.37	6.55	4.60	7.50
$\text{H}^+$	21.7	10.8	0.45	89.1	11.4	9.55	0.40	35.5	2.03	0.28	0.03	25.1
$\text{HCO}_3^-$	1.24	0.00	0.00	7.40	0.77	0.00	0.00	9.39	3.93	2.80	0.00	13.5
$\text{SO}_4^{2-}$	2.54	2.60	0.60	4.90	1.66	1.06	0.31	6.10	2.32	1.70	0.40	8.70
$\text{Cl}^-$	13.2	10.9	3.00	39.5	10.4	7.09	2.13	34.9	7.09	6.80	1.30	20.90
$\text{NO}_3^-$	2.90	3.20	0.50	6.50	2.97	1.50	0.45	16.2	2.23	1.90	0.70	5.00
$\text{Ca}^{2+}$	5.96	4.50	1.10	21.0	5.03	3.45	0.68	18.9	4.29	3.70	0.80	11.0
$\text{Mg}^{2+}$	0.34	0.20	0.10	1.60	0.19	0.09	0.02	1.12	0.21	0.20	0.00	0.50
$\text{Na}^+$	1.71	1.40	0.30	4.90	0.50	0.35	0.07	1.80	0.96	0.80	0.10	2.70
$\text{K}^+$	0.43	0.30	0.10	2.90	0.40	0.27	0.02	2.22	0.51	0.40	0.10	3.30
$\text{NH}_4^+$	1.73	1.50	0.30	4.30	1.39	0.97	0.27	4.90	1.36	1.20	0.30	3.20

ties in the physical meaning of the scavenging factors remain. The wet removal process may indeed be split into in-cloud processes, characterized by hygroscopicity-induced nucleation mechanisms, and below-cloud processes, a highly stochastic process based on the impaction of droplets (snowflakes) with aerosol particles with a huge dependency on particle size. Variability of  $\omega$  is also influenced by a large number of factors, such as wind speed, temperature, precipitation amount and type, the time elapsed between two precipitation events, nucleation efficiency, vertical concentration differences, cloud type, etc. (Cheng and Zhang, 2017; Duce et al., 1991; Luan et al., 2019; Oduber et al., 2021).

### 3. CONCLUSIONS

Characterization of ion composition together with anemological analyses sheds a light into the high seasonal variability and various sources of origin, therefore add the understanding of factors influencing aerosol and precipitation ion chemistry in Moscow urban background. Total inorganic ions compose the biggest fraction of aerosol  $PM_{10}$  mass, up to 27% in autumn. Degree of neutralization in summer and anions in autumn, and substantially electroneutrality in spring constraints by the season-related neutralized agents such as ammonia and carbonates. Dominance of secondary inorganic aerosols (SIA) over all the other ion species exists mostly as  $NH_4NO_3$  and  $(NH_4)_2SO_4$  in all seasons. Backward trajectories within a cluster of the prevalent air mass transportation indicate the highest regional SIA source in the northwestern direction in spring and summer. Sulfates and nitrates dominate among the SIA components, with maximum contribution of 38 and 34%, respectively, in autumn. Similarity of  $SO_4^{2-}$  and  $NH_4^+$  relationships among the wind direction and speed reflects the significant thermodynamic stability of ammonium sulfates originated from  $SO_2$  gas-to-particle conversion preferably in the southeast industrially developed Moscow area. High concentrations of  $NO_3^-$  are due to ground-level traffic as well as the centralized heating system operation. Salt components ( $Na^+$  and  $Cl^-$ ) are attributed to a

high amount of de-icing agents used in road management.  $Na^+$  shows a maximum in summer and minimum in autumn, with the largest variability between seasons, differently from  $Cl^-$ . While chloride is a highly reactive mobile substance and degassed by atmospheric processing, conservative potassium accumulates in soil and stabilizes by ion exchange chemistry then recirculates in the atmosphere due to soil resuspension. Chlorine depletion phenomenon follows the snow melt and demonstrates the biggest  $Cl^-$  displacing from  $NaCl$  promoted in summer by both a significant low-level turbulence and dryness, and the required  $HNO_3$  photochemistry.  $Ca^{2+}$  and  $Mg^{2+}$  relate to local soil resuspension after snow thaw,  $Ca^{2+}$  shows an additional source from intensive building activities in the New Moscow area. Biomass burning is indicated from remote sources in the region surrounding Moscow by high  $K^+$  concentrations in all seasons. High frequencies of backward trajectories from the European part of Russia in warm seasons confirm the large agriculture and wildfires impact to the air pollution of a megacity. Main sources of  $PM_{10}$  inorganic ions are secondary sulfates and nitrates, soil resuspension, road salt, and biomass burning in spring and autumn. Organic acid anions,  $K^+$ , and anhydrosugars detect biomass burning associated to summer wildfires. Concerning  $PM_{10}$  and ionic data there is no particularly critical issues about atmospheric pollution in Moscow urban background, in comparison to evaluated large European and Canadian cities. Lower content of  $SO_2^-$ , probably due to centralizing gas operated heating system, and comparable  $NO_3^-$  concentrations impacted by intensive traffic and industry, are found. Impact of deicing agents on  $Cl^-$  and  $Na^+$  concentration is similar to inland cities with cold climate.

Precipitation collected in the same period shows the link between aerosol and precipitation scavenging, with increasing acidity in spring and summer. The lowest values of scavenging factor for  $NO_3^-$  and  $NH_4^+$  was determined in summer and for  $SO_4^{2-}$  in spring, while the maximum for  $NO_3^-$  in spring. The finding obtained can support the mitigation efforts contributing to the reduction of aerosol mass load and consequently of aerosol and precipitation acidity.

## 6. ВОДЫ

### Anthropogenic factors affecting the Moskva River water quality: levels and sources of nutrients and potentially toxic elements in Moscow metropolitan area\*

#### INTRODUCTION

Population growth and urbanization pose challenges to water supply systems, especially considering that surface water is at risk of contamination from wastewater disposal and is greatly exploited in agricultural, industrial, and municipal activities (Giri & Singh, 2014). Pollutants in surface water could be of natural (chemical weathering of bedrocks, runoff from banks, groundwater supply, etc.) or anthropogenic (mining and industrial activities, pesticides application, vehicle exhaust and abrasion, fuel combustion, etc.) origin (Cengiz et al., 2017; Nordberg et al., 2011) and could migrate to aquatic systems in dissolved and suspended phases (Kasimov et al., 2020b; Le Pape et al., 2012; Shotyk et al., 2017). The dissolved phase of chemical elements is considered to be more bioavailable and therefore potentially toxic to different organisms compared with the suspended one (LeFevre et al., 2015; Shotyk et al., 2017) and even more toxic than the nano-form of metals (Notter et al., 2014). Urban areas are believed to be both polluters and consumers of freshwater. Thus, nowadays urbanized watersheds have gained the attention of various environmental scientists and medical specialists as water contamination by potentially toxic elements (PTEs) may cause a considerable risk of chronic poisoning to fishery resources (Lemly, 2004) and millions of urban residents (Berg et al., 2001; Khatri & Tyagi, 2015; Kominkova & Nabelkova, 2007).

The water quality problem is well pronounced in megacities due to the high population density together with the vast amount of pollutant sources. It has been investigated in many megacities all over the world: Jakarta (Costa et al., 2016), Delhi (Parween et al., 2017), Kolkata (Zaman et al., 2018), Beijing (Zhang et al., 2017), Shanghai (Zhao et al., 2016), Shenzhen (Wang et al., 2004), Tokyo (Kido et al., 2009; Saito et al., 2020), Seoul (Chang, 2005), Bangkok (Areerachakul & Sangansintukul, 2010), Ho Chi Minh City (Vo, 2007), Istanbul (van Leeuwen & Sjerps, 2016), London (Bowes et al., 2016; Whitehead et al., 2013), Paris (Billen et al., 2001), Kinshasa (Kayembe et al., 2018), Cairo (Abdel-Satar, 2005), Buenos Aires (Rigacci et al., 2013), Rio de Janeiro (Ribeiro & Kjerfve, 2002; Villas-Bos as et al., 2017), Mexico (Espinosa-García et al., 2015), New York (Mehaffey et al., 2005), and others. Moscow is the largest megacity in Europe with a population of about 12.6 million inhabitants (Demographics, 2021) and is located on the Moskva River, which experienc-

es high anthropogenic pressure from the city's industrial enterprises, water carriage, wastewater treatment facilities, municipal wastewater, etc. Landscape components where Moscow's pollutants accumulate (soil, road dust, sediment, snow cover, rain, and atmospheric aerosols) have been recently well studied. Thus, the results of 21 years of observations of nine heavy metals in the topsoils of the eastern district of Moscow showed a gradual increase in pollution levels and revealed Pb and Zn as the main pollutants (Kosheleva & Nikiforova, 2016). It was also proved that the level of soil contamination in Moscow depends on the parameters and arrangement of the buildings (Kosheleva et al., 2018) and their proximity to a road (Nikolaeva et al., 2017). Road dust itself is dominated by sand and silt-sized particles (Kasimov et al., 2019) and enriched in Ag, Cd, Sb, Zn, Sn, Cu, Pb, W, Bi, and Mo (Kasimov et al., 2020a) as well as Hg, As, Cr, and Ni (Ladonin & Mikhaylova, 2020). In the city center, due to a high level of traffic, road dust and PM<sub>10</sub> proved to be the most polluted (Vlasov et al., 2021a). Nanoparticles of road dust are characterized by high concentrations of Cu, Zn, Ag, Cd, Sn, Sb, Hg, Pb, Tl, and Bi (Ermolin et al., 2017). In Moscow's traffic zones, anthropogenic emissions contaminate snow cover with suspended Ca, W, Co, V, Sr, Ti, Mg, Na, Mo, Zn, Fe, Sb, and Cu (Vlasov et al., 2020). Due to the resuspension of contaminated particles of road dust and urban soils, industrial and traffic impact, and waste and biomass burning, the rainwater in Moscow is highly enriched in Sb, Pb, Cd, and S and less enriched in P, Ba, As, W, Mn, Sn, Na, Co, Ni, and Be (Vlasov et al., 2021b).

Since the historically developed system of water supply sources in Moscow is based on the use of surface water (the resources of the Moskva and Volga rivers) (Datsenko, 2016), the pollution of these aquatic systems should be closely monitored. At present, the natural hydrological regime is observed only in the upper reaches of the river, upstream from the Mozhaysk Reservoir (Hydroecological, 2015). Upstream from Moscow, the runoff of the Moskva is regulated by the hydroelectric complexes based at the Istra (since 1935), Mozhaysk (since 1960), Ruza (since 1966), and Ozerna (since 1967) reservoirs, as well as the reservoirs of the Vazuza hydrotechnical system. Within the Moscow megacity area, the upper Volga River waters are connected to the Moskva River through the Moscow Canal (Datsenko, 2016). At the mouth of the Moskva River, taking into account the regulation of reservoirs and their usage for the needs of the population, industry, and agriculture, the average minimum monthly discharge is 115–

\* Shinkareva G., Erina O., Tereshina M., Sokolov D., Lychagin M., Kasimov N. // Environmental Geochemistry and Health. 2022.



120 m<sup>3</sup>/s (Rybalsky et al., 2016). Nowadays, the share of the spring runoff from the Moskva River, upstream of the Mozhaysk Reservoir, is 63% of the annual, while in the regulated area it has decreased by more than two times, and the summer–autumn runoff has increased by more than 1.5 times. A similar intra-annual runoff distribution is typical for the river tributaries. In the Moskva River Basin, an ascending trend in the annual runoff from the mid-nineteenth century to the present time was revealed mostly due to the surface runoff from slopes during warm seasons with a decrease in low flow periods, caused mostly by urbanization growth (Koronkevich & Mel'nik, 2015). Monitoring of surface water quality within the boundaries of the city of Moscow is organized by the Department of Environmental Management and Protection of Moscow City, and the Mosecomonitoring Portal, which has more than 60 observation points on 24 main water bodies, including 13 points on the Moskva River, 31 points on its tributaries, 4 points on the Kosino lakes, and 14 points on other rivers (Kulbachevsky, 2021). Observations are carried out throughout the year during ice-free periods: monthly for most of the sections and at least once a quarter for the rest. The list of analyzed indicators includes up to 40 physical and chemical substances: pH, transparency, dissolved oxygen, suspended and organic substances, basic ions, nutrient elements (nitrogen and phosphorus compounds), some metals, petroleum products, surfactants, and some others (Kulbachevsky 2020, 2021). However, common urban pollutants (especially Sb, Mo, Pb, Zn) revealed in other Moscow environments are insufficiently researched in river water. In addition, the sources and spatial patterns of potential contaminants spreading in the Moskva River and its tributaries are still poorly investigated. Our research aimed to define (1) the main patterns of distribution and (2) likely sources of potentially toxic elements and nutrients in the Moskva River under different levels of anthropogenic stress, as well as (3) their influence on river water quality. To do so, three parts of the Moskva Basin with different anthropogenic loads were investigated: upstream, urban and downstream.

## MATERIALS AND METHODS

### Study area

The Moskva River is the main waterway to Moscow megacity. It flows out of the Star'kovo marsh, goes further through the territory of the Smolensk–Moscow Upland of the East European Plain, and joins the Oka River in the city of Kolomna (Fig. 1). The Moskva River Basin area is 17,600 km<sup>2</sup>, which accounts for 38% of the entire territory of the Moscow Region. The cities of Mozhaysk, Zvenigorod, Moscow, Zhukovsky, Bronnitsy, Voskresensk, Kolomna, and some others are situated on the banks of the Moskva River. According to their main hydrographic characteristics (length and catchment area), all rivers of the Moscow megacity are small ones, with the exception of the Moskva and the Pakhra, which are medium-sized rivers with a catchment area > 2000 km<sup>2</sup> and a length of 502 km and 135 km, respectively. The length of the Moskva River within the city is about 75 km, where the entire urban area serves as its catchment (Kulbachevsky 2020, 2021).

The average discharge in the upper reaches of the river (at the Roshydromet gauging station upstream the Mozhaysk Reservoir) is 5.8 m<sup>3</sup>/s, and at Zvenigorod–38 m<sup>3</sup>/s. As a result of the operation carried out at all

reservoirs, the average discharge in the section of the Rublevo Reservoir (11 km upstream of the western border of Moscow) is 51 m<sup>3</sup>/s, which is almost two times higher than the average natural annual discharge of the Moskva River in this section during an extremely dry year and eight times higher than the average natural minimum monthly discharge of the Moskva in this section (6.6 m<sup>3</sup>/s). Due to the supply of Volga water through the Moscow Canal, the natural discharge of the river more than doubles (Shchegolkova et al., 2016). These waters provide about 70% of the current water demand in Moscow and the Moscow Region (Kulbachevsky, 2020, 2021).

In Moscow city area, the main tributaries of the Moskva River are the Setun, the Yauza, the Moscow Canal, and the Pakhra rivers. Most of the water bodies in Moscow have an open channel, natural banks, and preserved floodplain–valley complexes, which ensure the rivers' ability to naturally self-recover in response to the increasing anthropogenic impact. The Pakhra River is a well-known, highly polluted Moskva tributary that flows through Podolsk Town, where enterprises of nonferrous and ferrous metallurgy, petrochemical industry, battery and element industry, cable industry, and instrument engineering are situated (Akhtyamova, 2009; Akhtyamova et al., 2012; Yanin, 2011).

The main sources of pollution of the Moskva River Basin are insufficiently treated household and industrial wastewater from the cities of Kolomna, Moscow, Voskresensk, and others, as well as agricultural wastewater flowing directly into rivers (Kulbachevsky, 2020, 2021). One of the key factors for the deterioration in the river water quality is the increase in the number and size of natural landfills on the floodplain, which leads to soil, vegetation (including vegetables), and groundwater pollution (Yashin et al., 2015). In the middle and lower parts of the Moskva Basin, the river is experiencing high anthropogenic pressure; its runoff is formed by 50% of the treated wastewater from Moscow city, as well as from settlements in the Moscow Region (Kulbachevsky, 2020, 2021; Rybalsky et al., 2016).

### Field data campaigns

Despite the fact that the Moskva River itself and some of its tributaries are dammed and have a regulated flow regime, which is significantly different from the natural one, several hydrological seasons can be distinguished for these rivers. Thus, field campaigns were planned to cover the most important of them (Fig. 2; Table 1): spring flood (April 4–5, 2019, and March 11–15, 2020) and summer low water period (August 6–8, 2019, and August 17–23, 2020).

To assess the impact of Moscow megacity on the dissolved pollutants' migration patterns and river water quality, the Moskva River Basin was divided into three parts: (1) the upstream part from the source area to the upper Moscow boundary, which includes in addition 10 tributaries; (2) the urban part within the Moscow area (river inside Moscow up to the Kuryanovo aeration station) with four extra points on tributaries; and (3) downstream Moscow and to the mouth with six tributaries. We considered Moscow to be a single combined pollution source, so our research focused on upstream and downstream parts mostly.

The upstream part was repeatedly sampled during each of four seasons (Table 1). The analysis for urban part, with-

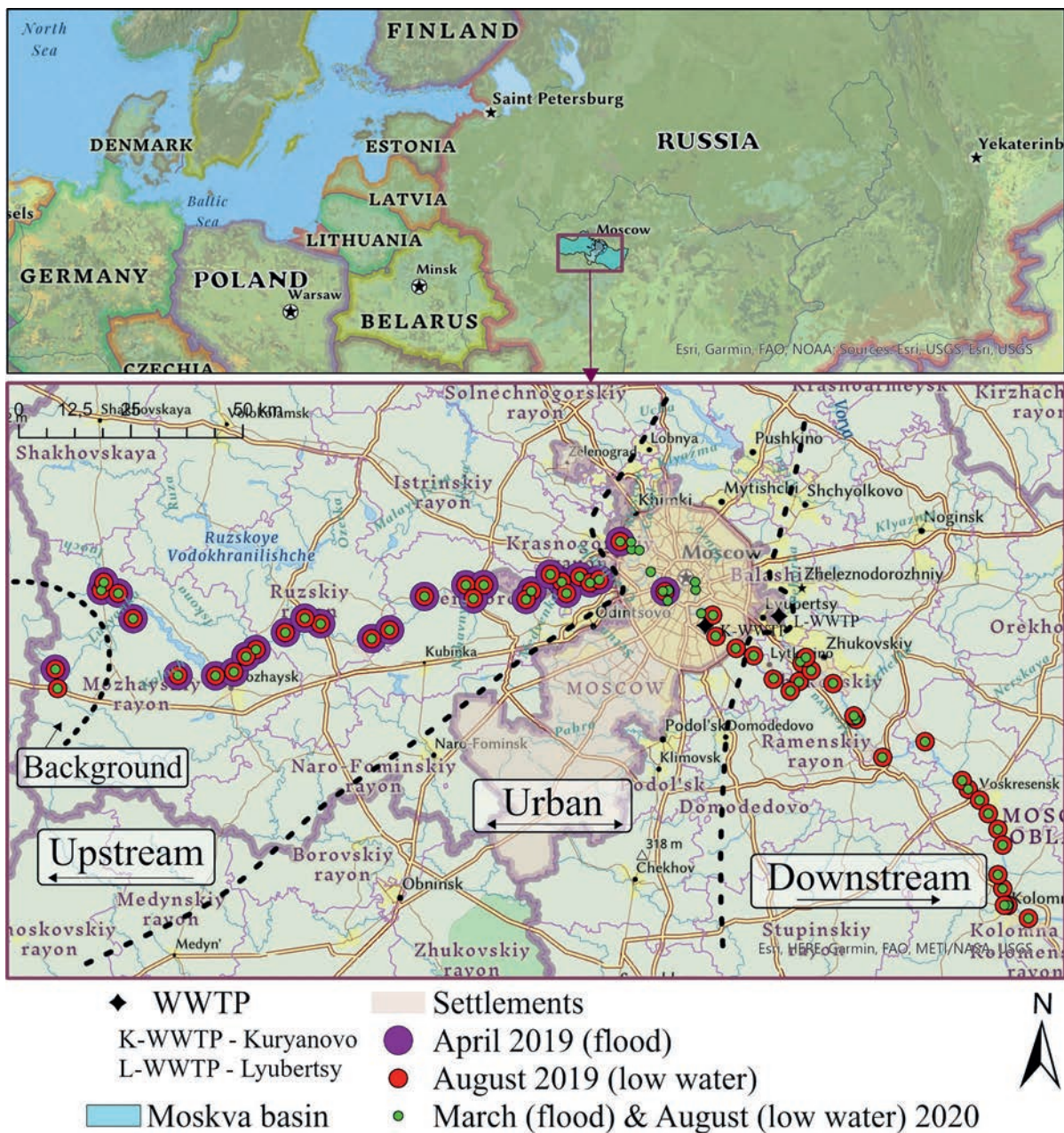


Fig. 1 Sampling stations of river water in the Moskva Basin

in Moscow city, was based mostly on data gathered during the March and August campaigns of 2020. Samples for the downstream part were taken during August 2019 and March and August 2020 (Fig. 1). The total amount of collected river water samples was 215 (147 in Moskva River and 68 in tributaries, Table 1). All stations are confined to the most significant sources of flow transformation along the river systems: the confluence with the largest or most polluted tributaries, near large settlements, wastewater discharge points from city treatment facilities, etc.

To estimate background level of PTEs and nutrient concentrations, the mean of three sampling stations in the most upper part of the Moskva River for all seasons ( $n = 12$ ) was calculated.

The 15 key tributaries of the Moskva River, on which sampling sites were organized, included rivers with a length of more than 30 km and a catchment area of more than 150 km<sup>2</sup>: the Gzhelka, Inoch, Iskona, Istra, Koloch, Kolomenka, Lusyanka, Nerskaya, Pakhra, Pekhorka, Ruza, Setun, Severka, Skhodnya, and Yauza. Also, ob-

servations were organized on the Moscow Canal and four small tributaries: the Nakhavnya, Vyazemka, Medvenka, and Chachenka, since according to the data of long-term hydrochemical monitoring carried out by the Mosvodokanal, these rivers are polluted ones.

Samples were put into 5-L polyethylene terephthalate bottles from the surface layer of water. Vertical sample checks of the water column at several stations showed the absence of significant gradients in the measured parameters due to turbulent mixing, which allows the surface samples to be considered representative. Afterward, the water samples were filtered on a Millipore vacuum pump through 47-mm-diameter membrane filters with a pore size of 0.45  $\mu\text{m}$ .

The suspended sediments concentration (SSC) or turbidity in the river waters was determined by the direct weighted method. An optical method for estimating suspended sediments amount with the HACH 2100P photometer (Hach Company, Loveland, CO, USA) was used at the control sites.



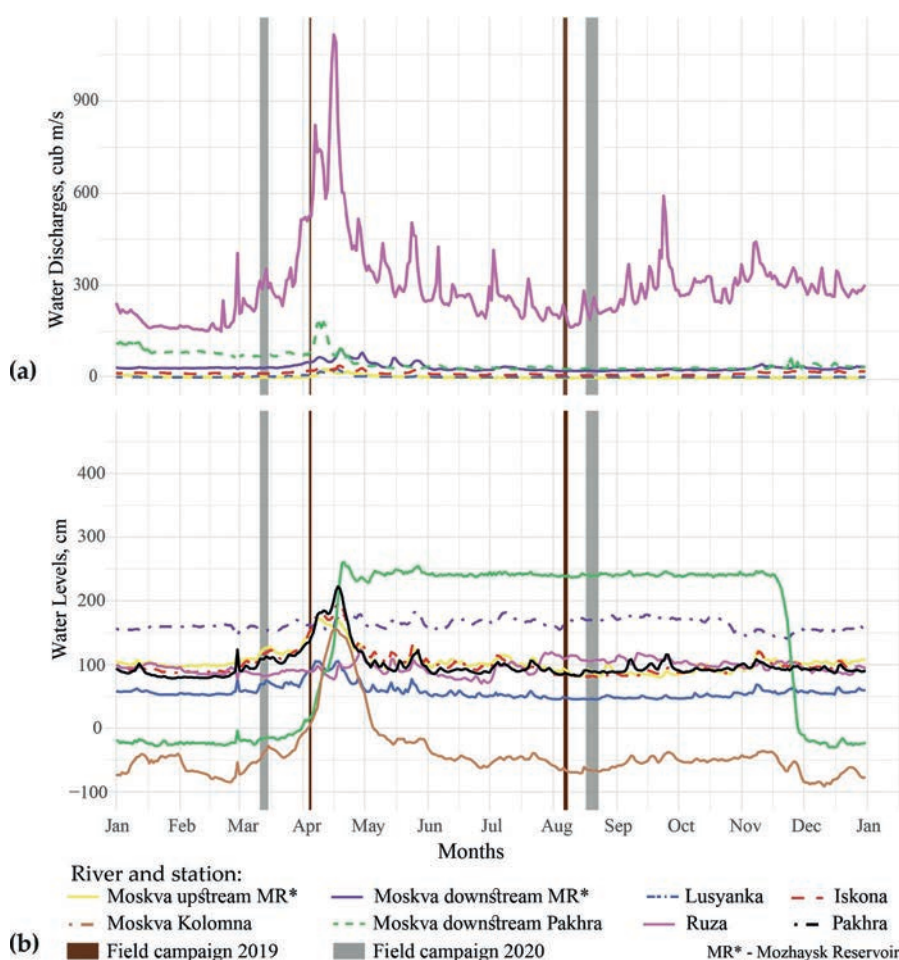


**Fig. 2.** Average annual water discharges (a) and water levels (b) of the Moskva River and its tributaries based on gauging stations data, and sampling campaign periods. Water levels of the gauging stations are calculated according to the Baltic Heights System BK77

**Table 1** Amount of samples collected in different field campaigns in Moskva River and its tributaries

Moskva River Basin part	Season	Sampling period	Number of samples*
Background	Flood	April 5, 2019	3(M)
	Flood	March 11, 2020	3(M)
	Low water	August 6, 2019	3(M)
	Low water	August 17, 2020	3(M)
	All seasons, total	–	12(M)
Upstream	Flood	April 4–5, 2019	15(M) + 10(T)
	Flood	March 11–15, 2020	16(M) + 10(T)
	Low water	August 6–8, 2019	16(M) + 10(T)
	Low water	August 17–23, 2020	16(M) + 10(T)
	All seasons, total	–	63(M) + 40(T) = 103
Urban	Flood	April 8, 2019	1 (T)
	Flood	March 11–15, 2020	8(M) + 4(T)
	Low water	August 6–8, 2019	2(M) + 1(T)
	Low water	August 17–23, 2020	8(M) + 4(T)
	All seasons, total	–	18(M) + 10(T) = 28
Downstream	Flood	March 11–15, 2020	18(M) + 6(T)
	Low water	August 6–8, 2019	18(M) + 6(T)
	Low water	August 17–23, 2020	18(M) + 6(T)
	All seasons, total	–	54(M) + 18(T) = 72
Total	All seasons	–	147(M) + 68(T) = 215

\*M stands for samples from Moskva River and T for its tributaries



## Laboratory procedures

Water temperature, pH, dissolved oxygen (DO) concentrations, and specific conductance (at 25 °C) were measured in situ by YSI ProSolo, YSI ProODO, and YSI Pro30 probes (Yellow Springs, Ohio, USA) at every sampling station. River water samples were taken in PET 5-L bottles. To separate suspended form of chemical elements from dissolved ones, samples of river water were filtered through pre-weighted membrane filters with a pore diameter of 0.45 µm using a Millipore Vacuum pump station. Laboratory analyses were carried out at the Krasnovidovo scientific station of Lomonosov Moscow State University.

In unfiltered samples, the amount of easily oxidized organic substances was assessed via the five-day biochemical oxygen demand (BOD<sub>5</sub>) using the iodometric method and the chemical oxygen demand (COD) using the dichromate method. The content of total dissolved nitrogen (TDN) and phosphorus (TDP), dissolved inorganic phosphorus (DIP), and nitrite nitrogen (N–NO<sub>2</sub>) was determined in filtered samples on a single-beam photometer using standard methods: the Murphy–Riley method (Murphy & Riley, 1962) for TDP and TIP, alkaline persulfate digestion (Nollet & De Gelder, 2013) for TDN, and Griess reaction (Nollet & De Gelder, 2013) for N–NO<sub>2</sub>. Concentrations of nitrate and ammonia nitrogen (N–NO<sub>3</sub> and N–NH<sub>4</sub>), as well as major ions (Ca<sup>2+</sup>, Mg<sup>2+</sup>, Na<sup>+</sup>, K<sup>+</sup>, SO<sub>4</sub><sup>2-</sup>, Cl<sup>-</sup>), were determined via ion chromatography on Concise IC Sep An2 and Shodex IC YS-50 columns (USA and Japan). HCO<sub>3</sub><sup>-</sup> and CO<sub>3</sub><sup>2-</sup> concentrations were determined by titration with hydrochloric acid. Total dissolved solids concentration (TDS) was calculated as the sum of eight major ions. After filtration, the filter with accumulated suspended matter was re-weighed to calculate the SSC in river waters (mg/L).

Concentrations of Li, B, Al, Ca, V, Mn, Ni, Cu, Zn, As, Sr, Zr, Mo, Sb, Ba, Pb, Bi, and U were determined using the ICP–MS and ICP–AES methods (Elan-6100 and Optima-4300, Perkin Elmer, Waltham, MA, USA) at the All-Russian Scientific Research Institute of Mineral Raw Materials named after N.M. Fedorovsky in Moscow in accordance with the European Communities Environmental Objectives (Surface Waters) Regulations, S.I. no. 272/2009 (2009), and ISO standards 5667-3 (2018). This laboratory is accredited by the international analytical system accreditation (AAC.A.0025) and the national accreditation system (RA.RU.21ГП11). The analysis was performed using blank samples and standard materials, “Trace metals in Drinking Water (TMDW)” (High-Purity Standards, USA). The detection limits (DLs) were as follows (µg/L): Li 0.008; B 0.63; Al 1.4; Ca 7; V 0.66; Mn 0.089; Ni 0.16; Cu 0.4; Zn 0.5; As 0.07; Sr 0.08; Zr 0.012; Mo 0.081; Sb 0.026; Ba 0.06; Pb 0.06; Bi 0.0023; U 0.0019. Only those PTEs for which the number of points with values below the detection limit did not exceed 40% were chosen for further analysis.

## Data analysis

The ratios of the PTEs concentrations in the Moskva River waters and its tributaries were compared with world average data (Gaillardet et al., 2014) (this ratio was called Kc). Descriptive statistics were calculated using the “pastecs” package (Grosjean & Ibanez, 2018), and all graphic illustrations were designed in “ggplot2” (Wick-

ham et al., 2021) and “tmap” (Tennekes, 2021) packages for R, as well as ArcGIS Pro software (developed by Esri). To define the common sources of PTEs, factor analysis (FA) with Varimax rotation was performed using the “nFactors” package (Raiche & Magis, 2020) and the correlation analysis using the “corrplot” package (Wei & Simko, 2021) for R. The suitability of the dataset for FA was assessed using the Kaiser–Meyer–Olkin (KMO) test and Bartlett’s test of sphericity (BoS). KMO is a measure of sampling adequacy for each variable in a dataset that points to the proportion of variance which may be caused by certain factors. Bartlett’s test of sphericity signifies whether the correlation matrix is an identity matrix, which would indicate that the variables are unrelated. High KMO values (> 0.6) together with low significance levels (p < 0.05) for BoS typically indicate that the sampling is adequate and there are significant relationships among the variables (Li et al., 2013; Liang et al., 2019; Mishra et al., 2018; Zhang et al., 2021); thus, FA may be useful, which is the case for this study (KMO = 0.71, the significance level for BoS << 0.05). KMO and Bartlett’s test of sphericity were checked using the “REdaS” package for R (Maier, 2015). All named packages were performed in R Studio Desktop version 4.0.3 (2020-10-10).

River water quality was assessed by the comparison of PTEs concentrations with the maximum permissible concentrations of chemical substances in the samples taken of water bodies of cultural and domestic water use (MPC<sub>D</sub>, this contamination factor was called CF<sub>D</sub>) (San-PiN 1.2.3685-21, 2021) and water bodies of fishery use (MPC<sub>F</sub>, CF<sub>F</sub> ratio) (Order, 2020) for the Russian Federation, as well as the World Health Organization drinking water quality standards (MPC<sub>W</sub> and CF<sub>W</sub>, respectively) (Guidelines, 2017) and the United States Environmental Protection Agency (US EPA) water quality standards (MPC<sub>USA</sub>, CF<sub>USA</sub>) (EPA 816-F-09-004, 2009).

For an integrated assessment of water quality, taking into account the complexity of the recurrence of pollution in different phases of the water regime, the Canadian CCME WQI index was calculated (Canadian, 2017) using formula (1):

$$\text{CCME WQI} = 100 - \frac{\sqrt{F_1^2 + F_2^2 + F_3^2}}{1.732} \quad (1)$$

where F<sub>1</sub> is the factor reflecting the complexity of pollution (Eq. 2):

$$F_1 = n/N, \quad (2)$$

where n is the number of indicators for which the excess of MPC is observed and N is the total number of indicators taken into account.

F<sub>2</sub> is a factor reflecting the frequency of quality standards in excess for each of the indicators (Eq. 3):

$$F_2 = n_{ij}/N, \quad (3)$$

where n<sub>ij</sub> is the number of analysis results for the i-th ingredient in the j-th section during the considered period of time, in which their content or value exceeds the corresponding MPC (or background values).

F<sub>3</sub> is a factor reflecting the frequency of exceeding the standard values for each indicator (Eqs. 4–6):

$$F_3 = \frac{0.01}{0.01 \cdot E_2 + 0.01} ; \quad (4)$$

$$E_2 = \sum E_1 / W; \quad (5)$$

$$E_1 = C_i / MPC - 1, \quad (6)$$

where  $W$  is the total number of tests and  $C_i$  is the concentration of the  $i$ -th component.

Depending on water quality, the CCME WQI values range from 0 to 100. Levels of water quality could be determined in accordance with the classification presented in Table 2.

**Table 2.** Water pollution level according to CCME WQI values (Canadian, 2017)

CCME WQI value	Water quality
95–100	Excellent
80–94	Good
65–79	Fair
45–64	Marginal
0–44	Poor

## RESULTS

### Physical and chemical parameters of river waters

The Moskva River and its tributaries are mostly characterized by low-to-medium mineralization. TDS (total dissolved solids) values in the Moskva River ranged between 158 and 580 mg/L, with the exception of the river's source, where it did not exceed 70 mg/L. In the upper reaches of the river, TDS changed direction along its course, but in the urban part it increased continuously, reaching a nearly constant value below the city. In the river's tributaries, TDS varied more greatly—between 124 and 841 mg/L, with the highest values observed in rivers of the central part of the basin draining most urbanized areas. Among major ions,  $\text{Ca}^{2+}$  and  $\text{HCO}_3^-$  dominated (over 50% of total cation and anion equivalent mass, respectively) in almost all of the taken samples, although in urban and downstream parts of the river the share of  $\text{Cl}^-$  and  $\text{Na}^+$  ions increased up to 35% and more (in equivalent form), almost reaching the levels of bicarbonate and calcium concentrations.

The influence of Moscow megacity on physical parameters appeared to be rather low (Table 3): pH and dissolved oxygen values dropped only slightly (by 0.2 and 2.6), whereas suspended sediment concentration and specific conductance increased slightly (1.5–1.8-fold) downstream from the city. Mean values of pH, specific conductance, and dissolved oxygen in the Moskva River and its tributaries did not show seasonal variations either. The range of pH values was equal to 3.7. Maximum pH was measured in the Pakhra (8.9, low water) and the Ruza (8.7, flood) rivers, where high dissolved oxygen concentrations indicated increased levels of photosynthetic

activity, as well as in the main channel of the Moskva, downstream at the Tuchkovo settlement where wastewater discharges of LLC “Tubeton” flow into the river. Minimum values were found for the Moskva source (5.2–5.3 depending on the season), the Gzhelka (7.5, low water) and the Nerskaya (7.6, flood) rivers.

Highest specific conductance values were measured in the Moskva River downstream from the Lyubertsy Waste Water Treatment Plant (Lyubertsy WWTP; 1013.5  $\mu\text{Sm/cm}$  during low water and 909  $\mu\text{Sm/cm}$  in flood), as well as in the Pakhra (979  $\mu\text{Sm/cm}$ , low water) and the Yauza (1364  $\mu\text{Sm/cm}$ , flood) rivers. Lowest specific conductance was found for the Skhodnya (321  $\mu\text{Sm/cm}$ , low water) and the Inoch (186  $\mu\text{Sm/cm}$ , flood) rivers, as well as the Moskva River source (151  $\mu\text{Sm/cm}$  during low water and 37  $\mu\text{Sm/cm}$  in flood).

Maximum dissolved oxygen concentrations (14.2–17.5 mg/L depending on hydrological season) were revealed in the Moskva River upstream part. Minimum DO levels (0.5–4.8 mg/L) were found at the Moskva River source. Among the Moskva tributaries, the highest DO concentrations were measured at the Pakhra River mouth (14.2 mg/L) during the low water period of 2020 and at the Ruza River mouth (16.8 mg/L) during flood. The lowest DO values were found in the Pakhra (3.4 mg/L, low water 2019) and the Pekhorka (8.5 mg/L, flood) rivers.

The highest mean suspended sediment concentrations were found in the urban part of Moskva River. Maximum SSC in the upstream part of Moskva River was two times higher than downstream one: 91.6 mg/L (in the Moskva River source area during low water period) versus 44.5 mg/L (downstream from Dzerzhinsky town during flood), respectively. The lowest SSC was measured for the Moskva upstream area (1.3 mg/L, low water) and downstream from Mozhaysk reservoir (2.9 mg/L, flood). The natural flow regime of the Moskva tributaries provided higher suspended sediment concentrations in flood period, when the mean SSC value was 5.7 times higher than in the low water one. The highest levels of SSC at about 176 mg/L and 31 mg/L were defined in the mouth of the Setun (flood period) and Kolomenka (low water) rivers, respectively.

### Nutrients concentrations

Mean nutrient concentrations and organic matter content in the downstream part of the Moskva Basin (the Moskva main channel and tributaries were considered together) were 1.4–14 times higher than in the upstream part and 1.6–92 times higher than the background values (Table 4, Fig. 3b). The greatest differences between upstream and downstream basin parts were found for  $\text{N-NO}_2$  and  $\text{N-NH}_4$ , whose concentrations increased 7.5–14 times in the downstream part. The smallest differences between the upper and lower parts of the river were observed for  $\text{BOD}_5$ , COD, and  $\text{N-NO}_3$ , although all of these parameters also increased steadily along the

**Table 3.** Water parameters (mean values) of the Moskva River parts and its tributaries

River or its part	TDS (mg/L)	pH	Specific conductance ( $\mu\text{Sm/cm}$ )	DO (mg/L)	SSC (mg/L)
Upstream	316.5	8.1	399.3	11.5	12.0
Urban	380.5	8.0	622.8	9.1	25.8
Downstream	503.7	7.9	711.8	8.9	18.1
Tributaries	444.9	8.1	629.7	10.3	21.2







**Table 4.** Descriptive statistics for nutrient concentrations and organic matter content in different Moskva River parts

Parameter	Upstream part			Urban part			Downstream part			BG <sup>c</sup>		
	Mean ± STD <sup>a</sup> (Min–Max)	M <sup>b</sup>	CV (%)	n	Mean ± STD (Min–Max)	M	CV (%)	n	Mean ± STD (Min–Max)		M	CV (%)
BOD <sub>5</sub> , mgO <sub>2</sub> /L	3.2 ± 1.9 (0.5–10.6)	2.6	59	101	2.2 ± 1.9 (0.6–9.1)	1.8	87	27	4.9 ± 2.6 (1.0–11.5)	4.7	53	71
COD, mgO/L	24.7 ± 18.7 (11.6–146)	20.2	76	103	32.3 ± 8 (24.6–60.6)	30.6	24	28	36 ± 8 (13–57)	36	23	71
N–NO <sub>3</sub> , mg/L	1.8 ± 1.4 (0.08–5.3)	1.7	78	45	1.98 ± 1.8 (0.3–4.5)	1.57	92	4	2.7 ± 2.5 (0.9–13)	2.1	90	22
N–NO <sub>2</sub> , µg/L	15.6 ± 35.1 (0.00–249)	0.12	225	102	44.9 ± 39.5 (0.04–185)	36.5	88	28	224 ± 284 (0.01–953)	168	127	71
N–NH <sub>4</sub> , mg/L	0.2 ± 0.3 (0.04–1.9)	0.14	126	45	1.3 ± 0.9 (0.3–2.4)	1.2	74	4	1.8 ± 0.9 (0.3–3.9)	1.7	49	22
TDN, mg/L	2.0 ± 1.4 (0.2–7.0)	1.63	67	102	2.5 ± 1.7 (1.1–8.4)	1.9	68	28	7.9 ± 4.9 (0.6–37)	7.5	62	72
DIP, mg/L	0.09 ± 0.1 (0.00–0.72)	0.06	124	103	0.07 ± 0.04 (0.03–0.2)	0.06	53	28	0.4 ± 0.4 (0.06–3.0)	0.4	96	70
TDP, mg/L	0.10 ± 0.1 (0.01–0.76)	0.07	109	103	0.09 ± 0.04 (0.04–0.3)	0.08	48	28	0.5 ± 0.4 (0.07–3.2)	0.4	94	65

<sup>a</sup>STD standard deviation value<sup>b</sup>M median value<sup>c</sup>BG mean value for background sampling subset (n = 12)**Table 5.** Descriptive statistics for PTEs concentrations (µg/L) in the Moskva Basin upstream, urban, and downstream parts

PTEs	Upstream part (n = 103)			Urban part (n = 28)			Downstream part (n = 72)			BG <sup>c</sup> , (n = 12) World <sup>d</sup> (µg/L)			
	Mean ± STD <sup>a</sup> (Min–Max)	M <sup>b</sup>	CV (%)	Mean ± STD <sup>a</sup> (Min–Max)	M <sup>b</sup>	CV (%)	Mean ± STD <sup>a</sup> (Min–Max)	M <sup>b</sup>	CV (%)	Mean ± STD <sup>a</sup> (Min–Max)	M <sup>b</sup>	CV (%)	World <sup>d</sup> (µg/L)
Li	3.5 ± 2.9 (0.6–18.7)	2.8	82	6.7 ± 4.2 (2.8–20)	5.5	63	8.5 ± 2.5 (4.8–22)	7.7	29	7.7	29	1.7/1.5	1.84
B	37 ± 41 (10–240)	23.0	111	65 ± 60 (29–310)	44.5	92	72 ± 29 (23–181)	67	40	67	40	27/20	10.2
Al	17 ± 82 (0.5–610)	1.7	485	7.6 ± 5.8 (1.7–33)	6.5	77	5.6 ± 3.4 (0.4–15)	5.2	64	5.2	64	6/5	32.0
Ca	58,712 ± 17,980 (3050–98,795)	58,800	31	66,726 ± 19,209 (41,300–108,900)	62,100	29	66,231 ± 7965 (41,000–98,500)	66,445	12	66,445	12	50,346/50,850	–
V	0.8 ± 0.4 (0.1–1.9)	0.76	43	1.2 ± 0.4 (0.6–2.5)	1.2	36	1.4 ± 0.5 (0.4–2.5)	1.5	34	1.5	34	0.54/0.57	0.71
Mn	15 ± 32 (0.2–210)	2.2	213	68 ± 136 (0.3–720)	39	200	29 ± 43 (0.3–140)	1.2	149	1.2	149	37/29	34
Ni	0.36 ± 0.6 (0.09–3.7)	0.1	165	1.1 ± 1.1 (0.09–4.9)	0.8	102	1.7 ± 0.8 (0.1–4.4)	1.7	48	1.7	48	0.7/0.6	0.8
Cu	1.6 ± 6.0 (0.25–61)	0.8	378	2.6 ± 1.1 (1.0–5.9)	2.6	43	1.9 ± 2.4 (0.3–21)	1.8	125	1.8	125	0.8/0.8	1.48
Zn	3.3 ± 6.5 (0.1–59)	1.9	194	7.3 ± 3.9 (2–18)	6.4	53	8.5 ± 4.9 (0.4–34)	7.9	58	7.9	58	5/2	0.60
As	1.5 ± 0.8 (0.3–3.0)	1.2	54	1.6 ± 0.8 (0.7–3.5)	1.8	46	1.9 ± 0.6 (0.5–4.1)	2.1	34	2.1	34	0.84/0.84	0.62
Sr	284 ± 448 (7.9–2966)	152	158	507 ± 388 (180–1810)	430	76	672 ± 275 (280–2340)	645	41	645	41	122/126	60
Zr	0.13 ± 0.19 (0.02–1.3)	0.07	150	0.11 ± 0.09 (0.02–0.4)	0.07	87	0.07 ± 0.06 (0.02–0.41)	0.05	87	0.05	87	0.17/0.15	0.04
Mo	0.57 ± 0.65 (0.04–3.6)	0.39	113	0.8 ± 0.3 (0.4–1.7)	0.67	44	0.8 ± 0.2 (0.2–1.2)	0.9	26	0.9	26	0.28/0.24	0.42
Sb	0.1 ± 0.05 (0.02–0.3)	0.09	47	0.27 ± 0.1 (0.1–0.5)	0.27	35	0.4 ± 0.1 (0.07–0.51)	0.38	31	0.38	31	0.07/0.07	0.07
Ba	44.6 ± 14.3 (14–108)	42.0	32	45.4 ± 7.7 (36–70)	43.5	17	34 ± 6 (20–44)	34	17	34	17	44/43	23
Pb	0.21 ± 0.30 (0.01–1.6)	0.06	143	0.26 ± 0.24 (0.02–0.8)	0.1	93	0.3 ± 0.2 (0.02–0.84)	0.3	75	0.3	75	0.19/0.1	0.08
Bi	0.002 ± 0.002 (0.001–0.01)	0.0009	102	0.0008 ± 0.0002 (0.00003–0.0015)	0.0009	29	0.001 ± 0.002 (0.0003–0.012)	0.0009	134	0.0009	134	0.002/0.001	–
U	0.47 ± 0.2 (0.02–1.1)	0.46	43	0.64 ± 0.32 (0.2–1.8)	0.6	50	0.6 ± 0.4 (0.1–2.4)	0.6	65	0.6	65	0.49/0.53	0.37

<sup>a</sup>STD standard deviation value<sup>b</sup>M median value<sup>c</sup>BG background mean/median values<sup>d</sup>From (Gaillardet et al., 2014)

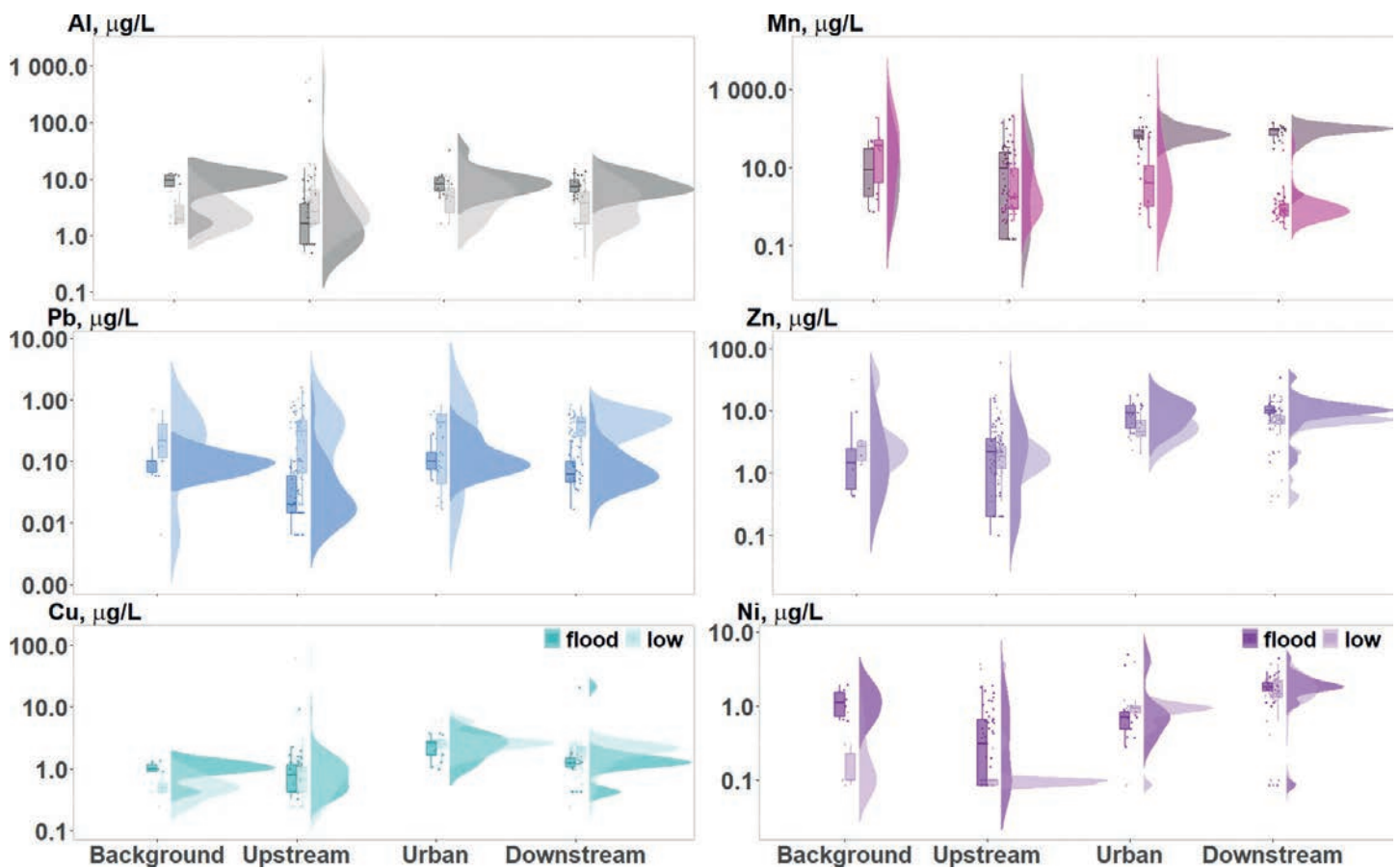


Fig. 4. Raincloud plots—data distribution (the “cloud”) with jittered raw data (the “rain”) supplemented by boxplots (Allen et al., 2021)—of dissolved PTEs concentrations in different Moskva Basin parts

### PTEs concentrations

Background PTEs concentrations in the Moskva Basin (Fig. 3c) usually were not higher than the world average PTEs values (Gaillardet et al., 2014). Exceptions were revealed only for Zn (8.3-fold higher), Zr (4.2), B (2.7), Pb (2.4), and Sr (2).

The upstream Moskva River part, relative to the background values (Kc coefficient, Fig. 3a), showed slightly higher concentrations of Al, Sr, Cu, Li, and Mo (Kc = 2–3). In the urban part, the amount of pollutants and Kc values were greater: Sr, Sb, Li, Cu, Mo, B, V, As, and Mn (Kc = 2–4). The highest Kc values were found in the downstream part of the Moskva Basin for Sr, Sb, Li (Kc = 4.0–5.5), Mo, B, V, Cu, Ni, and As (Kc = 2–3). Thus, the main pollutants of all the Moskva Basin parts are Sr, Sb, Li, Cu, Mo, B, V, and As. Concentrations of these elements in the entire Moskva Basin were higher than the background values.

Comparison of the Moskva Basin parts (KK coefficient, mean values, Fig. 3d) with world average PTEs content (Gaillardet et al., 2014) revealed high concentrations of Zn, Sr (KK = 4–6), B, Zr, Pb, and As (KK = 2–4) in the upstream part, the same elements accompanied with Sb, Li, Mn, Ba (KK = 2.0–3.9) in the urban part (Fig. 3d) and with the addition of Ni, Mo, V, Zr (KK around 2) in the downstream part (Fig. 3d). A significant increase in KK values was revealed for all studied elements and especially for Ni, Sb, Sr, Li, Zn, and B when moving from upstream to downstream river parts.

Descriptive statistical results calculated for the upstream Moskva Basin part showed high coefficient of

variation (CV) for elements of joint natural and anthropogenic origin such as Al, Cu, Mn (213–485%) and Zn, Ni, Sr, Zr, Pb, Mo, B, Bi (102–194%). Such high CV values are mainly due to extremely high concentrations of these elements (especially Al and Zr) in local areas—Moskva source and Setun mouth (Mn, Ni) areas. For other elements, it varied from 31 to 82% (Table 5).

For the urban part of the Moskva Basin, which is supposed to be more polluted, CV was significantly lower as the joint impact of different element sources and lack of unpolluted water supply contributes to smoothing out the variations in the concentrations of elements. The highest CV values were found for Mn and Ni (200% and 102%) here. Other PTEs had lower CV values (17–93%). For the downstream basin part, rather low CV values were characteristic—only Mn, Bi, and Cu exceeded 100% (125–149%). Thus, only Mn appeared to have high CV values (around 100% and higher) for all basin parts, while for Cu (upstream and downstream) and Ni (upstream and urban) only for two of the three basin parts CV values > 100% were calculated. Lowest CV values were defined for crustal elements Ca and Ba (Table 5). Highest CV values for almost all PTEs except for Bi and U were found for upstream part of Moskva Basin, where the presence of uncontaminated tributaries and river parts together with various local sources of pollution (small towns, farms, roads, etc.) leads to a large heterogeneity in the PTEs concentrations in the main channel of Moskva River.

The high variance of element concentrations was caused by the combination of anthropogenic and hydroclimatic factors (Fig. 4). However, the large variability of PTEs concentrations determines the use of

**Table 6.** Factor analysis results for PTEs and nutrient concentrations distribution in the Moskva River Basin.

Loadings	Factor 1	Factor 2	Factor 3	Factor 4	Factor 5
Sr	<b>0.91</b>	0.24	0.06	0.04	0.02
Li	<b>0.89</b>	0.29	0.02	0.22	0.07
B	<b>0.77</b>	0.28	0.15	0.19	0.02
Mo	<b>0.70</b>	0.16	0.02	0.25	0.00
Ca	<b>0.66</b>	0.02	-0.29	0.23	0.11
TDN	0.27	<b>0.86</b>	0.00	-0.10	0.12
TDP	0.32	<b>0.73</b>	-0.01	-0.05	0.03
Sb	0.33	<b>0.69</b>	0.01	<b>0.41</b>	0.17
Ni	0.16	<b>0.65</b>	0.32	0.03	0.07
N-NO <sub>2</sub>	0.03	<b>0.56</b>	-0.07	0.12	0.06
Al	-0.17	0.00	<b>0.94</b>	0.03	0.01
COD	0.21	<b>0.40</b>	<b>0.79</b>	0.05	0.06
Zr	-0.09	-0.06	<b>0.77</b>	0.00	-0.04
V	0.28	<b>0.35</b>	0.01	<b>0.89</b>	0.03
As	0.23	0.06	-0.18	<b>0.69</b>	0.01
Zn	0.11	<b>0.33</b>	0.18	0.02	<b>0.92</b>
Cu	0.00	-0.07	0.02	0.08	<b>0.68</b>
Pb	0.09	0.00	0.28	<b>0.46</b>	0.29
Mn	0.13	0.05	<b>0.31</b>	-0.04	0.15
Bi	-0.08	0.21	<b>0.39</b>	-0.23	0.08
Ba	0.07	-0.49	-0.23	0.09	0.01
U	<b>0.38</b>	-0.15	-0.14	<b>0.45</b>	0.00
BOD <sub>5</sub>	0.13	<b>0.44</b>	0.07	0.15	-0.08
% of total variance	17.1	16	12.2	9.4	6.5
Eigenvalue	6.6	3.6	2.2	1.8	1.5

PTEs with FL  $\geq 0.5$  are shown in bold italic and with FL = 0.3–0.5 in italic

median values instead of averages when comparing the basin parts. The most significant difference (> threefold) between median PTEs concentrations within urban and upstream basin parts was detected for Mn, Al, Pb, Zn, Cu, and Sr during flood season and for Ni and Sb during low water (Fig. 4). This fact proves the high anthropogenic input of these elements within the Moscow megacity area. Further downstream during both flood and low water seasons median PTEs concentrations did not significantly exceed urban part median values.

The highest concentrations of Bi, Zn, TDP, and DIP were found in the Moskva's main channel around the Lyubertsy WWTP. The lowest concentrations of most PTEs were found in the upper part of the Moskva River. Mean PTEs and nutrient concentrations in the Moskva's main channel and tributaries are close. For the tributaries, slightly higher (two–threefold) concentrations of N-NO<sub>3</sub>, Mn, and Ni were found at the urban part; N-NO<sub>2</sub>, N-NH<sub>4</sub>, DIP, and Mo at the upstream part; B and Sr at both the upstream and urban parts; and lower content of Al at the upstream part (6.7 times lower than in the Moskva's main channel). The highest PTEs concentrations were found in the Setun, Yauza, and Gzhelka and the lowest in the Inoch and Lusyanika rivers.

### Correlation analysis

A significant positive correlation was found within the following associations: Al-Zr-COD ( $r = 0.72-0.75$ ), COD-Ni (0.59), Li-Sb (0.61), Mo-B-Li-Sr-Ca (0.53–0.71), N-NO<sub>3</sub>-DIP-TDP-N-NH<sub>4</sub>-TDN (0.54–0.99), V-Sb-As-Li (0.55–0.71), Ca-U (0.55), and Cu-Zn (0.6

(Appendix, Fig. 7a). A negative correlation was revealed between Ba, Ni, Sb, and some nutrients (DIP, TDP, TDN, COD, BOD<sub>5</sub>;  $r = -0.42$  to  $-0.25$ ), as well as within Al-Ca-As-U-Zr-Bi ( $-0.18$  to  $-0.38$ ) association.

Al, COD, Zr, and N-NH<sub>4</sub> appeared to have a strong negative correlation with pH values ( $r = -0.74$  to  $-0.53$ ). Dissolved oxygen has a moderate negative correlation ( $-0.48$  to  $-0.30$ ) with COD, N-NH<sub>4</sub>, Pb, Sb, V, Li, TDP, TDN, DIP, Sr, As, Zn, and Ni. A positive correlation was found for Ca, Li, N-NH<sub>4</sub>, Sr, Mo, TDN, B, DIP, TDP, Sb, and specific conductance, as well as for As, V, N-NH<sub>4</sub>, and water temperature. SSC content did not show any significant correlation with PTEs, nor with nutrients (Appendix, Fig. 7b).

### Factor analysis

Factor analysis was performed using the entire dataset including all parts of the Moskva River and its tributaries in order to define element associations derived from common pollutant sources in the entire basin. There is a very strong correlation between TDP and DIP ( $r$  around 1), and missing data for N-NO<sub>3</sub> and N-NH<sub>4</sub>, therefore DIP, N-NO<sub>3</sub>, and N-NH<sub>4</sub>, were excluded from factor analysis. All remained variables passed KMO and Bartlett's test of sphericity. After Varimax rotation FA revealed five factors (Table 6) that explained 61% of the total PTEs variance (each group consists of elements with factor loadings (FL)  $> 0.5$ , elements with FL 0.3–0.5 are shown in brackets): (F1) Sr-Li-B-Mo-Ca(-TDP-U-Sb); (F2) TDN-TDP-Sb-Ni-N-NO<sub>2</sub>(-BOD<sub>5</sub>-COD-V-Zn); (F3) Al-COD-Zr(-Bi-Mn-Ni); (F4) V-As(-Pb-U-Sb); and (F5) Zn-Cu. Ba has negative FL ( $-0.5$ ) within factor 2.



### Compliance with water quality guidelines

To assess changes in water quality from the source to the mouth of the Moskva River, contamination factors (CF) were calculated as ratios between PTEs concentrations in the Moskva River Basin and different guidelines (Table 7, Fig. 5): the maximum permissible concentrations for drinking water ( $MPC_D$ ) and fisheries ( $MPC_F$ ), as well as to the WHO guidelines for drinking water ( $MPC_W$ ) and U.S. EPA water quality standards ( $MPC_{USA}$ ). The greatest excess, although sometimes insignificant, over any of guidelines was revealed in the downstream ( $BOD_5$ ,  $N-NO_3$ ,  $N-NO_2$ ,  $N-NH_4$ , As) and urban (Mn) parts of the basin (Fig. 5).

The highest contamination factors (CF) for most PTEs were found over  $MPC_F$  (Fig. 5) as regulations for these are the strictest among the others. Elements with the highest average  $CF_F$  values ( $CF_F = 1.5-4.8$ ) were  $N-NO_2$ , Mn,  $N-NH_4$ , Cu, and  $BOD_5$ . CF values calculated, according to other guidelines, are much lower and at average do not exceed the threshold. However, local maximum values of CF were much higher than average, especially for Mn, Cu,  $N-NO_2$ , Al, Zn, Sr,  $BOD_5$ , B, Mo, and  $N-NH_4$ .

*Russian Federation water quality guidelines for fisheries* Upstream and in most of the urban part of the river,

nutrient concentrations predominantly stayed within the fisheries guidelines, with occasional increases found in tributaries or in localized sections of the main river (maximum  $CF_F = 5.0$  for  $BOD_5$ , 6.2 for  $N-NH_4$ , 12.5 for  $N-NO_2$ ). Downstream from wastewater treatment stations,  $MPC_F$  for  $BOD_5$ ,  $N-NH_4$ ,  $N-NO_2$ , and DIP continuously were exceeded at the entire remaining section of the river. The most extreme  $CF_F$  values (up to 5.5 for  $BOD_5$ , 10.0 for  $N-NH_4$ , 47.7 for  $N-NO_2$  and 15.0 for DIP) were found directly below treatment plants and in some contaminated tributaries—the Pakhra, Pekhorka, and Medvenka.  $MPC_F$  for  $N-NO_3$  only were exceeded once with CF of 1.4 in the Pekhorka River.

Among PTEs, high  $CF_F \geq 10$  was calculated for Mn in the swamp area of the Moskva River source ( $CF_F = 10-21$ ), in the urban and downstream part of the Moskva Basin (10–12), as well as in the Setun (11–72), Yauza (19), Chachenka (17), and Nerskaya (14) rivers. Lower  $CF_F$  ( $CF_F = 3-10$ ) was found for Mn in the upstream part of the Moskva River (3.0–5.6) again and in the downstream part in Kolomna town ( $CF_F = 9.1-9.9$ ). Other points with medium  $CF_F$  values for Mn were revealed in such tributaries as the Pekhorka (9.8), Setun (9.0), Gzhelka (6.8), Lusyanika (6.8), and Skhodnya (5.4) rivers and the Moscow Canal (5.9), as well as sampling points in the Moskva's main channel downstream from the confluences

**Table 7.** Maximum permissible concentrations (MPC) according to different national and international standards ( $\mu\text{g/L}$ )

PTEs	$MPC_D$	$MPC_F$	$MPC_W$	$MPC_{USA}$
Organization:	Government of Russian Federation	Ministry of Agriculture of Russian Federation	World Health Organization	United States Environmental Protection Agency
Li	<b>30</b>	80	NA	NA
B	500	<b>100</b>	2400	NA
Al	200	<b>40</b>	NA	50
Ca	NA	180,000	NA	NA
V	100	<b>1</b>	NA	NA
Mn	100	<b>10</b>	NA	50
Ni	20	<b>10</b>	70	NA
Cu	1000	<b>1</b>	2000	1300
Zn	1000	<b>10</b>	NA	5000
As	<b>10</b>	50	<b>10</b>	<b>10</b>
Sr	7000	<b>400</b>	NA	NA
Zr	NA	70	NA	NA
Mo	250	<b>1</b>	NA	NA
Sb	<b>5</b>	NA	20	6
Ba	<b>700</b>	NA	1300	2000
Pb	10	<b>6</b>	10	15
Bi	100	NA	NA	NA
U	100	NA	30	30
$BOD_5$ , $\text{mgO}_2/\text{L}$	4	<b>2.1</b>	NA	NA
$N-NO_3$ , $\text{mg/L}$	10.2	<b>9.1</b>	11	10
$N-NO_2$ , $\mu\text{g/L}$	1000	<b>20</b>	900	NA
$N-NH_4$ , $\text{mg/L}$	1.5	<b>0.39</b>	NA	NA
DIP	1.2	<b>0.2</b>	NA	NA
Reference	1	2	3	4

NA stands for no data available; References: 1—(SanPiN 1.2.3685–21, 2021), 2—(Order, 2020), 3—(Guidelines, 2017), 4—(EPA 816-F-09-004, 2009). The lowest MPC values are shown in bold

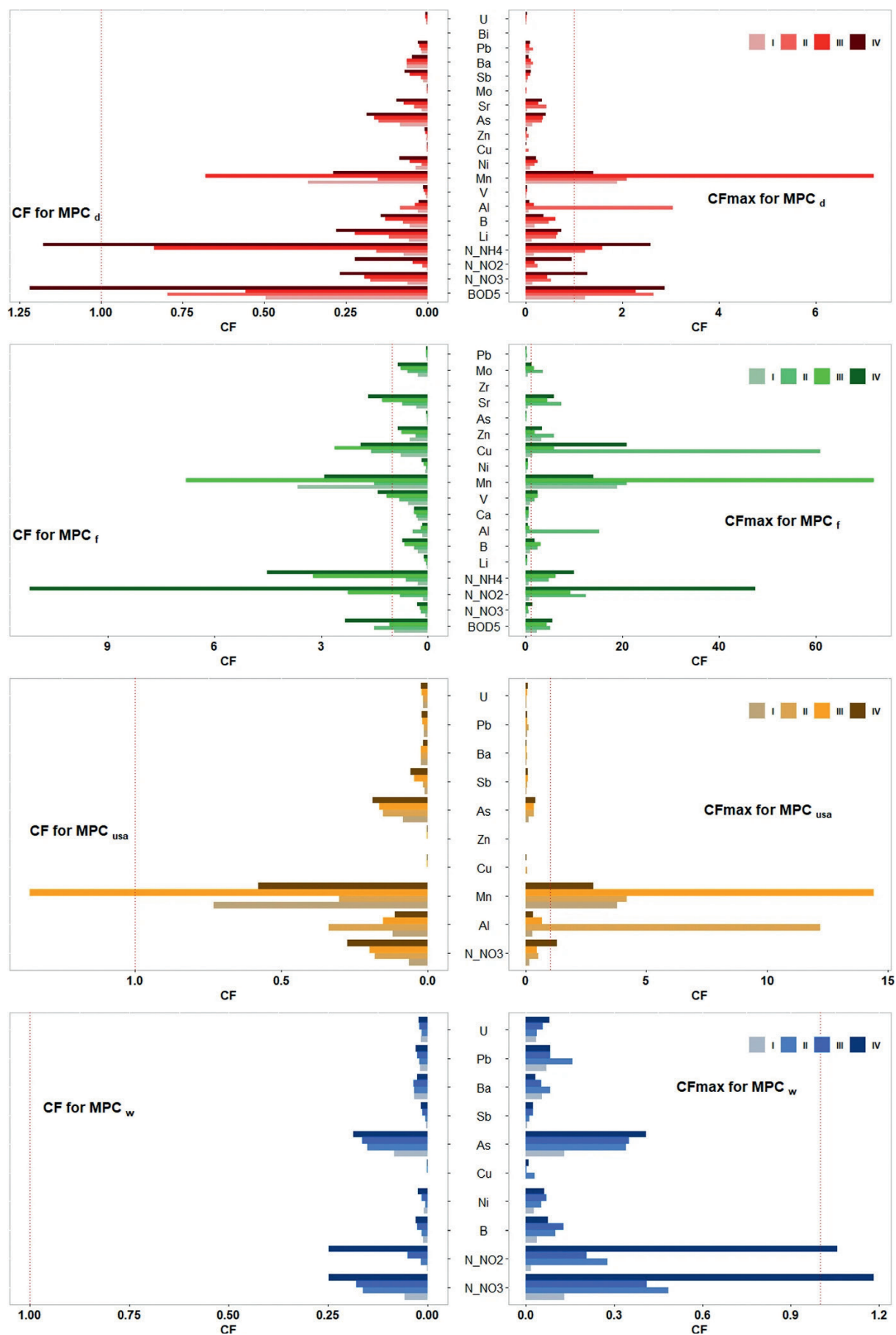


**Fig. 5.** Barplots for contamination factors (CF) according to Russian MPC<sub>D</sub>, MPC<sub>F</sub>, United States EPA MPC<sub>USA</sub>, and worldwide WHO MPC<sub>W</sub> guidelines for the four Moskva Basin parts (tributaries + main channel): I—background, II—upstream, III—urban, IV—downstream parts; average values are in left column and maximum are in right. Red dotted line indicates CF = 1

with mentioned tributaries (5.8–9.7). In addition, elevated Mn concentrations resulted in rather high  $CF_F$  being found downstream from some of Moscow city's industrial zones, TPP (7.9–8.3), Zhukovsky (9.0), and Bronnitsy (8.8) towns and the Lyubertsy WWTP (4.4). Ubiquitously high  $CF_F$  values for Mn were observed during the spring flood of 2020, during other sampling seasons only a sporadic decrease in  $CF_F$  for Mn was detected.

For Cu, two local maximums ( $CF_F \geq 10$ ) were found: in the Moskva River within Krasnogorsk town ( $CF_F = 61$ ) and in the Nerskaya River (21). Moderate  $CF_F$  were calculated for the Setun (3.5–5.5), Yauza (3.7–5.9), and Nakhavnaya (8.5) rivers, as well as the Moskva River upstream area (3) and the downstream Ruza tributary (9.2). All increases in  $CF_F$  for Cu were sporadic and not connected to any hydrological season.

High  $CF_F$  values were calculated also for Al (6–15) in the Moskva River source area; Sr in the Medvenka (3.3–35), Setun (3.1–4.5), and Gzhelka (4.3–5.9) rivers; and Mo (3.4–3.6) in the Chachenka River.

*Russian Federation drinking water quality guidelines* The Russian Federation Standard for drinking water ( $MPC_D$ ) for  $BOD_5$  was continuously exceeded during low flow periods in the lower part of the Moskva (maximum  $CF_D = 2.9$ ), and for other nutrient elements ( $N-NH_4$ ,  $N-NO_3$ , DIP), only occasional increases with  $CF_D < 2$  were detected. Among PTEs, excesses over  $MPC_D$  were detected only for several higher concentrations of Mn and Al. The highest  $CF_D$  value for Mn (7.2) was found in the Setun River, while the greatest  $CF_D$  values for Al (2.6–3.0) were calculated for the Moskva source.

*World Health Organization water quality guidelines* The maximum permissible concentrations of pollutants in drinking water according to the WHO standards ( $MPC_W$ ) are significantly higher than the Russian Federation standards for water bodies of fishery use ( $MPC_F$ ), except for As and Cd (Table 7). Therefore,  $CF_W$  values were much lower than  $CF_F$ . A slight excess over  $MPC_W$  was found only for  $N-NO_3$  in the Pekhorka (1.2) and  $N-NO_2$  in the lower Moskva River (1.1 at Cherkizovo). For PTEs, even maximum  $CF_W$  values did not exceed 0.41, i.e., pollutant concentrations were lower than the threshold values.

Thereby, the main pollutants of the Moskva River and its tributaries are Mn, Al,  $N-NO_3$ ,  $N-NH_4$ , Cu,  $N-NO_2$ , Sr, Zn, B, and Mo. However, they exceed guidelines only locally. Areas of the Moskva Basin found to be at least slightly contaminated are as follows: the Moskva source area (Mn, Al, Cu, Zn), the Moskva River from the Kuryanovo WWTP (Mn, Cu, Sr,  $BOD_5$ ,  $N-NO_2$ ,  $N-NH_4$ , DIP) and from the confluence with the Medvenka River to the very mouth (V, Sr, Cu), as well as the Lusyanka, Koloch, Nakhavnaya (Cu), Vyazemka (Sr, B, V, Mo), Medvenka (Mn, Sr, Mo, B,  $N-NO_2$ , DIP), Chachenka (Mn, Sr), Pakhra (Mn, Sr, V), Pekhorka (Mn, Sr, V, Cu, Zn,  $BOD_5$ ,  $N-NO_2$ ,  $N-NH_4$ , DIP), Gzhelka (Mn, Sr, DIP), Nerskaya (Mn, Sr), Severka (Mn, V), Kolomenka (Mn, V,  $BOD_5$ ), Skhodnya (Cu, Zn), and Setun (Mn, B, V, Cu, Sr) rivers.

*United States Environmental Protection Agency drinking water quality guidelines* US EPA permissible concentrations of PTEs are also lower than those of the  $MPC_D$  for all studied elements except for As (Table 7). However, significant  $CF_{USA}$  values for Mn (up to 4.2) and Al (up to 12.2) were obtained from the Moskva source sampling point and in the Setun River for Mn (14.4). The

$N-NO_3$  guideline was only exceeded once in the Pekhorka ( $CF_{USA} = 1.3$ ). The concentration of other elements did not exceed maximum permissible values.

## DISCUSSION

### PTEs and nutrient sources

Sources of potentially toxic elements and nutrients in the Moskva River and its tributaries were identified based on the factor and correlation analyses results for PTEs, nutrient concentrations and water parameters (Table 6).

*Mineral sources* Sr, Li, B, Mo, and Ca were mostly affected by the first factor; responsible for 17.1% of elements' variance. Distribution of TDP, U, and Sb could also be driven by this factor, although to a lesser extent as their FL were significantly lower (Table 6). Concentrations of Sr, Li, B, and Mo in the Moskva Basin were significantly higher than world average and background values, especially within the downstream basin part (Fig. 3). Elements of Factor 1 had moderate positive correlation with specific conductance ( $r = 0.62-0.81$ ) and rather high variance (Table 5). Tributary factor score values (FS) for Factor 1 were found to be up to 5.6 times higher than those for the main Moskva channel during all seasons, which proves non-anthropogenic origin of these elements. The highest FS values were found at the Medvenka (1.4–5.1), Setun (FS = 1.5–4.1), and Gzhelka (1.1–4.7) mouth areas. Downstream from the confluence of these tributaries FS increases slightly.

Often found in groundwater and wells, these elements are reported to come from various rocks weathering (Voutchkova et al., 2015; Xiao et al., 2019). Groundwater is supposed to be a preferable source of Ca due to the presence of carbonate deposits such as limestone, dolomite, and marl in the territory of the Moscow Region (Geological, 2020). Moreover, in the groundwater of the Moscow Region, elevated concentrations of Sr, Li, Ba, and B were systematically observed as these elements were found in high concentrations (exceeding the  $MPC_D$ ) at the Podolsk–Myachkovo aquifer (Information, 2020).

However, in the Moskva River, water concentrations of Sr, Li, B, Mo, and Ca were lower than all MPC values (Fig. 5), except for Sr (maximum  $CF_{max} = 7$ ) and B (3) in the Medvenka, Gzhelka, and Setun rivers, and B in the Medvenka and Chachenka ( $CF_{max} = 2-3$ ) river mouths when compared with fishery guidelines ( $MPC_F$ ). High concentrations of TDP and Ca in the Medvenka River could also be explained by the lithologic factor.

Rather, high concentrations of Li and Sr, determined in urban soils of Warsaw (Poland), can migrate during podzolization processes (Kabata-Pendias & Pendias, 2001) and therefore reach river water, which may take place in Moscow. A high content of Sb was previously found in Moscow soils, especially in industrial zones where its mobility is significantly higher than in natural soils (Kosheleva et al., 2015). This supports our findings for soils (Factor 1,  $FL_{Sb} = 0.33$ ), sewage sludge and road runoff (Factor 2,  $FL_{Sb} = 0.69$ ), and several industrial zones (Factor 4,  $FL_{Sb} = 0.44$ ) in Moskva River water.

*Urban sources: sewage and road runoff* Distribution of TDN, TDP, Sb, Ni,  $N-NO_2$ , and to some extent  $BOD_5$ , COD, V, Zn is defined by the second factor, which explains 16% of the pollutant variance. These elements are sensitive to specific conductance ( $r = 0.53-0.61$ , except for Ni and  $N-NO_2$  with  $r = 0.2-0.4$ ) and the dissolved



oxygen ( $r = -0.3$  to  $-0.45$  for main elements) content in river water. A significant excess of Sb was detected downstream from the Moskva River, in the Pakhra and Pekhorka rivers. Maximum values were discovered at the sampling point downstream from the Lyubertsy WWTP during all hydrological seasons.

In Moscow, Sb and Zn originate mostly from vehicle emissions and are reported to be the main pollutants of road dust (Kasimov et al., 2020a; Vlasov et al., 2021a), soils (Kosheleva & Nikiforova, 2016; Kosheleva et al., 2014, 2015), snow (Vlasov et al., 2020), and even rain water (Vlasov et al., 2021b), which could also participate in soil erosion and road dust washout during heavy rains. As a result, rainwater ensures the supply of these elements to the Moskva River through the city sewage system. The same is true for snowmelt water. In Koriyama City (Fukushima Prefecture, Japan), the origin of Sb in sewage water has also been reported to be found in brake dust (Ozaki et al., 2021). A high content of metals (e.g., Sb) in sediments from the Pakhra River (Yanin, 2002) is associated with sewage from Podolsk city. Tire abrasion is a well-known source of Zn in urban environments (Alves et al., 2020). Zn was reported to be among the main pollutants of road runoff around the world: Italy (Mangani et al., 2005), Queensland (Drapper et al., 2000), and Augsburg, Germany (Hilliges et al., 2017).

COD and BOD<sub>5</sub> parameters were used to identify the main source of elements associated with sewage in the Yamuna River, India (Kumar et al., 2014). A combination of increased TDN, TDP, COD, and BOD<sub>5</sub> with lowered dissolved oxygen is typical for treated municipal sewage with similar concentrations occurring in other effluents of treated wastewater of the world (Carey & Migliaccio, 2009; Ritter et al., 2002). N–NO<sub>2</sub> is more distinguished in the second factor than ammonia nitrogen due to its very low background concentration, variability, and changeability. N–NO<sub>2</sub> is not only directly supplied with treated water, but is also continuously generated downstream as it transforms from N–NH<sub>4</sub> to N–NO<sub>3</sub> during the nitrification process in oxygen-rich river water, so ratios of nitrogen forms in wastewater and at different points downstream can differ significantly (Zhao et al., 2020), and any form of nitrogen in wastewater may contribute to nitrite pollution at lower sections of the river.

Ni and Zn are also often found in urban wastewater (Singare et al., 2011; Singh et al., 2017). However, another source could be fuel combustion (Purushothaman & Chakrapani, 2007). Thus, Sb, Zn, and Ni could further migrate into the river as a part of road runoff and sewage water. Factor 2 has negative FS ( $-0.5$ ) for Ba which has a weak correlation with water pH. In natural aquatic systems, concentrations of Ba depend on aquifer lithologies and the physicochemical conditions of the water: dissolved Ba<sup>2+</sup> in water decreases as SO<sub>4</sub><sup>2-</sup> increases (Kravchenko et al., 2014).

Only Zn was found in excess over MPC<sub>F</sub> (three–five-fold) (Fig. 5) at sampling stations in the Moskva main channel in Krasnogorsk and downstream from the Pekhorka River.

*Swampy Moskva source area* The third factor (explains 12.2% of total variance) guides the distribution of Al, COD, Zr and to a lesser extent Bi, Mn, and Ni. The highest factor scores (up to 9.3) were found in the Moskva River source. The main elements (Al, Zr, and COD) have a strong negative correlation ( $r = -0.55$  to  $-0.74$ ) with the pH, with minimum values of 5.2–5.5

being measured exactly. Zr was revealed to be in excess of world average values (KK up to 3.3) and for Al (CF up to 15), both in the Moskva source area. High COD values are typical for acidic peatlands and bogs (Rathgeb et al., 2017). It was shown that organic acids enhance the dissolution of minerals such as kaolinite, goethite, and zircon and favor the transport of Al, Fe, Ti, Zr, and rare earth elements by chemical complexation (Oliva et al., 1999). Kaolinite was found in technogenic silts of the Pakhra River in Podolsk (Yanin, 2019) and zircon was present in the bed sediments of the Pakhra River (Yanin, 2018), proving the presence of these minerals within the Moskva Basin. A large deposit of sand and gravel material is being developed near the source area of the Moskva River—the Drovinskoe deposit. Thus, these elements, leached from carbonate rocks in the Moskva source area, could be transported with organo-mineral colloids in river water originating from soils of marshy areas.

*Groundwater and landfills leachate* The fourth factor is responsible for the 9.4% of total variance and drives the distribution of V and As and to a lesser extent Pb, U, and Sb (Table 6). The main elements of this association had a strong positive correlation with water temperature and a moderate negative correlation with DO concentrations, which indicates the considerable influence that hydrological seasonality has on the distribution of these PTEs. Thus, positive factor scores for these PTEs were revealed for summer low water seasons (August of 2019 and 2020) and negative factor scores for spring sampling campaigns (April, 2019 and March, 2020) when water temperature is rather low, and snowmelt provides a large share of water to the rivers. Calculated values of runoff of infiltration origin for the Moskva Basin highlighted the predominance of such a runoff for the winter-spring period (Koronkevich & Mel'nik, 2015), which also provides a larger share of groundwater supply between summer and autumn. Moreover, it was reported that the chemical pollutants that enter the aquifer usually discharge into the water body during the summer and winter low water seasons, but not in the period of snow melting and heavy rains (Yasinskii et al., 2019). Another element that could be associated with this factor is Pb (FS = 0.46, Table 6), which was also found in groundwater at the base of the landfill in Moscow (Shimko et al., 2018).

Maximum FS values for this factor were detected in the Setun (August, 2019), Kolomenka (both warm seasons), and Pakhra (August, 2020) rivers and in the Moskva River downstream from Voskresensk Town (both warm seasons). V and As, however, showed a rather low variance across the Moskva Basin. Although V and As concentrations did not exceed background values, an excess over world average concentrations were calculated for As (KK = 2.3–3.0, Fig. 3).

Significant concentrations of As were found in the landfill leachate in France (Pinel-Raffaitin et al., 2006). Soluble forms of As are known to follow soil-related pathways via runoff and leaching (Slimak & Delos, 1983; Wang & Mulligan, 2006). Thus, As could reach groundwater during the warm season when runoff from landfills can enter groundwater through thawed soils.

High concentrations of V (CF = 2 in comparison with MPC<sub>F</sub> guidelines) were detected in the Moskva main channel downstream from Voskresensk Town and its mouth, as well as in the Setun and Pakhra rivers. No other elements were found to be in excess.

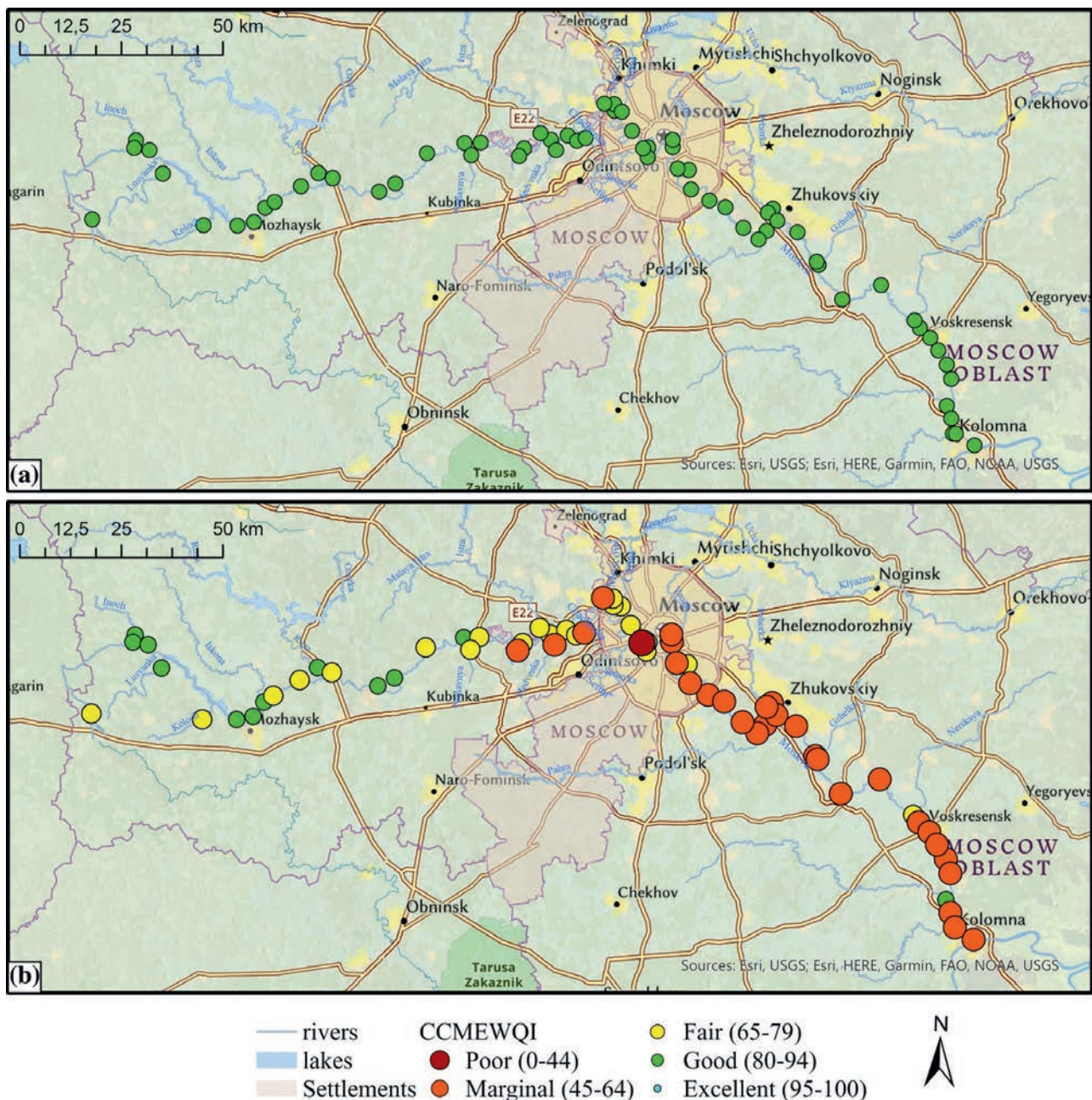


Fig. 6. CCME Water Quality Index calculated relative to Russian (a) drinking water  $MPC_D$  and (b) fisheries  $MPC_F$  standards

*Industrial zones (Krasnogorsk and Setun mouth area)* The fifth factor, responsible for changes in Zn and Cu concentrations, did not correlate with water properties and had great variability in concentrations across the basin due to several extra values: highest Cu and Zn content found in the Moskva River upstream area ( $KK-Zn = 53$ ,  $Kc-Zn = 6.4$ ), in Krasnogorsk ( $KK-Cu = 41.2$ ,  $Kc-Cu = 76.3$ ;  $KK-Zn = 98.3$ ,  $Kc-Zn = 11.8$ ), downstream Pekhorka River ( $KK-Zn = 56.7$ ,  $Kc-Zn = 6.8$ ), the Nerskaya ( $KK-Cu = 14.2$ ,  $Kc-Cu = 26.3$ ), and the Setun ( $KK-Cu = 2.5$ ,  $Kc-Cu = 4.6$ ;  $KK-Zn = 20.2$ ,  $Kc-Zn = 2.4$ ) rivers. This factor is responsible only for 6.5% of total variance. The highest factor scores for this association of PTEs were revealed also in Krasnogorsk (FS = 10.0, August, 2020), the Moskva, upstream from the Inoch (FS = 5.0, August, 2019), downstream Vyazemka (FS = 2.5, August, 2020), Pekhorka (FS = 4.5, March, 2020), and in the mouths of the Setun (FS = 1.9, March, 2020) and Yauza rivers. The main areas affected being

industrial zones in Krasnogorsk. Zn and Cu concentrations exceeded water quality guidelines ( $MPC_F$ ) only in the Moskva River in Krasnogorsk (CF = 6 and 61, respectively). Thus, showing that the main area affected by Factor 5 is the Moskva River in Krasnogorsk and downstream from the Pekhorka River, and the Setun mouth, all areas with high anthropogenic loads. It was reported that the main volume of wastewater and pollutants in the Setun Basin is discharged through the city drainage network of the State Unitary Enterprise "Mosvodostok" and accounts for more than 90% of the total wastewater discharge (Resolution, 2003). Cu and Zn were also revealed as the main soil pollutants around the Setun mouth area (Bashkin et al., 2004).

### River water quality

In order to carry out an integrated assessment of water pollution in the Moskva River and its tributaries, and its repeatability throughout the year the CCME WQI in-



dex distribution across the basin was analyzed. CCME WQI was calculated relative to each of the considered water quality standards (Fig. 6; Appendix, Fig. 8). Results showed that the river water quality in the Moskva Basin deteriorates upstream to downstream no matter which guidelines are used. However, at most sampling points the water quality rates as good (16.9–100.0% of sampling stations depending on the guidelines used for comparison).

If the  $MPC_F$  was used as a water quality objective, the worst water quality (CCME WQI < 45) was detected in the Setun River mouth (Fig. 6b). Regions with marginal water quality (46.2% of stations) included a wide range of sampling stations: the swampy Moskva source area, the Moskva River in Krasnogorsk, downstream from the Yauza River, as well as at the mouths of the Vyazemka, Medvenka, Chachenka, Yauza, Pakhra, Pekhorka, and Gzhelka rivers. Fair water quality was discovered upstream from the Moskva River where it joins the Iskona River to the confluence with the Setun River, and in the Nakhavnaya river mouth. Good water quality was detected in the Moskva River part where it flows into the Iskona River up to the Tuchkovo settlement, and at the Severka and Kolomenka river mouths (Fig. 6).

According to the CCME WQI calculated in regard to WHO water quality guidelines ( $MPC_W$ , Appendix, Fig. 8a), Russian drinking water quality standards ( $MPC_D$ , Fig. 7a) and United States EPA objectives ( $MPC_{USA}$ , Appendix, Fig. 8b), the Moskva River water could be classified mostly as good (96.9–100% all stations). Using the  $MPC_D$  as a reference, the Moskva source area was deemed fair (CCME WQI = 77). However, using the  $MPC_{USA}$ , the Moskva River was marginal (CCME WQI = 62) and the Setun mouth fair (CCME WQI = 79).

Thus, taking into account temporal variations in pollutant concentrations in the Moskva River and its tributaries, the level of water pollution for most sampling stations remained at a “good” level. However, if stricter guidelines such as those of the Russian Federation guidelines for fisheries ( $MPC_F$ ) were used, this would significantly reduce the CCME WQI to marginal or even poor. The most polluted areas of the Moskva Basin are the Moskva source area and the Setun River mouth.

## CONCLUSIONS

This research proved that contaminated areas of the Moskva River Basin are mostly confined to its middle and lower reaches. Several tributaries also contribute significantly to the contamination of the Moscow River at their confluences. Small tributaries often have more extreme pollutant concentrations than the main river and noticeably complicate the longitudinal changes in the Moskva River’s water chemistry.

The main pollutants of the Moskva River and its tributaries, as shown by their comparison with various environmental guidelines and the average composition of world river water, are Mn, Al, N-NO<sub>3</sub>, N-NH<sub>4</sub>, Cu, N-NO<sub>2</sub>, Sr, Zn, B, Mo, and Sb. This profile fits the specifics of the Moscow Megacity and its surroundings, with intensive residential nutrient loading and local industrial and city wastewater input, as well as reflects the local geochemistry of wetlands in the river’s source.

Five main sources of PTEs in the Moskva River Basin were identified: (1) mineral sources weathered by groundwater and river water supply Sr, Li, B, Mo, Ca (TDP, U, Sb); (2) urban sources such as sewage and road runoff are responsible for TDN, TDP, Sb, Ni, N-NO<sub>2</sub> (BOD<sub>5</sub>, COD, V, Zn) input; (3) the swampy Moskva source area provides Al, COD, Zr (Bi, Mn, Ni) input; (4) V, As (Pb, U, Sb) supply is seasonal and connected with landfill leachate, dissolution with snowmelt, and further groundwater inflow during the warm season; and (5) Zn and Cu in river water is related to the industrial zones in Krasnogorsk Town and the Setun Basin. However, mineral and urban sources have the most and almost equal contribution to total variance of pollutants (16–17%).

Water quality in the Moskva Basin in general is good (16.9–100.0% of sampling stations) according to the CCME Water Quality Index. Local deterioration of water quality is confined to a large stretch of the Moskva River starting downstream from the Kuryanovo WWTP and reaching the river’s mouth, as well as the mouths of the Setun, Medvenka, Pekhorka, Pakhra, and Gzhelka rivers.

The results of our study indicate that the main actions to improve water quality and reduce PTEs concentrations in the Moscow River Basin should be focused primarily on improving the mechanisms of treatment of domestic and road runoff in the cities of the Moscow metropolitan area.



# Rainstorms impacts on water, sediment, and trace elements loads in an urbanized catchment within Moscow city: case study of summer 2020 and 2021\*

## INTRODUCTION

The ongoing climate change is leading to complex and diverse changes in different precipitation characteristics. General estimates shows 1–2% per century growth of precipitation total amount from the middle of the twentieth century over the continents (Contractor et al. 2021); with respect to the mid-latitudes, there is a significant positive trend in mean precipitation in the Northern Hemisphere (Trenberth 2011). Moreover, the daily extreme precipitation intensity tends to increase almost everywhere over land (Donat et al. 2016), including the occurrence of heavy rain events over the Northern Eurasia (Semenov and Bengtsson 2002; Mokhov et al. 2005; Groisman et al. 2005; Zolina and Bulygina 2016; Ye et al. 2017). The contribution of heavy convective showers to the total precipitation increases with the statistically significant trend of 1–2% per decade in vast Northern Eurasia regions, reaching 5% per decade at a number of stations, is reported (Chernokulsky et al. 2019; Aleshina et al. 2021). The overall changes in the character of precipitation over the majority of Northern Eurasia regions are characterized by a redistribution of precipitation types toward more heavy showers.

Even more pronouncing effects on precipitation fields are seen under urban surface conditions (Varentsov et al. 2018). Due to specific urban climate which is characterized by deviations of the temperature and humidity from surrounding rural environment, known as urban heat island (UHI) (Lappalainen et al. 2018; 2022; Masson et al. 2020), intense precipitation amount growth, increase of turbulence mixing, and more favorable conditions for convective boundary layer uplift are typically observed. Megapolises experiences rainfall structure changes in context of short-live precipitation events intensity growth. Significant increase of extreme hourly rainfall sums is observed in Shanghai during the XX century, its frequency rose up during intense urbanization from 1981 (Liang and Ding 2017). European cities studies indicate also rainfall intensity growth (Faccini et al. 2015; Liang and Ding 2017). These effects have significant environmental and social impacts (Sokolov et al. 2020; Vlasov et al. 2020, 2021c, a; Kosheleva et al. 2022; Nikiforova et al. 2022; Popovicheva et al. 2022). In particular, urban regions are suspected to changes of the timing and magnitude of rainfall events as a result of climate change. Both with proliferation of impervious surfaces, these areas are predicted to significantly alter the flooding experienced in many urban areas of the world (Faccini et al. 2015; Liang and Ding 2017) and become extremely vulnerable to the rainstorm events. Climate change and urban water environment impacts at the global scale (Praskievicz and Chang 2009) with a particular exam-

ples from the cities of China (Liang and Ding 2017), UK (Ashley et al. 2005), cities of Europe (Faccini et al. 2015; Liang and Ding 2017).

As far as extreme rainfalls are associated with floods and increase in the amount of contaminants directly introduced into the rivers (Vlasov et al. 2021b), many cities are developing mitigation and adaptation strategies to reduce their vulnerability (Maragno et al. 2018). In this regard, Moscow city remains an exceptional example as the biggest monocentric agglomeration in Europe which has not yet developed green infrastructure (GI) areas and specifically low impact development measures. Due to this, recently large storm overflows, the overfilling of structures in stormwater networks and an increase in the number of the sewer floods have been observed here. Recent flooding across the Moscow city during the summer storms of 2020 and 2021 have highlighted the significant impacts that flooding can have on inundation of the urban areas, erosion with parks and huge sediment transport over urban rivers. In particular, the most significant events were observed during rainstorms on 29–30 May 2020 corresponding to 140% of monthly mean.

Due to lack of hydrological and hydrochemical monitoring by state and municipal agencies in Moscow, studies on flood prediction and adaptation effects are absent. To the best of our knowledge, there is no data regarding impact of extreme precipitation on timing and magnitude of floods, as well as their environmental impacts. Since 2019, Department of Hydrology of Lomonosov Moscow State University has been operating a network of gauging stations in the Setun River watershed (190 km<sup>2</sup>), which is the largest tributary of the Moskva River located entirely within the bounds of Moscow city. At these stations, autonomous stage-discharge stations are set up, supported by systematic investigations of major and trace element chemistry during flood events (Tereshina et al. 2020, 2021; Sokolov et al. 2021). Combined with the Meteorological Observatory of Moscow State University, which is located at downstream part of the Setun catchment and provides the atmospheric characteristics and specific weather conditions records including extreme precipitation since 1954 (Chubarova et al. 2011), this area presents an exceptional case to study the impact of rainstorm events on water, sediment and trace elements loads within Moscow city.

This paper summarizes a large dataset of water fluxes, dissolved and particulate element concentrations in the Setun River collected from 2019 to 2021 with a particular focus on comprehensive analyses of flow response to rainstorm-generated events that were observed in Moscow on 29–30 May 2020 and 28–29 June 2021. A high-quality data encompassing detailed flow and turbidity measurements at 3 stations along Setun River and

\* Chalov S., Platonov V., Erina O., Moreido V., Samokhin M., Sokolov D., Tereshina M., Yarinich Yu., Kasimov N. // Theoretical and Applied Climatology. 2022.

long-term precipitation records from the stations operated in Moscow region, as well as meteorological COSMO-CLM model outputs, were considered in the study to understand hydroclimatic impacts on water and sediment quality during high flow events. Specifically, we aim at statistical analyses of long-term extreme precipitation records (1); reconstructing precipitation patterns during 2020 and 2021 rainstorms over case study Setun River by COSMO-CLM model (2). Additionally, based on monitoring data we aim to assess the magnitude and the transit time of water and sediment flows during short-lived events (3) and to characterize the dynamics of particulate and dissolved element transport in response to precipitation (4). The prepared datasets allow us to show that transported elements can be classified into different groups reflecting their behavior during floods in a small urban river. We also discuss the accuracy and perspectives of the proposed hydroclimatic approach to predict extreme rainfalls and their hydrological impacts, define specific features of urban river floods compared to natural rivers, and outline possible implications for water management system development in Moscow.

## METHODS

### Moscow region precipitation data

The Moscow Region has a broad network of weather stations that provide standard precipitation measurements. However, there are only few long-term rainfall observations valuable for robust statistical estimates. We have used the original 6-hourly and daily precipitation sums from the Russian Institute of Hydrometeorological Information – World Data Center (RIHMI-WDC, <http://meteo.ru/data>) database according to the 10 stations within Moscow city and the nearest surrounding Moscow region for a 1966–2021 period, with the longest timeseries belong to Moscow State University Observatory (MSU), Balchug, Nemchinovka, Podmoskovnaya, Tushino, and VDNKh (Fig. 1). Data gaps were filled with <http://pogodaiklimat.ru/> site datasets, where it was possible and available. These stations were used for the long-term climatological estimates. Additional observational datasets were collected for specific periods of interest within the 2020 and 2021 cases (29–30 May 2020 and 28–29 June 2021) from the <http://pogodaiklimat.ru/> Web site,

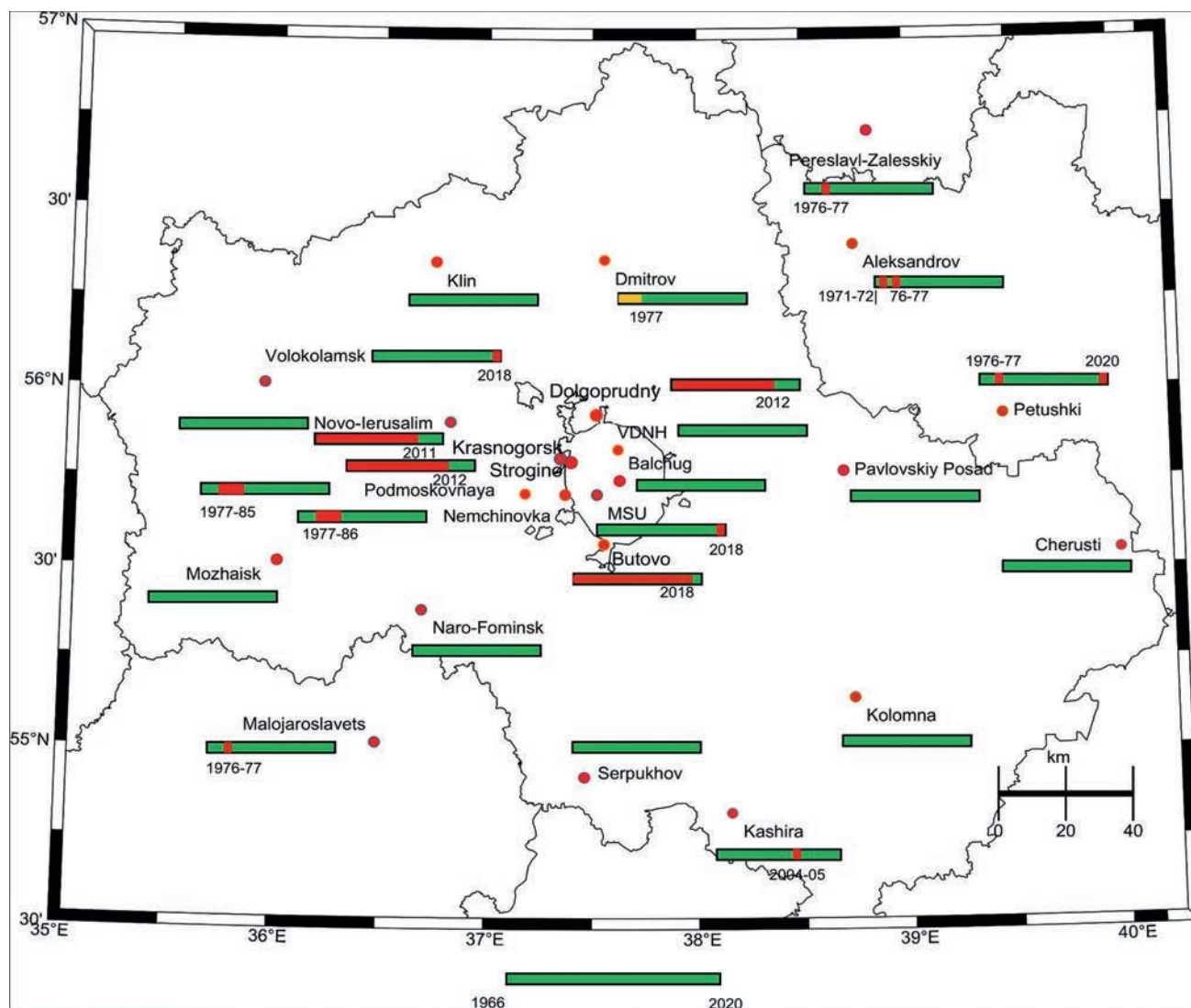


**Fig. 1.** Long-term precipitation data availability for the Moscow region. Data availability periods presented as colors: period without gaps is presented in green, gaps more than one month are presented in yellow, periods with no data are presented in red

since there are some novel station data available in Moscow region last decades and years. These data included also airport stations Domodedovo, Sheremetyevo, and Vnukovo, as well Strogino, Krasnogorsk, Dolgoprudny, and Butovo, and were used additionally for comparison with modelling results to provide reliable verification. The MSU and Nemchinovka stations are located within the Setun River basin, therefore specific attention was brought to data from these stations. Moreover, the pluviograph datasets from the MSU Observatory were digitized with 10 min time step for periods 29–30 May 2020 and 28–29 June 2021, and used for high-resolution comparison to model precipitation output data.

Long-term precipitation datasets were used to estimate extreme sums frequency, their changes for a considered period, trends estimation based on ETCCDI indices (Karl et al. 1999): Rx1day—monthly maximum 1-day precipitation; R10mm, R20mm, and R30mm—annual count of days when precipitation  $\geq 10$  mm, 20 mm and 30 mm, accordingly; PRCpTOT—annual total precipitation in wet days (i.e., days with precipitation  $\geq 1$  mm); R95pTOT and R99pTOT—annual total precipitation when daily precipitation amount  $> 95$  and  $> 99$  percentiles of precipitation on wet days, accordingly. Daily extreme precipitation sums are crucial for short-term flooding cases, especially in urban conditions (Yang et al. 2013; Zhou et al. 2017). Trends were estimated according to the t- and F-tests on the 5% significance level.

### COSMO-CLM (CCLM) model setup

The COSMO-CLM (CCLM) model (ver. 5.12) was used for atmospheric simulations. CCLM is the climate version of the non-hydrostatic mesoscale atmospheric COSMO model, including various modifications and extensions adapted to the long-term numerical experiments. It was developed by the German Weather Service (DWD) and CLM-Community (Rockel et al. 2008). The model equations are solved on the rotational Arakawa C-grid (Arakawa and Lamb 1977) in latitude–longitude ( $\phi$ ,  $\lambda$ ) coordinates with a pole tilt to minimize the issue of longitude convergence at the pole. The height coordinate is the terrain-following hybrid Gal-Chen coordinate ( $\sigma$ -z system) (Gal-Chen and Somerville 1975; Schär et al. 2002).

The standard configuration of the CCLM model includes the Runge–Kutta integration scheme with the fifth advection order. There is an option to apply the spectral

nudging technique (Schubert-Frisius et al. 2017). The Ritter and Geleyn radiation scheme (Ritter and Geleyn 1992) is based on the two-stream version of the radiation transfer equation. The moist and shallow convection is parametrized using Tiedtke mass-flux schemes with equilibrium closure based on moisture convergence (Tiedtke 1989). Turbulence is described by a prognostic turbulence kinetic energy (TKE) based scheme, with a 2.5-order closure (Herzog et al. 2002). A full description of the COSMO model physics, dynamics, and parameterizations is available elsewhere (<http://www.cosmo-model.org/content/model/documentation/core/default.htm>).

For the land grid cells, the TERRA (Schulz and Vogel 2020) surface active layer model is used. An important part of the COSMO-CLM model v.5.12 and the reason of its use in this work is the TERRA-URB urban canopy parameterization (Wouters et al. 2015, 2016; Varentsov et al. 2020) allowing to take into account canopy layer energy exchanges between atmosphere and surface and subsurface in detail, to reproduce meso- and microscale dynamics caused by urban canopy impact correctly. These processes consideration reflects the extreme precipitation formation in urban conditions (Varentsov et al. 2018). Since the TERRA-URB urban canopy model was developed taking into account impervious water storage based on a density distribution of water puddles (Wouters et al. 2015), it is well suitable for urban hydrology tasks. Therefore, it is crucial to use the last version of the TERRA-URB parameterization to simulate extreme precipitation cases in Moscow city successfully. The TERRA-URB requires an additional external parameters information about urban surface properties within each modelling domain. This information includes impervious area fraction, anthropogenic heat flux, building fraction and height, canyon height-to-width ratio, facet-level albedo, emissivity, heat capacity, and conductivity data. More detailed information about these data source availability, usability and verification provided in (Varentsov et al. 2020).

Model experiments used the standard nested domains scheme including base and inner domains. ERA5 (Hersbach et al. 2020) global reanalysis data ( $0.25^\circ$ ,  $\sim 30$  km) used as driving conditions for the base domain with grid size  $0.027^\circ$  ( $\sim 3$  km) and 500 grid cells in both directions, covering the most area of the East European Plain. The base domain output data used as driving conditions for inner domain simulations with  $0.009^\circ$  ( $\sim 1$  km) grid size focused on the Moscow region only (Fig. 2). Base domain

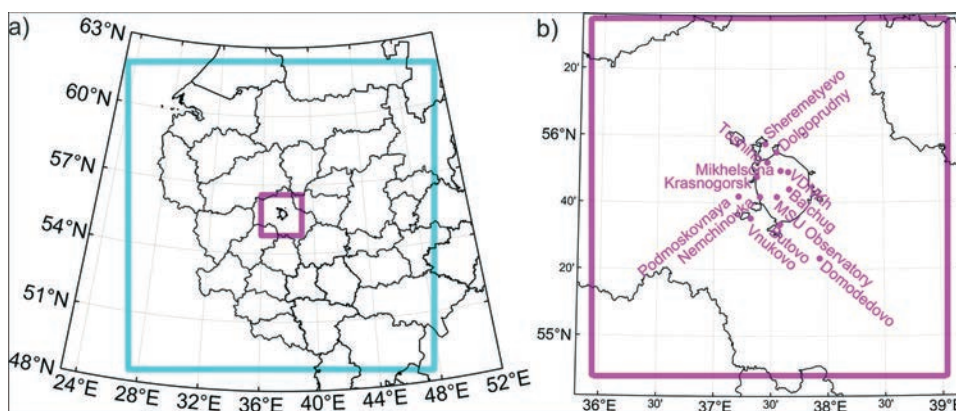


**Fig. 2.** COSMO-CLM model domains used for numerical experiments: large/base domain (in cyan) with  $\sim 3$  km grid size (a); nested domain (in magenta) with  $\sim 1$  km grid size and location of meteorological stations used in the study with precipitation data available during the considered 2020 and 2021 events (b)



experiments were simulated with 40 s time step, whereas inner domain experiments simulated with 10 s time step. Model used 50 vertical levels; no spectral nudging was applied. COSMO-CLM ~ 1 km grid cells getting inside the Setun River basin contour, 190 grid cells in total.

COSMO-CLM experiments were run using the Lomonosov Moscow State University High Performance Computing Center “Lomonosov-2” (Voevodin et al. 2019) resources. Two model experiments were conducted for periods 28.05–02.06.2020 and 27.06–03.07.2021 corresponding to considered 2020 and 2021 summer floods: 29–30.05.2020 and 28–29.06.2021, accordingly. Aims of these experiments were to estimate model capability to reproduce heavy rainfalls in Moscow region during cited periods, to get relevant input data for high-resolution runoff simulations by hydrological model, and to reveal opportunities to tune model parameters for further experiments and other case studies. The model output step was 15 min containing 15-min precipitation sums at each grid cell during the whole experiments period.

The model outputs were summarized over 1 h, 3 h, and 1 day. The 15-min and 1-h model precipitation amounts were compared with 10-min and 1-h summarized pluviogram values for MSU Observatory station; 3-hourly and daily precipitation sums by model compared with standard precipitation measurements according to data and stations listed in Sect. 1. In all cases, we have calculated errors as differences between model and observed values and common verification statistics: mean error, RMSE and correlation between samples.

## Hydrological monitoring

Since November 2019, three monitoring stations for discharge, sediment transport, and water and sediment quality were installed in the downstream reach of the Setun River (Fig. 3). Water stage was recorded with the Onset Hobo pressure sensors corrected for barometric pressure with 30-min interval and discharge was measured using the float method at all stages on the monthly basis. Sensors were installed in a stilling well fixed to the stream bank at a stable location. At very low stages, the discharge was measured with conventional impeller current meters and at high stages we used the Sontek River-Surveyor M9 acoustic doppler current profiler (ADCP). Based on discharge measurements data for each of the stations stage-discharge relationships  $Q = f(H)$  were assessed (Table 1). These were further used to recalculate streamflow discharges with 30-min frequency. Integrated gauged water discharges for S-1 and S-3 are presented in Online Resource 1.

## Water quality monitoring datasets

Water samples were collected about 20 cm below the surface, manually from the bank since November 2019 at the downstream station S-3 (Fig. 3). Relatively narrow river channel induces high water velocities (up to 1 m/s) and enhanced turbulence that ensures efficient homogenization of the suspended and dissolved matter across the section. Sampling was performed approximately once a month during the base flow periods. During the spring flood and

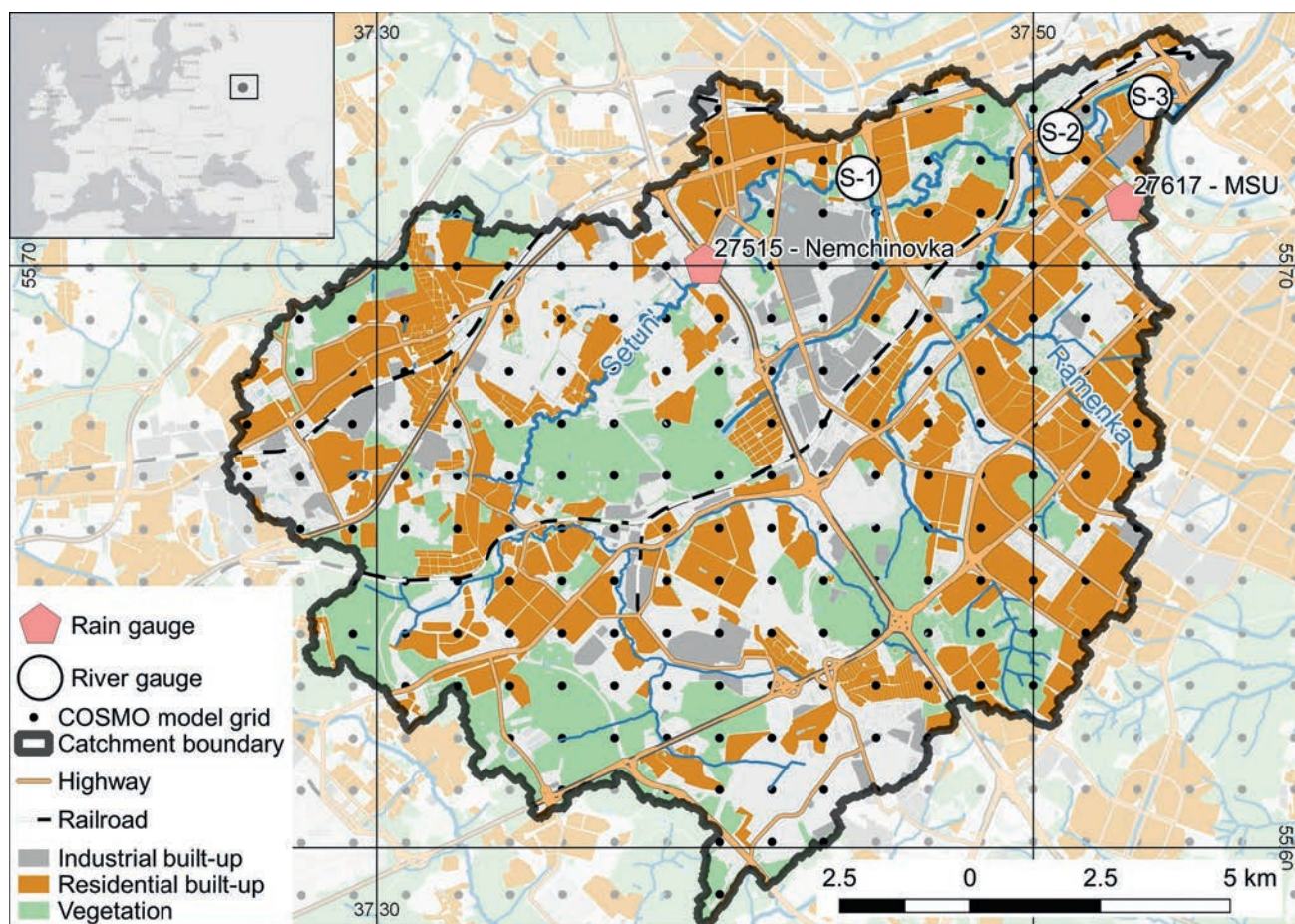


**Fig. 3.** Case study Setun River catchment and location of hydrological gauges S-1, S-2, S-3, and COSMO model 1-km grid size domain

**Table 1.** Stage-discharge relationships for the Setun River gauges

Gauge	Coordinates	Q = f(H) relationship <sup>a</sup>	Range of elevation, m abs	Catchment area, km <sup>2</sup>
S-1	55° 42' 51.4543" N 37° 26' 41.2004" E	$Q = 3.23 \cdot (H - 131.8)^3 - 4.62 \cdot (H - 131.8)^2 + 7.12 \cdot (H - 131.8) - 1.39$	132.0 – 134.5	115
S-2	55° 43' 21.3840" N 37° 30' 20.9602" E	$Q = 4.68 \cdot (H - 124.7)^2 - 0.91 \cdot (H - 124.7) + 0.44$	124.7 – 128.6	182
S-3	55° 43' 47.2894" N 37° 31' 46.1836" E	$Q = 1.33 \cdot (H - 122.5)^3 + 1.73 \cdot (H - 122.5)^2 - 0.53 \cdot (H - 122.5) + 0.12$	122.6 – 124.9	186

<sup>a</sup>H water level elevation (m abs)

summer flash flood monitoring frequency increased from monthly to daily. In particular, during 2021 spring freshet and summer rain floods, additional sampling was done. One week before the start of the spring flood (March 19) and 5 days before the start of the flash flood (June 23), samples were taken on the daily basis. In total, more than 50 water samples were collected from the Setun River in 2021; 25 of which were taken during the spring flood and flash rain flood. The freshet datasets were used to compare the effects in water quality driven by rainstorms and snow melting processes on the watershed.

Water temperature, pH, dissolved oxygen (DO) concentrations, and specific conductivity (at 25 °C) were measured in situ by YSI ProSolo, YSI ProODO and YSI Pro30 probes (Yellow Springs, Ohio, USA) at every sampling station. River water samples were taken in PET 5L bottles. Samples of river water were filtered through pre-weighed membrane 0.45 µm filters using a Millipore Vacuum pump station. The filters with suspended particulate matter (SPM) were weighed to determine SPM concentration. Two aliquots of 30 ml of filtered water were collected for cations and trace elements analysis. Processing of samples were carried out at the Krasnovidovo scientific laboratory of Lomonosov Moscow State University.

The amount of easily oxidized organic substances was assessed in unfiltered samples via the five-day biochemical oxygen demand (BOD<sub>5</sub>) using the iodometric method. Total organic matter concentration estimated via indirect parameter of chemical oxygen demand (COD) using the dichromate method. The content of total (TN) and total dissolved nitrogen (TDN), total (TP) and total dissolved phosphorus (TDP), total inorganic (TIP) and dissolved inorganic (DIP) phosphorus, and nitrite nitrogen (N-NO<sub>2</sub>) was determined in filtered and unfiltered samples on a single-beam photometer using standard methods: the Murphy-Riley method for TP, TDP, TIP, and DIP; alkaline persulfate digestion for TN and TDN; and Griess reaction for N-NO<sub>2</sub>. Concentrations of nitrate and ammonia nitrogen (N-NO<sub>3</sub> and N-NH<sub>4</sub>), as well as major ions (Ca<sup>2+</sup>, Mg<sup>2+</sup>, Na<sup>+</sup>, K<sup>+</sup>, SO<sub>4</sub><sup>2-</sup>, Cl<sup>-</sup>), were determined via ion chromatography on Concise IC Sep An2 (USA) and Shodex IC YS-50 columns (Japan). HCO<sub>3</sub><sup>-</sup> and CO<sub>3</sub><sup>2-</sup> concentrations were determined by titration with hydrochloric acid. The filter with accumulated suspended matter was weighed after filtration to calculate the suspended sediment concentration (SSC) in river waters (mg/L).

Dissolved (filtered water, < 0.45 µm) concentrations of Li, B, Al, Ca, V, Mn, Ni, Cu, Zn, As, Sr, Zr, Mo, Sb, Ba, Pb, Bi, U were determined using the ICP-MS and ICP-AES methods (Elan-6100 and Optima-4300, Perkin Elmer, Waltham, MA, USA) at the All-Russian Scientific Research Institute of Mineral Raw Materials named

after N.M. Fedorovsky in Moscow in accordance with the European Communities Environmental Objectives (Surface Waters) Regulations, S.I. no. 272/2009 (2009), and ISO standards 5667-3 (2018). This laboratory is accredited by the international analytical system accreditation (AAC.A.0025) and the national accreditation system (RA.RU.21ГП11), The analysis was performed using blank samples and standard materials, "Trace metals in Drinking Water (TMDW)" (High-Purity Standards, USA). The detection limits (DLs) were as follows (µg/L): Li 0.004; B 0.04; Al 0.78; Ca 4; V 0.2; Mn 0.079; Ni 0.05; Cu 0.1; Zn 0.2; As 0.06; Sr 0.028; Zr 0.0046; Mo 0.017; Sb 0.005; Ba 0.02; Pb 0.01; Bi 0.00053; U 0.00079. For low concentrations of MMs (< 5 DL), the relative standard deviation did not exceed 20%; for higher concentrations of MMs (> 5 DL), the relative standard deviation did not exceed 10%.

Dissolved and particulate major and trace element concentrations and water discharges in the water samples of Setun River are listed in Online Resource 2 which includes dynamics of chemical parameters of the Setun River during the summer storm flood of 2021, as well as the river's chemical profile below and after the flood.

## RESULTS

### Precipitation patterns

The long-term statistical analysis of daily precipitation over Moscow region indicated extreme values up to 70 to 80 mm during the twentieth century; however, values above 80 and 100 mm appeared 5 times since 2000–2002 (Fig. 4). Positive linear trends are insignificant over all stations on the 5% level with the exception of the Nemchinovka station located at the upstream of case study Setun River catchment. Here, the only significant positive trend has been observed. Therefore, most of the changes in daily precipitation maxima are insignificant with significant exception for 1 station within the Setun River basin.

Case study Setun River catchment stations (MSU and Nemchinovka) show similar extreme daily precipitation indices and patterns. R95TOT at MSU Observatory (Fig. 5) is comparable with daily maxima below 300 mm until 2010. At the same time, in 2013 and after there are values more than 400 mm, and R95TOT values are near 300 mm during 3 years. R99TOT has more striking variability and outliers (in 1973, 2004, 2020), which are larger at Nemchinovka (200–250 mm) than at MSU Observatory (near 200 mm). Both indices at both stations shows positive linear trends, which are significant for R95TOT at Nemchinovka at 5% significance level and for R99TOT at MSU Observatory at 15% level only.

Significant changes were not detected at the MSU Observatory by the R10mm, R20mm, R30mm indices



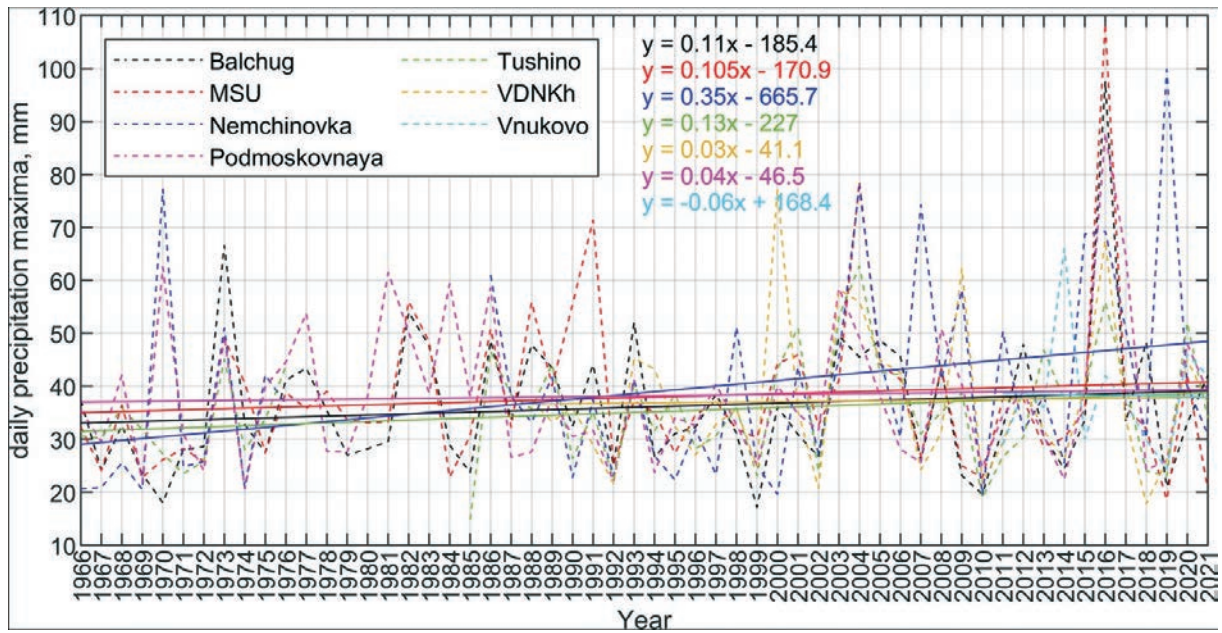


Fig. 4. Timeseries of yearly maxima of daily precipitation maxima (mm) according to 7 Moscow weather stations data having the longest period of records

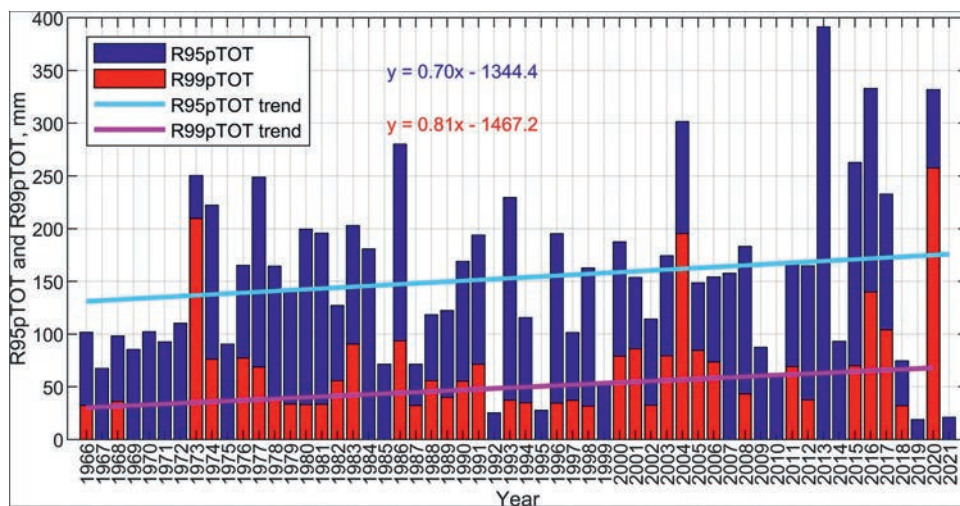


Fig. 5. R95TOT and R99TOT values (mm) and its trends according to the MSU Observatory weather station

(Fig. 6). R10mm reaches 20–25 days maxima at MSU Observatory, up to 30 days after 1996. Maximums are distributed more uniform at MSU Observatory, with more outliers at Nemchinovka, where the number of R20mm values more than 5 days increases after mid-1990s. R30mm values demonstrates more variability at MSU Observatory than at Nemchinovka (up to 3–5 days); however, there are no significant trends in this index at both stations. All indices at both stations shows positive trend, except of MSU Observatory R10mm, where an insignificant negative trend is observed. There are only significant positive trends in R10mm and R20mm at Nemchinovka at 5% significance level.

These long-term changing conditions underlie the formation of extreme floods observed on 29–30.05.2020 and 28–29.06.2021 in Moscow. The estimated corresponding daily sums percentiles and the corresponding 100-year days frequencies (Table 2) show extreme character of the observed patterns. Considered stations demonstrated the daily sums over 99% percentile during 29–31.05.2020

and 27–28.06.2021. Moreover, the corresponding number of days with such amounts reached just no more than 100 days, i.e., the recurrence of such events is less than once per year.

In May 2020, the low moved from the Black Sea area leading to the warm front passage in Moscow region. Large-scale precipitation enhanced by some meso-scale squall lines formed in warm and moist air mass. Moreover, warm front during this period was transformed into the occlusion front and intensified at evening and night times (Online Resource 3).

COSMO-CLM model showed two main rainfall periods on 29 and 31 May (see Fig. 8), the latter case is prevailing by intensity and modelled precipitation sums. Precipitation maxima differed significantly by extreme values (from 2 to 10 mm per 15 min) and time. The first maximum was observed on 29 May 2020 at the morning and early afternoon times (from 00 to 15 h UTC, local time is UTC + 3 h), with short extreme values in early morning near Podmoskovnaya, Vnukovo and Krasnogorsk, i.e.,



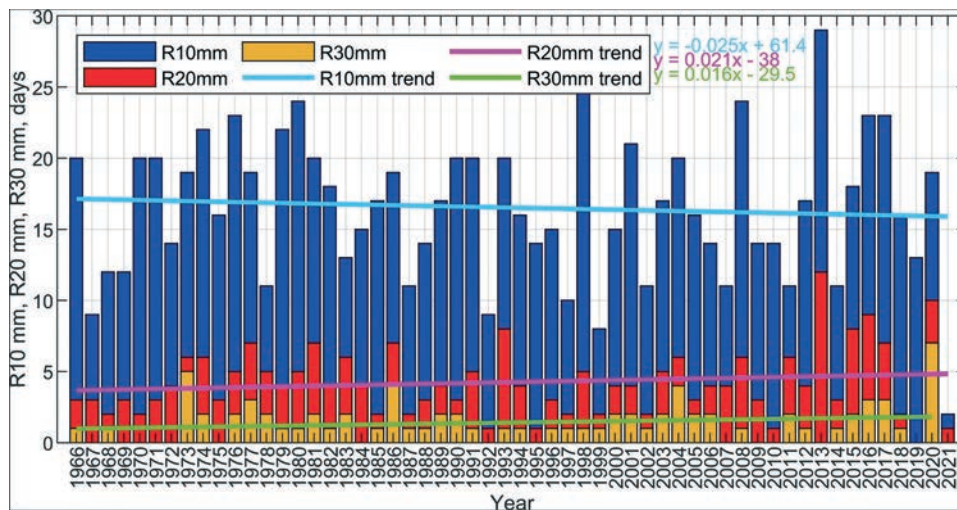


Fig. 6. R10mm, R20mm, and R30mm values (days) and its trends according to the MSU Observatory weather station

Table 2. Daily precipitation sums, percentiles and the corresponding number of days per 100 years at the Moscow region stations for 27–29.05.2020 and 27–29.06.2021 periods

Station	Daily precipitation sum, mm/percentile, %/number of days per 100 years				
	29.05.2020	30.05.2020	31.05.2020	27/28.06.2021	28/29.06.2021
Balchug	32/99.75/89	20/98.91/397	33/99.79/75	19/98.75/456	0/50.70/17982
MSU Observatory	38.7/99.86/51	31.7/99.68/114	32.5/99.71/103	-	-
Nemchinovka	23/99.28/218	36/99.77/68	32/99.69/93	22/99.24/233	0.8/67.76/9870
Podmoskovnaya	52/99.98/5	34.3/99.78/68	41/99.91/27	11/96.67/1042	0.6/65.18/10885
Tushino	41.5/99.90/35	26.4/99.50/180	34/99.77/83	33/99.73/97	37/99.83/59
VDNKh	38/99.82/64	23/99.23/277	34/99.76/86	20/98.93/388	0.4/59.42/14739

on the west–north–west edge of Moscow region, without significant and continuous maxima over the Setun River basin. The second simulated maximums on 30–31 May 2020 were much more intense and long-lasting (up to 2 or 3 maximums during the whole day).

However, the main rainfall meso-gamma squall-line rainfall system crossed the Setun River basin in the late evening–night (Online Resource 4, a–c) on 30 May from 22.00 to 23.30 UTC from the south to the north. The second rainfall maximum was observed on 31 May from 2.00 to 3.30 UTC which reached smaller values (2–3 mm per 15 min) and concerned less subcatchments over the east and south–west of the basin. The following rainfalls during the 31 May contributed to 3–4 mm per 15 min.

During the end of June 2021 cyclone was formed over the West regions of Russian plain within the low-gradient pressure field, intensified after anticyclonic blocking termination and moved to the Central part of Russian plain leading to enhanced mesoscale convection and squall lines (Online Resource 3) (Alekseeva et al. 2022). COSMO-CLM simulation results indicated three rainfall events on 27, 28 and 30 June with the main maxima on 28 June. The latter event was short-lived (from 13.00 to 16.30 UTC) as compared with the 2020 case. On the contrary, the 2021 rainfall was more intense including grids within area of interest – the Setun basin and developed during the late afternoon time. Maximal intensities reached 7.5 mm per 15 min at Nemchinovka and 11 mm at Vnukovo, there are the largest values among other considered grids. Spatial structure of this rainfall event

(Online Resource 4, d–f) model simulated two main precipitation intensity cores crossing the top parts of the Setun River subcatchments during a little more than a half of an hour with maximal intensities exceeding 15 and 20 mm per 15 min. Perhaps, these values and movement of rainfall core contributed significantly to the following flooding.

### Streamflow patterns

The event record on 27–29 June 2021 seen from the two weather stations (Table 2) data alongside the streamflow time-series shows an insight on how the rainstorm propagated over the catchment. The rain gauges are located in the central (27,515 – Nemchinovka), controlling the rainfall over the Setun headwaters, and eastern (27,617 – MSU) parts of the catchment, which is mainly covered by the Ramenka River–Setun's right tributary (Fig. 3). The 27,515 rain gauge reported the accumulated 12-h rainfall, the 27,617 rain gauge reported rainfall accumulation at 10-min intervals.

Starting from 17:00 27.06, the 27,617 rain gauge accumulated some 13 mm of rainfall, which almost immediately resulted in a sharp flood peak on the S3 streamflow gauge, which lasted over 5 h. The localization of rainfall was mainly over the eastern part of the catchment, as no significant rainfall or water level rise can be seen at 27,515 rain gauge (Fig. 7) and S1 gauge.

The next pluvial event starting from 13:00 28.06 covered the entire Setun catchment, as both rain gauges

reported significant amount of rainfall in several hours. This resulted in a sharp flood emergence with streamflow discharges rising more than tenfold in 10 h, from 2 to 20 m<sup>3</sup>/s on S1 gauge and from around 3 to 40 m<sup>3</sup>/s on S3 gauge. This first floodwave was relatively short-lived—nearly 5 h on S3 and 11 h on S3, but it was then followed by a smaller and longer secondary wave. It lasted from 15:00 to 23:00 28.06, and can be clearly traced on both gauges, but more pronounced on S1.

### Water quality patterns

Dissolved and particulate major, nutrient and trace element concentrations show a wide range of variations. During the flood, total major cation concentrations ranged from 79 to 192 mg·L<sup>-1</sup>. Among them, Ca<sup>2+</sup> was clearly dominant, contributing to 52–58% of total cation molar mass at concentrations 45–104 mg·L<sup>-1</sup>. Na<sup>+</sup> contributed to 22–28% of molar cation mass (20–56 mg L<sup>-1</sup>), Mg<sup>2+</sup> to 15–20% (7–22 mg·L<sup>-1</sup>), K<sup>+</sup> to 2–4% (6–10 mg·L<sup>-1</sup>). Total major anion concentrations ranged from 194 to 477 mg·L<sup>-1</sup>. Among them, hydrocarbonates (HCO<sub>3</sub><sup>-</sup>) dominated with concentrations of 122–289 mg·L<sup>-1</sup> (42–53% of total molar anion mass), followed closely by chlorides (Cl<sup>-</sup>, 51–117 mg·L<sup>-1</sup>, 25–41% of total anions), while sulphates and carbonates were less dominant (SO<sub>4</sub><sup>2-</sup> 20–60 mg·L<sup>-1</sup>, CO<sub>3</sub><sup>2-</sup> 0–30 mg·L<sup>-1</sup>).

Concentration of suspended particulate matter (SPM) reached 522.9 mg·L<sup>-1</sup> at peak flow, and then declined, reaching 48.1 mg·L<sup>-1</sup> by the end of observation.

Concentration of total inorganic silicon (Si) ranged within 3.4–6.5 mg·L<sup>-1</sup>, total nitrogen (TN) – 2.3–4.4 mg L<sup>-1</sup>, total phosphorus (TP) – 0.22–0.9 mg·L<sup>-1</sup>, 57–87% of TN (2.0–3.3 mg·L<sup>-1</sup>), and 19–44% of TP (0.08–0.18 mg L<sup>-1</sup>) was presented by dissolved form. Concentration of nitrite nitrogen (N-NO<sub>2</sub>) varied between 0.099 and 0.266 mg L<sup>-1</sup>. Concentration of phosphate (DIP) ranged between 0.054 and 0.072 mg·L<sup>-1</sup>; dissolved organic phosphorus (DOP), between 0.018 and 0.122 mg·L<sup>-1</sup>; particulate inorganic phosphorus (PIP), 0.11 and 0.35 mg·L<sup>-1</sup>; particulate organic phosphorus (POP),

0 to 0.473 mg·L<sup>-1</sup>. BOD<sub>5</sub> values ranged between 2.2 and 6.3 mgO<sub>2</sub>·L<sup>-1</sup>; COD, between 20.6 and 33.4 mgO·L<sup>-1</sup> in filtered samples and 33.0–100.7 mgO·L<sup>-1</sup> in unfiltered samples.

Among trace elements, concentration of Li during the flood lied within 0.009–0.017 mg·L<sup>-1</sup>; B, 0.098–0.130 mg·L<sup>-1</sup>; Al, 0.0011–0.0220 mg·L<sup>-1</sup>; V, 0.00099–0.00190 mg·L<sup>-1</sup>; Mn, 0.001–0.180 mg·L<sup>-1</sup>; Co, 0.00016–0.00046 mg·L<sup>-1</sup>; Ni, 0.00054–0.00250 mg·L<sup>-1</sup>; Cu, 0.0018–0.0032 mg·L<sup>-1</sup>; Zn, 0.0068–0.0210 mg·L<sup>-1</sup>; As, 0.0020–0.0024 mg·L<sup>-1</sup>; Br, 0.023–0.060 mg·L<sup>-1</sup>; Sr, 0.68–1.50 mg·L<sup>-1</sup>; Zr, 0.00006–0.00015 mg·L<sup>-1</sup>; Mo, 0.0015–0.0022 mg·L<sup>-1</sup>; Sb, 0.0005–0.0015 mg·L<sup>-1</sup>; Cs, 0.0000040–0.0000066 mg·L<sup>-1</sup>; Ba, 0.043–0.058 mg·L<sup>-1</sup>; Pb, 0.0012–0.0031 mg·L<sup>-1</sup>; U, 0.00054–0.00140 mg·L<sup>-1</sup>.

For some of the elements, concentrations during the flood sometimes were below detection limit; maximum concentrations for these elements during the flood were as follows: Cr, 0.0012 mg·L<sup>-1</sup>; Cd, 0.000092 mg·L<sup>-1</sup>; Sn, 0.000032 mg·L<sup>-1</sup>; La, 0.00012 mg·L<sup>-1</sup>; Nd, 0.0000086 mg·L<sup>-1</sup>.

The concentration of Mg<sup>2+</sup> at the flood peak was 3.3 times lower than during previous low flows; SO<sub>4</sub><sup>2-</sup> was 2.7 times lower; HCO<sub>3</sub><sup>-</sup>, Ca<sup>2+</sup>, and Na<sup>+</sup> were 2–2.5 times lower; and K<sup>+</sup> was 1.4 times lower. There was a slow increase in concentrations of these ions immediately after the flood peak, and the higher the concentration of the ion itself, the longer the recovery of the initial low-flow level. Peak concentrations of HCO<sub>3</sub><sup>-</sup> and Ca<sup>2+</sup> were reached on 28 June, while the remaining ions reached their peak on the evening of 29 June. All ions returned to their previous low flow levels between 30 June and 1 July. However, due to a slight rainfall on 1 July, there was a slight decrease in their concentrations. Mineral silicon, whose concentration at the flood peak was almost two times lower than previously, and orthophosphates (1.5 times lower) followed the same patterns. The concentration of total dissolved organic matter also decreased by 1.8 (according to the COD value in the filtered sample) when the flood passed.

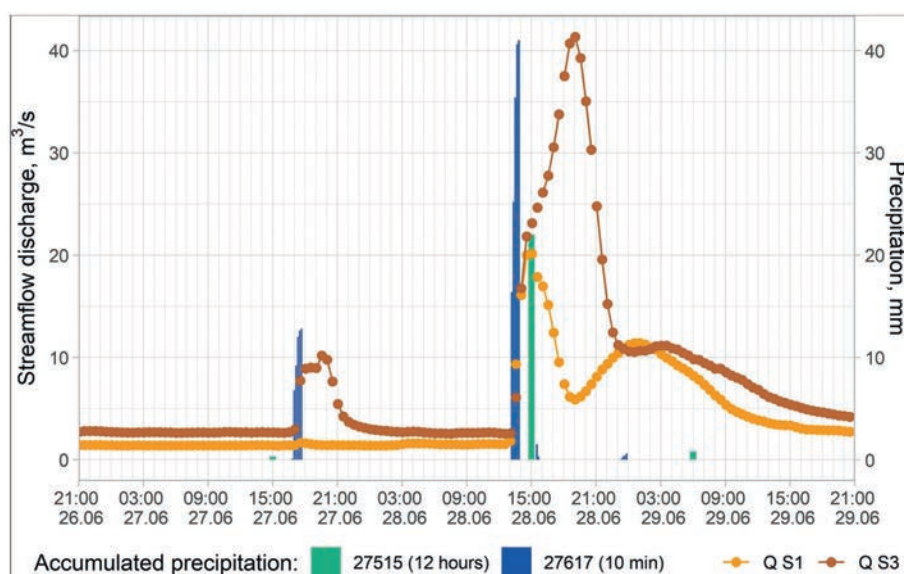


Fig. 7. Observed precipitation at two weather stations and streamflow at the two gauges during pluvial flood event on June 27–29, 2021

## DISCUSSION

### Simulation results verification and accuracy estimates

The COSMO-CLM simulations were verified according to standard approaches including timeseries comparison between stations observations and the nearest neighboring model grid point data. Timeseries compared on daily, 6-h scales for most stations cited in previous Sections and depicted on the Fig. 2. Pluviograph timeseries were compared on 10-min (observations) and 15-min (simulations) scales, as well hourly sums were calculated for both timeseries and compared. In all cases, average mean error (bias), RMSE and correlation were estimated. The simulated rainfall at the MSU Observatory station located within the Setun basin was compared with high-resolution 10-min observations using decoded and digitized pluviograph data (Online Resource 5). Despite the different time steps, we analyzed the overall precipitation intensity course according to model and measurements. The model successfully predicted first rainfall values on 29 May, but with average a half day time lag. The rainfall on 30–31 May was not captured; precipitation was reproduced during other time period and values were absolutely overestimated. At the same time, the main observed precipitation maximum on 29–30 May 2020 was not captured (5 mm per 10 min, up to 15 mm sum per 1 h). Overall verification according to these data shown just zero correlation ( $0 \dots -0.2$ ), however low biases ( $-0.15$  mm for hourly sums and  $-0.3$  for 10–15-min values) and significant RMSE (2.7 for hourly sums

and 0.88 for 10–15 min values) for both hourly sums and high-resolution intensities.

The estimates (Online Resource 5) include comparison between simulated and observed 3-h and daily precipitation sums for 2020 case. This follows the above-mentioned results including underestimating daily sums for 29. And 30. May and overestimating it for 31. May by the COSMO-CLM model. Table 4 provides verification statistics for stations data available. Although biases and RMSE are too large reaching 6–8 mm and more than 20 mm for separate stations accordingly, correlation coefficient values are satisfactory just for all stations. At the same time, comparisons on the smaller timescales (3–6 h precipitation sums, Table 3) demonstrates large biases and RMSE in addition to no correlation. These results justify the correct reproduction the large-scale factors of precipitation formation including the warm front intensification and ambient favorable conditions; however it reveals significant mismatches in meso-scale features, such as specific time and regions of squall lines formation, location, development and movement, which are subjects to improve in future investigations (Fig. 8).

The 10-min pluviograph observations at the MSU Observatory station compared with high-resolution simulation data for the nearest COSMO-CLM grid point precipitation amounts (Figs. 9 and 10). In this case model has underestimated the precipitation significantly, reproduced the first small rainfall on 27. June 2021 at 16.40–17.40 with a minimal time shift. However, the main rainfall event during 13.00–15.50 was not captured by the model absolutely. Overall verification according to these

**Table 3.** Daily precipitation sums verification statistics for 2020 and 2021 cases

Station/statistics	Daily precipitation sums 2020			Daily precipitation sums 2021		
	Bias	RMSE	Correlation	Bias	RMSE	Correlation
MSU Observatory	-0.020	24.233	0.556	-	-	-
Nemchinovka	5.333	25.102	0.619	-2.637	5.549	0.821
Podmoskovnaya	-7.354	19.950	0.625	-4.152	6.813	0.333
Balchug	-2.128	8.803	0.867	-1.264	3.398	0.998
VDNKh	-2.227	18.580	0.668	-2.922	7.360	0.386
Tushino	3.393	29.748	0.580	-9.858	16.184	0.992
Butovo	3.787	11.745	0.888	-7.064	15.535	-0.163
Sheremetyevo	-8.146	25.437	0.409	-4.829	8.108	0.723
Vnukovo	-4.097	18.580	0.633	-6.302	10.431	0.963
Domodedovo	0.929	12.913	0.082	-1.308	3.401	0.882

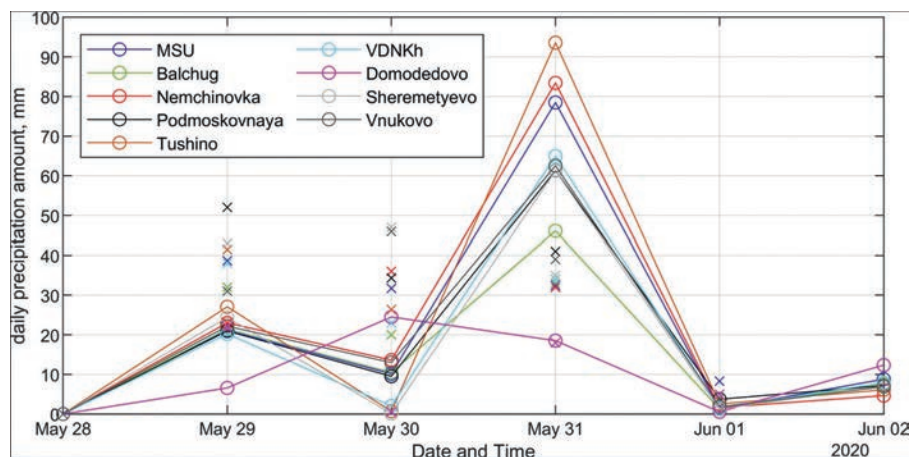


**Fig. 8.** Daily precipitation sums (mm) comparison for the 2020 COSMO-CLM model run (o) and observations (x)



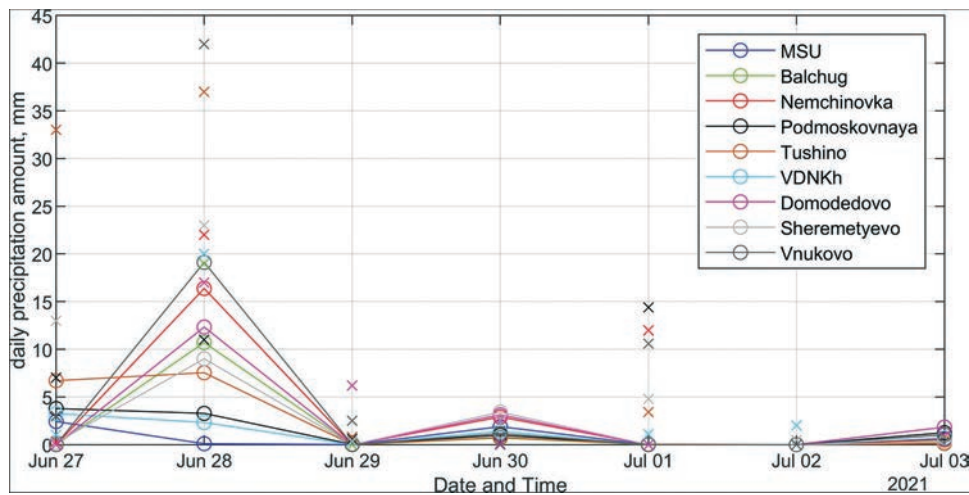


Fig. 9. Daily precipitation sums (mm) comparison for the 2021 COSMO-CLM model run (o) and observations (x)

data shown just zero correlation, however low biases ( $-0.35$  mm for hourly sums and  $-0.03$  for 10–15 min values) and significant RMSE (3.3 for hourly sums and 0.7 for 10–15 min values) for both hourly sums and high-resolution intensities. The key reason for such failed reproduction is that the main intense rainfall area shifted just few km to the west in the model (see Online Resource 4). In this way, the model has reproduced the precipitation maximum of similar intensity, but shifted on few model grids. This is an example of small-scale stochastic features impacting the model behavior and shortcomings of point-by-point comparisons for precipitation amount field, specifically.

According to daily sums comparison with simulated values (Tables 3 and 4), there are significant errors; however, RMSE is distinctly smaller than for 2020 case. Correlation coefficients are also less on average, but for some grid points are greater than 0.8 including points

corresponding to stations of specific interest Nemchinovka and Vnukovo within the Setun basin. In this case we can conclude the local conditions nearby the Setun River basin were reproduced more satisfactory compared with 2020 case, because the main rainfall events of smaller scales were observed and simulated within narrower time interval and resulted in more similar accumulated daily sums. Despite the model didn't reproduce the correct location of squall lines, it did this for the actual event of comparable intensity. At the same time, more detailed 3–6-hourly sums indicated less biases and RMSE, but poor correlation, which justifies satisfactory course of precipitation values. Therefore, the COSMO-CLM model has captured the mesoscale convective complex in general and formed squall lines correctly, but did not reproduce the time and locations of heavy rainfall events, although the one affected the Setun basin was reproduced satisfactory.



Fig. 10. Location of Setun (1) and Lusyanka (2) catchments in the Moscow region

The observed uncertainties require detailed analysis of unreproduced features and causes, as well application of the weather radar data for verification. Spatial verification methods could be useful to estimate mismatches in spatial location of extreme rainfall areas, etc. It is also important to consider the Setun River logger data and hydrological model evaluation to tune and correct the COSMO-CLM modelling workflow including the urban external parameters update, assessment of its linkage with precipitation and runoff, etc.

#### Precipitation impact of water runoff and urban conditions

We implemented statistical analyses to verify the observed impacts of extreme rainfalls on the flood events formation. Of the two events considered, the event on 28–29 June 2021 gives a much clearer insight on the propagation of the extreme rainfall into the river network in the Setun catchment. The first floodpeak demonstrated the concentration time of the impermeable part of the catchment, directly contributing the rainfall it received to the river network. For the western part of the catchment, it is estimated around 2 h, and for the whole catchment, around 6 h. This corresponds with the concentration time estimates derived from the long-term time-series rainfall-runoff correlation analysis in the Setun River catchment conducted earlier (Chalov SR, Platonov SV, Moreydo VM, et al. (2022) The small urban river runoff response on 2020 and 2021 extreme rainfalls on the territory of Moscow. Russ Meteorol Hydrol [Manuscript in preparation]). The entire catchment response, involving infiltrated and hillslope-routed fraction of rainfall can account for 6 to 11 h for the western and eastern parts, respectively. Compared to the average concentration time in the Lusyanka non-urbanized catchment, which is 16 h, it is more than twice as rapid. This can be explained solely by larger area of paved impermeable surfaces in the Setun River catchment.

To compare the catchment response to extreme precipitation event in urbanized and non-urbanized areas, we took a case study in the Lusyanka River catchment located in 120 km to the West of Setun catchment (Fig. 10). While the Lusyanka River catchment area is comparable—170 km<sup>2</sup> against 186 km<sup>2</sup> for the Setun River, the landscape cover is highly contrasting, mostly forested or covered with grassland.

To demonstrate the different catchment response, we analysed several rainfall events in July 2020, recorded at the nearby station located in Mozhaysk town (27,509 in Fig. 10) in 25 km to the East of the catchment (Fig. 11). On 7 and 8 July, 2020 the region was hit by a large rainstorm, resulting in over 80 mm rainfall in 6 h. The catchment response was rapid, but not pronounced, as the stage began gradually increase from around 50 cm to around 100 cm in the following hours. Next rainfall event on 12 July with only 20 mm of precipitation resulted in much larger catchment response—in nearly 6 h, the stage increased threefold from 60 to 180 cm. The last 40 mm rainfall on 14–15 July resulted in further ascent of river stage from 100 to 260 cm in 10 h.

In general, the hydrograph shape of the three analyzed events clearly shows the different response to large rainfall events as the catchment is gaining moisture. After the first extreme rainfall event, the response was slow and but gradual, as most of the water infiltrated into the soil and only a fraction was routed into the river network. The next two events show much faster response, as the infiltration capacity was exceeded and most of the rainfall resulted in overland flow. These evidences confirm that the urbanization effects might represent a significant increase in flooding for small catchments, whereas at larger scales, the effects are highly complex and a result of sub-catchment responses (Miller and Hutchins 2017).

#### Water quality impact of extreme flow events over urban catchment

There are several types of temporal trends in dissolved forms of chemical elements in the river during storm rainfall. Most of the trace element particulate concentrations increase with increasing discharge and reach more or less constant values during the floods, whereas dissolved concentrations decrease. Four main groups of elements might be considered based on their flood-driven behavior. The first group is composed of mostly soluble elements. All major ions (HCO<sub>3</sub><sup>-</sup>, SO<sub>4</sub><sup>2-</sup>, Ca<sup>2+</sup>, Mg<sup>2+</sup>, Na<sup>+</sup>, K<sup>+</sup>), mineral silicon, orthophosphates, total dissolved organic matter belong to the group of components whose concentrations decrease with the rise in water discharge (Fig. 12a). Concentrations found in groundwater supplying the river during low-water periods, especially in urban conditions, are always higher than those found

**Table 4.** Three to six-hourly precipitation sums verification statistics for 2020 and 2021 cases

Station/statistics	Three to six-hourly sums 2020			Three to six-hourly sums 2021		
	Bias	RMSE	Correlation	Bias	RMSE	Correlation
MSU Observatory	-3.735	10.676	0.075	-	-	-
Nemchinovka	-2.504	11.577	-0.102	-0.900	3.709	0.612
Podmoskovnaya	-5.507	11.762	0.046	-1.010	3.363	0.409
Balchug	-4.629	9.269	-0.144	-0.469	3.865	-0.028
VDNKh	-4.011	9.204	0.191	-0.738	3.820	-0.033
Tushino	-2.511	12.922	0.027	-2.361	8.400	0.778
Krasnogorsk	-4.125	7.015	0.309	-0.345	2.272	0.680
Dolgoprudny	-11.636	18.560	0.021	-1.202	4.936	0.586
Butovo	-7.589	11.456	0.416	-1.640	7.233	0.061
Sheremetyevo	-9.348	14.784	-0.005	-0.513	3.787	-0.032
Vnukovo	-3.597	9.285	-0.003	-0.657	6.330	-0.027

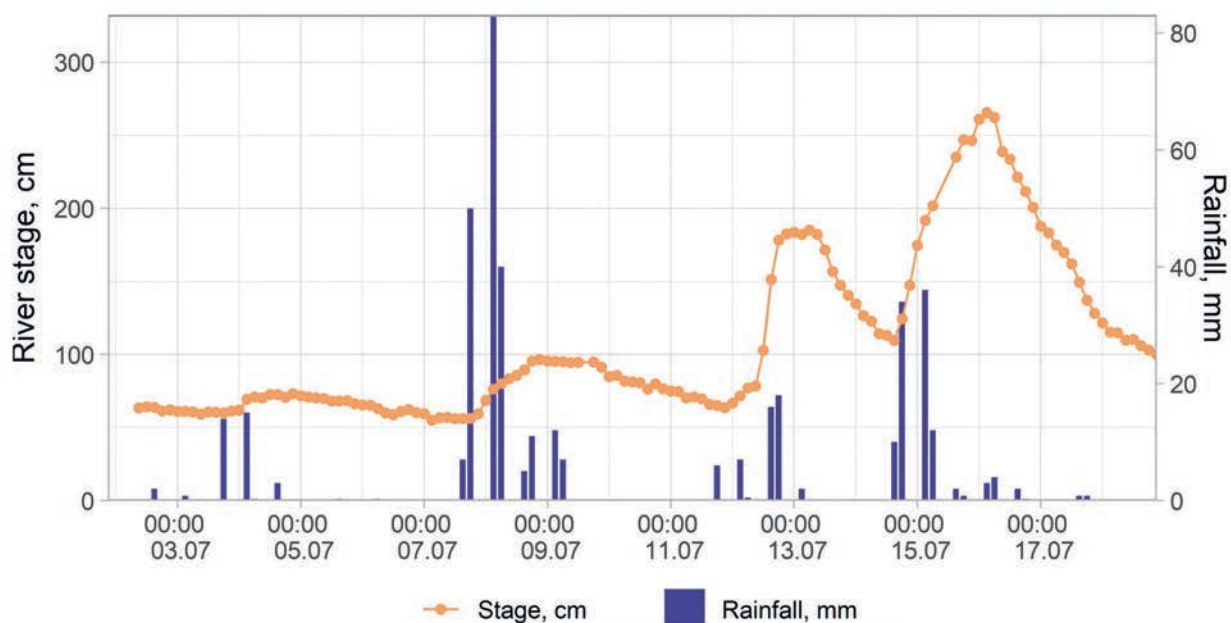


Fig. 11. Rainfall and river stage at Lusynka catchment in July 2020

in rainwater. However, there is no strong enrichment of rainwater by these ions with slope runoff.

The turbidity of the Setun River has a significant impact on the chemical concentrations during high water flow. During the June–July 2021 flood, the SSC was 2 or more times higher than the previous low-flow level (26 mg/l), and at the peak of the flood reached over 500 mg/l. Increased element transfer in suspended form significantly changes the total load and composition of nutrients and organic substances in the river. At the maximum

water discharge, concentration of dissolved inorganic phosphorus slightly decreased, while the concentration of its suspended inorganic form increased by 5.6 times, and that of the suspended organic form—by 8.8 times. The percentage of suspended forms of phosphorus thus increased from about 50 to 80% or more during the flood. The percentage of suspended form of total nitrogen also increased during the flood from 10–20% to a maximum of 40% (Fig. 12b). The values of BOD<sub>5</sub> and COD in unfiltered water samples increased by 2 and 2.8 times, re-

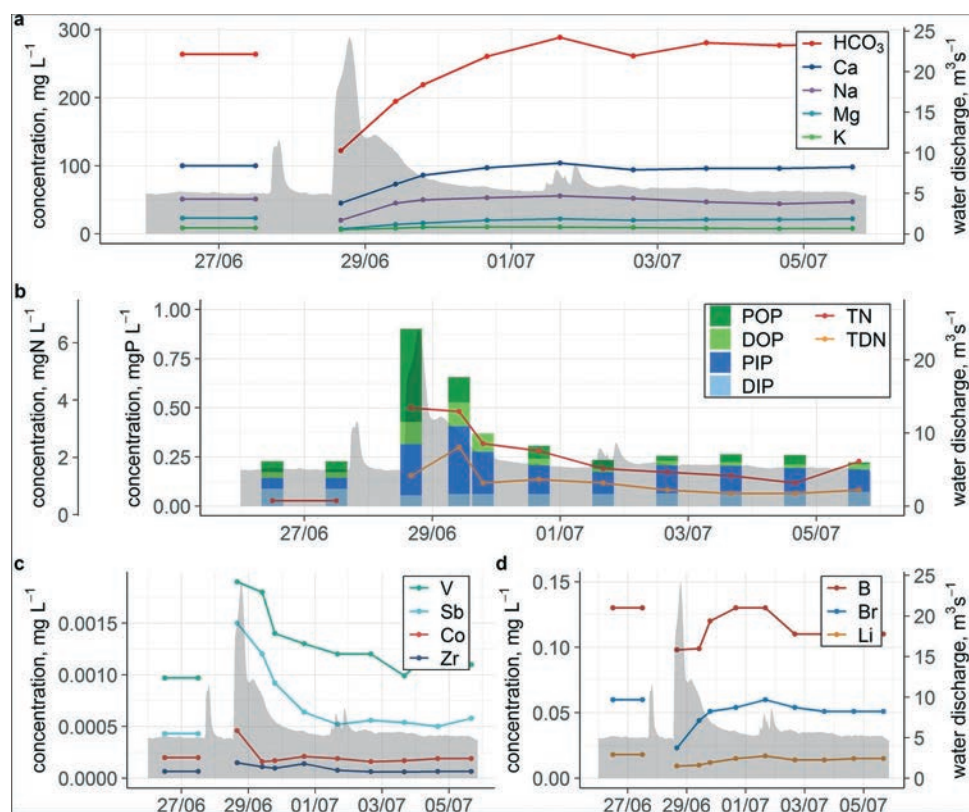


Fig. 12. Concentrations of major ions (a), nutrient elements (b), and some trace elements with positive (c) and negative (d) relationship to water discharge during a flash flood on the Setun River in June–July 2021



spectively, at the peak of the flood compared to low-flow levels. Therefore, flushing of particulate matter from the watershed is an important mechanism of nutrient and organic pollution of urban river water during heavy rainfall and flood formation. Among the nutrients, in contrast to orthophosphates and COD values, the content of dissolved organic phosphorus during the flood significantly increased by 5.7 times compared to the low-flow values, indicating probable flushing of phosphorus-containing organic compounds from the watershed. Similarly, concentrations of total dissolved nitrogen and phosphorus, as well as nitrite nitrogen, almost doubled at the flood peak, which is explained by strong relationship with particulate concentrations (Walling et al. 2008). The increase of sediment concentration induced growth in both particulate and dissolved concentration of wide range of trace elements (Fig. 12c). This group is composed of mostly elements linked to the particulate matter and mostly consists of insoluble and well-sorted elements. Both with increase of SSC, the intensification of sorption lead to significant increase of Mn (20.7-fold), Cs (11.6-fold), Cd (6.8-fold), Al, Nd, and Er (6.1–6.2-fold) dissolved concentrations. Concentrations of some other elements increased 2–3 times. The patterns of temporal variability of concentrations at the falling limb of the flood differed between these elements: for some (Al, Mn, Co, Cd), the rise at flood peak was followed by a sharp decline; by the next day, concentrations returned to almost low-flow level. For others, this decline was extended by several days.

Li, B, Cr, As, Br, and Sr were negatively related to water discharge during flood events—their concentrations (in dissolved form), as well as total dissolved solids concentration, decreased during higher water discharge (Fig. 12d). The decrease in concentrations at flood peak for these elements did not exceed 2.5 times in comparison with low-flow concentrations, and their return to initial values was relatively slow (to June 30–July 1, as was found for major ions).

There was no significant change in concentrations or range of variability for a number of elements, which included Cu, Zn, Mo, Sn, Pb, Ba, La, Cs, U, etc., during the rainfall flood when compared to periods of low flow.

The chemical composition of the river water during floods significantly varied from spring snowmelt floods. During the spring flood, concentrations of major ions were mostly negatively correlated with water discharge, although for  $\text{Ca}^{2+}$ ,  $\text{Mg}^{2+}$ ,  $\text{K}^+$ , and  $\text{SO}_4^{2-}$  a slight increase in the beginning of the rising limb was observed. Concentrations reached their minimum 1 day after the peak discharge. COD in filtered and unfiltered samples increased 2–2.4 times compared to preceding low flow (to 100–120 mgO/L). Dissolved N and P reached 1.3–2 times their baseflow concentrations, their particulate forms increased 4–9 times due to high suspended sediment content (> 300 mg/L), maximum nutrient concentrations were observed before peak water discharge. Minimum concentrations of Li, B, Br, Sr, Cu, Cd, and Ba coincided with peak discharge and were 1.2–3 times lower than their low flow concentrations, for Sb peak concentration was, on the contrary, was 4.3 times higher. Al, V, and Ni increased rapidly 2–4.9 times in the beginning of the flood and then returned to baseflow levels.

Major ions showed similar patterns during both spring flood and flash flood: their concentrations during the snow melt decrease. However, for some of the ions ( $\text{Ca}^{2+}$ ,  $\text{Mg}^{2+}$ ,  $\text{K}^+$ ,  $\text{SO}_4^{2-}$ ), as well as for the mineral

silicon, concentrations increased slightly along with the river discharge at the beginning of the spring flood. This may be the result of the intensive washout of salts that accumulated on the watershed during winter, along with insufficient dilution by low-mineralized snowmelt water. Due to the greater duration of the spring flood than that in summer one can determine that the minimum concentration of major ions comes with a delay of 1 day from the maximum water discharge. At the same time, the duration of the rising and falling limb for the flood wave itself, and for the ion flow, generally correspond, meaning that the rate of increase and decrease in river runoff is close to the rate of change in the chemical composition of the river.

In contrast to the flash flood, there is a more significant (up to 2.4) increase in the COD value in spring, as well as an increase in dissolved mineral phosphorus content.

The total concentrations of dissolved nitrogen and phosphorus during the spring flood are much higher than during low-flows (Erina et al. 2020); showing a non-linear relationship with water discharge: at the beginning of the flood their concentrations increase smoothly, while at the peak of water discharge the content of suspended nitrogen and phosphorus increases during the floods by 4–6 times, increasing the suspended matter content to 300 or more mg/l.

The maximum concentration of nitrites found locally during the spring of 2021 occurred in the middle of the rising limb of the flood, however, during the further rise and fall its concentration was close to that of the low-flows.

Among trace elements, the dynamics of Li, B, Br, and Sr generally mimicked the changes that occurred in the water discharge, while the dynamics of Cr and As content had a more complex form (Cr, monotonic decrease throughout the spring flood; As, increase in concentrations at the peak of the flood). In spring, however, the inverse was observed for Cu, Cd, Zr, Ba, and some other elements, for which such a relationship was not observed in summer.

### Implications for water management systems

The observed changes in water regime and high levels of suspended solids and pollutants concentrations during a storm event in the urban Setun River which significantly exceeds the Russian guidelines for surface water are explained by low standards of environmental protection. Moscow is currently operating a storm water drainage system constructed in the middle of the twentieth century. This system accumulates stormwater separately from domestic sewage and treats it primarily from suspended solids and oil products. This situation was quite common among large cities around the world just a few decades ago (Brown et al. 2009; Hale 2016; Goulden et al. 2018). Stormwater facilities, unable to absorb the increasing runoff and pollutants load from the urban watershed (Vorobevskii et al. 2020; Lu et al. 2021), often were unable to provide proper treatment. Therefore, during extreme rainfall and the combined sewage system, a mixture of fecal sewage along with stormwater entered urban rivers (Lee and Bang 2000; Gasperi et al. 2012), contaminating them dramatically.

Despite possible hazards due to hydrological changes and contamination with urban pollutants (Erina et al.

2021), small rivers of Moscow are vital for the city's functionality and its economic development. The Setun River catchment area is constantly integrating in the urban landscape with green parks and green infrastructure (Klimanova and Illarionova 2020) and provide, among others, aesthetic and recreation services. At the same time, the observed measures are not integrated into managing of stormwater loads which is widely developed in many cities (Qiao et al. 2019; Rosenberger et al. 2021). The Setun basin seems to have great potential for stormwater management by implementing Low Impact Development (LID) such as stormwater ponds, rain gardens and permeable pavements. The examples of other large cities in Europe, USA, China (Damodaram et al. 2010; Ahammed 2017; Prudencio and Null 2018; Bohman et al. 2020) show that the implementation of retention ponds leads to a 70% reduction of sediment load to the rivers and a 20–40% reduction of dissolved pollutants load to the rivers (Bedan and Clausen 2009; McPhillips et al. 2021). Natural based solutions for urban stormwater control also expand both social infrastructure and are widely supported by citizens (Darnthamrongkul and Mazingo 2021). At the same time, the implementation of green infrastructure requires a complete revision of the existing drainage system throughout the entire catchment (Barbosa et al. 2012; Cettner et al. 2013; Qiao et al. 2020) and designing the spatial organization of LID facilities, which needs a complete understanding of the hydrology and pollutant loads on different parts of the catchment (Rosenberger et al. 2021). Thus, this study is the first step toward designing sustainable stormwater management in the basin of Moscow's urban streams.

## CONCLUSIONS

The present study is the first attempt to use hydro-meteorological records and models for the largest urban area in Russia to investigate climate change and urbanization impacts on flooding and water quality. The study is based on the most comprehensive overview of the precipitation datasets for the 6 stations within Moscow city and the neighboring Moscow region for a 1966–2021 period. The standard configuration of COSMO-CLM model ver. 5.12 with the last version of the TERRA-URB urban canopy model has reproduced the synoptic-scale and main mesoscale features of 2020 and 2021 summer extreme precipitation events satisfactorily and could be applied and developed in further studies. In some cases, it failed to capture location, time span and intensity of rainfall events on hourly and sub-hourly timescales due to local shifts of precipitation areas in space and time. The COSMO-CLM outputs were combined with urban flow analyses for the Setun River basin which is based on 30-min frequency datasets. Two particular rainstorm events, on 29–31 May 2020, and on 28–29 June 2021 provided a clear insight on the propagation of the intense rainfall into the river network in the Setun catchment.

The key research outcomes of this study are grouped into three categories according to the results of precipitation, flow discharge and water quality data processing:

1. The long-term extreme precipitation data indicates mostly insignificant increase of absolute yearly daily maxima. At the same time, there is a statistically significant rise of moderate extremeness ETCCDI indices (R95TOT, R20mm) specifically within the Setun basin (at MSU Observatory, and Nemchinovka stations). Meanwhile, indices characterizing the largest precipitation amounts among the ETCCDI classification do not reveal any significant trends for a considered period. This suggests that urban precipitation patterns in Moscow city, emerging in moderate rainfall events frequency, are increased.
2. Whereas the observed increases in frequency and intensity of extreme rainfall are physically consistent with global warming in the twentieth century, the water discharges in small urbanized rivers are entirely driven by urbanization effects, firstly larger area of paved impermeable surfaces. The available evidence has been found for the Setun River catchment concerning twice as rapid rainstorm flood catchment response time compared to the average concentration time in the non-urbanized catchment which is 16 h; significant impacts of values and movement of rainfall core to the small river flooding.
3. The effects of rainstorms in the urbanized catchment of Moscow city are highly complex. It was observed that in spring there various genetic types of waters interact in a complex way within the urban landscape. This alongside the greater duration of the spring flood process itself in comparison to a flash flood, causes some differences in the flash flood dynamics of the chemical composition of water, and a more complex relationship between the chemical parameters and the water discharge. At the same time, many similarities were found between spring floods and flash floods: inverse dynamics of water discharge and concentrations of Li, B, Br, and Sr, attribution of the maximum concentrations of Al and Mn to a raising limb of the flood, and their sharp decrease immediately after that. It was also noted that the level of concentrations post flood returned almost immediately to pre-flood levels for both types of floods.

Due to lacks in wealthy hydro-meteorological records, especially in term of urban rivers flows, further research to combine rainfall intensity, convective storms, urban flooding and first flush events and their changes in the future will help to consider and make adequate decisions for designing sustainable stormwater management in the urban areas.

## ВМЕСТО ЗАКЛЮЧЕНИЯ

### Загрязнение Московского мегаполиса: мониторинг химического состава микрочастиц в системе «атмосфера–снег–дорожная пыль–почвы–поверхностные воды» \*

#### ВВЕДЕНИЕ

Развитие дорожно-транспортной сети и многопрофильной промышленности, высокие темпы застройки в Московском мегаполисе приводят к масштабному экологическому воздействию на природные компоненты и значительно ухудшению условий жизни горожан [1]. Доминируют эмиссии от автотранспорта, в твердой фазе которых присутствуют черный углерод (black carbon, BC), опасные органические соединения, тяжелые металлы и металлоиды (ММ). Многокомпонентный состав аэрозолей и его влияние на процессы седиментации и накопления в системе «атмосфера–снег–дорожная пыль–почвы–поверхностные воды» при множественности источников эмиссии создают одну из наиболее сложных экологических проблем. Накопление этих токсичных компонентов особенно велико в тонких фракциях, среди которых наиболее часто определяется массовая концентрация частиц размером 10 мкм и менее (PM<sub>10</sub>), которые негативно воздействуют на организм человека [8]. Оценка качества воздуха Москвы по газообразным соединениям и частицам PM<sub>10</sub> аэрозоля показывает уровень загрязнения, сопоставимый с крупными городами Европы [19]. Однако концентрация загрязняющих веществ в аэрозолях и накопление в депонирующих средах Москвы остаются недооцененными. Поэтому чрезвычайно важно проследить судьбу приоритетных поллютантов в городской среде и оценить их аккумуляцию в компонентах городских ландшафтов.

Для решения этой задачи особую актуальность представляет сопряженный анализ химического состава аэрозолей и микрочастиц PM<sub>10</sub> в снеге, дорожной пыли, почвенном покрове, взвешенных и донных наносах речных водотоков. Обогащенные поллютантами микрочастицы в транзитных и депонирующих средах увеличивают риск хронических и респираторных заболеваний в крупных городах вследствие высокого загрязнения BC [23], ПАУ [12] и ММ [32]. Цель данной работы – развитие технологии мониторинга городской среды и ее апробация в Московском мегаполисе на основе химического анализа микрочастиц PM<sub>10</sub> в системе «атмосфера–снег–дорожная пыль–почвы–поверхностные воды», которая необходима для оценки и прогноза ее эколого-геохимического состояния в условиях пространственно-временной изменчивости природных и антропогенных факторов.

#### ТЕХНОЛОГИЯ ЭКОЛОГИЧЕСКОГО МОНИТОРИНГА МИКРОЧАСТИЦ

Новая технология экологического мониторинга окружающей среды мегаполиса с использованием сопряженного анализа микрочастиц в различных средах включает четыре этапа: (1) полевой; (2) химико-аналитический; (3) покомпонентную оценку состояния окружающей среды; (4) сопряженный анализ микрочастиц в системе «атмосфера–снег–дорожная пыль–почвы–поверхностные воды», которая состоит из подсистем с близкими характерными временами протекания процессов миграции.

На полевом этапе организуются постоянные наблюдения на базовых станциях мониторинга атмосферы и речных вод, параллельно проводится площадная съемка отдельных депонирующих сред по регулярной сети в одних и тех же пунктах опробования. Размер ячеек сети обеспечивает характеристику геохимической неоднородности территории, частота наблюдений выбирается в соответствии с характерными временами процессов – аэрозоли и атмосферные осадки характеризуют суточную изменчивость загрязнения, снежный покров, дорожная пыль и поверхностные воды – сезонную, почвы – многолетнюю.

Подсистема «аэрозоли–атмосферные осадки» характеризует качество воздуха и геохимическую нагрузку на городские территории по концентрациям компонентов PM<sub>10</sub> (BC, ионов, ММ и др.). Для непрерывного автоматизированного мониторинга химического состава аэрозолей и атмосферных осадков на территории Метеообсерватории МГУ (юго-запад г. Москвы) создан Аэрозольный комплекс. Аэрозольная нагрузка измеряется в стандартах качества воздуха PM<sub>10</sub> [24] с помощью оптического счетчика числа частиц TSI OPC и аэталометра AE33, позволяющего по эффективному поглощению солнечного излучения на длине волны 880 нм определять массовую концентрацию эквивалентного BC (eBC). Проводится суточный отбор проб аэрозолей с последующим анализом химического состава в лаборатории. Параллельно выполняются наблюдения за осадками, температурой и относительной влажностью воздуха, давлением, скоростью и направлением ветра.

Мониторинг распределения ММ в подсистеме «снег–дорожная пыль–почвы» проводится на дорогах с разной интенсивностью движения, а также во

\* Касимов Н.С., Кошелева Н.Е., Поповичева О.Б., Власов Д.В., Шинкарева Г.Л., Ерина О.Н., Чалов С.Р., Чичаева М.А., Ковач Р.Г., Завгородняя Ю.А., Лычагин М.Ю. // Метеорология и гидрология. 2023 (принята к публикации). RINC 0.95



дворах жилых домов. Пробы дорожной пыли отбираются с поверхности дорожного полотна, из верхнего слоя почв – не далее 5 м от края дороги, снега – в точках отбора почвенных проб. Все пробы отбираются в 3-4 повторностях, из которых составляется одна смешанная проба.

Транспорт загрязняющих веществ в подсистеме «*речные воды–взвешенные наносы–донные отложения*» изучается на двух пространственных уровнях. На бассейновом уровне для оценки влияния города на р. Москве проводится установка станций мониторинга на разном удалении выше и ниже города. На локальном уровне станции размещаются на разных участках течения одного из притоков р. Москвы в пределах города. Мониторинг включает сезонные водно-балансовые, гидролого-геохимические исследования содержания ММ в микрочастицах речной взвеси и донных отложений, а также оценку вклада микрочастиц в транспорт загрязнителей городской рекой-притоком. Используются современные средства измерения (автоматические логеры уровня воды, мутности, доплеровские профилографы, а также зонд-ловушка для отбора проб взвеси).

На химико-аналитическом этапе определяются концентрации ММ, ПАУ и основных ионов во всех компонентах изучаемой системы в одной лаборатории с использованием единых методик и стандартов. Микрочастицы  $PM_{10}$  выделяются путем отмучивания с фильтрованием растворов через мембранные фильтры с диаметром пор 0,45 мкм. Содержание ММ анализируется с помощью атомно-эмиссионной спектроскопии (ICP-AES) и масс-спектрометрии (ICP-MS) с индуктивно-связанной плазмой, содержание ПАУ – методом жидкостной хроматографии высокого давления [5], концентрации водорастворимых неорганических катионов и анионов – методом ионной хроматографии [7, 21].

Покомпонентная оценка состояния городской среды включает определение геохимической специализации каждого компонента с использованием единого эталона сравнения (средний состав верхней части континентальной коры или кларки ММ по [27]) и одного нормирующего элемента. Наиболее часто при оценке загрязнения различных компонентов окружающей среды используется Al [36]. Перечень накапливающихся поллютантов определяется в соответствии со значениями коэффициента обогащения  $EF_i = (C_i/C_{ref}) / (K_i/K_{ref})$ , где  $C_i$  и  $C_{ref}$  – содержание  $i$ -го и нормирующего элемента в  $PM_{10}$ ,  $K_i$  и  $K_{ref}$  – кларки  $i$ -го и нормирующего элемента в верхней части континентальной земной коры.  $EF < 1$  указывает на поступление ММ от терригенных источников,  $EF$  1-10 – на воздействие и антропогенных, и терригенных источников, а  $EF \geq 10$  – на явно антропогенные источники ММ. Контрастность техногенных аномалий ММ характеризует коэффициент концентрации  $KK_i = C_i/C_k$ , где  $C_k$  – концентрация  $i$ -го элемента в верхней части континентальной коры,  $n$  – число элементов с  $KK_i > 1$ . Общее загрязнение депонирующих сред группой поллютантов при отсутствии фоновых аналогов оценивается с помощью суммарных показателей загрязнения также относительно верхней части континентальной коры  $Zc = \sum KK_i - (n - 1)$  и обогащения  $TEF = \sum EF_i - (n - 1)$ , где  $n$  – число элементов с  $EF_i > 1$  [6, 35]. Для ПАУ используются парные отношения флуорантен/пирен (Fln/Pyr), бенз(а)пирен/ бенз(ghi)перилен (BaP/ghi),

которые являются наиболее часто используемыми маркерами транспортных эмиссий, а также Pyr/ghi и BaA/ghi, где BaA – бенз(а)антрацен, которые диагностируют промышленные выбросы [29].

На этапе сопряженного анализа микрочастиц в городской среде создается цифровая база данных с содержанием поллютантов и результатами оценок загрязнения отдельных компонентов; отслеживаются геохимические связи в подсистемах, связанных потоками поллютантов; выявляются сезонные и многолетние тренды изменения геохимических показателей. Межсуточные вариации техногенной нагрузки на городскую среду характеризуются на основе распределения поллютантов в подсистеме «*аэрозоли–атмосферные осадки*». Вымывающая способность осадков оценивается с помощью коэффициента захвата  $SR = (C_{sum}/pprec)/(C_{air}/p_{air})$ , где  $C_{sum}$  и  $C_{air}$  – суммарная концентрация ММ в осадках и в аэрозолях, соответственно,  $pprec$  – плотность дождевой воды (1 кг/л),  $p_{air}$  – плотность атмосферного воздуха (1,2 кг/м<sup>3</sup>) [15].

Химический состав микрочастиц в подсистеме «*снег–дорожная пыль–почвы*» дает представление о пространственном распределении поллютантов в микрочастицах основных депонирующих сред мегаполиса на основе данных о содержании поллютантов в точках опробования регулярной сети мониторинга. Анализ распределения ММ в микрочастицах этой подсистемы предполагает: 1) сравнение концентраций и интенсивности накопления ММ во фракции  $PM_{10}$  относительно валового содержания ММ во всех компонентах с выявлением наиболее загрязненных компонентов; 2) определение геохимического взаимовлияния частей подсистемы с помощью статистических и геохимических методов.

Анализ переноса микрочастиц в системе «*речные воды–взвешенные наносы–донные отложения*» позволяет оценить доли транспорта и аккумуляции взвешенного материала, поступающего из антропогенных источников на территории мегаполиса и переносимого р. Москвой в основные фазы водного режима – половодье и межень. С этой целью рассчитывается коэффициент концентрации КК – отношение содержания ММ во взвеси или донных отложениях к содержанию этого элемента в верхней части континентальной коры. Для донных отложений дополнительно рассчитывается коэффициент накопления ММ относительно взвешенных наносов ( $K_d$ ). Как и для подсистемы «*снег–дорожная пыль–почвы*», дается покомпонентная оценка интенсивности обогащения ММ микрочастиц  $PM_{10}$  под воздействием мегаполиса и сравнение концентраций и интенсивности накопления ММ во фракции  $PM_{10}$  относительно валового содержания ММ во взвеси и донных отложениях.

## РЕЗУЛЬТАТЫ И ИХ ОБСУЖДЕНИЕ

### Подсистема «аэрозоли–атмосферные осадки».

Данные о сезонном варьировании среднесуточных концентраций  $PM_{10}$  и компонентов аэрозолей, их процентном вкладе в общее содержание приведены на рис. 1. Изменчивость массовой концентрации  $PM_{10}$  характеризуется средними значениями  $33 \pm 29$ ,  $20 \pm 9$  и  $9.4 \pm 2.8$  мкг/м<sup>3</sup> весной 2018 г., осенью 2019 г. и зимой 2019–2020 гг., что ниже принятого в России норматива качества атмосферного воздуха (60 мкг/м<sup>3</sup>) городских и сельских поселений [9].

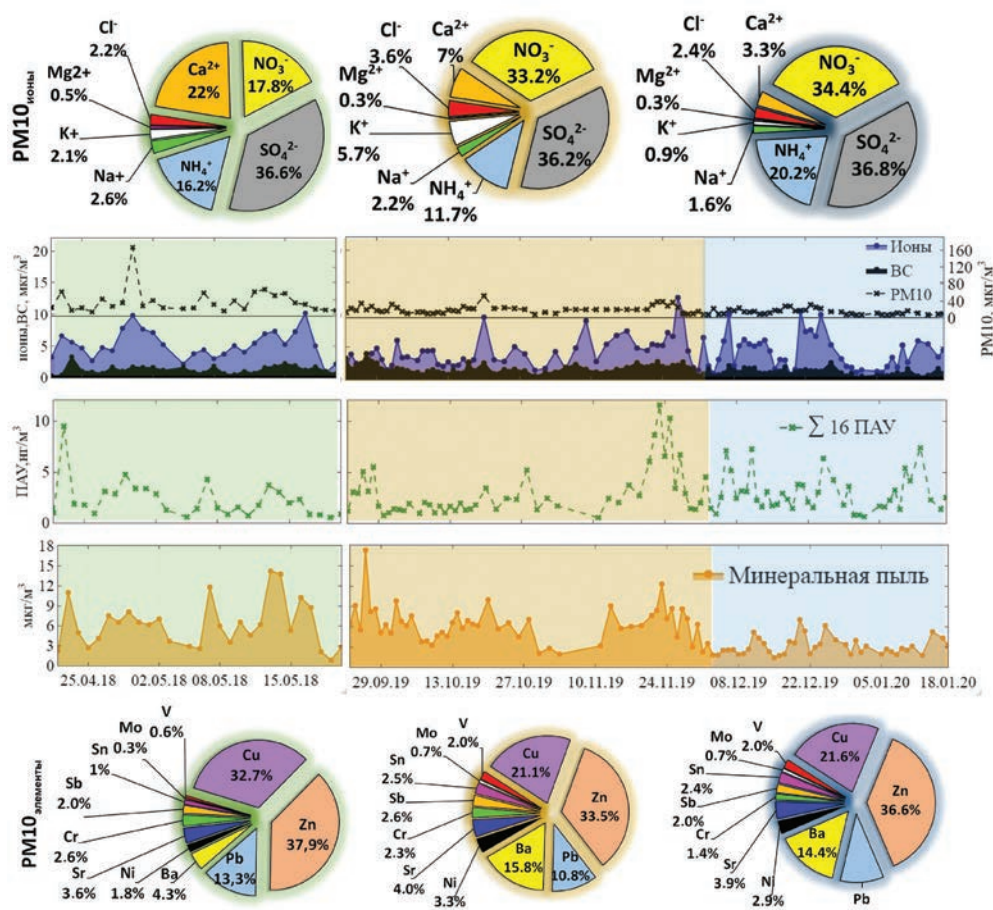


**Рис. 1.** Сезонное варьирование (весна 2018, осень 2019, зима 2019-2020) концентраций  $PM_{10}$ , черного углерода (BC), минеральной пыли, суммарной концентрации ионов и 16-ти ПАУ на Аэрозольном комплексе МГУ. Круговые диаграммы показывают процентный вклад ионов (вверху) и микроэлементов (внизу) в общее содержание в  $PM_{10}$

Во время новогодних праздников концентрация  $PM_{10}$  находилась в пределах 6.7-9.5  $\mu\text{г}/\text{м}^3$ , что ниже среднего за весь период наблюдений. Наибольшее превышение ПДК зарегистрировано 30.04.2018, когда содержание  $PM_{10}$  в воздухе возросло до 168  $\mu\text{г}/\text{м}^3$ . Это объясняется интенсивным пылением почвы после схода снежного покрова [3], а также сельскохозяйственными пожарами в Московском регионе [26]. В майские праздники концентрация частиц  $PM_{10}$  колебалась от 11 до 56  $\mu\text{г}/\text{м}^3$ , превышая среднюю концентрацию за весь период наблюдений.

Самый высокий вклад 27% в количество  $PM_{10}$  внесли водорастворимые ионы осенью. В сезонном ходе суммарных концентраций катионов и анионов максимум  $5.0 \pm 2.3$   $\mu\text{г}/\text{м}^3$  приходится на весну и минимум  $3.0 \pm 1.7$   $\mu\text{г}/\text{м}^3$  на зиму. Среди катионов в любой сезон доминировали сульфаты  $\text{SO}_4^{2-}$  (~36%) вторичных аэрозолей городских источников. Близкая доля нитратов  $\text{NO}_3^-$  (~34%) в эмиссиях транспорта наблюдалась в осенне-зимнее время. Среди анионов преобладал аммоний  $\text{NH}_4^+$  (11-20%), образующийся на городских свалках мусора, в сточных водах и мигрирующий из сельскохозяйственных районов Подмосковья. В основной массе неорганических аэрозолей преобладают сульфаты и нитраты аммония в результате реакции нейтрализации аммиаком  $\text{H}_2\text{SO}_4$  и  $\text{HNO}_3$  в городской среде [31]. Средняя за сезон концентрация иона  $\text{K}^+$  – маркера сжигания биомасс [25] варьировала от наибольшей  $0.2 \pm 0.1$   $\mu\text{г}/\text{м}^3$  осенью до минимальной  $0.02 \pm 0.01$  зимой, что указывает на

вклад эмиссий жилого сектора и сельскохозяйственных пожаров в Подмоскowie. Присутствие солевых компонентов  $\text{Na}^+$  и  $\text{Cl}^-$  в аэрозолях и осадках обусловлено противогололедными смесями [4].

Вклад минеральной пыли в концентрацию  $PM_{10}$  близок к ионным компонентам, а осенью даже их превосходил, составляя 32%. Ее сезонный ход характеризуется максимальными значениями  $5.9 \pm 3.5$  и  $6.5 \pm 2.8$   $\mu\text{г}/\text{м}^3$  весной и осенью, и минимальным  $2.8 \pm 1.0$   $\mu\text{г}/\text{м}^3$  зимой из-за постоянного снежного покрова. Аналогичный сезонный тренд наблюдался и в суммарной концентрации микроэлементов, поступающих с дорожной пылью [35], выбросами автотранспорта [22] и промышленных предприятий [18]. Среди ММ в любой сезон доминировали Cu, Zn и Pb, составляя 21–32, 33–37 и 10–13% от суммарной концентрации микроэлементов, осенью и зимой к ним присоединялся Ba, внося 14–15%.

Суточная и сезонная изменчивость концентрации BC свидетельствует о загрязнении атмосферы Московского мегаполиса продуктами сжигания топлив (дизельного, бензинового, газа) транспортом, теплоэлектростанциями и промышленными предприятиями и отражает эпизоды поступления в город шлейфов сжигания биомасс из Подмосковья. Самая высокая концентрация BC  $1.7 \pm 0.8$   $\mu\text{г}/\text{м}^3$  наблюдалась осенью, при высоком вкладе сжигания биомасс при отоплении частного жилого сектора Подмосковья [24]. Самая высокая вариабельность доли BC в полной массовой концентрации  $PM_{10}$  отмечена весной



2018 г. ~ 4% с максимумом 34% [26]. Период майских каникул характеризуется наибольшим влиянием сжигания биомасс и пожаров. В течение суток концентрации ВС обнаруживают устойчивые максимумы в 6-9 часов утра и с 22 часов вечера, обусловленные изменчивостью пограничного слоя и увеличением интенсивности движения автотранспорта. Отрицательная корреляция между концентрациями ВС и скоростями ветра подтвердила накопление загрязнений преимущественно в дни стабильной безветренной погоды.

Сезонный ход суммы концентраций 16-ти ПАУ выражен слабо с некоторым ростом к зиме. Наивысшая среднесуточная концентрация 23.11.2019 составила 11.6 нг/м<sup>3</sup>. С 22 по 25 апреля 2018 г. зафиксирован рост в 2-3 раза суммы 16-ти ПАУ, обусловленный переносом шлейфов сжигания биомасс из региона на фоне городских транспортных эмиссий. Это отразилось в увеличении отношения FLn/Pуг и уменьшении отношения ВаP/ghi. Осенью (21-26.11.2019) в составе ПАУ возросло относительное содержание 3- и 4-кольчатых полиаренов за счет повышения долей фенантрена (Fn), FLn и Pуг. Увеличение в 1,5-2 раза отношений Pуг/ghi и ВаA/ghi при высоком содержании Fn указывает на промышленное происхождение источников эмиссий с высоким вкладом петрогенных ПАУ. В период новогодних праздников 1–10.01.2020 снижение промышленной активности в городе сопровождалось уменьшением концентраций ПАУ в частицах PM<sub>10</sub> и уменьшением отношений Pуг/ghi и ВаA/ghi. Снижение транспортной нагрузки в это время привело к увеличению отношения FLn/Pуг и уменьшению – ВаP/ghi.

Наблюдения на МО МГУ в апреле-июле 2020 г. позволили выполнить сопряженный анализ ММ в системе «аэрозоли–атмосферные осадки», который подтвердил значительную роль атмосферных осадков в очищении атмосферы от ММ. В дни после осадков концентрации Be, Na, S, Ti, V, Ni, As, Sb, Cs, Tl сокращались на 30–60%, Li, Mg, Al, K, Ca, Sc, Co, Cu, Rb, Sr, Y, La, Ce, W, Pb, Th, U на 10–30%, возрастали лишь у P, Fe, Zr, Mo, Cd, Sn, Ba, Bi. В последующие сутки после выпадения дождей концентрации многих ММ в аэрозолях начинали восстанавливаться. Содержание Be, Na, S, K, Sc, V, Ni, Zn, As, Rb, Sr, Cs, Ba, W продолжало снижаться из-за слабого выдувания загрязненных частиц почв и дорожной пыли с увлажненной поверхности дорог после дождя.

Сравнение геохимической специализации нерастворенной фазы осадков и аэрозолей в дни выпадения осадков по величине  $EF$  показало интенсивное обогащение аэрозолей всеми ММ, особенно сильное Sb (в 62 раза), Cd (38), Sn (27), S (26), Mo (17), Cu (15), V, Sr, Zn (10 раз). Слабое обогащение микрочастиц в осадках связано с переходом части ММ из взвешенной фазы в растворенную [34]. Перечень активно накапливающихся ММ в аэрозолях и нерастворенной фазе осадков идентичен: Pb, Bi, Sb, Cd, Sn, Zn, S, Cu, Mo, что указывает на существенную роль поставки ММ из техногенных источников Москвы, отмеченную ранее в [11, 28, 33-35].

Значимые при  $p < 0,05$  коэффициенты корреляции  $r$  между содержанием ММ в нерастворенной фазе осадков и аэрозолях типичны для поступающих преимущественно из терригенных источников Y, Al, Li, Th, La, U ( $r = 0,50-0,62$ ), Co, Ce, Rb, Be, Cs (0,45-0,49), W, Tl, Zr (0,37-0,43), слабо переходящих в растворен-

ную фазу. Корреляционные связи для большинства ММ усиливаются при использовании в расчетах общего содержания ММ в осадках и становятся значимыми также у Sr ( $r = 0,90$ ), Ba (0,69), Mg (0,41) и Fe (0,36), для которых характерно растворение вымываемых дождями из атмосферы твердых частиц.

Вымывающая способность осадков по отношению к ММ в аэрозолях оценивалась по величине SR, при расчете которой учитывались концентрации ММ в пробах осадков и аэрозолей только в дни выпадения осадков. Убывающий ряд ММ имеет вид: Be (SR=14340) > Pb, P, Zn (8200–11100) > Na, Al, Ti, Mg, Ca (5000–6000) > Y, Ce, Th, La, K, Sc (4000–5000) > U, Zr, Rb (3000–4000) > Co, Ni, As, Fe, Li (2000–3000) > Mn, Cs, Sb, Sr, S, Ba (1500–2000) > W, Tl (1000–1500) > Cr, Cu, Cd, V, Bi (500–1000) > Mo, Sn (SR < 500). Показатель SR для V, Fe, Mn, Cr, Cd, Cu, Zn, Ca, Na и Co находится в диапазоне, установленном для других регионов мира [15], однако для Pb, Sb, As, Ni, Mg, K, Al и S величина SR в несколько раз выше из-за значительной поставки этих ММ из антропогенных источников, включая дальние, и выдувания частиц загрязненных почв и дорожной пыли. Эффективность очищения атмосферы от этих элементов при дождях особенно велика.

**Подсистема «снег – дорожная пыль – почвы».** Мониторинг распределения ММ в подсистеме «снег–дорожная пыль–почвы» проводился в пределах Западного административного округа (ЗАО) г. Москвы; дорожная пыль и верхний (0–10 см) слой почв опробовались летом 2017 г., снежный покров – весной 2018 г. перед снеготаянием. Элементный состав микрочастиц PM<sub>10</sub> в этих компонентах определялся для трех типов дорог с разной интенсивностью движения: 1) 52-ой км МКАД; 2) главные радиальные шоссе; 3) средние дороги, а также во дворах жилых домов и в районе МО МГУ. Пробы отбирались в трех повторностях: дорожной пыли – с дорожного полотна, верхнего слоя почв – не далее 5 м от края дороги, снега – в точках отбора почвенных проб на всю мощность снежного покрова пластиковой трубой.

Сравнение химического состава PM<sub>10</sub> в подсистеме «снег–дорожная пыль–почвы» выполнено на основе коэффициента  $K_y = C_{i1} / C_{i2}$ , показывающего отношение содержания  $i$ -го ММ в одном компоненте ( $C_{i1}$ , мкг/г) к его содержанию в другом компоненте ( $C_{i2}$ , мкг/г). Для фракции PM<sub>10</sub> пылевой составляющей снега характерны повышенные концентрации большинства ММ ( $K_y$  1–1,5) относительно PM<sub>10</sub> дорожной пыли, за исключением Ca ( $K_y \approx 3$ ) и Rb, Sr, Zn ( $K_y < 1$ ) (рис. 2А). Источниками Ca в PM<sub>10</sub> дорожной пыли являются карбонатные строительные материалы, истирающееся дорожное полотно и бордюрный камень, а также противогололедные реагенты, частицы которых даже при интенсивных дождях летом не полностью удаляются с поверхности дорог [35].

Наиболее высокие содержания в микрочастицах PM<sub>10</sub> снега по сравнению с PM<sub>10</sub> дорожной пыли характерны для Pb ( $K_y = 4,2$ ), Mo (3,2), Cu (3,1), Cd, Bi, Sn, Cr, Ni (2,1–2,5), V, W, Sb (1,7–1,8), что можно объяснить активным поступлением этих ММ с выбросами автотранспорта и промышленных объектов. Например, Mo, Cu, Cd, Cr, Ni, W, Sb поступают от предприятий машиностроения и металлообработки, электротехнических производств, Sb, Bi, Sn, Cr, V – при сжигании мусора, особенно в холодный период



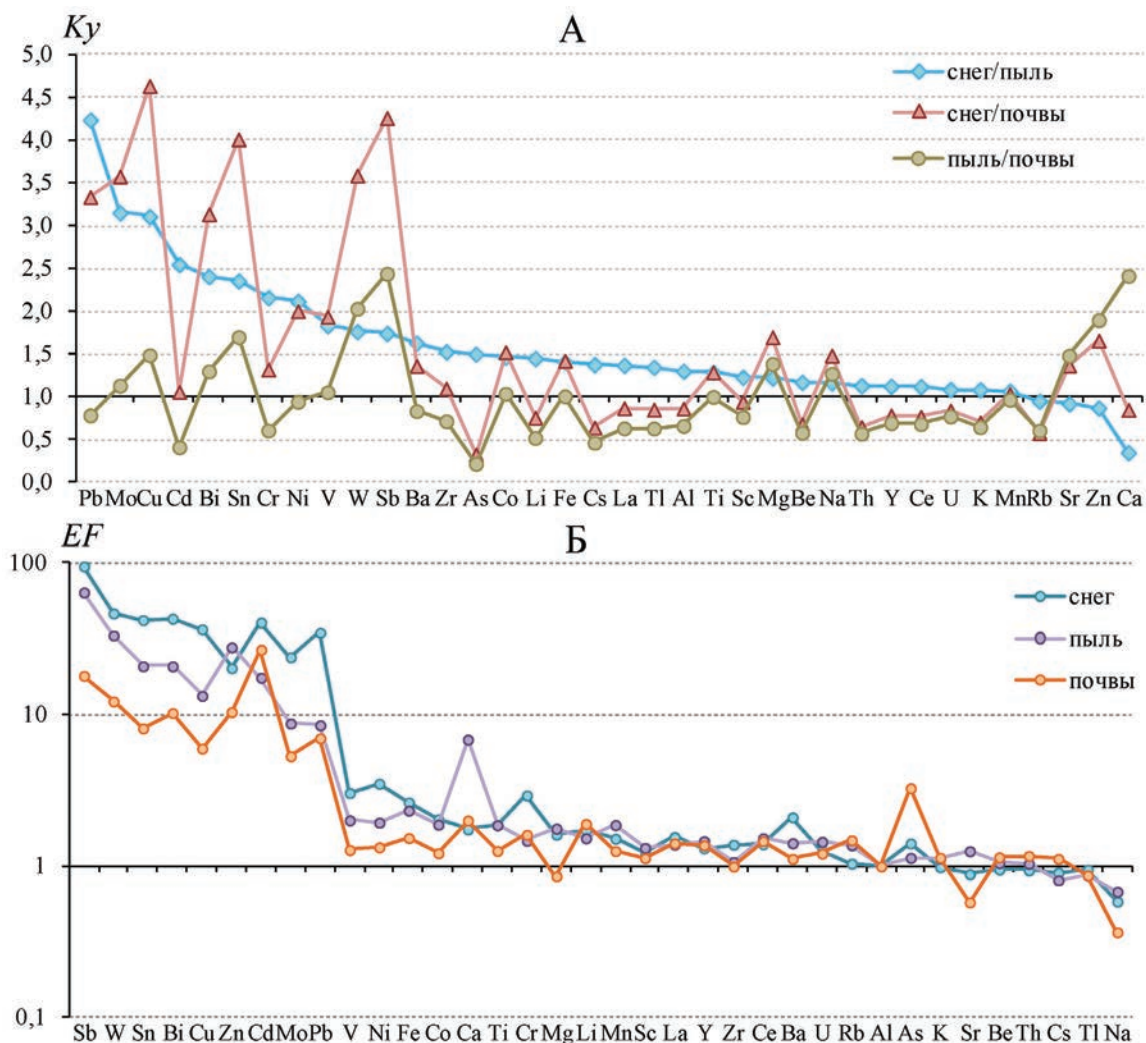


Рис. 2. Отношение концентраций ММ  $Ky$  (А) и коэффициенты обогащения  $EF$  (Б) в микрочастицах  $PM_{10}$  пылевой составляющей снега, дорожной пыли и почв в ЗАО Москвы

[6]. По сравнению с  $PM_{10}$  почв в снеге в 4,0–4,6 раза более высокие концентрации Cu, Sb и Sn, W, Mo, Bi, в 3–4 раза Pb и в 2 раза Ni. Обратное соотношение между Li, Cs, La, Tl, Al, Sc, Be, Th, Y, Ce, U, K, Rb в почвах и снеге обусловлено их незначительной поставкой из техногенных источников.

В подсистеме «дорожная пыль–почвы» концентрации Sb, W, Zn, Ca, Sn, Cu, Sr, поступающие с выхлопными и невыхлопными выбросами автотранспорта [13, 22, 35], в частицах  $PM_{10}$  пыли в 1,5 и более раз больше, чем в  $PM_{10}$  почв (рис. 2А). По содержанию большинства остальных ММ фракция  $PM_{10}$  почв слабо отличается от  $PM_{10}$  дорожной пыли ( $Ky = 0,6–1,5$ ). Более высокие концентрации As, Cd, Li и Cs в  $PM_{10}$  почв по сравнению с  $PM_{10}$  дорожной пыли объясняются поступлением этих ММ в почвы с удобрениями, торфо-компостными смесями, используемыми при разбивке газонов рядом с дорогами, а также с пестицидами при обработке городских растений [6].

В  $PM_{10}$  пылевой составляющей снега антропогенное происхождение имеют  $Sb_{95} W_{47} Bi_{43} Sn_{42} Cd_{41} Cu_{37} Pb_{35} Mo_{24} Zn_{20}$  (нижний индекс – средняя величина  $EF$ ), в дорожной пыли –  $Sb_{64} W_{33} Zn_{28} Bi_{21} Sn_{21} Cd_{18} Cu_{13}$ , в почвах –  $Cd_{27} Sb_{18} W_{12} Zn_{10} Bi_{10}$  (рис. 2Б). Вероятными источниками этих элементов явля-

ются износ тормозных колодок [18, 35], истирание шин [13], выбросы предприятий металлообработки, нефтехимии и нефтепереработки [14], приборостроения, химической и резиновой промышленности, по производству пластика [17], по переработке и сжиганию отходов [16].

Сравнение коэффициентов  $EF$  для микрочастиц  $PM_{10}$  в компонентах подсистемы «снег–дорожная пыль–почвы» позволило выявить поступающие из общих источников ММ и их миграцию между компонентами. Обогащение микрочастиц  $PM_{10}$  большинством ММ уменьшается в ряду: пылевая составляющая снега > дорожная пыль > почвы, за исключением Ca, уровень обогащения которым дорожной пыли ( $EF=7$ ) в 3,5 раза выше, чем почв и снега, и As с максимальным накоплением в почвах ( $EF=3,3$ ), что примерно в 3 раза больше, чем в снеге и дорожной пыли. Одновременно накапливаются во фракции  $PM_{10}$  снега, дорожной пыли и почв Sb, W, Bi, Sn, Cd, Cu, Pb, Mo и Zn, в снеге и дорожной пыли – Ni, V и Fe, аномалии которых не наблюдаются в подсистемах «снег–почвы» и «дорожная пыль–почвы», но где формируются аномалии Sr и Ca, соответственно. Некоторые ММ аккумулируются в отдельных компонентах: для  $PM_{10}$  пылевой составляющей снега типичны аномалии

Va и Co, образованные невыхлопными выбросами транспорта и не успевшие проявиться в почвах и в дорожной пыли из-за меньшей сорбционной способности последней. Во фракции  $PM_{10}$  почв накапливается As, аномалии которого в  $PM_{10}$  дорожной пыли и снега не обнаружены.

**Подсистема «речные воды – взвешенные наносы – донные отложения» р. Москвы.** Влияние городской территории на состав микрочастиц оценивалось на бассейновом уровне по данным наблюдений на 4-х станциях мониторинга на р. Москве в течение 2019 г. в период весеннего половодья (апрель) и летней межени (август). Всего отобрано 130 проб речной воды, взвеси и донных отложений. Их анализ показал, что поступление тонкодисперсных частиц, характерных для городских ландшафтов, определяет исключительную роль глинистой фракции  $PM_{10}$ , составляющую в среднем около 60% от объема переносимых взвесей при характерном значении для рек ЕТР 26% [10]. Основная масса (до 40%) взвешенного вещества связана с еще более тонкой фракцией  $PM_{1-5}$ . В половодье гранулометрический состав взвешенных наносов утяжеляется, доля фракции  $PM_{10}$  по сравнению с августом возрастает с 89 до 98%, что является характерным для урбанизированных территорий, тогда как в бассейнах рек с незначительной техногенной нагрузкой, как правило, наблюдается обратная картина.

Микрочастицы  $PM_{10}$  дают значимый вклад в валовое содержание элементов во взвеси и донных отложениях. Так, во фракции  $PM_{10}$  наносов р. Москвы в створе выше г. Москвы (д. Шишиморова) доминируют Pb, Cu, Fe, Cr и Cd, составляя от 50 до 95% общего содержания ММ во взвешенной форме. Однако для большинства элементов из техногенных источников, включая Pb, V, Zr, Ni, Cu, Be, средние концентрации во фракции  $PM_{10}$  оказались в 2,3 раза выше, чем в об-

щей пробе взвеси. Ниже г. Москвы доля микрочастиц в переносе V и Fe во взвеси р. Москвы достигает до 74% и 99% соответственно при 40% и 61% в верхнем створе. Доля  $PM_{10}$  в общем содержании Pb ниже г. Москвы, наоборот, снижается от 95 до 80% с одновременным ростом валового содержания элемента во взвеси, то есть обогащение происходит в основном за счет поступления более крупных частиц  $PM_{>10}$ .

В донных отложениях р. Москвы доля микрочастиц  $PM_{10}$  в общем содержании ММ не превысила 55-60%, что объясняется активной миграцией в составе взвеси более тонких фракций, тогда как крупные частицы осаждаются в донные отложения. Наиболее активно во фракции  $PM_{10}$  донных отложений накапливаются Bi, Cu, Ni, Pb и V. Свинец отмечался ранее как приоритетный загрязнитель столичных водоемов – его накопление выявлено в донных отложениях прудов восточной Москвы [2], источниками являются выбросы предприятий машиностроения, металлообработки и производства строительных материалов. Средняя концентрация ММ в тонких частицах донных осадков р. Москвы превышает содержание элементов в интегральных пробах в 2,5 раза, достигая максимума у Ni – в 5,3 раза.

В целом для фракции  $PM_{10}$  донных отложений и взвешенных наносов р. Москвы установлены сопоставимые уровни содержания ММ (рис. 3А). Наибольшие различия в концентрациях в  $PM_{10}$  донных отложений относительно взвешенных наносов обнаружены у As и Zn. На верхнем участке они преобладают в микрочастицах взвеси, а на нижнем участке их намного больше во фракции  $PM_{10}$  донных отложений (рис. 3А), так как в аквальных ландшафтах низовьев р. Москвы за счет более низких скоростей течения происходит аккумуляция поллютантов, поступающих со смывом почв и дорожной пыли [21, 28, 30]. Сходная тенденция выявлена у Mn, Mo, Bi, кото-

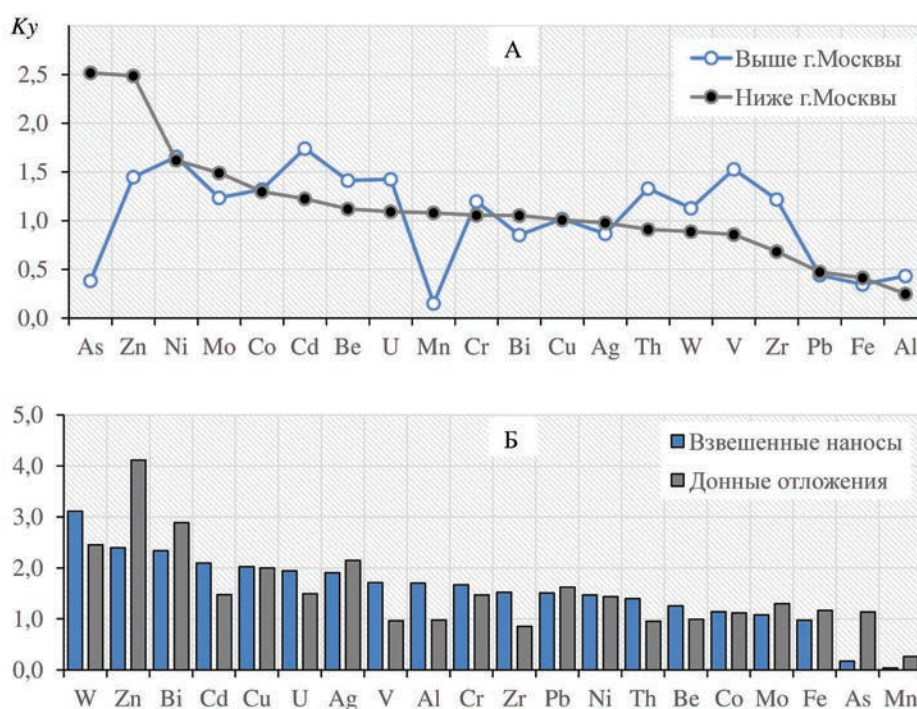


**Рис. 3.** Накопление ММ в донных отложениях ( $K_y$ ) относительно взвешенных наносов (А) и отношение концентраций ММ ниже и выше Московского мегаполиса в микрочастицах  $PM_{10}$  взвешенных наносов и донных отложений р. Москвы (Б)



рые так же могут поступать в аквальные ландшафты с загрязненными почвами и дорожной пылью и для которых установлены антропогенные источники в подсистеме «снег–дорожная пыль–почвы».

Миграция большинства поллютантов в речной системе р.Москвы ниже Московского мегаполиса происходит преимущественно в составе частиц  $PM_{10}$  взвешенных наносов. Концентрация Zn в донных осадках нижнего течения р.Москвы в  $PM_{10}$  увеличивается более чем в 4 раза, а концентраций Bi, W, Ag, Cu в 2,0–2,9 раза. В нижнем створе по сравнению с верхним во все фазы гидрологического режима концентрации W, Zn, Bi, Cd, Cu, U, Ag в  $PM_{10}$  увеличиваются в 1,9–3,1 раза (рис. 3Б). Zr, как правило, поступает в аквальные системы города вместе с дорожной пылью, куда он попадает при износе тормозных колодок и металлических частей автомобилей [6]. W, Cd, V и Bi, вероятнее всего, поступают в р. Москву в черте города со смывом дорожной пыли и почв, так как в этих компонентах выявлено активное накопление этих элементов в частицах  $PM_{10}$ . Другие техногенно обусловленные ММ более интенсивно аккумулируются в составе донных отложений по сравнению с взвешенной формой.

В донных отложениях ярко прослеживается накопление ММ из техногенных источников – ниже по течению Московского мегаполиса в р.Москве сильнее всего накапливаются  $Cd_{86}$   $Zn_{55}$   $Pb_{21}$   $Bi_{28}$   $Cu_{19}$   $As_{13}$  (нижние индексы – значения *EF*), для которых были также установлены высокие значения *EF* в дорожной пыли, пылевой составляющей снега и почвах (рис. 2). При этом во взвешенных наносах влияние городского загрязнения проявляется более слабо и ярко выражено только у  $Cd_{17}$  и  $Pb_{11}$ .

Таким образом, в подсистеме «вода–взвешенные наносы–донные отложения» микрочастицы  $PM_{10}$  играют ключевую роль в переносе многих ММ, особенно Pb, Cu, Ni, V. Водные объекты являются конечным звеном транспорта городских загрязнений, в связи с чем приоритетные поллютанты, обнаруженные в составе дорожной пыли и почв мегаполиса (например, W, Cd, Mo, Mn и Bi), накапливаются также в речной взвеси и донных отложениях. Это подтверждают результаты мониторинга р. Сетунь на локальном уровне [30].

\*\*\*

Мониторинг микрочастиц  $PM_{10}$  в Московском мегаполисе обеспечил покомпонентную оценку загрязнения и распределения поллютантов в системе

«атмосфера–снег–дорожная пыль–почвы–поверхностные воды». Исследование на базе Аэрозольного комплекса МГУ химического состава и свойств микрочастиц в атмосфере показало уровни аэрозольной нагрузки от ВС, водорастворимых ионов, минеральной пыли, ММ и ПАУ, а также эпизоды сильного загрязнения и его потенциальные источники при варьировании метеорологических условий в разные сезоны года. Изменение активности населения в периоды праздников отражается на полной массовой концентрации аэрозолей и компонентах их состава.

В подсистеме «аэрозоли–атмосферные осадки» вымывающая способность осадков по отношению к Pb, Sb, As, Ni, Mg, K, Al и S в аэрозолях в Москве в несколько раз выше, чем в других регионах мира из-за значительной поставки этих ММ из антропогенных источников, включая дальние, и выдувания частиц загрязненных почв и дорожной пыли. В дни после осадков концентрации практически всех ММ в аэрозолях значительно, до 60% снижались.

В подсистеме «снег–дорожная пыль–почвы» анализ распределения ММ в микрочастицах  $PM_{10}$  позволил уточнить источники ММ в теплый и холодный сезоны. Степень обогащения большинством ММ фракции  $PM_{10}$  уменьшается в ряду пылевая составляющая снега > дорожная пыль > почвы. В микрочастицах  $PM_{10}$  снега, дорожной пыли и почв одновременно накапливаются Sb, W, Bi, Sn, Cd, Cu, Pb, Mo и Zn, в снеге и дорожной пыли – Ni, V и Fe, а в подсистемах «снег–почвы» и «дорожная пыль–почвы» – Cr и Ca.

Изучение микрочастиц  $PM_{10}$  в подсистеме «вода–взвешенные наносы–донные отложения» показало, что под влиянием городской среды в зарегулированной речной системе содержание фракции  $PM_{10}$  и концентрации в ней ММ существенно возрастают в периоды повышенной водности, что не характерно для водотоков с низкой антропогенной нагрузкой. Воздействие Московского мегаполиса способствует значительному обогащению взвеси техногенными ММ, которые затем накапливаются в донных отложениях ниже по течению и могут ухудшать экологическое состояние водных экосистем.

Апробация разработанной технологии геохимического мониторинга в Московском мегаполисе показала, что она удовлетворяет современным мировым стандартам, позволяет достоверно оценить экологическую ситуацию и обосновать мероприятия по уменьшению загрязнения городских ландшафтов и создаваемого им риска здоровью населения.